MICROBEAM ANALYSIS
1991

D. G. Howitt

Editor

Proceedings of the 26th Annual Conference

of the

Microbeam Analysis Society

San Jose, Calif., 4-9 August 1991

PUBLISHER'S NOTICE

San Francisco Press, Inc., and the sponsoring society are not responsible for the information and views presented in this volume by the several contributors.

San Francisco Press is the publisher of the Proceedings of the MAS conferences, the AEM workshops, the EMSA conferences, and the XIIth International Congress for Electron Microscopy.

Permission to reprint portions of this volume in professional journals published by scientific or technical societies (with suitable acknowledgment) is automatically granted; for reprint rights given to book publishers, commercial journals, company publications, and other media, apply to the Society's secretary.

Participants at these meetings, MAS members, and EMSA members are entitled to a 20% discount from the list prices tabulated below, provided *prepayment is made personal check.* (Books ordered by organizations are sold at the full list price.) Add postage and handling of $2.50 for first book, $1 for each additonal book (foreign orders: $5 and $2); Californians add sales tax.

The following books are included in this offer.

AEM 1981, 1984—$30 each

AEM 1987—$50*

MAS 1975, 1976, 1977,** 1979, 1980. 1981, 1982—$25 each

MAS 1986, 1987, 1988, 1989—$50 each

MAS 1990, 1991—$65 each

EMSA 1983, 1985, 1986, 1987, 1988, 1989—$50 each

EMSA 1991—$72.50

XII ICEM (1990), 4 vols. (imaging, analytical, biological, materials), $65 each

Electron Microscopy Safety Handbook (Barber & Clayton, Eds.)—$15

Early History of the Electron Microscope (Marton; pref. Gabor)—$7.50

Electron Microscopy and Alzheimer's Disease (Metuzals, Ed.)—$10

Electricity and Medicine: History of Their Interaction (Rowbottom & Susskind)—$30

---

*Contains also MAS—1987 papers on surface effects.

**Proc. 8th ICXOM.

Send order to:
San Francisco Press, Inc., Box 6800, San Francisco, CA 94142-6800, USA

Preface

The 1991 Joint meeting in San Jose, Calif., marks the 25th Anniversary of the Microbeam Analysis Society. It has been both a pleasure and a privilege to organize this program for the Society. The breadth and size of the program are particularly gratifying in this Anniversary year and we look forward to an exciting week of scientific presentations.

I should like to extend my sincere appreciation to the people who chaired and organized the individual sessions; and to the members of the Local Arrangements Committee, who succeeded in producing a truly memorable Anniversary meeting. I should particularly like to thank Dr. Ernie Hall for his help in putting together the Joint program with the Electron Microscopy Society of America. The papers presented in the Joint sessions appear at the end of this volume, in the EMSA format in which most of them were submitted.

<div align="right">

DAVID G. HOWITT
University of California at Davis

</div>

TABLE OF CONTENTS*

*An author index begins on p 575.

---

*J designates sessions arranged jointly with the Electron Microscopy Society of America

J-3. ANALYTICAL ELECTRON MICROSCOPY (W. A. P. Nicholson, T. F. Kelly, P. S. Turner, V. P. Dravid, G. L'Espérance, A. J. Garratt-Reed)

J-4. EM APPLICATIONS IN ELECTRONICS (R. Sinclair, R. Anderson, J. Batstone, S. J. Rosner, I. Raaijmakers, H. Iwasaki, B. Tracy, A. G. Cullis)

J-5. HIGH-RESOLUTION SEM (D. C. Joy, M. T. Postek)

Officers of the Microbeam Analysis Society

MAS Executive Council

President: John. T. Armstrong, California Institute of Technology, Pasadena, Calif.
President Elect: David B. Williams, Lehigh University, Bethlehem, Pa.
Past President: Alton D. Romig Jr., Sandia National Laboratories, Albuquerque, N.M.
Treasurer: Harvey Freeman, Dow Corning Corp., Midland, Mich.
Secretary: John A. Small, National Institute of Standards and Technology, 222/A121,
        Gaithersburg, MD 20899, (301) 975-3945

Directors
Serge Cvikevich, IBM GTD, Hopewell Junction, N.Y.
John Friel, PGT, Princeton, N.J.
Jon McCarthy, NORAN, Middleton, Wis.
Ryna Marinenko, NIST, Gaithersburg, Md.
John R. Porter, Rockwell International Corp., Thousand Oaks, Calif.
Phillip E. Russell, North Carolina State University, Raleigh, N.C.

Honorary Members
L. S. Birks, Chapin, S.C., USA
A. A. Chodos, Monrovia, Calif., USA
Peter Duncumb, Great Shelford, Cambridge, Great Britain
T. A. Hall, Cambridge, Great Britain
K. F. J. Heinrich, National Institute of Standards and Technology, USA
James Hillier, Princeton, N.J., USA
R. E. Ogilvie, Massachusetts Institute of Technology, USA
Jean Philibert, Université de Paris Sud, Orsay, France
S. J. B. Reed, University of Cambridge, Great Britain
D. B. Wittry, University of Southern California, USA

Emeritus Members
G. W. Bailey, Baton Rouge, La., USA
Paul Lublin, Framingham, Mass., USA

1990 MAS Paper Awards

Birks Award: A. D. Romig Jr., S. J. Plimpton, J. R. Michael, R. L. Myklebust, and D. E. Newbury, *Application of parallel computing to the Monte Carlo scattering in solids: A rapid mmethod for profile deconvolution*

Macres Award: J. J. Donovan and M. L. Rivers, *PRSUPR: A PC-based automation and analysis software package for wavelength-dispersive electron-beam analysis*

Castaign Award: J. D. Pasteris, J. C. Seitz, Brigitte Wopenka, and I-Ming Chou, *Recent advances in the analysis and interpretation of C-O-H-N fluids by application of laser Raman microspectroscopy*

Cosslett Award: K. K. Soni, D. B. Williams, J. M. Chabala, R. Levi-Setti, and D. E. Newbury, *Imaging of Al-Li-Cu alloys with a scanning ion microprobe*

1991 MAS Presidential Awards

Presidential Science Award: Joseph I. Goldstein
Presidential Service Award: Thomas Huber
Special Service Award: Arthur A. Chodos
K. F. J. Heinrich Award for outstanding young MAS scientist: Alton D. Romig Jr.

SUSTAINING MEMBERS' INFORMATION

ADVANCED MICROBEAM SERVICES, INC.
4217C Kings-Graves Road
Vienna, Ohio 44473

Product Contact: Donald P. Lesher   (216) 394-1255

Product Line: Service of Electron Microprobes and accessories.

AMRAY, INC.
160 Middlesex Turnpike
Bedford, MA 01730

Product Contacts:
     Technical Data: Dr. Sheldon Moll   (617) 275-1400
     Delivery & Prices: Gerald Cameron, Jr   (617) 275-1400

Product Line: Manufacturer of scanning electron microscopes

Regional Sales Offices:

George Bruno	New England	(617) 275-8310
Ed Griffith	Mid-Atlantic North	(609) 662-3922
Tom Richards	Mid-Atlantic South	(609) 662-3922
Ken Lindberg	Southeast	(305) 767-4220
Rich Lantz	Southwest	(214) 247-3542
Gerry O'Loughlin	Northern California	(408) 748-1300
John Pong	Southern California	(714) 380-0289
Fred Feuerstein	Mid-West	(312) 695-6117
Matt Gohlke	Mid-East	(216) 579-0035

CAMECA INSTRUMENTS, INC.
2001 West Main Street
Stamford, CT 06902-4583

Product Contact: Thomas C. Fisher   (203) 348-5252

Product Line: Scanning electron microprobes and secondary ion mass spectrometers

CHARLES EVANS & ASSOCIATES
301 Chesapeake Drive
Redwood City, CA 94063

Product Contact: Donald H. Wayne   (415) 369-4567

Product Line: Specialists in materials characterization.

DAPPLE SYSTEMS
355 West Olive, Suite 100
Sunnyvale, CA 94086

Product Contact: Bill Stewart   (408) 733-3283

Product Line: Microcomputer-based analytical instrumentation including automatic image analysis and energy-dispersive x-ray microanalysis.

ELECTRON MICROSCOPY SCIENCES / DIATOME US
321 Morris Rd.
P.O Box 251
Fort Washington, PA 19034

Product Contact: Stacie Kirsch   (215) 646-1566   (800) 523-5874

Product Line: A complete line of the highest quality chemicals and supplies, as well as equipment for EM & LM in Biological and Materials Science. Also the Swiss Diamond Knife line.

Regional Sales Offices:

Midwest	Ed Immer	(800) 523-5874
Texas	Dick Rebert	"
East Coast	Matthew Irwin	"

ELECTROSCAN CORPORATION
66 Concord Street
Wilmington, MA 01887

Product Contacts: Mike Ruggiero (508) 988-0055

Product Line: Multi-environmental electron microscopes - operating up to 20 torr specimen chamber pressure. Secondary and backscattered high-resolution imaging is available throughout this pressure range (from 10 to minus 5 torr to 20 torr). Dynamic imaging provided by variable specimen chamber control and real-time (TV) imaging of any experiment irrespective of specimen's physical state.

Regional Sales Offices:

North East: Dick Harnman	(914) 268-9221
Middle Atlantic: Harry Freer	(703) 742-6216
California: John Treadgold	(213) 207-6478
South East: Al Pick	(214) 250-6663
New Jersey & New York: Roger Attle	(914) 368-3935

EMITECH USA, INC.
5206 F. M. 1960 West
Suite 100
Houston, Texas 77069

Product Contact: John Fitzpatrick	(713) 863-2067	(800) 444-3137
	FAX	(713) 893-8443

Product Line: TEM/SEM Sample Preparation Equipment

ENERGY BEAM SCIENCES
EBTEC Corporation
P.O. Box 468
11 Bowles Road
Agawam, MA 01001

Product Contact: Linda Standrowicz (413) 786-9322

Product Line: Electron microscope filaments (tungsten, LaB6 and prototype, apertures, scientillators, SEM mounts (aluminum, carbon) and mount storage, small instruments (sputter coaters, vibratome), complete range of EM supplies.

ETP-USA/ELECTRON DETECTORS INC.
1650 Holmes St. Building C
Livermore, CA 94550

Product Contaact:	Robert Ruscica	(415) 449-8534
	FAX	(415) 449-8996

Product Line: Robinson line of accessories for the Scanning Electron Microscope.

FEI COMPANY
19500 N. W. Gibbs Drive
Suite 100
Beaverton, OR 97006-6907

Product Contact: Doug Rathkey (503) 690-1512

Product Line: Emitters: LaB6 Vogel and Mini-Vogel Mounts, Cold-Field Emission, Schottky Emission and Liquid Metal Ion Sources. Ion and Electron Beam Columns: Single and two-lens, and Schottky Emission Components. Focused Ion Beam Milling Systems: Digital and Analog.

GATAN, INC.
6678 Owens Drive
Pleasanton, CA 94588-3334

Product Contact: CA Sheri Kurland   (415) 463-0200
                 PA Terry Donovan   (412) 776-5260

Product Line: Specialized accessories for transmission electron microscopy, TV imaging systems, parallel EELS analytical systems, side entry specimen holders for TEM, specimen preparation equipment for materials scientists, & specimen preparation & TEM analysis on a service basis.

Regional Sales Office:
Eastern Region: Terry Donovan, 780 Commonwealth Dr., Warrendale, PA 15086 (412) 776-5260

GW ELECTRONICS, INC.
6981 Peachtree Industrial Boulevard
Norcross, GA 30092

Product Contact: Larry Glassman   (404) 449-0707

Product Line: Electronic accessories for scanning electron microscopes and microprobes including Backscattered Electron Detectors, Specimen Current Amplifier, Signal Processor, Graphics Generator, and Microchannel Plate Detector.

HESSLER TECHNICAL SERVICES
44 Strawberry Hill Ave.
Suite 8G
Stamford, CT 06902

Product Contact: Robert Hessler   (203) 358-0266

Product Line: Sales and Marketing representative for High Technology products.

HNU X-RAY SYSTEMS, INC.
160 Charlemont St.
Newton Highlands, MA 02161

Product Contact: Therese Hipple   (617) 964-6690

Product Line: System 5000 Microanalysis and Imaging Instruments

INSTRUMENTS SA, INC.
6 Olsen Ave.
Edison, NJ 08820

Product Contact:
        Bruce D. Perrulli   (201) 494-8660
        Susan Maher   (201) 494-8660

Product Line: MOLE - Raman molecular microprobes, contact Bruce D. Perruli; Surface analysis microprobes, contact Susan Maher.

INTERNATIONAL SCIENTIFIC INSTRUMENTS, INC.
6940 Koll Center Parkway
Pleasanton, CA 94566

Product Contact: Dr. Robert Buchanan   (415) 462-2212
                 Mary Battle   (415) 462-2212

Product Line: Scanning electron microscopes and transmission electron microscopes.

JEOL USA, INC.
11 Dearborn Road
Peabody, MA 01960

Product Contacts: Charles Nielsen, Robert Santorelli   (508) 535-5900

Product Line: EPMA, Auger, SEM, TEM, NMR, Mass Specrometers.

Regional Sales Offices:
Thayer Brickman, Jack Francis, JEOL USA, Inc., 3500 Bayshore Road, Palo Alto, CA 94303   (415) 493-2600
Robert Steiner, JEOL USA, Inc., 9801 W. Higgins St. Suite 220, Rosemont, Il. 60018   (312) 825-7164
John Bonnici, JEOL USA, Inc., 23 Brunswick Woods Drive, East Brunswick, NJ. 08816   (201) 254-5600

KEVEX INSTRUMENTS, INC.
355 Shoreway Road
San Carlos, CA 94070-1308

Product Contacts:
    Technical Data: Tom Stark/Nancy Wolfe   (415) 591-3600
    Delivery & Prices: Helen J. Barker   (415) 591-3600

Product Line: Energy-dispersive x-ray spectrometers for materials analysis including instrumentation for EDS, WDS, EELS, and digital image processing.

Regional Sales Offices:
Frank Mannino, 9989 Windsor Way, San Ramon, CA 94583 (415) 828-2188, Home: (415) 828-1655
Rick Cumby, P.O. Box 850820, Mesqite, TX 75185-0820 (214) 226-0182, Ans. Serv.: (214) 699-1944 Home: (214) 240-4095
Dan Polakowski, 9918 Scots Circle, Crystal Lake, IL 60014 (815) 455-8448, Home: (815) 455-8444
Vic Balmer, 7600 Primavera Way, La Costa, CA 92009 (619) 436-2932, Home: (619) 944-1063
Joe Piersante, 16 Barberry Hill Dr., Gainesville, GA 30506 (404) 887-9965, Home: (404) 889-1363
Robert Fucci, 60-C Charles Dr., Manchester, CT 06040 (203) 646-6325, Home: (203) 645-6373
Rich Fiore, Rd. 3 Box 99, Harvey's Lake, PA 18618, (717) 639-2330, Home: (717) 639-2021
Karen McGranahan, 19635 Cottonwood Trail, Strongsville, OH 44136, (216) 238-8666 Home: (216) 572-3606
Barry Weavers, 7 Valley Forge Dr., North East, MD 21901 (301) 287-3955, Home: (301) 287-5285
Rod Palmberg, P.O. Box 200, Mercer Island, WA 98040 (206) 232-3444, Home: (206) 232-6097 FAX: (206) 232-8323
Karl L.R. Mahler, P.O. Box 505, Thornhill, Ontario, Canada L3T4A2, (416) 731-2161 Home: (416) 889-8907 FAX: (416) 731-2162
Kevex East Application Lab, 50 Valley Stream Parkway, Suite 180, Great Valley Corporate Center, Malvern PA 19355
      Office: (215) 647-4866 FAX: (215) 889-9050

R.J. LEE GROUP, INC.
350 Hochberg Road
Monroeville, PA 15146

Product Contact: Hank Beebe   (412) 325-1776
               FAX   (412) 733-1799

Product Line: Analytical services, consulting, contract research, materials characterization, TEM, SEM, PC-based microimaging.

Regional Sales Offices:
2424 6th. Street, Berkeley, CA 94710, (415)486-8319, FAX (415)486-0927
1036 Battleview Parkway, Manassas, VA 22110, (703)368-7800, FAX (703)368-7761

LEICA INSTRUMENTS, INC.
111 Deerlake Road
Deerfield, Ill 60015

Product Contact: Barry T. Gray   (708) 405-0123

Product Line: Scanning electron microscopes, Optical Microscopes, Cryo sample prep equipment.

Regional Sales Offices:
Dr. Joseph Keegan, 111 Deerlake Rd., Deerfield, Ill. 60015 (708) 405-8130

LINK ANALYTICAL INC.
Microscope Products
8017 Excelsior Drive
Madison, WI 53717

Product Contacts:
    Technical Data: Paul Mainwaring   (608) 836-3200
    Delivery & Prices: Donald Grimes   (608) 836-3200

Product Line: Advanced energy-dispersive x-ray microanalysis and imaging systems.

Regional Sales Offices:
Paul Smith, 9 Acton Road, Chelmsford, MA 01824 (508) 250-0855
Patrick Campos, 240 Twin Dolphin Dr, Suite D, Redwood City, CA 94065 (415) 595-5465
Gerald Dougherty, 1010 Huntcliff, Suite 1350, Atlanta, GA 30352 (404) 642-7666
Graham Bird, 5300 Hollister, Suite 230,, Houston, TX 77040 (713) 642-0200
Charles Lambright, 118 Hidden Tree Lane, Amherst, Ohio 44001 (216) 988-3124

MATERIALS ANALYTICAL SERVICES INC.
2418 Blue Ridge Road
Suite 105
Raleigh, NC 27607

Product Contacts: Donald S. Porterfield   (919) 881-7708
             John W. Bumgarner   (919) 881-7708
                       FAX   (919) 881-8227

Product Line: Fourier Transform Micro Infrared Spectrometer(FT-IR), Energy Dispersive X-ray Fluorescence (EDXRF), Scanning Electron Microscopy (SEM), Secondary Ion Mass Spectroscopy (SIMS), Auger Consultation, Scanning Tunneling Microscopy (STM), CG Pt/Ir STM Tips.

McCRONE ASSOCIATES, INC.
850 Pasquinelli Drive
Westmont, IL 60559

Product Contacts:
    Dr. John Gavrilovic   (708) 887-7100
    Dr. Timothy Vander Wood   (404) 368-9600

Product Line: Materials characterization, surface analysis, particle characterization and identification, forensic contamination, pharmaceuticals, dust, corrosion, semiconductors, wafers, electronics. Instruments available to apply: EMA, SIMS, ESCA, Auger, Raman, SEM, AEM, ultramicrotomy, class 100 cleanroom.

Regional Sales Offices:
McCrone Associates/Atlanta, Dr. Timothy Vander Wood, 1412 Oakbrook Drive, Norcross, GA 30093, (404) 368-9600

MICRON, INC.
3815 Lancaster Pike
Wilmington, DE 19805

Product Contact: James F. Ficca, Jr.   (302) 998-1184

Product Line: Analytical services including, Optical Microscopy (OM), Scanning Electron Microscopy (SEM/EDS), Transmission Electron Microscopy (TEM), Electron Probe X-Ray Microanalysis (EPA),

MICROSPEC CORPORATION
45950 Hotchkiss Street
Fremont, CA 94539

Product Contact: Joseph Carr   (415) 656-8820
                 FAX   (415) 656-8944
Product Line: WDX-3PC wavelength-dispersive x-ray spectrometer system for use on SEMs.

NISSEI SANGYO AMERICA, LTD.
HITACHI SCIENTIFIC INSTRUMENT DIVISION
460 E. Middlefield Road
Mountain View, CA 94043

Product Contact: Hideo Naito   (415) 961-0461

Product Line: Scanning electron microscopes, transmission electron microscopes, field emission.

Regional Sales Offices:
Nissei Sangyo America, Ltd., 2096 Gaither Rd., Rockville, MD 20850
Nissei Sangyo America, Ltd., 2850 E. Golf Rd., Suite 200, Rolling Meadows, IL 60008
Nissei Sangyo America, Ltd., 89 Galaxy Blvd., Suite 14, Rexdale, Ontario M9W 6A4, Canada

NORAN INSTRUMENTS INC.
2551 W. Beltline Hwy.
Middleton, WI 53562

Product Contacts:
 Technical Data: Joseph Mullen   (608) 831-6511
 Delivery & Prices: Dennis Masaki   (608) 831-6511

Product Line: Voyager Microanalysis System (new product), Series II Microanalysis System, I-2 Integrated Imaging System, TN-8502 Video Image Analysis System, and TSM Confocal Microscope.

OVONIC SYNTHETIC MATERIALS, INC.
1788 Northwood
Troy, MI 48084

Product Contact: Steven A. Flessa   (313) 362-1290
                 (800)366-1299   FAX (313)362-4043
Product Line: The OVONIX line of multilayer x-ray monochromators are replacing natural crystals and Langmuir-Blodgett psuedocrystals for improved light-element analysis in WD/XRF and EPMA spectrometers. Increased peak intensities and suppression of higher orders improves analysis of Al-B in XRF and of F-Be in EPMA.

OXFORD INSTRUMENTS NORTH AMERICA, INC.
130A Baker Ave.
Concord, MA 01742-2204

Product Contact: Glenn Kinnear   (508) 369-9933

Product Line: A range of accessories for scanning and transmission electron microscopes including: Cryopreparation and cryotransfer systems for SEM and TEM; Cooling (N2 and He), heating, tensile and X Y Z stages for SEM; Cathodoluminescence detection for SEM and TEM; Cooling, heating, and analytical holders for TEM; Rapid sample freezing equipment (SEM or TEM); Freeze replication/freeze etch equipment; Digital image processing.

Regional Sales Office:
Jeremy Sutton, Oxford Instruments North America, 1050F East Duane Avenue, Sunnyvale, CA 94086, (408) 732-3002

PERKIN-ELMER
6509 Flying Cloud Dr.
Eden Prairie, MN 55344

Product Contacts:
 Technical Data: Greg Carpenter   (612) 828-6100,
 Delivery & Prices: Customer Order Dept. (800) 328-7515   FAX: (612) 828-6322

Product Line: ESCA, Auger, SIMS and MBE instruments, vacuum products.

Regional Sales Offices:
Boston: 5 Medallion Center, Greeley St., Merrimack, NH 03054 (800)523-2310; in NH (603)424-6100, FAX: (603)424-0902
New York: 5 Progress St., Edison, NJ 08820 (201)561-6730, FAX: (201)561-0268
Wash. DC: 7310 Ritchie Hwy., Suite 520, Glen Burnie, MD 21061 (301)761-3053, FAX: (301)761-0479
Denver: 14818 W. 6th Avenue, PHI Suite, Golden, CO 80401 (303) 271-0040
San Jose: 2305 Bering Dr., San Jose, CA 95131 (408) 473-9000, FAX: (408) 434-0139

PHILIPS ELECTRONIC INSTRUMENTS
85 McKee Drive
Mahwah, N.J. 07430

Product Contact: Dr. M. N. Thompson   (201) 529-3800

Product Line: XL series Scanning Electron Microscopes, CM series Transmission Electron Microscopes, EDAX X-Ray Analysis Systems, and PHAX SCAN ultra fast microanalysis with SEM.

PRINCETON GAMMA-TECH
1200 State Rd.
Princeton, NJ 08540

Product Contacts:
       Technical Data: Doug Skinner   (609) 924-7310
       Delivery and Prices: Mark Smith   (609) 924-7310
              FAX   (609) 924-1729

Product Line: Princeton Gamma-Tech's product line consists of the PGT System 4+ microanalysis system with complete EDS x-ray analysis capabilities for SEM, TEM, and STEM. Also highlighted in our product line is PGT Imagecraft, digital image processing, enhancement, and quantitative image analysis for light microscopy as well as electron microscopy.

Regional Sales Offices:
Branch Officez: 568 Weddell Drive, Suite 1, Sunnyvale, CA 94089, (408)734-8124, FAX (408)734-8137
Western Region: Griot Group Inc., Los Altos, CA, (415)941-2533, FAX (415)941-2536
Southwest Region: Jake Brown, Euless, TX, (817)571-9075
Central West Region: Contemporary Science, Inc., Mount Prospect, IL, (312)255-3793
Central East Region: Tom Griffin, Rocky River, OH, (216)331-0120
Northeast Region: Scientific System Sales Corp, Jericho, NY, (516)822-4880, FAX (301)822-4887
Southeast Region: Robert Green, Atlanta, GA, (404)633-3904

SPECTRA-TECH, INC.
652 Glenbrook Road
P.O. Box 2190-G
Stamford, CT 06906

Product Contacts:
       Technical Data: John A. Reffner   (203) 357-7055
       Delivery & Prices: Faith Cornick   (201) 646-0421

Product Line: FT-IR microscopes and accessories

Regional Sales Offices:
Tom Driscoll, Spectra-Tech, 3 University Plaza, Hackensack, NJ   07601

SPI SUPPLIES
DIVISION OF STRUCTURE PROBE, INC.
P.O. Box 656
West Chester, PA 19381-0656

Product Contact:
       For SPI Supplies: Ms. Sue Morris (800) 2424-SPI, in PA (215) 436-5400, FAX (215) 436-5755
       For Structure Probe, Inc.: Ms Kim Royer   (Tel. and FAX as above)

Product Line: SPI Supplies: Complete line of sample preparation equipment, consumable supplies, standards and other accessory items for the microanalysis laboratory. Call for catalog. Structure Probe: Independent laboratory offering SEM, EDS, WDS, Auger, Metallurgical failure analysis a specialty. Accredited by American Association for Laboratory Accreditation.

Laboratories (Structure Probe, Inc.):
Ms. Kim Royer, 569 E. Gay St., West Chester, PA 19380   (215) 436-5400
Dr. A. Blackwood, 63 Unquowa Rd., Fairfield, CT 06430   (203) 254-0000
Mr. Ronald Bucari, 1015 Merrick Rd., Copiague, L.I., NY   (516) 789-0100

M.E. TAYLOR ENGINEERING, INC.
21604 Gentry Lane
Brookeville MD 20833

Product Contact: M.E. (Gene) Taylor   (301) 774-6246
                                    FAX   (301) 774-6711
Product Line: Scintillators, SEM supplies, secondary and backscatter electron detectors, vacuum foreline traps, specimen stubs, filaments and related items. Precision machine work and scientific glass blowing. Repair most EDS detectors.

VG INSTRUMENTS, INC.
32 Commerce Center
Cherry Hill Drive
Danvers, MA 01923

Product Contact: Bob Michael   (508) 777-8034

Product Line: UHV analytical instrumentation; those pertinent to MAS include high-resolution Auger, UHV dedicated STEM, imaging SIMS.

CARL ZEISS, INC.
One Zeiss Drive
Thornwood, NY 10594

Product Contact: Paul E. Henry   (914) 681-7741

Product Line: Transmission and scanning electron microscopes.

Presidential Symposium

Invited Speakers

    G. F. Bastin, Eindhoven University of Technology

    P. Duncumb, Cambridge, England

    C. E. Evans, Charles Evans & Associates

    C. E. Fiori, National Institute of Standards and Technology

    J. I. Goldstein, Lehigh University

    K. F. J. Heinrich, National Institute of Standards and Technology

    D. C. Joy, University of Tennessee

    A. LeFurgey, Duke University Medical Center

    R. Linton, University of North Carolina

    D. E. Newbury, National Institute of Standards and Technology

    P. E. Russell, North Carolina State University

    G. Shimizu, Osaka University

    D. R. Veblen, Johns Hopkins University

    R. Warner, Procter and Gamble Corp.

    O. C. Wells, IBM

    D. B. Williams, Lehigh University

CALCIUM REDISTRIBUTION FROM THE PERICELLULAR MATRIX DURING DEPOLARIZATION-INDUCED CONTRACTION OF CORONARY SMOOTH MUSCLE: RESULTS USING TWO ANALYTICAL ELECTRON MICROSCOPIC TECHNIQUES

E. S. Wheeler-Clark, G. B. Weiss, and L. M. Buja

The sarcoplasmic reticulum (SR) and extracellular space/matrix (ECS) are generally accepted as the two possible physiological sources of calcium (Ca^{2+}) for smooth muscle contraction.[1] In most vascular smooth muscle, the primary source of Ca^{2+} for agonist-induced contractions is the SR, which can provide sufficient Ca^{2+} even in the absence of extracellular Ca^{2+} influx.[2] In contrast, large, proximal coronary arteries appear to depend more on extracellular Ca^{2+} influx for contraction and are more sensitive to the vasodilatating effects of organic Ca entry blockers compared with arteries from other vascular beds.[3,4] Based on results from a previous study in rabbit renal arteries,[5] we hypothesized that Ca^{2+}-induced Ca^{2+} release from the SR could account for the apparent dependence of coronary artery contraction on extracellular Ca^{2+} influx. We tested this hypothesis by measuring Ca redistribution during depolarization-induced contraction of canine coronary arteries, using two complementary analytical electron microscopic (EM) techniques-- [45]Ca EM autoradiography and electron probe x-ray microanalysis (EPMA).

Methods

Canine coronary artery rings depolarized with solutions containing 80 mM K^+ (substituted for Na^+) and 0.75 mM Ca^{2+} developed greater than 1 g isometric tension; these contractions were inhibited virtually 100% by a 60min preincubation with 0.3 µM nitrendipine (N = 10). For [45]Ca EM autoradiography, similar coronary artery strips were incubated with [45]Ca prior for 60-65 min to freezing under four experimental conditions: (1) control, (2) 80 mM K^+-contracted (initiated 5 min before freezing), (3) nitrendipine (NTR) alone (60min exposure), and (4) NTR plus 80 mM K^+ (as in group 3, but high K^+ added 5 min before freezing). Phentolamine (5 µM) and propranolol (10 µM) were added to all muscle groups to prevent potential adrenergic stimulation by norepinephrine released from nerve terminals in the artery wall. Muscles in the control and both nitrendipine groups (conditions 1, 3, and 4) were relaxed, whereas muscles in group 2 were contracted by the high-K^+ solution immediately prior to freezing. Frozen muscles were freeze-dried, embedded, and analyzed using [45]Ca EM autoradiography procedures described previously.[5]

Although specimen preparation for [45]Ca EM autoradiography provides excellent visualiza-

tion of ultrastructural detail, this analytical EM technique is limited by relatively poor spatial resolution (550 nm) and associated difficulties in quantitation. Therefore, we also analyzed Ca redistribution from cell surface regions using EPMA of freeze-dried, unembedded sections of coronary arteries which had been frozen under either control of K^+-contracted conditions (no [45]Ca loading). Dextran (5 g/100 ml; 40 000 ave. MW; added to stabilize the extracellular matrix during EPMA), 1 mM Ca, and cobaltic EDTA (an extracellular marker) were present in both control and high-K^+ solutions for 30-45 min prior to freezing. Addition of dextran CoEDTA have nominal effects on osmotic pressure and no demonstrable effect on muscle function.[6]

Thin (150-200nm) frozen-hydrated sections of these muscles were transferred directly into a JEOL 1200 microscope, freeze-dried internally, and analyzed between -100 and -105 C. The electron source was a LaB_6 filament at 120kV acceleration voltage operated in the scanning transmission (STEM) mode. X-rays were collected and analyzed using a Tracor Northern (TN) detector and TN 5500 computer.

Results

In control and nitrendipine (± high K^+) muscle cells, relative [45]Ca activities determined by autoradiography were greater at the cell surface (about 7-fold) and in the SR (about 4-fold) than relative [45]Ca activities measured for the cytosol or ECS (Table 1). These data support the hypotheses that Ca is bound at the cell surface and sequestered by the SR in relaxed coronary muscle cells. However, the relative [45]Ca content of the SR in relaxed coronary artery muscle cells was between two and three times smaller than that previously measured for SR in rabbit renal artery smooth muscle cells.[5]

In response to high K^+-induced contraction, the [45]Ca activity of the cell surface was reduced 75% (p < 0.05) in K^+-contracted muscles (Table 1). Loss of [45]Ca occurred only from cell surface regions that contained no visible SR in close association with the cell membranes (cell surface region in Table 1) and was not observed in cell surface regions where the plasma membrane and SR closely approached one another (cell surface/SR region in Table 1). Preincubation with NTR completely inhibited the high K-induced translocation of cell surface associated [45]Ca. In contrast with previous results in rabbit renal artery, the [45]Ca activity of the SR remained the same or increased slightly (N.S.), indicating a lack of SR Ca release under these conditions in coro-

TABLE 1.--Relative ^{45}Ca activities (± S.E.) of individual sites in canine coronary arteries.

	Control	K-Contracted	Nitrendipine	Nitrendipine, K-Depolarized
Cell Surface	5.527+1.098	1.279+1.079*	6.435+1.111	6.485+1.505
SR	3.130+0.907	3.132+0.894	2.756+0.853	3.422+0.914
Cell Surface/SR	1.787+0.382	1.484+0.435	1.606+0.424	1.789+0.477
Cytosol	0.873+0.071	0.951+0.086	0.847+0.077	0.846+0.089
ECS	0.851+0.041	0.845+0.043	0.860+0.035	0.858+0.047

*Significantly different from relative ^{45}Ca activity of PM in control (p < 0.006), nitrendipene (p < 0.001), and nitrendipine, K^+-depolarized (p < 0.005) muscles; overall experimental data.

TABLE 2.--Elemental content (mean + S.E.M.) in mmoles/kg dry wt of cell surface-associated regions in canine coronary artery smooth muscle.

Region:	Expt'l Group (N):	Na[a]	K[a]	Co	Ca
A	Control (9)	960 + 108	162 + 27	50 + 6	19.3 + 2.4
	K-contracted (9)	348 + 60	1048 + 172	48 + 14	13.3 + 4.2*
B	Control (10)	635 + 64	452 + 68	28 + 5	13.7 + 2.0
	K-contracted (10)	276 + 34	874 + 69	28 + 3	14.6 + 1.7
C	Control (6)	60 + 17	719 + 24	0 + 2	3.1 + 1.9
	K-contracted (5)	56 + 13	929 + 47	4 + 2	0.0 + 1.6

[a]Decreased Na and increased K content in the high $[K]_o$-substituted solution are responsible for the decreased Na and increased K content of Regions A and B.
  *Significantly different from control values by the rank-sum test (p < 0.05).
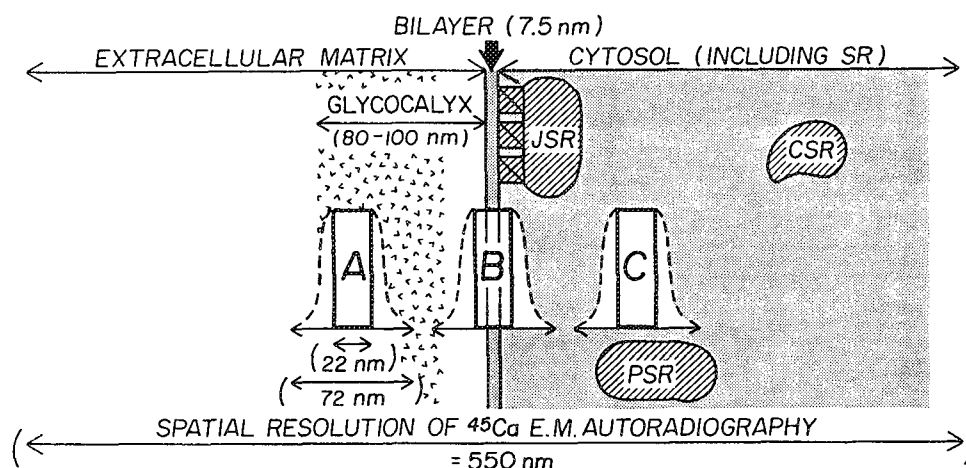
FIG. 1.--Cartoon illustrating difference in spatial resolution of ^{45}Ca EM autoradiography and EPMA with regard to underlying ultrastructure at smooth muscle cell surface. Rectangles A, B, and C indicate placement of visible rasters for EPMA: dashed lines indicate beam diameter and decrease in beam intensity with greater distance from edge of visible raster.

nary smooth muscle cells. These results suggested that substantial Ca may be translocated from cell-surface associated structures during depolarization-induced contraction of coronary arteries and that this Ca may be extracellular in origin.

EPMA data from three regions (A, B, and C) of the smooth muscle cell surface were obtained by rastering of the electron beam over the cell surface-associated regions in the manner depicted in Fig. 1. Table 2 compares the elemental content of these regions obtained by initial EPMA of control vs K$^+$-contracted smooth muscle cells. Table 2 shows that the mean Ca content of region A was reduced by about one third in the K$^+$-contracted muscle cells compared with control values, whereas the Ca contents of regions B and C were unchanged in response to high K$^+$. Moreover, six of the initial nine data obtained from region A of the K$^+$-contracted cells had values less than 10 (average of values < 10 = 5.8 mmoles/kg dry wt). In comparison, only one of nine values in the control group was less than 10 (= 9.6 mmoles Ca/kg dry wt). Because data from region A of K$^+$-contracted muscles were not normally distributed, they were compared with control values by the nonparametric, rank-sum test. The results suggest that the decreased Ca content of region A during high K$^+$-induced contraction is significant (p < 0.05), despite the inhomogeneous data obtained from this region. In contrast, there was little change in the ECS Ca content when analyses were made between 200 and 600 nm away from the cell surface (Ca content of nonpericellular ECS averaged 21.6 and 18.9 mmoles/kg dry wt for control and K$^+$-contracted muscles, respectively, N.S.).

Conclusions

Both the autoradiographic and EPMA results suggest that Ca mobilization from the extracellular matrix during Ca^{2+} channel activation and coronary smooth muscle contraction might be restricted to a narrow extracellular region closely associated with the membrane bilayer (i.e., pericellular matrix). Micrographs obtained from tannic acid-stained coronary artery smooth muscle indicate the glycocalyx normally extends between 70 and 100 nm out from the membrane bilayer (not shown). Therefore, the total Ca content of region A measured by EPMA is expected to include Ca bound to the outer portions of the glycocalyx, as well as free Ca^{2+} in the extracellular fluid. Comparison of Ca:Co (or Ca:Na) ratios in region A of control muscles vs Ca:Co (or Ca:Na) ratios in solution indicate that 50% or more of the Ca in region A of relaxed muscles might be bound. Thus, the apparent restriction of extracellular Ca^{2+} movements to the pericellular region might be due to passive, diffusion-limiting properties of the glycocalyx and/or local Ca^{2+} buffering by low-affinity, extracellular binding sites during Ca^{2+} channel activation.

In summary, both the autoradiographic and initial EPMA data support the hypothesis that substantial Ca^{2+} is mobilized from the pericellular matrix during depolarization-induced contraction of coronary arteries. Our original hypothesis--that Ca^{2+}-induced Ca^{2+} release from the SR can account for the apparent dependence of coronary artery contraction on extracellular Ca^{2+} influx--is not supported by the data. Based on the average diameter of coronary artery smooth muscle cells (2.0-2.5 μm) and the average Ca loss from region A (from EPMA data), we estimate that the amount of Ca^{2+} transported from the pericellular matrix could contribute as much as 50-100 μmoles total Ca/kg wet wt of cytosol. This amount of Ca is probably sufficient to cause maximal contraction even in the absence of SR Ca^{2+} release.

References

1. A. P. Somlyo, "Excitation-contraction coupling and the ultrastructure of smooth muscle," *Circ. Res.* 57: 497, 1985.
2. M. Bond et al., "Release and recycling of calcium by the sarcoplasmic reticulum in guinea-pig portal vein smooth muscle," *J. Physiol.* (London) 355: 677, 1984.
3. C. van Breemen and B. Siegel, "The mechanism of alpha-adrenergic activation of the dog coronary artery," *Circ. Res.* 46: 426, 1980.
4. S. Flaim, "Comparative pharmacology of calcium blockers based on studies of vascular smooth muscle," in S. F. Flaim and R. Zelis, Eds., *Calcium Blocker: Mechanisms of Action and Clinical Applications*, Baltimore: Urban and Schwarzenberg, 1982, 155.
5. E. Wheeler-Clark et al., "Cellular redistribution of ^{45}Ca in rabbit renal artery determined by electron microscopic autoradiography: Changes in response to K$^+$-induced depolarization and nitrendipine," *J. Pharmacol. Exp. Ther.* 239: 286, 1986.
6. J. Tormey and E. Wheeler-Clark, "Spatial resolution in electron probe analyses of sarcolemma and sarcoplasmic reticulum of cardiac muscle," *Proc. N. Y. Acad. Sci.* 483: 260, 1986.

CHANGES IN THE VACUOLAR CONCENTRATION OF CALCIUM IN TOBACCO LEAF TISSUE DURING GROWTH AND DEVELOPMENT AS MEASURED BY LOW-TEMPERATURE X-RAY MICROANALYSIS

Patrick Echlin

Nearly all plant and animal cells maintain very low levels of free Ca^{2+}. Temporary increases in cytoplasmic Ca^{2+} play a pivotal role in the regulation of a wide variety of metabolic and developmental process.[1] To maintain the necessary low concentrations of Ca^{2+} in the cytoplasm, excess calcium ions must be excluded from entering the cell, excreted from the cell, or sequestered as an insoluble salt within the cell. The roots of most plants have little or no control over the uptake of Ca^{2+} from the soil solution[2] and the cation is carried to all parts of the plant in the transpiration stream. Elimination of surplus Ca^{2+} is a major functional problem for plants. Although the plant cell membrane can actively pump Ca^{2+} into the apoplast, there are very few examples of specialized glands cells that excrete calcium salts in the same way many halophytes can excrete sodium chloride.[3] In many species the problem of excess calcium is solved by synthesizing oxalic acid, which in its anionic form precipitates the excess Ca^{2} as insoluble crystals of calcium oxalate.

Calcium oxalate crystals are found frequently either in specialized cells called idioblasts or in the vacuoles of cells in a wide range of plant species and tissue types. The calcium oxalates occur as mono- and trihydrate salts in many crystalline forms, and are usually clearly seen in the light microscope as highly refractile bodies that may fill the whole lumen of the cell in some cases.

There is very little information regarding the rate of calcium oxalate deposition in living plants. The studies of Kausch and Horner[4] and Borchert[5] indicate that the crystals are deposited over a period of several days; the more recent study by Xingxiang and Franceschi[6] indicates that the process may be much faster and, in the water plant *Lemma*, may be complete within 30 min.

The process of calcium oxalate crystal formation has been followed by direct observation of the appearance and growth of the crystals[4,5] or by the use of cytochemical methods[4,6] to follow the increased activity of enzymes such as glycolate oxidase and catalase which are directly involved in the principal pathway for oxalate formation.[7,8]

An alternative (and we suggest a more sensitive) procedure, would be to follow the changes

Patrick Echlin is at the Department of Botany, University of Cambridge, Cambridge, England, CB2 3EA. The experimental work associated with this study was carried out while the author was a visiting scientist at the Philip Morris Research Center, Richmond, Va.

in vacuolar calcium concentration as measured by x-ray microanalysis as this is the principal cation involved in the precipitation of oxalate in plant cells. This method has the advantage that it can detect the small (ca 1 mol m^{-3}) concentration of calcium shown[5] to be involved in calcium oxalate precipitation, but is insensitive to the very low cytosolic concentrations of a few hundred µmol m^{-3} of calcium, which are important in signaling processes in cells.

Quantitative x-ray microanalysis has been carried out on frozen, fully hydrated fracture faces of upper and lower epidermis, palisade, and spongy mesophyll cells in leaf tissue of tobacco plants at various stages of growth. The studies show that there is a gradual increase in the concentration of calcium in all cell types as the leaf ages; the highest concentration and greatest changes is found in the principal photosynthetic tissue of the leaf.

Methods

Plants of *Nicotiana tabacum* L. cv Coker 319 were grown under natural light conditions in a greenhouse at the Philip Morris Research Center in Richmond, Va., from April to September. Leaves were picked at five stages of growth from the midstalk position throughout the growing season. Strips, 1 × 3 mm, were cut from the leaf tissue in the inter-vein region and placed in small holes in a graphite specimen holder that had been previously partially filled with a buffered graphite suspension. The samples were quench frozen in turbulent liquid nitrogen within less than 1 min of being excised from the tissue.

The frozen samples were transferred under liquid nitrogen to the pre-cooled cold stage of the AMRAY Biochamber, where they were fractured at low temperatures (ca 100 K) and high vacuum (ca 5 µPa), and coated with a thin layer of evaporated chromium. The coated, frozen, hydrated fracture faces were transferred to the pre-cooled cold stage of an AMRAY 1600 scanning electron microscope, where they were examined in the fully frozen hydrated state at 110 K. A reduced raster approximately 3 × 3 µm was placed at the center of each fractured cell face to insure that only the vacuolar calcium was measured. Repeated analyses were carried out on upper and lower epidermal cells, spongy mesophyll, and palisade cells. No analyses were made of stomata or fascular tissue. Quantitative x-ray microanalysis was carried out with the peak-to-local background program available on a Link Systems 860 Series II en-

ergy-dispersive x-ray analyzer by procedures reported earlier.[9,10]

Results

Measurements of calcium concentration were made on 20 different leaves at each of the five stages of growth (10, 13, 16, 20, and 22 weeks from the time the seeds were sown). Three to four measurements were made on each of the four cell types of the leaf (Fig. 1). No analyses were made on cells in which calcium oxalate crystals were visible at a magnification of 100× (Fig. 2). A total of 46 plants from 15 different sets of plants were analyzed. Data from replicates of cell types within the same leaf were averaged to reduce the cell-to-cell variation. The results of the analyses are shown in Table 1.

TABLE 1.--Local concentration of calcium in the vacuoles of the four different cell types of tobacco leaves as a function of leaf age.

	Upper Epidermis	Palisade Cells	Spongy Mesophyll	Lower Epidermis
10 weeks (n = 65)	5 (± 0 25)	16 (± 0 8)	10 (± 0 5)	3 (± 0 09)
13 weeks (n = 67)	11 (± 0 56)	19 (± 0.93)	10 (± 0 51)	5 (± 0 27)
16 weeks (n = 64)	8 (± 0 38)	18 (± 0 9)	14 (± 0 65)	11 (± 0 55)
20 weeks (n = 62)	13 (± 0 7)	28 (± 1 8)	11 (± 0 56)	12 (± 0 6)
22 weeks (n = 64)	9 (± 0 44)	38 (± 1.9)	11 (± 0 53)	12 (± 0.59)

Values expressed as mol m^{-3} fresh weight rounded up to the nearest whole number (± SEM).

The calcium levels in the upper and lower epidermis show little significant variation as growth progresses, although there is considerable variation in the actual concentration at any given growth stage. The mean values for calcium for all growth stages are 9.2 mol m^{-3} for the upper epidermis and 8.6 mol m^{-3} for the lower epidermis. The low values recorded at the earliest growth stage (10 weeks) are of interest because the leaves are not fully expanded and photosynthesis would not be functioning at a maximum level. The level of calcium in the spongy mesophyll remains remarkably constant during all phases of growth. The most significant changes are seen in the palisade cells, the principal photosynthetic tissue of the leaf. The levels are higher than in the other tissues and show a progressive increase as the leaf matures and ages. During the first 10-16 weeks, during which the photosynthetic activity of the leaf reaches a peak, the levels of calcium remain fairly constant. As the leaves grow older the calcium level in the palisade cells nearly doubles.

Coefficients of correlation have been calculated between calcium and other elements (P, K, S and Mg) that were measured at the same time. Although there were positive correlations between some of these elements (e.g., P and K, and K and Mg), there was no positive correlation between any of these elements and Ca except for Ca and S at the later stages of growth.

Discussion

The variations in calcium concentration are considered to be associated primarily with oxalic-acid accumulation in the vacuoles, which in the early stages of growth are related to photorespiration, osmoregulation, and maintenance of pH, and in the later stages to the general phenomenon of senescence. The lower levels of calcium in the 10-week-old leaves are to be expected because cell-wall deposition and expansion is not complete and photosynthesis has not reached the maximum level. However, the higher levels in the photosynthetic tissue and in particular in the palisade cells are most certainly related to the formation of oxalic acid. In a comprehensive study of organic acid metabolisum in tobacco it has been shown that there is a slightly increased amount of oxalic acid at the early stages of growth.[11] Oxalate is generally considered to be an end product of metabolism[12] and it is unlikely that any calcium present in calcium-oxalate crystals would be returned to active metabolic processes. In some tobacco varieties, the high amounts of oxalic acid act as very effective "sinks" and may absorb so much of the calcium in the plant that they begin to exhibit calcium-deficiency symptoms. In the juvenile leaves of this present study, one might have expected that any oxalate would have been bound to the more abundant potassium ion rather than calcium, as the latter cation is present only in low concentration and is most certainly associated with the developing tobacco walls. However, potassium oxalate is much more soluble than the calcium salt and would not have the effect of sequestering the oxalate in a virtually insoluble form.

As the tobacco leaf expands and matures, there is a substantial increase in photosynthetic activity. By 13-16 weeks the calcium level is nearly doubled in the whole tissue, with a slightly greater increase in the photosynthetic tissue. This increase is considered to be related to two events going on in the leaves at this stage of growth. It has been shown that plants growing on nitrate as a nitrogen source produce an excess of hydroxyl ions, which cause the pH of the sap to rise.[13] Plants respond to this pH change by producing organic acids such as oxalate, which would neutralize the rise in pH. Soluble organic-acid salts such as potassium malate or oxalate would upset the ionic balance, but precipitation of oxalate as the insoluble calcium salt would restore the ionic balance. In differentiated cells this oxalate would be stored in the vacuole.

An additional source of oxalic acid would be
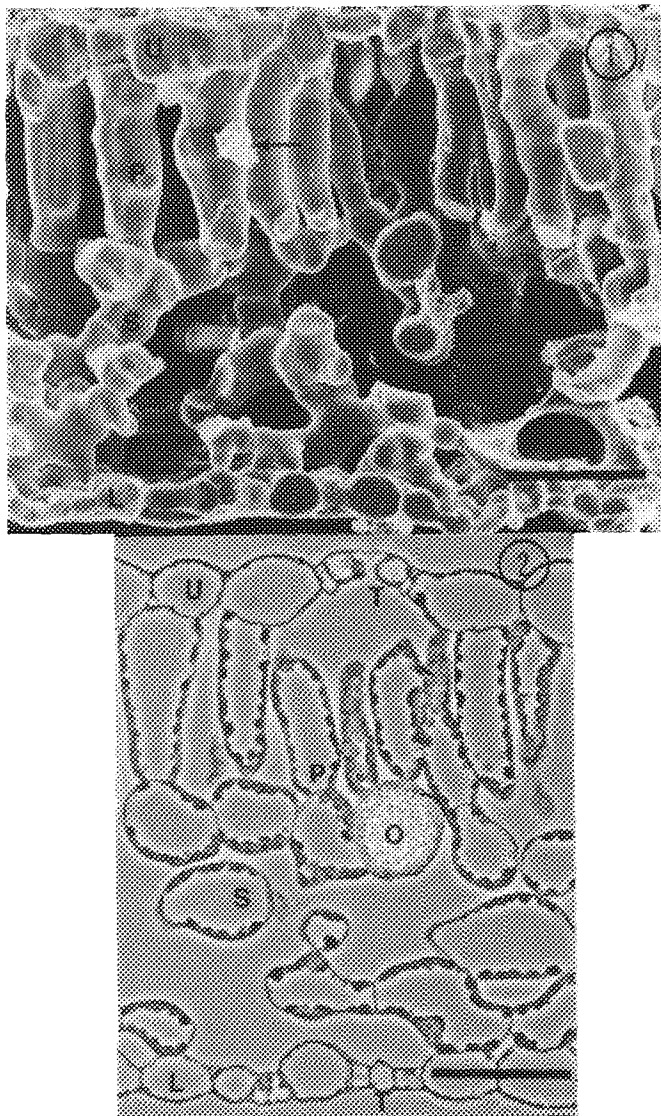
FIG. 1.--Scanning electron micrograph of frozen hydrated fracture face of mature tobacco leaf coated with ca 8 nm of evaporated chromium. This type of fracture face was used in analytical investigations. Arrow points to ice fragment broken off during fracturing process. U, upper epidermis; P, palisade cells; S spongy mesophyll; L, lower epidermis. Bar marker, 50 μm.

FIG. 2.--Light micrograph of thin section of mature tobacco leaf cut from resin-embedded material. Calcium oxalate crystals (O) can be seen filling vacuoles of cell at palisade (P)/ spongy mesophyll (S) interface. It is not possible to see calcium oxalate crystals in any of the other cells, even though measured calcium concentration is quite high. Such cells would not be included in the x-ray microanalytical studies described in this paper. U, upper epidermis; L, lower epidermis; T, stomata. Bar marker, 50 μm.

photorespiration. Tobacco is a C_3 plant, and it is known that in high light there is an increased production of oxalic acid. The glyco-

late and glyoxylate produced as a result of photorespiration (a feature of C_3 photosynthesis at high light levels) are oxidized to oxalate by glyoxylate oxidase which is known to be present in high amounts in tobacco plants.[14] The oxalate would be precipitated as the calcium salt to avoid upsetting the ionic balance. In this study on tobacco, where the plants were grown at high light levels (and at high nitrate levels), it is the palisade cells, the principal photosynthetic tissue, that have the highest amounts of calcium.

These higher levels of calcium are maintained during the later stages of growth, but not due to nitrate assimilation or photorespiration. It is well known that calcium is phloem immobile and that once it has accumulated in the leaf it shows very little movement out of the leaf into younger tissue. This factor would favor the maintenance of higher levels of calcium in older leaves, and there is some evidence that these higher levels may well presage and even stimulate the process of leaf senescence.[15] The presence of oxalic acid and inorganic phosphate and sulfate would tend to sequester calcium from the cytosol and reduce the cytosolic level to the point where membranes lose their functionality, which results in a leakage of cellular components and a disorganization of metabolic processes. The continued and progressive growth of calcium-oxalate crystals would also sequester calcium from the remaining pectic middle lamella of cell walls, which in turn would be progressively weakened. Many of the symptoms and processes of senescence can be reversed by addition of soluble calcium salts to the tissues concerned.[15] Although the calcium levels appear higher in the photosynthetic tissues, this increased level is due primarily to the substantially higher levels in the palisade cells. The calcium levels in this tissue show spectacular increases during the later phases of growth, which can be related to the finding that most of the calcium-oxalate crystals are found associated with this cell type.

This study reveals that low-temperature x-ray microanalysis is an effective way of measuring the in situ local concentration of calcium in cells. Because of the strong affinity of this element for the oxalate union, it is suggested that x-ray microanalysis is a sensitive way of measuring the potential sites of calcium oxalate crystal deposition in cells. It has been shown that there is a build-up of calcium (and hence, it is believed, oxalate) in the principal photosynthetic tissue of the tobacco leaf at a very early stage of growth, well before any calcium oxalate crystals can be detected by their morphological appearance.

References

1. P. K. Hepler and R. D. Wayne, "Calcium and plant development," *Ann. Rev. Plant Physiol.* 36: 397-439, 1985.

2. D. T. Clarkson, "Calcium transport be-

tween tissues and its distribution in the plant," *Plant Cell Env.* 7: 449-456, 1984.

3. A. Fahn, *Plant Anatomy*, 4th ed., Oxford: Pergamon Press, 1990.

4. A. P. Kausch and H. T. Morner, "Differentiation of raphide crystal idioblasts in isolated root cultures of *Yucca torreyi* (Agavaceae)," *Can. J. Bot.* 62: 1474-1484, 1984.

5. R. Borchert, "Calcium induced patterns of calcium-oxalate crystals in isolated leaflets of *Gleditsia triacanthos* L. and *Albizia julibrissen* Durazz," *Planta* 165: 301-310, 1985.

6. L. Xingxiang and V. R. Franceschi, "Distribution of peroxisomes and glycolate metabolism in relation to calcium oxalate formation in *Lemma minor* L." *Eur. J. Cell Biol.* 51: 9-16, 1990.

7. S. N. Seal and S. P. Sen, "The photosynthetic production of oxalic acid in *Oxalis corniculata*," *Plant Cell Physiol.* 11: 119-128, 1970.

8. K. E. Richardson and N. E. Tolbert, "Oxidation of glycolic oxalic acid by glycolic acid oxidase," *J. Biol. Chem.* 236: 128, 1961.

9. P. Echlin and S. E. Taylor, "The preparation and x-ray microanalysis of bulk frozen hydrated vacuolate plant tissue," *J. Micros.* 121: 329-348, 1986.

10. P. Echlin, "Changes in the cellular concentration of elements in tobacco leaf tissue during growth and senescence," *Beiträge zur Tabakforschung* 14: 297-312, 1989.

11. M. B. Vickery, "Chemical investigations of the tobacco plant: XI. Composition of the green leaf in relation to position on the stalk," *Conn. Agric. Exp. Stn. Bull.* (New Haven) 640: 221-236, 1976.

12. V. R. Franceschi and H. T. Horner, "Calcium oxalate in plants," *Bot. Rev.* 46: 161-421, 1980.

13. J. A. Raven and F. A. Smith, "Nitrogen assimilation and transport in vascular land plants in relation to intracellular pH regulation," *New Phytol.* 76: 415-431, 1976.

14. G. J. Kelly, E. Latzko, and M. Gibbs, "Regulatory aspects of photosynthetic carbon metabolism," *Ann. Rev. Plant Physiol.* 27: 181-205, 1976.

15. I. B. Ferguson, "Calcium in plant senescence and ripening," *Plant Cell and Environ.* 7: 477-489, 1984.

VISUALIZATION OF ULTRASTRUCTURE IN FREEZE-DRIED SECTIONS OF CORONARY SMOOTH MUSCLE

J. A. Maloney and E. S. Wheeler-Clark

The sarcoplasmic reticulum (SR) and extracellular space (ECS) are generally accepted as the two possible sources of Ca for smooth muscle contraction. However, few investigators have used electron-probe x-ray microanalyses (EPMA) to investigate Ca redistribution from the SR and ECS during smooth muscle contraction.[1,2] One limitation of SR analyses has been the inability to visualize SR directly in freeze-dried cryosections of smooth muscle. Most analyses of this structure have relied on separation of data obtained from the cytosol on the basis of high Ca content or P:K ratios (spectra) indications of SR inclusion) and theoretical modeling of %SR vs cytosolic volume in random analyses of nonmitochondrial cytosol.[2] Visualization of SR could be expected to improve the reliability of SR analyses and the accuracy of quantitation of the elemental content of this structure by reducing the number of assumptions inherent in such data acquisition.

Both freezing quality and section compression can limit the visualization of ultrastructural details such as the SR. Using improved freezing and sectioning procedures, we have recently visualized ultrastructure resembling the SR and lamina densa of the glycocalyx in freeze-dried sections of smooth muscle.

Methods

Large proximal coronary arteries were isolated from dogs that had been anesthetized with pentobarbital (30 mg/kg, i.v.). After dissection to remove adhering fat and cardiac muscle, coronary artery smooth muscle strips were suspended in a muscle bath containing warmed (34 C), oxygenated physiological salt solution. This solution contained 154 mM NaCl, 5.4 mM KCl, 6.0 mM TRIS, 11.0 mM dextrose and 1 mM $CaCl_2$ (pH 7.4 at 34 C). After a 2h equilibration, isometric force development in response to a high [K] solution (80 mM KCl substituted for NaCl) or 10^{-4} M phenylephrine (PE) was measured by a Grass FT.03 force transducer attached to one end of the coronary artery smooth muscle strip. After establishing that similar, repetitive force development could be achieved in response to various smooth muscle agonists, the muscle strips were ultrarapidly frozen in either the control (relaxed) or K^+-contracted state (ca 2min exposure to high [K] solutions) by clamping of the muscle strip between a pair of highly polished liquid N_2-cooled copper bars. All muscles were exposed to physiological solu-

tions containing similar amounts of $CaCl_2$ (1 mM), dextran (Sigma, 80 000 ave MW, 5 g/100 ml) and K[CoEDTA] (5 mM) for 30-45 min prior to freezing to facilitate comparison of EPMA analyses between different muscles.

Ultrathin (150-200nm), frozen-hydrated cross sections were obtained from these muscles by means of a Reichert-Jung Ultracut E ultramicrotome with a FC 4D cryo-attachment unit. Sections were cut with glass knives with an approximately 45° cutting edge (with a 5° clearance angle) and sectioning speed of 0.6-1.0 mm/s. The muscle block and knife were maintained at -120 C and the chamber (gas phase) at approximately -150 C throughout the sectioning process. Correct positioning of an ionizer (Diatome) within the cryochamber during sectioning appeared to reduce section compression substantially, possibly by inhibiting section sticking to the knife edge. Sections with vertical and horizontal dimensions similar to the block face and exhibiting uniform interference color were collected and sandwiched between carbon-coated Formvar films on folding copper grids.

The frozen hydrated sections were then transferred directly into a JEOL 2000× microscope with a cryotransfer stage (Gatan) and freeze-dried internally at temperatures between -120 and -80 C. Sections were analyzed at -100 C in the scanning transmission (STEM) mode at 120 kV acceleration voltage by rastering of the beam within selected visible regions (e.g., cytoplasm, cell edge, and putative SR, and lamina densa) of the sections. X rays were collected with a horizontal energy dispersive x-ray detector (Link Analytical) and analyzed by Tracor Northern computers (TN 2000 and TN 5500).

Results

Figures 1 and 2 demonstrate the high-quality ultrastructural preservation that could be obtained by use of the freezing and sectioning procedures described above. In well-oriented cross sections of smooth muscle cells, we frequently observed a "continuous filament"[3] approximately 70-100 nm external to (and running parallel with) the cell edge/plasma membrane (Fig. 2). Initial analysis of this filament indicated that it is an extracellular structure with high Na and Cl and low P content. The appearance of this structure is similar in density and position to the lamina densa of the glycocalyx as visualized in freeze-dried, embedded, and stained sections of smooth muscle cells.[3] Analyses of the visible cell edge immediately subadjacent to this filament yielded x-ray spectra with Na, Cl, and K content that were intermediate with cytosolic and
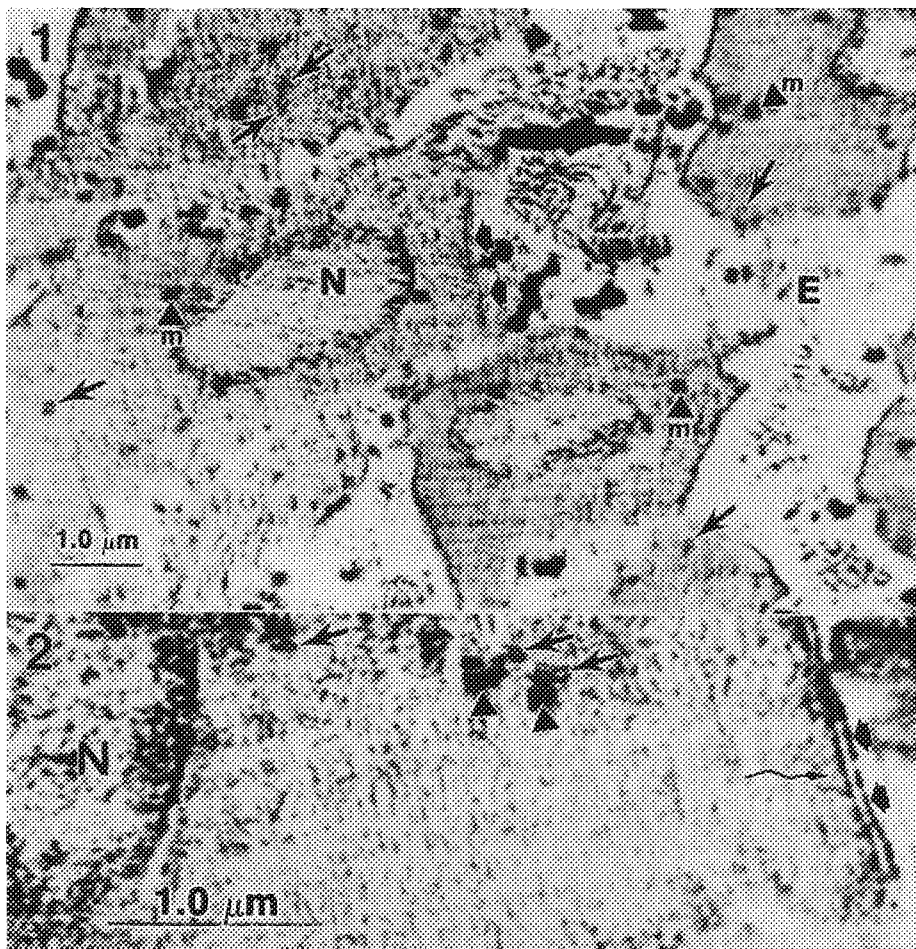
FIG. 1.--STEM micrograph of freeze-dried, unembedded cross section of large, proximal coronary arteries, showing smooth muscle cells surrounded by extracellular matrix (E). Inside cells, structures resembling SR (long, narrow arrows) can be visually distinguished from mitochondria (m, arrowheads) and nuclei (N). At right edge of central cell, filamentous structure resembling lamina densa of glycocalyx (broad, short arrows) runs parallel to cell edge/plasma membrane. FIG. 2.--Larger magnification STEM micrograph of another coronary artery smooth muscle cell, showing putative SR (narrow, long arrows), neighboring mitachondria (arrowheads), nucleus (N), and putative lamina densa (broad, short arrows). Small, wavy arrow points to possible surface vesicle budding from cell membrane at right.

extracellular analyses, but with higher P content than on either side (as expected if the raster is centered over the phospholipid-rich membrane bilayer). Occasionally, membrane-like structures resembling surface vesicles could also be observed in association with the cell edge/plasma membrane (Fig. 2).

Figures 1 and 2 also show examples of small structures that resemble SR as visualized in more conventionally fixed, embedded, and stained sections of smooth muscle. The appearance of the putative SR--i.e., a dense, membrane-like perimeter surrounding a more electron-lucent lumen--is distinct from that of mitochondria (which are larger in size and consistently dense) and putative surface vesicles (which have less inherent contrast and are more regular in shape). Our initial analyses of putative SR indicated high P content, high P:K ratios, and increased Ca content compared to analyses of adjacent cytosol.

Conclusions

With improved freezing quality and reduced section compression, we can visualize structures that resemble SR and the lamina densa of the glycocalyx in freeze-dried sections of coronary smooth muscle. Confirmation of our initial identifications of these structures will be sought by comparison of EPMA analyses of

these structures in relaxed vs high K^+- or phenylephrine-contracted smooth muscle strips. Routine visualization of the SR in smooth muscle could dramatically improve the reliability and accuracy with which elemental analyses of this structure can be obtained by EPMA. Analyses of changes in Ca content in the pericellular matrix during high K^+-contraction[4] also could be improved by visualization of specific components of the glycocalyx.

References

1. M. Bond et al., "Release and recycling of calcium by the sarcoplasmic reticulum in guinea-pig portal vein smooth muscle," J. Physiol. (London) 355: 677, 1984.

2. D. Kowarski, H. Shuman, A. P. Somlyo, and A. V. Somlyo, "Calcium release by noradrenaline from central sarcoplasmic reticulum in rabbit main pulmonary artery smooth muscle," J. Physiol. 366: 153-175, 1985.

3. M. Richardson, L. J. McGuffee, and M. W. C. Hatton, "Proteoglycan in fast-frozen, freeze-dried, plastic-embedded rabbit arteries," J. Ultrastructure Mol. Structure Res. 98: 199-211, 1988.

4. E. Wheeler-Clark et al., "Calcium redistribution from the pericellular matrix during depolarization-induced contraction of coronary smooth muscle: Results using two analytical electron microscopic techniques," this volume.

QUANTITATIVE MAPPING OF SKELETAL MUSCLE FIBERS BY X-RAY MICROANALYSIS: EFFECT OF LONG-TIME STORAGE OF FREEZE-DRIED CRYOSECTIONS

T. High, R. Nassar, I. Taylor, B. Scherer, P. Ingram, and J. R. Sommer

Electron probe x-ray microanalysis (EPXMA) is uniquely capable of performing quantitative topochemical analyses with high spatial resolution of elemental concentrations in cryosections from quick-frozen biological material. EPXMA requires very expensive instrumentation and maintenance, and data acquisition is very time consuming. For economic reasons, it is most desirable that any EPXMA facility should serve several users, who while waiting for their turn may need to store cryosections for a time. Storage of cryosections is associated with loss of structure and, under certain curcumstances, with changes in elemental distribution after short periods of time.[1] We have re-examined several cryosections by EPXMA mapping that had been stored under vacuum for very long periods of time.

Materials and Methods

Single, intact semitendinous muscle fibers from *R. temporaria* were quick-frozen as previously described.[2] The cryosections were freeze-dried in a Balzers FDU 101 and carbon-coated befor external transfer to plastic dessicators in which they were stored under vacuum. Quantitative EPXMA maps were obtained as previously described (Fig. 1).[3]

Results and Conclusions.

In the maps [Ca] was very high in the JSRs and occasionally (Fig. 1d) seen in hot spots that may correspond to spotty accumulations of negatively charged electron-dense material often seen in the free SR away from JSR.[2,4] Overall, only small variations in elemental distribution or concentration were observed after storage for over one year; the significance of these variations (especially with such elements as Na) is difficult to assess because of the small number (4) of muscle fibers examined. The lighter region in the center of Fig. 1b is a result of slight etching due to extended static probes that were taken from this area in addition to mapping. JSR [Ca] remained remarkably constant after one year of storage. Freeze-dried cryosections revealed some smearing of structural detail, ranging from minimal to moderate, especially in the myofibrial compartment (Figs. 1a and b). Our findings show that, when handled properly, carbon-coated cryosections can be stored over extended periods of time with minimal loss of structure or changes

in elemental distribution. Thus, quantitative EPXMA image maps after long storage present a rather accurate representation of the original. Proper storage of freeze-dried cryosections is a viable procedure for the effective participation of independent research groups in multiple-user EPXMA facilities, access to which may occasionally require prolonged storage periods.

References

1. T. v. Zglinicki and K. Zierold, *J. Microscopy* 154: 227, 1989.
2. R. Nassar et al., *SEM/1986* I, 309.
3. P. Ingram et al., *Applications in Biology and Medicine* (Berlin: Springer) 4: 251, 1989.
4. J. R. Sommer et al., *Acta Scand. Physiol. (Suppl.)* (in press).
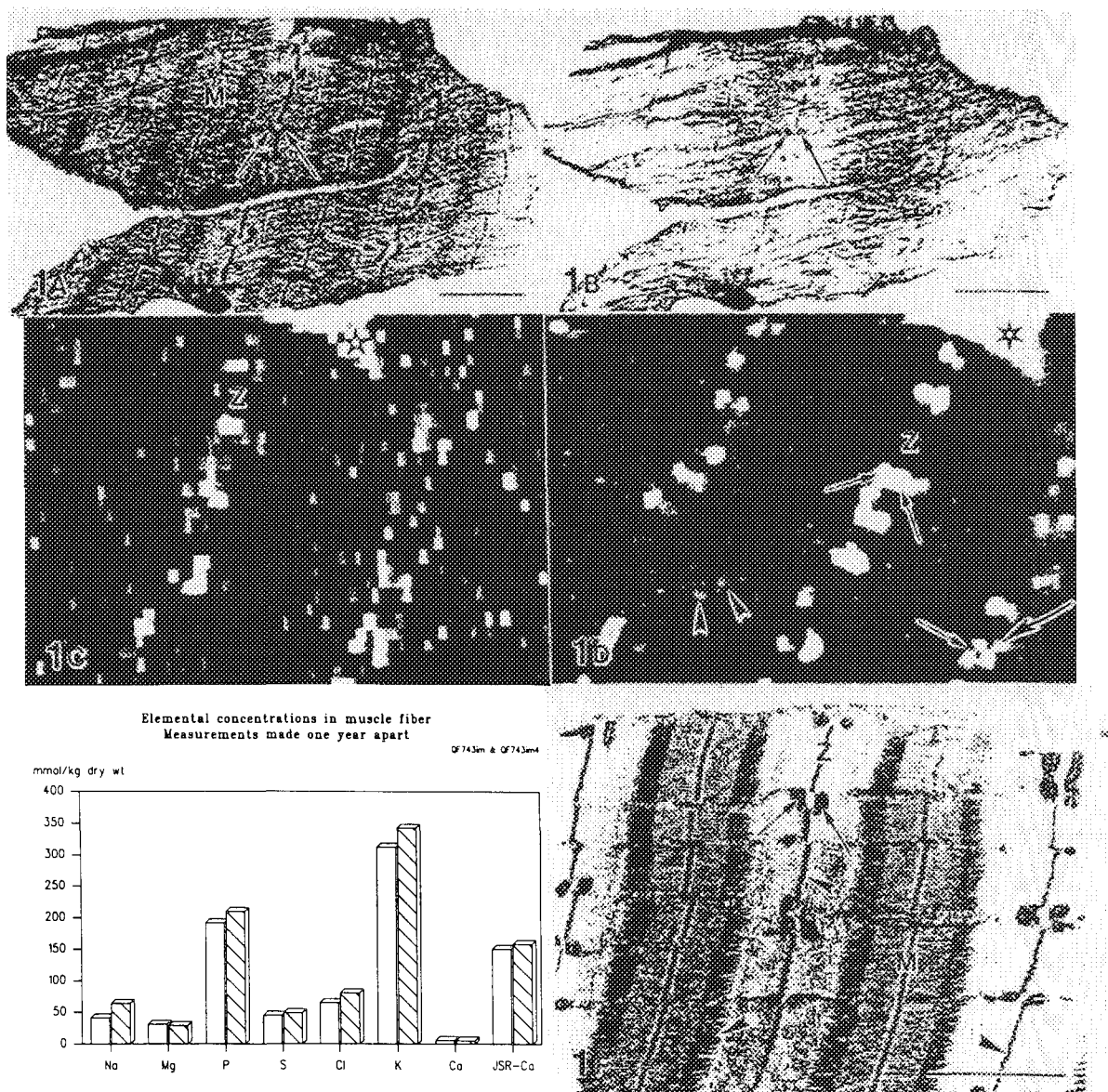
FIG. 1.--(a) Unstained freeze-dried cryosection after quick-freezing a single skeletal muscle
fiber at rest, TEM. Typical banding pattern with shearing artifacts (minute white holes) due to
sectioning. Z line (Z) bisects light I band; M line (M) bisects light H band which in turn bi-
sects dark A band. Junctional SR (JSR) with light core cylinders = arrows. Star = artifact(cf.
Figs. 1a-d; labels same in all figures). Bar ∿1.5 μm. (b) Same cryosection as in (a) after 1 yr
of storage under vacuum, TEM. Some smearing of borders between H and rest of A band has occurred.
JSRs (arrows) with core cylinders (small central white dots)[2] and overall section geometry are
well preserved after 1 yr. Bar ∿1.5 μm. (c) Quantitative x-ray [Ca] map of (a): 64 × 64 pixels (px);
dwell time, 1 s/px. The lighter the pixels, the higher the [Ca]. (For orientation, see bright
triangular artifact in upper right center (star); cf. (a)-(d). (d) [Ca] map of (b): 128 × 128 px;
dwell time, 2 s/px. Arrowheads: spots of high [Ca], probably in free SR. (e) Elemental concentra-
tions in cytoplasm and JSR did not differ significantly after 1 yr of storage. (f) Quality of cryo-
preservation: freeze-substituted region adjacent to Figs. 1(a), (b). Early cryoartifacts in A
and Z bands (arrowheads) increasing in severity with distance from surface.[2] JSRs = arrows. Bar
∿1.5 μm.

IMPROVED DECONVOLUTION OF K AND Ca BY FITTING WITH THE K RESIDUAL

L. G. Walsh and W. B. Greene

Application of electron probe x-ray microanalysis, EPMA, to biological investigations has its own set of difficulties that are different from those of the materials scientist. One of the most persistent difficulties is measuring low levels of Ca in the presence of large amounts of K. In the current study we investigate various methods of correcting for errors in Ca quantification introduced by variability in the centroid position and peak width of the overlapping K peaks. We also introduce a new method, using the residual of the K reference, to correct for errors due to changes in K peak width.

Small changes in total Ca content often produce profound changes in cellular physiology. For example, liberation of Ca ions often serves as a second messenger following stimulation or intercellular signaling. Moderate Ca accumulation activates a number of intracellular degredative processes that, if not stopped, may directly cause irreversible injury and cell death. Thus, measurements of low Ca concentrations and small Ca concentration shifts in cellular compartments are crucial for an understanding of normal and pathologic cellular physiology.

To make these measurements accurately with EPMA, large numbers of Ca counts are desired. Unfortunately, biological samples are sensitive to beam damage and are spatially inhomogeneous. Repeated measurements are usually necessary and studies of complex tissues may take many months to complete. In order to minimize the time it takes to make these studies, we continue to investigate more efficient methods for quantifying Ca.

Although Ca counting statistics ultimately limit quantification, the greatest impediment to analyzing Ca in biological samples with energy-dispersive x-ray spectroscopy, EDS, is interference from K. The K Kβ and Ca Kα peaks are separated by only 101 eV. Overlap between these elements with EDS is unavoidable. In most healthy cells, K is the most prevalent electrolyte and is 300 to 600 times more concentrated than Ca. Under these conditions the entire Ca Kα peak is dwarfed by the shoulder of the K Kβ peak. EPMA of most of the physiologically important Ca shifts hinges on the accu-

rate deconvolution of the K and Ca peaks.

The majority of laboratories utilize multiple least-squares (MLS) fitting to deconvolute this overlap. However, MLS fitting is very sensitive to small inconsistencies, the most important of which are (1) changes in detector calibration that lead to changes in peak position, and (2) changes in detector resolution that lead to changes in peak shape (predominantly a change in peak width).

The types of errors that are introduced are illustrated by the residual spectra in Fig. 1. (A residual spectrum is the portion of a spectrum that remains after the fitted peaks are subtracted.) As shown in Fig. 1(a), fitting a K standard, whose K Kα centroid is slightly shifted from that of the K reference peaks, produces an artifactual peak at the position where the Ca Kα is expected. Similarly, Fig. 1(b) shows that fitting K peaks with K reference peaks that are more narrow than the unknown will also produce a false peak where the Ca Kα is expected.
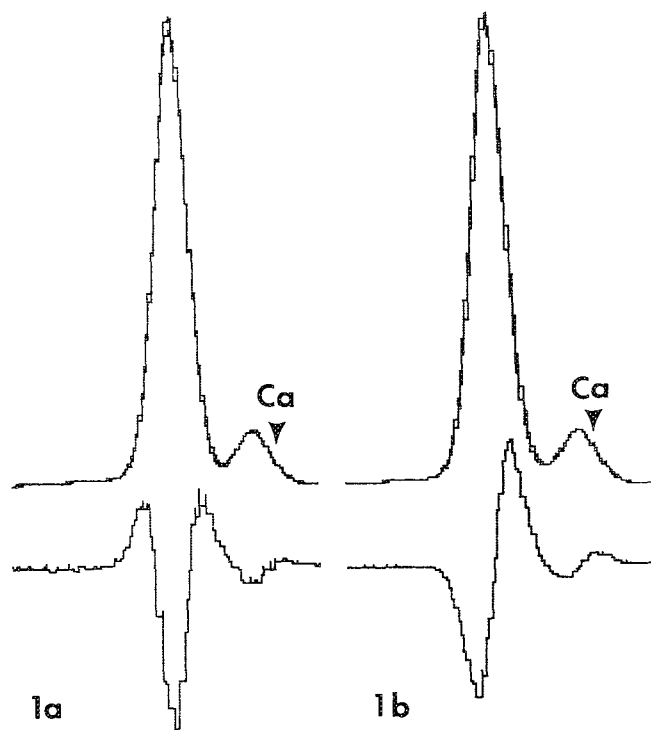
FIG. 1.--False Ca peaks are generated by errors in K peak position and width. (a) K Kα peak centroid shifted by 5 eV and resulting residual. Ca is not present in sample but appears in residual. (b) K peaks that are 5 eV wider than reference used for fitting generate similar false Ca peak.

The magnitude of these systematic MLS fitting errors is significant, often up to ±5 mmole/kg dry weight.[1] These errors affect every spectrum with large K peaks overlapping small Ca peaks. Failure to correct for these errors severely limits the accuracy and precision of Ca measurements in most biological samples.

Errors in K Centroid Position

Several methods have been devised to correct these systematic errors. For example, when the centroids of two widely separated peaks are well known (e.g., K and Cu), gain and zero errors can be calculated. Small changes in peak centroid can be corrected by recalibration of the spectrum, i.e., linearly shifting the spectrum by the new gain and zero factors to match the centroid positions of the reference peaks.[2]

Kitizawa et al. introduced another method for correcting for apparent peak shift.[3] They noted that the residual spectrum in the area around the K Kα resembles the first derivative of the K reference spectrum. That is, the first derivative of the K reference spectrum has peaks that match the position of the artifactual Ca Kα peaks in the residual spectrum. When they included the first derivative of the K reference spectrum in the MLS fit, they noted a marked improvement in Ca quantification in the presence of large concentrations of K.

Errors in K Peak Width

Two methods are commonly used for correcting for changes in peak width introduced by changes in detector resolution. Kitizawa et al. noted that the residual spectrum left after fitting K with a narrower K reference peak resembles the second derivative of the K reference spectrum.[3] When both the first and second derivatives of the K reference are included in MLS fits, K/Ca deconvolution is markedly improved.

Another approach is to degrade the resolution of the reference and unknown spectra until they match. Since peak width is now the same, peak shapes are more similar and there should be less variability in Ca quantification.

In this paper, we describe our experiences applying some of these methods for deconvoluting the K/Ca overlap and introduce a new procedure. We have examined these quantification methods at or near the limits of detectability for Ca in the presence of large amounts of K. We have found that the best accuracy and precision is obtained when gain and zero shifts are used to recalibrate K Kα peak centroid, followed by fits including a K residual to correct for changes in peak width.

Materials and Methods

The K reference[4] spectrum was generated from the summed spectra gathered at 125 keV from small crystals of KNO_3 that were thin enough for the electron beam to penetrate and yield about 75% of the screen current. Peak plus background count rate was kept at about 60 cps

for the K Kα. Ca reference spectra were similarly gathered from thin $CaCl_2$ crystals. The detector was calibrated to within 2eV of the Cu L and Cu K each day.

Standards were prepared from KNO_3 and Ca acetate in 25% dextran of 78 000 mwt, in 7-18 μmoh distilled and deionized water. The dextran contained 0.210 mmoles Ca/kg dry weight (by atomic absorption spectrophotometry). Five-milliliter droplets of mixed standards were plunge frozen in liquid propane. Cryosections 100-200 nm thick were cut at -120 C in a Reichert cryo-ultramicrotome and placed on 100-mesh folding copper grids that had a carbon-coated Formvar film on one side. The grids were stored under liquid nitrogen until use. Grids were freeze dried at -120 C to -80 C and analyzed on a GATAN cryo-transfer stage in a Hitachi H-7000 electron microscope. Analyses were made at -100 C in EDX STEM mode with a 125keV, 2-4nA beam (current calculated from screen current measurements calibrated using a Faraday cup stage). Spectra, 800 s live time, were collected with a horizontal KEVEX 30 mm² Si(Li) detector with 159.6eV resolution (measured at the Mn Kα, 1000 cps, with Mn evaporated onto a Formvar film on a Be grid). Spectra were anlyzed with a KEVEX delta IV analyzer. New software was developed for this project by John Konopka of KEVEX. All results are based on the fitted K integral, rather than [K], to remove inconsistencies in mass loss from the dextran or film.

The K residual (Fig. 2) was generated from the fit of a summed spectrum made of 43 spectrum from a standard that contained 597 mmole/kg dry weight K and 0.71 mmole/kg dry weight Ca. The gain and zero of the composite spectrum was shifted so that centroid positions of both the K and Cu Kα peaks matched our references. All the fitted K and the expected amount of Ca were subtracted from the spectrum to form the K residual reference spectrum. The residual was then included as a reference spectrum in some rounds of MLS fits to test its utility.

A variation of the K reference "spreading" method was also tested for its ability to counter errors in peak fitting due to changes in peak widths. For this test each standard spectrum was recalibrated and the K Kα peak width was measured. A temporary copy of the K reference was then mathematically spread so that the Kα peak width of the reference matched that of the standard. This spread K reference was then used in place of the narrower K reference in the "spread" fit of that standard.

Results and Discussion

As shown in Fig. 3, MLS fitting of spectra from standards with high K and low Ca content gives variable results, depending on the methods used in the deconvolution. Fitting the standards without concern for the K peak induced errors (the "raw" data) produced unacceptable errors in Ca quantification (Fig. 4).

2
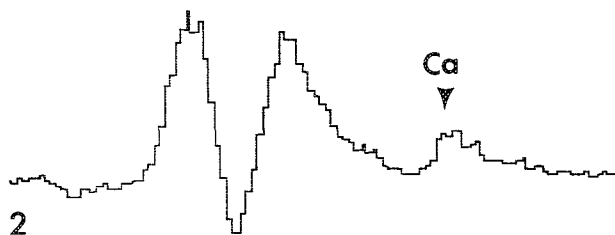
FIG. 2.--K residual used for this study.
FIG. 3.--Ca quantification of standards with 0
to 10 mmole Ca/kg dry weight in presence of
300-600 mmole K/kg dry weight using different
methods of K/Ca deconvolution. Expected re-
sults are shown by solid line.

Similarly, poor results were obtained when the
standard spectra were fit with the K residual
without recalibration or after recalibration
alone. In Fig. 5, all spectra were recalibrated
and then fit by inclusion of the K residual
and/or substituting the spread K reference peak
for the K reference. (The peak spreading rou-
tines were only used for 3 standards.) The
only method of quantification that produced
good results was fitting recalibrated spectra
with the K residual.

Virtually all these fitting methods reduced
the variability of the results when compared
with the raw data. Although the errors intro-
duced with all but the optimum fitting method
are disturbingly large, they do not appear to
be systematic. The mean errors are both posi-
tive or negative but are consistent for each
standard. This result appears to be linked to
changes in detector calibration where the K cen-
troid position and Kα peak width are consistent
within each standard, but vary slightly among
standards. Every effort was made to minimize
changes in detector calibration, but variability
in K Kα peak position of 4 eV, over the course
of the experiment, was unavoidable. The large
errors may be related to each method's sensitiv-
ity to peak shifts of a particular form.

We did not test the utility of using the sec-
ond derivative of the K reference to correct for
errors introduced by the variability in K peak
width, because the software was not available.
However, it is expected that the results would
be comparable, since the second derivative is
used as an approximation of the shape of the K
residual. Previous personal experiments with
the derivative method have shown that results
may vary with the choice of the original K ref-
erence. It has also been noted that fitting
with derivatives may add variability at moderate
to high levels of Ca.[5] It is likely that the K
residual would introduce similar errors at high-
er Ca concentrations.

Our experience with these methods leads us to
several conclusions about deconvoluting K and
Ca

1. The largest single improvement in MLS de-
convolution can be gained by shifting the K Kα
centroid position to match that of the K refer-
ence. Direct recalibration of the spectrum by
shifting gain and zero is probably superior to
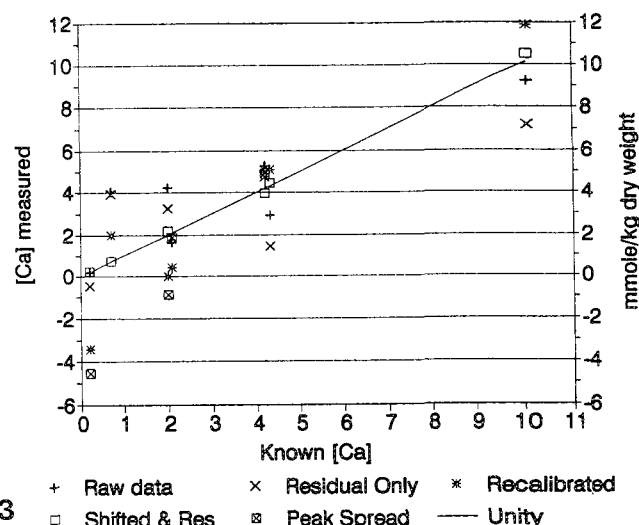
use of the first derivative of the K reference,
since each reference added to the deconvolu-
tion of an overlap region introduces signifi-
cant variability in the deconvolution of that
region.
2. None of the methods currently used to
correct for variable K peak width can adequate-
ly cope with a K peak in the unknown that is
narrower than the stored reference. For exam-
ple, all our attempts to use a residual gener-
ated from a K reference whose width equaled
the average K width in the standards were un-
successful. The reason is unknown, but the
results indicate that the changes in peak
shape with changes in peak width are not lin-
ear. Therefore, the K reference should be as
narrow as possible.
3. As the Ca concentration of the sample ap-
proaches one-tenth the K content, all of the
methods to correct for variable K peak width
are of little benefit.

We conclude that inclusion of the residual
of the K reference in deconvolution of K and
Ca, in recalibrated spectra, improves Ca
quantification. When this method is used, con-
centration differences of less than 0.5 mmole
Ca/kg dry weight can be confidently measured
in the presence of 600 mmole K/kg dry weight.

References

1. J. McD. Tormey, "Improved methods for
x-ray microanalysis of cardiac muscle," *Micro-
beam Analysis--1983*, 221.
2. J. J. McCarthy and F. H. Schamber,
"Least-squares fit with digital filter: A
status report," in *National Bureau of Standards
Special Publication 604*, National Bureau of
Standards, Washington, D.C., 1979, 273-296.
3. T. Kitazawa, H. Shuman and A. P. Somlyo,
"Quantitative electron probe analysis: Problems
and solutions," *Ultramicroscopy* 11: 251, 1983.
4. "Reference" spectra are those used in
MLS fitting as models of each element's peak
shape.
5. T. E. Bostrom and C. E. Nockolds, "Fil-
tered least-squares fitting of EDS spectra with

derivative references: Problems and limitations imposed by counting statistics," *Microbeam Analysis--1989*, 233.
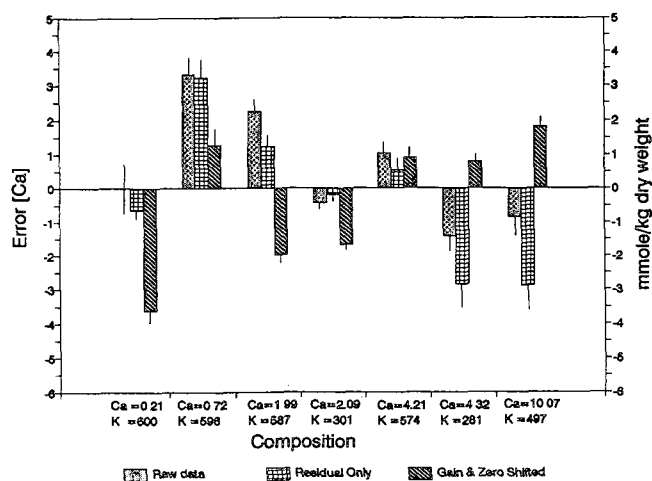
FIG. 4.--Errors in Ca quantification measured with different K/Ca deconvolution methods. Raw data were fitted without recalibration, fitting with K peaks spreading, or fitting with K residual. Residual only data reflect fits including the K reference residual without recalibration. Gain and zero shifted data were from spectra recalibrated to reposition K peaks in the correct positions. N's were 51 for Ca = 0.21, K = 600; 46 for Ca = 0.72, K = 596; 23 for Ca = 1.99, K = 587; 30 for Ca = 2.09, K = 301; 16 for Ca = 4.21, K = 547; 16 for Ca = 4.32, K = 281; and 40 for Ca = 10.07, K = 497 (mean error ± sem).
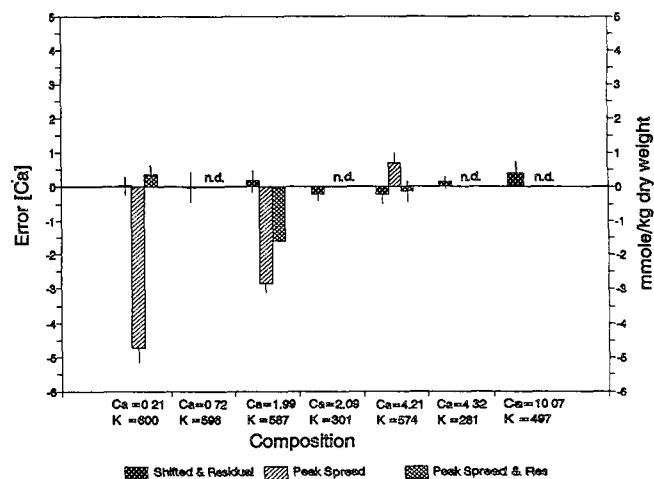
FIG. 5.--Errors in Ca quantification measured with different K/Ca deconvolution methods. Shifted and residual data were recalibrated by use of gain and zero shifts and then fitted with K residual included in deconvolution. Peak spread data were recalibrated and fitted with K reference peak spread to match width of each spectrum. "Peak Spread and Res" data were recalibrated and fit with both spread K reference and K residual. Peak spreading was not done on the four standards labeled "n.d." (Mean error ± sem).

ELEMENT COMPOSITION OF CARDIAC MYOCYTES FROM DIABETIC RATS STUDIED BY X-RAY MICROANALYSIS

Alice Warley and James Dedman

The incidence of heart disease is higher in diabetics than in the general population, and evidence has accumulated that in some cases the increase is due to the development of cardiomyopathy associated with the diabetic conditions.

Studies on heart muscle from animals with drug-induced diabetes have shown that there is a decrease in ventricular function, and that the contractile properties of isolated papillary muscles are altered after onset of the disease.[1,2] Biochemical studies have also shown that there is lowered activity of Ca activated myosin ATPase, altered permeability of the sarcolemma to Ca, and defective transport of Ca by the sarcoplasmic reticulum in hearts from diabetic animals.[2-4] These various findings have led to the suggestion that intracellular element concentrations are altered in heart tissue from diabetic animals.[5] However, there have been few direct studies on element composition of cardiac tissue after the onset of diabetes, and the results from these studies are contradictory. No significant changes in Na, K, or Ca but a decrease in Mg were reported for rabbits, whereas increases in tissue concentrations of both Na and K were reported for rodents and dogs.[6-8]

Electron probe x-ray microanalysis of heart tissue that has been cryofixed in vivo permits study of intracellular concentrations of elements without the need to correct for the extracellular contribution.[9,10] It should be possible, by use of this technique, to clarify whether any changes in element concentrations occur in cardiac myocytes from diabetic animals that could account for the altered contractility of the heart muscle.

Experimental

Diabetes was induced in male CSE Wistar rats (weight 300 g) by intraperitoneal injection of the drug streptozotocin (55 mg/kg). The progress of the disease was followed by monitoring of weight loss and the appearance of glucose in the urine.

Element concentrations were measured in heart tissue from animals 8 weeks after induction of diabetes. The animals were anaesthetized, the femoral artery was cannulated, and a blood sample was taken for measurement of blood

glucose. A ventral incision was made and the thorax was opened to expose the beating heart. The heart was gently lifted away from the thorax and cryofixed by clamping in the jaws of copper-clad pliers that had been cooled in liquid nitrogen and exposed to liquefied propane. Small pieces of the frozen ventricle were stored under liquid nitrogen.

Cryosections 200 nm thick were cut from the external edge of the frozen tissue at a temperature of -125 C. The frozen sections were transferred to Piloform-coated Ni grids and the sections were pressed onto the grids by means of a cooled polished copper rod. The grids were placed in a precooled brass block, which was transferred to a freeze drier; the sections were freeze dried overnight.

Analysis was carried out on a JEOL 100CX STEM electron microscope at 100 kV and a beam current of 1.5 nA. Spectra were collected for 100s live time and data were processed with a Link Analytical 860 series 2 EDS detection system and Quantem software.

Fractions of cardiac sarcolemma were prepared from control and diabetic animals, and ouabain-sensitive Na/K ATPase in the isolated cardiac sarcolemma was estimated.[11]

Results and Discussion

Induction of diabetes resulted in a decrease in body weight and an increase in blood glucose concentration (Table 1); circulating insulin levels were also decreased.

TABLE 1.--Body weight, heart weight, and blood glucose in diabetic rats.

	Start weight (g)	Weight loss (g)	Heart weight (g)	Glucose (mM)
Control	296±5		0.82±0.4	3.7±0.2
Diabetic	296±6	106±28	0.7 ±0.07	22.4±4.9

Estimation of element concentrations showed an increase in the concentrations of Na and S in cardiac myocytes from the diabetic animals when compared to control animals (Fig. 1). The increases in these elements were found in both myofibrils and mitochondria. There were no significant differences in the other elements. The concentration of Ca was low in both control (1 ± 2 mmole/kg, myofibrils) and diabetic animals (3 ± 2 mmoles/kg, myofibrils), and not significantly different between the two groups of animals.

The increase in intracellular Na concentration could be explained by a decrease in the activity of the sarcolemmal sodium pump, although a concomitant decrease in intracellular
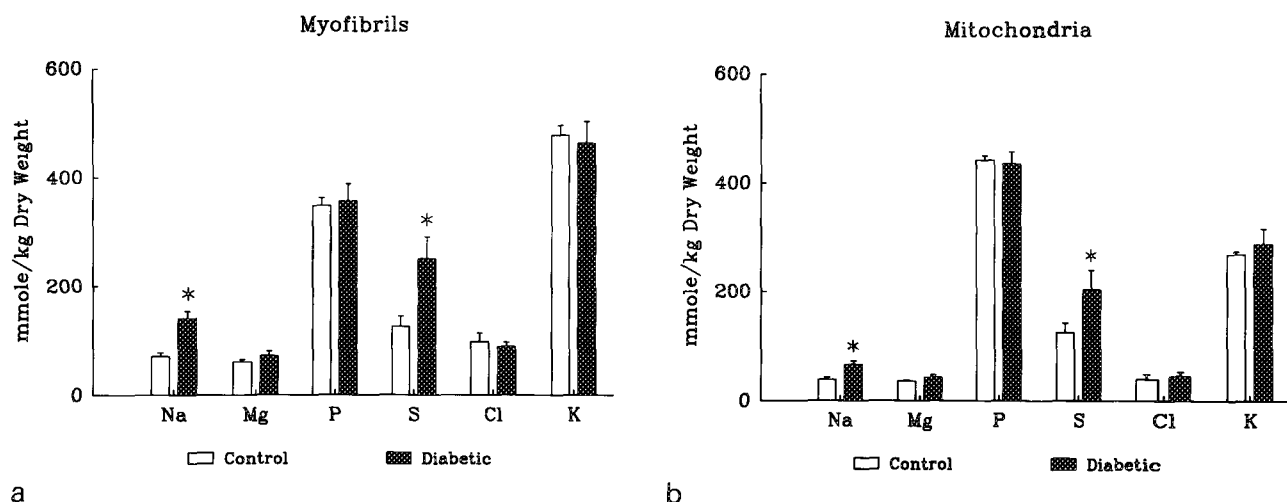
FIG. 1.--Concentrations of elements in (a) myofibrils and (b) mitochondria of cardiac myocytes from control (□) and diabetic (■) animals.

K would be expected.[7] However, the standard error of the K measurement is increased in the diabetic animals, and there is a significant negative correlation between the concentration values in individual cells for the elements Na and K. To determine whether there is a change in Na/K ATPase in the diabetic rats, sarcolemmal fractions were isolated from 6 control and 6 diabetic animals, and the specific activity of the ouabain-sensitive ATPase was determined. There was a decrease in the specific activity (μmole ATP hydrolyzed/mg protein/10 min) of this enzyme from 3.41 ± 1.67 (S.D.) in the control animals to 1.53 ± 0.57 (S.D.) in the diabetic animals. This decrease is statistically significant ($p < 0.05$, Student's t-test).

The measurements reported here show that changes in intracellular element composition can be detected in cardiac myocytes in vivo after the onset of diabetes, and confirm the validity of using this approach. Further experiments are being carried out to determine whether altered handling of Ca can be detected after the onset of diabetes.

References

1. F. S. Fein, L. B. Kornstein, J. E. Strobeck, J. M. Capasso, and E. H. Sonnenblick, "Altered myocardial mechanics in diabetic rats," *Circulation Res.* 47: 922, 1980.

2. D. W. Garber and J. R. Neely, "Decreased myocardial function and myosin ATPase in hearts from diabetic rats," *Am. J. Physiol.* 244: H586, 1983.

3. C. E. Heyliger, A. Prakash, and J. H. McNeill, "Alterations in cardiac sarcolemmal Ca pump activity during diabetes mellitus," *Am. J. Physiol.* 252: H540, 1987.

4. P. K. Ganguly, G. N. Pierce, K. S. Dhalla, and N. S. Dhalla, "Defective sarcoplasmic reticular calcium transport in diabetic cardiomyopathy," *Am. J. Physiol.* 244: E258, 1983.

5. G. N. Pierce, R. E. Beamish, and N. S. Dhalla, "Diabetic cardiomyopathy: Present status and future directions," in *Heart Dysfunction*

in Diabetes, Boca Raton, Fla.: CRC Press, 1988, 225.

6. S. Shimji, D. V. Godin, and J. H. McNeill, "Biochemical and functional changes in hearts from rabbits with diabetes," *Diabetolgia* 28: 452, 1985.

7. K. Kjeldsen, H. Braendgaard, P. Sidentius, J. S. Larsen, and A. Norgaard, "Diabetes decreases Na/K pump concentration in skeletal muscles heart ventricular muscle and peripheral nerves of rat," *Diabetes* 36: 842, 1987.

8. T. J. Regan, P. O. Ettinger, and M. I. Khan, "Altered myocardial function and metabolism in chronic diabetes without ischaemia in dogs," *Circulation Res.* 35: 222, 1974.

9. M. Bond and A. R. Jaraki, "Rapid freezing of hamster hearts in vivo at defined timepoints in the cardiac cycle," *Microbeam Analysis--1989*, 122.

10. A. Warley, "Cryofixation of heart tissue for x-ray microanalysis," *Scanning Microscopy* 3: 1247, 1989.

11. J. P. T. Ward and I. R. Cameron, "Adaptation of the cardiac muscle sodium pump to chronic potassium deficiency," *Cardiovascular Res.* 18: 257, 1984.

EVALUATION OF SILICONE BREAST IMPLANT SURFACES BY TRANSMISSION AND SCANNING ELECTRON MICROSCOPY

H. A. Freeman and R. T. Henrich

Several efforts reported in the literature[1-3] have attempted to describe degradation of silicone prosthetic materials which may follow surgical implantation of some mammary reconstruction and augmentation devices. Other, more recent published studies, completed with appropriate controls, investigated capsular tissue formation and Si distribution as it related to the alteration of both silicone and non-silicone devices.[4,5]

Procedures

It became evident from the earlier work that, with a knowledge of how the devices are made and of their typical microstructure, new microscopic techniques should be applied that address the issue of silicone elastomer surface integrity following implantation. A protocol was therefore developed to implant subcutaneously portions of mammary envelopes (disks) in the posterior dorsal regions of 30 mice for periods of up to 6 months. All animal preparation and surgical procedures conformed to accepted practice. Comparable disks from the same envelope were not implanted, but comprised a set of controls that were later compared with implanted specimens. The mice were sacrificed at intervals of 1, 3 and 6 months and the disks were removed along with any tissue capsule that had formed. Three implanted disks were randomly selected from each time period and their tissue capsules were removed. Transmission electron microscopy was performed on these implanted disks and their respective nonimplanted controls.

Two adjacent sites from each implanted disk and one section from the respective nonimplanted control were then embedded in dimethyl hydroxy terminated silicone polymer. This "DS polymer" provided good adhesion to the silicone and allowed the blocks to be trimmed across the envelope thickness while retaining polymer on inner and outer surfaces. Ultracyrotomy was completed at about -135 C and sections spanning the entire envelope thickness (Fig. 1) were examined in a JEOL JEM 2000FX analytical electron microscope (AEM) with EDS and scanning capabilities. Location of the outer surface of both the implanted and nonimplanted disks was facilitated by the block trimming operation and the presence of fluoropolymer inner surface layer (Fig. 2). Implanted and control surfaces were also carbon coated

---

The authors are at Dow Corning Corp., Midland, MI 48686.

to avoid charging and evaluated by an SEM mode.

Ultracryotome sections, 103 total, were generated from implanted and control specimens. Over 400 micrographs (typically at primary magnifications of 5000, 10 000, and 20 000) were taken to insure thorough characterization of the cross-sectioned envelope at its outer surface. Nearly half of the micrographs were taken at 20 000× and measurements were made on these enlarged prints (Figs. 3 and 4) to determine deviation (±2 nm) of this surface from a median plane.

Summary of Results

Body weight gain on all experimental animals was normal, which showed that the implantation of mammary envelope elastomer disks produced no adverse effects. No overt signs of inflammation were noted around the implants or in the surrounding tissue. Capsule formation appeared normal. No degradation or surface modification of the implanted elastomer surfaces was noted at any of the time intervals, when these surfaces were compared to the nonimplanted control surfaces by use of TEM. Amorphous fumed silica distribution (7-11nm particle size) appeared the same in both implanted and nonimplanted disks (Figs. 3 and 4).

In addition, SEM showed no unusual surface characteristics or particles on the surface of a disk 6 months after implantation when compared to its respective nonimplanted control (Figs. 5 and 6). Therefore, within the time frames investigated in this study, there were no significant changes in the surface of any envelope as a consequence of implantation and no evidence of surface degradation was found.

References

1. N. Kossovsky et al., "Analysis of the surface morphology of recovered silicone mammary prostheses," *Plast. Reconstr. Surg.* 70: 795, 1983.
2. J. P. Heggers et al., "Biocompatibility of silicone implants," *Ann. Plast. Surg.* 6: 38, 1983.
3. C. Rolland et al., "Nondestructive investigation on ninety-seven surgically excised mammary prostheses," *J. Biomed. Mater. Res.* 23: 285, 1989.
4. T. A. Fassel et al., "Scanning and transmission electron microscopy evaluation of bacterial adhesion morphology to breast prosthetic biomaterials," *Proc. XIIth ICEM* 3: 844, 1990.
5. D. Jennings et al., "Elemental silicone analysis in human breast and capsular tissue surrounding prostheses and expanders," *Proc. XIIth ICEM* 3: 846, 1990.
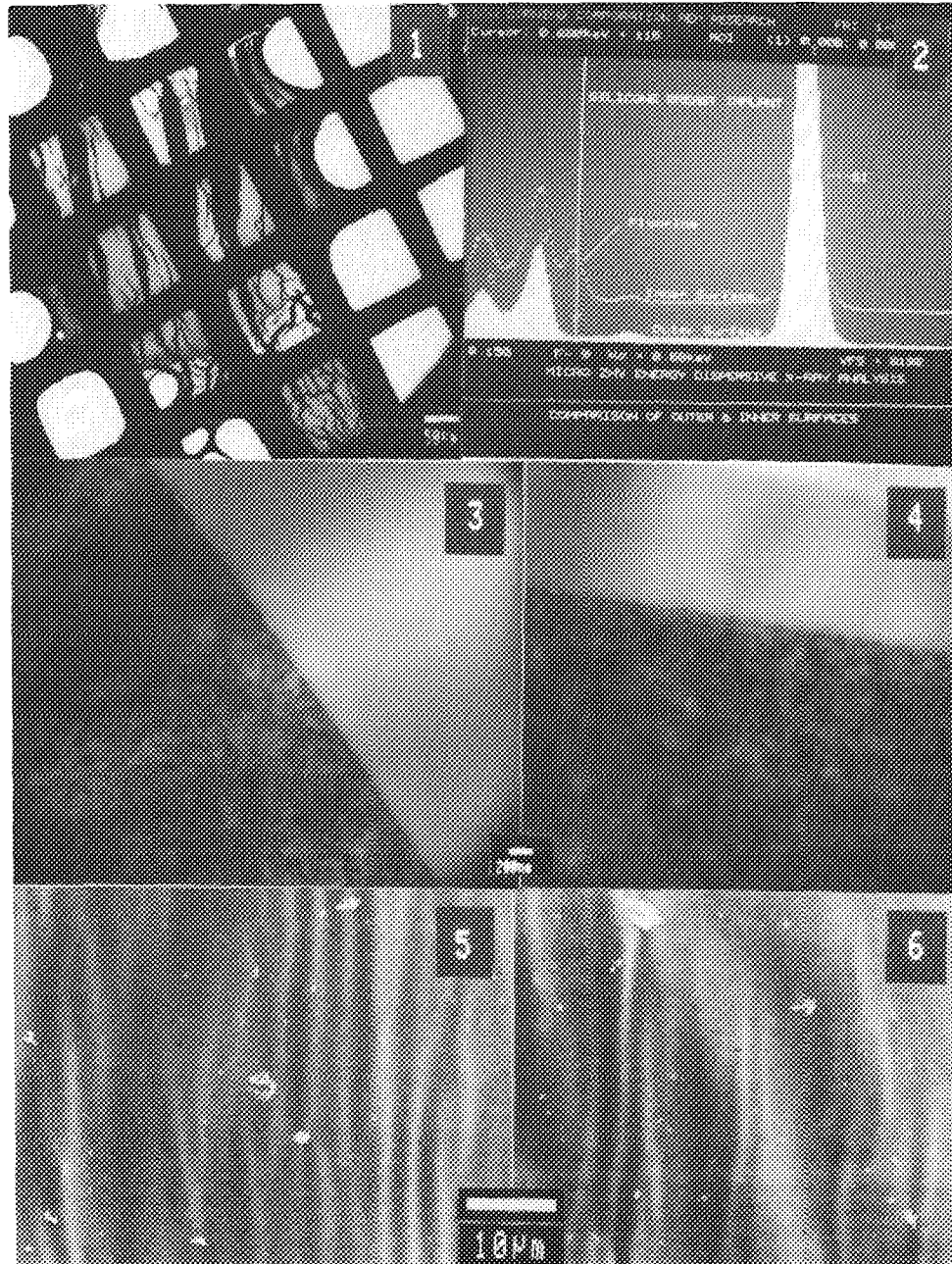
FIG. 1.--Complete ultracryotome section of mammary envelope resting on support grid. Outer surface is visible in upper left grid openings.
FIG. 2.--EDS spectra demonstrate the elemental distinction between dimethyl layer (upper spectrum) and fluorosilicone layer (lower spectrum).
FIG. 3.--Ultracryotome section of typical mammary prosthesis at outer surface 6 months after implantation.
FIG. 4.--Ultracryotome section of typical control (nonimplanted) mammary prosthesis at outer surface.
FIG. 5.--SEM of control (nonimplanted) mammary prosthesis surface.
FIG. 6.--SEM of mammary prosthesis surface 6 months after implantation.

MORPHOLOGICAL AND COMPOSITIONAL STUDIES OF *Helicobacter pylori* FOLLOWING BISMUTH SUBCITRATE EXPOSURE

N. A. Lilly and R. R. Warner

Helicobacter pylori are gram-negative microaerophilic bacteria implicated in the development of gastritis and peptic ulcers.[1] It has been shown that bismuth preparations are toxic to *H. Pylori* both in vivo[2] and in vitro.[3] Our investigations on the mechanism of in vitro bismuth toxicity show marked morphological changes coincident with Bi penetration into the bacteria. Bismuth often accumulates as masses within the cell interior. The morphological and chemical data suggest that Bi antibacterial effects are due to a nonspecific mode of action similar to that of organomercurials. Bismuth elemental distributions are similar in cryoanomercurials. Bismuth elemental distributions are similar in cryopreparations and conventionally prepared (glutaraldehyde-fixed) plastic-embedded sections. Unexpectedly, we noted extremely high intracellular iron levels in *H. pylori*. The iron distribution corresponds with elevated phosphorus within the bacterium.

H. pylori are found in the upper gastrointestinal trace of humans.[1,2] Increasing evidence suggests these bacteria play a causal role in the development of gastritis and peptic ulcers.[1] Bismuth preparations are toxic to H. *pylori*,[2,3] and treatment of recurrent ulcers with colloidal bismuth subcitrate (De-Nol) combined with antibiotics has become an established therapy.[4] A previous in vitro study showed that De-Nol was bactericidal to *H. pylori* as measured by viability, but its bactericidal actions resulted in no gross morphological alterations in cell ultrastructure.[3] The purpose of this investigation was to obtain morphological and elemental information that might elucidate a mechanism for bismuth antimicrobial effects on *H. pylori*. Secondarily, we wished to investigate the ability of conventional EM preparative procedures to preserve Bi elemental distributions.

Methods

Cultures of *H. pylori* ATCC 11638 were grown overnight in Brucella broth with 5% fetal bovine serum under microaerobic conditions. At T = 0, a 1:10 dilution of the culture was made into fresh broth (control) or into fresh broth containing De-Nol at a final concentration of 1000 μg/ml. Incubation times were 0, 4, and 24 h. Prior to fixation, aliquots of the bacterial cultures at each time point were pelleted in 10% albumin and frozen in a propane/isopentane cryogen. Other aliquots were pre-

pared by conventional TEM sample preparation techniques similar to those used by Armstrong et al.[3] Frozen samples were sectioned dry, 0.3 μm thick, at -115 C and freeze-dried. Morphological studies utilized thin sections of osmium postfixed and uranyl counterstained Spurr's-embedded bacteria. Elemental studies of conventionally prepared (glutaraldehyde-fixed) tissue embedded in LR White plastic were performed on unstained sections cut dry at 0.3 or 1.0 μm thickness. Morphological studies utilized the Zeiss EM-902 operated in the zero loss mode. Elemental analyses were done at 100 kV in the STEM mode with the Hitachi H-500 and Tracor Northern TN-5500 EDS system, or Philips CM12 and a Link eXL EDS system.

Results

De-Nol treatment has a small effect on *H. pylori* viability after 4 h, but is decidedly toxic after 24 h, with a complete kill obtained in some experiments (data not shown).

TEM examination of glutaraldehyde-fixed control *H. pylori* (Fig. 1a) reveals coccoid, spiral, and slightly curved bacillary forms as described previously.[3] In contrast, *H. pylori* exposed to 1000 μg/ml De-Nol for 24 h are degenerative and swollen, and contain electron-dense cytoplasmic aggregates (Fig. 1b). There is a large increase in bacteria displaying extremely distorted cell walls.

Analytical results from control *H. pylori* cryosections and LR White plastic sections are similar. Of some surprise, Fe localizations are generally detected in these bacteria (Fig. 2). Iron levels approaching 30 mM/kg (plasti-embedded) sample are observed. Generally the regions of enhanced Fe are coincident with P localizations, as shown in Fig. 2.

Bismuth is not detected in bacteria opposed to 1000 μg/ml De-Nol for 4 h, but is detected after 24 h. Results from cryosections and LR White plastic sections are similar. Point analyses of cryosections reveal Bi both in *H. pylori* retaining their bacillary shapes as well as those assuming a more degenerative form. X-ray maps show intracellular Bi in a variety of distributions, either localized or dispersed throughout the cytoplasm in bacillary forms, or dispersed primarily around the cell membranes in swollen and degenerated cells (Fig. 3). The regions of increased Bi are not associated with increased concentrations of either Fe or P.

Discussion

The reduction in cell viability upon expo-

N. A. Lilly and R. R. Warner are at the Miami Valley laboratories, Procter & Gamble Co., Cincinnati OH 45239.

sure to colloidal bismuth subcitrate (De-Nol) in vitro agrees with literature studies. However, unlike a previous study,[3] we see attendant and severe morphological changes upon Bi exposure.

Bismuth is detected within cells coincident with the onset of morphological changes, implying a causal relationship. The multitude of morphological effects produced by De-Nol is very similar to those produced by organomercurials,[5] which combine strongly with bacterial enzyme -SH groups[6] to disrupt a diversity of metabolic syntheses.

Of some interest is the very high Fe concentrations that we observe intracellularly in *H. pylori*. Iron is required for bacterial growth, and bacteria express specific chelating molecules (siderophores) specifically to acquire this element in low Fe environments.[7] Although high Fe levels in a variety of bacteria have been noted by others,[8] the extremely high intracellular concentrations that we observe are unexpected, as is the localized nature of Fe and its association with elevated P.

Conventional EM techniques of chemical fixation and plastic embedment are well known to remove and redistribute inorganic elements in biological tissue, particularly monovalent ions.[9] Our data from both conventional and the rigorous cryotechniques show similar Bi distributions, but perhaps less Bi in the plastic sections. Although it would appear that the conventional (easier) techniques are adequate to preserve Bi distributions, the comparisons are limited in number and are not quantitative, and additional study would be required to conclude that conventional techniques are truly adequate.

References

1. D. Y. Graham, D. G. Evans, and D. J. Evans Jr., "*Campylobacter pylori*: The organism and its clinical relevance," *J. Clin. Gastroenterol.* 11: S43-S48, 1989.

2. B. J. Marshall et al., "Antibacterial action of bismuth in relation to *Campylobacter pyloridis* colonization and gastritis," *Digestion* 37: 16-30, 1987.

3. J. A. Armstrong et al., "Responce of *Campylobacter pyloridis* to antibiotics and an acid reducing agent in vitro: An ultrastructural study," *J. Med. Microbiol.* 24: 343-350, 1987.

4. S. L. Gorbach, "Bismuth therapy in gastrointestinal diseases," *Gastroenterology* 99: 863-875, 1990.

5. Z. Vaituzis et al., "Effects of mucuric chloride on growth and morphology of selected strains of mercury-resistant bacteria," *Applied Microbiology* 29: 275-286, 1975.

6. A. D. Russell and I. Chopra. *Understanding Antibacterial Action and Resistance*, New York: Ellis Horwood, 1990.

7. M. D. Moody, "Microorganisms and iron limitation," *Bioscience* 36: 618-623, 1986.

8. M. Noll and K. Zierold, "Scanning electron microscopic and x-ray microanalytical studies on iron binding organisms," *Verh. Ges. Oekol.* 12: 417-424, 1984.

9. A. J. Morgan et al., "Specimen preparation," in D. A. Erasmus, Ed., *Electron Probe Microanalysis in Biology*, London: Chapman & Hall, 1978, 94-147.
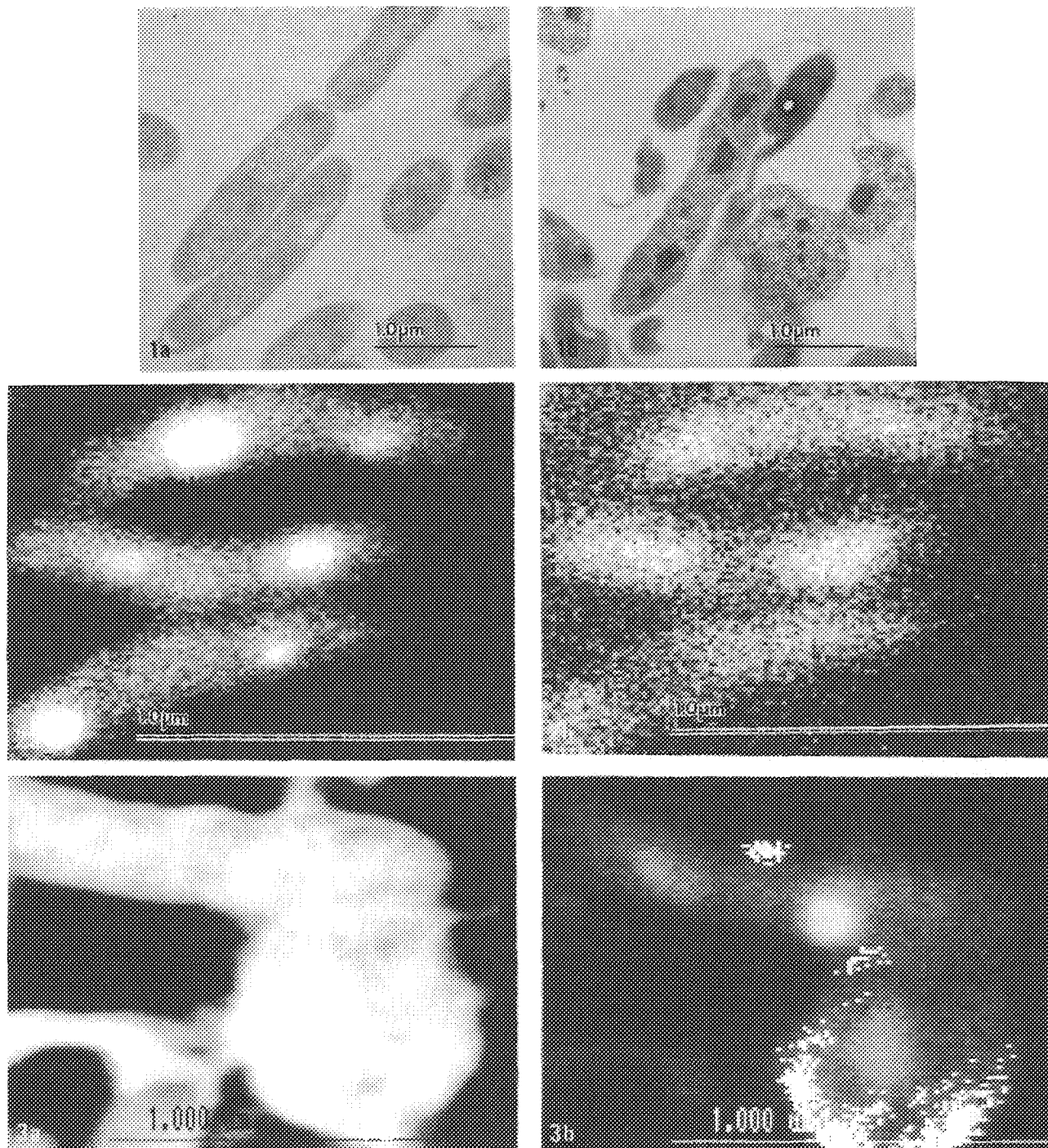
FIG. 1.--(a) Micrograph of control *H. pylori* bacteria. (b) Bismuth-treated bacteria showing cell wall blebbing, cytoplasmic aggregates, and degenerative forms.
FIG. 2.--Elemental distributions of Fe and P in a control *H. pylori* cryosection. (a) Elemental map showing the P Kα signal, (b) Fe Kα map. Note that Fe concentrations are found in same areas as P spots.
FIG. 3.--(a) Inverted brightfield STEM image showing treated bacteria. (b) Overlay maps of Bi (white) on P Kα signal, showing that Bi spots coincide with P spots.

THE COOL PLUME: HYDROCYNAMIC DESCRIPTION OF MATRIX-ASSISTED LASER DESORPTION (MALD)

Akos Vertes

Matrix-assisted laser desorption (MALD) as a soft volatilization and ionization technique was introduced three years ago.[1,2] Since then it acquired a reputation as a strong candidate for the analysis of high-molecular weight biopolymers. MALD remained in competition with electrospray ionization for the availability of a similar mass range and for their comparable detection limits. In other respects (e.g., the problem of interferences and coupling to separation techniques) they are considered to be complementary methods. However, in the atmosphere of excitement caused by the vast field of potential new applications, not too much attention has been paid to answering basic questions concerning the mechanism of the volatilization and ionization phenomena.

The experiment itself is relatively simple. Solutions of the large (guest) molecules and of the matrix (host) material are mixed, providing 1:1000 to 1:10 000 molar ratios. A droplet of this mixture is dried on metallic substrate and excited by a laser pulse in vacuum. The generated ions are typically analyzed by a time-of-flight mass spectrometer. The astonishing finding was that extremely large molecules (molecular weight exceeding 100 000 Da) could be transferred to the gas phase and ionized by this method.

Some early efforts were directed toward broadening the range of applicable matrices and laser wavelengths and resulted in a rough outline of required matrix material properties.[3] A promising candidate for a successful matrix should exhibit the following features:

(a) strong light absorption at the laser wavelength;

(b) low volatilization temperature (volatilization shall take place preferably in the form of sublimation);

(c) common solvent with the analyte; and

(d) ability to separate and surround the large molecules in a solid solution without forming covalent bonds.

The first systematic measurements describing several details of the desorption process have been reported only recently.[4] The most important findings included the establishment of accurate threshold irradiances and the revelation that the underlying process is collective in nature. Experiments in alternative configurations showed that the presence of a solid substrate is not indispensable and thus opened the possibility of performing MALD experiments in transmission geometry.[5] It was also shown that mass

Akos Vertes is at the Department of Chemistry, University of Antwerp (UIA), Universiteitsplein 1, B-2610 Wilrijk, Belgium.

spectrometry is not the only method to detect the large molecules.[6]

Theoretical investigations date back to efforts devoted to the understanding of plasma desorption and other high-energy-particle-induced desorption techniques.[7] An important basic question for all these methods is, how can we account for the transfer of large molecules to the gas phase without fragmentation or degradation? The intriguing similarity between MALD and the other soft ionization methods is that they all start with sudden energy deposition and they all yield large molecules in the gas phase. Energy deposition and redistribution processes seemed to be a key factor in the description of MALD mechanisms.[8,9] Attempts have also been made to account for the energy transfer to the large molecules during their volatilization.[8,9] A possible reason for the lack of degradation of these molecules is the presence of an energy-transfer bottleneck due to frequency mismatch between lattice vibrations in the solid and intramolecular vibrations in the large molecules.[10,11]

In this paper we outline a scenario in which the laser energy deposited in the solid matrix leads to heating and phase transition. The generated plume, in turn, undergoes gasdynamic expansion and exhibits strong cooling. The entrained large molecules are therefore also cooled and stabilized in the expansion. First we estimate the threshold irradiance to achieve phase transition in the matrix. In the second part of this contribution we also report preliminary hydrodynamic calculations of the plume expansion to check the feasibility of this idea.

Irradiance Threshold for Plume Formation

There are several regimes of laser-solid interaction for a given material, depending on the laser irradiance. The simplest case involves the following possibilities:

(a) surface heating with thermal desorption;

(b) surface melting with surface evaporation;

(c) volume evaporation;

(d) formation of optically thick plume;

(e) plasma absorption in the plume; and

(f) optical breakdown (in transparent insulators).

The separation of these regimes according to the principal determining factors (i.e., laser irradiance I_0 and solid optical absorption coefficient α) are shown in Fig. 1. The three different thresholds (volatilization threshold I_0^{volat}, plasma ignition threshold I_0^{plasm}, and optical breakdown threshold I_0^{break}) are marked by dashed lines. Although their values are
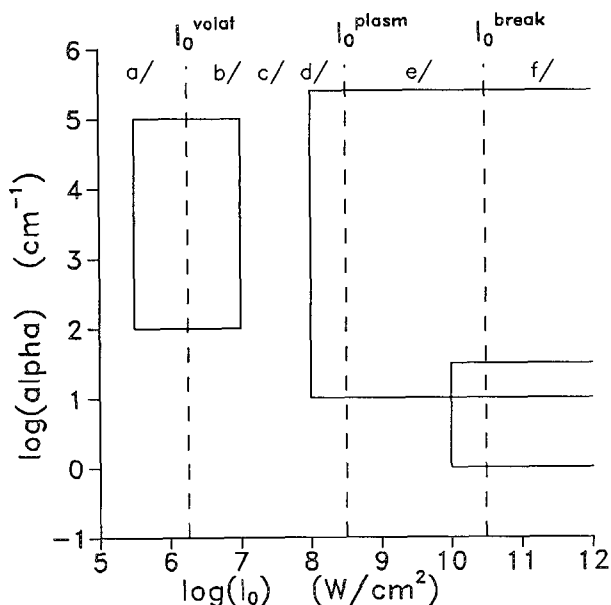
FIG. 1.--Various regimes of laser solid inter-
action are roughly divided according to laser
irradiance and optical absorption coefficient.

well defined, shifts can be expected in a given
experiment according to the choice of laser or
target material.

In an earlier study we dealt with the tran-
sition from normal absorption of the laser-gen-
erated plume to plasma absorption characterized
by 10^8-10^9 W/cm^2 threshold irradiance.[12] For
the high-irradiance transition between regimes
(d) and (e), the threshold was established on
the basis of the investigation of normal ab-
sorption vs plasma absorption.

Matrix-assisted laser desorption is a much
milder process, which typically requires about
10^6 W/cm^2 irradiance and low-melting-point or
low-sublimation-temperature materials. Recent-
ly, it has been shown by elaborate irradiance
threshold measurements that the underlying pro-
cess is a collective effect, similar in princi-
ple to phase transitions.[4] Furthermore, thresh-
old irradiance values change little when the
mass of the guest molecules is changed over an
order of magnitude.[13] Therefore, we assume
that the threshold of our concern marks the
transition between regimes (a) and (b) or be-
tween processes (a) and (c). To get an estimate
of the required irradiance, we set the following
condition. In order to reach volatilization,
the elevated surface temperature due to laser
heating must exceed the melting or sublimation
temperature of the matrix:

$$T_{surf} \geq T_{subl} \tag{1}$$

The rise of the surface temperature $\Delta T_{surf}(t)$
at time t under the influence of a uniform pen-
etrating light source with I_0 irradiance is:[14]

$$\Delta T_{surf}(t) = I_0 \{\delta/\pi^{\frac{1}{2}})$$
$$- \exp(\alpha\delta/2)^2 \ \mathrm{erfc}(\alpha\delta/2)]/\alpha\}K \tag{2}$$

where $\delta = 2(\kappa t)^{\frac{1}{2}}$; the thermal diffusivity

$\kappa = KV_m/c_p$; K, V_M, and c_p are the thermal con-
ductivity, the molar volume, and the specific
heat of the material, respectively. Although,
analytical formulas are shown to overestimate
the temperature jump in pulsed surface heating
at the irradiances of our concern ($< 5 \times 10^7$
W/cm^2) the error is negligible.[15]

If we substitute for the values for material
parameters for nicotinic acid (α_{265} 4 $\times$ 10^4
cm^{-1}; c_p = 150 J/mol K; V_M = 83.5 cm^3/mol;
K = 2 $\times$ 10^{-3} W/cm K), the end of a frequency-
quadrupled Nd-YAG laser pulse (t = 10 ns; I_0 =
10^6 W/cm^2), the surface temperature rise if
$\Delta T_{surf}(t)$ = 202 K. This value (if superim-
posed on the room temperature) compares ex-
tremely well with the sublimation temperature
of this matrix, T_{subl} = 236 C. Indeed, de-
tailed investigations show the threshold irra-
diance of ion generation with MALD for both
nicotinic acid[16] and sinapinic acid[4] matrix to
be around 10^6 W/cm^2. The most successful ma-
trices, their melting points, and their light-
absorption characteristics are listed in Table
1. Other quantities that affect Eq. (2) (such
as K, V_M, and c_p) show little variation for
these materials. Based on these data and on
the evaluation of Eq. (2) it seems understand-
able that all the listed matrices have similar
threshold irradiances.

Thus, we may infer that the phase-transition
scenario we put forward in the introduction
does not contradict the energy-deposition esti-
mates of this section. In the next section we
try to describe the processes in the generated
plume with special emphasis on plume tempera-
tures, for this is the parameter most relevant
to the fate of the entrained large molecules.

Plume Hydrodynamics

Laser-generated plume expansion has been de-
scribed earlier for a variety of condi-
tions.[18-20] In general, we are interested in
the density, temperature, and velocity distri-
butions of the laser-generated plume as they
develop with time. In contrast to the laser
plasma generation experiments, we expect mod-
erate temperatures during the volatilization of
the low-sublimation-point matrices.

In the course of laser-solid interaction,
two distinct phases can be recognized. The
first phase covers the period when the surface
of the solid does not reach the phase transi-
tion temperature. In this regime material
transport can be neglected and the description
only accounts for generation of a hot spot on
the solid surface. The temperature distribu-
tion is governed by the relation between the
laser heating and cooling of the spot by heat
conduction:

$$\partial[\rho e]/\partial t = -\partial[\kappa\partial(\rho e)/\partial z]/\partial z + \alpha_{solid}I \tag{3}$$

where ρe and α_{solid} stand for the energy densi-
ty and absorption coefficient of the solid ma-
terial. We have already seen a special solu-
tion of this equation for the case of a uniform
penetrating source, Eq. (2). Because we now
allow for both phase transitions in the solid

26

TABLE 1.--Melting temperatures and wavelengths and molar extinction coefficients of UV absorption maxima for most successful matrices used in laser desorption of peptides and proteins.[17]

Laser Desorption Matrix	T_m (°C)	λ_{max} (nm)	ϵ_{max} (L/mol·cm)
Nicotinic acid (3-pyridinecarboxilic acid)	236	266	3400
Pyrazinoic acid (2-pyrazinecarboxilic acid)	225	267	7820
Vanillic acid (4-hydroxy-3-methoxy-benzoic acid)	214	259	11900
Sinapinic acid ((3,5)-dimethoxy-4-hydroxy-(trans)cinnamic acid)	192	240	10000
Caffeic acid ((3,4)-dihydroxy-(trans)cinnamic acid)	225	297 235	?
Ferrulic acid (4-hydroxy-3-methoxy-(trans)cinnamic acid)	174	235	?

and various laser pulse profiles, a numerical solution of this equation shall now be sought. This solution can be used afterward as a boundary condition for the description of plume expansion.

The second phase starts when the surface of the solid is heated above the phase-transition temperature. At this stage the vapor pressure of the material becomes significant and the material transport across the surface cannot be neglected. To deal with the expansion problem we must solve a simplified set of hydrodynamic equations that express conservation of mass, momentum, and energy.

$$\partial[\rho]/\partial t = -\partial[\rho v]/\partial z \qquad (4)$$

$$\partial[\rho v]/\partial t = -\partial[p + \rho v^2]/\partial z \qquad (5)$$

$$\partial[\rho(e + v^2/2)]/\partial t \qquad (6)$$
$$= -\partial[\rho v(e + p/\rho + v^2/2)]/\partial z + \alpha_{plume}I$$

where ρ, v, p, and α_{plume} denote the density, hydrodynamic velocity, pressure, and absorption coefficient of the plume, respectively. We note that all the transport equations, Eqs. 3-6, are written in one-dimensional form. Therefore, only processes along the z corrdinate (perpendicular to the surface) are accounted for and transport is neglected in the model. Assuming a Gaussian beam profile, this approximation is good in the middle of the beam, where radial gradients are vanishing. However, the relevance of the results is not altered by this restriction, because at the volatilization threshold (where most of the experimental work is done) only the center of the spot is hot enough to

contribute substantially to the volatilization process.

Coupling between Eqs. (4) to (6) and Eq. (3) is provided by the Clausius-Clapeyron equation for the vapor pressure. Under laser desorption circumstances (i.e., near threshold irradiance), the plume remains optically thin; thus, the laser-absorption term in Eq. (6) can be neglected. The plume is heated only by the transfer of warm material across the interface, and is cooled by the expansion process. Due to the relatively low temperatures, thermal ionization and radiative cooling are not significant factors, either. Solutions of Eqs. (4-6) were found by a computer code developed and reported earlier.[18]

Results

Nicotinic acid/vacuum interface was investigated under the influence of a 10ns frequency-quadrupled Nd-YAG laser pulse. The temporal profile of the 10^7-W/cm^2 irradiance pulse was approximated by a square wave. Spatial distribution of plume density and temperature above the surface are shown in Fig. 2. Three time stages are depicted in order to visualize post-pulse behavior.

The spatial density profile at the end of the laser pulse (10 ns) showed monotonous decay (Fig. 2a). Subsequent cooling of the surface substantially lowered the rate of evaporation. Consequently, the density immediately above the target dropped quickly and the plume packet detached from the surface to produce a drifting and expanding plume packet (25 ns, 50 ns). We estimated the kinetic energy of the particles

stemming from plume translation. The drift velocity of the plume center of mass, V_{drift} = 3×10^4 cm/s, could be converted to kinetic energy: $E_{kin} \approx 60$ meV. This is a value quite close to the measured energies of molecules in the plume: $E_{kin} = 40$ meV (2×10^6 W/cm2, 248 nm, 13 ns excimer laser pulse, tryptophan target).[21] It is worthwhile to notice that the plume density was relatively high; at the 50ns time stage its maximum density still exceeded 1/10th of the solid density. With further expansion of the vapor cloud, its density dropped quickly. The high initial plume density has important repercussions regarding the possibility of gas phase processes. It seems possible that certain reactions are induced in this dense cloud of particles. Most important among them are protonation, alkalination, and adduct ion formation of the guest molecules. Indeed, there is clear experimental evidence that the appearance of sodium and/or potassium containing quasi-molecular ions are bound to the presence of sodium and/or potassium ion signals and to the generation of a dense plume.[22]

Another interesting feature of the plume was the spatial and temporal variation of the temperature. The surface of the nicotinic acid was heated to the phase-transition temperature, but a quick decay of plume temperature was observed with increasing distance from the surface (Fig. 2b). The actual value of the temperature drops well below room temperature due to the expansion cooling. Comparison of density and temperature distributions at 50 ns provided an estimate of 140K at the center of mass of the plume. The obvious consequence of such a cooling would be a stabilizing effect for the entrained large molecules. The situation is very reminiscent of the two laser experiments, in which jet cooling of the large molecules is usually introduced between the desorption and ionization step. Experimental verification of low plume temperatures by thermally labile molecules as molecular thermometers was reported earlier.[22]

However, simple heating of the matrix lattice by the laser pulse gives no satisfactory explanation of all the findings of UV MALD experiments. In contrast to the presence of intact guest molecules in the plume, host fragments can be abundant in the mass spectrum. This observation points to the importance of exploring the possible energy-transfer pathways in the system.[9] In the UV experiments, primary energy deposition leads to electronic excitation of the host molecules ($\pi \to \pi^*$ transition in the case of a nicotinic acid matrix). Quick internal conversion processes lead to vibrationally highly excited ground states. Part of the host molecules decompose from these vibrational states, but another part transfers its energy to the lattice. Thus, the lattice is heated and the phase transition temperature can be occasionally reached. At this stage the question arises: what prevents energy transfer to the guest molecules? According to our calculations of the energy transfer rates in this system, there is a bottleneck hindering the heating of internal vibrational degrees of freedom of the guest molecules.[10,11] This bottleneck is related to weak coupling between the lattice vibrations and the intramolecular vibrations of the large molecules.

Another important question is the origin of the ions in the system. It is clear from postionization experiments that the degree of
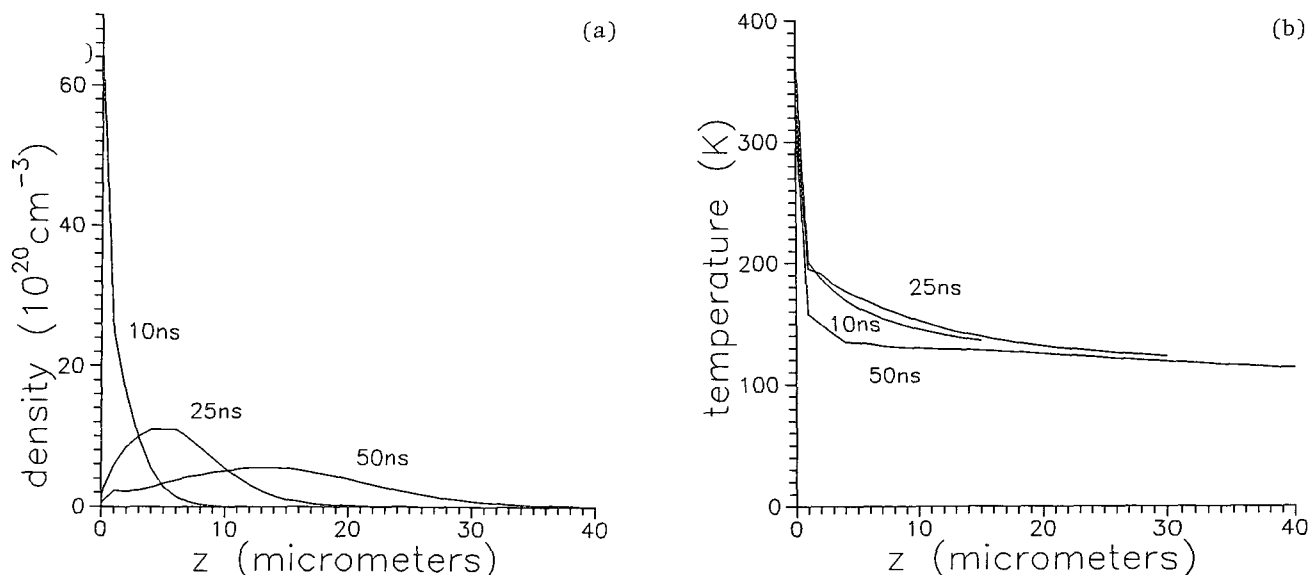
FIG. 2.--Evolution of plume above nicotinic acid surface as consequence of frequency-quadruples Nd-YAG laser pulse (10 ns; 10^7 W/cm^2). (a) Density profiles perpendicular to surface show detachment and expansion. (b) Although surface temperature reaches sublimation temperature, substantial cooling of plume is observed.

ionization in the plume is very low. In light of the calculated temperature values, it is also obvious that thermal ionization is not a feasible ion-production mechanism in these experiments. Rather, protonation and other adduct ion formation mechanisms shall be regarded as the primary source of ions. These processes can be discussed in terms of preformed ion volatilization and ion-molecule reactions. Guest particles that are already in their ionized form in the solid state (preformed ions) can give rise to gas phase ions extremely easily. Molecular ions of these substances in MALD experiments could be produced even without ion production from the matrix.[22] These findings support the suggestion that the role of the matrix is to embed and separate the guest particles in the solid phase and to entrain and cool them in the course of volatilization.

Conclusions

In this communication we suggested how to explain matrix-assisted laser desorption of intact large molecules. According to preliminary estimates of energy deposition, it seems likely that laser heating of the matrix to the phase-transition temperature is a prerequisite to carryng out successful MALD experiments. The generated plume has been described in terms of hydrodynamics and the results reflect several important features of the measurements. Most important, kinetic energies of neutral particles can be recovered. Furthermore, strong cooling of the plume is predicted, which would rationalize the absence of thermal degradation processes. Detailed calculations of plume expansion are under way to explore the effect of matrix and laser parameters on the desorption process.

References

1. K. Tanaka, H. Waki, Y. Ido, S. Akita, Y. Yoshida, and T. Yoshida, "Protein and polymer analyses up to m/z 100 000 by laser ionization time-of-flight mass spectrometry," *Rapid Comm. Mass Spectrom.* 2: 151, 1988.
2. M. Karas and F. Hillenkamp, "Laser desorption ionization of proteins with molecular masses exceeding 10 000 Daltons," *Anal. Chem.* 60: 2299, 1988.
3. R. C. Beavis and B. T. Chait, "The role of matrices and wavelength in the matrix assisted laser desorption of proteins," in R. M. Caprioli, Ed., *Proc. 38th ASMS Conf. Mass Spectrometry and Allied Topics*, Tucson, Ariz., 1990, 152.
4. W. Ens, Y. Mao, F. Mayer, and K. G. Standing, "Properties of matrix-assisted laser desorption; measurements with a time-to-digital converter," *Rapid Comm. Mass Spectrom.* (in press).
5. A. Vertes, L. Balazs, and R. Gijbels, "Matrix-assisted laser desorption of peptides in transmission geometry," *Rapid Comm. Mass Spectrom.* 4: 263, 1990.
6. P. Williams, "Mechanical approaches to volatilization of large biomolecules," in A.

Hedin, B. U. R. Sundqvist, and A. Benninghoven, Eds., *Ion Formation from Organic Solids (IFOS V)*, Chichester (England): Wiley, 1990, 131.
7. R. E. Johnson, "Mechanisms for the desorption of large organic molecules," *Int. J. Mass Spectrom. Ion Processes* 78: 357, 1987.
8. A. Vertes, "Laser desorption of large molecules: Mechanisms and models," in K. G. Standing and W. Ens, Eds., *Methods and Mechanisms for Producing Ions from Large Molecules*, New York: Plenum (in press).
9. A. Vertes and R. Gijbels, "Restricted energy transfer in laser desorption of high molecular weight biomolecules," *Scanning Microsc.* (in press).
10. A. Vertes, R. Gijbels and R. D. Levine, "Homogeneous bottleneck model of matrix-assisted ultraviolet laser desorption of large molecules," *Rapid Comm. Mass Spectrom.* 4: 228, 1990.
11. A. Vertes and R. D. Levine, "Sublimation versus fragmentation in matrix-assisted laser desorption," *Chem. Phys. Letters* 171: 284, 1990.
12. A. Vertes, M. DeWolf, P. Juhasz, and R. Gijbels, "Threshold conditions of plasma ignition in laser ionization mass spectrometry of solids," *Anal. Chem.* 61: 1029, 1989.
13. A. Hedin, A. Westman, P. Hakansson, and B. U. R. Sundqvist, "Laser desorption mass spectrometry: Some technical and mechanistic aspects," in K. G. Standing and W. Ens, Eds., *Methods and Mechanisms for Producing Ions from Large Molecules*, New York: Plenum (In press).
14. M. von Allmen, *Laser-beam Interactions with Materials: Physical Principles and Applications*, Berlin: Springer, 1987, 55.
15. J. M. Philippoz, R. Zenobi, and R. N. Zare, "Pulsed heating of surfaces: Comparison between numerical simulation, analytical models, and experiments," *Chem. Phys. Letters* 158: 12, 1989.
16. R. C. Beavis and B. T. Chait, "Factors affecting the ultraviolet laser desorption of proteins," *Rapid Comm. Mass Spectrom.* 3: 233, 1989.
17. J. G. Grosselli and W. M. Ritchey, Eds., *Atlas of Spectral Data and Physical Constants for Organic Compounds*, Cleveland: CRC Press, 1975.
18. L. Balazs, R. Gijbels, and A. Vertes, "Expansion of laser generated plumes near the plasma formation threshold," *Anal. Chem.* 63: 314, 1991.
19. A. Vertes, P. Juhasz, M. DeWolf, and R. Gijbels, "The role of energy deposition processes in the understanding of laser microprobe analysis mechanisms," *SEM/1988* II, 1853.
20. A. Vertes, P. Juhasz, M. DeWolf, and R. Gijbels, "Hydrodynamic modeling of laser plasma ionization processes," *Int. J. Mass Spectrom. Ion Processes* 94: 63, 1989.
21. B. Spengler, U. Bahr, M. Karas, and F. Hillenkamp, "Postionization of laser-desorbed organic and inorganic compounds in a time of flight mass spectrometer," *Anal. Instr.* 17: 173, 1988.

22. J. Clareboudt, M. Claeys, R. Gijbels, and A. Vertes, "Aryltriphenylphosphonium halides as 'molecular thermometers' in matrix assisted laser desorption," *Proc. 39th ASMS Conference on Mass Spectrometry and Allied Topics*, Nashville, Tenn. (in press).

CHARACTERIZATION OF THIN POLYMER FILMS BY LAMMS

P. J. Cunningham, J. A. Leake, and E. R. Wallach

The analysis of bulk polymers by laser micro-probe mass spectrometry (LAMMS) generally yields little structural information, as the laser power densities required to remove the polymer molecules from the solid phase cause degradation of the polymer to form carbon clusters. One possible solution is to use post-ionization to separate and hence gain more control over the ablation and ionization stages.[1] An alternative solution is to use matrix-assisted ionization[2] to favorably change the ion formation process; for instance, Karas and Hillenkamp[3] have described the use of strong ultraviolet (UV) absorbing matrices such as nicotinic acid/glycerol to allow the detection of high mass bioorganic ions. However, such organics have specific molecular weights, and the use of UV absorbers to assist ionization is not generally applicable to the detection of high-mass ions of synthetic polymers, each of which has a distribution of molecular weights. Alternative methods are therefore being investigated. The use of inorganic matrix additions to produce characteristic fragment spectra from synthetic polymers is considered in this paper. Results demonstrating the characterization of synthetic polymers by LAMMS after deposition from solution onto various substrates are presented together with initial semiquantitative results from a series of liquid crystal copolymers on a metal substrate. The use of pattern recognition as an aid in characterization of these polymers is also demonstrated. Finally, the relative success in performing semiquantitative analysis of polymers by LAMMS is explained in terms of the energy distributions for the resulting characteristic ionized polymer fragments and the transmission of these ions through the instrument.

Effect of Ionization Energy of the Substrate on Formation of Characteristic Ions

Ion attachment reactions are generally recognized to be a major ion formation process occurring in the LAMMS analysis of organics, with anions or cations attaching to neutral molecules to form charged complexes.[4] In the analysis of thin polymer films on metal substrates, characteristic fragment spectra are formed in place of the carbon cluster spectra usually observed at the same laser power density. In the

current work, specimens of polystyrene oligomers (peak molecular weight = 867 a.m.u.) were prepared by deposition from methylene chloride solution onto substrates (polished to a 1μm finish where possible). To investigate the role of the matrix additions, a number of substrates were selected with a wide range of ionization energies; Al (ionization energy of 5.98 eV), Cr (6.76 eV), Ni (7.63 eV), Si (8.15 eV), Zn (9.39 eV), and graphite (11.26 eV) were used. The specimens were analyzed by a LIMA-2A instrument, described in detail elsewhere,[5] and the laser power density at the sample was varied in the range $10^7 - 10^{10}$ W cm^{-2} in order to obtain transmission curves, i.e., graphs of the number of ions detected at the electron multiplier plotted against the number of ions produced at the sample (proportional to the incident laser energy density).

In repeated analysis of the same region, carbon cluster ion spectra were observed until the polymer/substrate interface was reached, when characteristic fragment spectra of polystyrene were obtained for most substrates (Fig. 1). This result was observed for all laser power densities. On the graphite substrate, carbon clusters were formed at low laser power densities and only at a laser power density of 5×10^8 W cm^{-2} was the substrate ionized with sufficient energy to initiate the ionization mechanism for producing characteristic fragment ions (Fig. 2). Similar results were also observed for silicone oil on graphite. Thus, it is evident that the substrate does not merely absorb the radiation from the laser pulse; it permits controlled fragmentation rather than disintegration of the polymer and the mechanism appears to be related to the ionization energy of the substrate. In addition to the characteristic fragment ion spectra, molecular adduct ions were formed for polystyrene oligomers on Al, Cr, and Ni substrates (e.g., Fig. 3) and the yield of these adduct ions was found depend inversely on the ionization energy of the metal. The yield was highest for Al and lowest for Ni, whereas no molecular adduct ions were obtained with Si, Zn, or graphite substrates for any of the laser power densities used. The yield of adduct ions also increased with increases in the laser power density over the entire range of laser power densities used.

Transmission of Organic Ions in the LAMMS Instrument

Transmission curves for inorganic samples show that, as the laser power density is varied, the number of ions detected initially
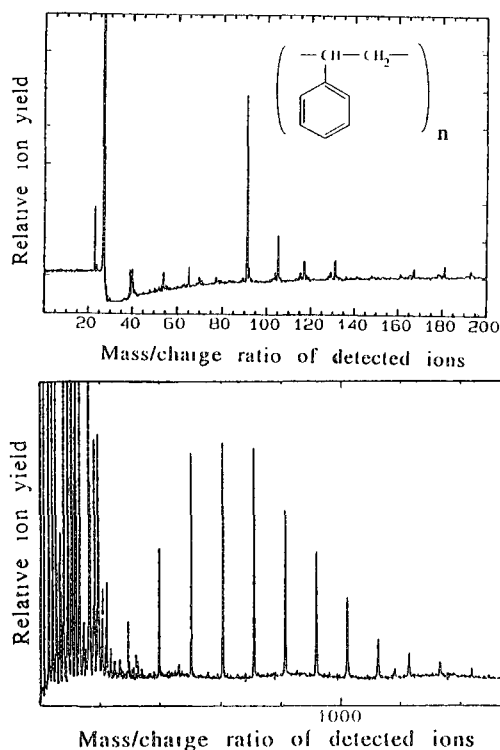
FIG. 1.--Composition of BN copolymers.

FIG. 2.--Mass spectrum showing characteristic fragment ions obtained from polystyrene deposited on an aluminum substrate.

FIG. 3.--Molecular adduct ion distribution observed for polystyrene on aluminum, chromium, and nickel substrates.

FIG. 4.--Transmission curve obtained for complete fragmentation to carbon, hydrogen, and oxygen ions of thin film of polystyrene deposited on chromium substrate.

FIG. 5.--Transmission curve obtained for formation of molecular adduct ions from thin film of polystyrene deposited on chromium substrate.

increases in the number of ions produced.[5] Figure 4 shows the transmission curve for carbon, hydrogen, and oxygen ions detected in the mass range 0-20 a.m.u. due to the fragmentation of polystyrene to its elemental constituents. This curve shows a similar trend to that observed for inorganic samples. As the density of the plume of charge increases, the individual charges can no longer be considered to act independently, and collisional and space-charge effects lead to the ions of a particular mass-to-charge ratio having a wide energy spread rather than the unique value expected as a consequence of the extraction voltage used. Thus, in the LAMMS instrument used in the current work, ions with energies outside a narrow 200eV energy window (i.e., greater or less than 100 eV from the 3000eV extraction voltage) are filtered out. In contrast, Fig. 5 shows the transmission curve for the polystyrene oligomer ions of mass 250-1500 a.m.u.; the plot does not saturate and the yield of ions detected is proportional to the yield of ions produced. Similar trends are observed for the characteristic fragment ions of polystyrene in the mass
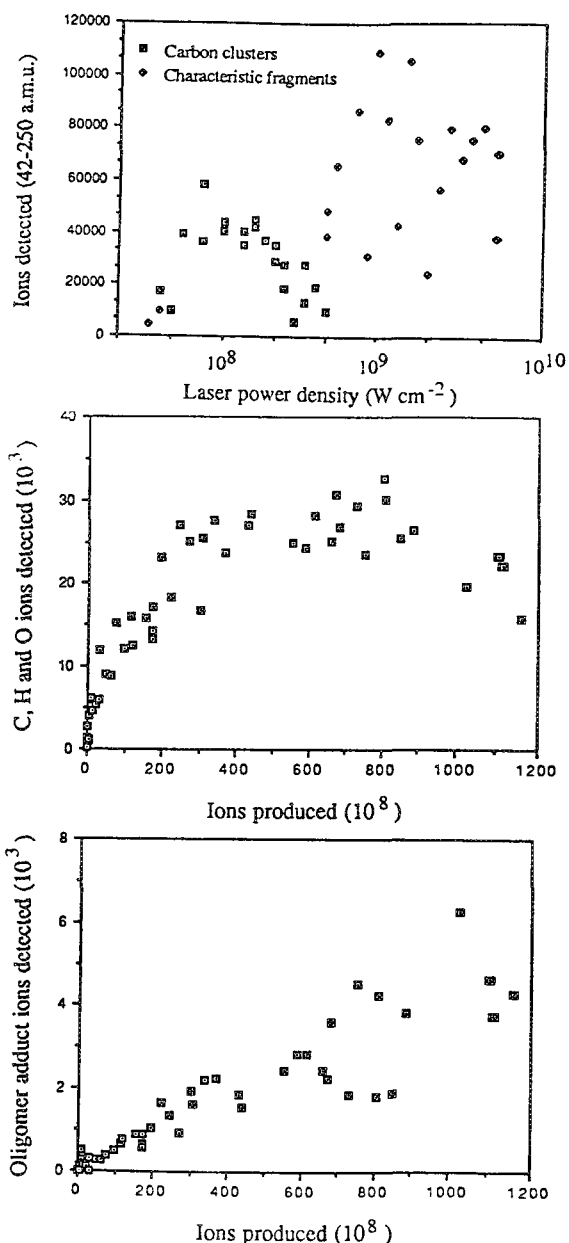
range 40-250 a.m.u. The explanation is that the total number of fragment ions and oligomer adduct ions produced is significantly smaller than the total ion yield for carbon, hydrogen, and oxygen. Also, the ions begin to separate out depending on their mass as soon as they are formed and the organic fragment and molecular adduct ions are formed over an extensive mass range. Hence, the plume of organic ions is less dense and space-charge and collisional effects are less significant. We confirmed this explanation by placing an electron multiplier detector in the reflectron position, which allowed measurements of the full range of ion energies without any ion energy filtering.[6] A typical resulting spectrum of polystyrene on a chromium substrate is shown in Fig. 6, in which the chromium peak (A) has a very broad energy spread and is typically split. (Although saturation of the detector has occurred for the chromium peak, the peak splitting is still obvious.) The shaded re-

gion of peak A shows the area that would have been measured after ion filtering if the standard operating mode had been used, and it is evident that this region is not representative of the yield of unfiltered ions. In contrast, the ion energy spreads of the organic peak (e.g., B) are much narrower and the peaks are reasonably symmetrical. Hence, the yield of organic ions detected after energy filtering would remain representative of the initial yield of ions produced; and this evidence provides the basis for quantitative analysis of polymer films.

Quantitative LAMMS Analysis of BN Liquid Crystal Copolymers

In order to investigate the quantitative capability of the LAMMS technique for the analysis of polymers films, a series of liquid crystal copolymers were chosen consisting of varying amounts (see Table 1) of the two components, hydroxybenzoic acid (B) and hydroxynaphthoic acid (N). The insoluble BN liquid crystal copolymers were deposited onto an aluminum substrate by melting a crystal onto the substrate and allowing it to spread into a thin film. Six accumulations, each of 10 spectra, were recorded at a laser power density of

TABLE 1.--Composition of BN copolymers.

Specimen	HBA content (%)	HNA content (%)
BN 13	75	25
BN 14	66.7	33.3
BN 15	50	50
BN 17	25	75
BN 18	80	20
poly HBA	100	0

approximately 10^8 W cm^{-2} for each copolymer composition and also for the individual homopolymers. A typical resulting spectrum for the 50/50 composition is shown in Fig. 7. The important features to note are that there are prominent peaks at 121 a.m.u. and 171 a.m.u., corresponding to ions of the repeat monomer units plus hydrogen; and that few ion peaks are observed above these masses. These peaks occur because the copolymer fragments at the weak C-O bonds and it is a common feature of LAMMS spectra of polymers that the monomer
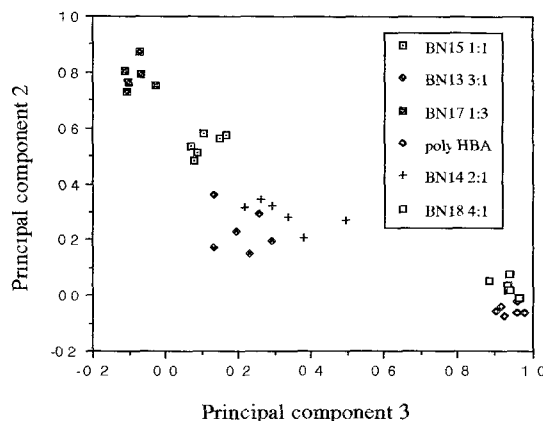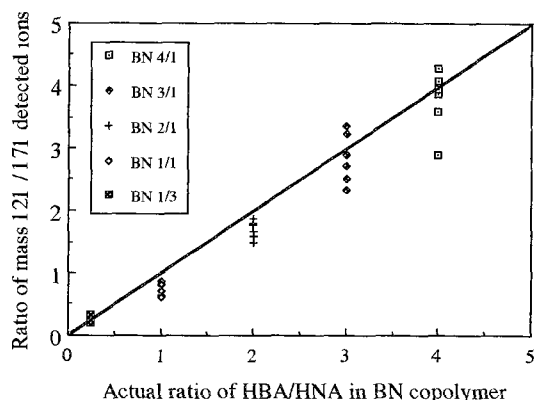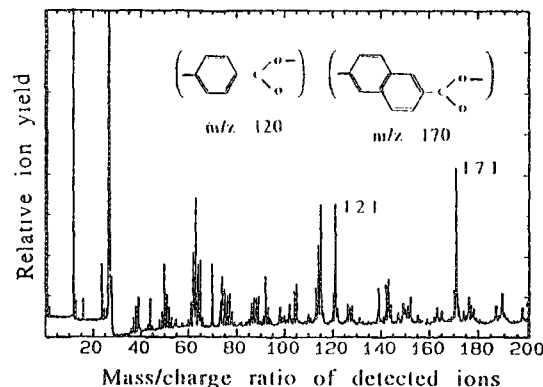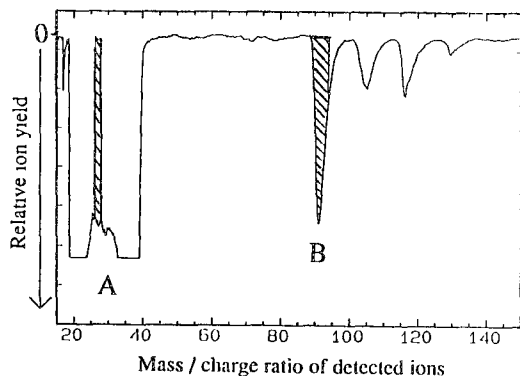
FIG. 6.--Spectrum obtained from thin film of polystyrene on aluminum substrate recorded with the electron multiplier in the reflectron position; i.e., without energy filtering. (Note that the mass spectrum is inverted in this mode of operation.)

FIG. 7.--Structure and characteristic fragment mass spectrum of BN liquid crystal copolymer.

FIG. 8.--Comparison of actual and detected compositions of BN copolymer series.

FIG. 9.--Principal component score plot showing separation of BN copolymers of different compositions.

unit plus hydrogen ion signal is often the highest mass ion signal of significance. It is also significant to note that the relative intensities of the 121 a.m.u. and 171 a.m.u. peaks are similar to the concentrations of the two components in the copolymer and so can be used to distinguish BN copolymers of different compositions. The results are shown in Fig. 8, in which the ratios of ions detected for the 121 a.m.u. and 171 a.m.u. peaks are plotted against the actual ratios of the hydroxybenzoic acid and hydroxynaphthoic acid concentrations for each sample. Each point represents the average of 10 mass spectra; it is clear that the 1/3, 1/1, and 2/1 copolymers can be distinguished using this method but that the 3/1 and 4/1 compositions overlap to some extent. It is also observed that the experimentally measured ratios are generally lower than the actual ratios, because the ions of 171 a.m.u. are slightly more stable than those of 121 a.m.u. due to their greater aromaticity and so are less likely to fragment. The scatter in the results is a consequence of problems in defining peaks due to relatively poor mass resolution (associated with the ion formation mechanism) and also relatively few data points sampled in each peak. The latter problem can be overcome by improved data collection (e.g., use of a faster transient recorder).

Pattern Recognition Analysis of LAMMS Data

The BN copolymer series is ideal for quantitative analysis in that the repeat monomer units plus hydrogen ions are particularly stable. However, for many polymers the equivalent characteristic monomer peaks are not so prominent in the resulting mass spectrum because the ions fragment further to form more stable ions of lower masses. In general, the characteristic fragment spectra of polymers consist of many ion signals of different masses and it is useful and often necessary to consider the whole spectrum in order to identify a polymer uniquely. Seydel[7] and Odom[8] have given comprehensive accounts of the use of computerized statistical multivariate analysis techniques to classify successfully biological samples and polymers by finding trends in a large number of spectra. In the present work, principal component analysis (PCA)[9] has been applied to the series of BN copolymers; the resulting component plot is shown in Fig. 9. Similar spectra result in points plotted close to each other. It is evident that the different copolymers are well separated except for the 2:1 and 3:1 compositions, which overlap. It is also noticeable that the 4:1 composition is regarded as very similar to the pure polyhydroxybenzoic acid. This is because only the 20 most significant ion peaks were sampled in each spectrum and most of the peaks representing the N component of the 4:1 composition did not fall into this category. The separation of the 4:1 BN composition and the polyhydroxybenzoic acid could be improved by sampling of more ion peaks in the spectra. The scatter in the data is

again largely due to the problems discussed earlier, namely the mass resolution and the number of data points in each peak.

Conclusions

It has been shown that reproducible characteristic mass spectra may be produced from thin polymer films deposited onto various substrates, and that the formation and intensity of the spectra depend on the ionization energy of the substrate. Even at high laser power densities, the yield of organic ions detected remains representative of the population of ions produced in the plasma. Thus, initial results have shown that quantitative LAMMS analysis of polymers is feasible and not restricted by transmission losses in the instrument due to space charge and collisional effects which are observed for inorganic materials. The pattern-recognition results confirm the usefulness of statistical analysis to separate LAMMS spectra of different polymers and also confirm that deposition of thin polymer films on metal substrates is a successful way of obtaining reproducible mass spectra.

References

1. J. B. Pallix, U. Schuhle, C. H. Becker, and D. L. Huestis, "Advantages of single-photon ionisation over multiphoton ionisation for mass spectrometric surface analysis of bulk organic polymers," *Analytical Chemistry* 61: 805, 1989.
2. M. Karas, D. Backman, U. Bahr, and F. Hillenkamp, "Matrix-assisted ultraviolet laser desorption of non-volatile compounds," *Int. J. Mass Spectrometry and Ion Processes* 78: 53, 1987.
3. M. Karas and F. Hillenkamp, "Laser desorption ionisation of proteins with molecular masses exceeding 10 000 daltons," *Analytical Chemistry* 60: 2299, 1988.
4. D. M. Hercules, "Organic mass spectrometry using the laser microprobe," *Pure and Applied Chemistry* 55: 1869, 1983.
5. K. W. Hutt, J. Housden, and E. R. Wallach, "Anomalous ion transmission in a laser microprobe (LAMMS): Investigation by high frequency monitoring of the current through the sample/target," *Int. J. Mass Spectrometry and Ion Processes* 94: 237, 1989.
6. J. Housden, K. W. Hutt, and E. R. Wallach, "Evolution of ion energy distributions with increasing ion yields in a laser microprobe mass spectrometer (LAMMS)," *Microbeam Analysis—1989*, 269.
7. B. Lindner and U. Seydel, "Pattern recognition as a complementary tool for the evaluation of complex LAMMS data," *Microbeam Analysis—1989*, 286.
8. R. W. Odom, F. Radicati di Brozolo, P. B. Harrington, and K. J. Voorhes, "Polymer characterization and classification by use of LAMMS and principal component analysis," *Microbeam Analysis—1989*, 283.
9. "FACTOR analysis," *SPSS-X User Guide*, 3rd ed., SPSS Inc., 1988, 480.

MICROANALYSIS OF TRACE ELEMENTS AND NOBLE GAS ISOTOPES IN MINERALS AND FLUID INCLUSIONS

J. J. Irwin and J. K. Bohlke

The low abundances of the noble gases in most minerals and in the atmosphere, combined with effective high-vacuum technology, enables construction of mass spectrometers having very low backgrounds. For some isotopes of Kr and Xe, the blank in a mass spectrometer can be a few thousand atoms, which permits analysis of a sample containing the equivalent of less than 10^{-6} cc of "air." Measurement of the abundance of the noble gas isotopes (NGI) in rocks is important, largely as a consequence of production of some isotopes by natural nuclear processes such as radioactive decay, spontaneous fission, and reactions between subatomic particles and nuclei. Noble gas isotopes can also be "synthetically" produced from Cl, K, Ca, Br, Se, I, Te, Ba, and U by neutron irradiation of a sample in a nuclear pile, which makes measurement of very low concentrations of these elements possible.[1] Simultaneous analysis of natural and pile-produced isotopes in the same gas sample enables measurement of the abundance of some "parent" elements and daughter-product isotopes at the same time, an approach initially used to identify the extinct decay of ^{129}I[2,3] which was followed by development of the $^{40}Ar/^{39}Ar$ age-dating technique.[4]

In the most common procedure, rock fragments are incrementally heated under vacuum, which releases NGI progressively in a stepwise fashion up to the point of fusion. Although useful for distinguishing separate components of gas in heterogeneous samples, this approach does not permit identification of the exact source of the gas, a problem circumvented by the development of the laser-microprobe gas extraction method.[5] A high-sensitivity, low-blank-mass spectrometer, coupled with a laser-microprobe gas extraction system designed for simultaneous analysis of Ar, Kr, and Xe in submilli-gram sized samples of rocks, was developed and initially used to identify the phases in meteorites carrying extinct ^{129}I.[6] More recently

the laser-microprobe mass spectrometer (LMMS) technique has been applied to terrestrial problems, with emphasis on the nature and origin of fluid inclusions (FI) in minerals.[7,8] The purpose of this report is to document the capabilities of this instrument and to present data that illustrate the significance of the LMMS appraoch to some aspects of geochemistry.

Equipment and Procedure

The mass spectrometer used in these analyses is a glass envelope, 60° sector, statically operated machine[9] constructed specifically for microanalysis.[6] Noble gases are usually extracted by use of a Jarrell-Ash model 46-606 Nd-YAG laser microprobe. The laser directs its energy to a mineral grain through the microscope optics, which permits visual targeting. The laser microprobe can be operated in two modes. In non-Q-switched mode, the laser delivers a series of 1 s pulses that last for ∿200 μs. The laser is operated in non-Q-switched mode to extract gas from materials that absorb the wavelength of light emitted by this laser (1 μm) such as hornblende, biotite, garnet, and basalt galss. Scanning electron microscope images of laser craters indicate that single-laser craters are cone shaped and approximately 70 μm deep, thinning with depth from ∿100 μm in diameter at the surface, with a volume estimated to be 2×10^{-7} cc (Fig. 1). In order to observe and characterize FI by petrographic techniques, most studies of FI in rocks are of minerals transparent or translucent to visible light (i.e., quartz, calcite, fluorite, barite, topaz, feldspars) that do not usually absorb the wavelength of light emitted by the laser. Noble gases are extracted from FI in these minerals by operation of the laser in Q-switched mode, which yields a 1-2 s pulse of energy of ∿1 Joule. The laser is fired repeatedly until the mineral is visibly fractured or ablated, which releases the gases from FI (Fig. 2). The mechanism by which the short, high-energy Q-switched laser pulse causes FI to rupture is uncertain. Data from synthetic and natural FI samples indicate that significant amounts of gases are not released from the "host minerals"; the effect is that of "micro crushing,"[10] although it is possible that a small degree of melting occurs.

It is also possible to extract NGI from samples by passing a current through beehive-shaped, tightly wound conical coils of Ta or W that are mounted inside a vacuum-tight flange and connected to an electrical feedthrough.[11] One or more grains (usually 50-200 μg) are loaded into each coil. These miniature coils can be used as "micro furnaces" to fuse standards, neutron irradiation monitors,[10] and

FIG. 1.--Typical laser craters in basalt glass, formed by non-Q-switched laser shots. Scale bar, 100 μm. Each pit was formed by one or two laser shots.

FIG. 2.--Typical laser ablation of quartz, caused by 20 Q-switched laser shots in small area. Scale bar, 100 μm. Breached FI are visible both in smooth sample surface and in laser excavation.

FIG. 3.--Plot of ^{38}Ar vs ^{36}Ar in basalt standard (which contains atmospheric NGI) and FI in high-grade metamorphic rocks (HGMR) from Sri Lanka. There are at least two components of Ar distinct from "air" that occur in different types of FI in the HGMR from Sri Lanka: (1) ^{36}Ar/^{38}Ar $\sim$10, probably caused by production of ^{36}Ar from ^{38}Cl by thermal neutron capture, (2) ^{36}Ar/^{38}Ar $\sim$3.5, probably caused by production of ^{38}Ar from ^{35}Cl by α-particle-induced reactions. One analysis (upper left) probably indicates localized in situ production of ^{38}Ar from reactions with α particles. Analysis of bulk sample of this rock would yield average composition similar to "air," which would obscure presence of nucleogenic gases. Each count/s corresponds to 1.07×10^5 atoms of Ar.

FIG. 4.--Plot of ^{80}Kr/^{84}Kr vs ^{82}Kr/^{84}Kr in basalt standard (which contains atmospheric NGI, ^{80}Kr/^{84}Kr = 0.04, ^{82}Kr/^{84}Kr = 0.2) and FI in Stripa granite.[19] Data from standards and samples were gathered at similar count rates (Fig. 3). Measured "excesses" (abundances greater than atmospheric) of ^{80}Kr and ^{82}Kr are correlated, with average ratio of excess ^{80}Kr:^{82}Kr = 2.8 ± 1. This ratio of ^{80}Kr:^{82}Kr is appropriate for production of these isotopes from neutron capture on ^{79}Br and ^{81}Br, respectively, in the Stripa granite, nucleogenic reactions not previously reported in rock samples.

(Cont'd.)
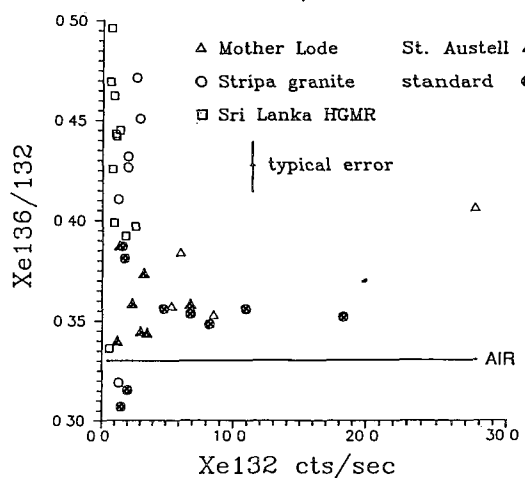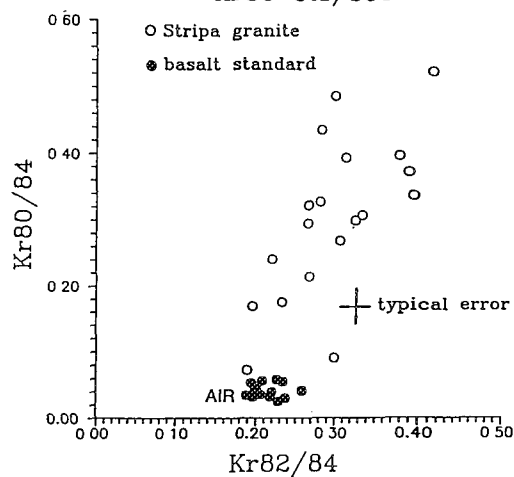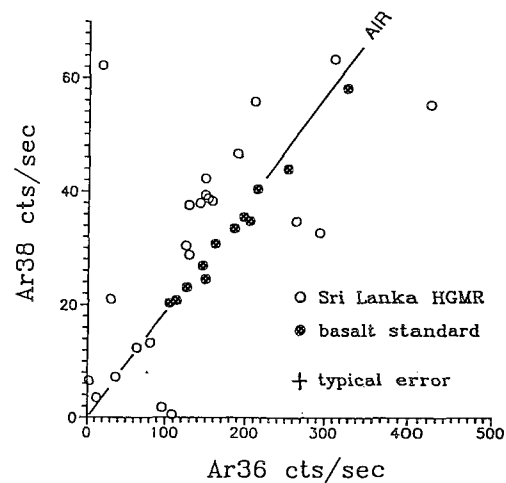
samples that have very high melting temperatures (such as quartz); to outgas samples incrementally, and to heat materials transparent to laser light. The combined capabilities of laser-microprobe and Ta-coil extraction methods enable extraction of gas in samples ranging from $\sim 5 \times 10^{-7}$ g (the mass of a single non-Q-switched laser shot) to nearly 1 mg.

Sample Preparation

In preparation of samples, care is taken to avoid contamination of samples with hydrocarbons, which can cause increased background at important masses (e.g., ^{39}Ar) and are notoriously difficult to remove from high vacuum systems. Saw blades, drills, and grinding laps are cleaned before use. In studies of FI, all samples are prepared by thinning and polishing in pure silicon carbide or alumina grit, lubricated with distilled water. Although it is often desirable to thin and polish rock specimens in order to observe microscopic features, this process usually requires mounting the rock in an epoxy, which is invariably a hydrocarbon compound that cannot be admitted into the mass spectrometer. A high-vacuum leak sealant ("Vac Seal") has been used to mount samples on a glass slide during thinning and polishing, with modest success, as it does not form a very "hard" epoxy. By use of Vac Seal as a mounting medium, some rock samples containing muscovite, amphibole, garnet, and pyroxene have been made into polished petrographic "thick sections" ~ 100 μm thick, neutron irradiated, and laser-microprobed without evidence of interferences.[12]

Standards

In order to monitor the accuracy of measurement of isotope ratios; to determine the absolute and relative sensitivity of the machine for Ar, Kr, and Xe; and to calibrate production of NGI during neutron irradiation, four types of standards have been developed.

1. To determine the accuracy of measurement of Ar, Kr, and Xe isotope ratios over a range of count rates similar to most natural samples, gases are extracted from a synthetic basalt glass containing known concentrations of atmospheric NGI measured by isotope dilution,[13] with the laser-microprobe in non-Q-switched mode (Fig. 1). Each laser shot outgasses a fairly consistent volume of the basalt ($\sim 2 \times 10^{-7}$ cc), so by firing the laser between one and 50 times it is possible to extract a variable and pre-

dictable amount of gas (Figs. 3 and 4).

2. Aliquots of "air," typically $\sim 5 \times 10^{-7}$ cc, are sealed in glass microcapillary tubes by a fine torch. The tubes are broken open by the laser microprobe (operated in a Q-switched mode), releasing a small volume of "bona fide air" into the mass spectrometer sample system. The data from these microcapillary tubes are used to calibrate the sensitivity of the machine and to assess the accuracy of measurement of Xe isotope ratios at low count rates (Fig. 5).

3. A standard for measurement of relatively large amounts of Xe was prepared by implantation of aluminum foil with 340 atoms/μm^2 of atmospheric Xe.[6] A single laser shot releases Xe from an area of foil of typically 10^{-4} cm^2. The data from the foil are useful for assessing possible effects of isotopic "memory," which can be a problem in the study of Xe,[14] and for calibration of the sensitivity of the instrument for measurement of Xi.

4. Fluid inclusions containing measured concentrations of K, Cl, Br, I, and Ba were synthesized in pure quartz using established procedures,[15] neutron irradiated, and then analyzed by firing the laser-microprobe in Q-switched mode in preselected areas, thereby releasing natural and neutron-induced gases from FI. The data from synthetic FI were used to calibrate production of ^{38}Ar$_{Cl}$, ^{39}Ar$_K$, ^{80}Kr$_{Br}$, ^{128}Xe$_I$, and ^{131}Xe$_{Ba}$ in neutron irradiation and to establish the reproducibility and accuracy of measurement of some natural isotope ratios such as ^{40}Ar/^{38}Ar[10].

Detection Limits

Measurement of the halogens and K in artificially irradiated samples and production of nucleogenic isotopes in rocks is facilitated by the relatively high neutron capture cross sections of some "parent" nuclides (^{37}Cl, ^{39}K, ^{79}Br, ^{127}I), coupled with very low initial abundances of the "product" isotopes (^{38}Ar, ^{39}Ar, ^{80}Kr, and ^{128}Xe, respectively). In absolute terms, the smallest quantity of an isotope that can be detected must exceed the standard deviation of the blank, as blanks are analyzed before every sample and data are corrected for blank by use of the mean and standard deviation of a representative suite of blanks (usually 10, see Table 1 for a typical blank), plus the error on the analysis. In neutron-irradiated samples, the amount of an isotope that must be present in order to obtain an accurate measurement of the abundance

◄ FIG. 5.--Plot of ^{136}Xe/^{132}Xe vs ^{132}Xe in FI from high-grade metamorphic rocks from Sri Lanka, the Stripa granite, the St. Austell granite, quartz veins from the Mother Lode (Sierra Nevada, California), and capillary tube standards containing atmospheric NGI. Each count/s = 1.56×10^5 atoms of Xe. These data illustrate importance of analyzing samples and standards at similar count rates: note change in accuracy and precision of measurement of ^{136}Xe/^{132}Xe ratios with higher count rates. Many data from standards indicate slightly higher than atmospheric ^{136}Xe/^{132}Xe ratios, presumably caused by memory in the machine. Some data from samples indicate ^{136}Xe/^{132}Xe ratios greater atmospheric and outside "envelope" of data from standards, consistent with presence of Xe derived from spontaneous fission of ^{238}U, which was confirmed in the same data by presence of excess ^{134}Xe.

TABLE 1.--Detection limits of neutron-irradiation products.

product/reactant@	production rate * x 10 E -8	blank atoms E5	atoms of parent req'd for 5 x blank#	grams of parent req'd for 5 x blank	ppm in 1.2 E-5 g$
39Ar/K	5.58	4 ± 1	3.60E+13	2.32E-09	1.93E+02
37Ar/Ca	2.54	2300 ± 300	4.50E+16	3.00E-06	2.50E+05
38Ar/Cl	105.5	10 ± 1.5	4.70E+12	2.80E-10	2.30E+01
80Kr/Br	5204	0.08 ± 0.02	7.20E+08	9.60E-14	8.00E-03
82Kr/Br	1487	0.15 ± 0.03	5.00E+09	6.70E-13	6.00E-02
83Kr/Se	4.15	0.15 ± 0.03	1.80E+12	2.40E-10	2.00E+01
83Kr/U	23.3	0.15 ± 0.03	3.20E+11	1.26E-10	1.05E+01
84Kr/U	43.1	0.45 ± 0.12	5.20E+11	2.06E-10	1.71E+01
86Kr/U	86.3	0.15 ± 0.05	8.70E+10	3.40E-11	2.80E+00
128Xe/I	8562	0.10 ± 0.02	1.30E+09	2.80E-13	2.00E-02
129Xe/U	27.4	0.3 ± 0.1	5.50E+11	2.20E-10	1.83E+01
131Xe/Te	83.9	0.3 ± 0.1	1.80E+11	3.80E-11	3.20E+00
131Xe/U	124	0.3 ± 0.1	1.20E+11	4.70E-11	3.90E+00
131Xe/Ba	15.7	0.3 ± 0.1	9.60E+11	2.2 E-10	1.83E+01
132Xe/U	185	0.3 ± 0.1	8.10E+10	3.10E-11	2.60E+00
134Xe/U	341	0.15 ± 0.05	2.20E+10	8.70E-12	7.00E-01
136Xe/U	274	0.15 ± 0.05	2.70E+10	1.10E-11	9.20E-01

@ assumes neutron-irradiation of 1E19 n/cm^2 in Missouri reactor.
* atoms of noble gas produced in irradiation/atoms of parent element.
# atoms of parent element required to produce count rate of 5 × background (blank) in mass spectrometer.
$ volume of a mineral grain outgassed by ∿20 non-Q-switched laser shot (a typical sample).

of the "parent" element is greater than the absolute detection limit due to propagated errors in the sensitivity for Ar, Kr, and Xe, neutron irradiation production rates, and the blank correction. For the purpose of this report, detection limits for measurement of the abundances of Cl, K, Ca, Br, Se, I, Te, Ba, and U are defined as the quantity of an element that will produce (in neutron irradiation) an amount of the relevant NGI equal to at least five times the blank for that isotope (Table 1). Data from synthetic FI indicate that the abundances of Cl, K, Br, and I can be measured to within ±10-15% at this level.[10] The values listed in Table 1 are for an irradiation of 1 × 10^{19} n/cm^2 in the rotating can position in the Missouri Research Reactor, based on a compilation of data from irradiated synthetic FI and the hornblende standards MMHb-1 and Hb3Gr.[10]

With a few notable exceptions (such as [40]Ar produced by decay of [40]K), deviations in natural isotopic abundances from the composition of the modern atmosphere are usually relatively small. It has been found that some FI in rocks contain NGI distinct from the composition of the modern atmosphere in relatively subtle ways that have not been previously noted (Figs. 3 and 4). The isotopes present "in excess" can be produced by nuclear reactions in rocks and are thought be indicate the presence of nucleogenic NGI in some FI. (Folloiwng convention, the term "nucleogenic" refers to nuclides produced by processes other than radioactive decay or fission.) Analysis of neutron-irradiated

samples can create memory effects in the mass spectrometer; the precision of an isotope ratio (if calculated solely from reproducibility of a measurement) can be a misleading underestimate of the real uncertainty, which must be evaluated by analysis of standards containing similar amounts of gas as the samples (Figs. 3-5). The presence of a nucleogenic or radiogenic NGI is usually noticed when an isotope ratio deviates from atmospheric composition, so the smallest amount of a nucleogenic or radiogenic isotope that can be detected must be determined on the basis of data from standards. An indication of how much of an isotope must be present to be measured (summarized in Table 2) is given by the sum of the error in reproducibility of a standard (the standard deviation in an isotope ratio) plus the deviation of the mean value of an isotope ratio in a standard from its known value (i.e., the deviation in an isotope ratio from atmospheric composition), plus the typical error on the measurement of the same isotope in a sample.

Applications

The LMMS technique was initially applied to problems in cosmochemistry.[5] In the Allende meteorite, sodalite was identified as the main carrier phase for extinct [129]Xe.[6] In the first studies of terrestrial samples it was shown that [40]Ar/[39]Ar ages of microscopic laser "pits" in micas and garnets can be measured, and that some individual crystals of garnet formed in more than one stage.[12,16] Most

TABLE 2.--Detection limits for natural NGI.

Isotope	Detection limit# (atoms $\times 10^5$)	Isotope	Detection limit# (atoms $\times 10^5$)
36Ar	21	124Xe*	0.1
37Ar	2000	126Xe*	0.1
38Ar	9.5	128Xe	0.37
39Ar	5	129Xe	0.6
		130Xe	0.08
78Kr	0.16	131Xe	0.6
80Kr	0.16	132Xe	0.6
82Kr	0.27	134Xe	0.45
83Kr	0.23	136Xe	0.45
84Kr	0.4		
86Kr	0.4		

Amount of an "excess" of each isotope that can be measured in a sample containing natural, nucleogenic, and radiogenic gases, calculated from the sum of the standard deviation of standards and the tupical analytical error.

* Estimated by comparison with isotopes having similar abundances.

rocks contain microscopic inclusions of fluid; it has long been known that these inclusions are samples of fluids present during crystallization of some minerals and deposition of metals in ancient hydrothermal systems. In many rocks the composition of FI varies over a distance of less than a few millimeters, a situation that has frustrated attempts to determine their composition.[17] The LMMS-NGI technique is nearly ideally suited for analysis of materials that are heterogeneous on this scale, and each measurement of Ar, Kr and Xe in a FI sample provides a wealth of information. As discussed in a previous section, it is possible to analyze less than 10^{-11} L of fluid containing "typical" concentrations of Cl, K, Br, and I, or a single cubic FI ∿20-50 μm on a side.[10] Data from neutron-irradiated FI provide a measure of the abundances of elements that control the ability of a fluid to transport metals in solution (Cl), provide important information about the sources of fluids from the relative abundance of the halogens (Cl, Br, and I), and in principle should yield an $^{40}Ar/^{39}Ar$ age of the fluid. The halogens can be useful tracers of sources of fluids, largely because they are not fractionated by temperature-sensitive processes (such as boiling) and are strongly affected by some other processes such as precipitation or dissolution of salts or mixing of different fluids. Variations in the halogen composition of FI that we have measured so far are summarized in Fig. 6.

The abundances of naturally occurring NGI provide information about the origin of FI in several different ways.

1. The abundance of Ar, Kr, and Xe is an indication of the source of gas in FI, as terrestrial fluid reservoirs differ in their elemental composition[18] and some processes common in ancient hydrothermal systems fractionate NGI. Meteoric waters acquire specific concentrations

of gases by equilibrating with the atmosphere and can be changed in the subsurface by a variety of processes: gas loss by boiling, gas loss or gain by interaction with rocks, etc. Metamorphic and magmatic fluids could have a wide range of NGI contents, but are not yet well characterized.

2. Some NGI are formed by radioactive decay or spontaneous fission (such as ^{40}Ar, ^{136}Xe, ^{134}Xe, ^{132}Xe, ^{131}Xe), and the abundance of these isotopes is an unambiguous indication of the presence of the parent isotope in the FI and/or in a source of the fluid prior to trapping of the FI (Fig. 5).

3. In much of the Earth's continental crust, radioactive decay of U and Th has resulted in a significant fluence of α particles and neutrons. Reactions between these nuclear particles and elements that occur in minerals produce NGI. Partly because fluids are enriched in the elements that react with nuclear particles to form NGI (e.g., Cl. Br, I) and partly because fluids can collect and concentrate gases (inert and otherwise) from large volumes of rocks, FI in ancient hydrothermal systems are particularly likely to contain nucleogenic NGI (Figs. 3 and 4). The importance of microanalysis is illustrated by data from some precambrian metamorphic rocks (Fig. 3), in which various types of FI are heterogeneously distributed on a scale of less than 1 mm. Measurement of NGI in these rocks by any bulk analytical technique, using even as little as 1 mg of sample, would tend to average the observed variations and give a mean isotopic composition similar to the modern atmosphere-- when in fact few of the FI contain this composition of gas.

References

1. G. Turner, "Trace elements and extinct ^{129}I in chondrites," *J. Geophys. Res.* 70: 5433-5445, 1965.

2. J. H. Reynolds, "I-Xe dating of meteorites, *ibid.*, 65: 3843-3846, 1980.

3. P. M. Jeffery and J. H. Reynolds, "Origin of excess ^{129}Xe in stone meteorites," *ibid.*, 66: 3583-3583, 1961.

4. C. M. Merrihue and G. Turner, "Potassium-argon dating by activation with fast neutrons," *ibid.*, 71: 2852-2857, 1966.

5. G. H. Megrue, "Isotopic analysis of rare gases with a laser-microprobe, *Science* 257: 1555, 1967.

6. C. L. Kirschbaum, "Carrier phases for iodine in the Allende meteorite and their associated $^{129}Xe/^{127}I$ ratios: A laser microprobe study," *Geochim. Cosmochim. Acta* 52: 679-699, 1988.

7. J. K. Bohlke, C. Kirschbaum, and J. J. Irwin, "Simultaneous analysis of noble gas isotopes and halogens in fluid inclusions in neutron-irradiated quartz veins using a laser-microprobe noble gas mass spectrometer," *U.S.G.S. Bulletin 1890*, 1989, 61-88.

8. J. K. Bohlke and J. J. Irwin, "Sources of salinity in ancient hydrothermal systems:

Laser microprobe analyses of Cl, Br, I, and K in fluid inclusions from Salton Sea (Calif.), St. Austell (U.K.), Creede (Colorado), and Alleghany (Calif.)," *Geochim. Cosmochim. Acta* (PACROFI III) (in press).

9. J. H. Reynolds, "High sensitivity mass spectrometer for rare gas analysis," *Rev. Sci. Instr.* 27: 1956.

10. J. K. Bohlke and J. J. Irwin, "Laser microprobe analyses of noble gas isotopes and halogens in fluid inclusions in minerals: Analyses of noble gas isotopes and halogens in fluid inclusions in minerals: Analyses of microstandards and synthetic fluid inclusions in quartz," Ref. 8.

11. J. H. Reynolds, J. R. Lumpkin, and P. M. Jeffery, "Search for ^{129}Xe in mineral grains from the Allende inclusions: An exercise in miniaturized rare gas analysis," *Z. Naturforsch* 35A: 257-266, 1980.

12. J. J. Irwin et al., "A laser-microprobe study of argon isotopes in deformed pegmatites from the Northern Highlands of Scotland," *Geo. Soc. (London)* 42: 149-160, 1989.

13. G. Lux, "The behaviour of noble gases in silicate melts: Solution, diffusion, bubbles and surface effects, with applications to natural samples," *Geochim. Cosmochim. Acta* 51: 1549-1560, 1988.

14. S. P. Smith and J. H. Reynolds, "Excess ^{129}Xe in a terrestrial sample as measured in a pristine system," *Earth and Planet. Sci. Lett.* 54: 236-238, 1981.

15. S. M. Sterner and R. J. Bodnar, "Synthetic fluid inclusions in natural quartz: 1. Compositional types synthesized and applications to experimental geochemistry," *Geochim. Cosmochim. Acta* 48: 2659-2668, 1984.

16. J. J. Irwin, C. Kirschbaum, J. Rosenfeld, and W. E. Glassley, "A study of argon isotopes in an unconformity garnet from SW Vermont, using a laser-microprobe," *EOS* 68: 1514, 1987.

17. E. Roedder, "Fluid inclusions," *Revs. Mineralogy* 12:, 1984.

18. S. P. Smith and B. M. Kennedy, "Noble gas evidence for two fluids in the Baca (Valles Caldera) geothermal reservoir," *Geochim. Cosmochim. Acta* 49: 893-902, 1985.

19. D. K. Nordstrom et al., "Fluid inclusions in the Stripa granite and their possible influence on the groundwater chemistry," *ibid.*, 53: 1711-1755, 1989.
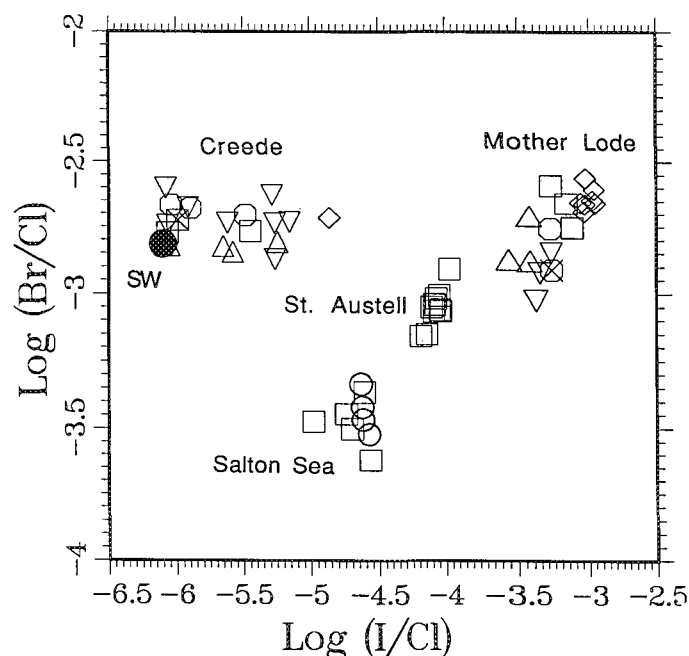
FIG. 6.--Summary of halogen abundance data from FI. Data are from 4 districts, each representative of different type of hydrothermal system: (1) Creede, Colo., an area of metalliferous sulfide deposits that fill Tertiary fractures in volcanic rocks; (2) Mother Lode, Sierra Nevada, quartz-vein-hosted gold deposits near Alleghany, Calif., (3) St. Austell granite, S.W. England, an area of high-temperature FI associated with Sn and Cu deposits, inferred to be derived from crystallizing magmas; (4) Salton Sea, California, an area of active sulfide mineralization and metamorphism, characterized by high-temperature, highly saline fluids. The different symbols shown within data groups from each area indicate different types of FI, illustrating the variations of FI composition within these hydrothermal systems. In contrast, data from St. Austell granite are tightly clustered, as there is a single source of FI in the rocks under study. SW is composition of modern seawater.

LAMMS AND RAMAN SPECTROSCOPY OF METAL PHTHALOCYANINE PARTICLES AND FILMS

R. A. Fletcher, J. A. Bennett, S. Hoeft, and E. S. Etz

Two recent papers summarize the chemical and physical properties of metal phthalocyanes (Pc's) and give examples of their many applications.[1,2] Pc's have the interesting property of being extremely thermally stable organic materials with stoichiometric single metal attachment. Because of their thermal stability, Pc's can be made into thin films by evaporation.

We are studying metal Pc's because they have (in addition to their thermal stability) low solubility, and are thus potential candidates for the preparation of thin-film standards. We previously examined several Pc's in powder form by laser microprobe mass spectrometry (LAMMS) and Raman spectroscopy.[3] In this paper, we characterize Pc's in thin-film form and compare the spectra generated with those from the particulate material. In addition, for both powder and thin-film form, we compare mass spectra generated by two laser microprobes with different ionization/extraction geometries. One instrument (LAMMA) is optimal for characterizing particles; the other (LIMA) is designed for analyzing supported thin-film and bulk materials. Independently, micro-Raman spectroscopy is used to characterize the structure of the thin films.

Experimental

The samples analyzed were commercial metal Pc powders (InPcBr, CuPc, H_2Pc, VOPc, and AlPcCl) and thin films formed by thermal evaporation/vacuum deposition of the same powders onto various substrates. The substrates used were quartz coverslips, microscope slides, and single-crystal Si. Profilometer measurements on the Pc films indicated that the films' thickness is between 10 to 50 nm. The Pc particles and the films were analyzed directly from coverslips.

Figure 1 schematically illustrates the sampling geometries of the three instruments. The laser microprobe mass analyzer (LAMMA 500) has transmission geometry with respect to laser

R. A. Fletcher, J. A. Bennett, and E. S. Etz are at the Chemical Science and Technology Laboratory, National Institute of Standards and Technology, Gaithersburg, MD 20899; S. Hoeft is a graduate student at the Chemistry Department, Washington University, St. Louis, MO 63130, conducting his experimental work at NIST. Certain commercial instruments are identified in this report to specify adequately the experimental procedure. Such identification does not imply recommendation or endorsement by NIST, nor does it imply that the materials or equipment identified are necessarily the best available for the purpose.
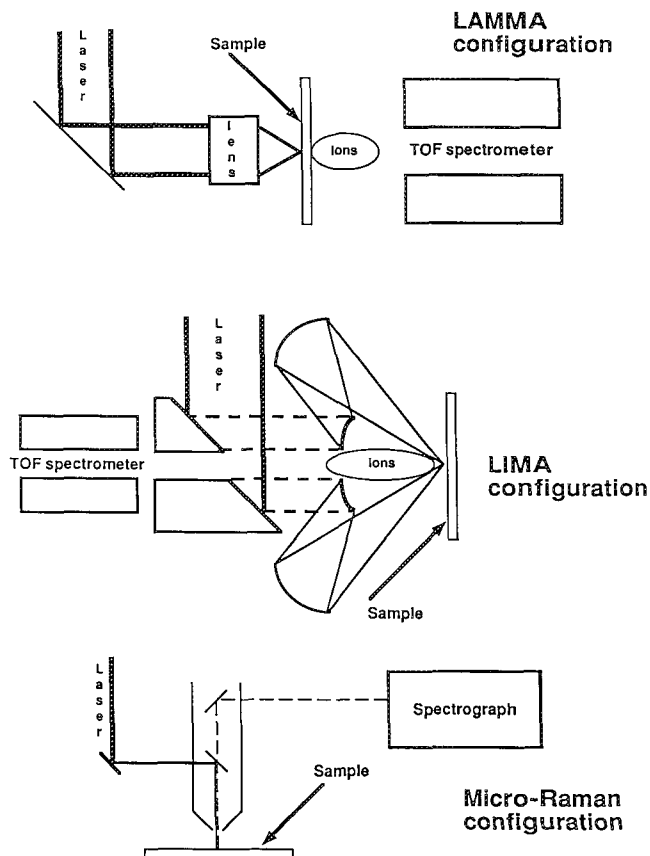
FIG. 1.--Schematic of sample/laser beam detection geometries for LAMMA 500, LIMA, and micro-Raman.

and mass spectrometer, whereas the laser induced ion mass analyzer (LIMA) has reflection geometry, and the laboratory-constructed micro-Raman system employs backscattering geometry. An important difference between the LAMMA 500 and the LIMA is that in the former instrument, ions are detected from the full thickness of the sample, which requires penetration; whereas in the latter instrument, ionization comes from the front surface of the sample. Both laser microprobes have time-of-flight mass spectrometers and Nd:YAG lasers, which are frequency quadrupled to provide 266nm radiation. In the LAMMA 500, the laser has a near-Gaussian beam intensity profile; in the LIMA, the laser beam has an annular intensity profile. Laser energies are lower by approximately an order of magnitude in the LAMMA 500 than the LIMA. The Raman instrument uses a Gaussian profile Ar^+ 20mW laser beam (514.5 nm) focused to 2 μm onto the sample as the excitation source.

LIMA positive ion mass spectrum of InPcBr film

LAMMA positive ion mass spectrum of InPcBr film

LIMA positive ion mass spectrum of InPcBr particle

LAMMA positive ion mass spectrum of InPcBr particle
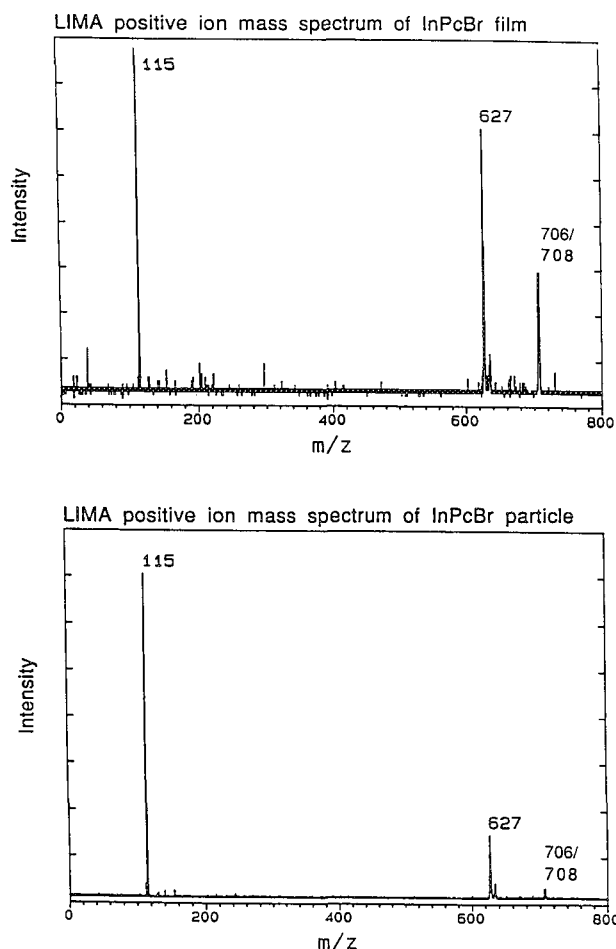
FIG. 2.--Mass spectra of InPcBr: thin film (top) and powder (bottom) obtained on the LIMA. Intensity scale of film spectrum is 0.02 V/division, intensity scale of particle spectrum is 0.125 V/division.

FIG. 3.--Mass spectra of InPcBr: thin film (top) and powder (bottom) obtained on the LAMMA 500. Intensity range, 50 mV full scale, is the same for both film and particle.

Results and Discussion

Positive ion mass spectra of InPcBr obtained from the LIMA and LAMMA 500 are shown in Figs. 2 and 3, respectively. The top spectrum in each figure is of the thin film; the bottom spectrum is of the Pc powder. Qualitatively, the mass spectra obtained from the two laser micro-probes contain very similar mass peak patterns, and the spectra generated from powders provide the same qualitative information as those pro-uced from thin films. However, there are some differences. Molecular ion production appears to be enhanced for the film over the particu-late form of the material. In spectra from both LIMA and LAMMA, there is an increase of peak intensity at m/x 706, 708 (molecular ion signal) compared to the peak intensity at m/z 627 (corresponds to InPc$^+$). Only a slight increase in the relative peak intensity at m/z 706, 708 is observed in the LIMA spectra, but there is a pronounced difference for the LAMMA.

In the LIMA spectrum, the large peak at m/z

115 is In$^+$ librated from the molecule. However, in the LAMMA 500 mass spectrum (top of Fig. 3), In$^+$ is absent. The spectral result is reproduced by a large defocusing of a low-energy beam (~1 µJ) to affect laser-Pc interaction. Under these conditions, the molecular ion peak was more intense than the InPc$^+$ peak. The energy is presumably suffic-ient to ionize the molecular species, but not high enough to liberate either the In or ionize In neutrals that could be released from the molecule. Most likely we are looking at a fragment of the molecular species that is preferentially generated by a break in the In-Br ionic bond. As laser irradiance increased, stronger bonds were broken and more fragments were produced. The next in terms of ease of ionization appears to be associated with the In-N covalent bond. This high mole-cular ion yield is surprising given that the LAMMA 500 must have enough irradiance to per-forate the film to produce detectable ions in the instrument.

FIG. 4.--Micro-Raman spectra of InPcBr: thin film (top) and powder (bottom).
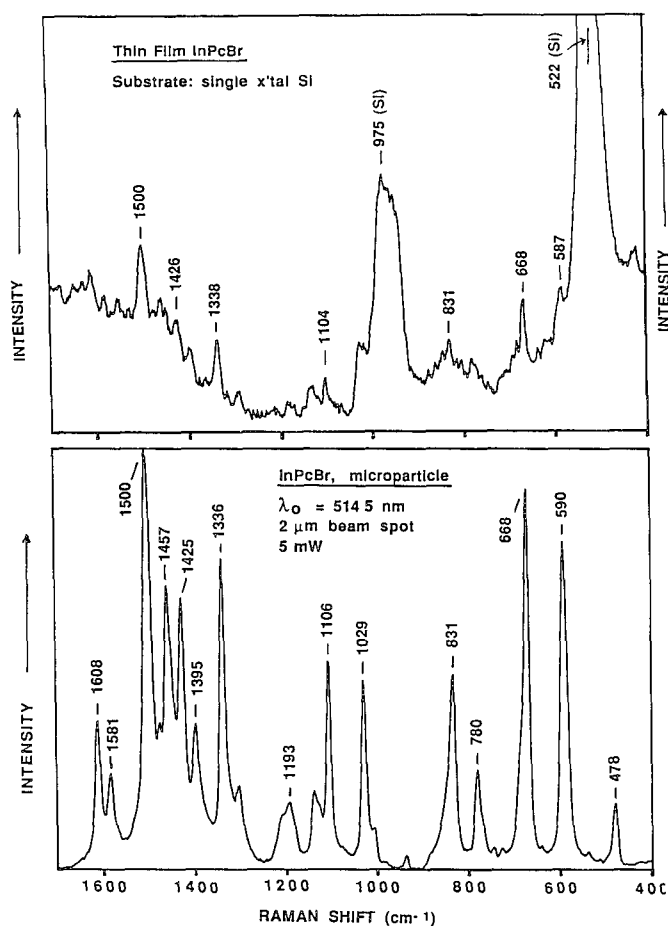
FIG. 5.--Micro-Raman spectra of VOPc: thin film (top) and powder (bottom).

Previous results reported for AlPcCl indicated that (AlPc + H)[+] was formed from the powder sample.[3] Work on the thin-film AlPcCl does not show a peak that corresponds to this unusual ion; rather, the expected AlPc[+] is observed. The molecular ion (AlPcCl)[+] was observed for the film, but not for the particle.

Measurements by Raman spectroscopy and x-ray diffraction in our study confirm that the films are polycrystalline; these results agree with results obtained by others.[4] The Raman spectra of InPcBr shown in Fig. 4 are for the powder (top) and the thin film (bottom). The substrate for the thin film was a silicon wafer (single-crystal Si) and the peaks at 975 and 522 wave numbers are due to the Raman bands of Si (as noted in the figure). Clearly the InPcBr lines are not strong for the thin film, but the compound is detected even at this low coverage (film thickness, some tens of nanometers).

Raman spectra (Fig. 5) taken of a film of VOPc deposited on amorphous Si indicate a near one-to-one correspondence of peaks from particulate VOPc and film VOPc. This film is somewhat thicker than the InPcBr film, but it is most likely less than 100 nm. One interesting observation is that of distinct frequency shifts from bands in spectra of particles when compared with films (especially most convincing

for CuPc on several types of substrates). We are following up on these observations with a view to relating these shifts to preferred molecular orientation on the substrate.

In summary, metal Pc's in powder and thin-film morphologies have been characterized by two laser microprobes and a Raman microprobe. The results for the laser microprobes indicate that qualitatively the instruments generate the same mass peak patterns. It is valuable to know, for analytical reasons, that the instruments produce spectra that are qualitatively the same for a given sample. A quantitative characterization of instrumental response between these two laser microprobes is under way. The Raman spectra are consistent with those published in the literature and are very similar from powder to film morphology, with a noted shift to higher frequencies.

References

1. D. D. Eley, *Mol. Cryst. Liq. Cryst.* 171: 1, 1989.

2. R. Brina, G. E. Collins, P. A. Lee, and N. R. Armstrong, *Anal. Chem.* 62: 2357, 1990.

3. R. A. Fletcher, E. S. Etz, and S. Hoeft, *Microbeam Analysis--1990*, 89.

4. T. D. Sims, J. E. Pemberton, P. Lee, and N. R. Armstrong, *Chemistry of Materials* 1:26, 1988.

A Characteristic X-ray Fluorescence Correction for
Thin-Film Analysis By Electron Microprobe
R. A. Waldo

The characteristic x-ray fluorescence correction in most thin film systems is negligible so no significant error usually results from its omission. Nevertheless, some cases exist where uncertainty about the size of the fluorescence correction may result in significant errors in the analytical results. Examples include films containing elements which would have a significant fluorescence contribution if present in bulk form, and film systems which might mistakenly be treated with bulk correction models because the films are thicker than the electron penetration depth.

Several characteristic fluorescence corrections for thin film systems are described in the literature..[1-5] Most, however, are limited in scope and application; use approximations; or only evaluate one-third or two-thirds of the triple integral in the fluorescence intensity equation with the remaining integrals to be evaluated by numerical methods.

de Boer[6] developed a comprehensive procedure to calculate the fluorescence correction for the x-ray fluorescence (XRF) analytical technique. He showed that the triple integral equations can be solved exactly for the general case of the exciting and excited element being in any layer. In XRF, however, the function describing the distribution of primary generated x rays is an exponential which is less commonly used to approximate the primary x-ray depth distribution function, $\phi(z)$, in electron probe microanalysis (EPMA).

Göhler and Hänisch[7] describe a solution for $\phi(z)$ models which have a $k_1 e^{-k_2 z} + k_3 z e^{-k_2 z}$ (linear– exponential) dependence.[8,9] They did not include the solution for the $k_3 z e^{-k_2 z}$ term, however, so their solution is equivalent to the solution of de Boer.

The two functional forms most commonly used to describe $\phi(z)$ in EPMA which are also applicable to film systems are the modified–gaussian model of Packwood and Brown[10] and the parabolic model of Pouchou and Pichoir (PAP).[11,12] Any treatment of fluorescence in thin film EPMA would have to consider these functional forms.

In this paper I develop the equations describing the total emitted characteristic x-ray fluorescence intensity for all geometries in a multilayer system and evaluate the resultant triple integral exactly in the case of the parabolic PAP and linear–exponential models and by numerical methods in the case of the modified–gaussian model. The solution for the modified–gaussian model is general and can be used for any functional form for $\phi(z)$. The solution for the linear–exponential models is shown to be a subset of the solution for the parabolic PAP model.

Fluorescence in a Multilayer Film System

There are n^2 possible exciter layer→ excited layer fluorescence interactions in an n-layer film system. Only three three basic geometries are necessary, however, to account for all of these interactions:

Case A) The exciting element is in a layer below the excited element. Only upward directed primary radiation need be considered in the calculation of the fluorescence intensity.

Case B) The exciting and excited element are in the same layer. If both elements are in the substrate, the equations are a subset of the general solution (Case B'). Case B' includes the bulk specimen fluorescence correction. Both upward and downward directed primary radiation are included in the calculations.

Case C) The exciter element is above the excited element; only downward directed primary radiation is considered. If the excited element is in the substrate, the solution is a simplified form of the general case (Case C').

I will use case A to illustrate in detail the derivation of the characteristic x-ray fluorescence intensity; the derivations for the other cases are analogous.

Figure 1 shows the geometry of the generation of characteristic x-ray fluorescence in a multi-layered film system for case A. The x and y directions (plane of the surface of the specimen) are assumed to be of infinite dimensions and each layer homogeneous in composition. It is desired to find the total emitted characteristic fluorescence intensity, $I'^{sp}_{f A_k}$ in the direction ψ toward a detector with solid angle $\Omega/4\pi$ and detection efficiency P. ($\Omega/4\pi P$ cancels when the specimen intensity is divided by the standard intensity.) The secondary A k-line x rays (A_k) may result from fluorescence by several j-line x-rays of elements B (B_j) in any of the layers or substrate.

In the particular case illustrated in Figure 1, primary B_j x rays originating from point P_1 in a deep layer b excite secondary A_k x rays at point P_2 in a layer a nearer the surface. The thickness of a layer i is t_i. The mass absorption

The author is with General Motors Research Laboratories (Analytical Chemistry Department), Warren, MI 48090-9055.

coefficient of primary B_j radiation in the layer i is denoted by μ_i and the mass absorption coefficient of the A_k secondary radiation in layer i times the cosecant of the x-ray takeoff angle, ψ, is designated by χ_i.

$I_{fA_k}^{'sp}$ is calculated after setting up the triple integral in the usual manner (e.g., Armstrong[4]) by

i) integrating over

     a) all depths z of the production of B_j x rays,

     b) all angles β of emission of the B_j x rays, and

     c) all depths s of possible excitation of A_k x rays;

ii) multiplying by

     a) a term $g = e^{\sum_{l=a-1}^{1} -\chi_l}$, accounting for x-ray absorption in the $a-1$ overlayers, and

     b) a term D' which contains several constants:[4]

$$D' = \frac{1}{2}C_A \mu_{B_j}^A \frac{r_{A_k}-1}{r'_{A_k}} \omega_{A_k} p_{A_k} \frac{\Omega}{4\pi} P \; ; \tag{1}$$

where

     1) C_A is the weight fraction of element A in the layer a;

     2) $\mu_{B_j}^A$ is the mass absorption coefficient of B_j radiation in pure element A;

     3) r_{A_k} is the absorption jump ratio at the k-absorption edge and $\frac{r_{A_k}-1}{r'_{A_k}}$ is a generalized notation for the ratio of ionizing absorptions to total absorptions;

     4) ω_{A_k} is the effective fluorescence yield of the k-shell; and

     5) p_{A_k} is the relative weight of the A_k line of interest

iii) and finally summing over all lines j of all elements B in all layers l capable of exciting A_k x rays. Thus,

$$I_{fA_k}^{'sp} = g\sum_B \sum_j D' \int_{z=\delta_{b-1}}^{\delta_b} \int_{\beta=\pi/2}^{\pi} \int_{s=\delta_a}^{\delta_{a-1}} F'_{B_j}(z,\beta,s)\,\mathrm{d}s\,\mathrm{d}\beta\,\mathrm{d}z \tag{2}$$

where the integrand F'_{B_j} can be found by following the paths of primary and secondary x rays:

$$F'_{B_j}(z,\beta,s) = I_{B_j}^{sp}(z)\tan\beta\, e^{-[\mu_b(\delta_{b-1}-z)-\sum_{i=b-1}^{a+1}\mu_i t_i]\sec\beta}\, e^{-[\mu_a(s-\delta_a)\sec\beta+\chi_a(s-\delta_{a-1})]}. \tag{3}$$

The depth distribution of generated primary B_j x rays in the specimen, $I_{PB_j}^{sp}(z)$, is related to the $\phi_{B_j}^{sp}(z)$ distribution by

$$I_{PB_j}^{sp}(z) = \frac{C_B}{A_B}z_{B_j}\omega_{B_j}p_{B_j}Q_{B_j}(E_0)\phi_{B_j}^{sp}(z) \tag{4}$$
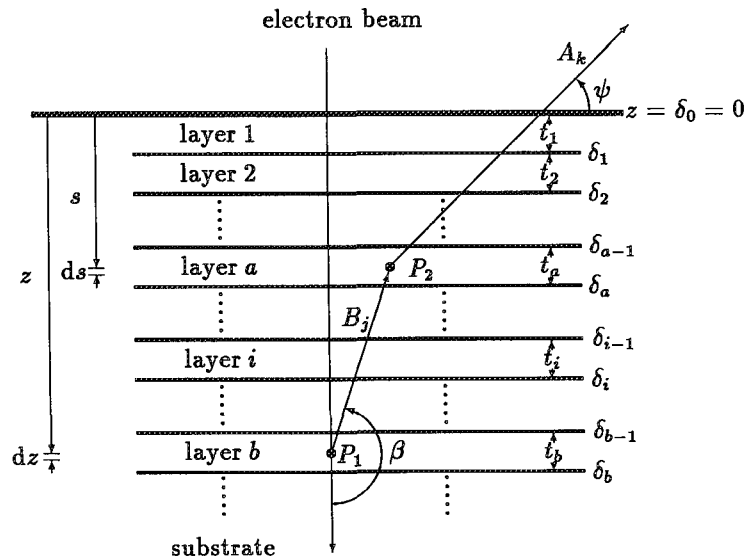
FIG. 1.- - Characteristic x-ray fluorescence in a multi-layer specimen.

where $Q_{B_j}(E_0)$ is the ionization cross section of the j-shell at the energy E_0, z_{B_j} is the number of electrons in the filled j-shell, and A_B is the atomic weight of B.

The function G'_{B_j} is defined here by

$$G'_{B_j}(z, \beta, s) = \frac{F'_{B_j}(z, \beta, s)}{\frac{C_B}{A_B} z_{B_j} \omega_{B_j} p_{B_j} Q_{B_j}(E_0)} \tag{5}$$

so

$$G'_{B_j}(z, \beta, s) = \phi^{sp}_{B_j}(z) \tan \beta e^{-[\mu_b(\delta_{b-1}-z) - \sum_{i=b-1}^{a+1} \mu_i t_i] \sec \beta} e^{-[\mu_a(s-\delta_a) \sec \beta + \chi_a(s-\delta_{a-1})]}. \tag{6}$$

The integral limits and integrand $G'_{B_j}(z, \beta, s)$ in Equations 2 and 6 are specific to each case of exciter layer–excited layer interaction and the evaluation of the triple integral has different solutions for each case.

We will see that the triple integral for a particular case cannot always be evaluated exactly for all functional forms of $\phi(z)$. The integrals with respect to s and β, however, can always be resolved exactly in terms of the exponential-integral function. I therefore introduce here the function $Y(z)$

$$G_{B_j} = \int_z \phi(z) \cdot Y(z) dz \tag{7}$$

with

$$Y(z) = \int_\beta \int_s f(z, \beta, s) \cdot ds\, d\beta. \tag{8}$$

Evaluation of the Double Integral $Y(z)$

After rearranging and combining terms of the same variable in Equation 6, $Y(z)$ for case A can be written

$$Y(z) = Y(z)\uparrow = \int_{\pi/2}^{\pi} \tan \beta e^{-[\mu_b(\delta_{b-1}-z) - \sum_{i=b-1}^{a+1} \mu_i t_i] \sec \beta} d\beta \int_{\delta_a}^{\delta_{a-1}} e^{-[\mu_a(s-\delta_a) \sec \beta + \chi_a(s-\delta_{a-1})]} ds. \tag{9}$$

$Y(z)\uparrow$ indicates that only upward directed B_j primary radiation need be considered.

1. Evaluation of the Integral With Respect to s

The integral with respect to s in Equation 9 is of the form $\int_z c_1 e^{-c_2 s + c_3} ds$ and is easily evaluated

$$Y(z)\uparrow = -\int_{\pi/2}^{\pi} \sin \beta e^{(\mu_b z - \mu_b \delta_{b-1} + \sum_{i=b-1}^{a+1} \mu_i t_i + \mu_a t_a) \sec \beta} \frac{\sec\beta}{\mu_a \sec \beta + \chi_a} d\beta$$

$$+ e^{-\chi_a t_a} \int_{\pi/2}^{\pi} \sin \beta e^{(\mu_b z - \mu_b \delta_{b-1} + \sum_{i=b-1}^{a+1} \mu_i t_i) \sec \beta} \frac{\sec\beta}{\mu_a \sec \beta + \chi_a} d\beta. \tag{10}$$

2. Evaluation of the Integral With Respect to β

Both of the definite integrals in Equation 10 are of the form

$$H(c_1, c_2, c_3) = \int_{\pi/2}^{\pi} e^{c_1 \sec \beta} \frac{\sec\beta}{c_2 \sec \beta + c_3} \sin \beta d\beta. \tag{11}$$

This type integral can be evaluated with the substitution $x = c_2 \sec \beta$:

$$H(c_1, c_2, c_3) = \frac{1}{c_3} \left[\int_{-\infty}^{-c_2} \frac{e^{\frac{c_1}{c_2} x}}{x} dx + e^{-\frac{c_1}{c_2} c_3} \int_{-\infty}^{-c_2 + c_3} \frac{e^{\frac{c_1}{c_2} u}}{u} du \right]. \tag{12}$$

where the second integral has been reduced to the same form as the first with the substitution $u = x + c_3$.

Integrals of the form

$$\int_{-\infty}^{x} e^{-t}/t\, dt$$

are defined as the exponential-integral function and are designated Ei(x). For $x \neq 0$, Ei(x) can be represented by the series expansion

$$\text{Ei}(x) = \gamma + \ln[\text{abs}(x)] + \sum_{k=1}^{\infty} \frac{x^k}{k \cdot k!}, \quad [x \neq 0] \tag{13}$$

47

where $\gamma = 0.5772158\ldots$ is Euler's constant.[13] The evaluation of Equation 11 is thus

$$H(c_1, c_2, c_3) = \frac{1}{c_3}\left[Ei(-c_1) - e^{-\frac{c_1}{c_2}c_3}\,Ei\left(-c_1 + \frac{c_1}{c_2}c_3\right)\right] \tag{14}$$

and $Y(z)$ for case A is

$$Y(z)\!\uparrow = \frac{1}{\chi_a}\left[-Ei(f_1 z + g_1) - e^{a_1 z + b_1}\left[Ei(f_2 z + g_2) - Ei(f_2 z + g_3)\right] + e^{b_2}\,Ei(f_1 z + g_4)\right] \tag{15}$$

with

$$
\begin{aligned}
&a_1 = \tfrac{-\chi_a}{\mu_a}\mu_b & &g_1 = \mu_b\delta_{b-1} - \textstyle\sum \mu_i t_i - \mu_a t_a \\
&b_1 = \tfrac{\chi_a}{\mu_a}(\mu_b\delta_{b-1} - \textstyle\sum \mu_i t_i) - \chi_a t_a & &g_2 = -(\mu_b\delta_{b-1} - \textstyle\sum \mu_i t_i)(\tfrac{\chi_a}{\mu_a} - 1) \\
&b_2 = -\chi_a t_a & &g_3 = g_2 + (\chi_a - \mu_a)t_a \\
&f_1 = -\mu_b & &g_4 = \mu_b\delta_{b-1} - \textstyle\sum \mu_i t_i \\
&f_2 = \mu_b(\tfrac{\chi_a}{\mu_a} - 1).
\end{aligned}
$$

The summations in the terms b_1 and $g_1 - g_4$ are over the i layers between layers b and a.

Solutions for the other geometries are:

Case B.

$$Y(z) = Y(z)\!\uparrow + Y(z)\!\downarrow \tag{16}$$

with

$$Y(z)\!\uparrow = \frac{1}{\chi_a}\left[-Ei(f_1 z + g_1) + e^{a_1 z + b_1}\left\{Ei(f_2 z + g_2) - r_2\right\}\right] \tag{17}$$

$$Y(z)\!\downarrow = \frac{1}{\chi_a}\left[e^{b_2}\,Ei(f_3 z + g_3) - e^{a_1 z + b_1}\left\{Ei(f_4 z + g_4) + r_1\right\}\right] \tag{18}$$

where

$$
\begin{aligned}
&a_1 = -\chi_a & &f_1 = -\mu_a & &g_1 = \mu_a\delta_{a-1} \\
&b_1 = \chi_a\delta_{a-1} & &f_2 = \chi_a - \mu_a & &g_2 = (-\chi_a + \mu_a)\delta_{a-1} \\
&b_2 = -\chi_a t_a & &f_3 = \mu_a & &g_3 = -\mu_a\delta_a \\
& & &f_4 = \chi_a + \mu_a & &g_4 = -(\chi_a + \mu_a)\delta_a
\end{aligned}
$$

and r_1 and r_2 have the values

$$r_1 = \ln\left(1 + \tfrac{\chi_a}{\mu_a}\right) \quad \text{and} \quad r_2 = \ln\left(\text{abs}\left[1 - \tfrac{\chi_a}{\mu_a}\right]\right).$$

Case B'.

$$Y(z)\!\uparrow + Y(z)\!\downarrow = \frac{1}{\chi_a}\left[-Ei(f_1 z + g_1) + e^{a_1 z + b_1}\left(Ei(f_2 z + g_2) + r_1 - r_2\right)\right]. \tag{19}$$

For bulk specimens $b_1 = g_1 = g_2 = 0$ in Equation 19.

Case C.

$$Y(z)\!\downarrow = \frac{1}{\chi_a}\left[-Ei(f_1 z + g_1) + e^{a_1 z + b_1}\left[Ei(f_2 z + g_2) - Ei(f_2 z + g_3)\right] + e^{b_2}\,Ei(f_1 z + g_4)\right] \tag{20}$$

with

$$
\begin{aligned}
&a_1 = \tfrac{-\chi_a}{\mu_a}\mu_b & &g_1 = -(\mu_b\delta_b + \textstyle\sum \mu_i t_i) \\
&b_1 = \tfrac{\chi_a}{\mu_a}(\mu_b\delta_b + \textstyle\sum \mu_i t_i) & &g_2 = -(\mu_b\delta_b + \textstyle\sum \mu_i t_i)(\tfrac{\chi_a}{\mu_a} + 1) \\
&b_2 = -\chi_a t_a & &g_3 = g_2 - (\chi_a + \mu_a)t_a \\
&f_1 = \mu_b & &g_4 = -(\mu_b\delta_b + \textstyle\sum \mu_i t_i) - \mu_a t_a \\
&f_2 = \mu_b(\tfrac{\chi_a}{\mu_a} + 1).
\end{aligned}
$$

Case C'.

$$Y(z)\!\downarrow = \frac{1}{\chi_a}\left[-Ei(f_1 z + g_1) + e^{a_1 z + b_1}\,Ei(f_2 z + g_2)\right]. \tag{21}$$

3. Evaluation of the Integral with Respect to z

The triple integral for case A is now given by

$$G_{B_j} = \int_{\delta_{b-1}}^{\delta_b} \phi_{B_j}^{sp}(z) \times \frac{1}{\chi_a} \left[-\mathrm{Ei}(f_1 z + g_1) - e^{a_1 z + b_1} \left[\mathrm{Ei}(f_2 z + g_2) - \mathrm{Ei}(f_2 z + g_3) \right] + e^{b_2} \mathrm{Ei}(f_1 z + g_4) \right] \mathrm{d}z. \tag{22}$$

G_{B_j} can be evaluated exactly (in terms of the exponential–integral function) when $\phi(z)$ has certain functional forms including exponential, polynomial and linear–exponential. For such $\phi(z)$ models, Equation 22 can be written as linear combinations of integrals of the form

$$\int_z z^n e^b \mathrm{Ei}(fz+g) dz \quad \text{and} \quad \int_z z^n e^{az+b} \mathrm{Ei}(fz+g) dz \quad ; \quad n = 0, 1, 2.$$

3a. Indefinite integrals of the form $s_n = \int z^n e^b \mathrm{Ei}(fz+g) \mathrm{d}z$.

The indefinite integrals are found by integrating by parts:

$$s_n = \int z^n e^b \mathrm{Ei}(fz+g) \mathrm{d}z = \frac{e^b}{(n+1) f^{n+1}} \left[u^{n+1} \mathrm{Ei}(u) - e^u \mathrm{E}_n(u) \right] - T_n + C, \ n = 0, 1, 2 \ldots \tag{23}$$

where $u = fz + g$; T_n is given by

$$T_0 = 0 \quad \text{and} \quad T_n = \sum_{r=1}^{n} \frac{n!}{(n-r)! r!} \cdot \left(\frac{g}{f}\right)^r s_{n-r}, \quad \text{for } n = 1, 2, \ldots \ ;$$

and $\mathrm{E}_n(u)$ denotes the exponential–polynomial

$$\mathrm{E}_n(u) = \sum_{r=0}^{n} (-1)^r \frac{n! u^{n-r}}{(n-r)!}.$$

Equation 23 evaluated at $u = 0$ ($z = -g/f$) contains terms of $0^{n+1} \mathrm{Ei}(0)$ ($\mathrm{Ei}(0)$ is undefined). With Equation 13 and l'Hospital's rule, these terms can be shown to be equal to zero. Thus,

$$\lim_{u \to 0} s_n = \frac{e^b (-1)^{n+1} n!}{(n+1) f^{n+1}} - T_n + C \tag{24}$$

where T_n has the same values as in Equation 23.

3b. Integrals of the form $s_n' = \int z^n e^{az+b} \mathrm{Ei}(fz+g) \mathrm{d}z$.

The indefinite integrals are found by integrating by parts:

$$s_n' = \int z^n e^{az+b} \mathrm{Ei}(fz+g) \mathrm{d}z = \frac{e^{\frac{-ag}{f}+b}}{a^{n+1}} \left[e^{\frac{a}{f}u} \mathrm{E}_n(\frac{a}{f}u) \mathrm{Ei}(u) - (-1)^n n! \mathrm{Ei}\left[\left(\frac{a}{f}+1\right)u \right] - T_n' \right] + C \tag{25}$$

where $u = fz + g$ and T_n' is given by

$$T_0' = 0 \quad \text{and}$$

$$T_n' = \sum_{r=1}^{n} e^{(\frac{a}{f}+1)u} (-1)^{n-r} \left(\frac{a}{a+f}\right)^r \mathrm{E}_{r-1}[(\frac{a}{f}+1)u] \frac{n!}{r!} + \frac{a^{n+1}}{e^{\frac{-ag}{f}+b}} \frac{n!}{(n-r)! r!} \cdot \frac{g^r}{f^r} s_{n-r}', \text{ for } n = 1, 2 \ldots$$

Equation 25 evaluated at $u = 0$ ($z = -g/f$) contains multiple terms of $\mathrm{Ei}(0)$. With Equation 13 and l'Hospital's rule s_n' can be shown to have finite values as $u \to 0$. Thus,

$$\lim_{u \to 0} s_n' = \frac{e^{\frac{-ag}{f}+b}}{a^{n+1}} \left[(-1)^n n! \ln(\frac{a}{f}+1) - T_n' \right] + C \tag{26}$$

now with

$$T_0' = 0 \quad \text{and} \quad T_n' = \sum_{r=1}^{n} (-1)^{n+1} \left(\frac{a}{a+f}\right)^r \frac{n!}{r} + \frac{a^{n+1}}{e^{\frac{-ag}{f}+b}} \frac{n!}{(n-r)! r!} \cdot \left(\frac{g}{f}\right)^r s_{n-r}' \ , \quad \text{for } n = 1, 2, \ldots$$

Exact Solutions for Certain $\phi(z)$ Models

The functions $S_n(\delta_1, \delta_2, b, f, g)$ and $S_n'(\delta_1, \delta_2, a, b, f, g)$ are defined here by

$$S_n(\delta_1, \delta_2, b, f, g) = \int_{\delta_1}^{\delta_2} z^n e^b \mathrm{Ei}(fz+g) \mathrm{d}z = s_n \big|_{\delta_1}^{\delta_2} \tag{27}$$

and

$$S_n'(\delta_1, \delta_2, a, b, f, g) = \int_{\delta_1}^{\delta_2} z^n e^{az+b} \mathrm{Ei}(fz+g) \mathrm{d}z = s_n' \big|_{\delta_1}^{\delta_2}. \tag{28}$$

49

1. Parabolic PAP $\phi(z)$ Model

The parabolic PAP model is given by

$$\begin{aligned}
\phi(z) &= A_1(z - R_m)^2 + B_1 \qquad \text{for } z \leq R_c \\
\phi(z) &= A_2(z - R_x)^2 \qquad\qquad\ z > R_c.
\end{aligned}$$

(29)

The integral with respect to z for case A can now be expressed as

$$G_{B_j} = \int_{\delta_{b-1}}^{\delta_b} (d_2 z^2 + d_1 z + d_0) \times \frac{1}{\chi_a} \left[-\mathrm{Ei}(f_1 z + g_1) - e^{a_1 z + b_1} \left[\mathrm{Ei}(f_2 z + g_2) - \mathrm{Ei}(f_2 z + g_3) \right] + e^{b_2} \mathrm{Ei}(f_1 z + g_4) \right] dz$$

(30)

with

$$\begin{aligned}
d_2 &= A_1, \quad d_1 = -2A_2 R_m, \quad \text{and} \quad d_0 = R_x^2 + B_1 \quad \text{for } z \leq R_c \\
d_2 &= A_2, \quad d_1 = -2A_2 R_x, \quad \text{and} \quad d_0 = R_x^2 \qquad\quad \text{for } z > R_c.
\end{aligned}$$

The integral G_{B_j} is expressed in terms of S_n and S_n' for case A as

$$G_{B_j} = \sum_{n=0}^{2} d_n \left[-S_n(\delta_{b-1}, \delta_b, 0, f_1, g_1) - S_n'(\delta_{b-1}, \delta_b, a_1, b_1, f_2, g_2) + S_n'(\delta_{b-1}, \delta_b, a_1, b_1, f_2, g_3) + S_n(\delta_{b-1}, \delta_b, b_2, f_1, g_4) \right].$$

(31)

This is an exact solution of the triple integral G_{B_j} in terms of the exponential–integral function. Solutions for cases B and C are analogous.

2. Heinrich Exponential Model

The exponential model of Heinrich is given by

$$\phi(z) = \alpha\beta e^{-\beta z} + (1 - \alpha)\beta^2 z e^{-\beta z}$$

(32)

so G_{B_j} can be expressed in terms of S_n' by

$$\begin{aligned}
G_{B_j} &= \sum_{n=0}^{1} d_n \cdot \left[-S_n'(\delta_{b-1}, \delta_b, -\beta, 0, f_1, g_1) - S_n'(\delta_{b-1}, \delta_b, a_1 - \beta, b_1, f_2, g_2) \right. \\
&\quad \left. + S_n'(\delta_{b-1}, \delta_b, a_1 - \beta, b_1, f_2, g_3) + S_n'(\delta_{b-1}, \delta_b, -\beta, b_2, f_1, g_4) \right]
\end{aligned}$$

(33)

with $d_1 = (1 - \alpha)\beta^2$ and $d_0 = \alpha\beta$.

3. PAP Simplified Exponential Model

G_{B_j} for the PAP simplified exponential model,

$$\phi(z) = Ae^{-\alpha z} + (Bz + \phi_0 - A)e^{-\beta z},$$

(34)

can be expressed in terms of the function S_n' in a similar manner.

Solution for Modified Gaussian $\phi(z)$ Models

When the x-ray depth distribution function $\phi(z)$ is a modified–gaussian,

$$\phi(z) = \gamma_0 e^{-\alpha^2 z^2} - (\gamma_0 - \phi_0)e^{\alpha^2 z^2 - \beta^2},$$

the integrals in equations of type 22 are of the form

$$\int_z e^{-(bz+c)^2} Ei(f_n z + g_m) dz$$

which cannot be solved in closed form. This type integral can be easily approximated, however, with numerical integration techniques.

Simpson's Rule of numerical integration for n intervals requires evaluating the integrand at the integral limits and at 2n-1 interior points. Evaluation of the integrand for the interior points poses no problems, but when a boundary of layer a coincides with a boundary of layer b for any geometry, some of the Ei function terms in equations of type 22 may contain zero argument.

Case A. If there are no intervening layers between layers a and b, then the summation terms in Equation 15 are eliminated and the arguments of the exponential-integral terms $\mathrm{Ei}(f_2 z + g_2)$ and $\mathrm{Ei}(f_1 z + g_4)$ are both 0. $Y(z)\uparrow$ at the layer a–layer b boundary, however, now has the simplified form

$$Y(z)\uparrow = -\int_{\pi/2}^{\pi} \sin\beta\, e^{\mu_a t_a \sec\beta} \frac{\sec\beta}{\mu_a \sec\beta + \chi_a}\, d\beta + e^{-\chi_a t_a} \int_{\pi/2}^{\pi} \sin\beta \frac{\sec\beta}{\mu_a \sec\beta + \chi_a}\, d\beta.$$

(35)

with solution

$$Y(z)\uparrow \;=\; \frac{1}{\chi_a}\left[-\mathrm{Ei}(g_1) + e^{b_1}\left\{\mathrm{Ei}(g_2) - r_2\right\}\right] \tag{36}$$

where $b_1 = -\chi_a t_a$, $g_1 = -\mu_a t_a$, and $g_2 = (\chi_a - \mu_a)t_a$.

The arguments of the Ei functions in Equation 36 are independent of z and non-zero. For the other cases:

<u>Case B.</u> At the upper interval endpoint

$$Y(z)\downarrow \;=\; \frac{1}{\chi_a}\left[e^{b_1}Ei(g_1) - Ei(g_2) + r_1\right] \tag{37}$$

where $b_1 = -\chi_a t_a$, $g_1 = -\mu_a t_a$, and $g_2 = -(\chi_a + \mu_a)t_a$.

Case B at the lower interval endpoint is equivalent to case A.

<u>Cases A′, C′ and Bulk Specimens.</u> These geometries are equivalent. The Ei(0) terms occur at the layer a boundary nearest the specimen surface.

$$Y(z)\downarrow \;=\; \frac{1}{\chi_a}r_1 \tag{38}$$

<u>Case C.</u> This is equivalent to case B downward directed radiation.

Accuracy of Numerical Integration

The choice of the number of numerical integration intervals for a desired accuracy can be made with the aid of the exact solution of the triple integral, G_{B_j}, derived for the parabolic PAP model. A hypothetical sample of a 300 μg/cm^2 film of gallium arsenide (GaAs) on GaAs substrate was modeled. The operating potential was 30 keV and the takeoff angle, ψ, was 40 deg for the calculations. The mass absorption coefficients are those of Heinrich.[14] Integration was done with the exact formula (Equation 31 for case A, etc.) and with Simpson's rule for numerical integration (Equation 22 for case A, etc.) with the number of Simpson intervals variable. Four exciter–excited layer fluorescence geometries are present in this system. The results are listed in Table 1.

For better than 1% accuracy only 4 Simpson intervals (2n+1=9 evaluations of equations of type 15-21 and 36-38) are needed for the calculation of the fluorescence of Ga when As is in the film. When the exciting element As is in the substrate, 4-8 intervals are needed.

The k-ratio Equation for Thin Film Microanalysis

The k-ratio for A_k radiation is (neglecting continuum fluorescence):

$$k_{A_k} \;=\; \frac{I'^{sp}_{pA_k} + I'^{sp}_{fA_k}}{I'^A_{pA_k}}. \tag{39}$$

For a layer containing A extending from δ_{a-1} to δ_a in a multilayer film system this is (from Equations 1-6)

$$k_{A_k} \;=\; gC_A\frac{\omega_{A_k,e}\int_{\delta_{a-1}}^{\delta_a}\phi^{sp}_{A_k}(z)e^{-\chi_a z}dz + \frac{1}{2}\sum_B\sum_j G_{B_j}\mu^A_{B_k}\frac{r_{A_k}-1}{r'_{A_k}}C_B\frac{A_A}{A_B}\frac{z_{B_j}}{z_{A_k}}\frac{Q_{B_j}(E_0)}{Q_{A_k}(E_0)}\omega_{B_j}p_{B_j}\omega_{A_k,B_j}}{\omega_{A_k,e}\int_0^\infty\phi^A_{A_k}(z)e^{-\chi^A_{A_k}}dz}. \tag{40}$$

Table 1. - - Evaluation of the triple integral G_{B_j} of Equation 31 by exact and numerical integration for the hypothetical sample described in the text.

Integration Method	$G_{B_j} \times 10^6$			
	1x1	1x2	2x1	2x2
exact (Equation 31)	0.3743	0.3942	1.708	4.272
numerical, n=2 intervals	0.3738	0.4099	1.710	4.252
" n=4 "	0.3741	0.3980	1.708	4.268
" n=6 "	0.3742	0.3959	1.708	4.270
" n=8 "	0.3742	0.3951	1.708	4.271

1x1=Fluorescence of Ga Kα in the film by As Kα in the film

1x2=Fluorescence of Ga Kα in the film by As Kα in the substrate

2x1=Fluorescence of Ga Kα in the substrate by As Kα in the film

2x2=Fluorescence of Ga Kα in the substrate by As Kα in the substrate

ω_{A_k,B_j} represents the effective fluorescence yield of A_k radiation after ionization by B_j x-rays which may differ from the fluorescence yield $\omega_{A_k,e}$ after electron ionization (Coster-Kronig transitions may differ). The transition probability, p_{A_k}, cancels in Equation 40. Because the B_j and A_k primary intensities are implicitly contained in this equation, the calculation of $K \to L$ and $L \to K$ fluorescences are simplified as in the method of Henoc et al.[15] This equation is strictly applicable, however, only to $\phi(z)$ models in which the primary x-ray intensity is a parameter of the model.[9,11,16]

Alternatively, a method based on Reed's[17] fluorescence correction procedure can be used. For this method we need an approximation for the ratio of generated (unattenuated) primary intensities of B_j and A_k x rays in the specimen. Reed's approximation is

$$\frac{I^{sp}_{PB_j}}{I^{sp}_{PA_k}} = \frac{C_B}{C_A}\frac{\omega^j_B}{\omega^k_A}\frac{p_{B_j}}{p_{A_k}}\frac{A_A}{A_B}\frac{(U_{B_j}-1)^{1\,67}}{(U_{A_k}-1)^{1.67}}P_{kl} \ , \tag{41}$$

where U_{B_j} and U_{A_k} are the overvoltage ratios for B_j and A_k radiation, and P_{kl} is a factor accounting for the ratio of primary intensities when B_j and A_k are from different shells. This formula is for bulk specimens. For thin film specimens we can assume B_j and A_k intensities from theoretical bulk specimens having the same $\phi(z)$ distributions as for the thin film specimen. From Equation 4 the intensity for the theoretical bulk B_j radiation is

$$I^{sp}_{PB_j} = \frac{C_B}{A_B}z_{B_j}\omega_{B_j}p_{B_j}Q_{B_j}(E_0)\int_0^\infty \phi^{sp}_{B_j}(z)\mathrm{d}z \tag{42}$$

with a similar equation for the A_k x-ray intensity. Multiplying the numerator and denominator of the second term of equation 40 by the B_j and A_k theoretical intensities of Equation 42 and substituting Reed's approximation of Equation 41 we obtain

$$k_{A_k} = gC_A\left[\frac{\int^{\delta_a}_{\delta_{a-1}}\phi^{sp}_{A_k}(z)e^{-\chi_a}\mathrm{d}z}{\int_0^\infty \phi^A_{A_k}(z)e^{-\chi^A_{A_k}}\mathrm{d}z} + \frac{\frac{1}{2}\sum_B\sum_j G_{B_j}\mu^A_{B_k}\frac{r_{A_k}-1}{r'_{A_k}}C_B\omega_{B_j}p_{B_j}\frac{A_A}{A_B}\frac{(U_{B_j}-1)^{1\,67}}{(U_{A_k}-1)^{1\,67}}P_{kl}\frac{\int_0^\infty \phi^{sp}_{A_k}(z)dz}{\int_0^\infty \phi^{sp}_{B_j}(z)dz}}{\int_0^\infty \phi^A_{A_k}(z)e^{-\chi^A_{A_k}}\mathrm{d}z}\right] .$$

Reed's method does not account for differing effective fluorescence yields from x-ray or electron excitation.

Conclusion

Exact equations for the calculation of the characteristic x-ray fluorescence intensity in homogeneous thin film systems were derived. The equations were substituted into the k-ratio equation showing that the fluorescence correction for thin film systems can be calculated directly without the need to use approximations for the ratio of generated intensities. The equations in this paper and the iteration procedure described in a previous paper[18] were incorporated into a computer program to calculate the compositions of thin film systems from experimental k-ratio data.

References

1) L. S. Birks, D. J. Ellis, B. K. Grant, A. S. Grant, A. S. Frisch, and R. B. Hickman, "Distribution of Secondary Fluorescence With Depth Using Monte Carlo Calculations," in McKinley et al., Eds., *The Electron Microprobe*, New York:Wiley, 1966,199–216.

2) M. G. C. Cox and V. D. Scott, "A Characteristic Fluorescence Correction for Electron Probe Microanalysis of Thin Coatings," *Journal of Physics D: Applied Physics* 12: 1441–1451, 1979.

3) A. Armigliato, A. Desalvo, and R. Rosa, "A Monte Carlo Code Including an X-ray Characteristic Fluorescence Correction for Electron Probe Microanalysis of a Thin Film on a Substrate," *Journal of Physics D: Applied Physics* 15: L121–L124, 1982.

4) J. T. Armstrong and P. R. Buseck, "A General Characteristic Fluorescence Correction for the Quantitative Electron Microbeam Analysis of Thick Specimens,Thin Films and Particles," *X-ray Spectrometry* 14: 172–182, 1985.

5) Y. H. Hu, Y. C. He, and J. G. Chen, "The Calculation Equations of Characteristic Fluorescence for Multilayer Films," *Journal of Physics D: Applied Physics* 21: 1221–1225, 1988.

6) D. K. G. de Boer, "Calculation of X-ray Fluorescence Intensities from Bulk and Multilayer Samples," *X-ray Spectrometry* 19: 145–154, 1990.

7) K.Göhler and M. Hänisch, "Characteristic Fluorescence Correction for Layered Samples Part I. Closed Solution for Film – Substrate Combination," *Scanning* 13: 1–5, 1991.

8) K. F. J. Heinrich, "A Simple Accurate Absorption Model," *Microbeam Analysis–1985*, 79–81.

9) J. L. Pouchou and F. M. A. Pichoir, "A Simplified Version of the "PAP" Model for Matrix Corrections in EPMA," *Microbeam Analysis–1988,* 315–318.

10) R. H. Packwood and J. D. Brown, " A Gaussian Expression to Describe $\phi(\rho z)$ Curves for Quantitative Electron Probe Microanalysis," *X-Ray Spectrometry* 10: 138–146, 1981.

11) J. L. Pouchou and F. Pichoir, "Basic Expression of "PAP" Computation for Quantitative EPMA," in *Proc. 11th ICXOM,* London, Ont.,249–253.

12) J. L. Pouchou and F. Pichoir, "Surface Film X-ray Microanalysis," *Scanning* 12: 212–224, 1990.

13) J. Spanier and K. B. Oldham, *An Atlas of Functions,* Washington: Hemisphere, 1980, 351–360.

14) K. F. J. Heinrich, "Mass Absorption Coefficients for Electron Probe Microanalysis," in *Proc. 11th ICXOM,* London, Ont., 67–119.

15) J. Henoc, K. F. J. Heinrich, and R. L. Myklebust, *NBS Tech. Note 769,* 1973.

16) G. F. Bastin and H. J. M. Heijligers, "Quantitative Electron Probe Microanalysis of Ultra-Light Elements (Boron–Oxygen)," *Scanning* 12: 225–236, 1990.

17) S. J. B. Reed, "Characteristic Fluorescence Corrections in Electron-Probe Microanalysis," *British Journal of Applied Physics* 16: 913–926, 1965.

18) R. A. Waldo, "An Iteration Procedure To Calculate Film Compositions and Thicknesses In Electron-Probe Microanalysis," *Microbeam Analysis–1988,* 310–314.

CHARACTERIZATION OF STANDARDS FOR QUANTITATIVE EPMA OF OXYGEN

A. V. McGuire, C. A. Francis, and M. D. Dyar

The recent development and application of multilayer W-Si thin-film crystals (LDE1) for electron microprobe makes routine and precise analysis of oxygen possible.[1,2] The high count rates and high peak-to-background ratio obtained with these crystals offer excellent statistical precision in oxygen analysis. However, accuracy is strongly tied to availability of well-characterized standard materials.

To date microprobe analyses of oxygen have been performed with standards whose oxygen content is unmeasured. Generally, calculations of oxygen contents of standards are based on assumptions of perfect stoichiometry and charge balance. Mineralogists have known for some time that naturally occurring minerals are very often not stoichiometric. Recent work on oxygen in naturally occurring biotites[3] has shown that their oxygen contents may vary by 19.9 to 24.5 cations per formula unit (p.f.u.), as compared to the stoichiometric value of 24 oxygens p.f.u. Lack of standard materials with measured oxygen contents represents a setback to the achievement of both precise and accurate oxygen analyses with the electron microprobe.

This project involved the characterization of oxygen contents of natural mineral samples with the aim of using these materials as standards for electron microprobe analysis of oxygen. Measurement of oxygen was done by fast neutron activation analysis (FNAA). This paper presents preliminary data for 8 mineral standards for which oxygen content has been measured by FNAA. Additional standards are in preparation.

Analytical Methods

Samples were selected to include as wide as possible a range of oxygen contents, mineral compositions, and structural types (oxides, carbonates, orthosilicates, tectosilicates, etc.), and to represent naturally occurring compositions of common rock-forming minerals. Many of these samples were obtained from the Harvard Mineralogical Museum. Data are presented in this paper for olivine, amphibole, quartz,[4] sillimanite, albite,[5] corundum, gahnite,[5] and dolomite.[6] Three of these minerals (Amelia albite; gahnite; and Hot Springs, Arkansas, quartz) are already commonly used microprobe

standards. Garnet, hematite, muscovite, and biotite are also being prepared.

Thin sections or grain mounts were made for each sample. Care was taken to avoid heating during mounting in epoxy. Homogeneity was tested by running a series of linescans (60 points total/sample) to collect peak counts for all elements including oxygen. Oxygen was counted with a W-Si multilayer crystal (LDE1) on one spectrometer. The microprobe used was a JEOL 8600 Superprobe equipped with four wavelength spectrometers, one Tracor Northern EDS spectrometer, and the Tracor Northern 5600 automation system. The system is equipped with an LDE1 (W-Si) crystal for light element analysis. Analyses were run at 15 kV accelerating voltage, 20 nA beam current (Faraday cup), and focused beam, except for analyses on albite which used a 10μm-diameter defocused beam.

Samples whose peak counts showed standard deviations of less than 1% of the average peak count value were considered to be homogeneous. For further confirmation of homogeneity, quantitative analyses (20 per sample) were then done with normal analytical procedures (60s count times, Tracor Northern ZAF matrix correction, oxygen by difference). Because fluorine interferes with the FNAA oxygen analysis, WDS scans were done on all samples to confirm the absence of fluorine.

Samples that were found to be homogeneous were then crushed, sieved, and handpicked to produce pure mineral separates. Fe^{3+}/Fe^{2+} ratios in iron-bearing samples were determined by Mössbauer spectroscopy, performed by one of us (MDD) at the Mineral Spectroscopy Laboratory at the University of Oregon. Samples, for which published cation analyses do not exist, are being analyzed at present by wet chemical analysis.

Five aliquots (60 mg each) of each sample were analyzed by FNAA for oxygen content at the University of Kentucky Radioanalytical Service Laboratory under the supervision of Dr. W. D. Ehmann.[7,8] Within 2 h of analysis, the samples are weighed into polyethylene vials under extra-dry nitrogen. For the FNAA analysis, samples were placed in an automated transfer system between the neutron flux source (Kaman Nuclear A-711 neutron generator) and the detectors (a pair of NaI(Tl) scintillation counters). Analytical errors of the FNAA analyses are about +1.0 wt% due to small aliquot size. Larger aliquots (150 mg) of the same samples have been resubmitted for repeat FNAA analysis.

A. V. McGuire is at the Department of Geoscience, University of Houston, Houston, TX 77204-5503; C. A. Francis is at the Harvard Mineralogical Museum, 24 Oxford St., Cambridge, Mass., and M. D. Dyar is at the Department of Geological Sciences, University of Oregon, Eugene, Oreg. This work was supported by NSF grant EAR-9017167 awarded to A.V.M.

Results

The 15 oxygen analyses for each sample (3 successive analyses per aliquot, 5 aliquots per sample) were averaged and the results and the standard deviations are reported in Table 1. Only corundum had a measured oxygen content that agrees closely with the calculated value. Disagreement of FNAA and calculated oxygen for the amphibole sample may be due to unmeasured hydrogen in the mineral. The observed substantial disagreement between measured and calculated oxygen contents should serve as a warning against the use of calculated or "assumed" oxygen contents in microprobe standards. ZAF correction factors for oxygen, calculated for these samples for both calculated and measured oxygen contents, are shown in Table 1. In some cases the difference between the two is quite large, and certainly large enough to introduce substantial error if the correct matrix correction factor is not used in microprobe analyses of oxygen.

Conclusions

Calculation of oxygen content by assumptions of charge balance and stoichiometry may be invalid. Use of calculated oxygen contents in calibration of the electron microprobe may lead to gross errors in microprobe oxygen analyses. Microprobe standards can (and

TABLE 1.--Compositions (elemental wt%) of oxygen standards with calculated and measured oxygen contents and ZAF correction factors for oxygen.

	Quartz[4] H122838	Sillimanite[*] H131013	Amphibole[*] 366-92	Albite[5] H131705	Olivine[*] 30-B1	Gahnite[5] H111989	Corundum[*] H126097	Dolomite[6] H105064
Si	46.74	17.31	18.90	31.85	19.58		0.00	
Al	4 ppm	33 54	7.57	10.46	0.00	29 28	52 92	
Fe^{2+}		0 20	1.82	0.01	6.86	1.53	0.00	0.06
Fe^{3+}			7.29					
Mg		0 04	7.36		29.76		0 00	13 13
Mn	2 ppb	0 01	0.09		0.10	0.29	0 00	0 02
Ti	1 ppm	0 01	3.00		0.00		0 00	
Cr		0.01	0.00		0.00		0 00	
Ca		0 00	7.40	0.27	0.02		0 00	21 75
Na	3 ppm	0.01	2.06	8.50	0.01		0 00	
K	2 ppm	0.00	1.22	0.19			0.00	
Ni					0 34			
Zn						34.14		
Li	2 ppm							
C								12 93
SUB total	46 74	51.13	56.71	51.28	56.67	65.24	52.92	47 89
O (calc)	53 25	49.65	42.71	48.70	43.98	34.92	47.08	51 79
TOTAL (calc)	99.99	100.78	99.42	99.98	100.65	100 16	100 00	99 68
O (FNAA)	50.40	44.82	44.03	49.95	40.38	31.73	47.30	49 27
TOTAL	97.14	95 95	100.74	101.23	97.05	96.97	100.22	97 16

Tracor Northern ZAF correction factors for oxygen

O by calc	0.2591	0 2596	0.1781	0.2596	0.2439	0.1900	0.2598	0.1589
O by FNAA	0 2375	0.2395	0.1824	0.2543	0.2276	0.1756	0 2607	0.1595

[*] Microprobe analyses at University of Houston and Fe^{3+} by Mössbauer; see references for other analyses

should) be characterized for oxygen content by
FNAA. The standards developed in this project
provide a small number of materials with well-
characterized oxygen contents. Use of these
materials as oxygen standards may allow for
more accurate oxygen analyses than may be ob-
tained with standards of unmeasured oxygen con-
tent. There are still many problems with oxy-
gen analysis, such as changes in peak shape
with material composition,[1,2] matrix correc-
tion factors,[1,2] etc. However, availability of
standards with characterized oxygen contents
should aid in study and eventual solution of
these problems, and provide some means of eval-
uating oxygen analyses being produced at pres-
ent in many microprobe laboratories.

Availability of Standards

The standards developed in this project will
be available to members of the microanalysis
community beginning in September 1991. Anyone
interested in obtaining these standards should
contact Carl A. Francis, Curator, Harvard Min-
eralogical Museum, 24 Oxford Street, Cambridge,
MA 02138.

References

1. J. T. Armstrong, "Accurage quantitative
analysis of oxygen and nitrogen with a W/Si
multilayer crystal," *Microbeam Analysis--1988*
301.
2. G. F. Bastin and H. J. M. Heijligers,
"Quantitative EPMA of oxygen," *Microbeam Analy-
sis--1989*, 207.
3. M. D. Dyar, "H, O, and Fe^{3+} in biotite
and muscovite," *GSA Abst. with Prog.* 22: A215,
1990.
4. C. Frondel and C. S. Hurlbut Jr., "Deter-
mination of atomic weight of silicon by physical
measurements on quartz," *J. Chem. Physics* 23:
1215-1219.
5. E. Jarosewich, J. A. Nelen, and J. A.
Norberg, "Reference samples for electron micro-
probe analysis," *Geostandards Newsletter* 4: 43-
47.
6. R. M. Garrels, M. E. Thompson, and R.
Siever, "Stability of some carbonates at 25° C
and one atmosphere total pressure," *Amer. J.
Sci.* 258: 402-418.
7. W. D. Ehmann, "Nondestructive techniques
in activation analysis," *Fortschr. der chem.
Forschung* 14: 49, 1970.
8. W. D. Ehmann and J. W. Morgan, "O, Si,
and Al in Apollo 11 rocks and fines by 14 MeV
neutron activation," *Geochim. Cosmochim. Acta*
(Suppl. 1), 2: 1071, 1970.

THE INFLUENCE OF SURFACE OXYGEN CONTAMINATION OF BULK EPMA OF OXYGEN IN TERNARY TITANIUM-OXYGEN-COMPOUNDS

J. J. Goldstein, S. K. Choi, F. J. J. van Loo, H. J. M. Heijligers,
J. M. Dijkstra, and G. F. Bastin

Surface oxide layers form on most materials at room temperature. The presence of these contamination layers makes it very difficult to analyze the oxygen content of the bulk material.[1] We have shown experimentally that for example the use of an air jet to prevent carbon contamination on sensitive nitride specimens can lead to dramatic in situ oxidation phenomena. On the most sensitive specimens (HfN, ZrN) such phenomena can even be observed without the use of an air jet: the mere positioning of the electron beam on the specimen can already start this (continuous) oxidation process. However, apart from these dynamic oxidation phenomena, which can easily lead to erroneous interpretations, there is also a problem related to the presence of native oxide skins on sensitive metals like T, Zr, and Hf or their alloys.

It is not usually realized how large the influence of a 5nm-thick TiO_2 layer on an otherwise oxygen-free piece of titanium can be on the experimentally O-Kα count rate. If the presence of a Ti-oxide skin is ignored and all the O Kα counts are attributed to an alleged bulk oxygen content, most bulk matrix correction programs would translate this to something like between 1 and 2 wt.% oxygen, no matter which accelerating voltage is used. Very large errors in the bulk oxygen content can be made under these circumstances. These problems find their origin in the fact that the O Kα emission volumes in metals like Ti are extremely shallow (approx 200 nm) due to the large absorption of O Kα x rays. (The mass absorption coefficient of O Kα in Ti is of the order of 20 000 cm^2/g). An oxide skin of even a few tens of nanometers can therefore occupy a surprisingly large proportion of the total emission volume and its influence on the total O Kα count rate can be disproportionally large due to the relatively low self-absorption of the O Kα intensity. It follows that when efforts are undertaken to measure low bulk levels of oxygen in titanium or its alloys, it is vital to know the oxide film thicknesses on each of the specimens in order to subtract the count rates from these films from the total observed O Kα count rate.

From a chemical point of view it might be expected that the oxide skin thickness is related to the titanium content and will thus vary from one compound to another. Therefore, it is necessary to use thin-film analysis software,[2] coupled with analyses over a wide range in voltages, in order to distinguish surface from bulk effects.

It was necessary to use thin film analysis procedures in our attempts to measure bulk oxygen contents in ternary Ti-Si-O and Ti-Al-O phases produced during diffusion bonding of metal-ceramic joints. Our preliminary results indicate that in the analysis of the solid solution of oxygen in titanium, the apparent bulk oxygen content is doubled by the presence of an oxide skin. This means that errors of up to 100% in the bulk oxygen content can easily be made if the presence of an oxide skin on the specimens is not taken into account.

Experimental

In order to establish the variation of oxide skin thickness with Ti-content in the Ti-Si-O system, a binary Ti-$TiSi_2$ diffusion couple was prepared from (presumably) "oxygen-free" starting materials by diffusion bonding in a vacuum furnace, and subsequently annealed for a prolonged period on time at 900 C. After annealing, the couple contained the Ti_3Si, Ti_5Si_3, Ti_5Si_4, and TiSi compounds in parallel layers between the unreacted Ti and $TiSi_2$ starting materials.

The oxygen measurements were carried out in a JEOL 733 Superprobe, equipped with a W/Si multilayer crystal (2d-spacing 59.8 Å), with natural hematite (Fe_2O_3) as a standard. Standard and sample were mounted in copper-filled conductive polymer and no conductive coatings were applied. Measurements of O Kα were made for each titanium-silicon compound and the Fe_2O_3 standard at accelerating voltages of 2, 3, 4, 5, 6, 8, 10, 12, and 15 kV. The measured k-ratios for O Kα were processed with our thin-film program ("TFA"[2]), assuming that the oxide skins consist exclusively of TiO_2 and that all O Kα counts can be attributed to this surface layer.

Results and Discussion

The results for the unreacted Ti specimen are shown in Fig. 1. The open circles represent the measured k ratios for Ti as a function of the accelerating voltage. The thin-film program ("TFA") was used to calculate k ratios. The major input parameters were the accelerating voltage and the assumed thickness
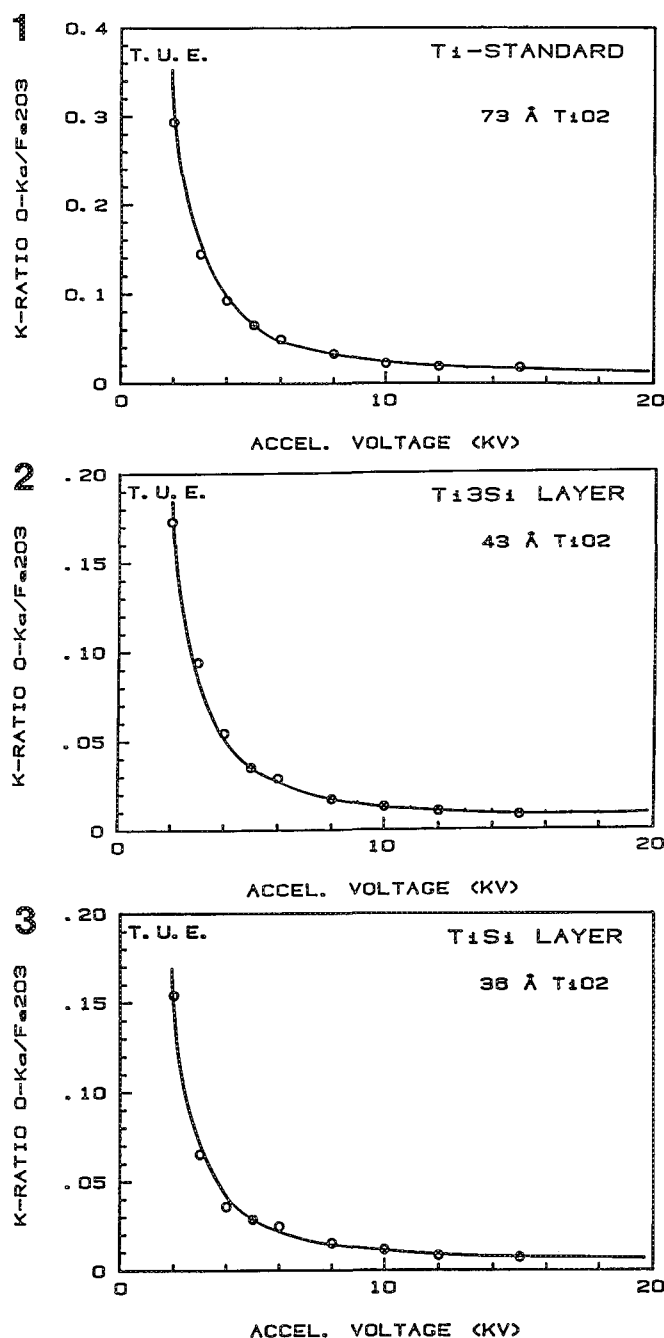
FIG. 1.--Agreement between measurements (circles) and predictions (solid curve) of our TFA program for 73Å-thick TiO$_2$ film on Ti. Take-off angle 40°.

FIG. 2.--Agreement between measurements (circles) and predictions (solid curve) of our TFA program for 43Å-thick TiO$_2$ on Ti$_3$Si.

FIG. 3.--Agreement between measurements (circles) and predictions (solid curve) of our TFA program for 36Å-thick TiO$_2$ film on TiSi.

of 73 Å fits the measured k ratios quite well (Fig. 1).

The oxidation of titanium at low temperatures has been studied by a number of investigators using Auger and x-ray photoelectron spectroscopy.[3] Early photoemission results showed the formation of a layer of TiO$_2$ which was thicker than the photoelectron sampling depth. The sub-

sequent literature gives conflicting results from oxide film thicknesses less than two monolayers to 40 Å and the presence of inhomogeneous oxides.[3] However, the Ti oxidation studies are carried out in clean vacuum systems that may not simulate oxide formation after metallographic polishing in the laboratory.

It is possible, and perhaps even likely, that any adhering atmospheric oxygen is inadvertently included as a contribution to the total film thickness of TiO$_2$. However, the very small thickness of the TiO$_2$ film makes it impossible to do meaningful EPMA measurements that are completely contained inside the film, even at the lowest accelerating voltages applied.

Alloying the titanium with 16.35 wt.% of Si as in the Ti$_3$Si compound (Fig. 2) reduces the oxide skin to 43 Å. This trend is continued in the Ti$_5$Si$_3$ (42 Å) and Ti$_5$Si$_4$ (38 Å) compounds. The lowest value of 36 Å so far has been found on the TiSi compound (Fig. 3). (TiSi$_2$ was not measured.) All efforts to reduce the surface oxide skin thickness by mechanical polishing procedures and/or chemical etching techniques have proved futile. Apparently the presence of such skins cannot be avoided. It is therefore all the more important that the influence of such a skin on the measurements of bulk oxygen contents is not underestimated or neglected. The work presented here is a necessary prerequisite for a correct evaluation of the O Kα microprobe data in order to arrive at the correct ternary phase relationships in the Ti-Si-O and Ti-Al-O systems.

At the moment investigations based on Auger and XPS techniques into the nature and thickness of the oxide skins on the various phases in both systems have been started. Apart from backing up our EPMA results we also hope that these techniques will supply more detailed information on the exact nature and layer sequence of oxides on top of the surfaces in case more than one oxide is involved.

References

1. G. F. Bastin and H. J. M. Heijligers, "Contamination phenomena in the electron probe microanalyzer," *Microbeam Analysis--1988*, 325.
2. G. F. Bastin, H. J. M. Heijligers, and J. M. Dijkstra, "Computer programs for the calculation of x ray intensities emitted by elements in multi-layer structures," *Proc. XIIth ICEM* 2: 216, 1990.
3. A. F. Carley, P. R. Chalker, J. C. Rioviere, and M. W. Roberts, "The identification and characterisation of mixed oxidation states at oxidised titanium surfaces by analysis of x-ray photoelectron spectra," *J. Chem. Soc.* (Faraday Trans. 1) 83: 351-370, 1987.

EXPLORING THE MINIMUM DETECTION LIMIT WITH THIN FILMS ON A SUBSTRATE USING EDS

R. H. Geiss and R. J. Savoy

The conventional determination of the minimum detectable limit (MDL) for an element is given with reference to measurements made on a standard with known concentration, C_{std}, of the element. Measurements of the peak (-background) intensity P and the background B allow the MDL concentration C_{MDL} to be determined from

$$C_{MDL} = 3.29 n C_{std} \sqrt{(B/P^2)}$$

where n is multiplying factor $[C_{std}/(1 - C_{std})(1 - k/k)]$ (n = 1 for a pure element standard).

In terms of counting rate, where 1_p and 1_b are the peak and background counting rates, respectively, and t is the t-me of the measurement,

$$C_{MDL} = 3.29 n C_{std} \sqrt{(I_b/I_p)}(I_p t)$$

For example, with a pure-element standard, using WDS, $I_p = 10$ cps, $I_p/I_b = 1000$, and t = 100 s.

$$C_{MDL} = 3.29 \sqrt{(1/10^{-10})} = 3.29 \times 10^{-5} = 32.9 \text{ ppm}$$

for 100s counting. For 1000s counting, $C_{MDL} \cong 10$ ppm.

With EDS the problem is a bit confused with respect to what values are to be used for the intensities of the peak and background. The natural line width of the emitted x rays is about 2-3 eV, but due to electronic noise and the statistics of electron-hole pair counting, the measured line widths in an EDS spectrum (as defined by the FWHM) are 50 to 100 times broader.

Consider the EDS spectral peak shown in Fig. 1. There are at least three ways in which we may define the peak and background intensities: (1) the peak and background intensities P and B, given by the intensities in the single channel at the peak maximum; (2) the integrated area under the peak A_p and the integrated area under the corresponding background region A_B; and (3) the integrated area under the peak A_p and the intensity of the background in a single channel under the peak B. Other definitions have been proposed that include use of the integrated areas of the peak and background as defined by the FWHM or 1.2 FWHM of the peak.

An EDS experiment on a pure palladium sample at 10 keV with a 40° TOA and counting for 5000 s gave $I_p = 563$ cps and the following for the peak/background given by the three options described above: (1) $A_p/A_B = 2.24$, (2) P/B =

11.4, (3) $A_p/B = 166.1$. The calculated MDL for these three options are then $C_{MDL} = (1)$ 1310 ppm, (2) 2216 ppm, (3) 152 ppm.

Consider that the volume irradiated in this experiment is about 1 μm on a side. The number of atoms in the irradiated volume is $N_{atoms} = V_p N/A = 10^{-12} \times 12 \times 6.02 \times 10^{23}/106.4 = 6.8 \times 10^{10}$ atoms, where V is the volume, p is the density, N = Avogadro's number, and A the atomic weight.

For the standard definition of peak/background, as given by P/B here, $C_{MDL} = 2216$ ppm, the minimum number of atoms detectable in this volume would be $N_{atoms} = 6.8 \times 10^{10} \times 2216 \times 10^{-6} = 15.07 \times 10^7$ atoms.

In terms of monolayers, one monolayer of Pd covering a 1μm square area would contain approximately 10^7 atoms. Therefore, the calculation for the number of Pd atoms detectable at a C_{MDL} of 2216 ppm corresponds to approximately 15 monolayers.

On the other hand, by use of the value for C_{MDL} given by the expression containing the area of the peak divided by the background in a single channel, $C_{MDL} = 152$ ppm, the minimum number of Pd atoms detectable should be 1.02×10^7 atoms, which is equivalent to about one monolayer.

To ascertain which is the best definition for C_{MDL} in the case of EDS, and therefore to determine which values for the peak and background intensities should be used in the evaluation of the C_{MDL}, we measured the EDS spectrum from a series of 2, 4, and 6Å films of palladium evaporated onto tantalum substrates. It can be shown that a 2Å palladium film corresponds to approximately one monolayer of palladium. Thus, in this experiment we are measuring film consisting of approximately 1, 2, and 3 monolayers of palladium, respectively.

Analysis of the data began with the creation of an ASCII file from the EDS spectrum and its importation into a PC spreadsheet program. Here the background, as determined from a Ta standard and normalized to the Pd background, was subtracted from the Pd data. The result left the expected series of overlapped peaks comprising the Pd L spectrum. These peaks were then fitted to a previously determined Pd L spectrum standard by use of a fractional multiplying factor. The Pd standard was deconvoluted into 5 Gaussians consisting of the Lα through the Lβ4, by means of a template developed for a PC spreadsheet. For the best fit, as determined by a least-squares analysis of the experimental and fitted data, we had to include the Lβ4 peak! In the determination of the k-factors, only the integrated intensity of the Lα peak was used.

The EDS Pd L spectra obtained from the 2, 4,

and 6Å samples are given in Figs. 2(a), (b), and (c), respectively. The peaks are shown after careful subtraction of the Ta background and include the fitted Gaussian curves. (As mentioned previously, for background subtraction the data from bulk Ta were used, which was found to be critical to obtaining the best background fit under the Pd L spectrum.) From the figures it is seen that the Pd peaks are easily identified and the Lα Gaussian is clearly defined even for the 2Å-thick film.

Using the integrated areas under the L peaks and the corresponding area from the pure Pd standard, k-factors can be calculated (k = $I_{sample}/I_{standard}$). The k-factors measured for both 5000 and 1200s collection times are compared with calculated k-factors for the appropriate Pd films on a Ta substrate in Table 1. The calculated values were obtained using the Pouchou and Pichoir,[2,3] $\phi(\rho z)$ model in the GMRFILM program of R. Waldo.[4] This program is available free in the MAS PC computer library.

TABLE 1

Pd film thickness (Å)	Calculated k-factor	Meas. 5000 s	Meas. 1200 s
2 Å	0.00140	0.00175	0.00075
4 Å	0.00281	0.00325	0.00146
6 Å	0.00423	0.00485	0.00130

The agreement between the measured and calculated k-factors for spectra collected with the 5000s counting time is very good. Considering the clarity of the peak from the 2Å film shown in Fig. 2(a), it should be possible to measure even less than a single monolayer of Pd on Ta at a data collection time of 5000 s. Spectra collected under the same instrumental conditions but for 1200 s were too noisy for reliable film thickness determination. That is, one could see the peaks and measure areas under the peaks, but the k-factors derived from these measurements were not consistent with the known film thickness, as can be seen from the data given in the last column of Table 1.

From the experimental evidence shown here and the three ways of calculating C_{MDL} discussed previously, we conclude that the best peak and background measurements to use to estimate the MDL from measurements on pure standards are the integrated area under the peak for the peak intensity and the intensity of a single channel under the peak for the background. Use of the integrated intensity for the peak has physical meaning in that the total x-ray emission from a specific atomic transition is contained in the integrated area of the peak. In the case of the background, the concern is with the counts in a single channel, not an integrated area. Liebhafsky et al.[5] note the minimum detectable limit is determined by that value of the peak intensity P which exceeds the background intensity B by $3\sqrt{B}$. In the experimental data collected here, B ≅ 8000 counts for the 2Å Pd film, so that $3\sqrt{B}$ ≅ 268,

which compares favorably with the measured peak intensity of 295 counts for the Pd Lα.

References

1. T. O. Ziebold, *Anal. Chem.* 39: 858, 1967.
2. J. L. Pouchou and F. Pichoir, *Proc. 11th ICSOM*, 1986, 249.
3. J. L. Pouchou and F. Pichoir, *Proc. 1st Eur. MAS*, 1989, 127.
4. R. A. Waldo, *Microbeam Analysis--1988*, 310.
5. H. A. Liebhafsky, H. G. Pfeiffer, and P. D. Zemany, in A. Engstrom, V. Cosslett, and H. Pattee, Eds., *X-ray Microscopy and X-ray Microanalysis*, Amsterdam: Elsevier/North Holland, 1960, 321.
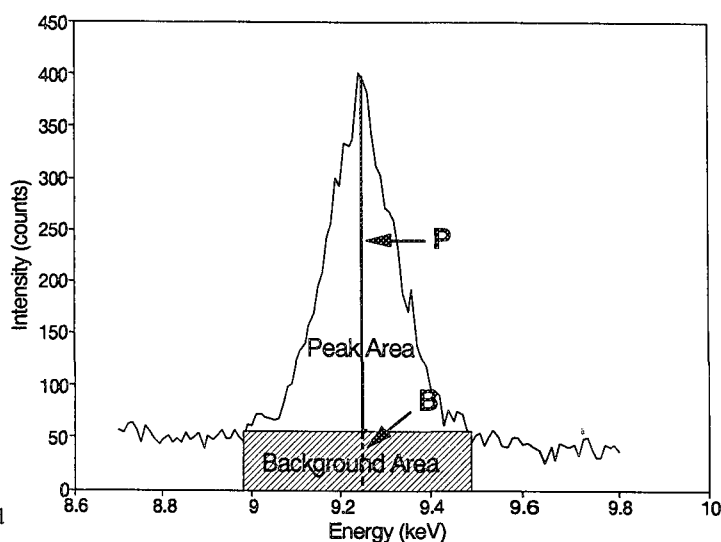
Fig. 1.--Definitions of peak and background areas and at peak P and background B, single-channel intensities.
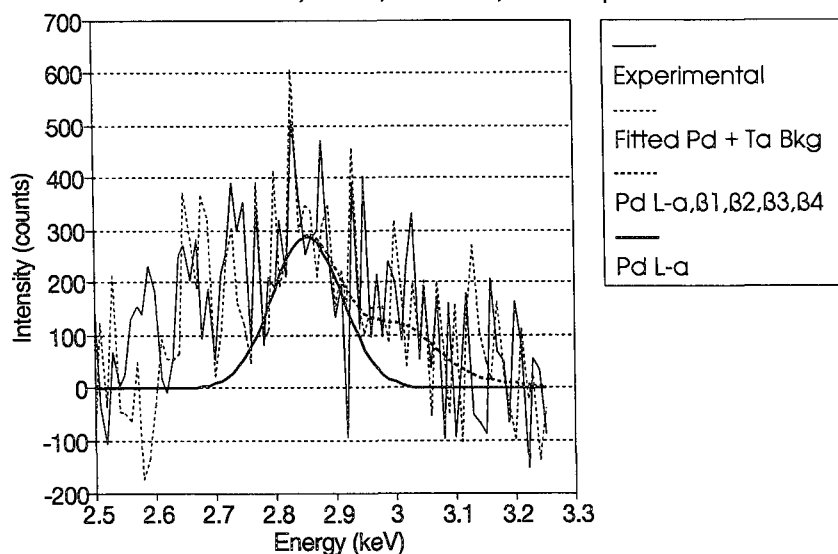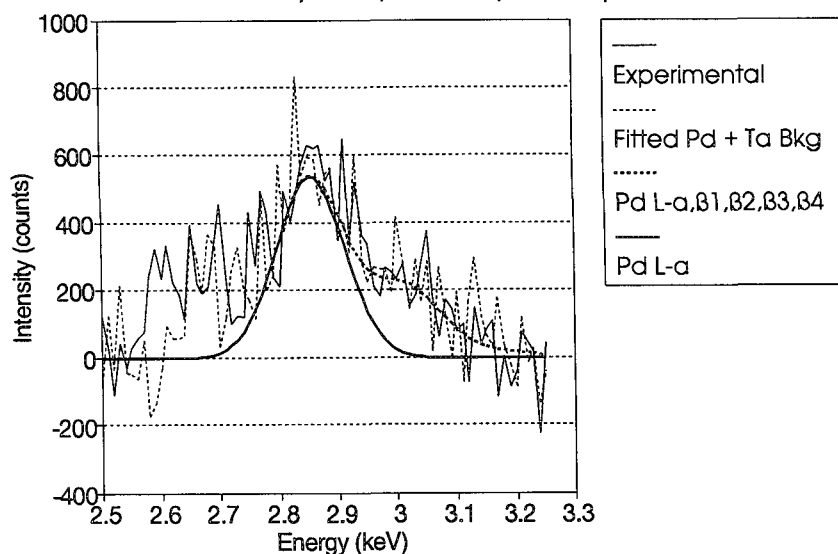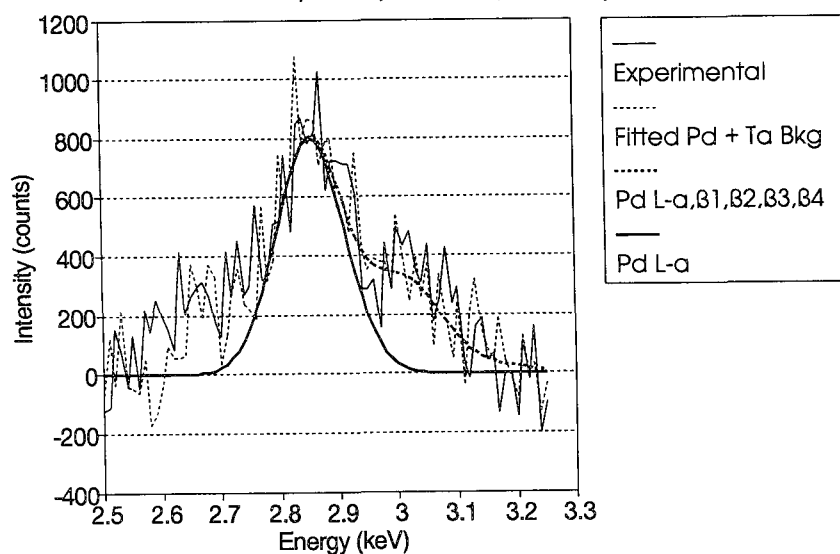
FIG. 2.--EDS spectra from 2, 4, and 6Å-thick films of Pd on a Ta substrate. Background has been subtracted by use of background from pure Ta sample as a model. Experimental and fitted Pd + Ta spectra are shown with solid and dotted lines, respectively. Calculated Pd Lα through Lβ₄ combined spectra and Lα line alone are shown by heavy dotted and solid lines, respectively. Areal intensity of Lα line was used to determine k-factors given in Table 1.

A MODIFICATION OF KYSER AND MURATA'S APPROACH FOR THE CHEMICAL QUANTIFICATION OF SPHERICAL PARTICLES IN A STEEL MATRIX

Raynald Gauvin, Gilles L'Espérance, and Sylvain St-Laurent

The current schemes of quantification of x-ray microanalysis in the S.E.M. [ZAF and $\phi(\rho Z)$ methods] are valid for specimens of homogeneous composition. The determination of the chemical composition of small particles embedded in a matrix using these techniques is impossible because the volume of x-ray emission is not of homogeneous composition. A scheme of quantification to determine the composition of small inclusions embedded in a matrix has been developed by use of Monte Carlo simulations. This scheme is similar to that developed by Kyser and Murata for the quantification of thin foils deposited on a substrate by x-ray microanalysis in the S.E.M.[1]

Description of the Method

The method of Kyser and Murata[1] to determine the composition and thickness of a thin foil deposited on a substrate is based on the experimental measurement of the K_i factor used in the conventional correction procedures:

$$K_i = I_i / I_{(i)} \tag{1}$$

where I_i and $I_{(i)}$ are the net intensities of element i emitted from a thin foil of specific thickness and composition deposited on a substrate and from a standard of known composition. These net intensities should be measured under the same experimental conditions. In their method, experimental K_i values are related to the thickness and the composition of the thin foil with calibration curves that are computed by the Monte Carlo method.

Figure 1 shows the geometry of a spherical particle embedded in a matrix. When the top radius of the circle defined by the intersection of the spherical particle and the top surface of the sample b and the depth of the inclusion P are known, the geometry of this spherical particle inside the specimen is completely characterized: r is the radius of the inclusion and c is its geometrical center. Since it is possible to measure the top radius of a spherical particle in the SEM, the determination of the composition and the depth of a spherical parti-
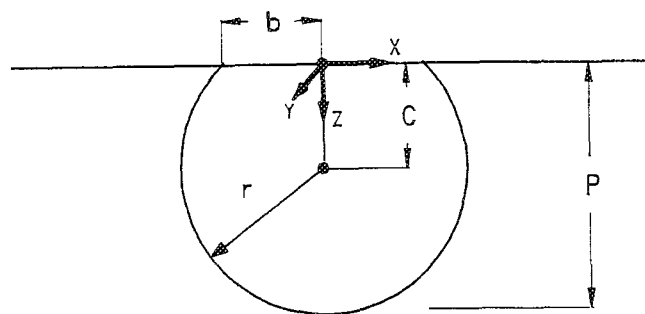
FIG. 1.--Geometry of spherical inclusion embedded in matrix.

cle is a problem similar to the determination of the thickness and composition of a thin foil deposited on a substrate. Monte Carlo simulations can therefore be used to compute calibration curves of K_i as a function of the thickness and composition of a spherical inclusion which has a given top radius. Experimental values of K_i, knowledge of the top radius of a spherical particle observed in the SEM, and these computed calibration curves can then be used to determine the composition and thickness of this particle. We have developed a Monte Carlo program to compute the x rays generated by the primary electrons as they are scattered in the particle and in the matrix in order to compute such calibration curves for a fixed b value.

Description of the Monte Carlo Program

The Monte Carlo program has been developed for a homogeneous spherical inclusion embedded in a homogeneous matrix. (Only an outline of the program can be given here; the detailed description of the program will be given elsewhere.[2]) Scattering of the electrons is computed by the method developed by Newbury and Myklebust.[3] Each time an elastic collision occurs, the elastic cross sections are weighted with composition, and a random number uniformly distributed between zero and one is used to determine which element interacts with the incoming electron. To generate uniform random numbers, we use the method developed by Press et al.[4] This method avoids the generation of sequences of random numbers.

When an electron is scattered in the specimen, its position with respect to the inclusion and the matrix needs to be known since the scattering process and the generation of x rays are different in the inclusion and in the matrix. If b and P are known, the equation of the surface of the inclusion is

$$X^2 + Y^2 + Z + \left(\frac{b^2 - P^2}{2P}\right)^2 = \left(\frac{P^2 + b^2}{2P}\right)^2 \qquad (2)$$

When an electron travels in the specimen, it is possible to determine at each moment of the simulation whether this electron is in the inclusion or in the matrix from Eq. (2) and the coordinates (X_i, Y_i, Z_i) of a given point of an electron in the specimen.

When an electron passes from an inclusion to the matrix or from the matrix to the inclusion, the distance between collisions is computed following Twigg.[5] When an electron travels between two collisions, the intensity I_x of characteristic x rays generated by this electron is computed using:

$$I_x = Q_x(E_m)\omega_x \alpha_x C_x (\rho/A_g) L_i \qquad (3)$$

where $Q_x(E_m)$ is the ionization cross section of element x calculated with the mean energy E_m of the electron between these two collisions; L_i is the distance between collisions; and ω_x, α_x, C_x, and A_x are the fluorescence yield,[7] the relative intensity factor,[8] the weight fraction, and the atomic weight of element x, respectively.

The background intensity I_b generated by an electron as it travels between two collisions is computed from

$$I_b = (\partial Q_b/\partial E) \; \Delta E \; \rho L_i/\bar{A} \qquad (4)$$

where $\bar{A}$ is the mean atomic number of the inclusion or of the matrix and $\partial Q_b/\partial E$ is the cross section for background generation[9] for photons having an energy E and a window energy ΔE.

Only a fraction of x rays generated in the specimen are measured by the x-ray detector because of absorption in the specimen. Characteristic and background intensities $I'_{x,b}$ measured by the detector are computed from Beer's law:

$$I'_{x,b} = I_{x,b} \exp\{\Sigma_j[(-\mu/\rho_j)|^{x,b}_j \rho_j d_j]\} \qquad (5)$$

where x and b refer to characteristic and background intensities, respectively, and $(-\mu/\rho)|^{x,b}_j$, ρ_j and d_j are respectively the mass absorption coefficient[10] for photon x or b, and the density and the distance traveled by the photons in the medium j (inclusion or matrix).

It is important to know in what region (or zone) relative to the detector x rays are generated to determine in what zone (inclusion and/or matrix) they are absorbed in order to use the appropriate values of $(-\mu/\rho)|^{x,b}_j$, ρ_j to compute $I'_{x,b}$ from Eq. (5). In the case of a spherical inclusion embedded in a matrix, five different zones exist, as shown in Fig. 2. A criterion to determine in what zone x rays are generated has been developed[2] from Eq. (2) and the equation of the detector axis.

The intensity $I''_{x,b}$ of characteristic or continuum x rays absorbed in the specimen is given by

$$I''_{x,b} = I_{x,b}[1-\exp\{\Sigma_j[(-\mu/\rho)|^{x,b}_j \rho_j d_j]\} \qquad (6)$$
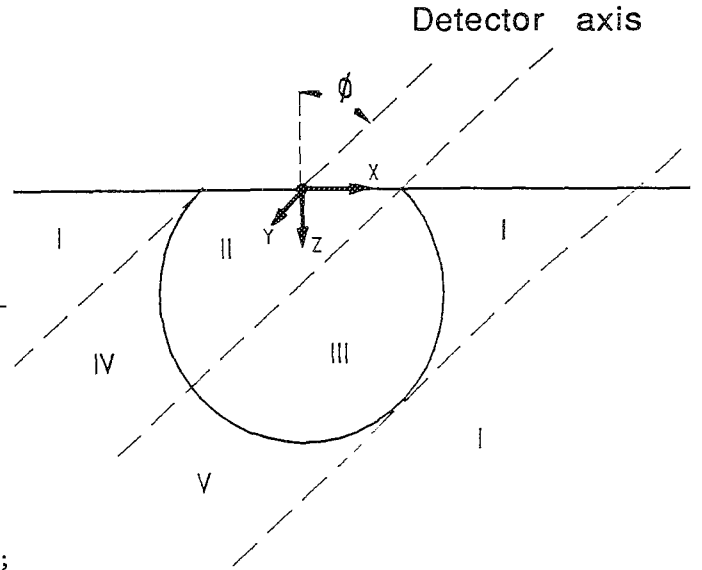
FIG. 2.--Zones of x-ray absorption: zone II, absorption in inclusion only; zone III, absorption in inclusion and in matrix; zone IV, absorption in matrix and in inclusion; zone V, absorption in matrix, in inclusion, and in matrix.

and the x-ray intensity I^f_A fluoresced by $I''^f_{x,b}$, if the energy of these photons is greater than the ionization energy of the atomic level of element A, is given by[11]

$$I^f_A = C_A \frac{(\mu/\rho)|^{x,b}_A}{(\mu/\rho)|^{x,b}_{spec}} \frac{\Gamma_A - 1}{\Gamma_A} \omega_A \alpha_A I''_{x,b} \qquad (7)$$

where $(\mu/\rho)^{x,b}_A$ is the mass absorption coefficient of photon x or b in element A, and Γ_A is the absorption edge jump ratio at the ionization energy of the atomic level of element A. The intensity of fluoresced x rays measured by the detector is given by

$$I^{f'}_A = I^f_A \exp\{\Sigma_j(\mu/\rho)|^x_j \; \rho_j \cdot S_j)\} \qquad (8)$$

where S_j is the distance traveled by photons A in the medium j in the direction of the detector. To compute S_1, the distance L_f from the midpoint between P_i and P_{i+1} to the position where fluorescence occurs is required (Fig. 3). To compute this value, we must know the distribution function of the fraction of x rays remaining in the specimen as a function of distance to compute the position where the fraction of primary x rays are absorbed ($I''_{x,b}$). It is assumed that the fraction of x rays remaining in the specimen decreases linear increasing distance with a slope equal to $(-\mu/\rho)|^x_i \rho_j$. Figure 4 shows this distribution function, $F(\gamma)$, as a function of the normalized distance γ when the photons are absorbed in three different zones.

We define the following normalized variables: $\gamma = L_f/Z_m \sec \phi$, $\Omega = d_{f1}/Z_m \sec \phi$, $\Delta = d/e = (\mu/\rho)^x_I [\rho_I/(\mu/\rho)^x_{II}]\rho_{II}$, $X = d_{f2}/Z_m \sec \phi$,

X-Ray detector

$f(\Upsilon)$
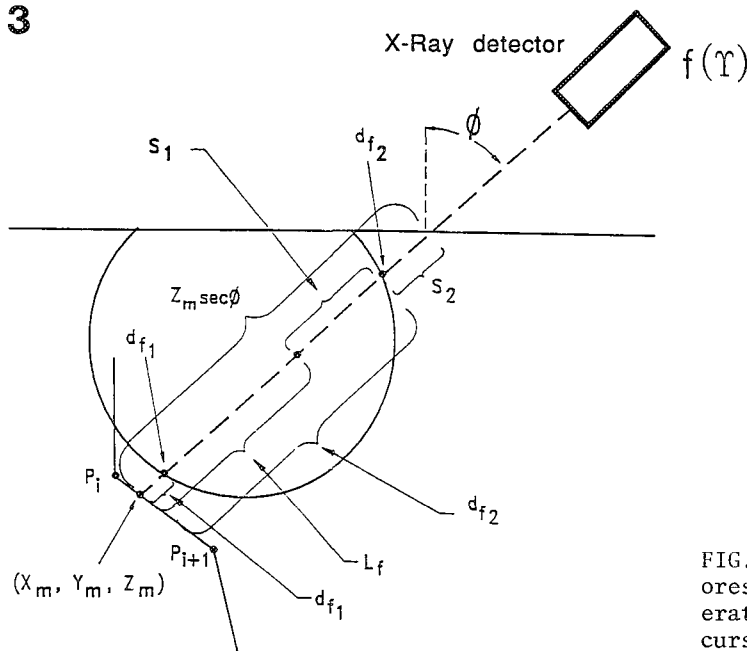
FIG. 3.--Geometry used to compute x-ray fluorescence. L_f is distance between x-ray generation and position where fluorescence occurs. S_1 and S_2 are distances used in Eq. (8). d_{f1} and d_{f2} are distances betwen point of x-ray generation and first and second interface between inclusion and matrix, respectively. $Z_m \sec \phi$ is total distance traveled by x ray in specimen toward detector.

FIG. 4.--Distribution function of x rays as a function of normalized distance γ when x rays are absorbed in three zones; -d, -e, and -f are slopes of this function in zones I, II, and II, respectively.

$\eta = e/f = (\mu/\rho)_{II}^X [\rho_{II}/(\mu/\rho)_{III}^X]\rho_{III}$ where Z_m $\sec \phi$; L_f, d_{f1}, and d_{f2} are defined in Fig. 3; and d, e, and f are defined in Fig. 4.

By stating that

$$\int_0^1 F(\gamma) \, d\gamma = 1 \qquad (9)$$

we obtain γ with the generation of a random number R uniformly distributed between 0 and 1 and by solving the equation

$$R = \int_0^\gamma f(\gamma) \, d\gamma \qquad (10)$$

When there is absorption in three zones, we obtain for $0 < \gamma \leq \Omega$ when $R \leq R'$ where R' is the area of the first zone:

$$R' = \Omega \frac{\Delta \eta \Omega + 2(1 - \chi) + 2\eta(\chi - \Omega)}{1 + \Omega^2 \eta(\Delta - 1) + \chi^2(\eta - 1)} \qquad (11)$$

$$\gamma = \frac{B - \sqrt{B^2 - A}}{\Delta \eta} \qquad (12)$$

where $A = R[1 + \eta\Omega^2(\Delta - 1) + \chi^2(\eta - 1)]$ (13)

and $B = \eta\Omega\Delta + (1 - \chi) + \eta(\chi - \Omega)$ (14)

For when $\Omega < \gamma \leq \chi$ when $R' < R \leq R''$ where R'' is the area of the first and second zone, and for $\chi < \gamma \leq 1$ when $R > R''$, similar formulas are obtained[2] as for cases II and I.

In this program, we consider the fluorescence of the Kα line of S by the Kα line of Mn and we also consider the fluorescence of the

Kα lines of S and Mn by the background. For these last two cases, I_b is computed from Eq. (6) with E equal to the ionization energy of the K level of S or Mn and ΔE is set equal to 300 eV.

Results

To test program simulations, experimental measurement of x rays emitted by MnS inclusions embedded in an iron matrix were performed in samples of iron powder that had been sintered at elevated temperatures. The periphery of the plane of interaction of the analyzed MnS inclusions with the top surface of the sample was always circular, indicating that these inclusions were spherical.

We measured K_i factors using for standards a pyrite sample (FeS_2) and pure manganese for the S and Mn Kα lines, respectively. All the measurements and the computations were made with the electron beam positioned at the center of the inclusions. In our computations, we assume that the initial diameter of the electron beam (including 90% of the electrons) is 50 nm. To compute x rays generated by the scattering of electrons in a spherical inclusion of a given size by use of our Monte Carlo program, the trajectory of 5000 electrons has been simulated. The experimental measurements were performed with a JEOL-840 SEM coupled with a Si(Li) Link detector operating with a Be window.

Figure 5 shows the ratio of net intensities for the Kα line of S and Mn emitted by the standards at an energy E_0 divided by the net intensities of the same Kα line at 15 keV as a

5

Inc: MnS, X = S, E_O = 15 KeV

- S K_α computed in FeS$_2$
- S K_α measured in FeS$_2$
- Mn K_α computed in Mn
- Mn K_α measured in Mn

6

p/d=2 21
p/d=0 5
p/d=0 116

- Experimental values
- Computed values
- — Fit of experimental values

Circular diameter (µm)

7

Circular Diameter = 1.0 µm , E_O = 15 KeV

o——o S
•——• Mn

Depth (µm)
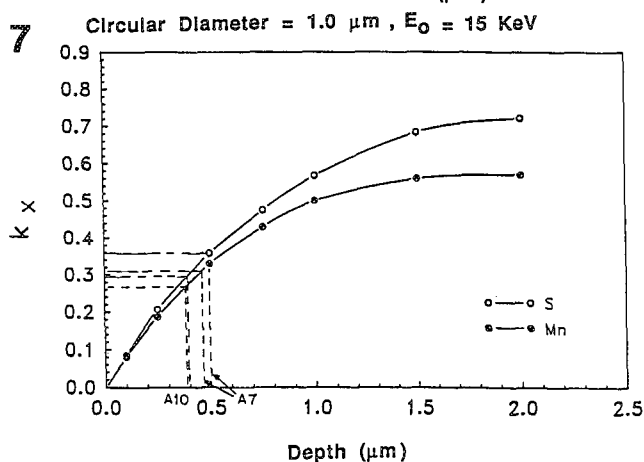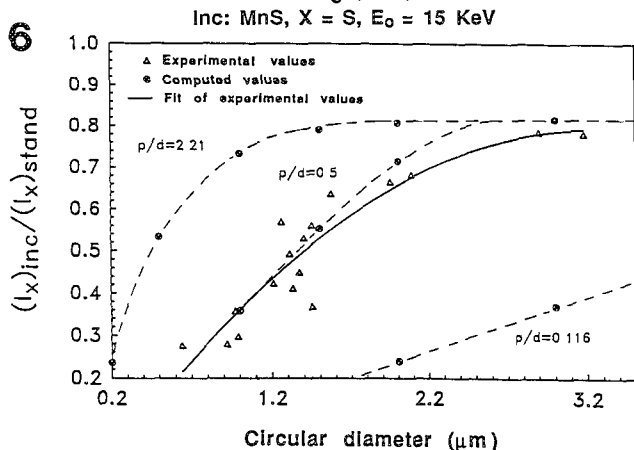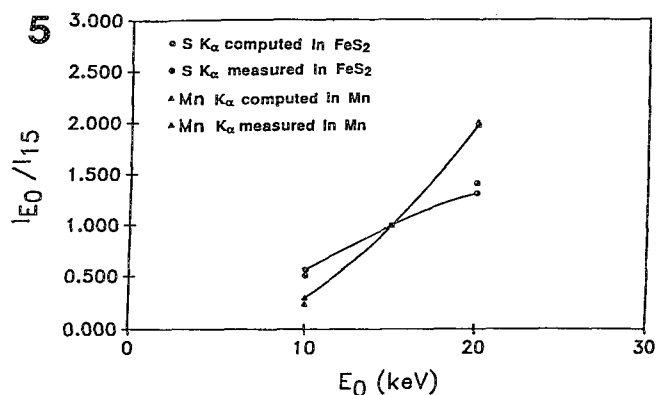
FIG. 5.--Ratio of net intensities for Kα line of S and Mn emitted by standards at energy E_0 divided by the net intensity of the same Kα line emitted at 15 keV as a function of E_0 measured experimentally at 10, 15, and 20 keV and computed with our Monte Carlo program.

FIG. 6.--K_i for x-ray Kα line of S at 15 keV as a function of superior diameter of inclusion measured experimentally for 17 MnS inclusions and computed by use of our Monte Carlo program for small inclusions (P/d = 0.116), medium inclusions size (P/d = 0.5), and large inclusions (P/d = 2.21) assuming that C_{Mn} = 0.63.

FIG. 7.--K_S and K_{Mn} as a function of P for E_0 = 15 keV, C_{Mn} = 0.63 and b = 0.5 µm. Results for inclusions A7 and A10 are also presented.

TABLE 1.--P values for five inclusions obtained with experimental values of K_S and K_{Mn} and computed curves of K_S and K_{Mn} as functions of P for fixed values of b and E_0, assuming that C_{Mn} = 0.63.

Inclusion number	Experimental		P obtained from experimental K_s (µm)	P obtained from experimental K_{Mn} (µm)	P average (µm)	ΔP/P x 100 (%)
	K_s	K_{Mn}				
E_0 = 20 KeV b = 0 7 µm A15	0 25	0 21	0 53	0.65	0 59	18
A1	0 33	0 255	0 75	0 8	0 775	6 2
A2	0 34	0 28	0 78	0 88	0 83	11 3
E_0 = 15 KeV b = 0 7 µm A15	0 42	0 36	0 5	0 47	0 485	6
A1	0 53	0 42	0 74	0 62	0 68	16
A2	0 56	0 44	0 8	0 7	0 75	12 5
E_0 = 15 KeV b = 0 5 µm A10	0 3	0 27	0 38	0 4	0.39	5
A7	0 36	0 31	0 5	0 47	0 485	6

function of E_0 measured experimentally (with the same beam current and acquisition time) at 10, 15, and 20 keV and computed with our Monte Carlo program. Clearly, there is excellent agreement between the measured and computed values.

Figure 6 shows the K_i values at 15 keV for the Kα line of S as a function of the top diameter d of the inclusion measured for 17 MnS inclusions. Similar results were obtained for the Mn Kα line. Since inclusions with the same top diameter can have different thicknesses, different values of K_i can be found for a specific d value. Thus, for a given top diameter d, the depth of the inclusion P is not known, and computed curves for small inclusions (P/d = 0.116), intermediate inclusions (P/d = 0.5), and large inclusions (P/d = 2.18) are shown. These curves were computed with the program assuming that the weight fraction of Mn is equal to 0.63. Deep inclusions have measured K_i values close to computed values, which also indicates (as seen previously in Eig. 5) that the program computes the x rays generated by the electrons well, because for these big inclusions, electrons travel only in the inclusions so that the x rays are generated in a specimen of uniform composition. The experimental K_i values for S and Mn are situated between the computed curves for P/d = 0.116 and P/d = 2.18 and these experimental values are near, on average, the values computed for P/d = 0.5. To interpret these results correctly, the average value of P/d for the top diameter of an inclusion d must be known in relation to the size distribution of the inclusions. We have computed these values[2] and, for the range of d for the 17 inclusions, the mean value of <P/d> is close to 0.5. (For d between 1.2 and 3.2 µm, <P/d> is between 0.62 and 0.5.) Thus, the fact that our experimental values are close, on average, to the values computed for P/d = 0.5 means that the modelization of x-ray generation presented here for spherical inclusion is very good.

65

One way to validate the quantification scheme of spherical inclusions embedded in a matrix, which has been described above, is as follows. First, calibration curves of K_S and K_{Mn} as a function of the depth P of the inclusion are computed for a fixed value of the top diameter d and C_{Mn} = 0.63 (the weight fraction of Mn in stoichiometry MnS). Experimental values of K_{Mn} and K_S are then measured and used with the calibration curves and the experimental value of d to obtain the depth P of the inclusion. One value is obtained with K_S and another with K_{Mn}, and these two values are compared to validate the quantification scheme. Thus, three inclusions (A1, A2 and A15) having a top diameter of 1.4 μm were analyzed at 15 keV and 20 keV; and two inclusions (A7 and A10) having a top diameter of 1 μm were analyzed at 15 keV. The calibration curves for inclusions A7 and A10 are presented in Fig. 7. Similar curves are obtained for inclusions A1, A2, and A15. The depth of these inclusions obtained with the experimental K_i values and the calibration curves are presented in Table 1. For inclusions A10 and A7, the difference between P values measured with K_S and K_{Mn} is of the order of 5%. For inclusions A1, A2, and A15, the difference between P values measured with K_S and K_{Mn} is of the order of 12%. These differences may be explained by a weight fraction of Mn which is different from 0.63 in some of these inclusions (a small peak of oxygen was detected in one of these inclusions when the x-ray detector was operated with an ultrathin window); and by the fact that some of these inclusions may not be perfectly spherical and since large inclusions were analyzed, the electrons which escape these inclusions have lost a significant fraction of their initial energy (E < 10 keV) and the scattering of electrons should be modelized more precisely with the use of the Mott elastic cross sections. The fact that the differences in P values are small indicates that our scheme of quantification is valid but that does not mean that our computed P values are good so that to validate these P values, distinct experimental measurements of the depth of inclusions should be performed.

The overall set of experimental data presented in this paper indicates that this method has a very good potential to perform the quantitative chemical analysis of spherical particles by x ray microanalysis in the SEM. This method gives very good results because the geometry of spherical inclusions is well characterized inside the specimen. Thus, this scheme of quantification is valid when the geometry of an inclusion, a particle, a second phase, or a fiber embedded in a matrix is well characterized inside the specimen and when both scattering media have a homogeneous composition.

Conclusions

A procedure to perform the quantitative chemical analysis of spherical inclusions embedded in a matrix using x-ray microanalysis in the SEM has been developed. This procedure is based on the measurement of the K_i ratios used in the usual procedure of quantification for all the elements present in the inclusion and the subsequent use of these values and calibration curves to determine the composition and the thickness of the inclusion.

A Monte Carlo program has been developed and applied to compute these calibration curves for a spherical MnS inclusion embedded in an iron matrix. The results obtained using this method indicates that this procedure of quantifying gives very good results because the geometry of a spherical inclusion is well known inside the specimen.

References

1. D. F. Kyser and K. Murara, in Proceedings of a workshop on the use of Monte Carlo calculations in electron probe microanalysis and scanning electron microscopy, *NBS Special Publication 460*, 129-138, 1976.
2. R. Gauvin, G. L'Espérance, and S. St-Laurent, "Quantitative x-ray microanalysis and a SEM" (in preparation).
3. D. E. Newbury and R. L. Myklebust, *Analytical Electron Microscopy--1981*, 91.
4. W. H. Press, B. P. Flannery, S. A. Teukdsky and W. T. Vetterling, *Numerical Recipes*, Cambridge University Press, 1986, 191.
5. M. E. Twigg, Ph.D. Thesis, University of Illinois, 1982, 70-71.
6. C. J. Powell, *ibid.*, Ref. 2, pp. 97-104.
7. W. Bambinek et al., *Rev. Mod. Phys.* 44: 716-813, 1971.
8. T. P. Schreiber and A. M. Wims, *X-ray Spectrometry* 11: 42-45, 1982.
9. P. Kirkpatrick and L. Weidman, *Phys. Rev.* 67: 321, 1945.
10. F. F. J. Heinrich, *The Electron Microprobe*, New York: Wiley, 1966, 296.
11. V. D. Scott and G. Love, *Quantitative Electron-probe Microanalysis*, West Sussex, England: Harwood Ltd., 1983.

CALCULATIONS OF X-RAY IONIZATION CROSS SECTIONS AT LOW OVERVOLTAGE RATIOS

Suichu Luo and David C. Joy

The x-ray ionization cross section σ_X is a quantity of great importance in electron-beam microanalysis because the magnitude and energy dependence of σ_X must be known accurately in order to implement any scheme of quantification. In the past microanalysis has been performed at beam energies in the range 10-25 keV, and in the regime where the overvoltage ratio U is of order 3 or greater. In this case the conventional expression for σ_X given by Bethe in the form $\sigma_X = (A/EE_C)\ln(BE/E_C)$ (where E is the electron energy, E_C is the critical excitation energy for the x-ray line of interest, and A and B are constants) is known to be reliable provided that care is used in selecting values of A and B.[1] However, with the availability of electron probe instruments using field-emission guns there is increasing interest in carrying out microanalysis at low beam energies (<10 keV) in which case for most common elements the overvoltage ratio U lies in the range 1 < U < 3, and the Bethe expression is neither accurate nor applicable because its underlying assumptions are no longer valid.

In this paper we present some initial results from first-principles calculations of σ_X using a quantum mechanical method developed with special attention to the low overvoltage case. Results from these computations are compared with alternative analytical expression for σ_X,[2,3] with other theoretical calculations,[4] and experimental data.[5]

Details of the Computation

The cross section is computed by a method similar to that described by Leapman, Rez, and Mayer[6] using first-order perturbation theory and Hartree-Slater-Fock wave functions, but because of the low electron energy and the low voltage ratio, both exchange energy and correlation effects are included. The bound wave-functions and the continuum ejected electron state wave-functions are calculated by solving the Schrödinger equation with a self-consistent potential. For all elements we have used as initial potential data values from the *Tables of Atomic Structure Calculations*.[7] To calculate the total electron impact ionization cross section, the differential cross section has to be integrated over both the transferred energy E and the momentum transfer q. The lower energy integration limit is the binding energy of the k shell and the upper limit is the total kinetic energy of the incident electron. The q limits of integration are functions of E and are ob-

---

The authors are at the EM facility, F239 Walters Life Sciences Building, University of Tennessee, Knoxville TN 37996-0810.

tained from the conservation of energy and momentum during the collision. The integral intervals of E and q strongly influence the accuracy of the results. To save computer time while still producing accurate data we adopted the following computational process. The initial interval for energy E is 1 eV, the initial interval of momentum Q (where Q = $h^2q^2/2m$) is about 1-6 eV, and the successive lengths of the intervals are determined by

$$\left[\frac{d\sigma(E + \Delta E)}{dE} - \frac{d\sigma(E)}{dE}\right] \frac{d\sigma(E + \Delta E)}{dE} < 0.1 \qquad (1)$$

$$\frac{F(Q + \Delta Q)d \ln(Q + \Delta Q) - F(Q)d \ln(Q)}{F(Q + \Delta Q)d \ln(Q + \Delta Q)} < 0.01 \qquad (2)$$

$$F(Q) = \frac{1}{Q} \sum_{1'} |\, <\varepsilon 1'|\ \exp(i\vec{q}.\vec{r})\ |\ nl> |^2 \qquad (3)$$

If these conditions are satisfied, then $\Delta E_{i+1} = \Delta E_i + \Delta E_i$ and $\Delta Q_{i+1} = \Delta Q_i + \Delta Q_i$; otherwise $\Delta E_{i+1} = \Delta Q_{i+1} = \Delta Q_i$. The integral over a grid in In Q and E is evaluated for about 60 points in energy space and 100 points in Q space. The code to implement these calculations is written in FORTRAN and the computation time for one element is about 24 h (with, for example, a 20Mhz IBM PS2/70 personal computer with a high-speed mathematics coprocessor chip). Decreasing the length of the initial intervals or the magnitude of the inqualities in Eqs. (1) and (2) substantially increases the computation time, although the precision of the result is improved by only a few percent.

Results

To illustrate the application of this method, Fig. 1 shows variation of σ_X with energy for aluminum Kα, for overvoltage ratios between 1 and 20, computed by the procedure discussed above. For comparison we also show experimental data for σ_X,[5] the value predicted by Bethe equation, using the parameters suggested by Powell[1] and by the classical Gryzinski equation,[3] the expression derived by Casnati et al. as a parametric fit to experimental data sets of σ_X, values at low overvoltage ratios,[2] and data computed by Rez using a method similar to that discussed here but not including exchange and correlation effects.[4]

It can be seen that the agreement between our computed result and the experimental data is excellent over the whole range of U; the maximum cross sections are obtained for an overvoltage just in excess of 2. By comparison, the Bethe-Powell,[1] Casnati et al[2] and Gryzinski[3] models predict that the cross section is a maximum for an overvoltage closer to 3. The
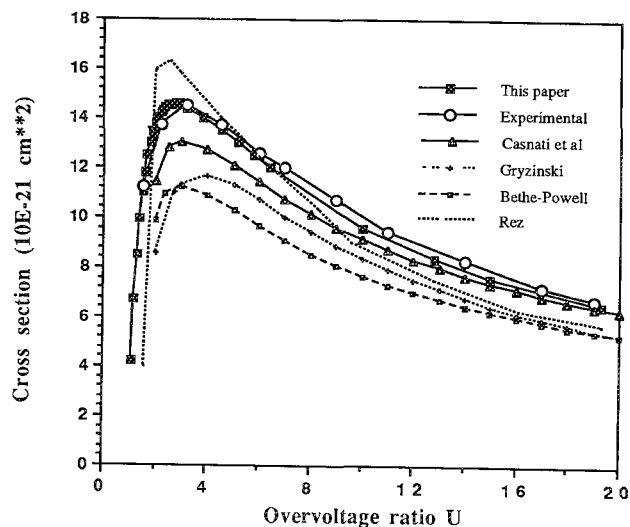
FIG. 1.--Comparison of computed ionization cross section for aluminum as a function of overvoltage ratio U with experimental data, and with other models for σ_x.

FIG. 2.--Fano plot of relative variation of ionization cross section σ_x with overvoltage ratio U in the range 1 to 3 for a variety of elements.

values of σ_x predicted by these models lie systematically below both our values and the experimental data in the low-overvoltage region, although at higher values of U the absolute discrepancy in all cases is small (<10%). It is to be expected that numerical methods will give a more accurate result than analytical methods because the calculation of wave functions, oscillator strengths, and cross sections is complicated and consequently most analytical approaches much employ simplifying assumptions in order to obtain integrable solutions.

The agreement between our data and those of Rez[4] is better, except near the threshold energy (U ~ 1) and at large U. The reason is probably that Rez's model did not take account of either exchange or correlation terms, and because we were able to employ smaller intervals for ΔE and ΔQ in the integration procedure. In particular, the discrepancy in the results as U → 1 indicates that exchange and correlations effects are significant and cannot be neglected in this regime.

Figure 2 shows a Beth-Powell-Fano plot for cross-section data in the range 1 < U < 3 for a variety of elements so far computed. Although there is some variation between one element and another, the data lie on a well-defined, and almost linear, trend line. This result is in agreement with the general behavior discussed by Powell. We are currently computing σ_x values for another dozen elements across the periodic table, and if these values display a similar variation in this overvoltage range, we shall attempt to use the approach of Casnati et al.[2] to derive a parametric fit through these data in such a form that the Bethe-Powell value approaches for high values of U. In this way we would hope to produce a readily evaluated expression which would give accurate values for σ_x for any overvoltage ratio.
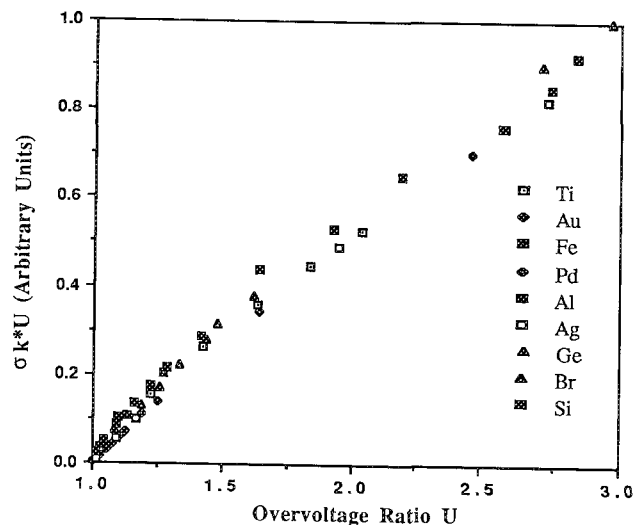
Conclusions

The technique described here is capable of computing x-ray ionization cross sections over a wide range of electron energies, including the low overvoltage region. Comparisons with the rather limited amount of experimental data available for the range 1 < U < 3 confirm the accuracy of these calculations and the relative inaccuracy of conventional analytical cross-section formulas in this same region. We are systematically computing data through the periodic table to provide a database for σ_x and, if the current trend in these data when displayed as a Fano plot proves to be consistent, we believe that it may be possible to obtain a parametric relation for the cross section as a function of the atomic number and U for convenience in computation. Work is also in progress to extend these computations to L and M shell ionization cross sections, again with the hope of obtaining a parametric relationship valid over the whole overvoltage range.

References

1. C. Powell, Rev. Mod. Phys. 48: 33, 1982.
2. E. Casnati, A. Tartari, and C. Baraldi, J. Phys. B15: 155, 1982.
3. M. Gryzinski, Phys. Rev. 138: A336, 1965.
4. P. Rez, X-ray Spectrometry 13: 553, 1984.
5. W. Hink and A. Ziegler, Z. Physik. 222: 222, 1969.
6. R. D. Leapman, P. Rez, and D. F. Mayers, J. Chem. Phys. 72: 1232, 1980.
7. F. Herman and S. Skillman, Atomic Structure Calculations, New Jersey: Prentice Hall, 1963.

QUANTITATIVE EPMA PROFILING OF Er CONCENTRATION IN OPTICAL FIBER PREFORMS

Jesse Hefter and G. P. Werber

Element profiling in electron probe microanalysis (EPMA) has found great utility in the determination of elemental distributions in many materials, particularly across interfaces. Recently, we have investigated the applicability of this approach for the determination of the concentration profile of Er in erbium-doped optical fiber preforms. Such materials are of current interest in the telecommunications industry as components of optical amplifiers.[1] Not only is the distribution of the Er in the preform center important, knowledge of its concentration is critical due to the effects that changes in concentration have on the overall optical properties.[2] For example, Singh et al. have recently shown that knowledge of the Er concentration profile together with data from modal field and spectral attenuation measurements can be used for the direct communication of Er^{+3} absorption cross sections in doped silica fibers.[3]

Since the rare earth concentrations are typically in the 100-1000ppma range, there are only a limited number of analytical methods capable of measuring their spatial distributions. Although secondary ion mass spectrometry (SIMS) has excellent sensitivity for trace elements, quantitation of the data is made difficult by the fact that there are wide variations in the relative sensitivities of the elements.[4] Nevertheless, experiments aimed at obtaining SIMS-based quantitative elemental line profiles of such materials have shown that the latter can be successfully obtained.[5]

The EPMA method, though lacking some of the sensitivity of SIMS, can facilitate providing quantitative information by use of standards similar in composition to the analyte. For example, Ainslie et al. have recently reported EPMA data obtained from rare earth-doped optical fibers.[6] The results below describe initial development work that has led to the successful determination of Er distributions in optical preform materials by EPMA.

Experimental

One optical fiber preform was studied. Sample Al-1027 contained Al_2O_3 (3 mole%), P_2O_5 (<0.5 mole %), and Er_2O_3. The preform was prepared by use of a modified chemical vapor deposition (MCVD) technique to deposit the SiO_2 core as well as the P_2O_5 additive.[7] Aluminum oxide and Er_2O_3 were added by solution doping of $Al(NO_3)_3$ and $ErCl_3$ in a water and ethanol mixture, respectively. The samples were cut

and polished sections from the optical fiber preform at one stage of the drawing process.

Erbium-doped silica glass standards were prepared to calibrate the EMPA experiment. These materials contained relatively low concentrations of additives to facilitate their synthesis. The nominal composition of the standards, LG17 (141 ppma Er) and LG18 (515 ppma Er), with respect to the SiO_2 matrix, are listed in Table 1.

TABLE 1.--Standard compositions (in mol%).

Compound	LG17	LG18
SiO_2	77.87	70.72
Al_2O_3	2.43	1.48
Li_2O (as Li_2CO_3)	1.50	1.49
CaO (as $CaCO_3$)	9.98	11.94
K_2O (as K_2CO_3)	2.23	3.89
Na_2O (as Na_2CO_3)	5.99	10.46
Er_2O_3	0.0055	0.0182

All EPMA data were taken with a JEOL-JXA840-II electron microprobe (W source, 20 keV, 50 nA) coupled with a Noran TN-5402 EDS/WDS analyzer along with a PAC system stage and spectrometer automation. An LiF crystal was used to provide excellent sensitivity for Er (at the $L\alpha_1$ peak). Damage arising from extended spot-mode irradiation was prevented by use of a raster-mode for the analysis. A magnification of 20 000× was thus used to define a scanned region about 4 × 5 μm on the specimen surface.

Elemental line profiles for Al, P, and Er were acquired by stepping of the stage along 100 points beneath the beam raster (with the Noran TASK program). Data points for the three elements were collected by simultaneous accumulation of x-ray counts for 50 s at a fixed stage position. Counting was performed at both the peak and background positions for each point. All the spectrometer data collected were captured dynamically with an Apple MacIntosh II connected as a serial output device of the Noran computer directing the microprobe. Software to extract the relevant spectrometer data was developed in the Microsoft QuickBasic™ environment.

Results and Conclusions

Determination of Er in Standards. Plots of

the peak and background for both LG17 and LG18 are shown in Figs. 1 and 2, respectively. There is some experimental variation in the signals over the ten analysis points. However, it is clear that the method can determine the presence of Er at the 125ppma level.

Use of the Standard for EPMA Calibration. Ten points on the standard (LG18) were analyzed to obtain an average "peak minus background" value for Er. The mean value obtained was found to be 0.732 ± 0.123 counts/s/nA. Wet chemical analysis (Parr bomb method of dissolution followed by inductively coupled plasma analysis) of LG18 yielded an Er concentration of 990 ppmw (= 510 ppma; expected: 515 ppma).[12] This value (in ppma) was used to obtain a factor for converting microprobe-based, background-corrected peak values to ppma values. The following equation was thus derived for this conversion: $ppma = (P - B)/(1.435 \times 10^{-3})$.

Loss of Er over time was studied by counting of the Er data (peak and background) 30 times at 5s intervals in one region. A plot of the Er (peak-background) values was then obtained to determine whether there was a point at which the Er counts began to decrease (Fig. 3). The data show that 150 s of sequential irradiation leads to no discernible decrease in the Er counts. This finding shows that the 50s counting time employed for collection of the line scan profiles is employed under conditions that do not lead to loss of the Er.

Preform Analysis. (a) *Elemental line plots.* An area of interest was located on the preform cross-section surface. Line plots were obtained for each of the three elements simultaneously during a single automated scan. The starting and ending points were adjusted to straddle the maximum of the preform diameter. The raster size of the probe beam 4 μm and accordingly, a step size was used to assure that no overlap of the prove occurred from point to point. A spacing of 4.84 μm was used, so that the total line profile length was about 480 μm.

The Er data were converted to ppma by use of the formula described above. The resulting quantitative profile is shown in Fig. 4. The Al and P data are plotted as (peak-background) vs probe position (Figs. 5 and 6). The Er concentration is relatively constant over the center of the preform, generally tracking along with the Al. In contrast, the P is seen to be depleted from the center of the preform. This result is consistent with the fact that P_2O_5 dopant can diffuse away from the center of the core during the preform consolidation process. Further, the asymmetrical nature of the observed peaks suggests that uneven volatilization of the P during processing has occurred.

(b) *High point determination.* The EPMA data can also be used to provide an accurate value of the [Er], which can in turn be utilized to assist in the quantitative calibration of other methods, e.g., SIMS. In order to obtain such a value, a long-term count at a position along the profile which was high in Er was made.

Thirty (30) readings (for a total of 93 865 peak counts, 50 s/pt) were taken at the highest Er concentration point in the Er plot (Fig. 4, 222.64 μm from the starting point). No degradation of the specimen as a result of this single-location data collection (25 min) was noted. Based on these accumulated counts, a mean value of 1.129 ± 0.055 counts/s/nA was obtained, which resulted in a calculated Er concentration of 787 ± 2 ppma.

Conclusions

The results described provide a preliminary demonstration that the EPMA method can yield a reasonably rapid (1-2 h analysis time) and accurate determination of the distribution of dopants as well as major elements in fiber preforms. With the use of suitable standards, quantitative line profile data can be readily obtained. Tests can be made for beam-specimen degradation. The knowledge of the damage threshold can aid in determining the maximum dwell time. It has been shown that close to 100 000 counts can be collected from a point on this preform without degrading the specimen. This result suggests that EPMA can provide calibration values useful in quantitation of SIMS experimental data. Finally, the electronic capture of the EPMA data to a powerful, personal microcomputer provides the opportunity for further post-processing (e.g., curve fitting, integration, and peak deconvolution), as well as for the use of extended graphics and software development environments available for the Macintosh platform that are not as generally as readily accessible in commercial microprobe analysis packages.

References

1. E. Desurvire, J. R. Simpson, and P. C. Becker, *Opt. Lett.* 12: 888, 1987.
2. J. Sandoe, P. H. Sarkis, and S. Parke, *J. Phys.* D5: 1788, 1988.
3. M. P. Singh, D. W. Oblas, J. R. Reed, W. J. Miniscalco, and T. Wei, *Symposium on Optical Fiber Measurements*, NIST Special Publication 792, 1990, 93.
4. H. A. Storms, K. Brown, and J. D. Stein, *Anal. Chem.* 49: 2023, 1977.
5. D. W. Oblas, F. Pink, M. P. Singh, J. Connolly, D. Dugger, and T. M. Wei (manuscript submitted).
6. B. J. Ainslie, S. P. Craig, T. S. Davey, and B. Wakefield, *Materials Letters* 6: 6, 139, 1988.
7. S. B. Poole, D. N. Payne, R. J. Mears, M. E. Fermann, and R. I. Laming. *J. Lightwave Technology* (LT-4), 1986, 870.
8. E. Gutman (unpublished data).
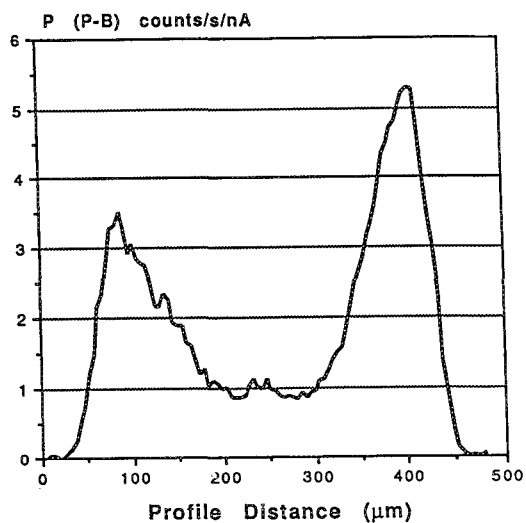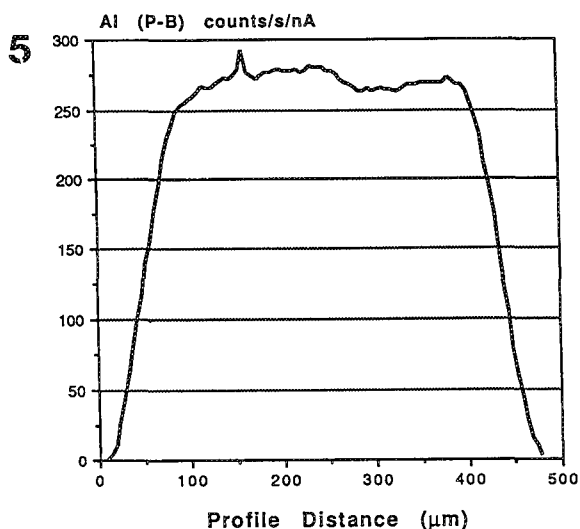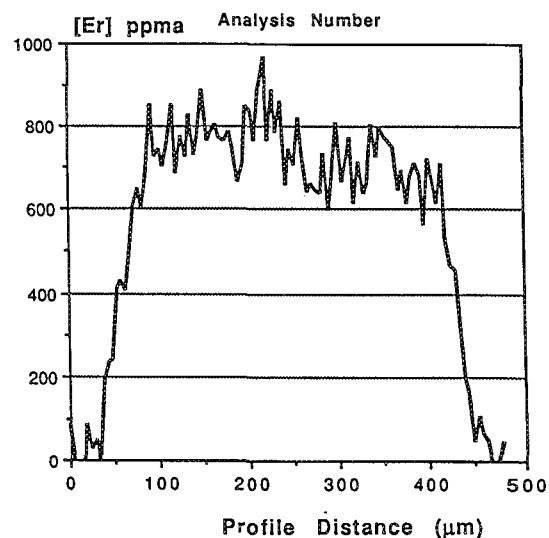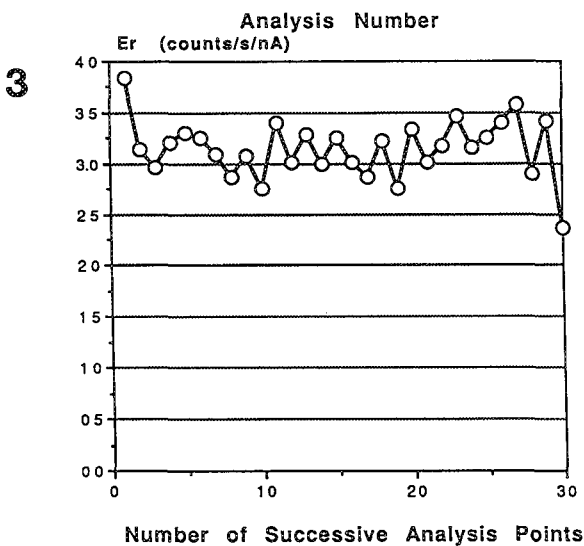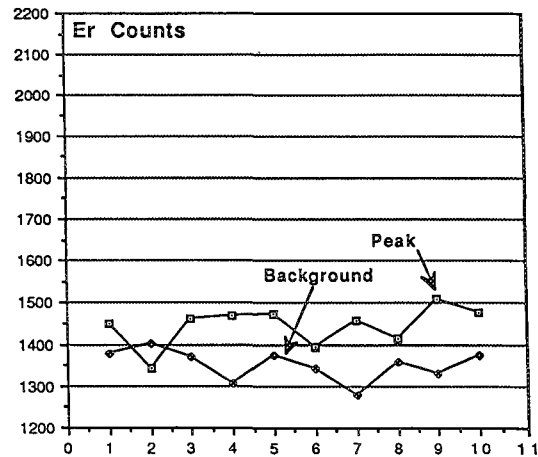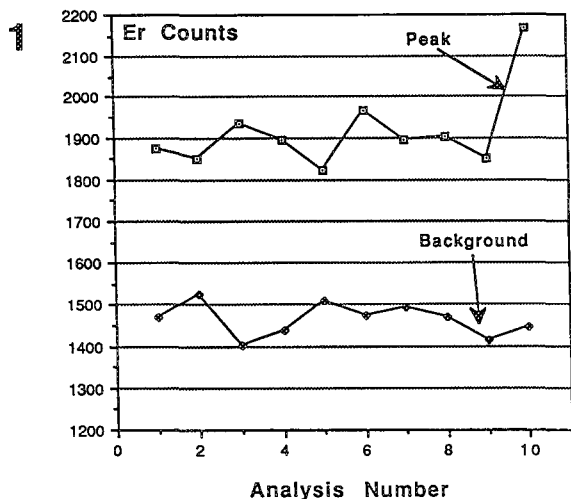
FIG. 1.--Analyses of 510ppma Er standard showing variability in peak and background counts for Er over 10 regions.

FIG. 2.--Analyses of 125ppma Er standard showing variability in peak and background counts for Er over 10 regions.

FIG. 3.--Loss of Er with time as a function of counting time at the same location on the specimen.

FIG. 4.--Quantitative line profile for Er expressed in ppma obtained from analysis of preform center.

FIG. 5.--Elemental profile for Al obtained over the same region of the preform as that for Er shown in Fig. 4 (Al expressed as background-corrected value in counts/s/nA).

FIG. 6.--Elemental profile for P obtained over same region of preform as that for Er shown in Fig. 4 (P expressed as background-corrected value in counts/s/nA).

ELECTRON MICROPROBE ANALYSIS OF CARBON IN CARBURIZED M50NiL

F. J. Galli and K. P. Gumz

M50NiL (AMS 6278) is a new carburizing grade steel (Table 1) with improved fracture toughness, fabricability, and core fracture toughness that is being evaluated in the aerospace bearing industry.[1] Carburizing continues to be an important manufacturing process for bearings and gears because it can improve the surface properties of these components. The analysis of carburized materials requires an analytical technique for determining case depth uniformity and carbon gradients, particularly on irregular surfaces such as gears. Rigorous electron microprobe analysis (EMPA) techniques have been developed[2] but are often difficult to employ given the various constraints of an industrial laboratory. In this study, emphasis was placed on the development of a simplified yet reliable EMPA technique for producing carbon gradients using both iron-nickel-carbon and M50NiL standards. The accuracy of the EPMA procedure was checked by comparison to established wet chemical techniques.

TABLE 1.--Nominal composition (wt%) of M50NiL. (Values for Mn and Si represent maxima.)

Fe	Cr	Mo	V	Ni	C	Mn	Si
Bal.	4.1	4.3	1.3	3.5	p.13	0.25	0.25

Experimental

Carburized M50NiL specimens subjected to various postcarburization heat treatments were prepared metallographically for EMPA. The series of iron-nickel-carbon standards were obtained through Lehigh University. Four potential M50NiL standards were cast and homogenized by swagging and heat treatment at Pratt & Whitney. The carbon content of these samples was determined by conventional bulk chemical techniques was 0.12wt%, 0.65 wt%, 0.83 wt% and 1.89 wt%. Analyses were carried out with an automated JEOL 733 Superprobe equipped with four wavelength-dispersive spectrometers and a Noran TN-5500 EDX analyzer. A conventional Pb-Stearate (STE) crystal was used to measure carbon intensity at an accelerating potential of 15 kV and a Faraday cup current of 40 nA. A liquid nitrogen cooled cold finger was inserted above the specimen to minimize carbon contamination from the electron beam.[3] A 30μm defocused beam was used to measure the standards and to obtain an average carbon gradient of the carburized samples. Due to the high volume fraction of carbides near the surface, a point analysis was

needed to measure the "matrix only" (area free of visible carbides) within the carburized layer. Wavelength scans were run on the several matrix standards to determine the appropriate background intervals, changes in carbon
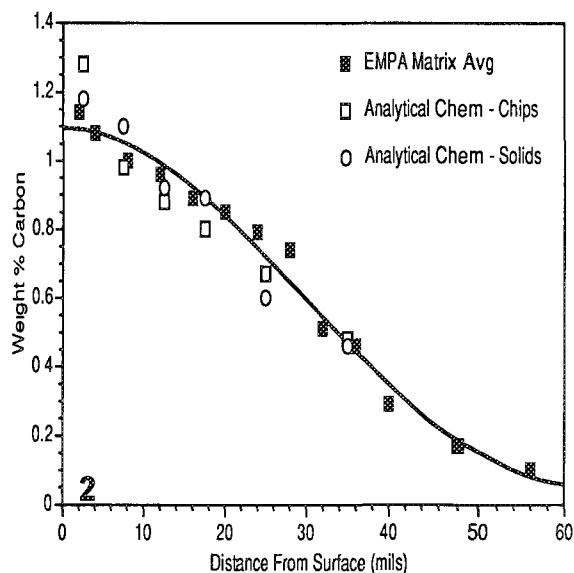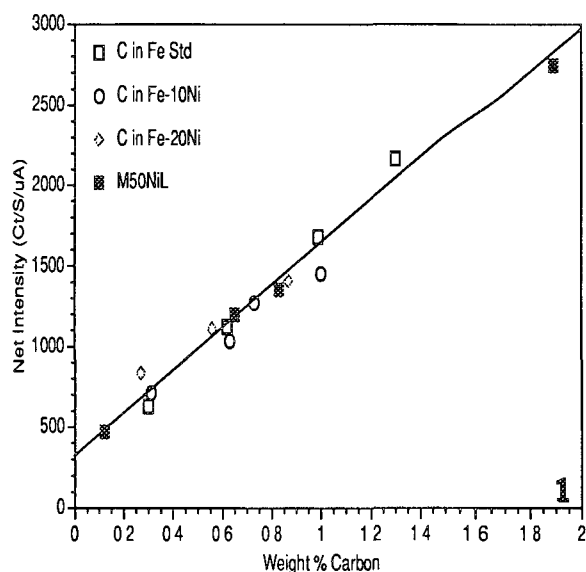
FIG. 1.--Calibration curve for Fe-Ni-C alloy standards. M50NiL data are superimposed on plot but not used in linear regression.
FIG. 2.--Comparison of carbon depth profiles obtained by EMPA and wet chemical techniques.

The authors are at Pratt & Whitney, M/S 114-45, 400 Main Street, East Hartford CT 06118.

peak position and peak shape, and potential interferences.

Results

The initial focus of this study was to determine the carbon content of the potential M50NiL standards from the calibration curve obtained from the iron-nickel-carbon standards. In general, the standard plot appears to be linear throughout the concentration ranges studied (Fig. 1). Results of the EMPA of these samples compare favorably with the nominal values obtained by wet chemical techniques (Table 2). Although the carbon in the standards appears to be in solution, the 0.65 wt%, 0.83wt%, and 1.89 wt% M50NiL samples contain increasing amounts of carbides, which appear to be uniformly distributed. In this case, performing analyses with a defocused beam appears to alleviate some of the large fluctuations in peak intensity measurements expected with a point analysis. Once evaluated, these M50NiL samples were used as secondary standards to adjust the calibration curve for subsequent analyses.

TABLE 2.--Comparison of EMPA and wet chemical techniques on four M50NiL samples (wt%).

Sample *	EPMA	Wet
1	0.14	0.12
2	0.66	0.65
3	0.81	0.83
4	1.87	1.89

Further comparison of EMPA and wet chemical techniques involved analyzing the same piece of carbonized M50NiL. EMPA was performed on one portion of the sample while chips and solid wafers were machined from another portion for chemical analyses. Good agreement was found among the methods; the largest variation was 0.2 wt% (Fig. 2). The EMPA technique offers certain advantages over wet chemical analysis, including simplified sampling procedures that can be applied to irregular surfaces such as gears, decreased potential for external contamination, greater certainty in determining the actual sampling depth, and the fact that EMPA is nondestructive.

EPMA of a series of carburized samples with a carburized zone 1-2 mm thick showed an average carbon content of ∿1 wt% at the surface and ∿0.5 wt% in the matrix near the surface (Fig. 3). Measurements were made at 100μm intervals to a depth of 1 mm and at 200μm intervals thereafter. The carbon gradients were used to verify processing conditions and to compare the experimental results with results predicted by computer programs.

Conclusions

A simplified EMPA technique has been successfully used to measure the carbon gradients in carburized M50NiL alloys. Carbon is determined, without use of mathematical matrix correction programs, from a calibration curve of peak height intensities of a series of iron-nickel-carbon and M50NiL standards. In addition, most aspects of the technique can be readily automated. Good agreement was found between results from samples analyzed by EMP and by established wet chemical techniques.

References

1. C. C. Law, K. P. Gumz, A. V. Karg, L. S. Lin, and J. E. Morral, "Physical metallurgy of carburized M50NiL," *Proc. 26th Joint Propulsion Conf. AIAA/SAE/ASME/ASEE*, AIAA 90-2288, 1990.

2. J. S. Duerr and R. E. Ogilvie, "Electron probe microdetermination of carbon in ferrous alloys," *Anal. Chem.* 44: 2361, 1972.

3. G. F. Bastin and H. J. M. Heijligers, "Contamination phenomena in the electron probe microanalyser," *Microbeam Analysis--1988*, 325.
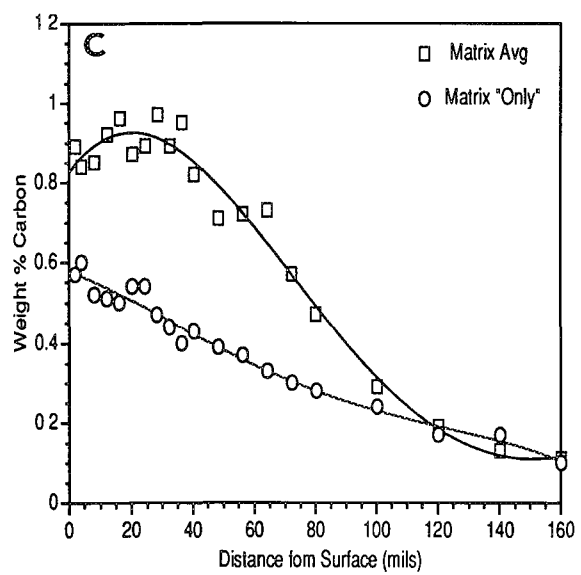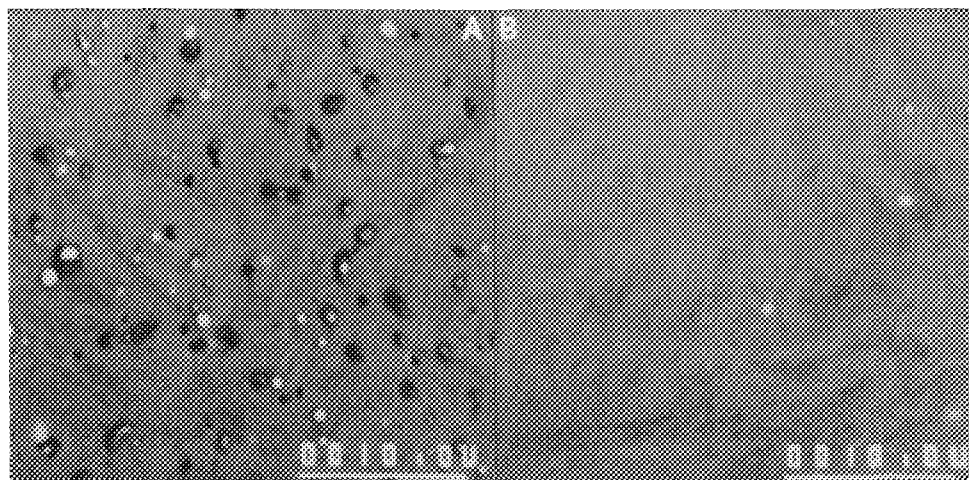
FIG. 3.--(a) BSE image of carburized
layer of M50NiL sample, (b) BSE image
of normal matrix, (c) carbon gradients
of sample.

CORRECTION OF THE RASTER-ANALYSIS DATA IN WDS QUANTITATIVE ELECTRON MICROPROBE ANALYSIS

S. V. Yang, J. H. Wagstaff, and G. A. McKay

A rastered beam is commonly used to acquire bulk chemical compositions or to minimize volatilization and/or ion mobility in WDS quantitative electron microprobe analyses. A major disadvantage of this method is that the analyses tend to have low totals and systematic errors if the standard intensities are acquired in the spot mode. This report offers a simple and reliable method to correct problems associated with rastered beam analyses acquired with spot mode standard intensities.

Procedures

In a typical electron probe analytical session, the analyst wishes to acquire as many normal spot analyses of adequate precision as is possible within the limited time of the analytical session. An electron microprobe analyst exploring a complicated multiphase sample may determine that some phases are too volatile to endure the electron beam in the spot mode without damage or, in the worst case, that a bulk chemical analysis is required for an area consisting of micron-sized (too small to be analyzed in the spot mode) heterogeneous phases. To handle such an awkward situation, the analyst may decide to mix point analyses and raster analyses in a single standard setup.

As noted, the raster-analysis data tend to have low totals relative to the spot-analysis data, because inside the rastered square only a line of the rastered area is in focus with respect to the diffracting crystal and x-ray counter, and the sum of the in-focus and the out-of-focus areas gives relatively lower total counts than in spot mode (Fig. 1). A straightforward correction to this problem is to normalize the results to make a 100% total. This method may provide acceptable results for analyses that cover a very small rastered area. However, for large-area raster analyses, new errors (to be discussed later) are introduced by normalization of the results.

To document these errors and develop correction procedures, we performed an experiment with the NASA Johnson Space Center CAMECA MBX scanning electron microprobe, in which we used a kaersutite (KAER) mineral standard to analyze Si, Ca, and Fe in an andradite (ANDR) mineral standard at 15 kV accelerating voltage and 29 na sample current. Standard intensities were

always acquired in spot mode; unknown intensities were acquired in both spot and raster modes. The analytical results, as well as the corresponding intensity ratios, are listed in Table 1 (the intensity ratio is I.X./I.STD., where I.X. is the net peak intensity of the unknown and I.STD. is that of the standard).

In these raster-mode analyses, the raster coverage area is approximately 140 × 140 μm (800 magnification). Data for ANDR in Table 1 show that the uncorrected raster analyses have unacceptably low totals. Normalizing the uncorrected data to a total of 100% over-corrects data for Si and Fe, and under-corrects data for Ca (Table 1). However, correcting the raster analysis by use of correction factors determined by both spot and raster analyses of KAER yields agreement with the spot analysis within analytical uncertainty (Table 1). Correction by the more rigorous procedure of applying a ZAF matrix correction to the raster-corrected intensities also yields agreement with the spot analysis within analytical uncertainty. Thus, compared to uncorrected or normalized raster data, analyses corrected either by applying simple correction factors to oxide concentrations, or by application of these factors to x-ray intensities and then a full ZAF matrix correction, show a significant improvement in the quality of the data.

Discussion

In reality, the focus line shown in Fig. 1 is a focus "band" rather than a theoretical line. The width of the band is determined by the type, the quality, and the position of the crystal, the alignment of the spectrometer, the acceleration potential, and the size of the electron beam. If the rastered area is relatively small, there might be no recogniz-
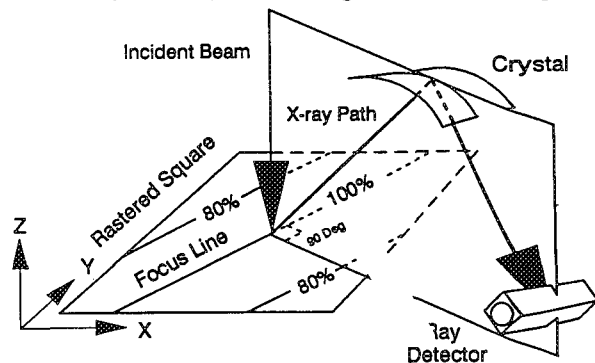
FIG. 1.--3-D view of spectrometer geometry in raster analysis. Rastered area is enlarged to show details of focus line.

S. V. Yang and J. H. Wagstaff are with Lockheed Engineering and Science Co., 2400 NASA Rd. 1, C23, Houston, TX 77258; G. A. McKay is at the NASA Johnson Space Center (JSC), SN2, Houston, TX 77058.

TABLE 1.--Point and raster analyses of ANDR using KAER as standard. ANDR raster data are shown for uncorrected analyses, analyses normalized to a total of 100%, analyses corrected by multiplying uncorrected oxide values by factors obtained from point and raster analyses of KAER, and analyses corrected by multiplying uncorrected intensity ratios by correction factors, then performing a full ZAF matrix correction.

	Wt %				I.X./I.STD.		
	SiO_2	CaO	Fe_2O_3	Total	Si	Ca	Fe
$ANDR_{Point}$, point mode	35.15	33.28	30.75	99.18	0.9466	3.5459	2.3782
$\pm$ 2 sigma	0.16	0.27	0.39				
$ANDR_{Raster}$, raster mode, uncorrected	31.95	28.58	28.14	88.66	0.8556	3.0390	2.1675
I_{Point}/I_{Raster} for ANDR[1]	--	--	--	--	1.1064	1.1668	1.0972
$KAER_{Point}$, point mode	--	--	--	--	1.0000	1.0000	1.0000
$KAER_{Raster}$, raster mode	--	--	--	--	0.9073	0.8585	0.9242
KAER raster correction factors[2]	--	--	--	--	1.1022	1.1648	1.0820
$ANDR_{Raster}$, normalized to 100%	36.03	32.23	31.74	100.00			
$ANDR_{Raster}$, corrected by KAER raster factors	35.21	33.29	30.44	98.95	0.9431	3.5400	2.3452
$ANDR_{Raster}$ analysis, raster- and ZAFcorrected [3]	35.01	33.23	30.33	98.58			

Notes.

[1] I_{Point}/I_{Raster} = (I.X.$_{Point}$/I.STD.)/(I.X.$_{Raster}$/I.STD.)

[2] I_{Point}/I_{Raster} for ANDR

[3] $ANDR_{Raster}$ Intensity ratios, corrected by KAER raster correction factors and processed through ZAF matrix correction.

able difference between the raster analysis and a corresponding spot analysis on a single stable phase. However, when a larger rastered area is selected, the peak count rate of the analyzed band element drops because the x rays generated outside of the focus band are not focused properly by the crystal onto the x-ray detector. The most important factor in these considerations is that *each analyzed element responds differently* in the amount of elemental peak intensity lost due to these effects. As shown in Table 1, the Ca Kα line dropped more than 14% of its peak intensity, whereas Fe Kα and Si Kα dropped less than 10% of their peak intensities. Treating all elements equally by normalizing the total to 100% will create systematic errors in the analysis. To determine proper correction factors, the user should acquire the peak intensities both in spot mode and selected raster mode on the appropriate standards and calculate the ratio of the two values for each element. The easiest method is to collect the intensity ratios of rastered beam against spot beam for all essential elements under the appropriate operating conditions. Graphs of correction factors vs raster size can be prepared from these data (e.g., Fig. 2). By having such graphs on hand, the probe analyst can make a simple and efficient, yet reliable, correction of the raster data after the analyses are completed.

The graph of the correction factors vs the raster size should produce a smooth curve that displays an increase in the correction factor as the raster size increases. A reversal of

the curve might indicate an alignment problem with the corresponding spectrometer, or it could indicate that another x-ray line has been brought into focus by the diffracting crystal during the raster mode data acquisition.
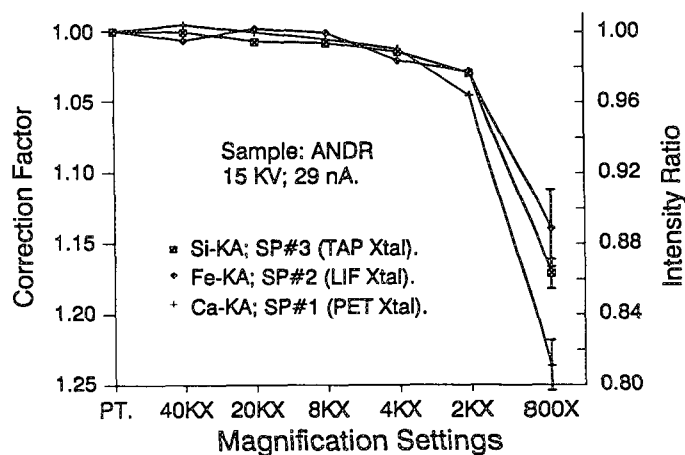
FIG. 2.--Plot of correction factor and intensity ratio vs point mode and raster magnification setting.

DETERMINING RESIN FLOW IN COMPOSITE LAMINATES BY MICROANALYSIS

M. G. Mager, Golnar Riahi, and Anoush Poursartip

Thermoset matrix polymer composites form an important class of strong and light-weight structural materials. An important factor in controlling the fabrication of these materials is the flow and mixing of the resin between the layers of pre-impregnated fibers ("prepreg") in the composite stack as heat and pressure is applied during the "curing" cycle. Various theoretical models have been developed to predict the resin flow in straight and curved composite sections, but little direct experimental evidence of the nature of resin flow is available.[1-3] In the current work an experimental method was developed to trace the flow and mixing of resin in prepreg by "tagging" of one layer with a brominated resin. The final distribution of the brominated resin was traced by use of the wavelength-dispersive x-ray spectrometer (WDX) on a scanning electron microscope (SEM).

Experimental

Brominated resin with a Br content of about 10 wt. % (Fiberite 7714) was used as the resin in one layer in a 16-layer composite lay-up. A nonbrominated resin (Fiberite 7409) was used for the other prepreg layers. The layers are numbered for convenience so that layer 1 is at the top, next to the bleeder layer which absorbs the excess resin, and layer 16 is at the bottom, next to the toolplate. The laminate stack was laid up and autoclave-cured according to the manufacturers' directions, then mounted in epoxy and polished in cross section (Fig. 1). Samples were then vacuum-coated with approximately 30 nm of carbon and analyzed with a Microspec WDS-3PC wavelength spectrometer on a Hitachi S-570 SEM. The spectrometer was standardized on a potassium bromide standard before each use and the SEM was operated at 20 kV accelerating voltage and 30 nA beam current. Each layer was analyzed by scanning areas of 90 × 75 μm for a 2min count, in order to get a good, statistically valid result and avoid errors due to varying numbers of fibers in the analysis area.

Results and Discussion

In Panel A, which is a unidirectional laminate with the brominated resin in layer 8, the layers were difficult to distinguish on the SEM. Therefore only four determinations

TABLE 1.--Bromine analysis of Panel A. Counts are background corrected.

Layer	KBr count (c/sec.)	Br count (c/sec.)	Br K-ratio
3	21567	57.3	0.00266
7	21567	210.8	0.00977
11	23774	10.5	0.00044
15	23774	6.2	0.00026
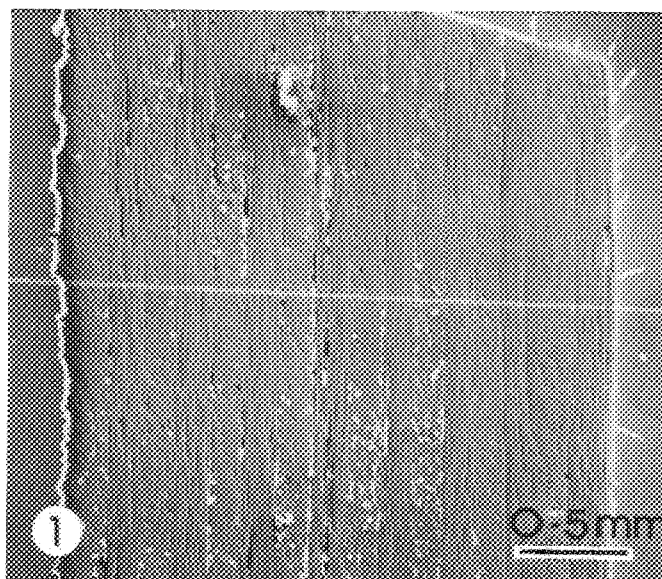
FIG. 1.--Polished section of Panel B. White line marks one line of Br analysis. Layer 1 is on left, layer 16 on right.

were taken, roughly corresponding to layers 3, 7, 11, and 15. The results, shown in Table 1, show significant Br counts in all layers tested, with higher levels toward the bleeder layer. The evidence of backflow and resin mixing suggest a more complex resin flow pattern than predicted by the existing flow models.[1-3]

Panel B, shown in Fig. 1, was laid up with the fiber orientation alternating at right angles in successive layers to make the layer identification easier. Because the fiber diameter is smaller than the penetration depth of the electron beam (about 5 μm in this matrix at 20 kV), the direction of fiber orientation does not affect the determination of the resin volume fraction. Layer 15 originally contained the brominated resin. Two traverses of the laminate were taken, about 20 mm apart. The final distribution of bromine is shown in
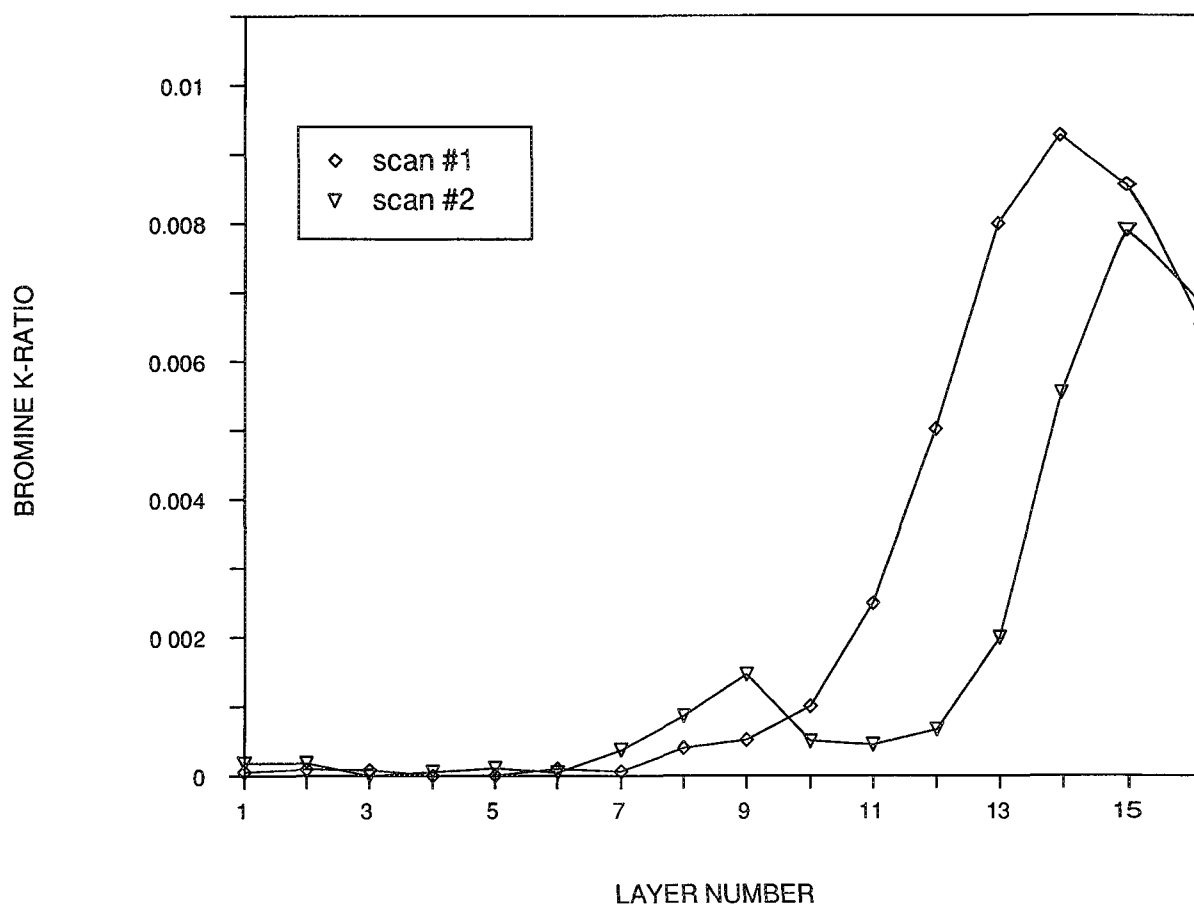
FIG. 2.--Distribution of bromine across Panel B on two lines.

Fig. 2. These results clearly show both back-flow into the 16th layer and mixing of the two resins up to at least the seventh layer. There is a small bulge of bromine counts in one of the scans at the 8th and 9th layers, suggesting a complex mixing pattern. Comparison of the scan results to the analysis of the bromine in the neat cured resin allows the bromine content of the final laminate to be converted to a volume fraction of the resin at any point in the laminate.[4]

The study of graphite-fiber reinforced resin composites has not benefited from electron microprobe microanalysis (EPMA) in the past because all the components are composed of light elements with few compositional differences. Bromine, added to some resins by the manufacturers to promote fire retardancy, proved ideal as a marker element because of its strong x-ray peak. The marker element must be molecularly bound to the resin monomer, so that there is no concern about diffusion of the marker. In this study we are confident that the brominated resin Fiberite 7714 is an accurate indicator of resin flow in straight and curved laminates are continuing.

References

1. A. C. Loos and G. S. Springer, "Curing of epoxy composites," *J. Composite Materials* 17: 135, 1983.

2. T. G. Gutowski, T. Morigaki, and C. Zhong, "The consolidation of laminate composites," *J. Composite Materials* 21: 172, 1987.

3. R. Dave, J. L. Kardos, and M. P. Duduković, "A model for resin flow during composite processing: 1. General mathematical development," *Polymer Composites* 8I: 29, 1987.

4. A. Poursartip, G. Riahi, L. Frederick, and X. Lin, "A method to determine resin flow during curing of composite laminates," *Polymer Composites* (in press).

THE RAMAN MICROPROBE: A PERSPECTIVE ON THE SYNERGISM BETWEEN CLASSICAL MICROANALYSIS AND MICROSTRUCTURAL CHARACTERIZATION

Fran Adar

The Raman microprobe was developed simultaneously during the early 1970s at the University of Lille in France and at the National Bureau of Standards (now NIST) as the molecular analog of the vacuum microprobes that provide elemental information. Its potential for studying the microstructure of engineered materials that has evolved since its introduction will be discussed.[1,2]

Background

The development of the Raman microprobe was based on the recognition that a narrow, collimated laser beam could be efficiently focused on a sample in a diffraction-limited spot of the order of 1 μm. The designs of the two instruments cited above were quite different, but they were both created for chemical microanalysis. Some of the early areas of applications of the technique included identification of atmospheric particulates,[3] contaminants in manufactured products[4] and biological tissues,[5] and the gas, liquid, and solid phases in fluid inclusions in minerals.[6,7] In these and other applications, the principal goal was chemical identification. The Raman spectrum from a region as small as 1 μm was used to fingerprint a chemical species.[3]

In reality, however, implicit in the geological applications was a recognition that the information from the Raman microprobe provided a history of the geological formation. In addition to the work on fluid inclusions, there were several short publications demonstrating the co-existence in certain geological thin sections of two or more crystalline polymorphs of the same chemical species which has certain implications on the formation of the rocks from which the sections were removed.[8]

The use of the Raman microprobe in the study of many engineered materials is analogous to the geological studies. The Raman spectra provide information for the clever researcher to make inferences on the history and/or structure of his material.

Applications to Engineered Materials

Raman microprobe spectra of high-T_c superconductors have enabled one to follow oxygen stoichiometry, to confirm crystal twinning,[9] and to observe the superocnducting gap.[10]

Many researchers have used the stress-induced shift in the Raman spectra of silicon films to measure strain that impacts the electrical properties of semiconductor devices.[11,12] Study of strain in composites is also of interest.[13]

One can study orientation in extruded polymers by performing careful polarization analysis.[14] In addition, there are often regions of the spectrum where the amorphous phase can be distinguished from the crystalline phase. Information on orientation and crystallinity is helpful in understanding the performance of engineered polymers.[15]

Raman microprobe spectra of diamond films not only enable confirmation of the deposition of diamond,[16] they also enable detection of the various sp^2 phases. Raman scattering, in fact, is the only technique that can detect the sp^2 noncrystalline carbon, and can detect it with quite high sensitivity.[17,18]

In addition, the Raman spectra of films deposited under conditions where diamond is just beginning to form show definite features at about 1135 and 1460 cm^{-1}. X-ray diffraction confirms the presence of diamond even though the $1332 cm^{-1}$ diamond band is comparatively weak. The film has been described as nanocrystalline diamond[19] and the extra unusual features could be attributed to π bonds on the surface due to surface reconstruction.

There is also interest in carbon films that are described as diamond-like carbon (DLC). These films are insulating and hard like diamond, but deposit quite smoothly, which makes them useful in many areas of manufacture such as computer hard disks. The Raman spectra indicate that the bounding in these films is, in actuality, more graphitic than diamond-like. A broad spectrum (stretching from about 900 to about 1700 cm^{-1}) can be band-fit to the two disordered carbon lines. The excitation wavelength dependence of the Raman bands can be explained by resonance with the bandgap which depends on the size of the cluster of aromatic rings.[20]

The Raman microprobe spectra of GaAlAs structures under patterned dielectric films enabled measuring stress by following the shift of the longitudinal optic (LO) phonon. In this case, however, rapid thermal annealing reduced the frequency shift (i.e., the stress) under the Si_3N_4 stripe. At the same time, the optical waveguiding properties under the stripe, as determined by the polarization behavior, changed dramatically.[21]

Other workers studied the optical properties and durability of titania dielectric films that were either sputter deposited or sol-gel deposited. The durability can be studied by the films' response to stress. Rutile films made by the two processes responded to stress in a similar fashion. However, the anatase sol-gel film was more compressible than bulk material and was consequently resistant to a

Fran Adar is at Instruments S.A., Inc., Edison, N.J.

pressure-induced phase transformation normally observed. This behavior was correlated with the observation by TEM of crystalline microspheres surrounded by voids.[22]

Conclusions

The Raman microprobe has evolved from an instrument for molecular fingerprinting into a tool for microstructural characterization. The examples cited indicate the potential types of applications. All areas of materials research can be fertile ground for future work.

References

1. P. Dhamelincourt and P. Bison, "Principle and realization of an optical microscope using the Raman effect," *Microscopica Acta* 79: 267-276, 1977.

2. G. J. Rosasco, "Raman microprobe spectroscopy," in R. J. H. Clark and R. E. Hester, Eds. *Advances in Infrared and Raman Spectroscopy*, vol. 7 London: Heyden, 1980.

3. E. S. Etz, G. J. Rosasco, and W. C. Cunningham, "The chemical identification of airborne particles by laser Raman spectroscopy," in *Environmental Analysis*, New York: Academic Press, 1977, 295-340.

4. M. Delhaye, P. Dhamelincourt, and F. Wallart, "Analysis of particulates by Raman microprobe," *Toxicological and Environmental Chemistry Rev.* 3: 71-87, 1979.

5. J. L. Abraham and E. S. Etz, "Molecular microanalysis of pathological specimens in situ with a laser-Raman microprobe," *Science* 206: 716-718, 1979.

6. G. J. Rosasco and E. Roedder, "Application of a new Raman microprobe spectrometer to nondestructive analysis of sulfate and other ions in individual phases in fluid inclusions in minerals," *Geochim. Cosmochim. Acta* 43: 1907-1915, 1979.

7. J. C. Touray, C. Beny-Bassez, J. Dubessy, and N. Guilhaumou, "Microcharacterization of fluid inclusions in minerals by Raman microprobe," *SEM/1985*, 103-118.

8. R. Lefevre, J. Barbillat, J. P. Cuif, P. Dhamelincourt, and J. Laureyns, "Caractérisation minéralogigue directe, par microsonde laser à effet Raman, des alternances calcite-aragonite mises en évidence chimiquement par microanalyse ionique dans une Algue Solenopore triasique," *C. R. Acad. Sci.* (Paris) 288D: 19-22, 1979.

9. C. Thomsen, M. Cardona, and R. Liu, "Raman scattering as an analytical tool for high T_c superconductors," *J. Less-Comm. Metals* 150: 33-37, 1988.

10. S. L. Cooper, F. Slakey, M. V. Klein, J. P. Rice, E. D. Bukowski, and D. M. Ginsberg, "Gap anistropy and phonon self-energy effects in single crystal $YBa_2Cu_3O_{7-\delta}$," *Phys. Rev.* B38: 11934-11937, 1988.

11. S. Nakashima, Y. Inoue, M. Miyauchi, A. Mitsuishi, T. Nishimura, T. Fukumoto, and Y. Akasaka, "Characterization of ion-implanted and laser-annealed polycrystalline Si by a Raman microprobe," *Appl. Phys. Lett.* 41: 524-526, 1982.

12. P. Zorobedian and F. Adar, "Measurement of local stress in laser-recrystallized lateral epitaxial silicon films over silicon dioxide using Raman scattering," *Appl. Phys. Lett.* 43: 177-179, 1983.

13. Y. M. Cheong, H. L. Marcus, and F. Adar, "Raman microprobe measurements of residual strains at the interfaces of Si on quartz," *J. Maber. Res.* 2: 902-909, 1987.

14. M. E. Andersen, "Molecular Optical Laser Examiner (MOLE): Application to problems encountered by electron microscopists in the analysis of polymers, *ACS Adv. in Chem. Series* 203, 1983, 383-400.

15. F. Adar, D. Armellino, and H. Noether, "Raman microprobe spectroscopy of polyethylene terephthalate fibers: Separation by band-fitting of amorphous-oriented and crystalline components," in SPIE 1336, *Raman and Luminescence Spectroscopies in Technology* II, 1990, 183-193.

16. L. S. Plano and F. Adar, "Raman spectroscopy of polycrystalline diamond films" Ref. 15, 1987, 52-56.

17. N. Wada and S. A. Solin, "Raman efficiency measurements of graphite," *Physica* 353-356, 1981.

18. R. J. Nemanich, J. T. Glass, G. Lucovsky, and R. E. Shroder, "Raman scattering characterization of carbon bonding in diamond and diamond-like thin films," *J. Vac. Sci. Technology* A6: 1783-1787, 1988.

19. M. Yoshikawa, "Raman spectra of diamond-like amorphous carbon films," *Materials Science Forum* 52 and 53, 365-386 (Trans. Tech Publications, Switzerland, 1989).

20. W. A. Yarbrough and R. Roy, "Nano-composite diamond films by hot filament assisted CVD," in MRS Extended Abstracts: Johnson, Badzian and Geiss, Eds., *Diamond and Diamond-like Materials Synthesis*, 1988, 33-38.

21. C. J. Radens, B. Roughani, H. E. Jackson, J. T. Boyd, and R. D. Burnham, "Raman microprobe analysis of strain induced by patterned dielectric films on GaAlAs structures structures, *IEEE J. Quan. Elect.* 25: 989-992, 1989.

22. N. J. Hess and G. J. Exarhos, "High pressure Raman spectroscopy of TiO_2 thin films," SPIE 1055, Ref. 15, 1989, 195-203.

APPLICATION OF SCANNING FOURIER TRANSFORM INFRARED MICROSCOPY TO PETROGRAPHY AND PETROPHYSICS

K. K. Liang

Minerals exhibit most of their fundamental molecular vibration modes in the mid-infrared (4000-400 cm^{-1} or 2.5-25.0 μm) spectrum.[1-5] Transmission measurement is the most common method for mineralogy characterization. The sample has to be ground, blended with alkali halide power (which is transparent in the infrared), and then pressed into a solid disk for analysis. It is well known that the grinding process tends to incur structural breakdown of minerals and thus leads to alteration of the corresponding infrared spectra.[5] Moreover, sampling is bound to be selective because of the laborious sample preparation procedure. Visual examination under an ordinary light microscope is usually employed to isolate a small region or to separate out the material of interest. Such practice can itself be tedious and highly subjective. For a sample of large size, the completeness of coverage and the thoroughness of characterization invariably depends on the dexterity and diligence of the operator. Scanning Fourier Transform Infrared Microscopy (SFTIRM) is a measurement technique that combines spectroscopy and scanning microscopy and is capable of producing two-dimensional maps of the distribution and abundance of constituent minerals in rock samples on a microscopic scale. The technique is essentially nondestructive and sample preparation typically only involves polishing the rock specimen flat. Mineral identification is based on specular reflectance measurement in the mid-infrared and the abundance of the identified minerals is extracted by fitting of mineral spectral standards to the measured spectrum. The rock sample is automatically scanned and analyzed over a sampling grid to generate two-dimensional images, one for each mineral. Spatial resolution of the order of tens of micrometers can be achieved. Such a detailed description of the mineralogy distribution and abundance will provide geologists and geophysicists with a powerful analytical tool to infer the formation process and geological evolution of rocks. Combining high-resolution mineralogical data with appropriate physical modeling, one may obtain accurate estimates of petrophysical properties such as porosity and permeability. Furthermore, if the mechanical properties of the minerals are known, one can develop detailed models to assess the mechanical strength of rocks.

NICOLET 60 SX (MICHELSON INTERFEROMETER)

SPECTRATECH IR MICROSCOPE
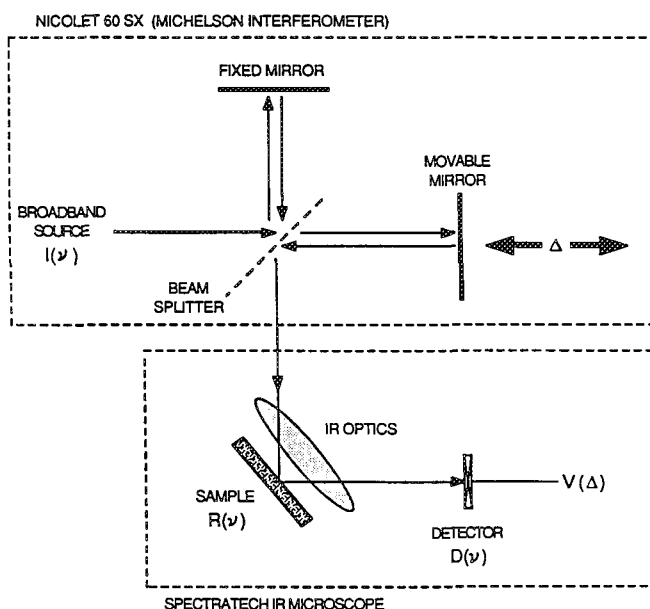
FIG. 1.--Scanning Fourier transform infrared microscopy (SFTIRM).

SFTIRM combines Fourier Transform Infrared (FTIR) Spectroscopy and scanning microscopy into a quantitative imaging technique. The key component in most Fourier transform spectrometers is the Michelson interferometer (Fig. 1). The source illumination is split into two beams which are bounced off of two mirrors, one of which is movable. The return beams are then recombined and reflected from the sample before being detected to generate an interferogram. It can be shown that the detector output voltage V' as a function of the movable mirror displacement Δ (Δ = 0 is defined where the optical path lengths for the two beams are identical) is given by

$$V'(\Delta) = \int R(\nu)I(\nu)D(\nu) \cos(2\pi\nu\Delta) \, d\nu + \text{constant} \quad (1)$$

where $I(\nu)$ is the source power spectrum, $D(\nu)$ is the detector spectral response, $R(\nu)$ is the reflectance spectrum of the sample and ν is the wavenumber; $\nu = 1/\lambda$, where λ is the wavelength. If the interferogram $V'(\Delta)$ is high-pass filtered to remove the constant term in Eq. (1), we can write in abbreviated form

$$R(\nu) = \frac{\text{Re}F\{V(\Delta)\}}{I(\Delta)D(\Delta)} \quad (2)$$

where Re$F\{\}$ denotes the real part of the

Fourier transform and

$$V(\Delta) = \int R(\nu)I(\nu)D(\nu) \exp(-j2\pi\nu\Delta) \, d\nu \qquad (3)$$

In general, the product term $I(\nu)D(\nu)$ in Eq. (2), corresponding to the inherent spectral characteristic of the interferometer, is not known a priori. However, it can be calibrated against a reference reflecting surface with $R(\nu) = 1$ for all ν within the bandwidth of interest. A gold coating, combining good tarnish resistance and an average normal reflectance of 99% for wavelengths of 2.5 μm and longer, provides an excellent calibration reference in the infrared spectrum. Therefore

$$I(\nu)D(\nu) = \text{Re}F\{V_{gold}(\Delta)\} \qquad (4)$$

and Eq. (2) becomes

$$R(\nu) = \frac{\text{Re}F\{V(\Delta)\}}{\text{Re}F\{V_{gold}(\Delta)\}} \qquad (5)$$

The availability of commercial infrared microscopes greatly simplifies the sample preparation and handling procedure. Typical IR microscopes are designed to be auxillary attachments to spectrometers. They provide both refractive lenses for direct viewing in the visible spectrum and IR optics for spectroscopic analyses. Selective examination of the sample is facilitated essentially by aperturing the IR optics to limit the spectroscopic measurement to an area with dimensions as small as tens of millimeters. The actual size of this area determines the effective spatial resolution of the system. The sample, in our case a rock specimen, can be mounted on a motorized X-Y state that can be stepped automatically to collect IR spectra over a two-dimensional grid of sampling positions. The spectra are processed to generate maps of mineral distribution and abundance.

Scanning FTIR microscopy embodies FTIR spectroscopy, microscopy, and the use of scanning for image formation. SFTIRM extends the power of IR microscopes, which are primarily intended for microspectrometry (i.e., isolating a small area for spectroscopic analysis), by use of scanning to carry out imaging. Spectral fitting is applied to the acquired data (1) to identify the constituent minerals in the sample, and (2) to extract the abundances of the identified minerals. Figure 2 shows the measured specular reflectance spectra in the 2000-700^{-1} range at two different locations on the surface of a sedimentary rock specimen. Specular reflectance spectral standards for pure dolomite, quartz, and illite are given in Fig. 3. Figure 2(a) clearly indicates the presence of both dolomite and quartz; Fig. 2(b) indicates the presence of dolomite and illite. We shall discuss two different spectral fitting and (b) linear area fitting (LAF).

We begin with a model that the specular reflectance spectrum of a mixture of minerals
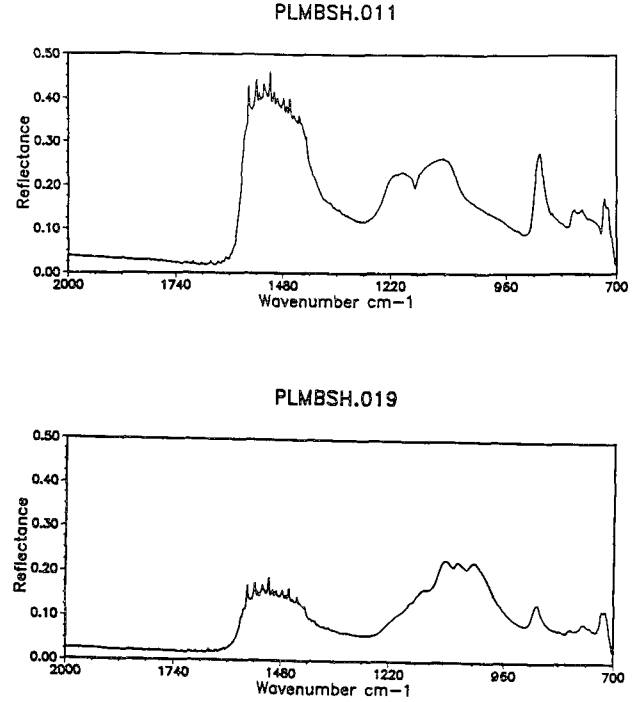
FIG. 2.--Specular reflectance spectra collected at two locations on sedimentary rock sample showing change in mineralogy.

is a weighted sum of the individual mineral spectra:

$$R_{mod}(\nu_j) = \sum_{i=1}^{N} c_i R_i(\nu_j) \qquad j = 1, 2, \cdots M \quad (6)$$

where i indexes the component minerals and c_i and R_i are the weighting coefficient and spectral standard for the ith mineral respectively. The weighting coefficient c_i's need not be linearly related to the concentrations (volume fractions or percentage weights) of the minerals, in which case the calibration curves have to be determined empirically.

In the LMS algorithm, the objective is to determine the c_i's such that the meansquares-error between $R_{mod}^i(\nu_j)$ and the experimentally meausred spectrum $R_{exp}(\nu_j)$ is minimized over the spectral interval ν_j, $j = 1$ to M:

$$\frac{d}{dc_i} \sum_{j=1}^{M} [R_{mod}(\nu_j) - R_{exp}(\nu_j)]^2 = 0 \qquad (7)$$

$$i = 1, 2, \cdots M$$

The solution to Eq. (7) is given by

$$\underline{C} = \{[\underline{R}\,\underline{R}^T]^{-1}\underline{R}\}\underline{R}_{exp} \qquad (8)$$

where $\underline{C}$ is a column vector with elements c_i's $\underline{R}_{exp}$ is a column vector with elements $R_{exp}(\nu_j)$'s, and $\underline{R}$ is an N × M matrix with N column vectors $\underline{R}_i$'s each representing a mineral spectral standard and M the total number of discrete frequencies used in the frequency

Quartz Standard QTZST.002

Illite Standard FILST.002
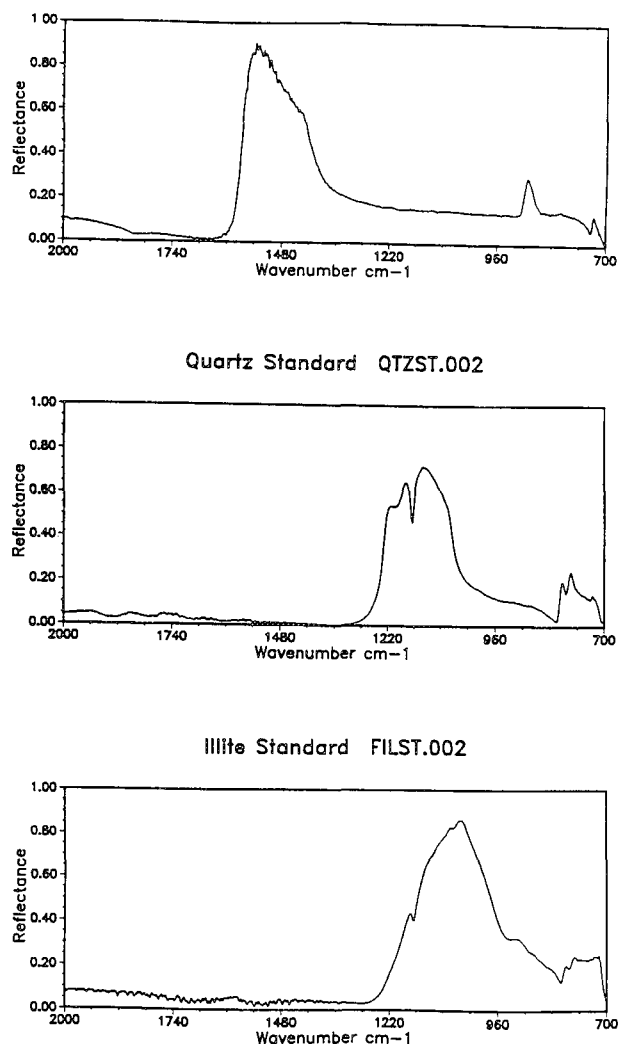
FIG. 3.--Spectral standards of pure laboratory samples of dolomite, quartz, and illite.

interval(s) where spectral fitting is applied. The overall operator matrix on the right-hand side of Eq. (8) is N × M in dimension and has to be calculated only once for a chosen suite of minerals. This algorithm gives the best fit to R_{exp} in the least meansquares-error sense and a unique solution is guaranteed.

In the LAF algorithm, instead of matching $R_{exp}(\nu_j)$ point by point, the areas under the curve in selective spectral windows are considered. For each mineral, a window is chosen so that as much of the reflectance peak is included as possible. No two windows can cover exactly the same spectral range. In fact, it is best not to have any overlap between windows. For the general case of N minerals, the area in each of the N spectral windows chosen can be expressed as

$$A_j = \sum_{i=1}^{N} c_i M_{ji} \qquad j = 1, 2, \cdots N \qquad (9)$$

Since the spectral windows are all distinct, we

have a system of N independent equations in N unknowns c_i's. The coefficients M_{ji}'s have a simple physical interpretation. They correspond to the area under the ith mineral spectral standard in the jth spectral window. The c_i's can be calculated from Eq. (9) as

$$\underline{C} = \underline{M}^{-1}\underline{A} \qquad (10)$$

The use of area in suitably chosen spectral windows to estimate c_i's has many advantages. Preference is given to the spectral region where the mineral has large reflectance and therefore good signal-to-noise ratio. This algorithm is insensitive to additive zero mean noise. The matrix $\underline{M}^{-1}$ has to be evaluated only once for a specific suite of minerals and eigenvalue analysis can be applied to check its numerical behavior. As in the LMS fit algorithm, a unique solution is assured.

The goodness of fit between R_{exp} and R_{mod} in each case is estimated by evaluation of the mean absolute normalized error:

$$E = \frac{1}{M} \sum_{i=1}^{M} \frac{\left| \sum_{j=1}^{N} c_j R_j(\nu_i) - R_{exp}(\nu_i) \right|}{\sum_{j=1}^{N} c_j R_j(\nu_i)} \qquad (11)$$

Experimental

To demonstrate the power of SFTIRM, we chose a sample with a relatively small set of minerals. The sample is a sedimentary rock composed mostly of dolomite, some quartz, and thin layers of illite. The only sample preparations applied were sawcutting and polishing to provide a flat surface for imaging. The flat surface together with the fine grain structure of the minerals (less than 10 μm from SEM images) give a good specular reflection surface. The mineral composition was determined by examination of the collected FTIR spectra at representative locations, as described in the previous section.

The experimental instrumentation includes a Nicolet 60 SX FTIR spectrometer with the 1280 processor, and a Spectra Tech IR-Plan Microscope with a 15×, 0.58 NA Cassegrain type IR objective with a built-in liquid nitrogen cooled mercury-cadmium-telluride (MCT) detector that operates in the 4000-700 cm^{-1} range. The IR microscope is equipped with a motorized X-Y stage that can be stepped automatically from the Nicolet processor via a serial port on the motor controller.

Specular reflectance spectral standards were obtained experimentally for dolomite, quartz, and illite. Dolomite from Lee, Mass., Brazilian quartz, and Fithian illite were available in fine powder form and were pressed into disks for reflectance measurement. The spectra are shown in Fig. 3.

The scanned area measures 1 × 1 cm. We made use of the full active area of the MCT detector for FTIR measurement to maximize photometric

83

throughput. The spatial resolution was therefore defined by the size of the detector to be 0.25 × 0.25 mm. The step size was 0.1 mm in both X and Y, which more than satisfies the Nyquist rate-sampling criterion. The total number of data points taken in each interferogram was 8192, corresponding to a spectral resolution of 4 cm^{-1}. Only 4 averages per interferogram were taken, since noise was not a problem due to the high photometric throughput from a large sampling area. At each pixel, the collected interferograms were processed right away by use of either the LMS or the LAF algorithm. Only the calculated mineral abundances and the error estimation were stored, so that the data-storage requirement was drastically reduced. The total time for each pixel was approximately 15 s. The whole 1 × 1cm area is divided into four subareas of 51 × 51 pixels each. The total time for each subarea scan was about 10 h, well within the liquid-nitrogen capacity of the detector dewar. At the beginning of each subarea scan, an instrument calibration was carried out against a gold coating and all the measured IR spectra were normalized by this calibration spectrum as prescribed by Eq. (5).

Results

The SFTIRM images of dolomite and illite obtained by LAF processing are consistent with the visible image.[6] The quartz image indicates that small quartz particles, less than 0.4 mm in size and not discernible in the visible image, are scattered throughout the sample.

The spectra for a small 4 × 4 mm (21 × 21 pixels) area were stored on disk for more exhaustive analyses. The corresponding images processed by both the LMS and LAF algorithms were compared. The error image was also generated for each processing algorithm. The two processing schemes essentially yield identical results in most cases, differing by 2 to 3%. Figure 4 shows how well $R_{mod}(\nu)$ matches $R_{exp}(\nu)$ for three cases with very different abundances of dolomite, quartz, and illite. The agreement between the LMS and LAF algorithms is especially good for the dolomite abundance where the reflectance is generally large. However, the fitting errors tend to be large where the signal strength is weak (i.e., small reflectance level across the entire spectrum), which happens mostly on the illite layers. The error can be thresholded to provide a quality check of the calculated abundance data.

Conclusion

We have described and demonstrated the principle and operation of Scanning Fourier Transform Infrared Microscopy in one application context: mineral characterization in rocks. The main advantages of this measurement technique over conventional IR spectroscopy and x-ray diffraction techniques for mineralogy characterization are that it is nondestructive and highly automated, and gives full coverage images that provide detailed spatial and quantitative
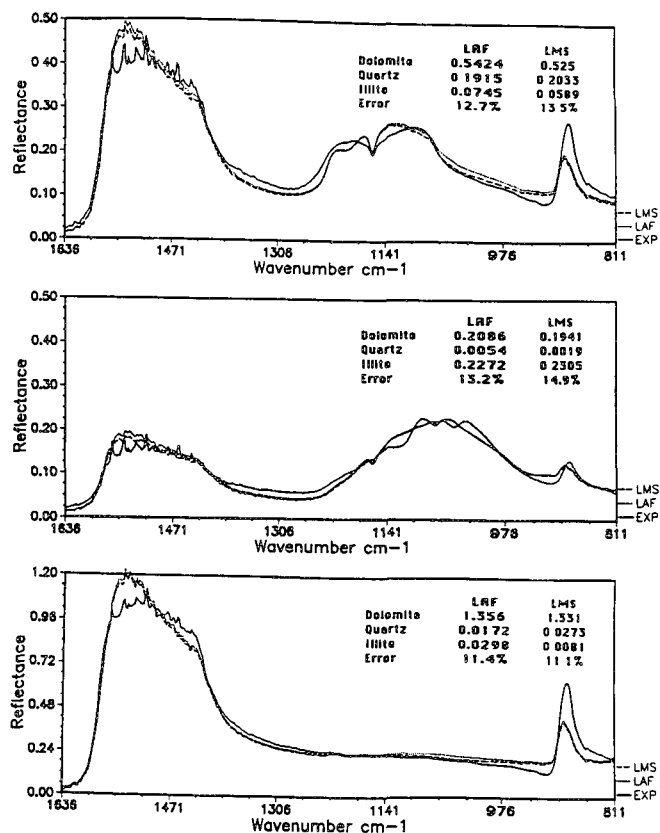
FIG. 4.—Match between modeled and experimental spectra.

description of the mineralogy in rocks. We have illustrated these advantages with a specific example of a sedimentary rock specimen where a relatively large area of coverage with submillimeter resolution was obtained. However, spatial resolution on the order of 10 mm can easily be achieved.

References

1. V. C. Farmer, Ed., *The Infrared Spectra of Minerals*, London: Mineralogical Society, 1974.
2. R. J. P. Lyon, *Evaluation of Infrared Spectrophotometry for Compositional Analysis of Lunar and Planetary Soils*, Final Report prepared for NASA, SRI Project PSU-3943, 1962.
3. R. J. P. Lyon, *Infrared Analysis of Soil Minerals*, Soil Clay Mineralogy, Chapel Hill: University of North Carolina Press, 1964.
4. J. W. Salisbury, L. S. Walter, and N. Vergo, *Mid-infrared (2.1 to 20.0 µm) Spectra of Minerals*, U.S. Geological Survey Open File Report 87-263, 1987.
5. W. M. Tuddenham and R. J. P. Lyon, "Infrared techniques in the identification and measurement of minerals," *Anal. Chem.* 32: 1630-1634, 1960.
6. K. K. Liang, M. Supp, and W. F. Murphy, "Mapping mineralogy distribution and abundance in rock samples by scanning Fourier transform infrared microscopy," *Scanning* 12: 168-178, 1990.

SINGLE CELLS AND CHROMOSOMES STUDIED BY CONFOCAL RAMAN MICROSPECTROSCOPY

G. J. Puppels, C. Otto, and J. Greve

The invention of the laser and its subsequent use as light source in Raman spectroscopic experiments has made this technique a valuable tool for molecular vibrational analysis. This development is due to the fact that the laser light can be tightly focused in a sample, which leads to high light intensities. In the first half of the 1970s it was realized that this feature could be further exploited in that it enabled the study of micro samples and made it possible to couple spatial and spectroscopical information.[1-3] Raman microprobes and even a Raman microscope[4] were developed. Applications included, among others, the identification of inclusions of small foreign bodies in tissue and environmental particulate pollution studies.[5 6]

Raman spectroscopy is an important technique in molecular biology.[7] It provides information about the structure and composition of nucleic acids, proteins, lipids, and other biological molecules, and about interactions among these molecules in complexes. However, little use has been made of Raman microprobing techniques in this field. An obvious reason is the small Raman scattering cross section of the above-mentioned biological macromolecules, which results in very low signal levels. For example, in single-cell studies, Raman spectroscopy has been used only in a limited number of cases. Its applicability was dependent on the possibility of resonance enhancement of the molecules under study (e.g., Ref. 8), on an extremely high compaction of material inside the cell,[9] or simply on the size of the cell. (Spectra of a giant lymphnode cell[10] and of large muscle cells[11] have appeared in literature.)

There are two ways around this problem of limited applicability. One is to enhance the Raman signal. To study nucleic acids and protein, that means one has to use UV excitation. With a recently developed UV Raman microspectrometer it was shown that single-cell resonant-Raman spectra could be obtained in that way.[12] However, the danger of radiation-induced damage has to be kept in mind. The other way is to improve the sensitivity of the instrumentation. This is the approach we used in our laboratory. It has led to the realization of a very sensitive confocal Raman microspectrometer (CRM)[13-16] Its features are briefly summarized below:

o high signal throughput from microscope objective to detector (∿40%)
o sensitive, essentially photon-noise-limited signal detection by means of a liquid-nitro-

gen-cooled CCD camera (quantum efficiency ∿40% at 700 nm, 10 electrons of read-out noise per channel, negligible dark current)
o confocal signal detection, leading to an effective suppression of background Raman signal from substrates or buffer (with a 1.2 NA objective and a 100µm pinhole, spatial resolution is ∿0.45 × 0.45 × 1.3 µm)
o laser light of 660 nm is used to prevent radiation damage to samples[17]

The CRM enables the recording of high-quality Raman spectra of cells and chromosomes. The high spatial resolution mentioned above makes it possible precisely to select the part of cell or chromosome that has to be investigated, as exemplified by Figs. 1-4.

Figure 1 shows spectra obtained from the nucleus (a) and cytoplasm (b) of neutrophilic granulocytes. The lines in the nuclear spectrum can be assigned to DNA and protein vibrations. No clear signal contributions indicating the presence of RNA or lipids are present. The line at 1048 cm^{-1} has not been assigned yet. It is not found in spectra of DNA, nucleosomes, chromatin, metaphase chromosomes, or polytene chromosomes[14,18-21] and its intensity varies strongly. The main signal contributions to the cytoplasmic spectrum come from myeloperoxidase, an enzyme that is present in a high concentration in the cytoplasmic granules. The enzyme is a heme protein that is activated during the process of phagocytosis (the ingestion of foreign bodies), when it catalyzes the production of hypochlorite. An exciting prospect is the possiblity of monitoring this enzyme activation in the cell by Raman microspectroscopy. Signal integration time during these measurements was limited to 30 s. With longer integration times spectral changes became visible, caused by the absorption of laser light by myeloperoxidase.[17]

In Fig. 2 spectra are shown from a (dark) band and three (light) interbands of a fixed polytene chromosome (Chironumus thummi thummi, chromosome II positions of measurements indicated in Fig. 3). Spectra obtained from different bands are virtually identical (and therefore so is the DNA and protein content). Spectra obtained from different interbands do show considerable variation. The intensities of the Raman lines at 1093 cm^{-1} (DNA-backbone) and 1448 cm^{-1} (protein CH-bending modes) were used to determine the DNA and protein concentration in eight neighboring bands and interbands (Fig. 3). This determination was made by a comparison of the intensities of these lines in the chromosome spectra with the intensity of the same lines in spectra of DNA and protein solutions of known concentrations[17,18] Figure 4 shows DNA and protein concentrations, DNA-
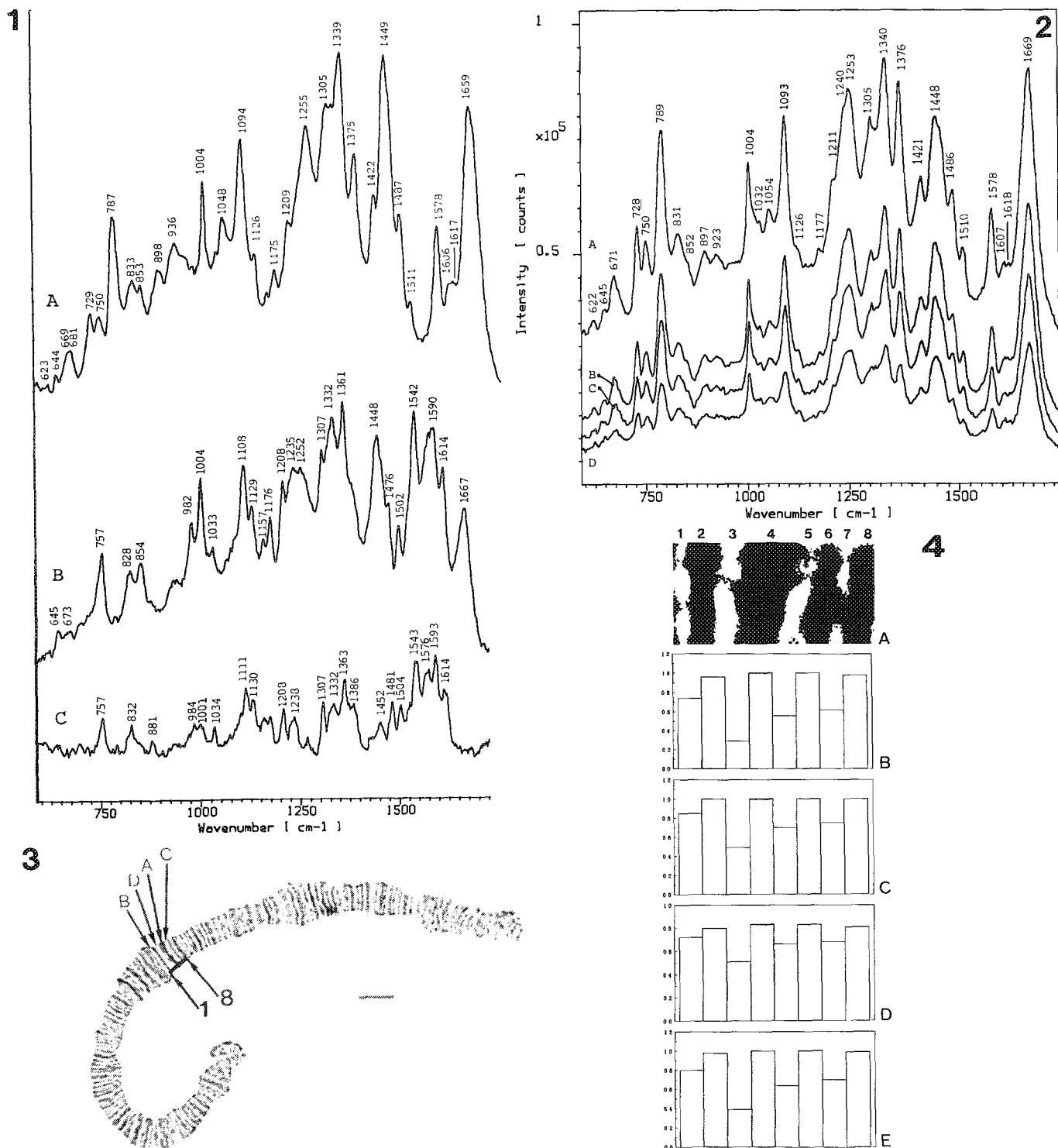
FIG. 1.--Raman spectra of intact neutrophilic granulocytes (a) focused in the nucleus (average of 5 measurements, 6 mW (660 nm), 150 s per measurement); (b) focused in cytoplasm (average of 5 measurements, 6 mW, 30 s per measurement); (c) Raman spectrum of purified myeloperoxidase (for experimental details see Refs. 17 and 18).

FIG. 2.--Raman spectra of a fixed polytene chromosome (see Fig. 3 for indication of measurement positions): (a) band (15 mW, 600 s); (b-d) interbands (15 mW, 600 s). (Work in cooperation with the laboratory of Dr. T. M. Jovin of the Max Planck Institute for Biophysical Chemistry, Department of Molecular Biology, in Göttingen, Germany.)

FIG. 3.--Light microscopic image of *Chironumus thummi thummi* (Ctt) chromosome II. Indicated are positions of measurements shown in Fig. 2 (a,b,c,d) and the eight bands and interbands for which relative DNA and protein concentration were determined (see Fig. 4). Scale bar, 10 μm.

FIG. 4.--DNA and protein concentrations in eight neighboring bands and interbands of a fixed Ctt-polytene chromosome: (a) magnification of Fig. 3 of chromosomal region under investigation (b) DNA concentration (normalized to band 4), ± 5%; (c) protein concentration (normalized to band 4), ± 5%; (d) DNA-protein weight ratio (absolute values), ± 19%; (e) total chromatin concentration (normalized to band 4), ± 5%.

protein ratio, and total chromatin concentration of the eight bands and interbands. In all cases DNA and protein content is lower in interbands than in bands. This finding correlates with a lower DNA-protein ratio in interbands than in bands. Furthermore, measurements on unfixed chromosomes have shown that overall protein secondary structure in interbands is different from that in bands.

These examples give a clear indication of the potentials of the CRM for in situ and in vivo studies of biological molecules. A great support for these studies is of course formed by the extensive amount of data already available from Raman spectroscopic studies on model systems or isolated molecules/molecular complexes.

Another major biological problem now open to investigation by means of Raman spectroscopy is the question of the origin of the banding patterns that appear on metaphase chromosomes after physico-chemical treatment and staining. This banding pattern is a reflection of a level of chromosomal organization that is still poorly understood.

Future instrumental developments will include the imaging of cells and chromosomes on the basis of the intensity of the Raman signal. Possibilities and instrumentation for Raman microscopy have been described before.[4,5,22,23] We do not expect serious difficulties in obtaining Raman images of cells and chromosomes now that the necessary level of instrumental sensitivity has been achieved.

References

1. T. Hirschfeld, "Raman microprobe: Vibrational spectroscopy in the femtogram range," *J. Opt. Soc. Am.* 63: 476, 1973.

2. G. J. Rosasco et al., "Investigation of the Raman spectra of individual microsized particles," *4th ICORS (abstracts)*, 1974.

3. M. Delhaye and P. Dhamelincourt, "Laser microprobe and microscope," *ibid.*

4. M. Delhaye and P. Dhamelincourt, "Raman microprobe and microscope with laser excitation," *J. Raman Spectrosc.* 3: 33, 1975.

5. E. S. Etz and J. J. Blaha, "Scope and limitations of single particle analysis by Raman microprobe spectroscopy," *NBSS Publication 533*: 153, 1980.

6. P. Dhamelincourt, "Developments and applications of the mole laser Raman microprobe," *Microbeam Analysis--1979*, 155.

7. For reviews see, for example, F. S. Parker, *Application of Infrared, Raman and Resonance Raman Spectroscopy in Biochemistry*, New York: Plenum Press, 1982.

8. B. Barry and R. Mathies, "Resonance Raman microscopy of rod and cone receptors," *J. Cell Biol.* 94: 479, 1982.

9. W. L. Kubasek et al., "Raman spectra of the model B-DNA oligomer d(CGCGAATTCGCG)2, and of the DNA in living salmon sperm show that both have very similar B-type conformations," *Biochemistry* 25: 7440, 1986.

10. J. L. Abraham and E. S. Etz, "Molecular microanalysis of pathological specimens in situ with a laser-Raman microprobe," *Science* 206: 716, 1979.

11. M. Pézolet et al., "A molecular probe of the contractile state of intact single muscle fibers," *Biophys. J.* 31: 1, 1980.

12. F. Sureau et al., "An ultraviolet micro-Raman spectrometer: Resonance Raman spectroscopy within single living cells," *Appl. Spectrosc.* 44: 1047, 1990.

13. G. J. Puppels et al., "Application of a highly sensitive confocal Raman microscope in biological studies," *Proc. 3rd European Conf. Spectroscopy Biological Molecules*, Esculapio, Bologna, 1989, 356.

14. G. J. Puppels et al., "Studying single living cells and chromosomes by confocal Raman microspectroscopy," *Nature* 347: 301, 1990.

15. G. J. Puppels et al., "A high throughout Raman notch filter set," *Rev. Sci. Instrum.* 61: 3709, 1990.

16. G. J. Puppels et al., "Description and performance of a highly sensitive confocal Raman microspectrometer," *J. Raman Spectrosc.* (in press).

17. G. J. Puppels et al. (submitted).

18. G. J. Puppels, *Confocal Raman Microstroscopy: A New Look at Cells and Chromosomes*, Ph.D. thesis, University of Twente, Enschede, 1991.

19. G. J. Thomas Jr., B. Prescott, and D. E. Olins, "Secondary structure of histones and DNA in chromatin," *Science* 197: 385, 1977.

20. R. Savoie et al., "Laser Raman spectra of calf thymus chromatin and its constituents," *Biophys. J.* 47: 451, 1985.

21. H. Hayashi et al., "The structure of nucleosome core particles as revealed by difference Raman spectroscopy," *Nucl. Acids Res.* 14: 2583, 1986.

22. D. V. Veirs, et al., "Mapping materials properties with Raman spectroscopy utilizing a 2-D detector," *Appl. Opt.* 29: 4969, 1990.

23. M. Bowden et al., "Line-scanned micro Raman spectroscopy using a cooled CCD imaging detector," *J. Raman Spectrosc.* 21: 37, 1990.

MULTICHANNEL RAMAN MICROANALYSIS WITH NIR EXCITATION

Jacques Barbillat, Edouard da Silva, Bernard Roussel, and S. G. Howard

Raman microanalysis is a powerful nondestructive method of obtaining molecular information at the microscopic level. Unfortunately, many samples, especially in industrial fields, are strongly fluorescent under visible excitation and cannot be studied. One of the best ways to overcome this fluorescence problem is to move the excitation toward the near infrared (NIR) part of the spectrum. This idea is not recent; it was proposed 30 years ago, well before the advent of laser sources.[1] However, it leads to a reduction in signal intensity, because Raman cross sections are inversely proportional to the fourth power of the wavelength. Moreover, the noise equivalent power (NEP) of common near-infrared detectors is several orders of magnitude higher than that of typical photomultiplier tubes (PMT) operating in the photon-counting mode, or than the intensified silicon photodiode array. NIR dispersive scanning techniques and single-channel detectors, as proposed some years ago to collect Raman spectra of large fluorescent samples sequentially, require long exposure of the sample to the laser beam.[2,3] Thus, they must be avoided in studies of microsamples irradiated with a laser beam focused down to the limit of diffraction, since it is not possible, without sample degradation, to increase laser power so as to compensate for the ν^4 dependence or the lower sensitivity of NIR detectors. Fourier transform Raman (FT Raman) microscopy is only emerging and currently does not allow spatial resolution better than 10-20 μm.[4,5]

In the work reported here, we describe the use of silicon-based charge-coupled devices (CCD) and of the more recently introduced multiplexed germanium array detector to obtain fluorescence-free multichannel Raman spectra with NIR excitation at 1064 nm. Until now, the only attempts to benefit from the advantage of multichannel spectroscopy to perform fluorescence elimination were done with for red excitation (up to 830 nm) and silicon-based CCD detection, but only for the study of large samples.[6,7]

The installation presented in this paper not only allows the complete elimination of fluorescence background, it also offers microanalysis and low-frequency performance comparable to that of available visible Raman microprobes. Spatial resolution better than a few microns (typically 2 μm) and Raman shift down to 30

J. Barbillat is at LASIR CNRS, Bât. C5 USTLFA, F-59655 Villeneuve d'Ascq, France; E. da Silva and B. Roussel are at DILOR SA, 244 rue des Bois Blancs, F-59000 Lille, France; S. G. Howard is at EG&G JUDSON, 221 Commerce Drive, Montgomeryville, PA 18936.

cm^{-1} are achievable routinely with this installation.

Experimental

The installation used in this work has been described in more details elsewhere.[8] It consists of a DILOR XY multichannel spectrometer which comprises a microscope attachment and a double subtractive premonochromator, followed by a spectrograph equipped with two exit ports that enable easy comparison of various detectors under similar experimental conditions.

This configuration provides the highest degree of Rayleigh and laser line rejection and the best transmission close to the Rayleigh line. Thus, unlike FT Raman interferometers, this system allows easy access to the low-frequency range even at Raman shifts as low as 30 cm^{-1}. By bypassing the double subtractive premonochromator and removing the Rayleigh line by means of a notch filter, one can achieve higher transmission and better signal-to-noise ratio for Raman lines beyond 450 cm^{-1} (or less, depending on the notch filter).

The visible microscope attachment has been modified to improve its transmission in the NIR. An especially designed NIR 100× Olympus microscope objective and an NIR beam splitter have been used in place of conventional elements employed with visible laser excitation. The positioning of the laser spot onto the sample can be viewed and adjusted by means of a CCD TV camera located behind the entrance slit of the spectometer.

We used two NIR laser sources: a cw unpolarized CVI-95 ND-YAG laser pumped with tungsten-halogen lamps and a linearly polarized Adlas ND-YAG laser pumped with a diode laser. The outputs of these lasers were filtered through a grating monochromator that exhibits an overall transmission better than 20% at 1064 nm.

Silicon-based CCD Detector. The silicon-based detector is a 512 × 512 sensor element The CCD is cooled to -110 C in a liquid-nitrogen cryostat in order to reduce the dark current to negligible levels. The associated electronics consists of a CE 200 electronic unit and a CC 200 camera controller from Photometrics.

The quantum efficiency is very high in the visible but drops rapidly in the far red until the phtoons no longer carry enough energy to create electron-hole pairs ($\lambda > 1100$ nm). However, the quantum efficiency remains at measurable values in the 1064nm region (Fig. 1).

The CCD detector exhibits extremely low
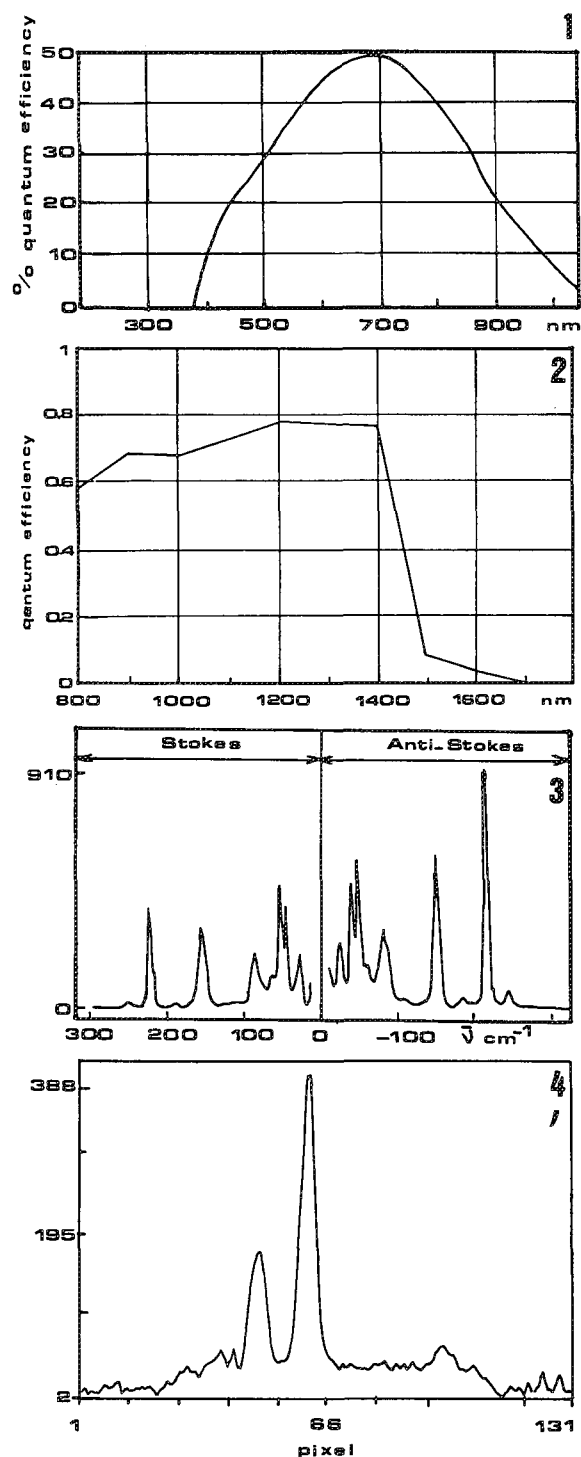
FIG. 1.--Quantum efficiency of silicon-based CCD detector (Photometrics PM512).

FIG. 2.--Anti-Stokes and Stokes low-frequency micro-Raman spectrum of sulfur (S_8). Excitation line, 1064 nm; silicon-based CCD detection; acquisition time, 500 s; power at the sample, < 50 mW.

FIG. 3.--Quantum efficiency of Ga0022 EG&G Judson NIR multiplexed germanium array detector.

FIG. 4.--Micro-Raman spectrum of industrial dye (7-4 dihydroxyflavilium chloride. Excitation line, 1064 nm; multiplexed Ge array detector; integration time, 10 s; power at the sample, < 50 mW.

noise, so that NEP and signal-to-noise ratio can be improved by integration of the signal for long periods of time. The senstivity can be increased by physically combining the photogenerated charge packets from a spectral line into a single charge packet. This process, called binning, reduces the total detector noise.

Multiplexed Germanium Array Detector. The EG&G Judson Ga0022 detector is a self-scanning germanium photodiode array for radiations extending from 800 to 1700 nm. The array has 128 elements in linear configuration. Individual element size is 2.5 × 0.1 mm with a center-to-center spacing of 100 μm. The photodiodes are operated in the capacitive-discharge mode, where the photovoltaic detector is both photon sensor and charge-storage device. A shift register scanning circuit reads the voltage change on each diode. The diode array and scanning circuitry are mounted in a dewar for operation at 77 K with liquid nitrogen.

Data from the detector are collected and analyzed by a 1461 detector interface from an EG&G PARC, which is interfaced to a PC/AT compatible computer. Detector control is supported via a EG&G PARC 1462 detector controller, which has a 14 bit ADC with a gain of 1500 electrons/count.

The array device has very high quantum efficiency, from 60% to 80% between 800 and 1450 nm (Fig. 2). NEP is of the order of 10^{-15} $W/H_2^{1/2}$ for an integration time of 1 s. In the same manner as for the CCD detector, better NEP can be obtained by an increase in the integration time. NEP of about 10^{-16} $W/H_2^{1/2}$ is achievable with integration time larger than 100 s.

Results

As illustrated in Fig. 3, the silicon-based CCD detector has a sufficiently high quantum efficiency around 1000 nm and very low noise to enable the observation of anti-Stokes and Stokes low-frequency spectrum of sulfur S_8 under the microscope with an integration time of 500 s. (For presentation of anti-Stokes and Stokes spectra we have adopted the following convention: anti-Stokes Raman shifts are negative, Stokes Raman shift are positive.) This spectrum and many other spectra collected with the CCD detection demonstrate that the rapid increase of silicon quantum efficiency as one moves toward shorter wavelengths can compensate for the exponential relationship of anti-Stokes Raman intensity. For instance, we were able to record acceptable anti-Stokes Raman lines of an industrial dye at -1600 cm^{-1}. This spectrum also illustrates the superior performance of dispersive multichannel technique in the low-frequency range, since one can easily observe Raman lines at about -30 cm^{-1} and -30 cm^{-1} from the exciting line.

Obviously anti-Stokes spectra do not illustrate the potentiality of NIR excitation for fluorescence elimination. According to Stoke's law, no fluorescence emission can occur at

wavelengths shorter than the excitation. Figure 4 presents the micro-Raman spectrum of an industrial dye (7-4 dihydroxylavilium chloride) around 600 cm^{-1} obtained with the multiplexed germanium array detector with an integration time of 10 g. Shorter integration time than with the CCD are possible owing to the very high quantum efficiency of germanium in the NIR. This dye sample is strongly fluorescent with visible excitation but does not exhibit any fluorescent background with 1064nm excitation.

Conclusions

We have demonstrated that silicon-based CCD detectors and multiplexed germanium array detectors can be successfully used to obtain fluorescence-free Raman spectra of good quality excited in the NIR, for instance at 1064 nm. These two devices are complementary, since a CCD has a very high quantum efficiency in the visible part of the spectrum with some extension into the NIR, so that it can detect anti-Stokes Raman spectra and the very low-frequency part of Stokes Raman spectra. The multiplexed germanium array detector has very high quantum efficiency from 1000 to 1700 nm and is the best choice for observation of Stokes Raman lines up to 3000 cm^{-1}. The noise characteristics of the Ge array detector are sufficiently low to allow the detection of weak Raman scattering from micrometric size samples close to the limit of diffraction.

The results obtained in the course of this work are very promising for the future development of NIR multichannel Raman microanalysis. The experience acquired during this study enables us to define more accurately the characteristics of the ideal multichannel NIR Raman microprobe.

Larger germanium arrays with more individual sensor elements are already under development and will extend the capabilities of the instrument by reducing the number of spectral ranges needed to obtain a complete spectrum. Furthermore, newly introduced NIR multichannel detectors such as InGaAs photodiode arrays are now commercially available and will be evaluated very soon at our installation.

References

1. H. Stammreich and R. Forneris, "High-resolution Raman spectroscopy in the red and near infrared-1," *Spectrochimica Acta* 17: 775-784, 1961.

2. D. Portfield and A. Campion, "Fluorescence-free scanning Raman spectroscopy," *J. Am. Chem. Soc.* 110: 408-410, 1988.

3. J. Barbillat and A. Chapput, "Near infrared Raman spectroscopy: potentialities of conventional scanning machines," *Spie Proc.* 1341: 233-238, 1990.

4. R. G. Messerschmidt and D. B. Chase, "FT-Raman microscopy: Discussion and preliminary results," *Appl. Spectrosc.* 43: 11-15, 1989.

5. F. J. Bergin, "A microscope for Fourier transform Raman spectroscopy," *Spectrochimica Acta* 46A: 153-159, 1990.

6. J. M. Williamson, R. J. Bowling, and R. L. McCreery, "Near-infrared Raman spectroscopy with a 783-nm diode laser and CCD array detector," *Appl. Spectrosc.* 43: 372-375, 1989.

7. J. E. Pemberton, R. L. Sobocinski, "Raman spectroscopy with He-Ne laser excitation and charge-coupled device detection," *J. Am. Chem. Soc.* 111: 432-434, 1989.

8. J. Barbillat, E. da Dilva, and B. Roussel, "Demonstration of low-frequency performance and microanalysis capability of multichannel Raman spectroscopy with near infrared excitation: Part 1," *J. Raman Spectroscopy* (in press).

TOWARD NANOMETER-SCALE OPTICAL DEVICES, MICROSCOPY, AND SPECTROSCOPY

Raoul Kopelman, Weihong Tan, S. J. Smith, Aaron Lewis, and Klony Lieberman

In conventional "far-field" light imaging, the image cannot be smaller than the diffraction limit, roughly $\lambda/2$, where λ is the wavelength.[1] In this case it is irrelevant whether the source is a laser beam, an ultrasmall lamp ($\leq\lambda/2$) or a simple luminescent center of atomic size. However, in "near-field" applications, the size of the image is only limited by the size a of the source and its distance d.[2,3] If $d < a$, the image size is roughly equal to the source size a. At this point the following questions become relevant: (1) What is the lowest limit for the source size a? (2) What is the brightness of such a source? (3) How stable is its position? (4) Can it be scanned? (5) How stable is the scanning? (6) How stable is the light intensity? (7) What are its spectral characteristics? (8) How robust is it mechanically and chemically? We discuss below some of these theoretical and practical considerations. We also give the principles and schematics of molecular exciton microscopy.

There is another set of questions: What is the nature of the "image"? Does it involve photons, evanescent photons, or energy (hv) packages? Can we at $a = d << \lambda$ distinguish an emission plus absorption event from an energy transfer event? Does it matter in practice? What is the detection sensitivity? What is the spectral resolution? Can one fully separate the nature of the target from the nature of the source or do they form a coupled system?

Theoretical Considerations

The simplest nanometer light source is a nanometer-sized hole, stopping down light from a larger light source, e.g., a laser. For the sake of contrast, the hole's surroundings must be totally opaque. The thinnest matrix for such a hole is typically aluminum, the metal with the shortest extinction length (6 nm). It is opaque enough for good contrast at a thickness of 50 nm.[4]

The thickness b of the plate is effectively the length L of the funnel defined by the hole (aperture a). For a $<\lambda$, the probability P of a photon to pass through the tunnel falls off as

$$P \sim a^6 \exp(-3.6L/a) \tag{1}$$

R. Kopelman is at the Departments of Chemistry and Physics, W. Tan is at the Department of Chemistry, and S. J. Smith is at the Department of Physics, University of Michigan, Ann Arbor, MI 48109; A. Lewis and K. Lieberman are at the Division of Applied Physics, Hebrew University, Jerusalem, Israel. They acknowledge support under DOE grant DE-FG02-GOER60984 and the Israeli National Council for R & D, respectively.

Obviously, when $a = L/10$ instead of $a = L$, the throughput is reduced by about 10^{22}. However, for a given size $a \simeq \lambda$, there will be significantly more throughput if the effective λ shrinks by a factor of 2 or more. This can be achieved, in principle, by filling the tunnel with a transparent material of high refractive index n (since $\lambda = \lambda_0/n$, where λ_0 is the wavelength in vacuum), or a high effective n (e.g., near a strong absorption edge).

To overcome the exponential decrease of light intensity with a, we transform the point source from a passive aperture to an *active emitter*, e.g., anthracene crystal fluorescence.[5] The submicron tip of a metal-coated glass micropipette is filled with the molecular crystal (Fig. 1). The incoming photons propagate through the super-micron portion of the pipette and get absorbed by the crystal. (The back-mirrored glass walls act as a light-pipe.) The absorbed photons generate Frenkel excitons that propagate (diffuse) toward the submicron tip; the glass walls may also serve as an effective light pipe. We note here that the diffusion length of anthracene is somewhat controversial. The old data[6,7] give about 500 Å (0.05 µm, perpendicular to the ab plane), but the more recent, room-temperature data give about 10 µm, i.e., 200 times longer.[8] Even if the latter data are contaminated by some emission-reabsorption events (radiative transport), it does not matter much from our point of view. Due to the overlap of the absorption and the emission spectra at room temperature (hot bands), the reabsorption process is fairly efficient (and includes some emitted light returning from the glass walls). The main point is that the exciton transport is largely controlled by the geometry of the crystal, i.e., the geometry of the tip's cavity. Thus, the efficiency decreases geometrically, rather than exponentially, with smaller aperture size. With a quantum efficiency of nearly unity, the major loss of photons is by fluorescence in the back-direction rather than forward direction. The forward/backward ratio of these two fluxes should be proportional to the ratio of cross sections. If the diameter of the crystal at the back is 0.5 and in front 0.05 µm, this forward/backward efficiency should be 1/100. Another loss channel is the exciton-plasmon transfer to the metal (gold) ring at the tip, which reduces the effective tip radius by about the *critical distance* (defined below), which is about 0.005 µm.

Of particular interest is the very-near-field interaction between the exciton at the tip and the sample. A metallic sample will quench the exciton with a typical critical distance d_c, defined as the distance at which

Molecular Exciton Microscope
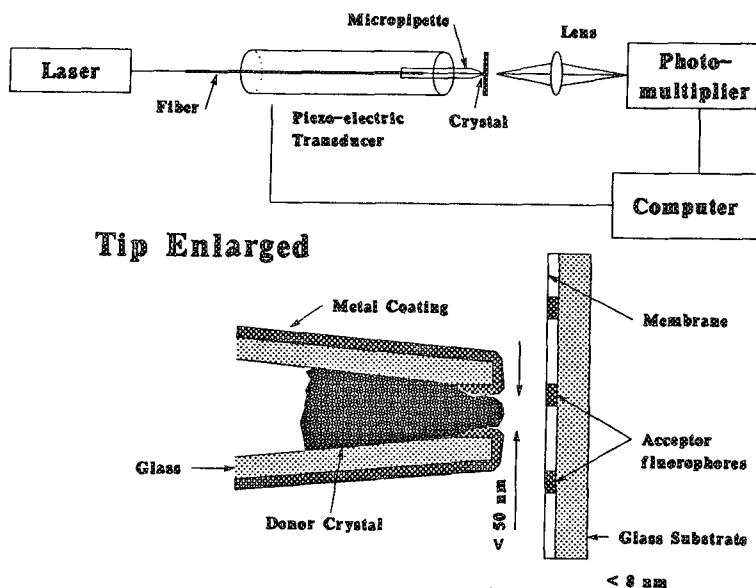
FIG. 1.--Schematic of microscope, tip, and sample.
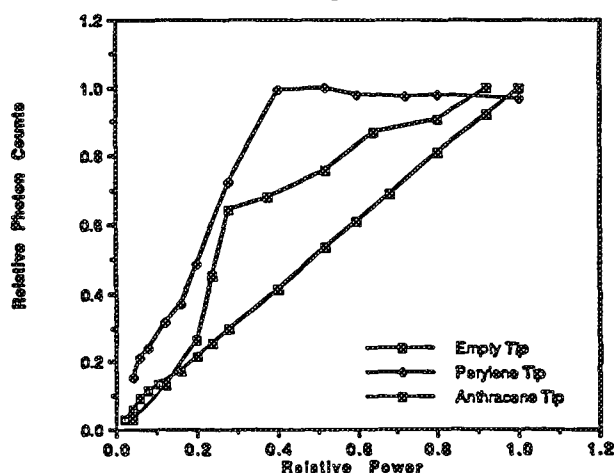
FIG. 2.--Normalized power characteristics of various tips (empty, perylene, anthracene). Only function forms should be compared.

this quenching probability is 0.5 (reducing the lifefime by a factor of two). Similarly, such a Foerster-Kuh-Drexhage distance also describes the quenching by a dielectric film of quenchers.[9,10] However, in the latter case, the quenching acceptors can also be efficient fluorophores.

How critical is exciton-exciton annihilation? The annihilation rate R is related to the density ρ quadratically:

$$R = k\rho^2 \qquad k \sim D \qquad (2)$$

where D is the diffusion constant. However, for dimensions smaller than the diffusion length (and with reflective boundary conditions) this relationship changes. For a one-dimensional wire (with diameter less than the diffusion length) one has:[11]

$$R' = k'\rho^3 \qquad k' \sim D \qquad (3)$$

so that

Thus, to maintain a steady state and keep up with annihilation, a much lower photon flux is required for a one-dimensional crystal, compared to a three-dimensional one. A typical exciton number density (per site) may be 10^{-4}, which yields a significant reduction factor of $R'/R \simeq 10^{-4}$. For a thicker wire, or one with a conical shape, with a diameter close to the diffusion length, an approximate relation may be $R' \sim \rho^{2.5}$. This would give $R' \sim \rho^{0.5}$ or $R'/R \sim 10^{-2}$ for $\rho = 10^{-4}$. On the other hand, the *trapping rate* R_T is linear in ρ for all geometries (but not linear in the trap concentration). Thus, an arrangement utilizing trapping or quenching at the narrow tip is more competitive with annihilation for smaller crystalline domains. Obviously, the fluorescence rate R_F is also linear with ρ. Whether one wants to optimize fluorescence or trapping, increasing the laser photon flux may quickly reach the limit of diminishing returns.

For biological and chemical analysis, the sensitivity to a single chromophore or fluorophore molecule in the sample is of particular interest. If the tip diameter is of the order of the Foerster radius or the Foerster-Kuhn-Drexhage critical distance, and the sample distance (including the fluorophore) is the same, the probability of detecting this molecule is extremely high (requiring just a few excitons at the tip). For a single highly efficient fluorophore (very high absorption coefficient and quantum efficiency near unity) about 10^9 photons are required to pass through such a sample (with a $\lambda/2$ distance from the molecule) to generate one fluorescence quantum (photon).[5,12,13] Will it also take 10^9 photons to create the required few excitons? Theoretically it will take only 10^4 to 10^5 photons with a single crystal. Furthermore, if the crystal surface is covered with appropriate "exciton traps" that act as donors for the fluorophore, the host crystal serves as an antenna. This effective antenna could easily consist of 10^6 or 10^7 host molecules. Thus, only about 10^3 or fewer photons will be required in this case. Such a reduced photon flux will significantly reduce linear or nonlinear effects that may reduce local heating, chemical decomposition, or Raman emission. Futhermore, not only will the single fluorophore be detected nondestruc-

tively, but its location is also established to within the Foerster radius (e.g., 25 or 50 A).

The photodestruction (degradation) of the fluorescent species (dye) is an important aspect.[2,14] The role (sec^{-1}) of photodestruction is given by

$$k_d = \sigma_a I \phi \qquad (5)$$

where σ_a is the absorption cross section (cm^2/molecule), I the incident beam intensity (photons/cm^2 sec) and ϕ the quantum yield of photodestruction.[13] For dyes in solution $\phi = 2.7 \times 10^{-5}$ for fluorescein and 1.1×10^{-5} for B-phycoerythrin.[13] However, in solid matrices this yield can be reduced to about 10^{-10}.[2] This involves optimization and purification of dye, matrix and solvent, addition of triplit quenchers, and use of barrier films to reduce gaseous exchange of oxygen and water.[2] Moreover, multiphoton or multiquanta destruction processes of the emitting "supertrap" can be largely circumvented by black-transfer into the host antenna. Thus, the reduction of the photodestruction efficiency is as much a molecular engineering job as is the enhancement of the EXCITOR's quantum efficiency and the scaling down of its effective size.

The above argument excluded the formation of exciton-polaritons. These are well studied at low temperatures.[15] Their role at room temperature is less well understood, but they may be responsible for the above mentioned literature discrepancies.[7,8] In general, the polaritons have a smaller cross section for trapping and annihilation, as well as a faster diffusion rate and a higher probability for escaping the crystal as fluorescence (photons). Alternatively, we note that effective refractive indices up to 30 have been claimed for anthracene crystals near resonance, due to the exciton-photon interation.[11] Classically, this gives an intracrystal "photon" (polariton) with a wavelength of about only 13 nm (i.e., with the size of soft x-ray wavelengths but the energy of visible light photons).

Experimental

Crystals of anthracene, DCM, and tetracene have been grown from solutions of benzene as well as hexane. Some details were given earlier.[5] The excitation was with a 20W argon ion laser (cw), using either the 360nm lines (for anthracene) or the blue line (for tetracene). While the anthracene emission was always blue, that of the tetracene varied from green to yellow and red.

Preliminary amplification factors for anthracene tips have been given earlier.[4,10] Order-of-magnitude amplification factors have also been found for 50 and 100nm tips of DCM [4-Dicyanomethylene)-2-methyl-6-(ρ-dimethylamino-styrly)-4*H*-pyran], by use of monochromatized Xe lamp excitation as well as the argon ion laser green line.

The extension of the anthracene crystal throughout the tip (see above) has also been shown by exciton quenching experiments. A 20nm gold film (transparent to blue light) on glass is Z-scanned by the anthracene tip. Only when the distance is below 10 nm is there significant reduction in the light intensity transmitted by this gold "mirror."

Using the same approach as in Refs. 5 and 12, we showed that perylene crystals have an intensity amplification effect similar to that of anthracene. However, the large shift from the ultraviolet exciting light to the orange-colored emission provides a wavelength increase of about two, compared to an empty pipette. This just about cancels the index of refraction increases inside the perylene crystal; i.e., the effective wavelength 1 is about the same for the empty and filled tips. Thus, the intensity amplification effect cannot be attributed to a simple index-of-refraction change but must be related to an exciton (exciton-polariton?) effect.

Figure 2 demonstrates the very different characteristics of empty tips, anthracene-filled tips, and perylene-filled tips. The empty micropipette shows a practically *linear* increase of *photon counts* with power (as expected), but that is no longer true for the crystal tips. The *sublinear* functional behavior of the anthracene crystal is consistent with an exciton annihilation effect. The reason for the *saturation behavior* of the perylene crystal is less obvious. We note that each curve describes a single micropipette, with a given tip size. Thus, no comparisons should be made among the different tips. They are shown just in order to demonstrate their different power characteristics. The perylene tip results, as those of the empty tip, are completely reproducible while the anthracene tip looses intensity in time, due to photo-oxidation.

References

1. E. Abbe, *Archiv f. Mikroskop. Anat.* 9: 413, 1873.
2. J. A. O'Keefe, *J. Opt. Soc. Am.* 46: 359, 1956.
3. P. S. Friedman and C. R. Parent, *Solar Energy Research Inst. Report. STR-211-3149 (DE87001172)*, Golden, Colo., 1987.
4. E. Betzig, A. Harootunian, A. Lewis, and M. Issacson, *Appl. Opt.* 25: 1890, 1986.
5. S. Lieberman, S. Harush, A. Lewis, and R. Kopelman, *Science* 247: 59, 1990.
6. V. M. Agranovich and M. D. Galanin, *Electronic Excitation Energy Transfer in Condensed Matter*, Amsterdam: North Holland, 1982.
7. D. Donati and J. O. Williams, *Mol. Cryst. Liq. Cryst.* 44: 23, 1978.
8. H. Nishimura, T. Yamaoka, K. Hattori, A. Matsui, and K. Mizuno, *J. Phys. Soc. Japan* 54: 4370, 1985.
9. K. H. Drexhage, *J. Lumin.* 1,2: 693, 1970.

10. K. H. Drexhage, in E. Wolf, Ed., *Progress in Optics*, XII, Amsterdam: North Holland, 1974, 163.

11. R. Kopelman, *Science* 241: 1620, 1988.

12. R. Kopelman, A. Lewis, and K. Lieberman, *J. Lumin.* 45: 298, 1990.

13. R. A. Mathies and L. Stryer, in D. L. Taylor, A. S. Waggoner, R. F. Murphy, F. Lanny and R. R. Birge, Eds., *Applications of Fluorescence in the Biomedical Sciences*, New York: A. L. Liss, 1986, 129.

14. E. B. Shera, N. K. Seitzinger, L. M. Davies, R. A. Keller, and S. A. Soper, *Chem. Phys. Lett.* 174: 72, 1990.

15. J. Aavikso, A. Freiberg, J. Lipmaa, and T. Reinot, *J. Lumin.* 37: 313, 1987.

SMALL-SPOT SURFACE ANALYSIS OF ORGANIC MATERIALS WITH A SCANNING INFRARED MICROPROBE

J. A. Reffner and W. T. Wihlborg

The surface of polymers, coatings and other organic materials, and thin films on metals can be studied by scanning infrared microscopy. Two infrared spectroscopic techniques are highly surface selective: attenuated total reflection (ATR) and grazing-incidence reflection. These techniques have been extended to the microscopic domain through the development of grazing-incidence and ATR objectives.

The grazing-angle microscope objective[1] is a modified Schwarzchild reflecting lens, with a numerical aperture of 0.996, providing a maximum incidence angle of 85° (Fig. 1). The high aperture requires an over-center primary mirror. The secondary mirror obscures the central area of the lens aperture, restricting the minimum incidence angle to 33°. Specific annular stops placed in the objective's Fourier plane (AP in Fig. 1) define specific angular apertures for viewing and recording spectra. For viewing, near-normal rays (33° to 45°) are used; for grazing-angle spectra are recorded at a 65°-85° angular range.

ATR is based on the total internal reflection of radiation at angles exceeding the critical angle. This requires that a high-refractive-index material (the ATR crystal) is in contact with the sample and that the incident radiation is totally reflected from this interface. Because the incident radiation penetrates a short distance into the sample when it is reflected at the interface, an absorption spectrum of the sample is produced. Since the sample's absorption diminishes the amount of the total internally reflected radiation, this is called attenuated total reflection.

The ATR objective for internal reflection microscopy is shown in Fig. 2. This objective provides a refracting optic for viewing the sample through the ATR crystal and a reflecting optic for spectral analysis. Before a spectrum is recorded, optical contact between the ATR crystal and the sample must be established. A microscopic area, down to the 10 × 10μm diffraction limit, can be analyzed. The depth that radiation penetrates into the sample is a fraction of a wavelength. When a ZnSe ATR crystal at an angle of incidence of 45° is used, the average sampling depth for weakly absorbing organic materials is 0.7 of a wavelength. This places the ATR technique as a method for near-surface analysis (the outer few micrometers).

At grazing angle, Fourier transform-infrared (FT-IR) microscopy is capable of detecting, identifying, and mapping molecular species in thin films on metal surfaces.[2] While XPS

The authors are at Spectra-Tech Inc., Stamford, CT 06906.
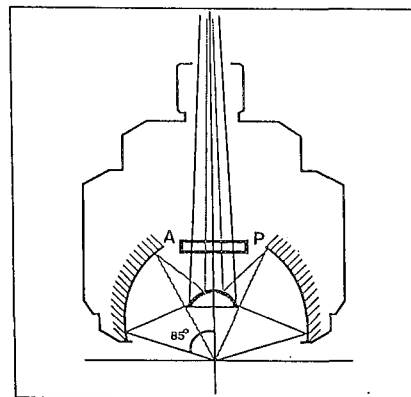
FIG. 1.--Grazing-incidence objective lens. AP is position for inserting annuli that define angular ranges for viewing and spectral analysis.

(ESCA), Auger, and SIMS are primary surface analysis techniques, grazing incidence FT-IR microscopy provides unique details about the molecular bonding. Organic materials on metal surfaces and spots as small as 20 × 20 μm can be studied.

Polycarbonate Residue on Aluminum

A polycarbonate (PC) residue on an aluminum surface was studied by grazing-angle FT-IR microscopy to determine whether debonding occurred at the metal-to-polymer interface or within the polymer matrix and to establish the chemical identity of the organic film. An earlier XPS analysis indicated that 1-2 nm of an organic material was present on the aluminum. The microscope was needed because the debonded areas were too small for macro measurements.

The GAM infrared spectrum of the aluminum surface provided detailed information about the presence of PC and its bonding to the aluminum. The spectrum reported in Fig. 3 was from a 100μm-diameter area. It showed that some PC remained on the aluminum surface after the debonding, but the strongest absorption band (1733 cm^{-1}) observed in this GAM spectrum was not present in the PC reference spectrum. The 1733cm^{-1} band is of particular interest. The formation of a bond between the PC and the aluminum surface could weaken the carbonyl bond and shift the 1775 band down to 1733 cm^{-1}.

In grazing-angle spectra, only bonds with components of their dipole moments perpendicular to the reflecting surface absorb radiant energy. The fact that the 1733cm^{-1} band is 6.8 times greater than the 1775cm^{-1} PC band strongly suggests that this carbonyl is perpendicular to the aluminum's surface.
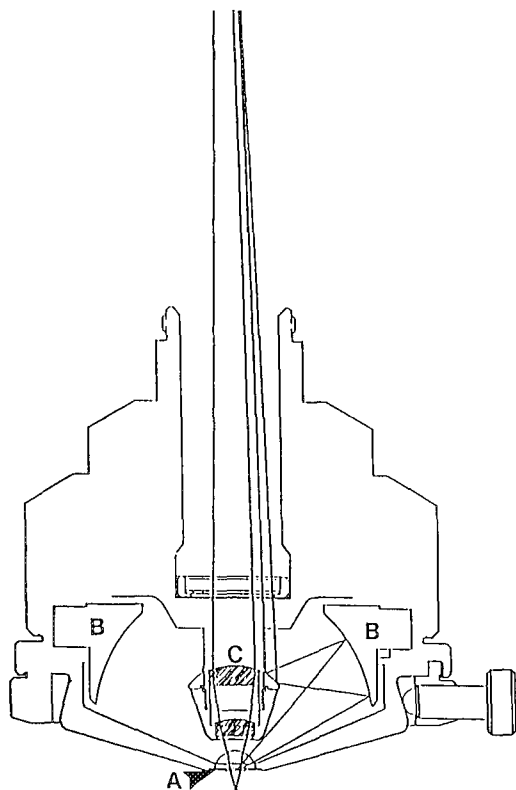
FIG. 2.--ATR objective lens ATR crystal A, mirror lens elements B, and refractive-lens elements C.

In this example, GAM spectra provided more details about the chemistry and structure of the aluminum surface than XPS, and it did so at higher spatial resolution and without requiring an ultrahigh vacuum.

Solder Flux Residue

Gold contact wires and solder pads are common in integrated circuits; flux residue can be a deleterious surface contaminant. GAM can be used to detect these thin-film contaminants. In this example, the increased detectability of GAM over standard microreflection analysis (RAS) is demonstrated.

A gold-plated surface was exposed to rosin solder flux and then washed with methanol prior to analysis. The gold surface appeared clean. Spectra of the same areas were recorded with the standard 15×, NA = 0.58 objective (near normal 15-35°) and with the grazing angle objective. A thick film of the rosin was also formed on a gold mirror as a standard. For comparison, spectra were recorded for the same 100μm-diameter area at both near normal and grazing incidence (Fig. 4).

The GAM infrared spectrum for the C-H band of the rosin flux residue has an absorbance ten times the reflection spectrum recorded at near normal incidence. The maximum band in the C-H region is at 2925 cm^{-1} and there are associated peaks at 2955 and 2875 cm^{-1}. Because of its greater sensitivity, there is a real advantage to using grazing incidence for the infrared

trace analysis of this clearn surface.

ATR is a near-surface-analysis technique, since the infrared photons only penetrate a fraction of a wavelength into the sample. Carbon-black-filled rubber was one of the first and remains a principal sample for ATR analysis. Glass-filled polymers are unyielding to other sampling modes. ATR's unique abilities to analyze surface degradation is also of great importance. For analytical microscopy, ATR provides a consistent penetration depth for quantitative analysis.

ATR Microscopy Examples

Examples of ATR microscopy are the best proof of its value. ATR microscopy is an exciting development that both extends and simplifies FT-IR microanalysis. The following examples illustrate its utility.

The spectra of PVC plastic tubing (Fig. 5) are for comparison of ATR-microscopy with the standard transmission measurement. The agreement of the absorbance band positions is excellent and the differences in band intensities are typical of ATR measurements. Although no sample preparation was needed for ATR, for the transmission measurement a sample was cut from the same piece of tubing with a microtome. A 100μm-diameter spot was analyzed by ATR, co-adding 250 scans (2 min) at 4cm^{-1} resolution.

The ability of ATR microscopy for quantitative analysis was demonstrated by analysis of liquid mixtures of corn and mineral oils. The intensity of the corn oil carbonyl band (1747cm^{-1}) was found to be directly related to the weight percent of corn oil in these mixtures. A direct quantitative relationship was established.

Conclusion

Grazing-angle and ATR FT-IR microscopy have become routine technologies. With these new objectives, small areas of a surface can be analyzed by GAM to detect monomolecular surface films and small areas of nonreflective materials can be analyzed by ATR. The biologist, chemical microscopist, and materials scientist now have these tools available to aid in their efforts to understand the molecular structure of the microscopic world. The microscope has become a primary accessory for FT-IR analysis; GAM and ATR advances the microscope a step closer to its being a univesal analytical tool.

References

1. U.S. Patent 4,810,077.
2. W. G. Golden, "Fourier transform infrared reflection-absorption spectroscopy," in *Fourier Transform Infrared Spectroscopy*, New York: Academic Press, 1985, vol. 4.
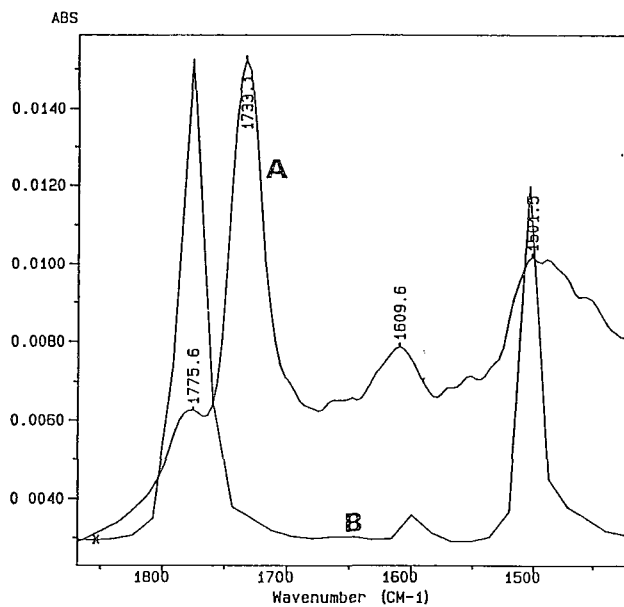
FIG. 3.--GAM infrared spectrum of (A) aluminum
surface from 100μm-diameter area, obtained by
co-addition of 1000 scans (4.5 min) at 8cm^{-1}
resolution; (B) scaled spectrum of polycarbon-
ate reference.
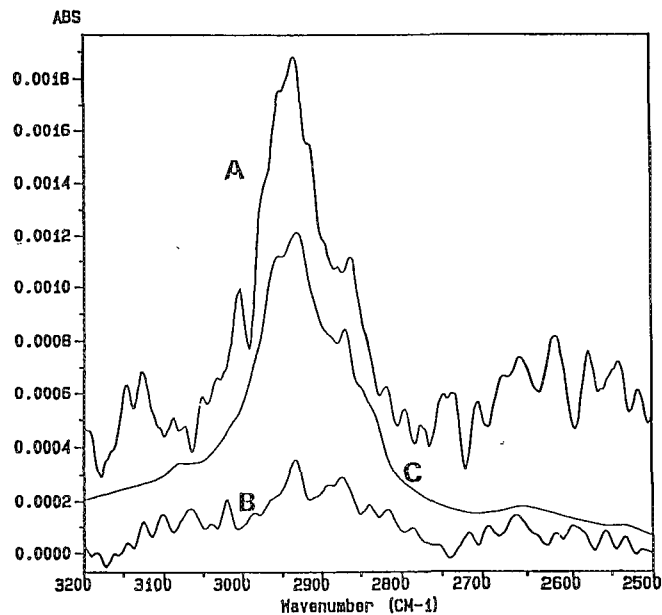
FIG. 4.--Infrared spectra of rosin residue:
(A) surface spectrum at grazing incidence,
(B) spectrum of same area at near-normal inci-
dence, (C) scaled spectrum of rosin.
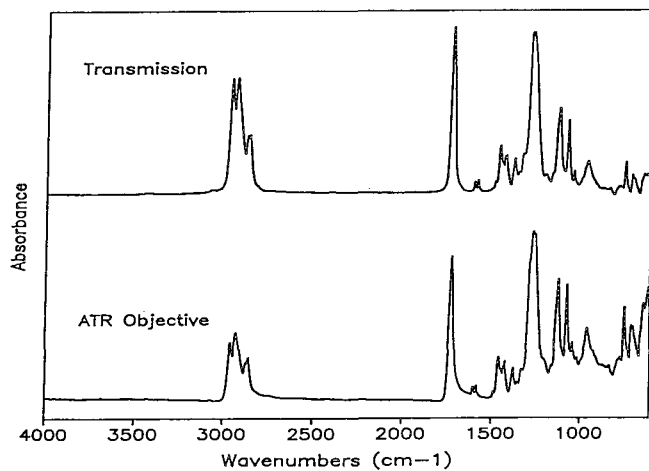
FIG. 5.--ATR and transmission spectra of PVC
plastic tubing obtained with microscope.

PHOTON SCANNING TUNNELING MICROSCOPY AND RAMAN MICROPROBE
SPECTROSCOPY: RECENT STUDIES OF OPTICAL WAVEGUIDES

H. E. Jackson

Recent results from our laboratory on the experimental characterization of optical waveguides are reviewed. Examples using two optical microprobe techniques, Raman microprobe spectroscopy, and photon scanning tunneling spectroscopy (PSTM) are discussed. Raman microprobe spectroscopy is used to explore the role of stress induced by a thin dielectric overlayer used to form channel waveguides in GaAlAs, and to explore photorefractive non-linearities in Ti:LiNbO$_3$ channel waveguides.[1-3] The PSTM, a new technique is used to investigate local surface and index variations by probing the evanescent field outside a planar and a channel waveguide.[3,4]

Raman spectroscopy is a sensitive technique for probing local structural and crystalline conditions, including compositional disorder, carrier concentration, crystalline damage, and strain in semiconductors. Raman microprobe spectroscopy allows one to probe these quantities on a spatial scale of 1 μm, an appropriate scale for the investigation of optical waveguide structures. As a first example, we discuss the use of this technique to measure the spatial distribution of strain associated with a particular waveguide structure and to understand the effects of the measured strain on waveguide behavior. Light of wavelength 839 nm was end-fire coupled into a single-mode channel waveguide structure formed on a GaAlAs heterostructure with a 3.5μm-wide stripe of Si$_3$N$_4$ patterned on top. The lateral waveguide mode field intensity distribution from the waveguide was measured and unexpectedly found to be a double-lobed pattern centered on the channel for both the transverse magnetic (TM) and transverse electric (TE) modes.

We sought to understand this behavior by utilizing Raman microprobe spectroscopy to obtain Raman spectra as a function of distance near and within the channel waveguide. A series of Raman spectra, taken at low power and concentrated on a narrow spectrum range around the GaAs-like longitudinal optic (LO) phonon, were obtained as function of position across the channel waveguide. A plot of the LO peak vs position is displayed in Fig. 1. This shift and its variation with position is attributed to a compressive stress induced in the GaAlAs material induced by the Si$_3$N$_4$ stripes under tension. Using a model for this stress distribution, we have shown that the photoelastic refractive index changes results in the double-lobe field-intensity distribution in these

samples. Raman spectra from the same sample after rapid thermal annealing revealed that the stress distribution was nearly eliminated and that the optical field distribution became a single symmetric peak.

As a second example, we briefly discuss the use of the Raman microprobe to investigate the photorefractive nonlinear optical process of polarization rotation within Ti:LiNbO$_3$ optical channel waveguides. We have used Raman scattering, where selection rules depend on the direction and polarization of the incident laser beam, as a probe of the polarization state of the wave propagating in the optical-channel waveguide. The technique is unique in providing a 1 μm spatial resolution both laterally and in the direction of guided wave propagation, and in utilizing the light scattered inelastically in a direction perpendicular to the waveguide surface. Figure 2 displays Raman spectra tkaen in this configuration and provides a comparison of the spectra obtained at incident laser powers of 64, 160, and 640 W/cm^2. The polarization rotation, as observed by changes in the Raman spectra, becomes more complete with increasing power. We have used these measurements and a theoretical model to calculate a value of β_{15}, an asymmetric component of the photovoltaic tensor.

The understanding of the local electromagnetic field associated with waveguide structures
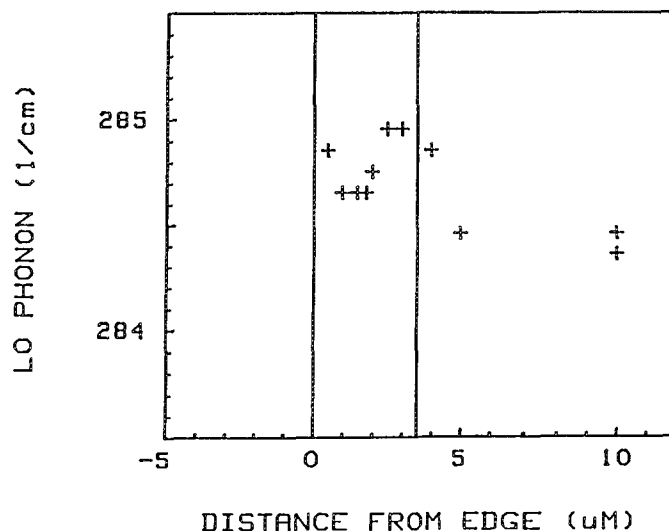
FIG. 1.--GaAs-like longitudinal optic phonon frequency, obtained by Raman microprobe, vs position across Si$_3$N$_4$ stripe defining channel in GaAlAs channel waveguide (from Ref. 3).

H. J. Jackson is at the Department of Physics, University of Cincinnati, Cincinnati, OH 45221.
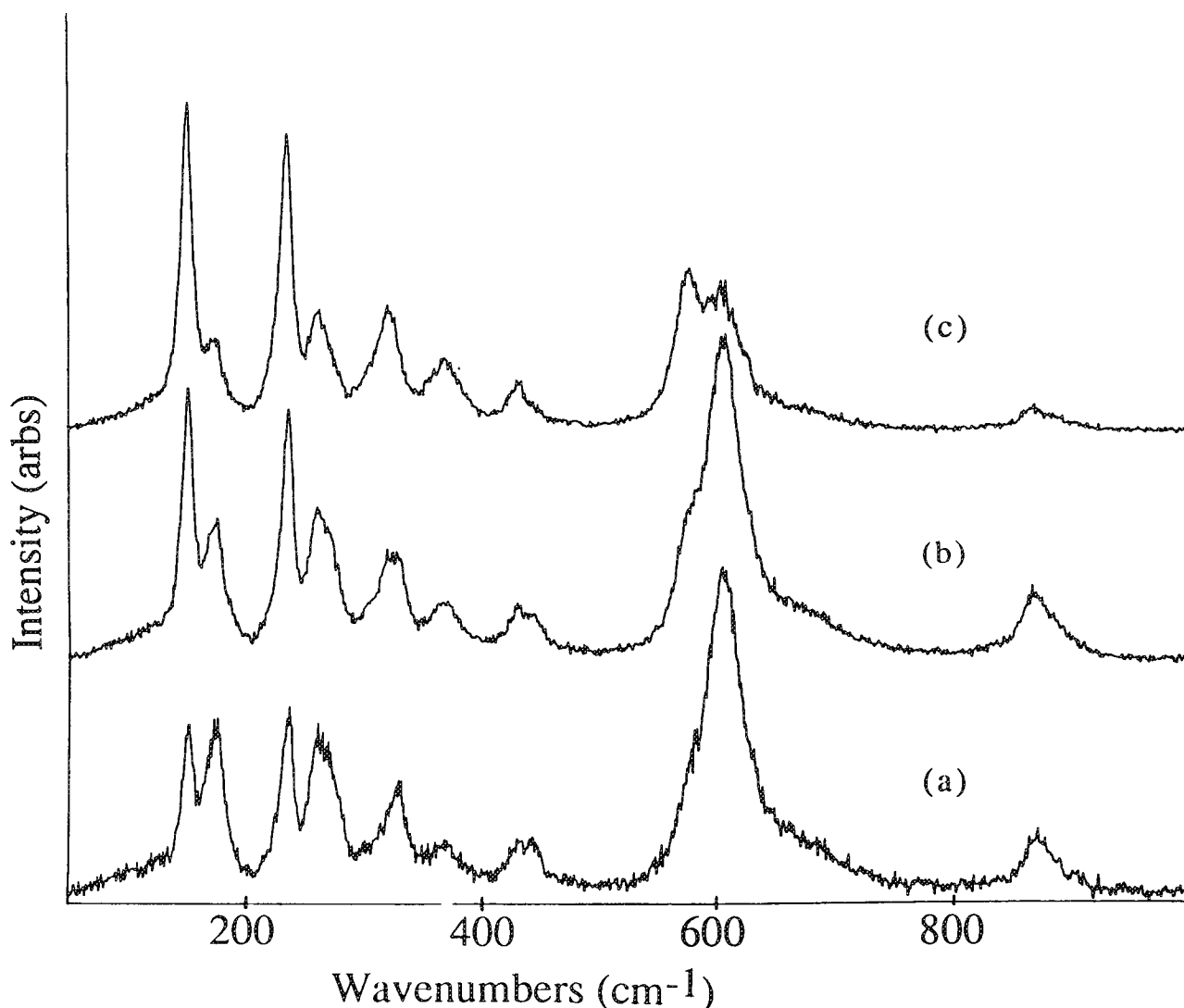
FIG. 2.--Raman spectra, offset for ease of viewing, obtained from channel waveguide Ti:LiNbO$_3$ sample with incident polarization along X direction and collection along Z. Power densities for spectra were (a) 63 W/cm^2, (b) 160 W/cm^2, (c) 640 W/cm^2 (from Ref. 2).

is of central interest to integrated optics. As a last example, we briefly discuss a recent technique, photon scanning tunneling microscopy, which allows one to probe the evanescent field outside the confined propagating optical field within the waveguide. The evanescent field above the surface of the waveguide depends exponentially on the height above the surface and on the local value of the index of refraction. Thus, if we can probe the evanescent field, we can measure with both high spatial resolution and sensitivity the local topographic features and index variations.

The measured evanescent field intensity vs the distance between the probe t$_1$p (an etched optical fiber) and the sample for a silicon oxynitride planar waveguide is displayed in Fig. 3. The predicted exponential dependence of intensity on distance between tip and sample is clearly seen; the slope of the fitted line gives a decay length of 55 nm for a transverse electric mode, in good agreement with theoretical modeling calculations. By using the scanning capabilities of the piezoelectric
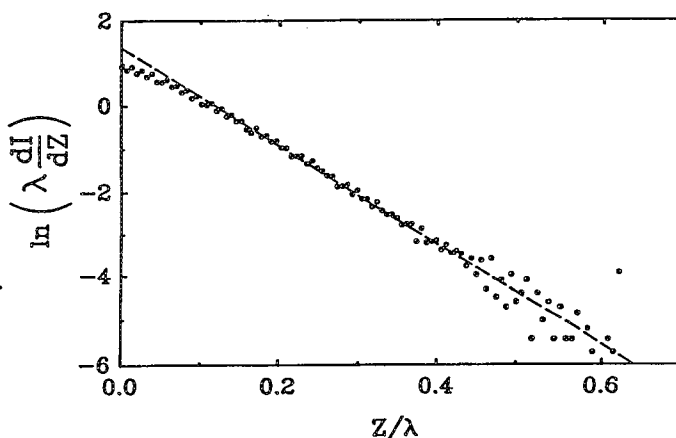
FIG. 3.--Dependence of light coupled from planar waveguide to nearby fiber tip separated by a distance z. Ordinate is log of derivative of measured intensity; exciting wavelength λ = 632.8 nm (from Ref. 4).

positioners to move the tip over a region of the waveguide surface, we can obtain a two-dimensional intensity image that may contain information on local surface roughness and local index of refraction inhomogeneities. Clear variations are observed on a local scale.

In summary, we have briefly reviewed several aspects of our recent optical microprobe characterization of optical waveguides, including examples of the use of the Raman microprobe to study local stress and nonlinear refractive effects, as well as the use of a new technique, PSTM, to probe local variations of topography and index of refraction by measuring the evanescent field associated with optical waveguides.

References

1. C. J. Radens, B. Roughani, H. E. Jackson, J. T. Boyd, and R. D. Burnham, "Raman microprobe analysis of strain induced by patterned dielectric films on GaAlAs structures," *IEEE J. Quantum Electronics* 25: 989, 1989.
2. U. B. Ramabadran, H. E. Jackson, and J. T. Boyd, "Raman microprobe characterization of photorefractive nonlinearities in Ti:LiNbO$_3$ channel waveguides," *Appl. Phys. Lett.* 58: 672, 1991.
3. H. E. Jackson and J. T. Boyd, "Raman and photon scanning tunneling microscopy of optical waveguides," *J. Opt. and Quant. Electronics* (in press).
4. D. P. Tsai, H. E. Jackson, R. C. Reddick, S. H. Sharp, and R. J. Warmack, "Photon scanning tunneling microscope study of optical waveguides," *Appl. Phys. Lett.* 56: 1515, 1990.

MICROPROBE RAMAN STUDIES OF SEMICONDUCTOR MICROSTRUCTURES

W. C. Tang and H. J. Rosen

With the advancement in epitaxial growth and processing techniques, device miniaturization has been progressing rapidly. The aim of miniaturization is not only to push forward the art of very large scale integration but also to explore new device and material characteristics due to the reduced dimensions. To characterize these small scale structures, often with an active region on a submicron scale, one requires a characterization tool with equally small spatial resolution. In this paper, we present results to demonstrate that microprobe Raman is a very useful tool to probe the localized temperature of devices as well as the variation of strain and material defects on a submicron scale. In addition, the technique is contactless and nondestructive.

Experimental

In this paper, the characterization of microstructures based on microprobe Raman is demonstrated to be extremely useful. The first part deals with measurement of temperature in a microscopic scale in an AlGaAs single-quantum-well (SQW) laser diodes. High localized temperature rise has detrimental effects on device performance. In the operation of semiconductor laser diodes, the temperature rise at the laser's emission facet is believed to play a major role in the laser's degradation.[1-9] In fact, under high-output-power operation, the laser can suffer a sudden catastrophic degradation in power. Physical damages can sometime be observed at the facet region after the catastrophic breakdown; this sudden death of the laser is often referred to as catastrophic optical damage (COD).[1] The COD is often attributed to a sharp rise in the facet temperature leading to localized melting. Hence understanding the facet temperature-rise behavior is critical to the control of the laser's reliability. Microprobe Raman permits the measurement of the facet temperature with a submicron-scale spatial resolution, as well as good temperature sensitivity. The samples studied in this part were AlGaAs SQW cleaved uncoated ridge waveguided laser diodes grown by molecular beam epitaxy (MBE) on $n^+(100)$ GaAs substrates. The active region of a SQW consists of 70Å $Al_{0.04}Ga_{0.96}As$ layer sandwiched between 2000Å graded AlGaAs regions with a parabolic Al concentration profile graded from 22 to 36%.

The second part deals with the microscopic

variation of strain and defect density across semiconductor microstructures. The detection of these microvariations is important to uniformity considerations, especially with the reduction of device dimensions. Another consideration arises from the recent interest in growing epitaxial films on top of prepatterned substrates.[10-14] Patterned growth has been generating a lot of interests, since it provides intrinsic waveguiding, current blocking, and lateral carrier confinement capabilities in laser and electronic devices.[10,11] Patterned growth also plays an important role in the growth of lattice-mismatched systems, since the growth of lattice-mismatched materials using patterned growth has been demonstrated to be promising in the reduction of defect density.[12-14] Samples studied in this part were MBE-grown $In_{0.25}Ga_{0.75}As$ (1000Å-thick) films on top of GaAs(100) substrates that contained both patterned and nonpatterned regions. The pattern consists of 1μm-wide parallel ridges along the [100] direction.

The Raman data were taken in air at room temperature in a backscattering geometry. An Ar ion laser (5145 Å) was used as the excitation source. The probe laser beam can be focused down to 0.75 μm (full width at half maximum) by a microscope objective lens. The unpolarized Raman signal was collected and analyzed via a microprobe Raman system. The facet temperatures were derived from the intensity ratio of the Stokes and anti-Stokes peaks of the GaAs-like longitudinal (LO) mode or the transverse optical (TO) mode, depending on the sample's orientation.[8] To minimize probe laser-beam-induced heating, a low probe beam power of 1 mW was used.

Results

SQW Laser Facet Temperature. The time-evolution behavior of AlGaAs SQW laser facet temperature and output power until COD under a constant operating current were measured. Figure 1 shows the behavior of three samples driven by different bias currents. Both output-power-degradation and facet-temperature-rise (with respect to room temperature) behavior can be separated into two regimes. The first is a slow gradual temperature rise right after the laser is turned on, accompanied by a gradual degradation of output power. The second regime shows a rapid nonlinear rise in the facet temperature and a concomitant degradation of laser power leading to COD. The most striking feature is that COD takes place at a facet temperature of approximately 140 C above room temperature for all samples studied, independent of the bias current. Therefore, it ap-

1

(a) I = 115 mA

(b) I = 106 mA

(c) I = 95 mA

Time (minute)

2 I = 0mA

Ar Probe Beam Power (mW)

3 I = 95 mA

Ar Probe Beam Power (mW)
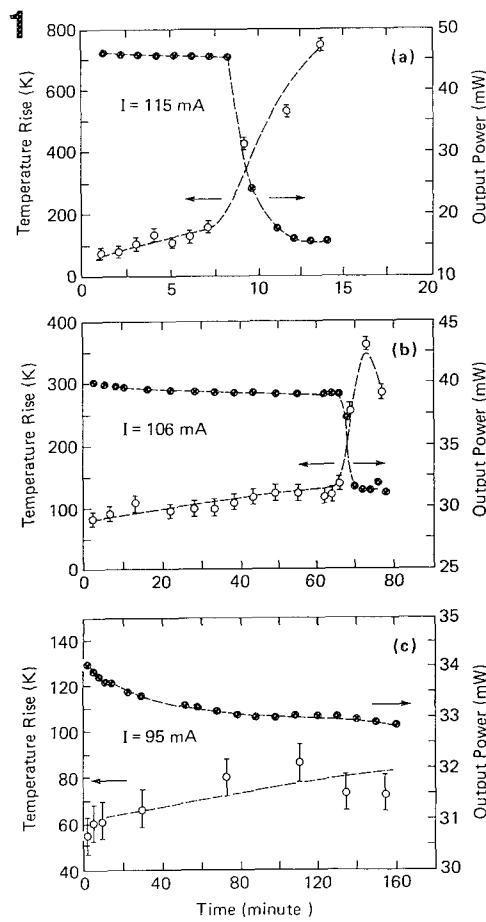
FIG. 1.--Facet temperature (open circles) and output power (closed circles) as function of time leading to COD under constant drive current. Initial power, (a) 46 mW (I = 115 mA), (b) 40 mW (I = 95 mA), (c) 34 mW (I - 95 mA).

FIG. 2.--Facet temperature as a function of Ar^+ probe beam power without laser being biased (I = 0 mA).

FIG. 3.--Facet temperature (open circles) and output power (solid circles) as a function of the Ar probe beam power with sample biased under 95mA drive current.
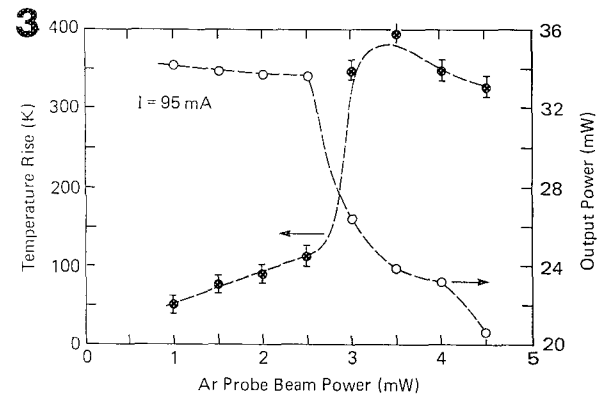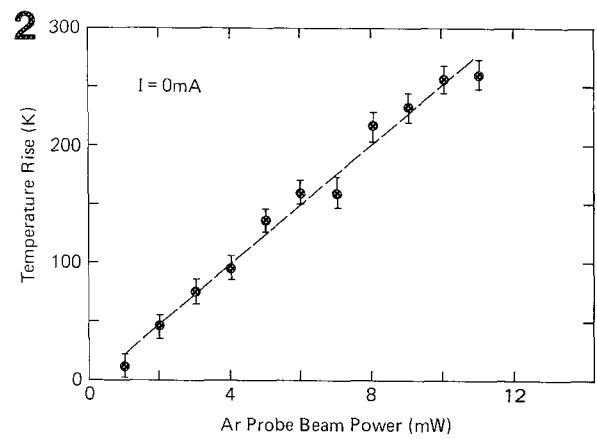
pears that a critical facet temperature exists. Once this critical temperature is reached, COD follows. Another feature illustrated in Fig. 1 is that the linear facet-temperature-rise rate before COD is a strong function of the bias condition. Hence, under high-bias-current operation, the linear temperature rise rate is correspondingly high and the time to reach the critical temperature is shorter, which leads to a short COD time. The measurement of the facet temperature thus identifies the important features that dictate the laser's COD lifetime: first, the existence of a critical temperature where COD occurs; second, the time needed to reach this critical temperature, which is decided by the initial facet temperature and the subsequent temperature rise rate during operation.

The underlying mechanisms responsible for the observed linear temperature rise and the rapid rise during COD were investigated via microprobe Raman. Adjacent lasers were biased under the same operating conditions, except the ambient. Various lasers were operated under various environments such as air, nitrogen, and helium. It was found that lasers operating in

air have a much higher facet-temperature-rise rate and power-degradation rate than lasers operating in nitrogen or helium at the same bias conditions. Indeed, lasers operating in air have a much shorter COD lifetime. These results indicate that the reaction of the facet with water vapor, oxidizing agents, and contaminants is a critical contributing factor to the initial degradation found in the lasers.

Now let us turn our attention to the nonlinear rapid temperature rise regime. To investigate whether the rapid temperature rise at the critical temperature point is merely a temperature issue, we studied the facet temperature behavior due to an external heat source. We used the Ar^+ probe beam as the external heat source and monitored the laser facet temperature as a function of the probe beam power without biasing the laser diode. As shown in Fig. 2, the facet temperature depends linearly on the Ar^+ probe beam power. Even when the temperature at a facet is much higher than the critical temperature, no nonlinear temperature rapid rise can be observed, which means that the nonlinear rise behavior is tied to the operation of the laser diode. We next repeated

102

4

(a) Ridge Edge Ridge

Valley

|←~/μm→|← ~3 μm →|

Anti Stokes Stokes

(b) Ridge

LO(GaAs)

TO(GaAs)

x2

(c) Edge

x2

Raman Intensity (arbitrary units)

(d) Valley

x2

-400 -320 -240 -160   160 240 320 400
Raman Shift (cm^{-1})

5

(a)

Temperature Rise (K)
260
240
220
200
180
160
-1.0 -0.5 0 0.5 1.0

Intensity Ratio:TO/LO
0.8
0.6
0.4
0.2
0.0

(b)

LO Peak Position (cm^{-1})
290
288
286
284
-1.0 -0.5 0 0.5 1.0

LO Peak Linewidth (cm^{-1})
22
20
18
16
14

Distance from Center of Ridge (μm)

FIG. 4.--(a) Schematic diagram of a patterned region. (b)-(d) Raman spectra of $In_{0.25}Ga_{0.75}As$ on various regions of patterned GaAs(100) substrate: (b) from center of a ridge, (c) edge of a ridge, (d) valley between two ridges.
FIG. 5.--Variation of Raman features across 2μm line scan over ridge and valley regions. (a) GaAs-like TO to LO intensity ratio (triangles) and probe laser beam induced temperature rise (circles). (b) GaAs-like LO peak linewidth (triangles) and frequency (circles).

the same probe-beam-heating experiment with the diode biased at a current 95 mA. As clearly shown in Fig. 3, a nonlinear rapid rise of the facet temperature at the critical temperature can be observed at a probe beam power of 3 mW. At a bias current of 95 mA, the laser diode should have a COD lifetime of at least 4 h. The laser in Fig. 3 suffered a COD after only ∿20 min of operation, which implies that we can shorten the time to COD with an external heat source as long as the diode is lasing. These results suggest that the critical facet temperature involves some solid-state phenomenon that ties to the emission photons of the diode. One possible mechanism is the occurrence of thermal runaway.[1-3] The gradual temperature rise found during the initial operation period causes a shrinkage of bandgap near the facet. This shrinkage leads to an increase of absorption of the emission photons near the facet. Thus, at some critical temperature, the bandgap shrinkage and the increase in absorption and temperature rise in the facet region form a rapid positive feedback cycle, which results in thermal runaway until the facet is damaged and COD occurs.

Micro-variation of Strain and Defect Density. Variation of strain and defect density on Microstructures, such as a $In_{0.25}Ga_{0.75}As$ film grown on patterned ridges on (100)GaAs substrates (Fig.a), can be probed by microprobe Raman. As illustrated in Figs. 4(b) to (d), substantial variations in the Raman spectra are observed even though the three spectra correspond to re-

gions less than 2 m apart. Two phonon modes are observed in all three spectra. The peak at 284.8 cm^{-1} found in the valley region (Fig. 4d) is near the reported frequency for GaAs-like LO mode from thick *unstrained* $In_{0.25}Ga_{0.75}As$ films on GaAs.[15,16] However, on top of a ridge, the frequency of this mode is shifted upward to 289 cm^{-1}, indicating a presence of strain.[17,18] A second phonon mode at ∿258 cm^{-1} in the valley region is attributed to the GaAs-like TO mode from unstrained $In_{0.25}Ga_{0.75}As$ on GaAs. This mode is also shifted upward to 268.7 cm^{-1} on top of a ridge. The TO mode is normally forbidden in the backscattering geometry from a (100) zinc-blende type of crystal.[19] The detection of this mode at the top of the ridge and valley is indicative of the presence of structural disorder and defects. It is interesting that the GaAs-like mode is most prominent in the edge regions of ridges (Fig. 4d). However, the strong TO mode in the edge region is attributed to the presence of non-(100) low index planes often seen in patterned growth.[13,14] Another difference in the Raman spectrum between the several regions is the presence of a phonon mode at 237 cm^{-1} in the valley region that is not resolvable in the ridge region. This mode can be ascribed to the disorder activated optical mode reported previously in $In_xGa_{1-x}As$ films.[15]
The sensitivity of the microprobe probe

Raman in mapping variation of strain and defect density is illustrated in Fig. 5. The results shown in Fig. 5 were obtained from a linescan across a 2μm distance in steps of 0.2 μm; Raman spectra were taken at each step. The center of a ridge is defined as the origin and the two edges of the ridge are found in ±0.5 μm. The data at a distance greater than 0.5 μm from the ridge center are thus from the valley region. The existence of non-(100) planes is manifested in the substantial increase in the GaAs-like TO to LO intensity ratio near both the edges (Fig. 5a). Also plotted in Fig 5(a) is the variation in the probe-laser-beam-induced temperature rise (with respect to room temperature). A sharp increase in temperature ($\sim$50 C) as we go from the ridge to the valley region is indicative of the higher disorder/defect density presence in the valley region. This result is consistent with the fact that the GaAs-like LO peak linewidth also broadens significantly when we go from the ridge to the valley (Fig. 5b). The variation in strain can be detected from the LO phonon frequency shift. As shown in Fig. 5(b), the GaAs-like LO phonon frequency decreases sharply from 289 cm^{-1} on top of a ridge to 285 cm^{-1} in the valley region. Since the value of 285 cm^{-1} is close to the value from an unstrained $In_{0.25}Ga_{0.75}As$, what is implied is that the film on top of the ridge is still under strain. The contrast in the strain and the defect density in the ridge and valley regions can be attributed to two factors. First, is the starting GaAs substrate morphology. It was found that the starting morphology in the valley region was poorer than the ridge region. The rougher morphology in the valley would then be expected to lead to a poorer epitaxial quality and a higher defect density in the subsequent growth of InGaAs. The higher defect density also provides a channel for the InGaAs film to relieve the lattice mismatch induced strain. The second factor is the result of epitaxial growth on a patterned substrate, which reduces defect density seen on the ridge region.[12,13] As a reduction of strain relieves defects, the strain found in the ridge region rises, as evidenced by the upward shift of the LO phonon frequency from the nonstrained value.

Summary

The usefulness of microprobe Raman has been demonstrated in the mapping of localized temperature as well as variation of strain and defect density on a microscopic scale. With microprobe Raman, the facet temperature rise behavior of AlGaAs SQW laser on route to catastrophic breakdown is identified. The sensitivity of microprobe Raman in mapping strain and defect density is demonstrated by the high-resolution scan across an $In_{0.25}Ga_{0.75}As$ film grown on patterned (100) GaAs.

References

1. C. H. Henry et al., "Catastrophic damage of $Al_xGa_{1-x}As$ double-heterostructure laser material," *J. Appl. Phys.* 50: 3729, 1979.
2. H. Yonezu et al., "Mirror degradation in AlGaAs double-heterostructure lasers," *J. Appl. Phys.* 50: 5150, 1979.
3. O. Ueda, "Degradation of III-V opto-electronic devices," *J. Electrochem. Soc.* 135: 11C, 1988.
4. S. Todoroki, M. Sawai, and K. Aiki, "Temperature distribution along the striped active region in high-power GaAlAs visible lasers," *J. Appl. Phys.* 58: 1124, 1985.
5. A. Moser, E. E. Latta, and D. J. Webb, "Thermodynamics approach to catastrophic optical mirror damage of AlGaAs single-quantum well lasers," *Appl. Phys. Lett.* 55: 1152, 1989.
6. F. R. Gfeller and D. J. Webb, "Degradation and lifetime studies of high-power single-quantum-well AlGaAs ridge lasers," *J. Appl. Phys.* 68: 14, 1990.
7. H. Brugger and P. W. Epperlein, "Mapping of local temperatures on mirrors of GaAs/AlGaAs laser diodes," *Appl. Phys. Lett.* 56: 1049, 1990.
8. W. C. Tang et al., "Probe beam heating of AlGaAs single-quantum-well laser facets in microprobe spectroscopy," *J. Appl. Phys.* 68: 5930, 1990.
9. W. C. Tang et al., "Raman microprobe study of the time development of AlGaAs single quantum well laser facet temperature on route to catastrophic breakdown," *Appl. Phys. Lett.* 58: 557, 1991.
10. E. Kapon, M. C. Tamargo, and D. Hwang, "Molecular beam epitaxy of GaAs/AlGaAs superlattice heterostructures on nonplanar substrates," *Appl. Phys. Lett.* 50: 347, 1987.
11. H. P. Meier et al., "Molecular beam epitaxy of GaAs/AlGaAs quantum wells on channeled substrates," *Appl. Phys. Lett.* 54: 433, 1989.
12. Fitzerald et al., "Nucleation mechanism and the elimination of misfit dislocations at mismatched interfaces by reduction in growth area," *J. Appl. Phys.* 65: 2220, 1989.
13. S. Guha, A. Madhukar, and Li Chen, "Defect reduction in strained $In_xGa_{1-x}As$ via growth on GaAs(100) substrates patterned to submicron dimensions," *Appl. Phys. Lett.* 56: 2304, 1990.
14. W. C. Tang et al., "Raman microprobe study of narrow $In_xGa_{1-x}As$ stripes on patterned GaAs(100) substrates," *Appl. Phys. Lett.* April 1991.
15. G. Landa, R. Carles, and J. B. Renucci, "Local bonding and long-range order: Raman investigation in III-V solid solutions," *Proc. 18th Intl. Conf. Phys. Semiconductors* 2: 1361, 1987.
16. Z. Sobiesierski, D. I. Westwood, and R. H. Williams, "Raman scattering from $In_xGa_{1-x}As$ grown on GaAs(001) by molecular beam epitaxy," *Materials Sci. and Eng.* B5: 265, 1990.
17. F. Cerdeira et al., "Stress-induced shifts of first-order Raman frequencies of diamond- and zinc-blende-type semiconductors," *Phys. Rev.* B5: 580, 1972.
18. G. Burns et al., "Phonon shifts and strains in strain-layered $(Ga_{1-x}In_x)As$," *Appl. Phys. Lett.* 51: 1919, 1987.
19. R. London, "The Raman effect in crystals," *Adv. Phys.* 13: 423, 1964.

104

PROFILING AND MAPPING OF ADVANCED MATERIALS USING SPATIALLY RESOLVED RAMAN MICROSCOPY

J. W. Ager III, D. K. Veirs, H. Q. Lee, and G. M. Rosenblatt

We have developed a technique to profile important physical and chemical properties of materials based on simultaneous acquisition of Raman spectra along a laser illumination line, coupled with extensive and rapid spectral analysis to extract the desired information. The technique uses a two-dimensional spectroscopic detector and, in contrast to Hadamard techniques, sample movement in one dimension that allows all collected light to be detected. Property maps comprised of the analysis results of more than 10 000 Raman spectra can be built up from successive profiles in a few hours. In order to increase efficiency, the data for one profile are analyzed while the data for the next profile are collected. Two recent applications are discussed: measuring spatial variations in crystalline quality in CVD-grown diamond thin films and mapping transformed zones produced by compressive stress in a bulk sample of phase-stabilized zirconia (PSZ).

Experimental

The spatially resolved Raman technique has been described previously.[1,2] As shown schematically in Fig. 1, a cw laser is focused on the sample by a cylindrical lens to form an illuminated line, which is imaged by the collection optics onto the entrance slit of the monochromator. The dispersed light is collected by a two-dimensional detector (1024 × 1024 wavelength × distance pixel format). Each row contains the entire Raman spectrum from the corresponding point along the illuminated line on the sample. The spectra are analyzed individually in real time to obtain the property of interest. The information obtained from the simultaneously acquired spectra produce a one-dimensional profile across the sample of chemical or physical properties that are distinguishable by their Raman spectra features. Sample translations perpendicular to the illumination line, along with repeated collection and analysis cycles, allow two-dimensional maps to be generated. The measured maximum spatial resolution and spectral precision are 5 μm and

and 0.16 cm^{-1}, respectively.

In the diamond measurements, the magnification of the collection optics was 8×, such that each row on the detector corresponded to the Raman spectrum from a 3μm long (25μm pixel size/8) by 15μm wide (120μm spectrometer entrance slit width/8) area of the sample. The laser power at the sample was 150 mW and the collection time was 1.5 h. Diamond peak frequencies and widths were computed for each spectrum (each row) in the data matrix by fitting a Lorentzian lineshape to the spectrum with a linear background term.

The Raman peaks in the spectrum of MgO-PSZ are broad and the changes in the sample occur over a distance scale of mm. Therefore, the maximum spatial and spectral resolution were not needed, and the data were collected in a 256 × 256 reduced image format (row and columns
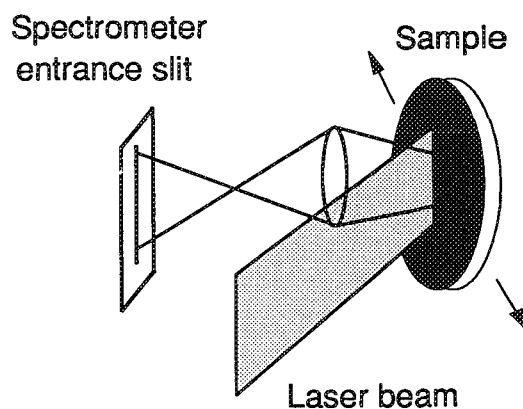
FIG. 1.--Schematic of illumination geometry for spatially resolved Raman spectroscopy.

summed together in groups of four) to reduce the collection and analysis time. The magnification of the collection optics was 1.8×, such that one image row corresponded to a 55 μm (25 μm * 4/1.8) by 90 μm (160μm slit width/1.8) area on the sample. Each spectrum (each row) was analyzed by fitting the observed spectrum to previously measured spectra of pure monoclinic and pure tetragonal zirconia. The spectral region used for the analysis included the 149 and 266 cm^{-1} peaks of tetragonal zirconia phase and the 181 and 190 cm^{-1} peaks of monoclinic phase zirconia. A map was built up using a translation step length of 0.5 mm. The collection time for each profile was 10 min. Fifteen profiles were collected for a total mapping time of 2.5 h; 2535 spectra were analyzed.

Sample Preparation

The diamond samples studied here were grown

by microwave-plasma-assisted chemical vapor deposition (CVD). The plasma used to grow sample 2C3 was smaller than the 10mm-diameter Si substrate. As a result, film growth was inhomogeneous. Scanning electron microscope (SEM) images of 2C3 show isolated higher-quality faceted microcrystals in the center of the film and fused lower-quality rounded microcrystals toward the edge. Sample 5W7 is a 200μm-thick free-standing film. The SEM images of 5W7 show uniform growth.

The zirconia sample is a 25mm-diameter hemisphere of commercial MgO-PSZ that was subjected to a two hemisphere compression test (Fig. 3(b)).[3] One of the hemispheres cracked almost exactly in half, forming the 25mm-diameter quarter sphere studied here.

Results and Discussion

Chemically synthesized diamond films have all of the attractive properties of natural diamonds such as hardness and high thermal conductivity; current and proposed applications include heat sinks, x-ray optics, tool coatings, abrasives, and high-band gap semiconductors. Current research is concentrating on refining the processing to produce higher-quality films and to increase the growth rate. Raman spectroscopy is the single most valuable tool available at present for the evaluation of diamond film quality; observation of the characteristic Raman line at 1332 cm^{-1} is definitive evidence of diamond growth. The focus of this work is to gain atomic-scale information from the frequency and shape of the diamond Raman line, and then to relate this to the important physical and mechanical properties of the film.

The one-dimensional spatial profiles of Raman linewidths and frequencies of samples 2C3 and 5W7 are shown in Fig. 2. For sample 2C3, the analyzed region extended from the center of the sample toward the edge. For sample 5W7, the region extended from the edge 1.6 mm toward the center of the rectangular piece. The Raman characteristics of sample 2C3 show continuous changes as a function of position. The diamond linewidth is narrowest near the center of the sample (where SEM showed better crystalline quality) and increases monotonically toward the edge of the sample (where SEM showed worse crystalline quality). In sample 2C3, shifts in the Raman frequency correlate with increases in the linewidth; the line frequency is 1332.7 cm^{-1} in the center of the sample and increases to 1334.4 cm^{-1} at the edge of the imaged area; and the linewidth increases from 7 to 14 cm^{-1}. Sample 5W7 does not show systematic changes in the Raman spectrum as a function of position. The average frequency and linewidth of the diamond Raman peak are 1332.5 cm^{-1} and 5.1 cm^{-1}.

The correlation of linewidth and frequency with film quality and with each other suggested by these spatially resolved spectra is interesting because linewidth and frequency are affected by different underlying physical factors. For example, the peak frequency is affected by strain (related to stress or temperature), whereas a peak is either homogeneously broadened by a decrease in phonon lifetime, or heterogeneously broadened by simultaneous sampling of sample regions with different Raman frequencies, or both. In these experiments, as discussed in detail elsewhere, shifts in the Raman peak frequency away from 1332.5 cm^{-1}, the peak frequency of single crystal diamond, are attributed to stress in the films. Compressive stress shifts the peak to higher frequency; tensile stress shifts the peak to lower frequency. The stresses probably are introduced during the cooling of the film from the growth temperature (typically 900 C). The Raman linewidth of single crystal diamond is 2 cm^{-1}; the linewidths of the films studies are larger (5-15 cm^{-1}). The broadening arises from a decrease in domain size caused by defects and by a stress distribution among in the many microcrystallites sampled in a Raman measurement. The stress gradient is probably primarily in the direction perpendicular to the film.
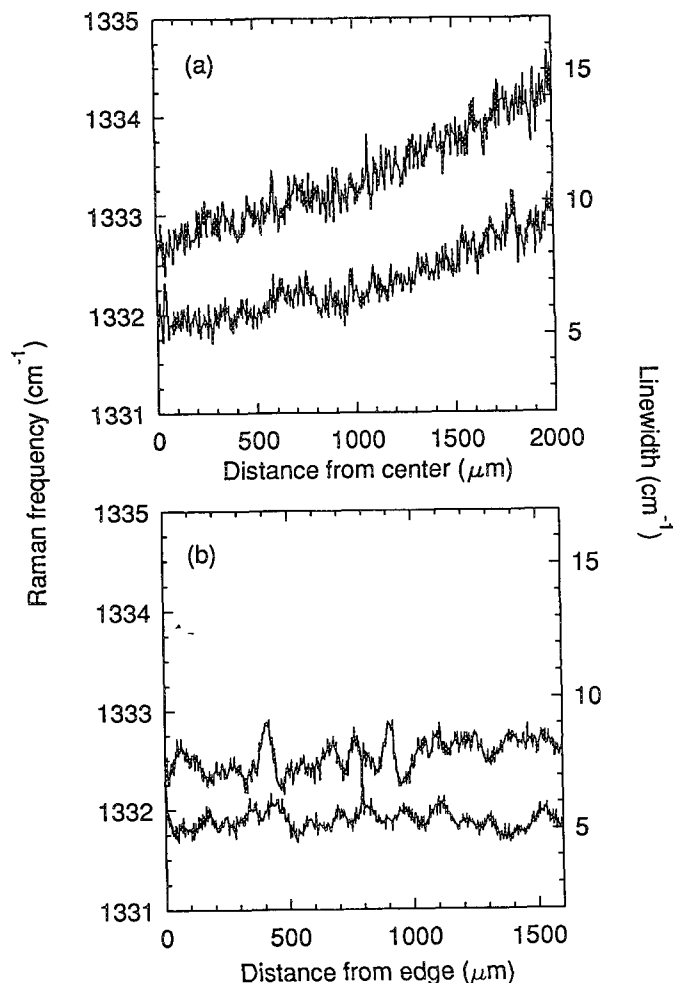
FIG. 2.--Profiles of diamond Raman frequency and linewidth across two CVD diamond films. Each profile was obtained from the analysis of 500 Raman spectra collected simultaneously over 1.5 h. (a) Sample 2C3 (inhomogeneous); (b) Sample 5W7 (more uniform).
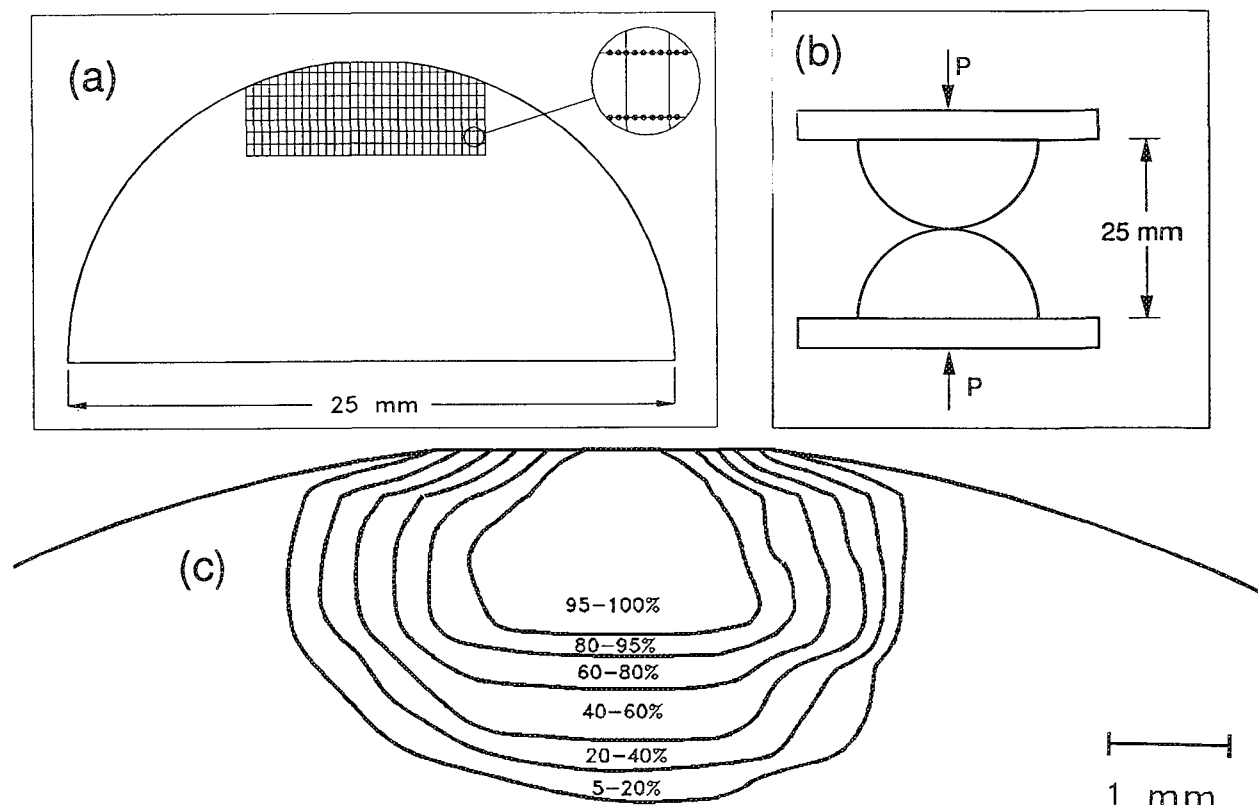
FIG. 3.--Map of fraction of monoclinic phase in the vicinity of the contact point of a MgO-PSZ quarter sphere produced in compression test: (a) full view of the face of the quarter sphere; grid indicates positions of measured profiles. As shown in magnified view, resolution parallel to sphere axis is grid spacing (0.5 mm), resolution perpendicular to sphere axis is one-fifth of grid spacing (55 μm); (b) schematic of double hemisphere compression test; (c) contour map of monoclinic fraction near contact point.

Phase stabilized zirconias are members of a new class of fracture-resistant ceramics based on the discovery that the stress-induced martensitic transformation from the tetragonal to the monoclinic phase occurs in fine ZrO_2 grains subject to stress fields in the vicinity of a propagating crack. The degree of toughening is related to the spatial extent and the amount of transformation of the transformed zone. For a complete understanding of these materials, a quantitative measure of the extent of transformation (spatial and amount) is required. Because the spectra of the tetragonal and monoclinic phases are easily distinguished, spatially resolved Raman spectroscopy can be used to measure the relative fraction of monoclinic phase as a function of position.[2,5]

In other work, we have studied fatigue cracking in a variety of PSZ systems.[2,5] Here, we study a PSZ sample cracked by steady state loading. The two hemisphere compression test discussed above and depicted in Fig. 3(b) is used to simulate powder compaction in studies of powder metallurgy.[3] A map of the fraction of monoclinic phase near the contact point of the PZR quarter sphere is shown in Fig. 3(c). Along the sphere axis there is a 1.5mm region of 100% transformation of tetragonal to monoclinic phase and a 1.7mm region of partial transformation. The transformed zone does not extend beyond 3.2 mm from the contact point. The transformed zone is approximately symmetric around the sphere axis. Work is in progress to compare the mapping results to the predictions of elasto-plasticity and crack propagation models.

Conclusions

Spatially resolved Raman spectroscopy allows one to obtain unique information not available from other characterization methods. This type of information can be of great use in commercial processes as well as in fundamental research. In the production of CVD diamond films for commercial applications, high-quality films with spatial uniformity may be of paramount importance. Spatially resolved Raman spectroscopy is a practical method to measure quality and uniformity simultaneously in these films. In fundamental research, the large number of spectra one can collect and analyze allow one to observe correlations which are not readily noticed with single-point techniques. Understanding complex behaviour in modern materials requires spatial information. In PSZ, Raman maps of phase composition are at present the only quantitative measure of the size and extent of the phase-transformed zones produced during fracture or under stress that lead to improved mechanical

properties in these materials. Spatially re-
solved imaging of chemical or physical proper-
ties based on spectroscopic data has resulted
in increased understanding of complex modern
materials.

References

1. D. K. Veirs, J. W. Ager III, E. T. Loucks,
and G. M. Rosenblatt, "Mapping materials prop-
erties with Raman spectroscopy utilizing a 2-D
detector," *Appl. Opt.* 29: 4969, 1990.

2. D. K. Veirs, G. M. Rosenblatt, R. H.
Dauskardt, and R. O. Ritchie, "Two-dimensional
spatially resolved mapping of solid materials,"
Microbeam Analysis--1989, 179.

3. C. W. Smith, P. D. Funkenbusch, and
J. C. M. Li, "Elasto-plastic analysis of the
two sphere compaction model applied to MgO-
PSZ," *Ceramic Trans.* 12: 497, 1990.

4. J. W. Ager III, D. K. Veirs, G. M. Rosen-
blatt, "Spatially resolved Raman studies of
diamond films grown by chemical vapor deposi-
tion," *Phys. Rev. B* (in press).

5. R. H. Dauskardt, D. K. Veirs, and R. O.
Ritchie, "Spatially resolved Raman spectroscopy
study of transformed zones in magnesia-partial-
ly-stabilized zirconia," *J. Amer. Cer. Soc.* 72:
1124, 1989.

THE APPLICATION OF POLARIZATION/ORIENTATION MICRO-RAMAN SPECTROSCOPY TO THE ANALYSIS OF SOLIDS

D. D. Tuschel

Methods such as x-ray diffraction, transmission electron microscopy, and Rutherford backscattering channeling have been extensively and successfully used to characterize the crystallinity and orientation of solids. Raman spectroscopy is another means of characterizing the physical structure of solids because Raman scattering depends on the polarization and direction of the incident light and the crystal symmetry and orientation of the solid sample. Micro-Raman spectroscopic methods for determining local crystal orientation in silicon have been developed which take advantage of these properties.[1,2]

To understand how this relationship can be applied to the characterization of solids, we consider the most fundamental expressions related to Raman scattering:

$$\vec{P} = \alpha\vec{E} \tag{1}$$

$$\begin{bmatrix} P_x \\ P_y \\ P_z \end{bmatrix} = \begin{bmatrix} \alpha_{xx} & \alpha_{xy} & \alpha_{xz} \\ \alpha_{yx} & \alpha_{yy} & \alpha_{yz} \\ \alpha_{zx} & \alpha_{zy} & \alpha_{zz} \end{bmatrix} \begin{bmatrix} E_x \\ E_y \\ E_z \end{bmatrix} \tag{2}$$

where α is the polarizability tensor, $\vec{E}$ is the incident electric field, and $\vec{P}$ is the dipole moment induced by the interaction of the incident field with the molecule. This relationship is orientation dependent and is part of the expression for Raman scattering intensity

$$S = AI_i \Sigma\int(E_i \cdot \alpha^j \cdot E_s)^2 d\Omega_s \tag{3}$$

where S is the Raman scattering intensity, A is a prefactor incorporating the dependence on incident frequency and the standard cross section, I_i is the intensity of the incident light, and E_s and Ω_s are the orientation and solid angle, respectively, at which scattered light is collected. The significance for our work is that Raman scattering intensity is proportional to $(E_i \cdot \alpha \cdot E_s)^2$, and the form (whether elements are zero or nonzero) of the polarizability tensor for crystals is dictated by the space group symmetry. There are 32 crystal classes and the forms of the tensors have been determined for all of them.[3] For a cubic crystal of class O_h such as Si, the optical phonon is triply degenerate and there are three tensors of the form

$$\alpha^1 = \begin{bmatrix} 0 & 0 & 0 \\ 0 & 0 & a \\ 0 & a & 0 \end{bmatrix}, \ \alpha^2 = \begin{bmatrix} 0 & 0 & a \\ 0 & 0 & 0 \\ a & 0 & 0 \end{bmatrix}, \ \alpha^3 = \begin{bmatrix} 0 & a & 0 \\ a & 0 & 0 \\ 0 & 0 & 0 \end{bmatrix} \tag{4}$$

An experimental arrangement can be envisioned in which the laser beam is incident along the x axis, an Si(100) chip is positioned in the xy plane, and backscattered light is collected with an analyzer parallel to either the x or y axis. A program has been written in ASYST® laboratory software to calculate Raman intensities of crystalline materials as a function of sample orientation for just such an arrangement. Raman scattering intensities have been calculated for the analyzer parallel and perpendicular to the incident polarization as the crystal is rotated in the xy plane. The theoretical polarization/orientation (P/O) plot for Raman scattering intensity from Si(100) is shown in Fig. 1. The parallel and perpendicular plots are sinusoidal functions 45° out of phase. Raman intensities for the same arrangement on Si(110) were calculated, and the method that was used transform the polarizability tensors from one coordinate system to another was that used by Wilson et al.[4] The P/O plot for Si(110) in Fig. 2 is distinct from Si(100). And, extending our calculations to a third orientation, the P/O plot for Si(111) in Fig. 3 demonstrates that this method is capable of distinghishing crystalline silicon orientation. In fact, this capability will be true for all cubic crystals because the shapes of the P/O plots depend only on the form of the tensor, which is dictated by the crystal symmetry and not its elemental or molecular identity, which determines the absolute magnitude of the tensor elements. Calculations and experiments for other crystal classes and compounds have been performed in our laboratory, but we limit our discussion here to cubic crystals.

The above discussion establishes the theoretical basis for the application of P/O micro-Raman spectroscopy to the analysis of solids. The significance of this method is its complimentarity to and superior spatial resolution over micro x-ray diffraction. P/O micro-Raman spectroscopy may be used to identify vibrational modes, distinguish allotropes and allomorphs, distinguish single from polycrystalline materials, and determine orientation of the crystal and degree of disorder, all on a micrometer scale.

D. D. Tuschel is at the Analytical Technology Division, Building 49, KP, Eastman Kodak Co., Rochester NY 14652.

Experimental

Raman spectra were obtained with an Instruments SA S3000 triple spectrograph outfitted
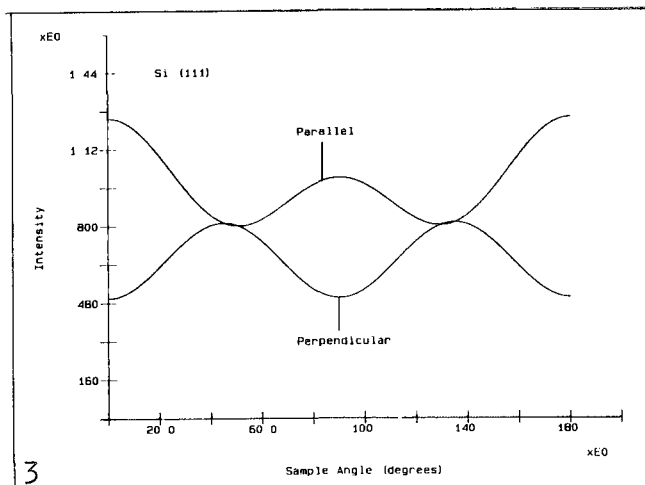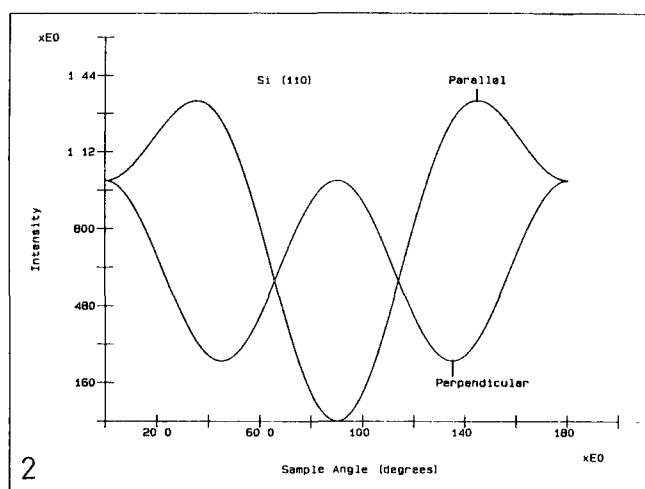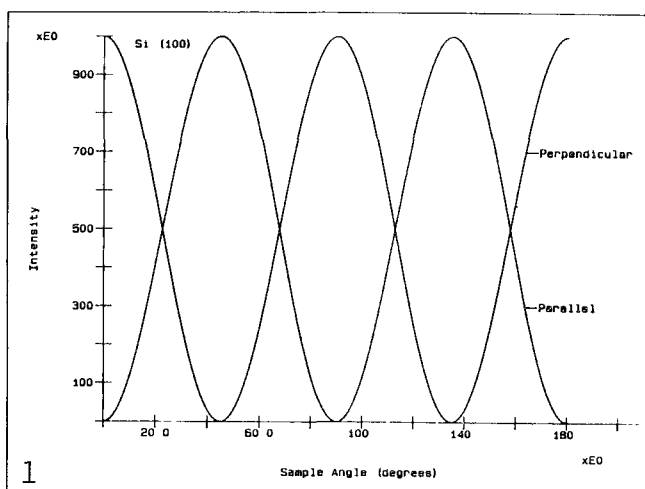
FIG. 1.--Theoretical Polarization/Orientation plot for Si(100).
FIG. 2.--Theoretical Polarization/Orientation plot for Si(110).
FIG. 3.--Theoretical Polarization/Orientation plot for Si(111).

with an Olympus microscope and rotational stage. The 514.5nm excitation from an argon ion laser was focused on the sample with a 100× Olympus 0.95 NA objective, and the same objective was used to collect backscattered light. Laser power at the sample was approximately 10 mW. The entrance and intermediate slits of the subtractive prefilter and the entrance slit of the spectograph were 200 μm, 2.0 mm, and 200 μm, respectively, for Si and diamond analysis; and 200 μm, 2.31 mm, and 200 μm for CCl_4 analysis. Raman scattering was detected with a Princeton Instruments IRY-1024G/R red-enhanced intensified photodiode array operating at a 2s integration time for 10 reads, and the spectral domains were 500 to 550 cm^{-1} and 1300 to 1350 cm^{-1} for silicon and diamond, respectively. Spectra of CCl_4 were obtained at a 5s integration time for 10 reads, and the spectral domain was 150 to 550 cm^{-1}, P/O spectra of Si (100), (110), (111), and diamond (100) were collected at 5° sample orientation increments. Peak areas were determined by use of Prism® software.

The silicon samples were 1 × 1 cm squares cut from wafers cleaved at (100), (110), and (111) orientations. The diamond was a type IIA(100) slice (0.25 × 4.00 × 4.00 mm) purchased from D. Drukker & ZN, N.V. The silicon and diamond samples were affixed to a glass microscope slide, which in turn was mounted on the microscope rotational stage.

Microscope and spectrometer optics are sensitive to polarization, and so each segment of the spectrometric system, from the point of the sample to the detector, was either calibrated for polarization aberrations or compensated with a $\frac{1}{2}$-wave plate. A white-light source, polarization scrambler, polarization analyzer, and power meter were used for the calibration.

Results

To verify that steps taken for polarization calibration and compensation were proper, polarized micro-Raman spectra of CCl_4 were obtained. The Raman spectrum of CCl_4 is well established as a standard. The bands at 219 and 316 cm^{-1} are depolarized and that at 465 cm^{-1} is polarized; the depolarization ratios ρ for them are 0.75, 0.75, and 0.0, respectively.[5] Several milliliters of CCl_4 were placed in a dimple dish microscope slide and sealed with a glass cover slip and tape. Five spectra were collected with the analyzer parallel, and five with the analyzer perpendicular, to the incident electric field. Two of the spectra are shown in Fig. 4. The average depolarization ratios obtained from all ten spectra were $\rho_{219} = 0.756$, $\rho_{316} = 0.739$, and $\rho_{462} = 0.00$. These ratios are in excellent agreement with reported values and establish the experimental arrangements and calibrations as proper for P/O experiments.

A schematic of the experimental arrangement for P/O micro-Raman spectroscopy is shown in Fig. 5. The Si(100) sample was put in position

110
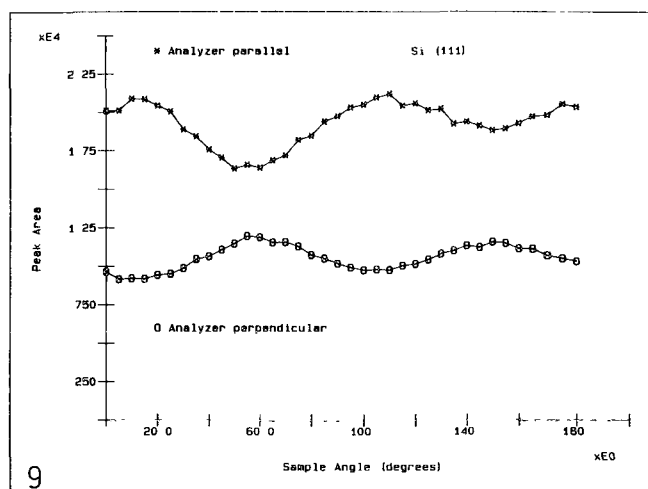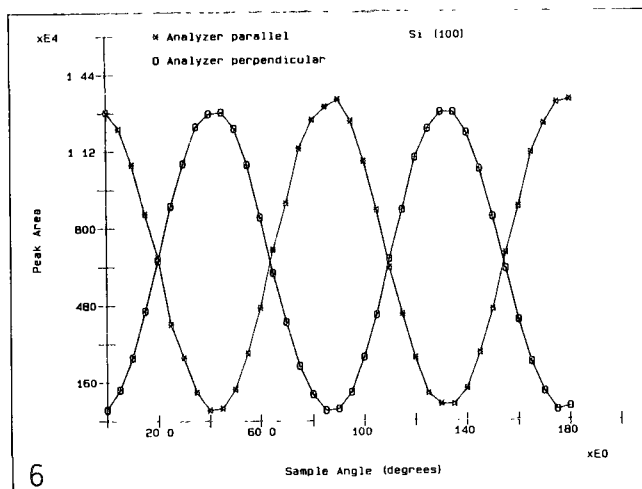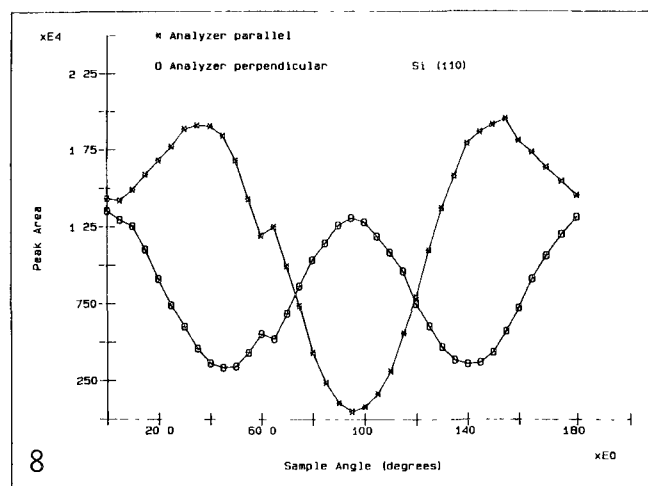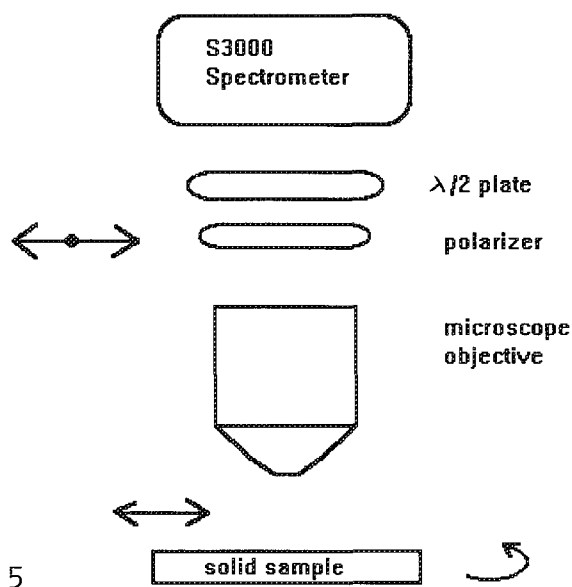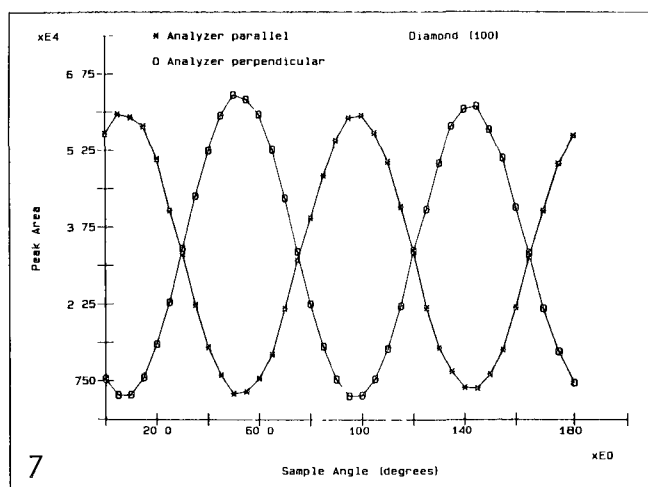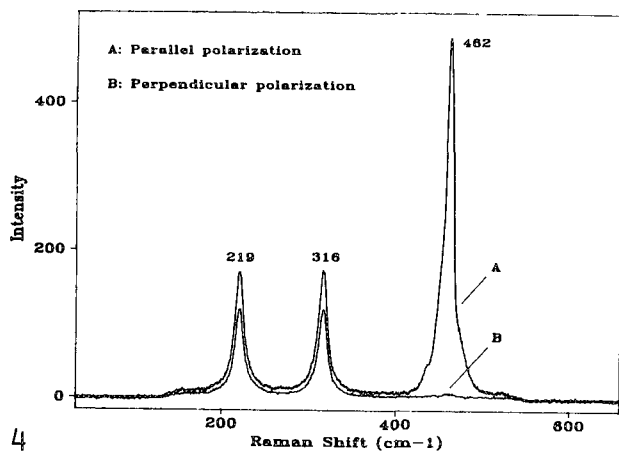
FIG. 4.--Polarized micro-Raman spectra of CCl$_4$.
FIG. 5.--Experimental arrangement for P/O micro-Raman spectroscopy.
FIG. 6.--Experimental P/O Plot of Si(100) 520cm^{-1} band.
FIG. 7.--Experimental P/O plot of diamond (100) 1334cm^{-1} band.
FIG. 8.--Experimental P/O plot of Si(110) 520cm^{-1} band.
FIG. 9.--Experimental P/O plot of Si(111) 520cm^{-1} band.

on the microscope rotational stage such that the cleaved side was approximately parallel to the incident polarization. (We note here that the experimental sample angle is only laboratory bookkeeping and any agreement with a crystallographic axis is coincidence.) The P/O plot of peak areas of the Si(100) 520cm^{-1} band is shown in Fig. 6. The data constitute two sinusoidal functions 45° out of phase and are in excellent agreement with the theoretical plot of Fig. 1. The approximately 45° phase shift between the experimentally obtained and theoretical Si(100) P/O plots is understood as a difference in the crystallographic starting points for data collection, and illustrates an application of P/O micro-Raman spectroscopy for the analysis of fabricated devices. P/O plot phase shifts can be used to quantitate the degree of crystallographic alignment of different features on a micrometer scale.

That the form of P/O plots depend on crystal symmetry is demonstrated by extension of our analysis to diamond. The crystal class of diamond is the same as that of silicon, and so the P/O plot of the 1334 cm^{-1} band of diamond (100) should agree with that of Si(100) (Figs. 1 and 6). The P/O plot of diamond (100) peak areas in Fig. 7 does indeed match. The phase shift of the diamond (100) P/O plot with respect to the theoretical plot of Fig. 1 is attributed to a difference in the crystallographic starting point for data collection.

We examined the utility of this method for differentiating crystal orientation by obtaining P/O spectra from Si(110). Experimentally, the sample was aligned such that the cleaved edge was approximately parallel with the incident polarization, and data were collected in the same fashion as for Si(100). The Si(110) P/O plot in Fig. 8 is indeed distinct from the Si(100) plot and is in excellent agreement with the theoretical Si(110) plot in Fig. 2. The same analysis was carried out on a chip of Si(111); the resultant P/O data plot in Fig. 9 is distinct from those of Si(100) and (110) and in agreement with the theoretical plot in Fig. 3.

Conclusions

The theoretical basis for Polarization/Orientation Raman spectroscopy has been discussed, and the feasibility of P/O Raman spectroscopic analysis on a micrometer scale has been established. The acquisition of depolarization ratios for CCl₄ in agreement with established literature values demonstrates that reliable polarized micro-Raman spectra can be obtained. Such polarized micro-Raman spectra can then be obtained in conjunction with the orientation of a solid sample to produce P/O plots that are directly related to crystal structure and orientation, demonstrated here with Si(100), (110), (111), and diamond (100). P/O micro-Raman spectroscopy may be used to identify vibrational modes, determine crystal structure, distinguish allotropes and allomorphs, distinguish single from polycrystalline materials, and determine

orientation of the crystal and degree of disorder, all on a micrometer scale. P/O micro-Raman spectroscopy promises to be an important analytical tool because of its complementarity to and superior spatial resolution over micro x-ray diffraction.

References

1. J. B. Hopkins and L. A. Farrow, "Raman microprobe determination of local crystal orientation," *J. Appl. Phys.* 59: 1103, 1986.
2. K. Mizoguchi and S. Nakashima, "Determination of crystallographic orientations in silicon films by Raman-microprobe polarization measurements," *J. Appl. Phys.* 65: 2583, 1989.
3. G. Turrell, "Raman sampling," in D. J. Gardiner and P. R. Graves, Eds., *Practical Raman Spectroscopy*, New York: Springer-Verlag, 1989, 24.
4. E. B. Wilson Jr., J. C. Decius, and P. C. Cross, *Molecular Vibrations: The Theory of Infrared and Raman Vibrational Spectra*, New York: Dover, 1955, 285.
5. K. Nakamoto, *Infrared and Raman Spectra of Inorganic and Coordination Compounds*, 3rd ed., New York: Wiley, 1978, 78.

MICRO-RAMAN CHARACTERIZATION OF IMPURITY PHASES IN CERAMIC AND THIN-FILM SAMPLES OF THE Y-Ba-Cu-O HIGH-T$_c$ SUPERCONDUCTOR

E. S. Etz, T. D. Schroeder, and Winnie Wong-Ng

We apply laser-Raman microanalysis to the investigation of high-T$_c$ materials, with emphasis on the Y-Ba-Cu-O system. The goal is to study the composition and microstructure of these materials, determine the extent of any compositional heterogeneity of the superconducting phase, and identify impurity phases. This communication focuses on the analytical characterization, based on the micro-Raman spectrum, of several of the common impurity compositions.

Previous papers reported results on the micro-Raman spectra of orthorhombic and tetragonal $YBa_2Cu_3O_{7-x}$ (YBCO, or Y-1:2:3 phase, for the composition range $0 \leq x \leq 1$) and various secondary phases in the YBCO system for ceramic powders, sintered pellets, and single-crystal material.[1,2] Our earlier studies have been extended to the broader high-Tc system represented by $LnBa_2Cu_3O_{7-x}$ (1:2:3 LnBaCuO, for Ln = lanthanides and yttrium) where we have mainly studied the erbium and europium analogs.[2] For the Ln-Ba-Cu-O system, the laser microprobe spectra were shown to consist of three types: (1) the normal Raman emissions from allowed vibrational modes, (2) structure-specific fluorescence emissions of Ln^{3+} ions in yttrium sites of YBCO, and (3) electronic Raman scattering from an electronic excitation in the Cu(11) atom.[2,3]

In this paper we discuss the Raman microprobe spectra of the impurity phases of composition CuO, $BaCuO_2$, $Y_2Cu_2O_5$, and Y_2BaCuO_5 with reference to the $BaO(BaCO_3)$ - Y_2O_3-CuO ternary system. These and other impurity phases tend to complicate the spectroscopic study of YBCO, and to date much controversy remains regarding the Raman spectra of the orthorhombic and tetragonal structures of $YBa_2Cu_3O_{7-x}$.[4-6] For these impurity compositions, we illustrate the sensitivity of the micro-Raman spectrum to differences, or

E. S. Etz is at the Chemical Science & Technical Laboratory and Winnie Wong-Ng is at the Materials Science & Engineering Laboratory of the National Institute of Standards and Technology (NIST), Gaithersburg, MD 20899; T. D. Schroeder is a summer guest scientist at NIST, from the Department of Chemistry, Shippensburg University of Pennsylvania, Shippensburg, PA 17257. They thank Ron Ono at NIST-Boulder for supplying the YBCO thin films for micro-Raman study, and Steven Robey and T. J. Hsieh of our laboratory for providing the DyBCO thin films. One of us (W.W.-N.) gratefully acknowledges partial support by the Electric Power Research Institute (EPRI) for the phase equilibrium studies of this work.

deviations (such as from presumed oxygen stoichiometry), in composition that are evident on the microscopic scale, and most often are not detected by bulk characterization methods. As a consequence, it is often difficult to relate the observed spectrum to a specific phase, structure, composition, or stoichiometry, or to conclude whether a mixed-phase material may in fact be at hand. These considerations are discussed with examples from the analysis of superconducting thin films of YBCO and DyBCO ($DyBa_2Cu_3O_{7-x}$).

Experimental

Two types of materials are examined: polycrystalline ceramic powders and polycrystalline thin films. The ceramic compositions $BaCuO_2$, $Y_2Cu_2O_5$, and Y_2BaCuO_5 were prepared by conventional solid-state reactions and ceramic processing techniques employing stoichiometric mixtures of Y_2O_3, $BaCO_3$, and CuO.[7] Bulk characterization of these ceramics was carried out by powder x-ray diffraction to determine phase purity. The superconducting samples, including the YBCO and DyBCO thin films, were also characterized with respect to their electrical and magnetic properties.

The YBCO and DyBCO thin films were grown on single-crystal [100] $SrTiO_3$, [100] $LaAlO_3$, and [100] MgO substrates. Two deposition methods were used to produce films of the superconducting stoichiometry. The Y-1:2:3 films were prepared by pulsed laser deposition using a single, stoichiometric YBCO target. The Dy-1:2:3 films were deposited by thermal co-evaporation of the pure elements (Dy, Ba, Cu). By both deposition techniques, the films were deposited to be 0.2-0.4 µm thick. At the upper end of this range, the films are nearly optically opaque and are not fully penetrated by the laser probe in the Raman measurement. The different microstructural and morphological properties of these films, on the various types of substrates, are currently under study. They tend to grow epitaxially and in preferred orientations. Our films have been found to be highly oriented, especially on $SrTiO_3$ and MgO substrates; on these crystals they exhibit a preferential orientation with the crystal c-axis perpendicular to the surface. The degree of epitaxy of thin LnBCO films can be determined by polarization-dependent Raman measurements.[8,9] The structure and composition of these films are being examined by x-ray diffraction (XRD), Rutherford backscattering spectrometry (RBS), and Auger electron spectrometry (AES). Their surface morphology is studied by scanning electron microscopy (SEM).

Limited measurements of several of the DyBCO films by transmission electron microscopy (TEM) have furnished information on microstructure, grain size, and various film defects. Good films exhibiting high critical temperatures (T_c = 86-89 K) have smooth surface morphologies resulting in high, mirror-like reflectivity. Bad areas in several of these film depositions are often recognized by their unusual nonuniform surface morphologies that give these areas the appearance of a dull scattering surface.

For the spectroscopic measurements we employed the multichannel-detection Raman microprobe described previously.[2] The spectra were excited with the 514.5nm line of an argon ion laser and were recorded with 5cm^{-1} spectral resolution. The spectra obtained with the microprobe are unpolarized. The focused laser spot directed at the sample has a diameter of about 2-3 μm. For the highly absorbing dark phases (e.g., CuO, $BaCuO_2$, $YBa_2Cu_3O_{7-x}$), power levels of 2-5 mW were used to acquire the spectrum in integration times of up to 30-45 min. For the less absorbing phases (e.g., $Y_2Cu_2O_5$, Y_2BaCuO_5), up to 20 mW could be safely directed at these particle samples without laser-induced sample modifications (such as localized heating with possible phase transformation). In the measurement of the superconducting YBCO and DyBCO thin films, up to 40 mW (in 2-3μm-diam. beam spot) of laser power could be employed to excite the spectrum. Film surfaces of highest reflectivity can tolerate the highest levels of laser irradiance because much of the incident energy is reflected and therefore not available for the Raman scattering process, not to absorption by the sample. Thus, the intensity of the Raman spectrum is considerably lower, at the same irradiance, than it is for a highly scattering nonreflecting film surface.

Results and Discussion

In the discussion of the Raman spectrum of "pure," presumed single-phase, superconducting $YBa_2Cu_3O_{7-x}$, it is necessary to consider the possible influence of any contaminating phases that are likely to affect the spectrum of YBCO. Many of the impurity phases have a number of Raman lines close to, or coincident with, those of YBCO.[4-6]

Compositional high purity of the superconductor is often difficult to achieve due to the fact that the most common impurities are intrinsic to the crystal chemistry, and therefore the synthesis, of YBCO. Furthermore, these secondary phases, the three most important ones considered here, have scattering properties that magnify their presence even in low concentrations. Becuase they are often less opaque, and thus less absorbing, than the black-phase superconductor, these oxides (especially the green phases $Y_2Cu_2O_5$ and Y_2BaCuO_5) offer a greater penetration depth for the probing laser spot, which leads to relatively more intense Raman scattering. One other factor is the presumed resonance enhance-

ment (at 514.5 nm) of the scattering by the 2:1:1 green phase Y_2BaCuO_5.[5,10]

The impurity phases considered here are all potential by-products of the calculation and sintering processes that lead to the preparation of the superconducting YBCO phase. The chemistry and phase relationships in the $BaO(BaCO_3)$ - Y_2O_3 - CuO system are complex, and a number of stable intermediate reaction products, and various solid solutions, can be formed.[7] The ceramic reactions that can lead to the formation of $BaCuO_2$, $Y_2Cu_2O_5$, and Y_2BaCuO_5, may be described by the following equations:[11]

$$BaCO_3 + CuO \rightarrow BaCuO_2 + CO_2$$

$$Y_2O_3 + BaCuO_2 \rightarrow Y_2BaCuO_5$$

$$Y_2O_3 + 2CuO \rightarrow Y_2Cu_2O_5$$

$$2CuO + Y_2BaCuO_5 + 3BaCuO_2 + 1/2O_2 \rightarrow 2YBa_2Cu_3O_{7-x}$$

$$Y_2Cu_2O_5 + 4BaCuO_2 + 1/2O_2 \rightarrow 2YBa_2Cu_3O_7$$
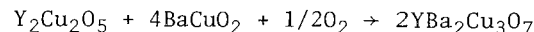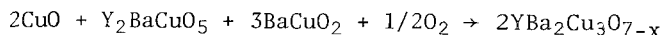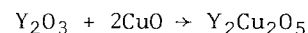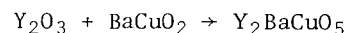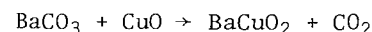
It is the outcome of these reactions that determines the microstructure. homogeneity, density, and composition of the YBCO sample. The Raman spectrum is sensitive to the compositional variability of the samples that are obtained.[4-6,11,12]

We can illustrate the sensitivity of the micro-Raman spectrum to deviations from stoichiometry and composition with the spectrum of $BaCuO_2$ (Fig. 1). This compound, which was prepared in air in the form of a pressed pellet, was expected to be of stoichiometric composition with respect to Ba and Cu, and the powder XRD pattern did not reveal any obvious contaminating phase, such as CuO and $BaCu_2O_2$. However, solid solution due to nonstoichiometry cannot be ruled out, so that this preparation may be represented by $BaCuO_{2+x}$ (where possibly $-0.2 \leq x \leq +0.2$). Other preparations of this phase, employing different annealing conditions, such as in oxygen or argon, are expected to yield a more consistent product. Numerous particles, varying in size from ∿2 to 20 μm, of this black-phase $BaCuO_{2+x}$ were examined in the Raman microprobe. The spectra of three particles, arbitrarily selected for analysis, are shown in Fig. 1. They show a great variability in the number of observed bands, their frequency positions, and their relative intensities. There are no contributions in these spectra from the starting materials ($BaCO_3$, CuO). Contrary to the equally black CuO, which is a very weak scatterer and has very weak bands at 295, 340, and 630 cm^{-1}, $BaCuO_2$ is a relatively strong scatterer (by a factor of about 15 stronger than superconducting YBCO[13]), and its spectrum has been reported.[13,14] For stoichiometric $BaCuO_2$ the principal band is at 640 cm^{-1}, with a weaker characteristic band at 585 cm^{-1}, and other bands at ∿500, ∿430, and ∿340 cm^{-1}. These latter bands are close to the bands observed for the YBCO superconductor. The five bands

FIG. 1.--Raman spectra of three arbitrary particles ($\sim$10 μm in size) of ceramic powder of nominal composition $BaCuO_2$.

oxygen stoichiometry is less than 2. One can apply these arguments to explain the variability in the particle spectra of Fig. 1 without invoking the presence of other particle constituents. This example illustrates the complexity in correlating the Raman spectrum with oxygen stoichiometry. Other preparations of $BaCuO_2$ are under investigation to clarify these issues further.

We have previously discussed the micro-Raman spectra of the green-phase impurity Ln_2BaCuO_5 and have compared the very similar spectra of Y_2BaCuO_5, Er_2BaCuO_5, and Eu_2BaCuO_5.[2] This composition is widely regarded as the most troublesome impurity phase, deriving not only from the reactions involved in the synthesis of YBCO, but often arising also from the atmospheric degradation of $YBa_2Cu_3O_{7-x}$. The compound has a large number of Raman allowed modes, but in practice only about 12 bands are observed.[10] Most of these bands are sufficiently removed from the bands of YBCO to make it possible readily to identify this impurity component. Principal bands appear at 210, 315, 390, 480, and 605 cm^{-1}. The latter band is the most pronounced, and when it is observed in the spectrum of YBCO with a companion band at $\sim$390 cm^{-1}, the presence of this green phase impurity is often invoked. Raman detection of this phase is possibly enhanced, as the spectrum of this compound is believed to be resonantly enhanced by the 514.5nm excitation.[5] However, a recent report concludes that a band at $\sim$600 cm^{-1} is also intrinsic to superconducting YBCO.[6]

The composition $Y_2Cu_2O_5$ as a potential impurity phase in YBCO has been discussed and its Raman spectrum is known.[17] It is a blue-green phase and gives rise to relatively intense (vs YBCO) Raman scattering, and therefore may lead to spurious lines in the spectrum of YBCO if present in low concentrations. As a segregated, microscopically small pure-phase impurity located at grain boundaries. $Y_2Cu_2O_5$ is readily detected and identified in the microprobe measurement. The compound has numerous sharp bands, and usually about 18 Raman active modes are clearly observed.[17] Pronounced and characteristic are sharp bands at 265, 330, 395, and 516 cm^{-1} There are no Raman bands of $Y_2Cu_2O_5$ at frequencies higher than 650 cm^{-1}.

We have studied several preparations of this phase, and the particle spectra of two preparations are shown in Fig. 2. The top spectrum is characteristic of $Y_2Cu_2O_5$ containing an impurity of the yttrium oxide (99.99% Y_2O_3) starting material which was found to have a trace concentration of Er_2O_3. The bulk concentration of Y_2O_3 (with trace Er^{3+}) in this sample of $Y_2Cu_2O_5$ was estimated to be about 5-6 wt% from powder x-ray diffraction analysis. Because of the intense, sharp-line fluorescence of Er^{3+} in the oxide matrix, these fluorescence emissions are easily detected and are comparable in intensity, at this low level of contamination, with the Raman emissions of $Y_2Cu_2O_5$. Thus, the features observed over the range

that can be always unequivocally identified as lattice vibrations of orthorhombic YBCO are the bands at $\sim$115, $\sim$150, $\sim$340, $\sim$435, and $\sim$500 cm^{-1}.[4-6] The appearance of a $\sim$640cm^{-1} band in the spectrum of YBCO is now generally attributed to a $BaCuO_2$ impurity phase.[5,13-16] The frequency position of the 640cm^{-1} band has been reported to shift with oxygen stoichiometry.[14] Furthermore, when the compound is reduced toward $BaCuO_{1.7}$ (by annealing in an argon atmosphere), a marked decrease in the intensity of the $\sim$640cm^{-1} band is observed, and even a disappearance of that mode.[13,14] Thus, in spectra of $BaCuO_2$ where the $\sim$640cm^{-1} band is not very pronounced, it can be assumed that the

FIG. 2.—Micro-Raman spectra of two preparations of the ceramic powder $Y_2Cu_2O_5$. Top: $Y_2Cu_2O_5$ with approx. 5 wt% Y_2O_3 impurity containing trace concentration (~10 ppm) of Er_2O_3; spectrum entails fluorescence emissions over range 650 to 1600 cm^{-1}. Bottom: $Y_2Cu_2O_5$ free of Y_2O_3 impurity; no trace Er^{3+} fluorescence observed.

FIG. 3.—Raman microprobe spectra of defect film areas in thin film samples of superconducting YBCO and DyBCO. Top: $YBa_2Cu_3O_{7-x}$ thin film on [100] LaAlO substrate; features analyzed are dendritic deposits in reflective area of film. Bottom: $DyBa_2Cu_3O_{7-x}$ thin film on [100] MgO substrate; area analyzed is non-reflective region of film.

650-1600 cm^{-1} are a part of the fluorescence spectrum of the Er^{3+} ion substituted for yttrium in the Y_2O_3 crystal lattice. We have previously discussed these laser-excited Er^{3+} fluorescence spectra of several Er^{3+}-substituted materials pertinent to the Er-Ba-Cu-O superconducting system.[2] The Y_2O_3 impurity is not homogeneously distribued in this sample of $Y_2Cu_2O_5$. A great variability was observed in the spectra of these particles, both in regard to the Raman and the fluorescence portion of the spectrum, indicating a substantial heterogeneity both in Y_2O_3 and $Y_2Cu_2O_5$ contents. However, the intense Raman line of Y_2O_3 at 378 cm^{-1} was not observed in this spectrum as it is masked by the scattering background of $Y_2Cu_2O_5$.

The bottom spectrum in Fig. 2 is that of a second preparation of $Y_2Cu_2O_5$ for which no unreacted Y_2O_3 or CuO could be detected by x-ray diffraction. Thus, if there is any Y_2O_3, it is below the 1-2% detection level of XRD and not likely to be detected by Raman scattering unless present as segregrated grains or microcrystallites. All the spectra from a number of particles were consistent with one another,

showing virtually no variability in the number of peaks and their relative intensities. This powder is free of any trace contamination by Er^{3+} since yttrium oxide of highest-available purity (99.999% Y_2O_3) was used in it preparation. This spectrum is entirely consistent with the best Raman results reported for $Y_2Cu_2O_5$.[17] We had shown earlier that the corresponding $Er_2Cu_2O_5$ (also a blue-green phase) can also be contaminated with unreacted starting material, namely trace Er_2O_3, as detected by the intense fluorescence emissions of the Er^{3+} ion.[2]

With the microprobe spectra shown in Fig. 3 we can illustrate some of the results for thin-film samples of YBCO and DyBCO. Here our microanalytical objective is to examine these polycrystalline films for homogeneity of composition and, in the case of the laser-deposited YBCO films, to relate the spectra of the films to that of the stoichiometric YBCO target. In contrast to the ceramic superconductors, thin films can in principle achieve higher critical-current densities, attributed in part to clean grain boundaries and a

116

textured microstructure. The largest critical currents have been found in films on $SrTiO_3$ and MgO substrates.[8,18,19] Though the aim is to produce stoichiometric films, the reality has been that a window of acceptable composition is often tolerated. This window may typically allow for a ±5% deviation in the stoichiometry of the deposited elements. The spectra of Fig. 3 show results from two different thin-film specimens where some parameters were not in control during the deposition, and partial areas of the films showed discontinuities. In each case, the thin-film sample has a good area of the film deposit, as determined by a standard four-probe electrical measurement, and a bad area of the film showing high resistivity. Good film areas are recognized by their mirror-like, reflective surfaces. Conversely, when film areas are highly scattering, they exhibit a dull gray appearance and show rough morphology. XRD and RBS measurements then confirm a mixed-phase composition and disordered structures.

The top spectrum (Fig. 3) of the YBCO film on a $LaAlO_3$ substrate is representative of numerous measurements on dendritic deposits found scattered about in the reflective (high-T_c) area of the film. Some variability was observed in this spectrum, from one dendritic microcrystalline deposit to the other. But the qualitatively same spectrum was also obtained in the dull-film areas of the specimen, where the deposit was determined to be an insulating phase, so far unidentified. The spectrum from these bad areas entails several features that we have previously associated with an oxygen nonstoichiometric $BaCuO_2$ phase (Fig. 1), but the ~640 cm^{-1} band is not fully developed relative to a ~585 cm^{-1} band. Thus it is not possible to relate this spectrum to a fixed structure and composition in the absence of other microprobe data, such as from quantitative electron probe microanalysis (EPMA), to get at least concentration data for the metals (Ba and Cu), even if reliable oxygen concentrations can as yet not be obtained by x-ray microanalysis.[12] It is also instructive to realize that the probe depth for optical vs electron-beam instruments may not be the same for opaque phases in the high-T_c systems. The penetration depth of the laser (at 514.5 nm) may only be about 0.1 μm, and is thus estimated to be smaller by a factor of ~5-10 compared to the penetration depth of the electron microprobe beam. Hence the two types of probe instruments may not be sampling the same specimen volume, with the Raman microprobe being more surface sensitive. Though the substrate materials utilized for these film depositions are themselves not strong Raman scatterers (in part also due to their high reflectivity), their Raman bands appear to be detected only when the film thickness is less than ~0.2 μm. As a result, we do not observe in the top spectrum the Raman bands of the $LaAlO_3$ substrate which has several bands in this region, with a sharp line at 490 cm^{-1}.

The bottom spectrum of Fig. 3 is characteristic of several probe spots in a bad dull-gray area of a DyBCO film on a MgO substrate. This is a film (thickness ~0.3 μm) produced by thermal co-evaporation where it was suspected that the resistive area of the specimen had been exposed to a thermal gradient during the deposition, changing the chemistry. Morphologically, this bad area was distinctly different from the good film areas and some localized areas showed luminescence. In areas that were free from luminescence, these spectra could be obtained and proved to be relatively invariant over large areas (several mm^2) of the film. There is a strong resemblance to the spectra from the bad areas of the YBCO film. It is surprising that the same, or a similar, insulating phase should have been found during these two different deposition processes, in which the chemistry leading to film formation ought to be so different. We are continuing our work on thin films and their formation, to clarify those factors we have been unable to elucidate as yet.

References

1. E. S. Etz et al., "Micro-Raman spectroscopy of high-T_c superconductors in the Y-Ba-Cu-O system," *Microbeam Analysis--1988*, 187-192, 1988.
2. E. S. Etz et al., "Raman and fluorescence spectra observed in laser microprobe measurements of several compositions in the Ln-Ba-Cu-O system," *Microbeam Analysis--1990*, 243-247, 1990.
3. W. R. Flavell and R. G. Egdell, "Observation of electronic Raman scattering in Y_2BaCuO_5," *Solid State Commun.* 69: 631-633, 1989.
4. R. Feile, "Lattice vibrations in high-T_c superconductors: Optical spectroscopy and lattice dynamics," *Physica* C159: 1-32, 1989.
5. J. R. Ferraro and V. A. Maroni, "The characterization of high-critical-temperature ceramic superconductors by vibrational spectroscopy," *Appl. Spetrosc.* 44: 351-366, 1990.
6. G. Burns et al., "Raman measurements of $YBa_2Cu_3O_x$ as function of oxygen content," *Solid State Commun.* 77: 367-371, 1991.
7. Winnie Wong-Ng et al., "Crystal chemistry and phase equilibria studies of the $BaO(BaCO_3)-R_2O_3-CuO$ systems: Part IV," *J. Solid State Chem.* 85: 117-132, 1990.
8. U. Weimer et al., "Investigation of the epitaxy of thin $YBa_2Cu_3O_{7-x}$ films," *Physica* C168: 359-362, 1990.
9. Y. Gao et al., "Microstructure and defects in a-axis oriented $YBa_2Cu_3O_{7-x}$ thin films," *Physica* C173: 487-500, 1991.
10. Z. Y. Popovic et al., "Optical phonons in Y_2BaCuO_5," *Solid State Commun.* 66: 43-47, 1988.
11. K. Schwartz, "High temperature superconductors: Theory, developments and perspective," *Mikrochim. Acta* (Vienna) II: 149-160, 1990.

12. P. Karduck et al., "Quantitative electron probe microanalysis of Y-Ba-Cu-O superconducting materials," *Mikrochim. Acta* (Vienna) II: 161-172, 1990.

13. A. Erle et al., "Characterization of the intergrain properties of $YBa_2Cu_3O_{7-x}$ by Raman spectroscopy," *Solid State Commun.* 73: 753-757, 1990.

14. R. M. Macfarlane et al., "Raman study of the effect of oxygen stoichiometry on the phonon spectrum of the high-T_c superconductor $YBa_2Cu_3O_x$," *Phys. Rev.* B38: 284-289, 1989.

15. H. Rosen et al., "Systematic Raman study of effects of rare-earth substitution on the lattice modes of high-T_c superconductors," *Phys. Rev.* B38: 2460-2465, 1988.

16. G. Burns et al., "Raman measurements of $YBa_2Cu_3O_{7-x}$ single crystals," *Solid State Commun.* 66: 217-221, 1988.

17. Z. Y. Popovic et al., "Infrared and Raman spectra of $M_2Cu_2O_5$(M=Y, Ho)," *Z. Phys.* B72: 13-16, 1988.

18. O. Eibl and B. Roas, "Microstructure of $YBa_2Cu_3O_{7-x}$ thin films deposited by laser evaporation," *J. Mater. Res.* 5: 2620-2632, 1990.

19. R. Ramesh et al., "Microstructural evolution of laser deposited superconducting Y-Ba-Cu-O films," *Physica* C173: 163-172, 1991.

X-RAY SPATIAL RESOLUTION AT INTERMEDIATE VOLTAGES: AN ASSESSMENT BY MASSIVELY PARALLEL MONTE CARLO ELECTRON TRAJECTORY SIMULATION

A. D. Romig Jr., J. R. Michael, and J. I. Goldstein

X-ray microanalysis in the analytical electron microscope (AEM) has proved to be a powerful tool for studying the spatial distribution of solute elements in both inorganic (metals, ceramics, semiconductors) and organic (biological, polymer) specimens. Most of the papers written on spatial resolution in the AEM have defined the spatial resolution as some measure of beam spreading in a single phase homogeneous specimen.[1,2] However, in the analysis of engineering materials, single-phase homogeneous specimens are rarely encountered. Most commercially important materials are multiphase and the AEM is typically used to measure the fine scale differences in composition between adjacent regions of the specimen (e.g., grain boundary segregation, precipitate/matrix compositions, artificial multilayer materials).

Traditionally, three parameters have been considered important in the determination of spatial resolution R: incident beam size d, specimen thickness t, and accelerating potential E_0. The development of field emission (FEG) AEMs with small beam sizes and high currents has permitted the improvement in spatial resolution, as it applies to multiphase specimens.[1] Taking advantage of the high beam current, investigators have clearly demonstrated an improvement in spatial resolution with decreasing specimen thickness.[3] However, the effect of accelerating voltage on spatial resolution has never been systematically studied. With the introduction of the new higher voltage AEMs, it is necessary to evaluate systematically the effect of beam energy on spatial resolution. Traditional wisdom has suggested that an intermediate-voltage (300-400kV) AEM with an FFG electron source would be the "ideal" analytical instrument, since the diameter of the electron scattering volume at the exit surface of the specimen, or beam broadening b is inversely related to E_0. Such high-brightness intermediate-voltage AEMs are not yet available (first deliveries in mid-1991).

The best approach to the characterization of spatial resolution under various conditions is

through the use of massively parallel Monte Carlo electron trajectory simulation. It is the objective of this work to investigate systematically the spatial resolution in multiphase materials at intermediate voltages as a function of beam size, specimen thickness, and electron beam energy by this method. To provide a baseline for comparison, electron scattering in single-phase homogeneous specimens has also been examined. Electron scattering in single-phase specimens and the fundamental definition of spatial resolution is discussed in more detail in the paper by Williams et al.[4]

There are many advantages to massively parallel Monte Carlo electron trajectory simulations as a method to assess spatial resolution for x-ray microanalysis in the AEM. The Monte Carlo simulation is more accurate and flexible than the analytical approach and the computer execution time using a parallel architecture is very short. A variety of analytical methods have been proposed to calculate R,[5,6] but all these analytical models require various assumptions that limit their application to single-phase homogeneous specimens thin enough so that only single-electron scattering events are considered. Furthermore, the analytical models do not explicitly include the beam diameter d in the calculation of the scattering volume.

Background

The spatial resolution R depends on the diameter d of the focused electron beam and the extent of beam broadening b in the thin-foil specimens.[1,6] The spatial resolution is given by

$$R = \frac{d + \sqrt{d^2 + b^2}}{2} \tag{1}$$

where

$$b = 7.21 \times 10^5 \left(\frac{\rho}{A}\right)^{1/2} \frac{Z}{E} t^{3/2} \tag{2}$$

as given by Reed.[5] The terms ρ, A, and Z are the specimen density, atomic weight, and atomic number, respectively. Most previous studies of x-ray spatial resolution have been performed at 100 to 200 kV. The results of these studies and the predicted decrease in beam broadening with increasing accelerating potential (Eq. 2) have been used to justify the construction of AEM instruments that operate at 300 kV and higher. However, there have been no experimental results to demonstrate the superiority of 300 kV over lower accelerating voltages. Studies that have attempted to make this comparison have been inconclusive because of the difficulty of performing the experiments under identi-

cal conditions (beam size, beam current, current distribution) and the fact that the electron beam diameter is a critical factor in the determination of R (Eq. 1).[1] In the most systematic study to date, 100kV FEG AEM spatial resolution data has been compared to that obtained from a 300kV LAB$_6$ AEM.[1] The great variation in beam size between the two AEMs used in these experiments did permit direct comparison of spatial resolution.

The effect of specimen thickness on the spatial resolution has been studied extensively.[3,7] Increased specimen thickness generally results in a degradation of the measured spatial resolution. The single-scattering model describes the diameter of the electron beam as it exits from a homogeneous single-phase specimen and states that the exit diameter of the electron beam is proportional to $t^{3/2}$ (Eq. 2).[5,6] The spatial resolutions observed in practice are much smaller than the exit diameters predicted by the single-scattering model. Also, the single-scattering model is of little use when inhomogeneous specimens are studied because the average atomic number of the entire scattering volume is used in the calculation.

Recently, the effect of fast secondary electrons (FSE) on the spatial resolution has been examined numerically.[8] Fast secondary electrons result from inelastic scattering of beam electrons and typically have energies from a few hundred eV to half the beam energy.[9] These electrons generate a significant number of x rays (⩾2% of the x ray generated by the primary beam may be excited by FSEs hundreds of nanometers from the point of beam impact), especially in light elements, and hence may degrade spatial resolution in thin-foil microanalysis. The deteriroration of spatial resolution due to the generation of FSEs is a consequence of the trajectory of the FSEs, which is inclined 45° to 90° from the trajectory of the primary electrons.[10] Therefore, high-energy FSEs can travel large distances in the foil and thus fluoresce atoms many beam diameters from the point of beam impact.

The Monte Carlo Model

The NIST (National Institutes of Standards and Technology) Monte Carlo algorithm was modified to utilize a parallel architecture.[11] The massively parallelized algorithm accurately models the backscattering yields from bulk specimens and the composition profiles obtained from thin specimens in the AEM.[11] The NCUBE 2 parallel computer used in this work has 1024 processors. Hence, 1024 trajectories (each with a unique starting random number) can be simulated concurrently. The NCUBE 2 is a MIMD (multiple instruction-multiple data) machine where each processor executes a copy of the program independently on a unique data set. Information can be passed between nodes at the end of a simulation to sum the results. The nodes in the NCUBE 2 are connected in a hypercube topology. The changes to the computer code to enable it to execute on the NCUBE 2

have been detailed previously.[11]

In the simulations used in this study, the electron beam was moved in discrete steps in a direction perpendicular to the interface between two regions of the specimen. For the baseline studies of spatial resolution in single-phase homogeneous materials, both halves of the specimen were defined to be the same material. For the multiphase specimens, materials of differing atomic number were used for each half of the specimen. The x-ray intensity for a given element was determined as a function of distance from the interface. At each beam position 100 000 electron trajectories were simulated. Usually 40 beam positions were simulated per specimen. Thus, about 4 000 000 electron trajectories were simulated per specimen. Each computer simulation required 100 to 300 s to execute, depending on the accelerating voltage (100 and 300 kV) and the specimen composition. All simulations specified an initial electron beam size of 1.0nm FWHM (full width at half maximum), the beam size of the Vacuum Generators HB501.[12] For comparison, some simulations were repeated with a 5.0nm FWHM electron beam, which is more typical of advanced thermionic source AEMs. To examine the effect of specimen thickness, both 50 and 100nm-thick specimens were considered. In order to determine the effect of fast secondary electron generation on the spatial resolution, the simulations were performed with and without fast secondary electrons included.

Numerical Experiments

To explore the effects of voltage, beam size, specimen thickness, and fast secondary electron generation on spatial resolution, specimens consisting of C/C (Z = 6), Al/Al (Z = 13), Cu/Cu (Z = 29) and Au/Au (Z = 79), and combinations of these elements (Cu/C, Al/Cu, and Al/Au) were examined. These elements were chosen to study spatial resolution in light, intermediate, and heavy element specimens, as well as multiphase specimens containing phases of different atomic number (e.g., different electron scattering powers and different efficiencies of FSE generation). The suggestion by Michael and Williams[1] of the following convention to measure spatial resolution has been adopted. The distance between the 2% and 98% points on a normalized composition profile (Fig. 1a) is defined as the profile width L. The spatial resolution R is 1.414 L.[1,4] If the x-ray generation volume has a Gaussian profile, 90% of the generated x ray falls between the 2% and 98% limits.

Results and Discussion

Figure 1 shows the normalized x-ray intensity profiles calculated for Cu at 100 kV for specimen thicknesses of 50 and 100 nm. Figure 2 shows the results of similar experiments for Au. Note the degradation in spatial resolution in the higher atomic number specimen. The results from profiles, such as those given in Figs. 1 and 2 for C, Al, Cu, and Au have been
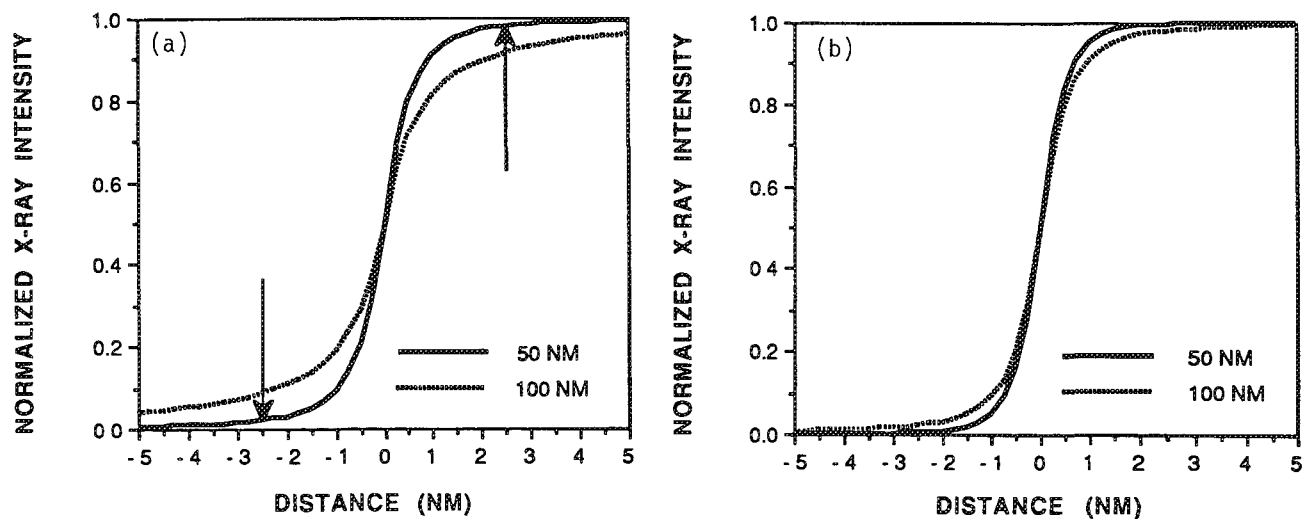
FIG. 1.--Normalized Cu x-ray intensity profiles obtained for 50 and 100nm-thick specimens at (a) 100 kV, (b) 300 kV. Effect of FSEs is not included. Profile width L is horizontal distance between 2-98% points on the composition profile (note arrows in (a)).
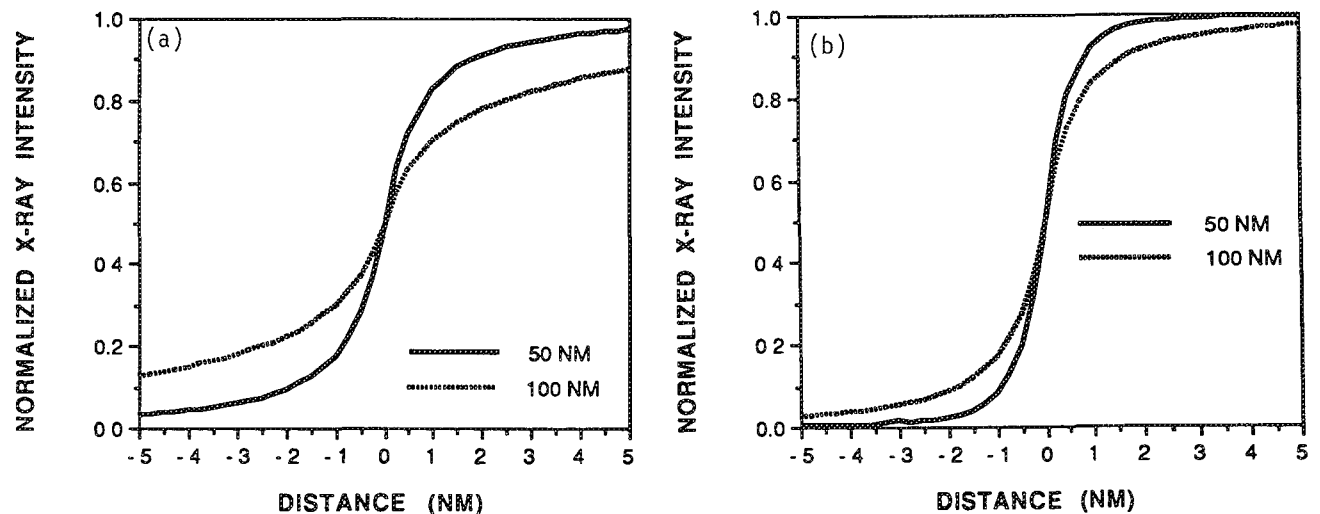
FIG. 2.--Normalized Au x-ray intensity profiles obtained for 50 and 100nm-thick specimens at (a)100 kV, (b) 300 kV. Effect of FSEs is not included.
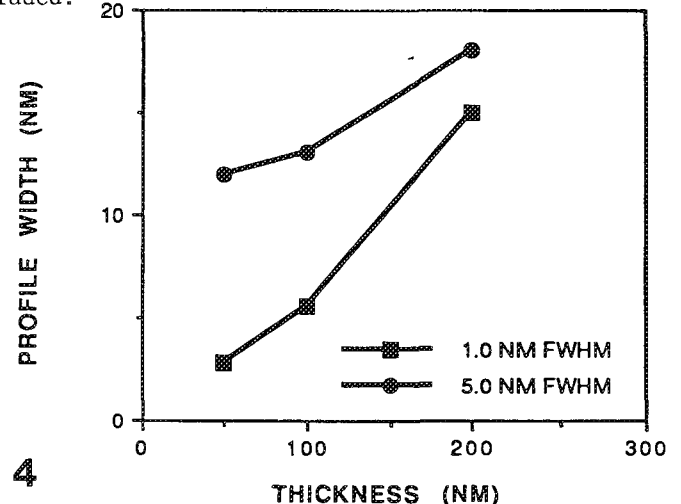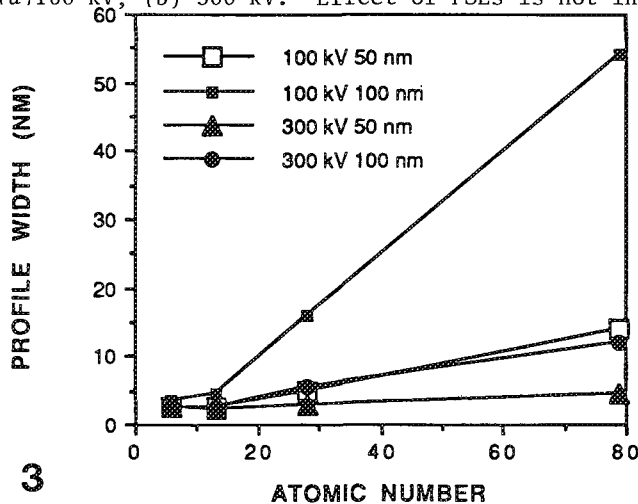
FIG. 3.--Profile widths (2-98% points) for 100 and 300 kV and 50 and 100nm-thick specimens vs atomic number. Effect of FSEs is not included.

FIG. 4.--Comparison of profile widths in Cu for range of specimen thicknesses at 300 kV for 1.0 and 5.0nm beam sizes. Effect of FSEs is not included.

121
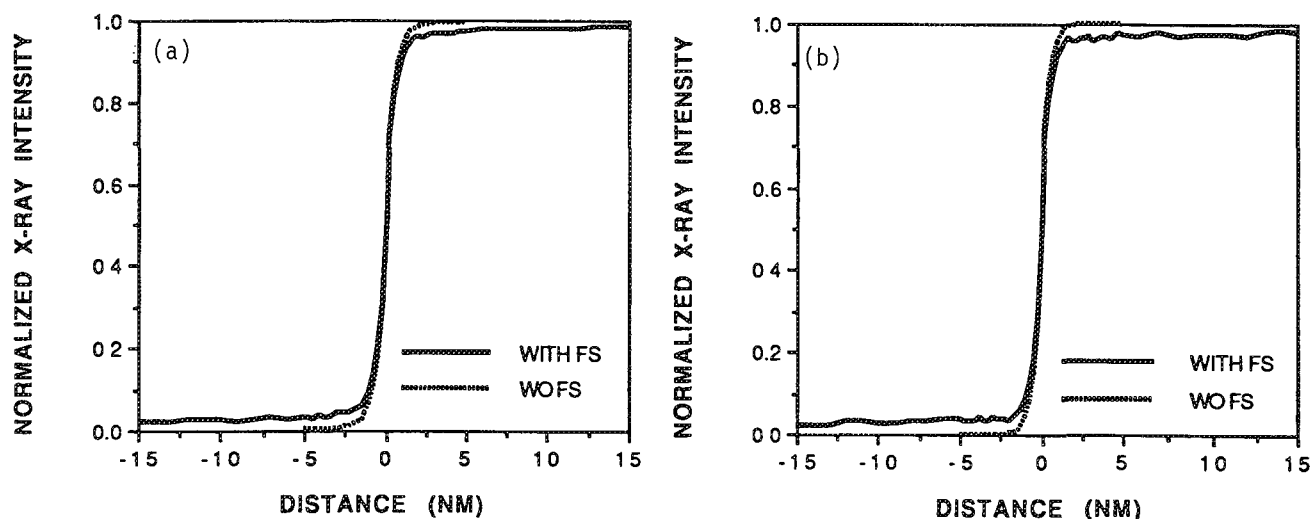
FIG. 5.--Normalized x-ray intensity profiles for C with and without FSEs for 100nm-thick specimen: (a) 100 kV, (b) 300 kV.
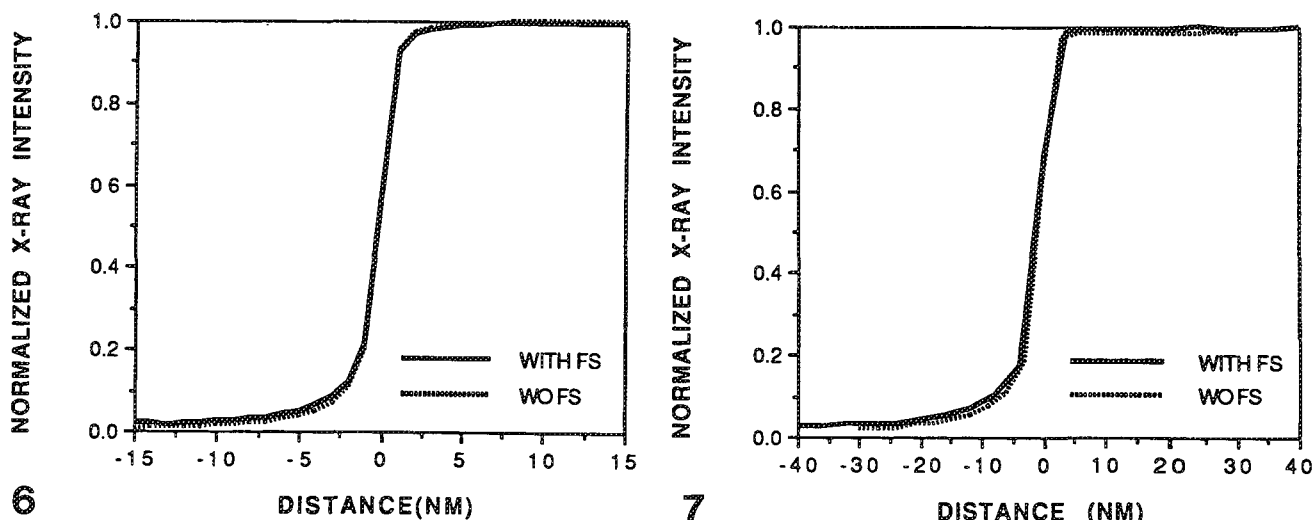
FIG. 6.--Normalized Al x-ray intensity profiles (with and without FSEs) across Al/Cu interface in 100nm-thick specimen at 100 kV.

FIG. 7.--Normalized Al x-ray intensity profiles (with and without FSEs) across an Al/Au interface in 100nm-thick specimen at 100 kV.

condensed into Table 1 where the distance between 2% and 98% points on the normalized intensity profiles, without the effect of fast secondary electrons, is given. Several critical observations can be made from these data regarding the effect of beam size, accelerating potential, specimen thickness, and average atomic number.

The use of higher voltage (300 vs 100 kV) results in improved spatial resolution, especially for materials of higher atomic number. The spatial resolution for carbon at 100 and 300 kV is nearly identical, which indicates that the major contribution to the spatial resolution is the initial beam size. For Au, the increase in kV results in a large improvement in the spatial resolution of approximately 3.1 and 4.5 times for specimen thicknesses of 50 and 100 nm, respectively.

These data may also be used to assess the effects of specimen thickness on the spatial resolution. The effect of thickness (50 vs 100 nm) on the resolution obtained for C is quite small and is almost undetectable at the spatial scale used in the simulation. In contrast, the effect of specimen thickness on the spatial resolution for Au is much more pronounced. Neither specimen follows the $t^{3/2}$ dependence given by the single-scattering model. This is a clear indication that the exit diameter b of the electron (Eq. 2) is not explicitly a measure of spatial resolution.

The synergistic effect of accelerating potential, specimen thickness, and average atomic number on spatial resolution, without the effect of fast secondary electrons, is shown in Fig. 3, where the calculated profile width L is plotted vs atomic number at operating

TABLE 1.--Profile width L (nm) without fast secondary electrons as a function of atomic number, thickness, and voltage.

ELEMENT	kV	50 nm	100 nm
C	100	2.5	3.5
C	300	2.5	2.5
Al	100	2.7	4.5
Al	300	2.5	2.5
Cu	100	5.0	16.0
Cu	300	2.8	5.5
Au	100	14.0	54.0
Au	300	4.5	12.0

TABLE 2.--Profile width L (nm) with and without fast secondary electrons as a function of atomic number, thickness, and voltage.

ELEMENT		kV	50 nm	100 nm
C	without FSE	100	2.5	3.5
C	with FSE	100	28.0	28.0
C	without FSE	300	2.5	2.5
C	with FSE	300	16.0	26.0
Al	without FSE	100	2.7	4.5
Al	with FSE	100	3.0	6.0
Al	without FSE	300	2.5	2.5
Al	with FSE	300	2.8	2.5

Table 3.--Profile width L (nm) for interfaces between Al/Cu and Al/Au with and without fast secondary electrons.

		kV	50 nm	100 nm
Al/Cu	without FSE	100	4.0	10.5
	with FSE	100	5.25	17.0
	without FSE	300	2.75	3.9
	with FSE	300	3.25	6.2
Al/Au	without FSE	100	9.0	36.0
	with FSE	100	13.0	45.0
	without FSE	300	3.25	7.5
	with FSE	300	5.75	14.0

Table 4.--Profile width L (nm) for interface between C/Cu with and without fast secondary electrons.

kV		50 nm	100 nm
100	without FSE	3.57	9.0
100	with FSE	16.0	32.5
300	without FSE	2.5	3.75
300	with FSE	19.0	55.0

voltages of 100 and 300 kV for specimens 50 and 100 nm thick. The FWHM incident beam size is 1 nm. These data show the advantage of 300 kV over 100 kV in terms of spatial resolution for most materials, especially for intermediate and heavy elements. The spatial resolution in a 100nm-thick specimen at 300 kV is essentially identical to that from a 50nm-thick specimen at 100 kV.

In order to study the importance of beam size, a number of simulations were run with a 5.0nm beam size. Figure 4 shows the results of these simulations for a 300kV electron beam in Cu of various thicknesses at 1.0 and 5.0nm FWHM beam sizes. This figure shows that improvements in spatial resolution accompany reductions in beam size for most practical specimens. In this example, the spatial resolution obtained for a 200nm-thick specimen can also be improved by decreasing the initial electron beam size. At some significantly greater thickness, the improvement due to reduced beam size is somewhat diminished. However, the thickness at which this effect occurs is much greater than any practical limit for microanalysis. Also, for lighter elements such as Al, the beam size dominates the spatial resolution to thicknesses well in excess of 200 nm. Similarly, for heavier elements such as Au, the spatial resolution is dominated by beam broadening at smaller thicknesses than Cu. The use of 100 kV results in the displacement of the curves shown in Fig. 4 to smaller thicknesses, thus reducing the thickness range over which beam size dominates the spatial resolution.

Effect of Fast Secondary Electrons

Fast secondary electrons are generated when a high-energy electron beam interacts with a solid specimen. A large number of fast secondary electrons (the FSE yield is 1% to 3% of the primary beam electrons, depending on E_0 and t) are generated in the specimen, with the vast majority of these electrons having rather low (a few keV) energy. A few percent ($\leqslant 5\%$) of the fast secondary electrons may have energies up to half the beam energy. Since the ionization cross section is inversely dependent on electron energy,[13] the FSEs are more efficient generators of x rays than the primary beam electrons! The cross section for high-energy ($\sim 0.5\ E_0$) fast secondary electron generation indicates that the fast secondary electrons follow a trajectory approximately orthogonal to the path of the primary beam electron.[10] As a consequence, high-energy electrons travel large distances parallel to the specimen surface and thus greatly degrade the spatial resolution. The magnitude of the effect of fast secondary electrons on spatial resolution depends on the average atomic number of the specimen. The current Monte Carlo calculations show that there is no significant difference between profiles calculated with or without fast secondary electrons in medium and high atomic number elements, such as Cu and Au. More generally, FSEs should have a significant degrading effect on

spatial resolution only in cases in which the ionization energy is approximately $\leqslant 2$-3 keV. Therefore, fast secondary electrons degrade the spatial resolution obtained from light elements with atomic numbers of 14 or lower analyzed in an AEM operating at 300 kV.

Figure 5 shows normalized x-ray intensity profiles for C at 100 and 300 kV for 100nm-thick specimens. Table 2 shows the calculated spatial resolutions obtained from C and Al at 100 and 300 kV for 50 and 100 nm thicknesses, including the effect of FSEs. It is quite apparent that the fast secondaries significantly degrade the spatial resolution in carbon. An order-of-magnitude increase in the profile width is observed for both 100kV and 300kV electrons in C. Furthermore, contrary to all the theoretical descriptions of beam broadening in thin specimens, the spatial resolution in C at 100 kV appears to be independent of specimen thickness when fast secondary electrons are included. This result is in agreement with other studies,[9,10] which found that the volume of fast secondary generation has a cylindrical shape. As a consequence, the spatial resolution is independent of specimen thickness up to the thicknesses at which elastic interactions result in beam broadening larger than the mean free path of the FSEs. This result may not be of significance in many materials studies, but is very important in the AEM study of organic specimens, which consist mainly of C and solute elements of relatively low atomic numbers. In light-element microanalysis (Z < 14), the fast secondary electrons introduce large tails for the x-ray emission volume.

The spatial resolution for microanalysis across interfaces between materials of different atomic number can be calculated by Monte Carlo simulations. This is fortunate since the single-scattering model and Gaussian-broadening models cannot accommodate variations in atomic number across the interface.[5,6,14] In addition, the effect of fast secondary electrons can be included only in Monte Carlo simulations. Hence, the advantage of a Monte Carlo simulation that executes very rapidly is very significant for a multiphase specimen in which there is a large compositional discontinuity at the interface. The short time required for a simulation greatly facilitates the use of Monte Carlo simulations for the interpretation of experimental data.

In order to assess the effect of fast secondaries on spatial resolution in multiphase specimens, a series of simulations across interfaces between elements of significantly different atomic number, Al/Cu and Al/Au, were performed. Figure 6 shows the normalized x-ray intensity profiles obtained for Al-Cu in a 100nm-thick specimen at 100 kV. Figure 7 shows a similar set of profiles for Al/Au. In each case, the tails caused by the generation of fast secondary electrons are apparent. Table 3 lists the results obtained from these specimens for two thicknesses at 100 and 300 kV. Several important observations must be made with

respect to these results.

To interpret the calculated data, it is important to recall several characteristics of fast secondary electrons. Although the energy distribution for fast secondary electrons includes a large number of low-energy fast secondary electrons, a significant number (≤5%) of the fast secondary electrons have energies up to half the beam energy. In addition, the cross section for fast secondary generation is inversely related to the mean free path between inelastic scattering events.[8] As a result, higher energy primary electrons have a longer mean free path between scattering events, so that fewer fast secondary electrons are generated. Similarly, the short mean free path in specimens of high atomic number results in a large number of fast secondary electrons. For Al, Cu, and Au the average number of fast secondary electrons generated per 100 000 100kV electrons in specimens 100nm thick is 740, 1852, and 3300, respectively. At 300 kV the average number of fast secondary electrons in similar specimens generated per 100 000 beam electrons is 319, 734, and 1185, respectively. Furthermore, the fast secondary electron distribution is shifted to higher energy for 300kV primary electrons. These features in the scattering phenomena account for the observed spatial resolution variations at Al/Cu and Al/Au interfaces with accelerating voltage (Tables 3 and 4). In Al/Cu and Al/Au specimens, the fast secondary electrons degrade the spatial resolution, since many of the fast secondary electrons generated in the Cu and Au have energies higher than the Al Kα absorption edge of 1.559 keV. Due to the increased generation of fast secondaries in Au relative to Cu, the spatial resolution is more severely degraded at the Al/Au interface than the Al/Cu interface (Table 3). The resolution for the Al/Cu and the Al/Au specimens should be compared with those shown in Tables 1 and 2. For example, the resolution obtained across an Al/Cu interface with FSEs at 100 kV for a 100nm-thick specimen is 17 nm, whereas the spatial resolution with FSEs obtained for pure Al and pure Cu are 6.0 nm and 16.0 nm, respectively. It is therefore apparent that the use of an average atomic number for the two element specimen would not yield reasonable results. The increased profile widths for the Al/Cu interface over that in pure Cu is due to the increased elastic scattering of primary electrons into the Al side of the interface, as well as the enhanced FSE generation on the Cu side of the interface.

An example of the effect of beam spreading and FSEs at an interface between a light element and a heavy element, such as in a graphite/metal composite, was obtained by simulating the x-ray profiles that would be measured across a C/Cu interface. The calculated results are given in Table 4. These results show the resolutions obtained for 100 and 300 kV for specimen thicknesses of 50 and 100 nm. In this case, it is apparent that there is little advantage in operating at 300 kV rather than 100 kV,

since the spatial resolution degrades in the 100nm-thick specimen. It is clear that Monte Carlo simulation is the technique of choice when considering the spatial resolution that can be obtained with the AEM in the analysis of multiphase specimens.

Conclusions

1. Massively parallel Monte Carlo electron trajectory simulations are the method of choice for examining spatial resolution in multiphase specimens. Only Monte Carlo methods have the ability to accommodate any incident probe size, multiple scattering, any specimen thickness, and the effects of fast secondary electrons.

2. Spatial resolutions on the order of a few nanometers will be possible in 300kV analytical instruments that can form beams a few nanometers thick.

3. For equivalent beam sizes, 300 kV is superior to 100 kV in terms of spatial resolution for specimens where all phases have an average atomic number higher than approximately 14.

4. For equivalent beam sizes, 300 kV is essentially identical to 100 kV in terms of spatial resolution for specimens in which there is a large atomic number difference between the phases, and one phase has an average atomic number lower than 14. This result is a consequence of the presence of fast secondary electrons.

5. The microanalytical spatial resolution at interfaces between elements of high and low atomic number is degraded both by the increased eleastic scattering and by the increased production of fast secondary electrons in the heavier element.

References

1. J. R. Michael and D. B. Williams, *J. Micros.* 160: 41, 1990.
2. A. D. Romig Jr. et al., *Microbeam Analysis--1982*, 72.
3. J. R. Michael, *Microbeam Analysis--1989*, 496.
4. D. B. Williams et al., *Proc. 49th Ann. Meet. EMSA*, 1991.
5. S. J. B. Reed, *Ultramicroscopy* 7: 405, 1982.
6. J. I. Goldstein et al., *SEM/1977* II, 315.
7. T. A. Stephenson et al., in *Quantitative Microanalysis with High Spatial Resolution*, London: The Metals Society, 1981, p. 53.
8. R. Gauvin and G. L'Esperance, *Microbeam Analysis--1989*, 527.
9. K. Murata et al., *J. Appl. Phys.* 52: 4396, 1981.
10. D. C. Joy, *Analytical Electron Microscopy--1984*, 43.
11. A. D. Romig Jr. et al. *Microbeam Analysis--1990*, 275.
12. J. R. Michael, *Microbeam Analysis--1988*, 60.

13. H. Bethe, *Ann. Phys.* (Leipzig) 5: 325, 1930.

14. P. Doig and P. E. J. Flewitt, *Metall. Trans.* 13A: 1397, 1982.

ELECTRON ENERGY LOSS SPECTROSCOPY ABOVE 200 kV

A. J. Gubbens, O. L. Krivanek, and M. K. Kundmann

Probably the most important limitation of electron energy loss spectroscopy is that it is best performed on specimens whose thickness is about one half of the mean free path for all inelastic scattering. This typically works out to about 20 to 50 nm at 100 keV primary (E_0), and is somewhat more than the very small thickness, typically 5 to 20 nm, required for lattice imaging, but it may present problems nevertheless. Increasing the primary energy makes inelastic scattering cross sections smaller, and increases the usable specimen thickness roughly as $\sqrt{E_0}$. This may be of paramount importance if a thin specimen cannot be prepared, as is often the case for biological sections, ion-thinned composite ceramics, and various other multiphase materials.

A second advantage of increasing the primary energy is that the characteristic angle for inelastic scattering, which is given by $\theta_E = \Delta E / 2 E_0$, decreases at higher E_0, which makes it easier to capture a large portion of the inelastically scattered electrons into a spectrometer. However, this effect is to a large extent canceled by the fact that in order to attain an energy resolution not much worse than at the lower voltage, the range of entrance angles into the spectrometer, and the size of the spectrometer entrance object, must be more restricted at higher E_0.

Another potential advantage is the smaller probe size theoretically possible at higher voltages. In practice, however, no 300kV or higher-voltage instrument currently available matches the probe-forming performance of a 100kV dedicated cold field emission STEM. Further, the theoretically attainable probe diameter for a 200kV microscope with a point emitter and an objective lens of $C_S = 0.4$ mm is only 1.2 Å ($d = 0.43 C_S^{1/4} \lambda^{3/4}$), so the further improvements available at 300 kV and higher will not be very important.

In most other respects, increasing the microscope voltage above 200 kV presents mainly difficulties, for instance to the EELS designer. The best energy resolution a particular spectrometer can achieve is constant when expressed as a fraction of the primary energy, i.e., as $\Delta E / E_0$. Attaining an energy resolution of 1 eV at 400 KeV is thus just as difficult (or as easy) as attaining 0.25 eV at 100 kV, or 0.06 eV

(20-25 keV was the energy used by Crewe and co-workers in their pioneering work on EELS.[1]) The actual resolution obtained at the lower voltages will of course be much worse because of the energy spread of the source, but if a monochromatic source were available, the figures quoted here would be realistic.

Another fundamental difficulty arises with the electron detector. Because a high-energy electron can travel several hundreds of micrometers in the detector, attaining the required spatial resolution and freedom from background and spurious signals is much harder to achieve at the higher voltages. Other problems are purely practical. For instance, the thickness of x-ray shielding required to make the instrument radiation-safe roughly doubles on going from 200 to 300 kV, and the doubles again on going to 400 kV. X-ray fluorescence and scattering also become much more important at higher voltages, resulting in new paths that let the x-rays get out of the instrument. These problems complicate the task of the instrument designer to the point that some attachments to a medium-voltage electron microscope plus the required shielding simply cannot be squeezed into the often tight space available.

Gatan has been designing and building electron energy loss spectrometers for 300 and 400kV microscopes for almost a decade now. Recently we designed, built, and delivered a parallel-detection EELS system for a 1.3MV electron microscope. Several problems were encountered in designing and testing this instrument, but none of them proved insoluble. Some of the problems are, to a large extent, also present in 300-400kV spectrometers, but 1.3MV operation made them much more obvious. Rather than reviewing the various current and potential applications of 300-400kV EELS, this contribution therefore reviews the design and the performance of the 1.3MV spectrometer, which will enable us to draw several conclusions that will be useful for "medium-voltage" operation by extrapolating downward from 1.3 MV. It will also give us a fresh perspective on medium voltage EELS, which has already been thoroughly reviewed elsewhere.[2,3]

Design of a 1.3MV PEELS

Figure 1 shows the configuration of the 1.3MV PEELS in relation to the overall instrument. The 1.3MeV electrons travel at 95% of the speed of light, and the x-rays that result when the electrons hit a solid target are heavily concentrated in the forward direction. Directing the electron beam in the PEELS instrument away from the operator is therefore an

FIG. 1.--Layout of 1.3 MV PEELS in relation to HVEM.

important safety feature.

The PEELS uses several design elements from the standard Gatan PEELS[4] designed for operation up to 400 kV. In order to increase the dispersion of the magnetic prism, and to avoid saturation of the magnetic material and excessive heating of the prism coils, the bending radius of the prism was increased to 25 cm (from 10 cm used in the standard design). The resultant prism gives an energy dispersion of 0.54 μm/eV at 1.3 MV. It has an entrance focusing distance of 956 mm, which is well suited to the space available below the camera chamber of the HVEM. The spectrum is magnified by five quadrupole lenses rather than the four used in the standard PEELS, to give energy dispersions as large as 500 μm/eV at 1.3 MV at the parallel detector. The quadrupoles are arranged in two separate groups; each group is water-cooled. The detector is situated 240 mm after the final quadrupole. It uses a thin single-crystal YAG scintillator to convert the electrons into light, and the light is detected by a 1024-channel linear photodiode array, very much as in the standard PEELS.

Tests of the Electron Optics

The electron optical performance of the HV

PEELS was first tested on a 200kV electron microscope at Gatan, and found to correspond exactly to the calculated properties. It was then installed on the 1.3MV Hitachi HVEM in the laboratory of Y. Bando, S. Horuichi, and Y. Matsui at the National Institute for Research in Inorganic Materials (NIRIM) at Tsukuba in Japan. Here again the electron optical performance was found as predicted at voltages up to 1.3 MV. The spectrometer was completely corrected for aberrations up to second order in the entrance angle, and the desired range of dispersion could be produced with the quadrupoles at all operating voltages from 400 kV to 1.3 MV.

Even though the electron optics design proved faultless, the narrowest profile of the zero loss peak obtained had a full width at half-maximum (FWHM) of 4 eV. The performance of the most critical element of the PEELS for energy resolution, the power supply of the magnetic prism, had been tested during initial component tests, and was found to have a short-term stability better than 0.3 ppm. That should have been more than sufficient for attaining 1 eV resolution. The suspicion therefore fell on the high-tension (HT) supply of the electron microscope. An oscillatory voltage was applied to the electrically isolated PEELS drift-tube, and the frequency was varied to determine whether a beat could be obtained by interference between the applied signal and a periodic disturbance already present. Such beat was detected at 3.93 kHz, the frequency used in the microscope's Cockroft-Walton generator. Further tests showed that the amplitude of the detected HT instability was about 4 V peak-to-peak, and that if the instability was not present, an energy resolution better than 2 eV should have been possible at the zero loss peak.

Efforts to eliminate the instability by fine-tuning the fast and slow HT feedback stabilization proved unsuccessful. However, because the instability was constant in magnitude, it should be possible to cancel it by generation of a compensating signal in much the same way as 60Hz stray magnetic fields are canceled in the standard Gatan PEELS. We have therefore built a circuit that takes the frequency signal from the Cockroft-Walton generator, adjusts its phase and amplitude, and feeds it to the spectrometer drift tube. Assuming that the circuit works as planned, it should enable the attainable energy resolution of the PEELS to be not much worse at 1.3 MV than at lower voltages.

Detector Performance

The YAG/fiber optics/linear photodiode array detector proved to be capable of detecting 1.3MeV electrons with an efficiency that was comparable to detecting 200kV electrons, but two problems arose nevertheless. The first concerned radiation damage to the scintillator. Its rate was quite rapid: working with the PEELS for just a few minutes produced irreversible browning of the scintillator and a loss of detection efficiency. Subsequent studies in
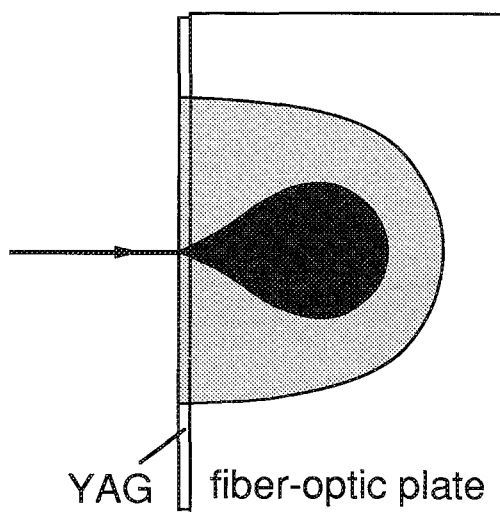
FIG. 2.--Schematic diagram of interaction of 1.3MeV electrons with scintillator. Dark region corresponds to incoming electron beam, lighter region to backscattered and secondary electrons.
FIG. 3.--Response of detector to narrow incoming beam of 1.3MeV electrons. No specimen, dispersion 2 eV/channel.

which the YAG and the fiber optics were irradiated separately showed that the damage was actually occurring in the fiber optics, which developed networks of microcracks wherever a concentrated beam of a few picoamperes of 1.3MeV electrons was incident on it. A search for materials with better radiation resistance showed that the damage varied by about three orders of magnitude in different glasses, and that glasses with a high refractive index normally used in fiber-optic manufacture were among the most sensitive ones. A custom-made fiber-optic plate from one of the more resistant glasses has been manufactured and is currently being tested for radiation resistance as well as all the other properties required of a fiber-optic plate, such as high numeric aperture and excellent uniformity.

The second problem concerned lateral spreading of the detected signal in the detector. The YAG crystal was the same thickness as used at 100 kV, with the result that most of the energy of each 1.3MeV electron was deposited into the fiber optics under the YAG. This decreased the number of photons generated per incoming electron to about the same number as produced by 100 keV electrons, but it improved the detector resolution, since each incoming electron generated a signal within the YAG before its trajectory spread substantially sideways (Fig. 2). However, backscattering of the primary electrons and the generation of back-diffusing secondary electrons within the fiber optics resulted in a second, much broader contribution to the signal produced by each primary electron. This effect is documented in Fig. 3, which shows the signal detected by the parallel detector when illuminated by a
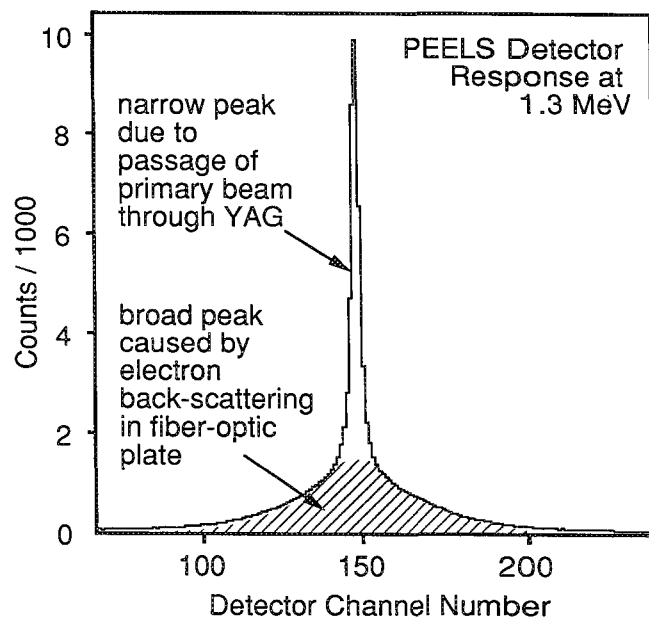
beam of 1.3MeV electrons incident in about channel 150, and about 3 channels wide. The detected signal consists of a central sharp peak with a FWHM of 4 channels, which is due to the fast electrons entering the YAG crystal, on top of a broad peak with a FWHM of about 40 channels, which is due to backscattered and secondary electrons reaching the YAG and producing light. The area under the broad peak is about double that of the sharp peak, showing that backscattering within the fiber optics is actually the more important source of the detected photons.

The back-scattering contribution can also cause a problem with viewing screens used in HVEMs.[5] It is normally minimized by use of an ultrathin support for the viewing phosphor, which allows the fast electrons to escape out the back side. However, the same solution applied to the present case would mean that the scintillator would have to be lens-coupled to the detector. Such a coupling typically delivers only about 10% of the photons that can be captured with a good-quality fiber-optic transfer plate. We have therefore chosen to keep the YAG mounted on a fiber-optic plate, and to deconvolve the tails of the detector response in much the same way as one would use deconvolution to remove the multiple inelastic scattering contribution in a spectrum from a thick specimen.[6]

Figure 4 shows (a) an as-recorded spectrum from boron nitride and (b) the result of deconvolving the spectrum with the detector response. The primary voltage was 1.3 MV, the energy dispersion was 0.3 eV/channel, the recording time was 0.8 s, and a 2mm entrance in front of the spectrometer was used. The poor jump ratio

129
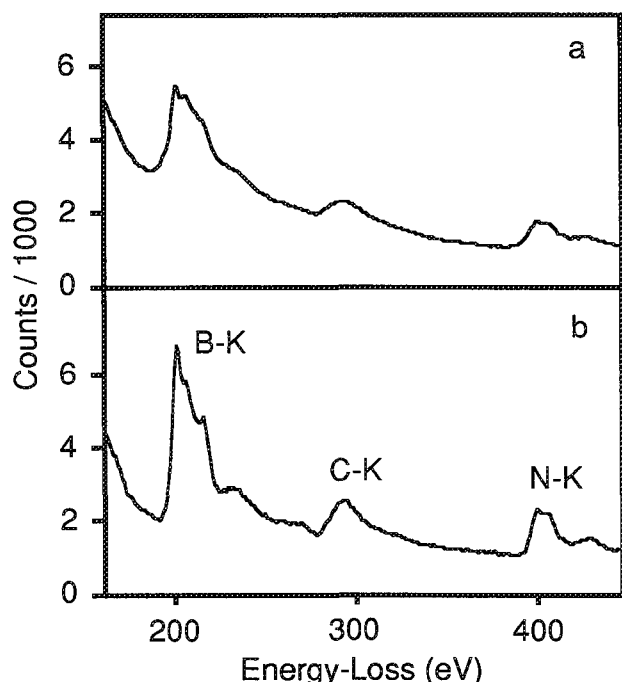
FIG. 4.--Spectra of boron nitride. 1.3 MV,
0.3 eV/channel, recording time 0.8 s (a) as-
recorded, (b) deconvolved with the detector
response shown in Fig. 3.

of the edges in spectrum (a) and the fact that
the normally abrupt rise at edge threshold has
been smoothed out are largely due to the broad
peak in the detector response. In carrying out
the deconvolution, we modeled the sharp peak in
the detector response by a Gaussian, and sub-
stituted a delta function of an equal area for
it. Thus, only the broad peak was deconvolved
from the spectrum, so that the unstable algor-
ithm was avoided, as was the large increase in
spectrum noise that would have resulted if we
had attempted to improve the spectrum resolution
by deconvolving with the sharp peak as well.
Apart from the currently unimpressive energy
resolution, and a small increase in the noise
component of the spectrum (which is unavoidable
in any deconvolution procedure), the decon-
volved spectrum looks similar to those obtained
at lower voltages, even though it came from a
boron nitride particle that would have been much
too thick to give a resonable spectrum at 100 or
200 kV.

Consequences for Medium-voltage EELS

Extrapolation of the 1.3MV results down to
300-400kV operation leads to several interest-
ing conclusions. First, the energy resolution
of the medium-voltage instruments may be partly
limited by high-frequency ripple present on the
HT. If the relative magnitude of such ripple
were the same as for the 1.3MV instrument, it
would amount to about 1 V peak-to-peak. Such
ripple would not give any obvious deteriora-
tion of high resolution images, and would be
difficult to identify in routine PEELS opera-
tions. The surest way of discovering its

presence would be to use a compensating
circuit similar to the one constructed for the
1.3MV PEELS and seeing whether it improved the
attainable resolution.

Second, since a part of the energy of 300
and 400keV electrons is deposited in the glass
under the YAG scintillator, the radiation
damage to the glass that occurs at these
voltages is probably significant, even though
much slower than at 1.3 MV. Once a radiation-
resistant fiber-optic YAG support has been
successfully developed, it should be used at
300 and 400 kV, too.

Third, electron backscattering within the
detector will broaden the detector response
function at 300 and 400 kV, although much less
than at 1.3 MV. Deconvolving the response
using either a no-specimen spectrum showing
only the zero loss peak, or a low-loss spec-
trum of the specimen (which will also contain
the "tails" to be removed) may therefore be
advisable at the lower voltages as well, par-
ticularly when the signal of interest lies on
a steeply varying background.

Provided these precautions are observed,
medium-voltage UELS should give results very
similar to those obtainable at 100 to 200 kV,
but from specimens about 2 times thicker, and
a further two-fold increase in usable specimen
thickness should be available on increasing
the operating voltage to 1.3 MV.

References

1. A. V. Crewe, M. Lsaacson, and D.
Johnson, "A high resolution electron spectro-
meter for use in transmission scanning electron
microscopy," *Rev. Sci. Instruments* 42: 411-420,
1971.
2. R. F. Egerton, "EELS at intermediate
voltage," in K. Rajan, Ed., *Intermediate
Voltage Microscopy and Its Application to
Materials Science* Mahwah, N.J.: Electron Optics
Publishing Group, Philips Inc., 1987, 67-71.
3. M. M. Disko and R. Ayer, "Electron
energy loss spectroscopy at 100 kV and 300 kV,"
in Ref. 2, 72-77.
4. O. L. Krivanek, C. C. Ahn, and R. B
Keeney, "Parallel-detection electron spectro-
meter using quadrupole lenses," *Ultramicroscopy*
22: 103-116, 1987.
5. R. Valle, B. Genty, A. Marraud, and B.
Pardo, "The influence of backscattering effects
on the detection of 1 MV electrons," *Proc.
Fifth Int. Conf. on High Volt. EM (Kyoto)* 1977,
163-166.
6. R. D. Leapman and C. R. Swyt, "Electron
energy loss spectroscopy under the conditions
of plural scattering," *Analytical Electron
Microscopy--1981* 164-172.

RADIATION DAMAGE IN INTERMEDIATE VOLTAGE MICROSCOPES

D. G. Howitt

At high voltages the electron beam can be much more destructive to electron microscopy specimens than at 100 keV. As the beam energy is increased, it is possible to transfer more and more energy to electron/atom collisions,and when this energy exceeds that necessary to displace the atom in the lattice, an atomic rearrangement occurs. The process begins with the creation of a Frenkel pair, an interstitial, which is the atom that has been moved away from the original site; and a vacancy, which is the hole that is left behind.

The continued production of Frenkel pairs usually leads to the formation of strain centers that vary in size, depending on the mobility of the interstitials and vacancies in the lattice. Most self-interstitials are mobile at room temperature, but the vacancies are not, so that a uniform microstructure of interstitial defects forms. The microstructure develops as the interstitials combine; the rate is controlled by the proportion that recombine with the vacancies that have already been created. If the sample is cooled sufficiently, usually to liquid helium temperatures, the interstitial mobility can be suppressed. Under these circumstances, the only defect aggregation that can occur is when the atoms are literally knocked into each other, so that the defect microstructure is considerably finer. When the specimen is heated, the microstructure can coarsen and clear away a lot of the so-called "black spot damage," which happens because the vacancies begin to move; but rather than inhibiting the radiation damage effect, the consequence is the opposite and the overall efficiency of the recombination declines rapidly becasue of vacancy aggregation.

In imaging, at moderate resolution, the defect formation is mostly an inconvenience because the vacancy and interstitial concentrations take some time to accumulate. Eventually the damage impinges on the microstructure being evaluated, either to modify the contrast directly, because of atomic rearrangement, or to introduce a phase decomposition because of the supersaturation of defects. In the case of defect imaging, for example, the dislocations may be decorated with additional defects (Fig. 1), but the Burgers vector analysis is still possible. In high-resolution imaging, the same sort of developments can be expected, except that defect accumulation is much more rapid, increasing as the square of the magnification. It is therefore very worthwhile to record sequences of images to confirm that no signifi-

D. G. Howitt is at the Department of Mechanical, Aeronautical, and Materials Engineering, University of California, 95616.

cant changes are being brought about in the image contrast.

The problems associated with analytical electron microscopy at high voltage are much worse because the ionization cross sections for x-ray production are of the same order as the cross sections for atomic displacement. A variation in the analytical signal is much more likely than a variation in image contrast, at the same magnification, simply because of the electron doses involved.

The amount of radiation damage which produces a noticeable effect corresponds to a resolution limit to the analysis. The problem of beam sensitivity is certainly not new and is well known, for example, to people who study biological materials at high resolution at conventional voltages. Organic materials undergo the same sort of degradation through radiolytic processes and in any situation, when the electron exposure in unit area has an upper limit N_{cr}, the resolution limit is

$$d \geqslant R/c\sqrt{fN_{cr}} \tag{1}$$

where R is the ratio of signal-to-background noise that must be obtained to distinguish the measurement, f is the collection efficiency of the detector, and c is the contrast.

When it is not possible to make a measurement before the radiation damage sets in, the data can sometimes be extrapolated back to the beginning, based on the changes that are observed. The basic idea is that one expects a constant rate of signal production from a specimen and a radiation damage process tends to change the rate.

We have made a systematic study of the x-ray production from materials that undergo distinctly different radiation damage processes, and by collecting spectra over short time intervals rather than all at once, one can infer what the initial x-ray production was. An example of such an extrapolation for sodium chloride is shown in Fig. 2, where the radiation damage is caused by the displacement of chlorine atoms to form a crowdion along <110>. The process is in fact a radiolytic one and the chlorine moves along all directions equally. The situation for displacement damage is different because the atoms move only in the forward direction. Although it is a fairly straightforward process to predict displacement damage, only in very thin specimens does the displacement rate reflect the change in the composition of the irradiated specimen, because the distance between the Frenkel pair (i.e., the distance between the displaced atom and the vacancy it leaves behind) is usually much smaller than the sample thickness. If that is the case, it is the effect of multiple

displacement events, rather than a single knock on, that determines the loss. In thicker specimens, under conditions of low beam flux or high temperature, the diffusion of the interstitials away from the region of analysis will be of increasing importance and will ultimately control the change in composition that is observed.

There is no simple solution, when radiolysis is going on, to improve the resolution once the signal collection has been maximized and the kinetics of the decomposition have been slowed, but there is one for materials that only undergo displacement. The problem disappears when the microscope is operated at an electron voltage below that which can provide sufficient energy to displace atoms. These voltages can be calculated in a straightforward way if the energies to displace atoms are known, and are given by

$$E_{th} = m_0 c^2 \left[\left(\frac{ME_d}{2m_0^2 c^2} + 1 \right)^{1/2} - 1 \right] \quad (2)$$

where $m_0 c^2$ is the rest energy of the electron, M is the mass of the displaced atom, and E_d is the energy to displace it.

Once this threshold has been crossed, there is little advantage in working at higher voltages because the cross sections for displacement have energy dependencies similar to those that produce the signal. An added disadvantage is that it is sometimes more difficult to collect the signal; but at best the resolution limit maintains the same square-root dependence on the inverse of whatever beam-current density sufficiently disrupts the specimen. The comparison between the resolution limit imposed by radiation damage and the limit set by the instrumentation at the subthreshold voltage is therefore the critical one.

Chlorine Loss from NaCl 14 keV

Au Loss By Sputtering 700 keV

$E_s = 5$ eV
30 nm Au

Oxygen Loss from Fe$_2$O$_3$

100 keV Electrons
298 K

L.E. Thomas
1985
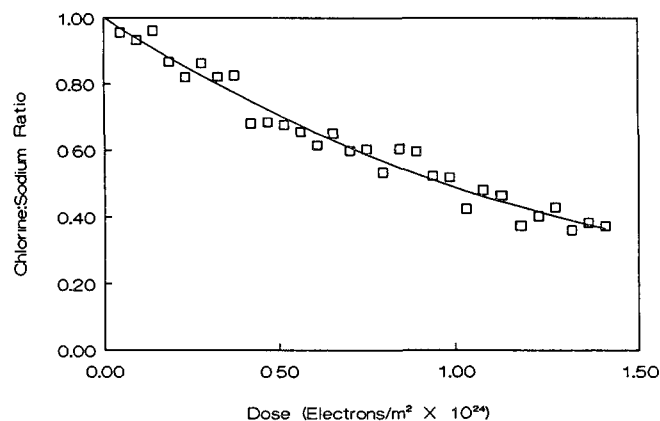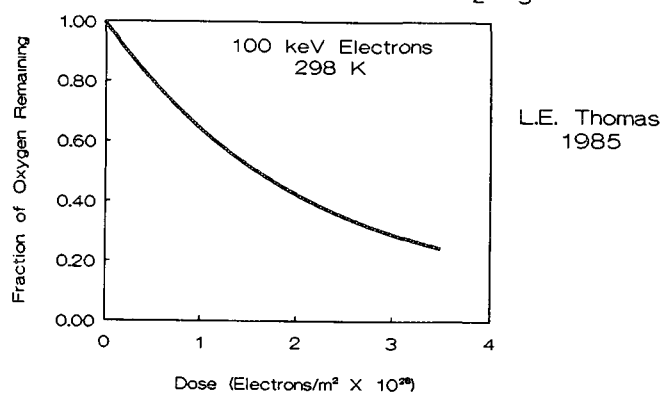
FIG. 1.--Dislocations in sapphire, decorated with clusters of vacancies (voids) and interstitials (loops) brought about by continued electron irradiation.
FIG. 2.--Composition ratio of sodium to chlorine for thin film of sodium chloride as it varies with electron flux at 100 keV.
FIG. 3.--Loss of gold from surface sputtering in thin film at high voltage. Data are based on experimental measurements made by Cherns.[1]
FIG. 4.--Loss of oxygen from iron oxide at 100 keV. Data are based on experimental measurements made by Thomas.[2]

ELECTRON ENERGY, keV
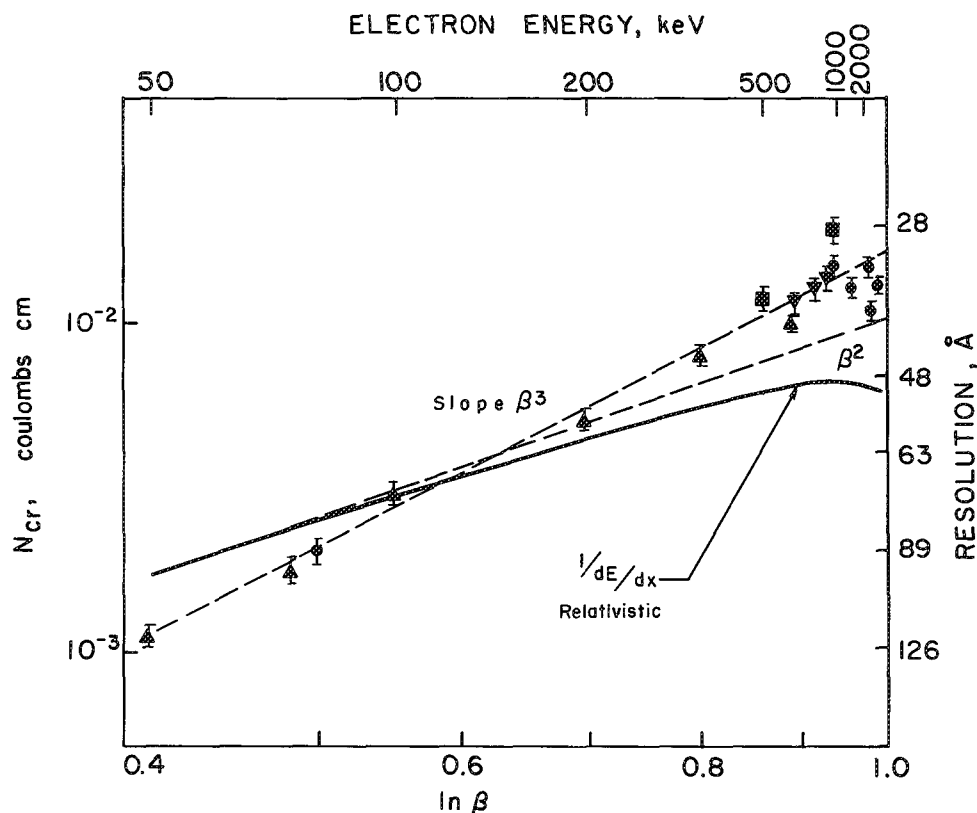
FIG. 5.--Variation in critical exposure (N_{cr}) with voltage for l-valine, an amino acid that undergoes a crystalline-to-amorphous transformation from electron-electron interactions; β is the ratio of electron velocity to that of light.

Below the threshold energy for direct displacement, subthreshold effects have been observed that are often associated with sputtering from the back surface. In metals, the energy required to displace atoms from a surface is substantially lower than that needed to displace them from the interior, so that considerable amounts of material can be lost.[1] The loss of material can produce a surface pitting or an injection of vacancies into the specimen. In either event it produces a change in composition that is determined by the rate at which atoms are displaced from the surface (Fig. 3).

Even lower displacement thresholds are associated with the displacement of atoms into the sites of adjacent vacancies and these are associated with electron energies below 100 keV. The effects are only significant in materials that contain a large concentration of vacant sites; the example of iron oxide is shown in Fig. 4. The composition losses are enhanced at high voltages simply because vacancies farther away from the displaced atoms are accessible. Eventually this process would be expected to contribute to a reduction of the recombination volume associated with conventional displacement. In other words, by encountering a vacant site, the displaced interstitial can be prevented from collapsing back, even though insufficient energy has been imparted to the atom to produce a displacement under normal circumstances.

As long as no new radiation damage processes are introduced, there is a distinct advantage

in going to high voltages in radiation-sensitive materials because the damage slows down. The amount of ionization damage follows the same dependence as the electron energy loss, which decreases in proportion to the square of the electron velocity. Some experimental values for thin films of l-valine are shown in Fig. 5 which show a slightly different dependence, closer to the cube of the velocity. If nothing else were affected, the advantage would be substantial; however, the events that produce the signal from the sample are also less likely to take place, so that there is a tendency for things to cancel out. Nevertheless, in some cases, for example if the image information can be averaged, there are good reasons for going to higher voltages to reduce the damage rate.

References

1. D. Cherns, M. W. Finnis, and M. D. Matthews, "Sputtering of gold foils in a high voltage electron microscope: A comparison of theory and experiment," *Phil. Mag.* 35: 693, 1977.

2. L. E. Thomas, *Ultramicroscopy* 18: 173, 1985.

X-RAY MICROANALYSIS OF HEAVY ELEMENTS OF L AND K SERIES LINES

S. M. Zemyan and D. B. Williams

Intrinsic Ge (IG) energy-dispersive detectors are now an alternative to Si(Li) detectors x-ray analysis on an analytical electron microscope (AEM). By virtue of its greater density, 3 mm of Ge is a more efficient absorber of x rays than the same thickness of Si. For example, the absorption efficiency drops to 75% for 25keV x rays in an Si(Li) detector (thereby including all L lines and the K lines of elements up to Sn), whereas absorption is ⩾75% up to 74 keV in an IG (including the K lines up to Pb). Consequently, IG detectors permit quantitative analysis of heavy elements ($Z \geqslant 50$) with use of either K or L lines, whereas Si(Li) detectors limit the analyst to L lines. The advantages and disadvantages of K and L line quantification are discussed below. In the present study, a sample of a silicate glass containing several elements, including 11.4 wt% Ba and 8.43 wt% Pb, was analyzed with a Link IG detector on a Phillips EM430 AEM operated at 300 kV. The glass is NIST standard K1070, described previously.[1] From these analyses the peak-to-background ratios (P/B) and detection limits for Ba and Pb in the glass are determined by use of K and L x rays. Relative sensitivity factors are estimated from these analyses and compared to theoretical values.

The principal advantage of K series spectra is that they are simple. At most there are four peaks ($K\alpha_1$, α_2, β_1, and β^2), of known relative intensities, on a background that is both low and slowly varying with energy (Figs. 1 and 2). Peak areas can be determined accurately by use of energy windows for the peaks and local backgrounds. Another advantage of the K lines of heavy elements is that absorption corrections are generally not needed because the x rays are highly penetrating in most materials. For example, the mass absorption coefficients μ (in units of cm^2/g) of Pb $K\alpha$ and Ba $K\alpha$ in the K1070 glass are 0.96 and 4.41. In comparison, the μ for Pb $L\alpha$ and Ba $L\overline{V}$ are 66.4 and 330.1, and the μ for Mg K, Si K, and Ca K (other elements in the K1070 glass) are 3378, 1691, and 425.

The main disadvantage of K x rays is that they are inefficiently generated by electron impact. Therefore, peak intensities are small and the statistical errors in measured concentrations are large. The number of $K\alpha$ or $L\alpha$ photons detected per unit beam current for

each element is proportional to $C_iQ_iX = C_i(\sigma\omega a\varepsilon/A)_{iX}$, where C_i is the wt% of element i, σ is the ionization cross section for the X shell, ω is the fluorescence yield of that shell, a is the relative fraction of α-radiation ($K\alpha$/K-total or $L\alpha/L_3$-total), ε is the detector absorption efficiency for the characteristic line, and A is the atomic weight.[2] To estimate relative intensities, values of σ are taken from Scofield, ω from Fink, and a from Salem et al.[3-5] The efficiency ε is 0.75 for Pb $K\alpha$; and 1 for Ba $L\alpha$, Ba $K\alpha$, and Pb $L\alpha$.

The normalized products C_iQ_iX for the $K\alpha$ and $L\alpha$ lines of Ba and Pb show the intensity advantage of L lines (Table 1). For example, Pb $L\alpha$ is nearly 18 times as intense as Pb $K\alpha$.

TABLE 1.--Theoretical intensities of Ba and Pb $L\alpha$ and $K\alpha$ lines, relative to the intensity of Pb $K\alpha$.

Element(i)/Line(X)	Relative Intensity C_iQ_{iX}
Ba $L\alpha$	30.3
Ba $K\alpha$	12.0
Pb $L\alpha$	17.9
Pb $K\alpha$	1.0

Background intensities are also lower for the K lines than for the L lines. However, the peak intensity falls more rapidly with increasing energy than does the background. Therefore, the P/B ratios are generally lower for the K than the L lines. This trend is especially true for the heavy elements, such as Pb (Table 2). K series detection limits are also adversely affected by the low peak intensities above background. The detection limit is defined as $C_i 3\sqrt{2B}/P$ (wt%), where P and B are the measured peak and background counts.[6] Table 2 shows detection limits of Ba and Pb in the K1070 glass derived from Figs. 1-4, which indicates for example that the detection limit of Pb is 15 times worse using $K\alpha$ than $L\alpha$.

The main advantage of the L spectra for quantification is their high intensity, which results in low statistical errors. The high intensity combined with high P/B ratios results in low detection limits (Table 2). The greatest disadvantage of L spectra is their complexity (Figs. 3 and 4). The L series of heavy elements contain many lines that may overlap with each other and with lines of other elements. Because the L lines originate from ionization of more than one subshell, the relative intensities depend on accelerating voltage and are difficult to predict. Because of

this complexity, estimating L peak areas may be difficult and inaccurate.

From the data in Tables 1 and 2, relative sensitivity factors (k factors) may be experimentally estimated and theoretically derived. The k factors are defined by $C_1/C_2 = k_{12}I_1/I_2$, where I_1 and I_2 are the measured peak areas of lines 1 and 2.[2] From above, the ratio I_1/I_2 may be calculated as $C_1(\sigma\omega a\epsilon/A)_{1\chi}/C_2(\sigma\omega a\epsilon/A)_{2\chi}$. Therefore, $k_{12} = (\sigma\omega a\epsilon/A)_{2\chi}/(\sigma\omega a\epsilon/A)_{1\chi}$. Experimental and theoretical k_{PbBa} factors based on both $K\alpha$ and $L\alpha$ lines, and k_{KL} factors for both Pb and Ba are given in Table 3. The experimental values are not highly accurate due to the small peak areas in Figs. 1-4; however, none differs from the theoretical values by

more than 30%.

Two features of our IG detector affect the ease with which spectral data may be used for quantification. First, Ta K x rays are visible between 56.3 and 67 keV in all high-energy spectra (Fig. 1). (The Ta K peaks are of sufficient intensity to complicate quantification of any elemental lines with which they may overlap.) These system peaks originate from Ta in the detector collimator. No Ta L or M x rays are detected, probably because they are absorbed in the collimator. Second, incomplete charge collection (ICC) is more severe in IG than in Si(Li) detectors, particularly below 10 keV. This problem is greatest for the Mg and Al K peaks, which are near the
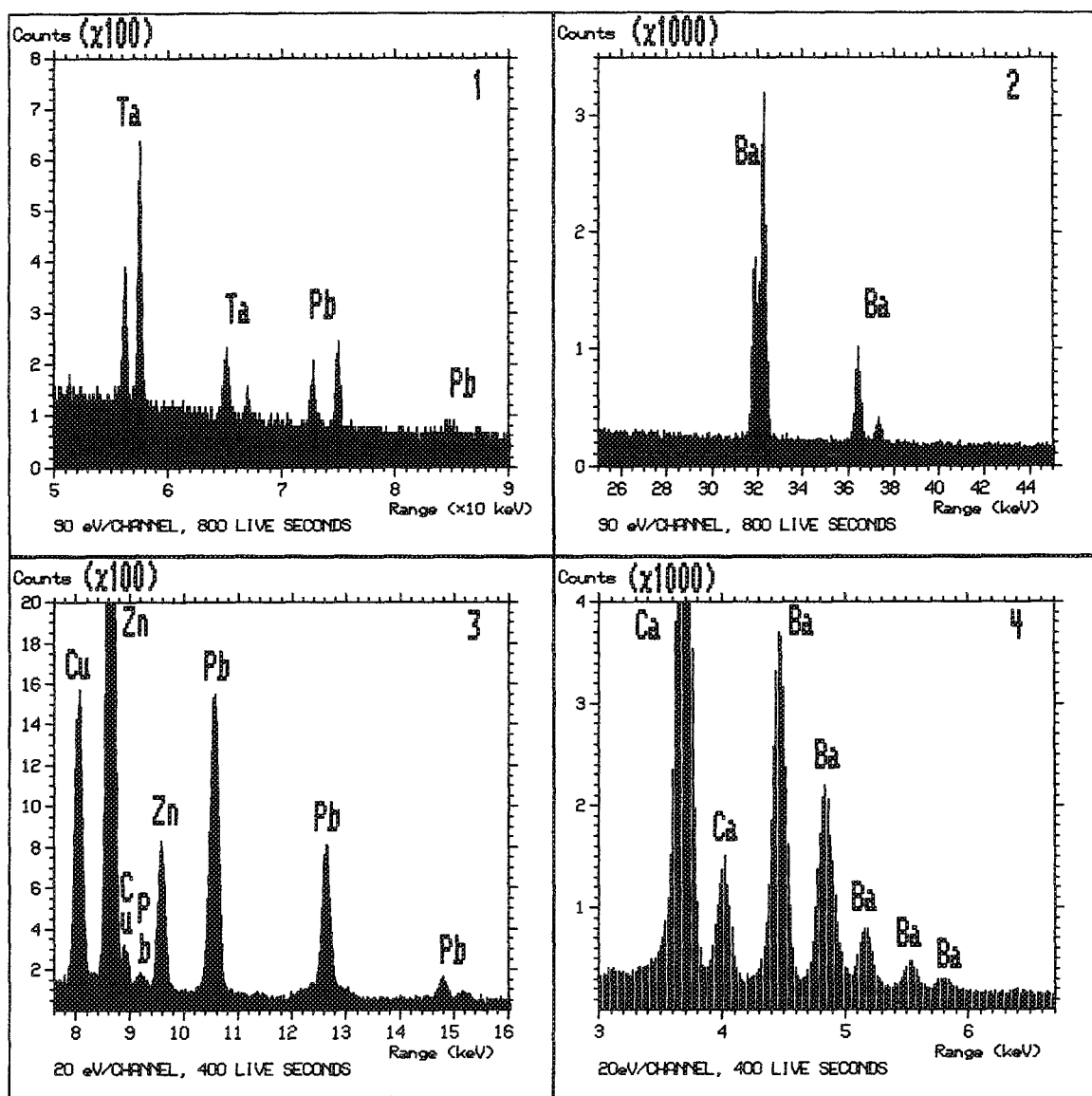
FIG. 1.--Pb K region of x-ray spectrum of K1070 glass, 800 live seconds, 1.22 nA beam current, 300 kV accelerating voltage.
FIG. 2.--Same as Fig. 1, for Ba K region of spectrum.
FIG. 3.--Pb L region of x-ray spectrum of K1070 glass, 400 live seconds, 1.22 nA beam current, 300 kV accelerating voltage.
FIG. 4.--Same as Fig. 3, for Ba L region of spectrum.

TABLE 2.--Determination of P/B ratios and detection limits for Pb and Ba in K1070 glass.

Element/Line	Ba Lα	Pb Lα	Ba Kα	Pb Kα1,2
Energy (keV)	4 467	10 549	32 065	74 957, 72 794
Peak intensity (cps/nA)	47 6	29 7	15 0	1 53
Background under FWTM (cps/nA)	7 14	2 54	2 27	1 59
P/B ratio	6 67	11 7	6 58	0 968
Detection limit, 800 s (wt%)	0 087	0 061	0 16	0 94

L absorption edges of Ge. ICC may not affect quantification of major or minor constituents, but could complicate detection and quantification of trace amounts of an element 1 or 2 atomic numbers below a major constituent. ICC is not noticeable in the K spectra of heavy elements.

TABLE 3.--Measured and theoretical k factors for Ba relative to Pb, and for K lines relative to L lines.

(Element/Line)$_1$	(Element/Line)$_2$	k_{12} (meas)	k_{12}(theo)
Ba Kα	Ba Lα	3.18	2.53
Pb Kα	Pb Lα	19.3	17.9
Pb Lα	Ba Lα	1.19	1.25
Pb Kα	Ba Kα	7.21	8.87

Conclusions

For heavy-element quantification, L x-ray spectra offer the advantages of high peak intensities and low detection limits. The K spectra offer simplicity in determining peak areas, little need for absorption corrections, and flexibility in cases where the L spectra have severe overlaps.

References

1. P. J. Sheridan, "Determination of experimental and theoretical k_{ASi} factors for a 200-kV analytical electron microscope," *J. Electron Microscopy Tech*. 11: 41, 1989.
2. J. I. Goldstein, "Principles of thin film x-ray microanalysis," in J. J. Hren, J. I. Goldstein, and D. C. Joy, Eds., *Introduction to Analytical Electron Microscopy*, New York: Plenum Press, 1979, 83.
3. J. H. Scofield, "K- and L-shell ionization of atoms by relativistic electrons," *Phys. Rev.* A18: 963, 1978.
4. R. W. Fink, "Tables of experimental values of x-ray fluorescence and Coster-Kronig yields for K-, L-, and M-shells," in J. R. Robinson, Ed., *Handbook of Spectroscopy*, vol. 1, Cleveland: CRC Press, 1974, 219.
5. S. I. Salem, S. L. Panossian, and R. A. Krause, "Experimental K and L relative x-ray emission rates," *Atomic Data and Nucl. Data Tables* 14: 91, 1974.
6. D. B. Williams, *Practical Analytical Electron Microscopy in Materials Science*, Mahwah, N.J.: Phillips Electronic Instruments, Inc., Electron Optics Publishing Group, 1987, 83.

PROGRESS ON THE ANL ADVANCED AEM PROJECT

N. J. Zaluzec

Commercial instrumentation on the market today, although labeled as "analytical electron microscopes," is in fact a transmission or scanning transmission electron microscope with analytical attachments. Although the manufacturers always optimize their instruments, they inevitably do so at the expense of analytical performance, and optimize instead for the best possible image resolution. In 1980 the Electron Miscopy Center (EMC) at Argonne National Laboratory (ANL) began a development project to specify and acquire a true analytical electron microscope (AEM). The instrument specifications were devised with the primary goal of attaining the best possible analytical sensitivity, resolution, and versatility consistent for state-of-the-art materials research and still provide moderate imaging capabilities. Early in the conceptual design it was determined that the instrument was sufficiently complex that it could not be built by the research staff at ANL alone, and the decision was made to enter into a development contract with a commercial manufacturer. After spending three years raising funds, two years visiting manufacturers to discuss and detail the specifications, and one year in bidding and negotiating a contract, the project was finally awarded to VG Scientific Instruments (now VG Microscopes Ltd) of East Grinstead, England. Progress has been deliberate; it appears that the instrument is nearing completion and may be delivered this year.

During the preliminary stages of this project, the most difficult task was to convince the manufacturers of the need and advantages of developing an analytical microscope operating at accelerating voltages of 300-500 kV and having an integral cold field-emission gun (CFEG). In 1980, when EMC began this project, instruments operating above 200 kV were few and far between (excluding HVEMs); commercial FEGs operated only at 100 kV. Today, 11 years later, medium-voltage (300-400kV) and 200kV FEGs are standard items in the repertoires of nearly all the manufacturers; but when the EMC began this project, the issue was in fact a major obstacle.

N. J. Zaluzec is at the Electron Microscopy Center for Materials Research, Materials Science Division, ARgonne National Laboratory, Argonne IL 60439. This project is supported by DOE contract BES-MS W-31-109-Eng-38. Many people contributed enormously to the success of this project; among them are all the staff in the EMC at ANL and at VG Microscopes Ltd. A special note of recognition for putting up with my relentless pressure, demands, and on-site visits goes to Drs. S. VonHarrach, R. Keyes (now at Cornell University), and J. Collings at VG.

The other important hurdles were the concept that image resolution was not the prime objective of the instrument; that true UHV ($<5 \times 10^{-10}$ Torr) at the specimen was an absolute requirement; and that the instrument must be modular in nature to allow the EMC to develop and install analytical detectors for future work, yet to be specified.

The general specifications of the instrument that were finally developed are listed in Table 1. Basically, the system consists of a CFEG with gun lens, triple condense, objective, and quadruple projector (Figs. 1 and 2). Although high-resolution imaging of the specimen is not important, imaging of the probe is considered essential; thus the four projectors allow sufficient magnification to do so under all conditions. All apertures (VOA, Cond, Obj, Diff, EELS) are electrically isolated and have eight position stops for electron dosimetry, together with a Faraday cup in the probe forming system. A conventional electrostatic beam blanking system is integral and is located between the C2 and C3 lenses. One of the most important features in the system design was the development of an objective-lens configuration that satisfied the ANL requirements. Figures 3 and 4 sketch out the geometrical configuration of this area, which includes seven experimental ports for analytical equipment development, and three for electrical connections. The polepiece gap is sufficient to allow complete inversion of the stage, although in practice (due to the need for gearing the motor drives) the actual rotation about the primary tilt axis is limited to ±85°. Initially three types of specimen stages are being constructed: ambient double-tilt Be, LN_2 double-tilt Be, and a single-tilt 1000 C heating stage. Image detection is accomplished by use of conventional NTSC video in the CTEM and BF/ADF imaging in the STEM, using one of four operator-selected YAG screen, the signals from which are flash digitized (8, 16, 32 bit) and routed to two independent frame scores (512 × 512 × 8 bit). A comprehensive specimen preparation chamber is directly interfaced to the column (Fig. 2) and allows complete extensive cleaning, characterization, and preparation of the specimen surface (Table 1). A "parking lot" for 12 specimens is also provided for in the specimen prep chamber. Two 400 l/s and two 60 l/s ion getter, four titanium subliminators, and 1 turbomolecular comprise the evacuation pumps for the system.

Consistent with the goal of maximizing the analytical sensitivity is minimizing spectral artifacts. Careful scrutiny has therefore been given to all parts of the probe-forming system, with special attention to the various beam-defining apertures. For example, multilayer

low/high Z material combinations have been employed in both beam- and nonbeam-defining apertures and at all critical su-faces to minimize potential sources of uncollimated hard x rays which give rise to the hole count phenomenon. The windowless XEDS system has been optimized to maximize the subtending solid angle and to allow retraction along a direct line-of-sight path to the specimen. This allows the instrument to achieve a continuously variable solid angle up to a maximum of 0.3 sR. A conventional hemispherical Auger spectrometer with extraction optics is interfaced to the center of the objective lens and both serial and parallel EELS detection capabilities will be present. In addition (not shown in Fig. 3), on the incident beam side of the objective lens between C2 and C3 is a drift space for secondary and Auger electron spectrometers that employs parallelizer optics installed within the objective prefield. The entire system is microprocessor controlled by a 386-level PC as system controller and a second 286-level system for image handling, by use of the two frame stores. The system may be controlled either directly by the operator using conventional multifunction dials and switches or using the PC and a mouse-directed interactive graphical user interface. The high voltage generator has already demonstrated combined ripple and noise of 150 mV at 300 kV (0.5 ppm!) under a full load bench test. With the column operating at
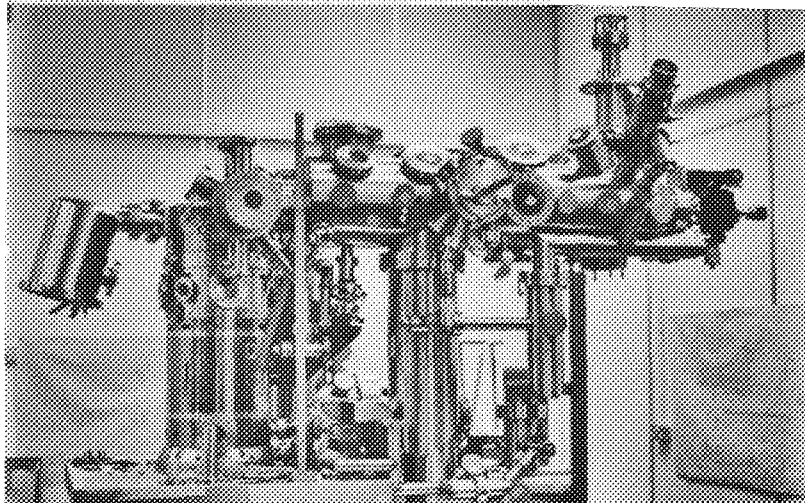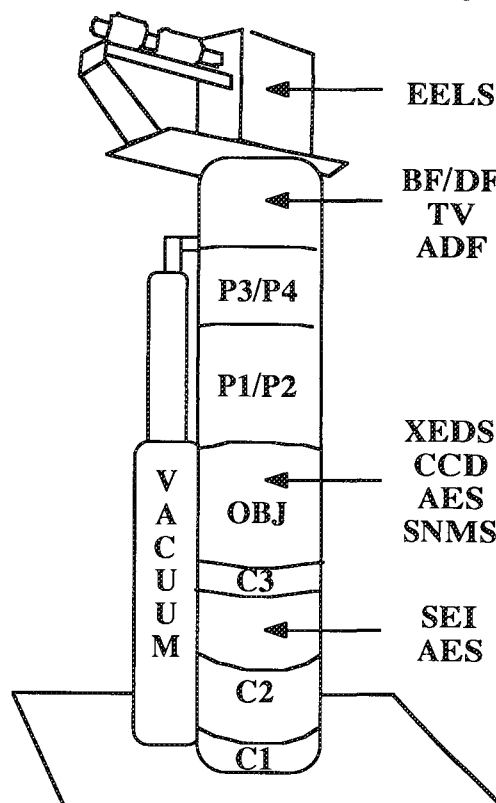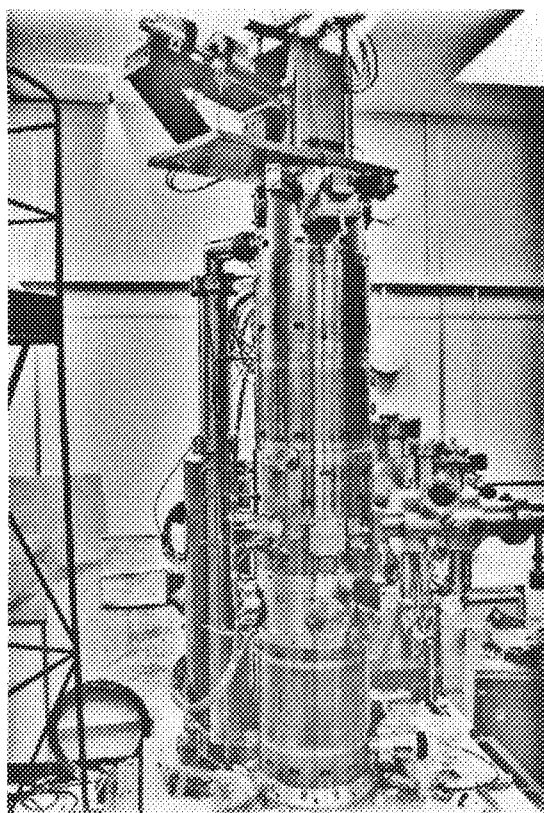
FIG. 1.--ANL AEM column assembly (top) and specimen preparation chamber (bottom). On the lower figure the column is assembled only up to the objective lens. See Fig. 2 for plan view.

250 kV graphite 3.4 Å STEM lattice images have **3**
been achieved. The expected gun brightness is
~4×10⁹A/cm²/sR at 300 kV and the nominal image
resolutions in both TEM and STEM should be <3Å
pt/pt BF, and <2Å in HADF-STEM. Figure 5 plots
a calculated contrast transfer function for the
Objective Lens at 300 and 100 kV, while Fig. 6
plots the calculated probe current/size rela-
tionships at 300 kV.

2

4

5

6
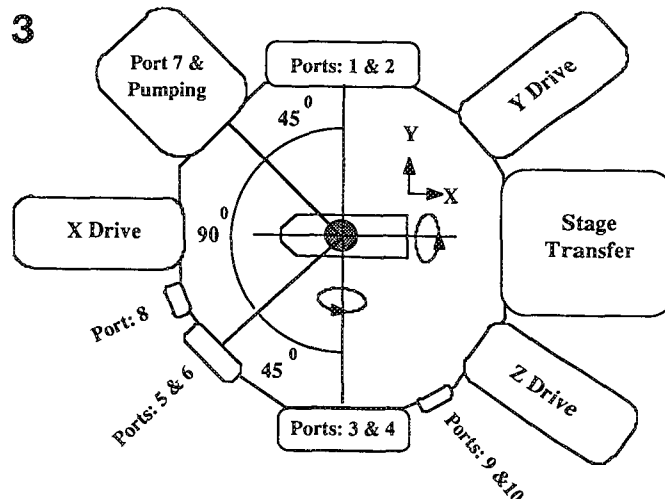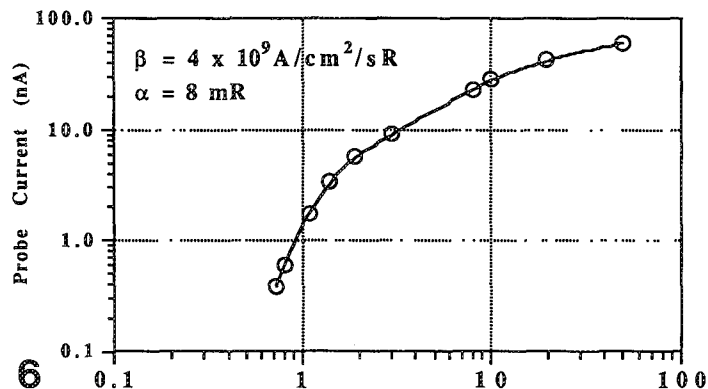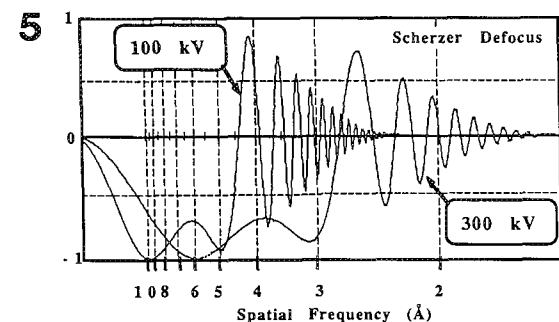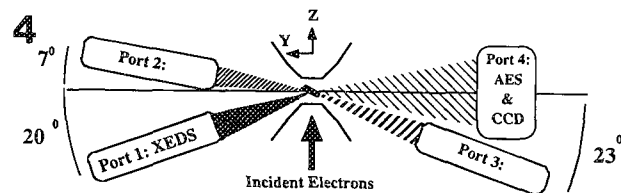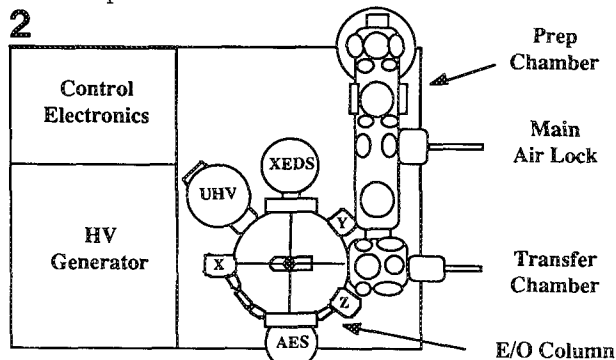
FIG. 2.--Plan view of system showing location
of preparation chamber relative to chamber.
FIG. 3.--Plan view of objective lens area
showing experimental port configuration.
FIG. 4.--Cross section through ports 1/2 and
ports 3/4 of Fig. 1. Ports 5/6 have the same
geometry as ports 1/2; port 7 is similar to
port 4. Ports 8-10 are for electrical connec-
tions.
FIG. 5.--Calculated contrast transfer function
for the ANL AEM at 300 and 100 kV; Scherzer
defocus, Cs = 4.4 mm, CFEG source.
FIG. 6.--Calculated probe size/current rela-
tionship for the ANL AEM at 300 kV.

TABLE 1.--ANL-EMC advanced AEM project goals.

- **Cold Field Emission Electron Source**
  - V_0: 50 - 300 kV, DV_{step} = 25 V, $DV/V_0 \leq 1$ ppm
  - $b300kV \sim 4 \times 10^9$ A/cm^2/sR and ultimate probes ≤ 3 Å
- **Ultrahigh vacuum (UHV) environment**
  - $< 2 \times 10^{-11}$ torr - Gun
  - $< 2 \times 10^{-10}$ torr - In the specimen region of the Objective Lens Column
  - $< 5 \times 10^{-10}$ torr - Specimen Preparation Chamber
- **Electron Optics capable of :**
  - STEM: Scanning Transmission Electron Microscopy
    - All the usual imaging/scanning modes - Frame/Line/Spot...
    - Mag : 50 X - 20 MX, Resolution BF STEM: ~3 Å, HADF ~1.85 Å
  - TEM: Transmission Electron Microscopy
    - Condenser/Objective Configuration-
      - Parallel probes down to ~ 100 Å, Convergent probes down to ~ 2-3 Å
    - Mag : 10 kX - 900 kX, Resolution: BF Pt/Pt : <2.8 Å, BF Lattice : < 3.4 Å
  - SEM: Scanning Electron Microscopy
  - TSEM: Transmission Scanning Electron Microscopy
  - TSED: Transmission Scanning Electron Diffraction
  - CBED: Convergent Beam Electron Diffraction, 8 aperture positions!
    - CL: 10 mm - 9 m , Distortion Free Mode: 10-50 mm
  - SAED: Selected Area Electron Diffraction : Only at > 30 kX
  - RHEED: Reflection High Energy Electron Diffraction
- **Side Entry Goniometer Stages**
  - Goniometer Stage capable of tilting to $\pm 85^{\circ}$ for special applications without hitting pole piece
  - RT Double Tilt Beryllium: $\pm 60^{\circ}, \pm 45^{\circ}$ Primary/Secondary
  - LN$_2$ Cooled Double Tilt Be Stage: $\pm 60^{\circ}, \pm 45^{\circ}$ Primary/Secondary , -165° C to +100 $^{\circ}$C
  - Single Tilt Heating Stage: $\pm 45^{\circ}$ Primary, RT to + 1000° C
- **Analytical SubSystems on the E/O Column**
  - XEDS - Windowless Detector @ 0.3 sR retractable along a line-of-sight to specimen
  - EELS - Serial/Parallel modes
  - AES - Hemispherical Analyzer on Objective Lens and with Parallelizer Configuration
  - Imaging - Two independent frame stores

- **Specimen Preparation Chamber**
  - Main AirLock and Transfer Cell with Sputter Cleaning Facilities
  - High Pressure/Temperature Gas Reaction Cell
  - Vacuum Transfer Vessel
  - Thin Film Evaporation Chamber
  - Mini-SIMS system - Gallium LMIS, Quad Mass Analyzer
  - RV LEED
  - ANL MultiPort Station for development work.
- **Computer Control**
  - PC Compatible 386 for Basic System Operation and Control
  - PC Compatible 286 for Frame Store and imaging
- **Special Objective Lens Port Configuration**
  - 7 Experimental Ports on Objective Lens for Analytical Equipment
  - 3 Additional Ports for Electrical Feedthrus etc...

MEDIUM VOLTAGE AEM: POTENTIAL AND PERFORMANCE

J. J. Hren

During the middle and late 1970s, analytical electron microscopy (AEM) was born for practical purposes and suffered the normal accompanying pains.[1-5] Not all cures to the recognized problems were in place when applications began pouring out, but working solutions were quickly developed wherever feasible (e.g., for contamination, etching, and high x-ray backgrounds), while others awaited time-consuming and costly improvements in instrumentation (e.g., higher voltage, better vacuum) or required breakthroughs (parallel detector for EELS, field-emission sources). The community of users spoke clearly to the manufacturers of their needs in small, directed meetings and this input was reinforced annually at the EMSA/MAS meetings. Several suggested improvements required major investments by manufacturers: better vacuums, smaller probes, better detectors, and higher voltages. The present session addresses specifically the effects of moderately higher voltage on AEM; however, the effects of related improvements are included where appropriate. The manufacturers have responded by making many of the suggested improvements and users have gathered a reasonable amount of new data. It is timely to ask: where do we stand? Were the projected improvements accurate assessments? What surprises were encountered? What are the important remaining needs?

Promise of Higher Voltage

Let us begin by stating the projected benefits of voltages higher than 100 kV and limiting our discussion to microscopes with accelerating voltages of 200-400 kV, which we define as medium voltage. Electron microscopes with this range of accelerating voltage remain reasonably compact, require only modest space preparation or user protection, use about the same peripheral instrumentation, and cost only a few times the price of 100kV instruments. In short, they can be purchased and used by many individuals or small groups and do not require a large staff to maintain. What about the major benefits of higher voltage to users? The number one gain will always be the ability to achieve useful data from thicker specimens. All other issues are esoteric to most users. Even though we shall touch on specimen effects only indirectly, analyzing thicker specimens remains the true *raison d'être* for medium voltage electron microscopes. Given that we want

J. J. Hren is at the Department of Materials Science and Engineering, North Carolina State University, Raleigh, NC 27695-7907. The author gratefully acknowledges helpful discussions with T. S. Headley, C. R. Hills, and J. R. Michael of Sandia National Laboratories.

to examine as thick a specimen as we can, what are the other benefits (disadvantages) of using voltages of 200-400 kV for AEM? We confine the discussion to the following topics:

X ray spectrometry and EELS
Microdiffraction
Specimen effects
Z contrasts

EDS

The bread and butter of AEM remains x-ray energy-dispersive measurements. Have higher voltages helped or hurt, how much, and why? There is still not a great deal of systematic data, but enough to give us some confidence to answer in a very positive way. In general, higher voltage has meant a better peak-to-background and better spatial resolution, and has made it possible to examine significantly thicker samples. Many of the quantitative indicators are reported in the present volume.[6] One especially positive result is that as voltage increases, spatial resolution for EDS is limited primarily by probe size. This is a somewhat unexpected but welcome result, especially when accompanied by the improvement in peak/background.

There are some negative consequences of increased voltage for EDS as well. The absolute mass sensitivity decreases with increasing voltage (primarily because of the decreased cross section) and the displacement threshold for many transition elements is exceeded at the upper end of medium voltage. In some cases, elements can be ejected from the specimen through its exit surface or stimulated to migrate away once they are displaced from their proper sites. Still, these are difficulties that can be partially overcome, e.g., by specimen cooling or selection of an optimum voltage. On balance, the results of measurements so far are good news; in fact, better than anticipated. In addition, improvements have come about in detectors and software, so the net result is highly favorable toward medium voltage SEM. In fact, with the use of ultrathin windows (or no windows), EDS has become somewhat competitive with EELS for light-element analysis.

EELS

Use of medium voltage has been beneficial to EELS as well. In fact, the absolute and relative gains in the utility of EELS because of higher voltages will be greater than EDS. Several papers at this meeting address these issues and the reader is referred to them. The bottom line is the ability to obtain useful data from a thicker specimen, but since the useful thickness at 100 kV is often only a fraction of that for EDS, higher voltages make

many more specimens accessible to analysis by EELS. Improved electron sources (brighter with less energy spread), much better spectrometers (parallel with improved energy resolution), and an ever-growing supply of reliable fundamental data, and data handling, make EELS more and more useful with time. Of course light-element analysis will remain an important capability, but rapid compositional mapping and various types of energy-filtered imaging will become increasingly important uses of EELS. There are other complementary advantages over EDS as well, so that EELS is taking its place more and more with EDS, partially because of the accessibility of higher voltages. As with EDS, absolute sensitivity in EELS is reduced with increasing voltage and radiation effects in the specimen increase. These are the prices exacted and we can compensate only partially. Optimization of the accelerating voltage to the specimen is one useful control.

Microdiffraction

Prospective advantages of the use of higher voltages for microdiffraction are marginal or even negative, on balance. The obvious gain in ability to penetrate thicker specimens is a marginal gain for diffraction. On the other hand, the larger radius of the Ewald sphere (and smaller convergence angle) makes it more difficult to obtain CBED data from higher-order Laue zones, and the increasing rate of radiation damage degrades the fine structure in diffraction patterns rapidly. On balance, it is fair to say increasing voltage per se gives few advantages. However, there is a related capability that is quite useful and could be routinely included. A *precisely variable* voltage (which can be conveniently measured) offers real advantages to CBED and microdiffraction in general.

Other Factors

A few less obvious points need to be made. Since thicker specimens can be analyzed with increased voltage, specimen preparation not only becomes easier, but significantly greater areas (volumes) of the specimen become amenable to analysis. In turn, this capability improves sampling procedures; that is, it makes the data statistically more significant and thereby makes comparisons with bulk properties more meaningful. It is hard to overstate the importance of this advantage. True, increased radiation damage is a price paid for higher voltages; but that can be minimized. For example, one can pick a voltage that minimizes damage when there are distinct thresholds, and doses can always be minimized. Parallel EELS provides an obviously useful way to minimize damage. Specimens can be cooled so as to minimize at least elemental migration and etching in the irradiated volume.

On balance, increasing the voltage for AEM is a very positive development, and it seems clear that negative effects can be minimized by choice of optimum operating conditions. It is timely to add an obvious reminder: careless specimen preparation will yield useless information no matter how optimized everything else may be. Users might well consider at least overseeing specimen preparation procedures periodically, especially if they consider the effort put into AEM measurements following specimen preparation.

Z-contrast

The recent development of Z contrast deserves special attention in the context of medium voltage electron microscopy.[7-8] Z contrast is best performed in the STEM mode, which in itself raises an additional issue: STEM or CTEM for medium voltage AEM? STEM is advantageous for Z contrast because the efficient collection of high-angle elastically scattered electrons is required, since they are proportional to the atomic number squared. High-angle collection is very efficiently performed in the STEM mode with an annular detector. Furthermore, inelastically scattered electrons can be detected simultaneously (e.g., for parallel EELS). With a field-emission source and an ultrahigh vacuum system, the effective spatial resolution of Z-contrast mode in the STEM mode is comparable to (or perhaps even better than) conventional HREM. Furthermore, interpretation of the contrast from high-resolution images seems to be significantly simpler than conventional HREM! Thus it seems possible to obtain an image with atomic resolution in which composition (Z) can be simultaneously mapped. So far extensive data have been published at 100 kV, but imminent results from 300 kV should provide a crucial test of anticipated improvements in resolving power. Does this assignment imply a crucial advantage of STEM over TEM for the future? The question is more than academic, as it was once thought to be.

Further Needs

Finally, some specific points about important gaps in present instrumentation should be made. These missing capabilities affect our ability to take full advantage of medium-voltage AEM. First, it should be clear that a conveniently adjustable voltage that can be precisely measured would be of considerable value. Second, and in parallel, the operational parameters of the microscope should be optimized without direct operator intervention. We should not have to rely on an individual's peculiarities and eyesight. Test images can be stored and digitally analyzed, and suitable corrections can be made with no subjective decisions required. The operator should be free to concentrate on getting useful data from the specimen, data that should not be variable with the operator. A third related improvement needed is the elimination of photographic material from the vacuum chamber. The time has finally arrived when electronic imaging can more than compete. Not only will the vacuum

benefit, but photographs will routinely become recognized as quantitative data, a psychological breakthrough of considerable importance to physicists. Fourth, STEM vs CTEM. In the case of Z contrast, the advantage of STEM is clear. Perhaps this advantage alone is a sufficient incentive to include STEM (along with an intense point source and a sufficiently good vacuum) in every medium-voltage electron microscope. A further advantage of STEM, often forgotten, is the potential for considerably reduced specimen damage *if* the signal collected is minimized (i.e., only the potential that is needed). This advantage becomes more significant as voltage is raised and radiation effects become more critical. In addition, with the evolution of parallel EELS, STEM imaging takes on new power.

Summary

Medium voltage AEM has already been shown to offer considerable advantages over earlier 100kV electron microscopes. For EDS and EELS the advantages of medium voltage are overwhelming. For microdiffraction, there is little advantage. The newly developed technique of Z contrast in the STEM mode seems to be a powerful addition to AEM, where medium voltage offers crucial advantages. Still needed in newer instruments are a variable accelerating voltage with digitally optimized electron optical control and digital imaging. Point electron sources and ultrahigh vacuum remain desirable objectives. The biggest advantage of higher voltages in AEM remains the ability to analyze thicker specimens, but only if specimen preparation is performed intelligently and preparation methods are constantly reviewed.

References

1. J. Silcox et al., Eds., *Analytical Electron Microscopy: Report of Specialist Workshop*, Cornell University, 1976.

2. J. A. Venables, Ed., *Developments in Electron Microscopy and Analysis*, New York: Academic Press, 1976.

3. J. A. Chandler, *X-ray Microanalysis in the Electron Microscope*, New York: Elsevier, 1977.

4. J. Silcox et al., Eds., *Analytical Electron Microscopy: Proceedings of Second Workshop*, Cornell University, 1978.

5. J. J. Hren, J. I. Goldstein, and D. C. Joy, Eds., *Introduction to Analytical Electron Microscopy*, New York: Plenum, 1979.

6. Present volume, session on Medium-voltage AEM, papers by Romig et al., Krivanek, Howitt, and Zaluzec.

7. S. J. Pennycook and D. E. Jessin, *Phys. Rev. Lett.* 64: 938, 1990.

8. D. E. Jesson and S. J. Pennycook, "High Z-contrast imaging or semiconductor interfaces," *MPS Bulletin*, March 1991, 34.

TOWARD STRUCTURE DETERMINATION USING CONVERGENT-BEAM ELECTRON DIFFRACTION

Michiyoshi Tanaka and Kenji Tsuda

Electron diffraction has not been useful to determine crystal structures reliably because of strong dynamical diffraction effects. However, convergent-beam electron diffraction (CBED) has a potential as a method of crystal structure analysis, because it can obtain diffraction patterns from such small specimen areas as to have a uniform thickness and no bending. Then, the intensity in CBED patterns can be compared with that obtained by dynamical calculation. If the crystal structure analysis due to CBED works, the method can be applied not only to perfect crystals but also to materials in which the crystal structure locally changes.

Vincent et al.[1] first applied the CBED method to determine atomic positions of AuBeAs, in which the positional parameters were determined by fitting the intensities of higher-order Laue-zone (HOLZ) reflections calculated under the quasikinematical approximation with the experimental intensities. We determined the rotation angle of the oxygen octahedron and the isotropic Debye-Waller factor of the oxygen ions in the low-temperature phase of $SrTiO_3$ by fitting HOLZ reflection intensities with those obtained by fully dynamical calculation.[2] Now we aim to determine the atomic positions of the intermediate phase of hexagonal $BaTiO_3$.

Analysis Procedure

We usually take high symmetry zone-axis patterns. The thickness of the specimen area used is necessary for fitting the calculated intensities with the observed ones. The zeroth-order Laue-zone (ZOLZ) reflection patterns are used to find the thickness. The accelerating voltage was determined in advance by use of a standard specimen of Si. HOLZ reflections are used to determine positional parameters because they are more sensitive to those parameters than ZOLZ reflections. The Debye-Waller factors are determined by use of the 1st and 2nd order Laue-zone reflections. We need CBED patterns taken at three different orientations to determine three components of an atomic coordinate. The number of independent reflections with respect to the symmetry of the CBED pattern is usually 20-40. The positional parameters and Debye-Waller factors are determined by fitting HOLZ reflection intensities with dynamically calculated ones using the nonlinear least square method (a modified Marquardt method). We indicate some important points for conducting structure analysis by use of CBED.

Dynamical Calculation

Due to the decrease in the computing cost of big computers, many a beam dynamical calculation is getting easier. Furthermore, such calculation can be also carried out by a laboratory-use engineering-work-station (EWS) at the cost of a little more time. The intensities of HOLZ reflections in a zone-axis CBED pattern barely converge when they are calculated with more than a hundred beams. In our experience, even for HOLZ reflections, fully dynamical calculation is necessary; a kinematical approximation to HOLZ reflections does not give the correct intensities of the reflections, even if ZOLZ reflections are calculated dynamically. To reduce the number of beams needed for the calculation, it is favorable to use lower accelerating voltages of the incident electron beam, for instance; 60 instead of 200 kV. When we use a thick specimen, HOLZ reflections do not show a uniform intensity along the azimuthal direction, but a complicated intensity change due to a strong interaction between HOLZ reflections. Thus, it is better to use a specimen <50 nm thick.

Imaging Plates

To determine atomic positions precisely, we have to obtain correct experimental intensities. CBED patterns usually have a wide dynamic range in intensity. However, it is quite difficult to record CBED intensities correctly with standard negative films due to their nonlinear properties and narrow dynamic range. Figure 1 shows the relation between the electron dose and the recorded intensity for a film and an imaging plate (IP). The excellence of IP in the linearity and the wide dynamic range is quite clear. Figure 2(a) shows a CBED pattern of FeS_2, which was taken by an IP and printed on photographic paper. Owing to the narrow dynamic range and nonlinearity of the photographic paper, the intensities in strong reflection disks are oversaturated. The same occurs in the case of negative films. Figure 2(b) shows a CBED pattern of FeS_2 recorded on the IP and processed using a comb-shaped filter. It is seen that the disks in Fig. 2(b) corresponding to oversaturated disks in Fig. 2(a) show an intensity gradient, indicating a wide dynamic range of IP. We record CBED patterns for crystal structure analysis using the imaging plate. A disadvantage of the IP is the need to have a large pixel size (80×80 µm) in comparison with films. However, this disadvantage is of no concern in the case of CBED, although the pixel size is an important factor by which to judge the superiority of the IP in the case of electron microscope images.

The authors are at the Research Institute for Scientific Measurements, Tohoku University, Katahira 2-1-1, Aobaku, Sendal 980 Japan.

Energy Filtering

To obtain accurate experimental data, it is a question how to subtract background intensity. It is not uniform on CBED patterns. The best way to remove background intensity is to apply energy filtering. Figure 3(a) shows an energy spectrum of FeS_2 without filtering. The pattern is smeared due to high background. Figure 3(c) shows an energy-filtered CBED pattern of FeS_2 formed by electrons with an energy spread of 7.8 eV. Background is greatly reduced and the details of the pattern can be clearly seen. It has been said that phonon scattering is worse than plasmon scattering because the former causes the interband transition but the latter the intraband transition. However, the present experiment indicates that it is essential to remove plasmon scattering to decrease background and that phonon scattering appears to spoil the patterns very little. The use of electrons with a smaller energy spread than the zero loss energy spread does not produce better CBED patterns but only needs a longer exposure due to the loss of intensity. Thus, energy filtering is quite effective in removing background intensity and obtaining data of good quality for comparison with dynamical calculation. It is desirable to develop an energy-filtering electron microscope that promises negligible aberration even at high scattering angles.

References

1. R. Vincent, D. M. Bird, and J. W. Steeds, "Structure of AuGeAs determined by convergent-beam electron diffraction," *Phil. Mag.* A50: 745 and 765, 1984.
2. M. Tanaka and K. Tsuda, "Determination of positional parameters by convergent-beam electron diffraction," *Proc. XII ICEM*, 1990, 518.
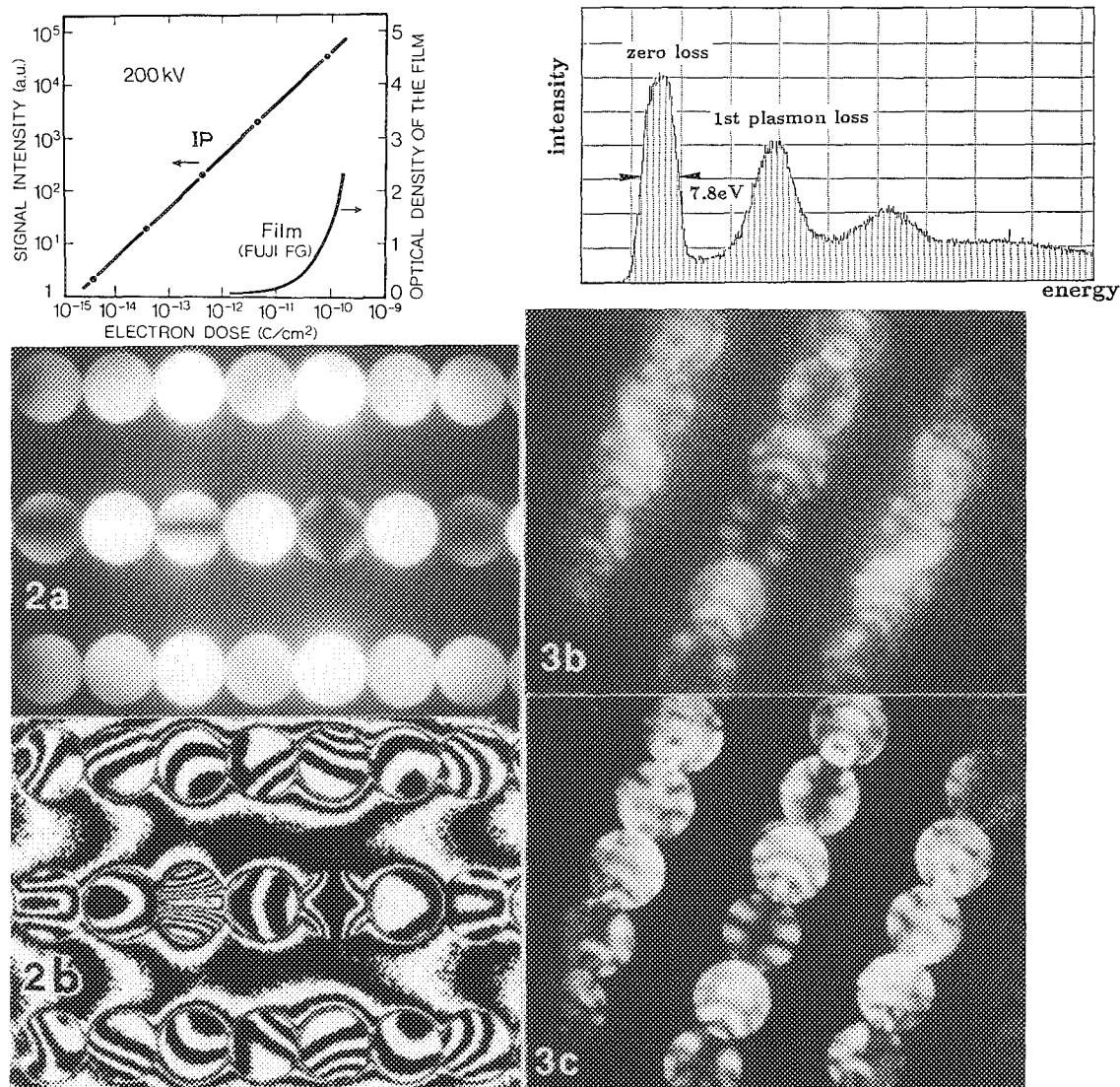
FIG. 1.--Relation between electron dose and signal intensity of imaging plate and Fuji FG film.
FIG. 2.--CBED pattern of FeS_2 recorded by IP: (a) photographic print from original data, (b) photographic print after processing with use of comb filter.
FIG. 3.--(a) Energy spectrum of FeS_2. (b) CBED pattern of FeS_2 without energy filtering. (c) CBED patterns of FeS_2 formed by zero loss spectrum of 7.8eV energy spread.

AUTOMATED STRUCTURE FACTOR REFINEMENT FROM ENERGY-FILTERED CONVERGENT-BEAM ELECTRON DIFFRACTION DATA

J. M. Zuo and J. C. H. Spence

We have automated the process of measuring structure factors, absorption coefficients, and thickness from energy-filtered convergent-beam electron diffraction data in the systematics orientation by defining a best fit parameter χ^2 and using an optimization routine to find the lowest χ^2--the best fit. By automating this process, we achieve the following: (1) speed up the whole process, (2) avoid systematic errors due to subjectivity, and (3) simplify the method. In this report we briefly describe the automation procedure and some applications. For a complete description, see Ref. 1.

The Definition of χ^2 and the Automation Procedure

We define a χ^2 similar to the standard definition of the goodness of fit parameter defined in statistics; for example, see Ref. 2.

$$\chi^2 = \sum_i \frac{f_i}{\sigma_i^2}(1_i^{theory} - 1_i^{exp}) \qquad (1)$$

The f_i is a weight coefficient, which can be adjusted to increase the importance of certain intensity points in the χ^2 that are sensitive to particular parameters. The σ_i^2 is the variance, which can be found from repeated measurements, or by

$$\sigma_i^2 = 1_i^{exp} \qquad (2)$$

assuming Poisson statistics of electron counting and DQE = 1. The automation program (called REFINE/CB) is shown as a simplified flow chart in Fig. 1. The experimental intensity data are assumed as energy-filtered parallel line scans along the systematics direction (Fig. 2). The scan coordinates are the coordinates of points 1, 2, and 3 of Fig. 2 in units of the two basic vectors g and h. The parameters that can be refined by this program are structure factor amplitudes and phases, absorption coefficients and phases, and thickness. For the parameter to be refined, an initial nonzero value is required. The initial structure factors may be calculated from spherical atoms or ions tabulated in the international tables for x-ray crystallography.[3] The initial absorption coefficients may be calcu-

lated from entered Debye-Waller factors by use of the Einstein model.[4,5] In our program the subroutine ATOM provided by King and Bird is used to calculate the absorption potential. The theoretical intensity is calculated by the Bloch wave method[6] and perturbation theory.[7] Perturbation theory is used when the change in the structure factors and absorption coefficients are smaller than a previously entered limit. The use of the perturbation method results in a saving of computing time proportional to the number of beams included in the calculation. The optimization method used in this program is the simplex method (subroutine AMOEBA in Numerical Recipes). We find that this optimization routine is more dynamic than other routines listed, although the convergence to the minimum is slower. That is less of a problem because of the use of perturbation method. The error in the determination of the parameters in the refinement is found by the standard method[8]

$$\sigma_{ak}^2 = \frac{\chi^2}{n - p} C_{kk}^{-1} \qquad (3)$$

where n is the number of data points, p the number of parameters, and the C_{kk}^{-1} is the kth diagonal term of the inverse matrix of C, which is defined by

$$C_{kl} = \sum_{i=1}^{n} \frac{f_i}{\sigma_i^2} \frac{\partial I_i}{\partial a_k} \frac{\partial I_i}{\partial a_l} \qquad (4)$$

A listing of this program can be found in a forthcoming book.[9]

The Refinement of Low-order Structure Factors in MgO: An Example

We have applied this program to the refinement of MgO (200) systematics. Figure 3 shows the CBED pattern used. It was obtained at 120 kV from an MgO smoke crystal on a Philips EM400 electron microscope. The path of scan is also shown, in which the pattern was deflected under computer control over the entrance aperture of a Gatan Model 607 serial ELS spectrometer. An energy window of 5 eV was placed around the zero loss peak. The ELS entrance aperture size was 1 mm and the camera length was 6500 mm (which together give an angular resolution of 0.15 mRad). The refinement was carried out in the following steps:

1. The incident beam direction was measured from the Kikuchi line features in the diffraction pattern according to Fig. 2.
2. The initial thickness refinement was performed using 9 systematic beams. The thickness
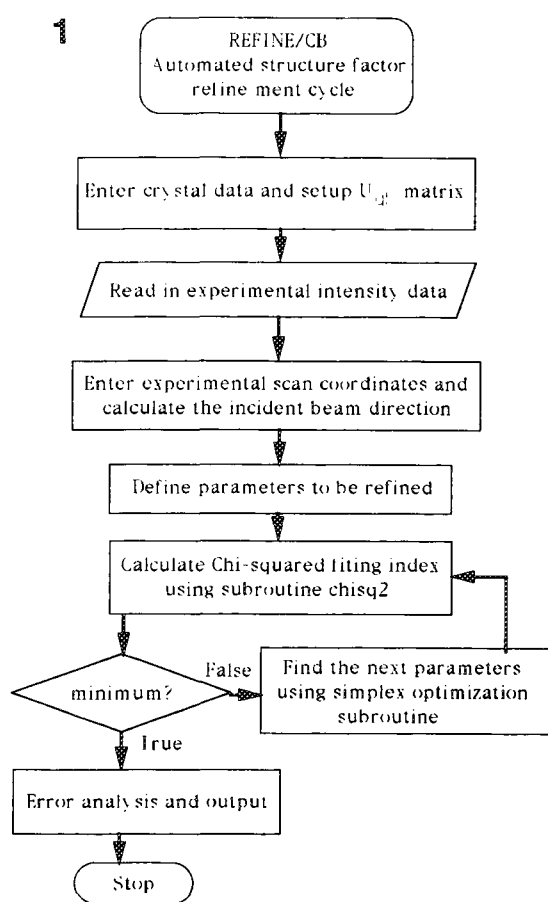
FIG. 1.--Simplified flow chart of automated re-finement program.
FIG. 2.--Method used to define incident beam direction.
FIG. 3.--Experimental CBED pattern used for this refinement. Line AB shows line scan trace.
FIG. 4.--Final refinement. Comparison of cal-culation (continuous line) and experimental data (crosses). Difference between them is shown below.

was found to be 80 nm. Structure factors from neutral atoms were used, together with absorp-tion coefficients from the "atom" subroutine of D. Bird. The starting values were therefore $U(200) = 0.0592$, $U'(200) = 0.0007632$, $U(400) = 0.02533$, $U'(400) = 0.000585$.

3. The incident beam direction was varied manually within the error range of measurement (see step 1 above) until the lowest χ^2 was found, and until no systematic error features (such as an as asymmetric peak) appeared in the difference plot.

4. An initial structure factor refinement was performed using 9 systematic beams, starting with the parameters obtained in step 2. This took about 17 min of cpu time on our VAXsta-tion 3200 computer. The results were $U(200) = 0.00163$, $U'(200) = 0.00163$, $U(400) = 0.02535$, $U'(400) = 0.000577$ and thickness 81.02 nm.

5. The final refinement was performed with 33 beams, including HOLZ beams. A weight win-dow was used with $f = 1.0$ for each point on the rocking curve except point 2 and 3 (Fig. 4),
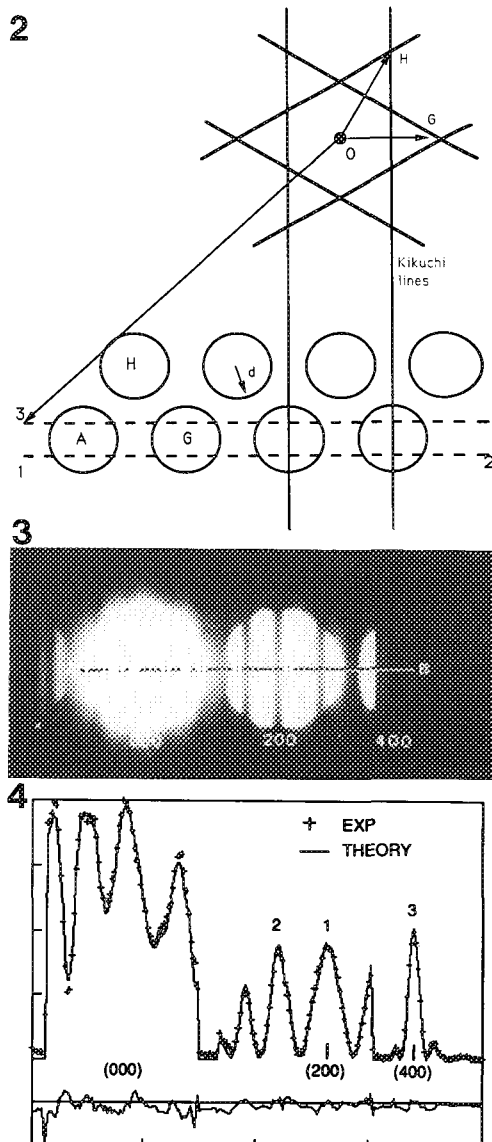
where $f = 20.0$. Point 1 was used for normal-ization. The values obtained in the last step were used as the initial values. The results were $U(200) = 0.05847 \pm 0.00051$, $U'(200) = 0.00158 \pm 0.00014$, $U(400) = 0.02484 \pm 0.00096$, $U'(400) = 0.00059 \pm 0.00028$, $t = 808.0 \pm 5.4$.

This process took about 6 h of cpu time without the use of perturbation and 0.5 h with the use of perturbation.

Conclusions

We have demonstrated that the automated re-finement of low order structure factors by quantitative CBED is possible with the use of energy-filtered data. A similar conclusion was reached in Ref. 10, which described the use of the steepest decent method for the measure-ment of structure factors in a nonsystematic case. We have concentrated on the one-dimen-sional systematic case in this report. A "goodness of fit" index has been defined, and the propagation of errors through the analysis

148

has been analyzed. The use of perturbation methods is found to result in large time savings.

References

1. J. M. Zuo and J. C. H. Spence, *Ultramicroscopy* 1991 (submitted).
2. P. R. Bevington, *Data Reduction and Error Analysis for the Physical Science*, New York: Springer-Verlag, 1976.
3. *International Tables for X-ray Crystallography*, Birmingham, England: Kynoch Press, 1972.
4. Q. A. King and D. Bird, *Acta Cryst.* A46: 202, 1990.
5. A. Weickenmeier, *Proc. XIIth ICEM*, San Francisco Press, 2: 536, 1990.
6. J. M. Zuo, K. Gjønnes, and J. C. H. Spence, *J. Electr. Micros. Technique* 12: 29, 1989.
7. J. M. Zuo, *Acta Cryst.* 1991 (in press).
8. J. R. Wolberg, *Prediction Analysis*, Princeton: Van Nostrand, 1967, p. 60, Eq. (3.10.40).
9. J. M. Cowley et al., Eds., *Techniques of Transmission Electron Diffraction*, Oxford University Press, 1991.
10. K. Marthinsen, R. Hoier, and L. Bakken, *Proc. XIIth ICEM*, 2: 492, 1990.

INELASTIC ELECTRON SCATTERING AT RHEED ENERGIES

H. A. Atwater, C. C. Ahn, S. Nikzad, and P. A. Crozier

Reflection high-energy electron diffraction (RHEED) has assumed increased importance as an analytical technique for the study of surfaces, principally because of its great compatibility with typical requirements for epitaxial film growth, such as long working distance and compatibility with deposition sources. RHEED is the most widely employed in situ probe during film growth molecular beam epitaxy (MBE), and although it is sensitive to surface crystallographic structure and morphology, it cannot directly provide surface chemical information.

Reflection electron energy loss spectroscopy (REELS) can be combined with RHEED to provide chemical information and retains all the advantages of RHEED for application to analysis of epitaxial growth, as recent studies have shown.[1,2] In these recent experiments, which represented the first attempt to perform spectral analysis of reflected and diffracted high-energy electron beams from clean and growing crystal surfaces, it was found that REELS is highly surface sensitive, and is also capable of in situ quantitative compositional analysis of epitaxial alloy films. More fundamentally, RHEED and REELS combined with MBE also afford a unique opportunity to examine inelastic scattering processes for clean crystal surfaces and thin epitaxial overlayers.

In this paper, several inelastic RHEED phenomena are discussed, including (i) evidence for increased core loss intensity due to surface channeling of high-energy electrons along high-symmetry azimuths in thin epitaxial films of Ge on Si (001); (ii) the roles of beam incidence angle and surface resonant scattering in determining core loss surface sensitivity; and (iii) the ratio of elastic to total inelastic scattering at Ge (001) surfaces for resonant and nonresonant scattering. We discuss inelastic electron scattering at typical RHEED energies in two experimental contexts: first, a conventional RHEED electron gun used for in situ analysis during MBE, and second, a conventional electron microscope.

In order to elucidate the role of electron channeling or surface resonant scattering in REELS, we have analyzed core level signals

H. A. Atwater, C. C. Ahn, and S. Nikzad are at the California Institue of Technology, Pasadena, CA 91125; P. A. Crozier is at Arizona State University, Tempe, AZ 85287.

from thin (1 monolayer) epitaxial Ge "marker" films on Si(001), using a conventional RHEED gun in an MBE system equipped with a Gatan energy-loss spectrometer mounted behind the RHEED screen. This thin-marker-layer technique is a powerful tool for analysis of the surface sensivity of REELS in resonant and nonresonant scattering, since the relative core loss yields can be measured for both a film of well-defined thickness and the substrate.

The samples used in the analysis of surface channeling and resonant scattering were 0.3nm-thick Ge films on Si(001). The Ge films were grown by MBE at a growth rate of 0.05 nm/s at T = 400 C, following growth of a 75nm-thick epitaxial Si buffer layer. Thickness was indicated by a quartz crystal thickness monitor
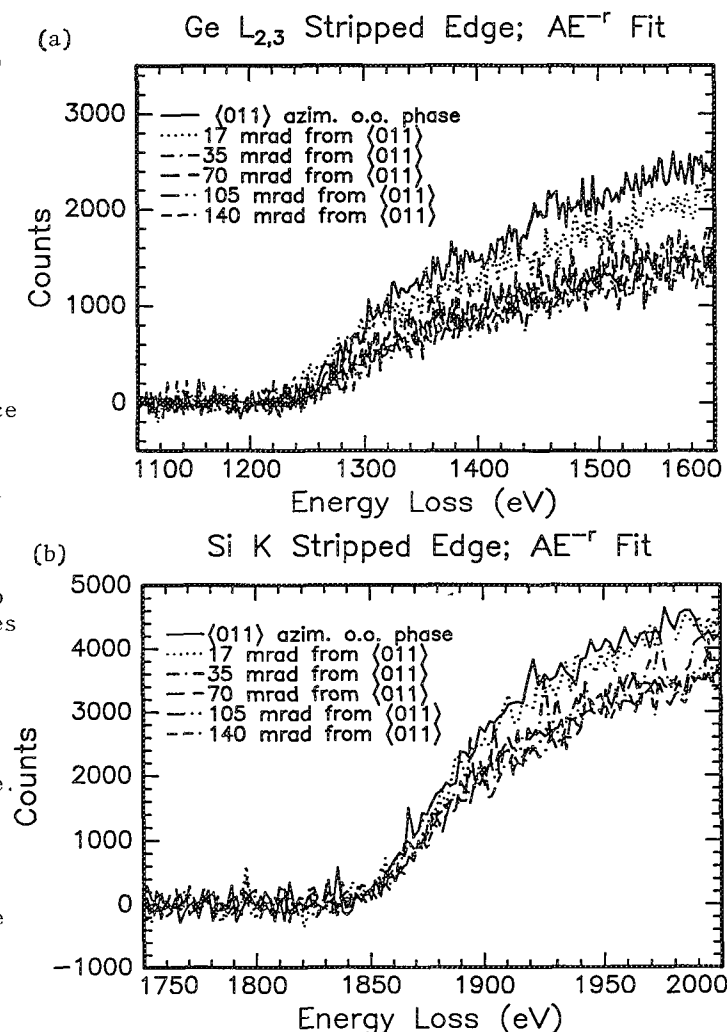
FIG. 1.--(a) Variation in Ge $L_{2,3}$ core loss intensity with azimuthal deviation from <011> for 0.3 nm Ge film on Si (001) (2 × 1); (b) Si K core loss intensity for the same sample.

previously calibrated against results from Rutherford backscattering spectrometry. The REELS scattering configuration is similar to a conventional RHEED configuration, with an electron-beam incidence tilt angle of $\phi = 10$-35 mrad. Structural analysis by reflection high-energy electron diffraction (RHEED) at 30 keV with an emission current of 30 μA was performed simultaneously with the REELS measurements. Both before and after growth, the RHEED pattern consisted of continuous Bragg rods and half-order reflections associated with a (2×1) surface reconstruction of the (001) surface, indicating a clean surface.

Figure 1(a) illustrates the variation of Ge $L_{2,3}$ core loss intensity with incident beam angle near a <011> zone axis. For these measurements the sample was inclined so that specular beam was in the out-of-phase condition, i.e., nonresonant with a Bragg reflection. Along a <011> zone axis the specular beam reflected in a $1/2(2,0,0)$ direction (15 mrad sample tilt), and this sample tilt was preserved during azimuthal rotation in the range 0-140 mrad. As the deviation of the incident beam azimuthal direction from <011> increases the Ge $L_{2,3}$ core loss intensity drops in the range 0-35 mrad. This finding suggests that the mean traveling distance of the electron beam directly along <011> is larger than at azimuths ≥ 35 mrad. For azimuthal deviations in the range 35-140 mrad, the core loss intensity remained constant, which suggests that the incident beam is not channeled in this range of orientations and that the mean traveling distance of the electron beam is nearly constant.

The variation of Si K core loss intensity from the same sample with azimuthal deviation from <011> is shown in Fig. 1(b). The Si K core loss intensity also decreases for angular deviations ≥ 35 mrad. This result is also consistent with an interpretation of surface channeling of the incident beam, since for a monolayer Ge film, the second layer contains Si. Hence Si atoms are located at the bottom of a channel formed by an axially aligned dimer row. Thus an increased mean traveling distance due to channeling betweem dimer rows on the (2×1) reconstructed (001) surface would also increase the number of Si atoms available core level excitation by the incident beam.

Surface resonance scattering of high-energy electrons has been attributed[3,4] to either of two processes. A "first kind of intensity anomaly" occurs when a Bragg spot in the RHEED pattern is coincident or in phase with the specularly reflected beam. This coincidence of specular and Bragg reflection is associated with dynamical scattering and often leads to spot splitting. A "second kind of intensity anomaly" is observed at coincidence of the specular reflection with an oblique Kikuchi line, and is indicative of a Bragg reflection for which the reflected wave propagates almost parallel to the surface.

The Ge $L_{2,3}$ and Si K core loss intensities

for the first and second intensity anomalies at a sample tilt of 35 mrad relative to non-resonant core loss intensities at 17 mrad are shown in Fig. 3(a) and (b), respectively. It is apparent that (i) both Ge $L_{2,3}$ and Si K core loss intensities are greater for an out-of-phase condition with specular beam along the $1/2(2,0,0)$ direction than for an in-phase condition with specular beam along the (2,0,0) direction; and (ii) the ratio of Ge $L_{2,3}$ to Si K core loss intensities is greater for specular beam along the $1/2(2,0,0)$ direction than along the (2,0,0) direction. A gain in surface sensitivity for (2,0,0) (30 mrad beam tilt) relative to out-of-phase scattering at the same tilt is anticipated via resonant enhancement of the core loss intensity. However, this effect is apparently small compared to the enhancement in surface sensitivity due to the smaller incident beam angle (15 mrad tilt) for $1/2(2,0,0)$ scattering.

Core-loss intensities due to the second kind of intensity anomaly are also illustrated (dotted line) for beam incidence at 70mrad azimuthal deviation from the (2,0,0) direction, which corresponds to a condition in which a total scattering intensity enhancement occurs due to the resonance of the specular beam with an oblique Kikuchi band. It is seen that in this case the Ge $L_{2,3}$:Si K intensity ratio is greater than for specular beam along the (2,0,0) direction. The enhancement in surface sensitivity is presumably due to an increase in the mean traveling distance when the specular beam is resonant with an oblique Kikuchi band.

Although much of our prior understanding of inelastic scattering in the reflection mode comes from work done in the TEM,[5] inelastic scattering from the bulk appears to dominate and obscure features of interest from the standpoint of surface sensitivity. Gains in surface sensitivity of inelastic scattering have been made by adoption of resonant scattering conditions corresponding to the second kind of intensity anomaly. However, it appears that the greatest gains in surface sensitivity come about from the use of a dedicated growth chamber with a RHEED gun, which has made it possible to control the sample surface smoothness and thus permit the use of shallower incident scattering geometries. For instance, it has made it possible to obtain core loss jump ratios[1] that are much higher than those seen in the work of Wang,[6] even though no attempt was made to fulfill the diffraction criterion of the second kind of intensity anomaly, or resonance condition. In order to discern the relationship between incidence angle and inelastic scattering in a more systematic way, we have examined the nature of low-loss features as a function of incidence angle for a Ge surface in a Philips EM430 TEM equipped with a Gatan 666 energy loss spectrometer.

Figure 4 shows 100keV RHEED patterns under parallel illumination in which the sample tilt and incidence angle are optimized so that the
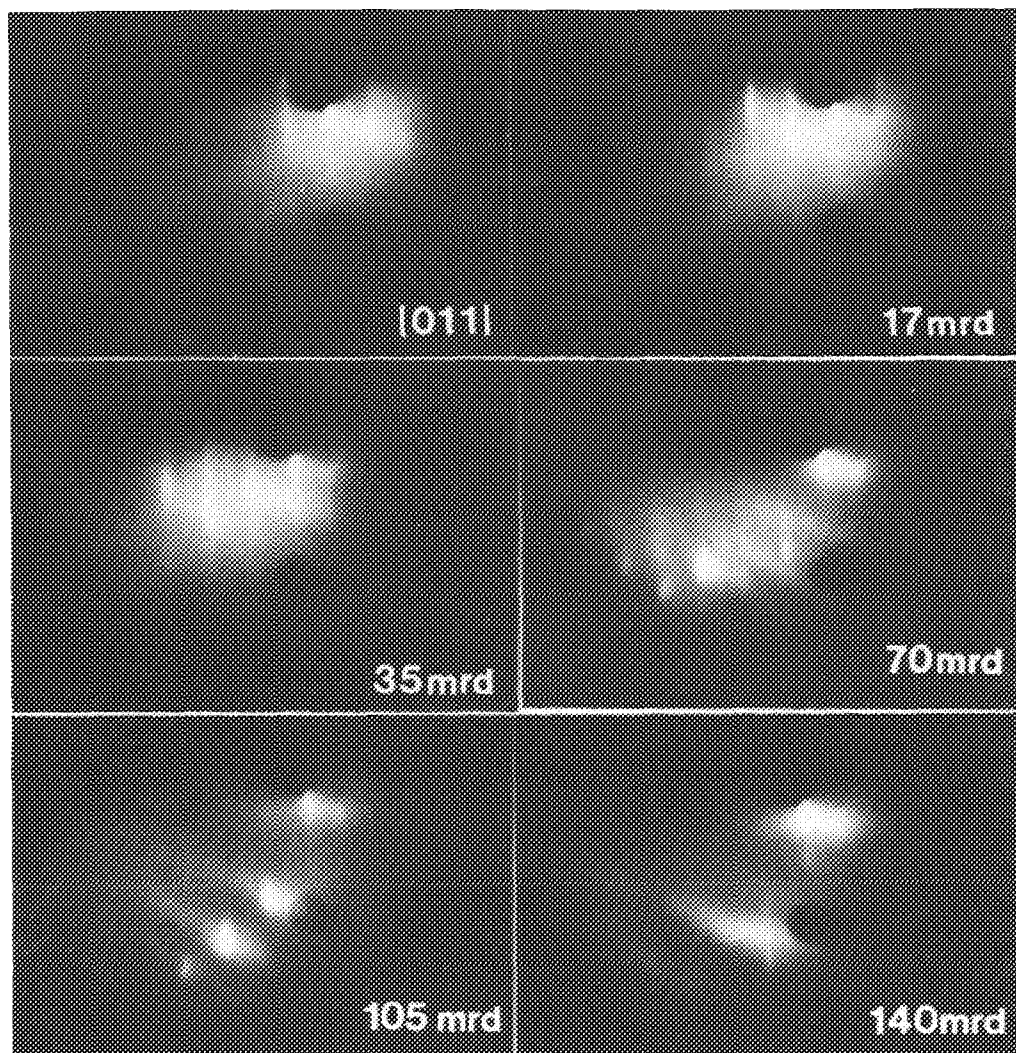
FIG. 2.--Reflection high-energy electron diffraction patterns at 30 keV for azimuthal deviations from <011> in 0-140mrad range corresponding to electron energy loss spectra in Fig. 1.
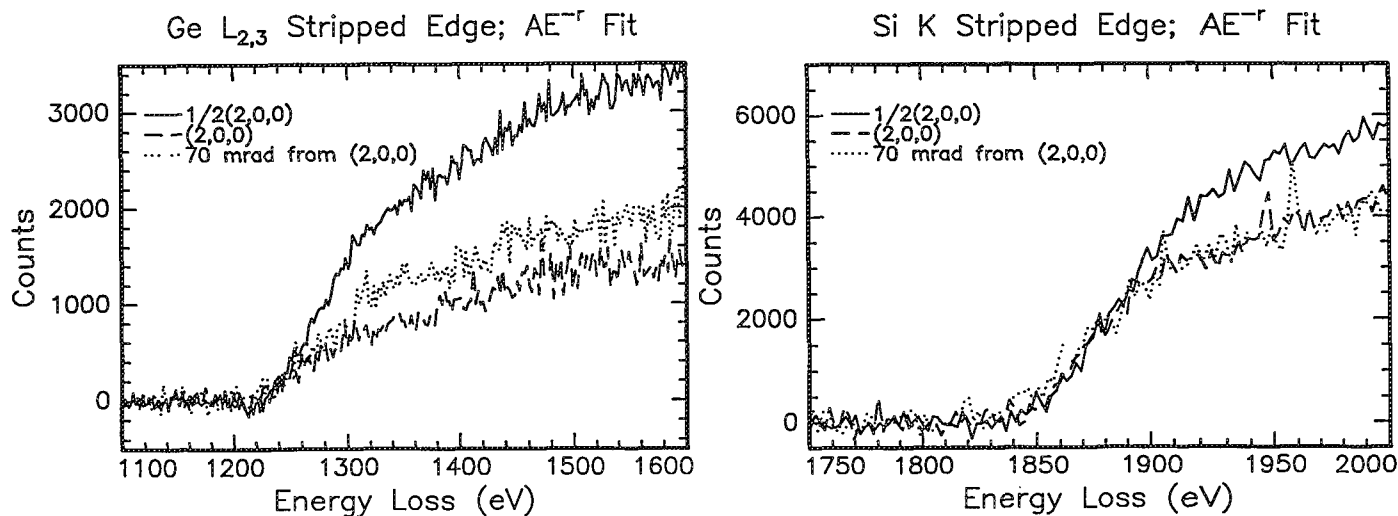
FIG. 3.--(a) Ge $L_{2,3}$ core loss intensity for out-of-phase conection with specular beam along 1/2(2,0,0) direction (solid line); in-phase condition with specular beam along (2.0.0) direction (dashed line); in-phase condition at 70 mrad azimuthal deviation from (2,0,0) direction (dotted line). (b) Si K core loss intensity for the same sample.
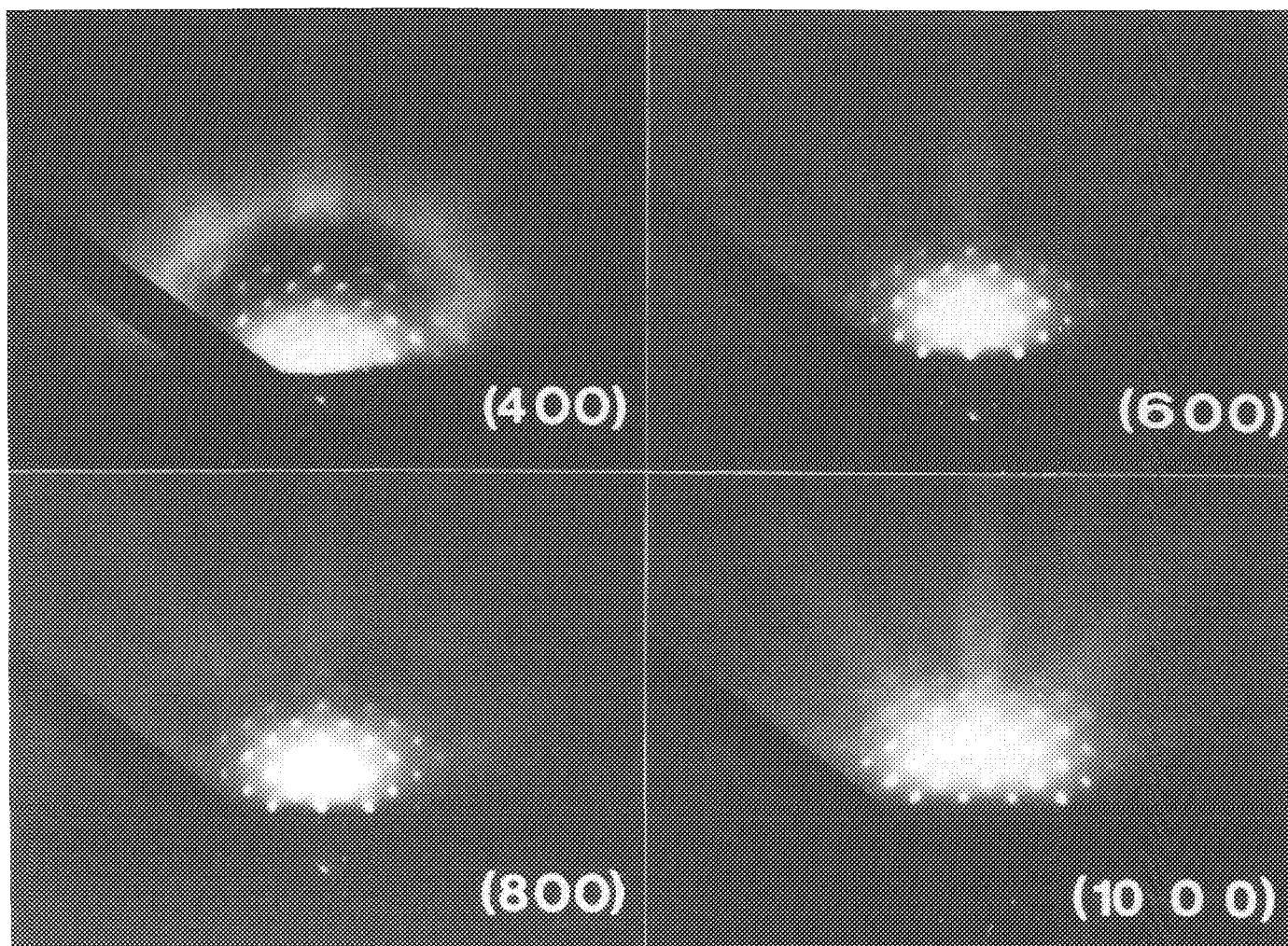
FIG. 4.--Reflection high-energy electron diffraction patterns at 100 keV for various beam tilts from the <011> azimuth corresponding to electron energy loss spectra in Fig. 5.
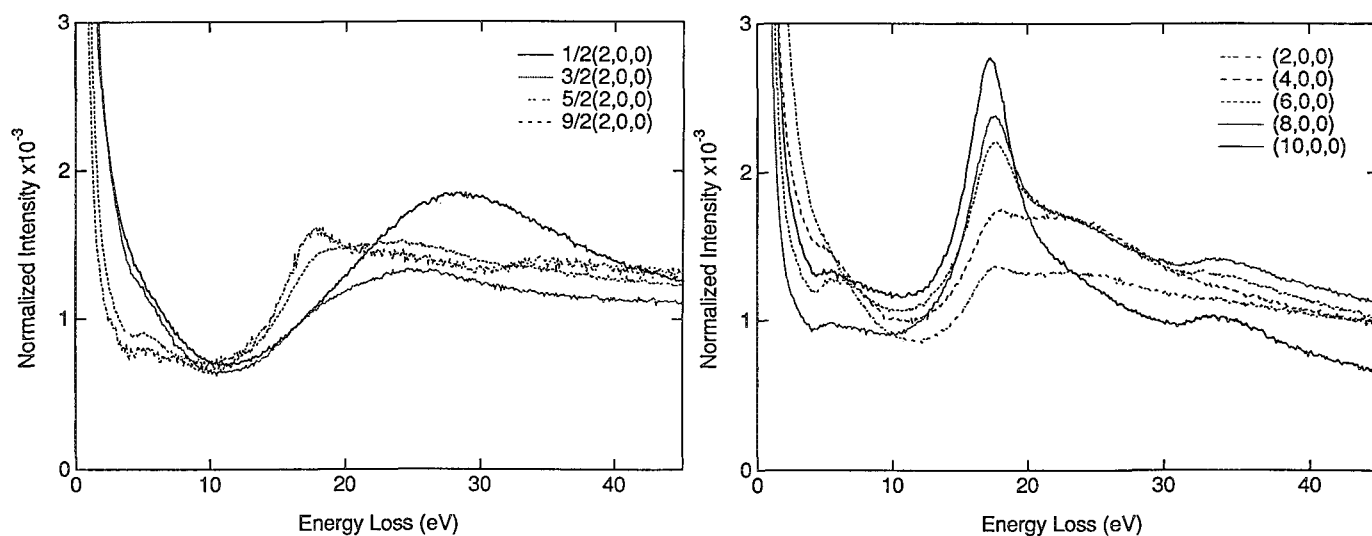
FIG. 5.--Low-loss spectra for 100keV scattering from Ge (001) surface in electron microscope for (a) out-of-phase, (b) in-phase specular beam conditions at various tilt deviations from (0,0,0) along <011> azimuth. Out-of-phase conditions occur with specular beam along 1/2(2,0,0), 3/2(s,0,0). 5/2(2,0,0), and 9/2(2,0,0); in-phase conditions are (2,0,0), (4,0,0), (6,0,0), (8,0,0), and (10,0,0).

specular reflection coincides with (4,0,0), (6,0,0), (8,0,0), and (10,0,0) reflections for a (001) Ge surface aligned along <011> direction. Low-loss spectra were obtained at the specular maximum for an entire tilt and incidence range of 1/2(2,0,0) to (10,0,0) under both in-phase conditions, where the specular beam was coincident with Bragg reflections, as well as out-of-phase conditions where the specular intensity maximum was peaked between Bragg reflections. These findings are illustrated in Fig. 5. Although Ge samples were polished and etched before insertion into the microscope, the observation of Bragg spots rather than Bragg rods in the RHEED pattern indicated that the surfaces were not as smooth as samples prepared and analyzed in our MBE chamber.

All the data in Fig. 5 are normalized to total intensity. Out-of-phase low-loss spectra are shown in Fig. 5(a). Of special note is the large broad inelastic contribution at 1/2(2,0,0), which shows that this shallow angle should generate and be sensitive to surface inelastic scattering, in this case presumably due to C contamination at the sample surface. Figure 5(b) shows low-loss data taken for the in-phase condition. Here the bulk plasmon contribution at 17 eV becomes a more prominent part of the low loss as the incidence tilt is increased to (10,0,0). Consequently, any energy-loss data taken at such steep angles would result in inelastic scattering phenomena dominated by the bulk and not the surface.

A plot of the ratio of integrated inelastic intensity to elastic intensity in the out-of-phase condition as a function of incidence tilt (Fig. 6) shows the shallowest angle to yield a large inelastic contribution, which drops almost immediately as the incidence angle is increased and then rises more slowly as the incidence angle is increased. This observation suggests that the greatest gain in surface sensitivity for inelastic scattering comes not by adoption of surface resonance conditions at relatively steep incident beam tilt angles,

but simply by adoption of shallow incident beam tilt conditions. This is of course only meaningful for clean, smooth surfaces, such as those achievable in epitaxial growth by MBE rather than in a conventional transmission electron microscope, since for surfaces that are not truly clean, inelastic scattering from surface contamination can obscure the desired results.

References

1. H. A. Atwater and C. C. Ahn, *Appl. Phys. Lett.* 58: 269, 1991.
2. C. C. Ahn, S. Nikzad, and H. A. Atwater, *Mat. Res. Soc. Symp. Proc.* (in press).
3. S. Miyake and K. Hayakawa, *Acta Cryst.* A26: 60, 1970.
4. E. G. McRae, *Rev. Mod. Phys.* 51: 541, 1979.
5. Z. L. Wang and J. M. Cowley, *Surf. Sci.* 193: 501, 1988.
6. Z. L. Wang, *Surf. Sci.* 214: 44, 1989; Z. L. Wang and R. F. Egerton, *Surf. Sci.* 205: 25, 1988.
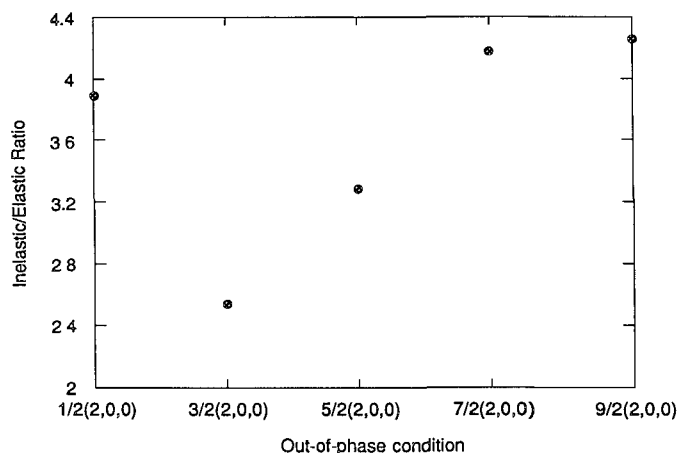
FIG. 6.--Ratio of integrated inelastic intensity to elastic intensity for out-of-phase condition as a function of beam tilt; 100keV scattering from Ge (001) surface.

STRUCTURE DETERMINATION FROM CBED PATTERNS

D. M. Bird and M. Saunders

Convergent-beam electron diffraction (CBED) has developed into a very widely used microanalytical tool for the determination of lattice parameters, crystal thickness, point and space groups, etc. Over recent years there has been an increasing amount of work addressing the question of whether complete crystal structure determination by CBED is possible. In this paper we briefly review some of the methods used to date and discuss a technique that may offer the prospect of determining a completely unknown crystal structure by inversion of a CBED pattern.

Background

The problem of determining crystal structures is essentially one of finding the Fourier components of the potential, i.e., the structure factors V_g. Several methods have been developed to measure structure factors and were nicely represented in the electron crystallography symposium of last year's ICEM conference.[1] They include:

(i) The measurement of highly accurate, low-order structure factors for known crystal structures by fitting to CBED intensities or critical voltages.[2,3] This procedure gives the valence charge distribution in the crystal and probes the bonding or details of the stoichiometry.

(ii) The measurement of kinematic or quasi-kinematic high-order structure factors in approximately known structures. It is possible to refine atomic coordinates by these methods to an accuracy of a few thousandths of an Ångstrom.[4-7]

(iii) The measurement of many approximately kinematic, medium-order structure factors using large-angle CBED patterns.[8] X-ray crystalography techniques are then used to find possible crystal structures.

(iv) The measurement of structure factor phases by detailed fitting of the intensity distribution around three or four beam diffraction situations.[9,10]

By combining these methods we are approaching the point where it will be possible to determine unknown crystal structures by CBED. The most difficult part of the process is finding an approximate structure that can then be refined. It is this step that is discussed in this paper. The method we propose is very similar to that described in Ref. 10: a set of structure factors is varied until a good match is obtained between a computed CBED pattern and the experimental

pattern. The method is still very much in the development stage and at this point no attempt is made to fit to real experimental data. Instead, other simulated patterns are taken as the idealized "experimental" data.

Simulated CBED Patterns

In order to be specific, we base our analysis entirely on the [1$\bar{1}$0] axis of GaP. However, the method is expected to be valid for any zone axis CBED pattern, including those where the structure really is unknown! The assumed crystal thickness is 250 Å and the accelerating voltage is 300 kV. The reason for working with such a thin crystal will be discussed later. We have chosen this axis because although GaP has a very simple crystal structure, it is noncentrosymmetric and the [1$\bar{1}$0] projection has a noncentric projection. The full projected potential is shown in Fig. 1(a), where we see the familiar dumb-bell pattern, with the heavier Ga atom forming a stronger potential than the P atom. GaP has been chosen so that the two atomic strings are reasonably distinct. In this sense the [1$\bar{1}$0] axis is quite a difficult case, because we must extract the phases of the structure factors as well as their amplitudes in order to reproduce the projected potential.

A computer simulation of the CBED pattern is shown in Fig. 2(a). It has been calculated by use of a many-beam program, including 43 beams (which gives a well-converged pattern) and ignoring absorption. The simulated pattern has the general form we would expect in thin crystals, with the disks beginning to show some structure, but no well-developed ring or fringe patterns. In trying to perform a fully *ab initio* fit to the CBED pattern, the full 43-beam pattern proves to be too complicated; and so for our preliminary work we have decided to concentrate on the 19-beam pattern shown in Fig. 2(b). This simpler case will enable us to try out various methods on a still moderately difficult example (there are still phases as well as amplitudes to be found), but the computer time required for testing is considerably shorter than for 43-beam calculations. The 19-beam computation is therefore taken as our ideal, "experiment" pattern, and it is this pattern that we shall try to match. It can be seen that the 19-beam pattern is not identical with the 43-beam pattern, but the general form is fairly similar. Also, in more realistic work, it will be important to include absorption, but for simplicity we ignore it in these preliminary calculations.

The process of going from the potential of Fig. 1(a) to the CBED patterns of Fig. 2 is

---

The authors are at the School of Physics, University of Bath, Bath, England BA2 7AY.

well understood, but the problems start when we think about going the other way. Before discussing our fitting method in detail, we might consider whether this inversion problem should be soluble in principle. How many structure factor amplitudes and phases are included in the many-beam computation of the 19-beam pattern of Fig. 2(b)? The 19-beam pattern goes out to the (004) disk, and so the highest-order structure factor present must be $V_{(008)}$. The structure factors that contribute are therefore (111), (002), (220), (113), (222), (004), (331), (224), (333), (115), (440), (006), (442), (335), (226), (444), (117), and (008). In principle, each has an amplitude and a phase, but in practice we can fix the origin to make some of them real. The [1$\bar{1}$0] axis has a mirror lying through the (001)
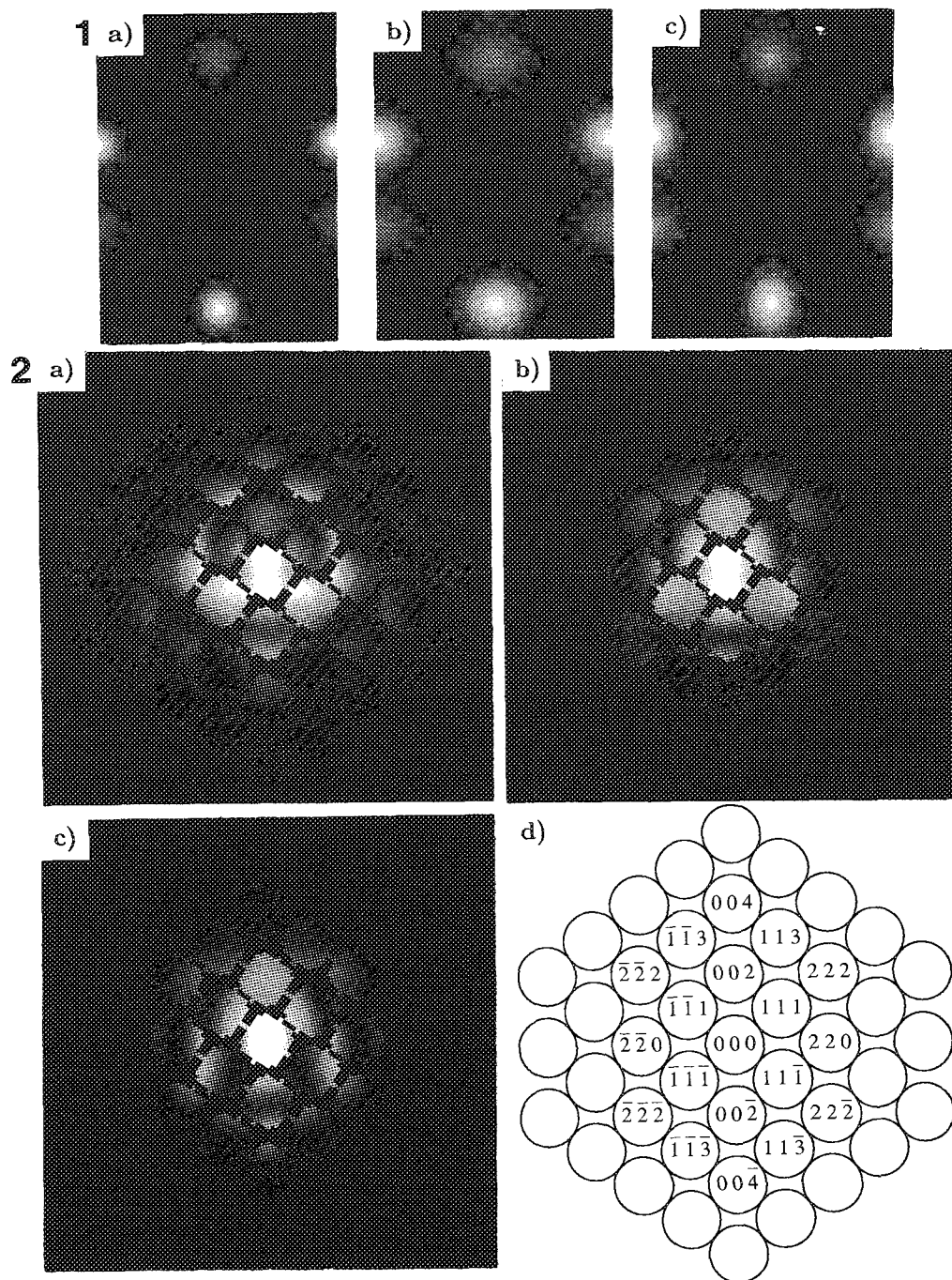
FIG. 1.--Projected potentials of GaP [1$\bar{1}$0]: (a) full potential, (b) potential using only first 6 structure factors, (c) potential derived from fitted structure factors. Note: (a) and (b) are calculated using Doyle-Turner form factors.

FIG. 2.--Simulated CBED patterns of GaP [1$\bar{1}$0]: (a) 43-beam calculation, (b) 19-beam calculation, (c) 19-beam calculation using 6 fitted structure factors. (In all cases thickness is 250 Å and accelerating voltage is 300(kV). (d) Pattern indexing.

154

disks and it makes sense to put the origin on the associated mirror in real space (Fig. 1a). This choice forces $V_{(220)}$ and $V_{(440)}$ to be *real*, although their amplitudes can still be of either sign. There is still one free parameter that gives the origin in the [001] direction; we fix it by choosing the (111) structure factor to be real, too. This choice of origin is consistent with the projected potential shown in Fig. 1(a). In principle, therefore, the full 19-beam pattern is constructed from 33 structure factor parameters; 3 structure factors have an amplitude only and the remaining 15 have an amplitude and a phase. The crystal thickness will in practice be another free parameter, but in this work we treat it as being known and fix it at 250 Å in all calculations.

Have we enough information to retrieve these 33 parameters? In principle the answer would seem to be yes. Because of the mirror in the CBED pattern there are only 10 independent disks, but each of them contains a considerable amount of information because of their internal structure. Even if there were only 4 bits of independent intensity information in each disk, it should be sufficient (there would be about 40 bits of data for 33 unknowns), and it is clear from looking at the patterns that there are considerably more than 4 independent orientations per disk. The precise amount of information present is rather difficult to quantify, but in our fitting procedures we have included 13 pixels taken uniformly over each disk, and we are happy that they represent essentially independent bits of information. The problem is therefore highly overdetermined, which implies that fitting procedures should be robust. It is also clear that by increasing the crystal thickness we could increase the amount of information in each disk, but as we shall discuss later there are good reasons for not doing so.

Although in principle we might be able to extract all 33 structural parameters from a fit to Fig. 2(b), in practice that is highly unlikely, since the higher-order structure factors will not have a great influence on the pattern and their effect will be masked by small variations in the more important, lower-order structure factors. Our experience to date indicates that it will be difficult to obtain reliable structure factors for any g-vector which does not have an associated disk in the CBED pattern we are matching. In our 19-beam example this means that we attempt to fit with only the first 6 structure factors in the above list because only these have associated disks in the "experimental" pattern of Fig. 2(b). The 33 parameters then reduce to 10: $V_{(111)}$ and $V_{(220)}$ have an amplitude only, and $V_{(002)}$ have an amplitude only, and $V_{(002)}$, $V_{(113)}$, $V_{(222)}$, and $V_{(004)}$ have an amplitude and a phase. This limited set of V_g cannot give a perfect match to the ideal pattern and so we cannot expect to reproduce the true structure factors exactly. However, if good approximations to this set of V_g could be found, the structure would effectively be solved, because these factors alone give the projected potential shown in Fig. 1(b),

which agrees well with the fully converged potential (Fig. 1a). It is clear that this method will not produce highly accurate atomic structures, but it has the potential to give approximate coordinates that can then be refined by the methods outlined above.

Methods

Our fitting procedure is very straightforward. We take an arbitrary set of the ten fitting parameters discussed above and generate a "trial" CBED pattern. The sum of squared differences between the intensities of the trial and ideal patterns is then evaluated:

$$S = \sum_{\underline{K}} \sum_{\underline{g}} [\sqrt{I}_{trial}(\underline{K},\underline{g}) - \sqrt{I}_{ideal}(\underline{K},\underline{g})]^2 \qquad (1)$$

where the sum over orientations $\underline{K}$ covers the chosen pixels in the CBED disks (in our case, 13 of them) and the $\underline{g}$ sum is over all 19 disks in the pattern. We choose to use square roots of the intensity to enhance the weaker features in the pattern, but that is not essential. The structure factors are then varied in such a way as to reduce S to a minumum. The global minimum of S reprsents the best 10 parameter fit to the 19-beam CBED pattern, and the corresponding structure factors may be assumed to give a good representation of the true projected potential. As noted this method is very similar to that of Ref. 10. However, we are attempting to fit considerably more parameters (although to a lesser degree of accuracy) and we choose to use the sum of square difference as our measure of fit instead of an R-factor. This choice is determined by the nicer analytic properties of S, which allow for more efficient minimization methods.

Although the method is simple in principle, several difficulties arise. The most important is that S has no global minimum in the parameter space we consider. It follows that any minimization run will tend to "fall down" to the *local* minimum nearest to the starting point. We have explored the structure of the S function computationally and believe it to have several local minima in the 10-parameter space we consider. When thickness is included as another variable, the situation gets worse with more minima being produced, and the number of local minima increases as the crystal thickness is increased. It is for this reason that we work with thin samples, although the crystal must not become so thin that the CBED disks become featureless. For GaP [1$\bar{1}$0] a thickness of 250 Å appears to be a good compromise. In the present studies we have adopted a rather crude procedure to overcome the local minimum problem. We use random starting points for the 10-structure factor parameters and perform many minimization runs. The structure of the S function then becomes apparent, and to date we have always found that the global minimum is fairly obvious--it has a considerably lower S value than the local minima and we tend to find it in a relatively

high proportion of runs. For the 19-beam GaP pattern we perform 150 minimization runs and the global minimum occurs 10 times. Although there is no absolute guarantee that this is the global minimum, we are quite confident that it is.

The method of using random starting points is good because it is completely unbiased, but has the disadvantage that many minimization runs are required to find the true minimum. It follows that we must have highly efficient minimization routines. In our present studies we use NAG routine E04GBF, which uses a quasi-Newton method to minimize a sum-of-squares function. The performance of the minimization is vastly improved by being able to calculate the *gradients* of S with respect to the structure factor parameters. That can be done by use of perturbation theory, which gives the first-order change in the diffracted intensities when the structure factors are varied.[11,12] The addition of gradients has been essential for performing the calculations in a reasonable time. Even so, the 150 minimization runs still take about 30 CPU hours on a 2Mflop workstation.

Results

The results for the 10 structure factor parameters at the global minimum of S are given in Table 1 and the projected potential derived from them is shown in Fig. 1(c). The corresponding CBED pattern is shown in Fig. 2(c). It can be seen that the structure factors are reproduced extremely well (both amplitudes *and* phases), with the largest error occurring for the phase of the weak (002) structure factor. The projected potential is in excellent agreement with Fig. 1(b), which is produced by use of the same number of correct structure factors. The Ga and P string potentials are well defined; the Ga string is clearly the stronger. The results of Table 1 and Fig. 1(c) are produced with essentially *no* prior knowledge of the atomic structure and are simply derived from the best available fit to the ideal "experimental" CBED pattern.

Conclusion

The fitting of computer-generated CBED patterns to experimental patterns appears to hold out the prospect of a considerable advance in quantitative microanalysis. However, many questions remain to be answered. Will the method work when there are many more structure factors to be fitted? Will the problem of local minima become unmanageable? How robust is the method against noise in the experimental pattern when real digitized CBED patterns are used instead of our idealized data? Will absorption cause a major problem? It is our belief that with improved minimization strategies and steadily increasing computer power, all these problems can be overcome and that structure determination could become as routine as the other tried and tested CBED techniques.

References

1. *Proc. XIIth International Congress for Electron Microscopy*, San Francisco: San Francisco Press, 1990, vol. 2.
2. J. M. Zuo, J. C. H. Spence, and W. Petuskey, Ref. 1, 508.
3. K. Kuroda, H. Matsuhata, and H. Saka, Ref. 1, 512.
4. D. R. Exelby and R. Vincent, Ref. 1, 510.
5. J. Gjønnes, N. Boe, and K. Gjønnes, Ref. 1, 516.
6. M. Tanaka and K. Tsuda, Ref. 1, 518.
7. Y. Tomokiyo and T. Kuroiwa, Ref. 1, 526.
8. R. Vincent and D. R. Exelby, Ref. 1, 524.
9. J. C. H. Spence and J. M. Zuo, Ref. 1, 530.
10. K. Marthinson, R. Hoier, and L. N. Bakken, Ref. 1, 492.
11. D. M. Bird, *Acta Cryst.* A46: 208, 1990.
12. S. Speer, J. C. H. Spence, and E. Ihrig, *Acta Cryst.* A46: 763, 1990.

TABLE 1.--Comparison of exact and fitted structure factors. A_g and ϕ_g are the structure factor amplitudes and phases, respectively.

	A_{111}	A_{002}	A_{220}	A_{113}	A_{222}	A_{004}	ϕ_{002}	ϕ_{113}	ϕ_{222}	ϕ_{004}
exact	2.63	0.51	-2.26	1.37	0.47	1.48	1.85	-2.48	1.85	0.53
fitted	3.06	0.39	-2 01	1.13	0.79	1.41	0.71	-2.89	1.40	1.21

ATEM OF A CERAMIC-METAL INTERFACE

R. H. J. Hannink, P. R. Miller, and Edward Summerville

Ceramic-metal bonding is becoming a common method which the physical properties of engineering ceramics can be more fully utilized. Oxide ceramics such as transformation toughening magnesia-partially stabilized zirconia (Mg-PSZ) have been successfully bonded to steel substrates with the use of an aluminum metal interlayer. The present study was undertaken to investigate and explain the mechanism by which the aluminum metal forms an interfacial bond whose strength can exceed the tensile strength of bulk aluminum.

Experimental

Bonded composites were prepared from a commercial 9mol%MgO-ZrO_2 (Mg-PSZ) ceramic[1] and a 5005 aluminum alloy in the form of 12mm-diameter Mg-PSZ slugs separated by an 0.6mm interlayer of the aluminum alloy. The surfaces of the Mg-PSZ were either diamond ground or polished to a 1μm diamond finish. The bond was formed by heating under pressure to about 550 C in air for 1, 45, or 1500 s in the case of the ground surfaces and 60 s in the case of polished surfaces.

Analytical transmission electron microscope (ATEM) samples were prepared by either Ar-ion thinning of previously cut, polished, and dimpled interface sections, or by ultramicrotomy. A thin carbon coat was deposited on the samples to prevent charging during TEM observation.

Analytical examination was carried out in a Philips CM30 ATEM operated at 300 kV and fitted with an EDAX energy-dispersive x-ray (EDS) analyzer and a Gatan parallel electron energy loss spectrometer (PEELS). To obtain the PEELS data, the magnification of the image was adjusted so that the entrance aperture of the PEELS unit became the selected area aperture for analysis. It was found that the zirconia, interface, and aluminum regions could be readily distinguished by use of the low-loss region of the electron energy loss spectrum. Zirconia has three broad peaks, the interface one broad peak at about 24 eV, and the aluminum the sharper plasmon peak at about 15 eV. In

R. H. J. Hannink, P. R. Miller, and Edward Summerville are at the CSIRO Division of Materials Science and Technology, Normanby Rd., Clayton, VIC 3168, Australia; E. Summerville is at the CSIRO Division of Manufacturing Technology, Leeds Crescent, Woodville North, SA 5012, Australia. They take pleasure in acknowledging Mr. P. G. Lloyd for providing the bonded specimens and Mr. B. Muldowney for providing assistance with the electron microscope specimen preparation.

order to determine the composition of the interface PEELS, spectra were acquired with a small STEM-probe of dimension similar to that of the interface with the microscope in the STEM-diffraction mode.

Results and Discussion

Mechanical property tests and transmission electron microscope observations of the interface showed that the bonding had been equally successful on ground and polished faces. Initial observations show that the Mg-PSZ is essentially unaffected by the bonding process. Visual examination the polished cross section of a bonded interface showed a dark coloration at the interface. This discoloration may be due either to the reduction of oxygen in the zirconia or an internal reflection of the aluminum through the translucent zirconia. Transmission electron microscopy of the Mg-PSZ adjacent to the interface showed that when metastable tetragonal precipitates were present, they had not transformed as a result of the applied pressure or thermal expansion mismatch stresses generated at the interface; nor did any immediately obvious microstructural changes result from a possible variation in stoichiometry or alloy composition. The aluminum alloy interlayer was completely recrystallized after the application of pressure with a small number of dislocations present, just away from the interface. The dislocations were assumed to be generated as a result of the thermal expansion mismatch stresses. Figure 1 shows the interface of the 60s hold time sample, polished surface, where a definite interfacial layer can be observed. Poor detail in the Mg-PSZ and aluminum phases is due to specimen orientation, close to [001] for both materials.

Figure 2 shows the Zr m-edge and O k-edge from zirconia near the interface. There is also a significant C k-edge overlapping the Zr m-edge due to carbon contamination. Figure 3 shows the PEELS spectrum from the interfacial layer. It can be seen from this spectrum that zirconium is absent and that there is a significant amount of oxygen in the interface. The low-loss region and shape of the O k-edge are consistent with that of alumina. PEELS spectra from the aluminum showed a much smaller O k-edge.

Contrary to the results of Tremouilles and Portier,[2] an interfacial reaction oxide layer between the Mg-PSZ and aluminum alloy was observed even after a hold time of 1 s. Tremouilles and Portier studied 8wt% yttria-zirconia/99.999% pure single-crystal aluminum sheet couples. These workers found that a reaction interlayer of aluminum oxide was formed only after heating to 590 C for 4 h

under a pressure of 60 MPa in argon atmosphere. Under these conditions the interlayer was 100 nm thick, whereas a reduction of bonding time to 30 min (1800 s) did not produce a satisfactory bond nor evidence of an inter-facial oxide layer.

In the current experiments the thickness of the interfacial layer varied as a function of hold time from about 5 to 30 nm for the short-est to longest hold times, respectively. This variance in the observation of a reaction oxide layer with the previous studies[2] may be due in part to the resolution of the analyzer system and oxygen-rich fabrication conditions.

Further analyses are currently under way to determine the species of the oxide layer. Preliminary nanoprobe EDS analyses suggest that the oxide layer, in addition to aluminum, is high in magnesium; crystallographic analyses will be used to determine the orientation relationship.

The observation of an oxide interlayer rich in magnesium suggests that the bonding mecha-nism in the metal-oxide system studied here involves a chemical interaction rather than physical bonding mechanism.

Conclusions

A number of conclusions can be drawn from the experimental observations.

1. Contrary to previously reported data,[2] mechanically sound bonds could be achieved between commercial alloys of aluminum and magnesia-partially stabilized zirconia (Mg-PSZ) in times as short as 1 s.

2. An oxide layer, high in magnesium, was observed in all the samples, even for bonding times as short as 1 s.

3. Bond thickness, for the times studied here, varied but was in general of the order 5-30 nm.

4. The bonding mechanism between aluminum and Mg-PSZ is chemcial rather than physical.

References

1. MS grade Mg-PSZ from ICI Advanced Ceramics, Redwood Drive, Mt. Waverley, VIC 3168, Australia.

2. G. Tremouilles and R. Portier, "TEM study of a ZrO$_2$/Al interface," *J. de Physique*, Colloque C5, Suppl. 10, vol. 49, 1988.

FIG. 1.--Bright field TEM image of Mg-PSZ/Al interfacial region for 60s bonded sample. The Mg-PSZ was polished to a 1μm diamond finish prior to bonding.
FIG. 2.--PEELS spectrum from interface region of 60s bonded sample; note presence of oxygen and no zirconium. Aluminum signal has been presumed lost in the C k-edge as a result of peak overlap. Note also detail of near-edge-fine-structure of O k-edge, indicating "alumina" type bonding.
FIG. 3.--PEELS spectrum of Mg-PSZ sample, obtained just back from interfacial region and showing oxygen k-edge for Mg-PSZ phase.

STUDIES OF CERAMICS BY USE OF BACKSCATTER DIFFRACTION PATTERNS IN THE SCANNING ELECTRON MICROSCOPE

M. D. Vaudin and W. C. Carter

Electron backscatter diffraction patterns (EBSP) may be obtained in the scanning electron microscope (SEM) from crystals as small as 0.2 µm. The patterns can be recorded in real time with a phosphor screen and a video camera. Computer analyses of these patterns may be used to determine crystal orientation to within 0.5°, and comparative dislocation density information can also be obtained. In this paper, the application of this technique to ceramic systems is discussed. The particular difficulties encountered when ceramics as compared to metals and semiconductors are studied arise because many ceramics are of relatively low symmetry and are poor electrical and thermal conductors. EBSP patterns from noncubic materials cannot be indexed by inspection, and therefore an efficient algorithm for automatically indexing diffraction patterns from any crystal system has been developed. The accuracy of both orientation determination and indexing depend to a large degree on the uncertainty in the position of the pattern source: i.e., the position of the stationary electron probe on the specimen. A least-squares algorithm has been developed to calculate the source position. In addition, the video camera introduces up to 5% distortion into the pattern, so a method of calibrating the video camera has been developed. Problems associated with the poor thermal and electrical conductivities of ceramics are being solved by a variety of techniques, including the careful application of very thin conducting films. The use of digital frame grabbers and processors has had a beneficial effect on most of the data acquisition aspects of this technique. Illustrative examples are cited from experiments on diverse ceramic materials.

Experimental Considerations

The electron backscatter pattern technique has been developed over the past ten years, mainly by Dingley and his group at the University of Bristol, to the point where orientation and point group information can be obtained with 0.25 µm spatial resolution and 0.5° angular resolution from a variety of materials.[1-5] The specimen is oriented in the SEM with its surface normal at 70° to the beam and the backscattered electrons strike a phosphur screen 45 to 50 mm from the specimen. The electron diffraction pattern that forms on the phosphor is imaged with a low-light TV camera

and the image is displayed on a computer monitor together with a cursor that is used to measure the position of zone axes in the diffraction pattern. To date orientation studies have typically been carried out on metals[6] and semiconductors[7] with cubic symmetry. The application of EBSP to ceramics is more difficult because ceramics usually have low electrical and thermal conductivity and moreover are frequently not cubic. The low electrical and thermal conductivity leads to the charging and contamination in the SEM discussed in this section; problems associated with the low symmetry of ceramics are discussed in subsequent sections.

The high beam currents used in this technique (1 nA or more) can cause considerable carbon contamination where the stationary electron probe strikes the specimen and creates a hot zone. "Flaring" on the diffraction pattern can occur once a significant charge has developed on the specimen during real-time analysis of a pattern for which the focused probe remains on the specimen throughout the analysis. The high angle of incidence reduces the charging problem to a certain extent, since a high proportion of the incident electrons are reflected. However, imaging may be extremely difficult with good insulators such as alumina, and sometimes the charging is so extensive that images must be obtained in the backscattered mode with some loss in contrast. Thin carbon coatings on the specimen surface can eliminate the charging problem, but only at the expense of diffraction-pattern quality. It has been shown recently that the use of frame grabbers and averagers solves a number of these problems: once a pattern has been averaged for a few seconds and stored in a frame buffer, the electron probe can be rastered to stop contamination and flaring. Also, if the carbon coat applied to reduce charging degrades the pattern, the quality of the pattern image can frequently be considerably improved by averaging and contrast enhancement.

The preparation of the specimen surface is critical to obtaining good diffraction patterns. A rough surface often presents problems because the source point may be shielded from the phosphor by other parts of the specimen. The technique used to produce a planar surface must not introduce defects such as dislocations and microcracks into the near surface region (top ≈10 nm). Investigators have obtained good results on hard materials such as alumina and silicon nitride by grinding the sample flat with 400-grit SiC paper, polishing with diamond paste, using grades from 30 µm down to 1 µm, and doing a final polish with basic colloidal

---

The authors are at the NIST Materials Science and Engineering Laboratory, Ceramics Division, Gaithersburg, MD 20899.

silica. A final polish with 0.05μm alumina or magnesia is also often successful.

Accurate Measurement of Zone Axis Positions

Many ceramic materials of interest are tetragonal or orthorhombic with c/a and b/a ratios close to an integer; e.g., $BaTiO_3$ and lead zirconate titanate (PZT) have c/a ratios of ≅1.01 and ≅1.03, respectively, and $Ba_2YCu_3O_{6+x}$ has b/a = 3.007 and c/a = 0.983. In these cases, the diffraction patterns at the three <001> axes do not differ much in the angles between the major zone axes, which presents considerable problems when the patterns are indexed. To differentiate between similar arrangements of zone axes, the positions of both the zone axes and the pattern source must be accurately measured. The clarity and contrast of the diffraction patterns are significantly enhanced by use of digital-averaging and contrast-enhancement techniques. A clear image of the intersecting lines that form a zone axis will show at least two pairs of lines intersecting in a slightly distorted parallelogram. It is easily shown that the exact position of the zone axis is at the intersection of the diagonals of the "parallelogram" (Fig. 1). Only two pairs of lines are shown in the figure for clarity.

The distortion introduced by the video camera is of the pincushion type, as can be seen by imaging a piece of graph paper whose axes are aligned with the cursor axes. The corners of the image are seen to be displaced away from some "center of distortion" that does not necessarily correspond to the center of the screen. From the positions of the graph paper intersection points on the monitor screen, a mapping from the distorted space of the monitor to the Cartesian space of the graph paper can be calculated by use of least-squares criteria. The data have been collected and the analysis is in progress.

Locating the Source of the Diffraction Pattern

The accuracy of the orientation information that can be obtained from this technique de-
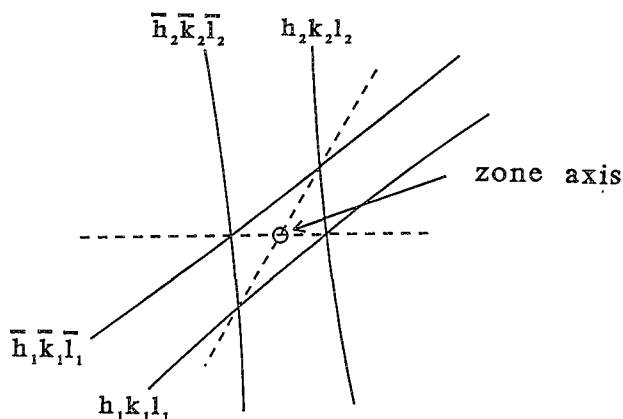
FIG. 1.--Position of zone axis relative to Kikuchi line intersections.

pends strongly on the accuracy with which the position (X,Y,Z) of the source of the pattern can be determined. That is particularly true for absolute orientation determinations, and less so for relative orientations that are found by determination of the misorientation between absolute orientations, so that the errors tend to cancel out. Several techniques exist for determining X, Y, Z. We have employed two different methods, both of which use the position on the screen of at least three indexed zone axes in a diffraction pattern taken from a well-annealed single crystal of a cubic material, typically silicon.

The first technique is a least-squarea algorithm. A best estimate for the position of the source point is desired for the number N_Z of zone axes whose positions have been measured with some experimental error. The angle between each pair of zone axes is known exactly. For N_Z = 3, an exact solution may be found, but that requires solution of a set of polynomial equations; the solution is very sensitive to small experimental errors. For N_Z > 3, no exact solution for the source point is available in general and a numerical scheme is applied: the (X,Y,Z) point is found that minimizes the squared differences between the exact angles between the zone axes and the angles calculated from (X,Y,Z) and the measured positions. The conjugate-gradient method is employed for this minimization,[8] and since the function that is being minimized has very small gradients near the minimum, the algorithm is relatively slow and sensitive to errors in zone-axis position.

The second technique is due to Pitsch and coworkers; an analytical solution for X,Y,Z is found from the positions and indices of four zone axes.[9] If more than four zone axes are clear in the calibration diffraction pattern, all possible combinations of four are employed and an average is taken. This average is weighted in favor of those zone axis combinations whose configuration is least sensitive to errors in zone axis position. As the Pitsch method finds analytical solutions, it is inherently faster than the least-squares method, but, as discussed below, it is more sensitive to experimental errors.

The sensitivity of the least-squares technique to errors in the positions of the zone axes has been comprehensively tested. A set of 10 silicon zone-axis positions and the angles between them were calculated for a given source point and crystal orientation. The least-squares calculation of (X,Y,Z) was carried out for N_t trials with errors, of defined size E but in random directions, added to the positions of the zone axes. Various numbers of zone axes N_Z, from 4 to 10, were used; for each test, the mean and standard deviations (δX, δY, δZ) of the X, Y, Z values were calculated, together with the magnitude of the source point error given by $\delta R = (\delta X^2 + \delta Y^2 + \delta Z^2)^{\frac{1}{2}}$. Figure 2 is a plot of δR vs N_Z with E = 0.25 and N_t = 200. In this test, for each value of N_Z all the possible combinations of 10 zone axes tak-
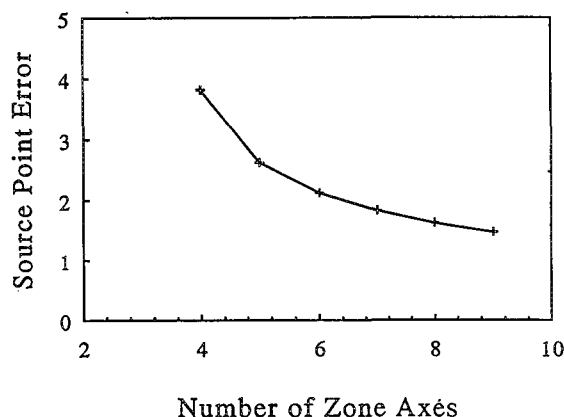
FIG. 2.--Source point error (δR) vs number of zone axes N_z with $E = 0.25$, $N_t = 200$.

FIG. 3.--Source point error (δR) vs zone axis error E with $N_t = 200$, $N_z = 4$, 6, and 8.

ing N_z at time t were used. As expected, the source point error δR decreases as more zone axes are used, going as approximately $1/N_z$; the total deviation is at least 6 times the forced error E even for 8 zone axes. Figure 3 shows δR vs E with $N_t = 200$ using three different zone axis sets with $N_z = 4$, 6, and 8; δR is approximately linear with E and the slopes of the lines are approximately proportional to $1/N_z$, in agreement with Fig. 2. It was also found that δR depends strongly on the average angle between the zone axes used in the calculation, $\bar{\Phi}$. Different sets of 4 zone axes were used for 200 trials each; for $\bar{\Phi} = 13.2°$, δR was nearly 4 times as large as for $\bar{\Phi} = 35.9°$. Analysis of the accuracy of the Pitsch method is not as far advanced. However, without weighting of the average as described above, the Pitsch method is approximately two to three times less accurate than the least squares method.

Automatic Indexing

The algorithm developed to index EBSP patterns obtained from known structures requires accurate knowledge of the position of the pattern source and at least three low index zone axes in the pattern. The zone axis positions are determined from the diffraction pattern on the video screen by use of a cursor. The aim of the algorithm is to find the set of zone axes in the known structure whose relative orientations best match those of the measured zone axes. Thus, the first step in the process is to calculate the angle between each pair of experimentally measured zone axes, which is determined from the coordinates of the zone axes and the position of the pattern source. These angles are then matched, in a systematic way, against a two-dimensional array that contains the calculated angles between selected zone axes in the structure. Zone axes are selected that are readily visible in an EBSP from the material, and unnecessary duplication caused by the crystal symmetry is avoided. For each set of zone axes matched against the measured zone axes, the sum of the absolute differences be-

tween the calculated and experimental angles is determined. The diffraction pattern lines corresponding to the match with the lowest sums are overlaid on the experimental diffraction pattern, so that the user can confirm that the indexing is correct.
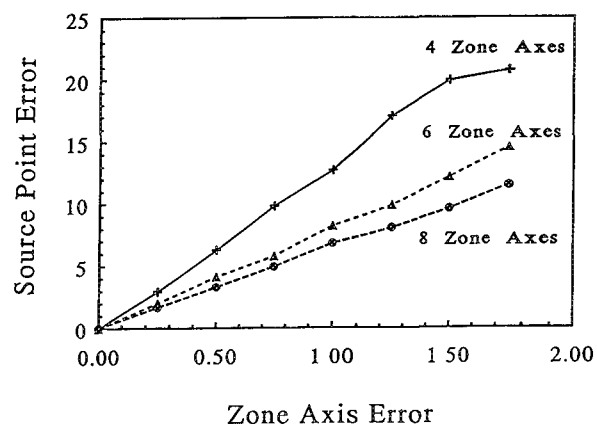
The success of the indexing depends largely on the accuracy of the measured zone axis positions and the source point. With the current real-time experimental setup (no frame averaging, 80286 PC with a processing speed of 8 MHz, 80287 coprocessor operating at 8 MHz), this algorithm can index cubic patterns from cubic materials with 100% accuracy in less than 1 s and rhombohedral patterns (e.g., alumina) with 80% accuracy in 1 to 3 s. With the improvements in the system described above, it is expected that we shall be able to index all systems except monoclinic and triclinic with 100% accuracy in 2 s or less.

Selected Experimental Results

The ceramic materials from which diffraction patterns have been obtained and grain misorientations measured include pure alumina, aluminua-chromia solid solutions, $Ba_2YCu_3O_{6+x}$ (in both bulk and thin-film form), PZT, and silicon nitride. In experiments on diffusion-induced grain boundary migration in the alumina-chromia system, various grains in alumina that had been polished and exposed to chromia vapor were found to develop different surface morphologies and varying chromia concentrations, depending on the surface orientation.[10] Grains further from (0001) orientation had higher chromia concentrations and rougher surfaces. In other experiments, alumina in which discontinuous grain growth had occurred was investigated to determine whether the misorientations in colonies of anomalously large grains were "special" (e.g., twin-related). No special relationships were found.[11]

When single crystals of the high-temperature superconductor $Ba_2YCu_3O_{6+x}$ c-axes are often formed.[12] As part of a study of the nature of the [001] tilt boundaries that form between the crystals in the cluster, the angle between

161

the [001] axes on either side of each boundary
was measured. Typically, the angle was 2° or
less and the boundary was therefore almost
pure tilt in nature, but it was found that the
[001] axes of grains at the edge of a cluster
were frequently misaligned with their neigh-
bors, in some places up to 10°. In all these
studies, the EBSP method provided useful in-
formation on absolute and relative grain orien-
tations that it would be difficult or impossi-
ble to obtain in any other way. Some of the
technique improvements described in this paper
have not yet been fully implemented; when they
are, the technique will become easier to use
and even more accurate.

References

1. D. J. Dingley, *SEM/1984* II, 569-575.
2. D. J. Dingley and K. Baba-Kishi,
SEM/1986 II, 383-391.
3. D. J. Dingley and K. Baba-Kishi, *Scan-
ning* 11: 305-312, 1989.
4. K. Baba-Kishi and D. J. Dingley, *J.
Appl. Cryst.* 22: 3, 189-200, 1989.
5. D. J. Dingley, *Proc. Electron Micros-
copy and Analysis Group and Royal Microscopical
Soc. Conf.* , Bristol: Institute of Physics,
1990, 473-476.
6. W.-H. Rhee, C. A. Handwerker, M. D.
Vaudin, and D. N. Yoon (in preparation).
7. D. J. Dingley, M. Longden, J. Weinbren,
and J. Alderman, *Scanning Microscopy* 1: 451-
456, 1987.
8. W. H. Press, B. P. Flannery, S. A.
Teukolsky, and W. T. Vetterling, *Numerical
Recipes*, Cambridge: Cambridge University
Press, 1989.
9. P. L. Ryder, H. Halbig, and W. Pitsch,
Proc. 5th Cong. X-ray Optics and Microanalysis,
Berlin: Springer-Verlag, 1969, 388-395.
10. M. D. Vaudin, J. E. Blendell, and C. A.
Handwerker, *Proc. Structures/Properties Rela-
tionships for Interfaces*, ASM, 1991.
11. C. A. Handwerker and M. D. Vaudin (un-
published work).
12. F. W. Gayle and D. L. Kaiser, *J. Mat.
Res.* (in press).

GRAIN BOUNDARY CHEMISTRY AND THE PROPERTIES OF ZIRCONIA CERAMICS

M. L. Mecartney and Y. J. Lin

Silicate grain boundary phases in zirconia ceramics have commonly been detected when these ceramics have been observed by analytical transmission electron microscopy (AEM).[1-3] The chemistry of these grain boundary phases can be manipulated in order to obtain desired micro-structures and subsequent properties.[4-7] AEM is the key for determining the grain boundary chemistry, precipitation/crystallization reactions, and solubility limits in zirconia materials doped with specific glass compositions. Using this grain boundary engineering method, one can design zirconia ceramics with enhanced mechanical properties.

Experimental

Sintered zirconia ceramic bodies were fabricated with 5 wt.% added glass phases. Three types of zirconia were used: pure zirconia (monoclinic at room temperature), zirconia stabilized by 3 mol% yttria in solid solution (tetragonal at room temperature) and zirconia stabilized by 8 mole % yttria (cubic at room temperature). The composition of the glass phases used in this study is given in Table 1. Analyses of the structure and composition of the materials were conducted by scanning and transmission electron microscopy with energy dispersive spectroscopy.

Results

The silicate glass phases completely wetted the zirconia grains and formed a continuous grain boundary phase. In the absence of glass, the grains were highly facetted (Fig. 1). No strong dependence on anisotropic surface energy was observed in the glass-containing samples, since rounded zirconia grains were formed (Figs. 2 and 3). EDS analyses showed that the solubilities of zirconia in both the alumino-silicate and borosilicate glasses were a few mol%. However, the yttria solubility in boro-silicate glass was much lower than that in aluminosilicate glass (Figs. 5-7). The samples containing high yttria solubility glass phases had yttria depleted from the zirconia grains (Fig. 5), which would make the grain less stable and more prone to transformation to the equilibrium monocli ic phase. The low-

M. L. Mecartney is at the Department of Materials Science and Engineering, University of California, Irvine, CA 92717; Y. J. Lin is at the Department of Materials Science and Engineering, University of Florida, Gainsville, Fla. The work was conducted at the Department of Chemical Engineering and Materials Science, University of Minnesota, Minneapolis, Minn., with support from the Packard Foundation.

TABLE 1.--Compositions of the initial phases added to the zirconia.

mol%	SiO_2	Al_2O_3	B_2O_3	Na_2O	K_2O
AS	79.8	20.2	----	----	----
BS	83.3	1.5	11.2	3.6	0.4

solubility glasses would be expected to limit mass transport and the grain growth rate.

The grain size of yttria-zirconia/glass composites depended on yttria concentration, as well as on the composition of the grain boundary glassy phase. The grains grew fastest in 8 mol% yttria-zirconia (cubic phase) samples and slowest in 3 mol% yttria-zirconia. Since most of the zirconia grains were surrounded by the glass phase, the grain growth was most likely accomplished via a dissolution-reprecipitation process. The effect on grain was then closely tied to the solubilities of yttria and zirconia in the glass. Figures 1-3 illustrate the difference in grain size for samples with and without glass. The addition of glass usually hindered the grain growth by limiting the dissolution of yttria and/or zirconia. However, the glass/zirconia samples containing a glass with high yttria solubility only moderately slowed grain growth, whereas the samples with low-solubility yttria glass dramatically decreased the grain growth.

An addition of MgO to borosilicate glass significantly modified the effects of this glass. Compared with pure borosilicate glass, MgO/borosilicate glass greatly increased the solubility of yttria in the glass. This drastic change resulted in extraordinarily large (3-5 μm) zirconia grains and large amounts (~60%) of monoclinic phase. A low solubility of zirconia and yttria in the glass appears to be crucial for controlling grain size. Since the size in yttria-zirconia samples containing a glass phase increased with increasing yttria solubility in the glass, in order effectively to suppress the grain growth, glass with little yttria solubility (such as borosilicate glass) should be used. On the other hand, a glass with high yttria solubility (e.g., borosilicate/ MgO glass), which promotes fast grain growth and severe yttria depletion, makes the zirconia grains unstable and promotes the monoclinic transformation on cooling from the sintering temperatures. A simple modification of the glass composition (addition of MgO) turned a grain growth suppressor (borosilicate glass) into a grain growth enhancer (borosilicate glass/MgO). The precise selection of the starting glass composition and the control of contamination during powder processing are therefore of utmost importance.

163

Crystallization of the glass phases depended on the starting compositions of the grain boundary glass and the size of the amorphous pockets. Mullite and zircon formed in large pockets of the aluminosilicate glass (Fig. 4). No crystalline phases formed from the borosilicate glass in samples containing high amounts of Y_2O_3 (8 mol % Y_2O_3 samples). In zirconia samples with a low yttria concentration, trace amounts of zircon formed from reactions of zirconia in the borosilicate glass. Upon crystallization, all the silicate phases became nonwetting with respect to the zirconia surfaces. The presence of MgO also enhanced the crystallization of zircon from the borosilicate glass in yttria-zirconia. In general, crystallization of the silicate glassy grain boundary phase was not desirable. The crystallization occurred only in large glass pockets and differences in the thermal expansion coefficients between the crystallized phase and zirconia generated microcracks at the interfaces. Crystallization also altered the composition of the remaining glass.

The mechanical properties of these zirconia ceramics could be modified by the addition of the glass phases. The fracture toughness of yttria-zirconia could be enhanced or degraded by the presence of glass (Fig. 8). The factors that determine the transformation toughness (grain size, grain morphology, yttria content in the grains, yttria partitioning among the grains and the residual stresses) could be changed by the interaction of the glass and zirconia. The borosilicate glass stabilized the tetragonal zirconia by removing the sharp corners of the grains. The aluminosilicate glass additions generated larger, round zirconia grains and also depleted the yttria from zirconia. The yttria depletion seemed to
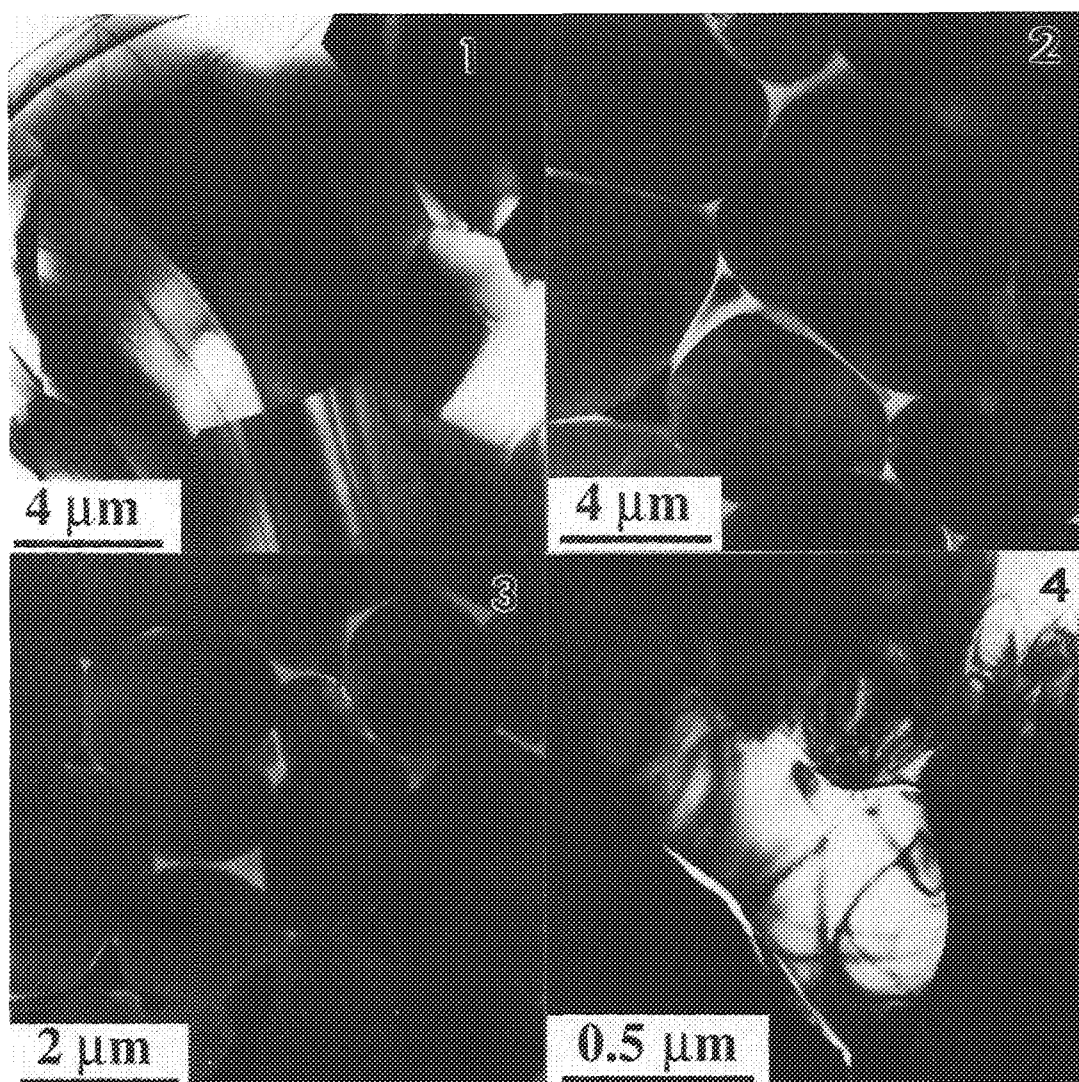
FIG. 1.--TEM of 8 mol% yttria stabilized zirconia.
FIG. 2.--TEM of 8 mol% yttria stabilized zirconia and aluminosilicate glass (DF image).
FIG. 3.--TEM of 8 mol% yttria stabilized zirconia and borosilicate glass (DF image).
FIG. 4.--TEM of zircon phase crystallized from aluminosilicate glass/zirconia sample.
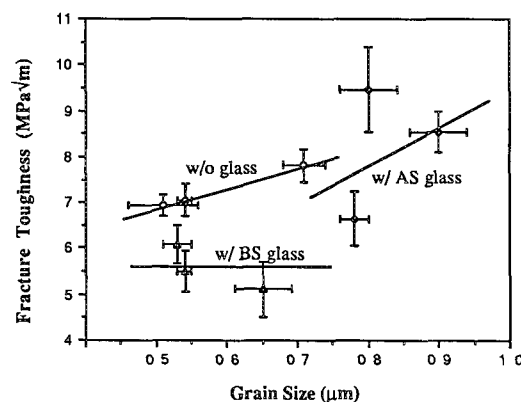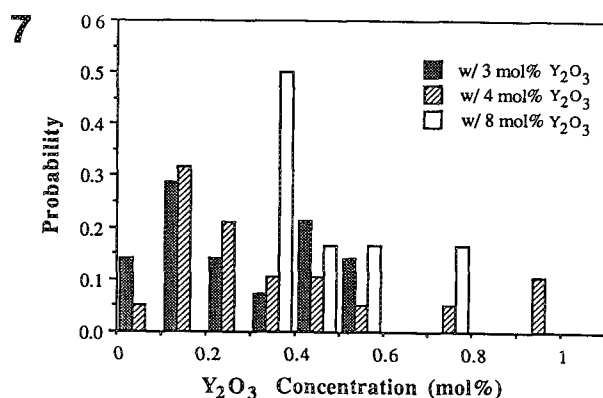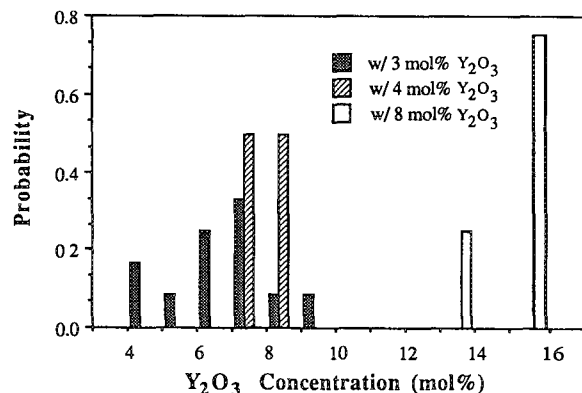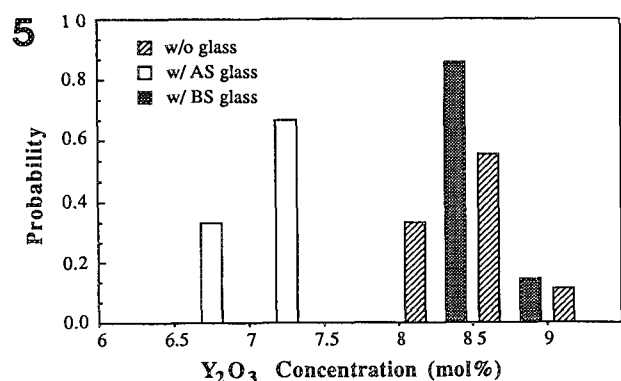
FIG. 5.--Distribution of yttria concentration in zirconia grains in 8 mol % Y_2O_3-ZrO_2 (w/o glass: sample without glass; w/AS glass: sample with aluminosilicate glass; w/BS: sample with boro-silicate glass. (Same notations are used in following figures.)
FIG. 6.--Yttria concentration in aluminosilicate grain boundary phase.
FIG. 7.--Yttria concentration in borosilicate grain boundary phase.
FIG. 8.--Fracture toughness vs grain size in 3 mol% yttria-zirconia with and without glass.

have a similar effect on increasing the tough-ness as the facetted grain morphology. Super-plastic deformation under constant load at 1400 C of all samples was successfully accom-plished with 50% reduction in height by com-pression. However, the samples with glass deformed much easier and proved the potential for superplastic deformation at low tempera-tures and minimal flow stresses.

Conclusions

A thorough understanding of the role of silicate glass in ceramics allows one to take advantage of the glass phase in the design of ceramic materials. Using an appropriate glass in yttria-zirconia, one can suppress the grain growth, enhance the yttria partitioning, pro-mote superplastic deformation, or increase the fracture toughness. The effect of these glass phases depends not only on the composition of the glass but also on the composition of the zirconia. The addition of small amounts of a suitable glass should provide a convenient and effective way to manipulate the microstructure and properties of yttria-zirconia.

References

1. M. Ruhle, N. Claussen, and A. H. Heuer, "Microstructural studies of Y_2O_3-containing tetragonal ZrO_2 polycrystals (Y-TZP)," *Advances in Ceramics*, 12: 352-370, 1984.
2. G. Wahlberg, L. K. L. Falk, L. Dunlop, and K.-O. Axelsson, "The intergranular micro-structure of a partially stabilized ZrO_2 material," *J. Mater. Sci. Lett.* 4: 1353-1355, 1985.
3. M. L. Mecartney, "The influence of an amorphous second phase on the properties of yittria tetragonal zirconia polycrystals (Y-TZP)," *J. Amer. Ceram. Soc.* 70: 54-58, 1987.
4. E. P. Butler, P. K. Slotwinski, N. Bonanos, J. Drennan, and B. C. H. Steele, "Microstructural-electrical property relation-ships in high conductivity zirconias," *ibid.*, 572-584.
5. J. Drennan and R. H. J. Hannink, "Effect of SrO additions on the grain boundary micro-structure and mechanical properties of magnesia-partially stabilized zirconia," *J. Am. Ceram. Soc.* 69: 541-546, 1986.
6. C. A. Leach, P. Taner, and B. C. H. Steele, "Effect of rapid cooling on the grain boundary conductivity of ÿttria partially stabilized zirconia," *J. Mater. Sci. Lett.* 5: 893-894, 1986.

7. Y. J. Lin, P. Angelini, and M. L. Mecartney, "Microstructural and chemical influences of silicate grain boundary phases in Yttria stabilized zirconia," *J. Am. Ceram. Soc.* 73: 2728-2735, 1990.

THE MICROSTRUCTURE AND MICROCHEMISTRY OF ORGANOCERAMICS

W. M. Kriven and O. O. Poppola

The term "organoceramics" is commonly used in the literature to identify two types of materials: organic-ceramic composites and ceramic materials that incorporate organic chains into their cell structure. Reactions between the constituents of the first category may lead to the formation of products that belong to the second. The presence of the organic phase in these materials can result in site-directed nucleation or inhibit nucleation. They can also modify crystal structure and morphology and favor particular topotaxial relationships between various phases.[1,2] In ceramic-organic composites, the polymer generally reduces porosity (by filling the pores), and serves as lubricant during processing, and thus optimizes particle packing. This effect results in a composite with better mechanical and electrical properties. For example, the flexural strength of a calcium aluminate-polyvinyl alcohol acetate composite is about 250 MPa, compared to about 5 MPa for a calcium aluminate cement. The incorporation of organic molecules in a ceramic lattice can occur by interlamellar absorption between neutral sheets in a layered structure or by encapsulation in cages in certain frameworks. For example, clathrasils $(17SiO_2 \cdot C_5H_5N)$ are made up of pyridine molecules encapsulated within hexadecahedral cages formed by a silica host framework.[3,4] Organic molecules of certain alcohols (e.g., ethylene glycol, decanedethiol) and acids (e.g., malic acid, α-naphthoic acid) can be absorbed within the interlayers of $4CaO \cdot Al_2O_3 \cdot xH_2O$.[5] Whatever the mechanism, this incorporation leads to lattice swelling, the extent of which depends on organic molecule type and the original crystal structure (e.g., sizes of cages, interlayer distances) of the host matrix.

These materials are generally processed at relatively low temperatures (<250 C) and have mechanical and electrical properties that make them attractive for applications such as electronic substrates and second-harmonic generators.[4,7] However, they are generally sensitive to moisture, which may limit their applications.

This paper reports on the effect of polyvinyl alcohol acetate (PVA) on the hydration

behavior of monocalcium aluminte. A brief description of the microstructure of the single-phase organoceramic hybrid of $4CaO \cdot Al_2O_3 \cdot 13H_2O$ will also be presented.

Experimental Procedures

Commercially available calcium aluminate powder (Lafarge Secar 71, high-alumina cement) was pressed into pellets and sintered at 1350 C. These pellets were then hydrated in 50 cm^3 of deionized water at 5, 35, and 80 C for 10 h and 14 days respectively. Samples of a calcium aluminate-PVA composite (macro-defect free cement MDF) were also hydrated under similar conditions. As a control experiment, some of the MDF samples were heat treated at 550 C for 24 h in order to burn out the polymer and were hydrated under the above specified conditions. After hydration, the samples were oven dried for 1 h and the microstructures were observed on an ISI DS 130 scanning electron microscope (SEM).

Powder of the organoceramic hybrid of $4CaO \cdot Al_2O_3 \cdot 10H_2O$ was produced by the method described in Ref. 6. The microstructure was studied on a Philips EM 420 transmission electron microscope operated at 80 kV.

Experimental Results

Hydration of Calcium Aluminate Pellets. Figure 1 summarizes the microstructures obtained on 10 h hydration of monocalcium aluminate at various temperatures. At 5 C, platelets (Fig. 1a) were observed at the surface. These platelets were typically arranged in a concentric manner (see arrowed region). EDS analyses of these platelets gave [Al]-[Ca] atomic ratios of 2, which shows that the platelets were $CaO \cdot Al_2O_3 \cdot 10H_2O$. At 35 C, a "mop-like" morphology was observed (Fig. 1b). After hydration at 80 C, the surface was completely covered with well-formed crystals of cubic and icositetrahedral morphologies and some irregularly shaped structures. Most of the hydration products were single crystals but some bicrystals were also observed (see arrows in Fig. 1c). EDS analyses confirmed the "mop-like" crystals to be $2CaO \cdot Al_2O_3 \cdot 8H_2O$ and the well-shaped cubic crystals to be $3CaO \cdot Al_2O_3 \cdot 6H_2$(.

The morphologies of the products formed after 10 h of hydration of a calcium alunina PVA composite are shown in Fig. 2. In most cases the surface of the hydrated samples were cracked and the polymer appeared to have been leached out from certain areas (Fig. 2a). No detectable product was present on the sample hydrated at 5 C. After hydration at 35 C, spherulitic crystals were observed at the surface (Fig. 2b). The surface of the sample
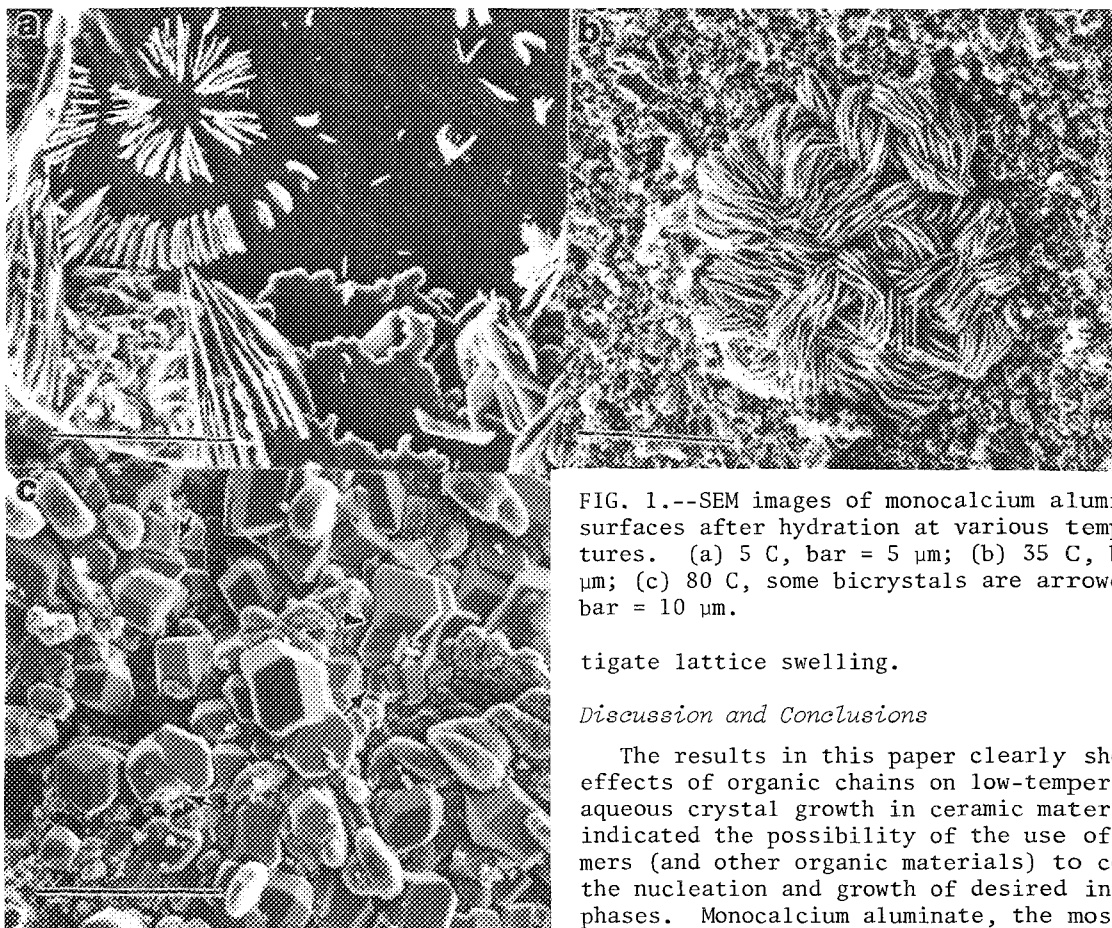
FIG. 1.--SEM images of monocalcium aluminate surfaces after hydration at various temperatures. (a) 5 C, bar = 5 μm; (b) 35 C, bar = 5 μm; (c) 80 C, some bicrystals are arrowed; bar = 10 μm.

tigate lattice swelling.

Discussion and Conclusions

The results in this paper clearly showed the effects of organic chains on low-temperature aqueous crystal growth in ceramic materials and indicated the possibility of the use of polymers (and other organic materials) to control the nucleation and growth of desired inorganic phases. Monocalcium aluminate, the most reactive component of aluminate cements, generally hydrate into three main phases: $CaO \cdot Al_2O_3 \cdot 10H_2O$ at temperatures below 20 C, $2CaO \cdot Al_2O_3 \cdot 8h_2O$ at temperatures between 20 C and 35 C, and $3CaO \cdot Al_2O_3 \cdot 6H_2O$ at 80 C.[7,8] The first two products are pseudohexagonal in structure and readily convert into the last one, which is cubic, provided enough moisture is available.[8] Polyvinyl alcohol acetate apparently had three important effects:

(1) $2CaO \cdot Al_2O_3 \cdot 8H_2O$ was stabilized at 80 C (Figs. 2b and c).

(2) The morphology of $2CaO \cdot Al_2O_3 \cdot 8H_2O$ was changed from "mop-like" at 35 C to spherulitic or "bowtie" like at 80 C (Figs. 2c and d).

(3) Only certain cubic habit planes were activated in the presence of the PVA at 80 C.

Any discussion of the tentative mechanism of the action of PVA on nucleation and growth of the hydrates must take into consideration

(i) the viscosity change of the solution as the polymer progressively dissolves in water and calcium and aluminate ions are released into solution;

(ii) ionic interactions between the calcium and the aluminate ions and the functional groups of the polymer chain; and

(iii) steric effects if the polymer is intercalated into the crystal structure.

The polymer apparently reduces the number of hydration product nucleation sites. Generally,

hydrated at 80 C was filled with crystals having two types of morphologies: cubic crystals and "bowtie" shaped ones (Fig. 2c). All the cubic crystals observed showed either cubic or rhombohedral morphologies. The underlying calcium aluminate grains had a rounded appearance (Fig. 2d). The numbers and sizes of hydration products in the presence of PVA were significantly reduced. Microchemical analyses by SEM-EDS showed that the spherulitic and the bowtie-like crystals were $2CaO \cdot Al_2O_3 \cdot 8H_2O$, and the cubic or rhombohedral ones were $3CaO \cdot Al_2O_3 \cdot 6H_2O$. The calcium aluminate/PVA composites, heat treated at 550 C and hydrated at 80 C, had on their surfaces products with the same morphology as those shown in Fig. 1(c).

Microstructure of the Organoceramic Hybrid of $4CaO \cdot Al_2O_3 \cdot 13H_2O$

The microstructure of the hybrid is shown in Fig. 3(a). It consisted of pseudo hexagonal crystals about 7 μm in size and lying preferentially on their basal plane. The associated selected-area diffraction pattern (Fig. 3b) clearly showed the {0001} of an hexagonal structure. This finding confirms x-ray results.[1] These crystals were extremely beam sensitive; diffraction patterns from other beam directions could not be obtained to inves-
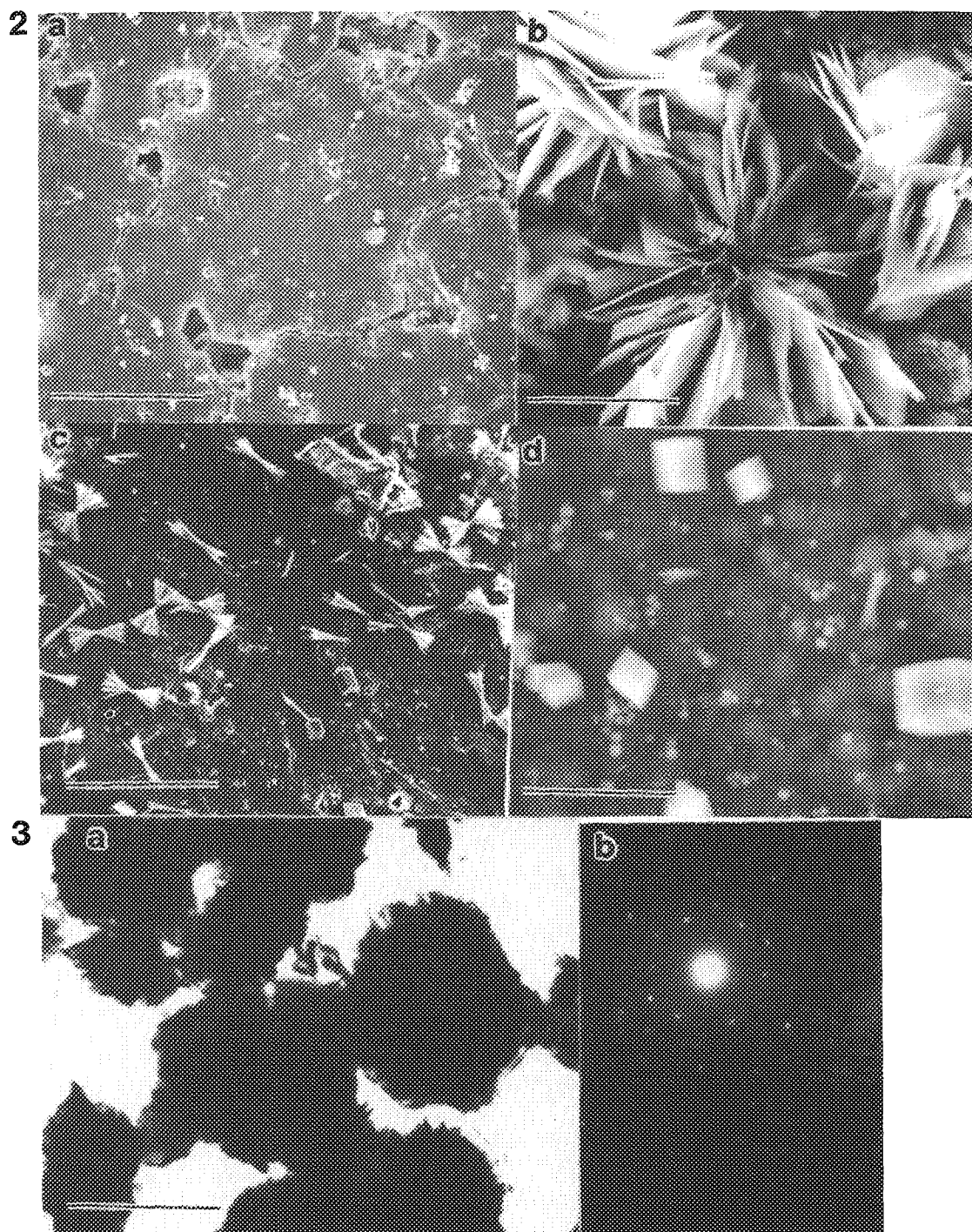
FIG. 2.--SEM images of calcium aluminate-polyvinyl alcohol acetate composite surfaces after hydration. (a) Cracks and areas where polymer had been leached out; bar = 30 μm. (b) Specimen hydrated at 35 C, bar = 10 μm. (c) Specimen hydrated at 80 C, bar = 20 μm. (d) Rounded calcium aluminate grains; bar = 10 μm.

FIG. 3.--(a) TEM bright-field image showing microstructure of organoceramic hybrid of $4CaO \cdot Al_2O_3 \cdot 13H_2O$; bar = 5 μm. (b) Selected area diffraction pattern showing the {0001} zone axis of hexagonal crystal structure.

the polymer tends to absorb into high-energy
crystallographic planes and renders them less
active toward nucleation and growth of inorgan-
ic hydrates. Even on planes that remain active
for nucleation, the formation of a viscous pol-
ymer layer at the surface of the nucleus may
offset the thermodynamic driving force for ac-
celerated growth. The "mop-like" morphology
resulted from abundant nucleation of the hy-
drate, which gave rise to interwoven spheru-
lites during growth. The "bowtie" morphology
actually resulted from a spherulitic and hori-
zontal growth on both sides of a reoriented
nucleus.

References

1. Werner Dosch, "Interlammelar reactions of
tetracalcium aluminate hydrates with water and
organic compounds," in S. W. Bailey, Ed., *Clay
and Clay Minerals*, New York: Pergamon Press,
1967, 273.
2. Ladislav Pach, Zdenec Hrabe, Sridhar
Komameni, and Rustum Roy, "Controlled crystal-
lization of vaterite from viscous solutions of
organic colloids," *J. Mater. Res.* 5: 2928,
1990.
3. H. K. Chae, W. G. Klemperer, D. A. Payne,
C. T. A. Suchicital, D. R. Wake, and S. R. Wil-
son, "Clathrasils: New materials for non-linear
optics," in G. Stucky, Ed., *New Materials for
Non-linear Optics*, Am. Chem. Soc. (in press).
4. H. K. Chae, W. G. Klemperer, D. A. Payne,
and C. T. A. Suchicital, "Molecular engineering
of phase transition temperatures in dodecasil-3
C clathirasils," *Proc. 7th ISAF* (in press).
5. J. F. Young, "Effect of organic compounds
on the interconversions of calcium aluminate
hydrates: Hydration of tricalcium aluminate,"
J. Amer. Cer. Soc. 53: 65, 1970.
6. P. B. Messersmith and S. I. Stupp, "Syn-
thesis of polyvinyl alcohol organoceramic," *J.
Mat. Res.* (submitted).
7. Paul Sliva, L. E. Cross, T. R. Gururaja,
and B. E. Scheetz, "Macro-defect-free process-
ing and low-frequency dielectric response of
calcium aluminate cement," *Materials Letters*
4: 409, 1986.

CORRELATED OPTICAL AND ELECTRON MICROSCOPY FOR CHARACTERIZATION OF COKE AND CATALYSTS

V. A. Munoz, W. W. Lam, Christine Payette and R. J. Mikula

The microstructure of coke deposits on reactor walls and on catalyst surfaces gives important clues to the efficiency of the coking process. In the upgrading of heavy oils and bitumen to synthetic crude oil, coke (or solids) production must be minimized in order to maximize liquid yield. Coke on catalyst surfaces can restrict access of organic material to the active catalyst sites, and coke on reactor walls limits the efficiency of heat transfer. Reduction of coke on catalyst and reactor surfaces requires an understanding of the mechanism of coke formation in order to minimize the detrimental effects of coke deposition. The synergism between isotropic and anisotropic coke production and the role of mineral impurities in catalyzing or hindering this process can only be understood via a combination of optical (OM) and electron microscopic (SEM) techniques. Examples are shown to illustrate the utility of correlated optical and electron microscopy in elucidating both the organic and mineral composition of coke deposits.

Experimental

The coke samples were prepared for analysis by mixing of the solids with epoxy resin in a 2:1 ratio and pouring of the mixture into a cavity made in a blank epoxy pellet. Afterward, they were polished by a procedure similar to that recommended by ASTM.[1] The catalysts were prepared by horizontal setting of the catalyst rods in cylindrical molds and filling of the molds with epoxy resin. The polishing was performed at lower pressure (20 psi) than for the coke samples (30-40 psi) in order to prevent disintegration of the brittle catalyst rods. The polishing eliminated about 50% of the diameter of the catalyst rods, exposing a cross section of the interior as well as the deposits found on the outer surface of the catalysts.

The samples were then marked using a Buehler Micromet II digital microhardness tester. Indentations of about 10 μm were made on the epoxy resin adjacent to the areas of interest by use of the diamond indentor available on this instrument. This procedure provides fiducial marks that facilitate the orientation and correlation of the optical and electron microscope images.

The optical micrographs were taken with a Carl Zeiss research microscope photometer by use of a reflected-light system operated with white light, with bright field illumination and

partially crosspolarized light. Blue violet light (450-490 nm) was used to determine the fluorescence properties of the microscopic entities. The identification of coke components is accomplsiehd by virtue of their reflectance, morphology, and texture; isotropic or anisotropic character; and fluorescent properties.

Polarized incident light was used to determine the proportion of organic species that form anisotropic coke. This type of coke is formed as a consequence of reactions leading to the presence of a nematic mesophase.[2-5] During this process, a liquid crystal type of structure is created due to a parallel alignment of planar aromatic molecules. The resulting coke rotates polarized incident light; by rotating the analyzer (second polarizer), one produces extinction patterns and polarizing colors that identify the anisotropic coke. Blue violet incident light excites fluorescence in certain organic components and helps to distinguish organic components from those transformed into coke due to the fact that at the mesophase stage the fluorescent properties are destroyed.[6-9] An increase in anisotropic coke formation generally means a decrease in liquid yield, so that characterization and control of this component are important in order to optimize conversion of bitumen and heavy oil to synthetic crude oil.

A Hitachi X-650 scanning electron microscope equipped with both EDX and WDX detectors was used to provide detailed information on the chemical and mineral composition of solid deposits on catalyst or reactor surfaces. The use of the fiducial marks allowed analysis of exactly the same fields of view of the samples which were characterized by the optical microscope. The OM provides only limited information on the elemental composition of a sample, and it is generally not possible to identify organic species or to distinguish between anisotropic or isotropic cokes in the SEM. In order to understand the role of mineral components in the nucleation and formation of coke species, a method of correlating the images and compositional information has been developed that combines the strengths of both techniques. By correlation of the OM and SEM information, it has been possible to generate a more complete understanding of the coke deposition mechanisms.

Due to differences in the imaging characteristics of the optical and of the electron microscopes, the micrographs obtained in the optical microscope were printed in reverse in order to obtain a correlation with the images formed in the SEM. With digital imaging and a computer-controlled display, it is also possi-

The authors are at the Department of Energy, Mines and Resources, CANMET, Fuel Processing Laboratory, P.O. Bag 1280, Devon, Alberta, Canada T0C 1E0.

ble to reverse the electron microscope image, although it is easier to work from an appropriately developed OM image.

Results

Coprocessing of bitumen and heavy oils with coal is considered to be a technically feasible approach to the production of synthetic crude oil. It is thought that there are mutually beneficial synergistic effects during the coprocessing operation that provide liquid yields greater than the sum of what would be obtained by individual processing. The addition of coal during heavy-oil upgrading also seems to reduce coke formation and minimize its deposition on reactor walls.

Examination of carbonaceous solids from a coprocessing reactor revealed that the coke particles are quite distinct from the coal phase (Fig. 1). The OM examination demonstrated that the coke component has an anisotropic character that varies from fine mosaic to large domains. The processed coal particles are isotropic with characteristics similar to the feed coal, but with higher mean random reflectance, from 0.4% to 1.1%, which indicates an increase in aromaticity.

The micrograph in Fig. 1(B), taken with the backscattered electron detector on the same field of view as in the optical micrograph (Fig. 1A), reveals the distribution of the inorganic components: they are concentrated in the fine mosaic anisotropic coke marked F in the micrographs. The x-ray spectrum of area F is shown in Fig. 1(E). This situation is representative of the particles analyzed, which demonstrates that the inorganic components play an important role in determining the size of the anisotropic domains of the resulting coke. The presence of iron sulfate serves to catalyze the process and at the same time hinders the formation of large anisotropic coke domains. The x-ray spectra obtained by the correlated OM/SEM technique show significant iron and sulfur (from an iron sulfate catalyst) in the fine mosaic anisotropic coke; the large domain anisotropic coke (D) shows little evidence of this catalyst.

This particular coprocessing operation did not produce any dramatic reduction in coke formation, but did result in a significant reduction on the deposition of coke on the reactor walls. Most of the coke was found cementing the coal particles as depicted in Fig. 1.

The micrographs in Fig. 2 illustrate the deactivation of catalysts due to coke formation and mineral deposition. Coke and inorganic or mineral deposits on the catalyst surface form an impervious outer layer and also reduce catalyst porosity in the interior of the catalyst body, which prevents liquid flow through the catalyst and significantly degrades the catalytic activity.

Figure 2(B) is an SEM backscattered electron image showing a catalyst rod with a thick outer layer of deposits; Fig. 2(A) is an optical micrograph at similar magnification. Figures 2(C) and (D) are optical micrographs at higher magni-fication and show the deposits of coke and minerals (mostly clays) in the interior as well as in the outer layer of the catalyst. The indications are that a combination of the mineral and coke deposition from the liquid phase is responsible for the degradation of catalyst activity as the coating builds up. The effect of the coating, by restricting access to the catalyst sites, is illustrated in the linescan of vanadium concentration across the catalyst cross section (Fig. 2E). Vanadium is a common constituent in the large organo-metallic molecules present in the heavy oil and bitumen feedstocks. As the larger organic constituents are cracked to the smaller molecular weight synthetic crude oil, the vanadium component is released and reacts to deactivate the catalyst. Normally the porosity of the catalyst is such that access throughout the catalyst is uniform and vanadium concentration is constant because of equal access of the large organic molecules to the active catalyst sites. The exponential decrease in vanadium from the edge to the center of the catalyst shown in Fig. 2(E) indicates blocking of the larger pore spaces at the catalyst surface, resulting in poor catalyst performance.

Figure 3 is an example of coke deposition on a reactor wall. Figure 3(A) is an optical micrograph showing anisotropic coke (A) which has a reflectance value of 5.0%, isotropic coke (I) with a reflectance of 1.2%, and isotropic grooves (G) with a reflectance of 0.7%. The high reflectance of the anisotropic coke (A) is indicative of much higher aromaticity than cokes (I) and (G). Coke (G) exhibited some fluorescence under excitation with blue violet light, indicating that the organic components in this area have not been completely transformed. Figure 3(B) is an SEM micrograph taken at a similar magnification and over the same field of view as the optical micrograph in Fig. 3(A). Figure 3(C) is a high-magnification optical micrograph taken with differential interference contrast to reveal the anisotropic nature of the particle marked (A).

The correlation of the OM and SEM images allows one to characterize the elemental composition of the three types of coke described. Figures 3(D), (E), and (F) are the spectra from the isotropic coke (I), the anisotropic coke (A), and the grooves (G), respectively. The Si and Al in the isotropic coke and in the groups are typical of clays found in the bitumen feed material. The association of minerals with the isotropic coke but not with the anisotropic coke indicates that the mineral matter is affecting coke formation. The S is characteristic of the organic components; in the case of the anisotropic coke (A), there is very little inorganic component. Based on the high aromaticity of the anisotropic coke (A) and its different elemental composition, it is clear that it was formed at a different stage in the process than the components (I) and (G). The fluorescence of the area G indicates that this organic component has not yet been completely transformed into coke.
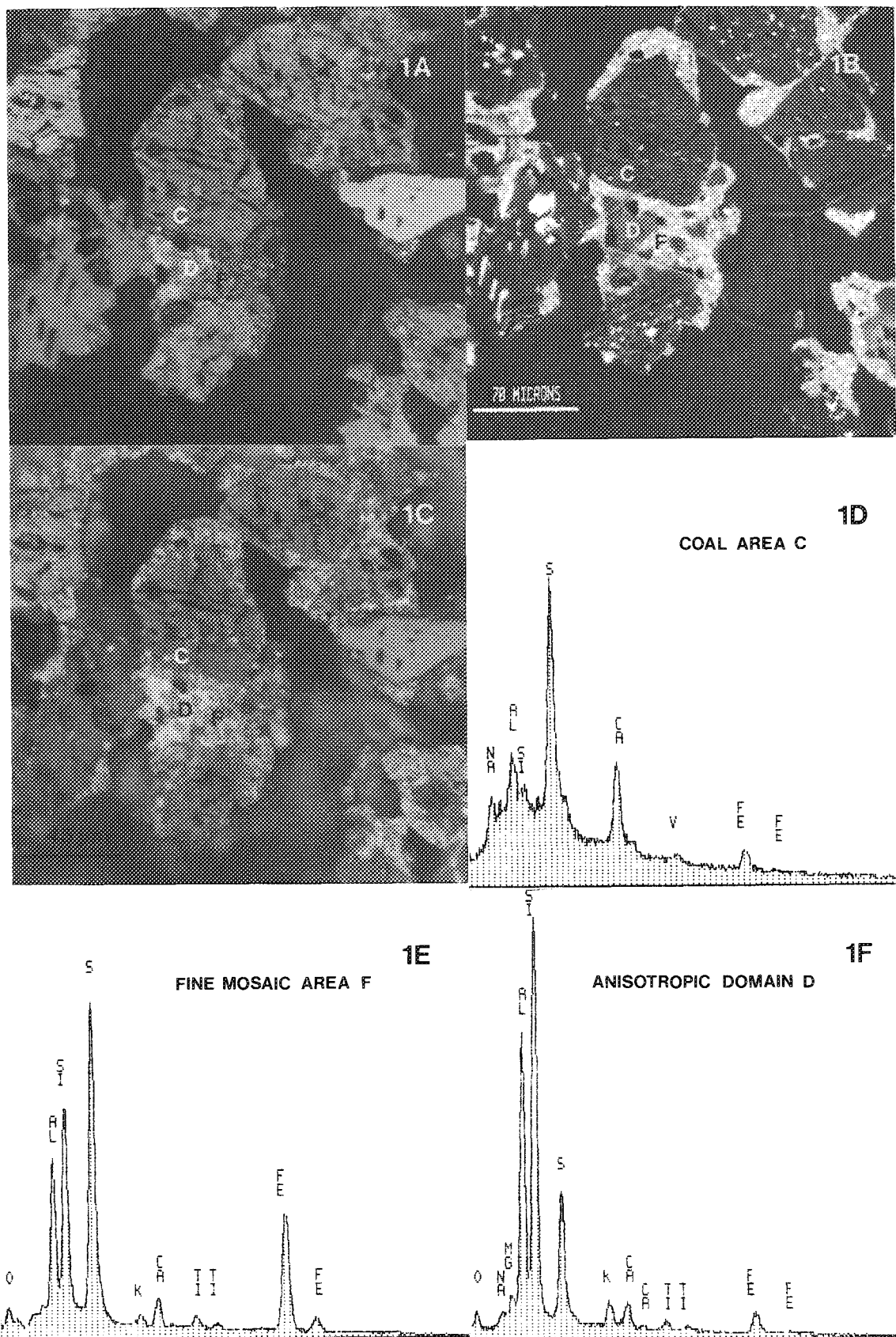
FIG. 1.--(A) Optical micrograph of coal particles (C) fused by coke. Anistropic coke domain (D), fine mosaic coke (F). (B) SEM backscattered electron detector image corresponding to (A). (C) Optical micrograph (partially cross-polarized light) showing anisotropic domain (D) and fine mosaic coke (F). (D) Coal particle (C) x-ray spectrum. (E) Fine mosaic anisotropic coke (F) x-ray spectrum. (F) Anisotropic domain (D) x-ray spectrum.
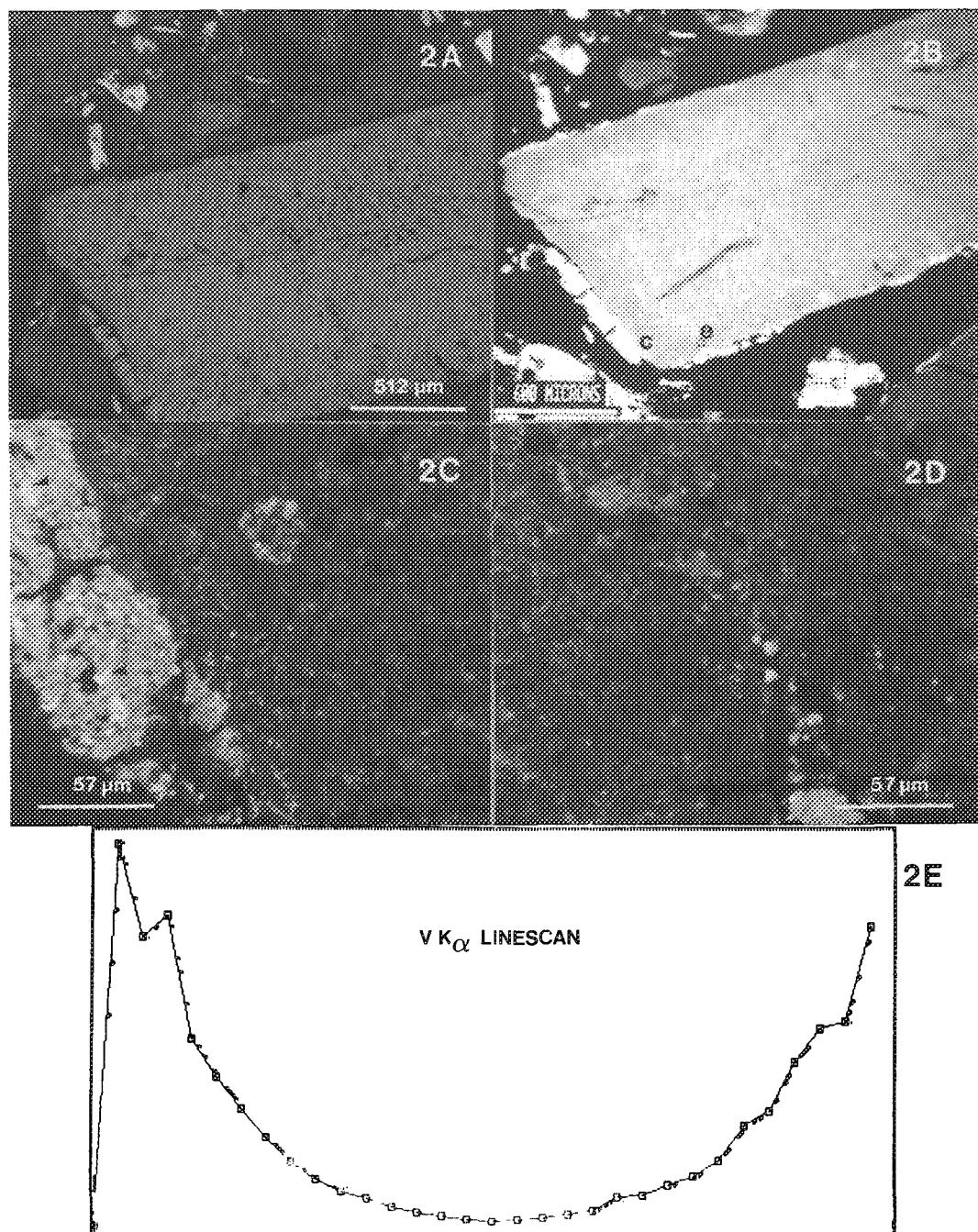
FIG. 2.--(A) Optical micrograph of catalyst rod exhibiting thick outer layer. (B) SEM backscat-
tered electron detector image corresponding to (A). (C) Optical micrograph of area (c) in (B)
showing coke and inorganics (arrows) in outer and interior regions. (D) Optical micrograph of
area e in (B). (E) Vanadium Kα linescan across catalyst cross section (32 points, 30 s/pt),
0.15 nA at 35 keV).
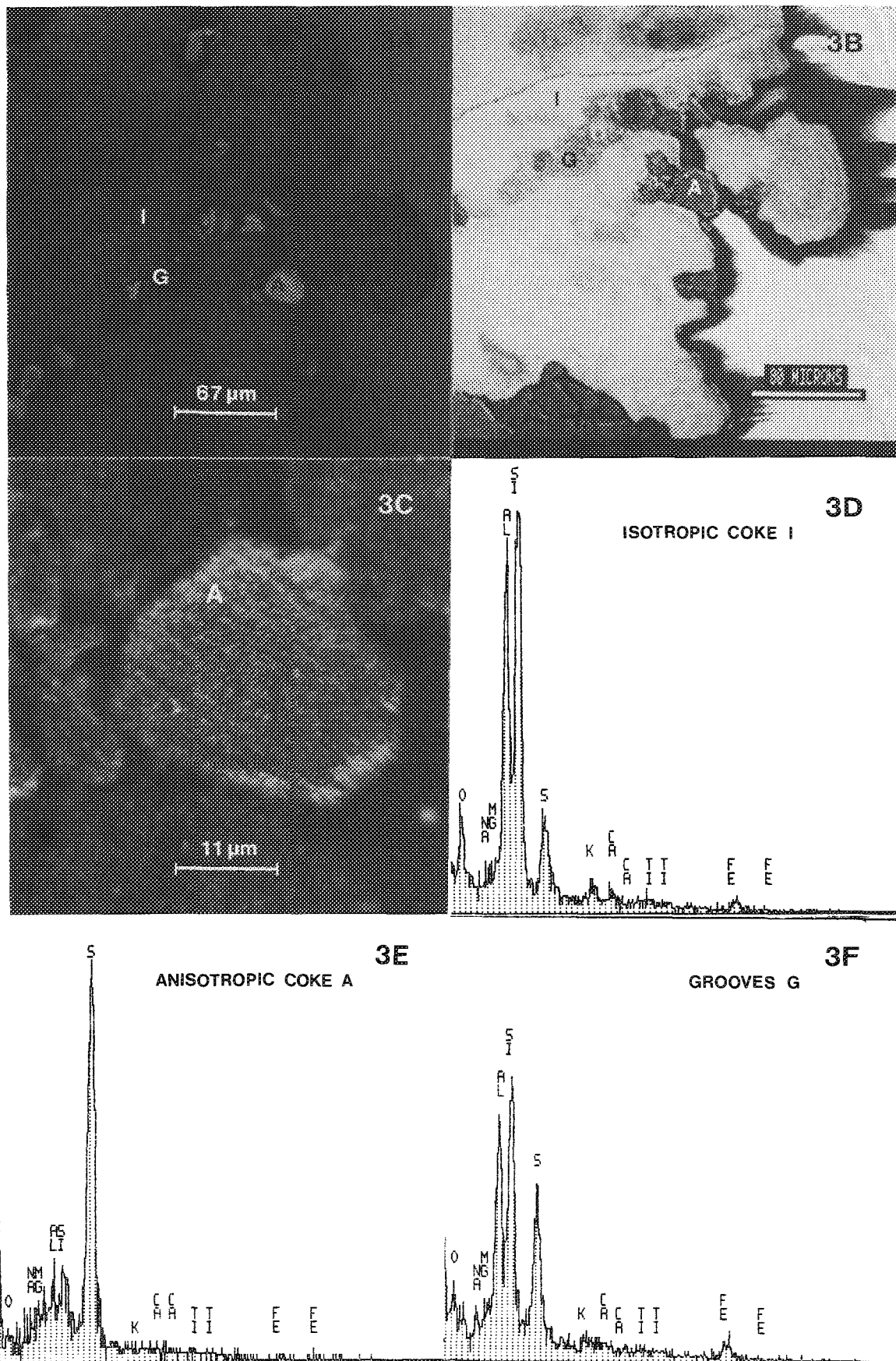
FIG. 3.--(A) Optical micrograph of coke deposited on reactor wall showing isotropic coke (I), isotropic grooves (G), and anisotropic coke (A). (B) SEM micrograph corresponding to (A). (C) Differential interference contrast micrograph (particle A). (D) Isotropic coke (I) x-ray spectrum. (E) Anisotropic coke (A) x-ray spectrum. (F) Isotropic grooves (G) x-ray spectrum.

Conclusions

Correlation of optical and scanning electron microscopic images gives a degree of detail in the characterization of coke not achievable by either technique alone. The complementary nature of the OM and SEM techniques allows one to correlate mineral composition with the nature of the organic or coke components phase; to determine the source of coke deposition, whether it is from the liquid or gas phase; and to determine the role of mineral matter and catalysts in preventing or enhancing coke deposition.[10]

References

1. American Society of Testing Materials (ASTM), D-2797 (Reapproved, 1980), *Preparing Coal Samples for Microscopical Analysis by Reflected Light*, ASTM, Part 26, Philadelphia, Pa., 1983.

2. H. Marsh and C. Latham, "The chemistry of mesophase formation," in J. D. Bacha, J. W. Newman, and J. L. White, Eds., *Petroleum-Derived Carbons*, Washington D.C.: ACS Symposium Series 303, 1986, 1-28.

3. L. S. Singer, "The mesophase in carbonaceous pitches," *Faraday Discuss. Chem. Soc.* 79: 265-272, 1985.

4. V. A. Weinberg and T. F. Yen, "Mesophase formation in coal derived liquid asphaltene," *Fuel* 61: 383-388, 1982.

5. V. A. Weinberg and T. F. Yen, "Mesophase formation in coal liquid solvent fractions," *Carbon* 21: 39-45, 1983.

6. I. M. Warner, "Molecular fluorescence and phosphorescence," in G. D. Christian and J. E. O'Reilly, Eds., *Instrumental Analysis*, Allyn and Bacon, 2nd ed. 1986, 274-277.

7. C. N. R. Rao, *Ultra-violet and Visible Spectroscopy: Chemical Applications*, Butterworths, 3rd ed., 1975.

8. C. E. White and R. J. Argauer, *Fluorescence Analysis: A Practical Approach*, New York: Marcel Dekker, 1970.

9. V. A. Munoz, R. J. Mikula, and W. W. Lam, "Microscopic techniques for the identification of coke," *Proc. 16th Ann. Mtg. Microscopical Society of Canada*, 1989, 56-57.

10. The authors thank K. C. McAuley for preparation of the figures.

GROWTH OF LARGE SINGLE CRYSTALS IN THIN-F   OXIDES

M. C. Boettcher and D. G. Howitt

Large grained metal oxide films show promise for use as quantitative standards for analytical microscopy. They have well-described reproducible chemistry that can be determined from selected area diffraction patterns; their thickness is uniform and can be monitored by cross-sectioning techniques. The growth of these films and the structures they form have been investigated by transmission electron microscopy.

Thin-film metal oxides of titanium aluminum, chromium, molybdenum, and niobium were prepared by ion beam sputtered by use of pure metal foil targets. The films were deposited on freshly cleaved sodium chloride <100> substrates, approximately 1 cm square. The salt was located directly below the target at a distance of 5 cm and tilted through ±15° during deposition. A focused ion gun was positioned below the target, impinging at an angle of 30°. The chamber is held under vacuum while a 3.4×10^{-4} Torr back pressure of oxygen gas was bled into the chamber, near the substrate surface, so that oxidation of the metal atoms occurred as the material was deposited. The films were prepared at thicknesses between 300 to 400 Å and were completely amorphous, as determined by selected-area diffraction.

The films were floated, annealed for 1 h, then rapidly quenched ($\sim$500 C/s). After annealing, planar crystals were observed as a result of the amorphous to crystalline transition. Explanation of microstructural features is based on the latent heat of the transformation.[1] Argon, which is incorporated in the growing film during deposition,[2] prefers to aggregate during the annealing process. This dissolution reaction causes planar recrystallization to become more favorable than random grain growth throughout the thickness of the film. Diffraction analysis of the large crystals and determination of the oxide structure indicates that most of the films form the terminal oxides, unless the oxygen partial pressure is carefully controlled. The annealing temperatures were determined by trial and error, increasing the furnace temperature until crystallization was observed.

References

1. D. G. Howitt and A. B. Harker, "The oriented growth of anatase in thin films of amorphous titania," *J. Mater. Res.* 2: 201, 1987.
2. H. F. Winters and Eric Kay, "Gas incorporation into sputtered films," *J. Appl. Phys.* 38: 3928, 1967.
3. R. C. West, Ed., *CRC Handbook of Chemistry and Physics*, 4th ed., 1983, D-70.
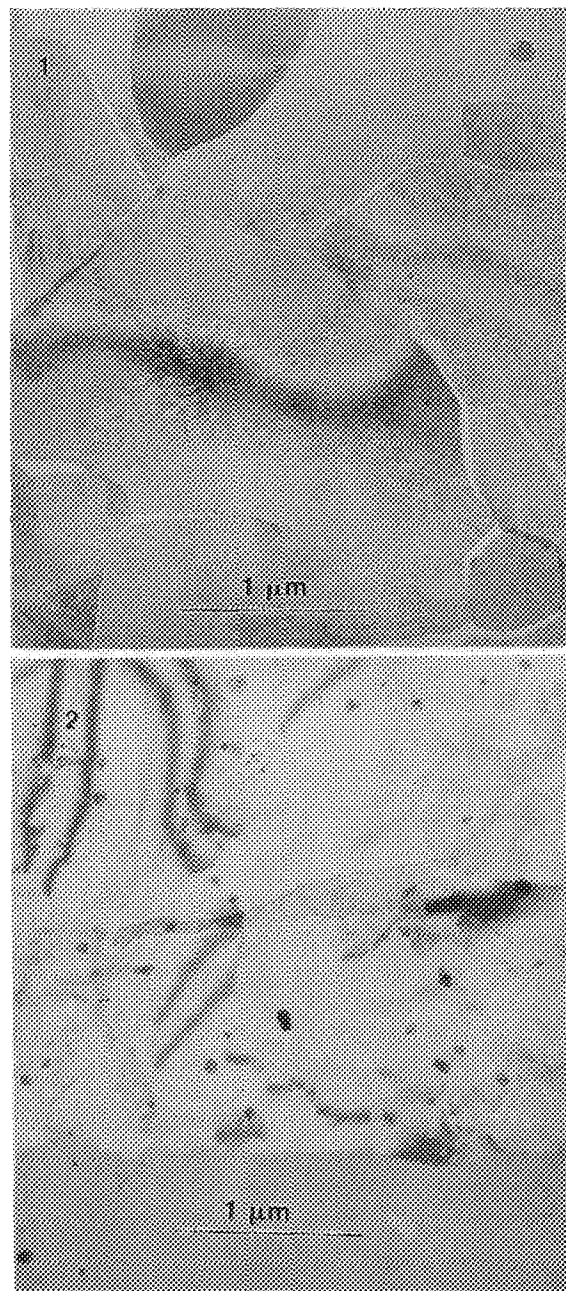
FIG. 1.--Large crystals of annealed Cr_2O_5.
FIG. 2.--Annealed Al_2O_3.

The authors are at the Department of Mechanical, Aeronautical, and Materials Engineering, University of Davis, Davis, CA 95616.

EFFICIENT USE OF MULTIPLE SIGNAL SOURCES IN IMAGE ANALYSIS

P. J. Statham and J. N. Jefferson

A digitized 2-D optical image or an electron micrograph typically consists of less than 1 Megabyte of data. When multiple signal sources are available, considerably more data may be involved. Spectrometers sensitive to x rays (e.g., EDX) or electron energy loss (e.g., EELS) introduce the additional dimension of energy, so that at every pixel a spectrum of values is available rather than a single intensity reading. Such signal sources are "expensive" both in storage (at least 2K bytes per spectrum) and in acquisition time when compared to a "low-cost" signal such as from a backscattered electron detector (BSED), which only requires a single byte for storage and gives a good signal-to-noise ratio (S/N) in a short acquisition period. Therefore, when EDX or EELS sources are involved, there is the potential for spending hours to acquire information at the same resolution as a typical micrograph and generating some Gigabytes of stored data. The answer to some question about a sample can be represented as a single bit (yes or no); in this respect, image analysis can be seen as a method to extract a small amount of "relevant" information from a vast pool of mainly "uninteresting" data. What is "relevant" and what is "uninteresting" depends on the study in question. When we have some prior knowledge of what to expect, we can use it to enhance the interesting parts of the data. If, by doing so, we can reduce data storage requirements and increase the speed of reaching a conclusion, the overall efficiency will have been improved.

In many cases we can reduce storage requirements simply by preselecting analytical information. For example, instead of storing a whole spectrum at each pixel, we can record a single number for each of several energy bands. This change will not affect the overall acquisition time but will reduce the Gigabytes of available data to a more manageable collection of images. Multivariate statistical techniques (e.g., principal-component analysis, PCA, or factorial analysis of correspondence, FAC) can then be used to condense these data even further into a few images that maximize the contrast for relevant information.[1,2]

The approach of using simple integrals over energy bands together with a sophisticated statistical analysis is one way of avoiding explicit correction for background in every spectrum. By not making any assumptions about the form of the background, systematic errors

---

The authors are at Link Analytical Ltd, Halifax Road, High Wycombe, Bucks, England HP12 3SE. Experimental results were provided by Julie Sheffield-Parker and Lorna Thomas.

due to an inaccurate background model will not be present in the data set and misinterpretation of artifacts can to some extent be avoided.[2] However, for EDX spectra, background-modeling and multiple-least-squares fitting can be applied reliably at each pixel and these quantitative corrections result in elemental images that give higher contrast and are more representative of elemental content than with uncorrected spectral samples. Statistical standard deviation images can also be derived and used to confirm hypotheses about the presence or absence of certain elements or the likelihood of two analyzed points being of different composition.[3]

The multiple image approach is useful because it offers analytical information for every pixel. However, in practice, there can be computational problems when extracting and manipulating pixel intensities from a series of large and separate images. Moreover, if there are only a few features of interest in the field of view, both storage and acquisition time are wasted on nonfeature pixels. When there is little prior knowledge about the sample, it may indeed be necessary to process all the data to discover the best way to delineate features and identify suitable classifications for chemical composition. However, where there is prior knowledge, or where a comprehensive analysis can be used as a "training" exercise to build up this knowledge, considerable savings can be made in both time and storage by allowing the computer to make decisions during image acquisition and thus to avoid recording superfluous analytical information.

These principles have been adopted in a software program we have developed called FEATURESCAN. On-line decision making is the function of the FEATURE FILTER facility, which is designed to optimize acquisition time when compositional analysis is required. First a run-length encoded binary image is obtained by thresholding an electron signal during a fast scan over the field of view. During this stage, no x-ray data are recorded. The selected pixels are collated into "features" that are subjected to a number of measurements, and various shape factors can be calculated. A simple example is shown in Fig. 1, in which the features have been highlighted where the fiber aspect ratio (length/width) is greater than 6. Since the features only occupy a small fraction of the total area of the field, considerable time is saved if x-ray data are only acquired within recognized features, rather than from all pixels as in an x-ray map. Furthermore, if only specific shapes are of interest, one can save further analysis time by invoking the FEATURE FILTER and only acquiring x-ray data

from features that fulfil certain shape criteria, as do the fibers for example in Fig. 1.

Once features have been selected for analysis on a morphological basis, a variety of signals can be used to determine composition. If the aim is to decide to which of several chemical classes each feature belongs, it is often possible to decide on some of the classes on the basis of a fast "inexpensive" measurement such as BSE. Further classes may need to be identified on the basis of x-ray analysis with a short dwell time. If the feature still cannot be classified unambiguously, a longer dwell time can be used to improve the precision. The FEATURE FILTER is thus used to minimize both the number and duration of measurements necessary to insure an accurate classification for each feature of interest.

If each feature is homogeneous in composition, there is no need to acquire data at every pixel position within the feature; a single analysis result can be obtained by acquisition of data at a single point or by continuous rastering within the feature. However, variations of composition within each feature may actually be the subject of study. Although it would be possible to refer to a series of x-ray maps and extract the data at each pixel position within each feature, the overall analysis time can be reduced considerably by limitation of data acquisition to individual pixels within each feature rather than over the full field. Furthermore, if the aim is to sort each pixel into one of a number of compositional classes, acquisition time can be reduced even further, as shown in the following example.

The histogram of gray levels below the right-hand image in Fig. 2 shows how the BSED signal can be used to provide a broad characterization of composition. Pixels with gray levels 0-15 are assumed to be of no interest (epoxy resin) and therefore a threshold equivalent to 16 is used in a fast preliminary scan to isolate features from background, as shown in the binary image top left in Fig. 2. Quartz and lead sulfide can be identified on the basis of mean atomic number alone, so that a rapid BSED measurement is sufficient for classification. Only if the BSED measurement gives 40-185 is it necessary to acquire any x-ray data to resolve whether a pixel is iron or zinc sulfide or does not fit in any class. In principle, the iron and zinc sulfides could also be separated on the basis of mean atomic number, but small variations in geometry and imperfections, coupled with electronic noise, produce a spread in BSED signal, so that the distributions overlap as shown in Fig. 2.

Electron scattering and inferior statistical precision make the intrinsic spatial resolution for x-ray data much less than for an electron image. Since there is usually a practical lower limit on the dwell time suitable for EDX analysis, it is often better to acquire compositional data on a coarser grid than that used for delineating features. Thus, prior knowledge again suggests how to optimize the experiment. Figure 3 shows the result of performing compositional analysis within each feature on a grid four times coarser than that used for digitizing the original image. Since the figure is reproduced in monochrome, the separation of pixels into colors representing individual phases is not apparent, but some of the areas of different compositions can be seen. In this example, a PHASE FILTER facility has been used to augment the FEATURESCAN program and optimize the acquisition time in the same way as the FEATURE FILTER did for whole-feature analysis. Thus, the areas of quartz and lead sulfide have been classified rapidly on the basis of BSED intensity alone (50 μm per pixel) and "expensive" x-ray data (50 mS per pixel) have only been acquired where essential.

In this last example, information has been obtained about both grain size and distribution of certain minerals within grains, which can be used in a study of mineral liberation to confirm a proposed course of action by a minerals processing engineer. In effect, the information has been selected from a database 512×512 pixels with roughly 2K bytes of spectral information at each pixel; i.e., approximately 0.5 Gigabytes of data. These data would have taken around 4 h to obtain at 50 ms/pixel. If only 10% of the field were occupied by grains, feature and phase filtering as described would reduce analysis time to the order of 1 min. Furthermore, by using run-length encoding of the binary image, extracting only relevant characteristic x-ray intensities from spectra and only storing measurements and accumulated totals of classified pixels for each identified feature, one can reduce the overall storage requirement typically to 10 K-100 K bytes. Thus, the overall expense of doing the study is reduced dramatically by use of prior information.

The general principles of on-line filtering are illustrated by Fig. 4, where the total volume of solid regions represents the cost of an experiment; if some signals are expensive to measure, particularly in terms of time, they should only be recorded where absolutely necessary. By using a low-cost signal to delineate features in layer A, one can avoid superfluous analytical measurements of background regions in the more expensive layer B, and the most expensive signal (e.g., EDX) is measured in C only where the results from B are inconclusive. The overall volume (that is, cost) of the experiment is therefore much lower than it would be if all the data had to be acquired first and computer processing applied retroactively.

References

1. J. M. Paque et al., "Quantitative analysis of x-ray images from geological materials," *Proc. XII ICEM*, 1990, 244.
2. P. Trebbia and N. Bonnet, "EELS elemental mapping with unconventional methods," *Ultramicroscopy* 34: 165, 1990.
3. P. J. Statham, "Pitfalls and advances in quantitative elemental mapping," *Scanning* 10: 245, 1988.
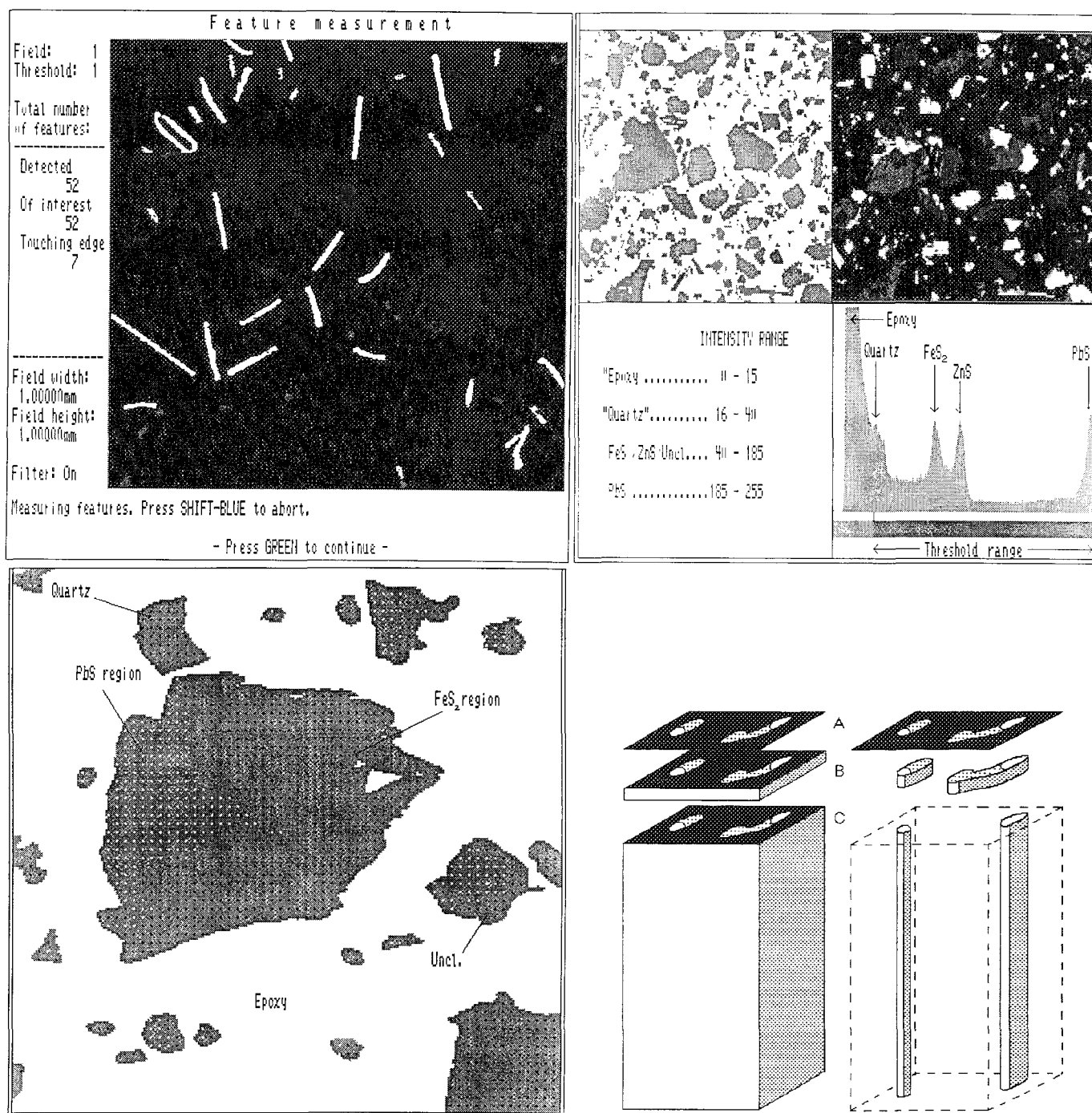
FIG. 1.--Image from airborne dust filter. Gray-level discrimination has been used to delienate features. Those highlighted have satisfied criteria for FEATURE FILTER which elminates features with fiber length/fiber width <6.0.

FIG. 2.--Data from sample of base metal sulfide concentrator product. Top right is BSED image and histogram beneath shows relationship between gray level and mean atomic number of minerals present. Thresholding segments image at top left into particles of interest and areas of epoxy rein.

FIG. 3.--Enlarged area from same sample as for Fig. 2, showing results of chemical classification at pixels within each particle. Acquisition time for PbS and quartz pixels is only 50 μs because they can be identified on the basis of a single BSED measurement. A further 50 ms was used for EDX to identify FeS_2 pixels. Unclassified pixels at right correspond to imperfections visible in original electron image.

FIG. 4.--The principle of on-line filtering to improve efficiency of image analysis with multiple signal sources. Left-hand diagram symbolizes cost of acquiring data from three signal sources over whole image field. Vertical axis represents cost per pixel (e.g., acquisition time), so that volume represents total cost. Right-hand diagram shows how cost can be reduced by measuring B only on features of specific shape selected by lowest-cost signal A and C performing expensive measurements only at pixels that cannot be uniquely identified by B.

181

QUANTITATIVE DIGITAL IMAGING APPLIED TO THE STUDY OF WELD DEFECTS

D. L. Parker and R. L. Ornberg

Quantitative images of the elemental composition of bulk and thin-sectioned specimens provide correlations between structural features and microchemical composition. Elemental composition data in image format are equivalent to numerous simultaneous point measurements. The advantages and use of elemental images produced by both wavelength-dispersive (WDS) and energy-dispersive (EDS) procedures have been previously reported.[1-3] Images generated by WDS techniques, as opposed to EDS procedures, take advantage of the improved peak-to-background, sensitivity, and ease of spectral processing in generating quantitative images. This paper describes the use of a commercially available electron microprobe WDS imaging system to determine the metal composition of defective weld joints in a Monel alloy hose. We have found that defect cracks can be directly correlated to narrow, 2-3μm-wide regions of high copper/nickel alloy within Monel weld joints.

Procedures

A Cameca MicroBeam system (Cameca Instruments, Inc.) equipped with three wavelength spectrometers and interfaced to a KEVEX 8000 digital imaging system (KEVEX Corp.) was used for this study. The three spectrometers were interfaced to the image processor, which was controlled by KEVEX Advanced Digital Imaging software. This configuration permitted the collection, storage, and display of data from all WDS units in the conventional KEVEX format. To avoid the problem of spectrometer defocus at low magnifications, all images were obtained at magnifications of 800× or more.[4] The Advanced Digital Imaging software routines as supplied by KEVEX were converted from the RT/11® (Digital Equipment Corp.) operating system to RSX/11M® (Digital Equipment Corp.) by Cameca Instruments to facilitate system operation under a consistent computer environment. The RSX/11M® operating system is a multitasking environment that allows collection of a multiple element image file from the three spectrometers while maintaining EPM system calibration and control. Images typically collected contained 256 × 128 pixels.

Image files were transferred to an IBM 80386 PC for processing, by use of Kermit communications software.[5] Raw x-ray intensities for each element at selected pixel locations were first corrected for dead time and then trans-

formed into K-ratios by means of software written in the C language. K-ratios were calculated with intensities from standard spectra obtained under identical instrument conditions. Background intensities for each element were obtained from the spectra file of the interfering element. This C-based routine returns a data file compatible with and processed for ZAF corrections by the standard Cameca routines.
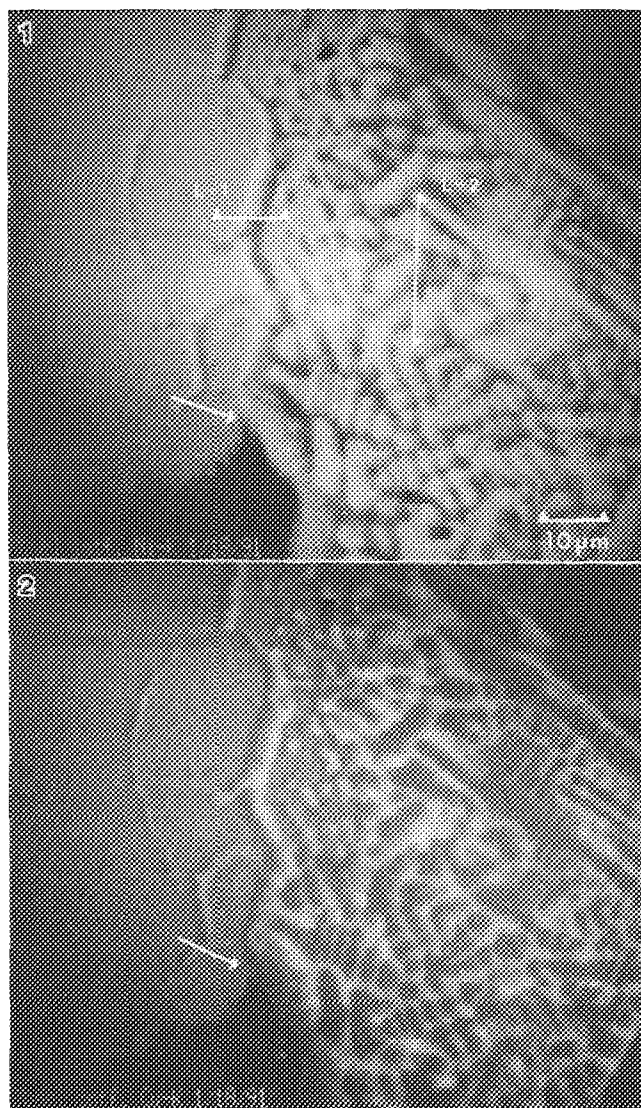
FIG. 1.--Image of nickel x-ray intensities in cross section of Monel hose weld interface. Arrow indicates edge of crack at high Ni/low Cu domain.
FIG. 2.--Image of copper x-ray intensities from area shown in Fig. 1.

The authors are with Monsanto Co., Physical Sciences Center/Monsanto Corporate Research, St. Louis, MO 63167. We acknowledge the collaboration of J. Scott Parker in the development of critical computer routines.

(a) Profile of Nickel and Copper Content

Profile of Nickel and Copper Content (b)
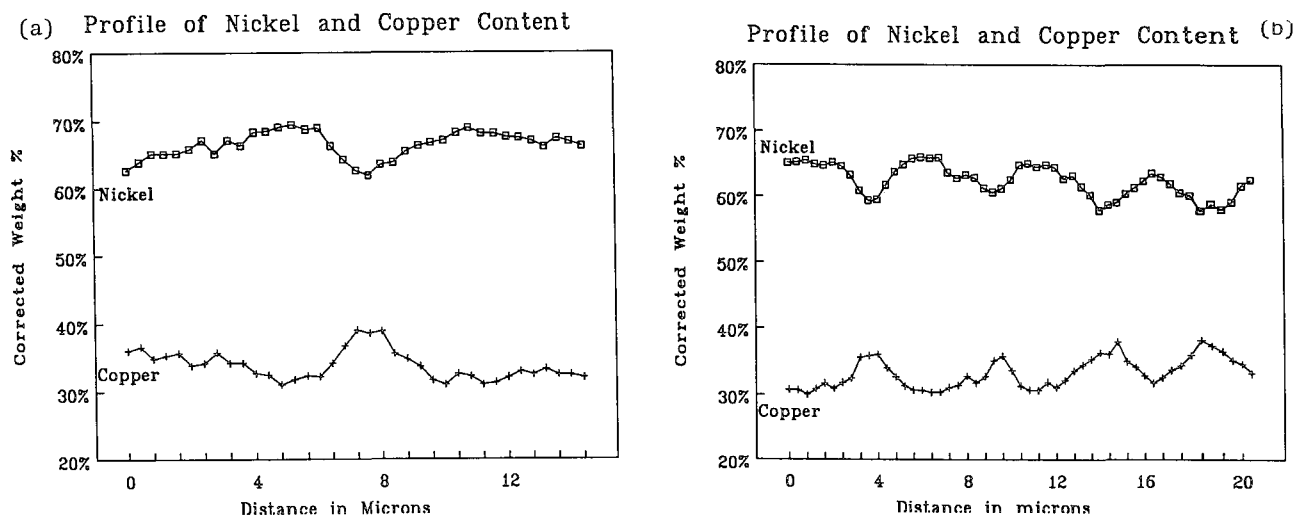
FIG. 3.--ZAF-corrected weight-percent concentration profile measured at (a) 38 pixels (15 μm) on line 1 of Fig. 1, (b) at 53 pixels (20 μm) on line 2 of Fig. 1.

Results

Weld joints in a seamless Monel bellow type transfer hose were found to develop cracks in applications involving the transfer of liquid chlorine. In worst cases, the cracks were found to perforate the hose completely at the weld structure. Conventional point mode EPM analysis provided no indications of abnormal surface composition at the failure sites. Detailed examination of unexposed cracks emanating from major defects within the weld also failed to elucidate a source of failure. Elemental images of failed areas provided the first indication of a nonuniform distribution of Monel constituents within the weld. The interface between the Monel hose matrix and the weld area is shown in cross section in the nickel and copper composition images (Figs. 1 and 2). As expected, the Monel hose had a uniform distribution of copper and nickel. However, the weld region contained numerous discrete regions of high copper and nickel which varied from 0.5 to 2 μm.

To verify the copper and nickel distributions in these images, data from the uniform Monel alloy obtained by conventional point-mode EPM analysis and from images were compared. For this comparison, a conventional step-scanned EPM procedure, using 30s counting times, was compared to 14 randomly selected pixel analyses of 1s dwell time. The weight percent values were 34.81 ± 0.28% copper and 62.96 ± 0.47% nickel for the EPM data, and 34.98± 0.53% copper and 61.95 ± 0.71% nickel for the image data. Although the standard deviation of the image data is twice that of point mode data, the copper and nickel are not statistically significant. The slight decrease in precision of the image data is most probably due to the short pixel dwell times (and hence lower intensity values) of the image data. The good agreement for copper and nickel demonstrated the validity of WDS analy-

sis from the image processing system.

Within each matrix/weld interface area, enriched nickel/depleted copper domains were found on the matrix side of the weld mixture. Immediately adjacent to these enriched nickel domains, in every case, were depleted nickel/ enriched copper domains. To characterize these nonuniform metal distributions further, the weight percent values for two rows of pixels (lines 1 and 2 in Fig. 1) were collected and plotted in Fig. 3. Line 1 represents a 14μm segment (38 pixels) extending, perpendicular to the joint, from the Monel hose matrix to the weld area. Line 2 represents a 19μm segment which runs parallel to the joint. As shown in Fig. 3, the variations in copper content are inversely related to variations in nickel; changes of 8% by weight are observed. For the entire image, the maximum deviation was 14% for Ni and 16% for Cu.

The role of these high copper and high nickel domains in the development of cracks within the hose was apparent from the coincidence of the cracks and the domains and the shape of the edge of the crack and the domains. The dark region (arrow) in Figs. 1 and 2 illustrates a crack in the weld joint lying next to an enriched nickel domain. In images not shown, fine micro cracks appear to propagate along these domains. Therefore, we believe that these subtle but detectable changes in composition within the Monel weld play an important role in crack formation and weld failure.

Conclusion

In this paper we have described a WDS electron probe imaging system and illustrated its use in obtaining microchemical and structural information where conventional SEM imaging methods failed. As with previous reports, our results demonstrate the many advantages of ana-

lytical imaging in electron microscopic exam-
ination of bulk specimens.

References

1. C. E. Fiori, R. D. Leapman, and K. E.
Gorlen, "Computer-aided compositional mapping
in scanning electron column devices," *Micro-
beam Analysis--1985*, 219.
2. R. B. Marinenko, R. L. Myklebust, D. S.
Bright, and D. E. Newbury, "Wavelength-disper-
sive techniques for compositional mapping in
electron-probe microanalysis," *Microbeam Anal-
ysis--1985*, 159.
3. D. E. Newbury, "Compositional mapping of
thick specimens," *Microbeam Analysis--1985*,
204.
4. D. E. Newbury, C. E. Fiori, R. B. Mari-
nenko, R. L. Myklebust, C. R. Swyt, and D. S.
Bright, "Compositional mapping with the elec-
tron probe microanalyzer: Part I," *Analytical
Chemistry* 62: 1159A, 1990.
5. J. M. Page, R. Browning, P. L. King,
and P. Pianetta, "Quantitative information
from x-ray images of geological materials,"
Microbeam Analysis--1990, 195.

VISIBILITY OF OBJECTS IN NOISE IMAGES AS A FUNCTION OF CONTRAST, NOISE LEVEL, AND OBJECT SIZE

D. S. Bright, E. B. Steel, and D. E. Newbury

In electron microscope or microprobe images, noise obscures objects and usually sets the basic limit to microscope performance. The noise level can be reduced by an increase in the image collection time, beam current, detector efficiency, etc. We wish to define an adequate image quality by determining the experimental imaging conditions for which objects of various sizes, densities and shapes are visible or not. It is reasonable to assume that objects are more visible if they are larger, if they have greater contrast, or if the relative noise level is less. Other parameters that might be of interest are the shape of the object, sharpness of the edges, and whether the objects are darker or lighter than the background. In our previous paper[1] we related visibility to object contrast and size for thin, straight objects. In this paper we generalize the study to a variety of objects and we relate visibility of these objects to a signal/noise parameter rather than to brightness and constrast per se.

In his 1948 paper[2] on the quality of television transmission of images, Rose[1] defined a parameter k that related visibility to the signal-to-noise of an image in this way: let b be the mean background level (assumed constant) and n be a characteristic signal level for the object. Then the contrast c above (or below) background, is

$$c = \frac{|n - b|}{n} \tag{1}$$

The signal-to-noise ratio (Poisson statistics)

$$S/N = n/\sqrt{n} \tag{2}$$

is related to the contrast in terms of a constant k that we call the Rose visibility constant:

$$c \geq k\sqrt{n}/n \tag{3}$$

Rose stated that for objects one pixel in size to be visible or to be distinguishable from background, the value for k is greater than unity and probably close to 5. If we combine Eqs. (1)-(3), we obtain k in terms of n and b:

$$k = (n - b)/\sqrt{n} \tag{4}$$

The authors are at the Surface and Microanalysis Science Division, National Institute of Standards and Technology, Gaithersburg, MD 20899. Certain commercial equipment and instruments are identified in this paper to describe the subject more fully. Such identification does not imply recommendation or endorsement by NIST, nor does it imply that the equipment identified is necessarily the best available for the purpose.

Solution of Eq. (4) for the object signal level n in terms of k and b yields

$$n = \tfrac{1}{2}(k \pm \sqrt{k^2 + 4b})^2 \tag{5}$$

where n can be greater than or less than b, depending on whether objects are to be brighter or darker than the background. To make test images, we select a background level b and then add objects of random type, size, position, orientation and k (affects contrast) by use of Eq. (5). Computer algorithms first generate images with zero noise levels and then substitute an appropriate random value for each pixel in the noiseless image. Each value is a random deviate from a Poisson distribution, with the mean value equal to the corresponding pixel value in the noiseless image.

We display and score the images with a Macintosh II using NIH_IMAGE.[3] We allow the use of arbitrary contrast stretch to provide measurements of visibility in a way that is independent of the display device, room lighting conditions, eye adaptation, and perhaps other factors. This arrangement models the situation with typical instruments that allow adjustment of the video gain and contrast. Objects become more visible up to a point, beyond which the noise is enhanced along with the objects of interest and the visibility is no longer improved.

We generated charts to show the effect of k on the visibility of various types of objects. The chart consists of disks, or other simple shapes, ranging from 1 to 20 pixels in radius and with contrasts corresponding to k values from 0.1 to 9.0. Figure 1 is a noiseless version of the image in Fig. 2, and shows the structure of the charts in Figs. 2-6. The visibility of the objects decreases downward (decreasing k or contrast) and to the left (decreasing size). In Fig. 1, the lower disks cannot be seen because of insufficient contrast in print, which illustrates the need for contrast stretch on the display screen. Figure 2 and all the other images in this paper have been enhanced with a linear contrast stretch to render them much as they might appear on the screen when one is trying to see the dimmest objects. Such high contrast does not show the shades of gray, seen in Fig. 1, which are present and are visible at lower contrast.

Similarities of visibility of the dimmer disks in Figs. 2-4 show that k is a good measure of visibility for a very wide range of background level and for objects darker or lighter than background. Figure 3 has dark disks and Fig. 4 has the background level b increased by two orders of magnitude; n is also much larger, from Eq. (5). In Fig. 5, the

185
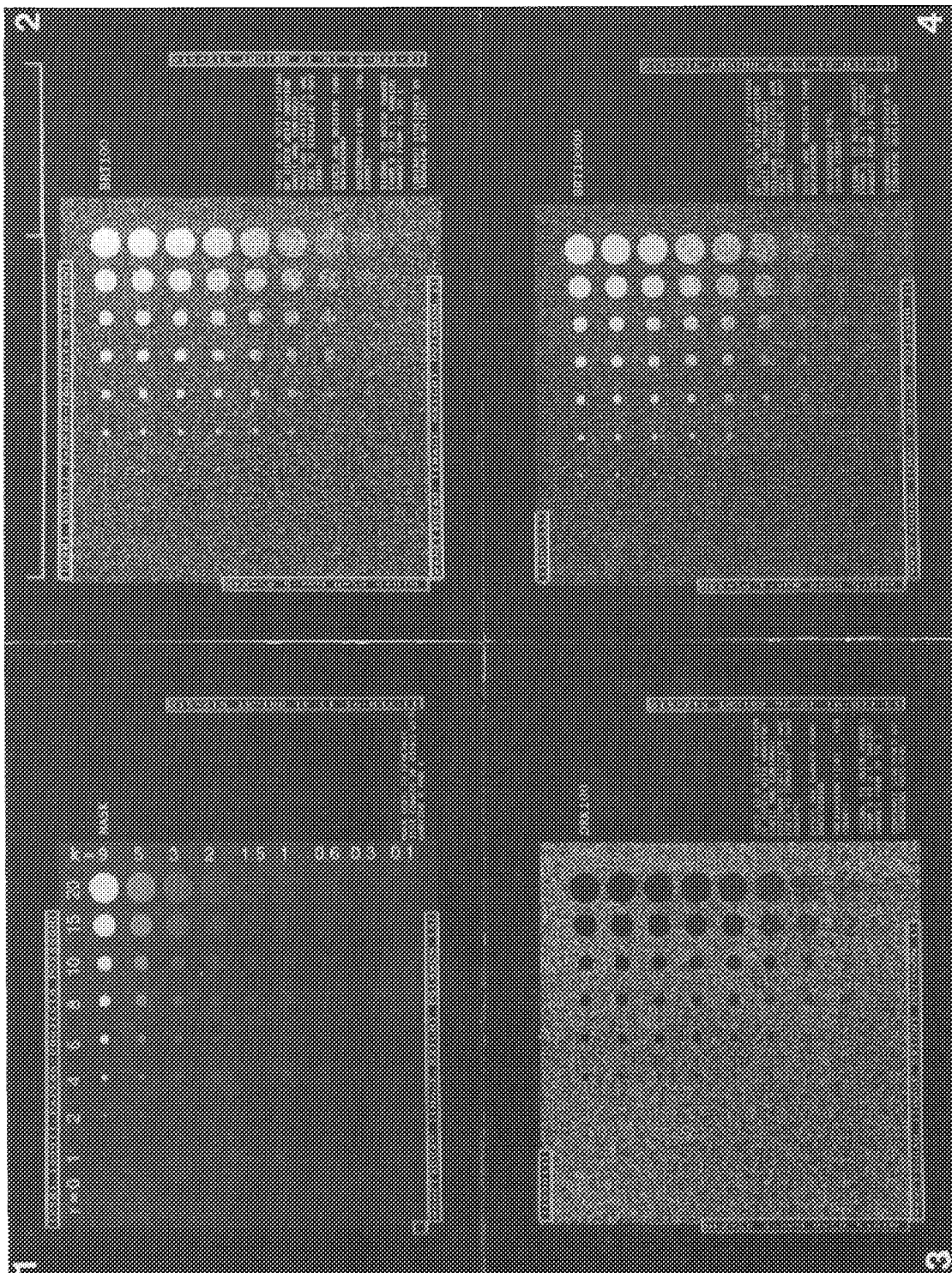
FIG. 1.--Computer-generated chart used to generate 512 × 512 pixel images in Figs. 2-b. Radii and k value in other disk charts are the same. Image is not contrast enhanced.
FIG. 2.--Test with b = 100 (background variance = 100). Contrast stretch applied (as human test subject might do it) to enhance visibility of dim objects. Other charts enhanced in same way. Image is 512 × 512 pixels.
FIG. 3.--Test with b = 100, objects darker than background.
FIG. 4.--Test with b = 10 000 (100× signal level of Figs. 2-6).
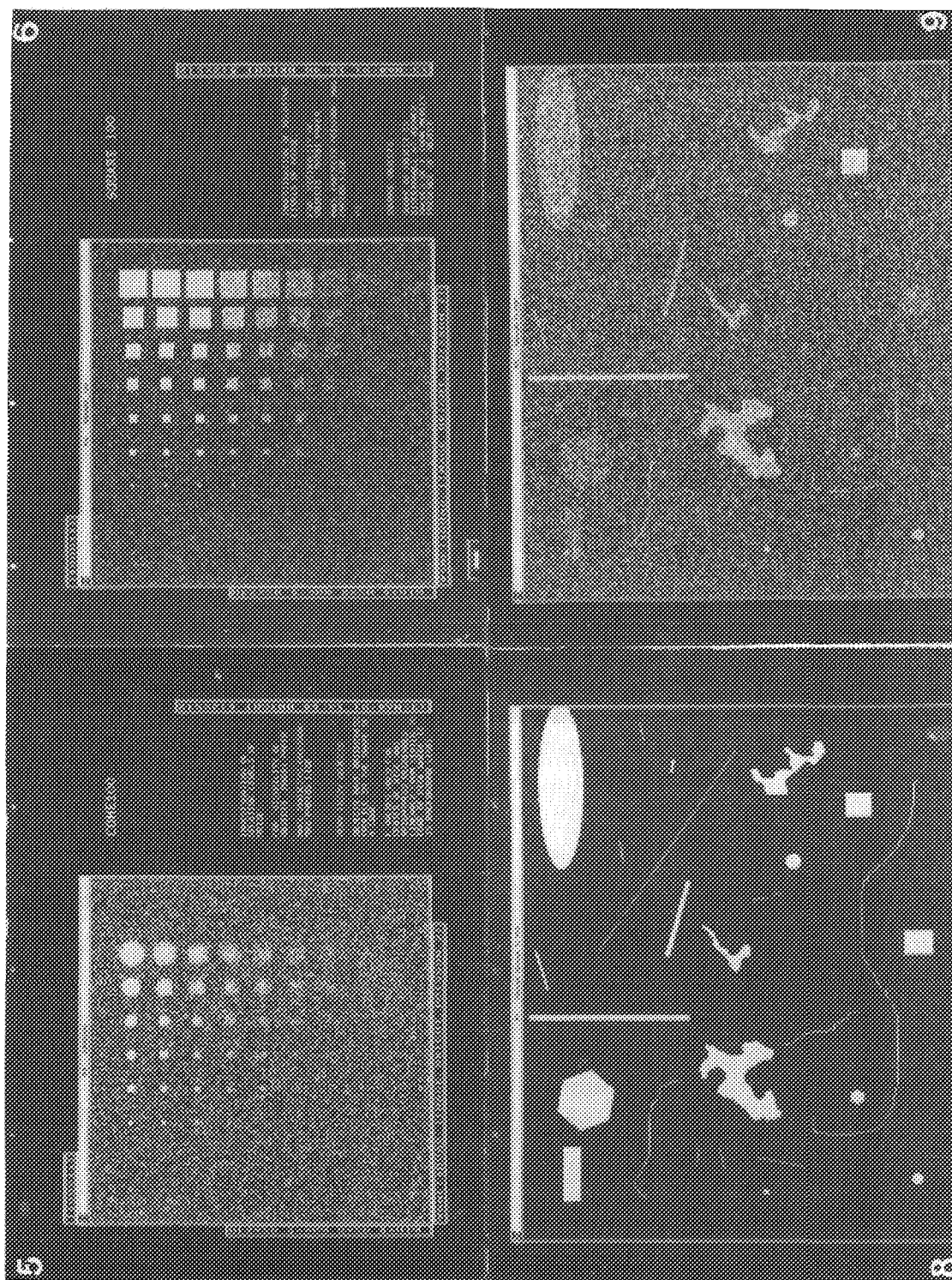
FIG. 5.--Test with b = 100. Fuzzy disks or brightness cones. Same cone intensity as in Fig. 2, but intensity drops off linearly to background level at edge.
FIG. 6.--Test with b = 100, showing squares rather than disks.
FIG. 8.--Mask of sample test image. All objects shown in white so they can be seen.
FIG. 9.--Sample test image, b = 100, k values for objects chosen at random.

187

disks have the same center or core intensity as in Fig. 2, but the intensity drops off linearly to the background level b at the rims. Comparison of Figs. 2 and 5 suggests that edge sharpness does not greatly affect visibility. That the fuzzy disks should be roughly as visible as their sharp counterparts is perhaps the most surprising result, but is consistent with our finding that the presence of an object may be clear while the shape of the object is not: note the larger but barely visible squares in Fig. 6 which look like amorphous blobs. Squares have about the same visibility as disks of similar size, but greater contrast is needed to distinguish the corners. Distinguishing shape evidently requires more contrast or signal-to-noise ratio (a higher value of k) by a factor of 2 or 3, as seen in Fig. 7 (triangles). Figure 7 shows the k values for barely detectable objects for these images, as determined by one subject. We use the value as estimates to determine ranges of k for the test images. The values of k plotted for Fig. 7 are for distinct visualization of the corners and edges of each square.

We shall evaluate results of test images analyzed by volunteers to determine more precisely the values of k for various levels of visibility and different parameters such as object size and shape. Figures 8 and 9 show a sample trial image for "scoring" by human subjects. Objects are chosen at random from a collection of objects, and placed with random position, orientation, size, and k with the one restriction of not overlapping other objects. Objects include thin and thick lines, various geometric shapes, and irregular shapes obtained from polished surfaces of a bimetal alloy. Fuzzy objects such as the disks in Fig. 5 are also included but not shown here. Subjects will identify the objects by drawing an outline (on Fig. 8) with the mouse, and will be scored (using Fig. 7) on the bases of detecting the presence of an object and indicating the size and shape.

References

1. D. S. Bright, E. B. Steel, and D. E. Newbury, "The problem of visibility in noise images," *Microbeam Analysis--1989*, 37 .
2. A. Rose in *Advances in Electronics*, vol. 1, New York: Academic Press, 1948. 131.
3. W. Rasband, *NIH IMAGE: An Image Processing Software Package for the Macintosh II*, 1990. (Available free of charge from Wayne Rasband, NIH Bldg 36, Rm 2403, Bethesda, MD 20892.)
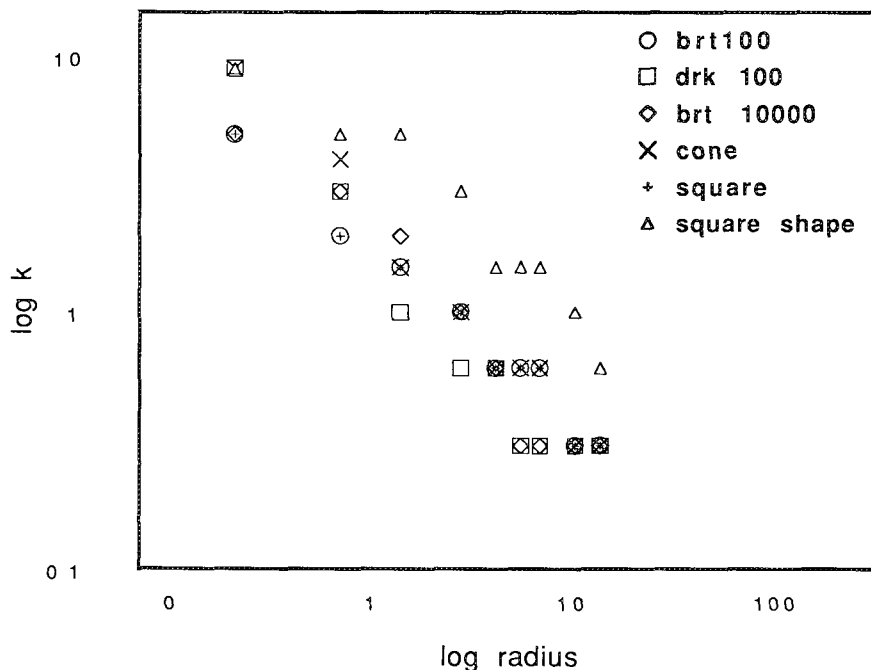
FIG. 7.--Measurements of k for barely detected objects in Figs. 2-6, plotted as logarithm of k vs logarithm of (nominal) radius in pixels.

SEGMENTATION OF GRAY-SCALE IMAGES BASED ON TEXTURE AND ORIENTATION

John C. Russ

Prior to performing measurements on features or structures in gray-scale or color images, it is usual to reduce them to binary images in which pixels are "on" or "off" depending on whether they are part of the features or part of the background, respectively. This operation is broadly described as segmentation of the image, and may be performed in a variety of ways. The most common is to define a range of brightness (or color) values that are considered to represent the features. These values may either be set interactively by the user, based on *a priori* knowledge such as stain densities or fluorescence intensities, or based on calculation from the image itself (e.g., by use of the brightness histogram to locate minima or adjusting limits to minimize variation in perimeter). However it is done, the threshold settings are global, applying to the entire image. It is generally assumed that any required processing to correct for nonuniform illumination, camera response, section thickness, etc., has been performed beforehand. Nevertheless, this method is inadequate to deal with some types of images, because there is not a unique and global relationship between brightness and structure. Closely related to range thresholding is the use of contour lines that mark boundaries where the brightness crosses set threshold values. The advantage of contour lines is that they are always continuous, but the same limitations for selecting the threshold values are present and the additional difficulty arises of defining which is the inside and which the outside of the lines.

Other approaches that are more independent of global variations and use local information include edge-following and split-and-merge classification. Although these approaches appear to work in very different ways (from the bottom up or from the top down), they are in fact very similar in the criteria applied to locate boundaries. Edge following starts at some location on a boundary and then progresses along the boundary, examining the neighboring pixels in some small region, at a minimum just the next touching pixels. A decision is made at each location for the direction to proceed based on local pixel differences. This method continues until it forms a closed path (or intersects the edge of the frame). The major difficulties with the method are the possible branching of boundaries at touching points, the effect of local noise obscuring the boundary, the need to start each new boundary line somewhere in the image, and the difficulty of know-

ing when to stop looking for more boundaries. The iterative nature of the procedure makes it quite slow for use with small computers.

Split-and-merge classification starts by dividing the image into (typically) four quadrants. The brightness histogram for each region is tested to determine whether it is homogeneous; if it is not, it is also subdivided into four more pieces. The process continues until all heterogeneous regions have been split (or until individual pixels remain). At the same time, after each reduction cycle, neighboring regions that originated in different higher-level divisions are compared to determine whether they are similar enough to merge. The final result is an image containing many regions, each one presumably uniform. The advantages and limitations of this approach both come from the criteria used to define homogeneity. Simple brightness statistics such as standard deviation are not sensitive to the presence of small numbers of different pixels; this permits ignoring noise, but hides small regions. Tests based on neighbor differences over small distance or on the construction of a co-occurence matrix ignore gradual shading variations and find abrupt changes, but may miss smaller or broad steps, are sensitive to noise, and are computationally intensive.

In principle, one can convert any of the criteria used for split-and-merge classification to a simple global thresholding operation by first applying one or more image processing steps to convert the original image to new values. These operations, performed in either the spatial or frequency domains, produce pixel values that are in effect the probability that the pixel belongs to a particular class. This separate processing is preferred from an implementation point of view, as well as in terms of user understanding. The types of processing operations include linear convolutions, such as first and second derivatives, or high- and low-pass filters, which can be applied in either the spatial or the frequency domains, as well as nonlinear neighborhood operations such as rank operations that can only be performed in the spatial domain.

Figure 1(a) shows a transmission light micrograph of cardiac muscle. The orientation of the fibers is visually evident, and a human observer can rather easily delineate the boundary between groups of fibers running in different directions. This information can be used to determine the volume of each orientation, or to mark areas for counting of mitochondria, localization of chemical activity by stains, etc. However, the boundary is a gestalt property of the image (based on grouping of infor-

J. C. Russ is at the Department of Materials Science and Engineering, North Carolina State University, Raleigh, NC 27695.
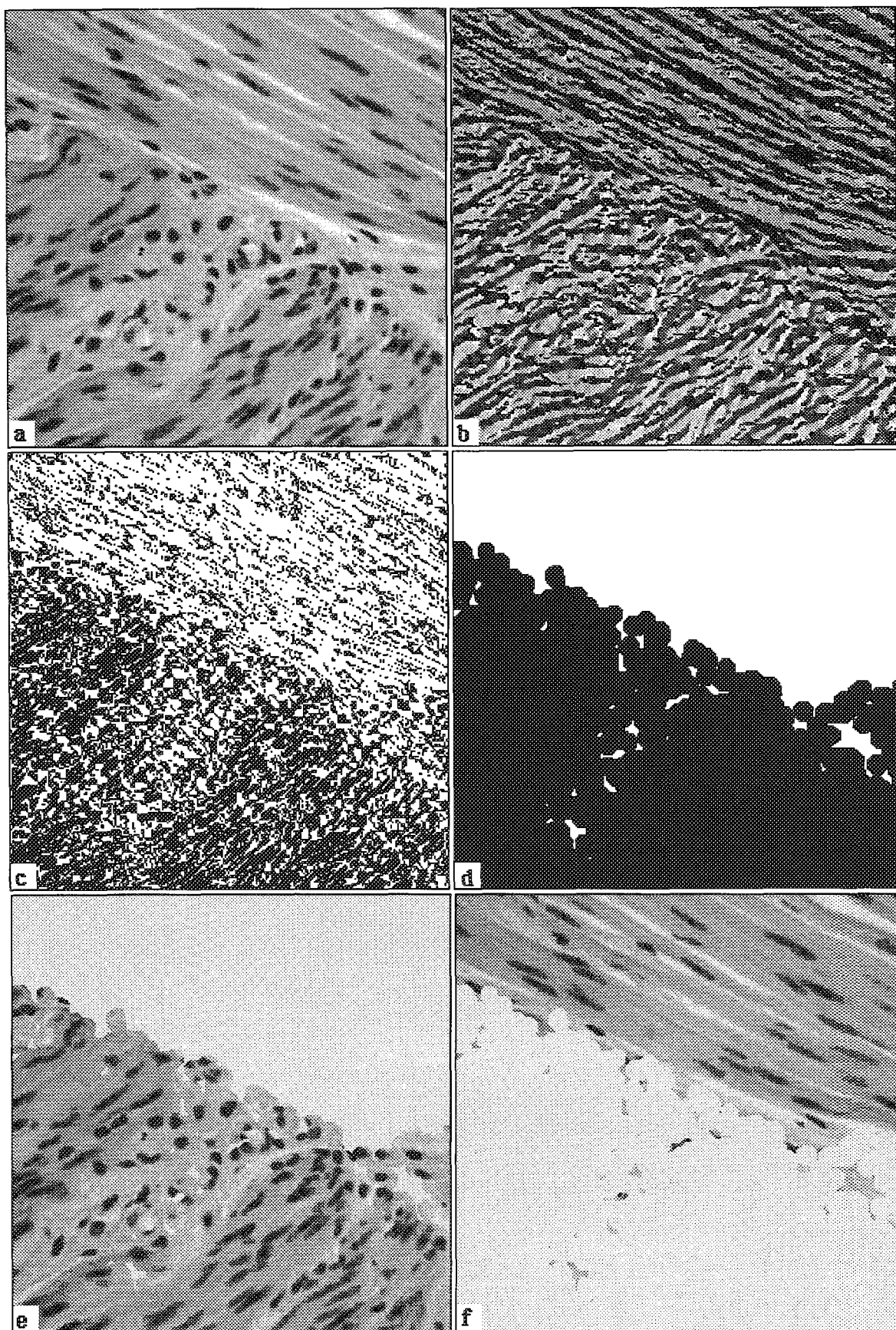
FIG. 1.--Classification based on orientation: (a) cardiac muscle (light microscope image of micro-
tomed section); (b) Sobel orientation image (gray scale indicates direction of maximum gradient);
(c) image (b) thresholded by direction; (d) image (c) after erosion (4 cycles, coefficient = 3)
and dilation (4 cycles, alternating coefficient = 1 and 0); (e) muscle fibers in one orientation
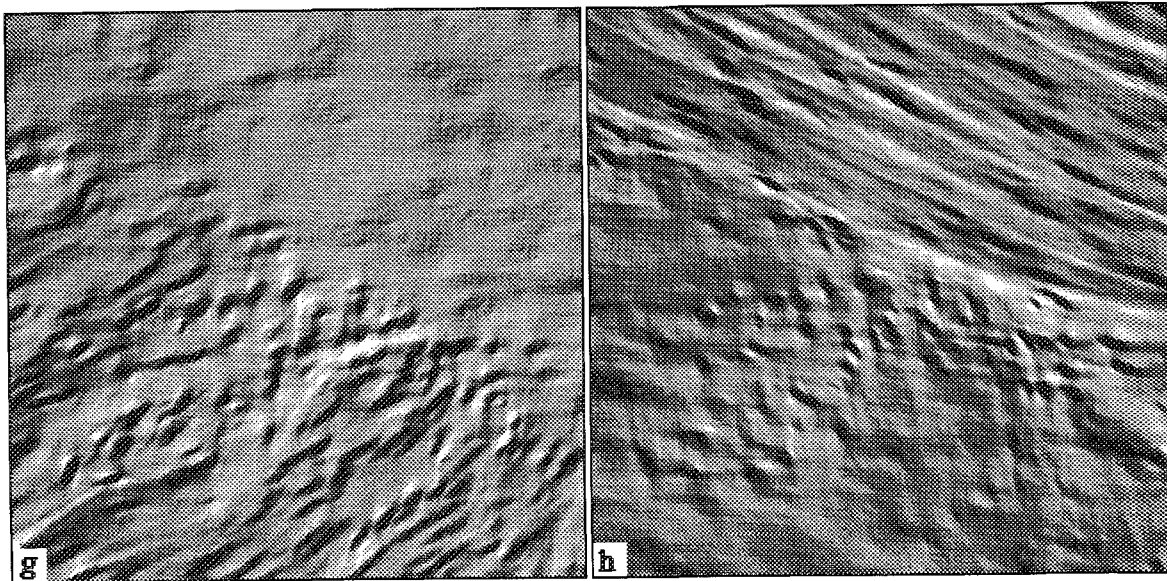
(Fig. 1, cont'd) selected by use of image (d) as mask for image (a); (f) other set of muscle fiber, with inverse of image (d) used as mask for image (a); (g) attempt to produce the same result in frequency space by multiplication by directional filer (a wedge-shaped mask) on two-dimensional FFT of image (a) and retransformation; (h) same operation as image (g) but with complementary directional filter.

mation) rather than a purely local one, and it is quite difficult to perform the same delineation with computer-based image analysis. The gray levels, texture, and other values are the same in both regions of the image. The classical approach to isolating orientation uses a two-dimensional frequency transform. Figures 1(g) and (h) show the results for this example. Performing a two-dimensional FFT, multiplying by a wedge-shaped mask that accepts all frequencies with a 90° range of orientations, and transforming produces the images shown. They clearly do not preserve the detail in each region, nor is it even possible to locate a simple boundary between them.

Figure 1(b) shows the Sobel direction image. The Sobel operator is most commonly used as a gradient or edge-locating convolution. Two derivatives, one in the x and one in the y direction, are formed by multiplication by kernels such as

$$
\begin{array}{ccc}
-1 & 0 & +1 \\
-2 & 0 & +2 \\
-1 & 0 & +1
\end{array}
\qquad
\begin{array}{ccc}
-1 & -2 & -1 \\
0 & 0 & 0 \\
+1 & +2 & +1
\end{array}
$$

The gradient image is calculated as the square root of the sum of squares of the magnitudes of the two-directional derivatives, producing a result whose magnitude is independent of direction. If the two-directional derivative values are combined instead as the arc tangent of $(\partial B/\partial y)/(\partial B/\partial x)$, the Sobel direction image is obtained. The gray values correspond to orientation, which is present throughout the muscle fiber regions regardless of the magnitude of the original gray value, because of the orientation of the fibers and organelles. Thresholding this image to select directions in a 90° range of values (and the 180° complementary directions) produces the binary image shown in Fig. 1(c). Due to noise in the original image

(and structure), this binary image does not correspond perfectly to the fiber regions. Some pixels within each region have an orientation value matching the opposite region. However, these tend to be isolated and morphological processing can improve the result.

Application of an erosion followed by a dilation produces the result shown in Fig. 1(d). The erosion was to a depth of four iterations, using a neighbor coefficient of 3. That is, any black pixel which touched more than 3 white pixels was removed. This removes the isolated noise pixels without altering the larger regions. The dilation was also performed to a depth of four iterations, using an alternating-neighbor coefficient of 0 and 1. Zero corresponds to classical dilation, in which any white pixel that touches any black pixels is changed to black. One requires that there be more than 1 touching black pixel. This alternating pattern produces octagonal shapes, and is sometimes referred to as an octagonal structuring element. It is the nearest approximation to the ideal isotropic circle in a small area of a square pixel grid. After the erosion and dilation operations, the binary mask corresponds rather well to the fiber regions. Its use as a mask to select the portion of the image to suppress or display produces the two images shown in Figs. 1(e) and (f) of the fibers having selected orientations.

Figure 2(a) shows a transmission electron micrograph of liver in which the human eye readily discerns two different textures, corresponding to the regions with many dark granules and the large, relatively smooth organelles. Simple thresholding does not work because the regions between the dark granules are the same in brightness as the smooth areas. Figure 2(b) shows a derived texture image. For each pixel in the original image,

191

the texture has been calculated as the slope of a regression line on a plot of brightness range vs distance for the neighboring pixels in a 7-pixel-wide circular region. In this process, the 37 pixels within the neighborhood are classed as to distance from the center, with values of 1, $\sqrt{2}$, 2, $\sqrt{5}$, $\sqrt{8}$, 3, and $\sqrt{10}$ pixels. The greatest difference in brightness for pixels within each distance range (inclusively) is then plotted against distance. The slope of this line is scaled to the one-byte depth of the image, and a new image is constructed. (For the image shown, this process takes 8 s on a Macintosh II.)

The texture image measures the local "busyness" of the original so that it can be thresholded (the brightness histogram has a well-defined minimum) to produce the binary image shown in Fig. 2(c). This may be used as a mask to select either the high- or low-texture regions for further measurement (Fig. 2d).

Other similar processing operations, which may be preferred in some cases because they require less computation, are the calculation of the variance around each pixel (by squaring and adding the differences between each pixel and its neighbors in some region such as a 5 × 5 or 7 × 7 octagon), or the local range (the difference between the brightest and darkest pixels obtained by ranking the brightness values in a local region, such as the same 5 × 5 or 7 × 7 octagon around each pixel). All these operations are far more computationally demanding than application of convolution kernels, and less amenable to the use of specialized array processors. However, in many cases they can extract information in the image similar to that which the human observer sees, and permit efficient thresholding to select regions based on texture or orientation.
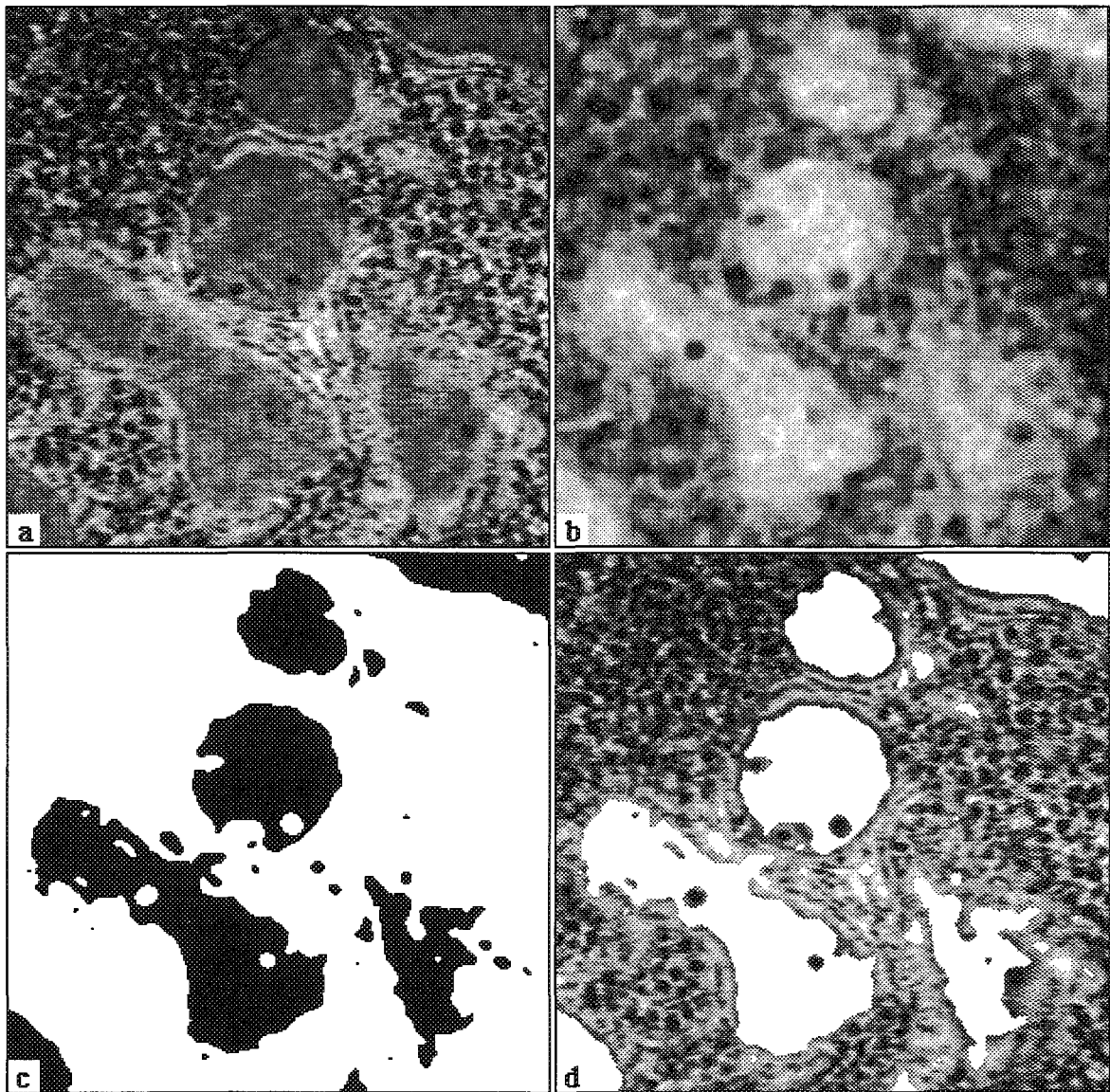
FIG. 2.--Classification based on texture: (a) liver (transmission electron micrograph of thin section); (b) texture image using 7-pixel diameter circular region; (c) thresholded binary from image (b); (d) high-texture regions in original using image (c) as mask.

BIOLOGICAL ENVIRONMENTAL SCANNING ELECTRON MICROSCOPY: THE EFFECT OF TANNIC ACID FIXATION IN AQUEOUS ENVIRONMENT ON PULMONARY SURFACTANT LIPID STRUCTURES

K.-R. Peters

Wet biological samples can now be analyzed with several new scanning microscopy techniques. The volume of fully hydrated tissues can be image in the scanning light microscope (LM) at a resolution of ∿50-100 nm utilizing advanced digital image enhancement techniques (image processing and volume reconstruction). Higher resolution on surfaces immersed in water is now possible with scanning stylus microscopy (SSM). In various signal modes, ultrahigh resolution of less than 1 nm is possible on atomically smooth surfaces or on the top of elevated features. The resolution gap between LM and SSM can be bridged by scanning electron microscopy if the specimen chamber is held at water vapor pressures high enough to maintain liquid water (4.5 Torr at 0 C and 17.5 Torr at 20 C). Such a pressure range can be provided in the environmental scanning electron microscope (ESEM)[1,2] for secondary electron imaging[3] of thin water films[4] and the fully hydrated surfactant film at the pulmonary air/tissue interface.[5] However, since the scanning electron microscope images only surfaces, free water covering the surface must first be carefully evaporated. Water removal can be controlled either by a slightly lowering of the water pressure in the specimen chamber or by a rise in the specimen temperature.

The fine structural investigation of the pulmonary surfactant surface is of great interest since its presence provides for the structural and functional integrity of the alveolar tissue. However, surfactant lipid structures are not easily maintained during established microscopic specimen preparation procedures. Recently it was shown[6] that traditionally used tannic acid[7,8] may stabilize surfactant lipids, but at the cost of severe structural alterations. We were able to confirm such alterations in the ESEM (Fig. 1). Fully hydrated liposomes that formed a protein-free surfactant lipid extract[9] could not be directly imaged in the ESEM because a monomolecular lipid film covered the surface of preparations and obscured the liposomes. In order to remove the surface film, we stabilize liposomes adsorbed to an Si support with our chemical crosslinking procedure, thiocarbohydrazide (TCH) and osmium tetroxide. Compared to this procedure, tannic acid treatment (1% in water) applied to adsorbed or suspended liposomes caused condensation and aggregation. Such alterations could not be observed in glutaralde-

hyde/osmium fixed or TCH/osmium stabilized liposomes. The ESEM allowed us to control the structural integrity of our samples in the fully hydrated state, elminating possible artifacts produced by dehydration for TEM sectioning of embedded surfactant structures or lung tissue.[9]

References

1. G. D. Danilatos, *Micron Microsc. Acta* 14: 307, 1983.
2. G. D. Danilatos, *Adv. Electronics and Electron Phys.* 71: 190, 1988.
3. K.-R. Peters, *Proc. Ann. EMSA Meeting* 47: 78, 1989.
4. K.-R. Peters, *Proc. XII Intern. Congr. Electron Microsc*, 1990, 374.
5. K.-R. Peters, *Scanning* 12: 1-40, 1990.
6. A. H. G. J. Schrijvers et al., *Mol. Cell. Biochem.* 88: 91, 1989.
7. M. Kalina and D. C. Pearse, *J. Cell Biol.* 74: 726, 1977.
8. C. J. Stratton, *Cell Tiss. Res.* 193: 219, 1978.
9. Surfactant lipids were obtained by collaboration with Dr. R. Notter, University of Rochester, Rochester, N.Y. Microscopy was performed in the Applications Laboratory, ElectroScan, Danvers, Mass., and the excellent help received is gratefully acknowledged. Supported by NSF Grant DIR-8907117.

The author is at the Molecular Imaging Laboratory, Department of Radiology, University of Connecticut Health Center, Farmington, CT 06030.
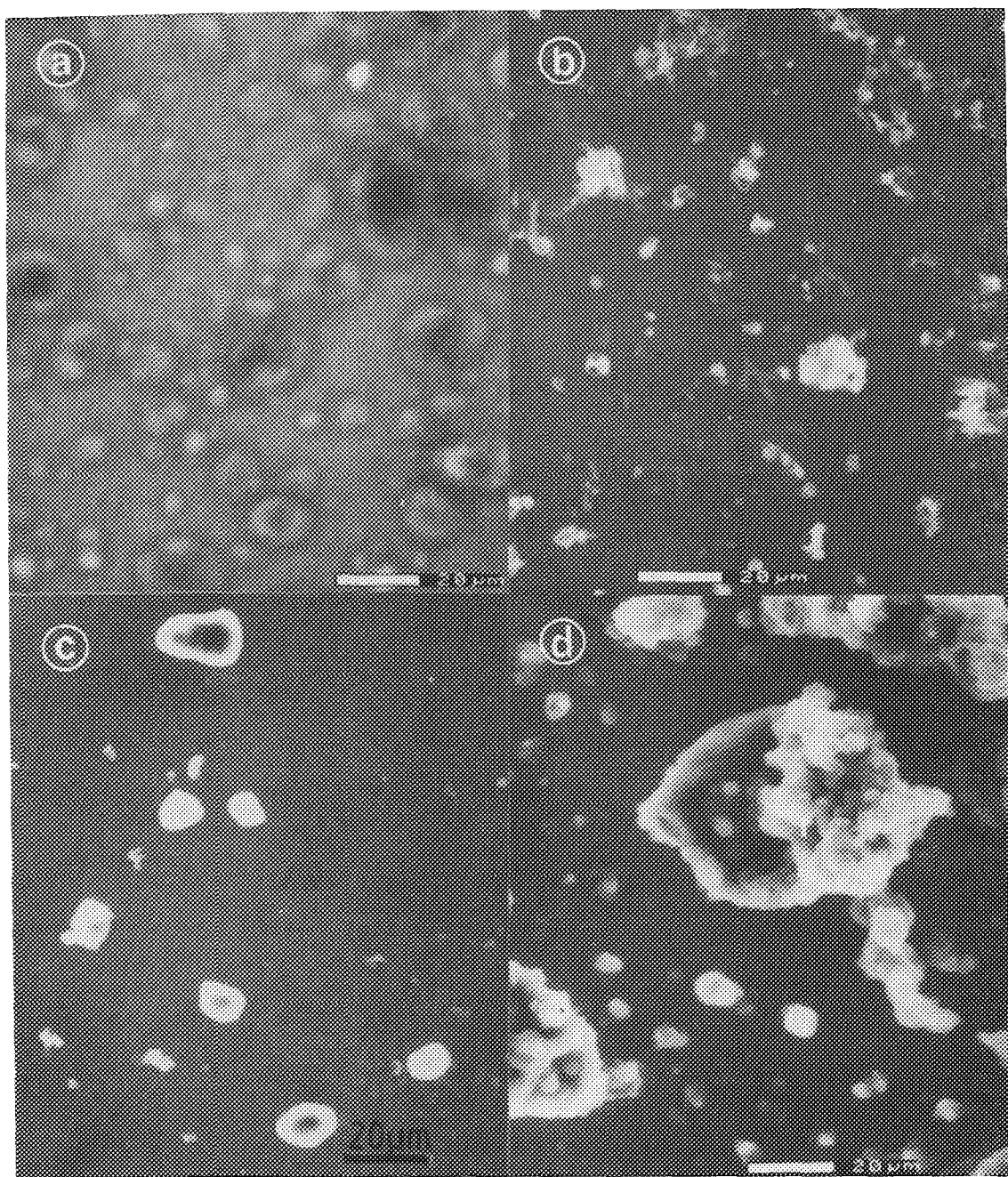
FIG. 1.--Fully hydrated pulmonary surfactant liposomes imaged without any metal coating at 100%
humidity and ambient temperatures in Environmental SEM at 25 kV with SE signal. (a) Surfactant
liposomes spread on Si support remained covered and obscured by monolamellar lipid film after
evaporation of most free water. (b) Adsorbed liposome preparation, stabilized while submerged
in thiocarbohydrazide and osmium teroxide. (c) Adsorbed liposome preparation treated while
submerged in tannic acid. (d) Suspended liposomes treated with tannic acid and then spread on
Si support, indicating massive structural alteration caused by tannic acid interaction.

PRELIMINARY STUDIES OF WET CEMENT PASTES BY AN ENVIRONMENTAL SCANNING ELECTRON MICROSCOPE

K. Sujata, T. B. Bergstrom, and H. M. Jennings

The environmental scanning electron microscope (E-SEM) has made possible in situ observations of materials in a moist environment.[1] This advance in scanning electron microscopy has had particular significance in the study of the microstructure of cement paste. The hydration of cement is a complex set of reactions that produces a microstructure which is itself sensitive to moisture content. This note reports on a model component of Portland cement as well as on the more complex multi-component system. (Conventional cement chemistry notation is used: $C = CaO$, $S = SiO_2$, $H = H_2O$.)

The most important constituent in cement is tricalcium silicate (C_3S), which reacts with water to produce an amorphous produce known as nonstoichiometric calcium silicate hydrate (C-S-H), and calcium hydroxide (CH).[2] During this study the hydration of C_3S was followed for several days after mixing.

A micrograph of C_3S before mixing with water is shown in Fig. 1. The grains are sharp and distinct. The C_3S and water were mixed at a ratio of 0.5 g water/1.0 g C_3S and the paste was allowed to react for 8 h, until approximately 10%[3] of the reactants was consumed. Micrographs were taken of specimens maintained at 3.6 Torr of water vapor and 20 C. Careful control of the specimen temperature and pressure allow the moisture content to be controlled exactly. The morphology of an 8h-old paste is shown in Fig. 2. An amorphous coating of C-S-H has formed on the surface of the grains. The coating is similar to that reported previously,[5] using TEM techniques. At this stage in the hydration process the particles are not highly interconnected and the bonding between them appears to be weak. After 16 h, or approximately 20% hydration,[3] the grains are completely engulfed with a hydration product and they are very connected (Fig. 3a). There are also indications of a needle-like structure radiating from the individual grains (Fig. 3b).

Most previous studies in conventional SEMs involved severe drying and other treatment of the samples that may have led to the damage of the coating. This effect is clearly illustrated by the crumpled surfaces of the particles shown in Fig. 4, a micrograph taken in a conventional SEM. The specimen in Fig. 4 is comparable in material and hydration time with those illustrated by Fig. 2. The latter also

demonstrates charging effects, even after the sample was coated with 500 Å of gold. The damage inflicted by the high vacuum of conventional SEM becomes more apparent in Fig. 5(a). This sample is comparable to Fig. 3(a). The needle-like structure has been pulled back from between individual grains (Fig. 5b), which demonstrates the delicate nature of the hydration product at this early age.

These micrographs document the general morphological development of C_3S hydration. The early stages of hydration show dramatically different microstructures when compared with those from a conventional SEM as shown above, which are influenced by sample pretreatments. Typically, the later stages of microstructural development appear to be similar in both a conventional (or high-vacuum) SEM, and in the E-SEM.

Ordinary Portland cement was also studied. In this case, however, instead of mixing water and cement, a few unhydrated grains of cement formed the sample (Fig. 6). Water was condensed on the surfaces of the cement particles in the E-SEM, by use of a cooling stage in conjunction with a high pressure in the chamber of the microscope. The details of this technique are described in detail by Sujata and Jennings.[4] When water comes in contact with the cement particles, certain parts of the cement dissolve to form an aqueous phase that is saturated[5] with various ions such as calcium, sodium, potassium, etc. Figure 7 shows the particles partially under water. During this process there is a small amount of particle rearrangement. Some of the grains of cement move close to each other, whereas others are repulsed. There is also a rotational rearrangement by which some of the grains change their angular positions, for better packing. These rearrangements may be caused by attractive forces such as surface tension and surface charges. A layer forms on the surface within the first half hour (Fig. 8). The formation of the amorphous C-S-H layer during the induction period in the hydration of cement has been deduced from indirect evidence.[6] These micrographs provide direct and clear evidence for the existence of the layer. This layer is continuous and may be the protective layer that has not been seen in a conventional SEM, where the continuity of the layer has often been broken by the high vacuum.

The influence on the microstructure of drying and other harsh treatments such as freeze drying and coating the samples with a conductive material for conventional SEM observation can lead to misinterpretation of information, which can be avoided by use of the E-SEM where the material under observation requires no pre-
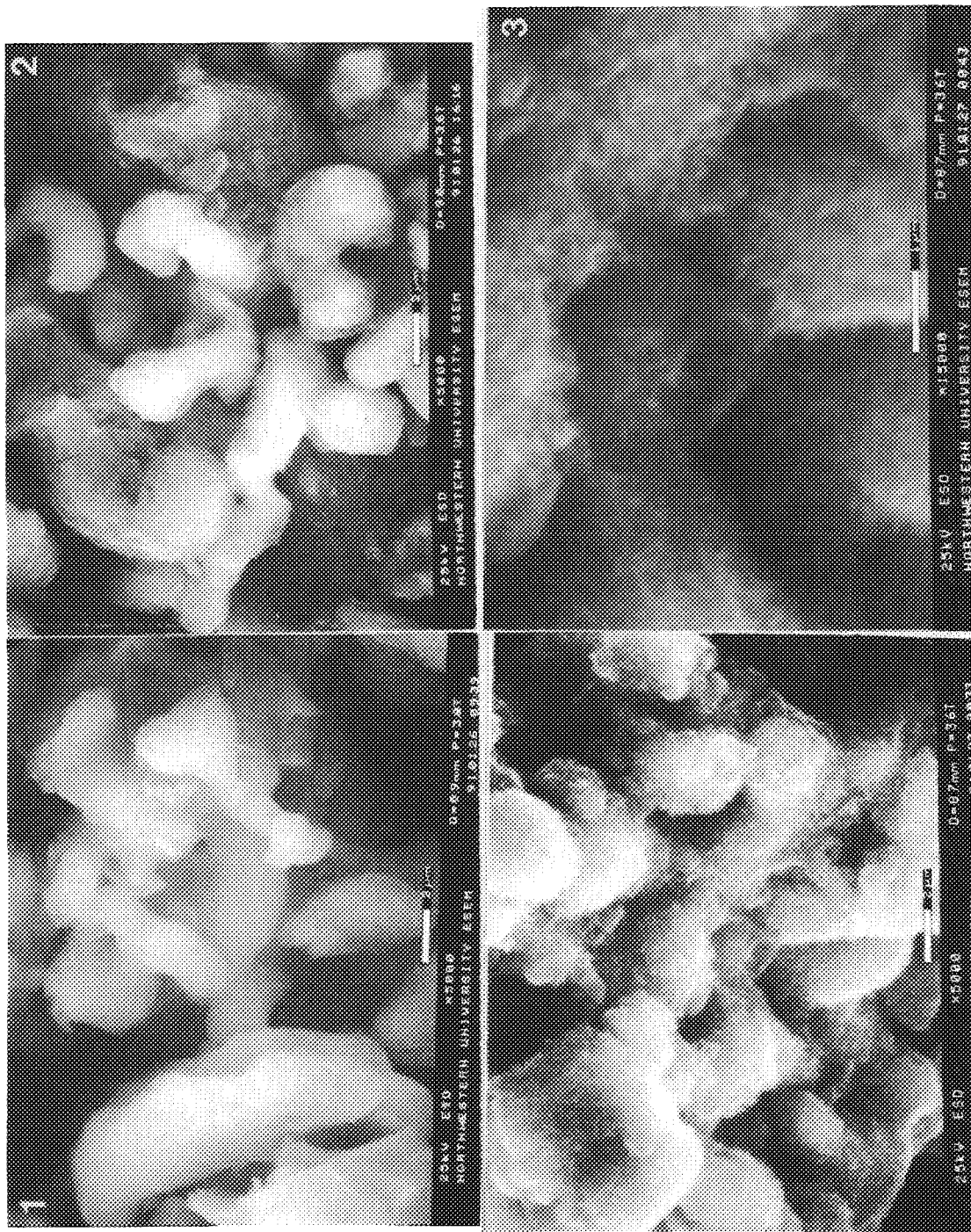
FIG. 1.--Dry, unreacted tri-calcium silicate.
FIG. 2.--Tri-calcium silicate paste after 8 h.
FIG. 3.-- (a) Tri-calcium silicate paste after 16 h; (b) magnified image of (a) showing needle-
like morphology.

treatment. The coating formed in the early stages of hydration is seen in the micrograph to be almost electron transparent, as demonstrated by a close look at the micrographs that show the unhydrated grains beneath the surface of the amorphous layer. Drying and coating leads either to damage or to covering of this delicate layer.

Most studies have focused on Portland cement or model tri-calcium silicate pastes that have been mechanically mixed. Another important variable that has not been addressed explicitly is the influence of physical mixing on the morphology of the early product. Indeed, mixing may in part have been the cause for the flake-like morphology and the exfoliation observed by Jennings et al.[6] using a wet cell in the HVEM. This observation was supported by observations made on pastes mixed outside the microscope. The mixed sample was about 30 min old. The layer no longer coats the entire sample, but is patchy. The micrograph in Fig. 9 shows the presence of a discontinuous flake-like structure on the surface of the cement grains of an age similar to the paste in the unmixed case.

References

1. N. Baumgarten, *Nature* 341: 81-82, 1989.

2. S. Mindess and J. F. Young, *Concrete*, Prentice-Hall, 1981.

3. H. F. W. Taylor, P. Barrett, P. W. Brown, D. D. Double, G. Frohnsdorff, V. Johansen, D. Menetrier-Sorrentiono, I. Odler, L. J. Parrott, J. M. Pommersheim, M. Regourd, and J. F. Young, *Mater. Constr.* (Paris), 17: 457, 1984.

4. K. Sujata and H. M. Jennings, *MRS Bulletin* 3: 1991.

5. H. M. Jennings, *J. Am. Cer. Soc.* 69: 614, 1986.

6. H. M. Jennings, B. J. Dagliesh, and P. L. Pratt, *J. Am. Cer. Soc.* 64: 567, 1981.
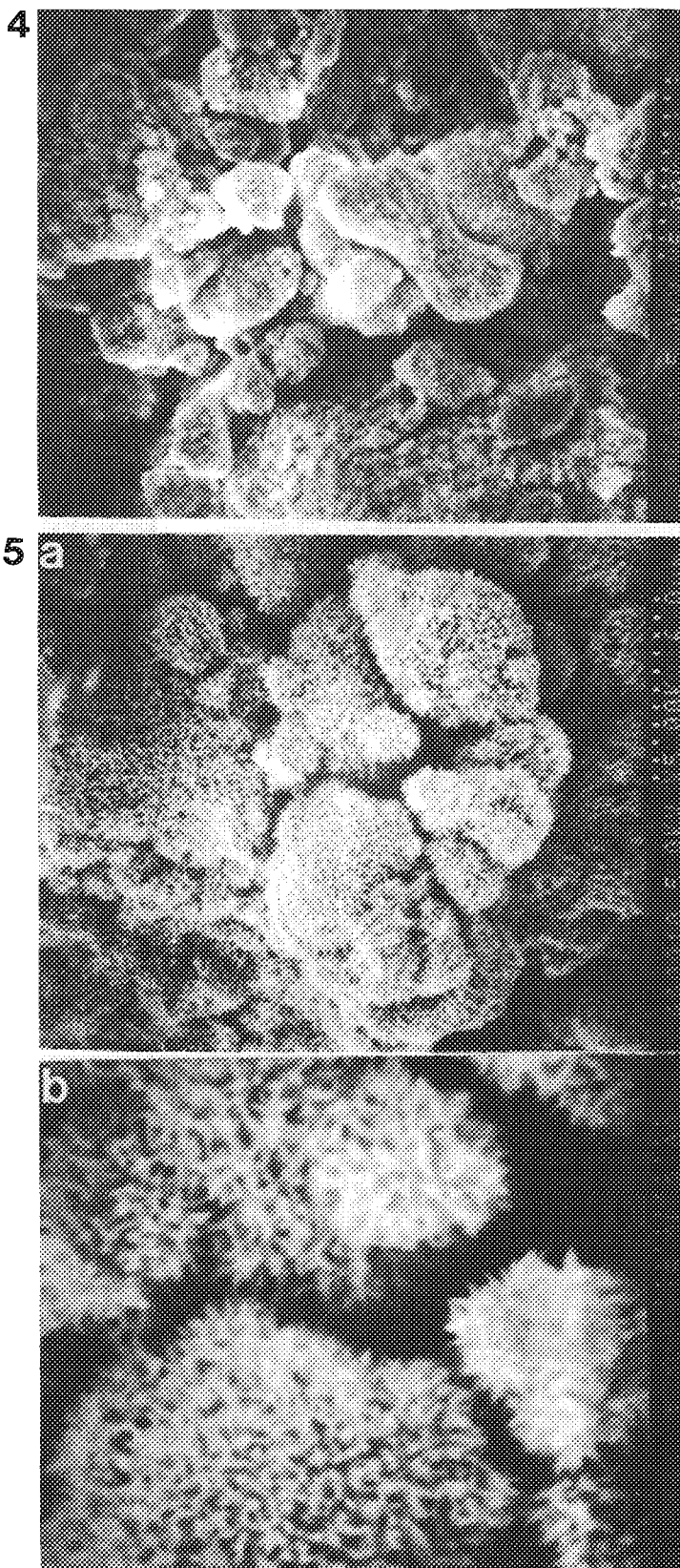
FIG. 4.--8-hour tri-calcium silicate paste in conventional SEM.
FIG. 5.--(a) 16-hour tri-calcium silicate phase in conventional SEM: (b) magnified image of (a) showing needle-like morphology.
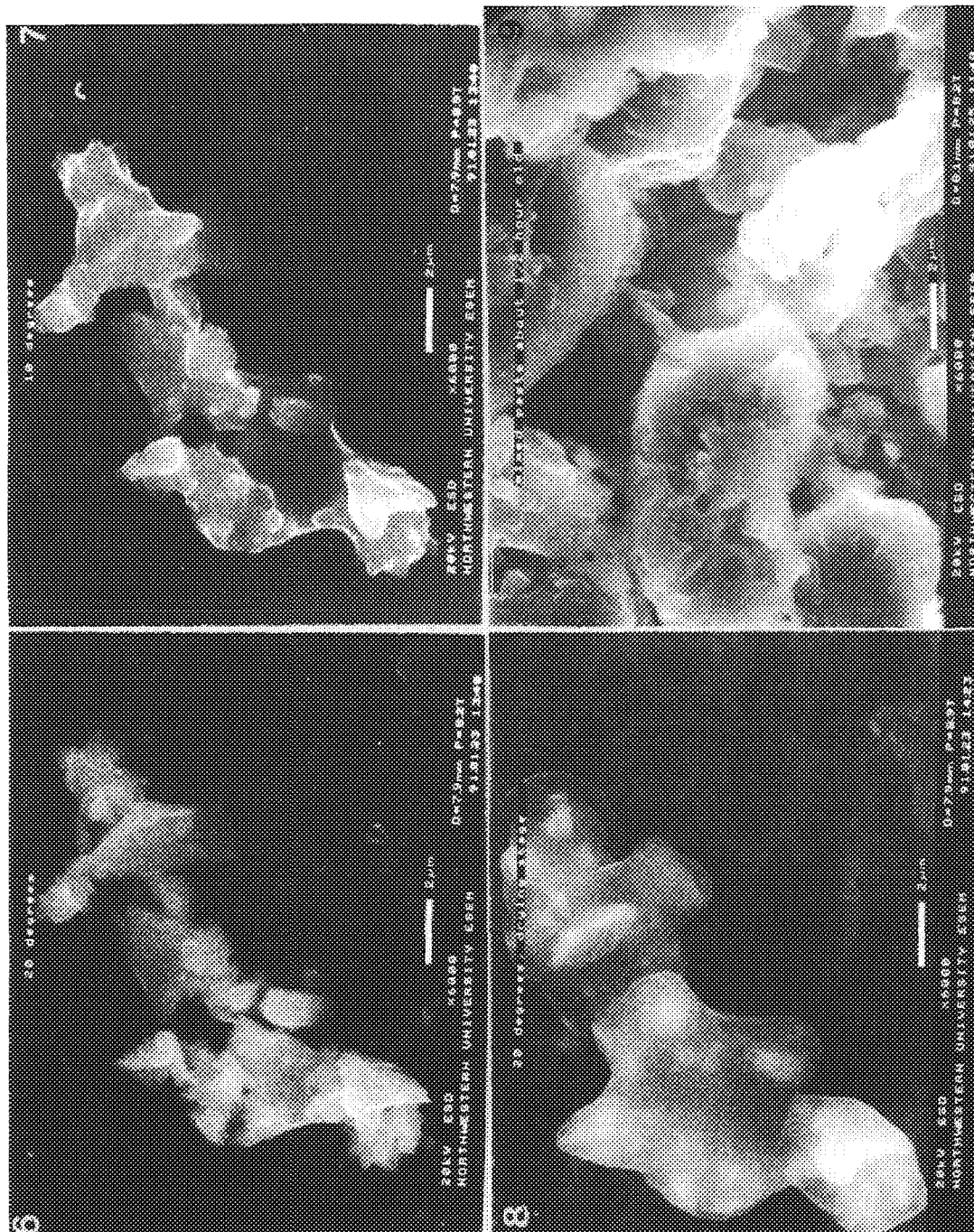
FIG. 6.--Unhydrated Portland cement grains.
FIG. 7.--Cement grains partially submerged under water.
FIG. 8.--Layer formed on surface of cement grains.
FIG. 9.--Mixed cement paste after 30 min showing broken layer on the surface.

X-RAY MICROANALYSIS IN THE ESEM

R. B. Bolon

Energy-dispersive electron beam microanalysis in the gaseous environment of an environmental scanning electron microscope is complicated by several factors not present in a traditional SEM. The most important of them is the loss of x-ray spatial resolution due to the extensive electron beam tail caused by electron scattering. This paper reports on an experimental evaluation of this effect and presents a procedure based on spectrum subtraction deconvolution, which makes it possible ot analyze structures down to and perhaps smaller than a micrometer in diameter.

Environmental scanning electron microscopy or high-pressure scanning electron microscopy is the technique of imaging specimens in a gaseous environment.[1] Although this capability was developed for biologists who wanted to study moist biological samples in their natural form, it also offers a variety of new capabilities for characterizing materials.[2,3] Most important is the ability to look at insulators without applying a conductive coating, made possible because ions generated in the gas by the electrons migrate to and neutralize surface charges.

Unfortunately, directing an electron beam into a gas creates several problems for microanalysis: degradation of x-ray spatial resolution due to scattered electrons, changes in beam current with pressure and working distance, low-energy noise caused by detected cathodoluminescence from the gas, low-energy x-ray absorption through ice deposits on the detector, and in some cases degradation of window and seal materials by the gas environment.

Experiment and Results

The x-ray spectrum generated by the scattered electrons is the most important problem and generally constitutes the majority of the spectrum collected under typical operating conditions. The spectrum was evaluated by the role count method,[4] as illustrated by data presented in Table 1. The data were collected from a Pt/Ni Faraday cage at a beam energy of 30 keV, a working distance of 15 mm, and water vapor at 3 torr pressure. The structure was made by pressing a 3mm-diameter Pt disk containing a 50μm aperture into a hole drilled in the center of a 25mm-diameter Ni block. Integrated peak intensities were obtained for Pt M and Ni K lines with the beam first positioned in the center of the aperture (hole), and then on the Pt and Ni (standards). The intensity ratio (hole count/standard count) for each element is a rough measure of the amount of scattering. At 2×10^{-5} torr, very few electrons are more than 25 μm from the center of the

R. B. Bolon is at General Electric Corporate Research and Development, Schenectady, NY 12301

TABLE 1.--ESEM hole count data.

H2O pressure	Pt (in hole)/ Pt		Ni (in hole)/ Ni	
2×10^{-5} torr	0 / 14,000 counts	(0%)	1/ 36,000 counts	(0%)
3 torr	4,100/ 9,100	(45%)	1,800/42,000	(4%)
5 torr	5,800/8,800	(66%)	3,200/41,000	(8%)

beam. At 3 torr, however, approximately 45% of the beam is scattered beyond 25 μm, onto the Pt aperture. An additional 4% is scattered beyond 1.5 mm, onto the Ni. At 5 torr, these values increase to 66% and 8%, respectively. Of course this method does not measure the fraction scattered less than 25 μm from the beam axis.

Efforts to eliminate or reduce this scattered component by placing apertures close to the sample are not feasible. A more practical approach is to use a background spectrum subtraction procedure. This method assumes that the electron beam consists of two components. One is the central unscattered fraction, which retains its focus and makes imaging possible. The other forms an extensive but relatively flat "skirt" or beam tail. In order to separate the x rays generated by these two components, two spectra are collected. One is obtained with the beam positioned on the feature of interest. The second is then collected either with a defocused beam or with a scanning beam, with a raster that best approximates the scattered distribution. This second spectrum is then weighted by an experimentally determined factor and subtracted from the first to yield a spectrum representative of the feature of interest.

Figure 1 shows an ESEM image of a polished section of a directionality solidified Mo,Ni,Al eutectic alloy. In this system the Mo segregates into 1.5 μm-diameter rods of almost pure Mo, aligned in a matrix of almost pure NiAl. Figure 2 includes a series of spectra collected from this structure with a 20keV beam, water vapor at 2 torr pressure, and a working distance of 15 mm. These spectra correspond to (a) the center of one rod, (b) the matrix between rods, (c) a rastered beam at 500×, (d) spectrum (a) minus 85% of spectrum (c), and (e) spectrum (b) minus 85% of spectrum (c). Although it is apparent from spectra (a) and (b) that the bright phase is rich in Mo and the matrix is rich in Ni and Al, their true compositions cannot be determined. With the knowledge that the Mo phase is essentially pure Mo, it was a simple matter to determine that 0.85 was the appropriate fraction of the "rastered" spectrum to subtract from the "rod" spectrum to remove the Ni and Al peaks.

This value can then be used to process other data collected in a similar fashion, provided that identical operating conditions are used.

References

1. G. D. Danilatos, "Foundations of environmental scanning electron microscopy," *Adv. Electronics and Electron Phys.* 71: 109, 1988.
2. R. B. Bolon, C. D. Robertson, and E. Lifshin, "The environmental SEM: A new way to look at insulators," *Microbeam Analysis--1989,* 449-452.
3. R. B. Bolon and C. D. Robertson, "X-ray and microstructural E-SEM analysis of reactions and nonconducting materials in gaseous environments," *Scanning,* 12: 41-42, 1990.
4. R. B. Bolon and M. D. McConnell, "Evaluation of electron beam tails and x-ray spatial resolution in the SEM," *SEM/1976* I, 163-170.
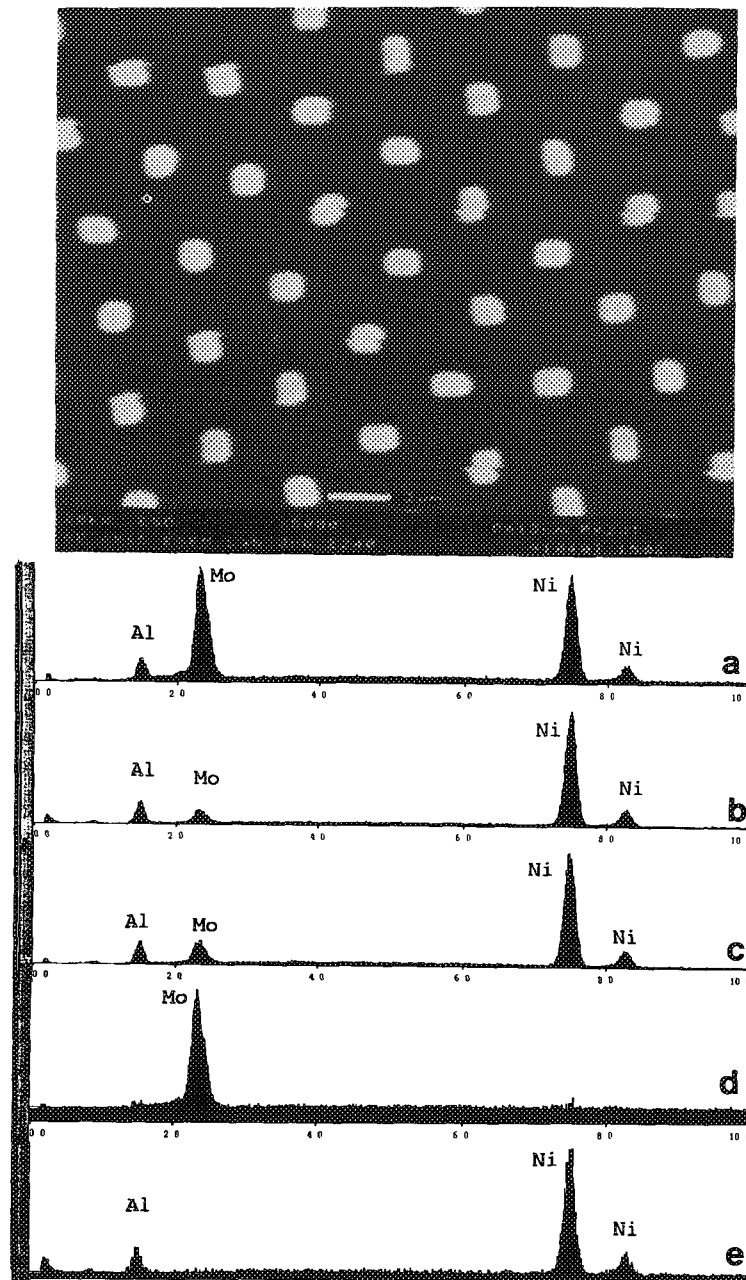
FIG. 1.--ESEM image of polished section of directional solidified No,Ni,Al eutectic alloy.
FIG. 2.--Spectra collected from Mo.Ni.Al eutectic alloy at 20 keV, water vapor at 2 torr pressure, 15mm working distance. (a) center of one rod, (b) matrix between rods, (c) rastered beam at 500×, (d) spectrum (a) minus 85% of spectrum (c), (e) spectrum (b) minus 85% of spectrum (c).

200

GAS FLOW PROPERTIES IN THE ENVIRONMENTAL SEM

G. D. Danilatos

The environmental SEM (ESEM) permits the introduction of a gaseous environment into the specimen chamber. Differential pumping is used to separate the high-pressure region from the high vacuum in the electron optics column. It is of great interest to know the state of gas in the chamber and around the specimen. It turns out that the gas properties are uniform throughout the specimen chamber except for a region within one diameter below the main (first) pressure-limiting aperture (PLA1). The variation of these properties in the neighborhood of PLA1 with or without the presence of a specimen is examined below.

Methods and Results

Experimental techniques have been employed previously to study the gas flow in the ESEM.[1] However, a more detailed description of the gradients of various properties is needed for the region just below and above the PLA1. In the present study, the direct-simulation Monte Carlo (DSMC) method has been employed and a series of computer programs developed by Bird have been used.[2] The real gas is modeled by many thousands of simulated molecules; the position coordinates and velocity components are stored and modified with time as the molecules are concurrently followed through representative collisions and boundary interactions in simulated physical space. There are compelling reasons that make this method the best choice. If the aperture were of a nozzle type with a well-defined geometry, where the variation of its diameter is smooth and known (e.g., a converging-diverging nozzle) all properties could be easily and accurately predicted for continuum (isentropic) flow. However, the PLA1 is formed on a very thin plate to produce a transition to low pressures as abruptly as possible. In addition, for pressures up to a few tens of millibars, the flow is in the transition regime from free molecule flow to continuum flow. Therefore, the DSMC method seems the best nonexperimental technique for the purpose.

Initially, good agreement between existing experimental measurements and predicted values by the DSMC method was established. Subsequently, the method was used to predict the behaviour of gas flow in new situations. Two representative cases are described below.

The first case describes the gas properties in the immediate vicinity of PLA1 in the absence of a specimen, i.e., when the microscope is idle and pressure is maintained constant as

The author is at ESEM Research Laboratory, 98 Brighton Boulevard, North Bondi (Sydney) NSW 2026 Australia, and Research Director for Electroscan Corporation, USA.

it is recorded by a pressure gauge very far from the aperture. Figure 1(a) shows the isodensity contours when the chamber pressure (stagnation value) is 10 mbar (corresponding to 1.64×10^{-2} kg/m^3) at 293 K and the diameter of the aperture is 0.4 mm. Initially, argon was chosen because it simplifies the calculation of electron beam scattering through it; the same stagnation conditions were maintained for both cases in this study. The corresponding temperature and flow speed contours are shown in Figs. 1(b) and (c). Because the flow field is axially symmetric, only half of a plane through the axis is shown.

The second case of interest is when we place a specimen near the PLA1 and inquire about the pressure gradients over the specimen. As an example, the circular surface of a cylinder 1.2 mm in diameter is positioned coaxially at 0.4 mm below the PLA1. The isodensity contours are given in Fig. 2(a), those of temperature in Fig. 2(b), and those of flow speed in Fig. 2(c). The pressure at the specimen surface vs radial distance from the axis is shown in Fig. 3. From density computations, we can find the mass-thickness of the gas over any given distance; from the mass thickness we can calculate the amount of beam scattering at various accelerating voltages.[3] We integrate along the optical axis as $\int [\rho(2)/\rho_0](dz/d_0)$, where the distance z along the axis and the gas density $\rho(z)$ have been normalized over the PLA1 diameter d_0 and the stagnation density ρ_0 for convenience in comparison. Here, the value of this integral in the distance from the specimen surface to a point at 4 aperture diameters above the PLA1 (not shown) is 1.27, whereas its value from the center of the aperture to the same point above the aperture is 0.39.

The ESEM allows the visualization of gas flows. One example, in Fig. 4, shows the gas jet just above a 0.1mm aperture subjected to atmospheric pressure in the region below it. The aperture was mounted at the tip of a hypodermic needle connected to ambient pressure via a plastic tube. The jet shown exhausts at 1.5 mm below the PLA1, normal to optical axis, inside the specimen chamber held at 2mbar pressure. The image was formed with the gaseous detection device.[4] The needle itself was used as the detecting electrode and was biased at only 2 V. To improve the signal contrast from the gas jet, the copper grid bearing the hole was thickly coated, first with aluminum and then with carbon. A Faraday cup placed below the gas jet measured the mass thickness of the jet normal to its axis from the collected beam current, without the limitations of good vacuum requirements imposed in the past (trans-

Density
(kg/cubic meter)
——— 1.48E-02
—‑‑— 1.32E-02
——— 1.17E-02
——— 1.01E-02
——— 8.56E-03
——— 7.00E-03
——— 5.45E-03
——— 3.89E-03
——— 2.33E-03
——— 7.78E-04

Stagnation value
1.64E-02

PLA1=4.00E-04 m

a

Temperature
(K)
——— 2.82E+02
—‑‑— 2.58E+02
——— 2.35E+02
——— 2.11E+02
——— 1.88E+02
——— 1.64E+02
——— 1.41E+02
——— 1.17E+02
——— 9.38E+01
——— 7.03E+01

Stagnation value
2.93E+02

PLA1=4.00E-04 m

b

Flow Speed
(m/s)
——— 4.59E+02
—‑‑— 4.11E+02
——— 3.64E+02
——— 3.16E+02
——— 2.68E+02
——— 2.21E+02
——— 1.73E+02
——— 1.25E+02
——— 7.76E+01
——— 3.00E+01

Stagnation value
0.00

PLA1=4.00E-04 m

c

Density
(kg/cubic meter)
——— 1.53E-02
—‑‑— 1.37E-02
——— 1.21E-02
——— 1.05E-02
——— 8.84E-03
——— 7.00E-03
——— 5.63E-03
——— 4.02E-03
——— 2.41E-03
——— 8.04E-04

Stagnation value
1.64E-02

a

Temperature
(K)
——— 2.85E+02
—‑‑— 2.58E+02
——— 2.30E+02
——— 2.02E+02
——— 1.75E+02
——— 1.47E+02
——— 1.20E+02
——— 9.19E+01
——— 6.43E+01
——— 3.67E+01

Stagnation value
2.93E+02

b

Flow Speed
(m/s)
——— 5.15E+02
—‑‑— 4.61E+02
——— 4.07E+02
——— 3.53E+02
——— 2.98E+02
——— 2.44E+02
——— 1.90E+02
——— 1.36E+02
——— 8.14E+01
——— 2.71E+01

Stagnation value
0.00

c

FIG. 1.—Flow field of argon through 0.4mm-diameter pressure-limiting aperture with (a) density (b) temperature, and (c) speed contours.
FIG. 2.—Same as Fig. 1 with specimen below aperture.

202
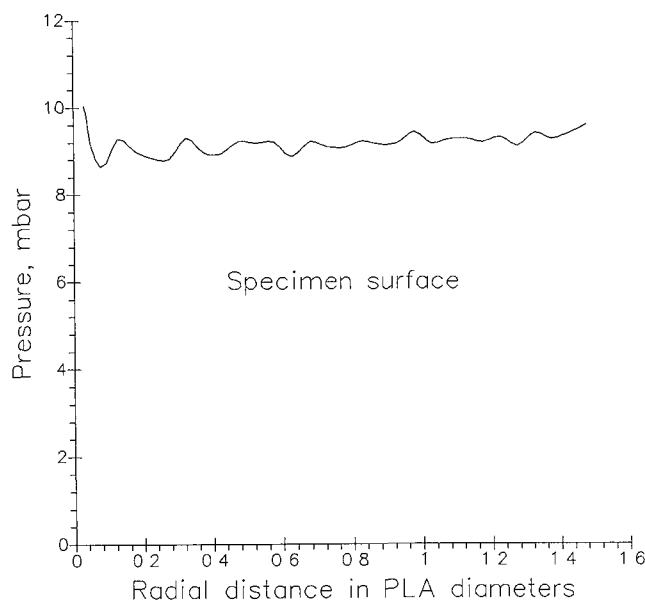
FIG. 3.--Pressure level on specimen surface.

FIG. 4.--Gas jet downstream from aperture plane. Image with 15 keV; horizontal field width = 0.14 mm.

mission microscopy).[5]

Discussion and Conclusions

The properties of the gas in the specimen chamber of an ESEM can be assumed to be uniform throughout the chamber; any significant deviation starts about one diameter below the PLA1. The gas density and temperature gradually increases and the flow becomes supersonic shortly above the aperture. The shear forces on surfaces, Mach number, and other properties can also be computed.

The specimen can affect the gas flow when it is placed very close to the aperture, but we can generally state that as long as the specimen distance is at least one PLA1 diameter, the gas properties are marginally affected. For the particular specimen of Fig. 2, the pressure at the surface is about 90% of the stagnation value. The speed of gas at any surface is effectively zero, but it can attain significant values as we move through a boundary layer into the free flow field. The small decrease of pressure on the surface should be taken into account when a fully saturated (wet) environment is to be maintained, which can be achieved by proper control of the specimen temperature.

It is suggested that mass spectroscopy be practiced from the gas sampling collected over the observed specimen area after the gas passes the PLA1.

The mass thickness above the PLA1 is small but significant. Its value depends also on the background pressure above the aperture and on the total distance traveled; its importance depends on the accelerating voltage used. This study shows that the specimen should be placed

as close to the PLA1 as possible to avoid unnecessary beam loss. The specially designed secondary backscattered electron and cathodoluminescence detectors are compatible with short specimen distances. X-ray work in an ESEM has been successfully implemented.[6] However, the existing x-ray detectors impose certain compromises; further research and development is needed to optimize the performance of this detection mode.

References

1. G. D. Danilatos, "Design and construction of an atmospheric or environmental SEM-2," *Micron* 14: 41, 1983.

2. G. A. Bird, "Monte Carlo simulation of gas flows," *Ann. Rev. Fluid Mech.* 10: 11, 1978.

3. G. D. Danilatos, "Foundations of environmental scanning electron microscopy," *Advances in Electronics and Electron Physics* 71: 109, 1988.

4. G. D. Danilatos, "Theory of the gaseous detector device in the ESEM," *Advances in Electronics and Electron Physics* 78: 1, 1990.

5. R. Wurster, "Transmission scanning electron microscopical investigation of a gas microjet," *Scanning* 8: 69, 1986.

6. R. B. Bolon, C. D. Robertson, and Eric Lifshin, "The environmental SEM: A new way to look at insulators," *Microbeam Analysis--1989*, 449.

TEM ANALYSIS OF CRYSTALLINE INTERFACE STRUCTURE: THE STATE OF THE ART

U. Dahmen

The characterization of the structure and chemistry of solid/solid interfaces is becoming increasingly important in materials science. Although electron microscopy has contributed a great deal to our present understanding of interfaces, many problems remain to be solved. A recent workshop held at the National Center for Electron Microscopy in Berkeley examined the field in some detail with the goal of pinpointing the most important problems, present limitations, and future developments. This paper will present a selective illustrated summary of the field on the basis of this workshop.[1]

The most clearly apparent conclusion was the call for a closer interaction between theory and experiment and a more quantitative approach to the interpretation of electron microscopy data. If electron microscopy is to continue to make a significant contribution to interface science, it is necessary but not sufficient to obtain improved spatial resolution: the problems of image interpretation, specimen noise and artifacts, chemical resolution, modeling of interfaces, and model/experiment comparisons must be addressed simultaneously. It is also clearly important to combine electron microscopy with the results from other techniques wherever possible, since the ultimate goal of interface characterization by TEM is the correlation between materials properties and the atomic atructure, chemistry, and bonding at interfaces.

The technique of high-resolution electron microscopy has now advanced to a level where it is possible to obtain high-quality images routinely. One of the main problems to be solved is the quantitative evaluation of these images and their comparison with theoretical predictions. This is particularly important in the determination of the atomic structure of interfaces for which accurate predictions have been made by molecular statics modeling. The necessity for refinement of projected atomic positions from experimental micrographs is illustrated by recent attempts to evaluate the matching between different models of a grain boundary and the experimentally observed structure.

The most common method of comparison is based on a visual judgment of the similarity between an experimental and a simulated image. Although the eye is a remarkably sensitive judge of likeness and difference, this method is fraught with error and subjectivity. An objective procedure must be developed to provide

---

The author is at the National Center for Electron Microscopy, MSD, Lawrence Berkeley Laboratory, Berkeley CA 94720.

a quantitative measure of the difference between the model and the experiment, similar to the R-factor in x-ray crystallography. Pattern recognition techniques have been successful for the special case of chemical discrimination at clean undistorted interfaces, but a general application to the case of structurally complex interfaces has yet to be developed. A number of critical problems must be dealt with before quantitative image analysis can become routine.

Mismatch between a simulated and an experimental image can be due either to real differences or to noise, microscope misalignments, or imperfections unrelated to the structure of the interface. To eliminate extraneous sources of error, images should be recorded under several conditions with known changes in defocus, beam tilt, specimen tilt, or thickness. Affinity with image simulations performed through the same range of conditions will yield improved accuracy and allow comparisons to be made with images recorded under nonideal, real-life conditions.

Specimen noise due to an amorphous surface layer of oxide or contaminant is a limiting factor that can be overcome by advances in specimen preparation (e.g., in situ UHV cleaning) or spatial averaging. The latter alternative is accomplished at the expense of localized spatial resolution.

Rigid body shifts are an important characteristic of interfaces because they are directly linked to the state of relaxation. Measurements can be made most accurately from inclined interfaces by the α-fringe technique, less accurately but with simultaneous information on localized atomic relaxations from edge-on interfaces in high-resolution micrographs and under special circumstnaces from face-on interfaces by convergent-beam diffraction.

Structure models usually deal with idealized interfaces of high symmetry in which two adjacent crystals are aligned along a common zone axis and the interface is periodic. These are precisely the conditions for the simplest TEM contrast and interpretable imaging; and because energy extrema tend to occur for special high-symmetry configurations, such structures are also often observed in nature. However, because of the prevalence of nonequilibrium conditions in most materials processing, interfaces in real materials are often nonrational in their crystallography. It is therefore necessary to progress along two directions: on one side, TEM analysis techniques need to be developed that allow quantitative evaluation of crystallographically nonrational interfaces, and on the other side high symmetry interfaces must be synthesized in the precise crystallography for which predictions are possible. It

is important to pursue both directions.

Crystallographically nonrational (real) interfaces are easy to obtain experimentally; here it is important to develop elastic, atomistic, thermodynamic, and crystallographic models. High-symmetry special interfaces are common in semiconductor materials, but are difficult to produce for the more general case such as interfaces resulting from martensitic transformations. Here it is important to find ways of synthesizing perfect model interfaces. For both alternatives electron microscopy must develop more quantitative analysis techniques.

However, the problem of quantification is not limited to high-resolution microscopy. Diffraction contrast techniques are very important, especially in the area of irrational interfaces, where HREM is severely handicapped by lack of crystal alignment. Image matching of interface dislocation structures is a powerful technique for the characterization of nonrational boundaries. The measurement of strain fields at interfaces and facet junctions and their quantitative comparison with elastic models requires further developments in elastic modeling and the measurement and mapping of strain fields from micrographs.

The quantitative characterization of interface roughness and diffuseness is limited as much by problems of technique as it is by a lack of clarity of concept. Interfaces can be rough but sharp, flat but diffuse. The expected appearance of interfaces rough with respect to structure, composition, or order can be illustrated schematically and inherent limitations discussed. Measurements of interface roughness and its power spectrum from diffraction peak shapes is an important characteristic of an interface and can often be related to materials properties.

Future developments in instrumentation in progress at present are reviewed briefly with regard to their impact on interface characterization.[2]

References

1. A copy of the workshop notes is available upon request.

HIGH-RESOLUTION ELECTRON MICROSCOPY OF GRAIN BOUNDARIES

K. L. Merkle and Y. Gao

High-resolution electron microscopy (HREM) has made considerable contributions to our understanding of grain boundaries (GBs) during the past several years, largely stimulated by the availability of instruments with spatial resolution of better than 0.2 nm. We review here some of the results of our HREM investigations on GBs in ceramic oxides, metals, and high-temperature superconductors. The emphasis of this paper is on (a) common features of GBs in different materials, (b) quantification of atomic scale structures in large-angle GBs, and (c) investigation of interrelationships between atomic structure and properties of GBs.

Grain Boundary Geometry

Irrespective of the crystal structure of the grains, the macroscopic characterization of a grain boundary involves five macroscopic and three microscopic degrees of freedom. This large multitude of possible arrangements of the interface makes it an extremely complex task to relate GB properties to GB structure.

The macroscopic geometry of a GB is usually described in terms of a bicrystal, where one crystal is rotated relative to the other via a misorientation (axis and angle) and a plane, which defines the boundary within this bicrystal. A special subset of possible bicrystals is given by the notionally interpenetrating lattices that form a coincident site lattice (CLS) with the reciprocal density of coincident sites Σ.[1]

An alternative description[2] uses the crystallographic planes $(h\ k\ l)_1$ and $(h\ k\ l)_2$ that are joined at the interface and a rotation ψ around the GB normal $\hat{n}$ to define the macroscopic GB geometry. For a general θ the GB contains both twist and tilt components, but for both of the special rotations $\psi = 0°$ and $\psi = 180°$, *asymmetric tilt* GBs are formed whenever $(h\ k\ l)_1 \neq (h\ k\ l)_2$; otherwise, i.e., for $(h\ k\ l)_1 = (h\ k\ l)_2$, $\psi = 0°$ and $\psi = 180°$ represent the ideal lattice and *symmetric tilt* GBs, respectively. Recent computer simulations of GBS in fcc and bcc metals have indicated that the GB energy as a function of ψ shows deep cusps at $\psi = 0°$ and $\psi = 180°$.[3,4] Therefore, tilt GBS are distinguished from all other configurations by their low energy. It is a favorable circumstance that these same boundaries,

provided their tilt axis coincides with a low index zone axis, are readily accessible to HREM observation

The GB *energy* is the most important factor in determining the types of GB geometries that occur in polycrystals and is also thought to play a central role in various GB properties; for example, in impurity segregation, fracture, and GB diffusion. Exploration of the connection between GB energy and structural parameters, such as macroscopic geometry, atomic-level geometry (rigid-body translations), and the detailed nature of the atomic relaxations at the GB core and near the GB, are therefore a prime goal of GB research. In the following we report results from HREM investigations of the fcc model systems NiO and Au in which the atomic structures have been explored for a range of macroscopic GB parameters. HREM investigations can also illuminate the connections between GB geometry, atomic-scale structure, and supercurrent transport properties in $YBa_2Cu_3O_{7-x}$.

The Role of the Grain Boundary Plane

Bicrystal experiments are particularly well suited for studies of the role of the GB plane in GB structure and energy. Figure 1 shows a TEM image of a $<1\bar{1}0>$ tilt GB in Au (near $\Sigma = 9$). The strong faceting of the GB into planar facets clearly indicates that some GB inclinations are preferred over others. However, atomic-scale resolution is needed to identify the facet planes and GB core structures. For example, the most prominent facets in Fig. 1 are of the (111)(551) type, for which the GB decomposes into triangular regions bounded by two (111)(111) and one (112)(112) GB. A single unit of this type from another $\Sigma = 9$ bicrystal is shown in Fig. 2. This dissociated GB is attached to a symmetric and an asymmetric GB on the left and right in Fig. 2, respectively. The occurrence of asymmetric GBs, where at least one of the GB planes is dense-packed (i.e., a low-index plane) is a common feature of many large-angle GBs, also in NiO (Fig. 3), which means that such boundaries may be low in energy.[5-8] Indeed, recent HREM studies in combination with computer simulation of $\Sigma = 9$ and $\Sigma = 11$ GBs in Au have shown that the facet formation agrees with GB energy calculations (including the dissociation of the (111)(115)GB) and that asymmetric GBs often have lower energies than the corresponding symmetric facets.[9,10]

On any given plane, the GB core structure is not necessarily unique, as illustrated in Fig. 4, which shows two variants of the (310)(310) tilt GB in NiO.[11] In atomistic

computer simulations of GBs one frequently finds GB structures that have similar energies for the same macroscopic GB parameters.[12] Multiple GB structures have recently been found by HREM in a number of materials.[13-15]

Another aspect of the role of the GB plane concerns the uniqueness of the structural repeat units. For example, when two low-index planes are joined together to form a GB, the atomic repeat distances would typically be incommensurate, at least in one direction along the plane of the GB. Therefore, no unique structural unit can be defined which would generate the atomic structure of the interface by periodic continuation. In contrast to computer simulation, which is largely limited to the investigation of periodic models of GBs, HREM can study the real structure of inter-
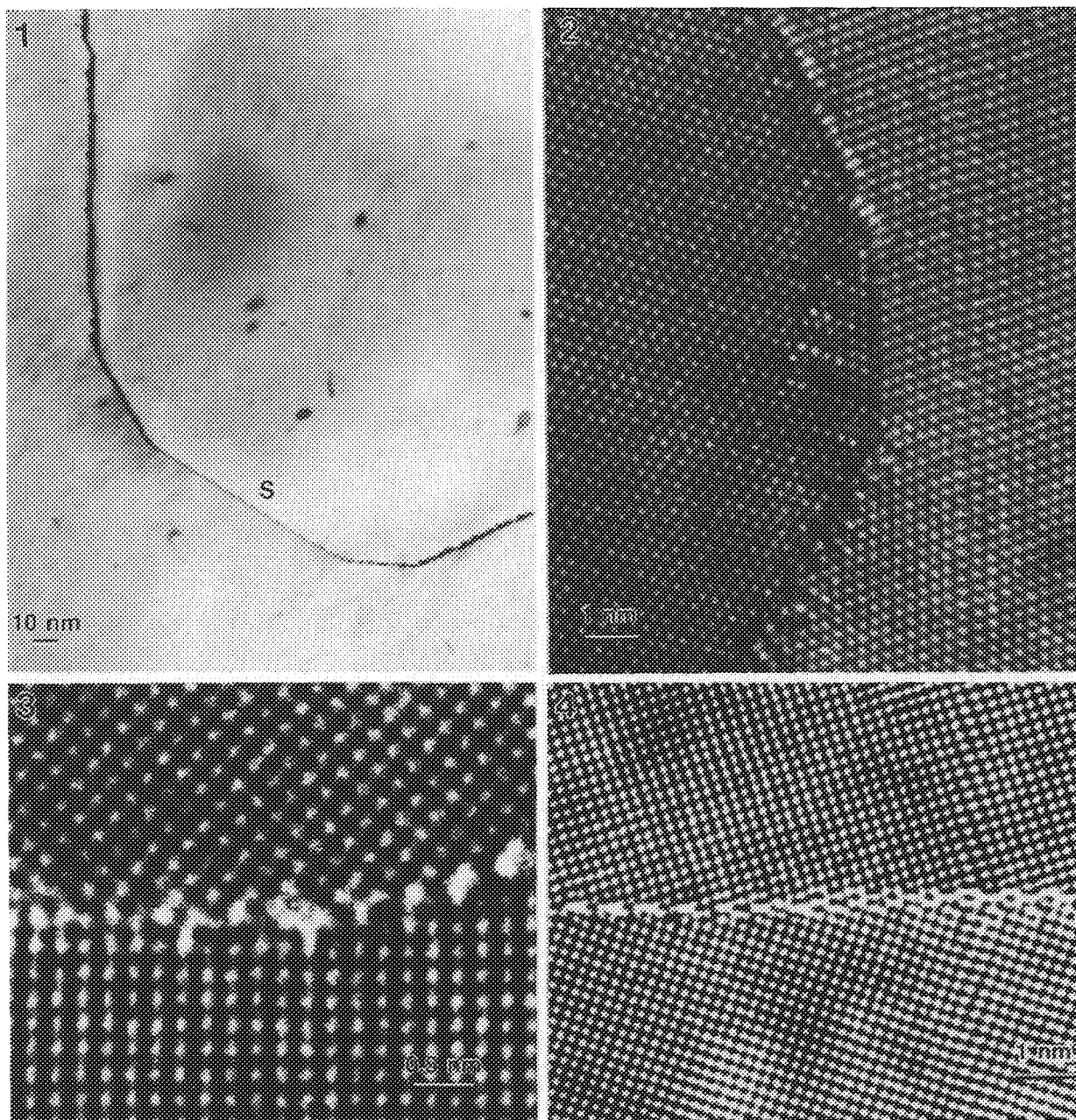
FIG. 1.—Transmission electron micrograph of <1$\bar{1}$0> tilt GB in Au. Coexistence of extended planar symmetric (S) with a number of asymmetric facets is evident.

FIG. 2.—Axial HREM image (white atomic columns) of <110> tilt bicrystal in Au, viewed along <110> tilt axis. Misorientation $\theta = 39°$ ($\Sigma = 9$). GB translates from (114)(114) GB (top) to dissociated (111)(115), and to (11,11,1)(111) (bottom).

FIG. 3.—NiO <001> $\Sigma = 5$ bicrystal (black atoms) with horizontal, asymmetric (430)(100) facet that translates to symmetric (210)(210) GB (right).

FIG. 4.—Small step separates two variants of (310)(310) GB in NiO (black atoms)

faces, including aperiodic features and structural defects. An interesting case in point is the (111)(001) GB, at the <1$\bar{1}$0>, θ = 54.73° misorientation, which is very close to the Σ = 41, θ = 55.88 misorientation. In Fig. 5 regions of good atomic match alternate with localized regions of misfit that are accompanied by lattice strain at rather short repeat distances. This boundary is quasiperiodic and represents the GB analogue to the formation of misfit dislocations in heterophase boundaries.[16] Similar to Au, quasiperiodic boundaries have also been observed in Ni((Fig. 6).[6]

Atomic Matching

Low-angle GBs have long been known to provide smooth transitions between the two lattices on either side of the GB by accommodating the misfit in spatially localized regions in the form of primary edge or screw dislocation. Misfit localization also plays an important role in large-angle GBs, as first suggested by Mott.[17] An example for misfit localization observed by HREM in a large-angle GB was given in Fig. 5. The localizations of misfit can take various forms, such as misfit-dislocation defects in quasiperiodic boundaries (Fig. 5), three-dimensional structures,[16] and localization of misfit within large structural units of GBs with large planar unit cells. Common features of all GBs are (a) the tendency of the atoms within the GB to assume positions
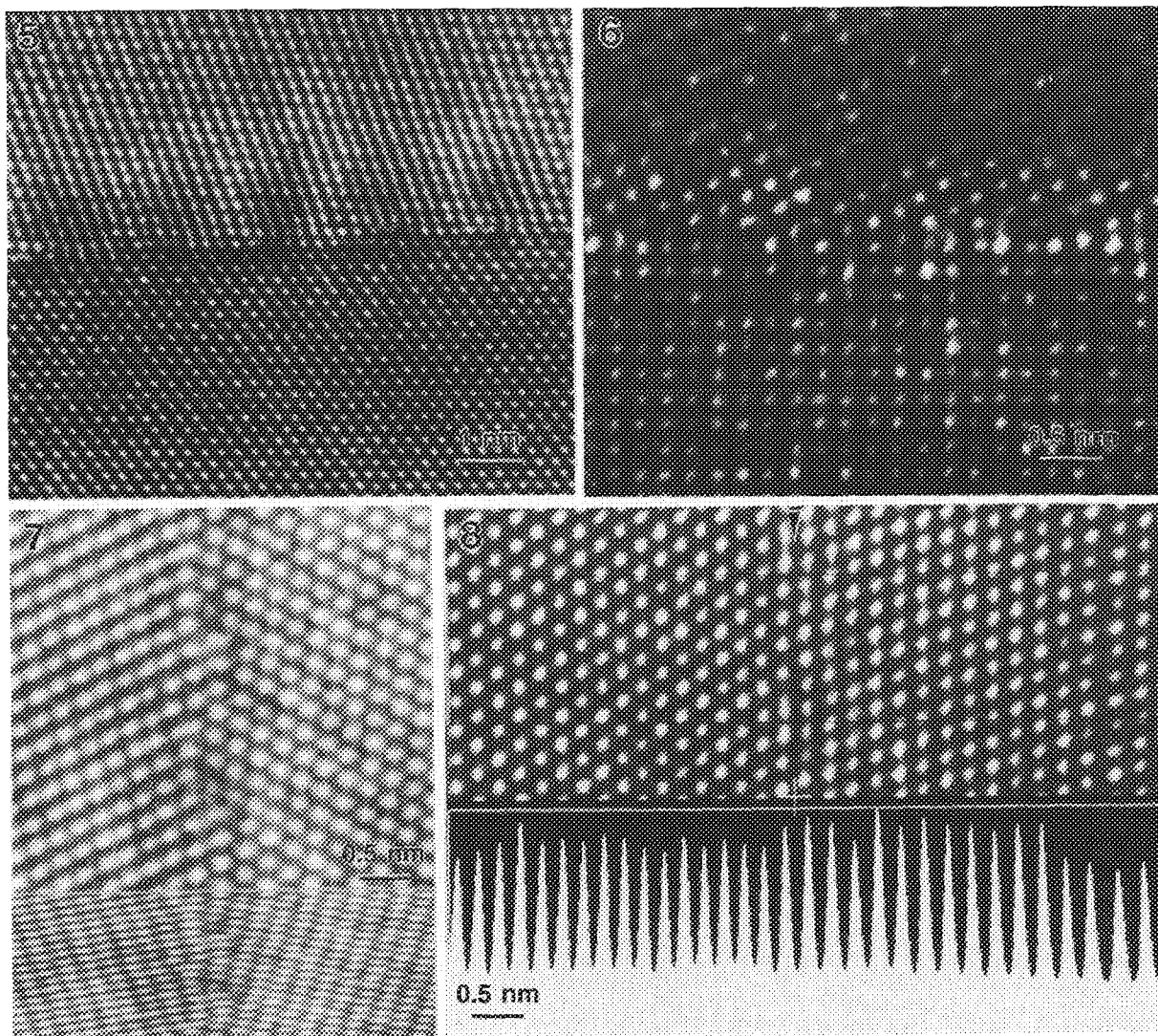
FIG. 5.--(111)(001), <1$\bar{1}$0> tilt GB in Au (θ = 55°). This GB is quasiperiodic and shows misfit localization in the form of·misfit-dislocation-like defects.
FIG. 6.--Incommensurate (210)(100) <001> tilt GB in NiO (black atoms). Grain boundaries often incorporate relatively dense-packed planes.
FIG. 7.--Atomically well-matched large-angle <1$\bar{1}$0> symmetric tilt GB in Au (white atoms). (443)(443), θ = 55°. Note misfit localization and relaxation of (111) planes in compressed image (bottom).
FIG. 8.--Analysis of volume expansion is based on digitized images and extrapolation of column positions from outside range of eleastic distortions associated with GB.

that resemble as much as possible the local en-
vironment in the ideal lattice; and (b) that
the atomic relaxations are rather local in
large-angle GBs. Therefore a boundary, such as
the $\Sigma = 41$ [near (111)(001), Fig. 5] with a
rather long structural period, seeks out its
minimum energy state more as a result of local
atomic relaxations rather than by preserving
its long-range structural periodicity. Atomi-
cally well-matched structures (Fig. 7) can of-
ten be recognized in HREM by an apparent elas-
tic continuation of low-index planes across
the GB.[18]

Quantification of Atomic-scale GB Parameters

The rigid-body displacements between the two
halves of a bicrystal have been recognized
since the earliest GB computer simulations as
providing an important relaxation mechanism for
the minimization of the GB energy.[19] Following
this discovery, several EM methods have been
developed to measure this important quanti-
ty.[20-24] Most of these methods are quite lim-
ited in their applicability (with the exception
of the Fresnel technique,[24,25] which is comple-
mentary to the HREM method), and only the HREM
technique allows the identification of the GB
core structure, which is important for the der-
ivation of absolute values of the rigid-body
translation normal to the interface.[26] We have
expanded the HREM technique used by Stobbs and
co-workers[23,27] (Fig. 8) to also allow highly
accurate measurements of the volume expansion
δ (i.e., the component normal to the GB) when
the GB is not parallel to major crystallograph-
ic planes on either side of the interface.[28]

Recent computer simulation results for a large
range of high-angle GB geometries have re-
vealed an approximately linear relationship
between GB energy and the volume expansion.[3,4]
With the exception of the coherent twin
(111)(111), which has practically zero volume
expansion, measured values of δ for Au are a
factor of two or more higher than the calcu-
lated values, based on embedded-atom-method
(EAM) potentials.[15,29] The origin of this
discrepancy between experimental and calcu-
lated volume expansions in Au is not known at
present. In contrast to Au, the volume ex-
pansion of the $\Sigma = 5$,(310) GB in NiO has been
found to be considerably smaller than calcu-
lated.[11]

A quantification of the unavoidable atomic
disorder at a GB can be attempted by consider-
ation of the local atomic environment of each
atom in the GB. Wolf has recently discussed
the correlation between GB energy and the num-
ber of "broken bonds" per unit GB area.[3,30]
Although the HREM technique gives at best a
two-dimensional projection of the atomic
structure and therefore requires observations
along more than one zone axis for a three-di-
mensional reconstruction of a GB, one can at-
tempt to construct three-dimensional models of
tilt GBs based on the assumption that there
are no shifts along the direction of observa-
tion. Using this simple model, we have ana-
lyzed HREM images, such as those in Fig. 9, in
terms of the number of "broken bonds" per GB
unit area.

By determining the number of atoms within a
shell that bisects the distance between first
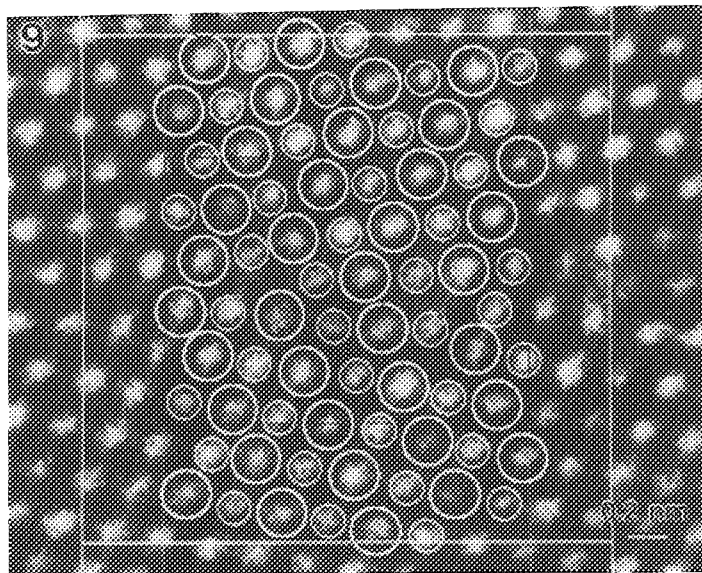
FIG. 9.--GB structural unit of (443)(443), <1$\bar{1}$0>
tilt GB in Au. Atom positions within repeat unit
are identified by circles. Small and large cir-
cles indicate assignment used for A and B layers,
respectively.
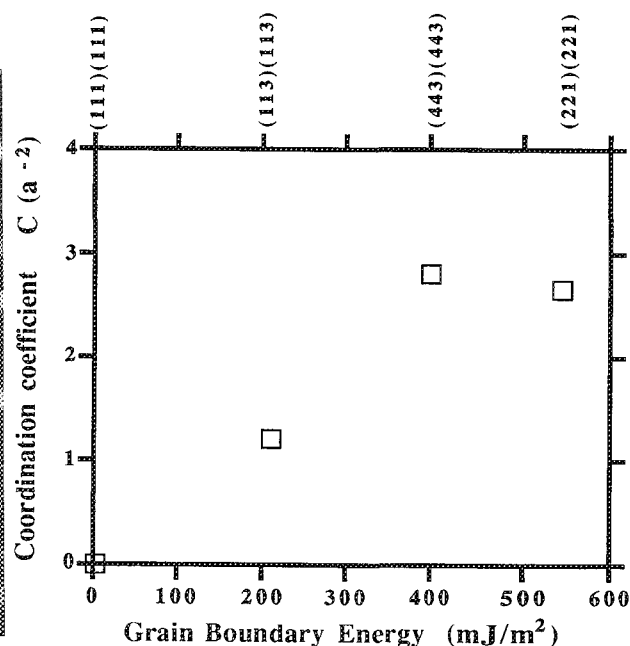
Fig. 10.--Coordination coefficient ("broken
bonds" per unit GB area) vs GB energy (from
EAM calculations[35]). Note practically linear
relationship between miscoordination and GB
energy.
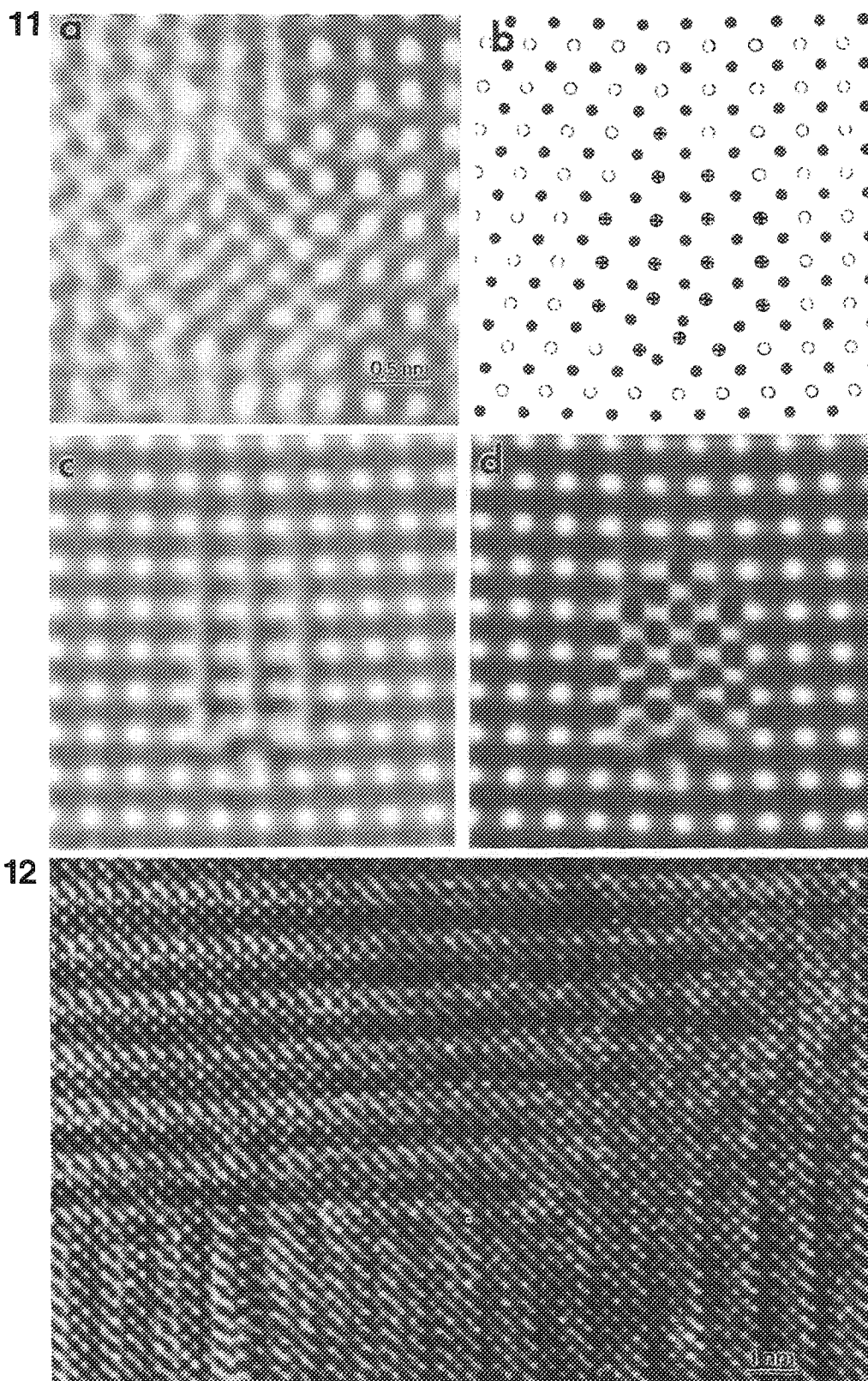
FIG. 11.--(a) HREM image of a dislocation core in low-angle <001> tilt GB of $YBa_2Cu_3O_{7-x}$. (b) Atomic structure of the dislocation core based on positions of atomic columns in (a). Full and open circles represent Cu-O and Y-Ba columns in <001> direction, respectively. (c) Simulated image where atomic columns at the core, marked by θ in (b), are, as in bulk, Y-Ba columns. (d) Simulated image based on model in which Y and Ba at the core are replaced by Cu columns. Image in (d) closely matches HREM image in (a) indicating material at core is nonsuperconducting. FIG. 12.--HREM image of <100>, $\theta = 90°$ tilt GBs in $YBa_2Cu_3O_{7-x}$. Both (010)(001) and (013)(013) GBs provide a good connection between Cu-O planes across GB and are therefore believed to be responsible for "weak-link-free" behavior.[33]

211

and second nearest neighbors in the ideal lattice, one can find the number of "broken bonds" for each atom n within the GB structural unit as the deviation $\Delta K_n = K_n - K_{id}$ from the perfect fcc crystal coordination number, $K_{id} = 12$. Following Wolf,[3,30] the coordination coefficient $C = (1/A)\Sigma_n|K_n - K_{id}|$; i.e., the number of "broken bonds" per GB unit area A is found by summing over all atoms in the GB unit cell. The number of "broken bonds" per GB unit area is plotted in Fig. 10 for several symmetric $<1\bar{1}0>$ tilt GBs in Au and shows a close to linear relationship to the calculated EAM energies for these boundaries.

Grain Boundary Structure and Properties

So far we have considered various aspects of the atomic structure of simple fcc GBs and their connection to GB energy. We shall now give two examples of HREM investigations of GBs in the orthorhombic high-Tc superconductor $YBa_2Cu_3O_{7-x}$. Here the atomic structure and chemical composition of the interface is related to the capacity for carrying electric current across the interface.

For $<001>$ tilt GBs in $YBa_2Cu_3O_{7-x}$ Dimos et al.[31] found that the critical current density across the GBs decreases by more than an order of magnitude as the misorientation angle θ increases from 0 to 11° and stays relatively constant at angles greater than 15°. We have observed small-angle GBs of the same geometry in MOCVD-grown $YBa_2Cu_3O_{7-x}$. As expected, the GBs consist of a set of appropriately spaced edge dislocations (Burger's vector a[100]). The lattices were smoothly connected between the two crystals in the GB regions separating the discrete dislocations. One dislocation core, observed by HREM, is shown in Fig. 11(a). Strong atomic relaxations are present, but the most striking feature is that the core region has a finite size, 2 nm in diameter. Image simulations based on a model that maintains the chemical composition of the lattice at the GB core (Fig. 11c) cannot reproduce the observed image. However, when the Y-Ba columns are replaced by Cu columns, one obtains a good match between observed and simulated images (Fig. 11d). To confirm this model, efforts will be undertaken to directly measure the composition of individual dislocation cores by analytical techniques.

Our HREM analysis suggests that the dislocation cores are not superconducting. In a dislocation model of the GB, the cores would start to overlap at 11°, given the observed size of the dislocation cores. Thus the rapid decrease of the critical current as a function of tilt angle observed by Dimos et al. could be explained by our observations.[32]

A large-angle $YBa_2Cu_3O_{7-x}$ GB of considerable interest is shown in Fig. 12. The misorientation for this GB is characterized by a $<100>$ tilt axis and a misorientation angle of 90°. Thus (001)(010) boundaries (horizontal section in Fig. 12) can be formed. The superconducting transport properties of bicrystal specimens with the same macroscopic configurations have recently been investigated by Babcock et al.

and their results suggested weak-link-free behavior for these GBs.[33] We have investigated the atomic structure of the (001)(010) GB in detail by comparisons between simulated images and the observation.[34] Two possible atomic models, both of which represent very well-matched structures that maintain the structural integrity of the superconducting phase at the interface, are consistent with the HREM images.

In spite of the atomically well-matched (001)(010) interface which maintains complete $YBa_2Cu_3O_{7-x}$ unit cells at the GB, the direct coupling of the supercurrent across the interface should be limited to Cu-O planes immediately adjoining the GB. However, at the $<100>$, $\theta = 90°$ misorientation we also find symmetric (013)(013) facets (Fig. 12). The latter provide a direct connection between the Cu-O planes, thus suggesting the possibility of strong supercurrent coupling across this large-angle interface.[34]

Summary and Conclusions

Systematic HREM investigations have provided new insights into the atomic structure of GBs. The application of this atomic-scale information to the understanding of GB properties may in the future allow for the possibility of prediction and modification of GB properties.

HREM studies of a number of GBs in Ni and Au have clearly demonstrated that a general tendency exists to produce atomically well-matched structures and to preserve a high degree of coherency across the interface. HREM observations have established that misfit-dislocation-like defects are formed in large-misfit incommensurate grain boundaries. We expect that these and other general structural features that have been investigated in NiO and Au are typical for other ceramic and metal GBs.

Considerable progress has been made regarding the quantification of structural GB parameters via HREM. Whereas several discrepancies between observed and calculated GB parameters remain, it is expected that the mutual feedback between HREM observations and GB computer simulation will serve as a stimulus to improve both the experimental and theoretical techniques and will lead to a better understanding of the complicated interrelations between GB structure and properties.

Atomic-structure information obtained from HREM observations on $YBa_2Cu_3O_{7-x}$ GBs has led to a much-improved understanding of the critical current behavior in these systems.

Direct correlations between atomic structure, including chemcial composition, and property measurements on individual GBs will be important for a full understnading of many grain boundary properties.

References

1. W. Bollmann, *Crystal Defects and Crystalline Interfaces*, Berlin: Springer, 1970.

2. D. Wolf and J. F. Lutsko, "On the geometrical relationship between tilt and twist grain boundaries," *Zs. f. Kristall.* 189: 239, 1989.

3. D. Wolf, "Structure-energy correlation for grain boundaries in fcc metals: III. Symmetrical tilt boundaries," *Acta Metall. Mater.* 38: 781, 1990.

4. D. Wolf, "Structure-energy correlation for grain boundaries in fcc metals: IV. Asymmetrical twist (general) boundaries," *Acta Metall. Mater.* 38: 791, 1990.

5. D. Wolf, "On the relationship between symmetrical tilt, twist, 'special,' and 'favored' grain boundaries," *J. de Physique* 46: 197, 1985.

6. K. L. Merkle and D. J. Smith, "Atomic resolution electron microscopy of NiO grain boundaries," *Ultramicroscopy* 22: 57, 1987.

7. K. L. Merkle, J. F. Reddy, C. L. Wiley, and D. J. Smith, "Structure of high-angle grain boundaries in NiO," in J. A. Pask and A. G. Evans, Eds., *Ceramic Microstructures '86: Role of Interfaces*, 1987, 241.

8. D. Wolf, "Comparisons of the energies of symmetrical and asymmetrical grain boundaries," in Ref. 7, 177.

9. K. L. Merkle and D. Wolf, "Structure and energy of grain boundaries in metals," *MRS Bulletin* 15: 42, 1990.

10. K. L. Merkle and D. Wolf, "Low-energy configurations of symmetric and asymmetric tilt grain boundaries" (submitted to *Phil. Mag.*).

11. K. L. Merkle and D. J. Smith, "Atomic structure of symmetric tilt grain boundaries in NiO," *Phys. Rev. Lett.* 59: 2887, 1987.

12. V. Vitek, A. P. Sutton, G. J. Wang, and D. Schwartz, "On the multiplicity of structures of grain boundaries," *Scripta Met.* 17: 183, 1983.

13. J. L. Rouvière and A. Bourret, "Multiple structures of a <001> Σ = 13 tilt grain boundary in Ge," in *Polycrystalline Semiconductors*, Springer Proceedings in Physics 35, Berlin: Springer-Verlag, 1988, 19.

14. M. J. Mills and M. S. Daw, "The study of defects in metals using HRTEM and atomistic calculations," *Mat. Res. Symp. Proc.* 183: 15, 1990.

15. K. L. Merkle, "High-resolution electron microscopy of grain boundaries in fcc materials," *Colloque de Phys.* 51C1: 251, 1990.

16. K. L. Merkle, "Quasiperiodic interfaces: HREM observations of grain and phase boundaries," in *Proc. XII ICEM*, 4: 332, 1990.

17. N. F. Mott, "Slip at grain boundaries and grain growth in metals," *Proc. Phys. Soc.* 60: 391, 1948.

18. K. L. Merkle, "Atomic matching across internal interfaces," *Mat. Res. Soc. Symp. Proc.* 153: 83, 1989.

19. M. J. Weins, H. Gleiter, and B. Chalmers, "Computer calculations of the structure of high-angle grain boundaries," *J. Appl. Phys.* 42: 2639, 1971.

20. R. C. Pond and D. A. Smith, "An experimental technique for detecting rigid-body translations between adjacent grains," *Can. Metall. Quarterly* 13: 39, 1974.

21. J. W. Matthews and W. M. Stobbs, "Measurement of the lattice displacement across a coincidence grain boundary," *Phil. Mag.* 36: 373, 1977.

22. R. C. Ecob and W. M. Stobbs, "The use of moiré techniques to measure rigid-body displacements," *J. Microsc.* 129: 275, 1983.

23. W. M. Stobbs, G. J. Wood, and D. J. Smith, "The measurement of boundary displacements in metals," *Ultramicroscopy* 14: 145, 1984.

24. C. B. Boothroyd, A. P. Crawley, and W. M. Stobbs, "The measurement of rigid-body displacement using Fresnel fringe intensity methods," *Phil. Mag.* A54: 663, 1986.

25. W. M. Stobbs, "The TEM of interfaces and multilayers," in A. Howie and U. Valdrè, Eds., *Surface and Interface Characterization by Electron Optical Methods*, NATO ASI Series B 191, Plenum Press, 1988, 77.

26. K. L. Merkle, "Rigid-body displacement of asymmetric grain boundaries," *Scripta Met.* 23: 1487, 1989.

27. G. J. Wood, W. M. Stobbs, and D. J. Smith, "Methods for the measurement of rigid-body displacements at edge-on boundaries using HREM," *Phil. Mag.* A50: 375, 1984.

28. K. L. Merkle, in *Proc. Workshop on Structure and Properties of Interfaces*, Wickenburg (submitted to *Ultramicroscopy*).

29. F. Dosandey, S.-W. Chan, and P. Stadelmann, "HREM studies of [001] tilt grain boundaries in gold," *Colloque de Phys.* 51: C1-109, 1990.

30. D. Wolf, "A broken-bond model for grain boundaries in fcc metals," *J. Appl. Phys.* 68: 3221, 1990.

31. D. Dimos, P. Chaudhari, J. Mannhart, and F. K. LeGoues, "Orientation dependence of grain boundary critical currents in $YBa_2Cu_3O_{7-x}$ bicrystals," *Phys. Rev. Lett.* 61: 219, 1988.

32. Y. Gao, K. L. Merkle, G. Bai, H. L. M. Chang, and D. J. Lam, "Structure and composition of grain boundary dislocation cores and stacking faults in MOCVD-grown $YBa_2Cu_3O_{7-x}$ thin films," *Physica* C174: 1, 1991.

33. S. E. Babcock, X. Y. Cai, D. L. Kaiser, and D. C. Larabalestier, "Weak-link-free behavior of high-angle $YBa_2Cu_3O_{7-x}$ grain boundaries in high magnetic fields," *Nature* 347: 167, 1990.

34. Y. Gao, G. Bai, D. J. Lam, and K. L. Merkle, "Microstructure and defects in a-axis oriented $YBa_2Cu_3O_{7-x}$ films," *Physica* C173: 487, 1991.

35. D. Wolf (private communication), 1991.

INTERFACIAL STRUCTURE OF Ω PHASE IN Al-4.0Cu-0.5Mg-0.5Ag ALLOY

Anita Garg and J. M. Howe

Al-Cu-Mg-Ag alloys combine the best features of 7000X and 2000X series Al alloys, attributed mainly to the precipitation of a coherent Ω phase on the $\{111\}_\alpha$ planes.[1] Addition of Ag to an Al-4.0Cu-0.5Mg (wt%) alloy is not necessary for precipitation of the Ω phase,[2] but its presence greatly enhances formation of Ω in preference to θ' and S'.[2,3] The exact role of Ag and Mg in the nucleation process of Ω is not known, but it is believed to be fundamentally different from that of θ' and S'.[4]

Experimental

Samples of Al-4.0Cu-0.5Mg-0.5Ag (wt%) alloy were homogenized for 36 h at 500 C, solution-treated for 24 h at 525 C, quenched into water, and aged for 48 h at 300 C. TEM foils were prepared by electrochemical thinning. The above aging treatment resulted in large plates with a well-developed interfacial structure. TEM and HREM were used to study the interfacial structure of the faces of Ω plates.

Results

A BF image of an Ω plate and the corresponding SADP close to a $\{111\}_\alpha$ zone-axis are shown in Figs. 1(a) and (b), respectively. The faint black and white contrast of different widths suggested that the interface contained a number of ledges of variable heights. A contrast analysis of these ledges (Figs. 1c-f) indicated that most of the ledges exhibited strain fields similar to Shockley partial dislocations with b = $a/6<112>_\alpha$, mainly in edge orientation. Occasionally, perfect glissile dislocations of the type $a/2<110>_\alpha$ were also found at the interface. These were not defects of the interface and were not connected to the interfacial structure. In thin regions of the foil, $a/2<110>_\alpha$ dislocations were found to glide on the adjacent $\{111\}_\alpha$ plane due to heating by the electron beam. At the edges of the plates, the ledges/dislocations were so close that their overlapping strain fields prevented an accurate determination of their actual character from conventional TEM images. HREM images (e.g., Fig. 2) showed the presence of Frank partials with b = $a/3<111>_\alpha$, spaced approximately 2.6-2.8 nm apart at the edges of the plate.

A transformation model from the fcc α matrix to the orthorhombic Ω phase has been proposed

which requires (i) glissile Shockley transformation dislocations of only one type, i.e., b = $a/6<112>_\alpha \parallel [100]_\alpha$ for each variant of the Ω phase; and (ii) misfit dislocations with b = $a/3<111>_\alpha$ to accommodate the large misfit normal to the habit place. Lattice dislocations play an important role in supplying these dislocations. In particular, a perfect dislocation (e.g., b = $a/2[110]_\alpha$) which is not glissile in the habit plane of the precipitate $(111)_\alpha \parallel (001)_\Omega$ and has b ⊥ $a/2[\bar{1}10]_\alpha \parallel [010]_\Omega$, upon dissociation at the interface would provide the right kind of Shockley partial $(a/6[11\bar{2}]_\alpha)$ to accomplish the transformation and also provide a Frank partial $(a/3[111]_\alpha)$ to accommodate the misfit. The other two types of nonglissile perfect dislocations could provide the $a/3<111>_\alpha$ misfit dislocations, but their Shockley counterparts are not needed for the transformation, and thus can combine to form glissile perfect dislocations that are not part of the interfacial structure.

Conclusions

The observed interfacial structure is in agreement with the model proposed for the fcc α to orthorhombic Ω transformation and is difference from that observed for similar precipitates such as γ' in Al-Ag alloys and the T₁ phase in weldalite alloys, where at least two or three types of glissile $a/6<112>_\alpha$ dislocations on the $\{111\}_\alpha$ habit plane accomplish the fcc (α) to hcp (γ',T) transformation.

References

1. I. J. Polmear and M. J. Couper, "Design and development of an experimental wrought Al alloy for use at elevated temperatures," *Metall. Trans.* 19A: 1027, 1988.

2. A. Garg et al., "Precipitation of the Ω phase in an Al-4.0Cu-0.5Mg alloy," *Scripta Metall. et Mater.* 24: 677, 1990.

3. B. C. Muddle and I. J. Polmear, "The precipitate Ω phase in Al-Cu-Mg-Ag alloys," *Acta Metall.* 37: 977, 1989.

4. K. M. Knowles and W. M. Stobbs, "The structure of {111} age hardening precipitates in Al-Cu-Mg-Ag alloys," *Acta Cryst.* B44: 207, 1988.

Anita Garg is at the Department of Metallurgical Engineering and Materials Science, Carnegie Mellon University, Pittsburgh, PA 15213; J. M. Howe is at the Department of Materials Science, University of Virginia, Charlottesville, VA 22903. This research was supported by ALCOA and NSF (Contract DMR-8915770).
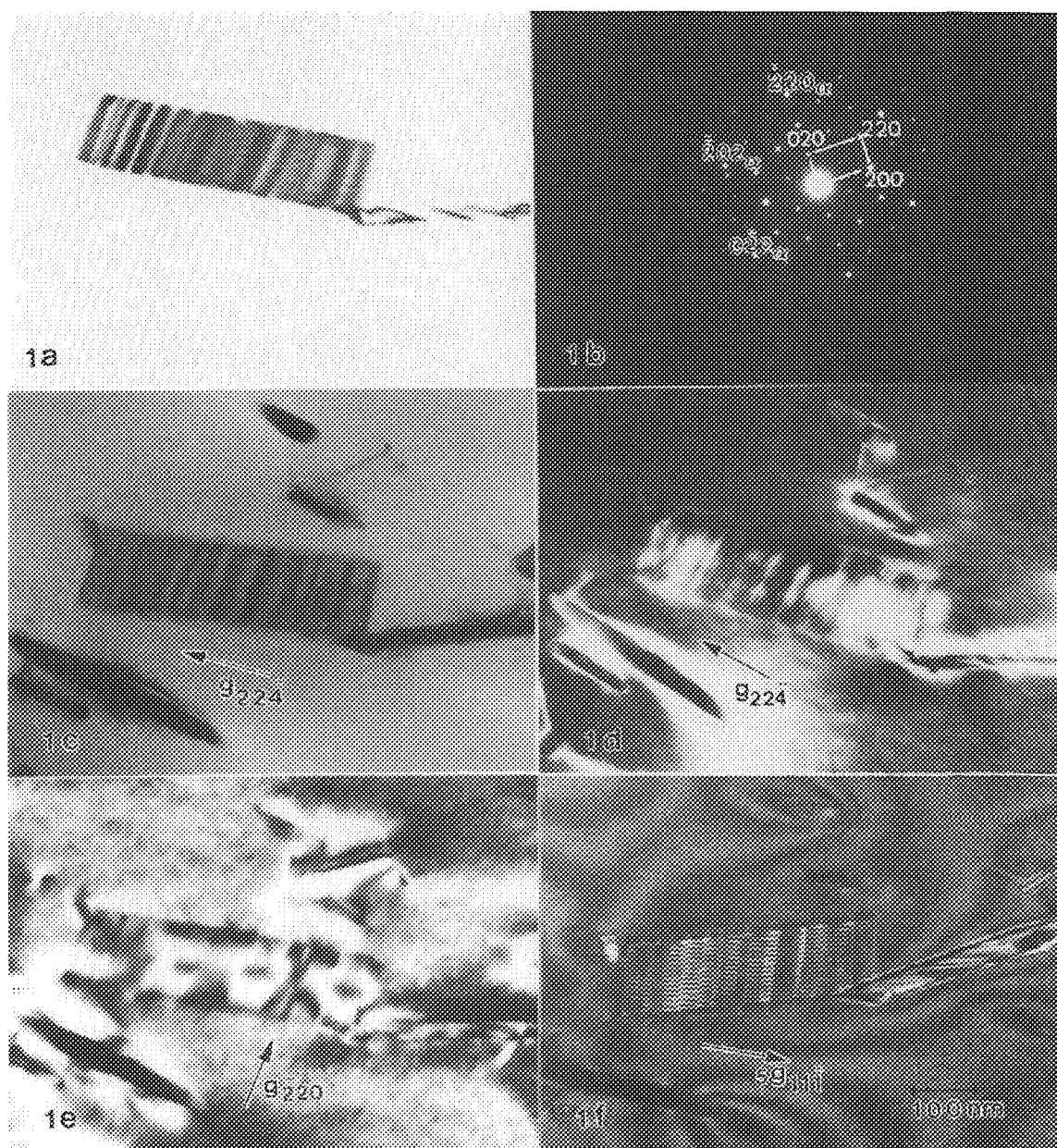
FIG. 1.--(a) Multibeam BF image of Ω plate close to $[111]_\alpha$ zone-axis; (b) corresponding SADP with Ω unit-cell outlined; (c) BF and (d) DF images of the ledges showing visibility of $a/6[11\bar{2}]$ dislocations with $g_{22\bar{4}}$; (e) DF image with $\bar{g}_{\bar{2}20}$ showing invisibility of the ledges; (f) WBDF image with $5g_{11\bar{1}}$ showing bending of displacement fringes at the ledges.
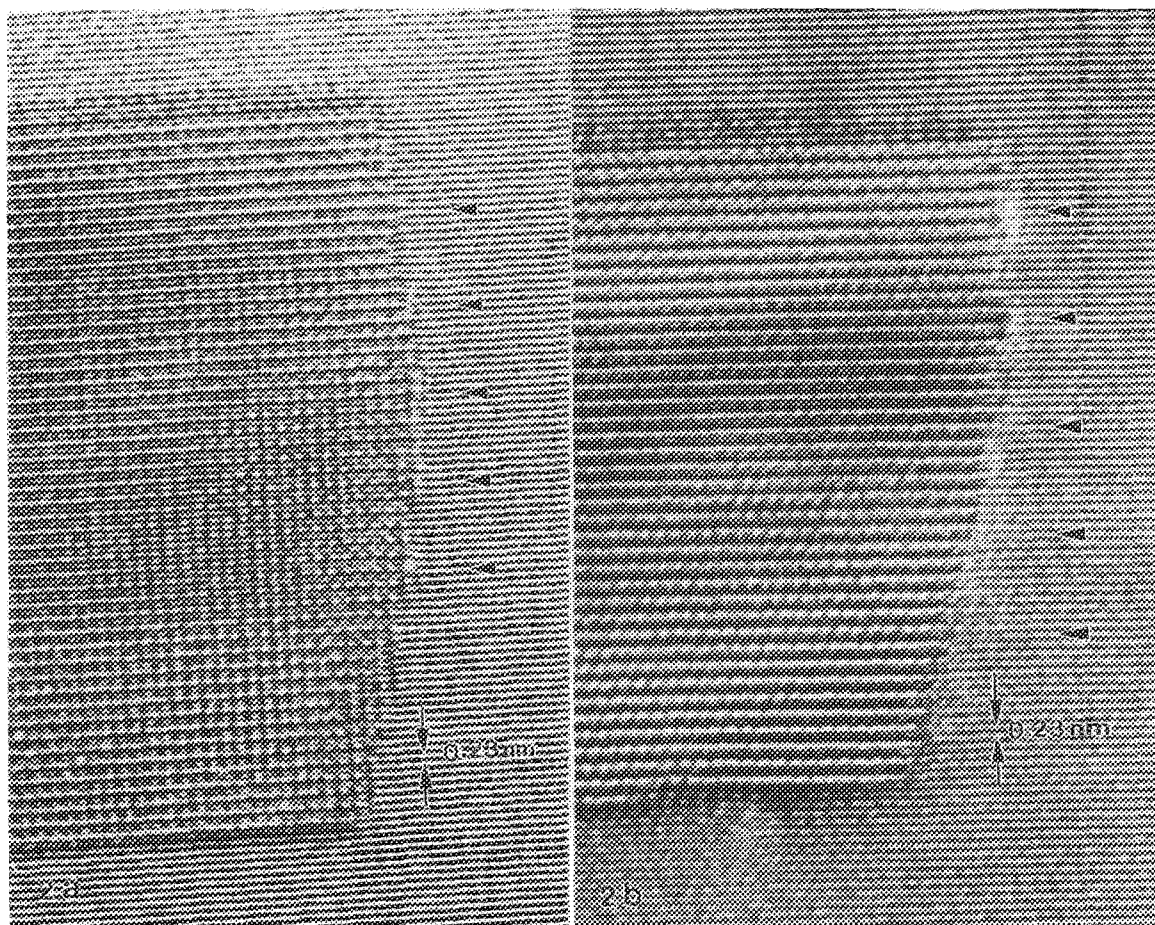
FIG. 2.--HREM images of the ends of two Ω plates in (a) <112>$_\alpha$ ‖ [100]$_\Omega$, (b) <112>$_\alpha$ ‖ [110]$_\Omega$ orientations. Approximate positions of Frank partials are indicated by arrowheads.

REFINEMENT OF INTERFACE ATOMIC STRUCTURES FROM HREM IMAGES

W. E. King and B. S. Lawver

In the past, extensive use has been made of high-resolution image simulation techniques to obtain qualitative and semi-quantitative validation of model atomic structures by comparison of simulated with experimental images. (Examples of such comparisons applied to interfaces can be found in Refs. 1 and 2). Simulation methods have advanced to the point where the calculated and experimental images are nearly indistinguishable. When such comparisons are made, two questions are invariably asked: (1) what are the positions of the atomic columns, and (2) what are the uncertainties in these positions? We have pursued these questions using a computational method that is commonly employed in structure refinement by x-ray diffraction and in the analysis of γ-ray and x-ray spectra, namely unconstrained, nonlinear least-squares optimization. The purpose of this work is to demonstrate the use of this method. As an example, we present a preliminary refinement of the structure of a $\Sigma 5(310)/[001]$ symmetric tilt grain boundary in Nb.

Experimental

Nb bicrystals with a single $\Sigma 5(310)/[001]$ symmetric tilt grain boundary were produced by the diffusion bonding method.[3] The bicrystals were sectioned and thinned to electron transparency. Images were acquired with the JEOL 4000EX high-resolution electron microscope (HREM).[4] The experimental image used in the present analysis (Fig. 1) has been averaged along the direction of the grain boundary to reduce noise. Three periods of this averaged image have been assembled for comparison with the simulated images.

Analysis

The embedded atom method (EAM) and the model generalized pseudopotential theory,[5] coupled with atomistic simulation, were used to predict a stable atomic structure for the $\Sigma 5(310)/[001]$ grain boundary. These structures were compared with the experimental image by use of image simulation. The experimental image, although not in exact agreement with any theoretical model, was qualitatively similar to images deduced from atomistic simulations. The lack of mirror symmetry at the experimentally fabri-

W. E. King is at the Chemistry and Materials Science Department, Lawrence Livermore National Laboratory, Livermore, CA 94550; B. S. Lawver is with LLNL Engineering Research Division. This work was performed under the auspices of the U.S. Department of Energy and LLNL under contract W-7405-Eng-48.

cated interface favors a structure predicted by EAM and shown in Fig. 2.[4,6] This structure was used as an initial guess in the optimized procedure; n atomic columns in the neighborhood of the grain boundary were included in the fitting procedure. Since the position of each column has two degrees of freedom, this gives rise to 2n free parameters referred to as x_1, x_2, ..., x_{2n}. It is the goal of a least-squares problem to fit a model $g(x)$ to the experimental data y, and thus to minimize the residuals f_i:

$$f_i(x) = y_i - g_i(x) \tag{1}$$

where y_i is the intensity value of the ith pixel in the experimental image and $g_i(x)$ is the intensity value of the ith pixel in the simulated image; that is,

$$\min \left\{ \sum_{i=1}^{m} f_i(x)^2 \right\} \tag{2}$$

This problem has been addressed in the current work by use of the MINPACK-1[7] unconstrained nonlinear least-squares optimization code coupled with the EMS image simulation code.[8] MINPACK-1 employs the Levenberg-Marquardt algorithm to solve the nonlinear least-squares problem.[9] A strength of this algorithm lies in its reliance on the calculation of the Jacobian matrix

$$\frac{\partial f_i(x)}{\partial x_j} \qquad 1 \leq i \leq m, \ 1 \leq j \leq 2n \tag{3}$$

which is used to correct the initial guess x_0. Functionally, MINPACK-1 calculates $F(x_0)$, then uses the forward-difference approximation to calculate the Jacobian matrix. The algorithm then estimates a correction p to x_0 such that

$$\|F(x_+)\| < \|F(x_0)\| \tag{4}$$

where $x_+ = x_0 + p$ and $\|F(x_+)\|$ is the Euclidean norm of F

$$\|F(x_+)\| = \left[\sum_{i=1}^{m} f_i(x_+)^2 \right]^{1/2} \tag{4}$$

This procedure is iterated with x_+, replacing x until specific convergence criteria are met. In this work n = 20 and m = 16 348, which corresponds to a 128 × 128 pixel image. The EMS computational cell was 4.2012 × 1.0503 nm². The simulated image was 512 × 128 pixels. Optimizations required 13 iterations corresponding to 173 multislice calculations. Simulations were run on a Silicon Graphics Personal IRIS 4D-25.
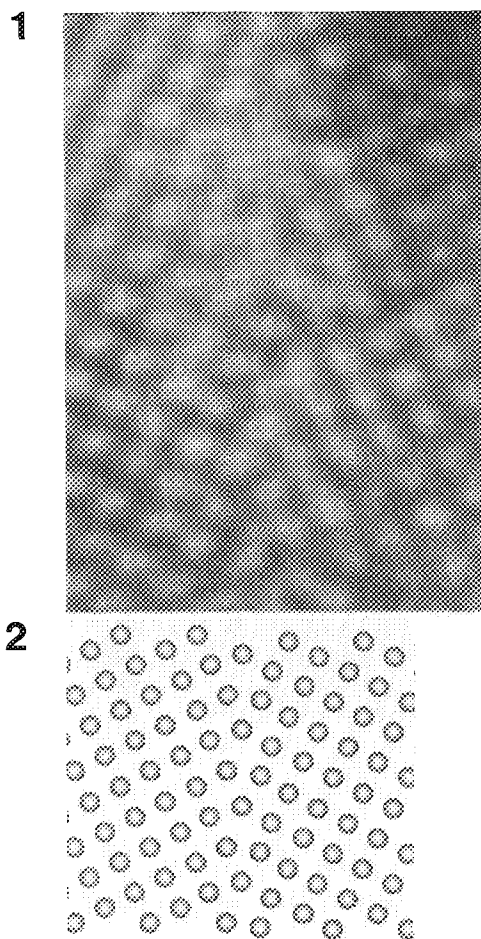
FIG. 1.--Experimental image of nearly symmetric segment of $\Sigma 5(310)/[001]$ tilt grain boundary in Nb. Image was acquired under thickness and defocus conditions that gave rise to a so-called "black-atom" image.[4]

FIG. 2.--Projection along [001] of atomic structure of $\Sigma 5(310)/[001]$ symmetric tilt grain boundary in Nb as predicted by EAM.[4,6]

Results

Figure 3 shows a plot of the 20 atomic positions that were included as free parameters in the optimization procedure as a function of the iteration number. Three atoms exhibited displacements of ~ 0.05 nm. Figure 4 shows a plot of $\|F(x)\|$ as a function of iteration number. $\|F(x)\|$ is very sensitive to small changes in the atomic positions. Figure 5 shows the experimental image (left), the image based on the initial guess (center), and the image based on the final solution (right). The marked improvement in $\|F(x)\|$ and the improvement in the fit that is visible by eye indicates that $\|F(x_+)\| < \|F(x_0)\|$. The fitting procedure gave rise to a general reduction in magnitude of the residuals. Figure 6(a) shows a surface and contour plot of the residuals between the experimental and simulated image as a function of position overlaid on the experimental image based on the initial guess. Figure 6(b) shows
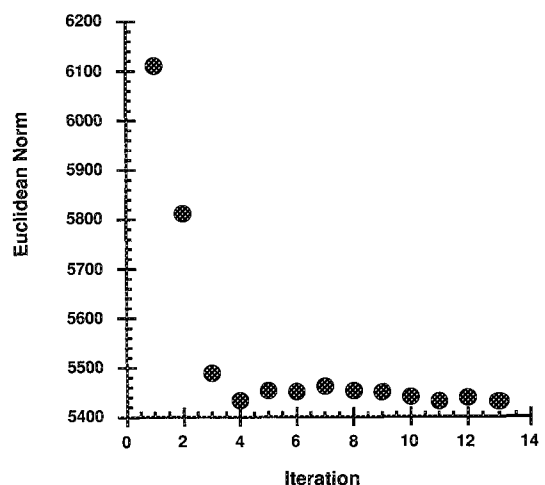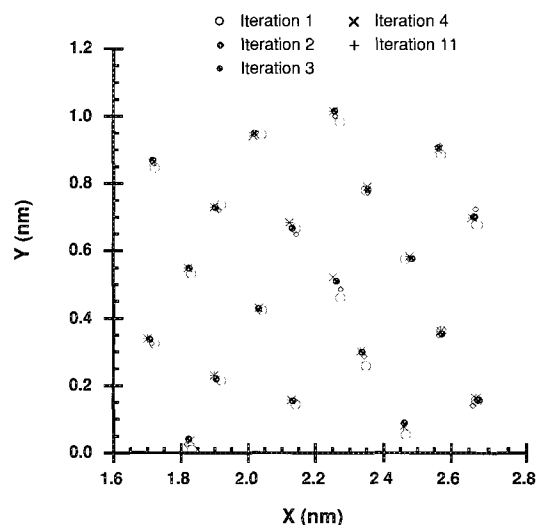
FIG. 3.--Evolution of the 20 atomic column positions in the neighborhood of grain boundary as a function of iteration of optimization procedure. Grain boundary is located at $x \approx 2.125$ nm.

Fig. 4.--$\|F(x)\|$ as a function of iteration number.

the contours defined by the residuals overlaid on the experimental image. Figure 7(a) shows a surface and contour plot of the residuals as a function of position overlaid on the experimental image based on final solution for x. Figure 7(b) shows the contours defined by the residuals overlaid on the experimental image. The amplitudes of the maxima and minima of the residuals have been reduced. Note that nearly all of the deivations of the experimental image from the simulated image are positive. This result may be associated with a nearly uniform background contrast in the experimental image revealed by Fourier filtering. This contrast was not included in the model.

The deviations of the fit from the experimental image are systematic and therefore indicate a deficiency in the model used to describe the simulated image. These deficiencies may include: (1) deviations in the crystal tilt from the exact zone axis, (2) additional
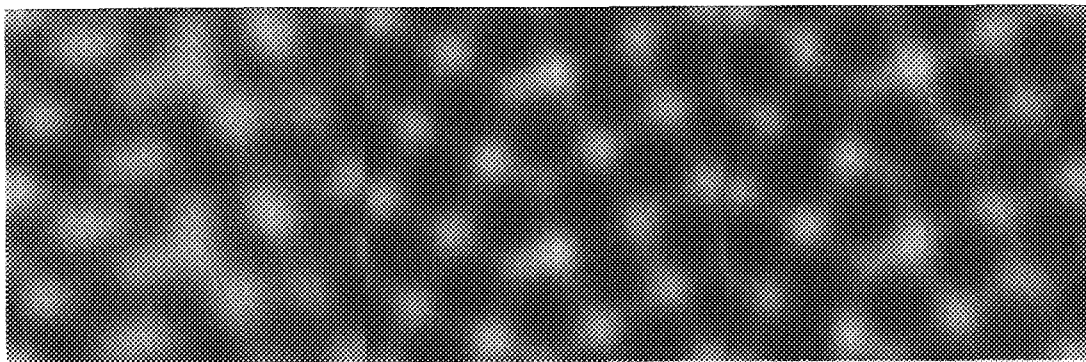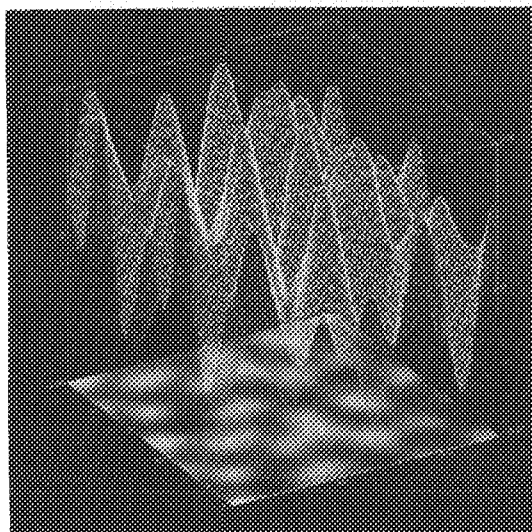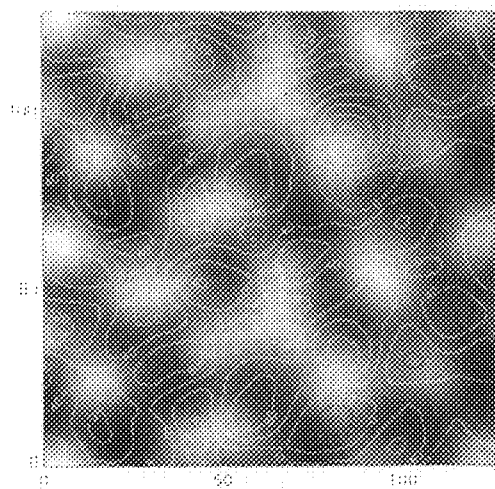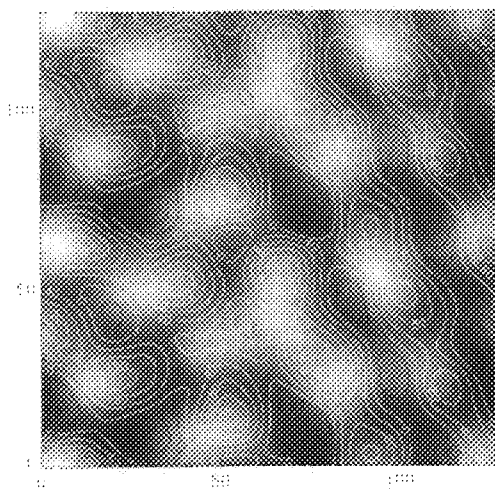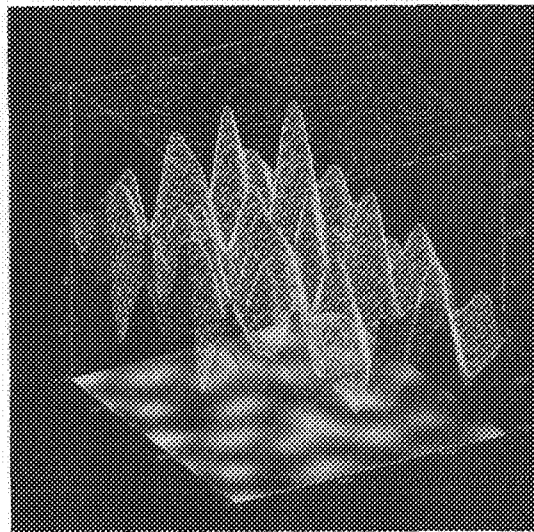
FIG. 5.--Experimental image (left), simulated image based on x_0 (center), and simulated image based on final solution (right).

FIG. 6.--(a) Experimental image overlaid by surface and contour plot of residuals between experimental and simulated image based on x_0; (b) experimental image overlaid by contour plot of residuals between experimental and simulated image based on x_0.

FIG. 7.--(a) Experimental image overlaid by surface and contour plot of residuals between experimental and simulated image based on final solution; (b) experimental image overlaid by contour plot of residuals between experimental and simulated image based on final solution.

219

contrast in the experimental image due to an amorphous layer on the top and bottom surface of the sample, and (3) failure of the model to include inelastic scattering. Deviation of the sample from exact zone axis orientation on both sides of the crystal is considered to be the largest contributor to $\|F(x)\|$, as evidenced by the elongated column contrast in the experimental image compared with the simulation.

This method does not reduce the need for clean, thin samples and careful microscopy, but it does provide a method for making quantitative comparisons of experimental and simulated images and to assess the uncertainty in the model atomic positions. However, we believe that this example demonstrates the usefulness and power of this method in refining the atomic structure of interfaces by use of the nonlinear least-squares approach.

References

1. K. L. Merkle and D. J. Smith, "Atomic structure of symmetric tilt grain boundaries in NiO," *Phys. Rev. Lett.* 59: 2887, 1987.
2. M. J. Mills and M. S. Daw, "The study of defects in metals using HRTEM and atomistic calculations," in U. Dahmen, D. J. Smith, and R. Sinclair, Eds., Pittsburgh, Pa.: MRS, 1990, 15.
3. H. F. Fischmeister, W. Mader, B. Gibbesch, and G. Elssner, "Preparation, properties, and structure of metal/oxide interfaces," in M. H. Yoo, W. A. T. Clark, and C. L. Briant, Eds., *Interfacial Structure, Properties, and Design*, Pittsburgh, Pa.: Materials Research Society, 1988, 529.
4. W. E. King, G. H. Campbell, A. Coombs, M. J. Mills, and M. Rühle, "HREM investigation of the structure of the $\Sigma 5(310)/[001]$ symmetric tilt grain boundary in Nb," in P. D. Bristowe, J. E. Epperson, J. E. Griffith, and Z. Liliental-Weber, Eds., *Defects in Materials*, Pittsburgh, Pa.: Materials Research Society, (in press).
5. J. A. Moriarty, *Phys. Rev.* B42: 1609, 1990.
6. S. M. Foiles, M. S. Daw, and R. B. Phillips, "Tilt boundaries in bcc metals: Comparison of results using different interatomic interactions," Ref. 4.
7. J. J. Moré, B. S. Garbow, and K. E. Hillstrom, *User Guide for MINPACK-1*, Argonne National Laboratory, 1980 (ANL-80-74).
8. P. Stadelmann, *Ultramicroscopy* 21: 131, 1987.
9. J. J. Moré, "The Levenberg-Marquardt algorithm: Implementation and theory, numerical analysis," in G. A. Watson, Ed., *Lecture Notes in Mathematics*, New York: Springer-Verlag, 1977, 630.

ON DETERMINING BODY TRANSLATION VECTORS FROM DIFFRACTION CONTRAST
IMAGES OF INTERFACES USING NONCOMMON REFLECTIONS

S. S. Sheinin and D. J. Seale

A technique for determining body translation vectors at interfaces between two crystals using diffraction contrast images has been well established.[1-4] This method is very useful in that it offers a completely independent check on values of the translation vector obtained from structure images. In the simplest and most common version of the technique, a reflection common to the two crystals is used to image the boundary.[1] Analysis of this image gives the component of the body translation vector in the direction of the common reflection. Thus, in order to define the body translation vector completely, this process must be repeated three times with noncoplanar common reflections. This requirement places unfortunate limitations on a determination of the body translation vectors since, in some situations of interest, obtaining strongly excited common reflections can present problems. For example, in some cases the range of orientations of the specimen available in the microscope does not yield strongly excited common reflections. Another problem arises in some materials in which noncommon reflections are very close to being common, giving spots in the diffraction pattern that are very closely spaced. This problem can arise, for example, in diffraction patterns from materials which contain both an HCP and an FCC phase. For an ideal c/a ratio some reflections such as $(13\bar{1})$FCC and $(\bar{2}112)$HCP are indeed common. However, for non-ideal c/a ratios, the reciprocal lattice vectors associated with these reflections no longer coincide but are separated by a very small amount.[5] Another example occurs in twin related crystals of high-T_c 123 compound superconductors. For example, a (001) orientation matrix and a (110) twin plane would give a $(1\bar{1}0)$ matrix reflection and a $(\bar{1}10)$ twin reflection, which have reciprocal lattice vectors equal in magnitude but differing in direction by only $\sim 2^0$. A natural question that arises in these cases is the following: can images obtained by allowing these closely spaced noncommon reflections through the objective aperture be used to determine body translation vectors? If yes, can these reflections be treated as a common reflection for the purpose of determining the body translation vector? In this paper we show that such a method can yield information about body translation vectors, but that treating these reflections as common reflections can lead to incorrect results. We also present

the theoretical basis for correctly interpreting these images.

Theoretical Basis for Interpreting Images Obtained with Noncommon Reflections

The interpretation of images obtained by allowing two closely spaced noncommon reflections through the objective aperture requires that the correct expressions for the amplitude of the electron wave in the image plane be used in calculating image contrast. To illus-the expressions to be used in this case, consider an image formed by including in the objective aperture a reflection $\underline{g}$ from the upper crystal in the specimen and another reflection $\underline{h}$ from the lower crystal. The expression for the amplitude of the wave in the image plane obtained in this case is given by

$$\Phi(t) = \exp[2\pi i(\underline{K} + \underline{g}) \cdot \underline{r}] \; \phi_g(t) \; \exp[2\pi i \underline{g} \cdot \underline{T}$$

$$+ \exp[2\pi i(\underline{K} + \underline{h}) \cdot \underline{r}] \; \phi_h(t) \qquad (1)$$

where t is the total specimen thickness, ϕ_g and ϕ_h are the amplitudes of the diffracted beams $\underline{g}$ and $\underline{h}$, $\underline{T}$ is the translation vector at the boundary, and $\underline{K}$ is the incident wave vector after correction for the mean inner potential of the crystal. The expressions for ϕ_g and ϕ_h can be obtained from Eq. (11) in Sheinin and Corbett.[7]

Results

In order to make an assessment of the image contrast obtained when two closely spaced diffracted beams $\underline{g}$ and $\underline{h}$ are included in the objective aperture, Eq. (1) has been used to calculate image intensity for the case of an FCC upper crystal with a zone axis in the $[\bar{1}10]$ direction, a lower twin crystal, and a $[\bar{1}2\bar{1}]$ twin axis. In this case, $\underline{g} = (2\bar{2}0)U$ and $\underline{h} = (0\bar{2}2)L$ are common reflections, where U and L indicate the use of coordinates in the upper and lower crystal, respectively. To determine the effects that are obtained when $\underline{g}$ and $\underline{h}$ are not equal, $\underline{h}$ was taken to be $\underline{g} + \Delta\underline{g}$, where $\Delta\underline{g}$ could be set to any desired value. The results shown in Figs. 1 and 2 were obtained for the case where $\Delta\underline{g}$ and $\underline{g}$ are in the same direction but $\Delta g/g = 0.05$. The translation vector $\underline{T}$ was chosen so that a value of $\underline{g} \cdot \underline{T} = 1/3$ was obtained. The overall thickness of the specimen used in the calculations was about one extinction distance and the tiepoint projection was taken to be such that the reflection $\underline{g}$ was in the Bragg condition. In Fig. 1, image contrast is compared in the following two cases: (a) a dark-field image formed with common re-
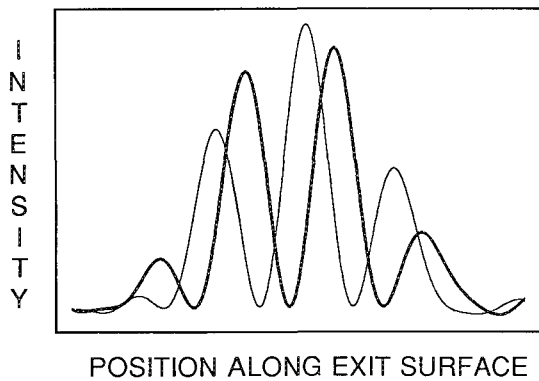
POSITION ALONG EXIT SURFACE

FIG. 1.--Intensity profiles showing image contrast obtained in dark-field image formed with (a) two common reflections passing through objective aperture and with translation at boundary (light curve) and (b) two closely spaced reflections and the same translation as in (a) at the boundary (heavy curve).
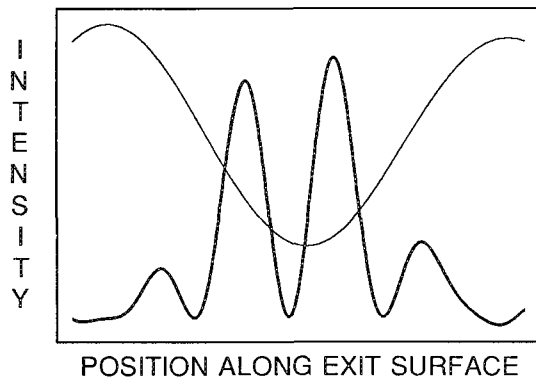

POSITION ALONG EXIT SURFACE

FIG. 2.--Intensity profiles showing image contrast obtained in dark-field image formed with (a) two closely spaced reflections as in Fig. 1 but without translation at boundary (light curve) and (b) two closely spaced reflections as in (a) but with translation at boundary (heavy curve).

flections g and h, and a translation vector at the boundary as described above, i.e., $\Delta g = 0$, $T \neq 0$ (this curve is the light line in the figure); and (b) a dark-field image formed with two closely spaced reflections passing through the objective aperture and again a translation vector at the boundary as described above, i.e., $\Delta g \neq 0$, $T \neq 0$ (this curve is the heavy line in the figure). It can be clearly seen that the image contrast obtained in the two cases is quite different, which shows that two closely spaced noncommon reflections cannot be treated as a common reflection for purposes of interpreting the image. In Fig. 2 image contrast is compared in the following two cases: (a) an image formed with two closely spaced reflections as above but with no translation at the boundary, i.e. $\Delta g \neq 0$, $T = 0$ (this curve corresponds to the light line in the figure), and (b) again an image formed with two closely spaced reflec-

tions but with a translation at the boundary, i.e., $\Delta g \neq 0$, $T \neq 0$ (this curve corresponds to the heavy line in the figure). Figure 2 shows that the intensity profiles obtained in the two cases are quite different, indicating that image contrast obtained when two closely spaced reflections are allowed to contribute to the image is indeed sensitive to the value of the body translation vector.

Conclusions

Two conclusions can be drawn from the results given in the previous section. The first is that body translation vectors can be determined from images formed with two closely spaced noncommon reflections if both diffracted beams are allowed to pass through the objective aperture. The second conclusion is that in interpreting image contrast in this case, these two reflections cannot be assumed to be common, even if they are very closely spaced. In order to obtain a correct interpretation of these images, equations of the form given in Eq. (1) above should be used to predict image contrast. (The extension to the many-beam situation is straightforward and will not be presented here.)

References

1. R. C. Pond, "The measurement of excess volume at grain boundaries using transmission electron microscopy," *J. Microscopy* 116: 105, 1979.
2. A. P. Sutton and R. C. Pond, "Electron microscope images of coincidence boundaries," *Physica Status Solidi* 45(a): 149, 1978.
3. S. S. Sheinin and R. Perez, "Dynamical theory of twin boundary contrast including effects of common reflections," *Physica Status Solidi* 79(a): 367, 1983.
4. H. S. Kim and S. S. Sheinin, "Dynamical theory of twin boundary contrast for the noncolumn and non-symmetrical Laue case," *Physica Status Solidi* 104(a): 519, 1987.
5. A. Fourdeux, R. Gevers, and S. Amelinckx, "Electron microscope contrast effects at the interface between two different polytypes," *Physica Status Solidi* 24: 195, 1967.
6. C. S. Pande, A. K. Singh, L. Toth, D. U. Gubser, and S. Wolf, "Domainlike defects observed in high temperature superconductor Y-Ba-Cu-O," *Phys. Rev.* B36: 5669, 1987.
7. S. S. Sheinin and J. M. Corbett, "Application of the multi-beam dynamical theory to crystals containing twins," *Physica Status Solidi* 38(a): 675, 1976.

DISLOCATION/GRAIN BOUNDARY INTERACTIONS IN A Σ13 GRAIN BOUNDARY IN SILICON

Laurent Sagalowicz and W. A. T. Clark

In near-exact coincidence site lattice (CSL) boundaries, it is expected that incoming crystal lattice dislocations will reduce their energy by dissociating into smaller grain boundary dislocations, with Burgers vectors obtained from the DSC lattice.[1] However, details of this precise mechanism are often difficult to observe. The purpose of this study is to understand in more detail the way in which special grain boundaries can impede the process of deformation by blocking the transmission of dislocation across interfaces, and hence how individual interfaces contribute to the observed macroscopic deformation of a polycrystal. We show that in Si the incoming dislocations can further dissociate into partial DSC dislocations, which separate regions in the boundary of different, but symmetry-related, structure.[2]

Experimental

The Si bicrystal studied here was grown by the Czochralski method and corresponds to a misorientation very close (i.e., within a few minutes of arc) to the exact Σ13 CSL, which is described as $22.6°/[001]_{1/2}$ axis. The plane of the boundary was one of those with the highest CSL site density, $(510)_1/(5\bar{1}0)_2$. This boundary is similar to the Σ5 and Σ25 studied by Bacmann et al.,[3][4] in that they are all obtained by rotation about [001] in the diamond cubic lattice.

Rectangular samples were cut from a large (∼30 × 13 cm) bicrystal, in the orientation shown in Fig. 1, so that the three faces corresponded to $(001)_{1/2}$, $(230)_1/(320)_2$, and $(3\bar{2}0)_1/(2\bar{3}0)_2$. They were then deformed in compression along $[3\bar{2}0]_1/[2\bar{3}0]_2$ by 1-10%, at a temperature of 800 C. (The elevated temperature is necessary to obtain plastic deformation in Si.) Slices were taken from both the deformed and undeformed specimens, as indicated in Fig.1, and 3mm-diameter disks were drilled from the slices so that the boundary lay along the diameter of the slice, inclined to 45° to its normal. Other slices were also taken from the $(001)_{1/2}$ face of the sample, with the common $[001]_{1/2}$ as their normal, and are used to obtain samples for high resolution electron microscope observations, but are not reported on here. The specimens were examined in the double-tilt stage of a JEOL 200CX TEM, operating at 200 kV.

Geometry of the Σ13 Boundary in Si

At a grain boundary at or close to CSL, orientation, simple energetic arguments indicate that there is a tendency for any crystal lattice dislocation that enters the boundary to dissociate into several smaller grain boundary dislocations, with Burgers vectors belonging to the DSC lattice. However, in the case of the diamond cubic lattice, additional defects can arise because the atom basis contains two, and not one, atoms. Thus the dichromatic pattern, the pattern formed by the interpenetrating lattices of the two crystals is different from the dichromatic complex, constructed by allowing the two crystal structures to interpenetrate. Furthermore, several energetically degenerate boundary structures can result, in this case three, which can be separated in the interface by partial grain boundary dislocations. The dichromatic pattern for the Σ13, $22.6°/[001]_{1/2}$ misorientations is shown in Fig. 2, on which are marked the three shortest vectors of the DSC lattice:

$b_1 = a/26[510]_1 : a/26[5\bar{1}0]_2$

$b_2 = a/26[\bar{1}50]_1 ; a/26[150]_2$

$b_{31} = a/26[\bar{3}\ 2\ 13]_1 : a/26[\bar{2}\ 3\ 13]_2$

There are three other equivalent b_3 dislocations, which can be obtained from the figure. Grain boundary partial dislocations can also be defined from this lattice, most of which have components along the common $[001]_{1/2}$ direction. For instance, the b, DSC dislocation can dissociate according to the following reaction (in the coordinate system of crystal 1):

$$\frac{a}{26}[\bar{3}\ 2\ 13]_1 \rightarrow \frac{a}{52}[\bar{5}\ \bar{1}\ 13]_1 + \frac{a}{52}[\bar{1}\ 5\ 13]_1 \qquad (1)$$

The two resulting partial DSC dislocations are translations that join an atom at a lattice site of one crystal to one displaced by $\pm(\frac{1}{4}, \frac{1}{4}, \frac{1}{4})$ from a lattice site of the other crystal, and can formally be identified as Class 3 interfacial dislocations.[2][5][6]

Electron Microscopy

The undeformed and deformed boundaries were imaged in a number of two-beam conditions, in order to determine the Burgers vectors of dislocations near and in the interface. Figure 3 shows the undeformed sample, imaged in a diffracting plane common to both crystals, and it is immediately evident that almost no grain boundary dislocation structure is visible. This was equally true for other reflections, and indicates the closeness of the misorientation to the exact CSL. However, some features are visible, such as a number of ledges (marked
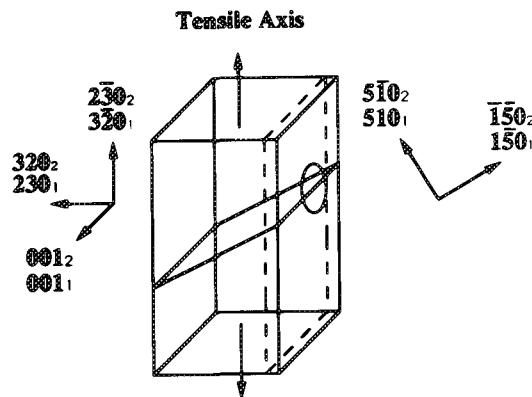
Tensile Axis

$2\bar{3}0_2$
$3\bar{2}0_1$

$5\bar{1}0_2$
510_1

$\bar{1}\bar{5}0_2$
150_1

$3\bar{2}0_2$
230_1

001_2
001_1

FIG. 1.--Geometry of $\Sigma13$ bicrystal used in this investigation.

$[\bar{1}50]_1:[\bar{1}50]_2 \longrightarrow$

$[5\bar{1}0]_1:[5\bar{1}0]_2$

b_2

010_2

b_1

100_1 100_2 010_1

b_3

FIG. 2.--Dichromatic pattern of $\Sigma13$ orientation, projected along $[001]_{1/2}$. Open squares and circles represent lattice sites of crystal 1 and crystal 2, respectively, in plane of the paper. Filled squares and circles are lattice sites of crystal 1 and crystal 2, respectively, displaced by $\pm a(0,0,\frac{1}{2})$. The three shortest DSC vectors, b_1, b_2, and one of four equivalent b_3s, are indicated.

at A), which are decorated with oxygen-rich precipitates (arrowed). At B is a dislocation, which appears (from the difference in contrast in the boundary on either side of it) to separate degenerate structures of the $\Sigma13$ CSL, and thus have some partial DSC dislocation character.

When the same boundary is imaged in the same diffracting vector after deformation, the difference in structure is evident (Figs. 4 and 5). The grain interiors contain many dislocations, predominantly on slip systems with the highest calculated Schmidt factor for this deformation geometry. One such dislocation is labeled C, and has Burgers vector $a/2[10\bar{1}]_1$; it is seen to interact with the boundary at D. From the foregoing remarks, energetically the most likely dissociation reaction for this dislocation is into one b_3 plus two b_2 dislocations, according to

$$\frac{a}{2}[10\bar{1}]_1 \rightarrow 2\frac{a}{26}[510]_1 + \frac{a}{26}[3\ \bar{2}\ \overline{13}]_1 \qquad (2)$$

However, it can be seen that, in the common $004_{1/2}$ reflection which gives $g \cdot b = 0$ for both b_1 and b_2 DSC dislocations, and $g \cdot b = 2$ for the b_3, the crystal lattice dislocation dissociates into not one but two visible dislocations in the interface. In addition, the contrast in the regions between alternate grain boundary dislocations is slightly different. In a different diffracting vector (Fig. 5), for which $g \cdot b$ for the b_3 dislocations is close to zero and $g \cdot b$ for the b_1 and b_2 dislocations is not, a fine network of grain boundary dislocations is evident at E and F. On the basis of their contrast in a series of reflections, these are identified as b_1 and b_2 DSC dislocations.

We explain this observation of the dissociation of a crystal lattice dislocation into four, and not the anticipated three, grain boundary dislocations by proposing that the b_3 DSC dislocation produced in reaction (1) further dissociates into two grain boundary partial dislocations, according to reaction

(2). The complete description of the dissociation of this incoming crystal lattice dislocation is, then:

$$\frac{a}{2}[10\bar{1}]_1 \rightarrow 2\frac{a}{26}[510]_1 + \frac{a}{52}[5\ 1\ \overline{13}]_1 \qquad (3)$$

$$+ \frac{a}{52}[1\ \bar{5}\ \overline{13}]_1$$

to produce four grain boundary dislocations, rather than three.

These observations indicate that grain boundary partial dislocations have an important role to play in the deformation of polycrystalline materials with the diamond cubic structure, and dislocation based model of deformation should be sure to take them into consideration. Confirmation of the atomic arrangement of these degenerate structures is currently being obtained by high-resolution electron microscopy.

References

1. W. Bollmann, *Crystal Defects and Crystalline Interfaces*, Berlin: Springer-Verlag, 1970.
2. R. C. Pond, "Line defects in interfaces," in F. R. N. Nabarro, Ed., *Dislocations in Solids*, Amsterdam: North Holland, 1989, 1.
3. J. J. Bacmann, G. Silvestre, and M. Petit, *Phil. Mag.* 43A: 189, 1981.
4. W. Bollmann, G. Sylvestre, and J. J. Bacmann, *Phil. Mag.* 43A: 201, 1981.
5. R. C. Pond, *Proc. Roy. Soc.* A357: 471, 1977.
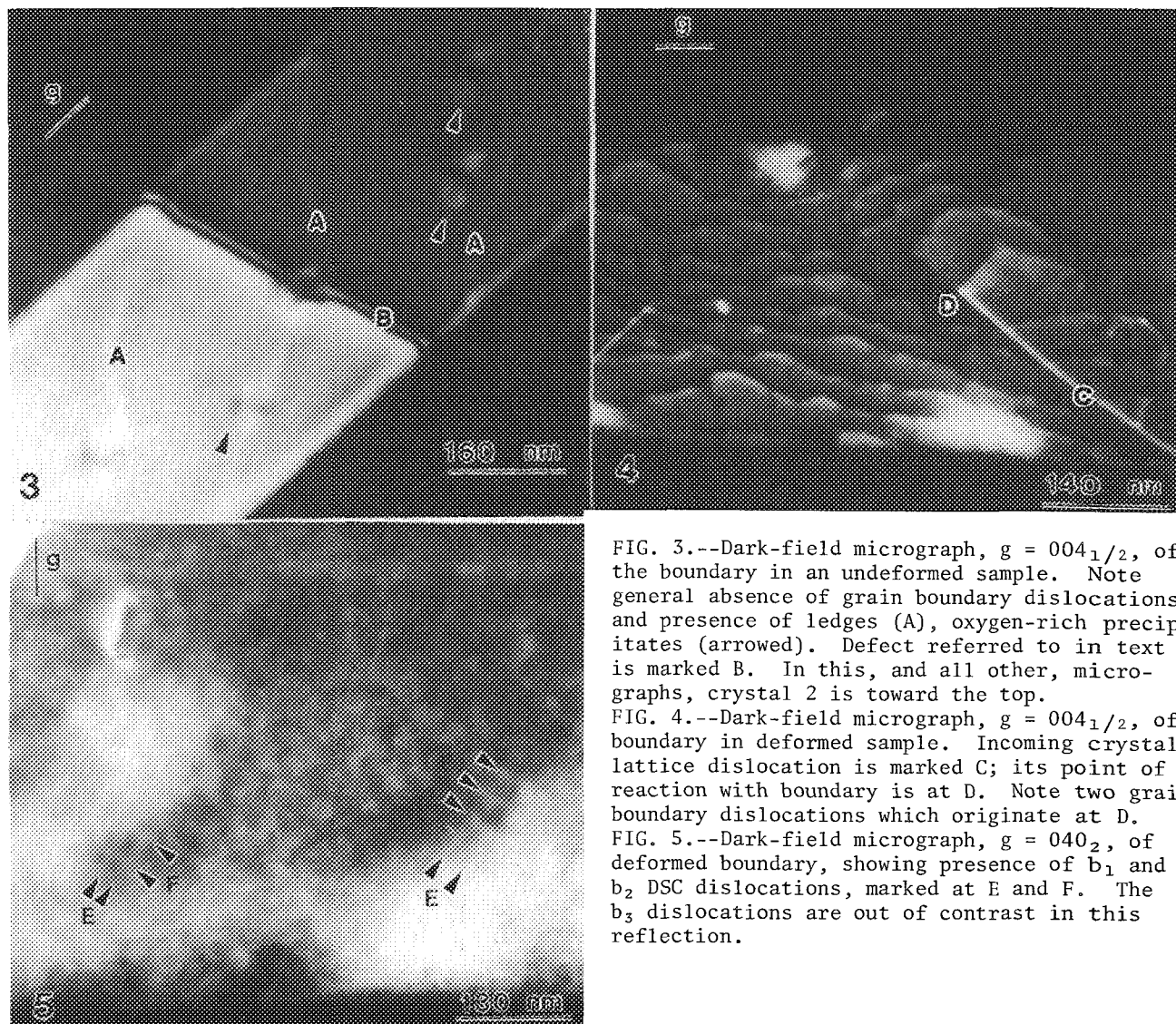
FIG. 3.--Dark-field micrograph, $g = 004_{1/2}$, of the boundary in an undeformed sample. Note general absence of grain boundary dislocations, and presence of ledges (A), oxygen-rich precipitates (arrowed). Defect referred to in text is marked B. In this, and all other, micrographs, crystal 2 is toward the top.

FIG. 4.--Dark-field micrograph, $g = 004_{1/2}$, of boundary in deformed sample. Incoming crystal lattice dislocation is marked C; its point of reaction with boundary is at D. Note two grain boundary dislocations which originate at D.

FIG. 5.--Dark-field micrograph, $g = 040_2$, of deformed boundary, showing presence of b_1 and b_2 DSC dislocations, marked at E and F. The b_3 dislocations are out of contrast in this reflection.

MISFIT DISLOCATIONS AT Ti₃Al/TiAl PHASE BOUNDARIES

W. Wunderlich, T. Kremser, and G. Frommeyer

The deformation mechanisms of two phase titanium aluminides are not fully understood.[1-4] The stoichiometry has a great effect on the mechanical properties in general and enhanced plasticity is achieved by additions of Cr and Si to the binary $Ti_{52}Al_{48}$ alloy. The improved ductility is caused mainly by glide of $<121]$ partial dislocations and subsequent twinning[1] of the TiAl phase. The present paper shows that also the Ti₃Al/TiAl phase boundaries make a considerable contribution to the nucleation of dislocations, so that improvement of the ductility of the two-phase TiAl base alloys occurs.

Experimental

TEM specimens were cut by spark erosion from the plastically deformed region, as well as from the grip section of tensile-test specimens of several $Ti_{52}Al_{48}$ alloys with and without additions of 1 and 3 at% Cr.

Results

The orientation relationship between the Ti₃Al phase and the TiAl matrix is $(111)_\gamma ||$ $(0001)_{\alpha2}$, $[110]_\gamma || [1210]_{\alpha2}$.[5] The (111)-plane in TiAl and the (0001) plane in Ti₃Al possess a hexagonal symmetry, so that the Ti and Al atoms fit well to each other. However, the spacing of the matching lattice planes is slightly different. The misfit is accommodated by dislocations at the interface, which were studied in detail by tilting experiments. The spacings of the misfit dislocations have been determined from the TEM micrographs. In the binary $Ti_{52}Al_{48}$ alloys three sets of dislocations with different spacings are observed. In TiAl base alloys with 1 and 3 at%, one set of misfit dislocations appears. The spacing is larger, indicating that the misfit is smaller. The TiAl/Ti₃Al interfaces in binary alloys are rather wavy and not so planar as observed in the Cr containing alloys. Similar misfit dislocations are present at incoherent twin boundaries of TiAl.

Discussion

The spacings of the misfit dislocations were calculated from the difference in the corresponding lattice constants. Addition of small amounts of Cr to the TiAl phase decreases the c/a ratio from 1.023 to 1.009, respectively, and both lattice constants c and a are decreased.[6] However, in the Ti₃Al phase the

spacing is increased. The misfit at the interface is lowered and the spacing of the misfit dislocation increases. With Cr present, only one set of misfit dislocation remains. This result implies that the misfit dislocations are not sessile and may partly contribute to the enhanced plasticity of the Cr containing TiAl base alloys.

References

1. W. Wunderlich, T. Kremser, and G. Frommeyer, *Z. Metallkunde* 81: 802-808, 1990.
2. Young Wim Kim, *J. Metals*, July 1989, 24-30.
3. V. K. Vasudevan, M. A. Stuke, S. A. Court, and H. L. Fraser, *Phil. Mag. Letters* 59: 299-307, 1989.
4. G. Hug, A. Loiseau, and P. Veyssiere, *Phil. Mag.* 57: 499-523, 1988.
5. C. R. Feng, D. J. Michel, and C. R. Crowe, *Phil. Mag. Letters* 61: 95-100, 1990.
6. T. Kawabata and O. Izumi, *Phil. Mag.* 55: 823-842, 1987.

The authors are at the Max-Planck-Institut für Eisenforschung GmbH, Max-Planck-Str. 1, D-@-4000 Düsseldorf 1, Germany.

ORIENTATION RELATIONSHIPS AT POLYMER/METAL INTERFACES

M. L. Bilaniuk and J. M. Howe

Interfaces are an integral part of composite materials, with the interfacial structure and properties often determining the physical, chemical, and mechanical performance of the composite. Although metal/metal and ceramic/metal interfacial structures have been extensively studied,[1,2] only a few polymer/metal interfaces have received much attention.[3] This study was undertaken to determine whether orientation relationships (OR) form across the interface between crystalline polymer and metal systems using electron microscopy techniques. The influence of metal reactivity on interface formation was also investigated.

Experimental

The interfacial system investigated consisted of a poly-DCH crystalline polymer metallized in vacuum with Au and Cr by evaporation and sputtering, respectively. Poly-DCH forms large single-crystal needles (monoclinic, $P2_1c$) with pronounced (100) facets, which facilitate metallization.[4,5] The metallized crystals were embedded in epoxy resin and ultramicrotomed to form cross-sectional samples. The samples were examined by conventional and high-resolution transmission electron microscopy (TEM) in Philips EM420T and JEOL 4000EX microscopes, respectively.

Results

The Au/poly-DCH interfacial region consisted of isolated Au droplets contained between the poly-DCH and mounting epoxy, indicating insufficient wetting of the polymer by Au (Fig. 1). Figure 2 shows a 0.3mm layer of Cr contained between the polymer and mounting epoxy. A few intact areas of interface, where Cr was not torn from the poly-DCH in the process of cutting, were sufficient to determine the orientation of the Cr layer by diffraction (Fig. 3). The Cr/poly-DCH interface was generally flat with evidence of columnar growth of Cr along the {110} direction. The OR at the Cr/poly-DCH interface was found to be $<110>_{Cr} \| (100)_{DCH}$ and $<001>_{Cr} \| [010]_{DCH}$ (Fig. 4). This finding was verified by high-resolution TEM, where one set of {110} planes of Cr was resolved perpendicu-

M. L. Bilaniuk is at the Department of Metallurgical Engineering and Materials Science, Carnegie Mellon University, Pittsburgh, PA 15213; J. M. Howe is at the Department of Materials Science, University of Virginia, Charlottesville, VA 22903. This research is sponsored by NSF Grant MSM 8714377. The authors are grateful to Dr. G. L. Baker (Bellcore Laboratories, Red Bank, N.J.) for providing the poly-DCH polymer.

lar to the Cr/poly-DCH interface (Fig. 5). The parallel directions $<001>_{Cr}$ and $[010]_{DCH}$ were also found to have the highest linear density of atoms by pattern matching across the interface,[6] indicating that the general principle of minimization of interfacial energy by maximizing atomic matching across an interface[1] may be important for crystalline-polymer/metal systems. The structure of poly-DCH was not resolved by high-resolution TEM due to extensive electron-beam damage.

Conclusions

Formation of an OR across an interface is a primary mechanism for interfacial energy reduction in metal/metal and ceramic/metal systems. Thus, it is somewhat intuitive that an OR might be obtained across crystalline-polymer/metal interfaces and that was confirmed in this study. It is postulated that for the Cr/poly-DCH interface, the OR is determined by matching of the most densely packed atomic directions. Formation of the interface also seems to be a function of the metal reactivity toward the polymer surface, but further research is needed to ascertain that.
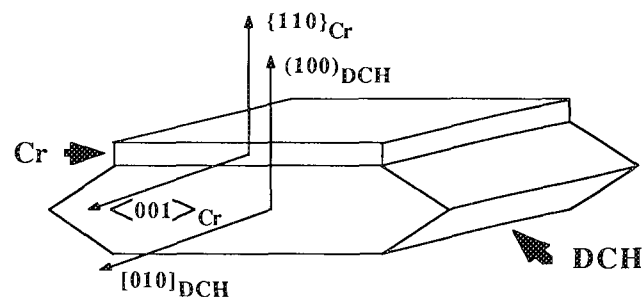
FIG. 4.--Experimentally determined OR at Cr/poly-DCH interface.

References

1. U. Dahmen, "Orientation relationships in precipitation systems," *Acta Metall.* 30: 63, 1982.
2. J. M. Howe, "Bonding, structure and properties of metal/ceramic interfaces," *Inter. Mater. Rev.* (submitted).
3. P. S. Ho et al., "Chemistry and microstructures at metal/polymer interfaces," *J. de Physique* 49: C5-49, 1988.
4. P. A. Apgar and K. C. Yee, "Poly-[1,6-di(N-carbazolyl)-2,4-hexadiyne," *Acta Crystallogr.* B34: 1957, 1978.
5. V. Enkelman et al., "Macroscopic single crystals of polymers by solid-state polymerication," *J. Mater. Sci.* 15: 168, 1980.
6. M. L. Bilaniuk and J. M. Howe (unpublished research).
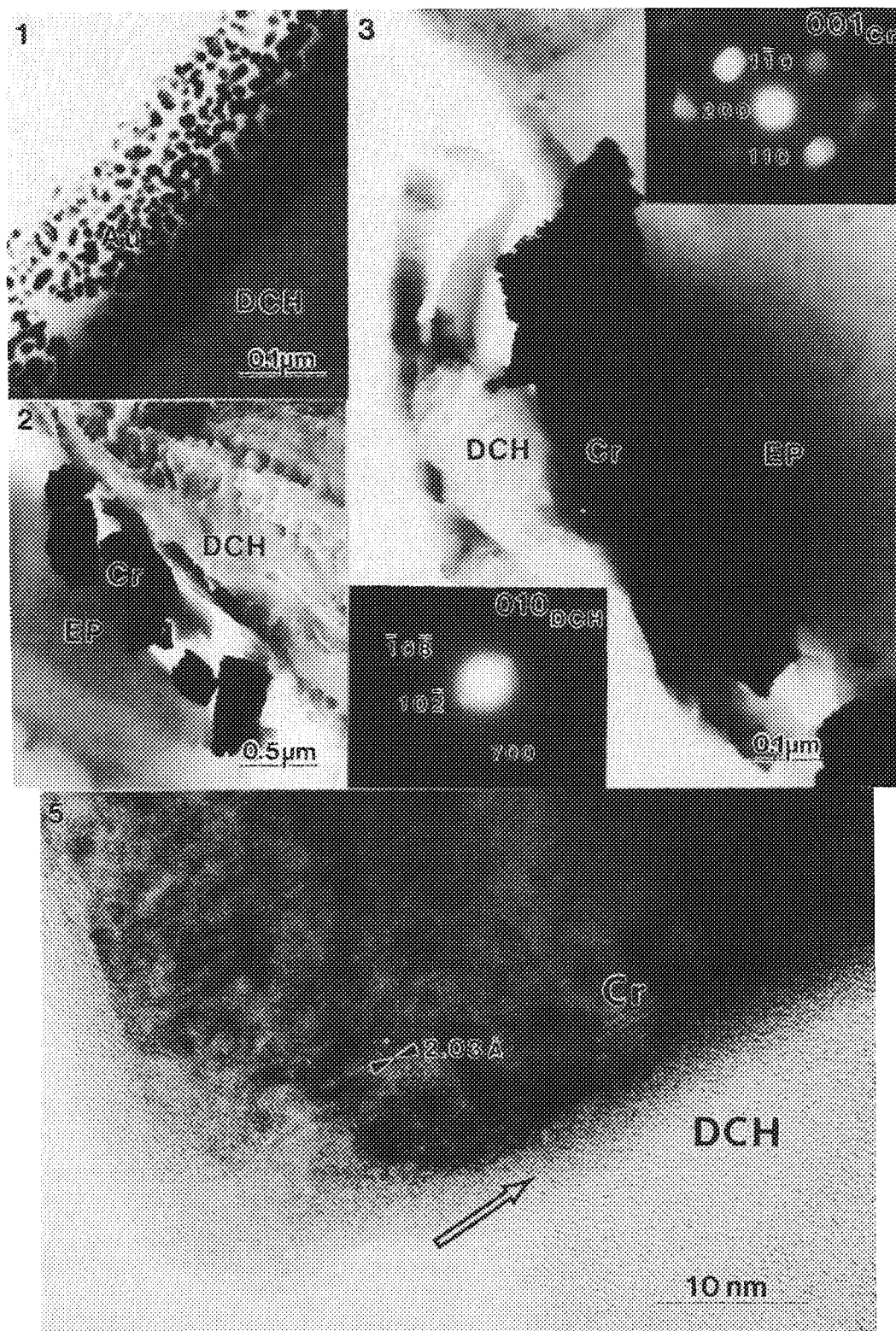
FIG. 1.--Microtomed Au/poly-DCH sample.   Inclined view of interface showing Au droplets.
FIG. 2.--Microtomed Cr/poly-DCH sample.   Cross-sectional view of interface.   EP--epoxy.
FIG. 3.--Same as Fig. 2. EP--epoxy.   Insets: respective diffraction patterns of Cr and poly-DCH.
FIG. 5.--Microtomed Cr/poly-DCH sample.   High-resolution TEM image of interface.   One set of
$\{110\}_{CR}$ planes visible.   Interface indicated by an arrow.

228

REACTION AND STABILITY AT MATERIAL INTERFACES

Robert Sinclair

In this paper, the application of cross-section high-resolution electron microscopy (HREM) to study interfacial solid-state chemical reactions is described. Microanalysis and microdiffraction are useful to complement the HREM results. Interpretation of interface stability or instability using high-order phase diagrams and basic thermodynmaic principles is shown to be extremely powerful.

One of the most valuable and impressive HREM applications has been the cross-sectional analysis of interface structure, especially at the atomic level. In thin-film technology, as dimensions become increasingly small, the material interfaces have a more dominant influence on the physical properties. For instance, small (e.g., 0.5nm) protrusions at the $Si-SiO_2$ interface can drastically alter the performance of thin oxides in microelectronic devices.[1] A most important aspect concerns the chemical reactions that can occur, which would result not only in the drastic alteration of the topography but also of the nature of the phases present. Cross-section HREM combined with microanalysis and microdiffraction allows phase identification, which is fundamental to understanding the stability (or lack thereof) of manufactured interfaces. The present paper illustrates the usefulness of electron microscopy in this field, and shows how it can support thermodynamic understanding of the observed behavior. Examples are drawn from problems in integrated circuit processing; a more complete discussion can be found elsewhere.[2]

The simplest system involves two elements at an interface, such as occurs at a metal-silicon electrical contact. One of the most scientifically and technologically interesting is Ti-Si. Annealing to equilibrium produces $TiSi_2$, which is desirable because of its low resistivity and excellent contact properties. However, heating at intermediate temperatures (400-500 C), commonly used during processing, brings about an intermixing reaction, which results in the formation of an amorphous alloy.[3] This reaction can have deleterious consequences on the electrical performance in submicron devices.[4] As described in Ref. 2, this effect corresponds to a solid-state amorphization reaction, which is explained by a reduction in free energy for the amorphous mixture compared to that of the physically separated elements. The composition of the amorphous phase can be determined at about 2nm spatial resolution using either the

Akashi 0002B or JEOL 2010 microscopes[4,5] and the compositions in contact with the elemental phases are consistent with the metastable Ti-Si phase diagram established independently from differential scanning calorimetry.[6,7]

Equivalent reactions have now been found at many metal-silicon interfaces,[2] and more recently at a Pt-GaAs interface.[8,9]

In many practical situations, three or more elements are present at a single interface, such as $TiSi_2-SiO_2$, $TiSi_2-TiN$, or (TiW)N-Al. Accordingly, understanding requires in the first instance application of ternary and higher-order phase diagrams,[2] many of which have never been established and so do not exist in the literature. We have developed a simple procedure to remedy this deficiency (see, for example, Refs. 10-12). An example concerns the comparison of TiW and (TiW)N as possible diffusion barriers between Al metallization and an Si semiconductor substrate; the nitride is considerably more stable upon annealing above 500 C. The problem arises from interaction of Al with the barrier layer. Inspection of the relevant ternary and quaternary phase diagrams (e.g., Al-Ti-W, Al-Ti-W-N) shows that Al is not thermodynamically stable with either material. However, for the nitride, cross-section HREM reveals the formation of a thin (5nm) continuous layer of AlN which is stable with Al (above) and (TiW)N (below).[13] By allowing a controlled partial reaction to bring about two thermodynamically stable interfaces, further degradation of the thin-film barrier is prevented.

Application of the same principles to GaAs allows prediction of thermodynamically stable contacts (e.g., CoAl) which do not react with the underlying substrate upon annealing.

In conclusion, our work serves to show that cross-section HREM is invaluable in revealing interfacial structure and reaction, and that the application of thermodynamic principles can be extremely effective in understanding the behavior and in designing mutually compatible material phases.

References

1. M. Niwa, M. Onoda, M. Matsumoto, H. Iwasaki, and R. Sinclair, *Jpn. J. Appl. Phys.* 29: 2665, 1990.
2. R. Sinclair, *Mater. Trans. Jpn. Inst. Met.* 31: 628, 1990.
3. K. Holloway and R. Sinclair, *J. Appl. Phys.* 61: 1359, 1987.
4. S. Ogawa, T. Yoshida, T. Kouzaki, and R. Sinclair (submitted for publication).
5. T. Kouzaki, S. Ogawa, and S. Nakamura, *Mats. Res. Soc. Proc.* 183: 111, 1990.

6. K. Holloway, P. Moine, J. Delage, R. Bormann, S. Capuano, and R. Sinclair, *Mats. Res. Soc. Proc.* (in press).

7. K. Holloway, Ph.D. thesis, Stanford University, 1989, 127.

8. K. H. Ko and R. Sinclair, *Appl. Phys. Lett.* (in press).

9. D. H. Ko and R. Sinclair, *Proc. 49th EMSA Ann. Meeting*, 1991, 858.

10. R. Beyers, *J. Appl. Phys.* 56: 147, 1984.

11. A. S. Bhansali, R. Sinclair and, A. E. Morgan, *J. Appl. Phys.* 68: 1043, 1990.

12. A. S. Bhansali, D. H. Ko and R. Sinclair, *J. Electron. Mater.* 19: 1171, 1990.

13. A. S. Bhansali, I. J. M. M. Raaijmakers, B. J. Burrows, A. E. Morgan, and R. Sinclair (submitted for publication).

HREM STUDIES OF Pd/Al$_2$O$_3$ INTERFACES

Thomas Muschik and Manfred Rühle

HREM studies were performed at Pd/Al$_2$O$_3$ interfaces formed after internal oxidation[1] of Pd-Al alloys (3 at.%) at ambient pressure for 24 h at 1273 K. Oxidized foils (Type I) were studied, as well as some specimens which were subsequently annealed for 1 h at 1273 K in Al vapor (Type II). The atomistic structure was evaluated by HREM studies, at the ARM in Berkeley (800 kV, C$_S$ = 1.3 mm, Δf ∿ 14 nm).

Results

A typical example of an Al$_2$O$_3$ precipitate in Pd matrix is shown in Fig. 1. Diffraction studies show that close-packed planes of the ceramic are parallel to close-packed planes in the Pd. Quantitative HREM revealed that the precipitate consists of η-Al$_2$O$_3$, which possesses a cubic spinel structure and whose particles are quite frequently twinned. The perfect lattices of the simulated and experimentally obtained image agree quite well (Fig. 2). The translation stage between the Pd and η-Al$_2$O$_3$ can be determined from Fig. 2.

Annealing in air and Al, respectively, resulted in a change of the structure of η-Al$_2$O$_3$ in regions up to the two outermost [111] planes of the alumina in both cases. A subtle difference can be identified between HRTEM images of the Pd/η-Al$_2$O$_3$ interfaces in as-oxidized (Type I) and Al annealed (Type II) samples (Fig. 3).

Interpretation and Conclusion

The experimental contrast of the Pd/η-Al$_2$O$_3$ interface in an Al annealed (Type II) specimen has been analyzed in detail. It is similar to the calculated contrast of a model structure in which the η-Al$_2$O$_3$ is terminated by Al ions located at octahedral interstices between a close-packed plane in the metal, and a close-packed oxygen ion plane in the alumina, and where Al is segregated in the metal close to the interface. The experimental contrast of Pd/η-Al$_2$O$_3$ interfaces in oxidized (Type II) samples are qualitatively consistent with the expected oxygen termination of the alumina. The results therefore support the interpretation of the hydrogen trapping experiments.[2]

References

1. W. Mader, *Mat. Res. Soc. Symp. Proc.* 82: 403, 1987.
2. X. Y. Huang et al., *Scripta Met.* 22: 109, 1988.
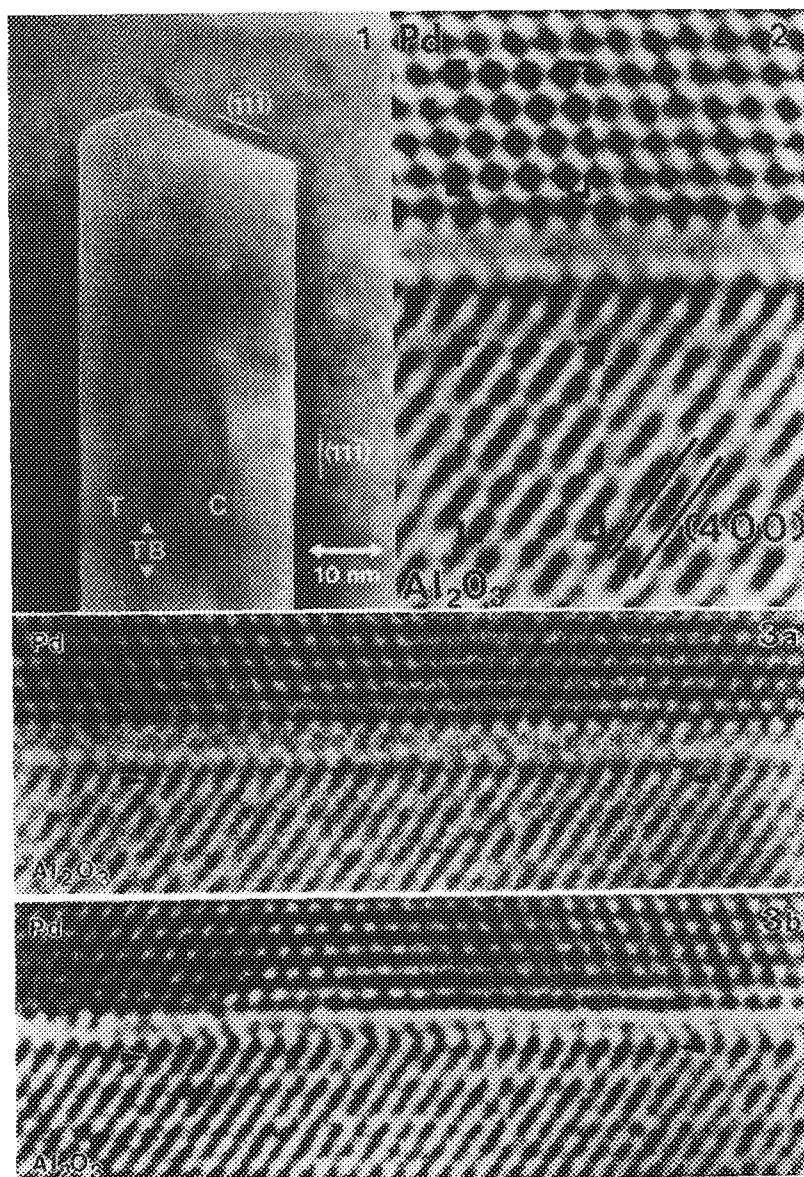
FIG. 1.--HRTEM image of typical twinned η-Al_2O_3 particle in Pd (110 projection). The twinned boundary (TB) separates part with cube on cube orientation relationship with matrix (C) from twinned relation parts (T).

FIG. 2.--Comparison between experimental and computer-simulated images. Excellent fit is obtained in both parts, η-Al_2O_3 and Pd.

FIG. 3.--Comparison between near interface contrast in (a) aluminum annealed type II specimen, (b) as-oxidized type I specimen. The crystals have approximately the same thickness; HRTEM images were taken at about the Scherzer focus of the ARM.

232

INTERFACE EVOLUTION DURING INTERNAL REACTION IN MIXED OXIDES

Monika Backhaus-Ricoult

During internal reduction of mixed oxides or during internal diffusion-controlled precipitation in a simple oxide, new phases are formed. The chemical composition and the crystallographic structure of the precipitated phase may change during the reaction or during ageing.

A detailed study of precipate evolution is shown for the formation of copper by internal reduction of (Mg, Cu)O and for the diffusion-controlled formation of $CaTiO_3$ in NiO. The microscopic reaction mechanism and the interface structure can be discussed in terms of analytical high resolution and traditional microscopy results.

M. Backhaus-Ricoult is at the CNRS Laboratoire des Materieux, F-92195 Meudon Cédex, France.

MICROSTRUCTURE AND CHEMISTRY OF EXTENDED DEFECTS IN R Ba Cu O SUPERCONDUCTING CERAMIC FAMILY (R = Y, Ho)

Jeanne Ayache

$RBa_2Cu_3O_{7-x}$ (R = Y and Ho) ceramics were studied by analytical transmission electron microscopy in order to characterize extended defects and determine structural and chemical phase transformations due to nonequilibrium states during sintering. EDX analysis was performed to follow chemical change of the matrix (excess or lack of cations and oxygen).

Various defects, such as intergranular phases, twins, dislocations, and stacking faults have been studied. Various orthorhombic structures, which are close to 123 phase and have various chemical compositions, have been found. An unexpected monoclinic phase was formed that has a new chemical composition.

J. Ayache is at the CNRS Laboratoire des Materieux, F-92195 Meudon Cédex, France.

INTERFACE MICROSTRUCTURE AND MICROMECHANICS IN GLASS AND GLASS-CERAMIC MATRIX COMPOSITES

S. M. Bleay and V. D. Scott

In recent years, much interest has focused on the potential of glass and glass-ceramic matrix composites as structural materials. The role of the fibers is to produce controlled fracture in the composite instead of the brittle failure seen in monolithic ceramics. The fiber/matrix interface plays a critical role in the fracture process, and this study relates interface microstructure to micromechanics and in turn to the nature of the composite fracture.

Experimental

Three composite systems were studied: (i) Pyrex glass reinforced with high modulus carbon fibers, (ii) Pyrex glass reinforced with Nicalon fibers; (iii) calcium alumino-silicate (CAS) glass-ceramic reinforced with Nicalon fibers. The composites were made by a hot pressing technique, with the fibers unidirectionally aligned to give a fiber volume fraction of ∿0.4.

Thin sections for transmission electron microscopy (TEM) were prepared by first cutting 3mm-diameter disks from the composite plate. The disks were ground to a thickness of ∿300 μm and then dimpled on both sides in a VCR model D500. Final thinning was accomplished by argon ion bombardment in a Gatan Duomill. The sections were examined in a JEOL 2000FX microscope fitted with a LINK AN10000 energy-dispersive spectrometer (EDS).

Samples cut from the composite plate were ground flat and a polished surface, perpendicular to the direction of fibers, was produced by grinding on successively finer grades of abrasive, finishing with a 1μm diamond slurry. Measurements of interfacial friction stress between fiber and matrix were made by application of a micro-indenter to the fiber, measurement of the indent size in fiber and surrounding matrix, and application of the formula given by Marshall.[1] Finally, some fractured specimens were examined in the scanning electron microscope (SEM).

Results

Carbon Fiber-reinforced Pyrex Glass. As with most types of carbon fiber, it was strongly oriented with basal planes lying parallel to the fiber axis. The Pyrex glass matrix contained a small amount of cristobalite (∿1 vol. %), insufficient to introduce any significant embrittling effect.[2] Figure 1 is a TEM picture of the interface. Between carbon fiber and Pyrex matrix is a layer approximately 100 nm

The authors are at the School of Materials Science, University of Bath, Bath, England BA2 7AY. This project was funded by Rolls Royce plc.

thick (labeled I in the micrograph) formed by chemical reaction. EDS showed that the layer was a sodium-rich silicon oxycarbide; the sodium present had diffused from the matrix material, as evidenced by a corresponding depletion in sodium level of the neighboring matrix. When carrying out the indentation test, the fiber slid easily within the matrix once the interface bond was broken and the interfacial shear stress was deduced to be ∿0.01 MPa (Table 1). The fracture surface of a specimen subjected to a three point bend test showed appreciable fiber pullout. to leave smooth fiber surfaces (Fig. 2).

TABLE 1.--Measurements of interfacial friction stress for glass and glass-ceramic matrix composite systems.

Composite System	Carbon/Pyrex	Nicalon/Pyrex	Nicalon/CAS	Nicalon/CAS (1100 C HT)
Interfacial friction stress/MPa	~0 01	4 1±1 0	3 1±0.5	up to 25

Nicalon Fiber-reinforced Pyrex Glass. The Nicalon fiber had a complex structure consisting of fine β-SiC crystals, silica, a substantial amount of free carbon (∿15 vol.%), and possibly some oxycarbide. The matrix contained ∿10 vol.% cristobalite but, again, not enough to embrittle it to any significant extent. A TEM picture of the interface (Fig. 3) shows an interface zone (I), ∿100 nm wide. EDS revealed that it contained silicon, oxygen, carbon, and sodium; the oxygen levels were higher than in the fiber interior. The sodium enrichment is, as with the carbon fiber-reinforced Pyrex, attributable to sodium diffusion from the matrix. Present in the outermost region of this zone is a layer, ∿10 nm thick, which is enriched in carbon. The carbon is believed to have been produced by some reaction between the Nicalon fiber and the matrix. The interfacial friction stress in this system was found to be 4.1 ± 1.0 MPa (Table 1). The fracture surface shows some fiber pullout (Fig. 4), although the lengths of exposed fiber are not as much as in the carbon/Pyrex system.

Nicalon Fiber-reinforced CAS. The matrix was found to be mainly anorthite, $CaAl_2Si_2O_8$. The microstructure of the interface showed evidence of a pronounced reaction (Fig. 5). A zone (I) of width ∿50 nm has formed that EDS

234

showed was enriched in carbon. A value of 3.1 ± 0.5 MPa was obtained for the interfacial friction stress, whereas the fracture (Fig. 6) shows clean fiber pullout, ∿100 μm in length. The Nicalon/CAS material was then subjected to exposure in air at 1100 C for 60 h, after which substantial change in its interfacial characteristics were recorded. The interface reaction zone was now ∿100 nm wide and contained voids. Only the elements oxygen and silicon were detected; the carbon had disappeared. Thus, it may be deduced that the silicon carbide in the Nicalon fiber has oxidized according to[3]

$$SiC_{(s)} + 2O_{2(g)} \rightarrow SiO_{2(s)} + CO_{(g)} \text{ or } CO_{2(g)}$$
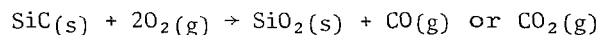
to leave a layer of silica between fiber and matrix. The carbon is oxidized also to either CO or CO_2 gas. The interfacial bond is increased by the heat treatment, giving values
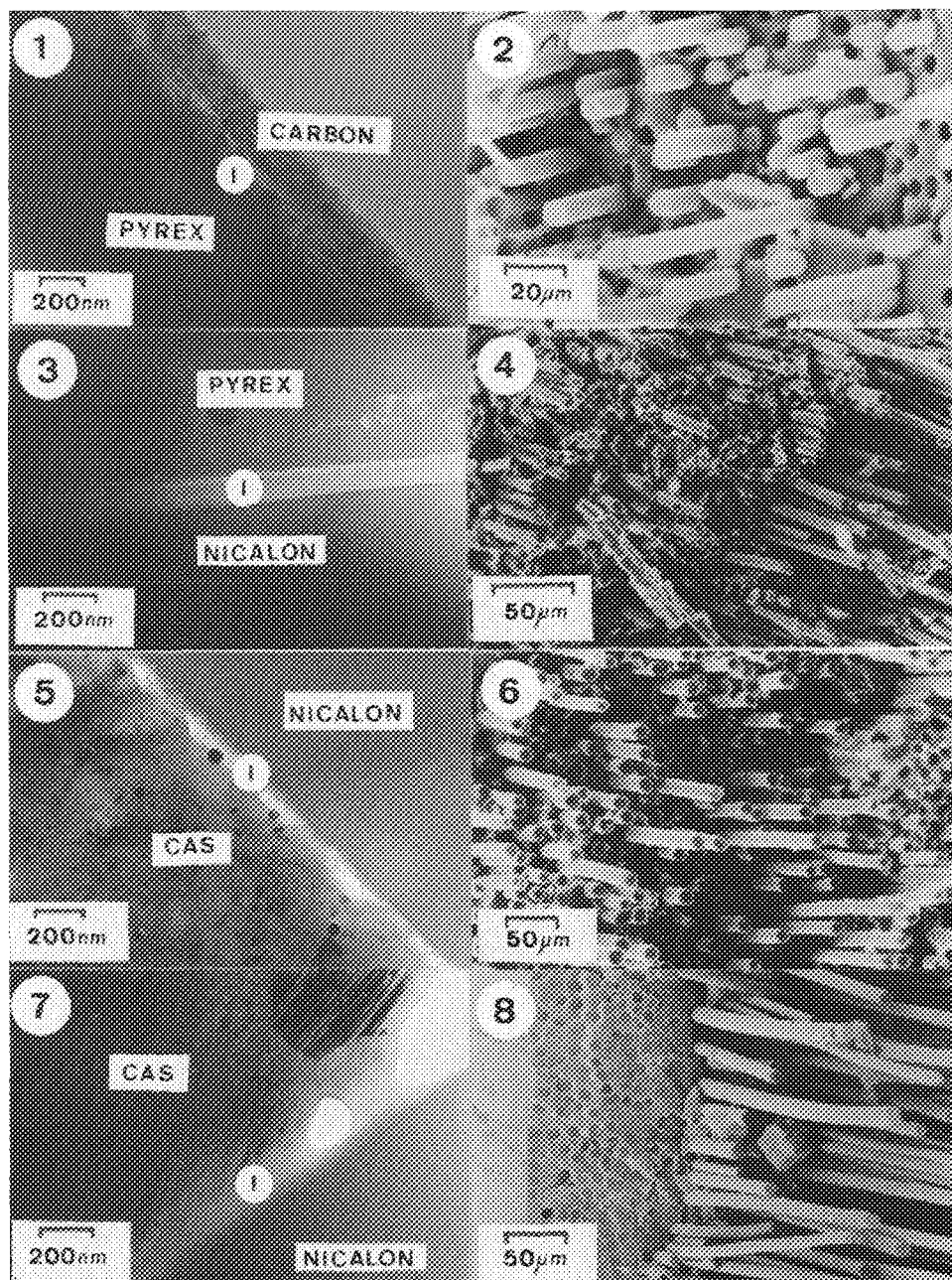
FIG. 1.--TEM of carbon/Pyrex interface.
FIG. 2.--SEM of carbon/Pyrex fracture surface.
FIG. 3.--TEM of Nicalon/Pyrex interface.
FIG. 4.--SEM of Nicalon/Pyrex fracture surface.
FIG. 5.--TEM of Nicalon/CAS interface.
FIG. 6.--SEM of Nicalon/CAS fracture surface.
FIG. 7.--TEM of 1100 C oxidized Nicalon/CAS interface.
FIG. 8.--SEM of 1100 C oxidized Nicalon/CAS fracture surface.

of interfacial friction of ∿25MPa in surface regions of composite. The fracture surface shows brittle behavior in the oxidized regions (Fig. 8).

Conclusions

Comparison of the interface characteristics of the three composite systems shows that fracture, interface micromechanics, and microstructure can be correlated in the following way.

With the carbon fiber/Pyrex composite, the highly enriched graphitic layers in the fiber give a low friction stress, ∿0.01 MPa, and long fiber pullout. Carbon is present at both Nicalon/Pyrex and Nicalon/CAS interfaces, but it is not oriented and consequently the friction stress is higher, although pullout still occurs; the slightly thicker carbon layer at the Nicalon/CAS interface gives the lower friction stress value and longer pullout.

After oxidation, however, a strong silica "bridge" is formed between fiber and matrix in the Nicalon/CAS material that leads to a higher value of interfacial friction stress. Since cracks can no longer be deflected at the interface, brittle fracture occurs in oxidized regions. The oxidation effects thus give further support to our contention that the carbon present at the fiber/matrix interface controls mechanical behavior in these composite systems.

References

1. D. B. Marshall and A. G. Evans, "Failure mechanisms in ceramic fiber/ceramic matrix composites," *J. Am. Ceram. Soc.* 68: 225-231, 1985.
2. S. M. Bleay and V. D. Scott, "Microstructure property relationship in Pyrex glass composites reinforced with Nicalon fibres," *J. Mat. Sci.* (in press).
3. R. F. Cooper and K. Chyung, "Structure and chemistry of fibre-matrix interfaces in silicon carbide fibre-reinforced glass-ceramic composites: An electron microscopy study," *J. Mat. Sci.* 22: 3148-3160, 1987.

HREM STUDIES OF Cu/MgO AND Pd/MgO INTERFACES

P. Lu and F. Cosandey

The structure of metal/oxide interfaces is of both scientific and technological interest.[1] With the resolution limit of electron microscopes better than 2Å, atomistic studies of metal/oxide interfaces are now possible. Two metal systems, Cu and Pd, were chosen for the present study because of the absence of any intermediate layer between the metals and MgO; and since two metal systems (Cu and Pd) have large misfits of 14.2% and 7.6% with respect to MgO, respectively, it is of interest to see the role of misfit on interfacial coherency. Internal oxidation of the Cu-1% Mg and Pd-1% Mg alloys were used to form the Cu/MgO and Pd/MgO interfaces, respectively, since low-energy interfaces can be formed by this method. Details of the oxidation processes have been reported elsewhere.[2] TEM specimens were prepared by cutting 3mm disks from the oxidized alloys, followed by grinding, dimpling, and ion thinning to perforation. An ISI-002B electron microscope with a resolving power of ~1.8 Å was used for the observations.

For the Cu/MgO system, it is found that the MgO particles exhibit the cube-on-cube orientation relationship with respect to the Cu matrix, and are octahedrally shaped with the predominant facets parallel to the {111} lattice planes of MgO and Cu. Figure 1 shows the TEM micrograph and diffraction pattern taken along the [110] direction. The (111) interface is found to be partially coherent despite the large misfit. Figure 2 shows a high-resolution electron micrograph of the interface taken in the [110] direction. The periodic contrast variation along the interface visible in the image is clearly indicative of misfit dislocations. The dislocation network has a periodicity of 16.8 Å in the direction perpendicular to the electron beam. Multislice image simulations confirm the presence of a hexagonal dislocation network.[2]

For the Pd/MgO system, two types of MgO particles are formed in the Pd matrix: (a) a tetradecahedrally shaped particle which exhibits the cube-on-cube relationship with the Pd with interfaces parallel to the {111} and {100} lattice planes (eight of {111} and six of {100} interfaces); and (b) a plate-like particle, which exhibits a twin relationship with respect to the Pd Matrix with two dominant interfaces parallel to the {111} lattice planes.[2] All three interfaces, i.e., (111), (100), and (111)$_T$, are found to be partially coherent. Figure 3 is the HREM image of (100) interfaces viewed along the [011] projection. The con-

trast due to misfit dislocations is clearly visible in the image. The dislocation network has a square structure with edge dislocations lying along the <110> directions with a/2<110> Burgers vectors. The distance between dislocation cores measured from the image has an average value of 38.3 Å, slightly greater than the 36.2 Å calculated based on Bollmann's O-lattice theory.[3] The square dislocation network has also been observed by weak beam microscopy.[2] A HREM micrograph of the (111)$_T$ interface is shown in Fig. 4. The misfit dislocations for this interface have a/6<112> Burgers vectors, which are the perfect dislocations of the twin interface but are associated with steps.[4] The contrast from these steps is clearly visible in the Fig. 4. Details of the dislocation structure is under further investigation.[5]

References

1. See, for instance, M. Ruhle, A. G. Evans, M. F. Ashby and J. P. Hirth, Eds., *Metal-ceramic Interfaces*, Acta-Scripta Metall. Proc. Ser. 4, 1990.
2. P. Lu and F. Cosandey, *Ultramicroscopy* (in press).
3. W. Bollmann, *Crystal Defects and Crystalline Interfaces*, New York: Springer, 1970.
4. J. P. Hirth and R. W. Balluffi, *Acta Metall*. 21: 929, 1973.
5. This research is supported by NSF under Grant NSF-MRG-89-07553.

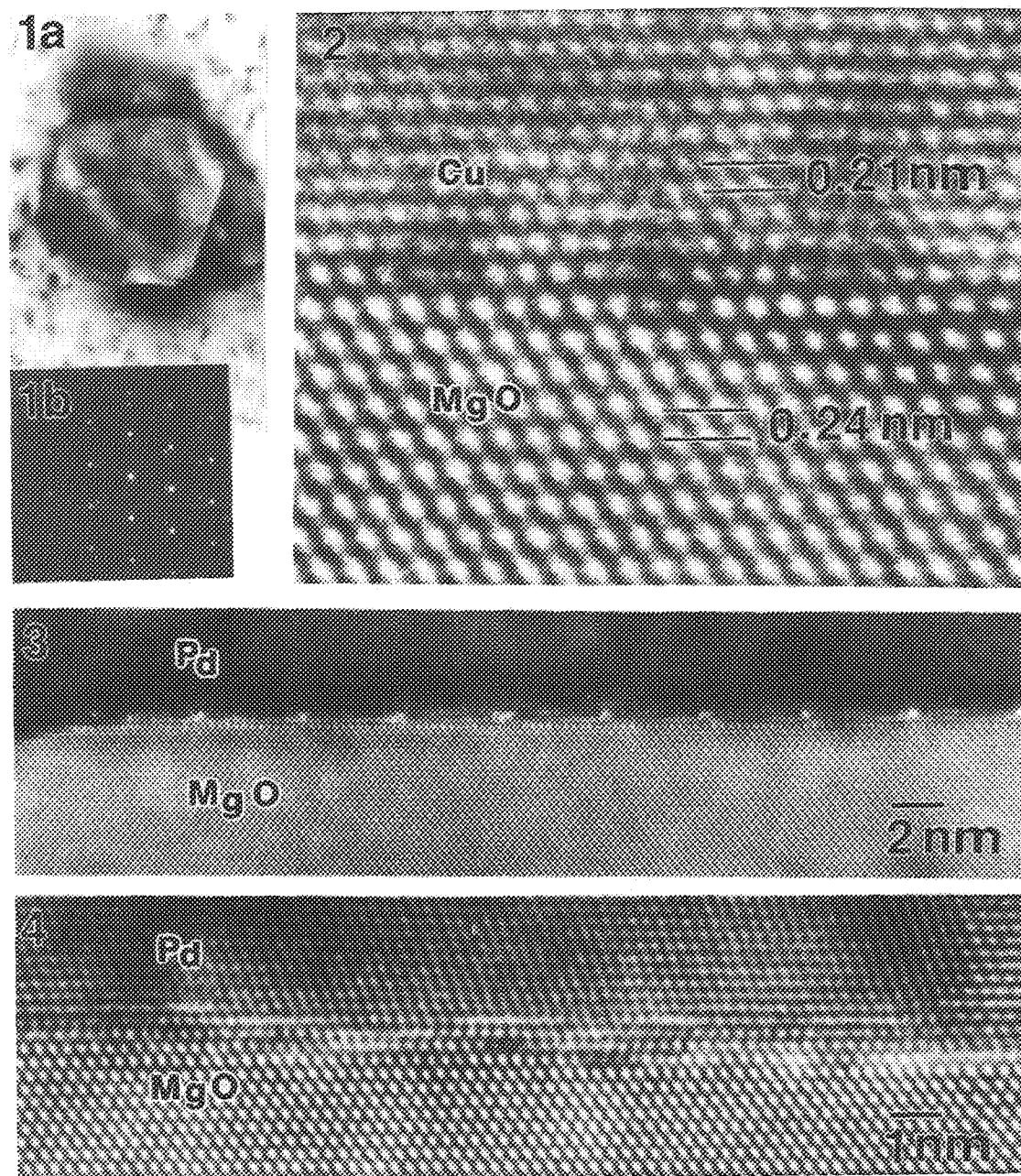The authors are at the Department of Mechanics and Materials Science, Rutgers University, Piscataway, NJ 08855.

FIG. 1.--(a) TEM micrograph, (b) diffraction pattern in [110] direction showing MgO particles in Cu matrix.
FIG. 2.--HREM micrograph of Cu/MgO(111) interface in [110] projection.
FIG. 3.--HREM micrograph of Pd/MgO(100) interface in [011] projection.
FIG. 4.--HREM micrograph of Pd/MgO(111)T interface in [110] projection.

INTERFACE MICROSTRUCTURES RELATING TO THE MECHANICAL PROPERTIES OF FIBER-REINFORCED ALUMINUM ALLOY

V. D. Scott, Ming Yang, and A. R. Chapman

The bond between fiber and matrix in a composite must be sufficient to permit load transfer between fibers via the matrix, yet should still allow some fiber pullout so as to achieve a measure of composite toughness. Such requirements are difficult to obtain simultaneously in a composite material, and it is recognized that the microstructure of the interface has a crucial role to play in controlling mechanical and chemical characteristics. This paper investigates interface microstructures in aluminum alloys reinforced with three different fibers by analytical electron microscopy techniques, and relates the information with fractographic observations on mechanically tested specimens.

Experimental

The metal matrix was an aluminum 7 wt% silicon alloy to which had been added 0.4 wt% magnesium. Reinforcements were low modulus carbon fiber (Courtaulds Ltd.) alumina (Safimax ICI Ltd.), and Nicalon (Nippon Carbon, Japan), all supplied as tows containing several thousand fibers in the case of alumina and carbon, and 500 in the case of Nicalon. The composites were manufactured by liquid metal infiltration of a fiber preform using a pressure of < 7 MPa and a melt temperature ∿750 C. Fibers were undirectionally aligned in the composites and fiber volume fractions were ∿0.4.

Cutting, grinding, and mechanical polishing of specimens was carried out with diamond-impregnated media, and finishing with colloidal silica for examination by optical and scanning electron microscopy (SEM). A LINK AN10000 energy-dispersive spectrometer (EDS) was fitted to the SEM for compositional analysis. SEM was also used for some fractography studies. Sections for transmission electron microscopy (TEM) were prepared by cutting 3mm-diameter disks from the composite plate, grinding them to 300 m thickness and then dimpling them on both sides in a VCR model 500. Disks were then thinned by argon ion bombardment in a Gatan Duomill and examined in a JEOL 2000FX microscope fitted with a LINK AN10000 EDS system.

Results

Concerning the microstructure of the aluminum-silicon alloy matrix, the silicon phase took the form of coarse rod-like particles which extended from fibers into matrix (Fig.

1a), often bridging across fibers. The network of silicon particles is clearly evidenced after deep etching (Fig. 1b). Frequently, the intermetallic FeSiAl$_5$ was found, the iron is an impurity introduced during manufacture.[1]

Carbon Fiber-reinforced Alloy. Figure 2(a) is a TEM picture of the interface between carbon fiber and aluminum metal. Many lath-like crystals are present which have nucleated on the fiber and grown into the matrix.[2] Selected area diffraction (SAD) combined with EDS identified the crystals as Al$_4$C$_3$, a rhombohedral structure with a = 0.334 nm and c = 250 nm, with basal planes oriented parallel to the length of the crystals (Fig. 2b). The interface structure was quite different where silicon made contact with a carbon fiber (Fig. 2c); the interface was well defined with no observable chemical reaction. The failure mode of this composite material exhibited brittle characteristics, with cracks tending to spread catastrophically across whole bundles of fiber (Fig. 2d).

Alumina-reinforced Aluminum Alloy. Figure 3(a) shows an interface between alumina fiber and aluminum metal. The interface is not very sharply defined, although SAD did not reveal any new phase. However, a detectable increase in magnesium concentration was recorded at the interface; Figs. 3(b), (c), and (d) illustrate EDS data from fiber, interface, and matrix, respectively. The presence of the magnesium signal together with a silicon signal indicates that the magnesium has diffused into a thin (∿50nm) surface layer of the fiber. No such magnesium enrichment was detected at a fiber/silicon interface. The fracture surface of a specimen tested in four-point bending shows some fiber pullout and separation from the matrix (Fig. 3e); the smooth appearance of the fibers confirms the absence of a chemical reaction at the interface.

Nicalon-reinforced Aluminum Alloy. A TEM picture taken from a region of the interface (Fig. 4a) shows a cluster of crystals growing outward from a fiber, which SAD combined with EDS identified as aluminum carbide, Al$_4$C$_3$. Another region of the interface reveals a group of aluminum oxide crystals extending into the metal matrix (Fig. 4b). However, much of the interface showed little evidence of a chemical reaction having taken place. Compositional analysis of the Nicalon fiber gave ∿33 wt% carbon, ∿58 wt% silicon and ∿9 wt% oxygen, all ± 2 wt%. Study of the shape of the carbon x-ray peak and a comparison with the carbon x-ray peaks from pure silicon carbide and from amorphous carbon indicated that ∿15 vol.% of
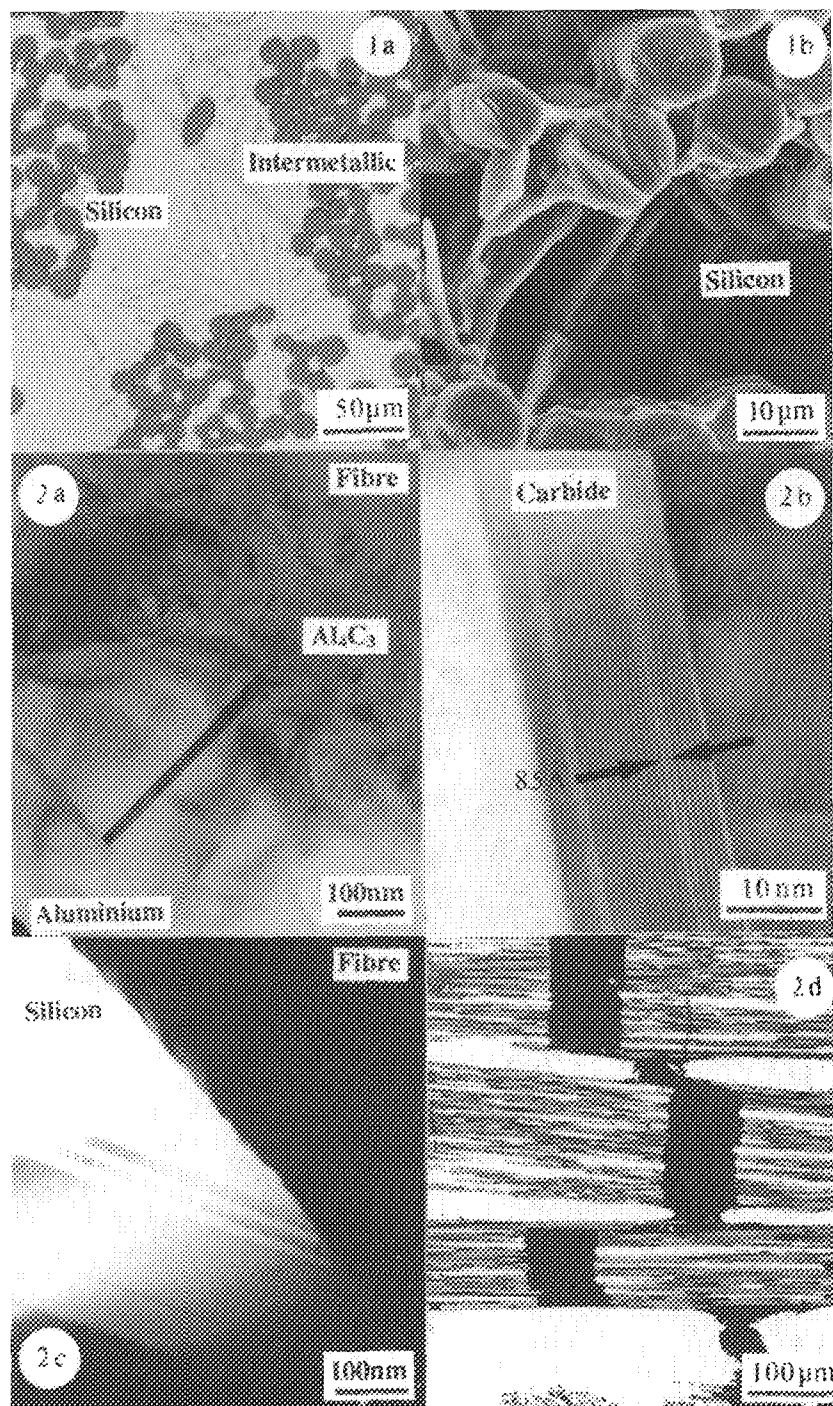
FIG. 1.--Transverse section from Nicalon fiber-reinforced alloy: (a) polished surface, optical microscopy; (b) deep-eteched surface, SEM.
FIG. 2.--Carbon fiber-reinforced alloy: (a) TEM of fiber aluminum interface showing aluminum carbide crystals; (b) lattice image from carbide crystal; (c) TEM of fiber/silicon interface; (d) section through fractured specimen showing brittle characteristics, optical microscopy.

free carbon was present in the fiber. (Details of this work will be reported elsewhere.) The fracture surface of this composite showed a mixed failure mode, with instances of interface separation as well as fiber splitting due to a strong interfacial bond.

Discussion

The matrix microstructure contains a network of silicon particles, often bridging fibers (Fig. 1b), which together with the presence of intermetallic phases acts to reduce ductility. However, comparison of the three composite systems indicates that the matrix
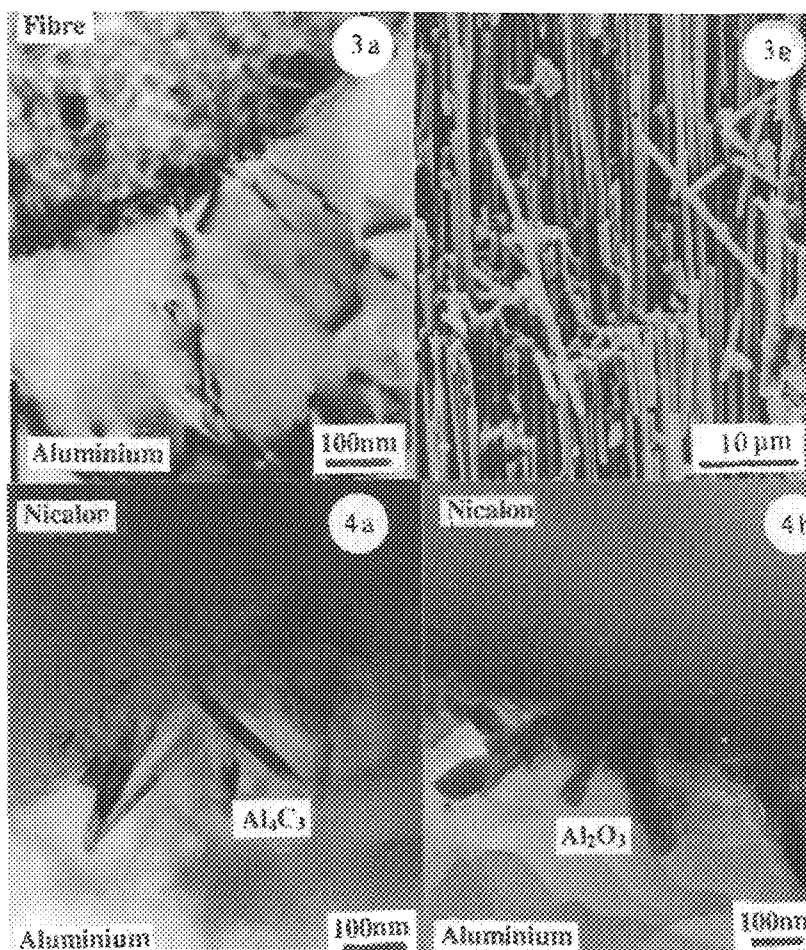
FIG. 3.--Alumina fiber-reinforced alloys: (a) TEM of fiber
aluminum interface, (b) EDS from matrix, (c) EDS from inter-
face showing Mg enrichment, (d) EDS from matrix, (e) fractured
specimen showing fiber matrix separation, SEM.
FIG. 4.--Nicalon fiber-reinforced alloy, TEM of fiber matrix
interface showing (a) aluminum carbide, (b) aluminum oxide.

plays only a secondary role with regard to
mechanical properties; the fiber matrix inter-
face characteristics are the more important.

In the carbon fiber-reinforced material,
for example, where extensive interface reaction
has occurred to form lath-like crystals of car-
bide extending into the matrix, a strong inter-
face bond has been developed, accompanied by
reduced matrix ductility and fiber degradation;
as a consequence, the composite is brittle and
a crack, once formed, spreads rapidly across
entire fiber bundles.

The alumina fiber-reinforced material shows
no evidence of a chemical reaction at the fi-
ber/matrix interface, although the strength of
the bond allows sufficient load transfer to
give reasonable strength, yet some degree of
fiber pull out to achieve a measure of magne-
sium at the interface has influenced the effi-
cacy of infiltration, but this effect is dis-
cussed elesewhere.

The behavior of the Nicalon fiber-reinforced
material is considered to be an intermediate
case. Some interface reaction occurs forming
carbide and oxide crystals. The carbide is
considered to be due to a reaction between
aluminum and the free carbon present in the
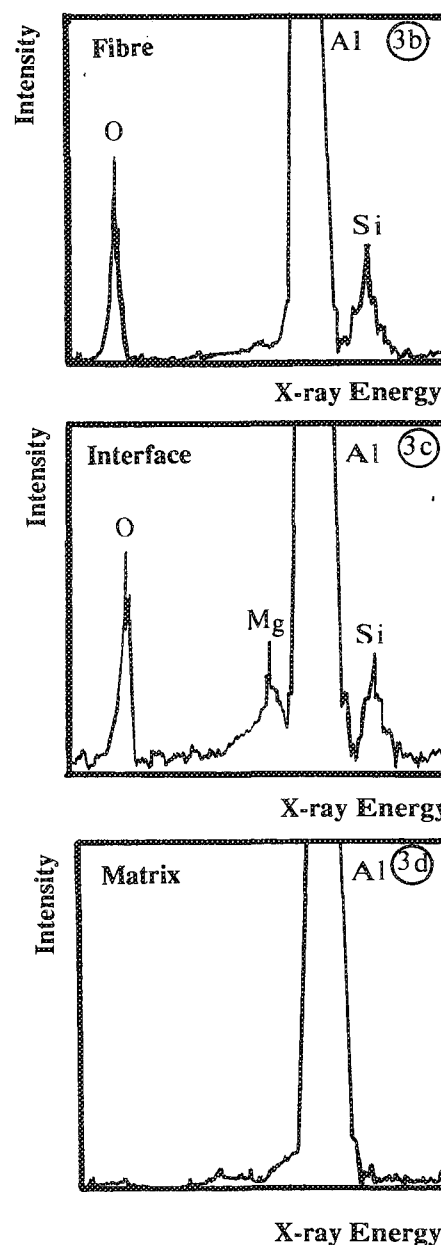
Nicalon fiber, and the alumina oxide results
from a reaction with the silica present, con-
clusions that accord with those of Viala et
al.[3] Nevertheless, the reaction product is
less extensive than in the carbon fiber com-
posite and, as a result, the material is not
as brittle.

References

1. M. Yang and V. D. Scott, "Microstructural
studies of aluminium-silicon alloy reinforced
with alumina fibres," *J. Mat. Sci.* (in press).

2. M. Yang and V. D. Scott, "Interface and
fracture of carbon fibre reinforced Al-7 wt.%
Si alloy," *J. Mat. Sci.* (in press).

3. J. C. Viala, F. Bosselet, P. Fortier,
and J. Bouix, "Chemical interaction between
silicon carbide Nicalon fibres and liquid alu-
minium or aluminium-silicon alloys,"
ICCM6/ECCM2 (F. L. Matthews, N. C. R. Buskell,
J. M. Hodgkinson, and J. Morton, Eds.), London:
Elsevier, vol. 2, 146-155.

PRECIPITATION, INTERLAYERS AND SEGREGATION AT INTERFACES: WHICH HIGH-RESOLUTION METHOD?

R. W. Carpenter, K. Das Chowdhury, and M. J. Kim

Analysis of 1-D, 2-D, and 3-D microstructural features such as segregation, interlayers and precipitates involve identification of local chemistry and atom positioning. Spectroscopic techniques such as electron energy loss (ELS) or energy dispersive x-ray (EDS) methods have unique capability for identification of local chemistry in complicated microstructures.[1] Conventional imaging methods can be used to determine atom positions with about 0.17nm resolution under rather restrictive conditions and can provide some relative information about elemental distribution in specimens through the variation in scattering amplitude with atomic number, but interpretation requires extensive careful simulations.[2] New applications of high angle annular dark-field STEM imaging show greater promise for elemental discrimination provided adequate differences in atomic number exist among the constituents.[3] In this case interpretation should be simpler because of the "incoherent" nature of the scattering. However, neither of these imaging methods is spectroscopic, and for complete analysis at current resolution limits both spectroscopic and imaging (and/or diffraction) methods must be used. In this note, some current examples of high spatial resolution electron energy loss (ELS) and high angle annular dark-field STEM analysis are discussed, with implications for future materials research.

Spectroscopy

Spectroscopic methods are generally count rate limited, so high spatial resolution requires careful consideration of small probe electron optics. The current in the small focused probe and the counting time, through probe/specimen positional stability, determines attainable spatial resolution and detectability. To attain spatial resolution better than about 10 nm, field emission sources of characteristic high brightness (typically 10^8 A/cm^2.str) and fast parallel detection systems are required.[1] An ELS system of this type was successfully used to determine that ribbon-like defects formed during the early stages of oxygen precipitation in silicon did contain oxygen, and were a metastable crystalline form of silicon oxide, not hexagonal silicon.[4] About 600 oxygen atoms were detected in small 2nm precipitates for that work. More recently the oxygen distribution at relatively simple inter-

faces between semi-insulating polycrystalline silicon (SIPOS) and single-crystal silicon-wafer substrates was examined by this ELS system and, in addition, by a computer system to control focused probe position at the specimen and spectrum acquisition, to enable position-resolved spectroscopy at interfaces. The oxygen solubility limit in silicon is about 10^{18} cm^3, i.e., about 0.002%, well below the detectability limit, so that these interfaces represent oxygen distribution step functions. They were used as test objects for interface spatial resolution under moderately restrictive electron optical conditions for small probe formation. Some results are shown in Fig. 1. The SIPOS layer is an oxygen-deficient amorphous silicon oxide deposited on the wafer substrate by chemical vapor reaction, containing 15at.% oxygen.[5] The interface image (Fig. 1a) shows that it is nearly atomically flat. The position-resolved oxygen-K edge spectrum (Fig. 1b) shows that the full width of the rise at the interface is about 7 nm. This spectrum was acquired with an incident probe about 3 nm in diameter, using a cold stage, with 2s collection time for the individual spectra used to derive the position resolved spectrum. The decrease in oxygen counts beyond the interface in the SIPOS region is attributed to local thickness variation developed during thinning. The full width of the oxygen rise is about what would be expected from convolution arguments.

Application of this method to oxygen distribution measurements at much more complex interfaces in ceramic matrix composites (CMC) reinforced with silicon carbide whiskers (SiC(w)) produced a much different result (Fig. 2). The matrix/SiC(w) interface image (Figs. 2a and b) exhibits considerable disorder and variable width. Position-resolved ELS spectra (Figs. 2c and d) from two regions of the interface showed that oxygen is present at one position but not at the other. The oxygen seems to be associated with the wider section of the interface, but both interface regions exhibit considerable disorder, and there is no firm basis for attributing oxygen to one part of the interface or the other in the absence of spectroscopic data. The oxygen distribution at region 2b of the interface has much larger spatial extent, by about a factor of 3 to 4, than the SIPOS example, but the two experiments were performed under the same conditions. In the CMC example oxygen diffused into the Si$_3$N$_4$ matrix grains during processing, as shown by the high oxygen background for Si$_3$N$_4$ in Figs. 2c and d. Diffusion of oxygen into the matrix is consistent with the physical chemistry of these materials, and has been observed by others using other experimental methods. Cation diffusion is also

---

1b

O-K

Si   SIPOS

Integrated Counts ($\times 10^3$)

Distance (Å)

2c

O-K

SiC Si_3N_4

Integrated Counts ($\times 10^2$)

Distance Å

2d

O-K

SiC Si_3N_4

Integrated Counts ($\times 10^2$)

Distance Å

InGaAs

InAlAs
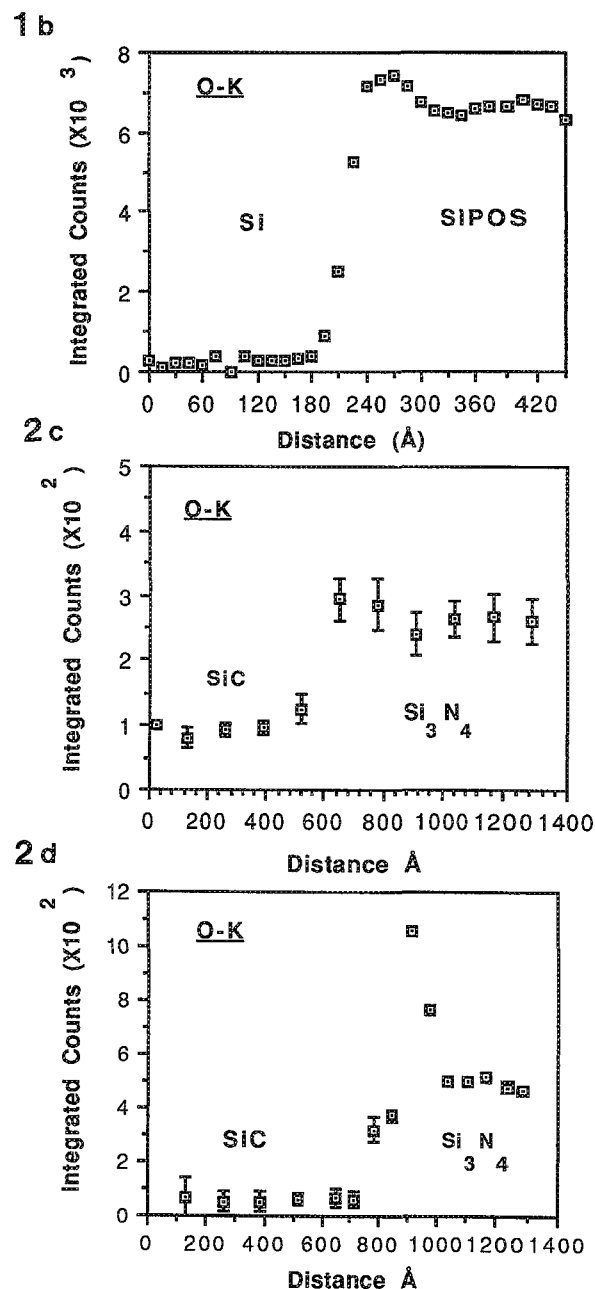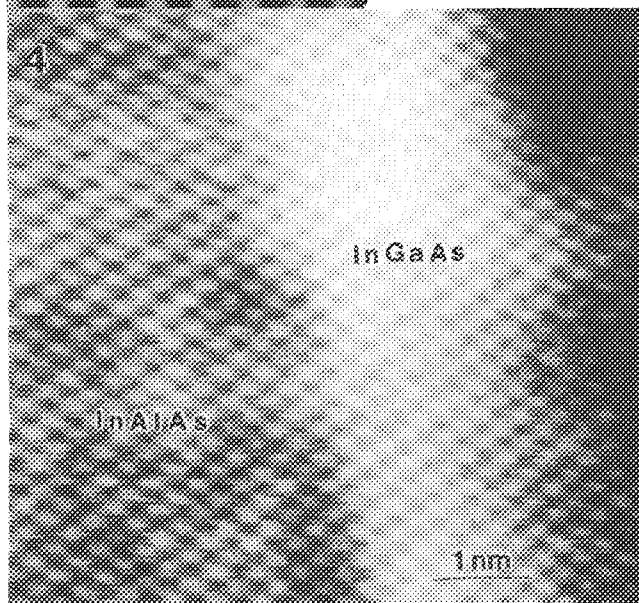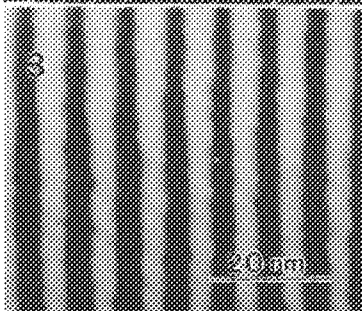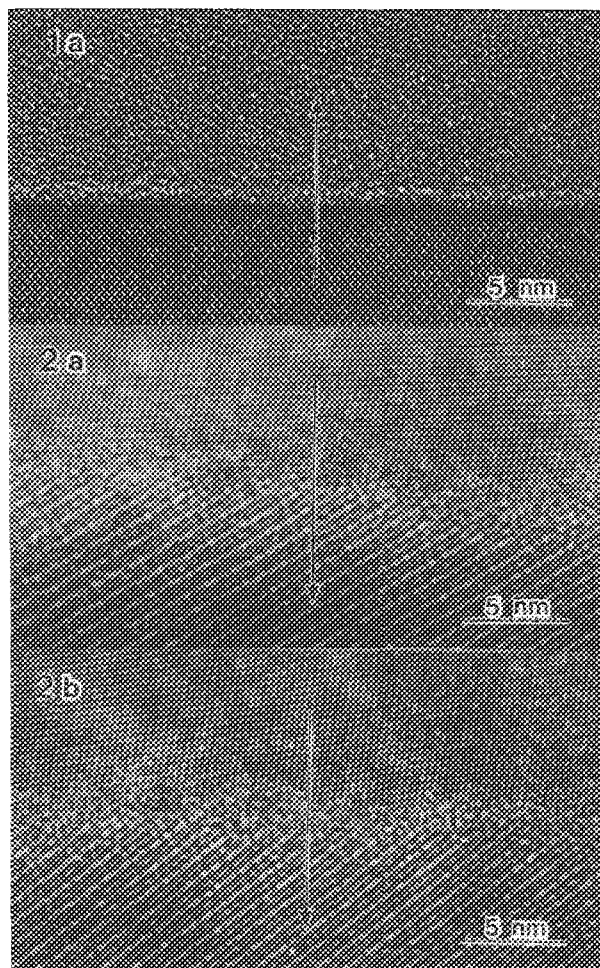
FIG. 1.--(a) SIPOS/Si <110> interface, HREM, 200 kV. Arrow shows trace of position-resolved ELS. Position-resolved ELS across interface, from oxygen-K edge; 100 kV.

FIG. 2.--(a) and (b) Si_3N_4 (bottom/SiC(w)(top)) interface in CMC. These two regions are adjacent to each other along same interface. Arrows show positions of traces for position-resolved ELS. (c) and (d) Position-resolved ELS spectra based on net integrated oxygen-K edge counts, showing oxygen distribution across interfaces of Figs. 2(a) and (b). Incident probe size at 100 kV, 3 nm, with step increment 1.3 nm and 2s acquisition time.

FIG. 3.--Low-magnification HAADF STEM image of Mo/Si multilayer specimen, 100 kV. Polycrystalline Mo layers are in bright contrast and amorphous Si layers are in dark contrast. Specimen thickness decreases from top to bottom of image.

FIG. 4.--High-resolution HAADF STEM image of quantum-well multilayer specimen taken at 100 kV with FEG/STEM. Ga-containing layer is in strongest contrast in this <110> projection. Note apparent chemically diffuse interfaces on the scale of ∿2 nm.

243

expected, to maintain electrical neutrality, and experiments to investigate this are in progress.[6]

The spatial resolution attainable for experiments of this type can be improved by reduction of the size of the probe incident at the specimen, given a suitably thin specimen in a manner consistent with desired limits for count rate and detectability, and the mechanical and electrical stability of the microscope itself. Our current results indicate that 1 nm may be near the limit attainable. The probe current cannot be increased without limit, even if that were physically possible, to improve spatial resolution without undesirable irradiation effects on the specimen, at least for covalent and ionic materials.[7]

Imaging

The most interesting and easily interpretable high-resolution imaging method sensitive to composition is high-angle annular dark-field STEM (HAADF).[3] Hollow-cone conventional dark-field imaging should produce equivalent results, provided that large enough illumination angles are used, but few results seem to be available. Fresnel imaging is often used to infer the presence of foreign chemical elements at interfaces, because it is sensitive to local mean inner potential. However, local changes in atom arrangement at interfaces without chemical segregation can also change the local mean inner potential. We recently investigated a clean $\Sigma 13$ grain boundary in Si and found that Fresnel images could be easily produced and correlated with local mean inner potential at the boundary.[8] We concluded that the presence of Fresnel fringes in an interface image is a necessary but not sufficient condition for the existence of segregation or an interlayer of differing chemistry.

Contrast in the HAADF imaging method depends strongly on the atomic number Z of the elemental distribution in the specimen, following from screened Rutherford high-angle elastic scattering cross sections.[3] The method was first used to image heavy atoms on light amorphous substrates.[9] For applications to crystalline specimens, care must be taken to exclude Bragg reflections from the detected distribution by appropriate choice of detector collection angle and beam direction in the specimen. When these conditions are satisfied, dynamical effects such as thickness fringes from wedge specimens, Fresnel fringes, and contrast reversals upon change in focus for atom column/tunnel images do not occur. An Mo/Si multilayer specimen images at low magnification in HAADF STEM is shown in Fig. 3. The Mo layers are bright and the Si dark. The thickness of each layer is about 4 nm and the thickness of the specimen decreases from top to bottom of the image. Line scans of the intensity distribution in such images yield information about the symmetry of the elemental distribution at the interfaces. Figure 4 is a high-resolution HAADF STEM image of an InAlAs/InGaAs interface in a $GaAs/Al_xIn_{1-x}As/Ga_yIn_{1-y}As$ quantum well multi-layer specimen. The interfaces do not appear to contain lattice defects, but are not chemically sharp on an atomic scale. The Ga-containing layer, with nominal thickness of 3.1nm, is in strongest contrast. The projection is <110> and the contrast variations at the interface indicate that chemical diffuseness exists over distances of about 1 nm at the interfaces. Interpretation of these images is subject to the same column approximation considerations for elemental information as are ordinary HREM images for atom position information.

Conclusions

Spectroscopic elemental resolution capability is now clearly at the 2nm level, with tangible evidence that 1nm spectroscopic and near 0.1nm elemental image resolution will be achieved in the near future. It is most likely that complementary spectroscopic and imaging methods will be required for complete characterization of material microstructures in the foreseeable future. Electronic image recording in both STEM and TEM may provide more direct elemental information than is now possible provided that suitably accurate elastic scattering cross sections become available and that filtering to eliminate inelastic contributions is used. However, to achieve chemical bonding information at interfaces (which is a major objective), high-energy/spatial resolution spectroscopy will be required.

Wide availability of these new capabilities will result in major advnaces in materials analysis capability and materials science research.

References

1. R. W. Carpenter, *Matl. Sci. and Engr.* A107: 207, 1989.
2. A. Bourret, *Mat. Res. Soc. Symp. Proc.*, vol. 139, Materials Research Soc., 1989, 3.
3. S. J. Pennycook, S. D. Berger, and R. J. Culbertson, *J. Microscopy* 144: 229, 1986.
4. R. W. Carpenter, Y. L. Chen, M. J. Kim, and J. C. Barry, *Proc. Microsc. Semicond. Mater. Conf.*, Oxford, Brit. Inst. Phys. Conf. Ser. 100, Sect. 7, IOP Pub., 1989, 543.
5. M. Catalano, M. J. Kim, R. W. Carpenter, and J. Wong, *Proc. 49th Ann. Mtg. EMSA*, 1991, 738.
6. M. H. Lewis, B. D. Powell, P. Drew, R. J. Lumby, B. North, and J. A. Taylor, *J. Mat. Sci.* 12: 61, 1977.
7. K. Das Chowdhury, R. W. Carpenter, and J. K. Weiss, *Proc. 47th Ann. Mtg. EMSA*, 1989, 428.
8. K. Das Chowdhury, M. J. Kim, Y. L. Chen, and R. W. Carpenter, *Proc. 49th Ann. Mtg. EMSA*, 1991, 1002.
9. A. V. Crewe, J. Wall, and J. P. Langmore, *Science* 168: 1338, 1970.
10. Figures 3 and 4 courtesy of Dr. J. Liu, ASU Center for Solid State Science.

QUANTITATIVE ANALYSIS OF OXYGEN SEGREGATION ON INVERSION DOMAIN BOUNDARIES IN ALUMINUM NITRIDE

A. D. Westwood, J. R. Michael, and M. R. Notis

Curved and planar inversion domain boundaries (IDB) in aluminum nitride (AlN) form in sintered AlN ceramics containing oxygen, and oxygen is known to segregate to them.[1-3] Several interface models (Table 1) have been suggested based on crystallographic constraints, chemical information, and observed high-resolution electron microscope (HREM) images.[4,5] Until recently, problems with simulation of HREM image from AlN have made accurate determination of the structure of the IDB interface difficult.[6]

The aim of the present study was to use quantitative analytical electron microscopy (AEM) to determine the oxygen concentration at the IDBs, and then to compare the experimental results with calculated oxygen concentrations for each of the IDB model by use of a Monte Carlo trajectory simulation program.[7] A match, if any, between the experimental and calculated oxygen concentrations would indicate the model that best described the IDB structure. The best match was obtained for Youngman's defect model (No. 2 in Table 1).

Experimental

An AlN pellet was fabricated by hot pressing of commercially available AlN powder containing ∿1wt% oxygen and cation impurities totaling <370 ppm (220 ppm C, 98 ppm Ca, 37 ppm Si, 10 ppm Fe), in a boron nitride (BN) coated graphite die, at 1800 C, under a 20MPa load, for 1h, in an N_2 atomosphere. No sintering aids were used, and it was therefore assumed that the ∿1 wt% oxygen present in the AlN powder was retained in the sample. Thin foils for examination by transmission electron microscopy (TEM) were prepared by first ultrasonically cutting 3mm disks from the substrate or pellet, followed by dimpling on both sides down to a final thickness of ∿10-20 μm. The specimens were then ion beam thinned until perforation. This preparation route allowed the samples to be self-supporting, eliminating the necessity of a supporting grid.

All analyses were conducted using a Vacuum Generators HB-501 dedicated scanning transmission electron microscope (STEM) operated at 100 kV, fitted with a Link LZ5 windowless Si(LI) x-ray detector and a Link Analytical AN10/95 x-ray system. An electron probe size of 1.0nm

full-width half-maximum (FWHM) with a probe current of ∿0.2-0.3 nA was used for all microanalyses. The N, O, and Al peak intensities were extracted from the x-ray spectra by the Link Analytical RTS2/FLS peak deconvolution program.

The extrapolation technique was used to determine the k-factors k_{NAl} and k_{OAl} necessary for the quantitative analysis.[8] An AlN sample having a thermal conductivity of 208 $Wm^{-1}K^{-1}$ was used for the k_{NAl} standard. The high thermal conductivity indicates a very low oxygen impurity concentration within the grains.[9] The AlN composition was assumed therefore to be stoichiometric within the grains, 65.18 wt% Al, 34.82 wt% N. A mullite $(3Al_2O_3.2SiO_2)$ sample was used for the k_{OAl} standard. X-ray analysis was conducted to determine the lattice parameter of mullite and the composition was determined from this value from a composition vs lattice parameter plot.[10] The reason for this approach is that mullite is an intermediate phase exhibiting a broad solid solution composition range. The composition of the mullite was found to be 36.8 wt% Al, 49.0 wt% O, and 14.2 wt% Si. A total of 28 EDS spectra were collected from the AlN sample to determine k_{NAl}; the k_{OAl} was determined from 16 EDS spectra collected from the mullite sample. The light element mass absorption coefficient for Kα lines used in the study were,[11] $\mu/\rho]^{NAl}$ = 13 830 cm^2g^{-1}, $\mu/\rho]^{N}_N$ = 1637 cm^2g^{-1}, $\mu/\rho]^{O}_{Al}$ = 6715 cm^2g^{-1}, $\mu/\rho]^{O}_N$ = 17 310 cm^2g^{-1} and $\mu/\rho]^{O}_O$ = 1200 cm^2g^{-1}. The conditions for collection of spectra were kept constant, 100s count time, count rates varies from about 400 to 1300 eps depending on specimen thickness, 12-15% dead time, and after every two spectra the beam current was measured by means of a Faraday cup. This procedure enabled the x-ray intensity from each spectra to be normalized to 1 nA and allowed the spectra to be accurately compared. The thickness of the specimen at the analysis point was measured through the use of the electron energy loss spectroscopy (EELS) log log-ratio method.[12] The required EELS data were collected by means of the VG serial EELS system with integrated intensities determined by the Link EELS software.

A large number of curved and planar IDBs were present in the sample. The planar IDBs lie on the basal plane (0001) of the AlN wurtzite structure (Fig. 1). The planar nature of the IDB allowed it to be accurately oriented parallel to the electron beam, which was necessary because even small deviations from the parallel orientation can have significant effects on segregation analysis.[13] The IDB was parallel to the x-ray detector line of sight where possible. The IDB analysis was conducted with the same instrument and collection conditions as in the k-factor determination. A total of three N, O, and Al concentration profiles were taken across three planar IDBs and

TABLE 1.--Proposed structural models for inversion domain boundaries.

Description	Width (nm)	Composition	Ref
1. Al_2O_3 platelet with only 1/3 of the unit cell along the c-axis.	0.433	AlO	4
2. Octahedrally coorindated Al sandwiched between two basal planes of substituted O, every 4th O being replaced by an N.	0.165	Al_3O_3N	5.6
3. Layer of AlON spinel, oriented with the {111} parallel to the AlN basal planes $d_{111} = 0.458$ nm.	0.458	$Al_6O_{18}N$	

TABLE 2.--Experimentally determined oxygen concentrations from IDBs. (Average oxygen concentration for the planar IDB was 6.0 ± 0.8 wt%.)

IDB Designation	Oxygen Weight %	Error Weight %	Thickness (nm)	IDB Type
IDB.PA	6 5	±0 9	109	Planar
	6 4	±0.9	106	Planar
	5.0	±0.7	117	Planar
	7 5	±1.0	103	Planar
IDB.PB	6.0	±0.8	106	Planar
	4 7	±0.7	103	Planar
	6 0	±0 8	108	Planar
	4 4	±0 7	101	Planar
IDB PC	7 8	±1 1	55	Planar
	5 7	±0 8	59	Curved
	5 9	±0.9	54	Curved
	7.3	±1 0	56	Curved
	5 7	±0 8	85	Curved
	7.1	±1.0	54	Curved

TABLE 3.--Calculated oxygen concentrations for proposed IDB models.

Description	Oxygen Weight (%)	
	60nm	110nm
1. Al_2O_3 platelet with only 1/3 of the unit cell along the c-axis.	15.2	12.8
2. Octahedrally coordinated Al sandwiched between two basal planes of substituted oxygen, every 4th oxygen being replaced by a nitrogen (Youngman et al.).	5.7	5.3
3. Layer of AlON spinel, oriented with the {111} parallel to the AlN basal plances $d_{111} = 0.458$ nm (Westwood).	20.6	17.8

one curved IDB. Several other data points were taken along the IDBs to determine whether any fluctuation in oxygen concentration was present. The data point spacing was 2.5 nm close to the boundary and 5 nm farther away from the boundary. For each spectrum collected, the collection was stopped every 15 s to make sure that the probe was correctly positioned; specimen drift was found to be negligible. After each spectrum, the foil thickness was measured by the EELS log-ratio technique. A computer program was written to take raw N, O, and Al x-ray peak intensities which, via an iterative process, allowed the concentrations of all three elements to be determined.

Monte Carlo electron trajectory simulations were conducted on a massively parallel processor by use of a program developed at National Institute of Science and Technology (NIST) and adapted to execute on the parallel processor.[7] The program treats the interface as a plate-like precipitate running through the foil thickness, with the precipitate oriented parallel to the electron beam. The input to the program required the assumed IDB composition and density, the specimen thickness, the electron probe size, and the number of electron trajectories to be simulated. The advantage of the parallel processor is the extreme speed with which the simulation is executed. Typically, 1×10^6 electrons were simulated to increase statistical accuracy. The output of the program provides the x-ray intensities generated in the IDB and the matrix (AlN). These intensities were converted to compositions by normalization with k-factors determined by the simulation for specimens containing Al, O, and N. The best match between the experimentally determined compositions and the Monte Carlo results indicated the most likely IDB model based on the microchemistry of the predicted interface structure.

Results and Discussion

The log k_{NAl} and log k_{OAl} values were plotted as a function of foil thickness (Fig. 2). A linear least-squares fit was used to generate the best fit line, which was extrapolated back to the ordinate axis to provide the absorption free k-factor at zero thickness. The extrapolated value for k_{NAl} at zero thickness was $k_{NAl} = 1.61 \pm 0.22$; the extrapolated value of k_{OAl} at zero thickness was $k_{OAl} = 0.88 \pm 0.10$.[14]

The oxygen concentration profiles taken across two of the planar IDBs are presented in Fig. 3. Oxygen segregation was found to be contained within a very narrow region, with a maximum concentration of (a) 6.5 ± 0.9 wt% (IDB.PA) and (b) 6.0 ± 0.8 wt% (IDB.PB), both at foil thicknesses of 110 nm. A number of other data points that were not part of the profile were taken from locations along the IDB interface; they revealed small fluctuations in oxygen concentration. Table 2, provides all experimentally determined oxygen concentration data obtained from points on the planar and curved IDBs. The variance present in the oxygen concentrations obtained from different locations

along the IDBs may be due to counting statistics, since the oxygen peak generally contained only 1500-2000 counts.

The aluminum, nitrogen, and oxygen profiles for IDB.PB are shown in Fig. 4. The nitrogen concentration appears to decrease at the boundary, whereas the aluminum concentration appears to be undeviated. This result would be expected, since in all the models oxygen is replacing nitrogen on the nitrogen sublattice in the AlN structure with aluminum concentration remaining fairly constant. An encouraging result is that within the matrix, the aluminum and nitrogen compositions are close to the stoichiometric AlN composition (Al 65.18 wt%, N 34.82 wt%). The matrix composition for IDB.PA was Al 64.32 wt%, N 34.21 wt%; and for IDB.PB was Al 64.84 wt%, N 34.00 wt%, which indicates that the k_{NAl} value was accurate.

There appears to be an oxygen-depleted region extending out to 20 nm on either side of the IDBs. The matrix oxygen concentration on either side of the IDB appears to be asymmetric outside the oxygen depleted zone. Analysis of the curved IDBs revealed oxygen segregation on both the curved portions and "planar" portions of curved IDBs. (Planar portions lie on the {10$\bar{1}$1} pyramidal planes.) It was previously reported that less oxygen segregated to the curved IDB variant than the planar variant.[2] The present analysis revealed this not to be the case: similar oxygen concentrations are present on both the curved and planar IDBs. Figure 5 shows a profile across adjacent planar and curved IDBs; the oxygen concentration was found to be 5.9 ± 0.9 wt% along the curved IDB. At random locations along the IDB, small amounts of Ca were detected; Ca is an impurity present in the starting AlN powder.

The Monte Carlo simulation was run for the three models listed in Table 1. The oxygen concentration calculated for each of the three models was determined for foil thicknesses of 60 and 110 nm. These values of foil thickness were chosen to match closely with the foil thicknesses of the experimentally determined data points, enabling comparisons to be made with the experimentally determined oxygen concentrations at the boundary (Table 2). The oxygen concentrations determined by Monte Carlo simulation for each of the three models are presented in Table 3.

A comparison between the experimentally determined oxygen concentrations and the Monte Carlo simulation of the oxygen concentrations at the boundaries shows that Model 2 provides a very good match between experimental and calculated values. It is therefore believed that this defect may be described as octahedrally coordinated Al sandwiched between two basal planes of substituted oxygen, and with every fourth oxygen replaced by a nitrogen atom. The slightly higher experimental values are attributed to the small quantities of oxygen contained within the AlN matrix. The Monte Carlo simulation program was executed with the AlN matrix assumed to contain no oxygen impurity.
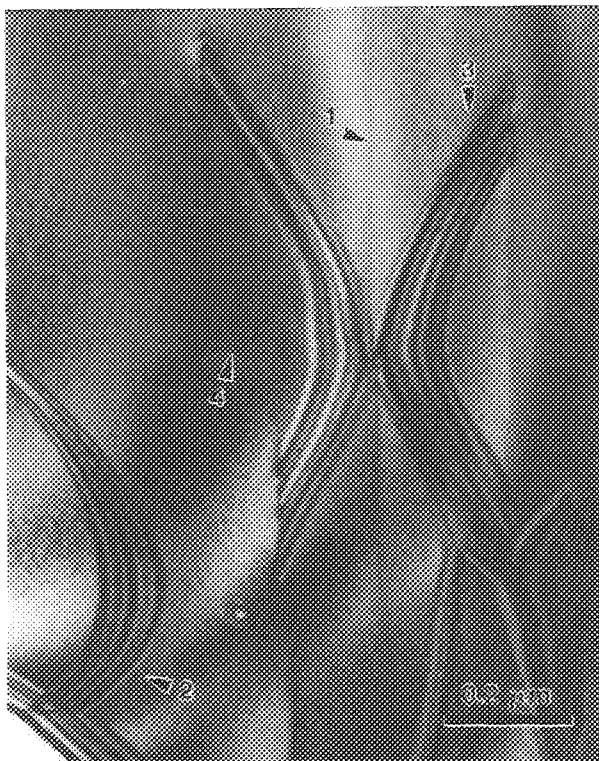
FIG. 1.--Bright-field TEM micrograph of inversion domain boundaries in undoped hot pressed aluminum nitride. IDB morphologies present in AlN are: planar and curved IDBs (arrows 1 and 2), characteristic "D"-shaped IDBs comprised of a planar and curved IDB (arrow 3), a "planar" curved portion lying on $\{10\bar{1}1\}$ pyramidal plane (arrow 4), and dislocations always present at intersection between planar and curved IDBs.
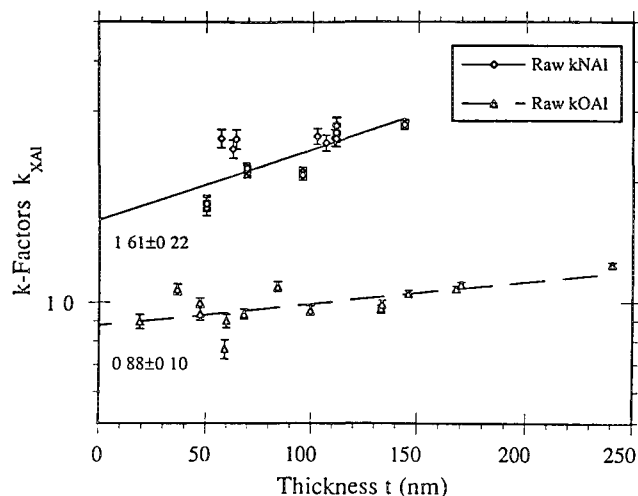
FIG. 2.--Plot of uncorrected k-factor data for log k_{NAl} and log k_{OAl} as a function of foil thickness. Extrapolated data at zero thickness provides absorption-free k-factors k_{NAl} = 1.61 ± 0.22 and k_{OAl} = 0.88 ± 0.10.

Oxygen concentrations calculated for models 1 and 3 were three to four times greater than the experimentally determined oxygen concentration.
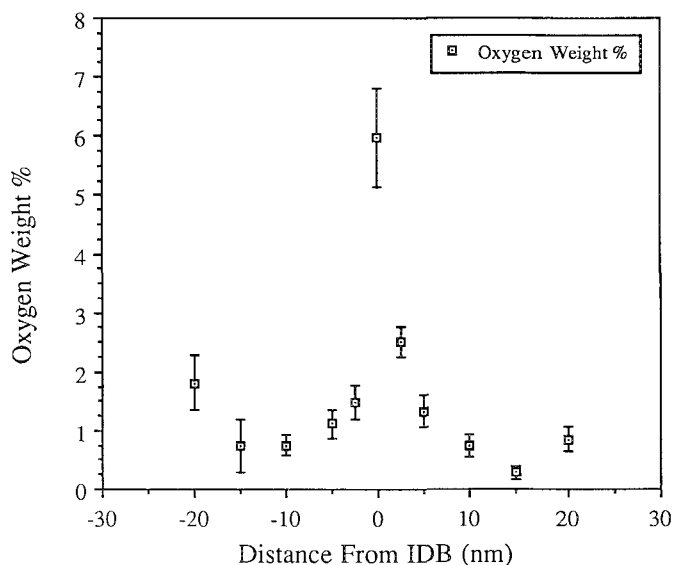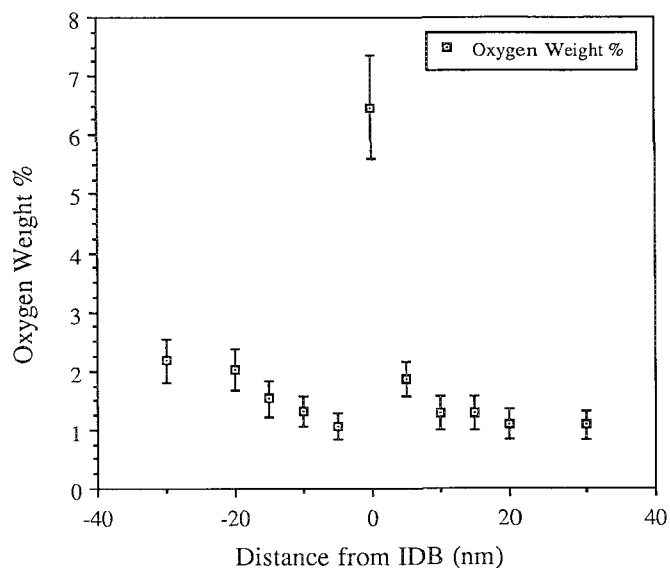
FIG. 3.--Oxygen concentration profiles across (a) IDB.PA and (b) IDB.PB revealed that oxygen segregation is confined within very narrow region; oxygen-depleted region is present extending 20 nm on either side of IDB, and oxygen concentration in matrix is not symmetrical on either side of IDB.

Conclusions

1. Oxygen is seen to segregate to both planar and curved IDBs.

2. Segregation of oxygen to the IDBs is confined within a very narrow region adjacent to these defects.

3. Oxygen-depleted regions are present in the matrix on either side of the IDBs.

4. The experimetnally determined oxygen concentrations at IDBs in AlN best matched the Monte Carlo simulations based on model 2 in Table 1 as proposed by Youngman).

5. Quantitative light-element (Z < 10) analysis and k-factor determination for light elements by EDS can be routinely conducted with
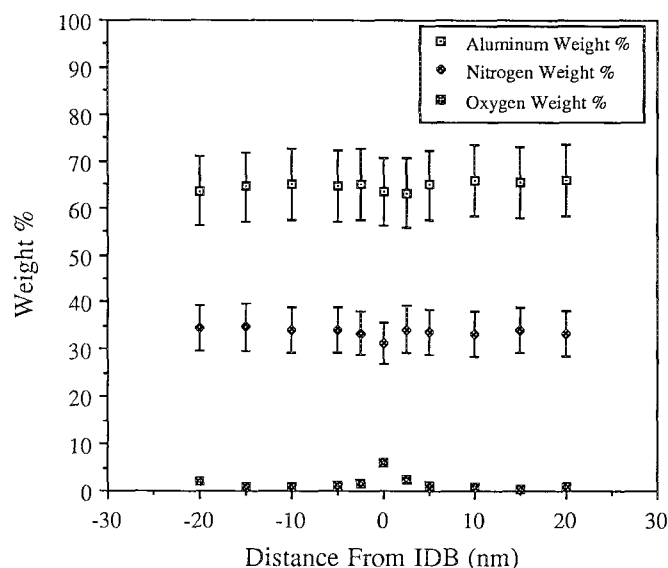
FIG. 4.--Concentration profile of aluminum, nitrogen, and oxygen across IDB.PB. Concentrations for aluminum and nitrogen in matrix are very close to stoichiometric concentrations of these elements, which indicates that experimentally determined k_{NAl} is accurate.

FIG. 5.--Oxygen concentration profile across planar IDB located at 0 nm and adjacent curved IDB positioned at 12.5 nm.

attention to the experimental details, analogous to quantification of elements with Z > 10.

References

1. A. D. Westwood and M. R. Notis, "On inversion domain boundaries in aluminum nitride," *J. Am. Cer. Soc.* (in press).

2. A. D. Westwood and M. R. Notis, "Planar and curved defects in aluminum nitride: Their microstructure and microchemistry," *Mat. Res. Soc. Symp. Proc.* 1989, 167, 295.

3. R. A. Youngman, J. H. Harris, P. A. Labun, R. J. Graham, and J. K. Weiss, "Inversion domain boundaries and oxygen accommodation in aluminum nitride," *Mat. Res. Soc. Symp. Proc.* 1989, 167, 301.

4. S. McKernan, M. G. Norton, and C. B. Carter, "High resolution electron microscopy of planar defects in AlN," *Mat. Res. Soc. Symp. Proc.* 1990, 183, 267.

5. J. H. Harris, R. A. Yongman, and R. G. Teller, "On the nature of the oxygen-related defects in aluminum nitride," *J. Mater. Res.* 5: 1763, 1990.

6. R. A. Youngman, M. McCartney, and R. G. Teller, "High resolution electron microscopy of planar inversion domain boundaries in aluminum nitride," *Ultramicroscopy* (in press).

7. A. D. Romig Jr., S. J. Plimpton, J. R. Michael, R. L. Myklebust, and D. E. Newbury, "Application of parallel computing to the Monte Carlo simulation of electron scattering in solids: A rapid method for profile deconvolution," *Microbeam Analysis--1990*, 275.

8. Z. Horita, T. Sano, and M. Nemoto, "An extrapolation method for the determination of Cliff-Lorimer k_{AB} factors at zero foil thickness," *J. Microsc.* 143: 215, 1986.

9. G. A. Slack, "Nonmetallic crystals with high thermal conductivity," *J. Phys. Chem. Solids* 34: 321, 1973.

10. F. J. Klug, S. Prochazka, and R. H. Doremus, "Alumina-silica phase diagram in the mullite region," *Ceramic Transactions* 6: 15, 1990.

11. B. L. Henke and E. S. Ebisu, *Advances in X-ray Analysis*, New York: Plenum Press, 1974, 17, 150.

12. T. Malis, S. C. Cheng, and R. F. Egerton, "EELS log-ratio technique for specimen thickness measurement in the TEM," *J. Electron Microsc. Tech.* 8: 193, 1988.

13. J. R. Michael, G. Cliff, and D. B. Williams, "A microcomputer-based Monte Carlo simulation and its application to grain boundary segregation studies in the AEM," *SEM/1984* 4: 1697.

14. A. D. Westwood, J. R. Michael, and M. R. Notis, "Experimental determination of light element k-factors using the extrapolation technique," *J. Microsc.* (submitted).

CORROSION AT Cr/Cu INTERFACIAL LAYERS

D. W. Kruger and Marina Plat

This paper discusses some of the analyses performed on a device consisting of two levels of metallurgy separated by a quartz insulating layer. The device is ultimately attached to a printed-circuit card and covered with a protective plastic coating. The particular failure mode discussed is corrosion of the first- and second-level metallurgy (Al-4% Cu and Cr/Cu/Au, respectively), and at the interconnecting vias that pass through the quartz. The corrosion was primarily due to the presence of ionic species. We discuss changes in the device and the packaging that were made to improve the corrosion resistance of the device. The search to identify and remove contaminants is also discussed.

Problem

Corrosion of second-level metal lines occurred during the development of the device. The corrosion was largely due to Cl left on the surface of the device from process chemicals, although residual S also played a role. Early parts sometimes failed prior to stress testing, showing corrosion and electrical opens in via test structures and conducting lines. The Cr/Cu adhesion was very poor; lines separated at the interface with a small applied force. The plastic coating offered minimal protection, and only slightly delayed the failure of the metallurgy.

Experimental

Microprobe analysis of corroded devices found large amounts of chlorine and sulfur on the parts. The Cl concentration was sufficient (1%) to make wavelength-dispersive spectroscopy (WDS) Cl x-ray dot maps (Figs. 1 and 2). Reaction products of first-level metal corrosion were observed outside the second-level metal that covered the vias. Reaction products, as well as chlorine and sulfur, concentrated in electrically open links of the test via chains. Back-side observations through the glass substrate revealed missing first-level metal and via attack, even when the second-level metal remained on the device. Cross-sectioned samples showed S above the first-level metals, as determined by energy-dispersive spectroscopy (EDS) and WDS. The S originated from an inadequate strip of the first-level photoresist.

Chlorine is a particularly insidious contaminant since it is a catalytic oxidizer of Cu. Thus, ionic chloride continues to oxidize the Cu as long as water is present and the chloride

The authors are at the IBM East Fishkill Facility, Z/E40 B/630, Route 52, Hopewell Junction, NY 12533.

ion can be transported to fresh metal. Water also serves as the transportation medium and electrical conductor for the Cl-accelerated corrosion process. A model for the corrosion mechanism emerged from the analyses. Chlorine, left on the part from an unknown process step, attacked the Cr/Cu at the bottom of the second-level metal stack. The Au cap enhanced the galvanic attack already active between the Cr and Cu layers. Crevice corrosion, accelerated by the Cl contamination, oxidized the Cu and/or Cr at the interface, and a path was opened to the interior of the via. During temperature and humidity stress testing, moisture entered the via region, reacted with residual sulfur, and attacked the first-level metal. Reaction products containing first- and second-level metal, Cl, and S were then forced back through the narrow gap between the Cr and Cu due to volume expansions associated with the reactions (Figs. 3-8).

Contaminant Sources

Analyses of the corroded devices indicated that they were very susceptible to Cl-driven corrosion. The majority of the Cl was introduced during the second-level metal photoresist strip that involved methylene chloride. The strip procedure was changed to eliminate the methylene chloride. The first-level photoresist strip was also improved to reduce the amount of residual S. Although these steps significantly decreased the severity of the corrosion problem, it was necessary to reduce the contamination on the devices still further.

Ion chromatographic analyses of corroded parts found 0.15-0.28 $\mu g/cm^2$ of ionic Cl, vs a background level of $\leqslant 0.01$ $\mu g/cm^2$. Additional Cl sources were traced to the dicing sector, where parts saw a 2.5 to 4.5-fold increase in Cl. Blank glass plates that were run through the sector also experienced an increase in Cl. After the postdicing cleaning procedure was made more rigorous, the Cl level was reduced to the background level.

The printed circuit card also contained Cl that spread over the device during a rinsing operation. A new card-cleaning procedure was implemented, and the Cl signals were reduced almost to background levels. The number of stress-tested devices that corroded decreased as a result of the new cleaning steps.

Additional Information

The Cr/Cu interface was phased to strengthen it against attack from Cl. A 50%Cr-50%Cu layer was added between the original Cr and Cu layers. The new structure was more resistant to interface attack and adhesion loss during

temperature and humidity stress testing than the unphased Cr/Cu interface.

In another episode, devices corroded along their periphery. The edges of the device substrate were left exposed to the processing environment by the original coating process. Small delaminations, nonwets, and bubbles occurred at the edges of the device. Tightening of the coating thickness measurement protocol, inversion of the card during the coating cure, and application of an additional layer of the coating improved the edge coverage. As a result of these changes, edge corrosion was no longer observed.

Conclusions

Eliminating Cl sources and trapped S significantly reduced the incidence of corrosion that occurred during stress testing. The large amount of Cl originally found on corroded parts was substantially reduced by removal of the methylene chloride from the first-level photoresist strip operation. Two other sources of

Cl contamination (the dicing operation and the printed-circuit cards) were addressed by addition or improvement of cleaning steps in the device fabrication. The cleaning procedures were shown to decrease the amount of ionic contamination on the dice to $<< 0.02$ $\mu g/cm^2$ of ionic Cl. The result was greatly improved reliability as determined by temperature and humidity stress testing.

The weak Cr/Cu interface was strengthened against corrosive attack and physical failure by the addition of a 50%Cr-50%Cu phased layer. The catastrophic attack of the via regions documented in Figs. 3-8 did not occur after the Cl levels were brought under control, and after the phased Cr/Cu layer was added. The improved uniformity and coverage of the plastic coating also protected the edges of the devices from corrosion.

The combination of removing major contaminants, phasing the Cr/Cu interface, and improving the application of the plastic coating eliminated corrosion as a concern for the device.

FIG. 1.--Micrograph of peeled-back conducting lines.   FIG. 2.--WDS Cl x-ray dot map of Fig. 1.
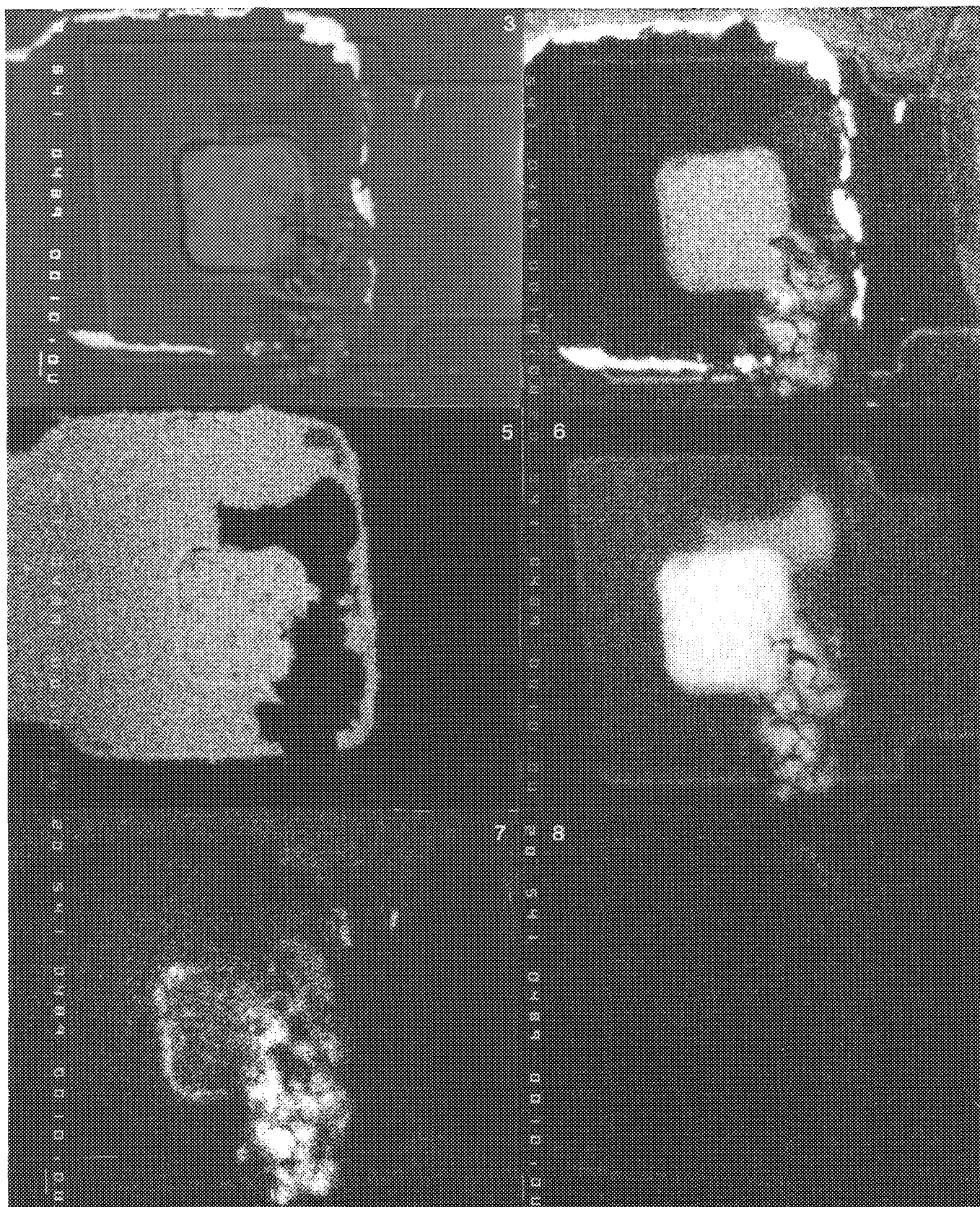
FIG. 3.--Micrograph of via region (2nd-level metal removed).
FIG. 4.--WDS Cr x-ray dot map of Fig. 3.
FIG. 5.--WDS Cu x-ray dot map of Fig. 3.
FIG. 6.--WDS Al x-ray dot map of Fig. 3.
FIG. 7.--WDS S x-ray dot map of Fig. 3.
FIG. 8.--WDS Cl x-ray dot map of Fig. 3.

252

ELECTRON MICROSCOPY OF THICK 304 SS-COPPER MULTILAYERS

M. A. Wall and T. W. Barbee Jr.

Multilayer nano-structures are dense synthetic ultrafine-grained high-interface-concentration solids. Such materials are of interest, since their unique structures often result in new or enhanced physical properties. In this paper we present the results of a TEM characterization study of a series of thick 304 stainless steel (ss)-copper (Cu) multilayered structures.

Experimental

The SS-Cu multilayers were made by planar magnetron sputtering.[1] Repeat periods are 20, 50, 200, 500, and 1000 Å with the total film thicknesses >15-20 µm. Specimens were examined in both plan and cross-sectional[2] views by TEM.

Results

Cross-section TEM specimens revealed well-defined layers in all samples and columnar growth structure for all repeat periods (Fig. 1). Columnar widths varied from 0.08-0.2 µm, with the smaller periods samples having the larger columnar widths. Plan-view specimens revealed a fairly equi-axed randomly oriented cross-section structure (Fig. 2).

Specimens with periods ≤200 Å were wholly (Fig. 1) with the (111) growth planes normal to the growth direction. Electron diffraction (SAD) did not show any difference in lattice parameters of the FCC-Cu and FCC-ss layers (Fig. 1).

Specimens with periods of ≥500 Å have bimodal FCC-Cu/FCC, BCC-ss structures (Fig. 3). The individual layers of ss have undergone a partial transformation to a BCC structure. Within a columnar section the Cu grains have a small number of low angle boundaries and twins and can be considered as single grains. The ss layers have retained FCC structure material at the ss on Cu deposition interface (Fig. 4). The remainder of the ss layer is polycrystalline BCC with grains of the order of 0.02-0.04 µm. The ss-BCC grains have at least two orientations relative to the FCC-ss phase (Figs. 4 and 5). The two main orientation relationships are:
$[110]_{fcc}//[111]_{bcc}$ with $(111)_{fcc}//(110)_{bcc}$ and
$[110]_{fcc}//[100]_{bcc}$ with $(111)_{fcc}//(110)_{bcc}$.

Conclusion

Magnetron-sputter-deposited ss films have a metastable BCC structure[3] with the (110) planes parallel to the stubstrate. This occurs as the mean energy of an incident adatoms are approximately 9 eV; all this energy is absorbed at the deposition surface. The surface of the material passes through the ∂ BCC phase of ss during deposition and this structure is quench stabilized due to the large (>10^{10} K/s) surface cooling rates.

At multilayer periods ≤200 Å, the epitaxial growth of ss on a FCC-Cu results in FCC-ss as deposited. Transformation of the FCC-ss to BCC is possibly held in check by coherency strains with the Cu lattice. For periods of ≥500 Å there is a bimodal FCC, BCC-ss structure. The FCC-to-BCC interface in the ss layer appears to lie at 50-100 Å from the ss-on-Cu interface. Since coherency strains are confined to regions near the interface, the retained FCC structure of the ss is limited to this region. The bimodal structure is believed to result from partial transformation of the ss during deposition in the larger-period (≥500Å) multilayers.

References

1. T. W. Barbee Jr., "Synthesis of multilayer structures by physical vapor deposition techniques," in *Synthetic Modulated Structures*, New York: Academic Press, 1985, 313.
2. C. Trybus et al., "Preparation of in-situ composite sheet and wire for TEM analysis," *Mat. Res. Soc. Proc.* 115: 1988.
3. T. B. Barbee and D. L. Keith, "Synthesis of metastable materials by deposition techniques," in *Synthesis and Properties of Metastable Phase*, New York: 1980, 93.

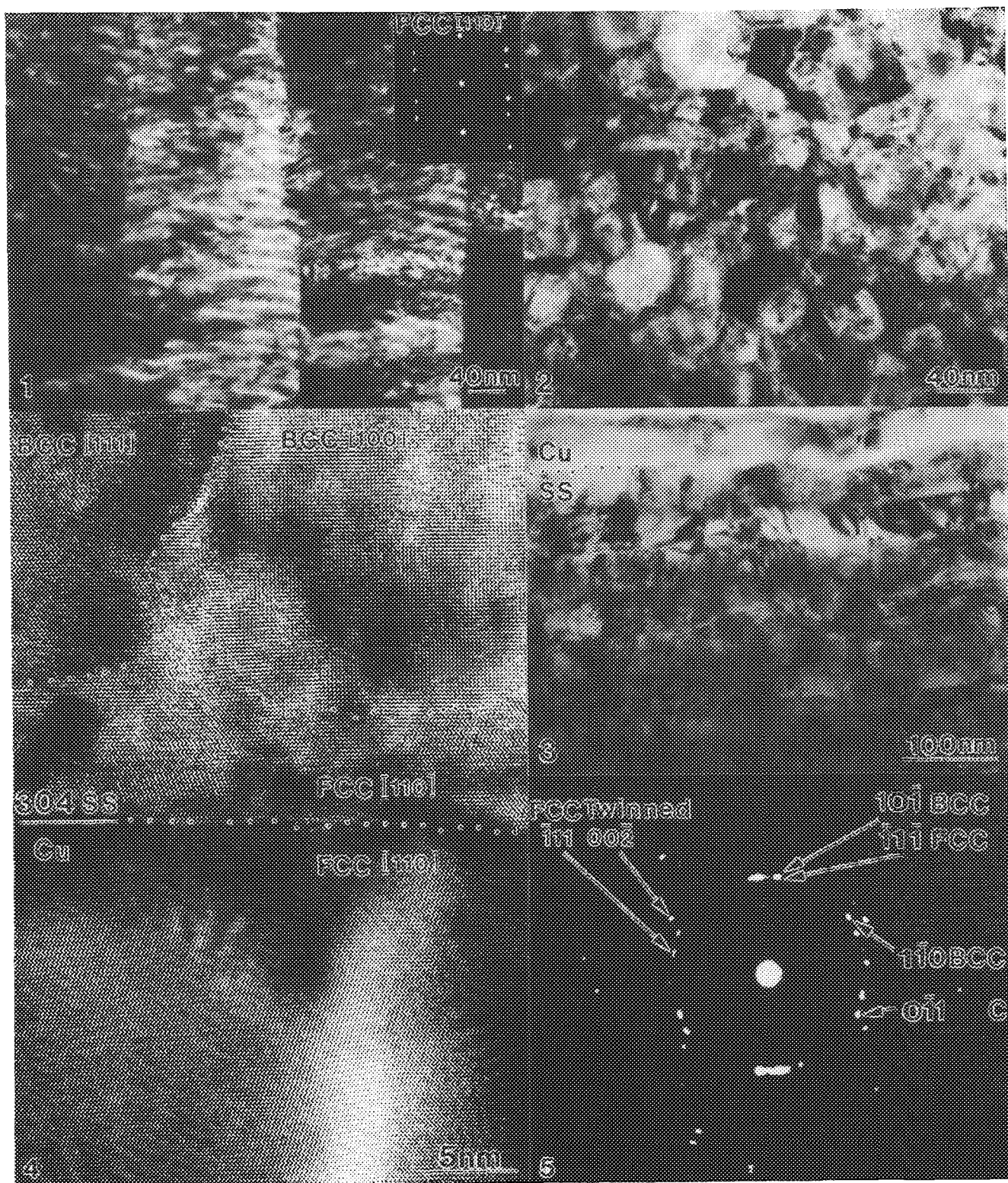FIG. 1.--BF and SAD in cross section of 200Å period copper/304ss multilayer showing typical columnar FCC structure.
FIG. 2.--BF in plan view of 200Å period copper/304ss multilayer.
FIG. 3.--BF in cross section of a 1000Å period copper/304ss multilayer.
FIG. 4.--HREM of 304ss on copper interface showing two BCC orientations of [100] and [111] on retained [110] FCC-304ss.
FIG. 5.--SAD patterns of [111] BCC on [110] FCC twin pattern.

MEASUREMENT OF PARTIAL SCATTERING CROSS SECTIONS FOR EELS QUANTIFICATION

Ferdinand Hofer

Electron energy-loss spectroscopy (EELS) is now an established technique that can be employed in electron microscopy for determining the elemental composition of solids in small volumes. The quantification of the EEL-spectra requires a knowledge of partial scattering cross sections for the inner-shell excitations, i.e., differential cross section integrated over angle and energy. These cross sections can be determined either experimentally by standards,[1,2] or theoretically by the hydrogenic model[3,4] or the Hartree-Slater model.[5,6] However, differences between experimental and calculated cross sections have been found, so that one must measure inelastic scattering cross sections under conditions of interest to the electron microscopist. By comparing such experimental scattering cross sections with calculated values, one can find any trends in discrepancies and make it possible to estimate the accuracy of quantitative microanalysis by means of EELS.

Experimental Methods

Absolute Measurements by Use of Thin-film Standards. This method has general applicability and can be used for almost all elements.[7] However, a difficulty associated with the measurement of cross sections is that a thin-film standard of known thickness, composition, and density must be manufactured for each element of interest. The problem introduced by this method is the thickness determination, which can be done in a sufficiently accurate way only by means of convergent-beam electron diffraction (CBED). This procedure can be time consuming and is moreover restricted to thick, crystalline specimens. That is why there are very few measurements of absolute inner-shell scattering cross sections in the literature. Apart from early measurements in the 1970s, this method was used only in a determination of partial cross sections of the elements C, Al, Fe, Cu, and Ag. (The results are included in Figs. 1-3.)[8] However, reasonably accurate measurements are somewhat difficult to perform because in the case of very thin metal films, thin surface oxide layers due to air oxidation and contamination films may introduce considerable systematic errors. If thicker samples are

used, the effect of such thin oxidation layers decreases but the spectrum has to be corrected for multiple scattering, a correction that may also introduce errors.

2. Relative Measurements (k-factor Method. The above-mentioned difficulties can be partially avoided if ratios of inner-shell scattering cross sections are measured.[1,2] In this method a thin-film standard is used that must contain one light element (B) that gives rise to a K-edge in the EEL-spectrum, and the element (A) whose cross section is sought. If the concentration of these two elements is known the cross-section ratio can be determined from

$$\frac{\sigma_B(\beta,\Delta)}{\sigma_A(\beta,\Delta)} = \frac{I_B(\beta,\Delta)}{I_A(\beta,\Delta)} \cdot \frac{N_A}{N_B}$$

where N_i is the number of atom per unit area, $I_i(\beta,\Delta)$ is the core-loss intensity integrated up to an energy-loss region of width Δ starting at the edge onset, and $\sigma_i(\beta,\Delta)$ is the partial scattering cross section integrated over a collection angle β and an energy-loss region Δ.

The measured cross-section ratios can be treated as EELS k factors in analogy with thin-film EDX. Cross-section values for the element A can be determined by insertion of a calculated cross-section value for the light element B. This can be done because the K edges of light elements can be accurately calculated.[9] Preferably, oxide compounds should be used as standards for determination of k factors, because the intensity of the K-edge of oxygen in the medium energy-loss region is relatively easy to measure, and oxides can be easily prepared and frequently have stoichiometric compositions.[2]

The experimental determination of partial cross sections (and k-factors) can be also influenced by the following effects, which must be taken into account or at least minimized:

multiple scattering due to thick specimens,
beam-convergence effects,
orientation effects in crystalline samples,
and
lens abberation effects (chromatic abberation in TEM image mode).

Results

Scattering cross sections and cross-section ratios can be experimentally determined only for particular values of β and E_0. Therefore, values determined under different experimental conditions can be directly compared only by representing $\sigma(\beta,\Delta)$ in terms of an integrated

F. Hofer is at the Research Institute of Electron Microscopy and Fine Structure Research, University of Technology, Graz, Austria. He thanks Dr. Beiping Luo (Fritz-Haver-Institut, Berlin) and Prof. Peter Rez (ASU, Tempe, Ariz.) for the calculation of Hartree-Slater cross sections and Prof. R. Egerton (SUNY Stony Brook) for providing computer programs.

dipole oscillator strength f(Δ) independent of β and E_0.[10] All measured k-factors and calculated values have been therefore converted to f(100) values. In the case of measurements on oxide standards, f(100eV) for oxygen has been taken as 0.41 (the Hartree-Slater value) rather than the hydrogenic value 0.45.

K Edges

K edges permit the detection of the elements Li to Si and generally show a simple sawtooth profile that can be well described by hydrogenic wave functions and by Hartree-Slater wave functions. Experimental GOS-values determined from k-factors[11,12] and absolute measurements[8] are compared in Fig. 1 with the predictions of the models. From this figure one can deduce that the Hartree-Slater values show a better agreement with the experimental values than with the hydrogenic values, a result that corresponds to previous findings.[10]

L_{23} Edges

More problems arise with the L edges, because they are not as simple as the K edges. For example, the elements Mg to Ar and Zn to As exhibit an edge with a delayed maximum, whereas the elements K to Cu respond with narrow and intense peaks right at the edge's onset (white lines). Figure 2 shows the f(100) values for the elements ranging from Al to Ge. For the elements Ca to Co the agreement between experimental and calculated values is quite good (within 10%), but there are large differences for the elements Al, Si, and Ni to Zn. (Note that for the experimental data the white lines have not been omitted as suggested by Auerhammer et al.[13] because the intense white lines are a very useful signal for microanalysis.)

M_{23} Edges

Since no quantitative measurements on M_{23}-excitations (K-Zn) have been published to our knowledge, we have measured the k-factors of some transition metals. The results for Ti, Mn, and Ni are presented in Table 1.

TABLE 1.--Oxygen K/metal M_{23} cross-section ratios for $E_0 = 120$ keV, $\Delta = 30$ eV, $\beta = 5.9$ mrad (TEM image mode).

	k-factor	Compound
Ti	7.66E-4 ± 1.2E-4	TiO_2
Mn	1.35E-3 ± 0.2E-3	MnO
Ni	4.90E-3 ± 0.4E-3	NiO

Although there are problems in subtracting backgrounds, since these edges are at low energies (below 100 eV) and are often affected by multiple scattering, there might be some prospects for electron spectroscopic imaging due to the high partial cross section of M_{23} excitations.

M_{45} Edges

The M_{45} edges permit the analysis of the elements Rb to W and also exhibit complicated edge shapes: The M_{45} edges of the elements Rb to Br and Lu to W have delayed maxima, and Cs, Ba, and the rare-earth elements exhibit intense white lines at threshold.

Figure 3 exhibits differences between experimental[8,14-16] and theoretical value.[13] The experimental values for the elements Sr to Cd show deviations of about 30% from the Hartree-Slater values. For the rare-earth elements, differences occur between experimental values measured by different authors. As to agreement between measured and calculated cross sections, note that the Hartree-Slater theory cannot predict the white lines included in the experimental data.[14-16] Therefore the calculated values are essentially lower than the experimental values (La to Dy).

N_{45} Edges

These edges can be useful for the microanalysis of elements ranging from Cs to Yg; the K-factors and f(100) values have been published recently.[9,17]

Conclusions

For quantification of EELS-spectra we recommend the use of partial scattering cross sections deduced from experimental k-factors via f(Δ) values. Tabulated f(50) and f(100) values have been published recently[9] and can be used to calculate the partial cross sections for particular experimental conditions (E_0 and β). However, since there are deviations among the measurements by different authors for some elements (e.g., Al, Ba, La, Lu, and Yb), further measurements on oxide standards seem to be necessary.

References

1. T. F. Malis and J. M. Titchmarsh, "A k-factor approach to EELS analysis," *Inst. Phys. Conf.* Ser. 78: 181, 1985.

2. F. Hofer, "EELS quantification of M edges by using oxidic standards," *Ultramicroscopy* 21: 63, 1987.

3. R. F. Egerton, "Formulae for light-element microanalysis by electron energy-loss spectrometry," *Ultramicroscopy* 3: 243, 1978.

4. R. F. Egerton, *Electron Energy-Loss Spectroscopy in the Electron Microscope*, New York: Plenum Press, 1986.

5. R. D. Leapman, P. Rez, and D. F. Mayers, "K, L, and M shell generalized oscillator strengths and ionization cross-sections for fast electron collisions," *J. Chem. Phys.* 72: 1232, 1980.

6. P. Rez, "Inner-shell spectroscopy: An atomic view," *Ultramicroscopy* 28: 16, 1989.

7. D. C. Joy, R. F. Egerton, and D. M. Maher, "Progress in the quantitation of electron energy-loss spectra," *SEM/1979* II, 817.

8. P. A. Crozier, "Measurement of inelastic electron scattering cross-sections by electron
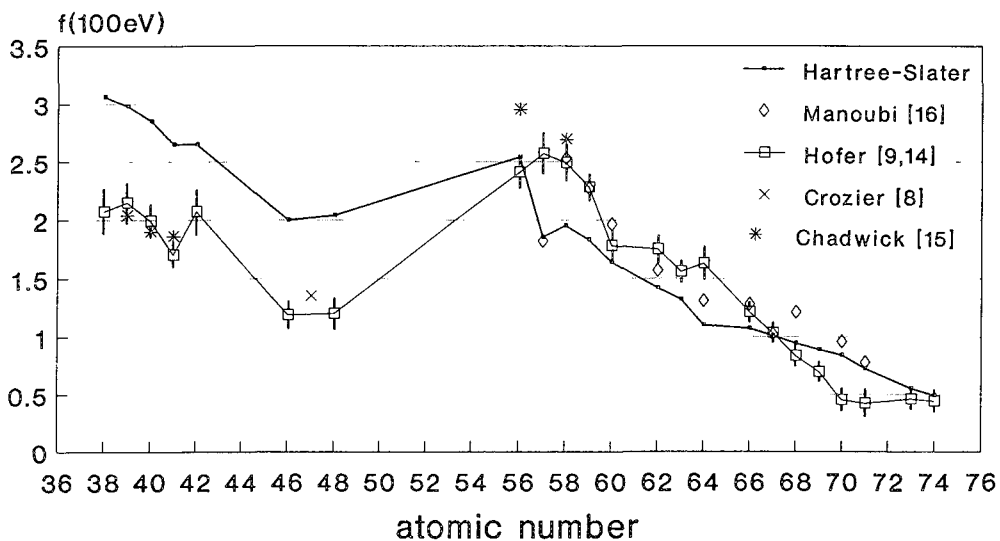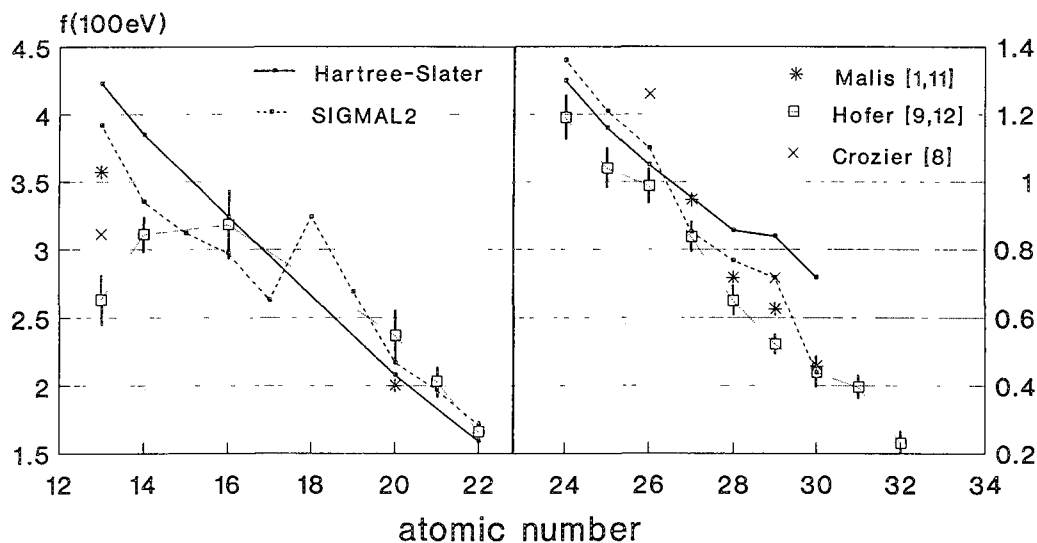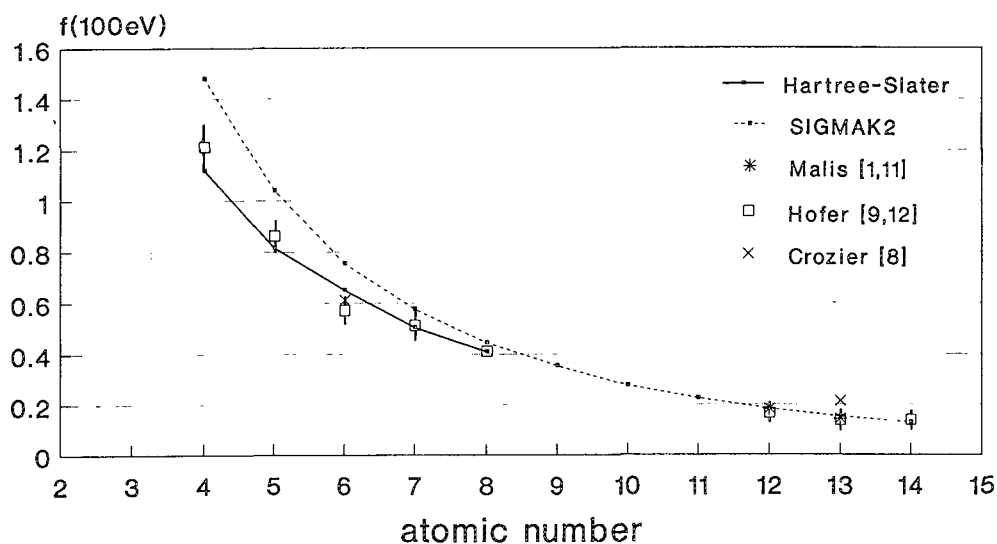
FIG. 1.--Dipole oscillator strengths f (100eV) for K-shells deduced from calculations and energy-loss experiments.

FIG. 2.--Dipole oscillator strengths f (100eV) for L_{23} shells.

FIG. 3.--Dipole oscillator strengths f (100eV) for M_{45} shells.

energy-loss spectroscopy," *Phil. Mag.* B61: 311, 1990.

9. F. Hofer, "Determination of inner-shell cross-sections for EELS-quantification," *Micros. Microanal. Microstruct.* (in press).

10. R. F. Egerton, "A simple parameterization scheme for inner-shell cross sections," *Proc. 46th Ann. Meet. EMSA* 1988, 532.

11. T. F. Malis (unpublished results).

12. F. Hofer and P. Golob, "Quantification of electron energy-loss spectra with K and L shell ionization cross-sections," *Micron and Microscopica Acta* 19: 73, 1988.

13. J. Auerhammer, P. Rez and F. Hofer, "A comparison of theoretical and experimental L and M cross-sections," *Ultramicroscopy* 30: 365, 1989.

14. F. Hofer, P. Golob, and B. Brunegger, "EELS quantification of the elements Sr to W by means of M_{45} edges," *Ultramicroscopy* 25: 81, 1988.

15. M. M. Chadwick and T. F. Malis, "AEM characterization of sintered silicon nitride with yttria and alumina additions," *Ultramicroscopy* 31: 205, 1989.

16. T. Manoubi, P. Rez, and C. Colliex, "Quantitative electron energy loss spectroscopy on M_{45} edges in rare earth oxides," *J. Electr. Spectr. and Relat. Phenom.* 50: 1, 1990.

17. F. Hofer, "EELS-quantification of the elements Ba to Tm by means of N_{45} edges," *J. Microscopy* 157: 279, 1989.

MEASUREMENTS OF IONIZATION CROSS SECTIONS FOR ELECTRON ENERGY-LOSS MICROANALYSIS UNDER WELL-DEFINED SCATTERING CONDITIONS

K. M. Krishnan and C. J. Echer

Partial cross sections required for electron energy-loss microanalysis have been measured for a series of high purity single crystal standards. For each sample four different scattering geometries were used. The experimental data were compared to theoretical calculations with both the standard hydrogenic model and parametrized Hartree-Slater cross sections. Best agreement between theory and experiment was observed for experiments performed in diffraction mode (image coupling) with the probe convergence angle (0.94 mrad) much smaller than the spectrometer collection angle (6.84 mrad). In addition, specimen thicknesses from the region of microanalysis were measured by convergent-beam electron diffraction. Absolute cross sections based on these measurements are also currently being determined.

Quantitative microanalysis using inner-shell ionization edges in electron energy-loss spectroscopy is straightforward and can be performed by relating the experimentally measured characteristic edge intensities (integrated over an energy window of width ΔE starting at the edge onset and a collection angle β) to the concentrations of the elements of interest through the simple equation[1]

$$\frac{N_a}{N_b} = \frac{I_a(\beta,\Delta E)}{I_b(\beta,\Delta E)} \frac{\sigma_b(\beta,\Delta E)}{\sigma_a(\beta,\Delta E)}$$

This method of obtaining relative concentrations of the two elements a and b can be carried out easily if the partial scattering cross sections of the inner-shell edges for the same energy window and collection angle, $\sigma_a(\beta,\Delta E)$ and $\sigma_b(\beta,\Delta E)$, can either be calculated from appropriate theoretical models or measured experimentally against suitable standard specimens. In practice, the implementation of this simple quantification procedure is complicated by problems of multiple scattering (if the specimens are more than 40-50 nm thick), channeling effects in crystalline specimens (which can be generally avoided by tilting the samples to orientations where no lower-order diffraction vectors are excited), convergence of the incident probe, and lens aberration effects. The theoretical models that are

normally used for the calculation of the partial cross sections assume that the inner shell cross sections are atomic in nature. In fact, for low-Z elements a hydrogenic model is used[2] with reasonable agreement with experiment. Alternatively, an atomic model using Hartree-Slater wavefunctions for transitions of inner shell electrons to the continuum has been developed[3] and is also available in a parametrized form.[4] Even if we can carefully overcome some of the experimental difficulties mentioned earlier, it is important to ascertain the accuracy of the theoretical models for various scattering geometries commonly used in experiments. Hofer[5] has carried out experimental measurements of partial cross sections for an extensive range of elements in the periodic table. Unfortunately, most of his published data are for only one scattering geometry, i.e., the image mode with β = 5.9 mrad. In this paper we present measurements complementary to Hofer's results for four different scattering geometries, but for a narrow range of elements. Single-crystal standards were used and specimen thickness was accurately measured by CBED. In addition to determining relative cross sections, we can thus determine absolute cross sections. The absolute measurements will be discussed in a subsequent paper.[6]

Experimental Details

All electron energy-loss measurements were recorded at 200 kV on a JEOL 200CX transmission electron microscope and a Gatan 666 parallel-detection spectrometer. Electron-transparent foils of high-purity single crystals of BeO, BN, SiC, Si_3N4, SiO_2, MgO, $TiC_{0.95}$, and $Y_3Fe_5O_{12}$, prepared by ion milling, were used in these experiments. Care was taken to tilt the foils away from any orientations where channeling effects could affect the interpretation of the results. All spectra were recorded from regions of the sample with thicknesses less than 0.2 inelastic mean free path lengths. Data were recorded under the following scattering geometries: (a) Probe convergence angle α = 0.84 mrad, Spectrometer collection angle β = 6.84 mrad, diffraction mode (image coupling); (b) α = 0.84 mrad, β = 6.82 mrad, image mode (diffraction coupling); (c) α = 3.5 mrad, β = 4.56 mrad, *diffraction mode*; and (d) α = 3.5 mrad, β = 50 mrad, image mode. The convergence angle was defined by the condenser aperture(s) and the collection angle was defined either by the objective aperture(s) calibrated against a well-known diffraction pattern (image mode) or the spectrometer entrance aperture radius

(diffraction mode). However the β = 50 mrad experiments were carried out in image mode with no objective aperture in the path of the electron beam. These results, interpreted in terms of relative cross sections (all ratios with respect to C-K edge) are discussed in this paper.

Precise measurements of the sample thickness were made by convergent-beam electron diffraction. The thickness of the same region of the sample, obtained in terms of the mean free path length for inelastic scattering from the electron energy loss spectrum, was used to measure the mfp accurately. The result was subsequently used to measure the thickness of the sample in regions where it was too thin for effective application of the CBED method. These results, interpreted in terms of the absolute cross sections, will be discussed in a later paper. In addition, we also measured x-ray emission spectra from the same regions of the sample, to permit a comparison of the EELS microanalysis with energy-dispersive x-ray spectroscopy using our ultrathin-window detector with experimentally measured K-factors.[7]

Spectra were processed by use of the SLEEP program developed at the NCEM. All spectra were normalized with respect to a channel-to-channel gain-variation spectrum to minimize any variation due to the difference in the detection efficiencies of the individual elements of the diode array. In addition, a dark-current spectrum, obtained under the same condition, was subtracted from each inner-shell ionization edge spectrum. For each edge, either a standard power law (AE^{-r})[8] or a log-polynomial[9,10] was used to model the background. All discussions in this paper are therefore well within the limitations of the reliability of the background subtraction models.

Results and Discussions

The results of our measurements of relative (with respect to the C-K edge) cross-sections $(K_{X/C})$ are summarized in Fig. 1 and 2. A 100eV energy window was used for the quantification of all edges. The experimental data are compared throughout with partial cross-section ratios calculated from both the hydrogenic model (i.e., the SIGMAK and SIGMAL2 programs[2] and an atomic model using Hartree-Slater wavefunctions.[3,4] To accommodate the wide range in values of $K_{X/C}$, a logrithmic scale was used in the plots. On such a scale, experimental error bars are well within the dimension of the data points shown in the plots.

Figure 1 is a comparison of the measurements of the K edges of Be, B, C, N, O, Mg, and Si. Of the four different scattering geometries used in this study, we observe the best agreement between the theoretical calculations (both SIGMAK and H-S) and the experimental measurements for the condition α = 0.84 mrad, β = 6.84 mrad (diffraction mode). The worst agreement is for the case α = 3.5 mrad, β = 50 mrad (image mode), with considerable deviation from the theory for Be, B, and O.

From a comparison of the results for identical scattering geometries but in the diffraction (Fig. 1a) and imaging (Fig. 1b) modes it is clear that the SIGMAK (and H-S) values are closer to the former experimental results. It also seems evident from the data that a modest disagreement between experiment and theory exists when the convergence angle is of the same order of magnitude as the collection angle (Fig. 1c), even if the experiment is performed in diffraction mode and a convergence-angle correction is incorporated in the calculations. Finally, if the experiment is to be performed with appropriate sensitivity to the microstructure (i.e., image mode), it seems to be preferable (comparing Figs. 1b and d) to define the collection angle with the use of an objective aperture. It can be argued that a large collection angle is required for accuracy in the retrieval of the single-loss profiles by the Fourier-log deconvolution procedure, but for thin specimens this argument is not relevant and our earlier observation reamins valid. In general, from the results shown in Fig. 1, we can conclude that lens-aberration effects, significant at large collection angles, need to be incorporated in the analysis. This makes comparisons with theory difficult under these scattering conditions.

Our discussion of the L-edges is based on the relative cross section (again $K_{X/C}$) measurements of four elements: Si, Ti, Fe, and Y (Fig. 2). For these four elements, the difference between the diffraction and image modes for the condition α = 0.84 mrad and β = 6.84 mrad is <10%. Apart from the condition where the convergence and collection angles are of the same order of magnitude (α = 3.5 mrad, β = 4.56 mrad, diffraction mode; Fig. 2c), the agreement between the Hartree-Slater theory and experiment is quite good, <20%. However, for Y, the error is considerably larger (50%) throughout for all experimental conditions. This result could arise from the fact that the calculations were carried out only for the L edge. It may be more appropriate to calculate the contributions from the L_3 and L_2 edges separately, scale them in the ratio of 2:1, and add them together.

In conclusion, for EELS microanalysis of light elements (4 < Z < 14) by use of K edges it is important to pay attention to the exact scattering geometry. Best agreement of currently used theoretical models with experiment is observed when the experiment is performed in difffraction mode with the collection angle substantially larger than the convergence angle. Comparisons of experiments carried out in image mode, without the use of an angle defining objective aperture, with theory (hydrogenic or Hartree - Slater), can be erroneous because of lens aberration effects. For L edges, within the limited data presented in this paper we can conclude that convergence corrections incorporated in the theory may be a source of error. Relative cross sections of M edges, absolute cross-section measurements,

and comparisons with low-Z microanalysis by use of a well-characterized ultrathin-window detector from the same set of samples were also measured. This material will be presented in a subsequent paper.

References

1. R. F. Egerton, *SEM/II* 505, 1984.
2. R. F. Egerton, *Ultramicroscopy* 4: 169, 1979; *Proc. EMSA* 39: 198, 1981.
3. R. D. Leapman, P. Rez, and K. L. Mayers, *J. Chem Phys.* 72: 1232, 1980.
4. P. Rez, *Ultramicroscopy* 9: 283, 1982.
5. F. Hofer, *Microsc. Microanal. Microst.* (in press).
6. K. M. Krishnan and C. J. Echer, unpublished results.
7. K. M. Krishnan and C. J. Echer, *Analytical Electron Microscopy--1983*, 99.

8. R. F. Egerton, *EELS in the Electron Microscope*, New York: Plenum Press, 1986.
9. K. M. Krishnan and M. T. Stampfer, *Proc. EMSA* 46: 538, 1988.
10. J. Bentley, G. L. Lehman, and P. S. Sklad, *Xth Int. Cong. Elec. Mic.* 1982, vol. 1, 585.
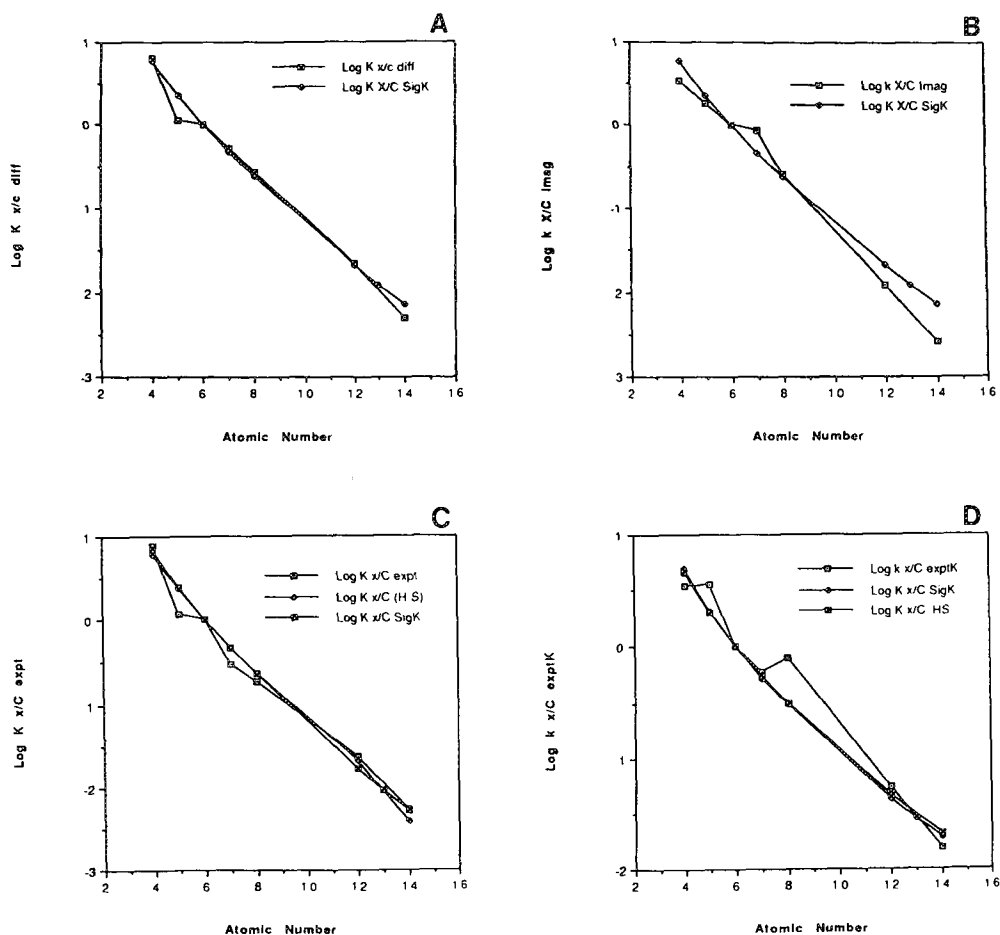
FIG. 1.--Experimentally measured ratios of cross section with respect to C-K. Four different scattering geometries are shown. (a) α = 0.84 mrad, β = 6.84 mrad, diffraction mode; (b) α = 0.84 mrad, β = 6.84 mrad, image mode. In both (a) and (b) results from SIGMAK program are also shown. (c) α = 3.5 mrad, β = 4.56 mrad, diffraction mode; (d) α = 3.5 mrad, β = 50.0 mrad, image mode. In both (d) and (d) theoretical results based on SIGMAK and Hartree-Slater parametrization are also shown for comparison.
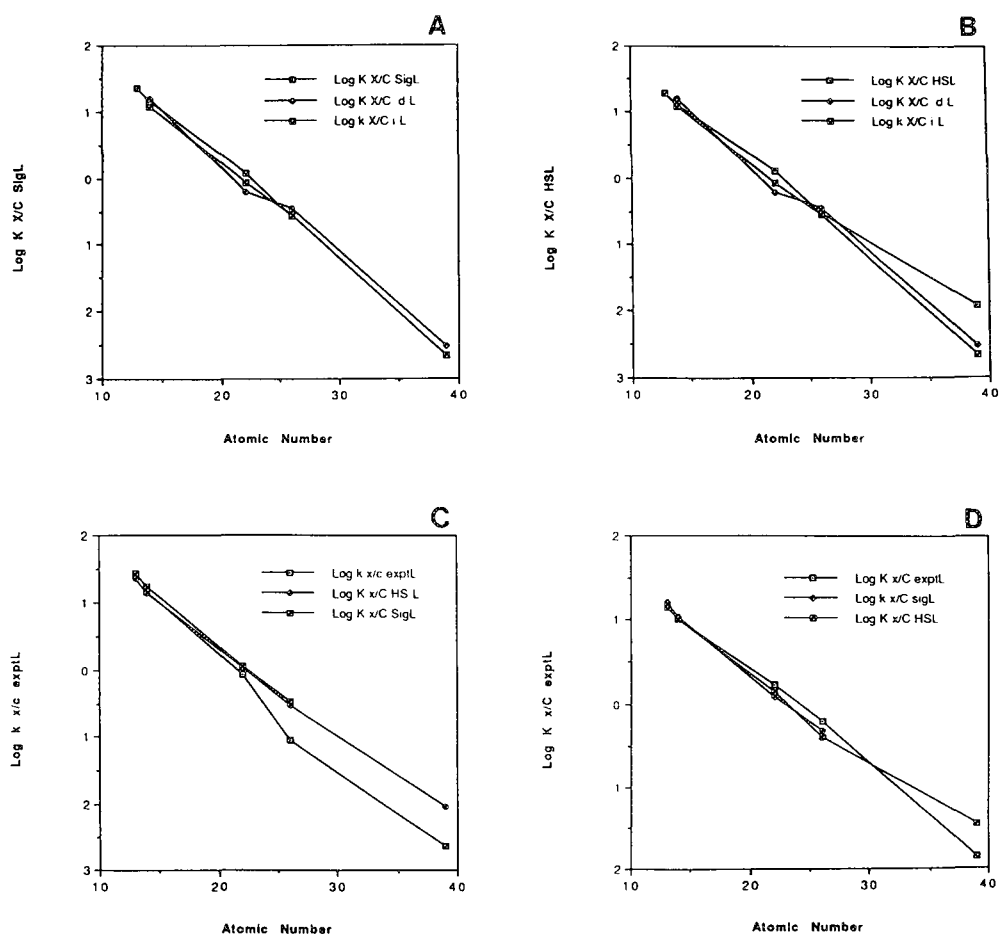
FIG. 2.--Experimentally measured relative cross sections for L edges (normalized with respect to CK edge). (a) Comparison of SIGMAL2 with both diffraction and imaging modes for α = 0.84 mrad, β = 6.84 mrad; (b) Comparison of Hartree-Slater calculations with both diffraction and imaging modes for α = 0.84 mrad, β = 6.84 mrad; (c) α = 3.5 mrad, β = 4.56 mrad, diffraction mode; (d) α = 3.5 mrad, β = 50.0 mrad, image mode. In both (d) and (d), experimental results are compared with SIGMAL2 and Hartree-Slater results.

AUTOMATED QUANTITATIVE ANALYSIS FOR PARALLEL EELS

M. K. Kundmann and O. L. Krivanek

Due to the high data-collection efficiency of parallel-detection electron energy-loss spectroscopy (parallel EELS), it is now possible to acquire rapidly high-quality spectra reflecting the elemental composition of a probed specimen area. Acquisition times of 1-10 s/spectrum for core-edge spectra out to 1000 eV energy-loss and beam currents of 10-100 nA are typical. Unfortunately, the time required to analyze each spectrum and extract the elemental composition is generally much greater; analysis times of 1-10 min/spectrum are common. The main reason for this bottleneck is that conventional spectrum analysis techniques rely heavily on expert judgments on the part of the analyst. We have developed algorithms that minimize the need for operator input and thereby reduce the time (and tedium) of analysis. Our goal is complete automation of EELS data reduction with spectrum analysis rates comparable to parallel EELS spectrum acquisitions times.

Specifications of the Task

The steps involved in EELS spectrum analysis are detailed in several standard texts.[1-3] As a framework for the present discussion, the task can be organized into three phases: (1) recognition and identification of ionization edges present in the spectrum, (2) extraction of the ionization edge signals, and (3) conversion of signal intensities to elemental concentrations (absolute or relative). The focus is on the instrument-independent part of the analysis; i.e., it is assumed that all spectrometer and detector calibrations have already been applied to the spectrum. Thus, automated energy-scale calibration and correction for the detector dark current and channel-to-channel gain variation are not discussed here.

In "traditional" EELS analysis, varying amounts of analyst intervention are involved in each of the above phases. Phase 1 is generally left entirely to the operator; the software at best provides a table of edge threshold energies against which to compare the observed edge thresholds. Phase 2 is concerned with corrections for multiple scattering and the modeling and subtraction of backgrounds to the ionization edges. This phase typically involves iterative interaction between the analyst and the software; e.g., the analyst repeatedly specifies fit windows and judges the accuracy of the background removal, while the software computes and subtracts the background model. Phase 3 involves the computation of ionization cross sections and the division of the extracted edge

---

The authors are with Gatan R&D, 6678 Owens Drive, Pleasanton, CA 94588.

signals by the cross sections to yield elemental concentrations. This phase is the most computation-intensive and accordingly requires the least amount of input from the analyst.

To achieve a higher level of automation, we have constructed algorithms for each of phases 1-3 that perform the tasks heretofore left to the analyst.

Recognition of Edge Thresholds

Recognition and identification of edges present in EELS spectrum is a straightforward task for a trained EELS analyst. By comparison of the energies of the observed ionization edge thresholds with tabulated values, identifications are quickly made. A computer program that carries out such a comparison is not difficult to write. However, it is surprisingly difficult to develop an algorithm to perform the initial task of recognizing and correctly locating the significant edge threshold in an EELS spectrum. Because EELS edges vary greatly in shape and intensity, and because the overall EELS spectrum intensity can vary over several orders of magnitude due to its underlying power-law dependence, it is not a trivial matter to define numerical criteria to characterize all possible edge thresholds.

We have succeeded in developing an edge-recognition and identification algorithm, as described elsewhere.[4] The basic steps of the algorithm are illustrated in Fig. 1. First, the edge signals are accentuated over the background by application of a log-difference transform, Δ_L, to the spectrum S(i). This transform is based on the logarithmic derivative $d(\ln S)/dE = (1/S)dS/dE$, and is defined as follows:

$$\Delta_L\{S(i)\} = [S(i + \Delta i) - S(i - \Delta i)]/S(i)$$

where i is the spectrum channel number and Δi represents a channel offset. The use and benefits of difference transforms for EELS analysis have been extensively described by others.[5,8]

Next, we remove any residual background by passing the transformed spectrum through a strong smoothing filter and subtracting the smoothed result from the log-difference spectrum (Fig. 1c). A special advantage of the log-difference transform is that it tends to compress the large dynamic range of EELS data while keeping the RMS noise fairly constant throughout the transformed spectrum. These characteristics make it possible to pick out the significant spectrum features in the background-subtracted difference spectrum by means of a straightforward statistical analysis.[4] Finally, the first peak in each highlighted range is interpreted as the edge threshold.
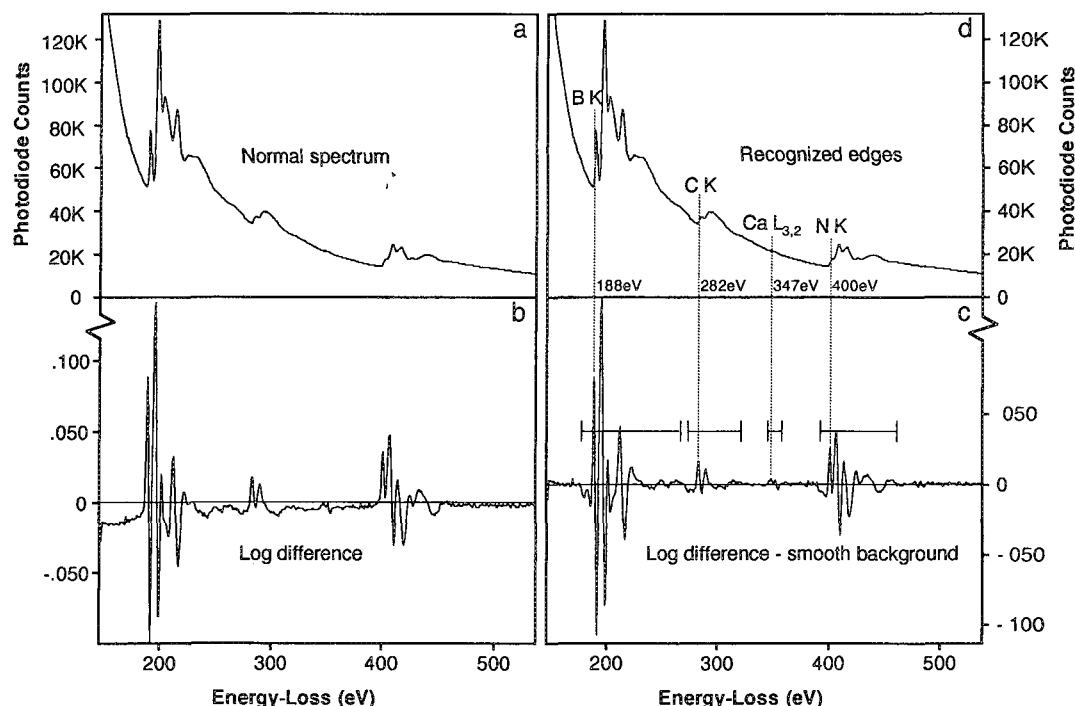
FIG. 1.--Illustration of edge-detection and identification algorithm.

Thresholds of overlapping edges are detected by an abrupt increase in the intensity of peaks within a highlighted interval (Fig. 2). The detected edges are subsequently identified by comparison of their measured threshold to tabulated values.[9,10]

The edge-recognition algorithm eliminates the need for operator input during this initial phase of EELS spectrum analysis. Although the algorithm, in its current implementation, misidentifies 5-10% of the edges it detects, such an error can be caught and corrected by the analyst during a postanalysis assessment of the results. Indeed, the edge-detection sensitivity of the algorithm can often be higher than that of an unsuspecting analyst. The weak but significant Ca $L_{2,3}$ edge in the spectrum of Fig. 1 went unnoticed until the edge-recognition routine identified it during a test run.

Extraction of Edge Signals

Once the significant edge thresholds in a spectrum have been located and identified, it is normally a straightforward task to fit a power-law to the pre-edge background, extrapolate it underneath the edge, and subtract it. The task of choosing an appropriate fit window is usually left to the analyst, because it is important to choose a part of the pre-edge background that is not affected by fine structure from a preceding edge nor by the finite' energy resolution tail of the edge of interest. However, with the information provided by the edge-recognition algorithm, a suitable fit window can be chosen automatically. The main function of the edge-recognition algorithm is to determine which parts of the spectrum display significant edge fine structure. It also

recognizes when the fine structure of two edges runs together. Thus, by passing this information on to the edge extraction algorithm, one can choose background fit windows to avoid
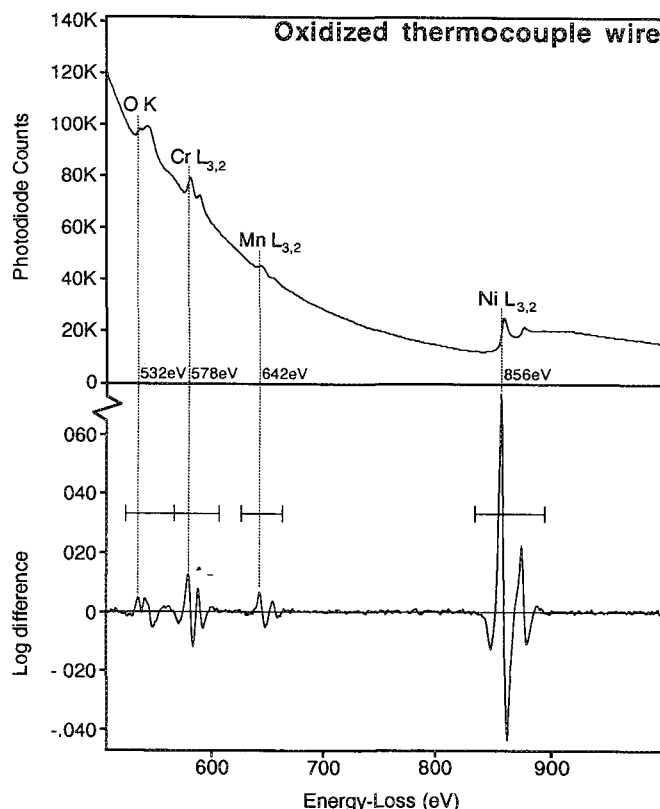

FIG. 2.--Illustration of edge-recognition algorithm's ability to resolve overlapping edges.

264

regions of edge fine structure so that an accurate power-law model is obtained.

This approach to edge extraction fails when two edges are too close together and the fine structure of one overlaps the threshold of the next. The only correct way to handle such a case is to use edge profiles measured from standards either to separate the overlapping edges or to attempt some form of least-squares fitting.[5,6,11] Our automated algorithm cannot currently handle such a case. However, it can recognize such cases and skip the quantification of such edges, rather than blindly attempting background subtraction and generating spurious results.

Conversion to Elemental Composition

The conversion to elemental composition requires the calculation of the appropriate partial ionization cross sections so that the extracted edge intensities may be converted to atomic concentrations. The standard routines for computing these cross sections are Egerton's SIGMAK and SIGMAL, which are based on a hydrogenic model and are readily available.[1] The data needed for the calculation are beam energy and collection angle in effect at the time of the data acquisition and the specification of suitable integration windows. The two experimental parameters can be entered by the analyst at the beginning of the data collection session and can then be automatically stored with each acquired spectrum. It is a trivial matter to give the analysis routine access to these stored data. As for the integration windows, the results of the edge-recognition algorithm once again prove useful. Since it has already identified the edge regions with significant structure and has ascertained the points of edge overlap, its output can be used to make intelligent choices for the integration windows, i.e., choices that will be large enough to integrate through the fine structure of the edge but not so large as to include erroneously counts from subsequent overlapping edges. Thus, all in-
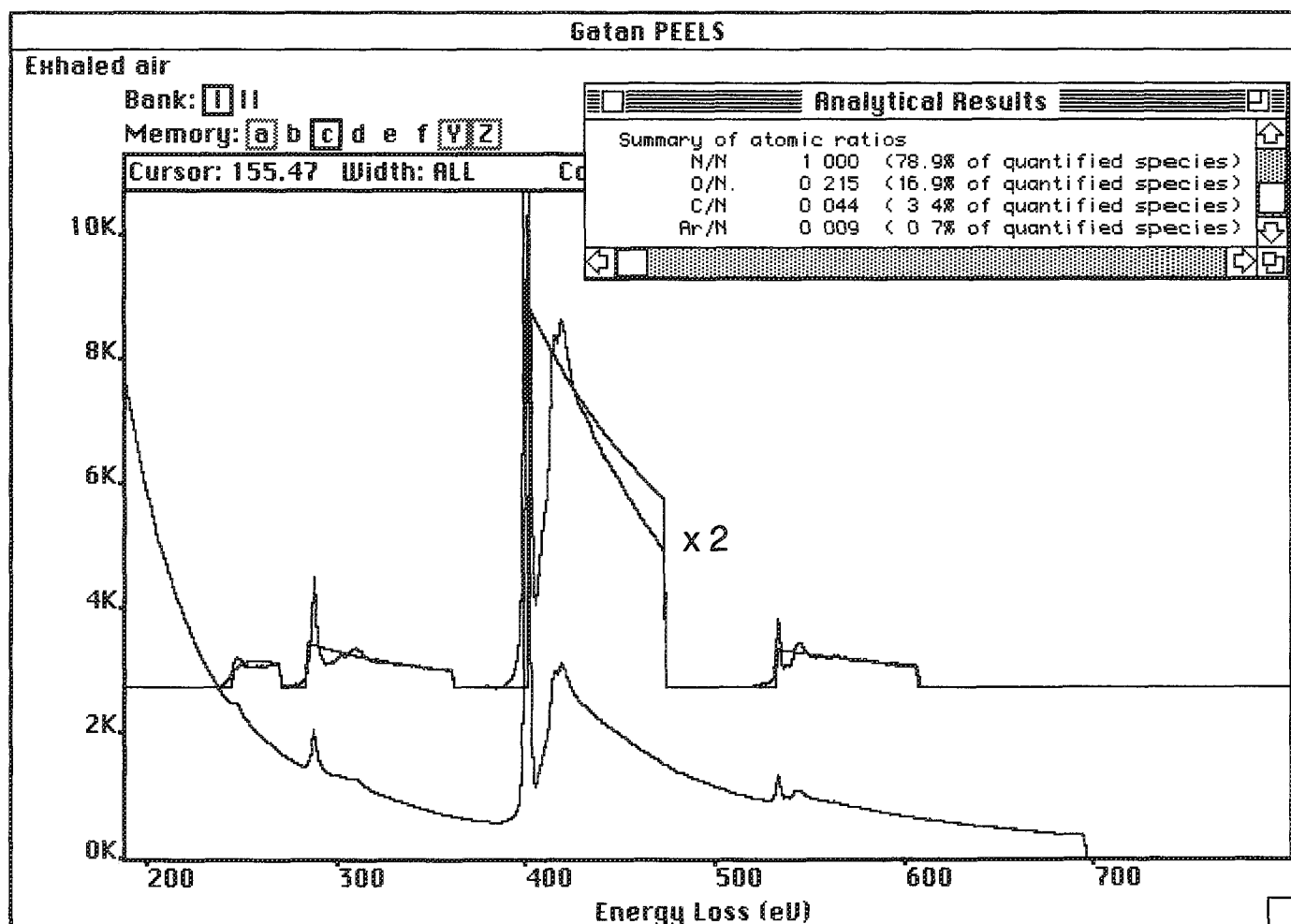
FIG. 3.--Results of automated analysis of parallel EELS spectrum from air sample exhaled into environmental cell. Extracted edges and calculated hydrogenic differential cross-section profiles are displayed with expanded and offset vertical scale.

formation necessary for the final data reduction step can be obtained by the algorithm without involving the analyst.

Examples and Discussion

A program that combines all the above techniques into a single automated routine has been developed for the Apple Macintosh II family of computers. It has been implemented as a single menu item labeled "Quantify Spectrum" in Gatan's parallel EELS acquisition and analysis program, EL/P. Figures 3 and 4 give the results obtained by the routine when applied to two typical spectra. Each spectrum was analyzed without analyst intervention once "Quantify Spectrum" was selected. The total time for each analysis was about 5 s.

Several of the advantages and disadvantages of the fully automated algorithm are demonstrated in these two examples. In both cases, the sensitivity of the routine is shown by its ability to extract and quantify even fairly weak edges. Both the Ar $L_{2,3}$ edge of the air sample and the Mn $L_{2,3}$ edge of the thermocouple sample were properly treated, even though they

reflect only about 1% atomic concentration. Certainly, the ability to do a complete spectrum analysis in only 5 s is also an advantage. One disadvantage of the algorithm is that it cannot properly handle overlapping edges, as indicated by the lack of a quantitative result for the Cr $L_{2,3}$ edge of the thermocouple sample, despite its clear presence in the spectrum. A further disadvantage of the routine is that it currently provides no estimates of the uncertainties in the results obtained. This is a very important feature that will have to be added to the algorithm, precisely because of its convenience. Assessment of the reliability of the computed results must still rely on a critical evaluation of the output on the part of the analyst. For example, although the computed partial cross-section profiles generally match the measured edge profiles quite well, for the N K edge of the air sample, the match is rather poor. To a trained EELS analyst, this feature immediately indicates that the error in the computed N K concentration can potentially be quite large. However, the algorithm currently makes
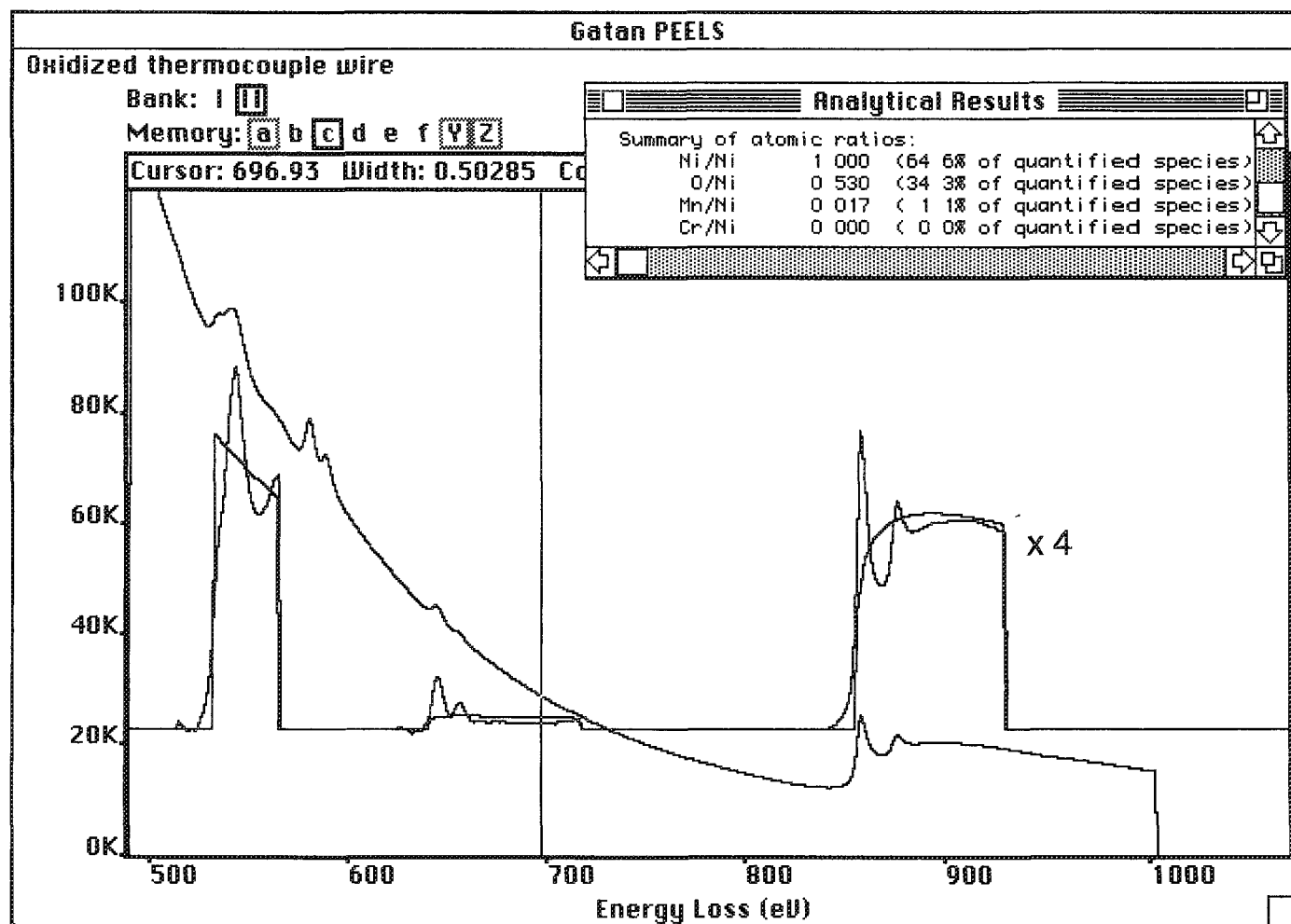

FIG. 4.--Results of automated analysis of parallel EELS spectrum from oxidized thermocouple wire sample. Extracted edges and calculated hydrogenic differential cross-section profiles are displayed with expanded and offset vertical scale.

no distinction between good and poor matches between the measured and calculated edge profiles.

Conclusion

We have developed an algorithm which, for straightforward cases involving no edge overlap, can carry out the reduction of EELS spectra to elemental concentrations without interruption for analyst input. Although the accuracy of the analysis must still be judged by the analyst, the tedious spectrum manipulations inherent to EELS analysis can now be carried out in less than 10 s/spectrum. However, assessment of the accuracy of the results still presents a considerable challenge to full automation of EELS data reduction.

References

1. R. F. Egerton, *EELS in the Electron Microscope*, New York: Plenum Press, 1986, ch. 4.
2. D. B. Williams, *Practical Analytical Electron Microscopy in Materials Science*, Mahwah, N.J.: Phillips Electronic Instruments, 1984, ch. 5.
3. D. C. Joy, in D. C. Loy, A. D. Romig, and J. I. Goldstein, Eds., *Principles of Analytical Electron Microscopy*, New York: Plenum Press, 1986, ch. 8.
4. M. K. Kundmann and O. L. Krivanek, *J. Microscopy, Microanalysis, and Microstructure* (in press).
5. H. Shuman, P. Kruit, and A. P. Somlyo, *Microbeam Analysis--1983*, 247.
6. H. Shuman and P. Kruit, *Rev. Sci. Inst.* 56: 231, 1985.
7. N. J. Zaluzec, *Ultramicroscopy* 18: 185, 1985.
8. N. J. Zaluzec, *Analytical Electron Microscopy--1987*, 275.
9. C. C. Ahn and O. L. Krivanek, *EELS Atlas*, Warrendale, Pa.: Gatan, 1983.
10. J. A. Bearden and A. F. Burr, *Rev. Mod. Phys.* 39: 125, 1967.
11. R. D. Leapman and J. A. Hunt, *J. Microscopy, Microanalysis, and Microstructure* (in press).

RESOLUTION, DETECTABILITY LIMITS, AND THICKNESS EFFECTS IN PARALLEL EELS IMAGING

Gianluigi Botton and Gilles L'Espérance

There has been a growing interest for EELS imaging since the commercial availability of parallel EELS (PEELS) systems due to the fast acquisition times and the high resolution inherent to energy loss spectroscopy. Problems in the quantification of imaging data have already been the subject of a study concerning short acquisition times, crystallographic effects, and electron optics.[1] The aim of this paper is to investigate the trade-off between detectability limits, and therefore quantification errors, and resolution when elements of different atomic number are imaged in a map. The effect of thickness is also shown to limit the range of applicability of the imaging method when simple extraction methods are used.

The configuration of the imaging system is described here briefly. A Gatan PEELS is coupled to a CM30 (S)TEM electron microscope; the control of the spectrometer and microscope is performed through a LINK AN10-85S MCA, which is interfaced to a IBM RT 125 via a DR11W line. Data acquired at each pixel are transferred in packets to the RT computer for processing and storage. A NiO thin film with multiple layers and BN flakes on a carbon film were used for the signal-to-noise ratio (SNR) measurements. Spectra were acquired in STEM mode at one fixed position on areas of the two samples of comparable t/λ. Statistical analysis was carried out on spectra containing the B_K and N_K edges for the Q_K and Ni_L edges for the NiO sample. The extrapolation and integration windows were 50 and 80 eV, respectively. Signal extraction and SNR calculations were carried out on the RT computer by use of maximum likelihood estimators.[2] Quantification errors were calculated by the methods described in Ref. 3. For imaging or line scan acquisitions, careful alignment of the microscope "descan" mode (post specimen de-scanning coils in the CM30) was performed in order to avoid shifting of the spectra during the scan at a magnification of 10 000×.
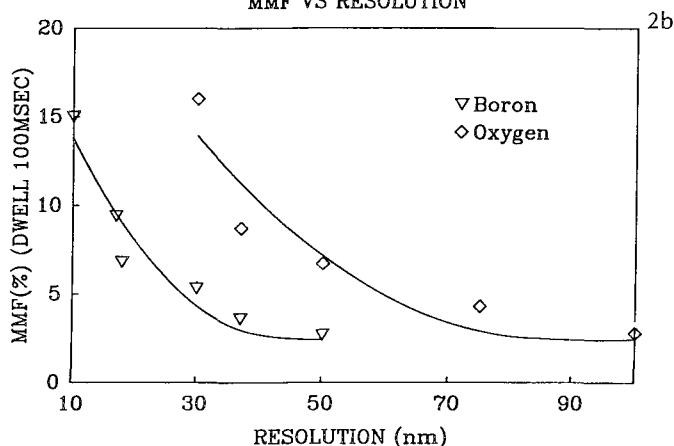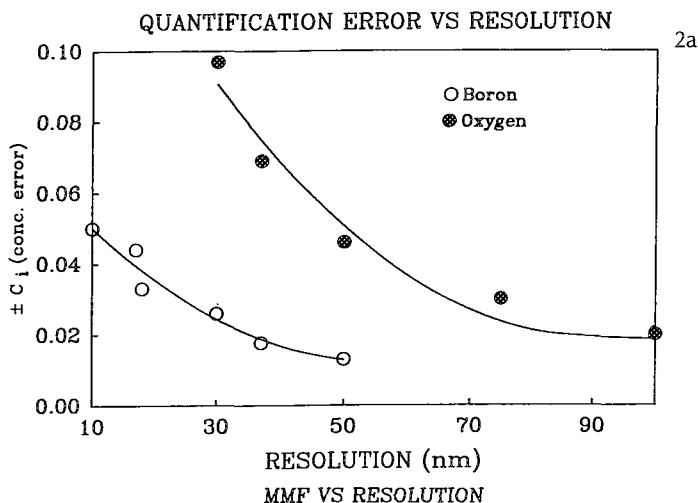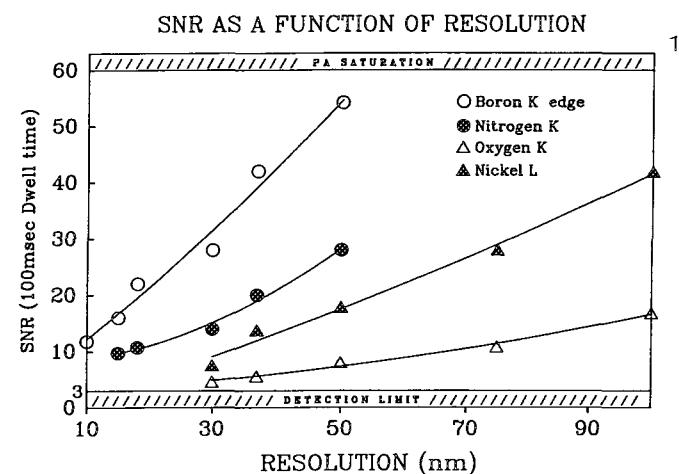
Second difference spectra line scans were acquired by successive line scans shifted in energy. Resolution conditions were varied by changes of spot size and the resolution was measured by the size of the probe in STEM mode with a sharp edge. The effect of collection angle on beam broadening and delocalization

effects were not considered in this work.

For a 100ms dwell time, which would be typical for image acquisitions, the SNR for various edges studied as a function of decreasing probe size (and therefore improved resolution) decreases (Fig. 1). This approach implies that under imaging conditions, and particularly when multiple elements are studied simultaneously, the detectability limits for these elements are substantially different and, for the same minimum mass fraction level required, resolution conditions change accordingly. For PEELS imaging, due to the level of saturation of the photodiode array (PA), an upper limit to the SNR appears for edges at low energies such as B_K (in BN) (Fig. 1). As a consequence, the N_K edge of Bn acquired simultaneously has a lower SNR limit (Fig. 1) than in the case where the N_K would have been the only edge of interest. Ranges of detectability limits in PEELS imaging therefore depend not only on the energy studied but also on the energy range relevant to the image acquisition. Concentration errors and minimum mass fraction (MMF) are high, yet better than expected from EDS mapping of light elements (Fig. 2)[4] and thus depend on acquisition conditions. Statistical analysis in quantitative mapping has to be carried out for each image acquisition condition and cannot be based solely on beam intensity and dwell time.

An effect that should be considered in the interpretation of EELS images is the thickness variation in the rastered area, since quantification by ratios is affected by thickness.[5] In order to show effects due to thickness and not statistical fluctuations, line scans were used. For 256 pixels line scans of 100 and 600ms dwell times and for samples with $t/\lambda <$ 1.3, variations of the O/Ni ratio in the NiO film, where multiple layers are found, are not discernible from statistical fluctuations. In a 1000ms dwell line scan in which the concentration error is 0.04, significant variations on the ratio are present and are related to changes in t/λ line scan (Fig. 3). The effect begins to be visible at $t/\lambda > 1.5$. For areas of $t/\lambda > 2$, background extraction fails and results cannot be interpreted (Fig. 3). An imaging system should therefore allow the monitoring of the process of signal extraction in order to identify areas of potential problems. Although in this particular case the effect shown is extreme, due to maximum $t/\lambda > 4$, in typical materials science samples variations will have to be interpreted with the help of t/λ maps acquired with the imaging system (Fig. 4). A possible method of eliminating the thickness effect is the acquisition of "difference" spectra and processing with spec-

SNR AS A FUNCTION OF RESOLUTION

QUANTIFICATION ERROR VS RESOLUTION

MMF VS RESOLUTION

EFFECT OF THICKNESS ON SIMPLE QUANTIFICATION OF IMAGING DATA

FIG. 3.--Effect of thickness on quantification of 256-pixel line scans: (a) $I(O_K)/I(Ni_L)$ 1000 ms, (b) t/λ for same area.

FIG. 1.--SNR of B_K, N_K, O_K, and Ni_L as function of resolution. Dwell time 100 ms.
FIG. 2.--Quantification errors: (a) error on concentration, (b) MMF.

tra containing multiple scattering contributions.[6,7] Although in principle the technique should account for thickness variations, our preliminary work on second-difference line scans has shown that for short acquisitions times (100 ms) and appropriate imaging conditions, second-difference spectra contain a significant noise level. The use of this acquisition technique for imaging can be therefore used only when appropriate statistical analysis is developed in order to extract the signal and evaluate quantification errors.

Finally, resolution in PEELS imaging may be influenced by the time-dependent detector response as the charge in the PA is not completely cleared out by the reading process when the detector is cooled. In regions where changes in intensity are important, a fraction of the charge of the previous pixel is accumulated at the readout and might therefore affect the resolution. Appropriate calibration of the time response of the detector and particular data processing can be implemented in order to reduce this effect.

As parallel EELS imaging becomes a new tool in AEM, quantification of data has to be carried out with appropriate statistical analysis in order to evaluate the limits of the technique in terms of quantification and resolution which depend not only on the analytical technique but also on the characteristics of the sample, the detection system, and the

269

FIG. 4.--t/λ map of aluminum-alloy thin foil with precipitates.

particular imaging conditions chosen.

References

1. G. Botton, G. L'Espérance, M. D. Ball, and C. F. Gallerneault, *Proc. XII ICEM*, 1990, vol. 2, p. 36.

2. M. Unser, J. R. Ellis, T. Pun, and M. Eden, *J. Microscopy* 5: 145, 1987.

3. P. Trebbia, *Ultramicroscopy* 24: 399, 1988.

4. G. L'Espérance, G. Botton, and M. Caron, *Microbeam Analysis--1990*, 284.

5. N. Zaluzec, *Proc. 41st Ann. Meet. EMSA*, 1983, 388.

6. H. Shuman and A. P. Somlyo, *Ultramicroscopy* 26: 393, 1988.

7. R. D. Leapman and C. R. Swyt, *Microbeam Analysis--1988*, 89.

THE ROLES OF SPUTTERING AND DISPLACEMENT DAMAGE IN ELECTRON IRRADIATION INDUCED MASS LOSS

D. L. Medlin and D. G. Howitt

Intense electron beams have been observed to cut holes in thin film samples in two distinct ways. In the first place, a pit develops at one or more surfaces and grows inward; in the second, the surfaces remain intact and void coalescence ultimately produces the penetration. The behavior in both cases can be described and predicted from an understanding of primary radiation damage mechanisms.

The radiation damage of thin gold foils was extensively studied by Cherns et al., who distinguished between sputtering at the electron exit surface and conventional displacement damage and subthreshold damage in the interior.[1] Similar observations regarding a subthreshold effect were also made by Urban in studies of lead, and it is clear that the mechanism involves the displacement of atoms into adjacent vacancies.[2] Hence, such subthreshold, or vacancy enhanced, displacements should require an energy comparable to the vacancy migration energy, which in metals is generally less than 1 eV.[3] In addition, the displacement distance should be one atomic spacing. It is the relative contributions of sputtering at the surface and subthreshold displacements in the interior that determine the mode of specimen damage.

These effects can be simulated numerically by solving flux equations which balance the rates of sputtering and bulk displacement within the sample. When sputtering is dominant, one expects a uniform thinning of the foil from the electron exit surface. This case is calculated in Fig. 1 for a material in which the sputtering cross section is ten times larger than that for internal displacement. Alternatively, if subthreshold displacements dominate over sputtering, vacancies created at the surface will be injected into the bulk where they can coalesce to form internal voids. This second case is illustrated in Fig. 2 for a material with a sputtering cross section only one-tenth of that for internal displacement.

References

1. D. Cherns, M. W. Finnis, and M. D. Matthews, "Sputtering of gold foils in a high voltage electron microscope: A comparison of theory and experiment," *Phil. Mag.* 35: 693, 1977.
2. K. Urban, "A study of athermal point defect migration at low temperatures by means of HVEM," in P. R. Swann, C. J. Humphreys, and M. J. Goringe, Eds., *High Voltage Electron Microscopy: Proc. 3rd Intern. Conf.*, London: Academic Press, 1974, 356.
3. J. P. Stark, *Solid State Diffusion*, New York: Wiley, 1976, 92.

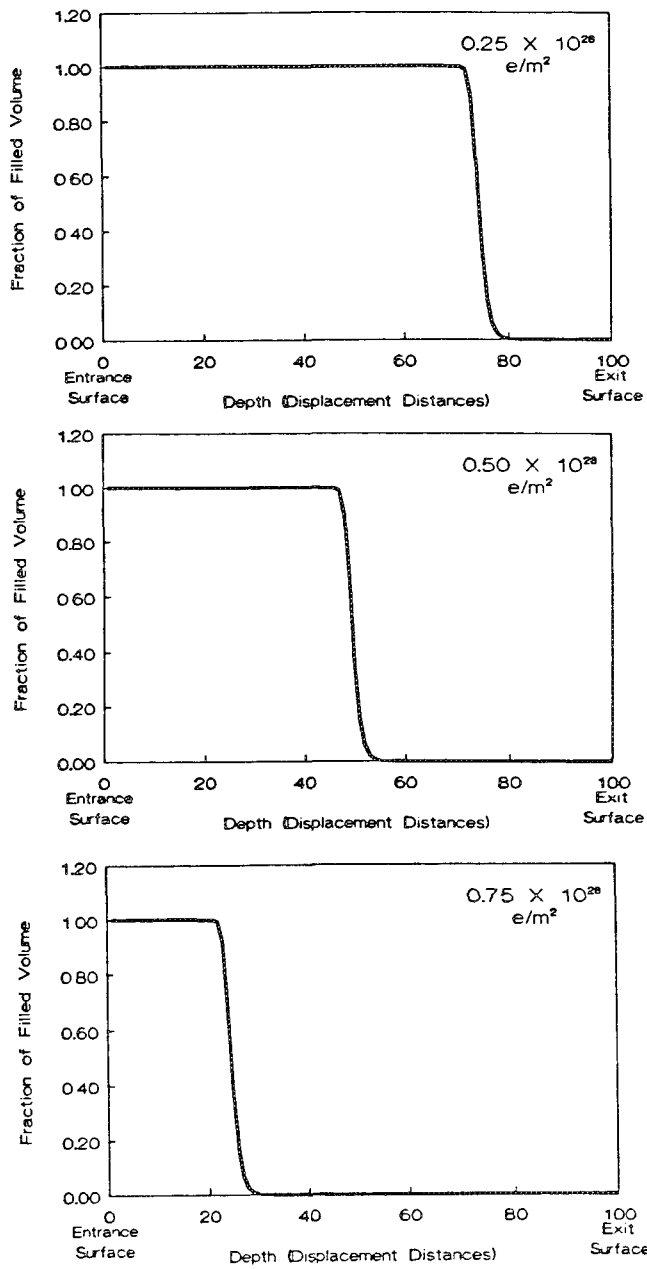FIG. 1.--Density profiles for material in which sputtering dominates, calculated at increasing levels of electron fluence. Sputtering cross section: 100×10^{-28} m^2. Displacement cross section: 10×10^{-28} m^2.
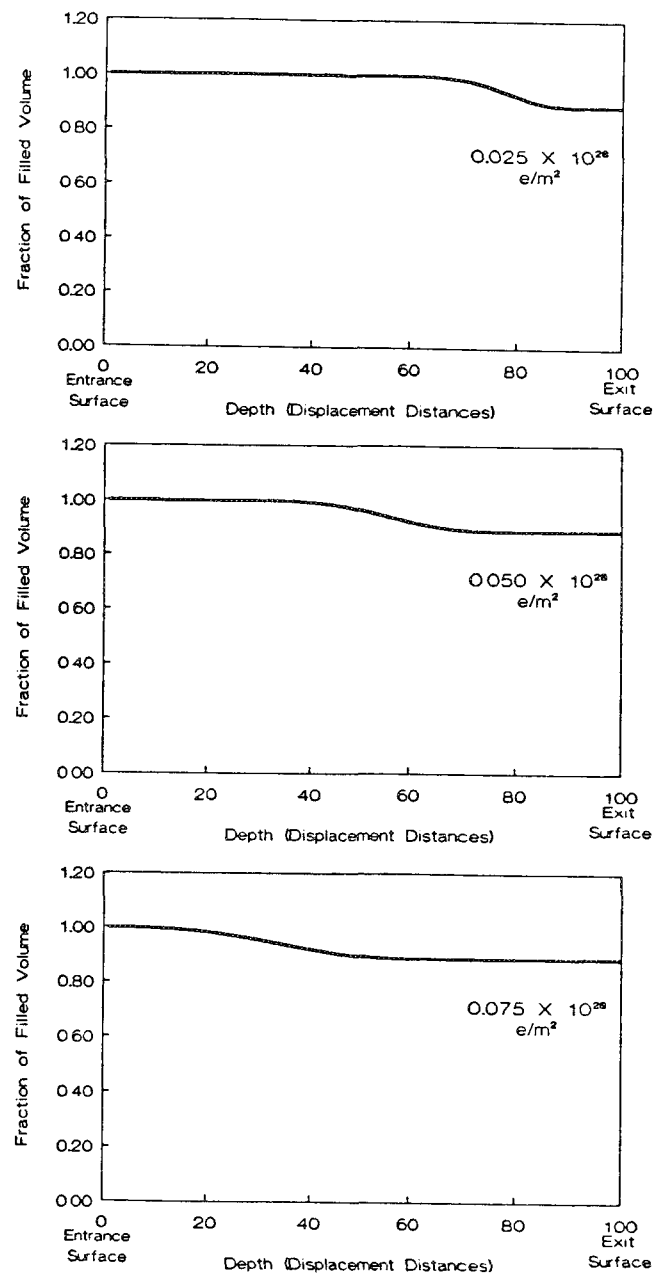
FIG. 2.--Density profiles for material in which internal displacements dominate. Sputtering cross section: 100×10^{-28} m^2. Displacements cross section: 1000×10^{-28} m^2.

EXELFS ANALYSIS OF Al K, Fe L_{23}, and Pd M_{45} EDGES

J. K. Okomoto, C. C. Ahn, and B. Fultz

Extended energy-loss fine structure (EXELFS) occurs above all the ionization edges in a condensed matter sample, but the analysis of EXELFS is usually performed only for K-edge data. The K edge data are simple to analyze because they correspond to transitions from 1s core states to only those unbound final states with p symmetry (assuming the dipole selection rule holds, as is typical in these cases). The L and M edge data, on the other hand, are complicated by the variety of possible initial and final angular momentum states. The L edges, for instance, have both 2s and 2p initial states, and transitions from the 2p initial states can result in final states with either s or d symmetry. In this paper we show that, in spite of the variety of possible transitions, useful EXELFS information can be extracted from L and M edges. In particular, we show that information about static and thermal disorder in the first nearest neighbor (1nn) shell can be obtained from Fe L_{23} and Pd M_{45} EXELFS data. In addition, we show that reasonable 1nn distances can be derived from the Fe L_{23} edge data.

Experimental Data

Thin metal samples were prepared by electropolishing pure foils of Al, Fe, and Pd. The spectra were collected with a Gatan 666 parallel detection magnetic prism spectrometer attached to a Phillips EM 430 electron microscope. Data was taken using 200 keV electrons at sample temperatures ranging from 96 K to 423 K. The illuminated sample areas had diameters of a few to several microns, and appeared thin enough so that plural scattering did not drastically alter the edge shape. Beam current fluxes ranged approximately from 0.01 to 0.1 A/cm^2. Collection angles were 12 mrad for the Al K and Pd M_{45} data, and 2 mrad for the Fe L_{23} data. To reduce channel-to-channel variations in the parallel detection system, each spectrum was gain-averaged over many data channels.[1] Cubic spline fits were used to isolate the EXELFS oscillations. The EXELFS data were normalized with the edge jump heights, and theoretically calculated differential cross sections were used to correct

for the basic nonoscillatory edge shapes. The experimental EXELFS data from the Al K, the F Le_{23}, and the Pd M_{45} edges are shown in Fig. 1, along with their Fourier transforms.

Theoretical Calculations

The electron scattering cross sections in the figures throughout this paper are calculated according to Bethe theory.[2] Atomic Hartree-Slater wave functions from the algorithm of Herman and Skillman[3] are used as the initial states. The final states are continuum states with the free electron density of states.[4] The collection angles chosen correspond to the conditions under which the experimental data were acquired. All the calculations ignore spin-orbit splitting.

Let ℓ_0 be the angular momentum quantum number for the core state of the ionized electron: $\ell_0 = 0$ for K, L_1, and M_1 edges; $\ell_0 = 1$ for L_{23} and M_{23} edges; $\ell_0 = 2$ for M_{45} edges. K edges correspond to transitions from 1s core states. Non-dipole transitions are not strictly forbidden in EELS because of the finite momentum transfer in the electron scattering. Nevertheless, Fig. 2 shows that in the region of the experimental EXELFS the dipole allowed 1s to p transition dominates in the Al K edge by a factor of over 100. It is thus a very good approximation to assume that the final state of the ionized electron is an outgoing p wave.

Consider the EXELFS analysis of the Fe L_{23} edge. The spin-orbit splitting between the L_3 and L_2 edges of about 13 eV can be neglected because it is small compared with the spacing between the EXELFS maxima far above the ionization threshold energy, and EXELFS oscillations from L_3 and L_2 edges will be in phase in this energy range. The presence of the Fe L_1 edge can complicate the analysis of the Fe L_{23} EXELFS for two reasons. First, the L_1 edge jump overlaps with the L_{23} EXELFS signal. This problem can be eliminated by using only L_{23} EXELFS data sufficiently past the L_1 edge jump. Second, the L_1 EXELFS overlaps with the L_{23} EXELFS. However, as shown in Fig. 3, the differential cross section of the Fe L_1 edge in the region of interest is about 4 times smaller than that of the Fe L_{23} edge. Moreover, transformation of the data from energy-loss space to the k space corresponding to the L_{23} edge effectively raises the frequencies of the L_1 EXELFS oscillations, and furthermore makes them incoherent. Figure 4 shows the Fourier transform (FT) of the theoretical L_1 EXELFS signal from the 1nn shell in Fe metal after being mapped to the k space of the L_{23} edge, and compares it with the FT of the theoretical 1nn shell Fe L_{23} EXELFS. The 1nn shell L_1 EXELFS was weighted by a factor of 1/4 to take into
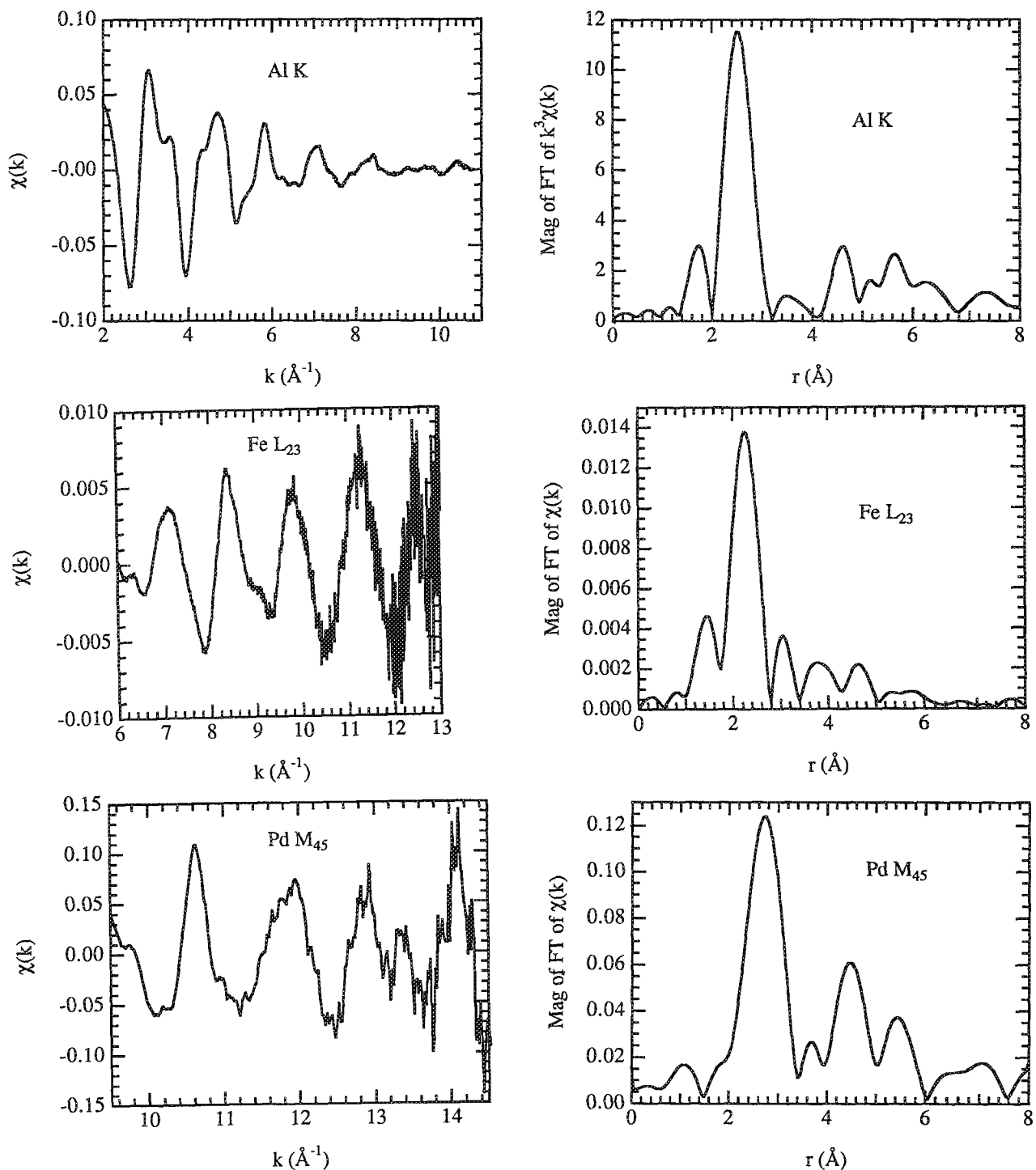
FIG. 1.--$\chi(k)$ from Al K, Fe L_{23}, and Pd M_{45} edges. Also shown are Fourier transforms of $k^3\chi(k)$ for Al K $(2.5 < k < 10.0 \text{ Å}^{-1})$, $\chi(k)$ for Fe L_{23} $(6.5 < k < 12.5 \text{ Å}^{-1})$, and $\chi(k)$ for Pd M_{45} $(9.8 < k < 14.2 \text{ Å}^{-1})$. Ends of windows in k-space smoothed with Gaussian lineshapes. Data taken from samples at 97 K.

account the smaller differential cross section of the L_1 edge. We see that the L_1 EXELFS should not greatly affect the lnn shell L_{23} EXELFS signal, although it may significantly distort the more distant neighboring shells.

Having dealt with the complications arising from the presence of different initial states in the Fe L edge, we now consider the variety of final states possible in transitions from the 2p core state. Figure 5 contains calculated partial differential cross sections for the excitation of 2p electrons in Fe into final states of s, p, d, or f character. We see that, in the EXELFS region, the 2p to d transition dominates over the sum of all others by a factor of about 25. This domination of the

274

2

3

4

5

6

7
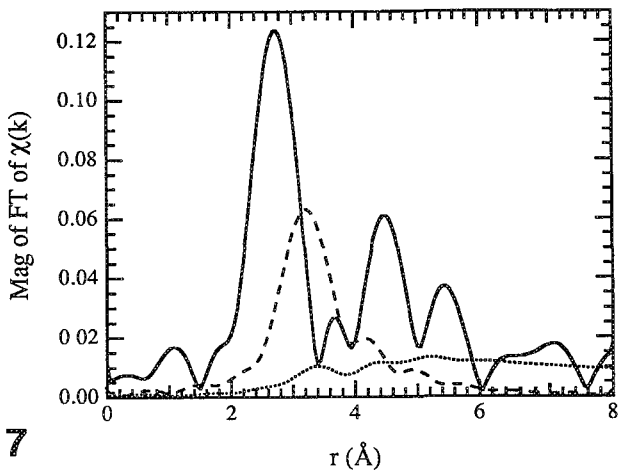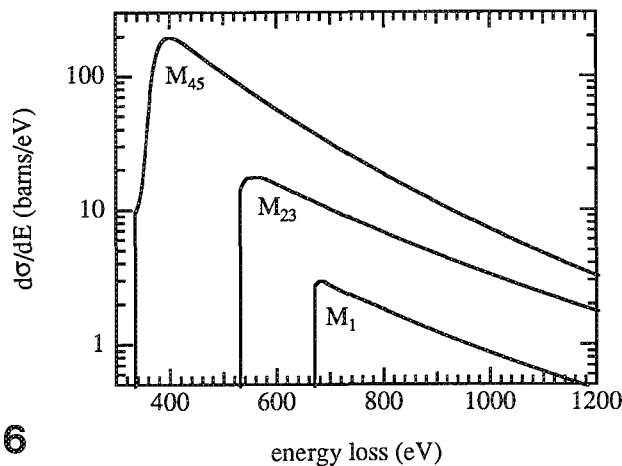
FIG. 2.--Partial differential cross sections for the excitation of 1s electrons in Al. Numbers correspond to orbital angular quantum numbers of unbound final states.

FIG. 3.--Differential cross sections for L_{23} and L_1 edges in Fe.

FIG. 4.--Magnitude of FT of $\chi(k)$ for theoretical 1nn shell L_{23} (solid line) and L_1 (dashed line) EXELFS signals.

FIG. 5.--Partial differential cross section for the excitation of 2p electrons in Fe. Numbers are orbital angular quantum numbers of final states.

FIG. 6.--Differential cross sections for M_{45}, M_{23}, and M_1 edges.

FIG. 7.--Magnitude of FT of $\chi(k)$ for theoretical 1nn shell M_{23} (dashed line) and M_1 (dotted line) EXELFS. FT of experimental M_{45} $\chi(k)$ (solid line) is shown for comparison.

2p to d transition makes possible the interpretation of the 1nn shell Fe L_{23} EXELFS using a generalization of the standard planeware EXAFS equation for polycrystalline samples:

$$\chi(k) = \frac{Nf(k)}{kR^2} \exp(-2R/\lambda) \exp(-2\sigma^2 k^2)$$

$$\cdot \sin[2kR + 2\delta_2(k) + \eta(k)] \qquad (1)$$

N is the number of atoms in the 1nn shell a distance R from the central atom; the sine term reflects the periodic interference between outgoing and backscattered waves; f(k) is the backscattering amplitude per 1nn atom, and $\eta(k)$ is the backscattering phase shift; $\delta_2(k)$ is the central atom phase shift for an outgoing d wave. The factor $\exp(-2R/\lambda)$ is a phenomenological term to account for the finite lifetime of the excited state, where λ is the mean free path of the photoelectron. Finally, the term $\exp(-2\sigma^2 k^2)$ is a Debye-Waller type factor due to vibrations between atoms where σ^2 is the mean-square relative displacement (MSRD) between the central atom and an atom in the 1nn shell. From Eq. (1) we see that the theoretical shift of the 1nn peak in the FT of the Fe L_{23} EXELFS can be determined simply from k dependence of the phase shifts due to the interaction between the outgoing d-like electron wave with the central and neighboring atom potentials.

The EXELFS analysis of the Pd M_{45} edge follows closely that of the Fe L_{23} edge. The spin-orbit splitting between the M_5 and M_4 edges of about 5 eV is ignored because it is much smaller than the spacing between the EXELFS maxima far above the edge onset energy. The M_{23} and M_1 edge jumps are removed from the M_{45} EXELFS signal by transformation of data only sufficiently past the M_1 edge jump. Figure 6 shows the differential cross sections of the Pd M_{45}, M_{23}, M_1 edges. In the experimental EXELFS region, the differential cross section

of the Pd M_{45} edge is apparently about twice as large as that of the Pd M_{23} edge and about 8 times as large as that of the Pd M_{23} edge. Figure 7 contains the FT of the theoretical M_{23} and M_1 EXELFS signal from the 1nn shell in Pd metal after being mapped to the k space of the M_{45} edge, and compares them with the FT of the experimental Pd M_{45} EXELFS. To make the comparison reasonable, the theoretical 1nn shell EXELFS from the Pd M_{23} edge was weighted such that its magnitude was roughly 1/2 that of the experimental 1nn shell PD M_{45} EXELFS. The theoretical 1nn shell EXELFS from the M_1 edge was weighted by a factor of 1/4 with respect to the theoretical 1nn shell EXELFS from the M_{23} edge. We see that the presence of the M_1 EXELFS affects primarily the data beyond the 1nn shell. The 1nn shell M_{23} EXELFS, on the other hand, overlaps in frequencies with the 1nn shell M_{45} EXELFS. This feature probably precludes the reliable determination of 1nn shell distances from Pd M_{45} EXELFS. However, it is still reasonable to determine changes in the statis or thermal disorder from the damping of the 1nn shell Pd M_{45} EXELFS signal.

Although the interference from the M_{23} EXELFS probably precludes the quantitative determination of 1nn distances from Pd M_{45} EXELFS data, nevertheless, for completeness, Fig. 8 contains the calculated partial cross sections for the excitation 3d electrons in Pd into final states of various angular momentum. The 3d to f transition is seen to dominate over the sum of all others by a factor of about 20.

Comparison Between Experiment and Theory

By comparing the FTs of the Al K and Fe L_{23} data in Fig. 1 with FTs of *ab initio* planewave calculations,[5] 1nn distances are found in Al and Fe which agree with x-ray diffraction results[6] to within ±0.05 Å. The uncertainty in the proper choice of edge onset energy E_0 con-

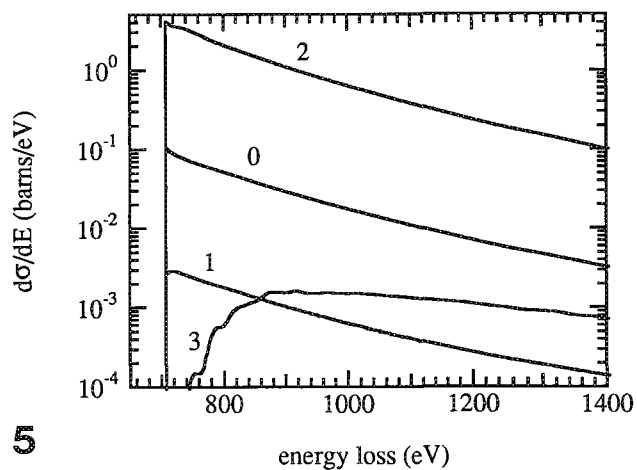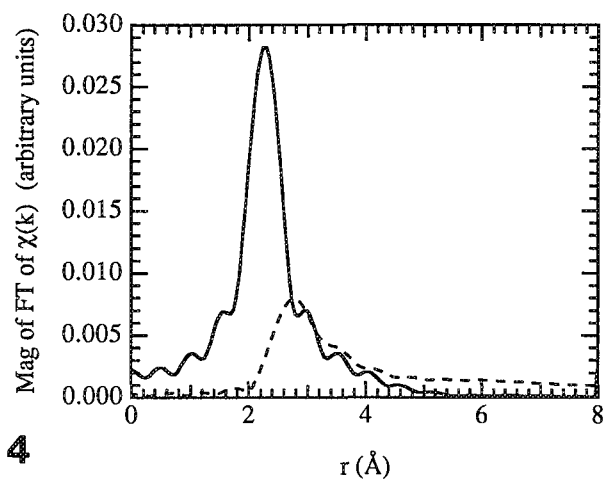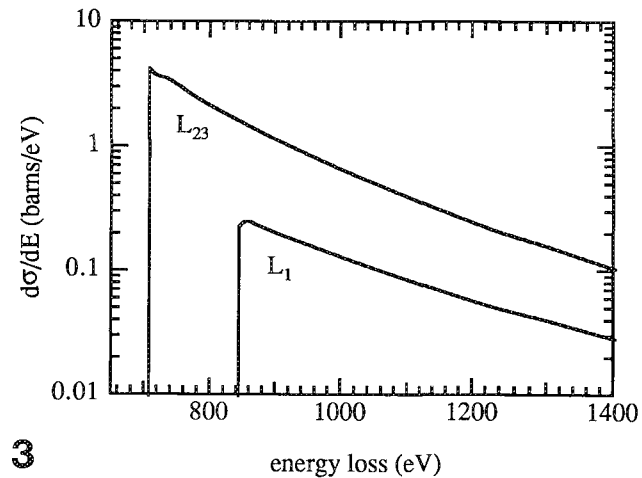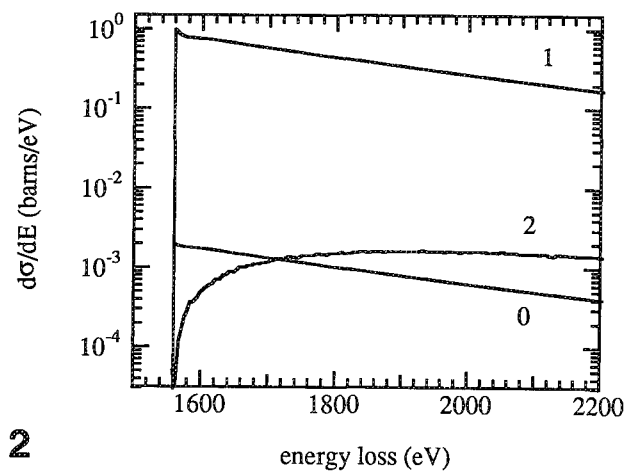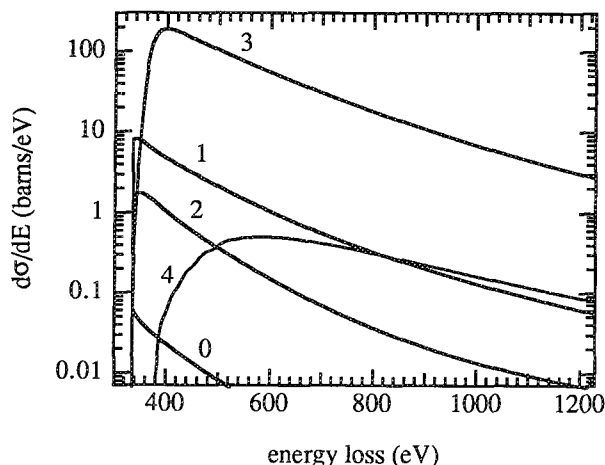

FIG. 8.--Partial differential cross sections for the excitation of 3d electrons in Pd. Numbers are orbital angular momentum quantum numbers of final states.

tributes to the error in the absolute determination of distances from our EXELFS data.

Mean-square relative displacements (MSRD) between atoms cause a damping of the EXELFS oscillations through the Debye-Waller type factor in the EXAFS equation. By use of this damping effect, EXELFS can measure the amount of static or thermal disorder in a sample. In particular, changes in the MSRD between the central atom and the 1nn shell can be determined from the damping of the 1nn peak in the FT of the EXELFS data. Such measurements can be done using the Al K, Fe L_{23}, and Pd M_{45} EXELFS data.

Debye temperatures can be extraced from temperature-dependent MSRD data by use of correlated Debye model. From the temperature-dependent damping of the 1nn peak, we determine "local" Debye temperatures in Al, Fe, and Pd to be 430 K, 415 K, and 390 K, respectively. These temperatures compare favorably with Debye temperatures derived from heat capacity measurements of 304 K for Al, 420 K for Fe, and 275 K for Pd.[7]

Conclusions

The cross section for high-energy electron scattering makes EELS possibl only for core edges at energy losses below about 5keV.[8] Only elements lighter than titanium (Z = 22) have K edges below 5 keV. However, that should not limit EXELFS experiments to elements of low atomic number. As we have known, useful EXELFS information can be extracted from L_{23} and M_{45} edges as well. The use of L_{23} and M_{45} edges opens up most of periodic table to EXELFS experiments.

References

1. H. Shuman and P. Kruit, "Quantitative data processing of parallel recorded energy-loss spectra with low signal to background," *Ref. Sci. Instrum.* 56: 231, 1985.
2. H. A. Bethe, *Ann. Phys.* 5: 325, 1930.
3. F. Herman and S. Skillman, *Atomic Structure Calculations*, Englewood Cliffs, N.J.: Prentice Hall, 1963.
4. R. D. Leapman, P. Rez, and D. F. Mayers, "K, L, and M shell generalized oscillator strengths and ionization cross sections for fast electron collisions," *J. Chem. Phys.* 72: 1232, 1980.
5. B. K. Teo and P. A. Lee, *J. Am. Chem. Soc.* 101: 2815, 1979.
6. N. W. Ashcroft and N. D. Mermin, *Solid State Physics*, New York: Saunders, 1976.
7. J. de Launay, in F. Seitz and D. Turnbull, Eds., *Solid State Physics*, vol. 2, New York: Academic Press, 1956. The temperatures were determined by fitting the observed specific heats c_V to the Debye formula at the point where $c_V = 3nk_B/2$.
8. C. C. Ahn and O. L. Krivanek, *EELS Atlas*, 1983. Copies from Center for Solid State Science, Arizona State University, Tempe, Arizona 85287, or from Gatan Inc., 780 Commonwealth Dr., Warrendale, Pa. 15086.

ANALYSIS OF MICROMETEOROIDS CAPTURED BY SPACECRAFT

D. E. Brownlee

There is a strong interest in the collection and subsequent laboratory analysis of both natural meteoroids and orbital spacecraft debris that impact spacecraft in low Earth orbit. The key interests in collection of natural meteoroids in space are obtaining an unbiased sample of meteoroids that approach the Earth, and collecting particles whose origin can be traced by electronic measurement of velocity and impact angle just before collection. Most of the particles are debris from comets and asteroids, and space collection provides a unique opportunity to collect samples that can be associated with both types of parentbodies. Particles collected in and below the atmosphere are influenced by the selection effects associated with survival of hypervelocity entry into the atmosphere and their trajectories no longer proide clues to their origins. Space collection has limitations, but it also has unique advantages and combined collection and trajectory measurement experiments are under development as a facility for the U. S. space station.[1] Analysis of anthropogenic orbital debris that also impacts spacecraft is of interest mainly in determining the hazard that these particles create for present and future satellites. Currently most of the analysis of hypervelocity particles captured in space is done by electron-beam and ion-probe studies of residual material found lining craters in returned spacecraft parts and in specially designed capture cells. Typical particles impact at velocities in the $3-80$km/s range and decelerate from cosmic velocity on a submicrosecond timescale. In most cases the particles are strongly modified by melting, partial vaporization, and dilution with collector substrate. In rare cases, such as some craters in gold, plastic and aluminum, actual unmelted debris is found lining the crater floors and walls. In future experiments the use of advanced materials such as low-density silica aerogels should permit the capture of totally unmelted particles impacting at speeds of over 10 km/s.

Collection

The impact rate of natural meteoroids of 0.1mm size is approximately 1 $m^{-2}yr^{-1}$; only recently have surfaces been returned from orbit with sufficiently long exposures to provide adequate numbers of impacts for study. The most significant were parts of the Solar Maximum Spacecraft that were returned after more than 4 years in orbit,[2,3] and the entire

D. E. Brownlee is at the Department of Astronomy, University of Washington, Seattle, WA 98195.

Long Duration Exposure Facility (LDEF) spacecraft that was exposed to space for over 5 years. With its approximately 100 m^{-2} of surface area, LDEF contains vast numbers of impact craters that range in size up to 5 mm in diameter.[5] LDEF carried several experiments designed specifically for collection of hypervelocity meteoroids, but most of the impacts on LDEF and all on "Solar Max" are on random spececraft materials. The experiments of LDEF included pure gold, aluminum, and other solid materials for direct cratering; and "capture cells" composed of layered metal and plastic foils into which impacting particles could penetrate. In a capture cell, both solid debris and recondensed vapor collect on internal surfaces, where they can be later analyzed by SIMS or other surface specific techniques. For craters in solid metal, the surviving debris is localized within a bowl shaped crater but volatilized material and even much of the melted projectile is ejected from the crater.

Analysis

Most of the analysis of meteoroids debris collected by Solar Max and LDEF is still in a preliminary stage; this paper concentrates on electron-beam techniques, although in the long run it is likely that SIMS and other methods will provide the most important data.[5,6] The impact craters into soft-metal targets are typically bowl shaped with raised petal-like rims; the crater/projectile size ratio is usually in the 3-4 range, depending on impact velocity and projectile density. In typical craters much of the projectile has been ejected and variable amounts remain as residue presumably dependent on factors such as particle composition, impact velocity, and angle. In some cases the residue is a very thin layer and only trace amounts of elements common in meteoritic materials are seen as EDX peaks that rise above the substrate continuum. The most common compositions for extraterrestrial particles that produce submillimeter craters are (a) mixtures of Mg, Si, Fe, S, Ca, Al, and Ni with relative elemental abundances that match those in the Sun and primitive meteorites, (b) single mineral grains of either forsterite or enstatite, or (c) iron sulfide. In craters with moderate amounts of residue, it usually occurs as a vesicular mixture of glass and small FeNi metal beads finely mixed with melted substrate material. In rare cases, the debris contains unmelted meteoroid materials up to micrometers in size. The debris that survives unmelted appears to be biased toward phases such as forsterite that have very high melting points. The spacecraft-generated debris that orbits the Earth dominates the natural flux of

incoming meteoroids only for particle sizes
below 25 µm and larger than 1 mm. The smaller
particles are dominated by elements such as Ti,
Zn, Cl, K, Si, and Al. The majority of the
smallest of these particles appears to be paint
that has degraded in low-earth orbit and shed
from satellites.[7] The largest are believed to
be dominated by Al, Ti, and steel structural
fragments from degraded spacecraft, but there
is not yet any direct analytical evidence to
support this belief.

Electron-beam analysis of the residue liners
in bowl-shaped impact pits provides special
challenges. The chief problems are the geom-
etry and the variable distribution of thin
samples on a thick metal substrate. The geom-
etry problem, getting electrons to the crater
bottom and x rays out to an EDX detector, has
been approached and only partially solved by
two different methods. One is to apply pres-
sure to the rear of the crater and deform it to
a flat surface. This approach is critical if
standard probe analysis is to be attempted.
The second approach is more directed to SEM-
EDX analysis and involves bending the SEM beam
into the crater. Typical craters have depth/
diameter ratios of 0.65, and it is not possible
to do even good qualitative studies of the
crater bottom with the usual take-off angles
of SEMs. With a small magnetic deflector we
found that it was possible to deflect the beam
into a crater inclined to point directly toward
a 35° take-off angle EDX detector. Like magic
the image in the SEM appears as if the crater
was pointing directly up the microscope's
optical axis. The beam is bent only a few
millimeters above the sample and can be made
to impact the sample at any angle depending on
the geometry and strength of the magnetic
field. The image quality is degraded but it is
certainly sufficient for submicron imaging.
This technique might be useful for other appli-
cations requiring EDX analysis and imaging of
deep holes.

Future Work

The present work on impact craters is pro-
viding information on the elemental composi-
tion of meteoroids and is providing valuable
insight for the development of future collec-
tion methods. Continued ion-probe work will
provide isotopic data, as well as light and
trace element data that cannot be derived
from electron-beam techniques on existing
samples. However, it is clear that the most
important future advances will require new
collection methods that more gently capture
unmelted phases where crystallographic infor-
mation and other properties such as trapped
gas and radiation damage is likely to be pre-
served. The major new advance required is the
use of improved capture materials that lessen
the shock and thermal damage during deceler-
ation from hpervelocity. The two major
approaches are to use stacks of very thin
films, or to use materials that are micro-
porous and have low bulk density. A very prom-
ising material that has been included in the
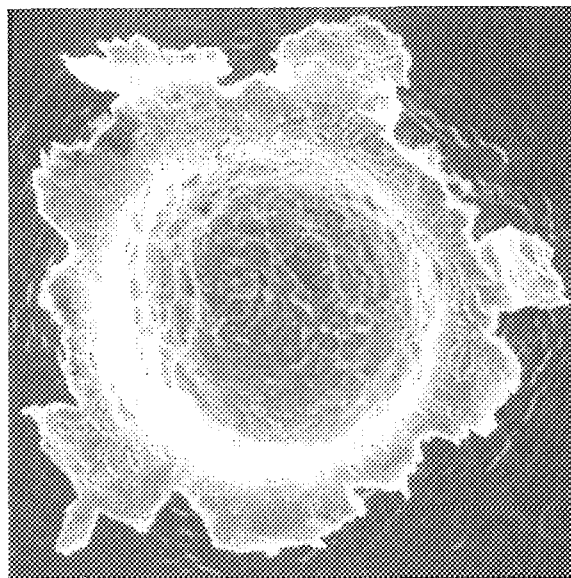
FIG. 1.--SEM image of 100µm diameter hyper-
velocity impact crater in aluminum from Long
Duration Exposure Facility spacecraft.
Material in crater bottom is mixture of alumi-
num and extraterrestrial material with an
elemental composition that approximately
matches that of the Sun for rock-forming
elements.

next generation of experiments is silica
aerogel. This material has a highly porous
structure composed of relatively uniformly
distributed 5nm silica particles. It is
optically transparent and has many of the
properties of glass but its density can be less
than 0.01 g cm^{-3}. Laboratory tests have shown
that this material can capture 6km/s silicate
particles with little thermal damage. Particles
penetrate into the aerogel leaving a long nar-
row track. They come to rest after traveling
of the order of 100 projectile diameters into
the medium. For microbeam analysis these
samples have to be extracted from the aerogel.
In tests the extraction has been accomplished
both by mechanical picking and by imbedding the
aerogel and microtoming down to the sample.

References

1. F. Horz, *Trajectory Determinations and
Collection of Micrometeoroids on the Space
Station*, LPI Tech. Rept. 86-05, Lunar Planet,
Institute, Houston, Tex., 1986, 102.
2. L. S. Schramm, "Analysis of micro-
meteorite material captured by the Solar Max
satellite," *Lunar and Planet. Sci.* 16: 736,
1985.
3. M. R. Laurance and D. E. Brownlee, "The
flux of meteoroids and orbital space debris
striking satellites in low Earth orbit,"
Nature 323: 136, 1986.
4. T. See, M. Allbrooks, D. Atkinson, C.
Simon, and M. Zolensky, *Meteoroid and Debris
Impact Features Documented on the Long
Duration Exposure Facility*, Planetary Science
Branch Publication 84, Johnson Space Center

No. 24608, NASA, 1990, 586.

5. H. Fechtig et al., "Measurements of the elemental and isotopic composition of interplanetary dust particles on LDEF," in R. H. Giese and P. Lamy, Eds. *Properties and Interactions of Interplanetary Dust*, D. Reidel, 1984, 121.

6. E. Zinner, N. Pailer, and H. Kuczera, "LDEF: Chemical and isotopic measurements of micrometeoroids by SIMS," *Adv. Space Res.* 2: 251, 1983.

7. D. J. Kessler et al., "Examination of returned Solar-max surfaces for impacting orbital debris and meteoroids," *Lunar and Planet. Sci.* 16: 433, 1985.

MICROPROBE ANALYSIS OF MICRON-SIZED GRAINS OF PLATINUM GROUP METALS IN A Ca-Al-RICH INCLUSION FROM THE ALLENDE METEORTIE

J. M. Paque

Ca-Al-rich inclusions (CAIs) from carbonaceous chondrites, such as the Allende meteorite, are among the most primitive materials available to us for study, dating from the early history of the solar system. These small, centimeter-sized objects have been studied extensively in an effort to get a better understanding of the conditions under which they formed and, by association, the conditions present during the formation of the solar system.[1] CAIs are composed of materials that are refractory, having very high melting or vaporization temperatures. Calculations have shown that the components in CAIs are those that would be predicted to have condensed from a gas of solar composition as it cooled.[2] The refractory siderophile elements Re, W, Os, Ir, Mo, Ru, Pt, and Rh are calculated to be some of the earliest of these condensates.[3,4]

In addition to the refractory minerals present in CAIs, the inclusions are often found to contain micron-sized grains consisting of varying proportions of the platinum group metals along with other refractory elements. These objects have been termed RMN (refractory metal nuggets).[5,6] One inclusion, A-WP1, is unique in that it is unusually rich in the element vanadium in both the oxide and the metal components.

This paper discusses the analytical problems associated with analysis of the metal grains in A-WP1. The results indicate that nuggets enclosed in melilite contain platinum group elements in approximately chondritic proportions, which suggests that these grains formed by condensation from a solar gas without further processing or alteration.

Experimental

Quantitative wavelength-dispersive analyses were performed on a JEOL 733 Superprobe at the Center for Materials Research (CMR) at Stanford University. Kevex Sesame automation, with ZAF corrections via Magic V, was utilized. Operating conditions for metal analyses were 20 kV accelerating voltage and 20 nA beam current. Pure metals were employed as standards.

Analyses of RMN grains presented several problems. First, the grain size was of the order of 1 μm, less than the analytical volume of the electron beam. For several grains, Ca, Al, Si, and Mg (the elements present in the surrounding minerals) were also analyzed and calculated as oxides. In these instances

totals, including metals and oxides, were near 100%. Replicate analyses without these elements gave nearly identical results for the refractory and platinum metal elements. Therefore, the elements in the nugget were normalized to 100% in all cases. Uncorrected totals for the platinum and refractory elements ranged from 11 to 63 wt.%.

A second analytical problem occurs when the RMN grain is adjacent to a spinel crystal. Both the spinel and RMN nugget contain V and Fe, and the relative amount of the contribution of these elements to the RMN analysis is not known. Analyses of RMN adjacent to spinel were used with caution in this study.

The third analytical problem involves the stability of the stage during the analysis. The movement of the spectrometers brings about a slight movement of the stage during some of the analyses, causing the beam to lose its centering on the RMN grain. The location of the beam was carefully checked both before and after each analysis and, if movement occurred, the analysis was rejected.

Finally, there are several minor peak interferences in this system. All the metals used as standards were analyzed as unknowns to determine the extent of this problem. The only significant interferences are the Ru Lβ line when the Rh Lα line (1.2%) is analyzed, and the presence of 1.2% Os when Pt is analyzed. The source of the Os/Pt interference has not been conclusively determined, but is most likely due to choice of background selection. Corrections were manually applied to the results to account for these interferences. The remainder of the interferences are significantly less than 1% and were ignored.

A total of 38 acceptable analyses of RMN grains were obtained for this study, including 8 replicate analyses.

Sample Description

The portion of the inclusion available for study in thin section is approximately 1 × 5.75 mm. The major minerals present in the sample, along with their chemcial compositions, are listed in Table 1. The majority of the minerals consist of oxides in the Ca-Al-Mg-Si system.

This inclusion can be roughly divided into three petrographic regions based on the silicate and oxide mineralogy: (1) melilite enclosing spinel and hibonite, (2) grossular-anorthite-nepheline-sodalite alteration, and (3) fine-grained aluminum-rich alteration. RMN were not found in the region of fine-grained aluminum-rich alteration.

J. M. Paque is at the Center for Materials Research and Geology Department, Stanford University, Stanford CA 94305-4045.

TABLE 1.--Major oxide and silicate minerals in A-WP1.

Melilite solid solution	$Ca_2MgSi_2O_7$-$Ca_2Al_2SiO_7$
Spinel solid solution	$(Mg, Fe)(Al, V)_2O_4$
Perovskite	$CaTiO_3$
Hibonite	$CaAl_{12}O_{19}$
Grossular	$Ca_3Al_2Si_3O_{12}$
Anorthite	$CaAl_2Si_2O_8$
Nepheline	$NaAlSiO_4$
Sodalite	$Na_8Al_6Si_6O_{24}Cl_2$

Melilite is the major phase in A-WP1, exhibiting kink-banding, up to 300 μm in size. Melilites often show effects of alteration along fractures and grain boundaries. Spinel, hibonite, perovskite, and RMN are poikilitically enclosed in the melilite. Spinel are subhedral to euhedral and up to 50 μm in diameter, and have a low iron content when enclosed within melilite compared with spinel in other regions of the inclusion. Anhedral blebs or bands of perovskite occur along the edges of spinel crystals. Hibonite occurs as euhedral laths associated with spinel.

Alteration products along melilite grain boundaries and fractures include grossular and anorthite, with minor amounts of a feldspar solid solution. Other alteration products include nepheline and sodalite. The grain sizes of alteration products are <20 μm.

The third petrographic area of the inclusion consists of a submicron aggregate of an iron-aluminum-rich material surrounding surviving mineral grains. A remarkable feature of this area is the presence of an extremely V-rich aluminate (up to 20 wt.% V_2O_3). This phase is associated with perovskite, laths of hibonite (<30 μm long), and anorthite; and is surrounded by the fine-grained Al-rich aggregate. Corundum occurs as anhedral grains, ∿8 μm in diameter, surrounded by an Fe-Al-rich submicron aggregate of grains.

Refractory platinum metal (RMN) nuggets are present in three different associations in A-WP1. RMN nuggets occur in the melilite (Fig. 1a), along the edges of spinel grains within the melilite (Fig. 1b), and in the alteration areas (Fig. 1c). It will be shown below that these associations are reflected in the chemistry of the individual grains.

Results

Two chemically distinct groups of RMN nuggets are found in A-WP1. RMN in melilite form one group (including RMN associated with spinel grains) and those in altered areas form the second group. Representative analyses from each of the areas are presented in Table 2.

Note the high Fe and Ni concentrations of the nuggets in the areas of melilite alteration. A plot of wt.% Ni vs wt.% Fe (Fig. 2) in RMN shows the variation in chemistry with petrography in A-WP1. In general, both Fe and Ni increase in the areas of alterations; however, several RMN increases in Fe without an associated increase in Ni. It is possible that the chemistry of these grains has been changed during the same event that produced the alteration of the melilite.

Examining only the RMN nuggets that are enclosed within melilite is logical in that these grains are likely to be the most primitive and least likely to have been affected by the alteration event that introduced Fe into spinel and altered melilite along fractures and grain boundaries. Indeed, these grains are found to contain nearly chondritic proportions of the refractory and platinum group elements. Figure 3 is a plot of the Os vs Ir concentrations of the RMN in melilite. The correlation with the cosmic Os/Ir ratio is very good, which shows that these elements were condensed from a solar gas into the RMN nuggets in chondritic proportions without further alteration.

All the analyzed elements from RMN within melilite are plotted in order of increasing volatility (decreasing temperature) in Fig. 4, normalized to condrites[7] and Os = 1.0. With the exception of the most volatile elements (V, Ni, and Fe), the elements are present in roughly chondritic proportions.

Discussion

Previous analyses of RMN in CAIs found grains that were enriched in a subset of the platinum and refractory metals. For example, Pt-rich and Os-rich nuggets were analyzed in an Allende inclusion and interpreted to be a result of condensation from gas over restricted temperature intervals.[5] Another possibility postulated by the authors for the origin of the Os-rich RMN is that they may be residues from a vaporization process. One hypothesis suggests that these elements may condense into alloys based on their high-temperature crystal structure,[8] but experiments have shown that synthetic alloys can be produced experimentally with all these elements in a hexagonal close-packed structure.[9]

The concentration of platinum group elements found in RMN in A-WP1 is the pattern that would be expected if there was full condensation of elements through Rh, with only partial condensation of the more volatile elements before incorporation into melilite. The grains in the altered areas could be formed in one of two ways: either they originally condensed at the same time as the RMN in melilite and were modified during the event that altered melilite along fractures and grain boundaries, or they are a product of a later, lower-temperature condensation event.
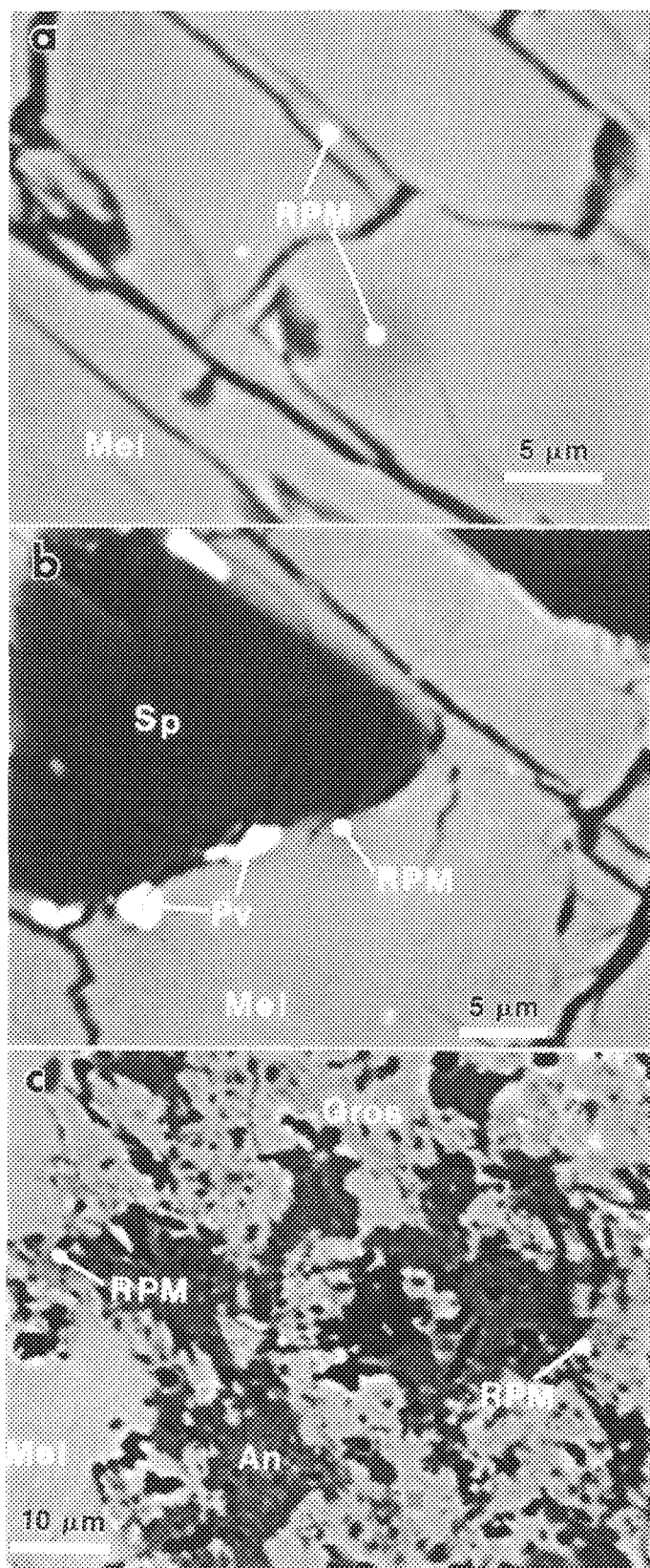
FIG. 1.--RMN (= RPM) occurrences in A-WP1: (a) in melilite, (b) with spinel in melilite, (c) in areas of alteration of melilite. (Abbreviations: Mel, melilite; Sp, spinel; Pv, perovskite; An, anorthite, Gros, grossular; RPM, refractory metal nugget.)

Conclusions

The RMN within melilite present a convincing case for condensation from a solar gas. A possible scenario for the formation of these nuggets could include condensation of the RMN grains followed by condensation of melilite, enclosing the RMN grains and segregating some of them from further reaction with the gas. At lower temperatures, the inclusion reacted with the gas to form the alteration along melilite fractures and grain boundaries. RMN that were present in these areas were exposed to this alteration process, which increased their Fe and Ni concentrations.

References

1. J. F. Kerridge and M. S. Matthews, Meteorites and the Early Solar System, Tuscon: University of Arizona Press, 1981, 746.

2. L. Grossman, "Condensation in the primitive solar nebula," Geochim. Cosmochim. Acta 36: 597, 1972.

3. L. Grossman, "Refractory trace elements in Ca-Al-rich inclusions in the Allende meteorite," Geochim. Cosmochim. Acta 37: 1119, 1973.

4. H. Palme and F. Wlotzka, "A metal particle from a Ca, Al-rich inclusion from the meteorite Allende, and the condensation of refractory siderophile elements," Earth Planet. Sci. Lett. 33: 45, 1976.

5. D. A. Wark, "Evidence of successive episodes of condensation at high temperatures in a part of the solar nebula," Earth Planet. Sci. Lett. 77: 129, 1986.

6. A. El Goresy, K. Nagel, and P. Ramdohr, "Fremdlinge and their noble relatives," Proc. Lunar Planet. Sci. Conf. 9: 1279, 1978.

7. E. Anders and M. Ebihara, "Solar-system abundances of the elements," Geochim. Cosmochim. Acta 46: 2363, 1982.

8. P. J. Sylverster et al., "Chemical compositions of siderophile element-rich opaque assemblages in an Allende inclusion," Geochim. Cosmochim. Acta 54: 3491, 1990.

9. D. A. Wark, The Allende Meteorite: Information from Ca-Al-rich Inclusions on the Formation and Early Evolution of the Solar System, Ph.D. Thesis, University of Melbourne, Australia, 1983.
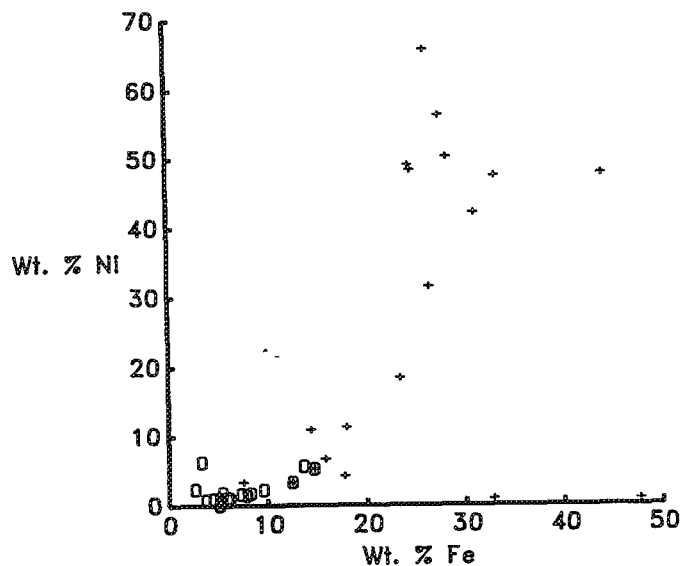
FIG. 2.--Petrographic relationship bewtwen con-
centrations of Fe and Ni in RMN and alteration
(+) or association with melilite or spinel (o).
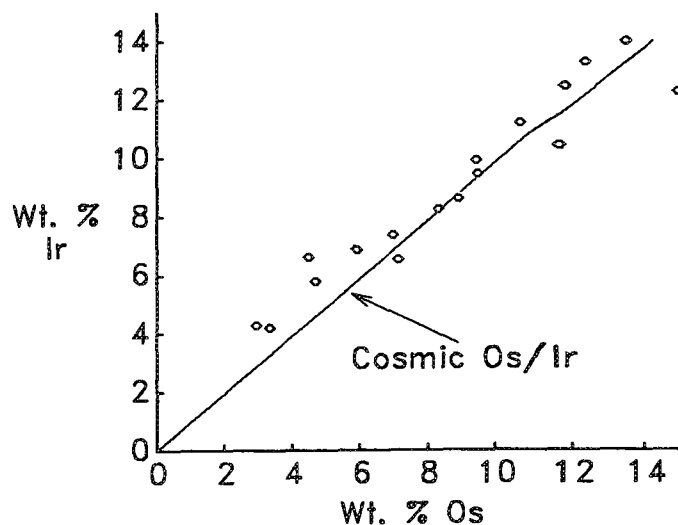
FIG. 3.--Plot of Os vs Ir concentrations in
RMN enclosed in melilite.
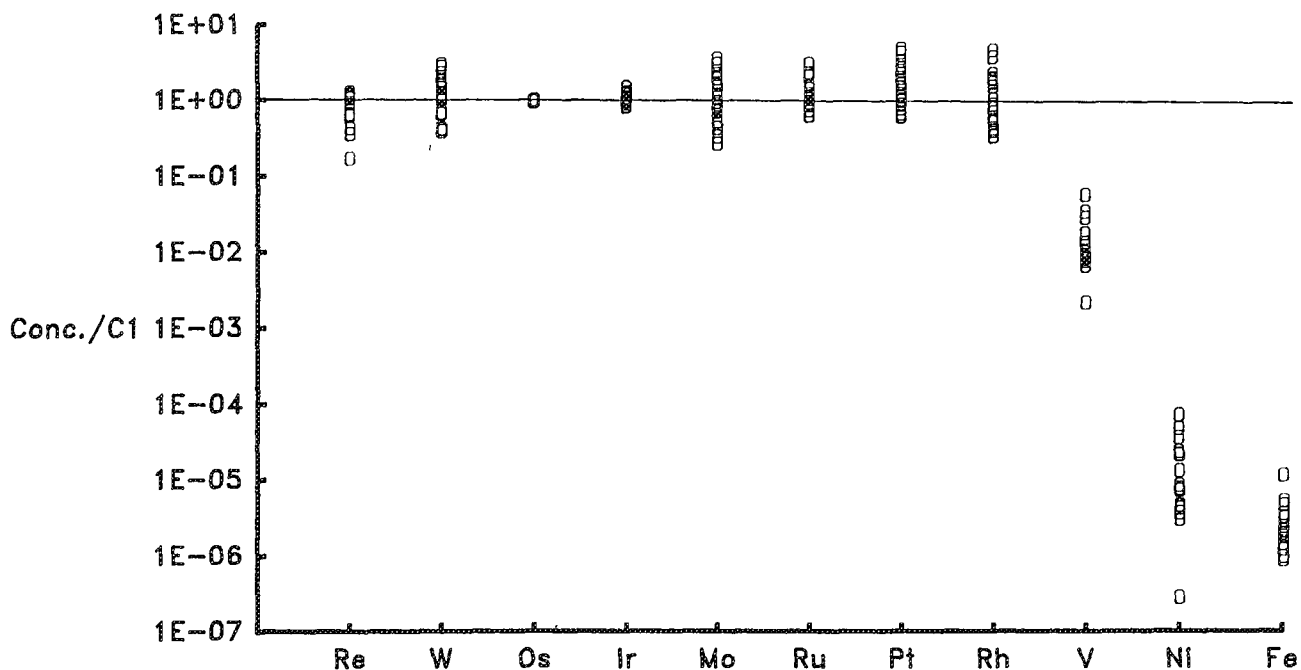
FIG. 4.--RMN from melilite with concentration relative to C1 chondrite values and normalized to
Os = 1.0. Elements are ordered on the horizontal axis in terms of increasing volatility.

TABLE 2.--Representative analyses of RMN from A-WPI.*

| Sample | R2 | R5 | R10 | R15 | R1 | R3 | R13 | R19 |
Assoc.**	MEL	MEL	MEL	MEL	SP	SP	ALT	ALT
V	25.7	4.9	14.5	11.1	4.0	33.0	0.2	0.2
W	2.1	1.5	1.6	1.8	0.7	1.4	0.0	0.0
Re	0.7	0.2	0.6	n.a.	0.9	0.3	0.1	n.a.
Os	7.2	4.6	12.4	8.3	13.9	5.2	0.0	0.1
Ir	6.6	5.7	13.3	8.2	13.8	10.0	1.1	6.2
Mo	22.3	20.1	10.2	13.1	7.4	13.3	2.9	4.3
Ru	9.7	14.5	13.4	14.8	17.7	8.6	0.0	0.7
Rh	2.2	4.1	1.9	5.0	2.9	1.7	0.0	1.0
Fe	5.2	9.6	5.9	7.9	10.6	11.0	44.1	26.5
Ni	0.7	2.3	1.2	1.4	5.1	0.6	47.7	31.5
Pt	17.7	32.4	25.1	28.3	23.0	14.9	3.9	29.6

* All analyses are normalized to 100 wt.%; n.a. = not analyzed.
**Mineralogical association of RMN: MEL, melilite; SP, spinel; ALT, alteration.

THE RELATIONSHIP BETWEEN HYDROUS AND ANHYDROUS INTERPLANETARY DUST PARTICLES

M. E. Zolensky

We have been examining the mineralogy of inter-planetary dust particles (IDPs) by AEM using ultramicrotomed samples, with the goal of elucidating their parent bodies and their physico-chemical histories. The least contaminated IDPs are harvested from stratospheric collectors and hardware returned from low-Earth orbit. The best of the latter samples were collected by Long Duration Exposure Facility (LDEF), which was retrieved in 1990 following 5.7 years in orbit. Consortium studies of IDPs by AEM, INAA, PIXE, noble gas, and isotopic techniques permit maximum information return from these nanogram-sized samples. The mineralogy of several dozen chondritic IDPs has not been reported.[1-8] We re-examine here the question of the relationship between hydrous and anhydrous varieties, and the identification of their parent bodies.

Comparisons of IDPs to Chondrites

Current models hold that the anhydrous particles are derived, at least in part, from completely unprocessed, primitive nebular condensates, specifically residing in perpetually cold outer-belt D-class asteroids and/or comets. The hydrous particles are believed to have originated in the regoliths of nearer, and warmer, hydrous main belt asteroids. Since these latter bodies are also believed to provide the bulk of chondritic meteorites, considerable effort has been expended in attempts to discover connections between hydrous IDPs and chondrites.[9,10] However, surveys of the mineralogy of these hydrous chondritic materials continue to show that there are interesting differences. For example, olivine is clearly the predominant anhydrous silicate in all chondritic meteorites, pyroxene and glass are more common in chondritic IDPS. The single exception are the (rare) serpentine IDPs, which are similar (and in one reported case identical[6] to CM chondrites, the most abundant carbonaceous chondrites. When present together in IDPs, serpentine and saponite (the most abundant hydrous phases in chondritic IDPs) are present as discreet crystals and aggregates. When these phases are present together in chondrites, they are commonly (though not always) intergrown at the molecular scale. Third, the carbon content of chondritic IDPs (as determined by quantitative windowless EDS) significantly exceeds chondritic meteorite matrix.[11]

Comparison of Hydrous to Anhydrous IDPs

Although it has become traditional to consider hydrous and anhydrous IDPs separately, the mineralogies of anhydrous and saponite IDPs (the latter being by far the most abundant hydrous variety) are basically identical when the presence of phyllosilicates is not considered (Table 1, Fig. 1a). Indeed, the phyllosilicate content of "hydrous" chondritic IDPs varies from only a few modal percent up to amounts exceeding 50%.
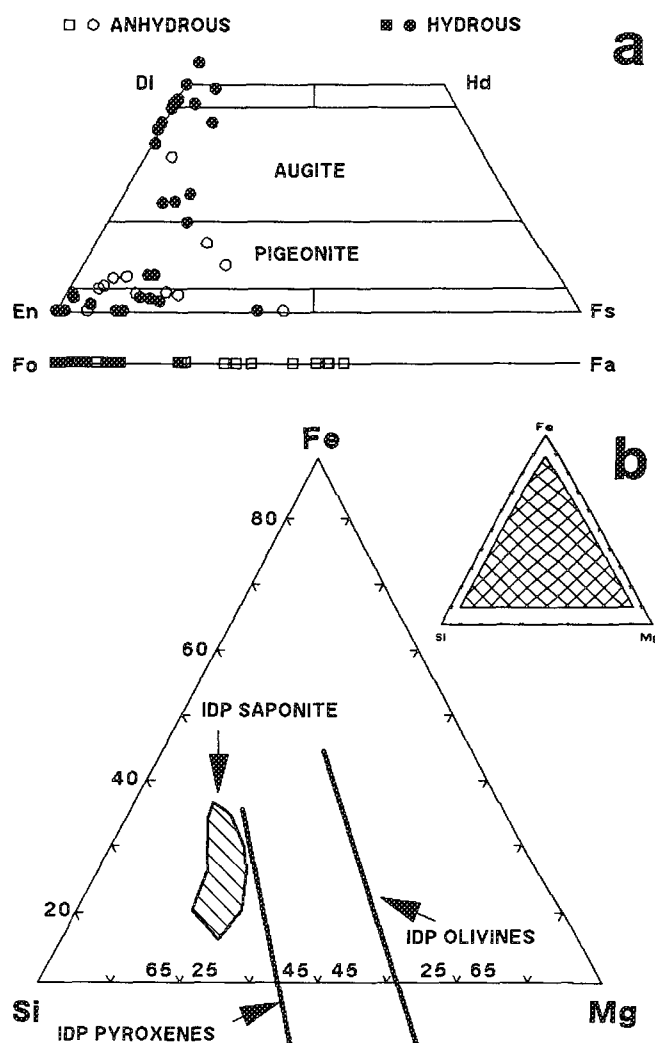

FIG. 1.--(a) Comparison of compositions of olivines and pyroxenes from hydrous and anhydrous IDPs. (b) Comparison of compositional ranges of olivines, pyroxenes, and saponite crystals from IDPs, all plotted on reduced-area ternary plot of atomic wt.% Fe-Si-Mg. (Data are from this work and Ref. 4.)

TABLE 1.--Mineralogy of chondritic IDPs (rare phases not listed).

Anhydrous	Hydrous	
	Saponite	Serpentine
Enstatite En57-100	Enstatite En61-100	
Diopside	Diopside	Diopside
Olivine Fo44-100	Olivine Fo76-100	Olivine Fo84
Pyrrhotite	Pyrrhotite	Pyrrhotite
Pentlandite	Pentlandite	Pentlandite
Magnetite	Magnetite	Magnetite
Chromite	Chromite	
Spinel	Spinel	
Carbonates	Carbonates	
Sulfates	Sulfates	
Metal	Metal	
Glass	Glass	
Carbides		
	Plagioclase	
		Schreibersite
		Tochilinite
	Saponite	
	Serpentine (minor)	Serpentine

Discussion

We therefore suggest that at least some, and perhaps most, anhydrous and hydrous IDPs are from identical parent bodies. In particular, the presence of carbonates and sulfates in some anhydrous particles clearly indicates derivation from bodies that experienced at least a mild aqueous alteration event. Such parent bodies would necessarily host a disequilibrium mineralogical assemblage, but this is practically the rule for samples from asteroids (meteorites). Since the compositional range of saponite in IDPs is very similar to that for pyroxene in the same (Fig. 1b), we suggest that pyroxene is a likely precursor for much of the saponite, rather than merely assigning that role to glass or olivine. The above scenario requires that either some main-belt asteroids have locally very low densities ($\sim$1 g/cc, to match that of some anhydrous IDPs), or that hydrous alteration has occurred on some comets or outer-belt asteroids (which seems unlikely). These results may indicate that cometary particles are underrepresented in our extraterrestrial collections, or that they do not typically exceed 10 μm in diameter, which is usually the lower size limit of particles that are studied).

References

1. W. Klock et al., *Nature* 339: 126, 1989.
2. J. P. Bradley, *Geochimica et Cosmochimica Acta* 52: 889, 1988.
3. M. S. Germani et al., *Earth and Planetary Science Letters* 101: 162, 1990.
4. R. Christoffersen and P. R. Buseck, *Earth and Planetary Science Letters* 78: 53, 1986.
5. I. D. R. Mackinnon and F. J. M. Rietmeijer, *Reviews of Geophysics* 25: 1527, 1987.
6. J. P. Bradley and D. E. Brownlee, *Science* 251: 549, 1991.
7. D. F. Blake et al., *Proc. Lunar Planetary Science Conference* 18: 615, 1988.
8. K. Tomeoka and P. R. Buseck, *Science* 231: 1544, 1986.
9. F. J. M. Rietmeijer and D. S. McKay, *Meteoritics* 20: 743, 1985.
10. K. Thomas et al., *Meteoritics* 25: 414, 1990.
11. G. E. Blanford et al., *Meteoritics* 23: 113, 1988.

MICROBEAM ANALYSES OF CARBON-RICH MATERIALS IN CHONDRITIC POROUS MICROMETEORITES

F. J. M. Rietmeijer

Solid particles in the Earth's lower strato-sphere have been collected by high-flying air-craft since 1965 with the aim to study the na-ture of solid aerosols that occur in the lower stratosphere.[1] Large amounts of micrometeor-ites in the 0.1-1mm size range enter the Earth's atmosphere and a fraction of solid aerosols in the lower stratosphere will be ex-traterrestrial material. In the lower strato-sphere, the concentration of micrometeorites of sizes (i.e., < 50 μm) that can be collected on inertial-impact flat-plate collectors at-tached to the wings of high-flying aircraft is very low (10^{-2}-10^{-3} m^{-3}) and large volumes of the stratosphere must be sampled to obtain statistically significant amounts of microme-teorites.[2] These micrometeorites are a cross section of asteroids and short-period comets that could be relic protoplanets preserved from the planet-forming era.[3] To a first approxima-tion, a chondritic major element distribution pattern supports the extraterrestrial origin of an individual micrometeorite[3] that also has a high bulk carbon content.[4] Unambiguous evi-dence for an extraterrestrial origin is present as solar flare tracks in olivine and pyroxene, large D/H ratios, and noble gas contents. De-tails on the mineralogy and chemistry[2,5] and physical properties[6] of chondritic micrometeor-ites are given in recent review articles that show chondritic micrometeorites to be uniquely different from any known meteorite class. Classification of fine-grained (~2-2000 nm) chondritic micrometeorites, or interplanetary dust particles (IDPs), relies on particle structure and mineralogy, namely (1) chondritic porous (CP) IDPs characterized by olivines plus carbons or pyroxenes plus carbons; and (2) chondritic smooth IDPs that consist mostly of phyllosilicates, smectites, or serpentine, plus carbons.[2,5] Chondritic porous IDPs are fluffy (low density) aggregates of hundreds (>10^4) of individual grains which range in size

from <100nm up to microns. A variable frac-tion of micron-sized grains are themselves compact subunits of even smaller grains (2-1000 nm in size) embedded in amorphous carbon and hydrocarbons. (In this context, the term hydrocarbons indicate all organic materials that are not elemental carbon.) Individual CP IDPs may contain micron-sized enstatite rods and plates.[2,5] The nominal mineralogy of CP IDPs is mostly (Fe,Mg) olivines and py-roxenes, including Mn-rich forsterite and en-statite;[7] Fe, Ni-sulfides, spinels, variable amounts of amorphous material with a chondrit-ic, magnesio-silica, or alkali-alumino-silica composition; and rare nonstoichiometric alkali-feldspar and plagioclase.[2,6,8] Minor amounts of smectites, kaolinite, and illite are common to many CP IDPs.[8] The fine-grained nonequi-librium mineral assemblages in these particles support a provenance in mineralogically active Solar System environments such as short-period (SP) comet nuclei. As dust from SP comets con-tains information on nebular and interstellar dust that accreted into the protoplanets of the Solar System, CP IDPs become windows through which we can view the onset of geolog-ical activity in the Solar System. I shall emphasize the carbon-rich constituents of CP IDPs in an attempt to determine the mineralog-ical signatures of individual carbon-rich grains that were part of Solar System proto-plants. The analytical electron microscope (AEM) results provide a mineralogical context for the abundant CHON, (H,C,O), (H,C,N), and (C,H) particles in the comet Halley nucleus as detected by mass spectrometers on board the Giotto and Vega spacecraft.[9,10]

Experimental

Chondritic porous IDPs present a consider-able challenge to the analyst who wants to de-termine the mineralogy and chemical composi-tions of the thousands of small-sized grains in these particles, in particular the carbon-rich materials. All samples were obtained from the NASA Johnson Space Center (JSC) Cos-mic Dust Collection. Prior to allocation, the chondritic elemental abundance pattern for each particle was determined using a JEOL-35CF scanning electron microscope (SEM) equipped with a PGT 4000T energy-dispersive spectrome-ter (EDS).[11] A high bremsstrahlung background in its EDS spectrum is taken to support the presence of low-atomic-number (Z < 10) materi-al in the particle.

Carbon-rich materials were analyzed in "dis-persed samples" and ultramicrotomed CP IDP thin sections. For the "dispersed samples," small fragments of a CP IDP were gently dis-
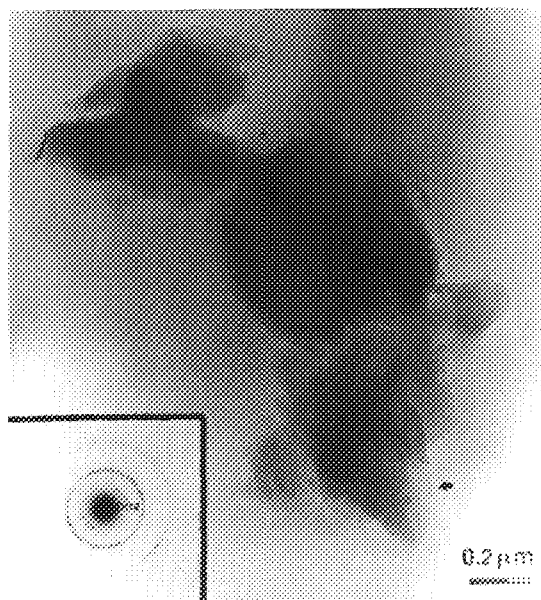
FIG. 1.-- Irregularly shaped turbostratic pre-graphitic carbon grain in CP IDP W7029E5 with artifacts of ultramicrotomy (open arrows). These areas give rise to basal 002 interplanar spacings in polycrystalline SAED pattern (in-set). Incipient formation of poorly graphi-tized carbon is visible along margin (solid arrow).

FIG. 2.--Irregularly shaped turbostratic pre-graphitic carbon grain in CP IDP W7029E5 show-ing moiré fringes (upper part) due to small, relative rotational misorientation of overlap-ping crystalline sheets. Polycrystalline SAED pattern shows hk 10 and 11 rings indicating presence of small polyaromatic molecules in pre-graphitic carbon. Double diffraction originated from six centers on hk 10 diffrac-tion ring.

persed onto a holey carbon film supported by a Be (150-mesh) grid, whereby individual grains in each sample became accessible to study. The samples were not provided with a conductive coating (e.g., C or Au/Pd) to reduce possible contamination during the coating process. In general, contamination of samples is negligible but recognizable in the rare instances when present.[2] The analytical data were obtained on a JEOL 100CX AEM equipped with a PGT System IV EDS. The AEM was operated at an accelerat-ing voltage of 100 keV. The microscope was modified to minimize the level of spurious x rays through thick apertures and a dual cold finger in the sample chamber for re-duction of specimen contamination.[1] Serial ultramicrotomed thin sections were obtained from CP IDPs that were embedded in epoxy at the JSC Curatorial Facility. Thin sections were prepared by means of a Reichert-Jung Ultrami-crotome E equipped with a diamond knife that moved at a speed of 0.3 to ∿0.6 mm sec^{-1}. In reflected light, the sections appeared silver to gold indicating a thickness of 90-110 nm. Artifacts related to thin sectioning are recog-nizable (Fig. 1). Each thin section was sup-ported by a holey carbon thin film on a trans-mission electron microscope (TEM) grid housed in a Gatan low-background, double-tilt specimen holder. The data were obtained on a JEOL 2000FX AEM fitted with TN5500 EDS for in situ

chemical analyses using a probe size of 15-20 nm. The AEM was operated at an accelerating voltage of 200 keV. With both microscopes, polycrystalline (or "ring") and single-crystal selected-area electron-diffraction (SAED) pat-terns have been obtained. The SAED patterns were calibrated with Au-coated holey carbon film by the exact experimental conditions for the unknowns. The resulting electron diffrac-tion data have a relative error of ∿1.5%.

Identification of carbon-rich materials re-lied on combinations of EDS, SEM, bright-field (BF), and centered dark-field (CDF) TEM and HRTEM imaging. Both EDS systems used in this study are suitable for the detection of ele-ments with Z > 10. Carbon-rich grains in the samples were selected by use of the absence of x-ray signals in the EDS after an effective acquisition time of 150 s. The embedding epoxy in ultramicrotomed samples contains chlorine that allows unambiguous distinction between indigenous epoxy and carbon-rich grains.

Results

The carbon mineralogy of primitive fine-grained CP IDPs is quite diverse and includes epsilon Fe,Ni-carbide and Mg-carbonate grains, filamentous carbon, graphite domains in amor-

phous carbon and abundant (as yet unidentified) hydrocarbon material.[2,5,6] Within individual CP IDGs platey and fluffy grains of carbon-rich materials co-occur, both as separate and in individual grains.

In CP IDPs W7029*A and W7010*A2, thin (< 10 nm), lobate electron-transparent sheets of well-crystalline lonsdaleite (or carbon-2H) are 0.2×0.3 μm to 0.6×2.0 μm in size.[12] Exposure to the incident electron beam causes wrinkling of the typically smooth surface of lonsdaleite sheets and suggests the release of volatiles from lonsdaleite. In both particles, lonsdaleite co-occurs with layer silicates. Thus, a model of in situ hydrous pyrolysis of hydrocarbons was adopted for lonsdaleite formation in CP IDPs.[12] To understand mineral properties of extraterrestrial materials we must necessarily rely on judicious comparison with terrestrial diagenesis. By this analogy, lonsdaleite could have formed by catalytically activated hydrous pyrolysis at temperatures < 350 C. This process produces a soft (i.e., graphitizable) carbon which during heat-treatment is able to transform into poorly graphitized carbon (PGC). Well-crystalline platey lonsdaleite conceivably formed as the result of catalytic support by co-occurring clay minerals in a manner similar to stabilization of nitrogen and oxygen bearing graphitic carbon formed from plyacrylonitrile interlayed in montmorillonite.[13] I conjecture that the observed electron beam damage of lonsdaleite could indicate the presence of oxygen or nitrogen.

Another type of platey carbon-rich material occurs in CP IDPs W7029E5, U2011C2, and U2022C7/C8, where it forms irregularly shaped grains of turbostratically stacked thin sheets that are between 0.3×0.3 μm and 4.5×1.3 μm in size. Although common (hkl) 201 and 116 and rare 112 and 114 diffraction rings in polycrystalline SAED patterns of these grains suggest considerable three-dimensional order of crystalline, pre-graphitic carbon basal (d_{002}) diffraction spots are rare. The SAED data are consistent with a graphitic unit cell of $c_0 = 0.75$ nm. Only a few grains in CP IDP @7029E5 have locally well-developed pre-graphitic layer stacking and their SAED patterns show discrete d_{002} diffraction spots with values between 0.42 and 0.345 nm. These d_{002} interplanar spacings are within three groupings of basal spacings in natural terrestrial pre-graphitic carbons that are centered around mean values at 0.45 nm, 0.371 nm, and 0.348 nm.[14] These groupings indicate alicyclic and aromatic structures in pre-graphitic carbons. By the analogy of terrestrial diagenesis, pre-graphitic carbons in CP IDPs are interpreted as mixed-layered carbons of individual sheets with variable C/[C+H+O+N] ratio.[14] Mixed layering in pre-graphitic carbons probably reflects kinetically controlled carbonization and graphitization in the early stages of hydrocarbon carbonization. As sulfur in CP IDP pre-graphitic carbons is below the detection limit of the EDS system, I infer C/[C+H+O+N] ratios in these grains to range between ∿0.35 and ∿0.75, with an average ratio of 0.5. This average ratio, as well as the inferred range, are comparable with ratios for two groups of CHON particles observed in SP comet Halley.[9]

Platey lonsdaleite and turbostratic pre-graphitic carbons in CP IDPs support considerable mineralogical activity in SP comet nuclei that affected hydrocarbons in these primitive bodies. When the platey carbon minerals are indeed soft carbons, (local?) increases in temperature (i.e., thermal metamorphism) could yield the fluffy PGC grains associated with lonsdaleite[12] and the less-developed PGC domains on turbostratic pre-graphitic carbon grains in CP IDP U2022C7/C8. The PGCs typically consist of tangled loops and concentric (sub)circular and polygonal structures.[15] In CP IDP W7029*A the mean apparent PGC interlayer spacing is 0.35 nm, and if PGC formation in this particle were uniquely temperature dependent, this value indicates PGC formation at ∿315 C.[15] The PGC structure is interpreted as a nonequilibrium growth form that may form in layered compounds. This interpretation implies either a long-duration and low-temperature or short-duration and high-temperature imprint on sustained thermal regimes (diagenesis) that produced platey carbon-rich minerals and layer silicates. During the lifetime of a micrometeorite the former may occur during parent-body evolution (diagenesis and metamorphism), whereas the latter conditions are present during micrometeorite deceleration in the Earth's atmosphere and cause pyrometamorphism that is probably the last process to leave its mineralogical imprint on a CP IDP prior to collection.

Conclusions

Platey carbon-rich minerals in CP IDPs, which form an important subgroup of micrometeorites reaching the Earth's surface, give evidence for diagenesis in primitive Solar System protoplanets that produced lonsdaleite and turbostratic pre-graphitic carbons from hydrocarbon precursors. Portions of these soft carbons underwent thermal metamorphism to poorly graphitized carbons. The wealth of carbon-rich minerals, including pre-graphitic carbons of variable C/[C+H+O+N] ratio, is consistent with abundant "low-Z particles" observed in SP comet Halley. The results show significant recrystallization of hydrocarbons that are among the most important Solar System materials. The AEM is an excellent tool for the study of carbon-rich materials, and the processes that determine their evolution, at the small-scale of individual grains in chondritic porous micrometeorites.

References

1. I. D. R. Mackinnon, F. J. M. Rietmeijer, D. S. McKay, and M. E. Zolensky, "Microbeam analyses of stratospheric particles," *Microbeam Analysis--1985*, 291-297.

2. I. D. R. Mackinnon and F. J. M. Reitmeijer, "Mineralogy of chondritic interplane-

tary dust particles," *Reviews Geophys.* 25: 1552, 1552, 1987.

3. D. E. Brownlee, "Cosmic dust: Collection and research," *Ann. Rev. Earth Plant. Sci.* 13: 147-173, 1985.

4. L. S. Schramm, D. E. Brownlee, and M. M. Wheelock, "Major element composition of stratospheric micrometeorites," *Meteoritics* 24: 99-112, 1989.

5. J. P. Bradley, S. A. Sandford, and R. M. Walker, "Interplanetary dust particles," in J. F. Kerridge and M. S. Matthews, Eds., *Meteorites and the Early Solar System*, 1988, 861-895.

6. S. A. Sandford, "The collection and analysis of extraterrestrial dust particles," *Fund. Cosmic Phys.* 12: 1-73, 1987.

7. W. Klöck, K. L. Thomas, D. S. McKay, and H. Palme, "Unusual olivine and pyroxene composition in interplanetary dust and unequilibrated ordinary chondrites," *Nature* 339: 126-128, 1989.

8. F. J. M. Rietmeijer, "Aqueous alteration in five chondritic porous interplanetary dust particles," *Earth Planet. Sci. Lett.* 102: 148-157, 1991.

9. E. K. Jessberger, A. Christoforidis, and J. Kissel, "Aspects of the major element composition of Halley's dust," *Nature* 332: 691-695, 1988.

10. B. C. Clark, "Carbon-rich particles in Comet Halley," *NASA Conf. Publ.* 3061: 27-36, 1990.

11. M. E. Zolensky, R. A. Barrett, A. L. Dodson, K. L. Thomas, J. L. Warren, and L. A. Watts, "Cosmic dust catalog, 11(1)," Washington, D.C.: U.S. Government Printing Office, 1990 (JSC 24461).

12. F. J. Rietmeijer and I. D. R. Mackinnon, "Metastable carbon in two chondritic porous interplanetary dust particles," *Nature* 326: 162-165, 1987.

13. T. Kyotani, N. Sonobe, and A. Tomita, "Formation of highly oriented graphite from polyacrylonitrile by using a two-dimensional space between montmorillonite lamellae," *Nature* 331: 331-333, 1988.

14. F. J. M. Rietmeijer, "Mixed layering in disordered Sri Lanka graphite," *Carbon* (in press).

15. F. J. M. Rietmeijer and I. D. R. Mackinnon, "Poorly graphitized carbon as a new cosmothermometer for primitive extraterrestrial materials," *Nature* 316: 733-736, 1985.

ANALYSIS OF COMETARY AND INTERSTELLAR ICE ANALOGS IN THE ELECTRON MICROSCOPE

D. F. Blake and Gary Palmer

Water-rich ices are a major component of many bodies in the solar system including the outer planets, satellites, comets, and the like. Outside the solar system, mixed molecular ices containing mostly H_2O are primary components of cold interstellar molecular clouds that are thought to be the birthplace of stars and protoplanetary nebulae. This interstellar ice represents the earliest and most primitive association of the biogenic elements. In these ices, solid H_2O serves as a matrix for the low-temperature (15-50 K) trapping of a variety of gases and small molecules in grains within interstellar molecular clouds.

During the formation of the solar system, most low-melting-point solids (including ices) in the inner portion of the solar nebula were volatilized. However, in the outermost portion of the solar nebula, beyond the orbit of Jupiter, original icy condensates from the parent cold molecular cloud may have persisted. It is believed that these condensates coalesced to form icy planetesimals (i.e., comets) which now inhabit the Oort cloud. Some of these icy planetesimals are thought to have bombarded the volatile-poor planets of the inner solar system, providing the earth with its rich complement of gases, volatiles, H_2O, and biogenic elements.

Since ' ₋r formation, all the larger bodies of the solar system such as the planets and satellites have undergone processing and differentiation that have destroyed original phases, components, and phase relationships. However, cometary bodies, residing in the coldness of deep space, too small in general to generate their own heat by compaction, are believed to have persisted relatively unaltered since the origin of the solar system (~4.55 × 10⁹ years before the present). Indeed, numerous remote observations of comets and ground-based analysis of materials thought to have originated in comets suggest that cometary bodies are the most pristine and primitive objects in the solar system. Thus, if one could deduce the physical and chemical state of components and phases within a cometary nucleus, one could gain a more complete understanding not only of cometary physics but also of the nature of volatiles and the biogenic elements as they were introduced to the earth ~4 billion years before

present.

One of the principal means by which remote observations are interpreted is through ground-based simulation and experimentation with analogous materials. This has been particularly true in the case of interstellar and cometary ices. Thus, much is now known about the chemistry of interstellar ices thanks to detailed laboratory studies of the growth and thermal and UV processing of mixed molecular ices.[1-4] The physics of cometary behavior has been studied by infrared (IR) and gas-release studies in bulk amorphous ices, and recently also by the processing of bulk quantities of cometary ice analogs. Although this work has provided insight into chemical and empirical vapor-pressure phenomena, very few direct experimental data exist that adequately address the phase equilibria and (apparently) numerous structural states of the solar system and interstellar ices. A knowledge of the petrology (phase relationships, microstructural associations and assemblages) of planetary, cometary, and astrophysical ice analogs is important because such physical properties control chemical reaction rates, vaporization behavior, bulk densities, and so on. These properties in turn determine how icy celestial bodies manifest themselves to us. Thus, the study of the petrology of ices grown under controlled conditions in the laboratory allows ground-based scientists to interpret more confidently remote observations of planetary surfaces, comets, cold molecular clouds, and the like.

The study of gas release from amorphous and crystalline water ice has only recently begun. Results from studies of this kind have direct application to cometary and planetary outgassing phenomena as well as to studies of the thermal properties of astrophysical ices. Several investigations report anomalous gas release or vaporization phenomena which are as yet only poorly understood. For example, eight different temperature regimes of gas release have been observed in pure water ice as it is warmed from 16 K to melting, yet water undergoes only two phase transitions in this temperature range.[5,6] Two (possibly three) of the temperature regimes of gas release which occur below the amorphous to crystalline transformation suggest that changes in morphology, porosity, or short-range local order ("annealing") are occurring even in the amorphous state. Various physical trapping mechanisms for CO have been reported in various ice matrices based on a detailed analysis of the fine structure of infrared spectra.[7] There is an increase of two orders of magnitude in the vapor pressure of amorphous ice relative to

crystalline ice at the same temperature.[8]
These data have been used to explain the gas
production rate of new comets vs old. Similar
studies have been made of the gas release and
crystalline structure states of low-tempera-
ture mixed molecular ices.[9] Large quantities
of cometary ice analogs have been grown, pro-
cessed by heat and irradiation, and analyzed
in the KOSI (comet nucleus simulation) experi-
ments.[10] Phase separation and migration of
frozen volatiles within the ice after irradi-
ation and temperature processing have been re-
ported.[11] Other studies have been performed
that address the presence or absence of ice
clathrates in solar-system objects and in lab-
oratory analogs.[12,13] The presence or absence
of clathrates bears strongly on the physico-
chemical nature of the ices and their structur-
al and gas release properties. However, the
only direct proof of the presence of an ice
clathrate is by analysis of structural data
contained in diffraction patterns. It is the
microstructural, micromorphological, and mi-
crochemical heterogeneity within astrophysical
ice analogs that must be characterized if the
mechanisms underlying the observed natural
phenomena are to be understood.

Previous Research

Water Ice. Two forms of amorphous water ice
have been described through x-ray diffraction
analysis.[14] These forms differ in density and
second-nearest-neighbor oxygen-oxygen distribu-
tion. The higher density form, whose density
is 1.1 g/cm^3, is made by vapor deposition at
about 10 K. The lower density form is made by
vapor deposition at about 77 K. It has a den-
sity of about 0.94 g/cm^3. When amorphous water
ice is heated above 125 K it irreversibly
transforms into the cubic polymorph.[15,16] This
transformation is kinetically controlled and
proceeds to completion relatively rapidly only
at higher temperatures, yielding submission
randomly oriented crystallites. Upon further
heating, a cubic to hexagonal phase change oc-
curs at about 153 K which is irreversible and
persists until the ice sublimes at about 160 K.

Electron Microscopy of Ice. There is a sub-
stantial body of literature on the electron mi-
croscopy of water ice, and it is not the intent
of this paper to provide a thorough review.
Most of the previous work can be classified
into three general areas: (1) the use of vit-
reous ice as a low-contrast embedding medium
for the EM of biological tissue in its native
state,[16,17] (2) the study of the phase equilib-
ria of mixed molecular ices used as cryopro-
tectants in the freezing and thawing of biolog-
ical tissue,[18] and (3) the study of defects in
"ideal" solids such as condensed gases at low
temperatures.[19,20] The largest body of re-
search pertains to the microscopy of biological
tissue; much of this information is directly
transferable to more general studies of ices
within the electron microscope.

Modification of the Electron Microscope

Modifications were made to our Hitachi
H-500H AEM to accomplish two purposes. (1)
Vacuum-system modifications were made to re-
duce the partial pressure of water vapor and
hydrocarbons so that vacuum-bom sample contam-
ination is substantially reduced or eliminated.
Bakeable micromaze alumina traps were placed in
the rough pump lines to reduce backstreaming of
oil vapor into the microscope. All the rubber
O-rings in the column were replaced by equiva-
lent O-rings made from Viton. (2) To improve
the vacuum in the objective lens polepiece gap,
a 20 1/s ion pump was put in place of the anti-
contamination cold finger in the front of the
microscope (Fig. 1). A lin pump-out line was
removed from the back of the objective pole-
piece area and a modified anticontamination
cold finger was installed in this orifice
through a bellows. These two modifications re-
sult in a differentially pumped volume inside
the polepiece that can be maintained at a vacu-
um level $1\frac{1}{2}$ orders of magnitude lower than that
in the main vacuum manifold of the instrument
(Fig. 2). To monitor polepiece vacuum, a quad-
rupole mass spectrometer was installed in an
unused objective lens aperture port. Finally,
a valve assembly and vacuum control logic was
installed so that as the specimen rod is intro-
duced into the microscope, it is both rough
pumped and diffusion pumped to high vacuum be-
fore the sample is inserted into the polepiece
gap. This procedure reduces the amount of air
and water vapor that can enter the polepiece
gap area during sample exchanges.

A low-electron-dose system was installed
with the intent of minimizing damage to elec-
tron beam-sensitive samples. This system in-
cludes a Gatan Corp. TV camera with video in-
tensifier whose output is digitized and dis-
played in real time on a Macintosh II computer.

Lastly, a gas inlet tube was installed so
that gases of selected compositions could be
bled into the sample chamber and frozen on the
stage. Samples are introduced into the AEM in
two ways: (1) Samples of ices collected or
grown elsewhere are introduced into the micro-
scope in the frozen state using a cryotransfer
holder, and (2) ices of selected compositions
are grown inside the AEM by bleeding of pre-
mixed gases from a sample bulb directly onto a
cryogenically cooled sample substrate (Fig. 1).
The same sample bulb is used for the introduc-
tion of gases into cryogenic sample cells mount-
ed in IR spectrometers in the Low Temperature
Spectroscopy Laboratory (LTSL) at NASA/Ames
Research Center. Thus, experiments can be per-
formed in which morphological and microstruc-
tural changes observed in ices inside the AEM
can be correlated with the evolution of fine
structure in the IR spectra of ices grown and
processed in like fashion.

We have two sample stages (fabricated by
Gatan Corp.) for cryogenic work at prsent.
(1) A liquid nitrogen cooled cryotransfer stage
with a beryllium tip, one tilt direction, and a
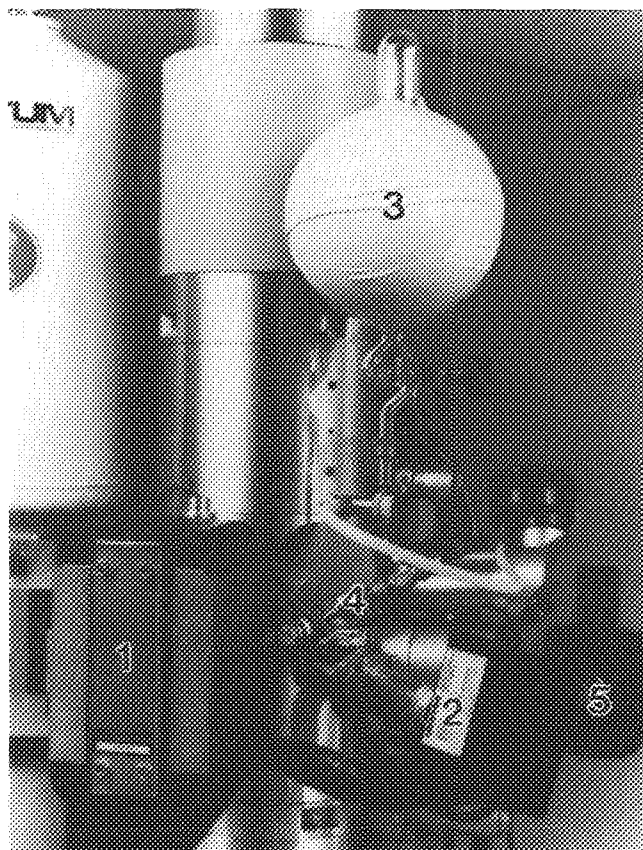specimen shutter that allows the sample and

FIG. 1.--Front view of microscope column show-
ing objective lens polepiece modifications to
allow for high vacuum operation and controlled
growth of mixed molecular ices in situ on sam-
ple substrates. 1, ion pump; 2, quadrupole
mass spectrometer; 3, bulk containing mixed
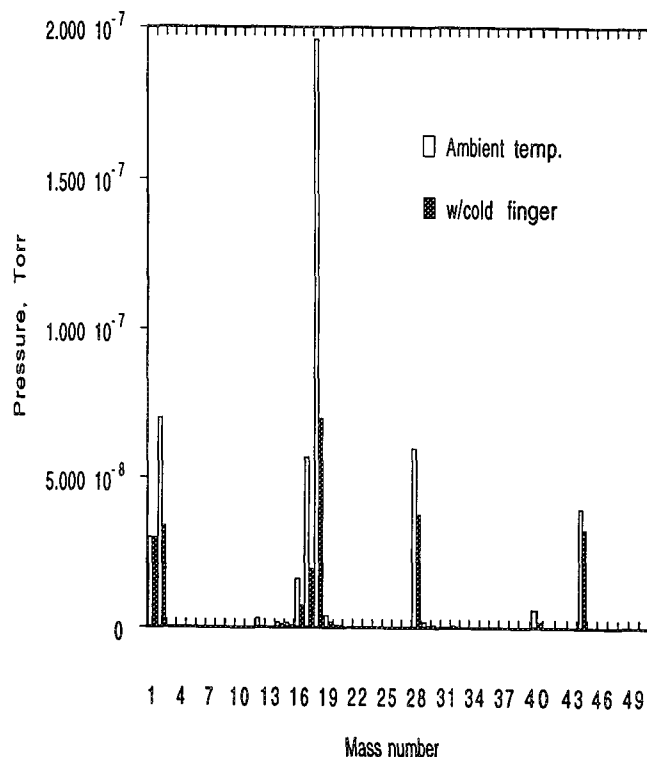gasses at ~40 m Torr; 4, gas inlet system; 5,
liquid He cold stage.

FIG. 2.--Objective lens polepiece gap pressure
(with ion pump in operation) before and after
cooling liquid-nitrogen cold finger surrounding
sample. Mass numbers due to water (18, 17, 16,
2) are reduced significantly when cold finger
is employed. The result is negligible contam-
ination from column-derived water vapor during
operation of cold stage.

specimen rod to be taken out of the microscope
while at low temperature (~110 K). Frozen sam-
ples can be loaded and unloaded from the holder
inside a cryotransfer station and transported
at low temperature in dewars. The stage can
operate in the range 110-363 K. (2) A second
cryostage is liquid helium cooled and can op-
erate in the range 12-363 K. The stage has a
single tilt and is equipped with a specimen
shutter that can be closed over the sample to
minimize contamination at low temperature.
Both cryostages have resolutions of ~3.4 Å at
their lowest operating temperature, although at
intermediate temperatures, when a heater is
used to warm the sample, resolution is some-
what lower. The unmodified Hitachi H-500H has
a resolution specification of 3.4 Å (symmetri-
cal illumination). We were pleased to find
that despite the modifications, which include
(among others) an ion pump bolted directly onto
the objective lens housing and a specially de-
signed, massive anticontamination cold shield
inside the objective lens pole piece gap, we
were able to achieve the resolution specifica-

tion for the machine.

Methods and Results

During operation of the microscope, the
polepiece gap can be maintained in the 6-7 ×
10^{-8} Torr range. Premixed gases are leaked
into the objective polepiece gap in the vicini-
ty of the specimen. The specimen consists of a
3mm EM grid covered with a solid or holey car-
bon film <10 nm thick, which is initially
cooled to 12 or 85 K. Typically, a 200-300nm-
thick layer of ice is formed during 5-10 min of
deposition. The thickness of the film cannot
be measured directly, but the progress of depo-
sition can be visually monitored on the video
display at low magnification. As-deposited
films at these temperatures are amorphous by
electron diffraction. Once a thin layer of
amorphous ice is deposited, the gas inlet sys-
tem is shut off and the shutter on the cryo-
stage is closed to protect the sample. Samples
can be viewed in the as-deposited condition or
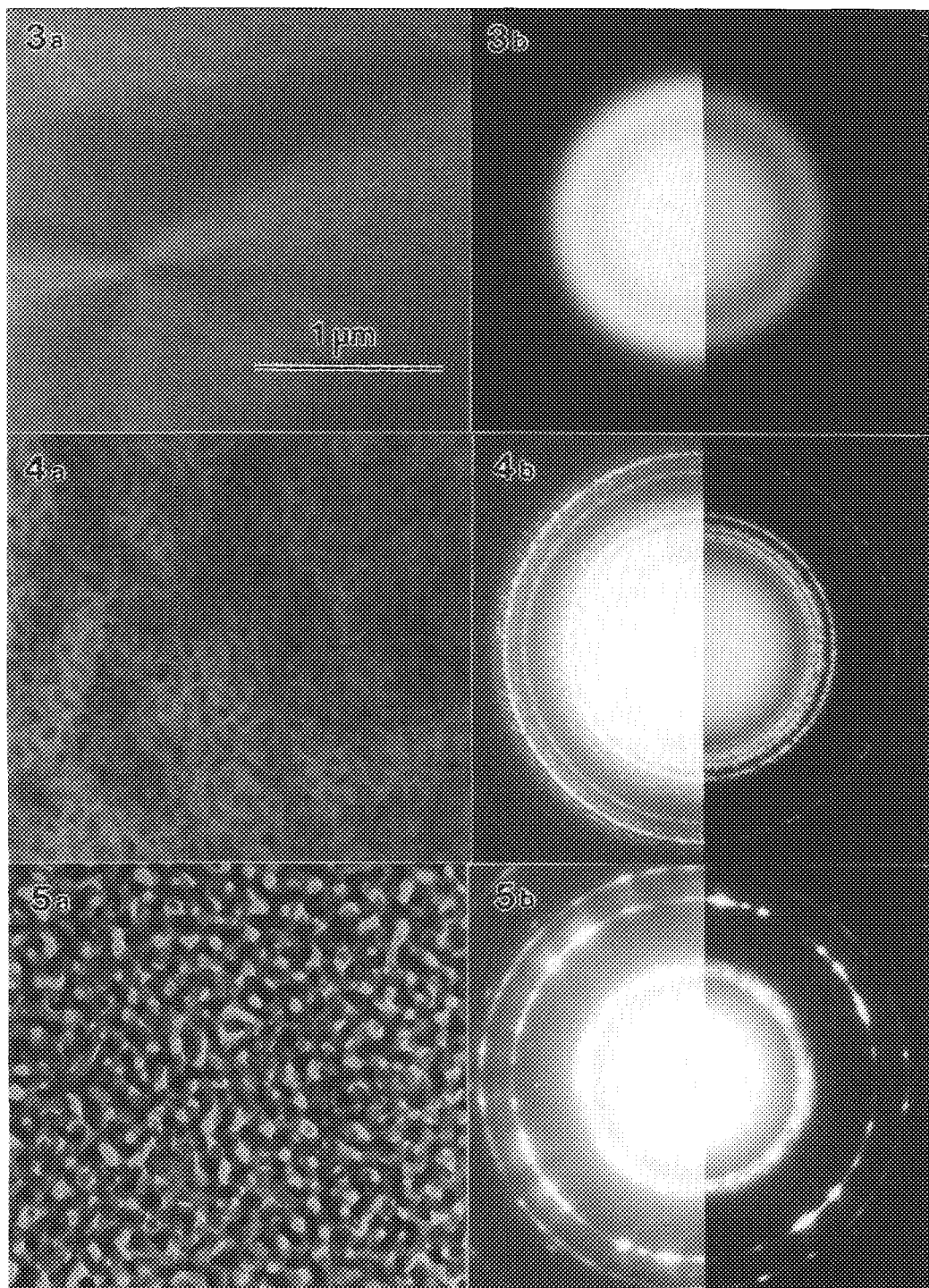after having been subjected to various tempera-

FIG. 3.--(a) Bright-field TEM micrograph of as-deposited 2:1 H_2O:CH_3OH ice, 85 K. No structure is evident in micrograph; weak contrast is due to shadowing of thin-film substrate by the vapor as it was directed onto the surface at a 30° angle. (b) Electron diffraction pattern for 85 K as-deposited pattern for 85 K as-deposited ice, showing characteristics of an amorphous solid.
FIG. 4.--(a) Bright-field TEM micrograph taken after 2:1 H_2O:CH_3OH ice was warmed to 130 K. Crystallization and phase separation are apparent. Magnification same as in 3(a). (b) Selection area electron diffraction pattern of ice after phase separation at 130 K. Powder rings can be indexed as type II clathrate hydrate structure with an a parameter of 16.3 Å.
FIG. 5.--(a) Bright-field TEM micrograph taken after volatilization of amorphous component and inversion of methanol lathrate hydrate to hexagonal ice (T = 150 K). Porous structure is a result of original sub-solidus phase separation during clathrate formation. Magnification same as Fig. 3(a). (b) Selected area electron diffraction pattern of ice after volatilization of amorphous phase. Pattern can be indexed as hexagonal polymorph of water ice (150 K).

ture histories, much as would be experienced by cometary ice during a transit through the inner solar system.

In the initial testing of the microscope modifications, pure H_2O ice was vapor deposited and studied. We are able to deposit and observe the two forms of amorphous H_2O ice,[14] and to view the amorphous to cubic phase transition and cubic to hexagonal transition.[15,16 21-23] With some attention to low-dose imaging technique, both bright- and dark-field imaging is possible at moderate magnification without apparent sample damage. Of course, that does not mean that no damage was experienced by the ice, only that no obvious sample damage is seen. To minimize the effects of radiolysis and beam-induced volatilization, we move to new areas for each micrograph or diffraction pattern.

The behavior of pure H_2O ice inside the microscope--the vapor deposition of amorphous H_2O ice and its transformation into cubic and hexagonal polymorphs--has been thoroughly addressed by others[16,17] and will not be described here. The first mixed molecular ice we studied in the microscope was a simple binary of H_2O and CH_3OH (methanol). We began with a 2:1 H_2O:CH_3OH mixture, which is close to the composition of ices within cold interstellar molecular clouds.[24] When this mixture is vapor-deposited on a thin carbon substrate held at 85 K inside the microscope, an amorphous solid is formed (Fig. 3a). Diffraction patterns from this ice show two diffuse maxima similar to that obtained from amorphous H_2O ice (Fig. 3b). When the temperature of the ice is increased slowly, a rapid and dramatic phase separation occurs at about 130 K (Fig. 4a). One of the components appears to be amorphous ice, and the second phase is crystalline with maxima at 0.39 nm (weak), 0.34 nm (strong), 0.297 nm (strong), and 0.206 nm (moderate). Occasionally, the (111), (220), and (311) maxima of cubic H_2O ice appear as well. When the amorphous H_2O:CH_3OH ice is deposited at 85 K and rapidly raised to 130 K, additional powder rings appear in the pattern (Fig. 4b). When the ice is warmed to about 145 K, the amorphous component disappears leaving behind a highly porous network of crystalline ice (Fig. 5a). At slightly higher temperatures, the ring pattern fades and is replaced by a spotty diffraction pattern that can be indexed as the hexagonal polymorph of H_2O ice (Fig. 5b).

One of the obvious candidates for the crystalline phase that forms at 130 K is methanol clathrate hydrate. Although methanol clathrate hydrate has not been described in the literature, a structure type II clathrate of ethanol has been reported.[25,26] The clathrate II hydrate structure is cubic, space group Fd3m, with a lattice parameter of about 17 Å.[27] In the clathrate II hydrate of ethanol the lattice parameter is reduced to 16.28 Å,[26] presumably due to the effect of hydrogen bonding between guest molecules and water molecules. The observed powder rings can be fit reasonably well to the clathrate II hydrate structure with a lattice parameter of 16.3 Å. Not all maxima

expected for the clathrate II structure are present, and some lines appear that are not allowed in space group Fd3m. However, similar deviations from the expected diffraction pattern have been reported for ethanol clathrate hydrate.[26] These differences were described by the authors as due to slight warping of the ideal structure (due to hydrogen bonding) and to order-disorder relationships among the guest molecules within the clathrate cages.

The ideal stoichiometry for a clathrate II hydrate is ∿1 guest molecule to every 17 H_2O molecules. When the clathrate forms, it can only accommodate about 6% of the CH_3OH and the rest is pushed out into the intercrystalline domains. In a 2:1 H_2O:CH_3OH ice, the result should be a CH_3OH-rich amorphous component, which would occupy the intercrystalline domains. When the amorphous ice sublimes, the remaining crystalline ice is highly porous as in Fig. 5(a). To confirm our identification of the initial crystalline phase as a type II clathrate hydrate, a second series of experiments was performed with a 20:1 mixture of H_2O:CH_3OH, which is much closer to the stoichiometry of the type II structure. After the ice is warmed to 150 K, the clathrate disintegrated leaving pure hexagonal H_2O ice as in the previous experiments, but little pore space was evident (Fig. 6).

Much additional work remains to be performed on this and other two-component and multicomponent ices. However, some observations can be made which may have relevance to the mechanical and gas release properties of comets. First, sub-solidus phase separations are capable of imparting a wide range of mechanical properties to solids. The best-known sub-solidus reaction occurs in the system Fe-C, in which small amounts of carbon and other alloying elements, along with thermal processing, produce the varied properties of steels. In like fashion, the mechanical hardness and physical integrity of cometary ice may be a specific (and predictable) function of composition and temperature history. Second, sub-solidus phase separations produce a complex microstructure which upon further heating and sublimation of one of the phases, may result in a highly permeable microporous architecture. The presence of such microstructures within cometary ice may allow volatile release from deep within the nucleus of a comet through interconnected pore systems, which may explain some of the observations of anomalous gas release such as were recently reported from comet Halley.

References

1. W. Hagen, L. J. Allamandola, and J. M. Greenberg, "Interstellar molecule formation in grain mantles: The laboratory analog experiments, results and implications," *Astrophys. Space Sci.* 65: 215-240, 1979.

2. M. H. Moore et al., "Studies of proton-irradiated cometary-type ice mixtures," *Icarus* 54: 388-405, 1983.

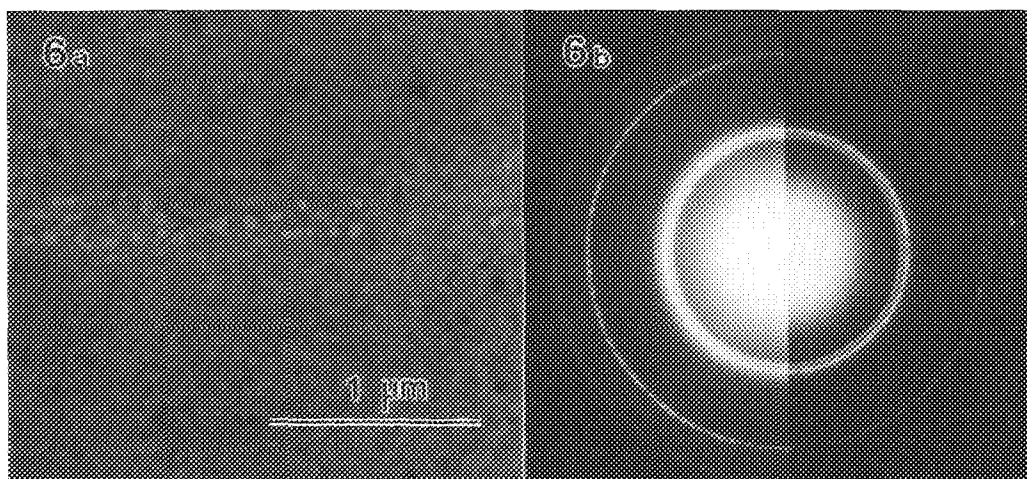3. L. B. d'Hendecourt and L. J. Allamandola,

FIG. 6.--(a) Bright-field TEM micrograph of original 20:1 $H_2O:CH_3OH$ amorphous ice, recorded after inversion of methanol clathrate hydrate to hexagonal ice (T = 150 K). Note absence of porous structure (cf. Fig. 5a), which suggests that almost entire volume of original ice became clathrated without any methanol left over. Magnification same as Fig. 3(a). (b) Selected area electron diffraction pattern of ice after volatilization of amorphous phase. Pattern can be indexed as hexagonal polymorph of water ice (150 K).

"Time dependent chemistry in dense molecular clouds: III. Infrared band cross sections of molecules in the solid state at 10 K," *Astron. Astrophys., Suppl. Ser.* 64: 453-467, 1986.

4. L. J. Allamandola, S. A. Sandford, and G. J. Valero, "Photochemical and thermal evolution of interstellar/pre-cometary ice analogs," *Icarus* 76: 225-252, 1988.

5. A. Bar-Nun, G. Herman, and D. Laufer, "Trapping and release of gases by water ice and implications for icy bodies," *Icarus* 63: 317-332, 1985.

6. D. Laufer, E. Kochavi, and A. Bar-Nun, "Structure and dynamics of amorphous water ice," *Phys. Rev.* B36: 9219-9227, 1987.

7. S. A. Sandford and L. J. Allamandola, "The physical and infrared spectral properties of CO_2 in astrophysical ice analogs," *Astro. J.* 357-372, 1989.

8. A. Kouchi, "Vapour pressure of amorphous H_2O ice and its astrophysical implications," *Nature* 330: 550-552, 1987.

9. A. Kouchi, "Evaporation of H_2O-CO ice and its astrophysical implications," *J. Crystal Growth* 99: 1220-1226, 1990.

10. H. A. Kochan et al., "Particle emission from artificial cometary surfaces: Material science aspects," *Lun. Planet Sci.* XX: 524-525, 1989.

11. P. Hsuing and K. Roessler, "Diffusion of volatiles in cometary analogs," *Lun. Planet Sci.* XXI: 538-539, 1990.

12. D. W. Davidson, Y. P. Handa, C. I. Ratcliffe, and J. S. Tse, "The ability of small molecules to form clathrate hydrates of structure II," *Nature* 311: 142-143, 1984.

13. L. A. Lebofsky, "Stability of frosts in the solar system," *Icarus* 25: 205-217, 1975.

14. A. H. Narten et al., "Diffraction pattern and structure of amorphous solid water at 10 and 77 K," *J. Chem. Phys.* 64: 1106-1121 1976.

15. L. G. Dowell and A. P. Rinfret, "Low temperature forms of ice as studied by x-ray diffraction," *Nature* 188: 1144-1148, 1960.

16. J. Dubochet et al., "Electron microscopy of frozen water and aqueous solutions," *J. Microscopy* 128: 219-237, 1982.

17. M. Adrian et al., "Cryo-electron microscopy of viruses," *Nature* 308: 32-36, 1984.

18. P. Mazur, "Cryobiology: The freezing of biological systems," *Science* 168: 939-949, 1970.

19. J. A. Venables, "Electron microscopy and diffraction of solid α-N_2," *Phil. Mag.* 21: 147-166, 1970.

20. J. A. Venables and C. A. English, "Electron diffraction and the structure of α-N_2," *Acta Cryst.* B30: 929-935, 1974.

21. D. F. Blake and L. J. Allamandola, "Direct determination of the morphology, structure and composition of cometary and interstellar ice analogs in the laboratory," *Workshop on Analysis of Returned Comet Nucleus Samples*, 9, Lunar and Planetary Institute, Houston, 1989.

22. D. F. Blake, L. J. Allamandola, and Gary Palmer, "Direct determination of the morphology, structure and composition of planetary, cometary and interstellar ice analogs," *Lun. Planet. Sci.* XXI: 369-370, 1990.

23. D. F. Blake, L. J. Allamandola, G. Palmer, and A. Pohorille, "Analytical electron microscopy of extraterrestrial ice analogs," *Proc. XIIth ICEM* 1: 594-595, 1990.

24. L. J. Allamandola, S. A. Sandford, and G. J. Valero, "Photochemical and thermal evolution of interstellar/precometary ice analogs," *Icarus* 76: 225-252, 1988.

25. A. D. Potts and D. W. Davidson, "Ethanol hydrate," *J. Phys. Chem.* 69: 996-1000, 1965.

26. P. Boutron and A. Kaufmann, "Metastable states in the system water-ethanol: Existence of a second hydrate; curious properties of both hydrates," *J. Chem. Phys.* 68: 5032-5041, 1978.

27. J. E. Bertie and S. M. Jacobs, "Infrared spectra from 300 to 10 cm^{-1} of structure II clathrate hydrates at 4.3 K," *J. Chem. Phys.* 69: 4105-4113, 1978.

MICRO-POWER SEEMANN-BOHLIN DIFFRACTOMETER FOR CRYSTAL-LOGRAPHIC IDENTIFICATION OF MINERALS

Songquan Sun, J. G. Bradley, and D. B. Wittry

X-ray powder diffraction is a useful technique for determining the composition of mineral mixtures in rocks and soils not only on the earth but also on planetary surfaces such as Mars. Basically, this technique involves the diffraction of monochromatic x rays by a powder specimen. Three geometries have been used for identification of minerals by arrangement of the relative position of the x-ray source, specimen and detector:[1,2] the Debye-Scherrer, Bragg-Brentano, and Seemann-Bohlin geometries.

The Seemann-Bohlin geometry is based on focusing x-ray optics. It has advantages of higher efficiency and simpler mechanism than the Debye-Scherrer or Bragg-Brentano geometry. However, for mineral analysis on planetary surfaces, the application of the conventional Seemann-Bohlin diffractometer has been limited because of the requirement for a power of hundreds to thousands of watts in the x-ray source and for precision alignment of the mechanical scanning mechanism. Despite considerable efforts[2,3] devoted to x-ray powder diffraction systems suitable for remote mineralogical analysis, large size, use of moving parts, and high power consumption are still the main obstacles for previously developed diffractometers being put into practical application. Although a low-power diffractometer has been described[4] based on a radioactive x-ray source and a position-sensitive detector, it has the problems of low intensity or a need for a strong radioactive source.

In this paper a modified Seemann-Bohlin (S-B) diffractometer has been proposed in order to solve these problems. The diffractometer has the advantages of no moving parts, very low x-ray source power (2 W), and convenient way of changing of the wavelength of the x-ray source.

Songquan Sun is at the Department of Materials Science and D. B. Wittry is at the Departments of Materials Science and of Electrical Engineering at the University of Southern California, Los Angeles, CA 90089-0241; J. G. Bradley is in the Infrared and Analytical Instrument Systems Section of the Observational Systems Division, Jet Propulsion Laboratory, Pasadena, CA 91109.

Principles of the Modified Seemann-Bohlin Diffractometer

For the conventional S-B geometry, the specimen satisfies the Bragg condition at various positions over an arc along the focal circle, so that the output of the x-ray source is utilized efficiently. In effect, the powder is like the curved crystal of the Johansson-geometry curved crystal monochromator.

Figure 1 shows a schematic view of the conventional S-B diffractometer, where a line slit, specimen holder, and detector are all on a focal circle. X rays from an x-ray source pass through the line slit and diverge on to the sample. For a given x-ray wavelength, x rays are diffracted through the same angle $2\theta_B$ corresponding to a set of (hkl) planes. The diffracted beams lying in the plane of the focal circle are focused to a point on the focal circle. However, the other diffracted beams lie on the surface of cones that have axes coincident with the incident beam. For a line source used with a Soller collimator, the locus of the focused points is a line along the cylinder. The focused line is typically recorded on photographic film, or detected by a suitable counter after passing through an exit slit that is rotated about the center of the focal circle.

The modified S-B diffractometer uses a spherical geometry instead of a cylindrical geometry. It has the following features: (1) specimens are mounted on a spherically curved surface, (2) a microfocus x-ray source is used, (3) moving parts would be eliminated by use of CCD or photodiode arrays, (4) the x-ray source operates at low power (2W), (5) multiple targets may be used by deflecting the electron beam of the microfocus x-ray source, (6) high resolution is obtained by a small x-ray source size, and (7) the overall size is small.

As discussed by James,[5] the x-ray optics of the focusing geometry for powder diffraction with a point source may employ a toroidally curved specimen surface. The S-B geometry is only a kind of approximation; i.e., the toroidal surface is replaced by a cylindrical surface tangent to it and the line source could be considered as an array of point sources parallel to the axis of the cylindrical surface. Figure 2 shows the x-ray optics for powder diffraction with a point source and a toroidal surface. If x rays of wavelength λ are incident on the arc of the focal circle and P is a point on the specimen diffracting the x rays through an angle $2\theta_B$, the diffracted beam cones will intersect the focal circle at intersection point I. If the specimen is rotated about a line joining the points S and I, a toroidal surface is ob-

tained. A significant portion of x rays diffracted from the toroidal surface will superpose to form a curved band. This configuration enables the entire specimen surface to be used for a given x-ray wavelength and diffraction line.

The spherical surface is another approximation to the toroidal surface; in this case the specimen is rotated about a line passing through the source and the center of the focal circle. Let the radius of curvature in the plane perpendicular to the focal circle be R_2 and the radius of focal circle be R; then for a cylindrical surface $R_2 = \infty$ and for a spherical surface $R_2 = R$. The intensity of the focused x rays from the spherically curved specimen is higher than that from a cylindrically curved specimen, particularly for the rays close to the point diametrically opposite the source.

Use of a point source is advantageous for three reasons: (1) the point x-ray source can have higher brightness than a line or area source, (2) the output of the x-ray source is utilized more efficiently because the slit is eliminated, and (3) the wavelength can be changed by a small displacement of the electron beam used to generate the x rays.

For the conventional S-B diffractometer an x-ray detector is mechanically scanned along the focal circle over a large diffraction angle range. The scanning operation results in slow and inefficient data acquisition; furthermore, the moving parts present a reliability problem. In the final form the modified S-B diffractometer would use a CCD array or photodiode array in combination with a scintillator to obtain the full diffraction pattern efficiently and reliably.

An interchangeable x-ray source makes it possible to identify the composition of mineral mixtures in rocks or soils with higher accuracy, which can be realized by deflection of the focused electron beam in the x-ray source from one metal target to an adjacent target of another metal. If the targets lie on the focal circle, the focusing properties of the modified S-B diffractometer will not change. By comparing the diffraction patterns of minerals ob-

tained from different wavelengths with the diffraction patterns of standards stored in a computer, the superimposed patterns from crystal mixtures could be unscrambled easily. Also, the use of multiple targets to obtain the diffraction pattern from the same powder sample can provide a solution to the usual difficulty in x-ray crystallography: to obtain a large number of reflections require a short wavelength, but high accuracy in determining large d spacing requires a long wavelength.

Instrumental Considerations

The prototype modified S-B diffractometer is shown in Fig. 3. A hollow 101.6mm-diameter stainless-steel ball is used as a housing which gives 50.8mm radius for the focal circle. Two openings on the top of the ball are for the source and sample; a slot at the bottom is for collection of signals. At present CCD or photodiode arrays have not been used; instead, the diffraction patterns were recorded on spherically curved Kodak TMAX P3200 negative film. The spherically curved negatives were made from readily available 36mm film cut to 15mm strips, which were sealed in light-tight, x-ray transparent flat plastic tubes. A loading/unloading mechanism curves the flat tube spherically against a base with a concave spherical surface.

The compact size affects the signal-to-background ratio drastically due to scattered radiation from the wall of the ball. Bafflers were used to reduce the background. Optimization of the electron beam voltage is another way of improving the signal-to-background ratio. The integrated continuum intensity $I_{con} \propto V^2$, whereas the intensity of a specific K line $I_K \propto (V - V_K)^{1.7}$. When the beam voltage decreases, the intensity decreases from continuum radiation more than it does for the characteristic line. In our experiments beam voltages of 30, 25, 20, 15, and 10 kV have been tried. A beam voltage of 15 kV gives the best signal-to-background ratio for Ti Kα radiation. The effective sample width is also important. If the width is too narrow, the
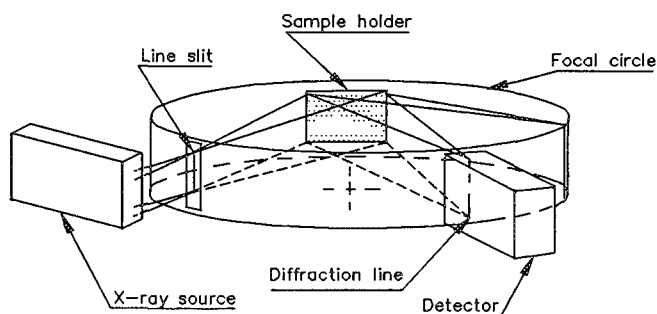

FIG. 1.--Conventional Seemann-Bohlin focusing diffractometer with line x-ray source and detector rotating about center of focal circle.
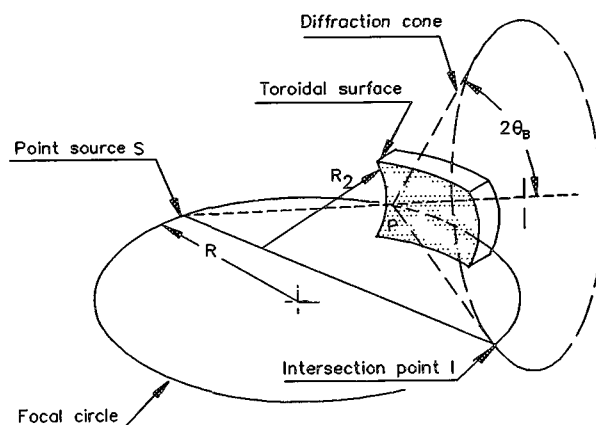

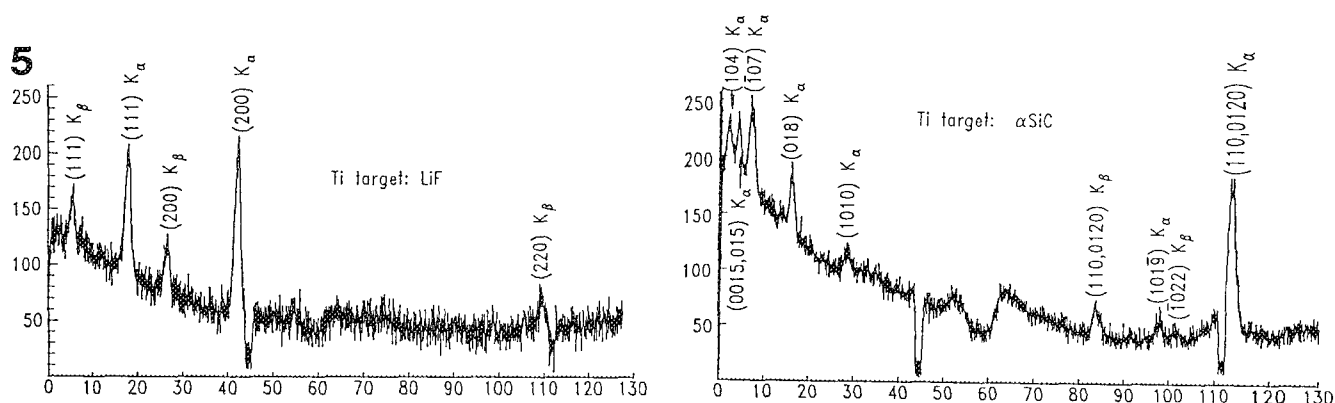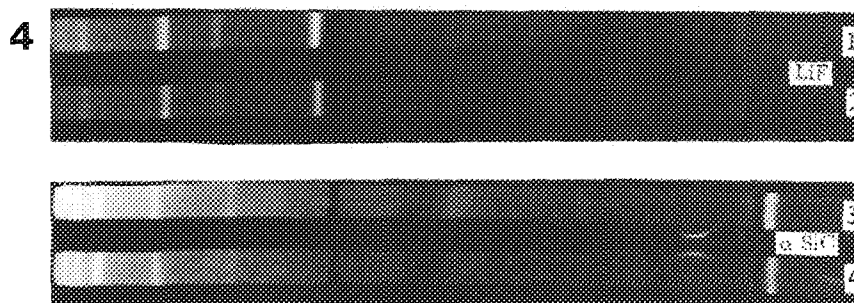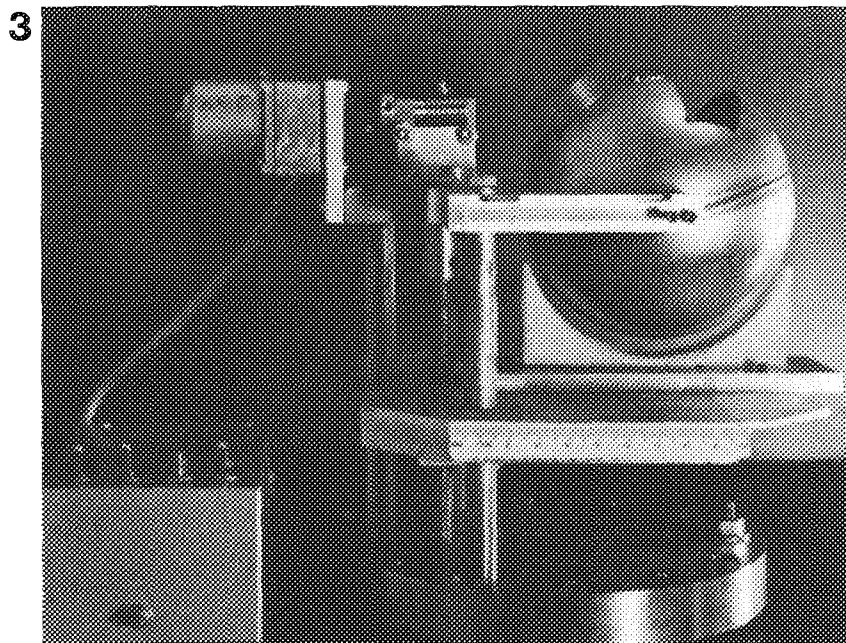FIG. 2.--Modified Seemann-Bohlin diffractomer with point x-ray source and toroidal or spherical holder.

FIG. 3.--Prototype modified Seemann-Bohlin diffractometer.
FIG. 4.--Positive print of diffraction patterns of LiF and αSiC crystal powders. Images were
recorded with Ti target, electron-beam voltage 15 kV, current 0.16 mA, on Kodak TMAX P3200 nega-
tive film. Exposure times were 12 min for LiF pattern 1 and 7 min for LiF pattern 2; 30 min for
αSiC pattern 3 and 20 min for αSiC pattern 4. The two black bands shown on each pattern were
due to two metal supports which increase ball strength. Supports also serve as references
for establishing zero and scale factor of patterns. Bright short arcs shown on pattern 4 were
due to kinks in film.
FIG. 5.--Intensity distribution profiles of diffraction patterns of LiF (pattern 2) and αSiC
(pattern 3) crystal powder. Profiles were obtained by densitometer scanning with aperture of
diameter of 25 μm and 25μmstep increment. Background increase near horizontal scale mark 65 due
to Ti Kα reflection of stainless-steel ball.

301

advantage of the spherical sample will be lost; in contrast, a greater width will affect the resolution..

Experimental Results and Discussion

So far, six kinds of samples have been tested: LiF, SiC, quartz, olivine, gypsum, and hematite. These crystal materials were ground and shifted through a 400-mesh screen or a 600-mesh screen. There was no obvious difference in diffraction patterns on the film for particle sizes of 400 mesh and 600 mesh. Hence we used 400-mesh powder for all samples.

The typical experimental conditions were as follows: electron beam voltage, 15 kV; electron beam current, 0.16 mA; exposure time, 7-30 min with Ti target; powder size, 400 mesh, effective sample area, 6.35×32 cm^2.

Figures 4 and 5 show the diffraction patterns of LiF and SiC samples and the intensity distribution profiles obtained by densitometer scanning. The powder pattern of a mineral can be described in terms of two sets of parameters: the position of the reflections and their relative intensities. Since the positions depend on the instrument geometrical factors and on wavelength, the usual procedure is to determine the values of d for various reflections and then to refer to standard data such as the ASTM Powder Diffraction File.

The LiF and SiC used were pure crystal materials and their diffraction patterns are easily indexed. However, the powders of quartz, olivine, gypsum, and hematite consisted of natural minerals, which are complex mixtures determined by the geological environment. Indexing these natural minerals by means of this diffractometer is theoretically possible but requires the use of more lines, which would require a better signal-to-background ratio. Nevertheless, the diffraction patterns of these minerals could be partially indexed with respect to the major constituents.

Cu and Ti targets were used in these experiments. Concerning these targets, it was found that the copper target resulted in the diffraction lines occurring at too small Bragg angles. The Ti Kα radiation provided better separation of the lines in the diffraction pattern. The pictures obtained with a Ti target show peaks from both the Kα and Kβ radiation, since no Kβ filter could be used for Ti K radiation.

Spherically curved samples gave peaks having the shape of an unsymmetrical triangle with the side of lower slope in the direction closer to the sample. This finding can be explained by reference to Fig. 6(a). For divergent x rays from the x-ray source S incident onto the spherical sample, if Bragg's condition is satisfied at a point P with grains oriented in all possible directions, then the diffracted beams form a cone with a half angle $2\theta_B$ at the vertex. A sphere containing the focal circle, source, and sample may be called a Rowland sphere. The cone intersects the Rowland sphere forming an arc; if all points along the focal circle on the sample behave as point P does, a

diffracted arc image A is formed by the intersection of a number of cones with the Rowland sphere. If we assume that point P rotates along the surface of the sphere to a point P', a new diffracted arc image A' is formed by another group of cones. Thus, if the powder particles distribute on the spherical surface continuously and uniformly, the superposition of these diffracted arc images forms a curved band in which the intensity distribution varies linearly up to the maximum intensity.

A picture of one line of a diffraction patterns of Al(111) polycrystalline film is shown in Fig. 6(b). This experimental result is a simulation obtained with Ti Kα radiation and a specimen substrate that had a spherical plate geometry with radius of the surface equal to the diameter of the Rowland sphere.

Further Work

The preliminary results show that the modified S-B diffractometer would be a candidate for planetary applications, particularly as a tool for sorting samples in the course of a "sample return mission." However, improvement of the signal-to-background ratio and resolution is still necessary. To achieve this goal, powder holders of toroidal shape, a Soller-type collimator, and other targets and filters will be tested. As mentioned in the foregoing section, a point source and a toroidal surface are necessary conditions for powder diffraction. Compared with cylindrical surface, a spherical surface appears to be a better geometry but may not be the best geometry. A toroidally curved x-ray diffractor having a geometry of $R_2 = 2R$ might give the best performance over a wide range of Bragg angles, as shown by Wittry and Sun for single-crystal diffractors.[6]

A Soller-type collimator will be used to reduce the length of the arcs making up the focused lines and to increase the resolution. A chromium target and vanadium filter will be employed to reduce the background and Kα line. If the thickness of the vanadium filter is 12.5 μm, the transmission of Cr Kα and Kβ would be 56.63% and 2.09%, respectively. In this way the signal-to-background ratio will be improved, since the filter also reduces the continuum on the high energy side of the filter's K absorption edge.

References

1. B. D. Cullity, *Elements of X-ray Diffraction*, Addison-Wesley, 1956, 149.
2. H. W. King, C. J. Gillham, and F. G. Huggins, "A versatile Bragg-Brentano/Seemann-Bohlin powder diffractometer," *Advances in X-ray Analysis*, vol. 13, New York: Plenum, 1969, 550.
3. K. Das Gupta, H. W. Schnopper, A. E. Metzger, and R. A. Shields, "A combined focusing x-ray diffractometer and nondispersive x-ray spectrometer for lunar and planetary analysis," Ref. 2, vol. 9, 1966, 221.
4. J. C. Gregory and T. A. Parnell, "A low

power x-ray diffractometer for soil analysis in remote locations employing a multiwire proportional counter detector array," *NS-19:* 24, 1972.

5. R. W. James, *The Optical Principles of the Diffraction of X-rays,* London: G. Bell and Sons, 1958, 334.

6. D. B. Wittry and S. Sun, "X-ray optics of doubly curved diffractors," *J. Appl. Phys.* 67: 1633, 1990.

(a)

(b)

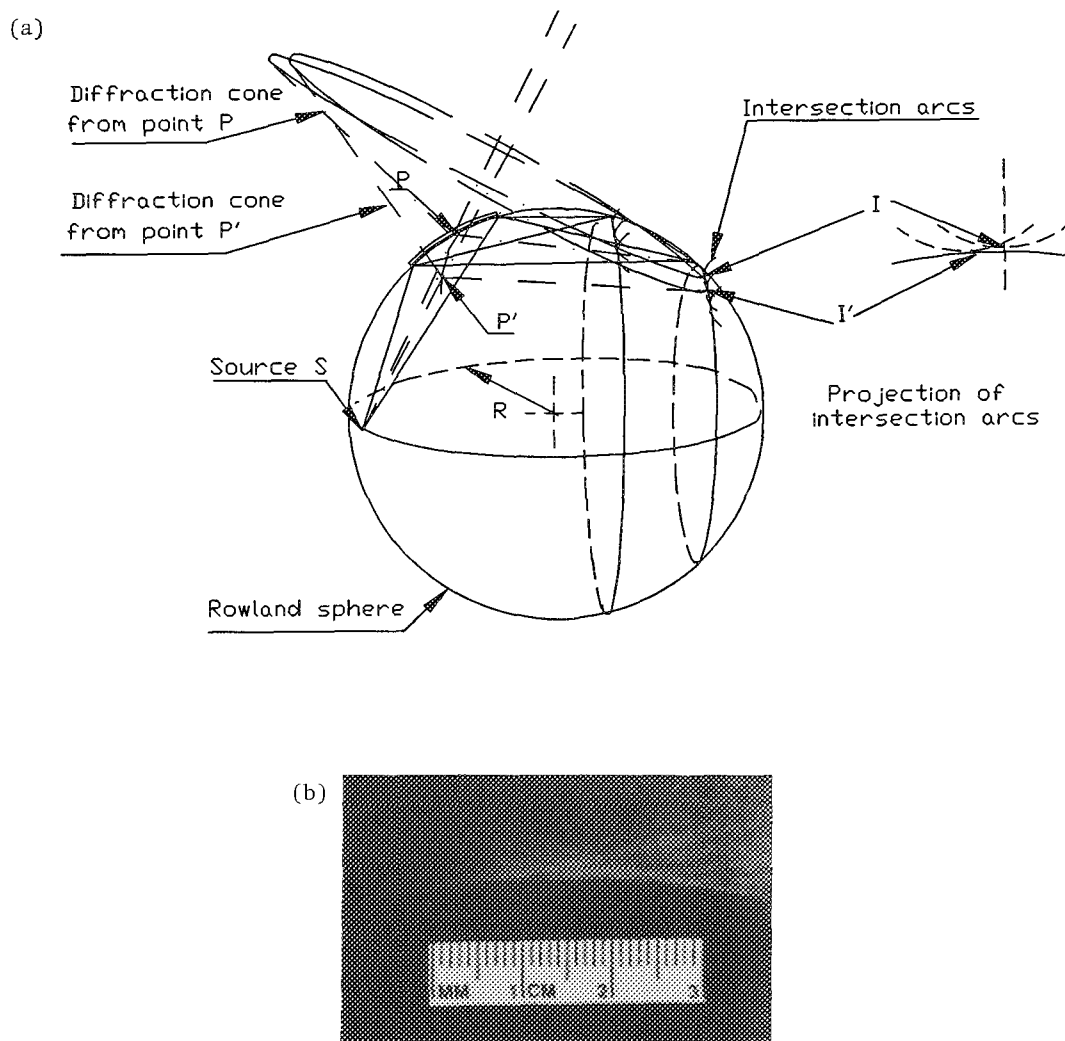FIG. 6.--(a) Theoretical and experimental explanation of diffraction line shape obtained from modified Seemann-Bohlin diffractometer. (b) Bright fringes are due to x rays passing through slots of 9-slot stainless-steel sheet mask placed between sample surface and point x-ray source. Pattern was recorded on Type 57 Polaroid film at 15min exposure time, beam current of 0.13 mA, beam voltage of 20 kV, and Ti target.

MICROSTRUCTURAL CHARACTERIZATION OF SOLDERS AND BRAZES FOR ADVANCED PACKAGING TECHNOLOGY

A. D. Romig Jr., D. R. Frear, P. F. Hlava, F. M. Hosking, J. J. Stephens, and P. T. Vianco

In the past the electronics industry has always attempted to increase the speed of electronic components and decrease the size of electronic assemblies by developing and manufacturing smaller and faster basic-level components (e.g., integrated circuits). However, it is now becoming apparent that the next significant advancement in electronic assembly size and speed may come not as a result of smaller and faster devices, but rather as a consequence of smaller and more closely spaced packages. This increased packaging density will occur at early levels of assembly as industry moves toward multichip modules. It will also occur at later packaging steps as industry continues to expand the use of surface mount technology (SMT) and mixed mounting technology (through hole attachment as well as SMT on one circuit board). Furthermore, there will be an increased propensity to use higher packaging density on printed wiring boards (PWB) and to place more PWBs in a given volume at yet the next level of packaging.

The robust packaging of electronic devices is as important to the overall reliability of the final assembly as the robustness of the individual components and subassemblies. The demands placed on the materials used to manufacture electronic subassemblies will be greatly increased by the trend to increase packaging density. These new needs will manifest themselves in two ways: (1) Manufacturing technology will need to be improved to accommodate the manufacture of components placed ever more closely to one another. In addition, the greater packaging density will make rework even more undesirable and require that industry build it right the first time. (2) The higher packaging density will increase the thermal load on the device, both in terms of the maximum temperatures experienced in service and in terms of the temperature range that will be created for the device. The long-time exposure to elevated temperatures can alter materials so that with time in service microstructure of the materials changes. The change in microstructure may result in detrimental changes in properties (e.g., electrical, thermal, mechanical). Furthermore, wide variations in temperature, such as heating and cooling between power-on and power-off cycles, can increase the

susceptibility of materials used in the assembly to thermomechanical fatigue.

One class of materials on which this advanced packaging technology will place severe new demands will be the alloys used to join assemblies and subassemblies (e.g., solders and brazes). These materials will be taxed both from the perspective of enhanced manufacturability as well as greater in-service robustness. For an excellent in-depth summary of the solder technology, both with respect to manufacturing technology and in-service performance of solders, the reader is referred to *Solder Mechanics: A State of the Art Assessment.*[1]

Advanced manufacturing technology will be required to make the new generation of robust and reliable packages. In addition, recent legislation requiring the discontinuation of halogenated solvents for cleaning is driving research in fluxless soldering/brazing technology. Pending legislation, which may outlaw the use of lead in solders, is driving research for lead-free solders that can be used for electronic assembly.

New technology, such as SMT, makes solder more than an electrical interconnect in that it requires the solder to be the structural material attaching the component to the PWB. At a peak service temperature of 120 C, a eutectic Pb-Sn solder is being used at 0.86 of its homologous melting point. At these temperatures, the microstructure of the solder joint will clearly evolve. Changes such as microstructural coarsening of the solder and extensive interaction between the solder and substrate are to be expected. Any attempt to use a continuum-mechanics approach (e.g., the finite-element method, FEM) to assess the performance of the solder joint will be inadequate unless the time-dependent properties of the materials in the joint are known and included in the constitutive relations of the FEM model. Lifetime predictions for such a joint will require a detailed understanding of the microstructure of the joint. To assess the performance of joints in advanced packages, the microstructure and any time-dependent microstructural changes must be completely characterized. Optical metallography, scanning electron microscopy (SEM) with secondary electrons (SE) and backscattered electrons (BSE), electron probe microanalysis (EPMA) by wavelength-dispersive x-ray spectrometry (WDS) for elemental mapping and the determination of phase compositions, and transmission electron microscopy (TEM) to examine fine-scale microstructural changes are techniques now being extensively used to characterize packaging

technology. It is the objective of this paper, through the use of selected case studies, to illustrate how advanced microstructural characterization techniques can be used to improve packaging technology. The specific case studies discussed are (i) microstructural characterization of solders, (ii) microstructural characterization of solder joint embrittlement of leaded, surface-mount transistors, (iii) microstructural characterization of metal/ceramic brazes in electronic applications (iv) microstructural characterization of direct brazing of grphite to copper.

Techniques for Microstructural Characterization of Packages

Solder and braze joints can be examined by a variety of techniques in order to characterize the materials in the joint. Techniques used for such characterizations range from simple optical microscopy to sophisticated analysis by transmission electron microscopy. The types of instruments and techniques actually used in a particular study will be dictated by the data required to solve the problem. All the materials characterization techniques are complementary and all might be used in the same study, although most studies will require only a few of them. Even the most time-intensive techniques are cost effective if they can supply the key information needed to solve the problem. Only a brief description of materials characterization techniques useful in the analyses of electronic packages are presented here. For further details on the microstructural characterization of solder joints, the reader is referred to the literature.[1-6] For further information on the characterization techniques, the reader is referred to classic texts such as *Practical Scanning Electron Microscopy and Microanalysis*[7] and *Materials Characterization*.[8]

Optical Microscopy (OM). Optical studies of polished cross sections are usually the first step in the examination of a solder or braze joint. Optical microscopy offers the materials scientist/engineer a readily available global view of the problem. These studies are accomplished by use of microscopes specially designed to illuminate the specimen with normally incident light. The light is reflected from the flat, polished surface of the specimen and through the objective lens of the microscope and viewing system (eye, camera, or TV). Most materials (metals, alloys, intermetallic compounds, and even ceramics) in a joint can be usually identified because each has a different total and spectral reflectance. The various materials reflect colors that range from the subtle yellow tint of nickel (relative to iron) to the intense colors of gold, copper, and the silvery-gold tint of certain intermetallic compounds. Boundaries between phases tend to be highlighted due to differing polishing characteristics of the phases. Etching of the speciman can be useful in distinguishing phases that are otherwise similar in appearance. Etching also allows for the easy observation of

grain structure in homogeneous materials by preferentially attaching the material at grain and twin boundaries. Optical micrographs display magnified views of the general distribution of materials in a joint and indicate the presence or absence of various components such as gold and other platings, the presence or absence of imperfections, pits, voids, contamination by flux, mixing and/or reaction between materials, and the formation of new phases such as intermetallic compounds. The resolution for optical microscopy is approximately 0.5 μm. In general, optical microscopy does not yield any chemical information.

Scanning Electron Microscopy (SEM): Secondary Electron Images. Secondary electrons (SE) are the most often used signal for imaging. They are produced in abundance and generally offer sufficient signal for producing images with good contrast. Secondary electrons are produced as a result of the inelastic scattering of the primary beam electrons in which a conduction band electron is ejected from the sample. The secondary electrons are low in energy (few eV) and escape from a shallow depth (5 nm). They carry predominantly topographic contrast information. These secondaries are collected by an Everhart-Thornley detector (scintillator/photomultiplier). They are efficiently attracted to the detector by a positively charged grid in front of the detector. When the beam is rastered over a surface and the resulting secondary electron signal used to modulate a cathode ray tube CRT, differences in topography of the surface give rise to differences in brightness on the image and the product is a detailed, high-magnification image of the surface. Structural details, such as the general appearance of a soldered assembly (before cross sectioning), phase boundaries, cracks, pits, inclusions, and other relief-producing features become quite distinct. Advantages of SEM over OM include much improved resolution (<50 nm in these types of specimens) and therefore yield more meaningful (not empty) magnification. SE images in the SEM also have tremendously increased depth of field relative to optical microscopy.

Scanning Electron Microscopy (SEM): Backscattered Electron Images. Backscattered electrons (BSE) are often used for imaging in the SEM, especially when qualitative compositional information is required. Backscattered electrons are produced when primary (beam) electrons are elastically scattered by the nuclei of the atoms in a material. The backscatter coefficient of a material is related primarily to the average atomic number of the material. The more massive the nuclei, the more efficient the backscattering (the higher the backscatter coefficient). The backscatter coefficient is secondarily related to density. By using the output from the BSE detector to modulate the CRT, an image displays contrast that is related to the composition of the materials. It is often possible to distinguish the mater-

ials in a soldered or brazed assembly in such a BSE image. Thus, it is one of the best tools for obtaining a general compositional assessment of a soldered or brazed joint. In addition, by using suitable detection systems and image processing, one can produce BSE images that reveal very subtle differences in the compositions of materials (e.g., the diffusion of nickel into originally pure copper braze metal).

Scanning Electron Microscopy (SEM) and Electron Probe Microanalyzer (EPMA): Element (X-ray) Maps. Characteristic x rays are the primary signal used to generate compositional information about microstructural constituents. X rays are produced when the high-voltage primary electrons in the beam of an SEM, EPMA, or TEM interact inelastically with atoms in the target material. The production of characteristic x rays requires that the primary beam electron dislodge an electron from an inner orbit of an atom in the material. The resulting configuration, in which the atom is said to be ionized, is energeticaly unstable. The atom will reduce its energy by transitioning an electron from an outer shell into the inner electron shell vacancy created by the initial ionization. In making this transition, the electron must lose a quantum of energy equal to the energy difference between the two shells. This energy will be emitted from the atom in the form of a characteristic x-ray photon or an Auger electron. The production of an x-ray relative to an Auger electron is more favored as the atomic number increases. Each element has a different configuration of electron shells with different energy level transitions and therefore produces a different characteristic x-ray spectrum. X-ray detectors can discriminate the x rays by wavelength (wavelength-dispersive spectrometry, WDS) or (energy-dispersive spectrometry, EDS), and thereby identify the elements present in the specimen. If the electron beam is rastered over a region of the specimen, and the signal from these detectors is used to modulate a CRT, an image revealing the distribution of a particular element in a solder or braze joint is created. A complete set of maps taken on an identical area of a specimen will show the distribution of all the elements in the scan area. In analog scanning/mapping, changes in the density of spots on the images are indications of the concentrations of the elements in the various parts of the assembly. Quantiative or semiquantitative mapping, with digital scanning and image processing, permits the comparison of elemental concentrations among maps of different elements. Maps reveal the elemental composition of the microstructural constituents that were merely differentiated by BSEs. It is routine to differentiate metals like copper, nickel, tin, lead, indium, gold, etc. as well as alloys such as brass, stainless steel, Kovar, etc. Elemental maps may also be useful in assessing compositional homogeneity in a specimen. Elemental x-ray maps, often used in conjunction with BSE images, are also useful in delineating the position and sequence of platings, their thicknesses, quality, and continuity. Elemental maps also disclose the presence of new phases, such as intermetallic compounds that may form between the solder and substrate either during processing or in service. The resolution for x-ray elemental mapping is governed by the size of the x-ray generation volume, which is typically 1 μm.

Electron Probe Microanalyzer (EPMA): Quantitative Analyses. X-ray intensity data can be used to determine the composition of phases and other microstructural constituents within a specimen quantitatively. X rays from each of the elements known to be in a sample are individually counted for a predetermined time under well-defined instrumental conditions and the integrated x-ray intensity is ratioed to similar data measured from suitable standards of known compositions. The resulting count rate ratios (k-ratios) are proportional to the amount of each element in that specific region of the specimen. Quantitative compositions can be determined from these ratios by the application of matrix correction algorithms which account for the perturbation (atomic number effects that describe the efficiency of x-ray generation, x-ray absorption and x-ray fluorescence) of the various x-ray intensities by the presence of the constituent elements in the specimen. This quantitative information can be used to verify that the proper alloys were used in a particular assembly, or to identify new phases, such as intermetallic compounds, formed by reaction between various starting materials. The extent of diffusion of one element into another (e.g., Ni into a Cu braze) can be quantified in order to assess whether the material has retained a microstructure and composition with adequate performance characteristics. The resolution for quantitative microanalysis is also governed by the size of the x-ray generation volume, which typically is 1 μm.

Transmission Electron Microscopy (TEM): Transmission electron microscopy is not often used in the analysis of braze and solder joints due to the extreme difficulty of specimen preparation. However, in cases where the power of TEM is really required, the efforts of specimen preparation are warranted. In TEM, the specimen must be made thin enough to be transparent to a beam of high-energy (100-400keV) electrons, which requires specimen thicknesses typically smaller than 150 nm. As the electrons pass through the specimen, they are scattered elastically and inelastically. These various scattering phenomena produce a variety of electron *types* that can be used to generate a variety of images. In the classical TEM mode, the specimen is illuminated by a beam of parallel electrons. Many of these electrons are scattered (diffracted) in specific forward directions and produce a diffraction pattern that contains crystallographic information about the specimen. These beams can be used to produce either a bright-

field (transmitted, or undiffracted, beam) or dark-field (diffracted beam) image. Microstructural features only a few nanometers in size can be examined in this imaging mode. Under specialized conditions, it is possible to use an interference phenemononon to *image* individual atoms and rows of atoms. Such images are called high-resolution (HREM) or atomic-resolution (AREM) images. They are particularly useful for characterizing interfaces. In many modern microscopes, called analytical electron microscopes (AEM), the beam can be focused to a probe and scanned, which allows one to produce transmitted-electron (bright-field or dark-field), secondary-electron, and backscattered-electron images by using the signal from the appropriate detector to modulate the CRT. The beam can also be stopped at a point for microanalysis by use of x rays. Because scattering in thin films is more limited than in bulk specimens, the resolution for microanalysis in the AEM is improved by approximately two orders of magnitude (10 nm).

Case Studies

Microstructural Characterization of Solders.
The solder alloys that are typically used in electronic applications are the Sn-Pb alloys, both near eutectic and high-Pb, and alloys containing In. Three such alloys are described here (all compositions given throughout this paper are in wt.%): 5Sn-95PB (T_{mp} = 311 C), 60Sn-40Pb (T_{mp} = 183 C), and 40In-40SN-20PB (T_{mp} = 121 C), where T_{mp} here indicates the start of melting. These solder alloys, because of their differing melting temperatures, can be used in a step soldering process in which successive joints are made with a series of solders with progressively lower melting points. Because of space limitations, only the binary Pb-Sn solders will be described here.

The 5Sn-95Pb solder, in the as-solidified state, consists of large grains of Pb with a dispersion of β-Sn precipitates. For slow cooling rates from the melt, a discontinuous precipitation process produces a "pearlitic-like" structure of Pb and Sn. At higher cooling rates, similar to those found in microelectronic solder joints, the β-Sn forms a nominally homogeneous distribution of precipitates as shown in the TEM micrograph in Fig. 1. The β-Sn precipitates lie on the $(111)_{Pb}$ habit plane with an orientation relationship of $(111)_{Pb}//(010(_{Sn}$ and $[0\bar{1}1]_{Pb}//[001]_{Sn}$.[9,10] This solder fails intergranularly under conditions of thermomechanical fatigue as shown in the SEM micrograph in Fig. 2.[11] It is possible that the β-Sn precipitates act to strengthen the interior of the Pb grains and thus make the Pb grain boundaries susceptible to failure.

The 60An-40Pb as-solidified solder has a near eutectic microstructure that consists of alternating Sn and Pb-rich phases with a small number of proeutectic Pb dendrites, as shown in the optical micrograph in Fig. 3. The microstructure of this solder is characterized by individual colonies, or cells, of similarly oriented lamella with slightly coarsened regions at the boundaries. The individual grain structure inside the lamella can only be observed by transmission electron microscopy. The microstructure in a lamellar and globular region is shown in the TEM micrograph in Fig. 4. The structure contains β-Sn grains 0.1 μm in diameter. During thermomechanical fatigue the microstructure of the 60Sn-40Pb solder evolves by heterogeneous coarsening at the cell boundaries, as shown in the optical micrograph in Fig. 5. Both the Pb and Sn phases coarsen. Eventual failure occurs through these coarsened regions via cracking at the β-Sn grain boundaries.[12,13]

Microstructural Characterization of Solder Joint Embrittlement of Leaded, Surface-mount Transistors. Surface-mount components may include several varieties of leaded packages. The conductor leads are typically made of Kovar (54Fe-29Ni-17Co), or similar alloys, and are plated with nickel (1 to 4 μm) to create a solderable surface. The nickel layer is then coated with gold (1 to 3 μm) to protect the nickel surface from excessive oxidation and contamination. Pretinning of the leads prior to attachment of the component to the printed wiring board replaces the gold coating with a fused (63Sn-37Pb) solder layer and thus reduces the likelihood of solder joint embrittlement caused by the formation of gold-tin intermetallic compounds. It has been shown that as little as 5 wt.% Au can severely degrade the mechanical integrity of the joint.[14] A pretinning procedure was developed in which each lead of a surface-mount transistor was immersed into a pot of 63Sm-37Pb solder (250 C) for approximately 2 s. The process was repeated in a second pot of solder. Data from wire dissolution experiments indicated that the accumulated immersion time was adequate to dissolve the gold film completely.[15] This case study will demonstrate that gold was in fact not sufficiently removed from the lead and solder film, with a resulting embrittlement of the circuit-board solder joints.

An optical micrograph of the transistor mounted on the printed wiring board is shown in Fig. 6. Figure 7 shows the same location on a similar board after loss of the transistor. Scanning electron microscopy (SEM) of the fracture surfaces of the bonding pads and transistor leads indicated limited ductility. Energy-dispersive x-ray analysis of the lead and pad fracture surfaces (Fig. 8) detected gold in addition to tin and lead, which led to the hypothesis that embrittlement of the solder joints by the formation of gold-tin intermetallic compounds was responsible for the failure. Several pretinned transistors were examined to determine whether gold was being retained in the solder film after the pretinning process. A gold x-ray map of the solder film cross section on a transistor lead pretinned by the schedule described above is shown in Fig. 9. Gold was present in the solder film and as an undissolved layer at the lead/solder inter-
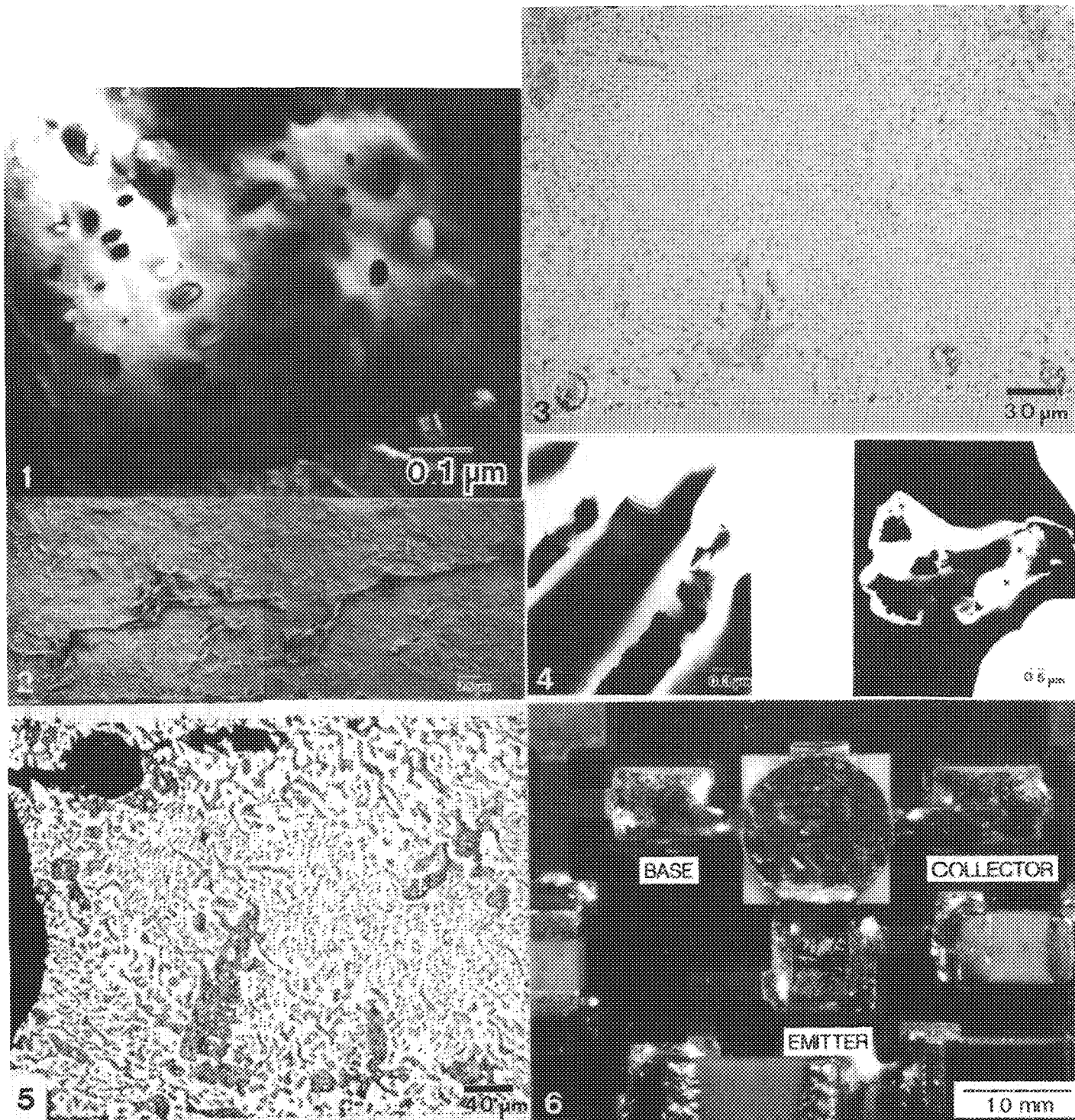
FIG. 1.--TEM micrograph of 5Sn-95Pb solder microstructure. Precipitates of β-Sn occur in homogenous distribution.
FIG. 2.--SEM of 5Sn-95Pb solder after imposition of thermomechanical fatigue. Failure process of this solder is intergranular at Pb grain boundaries.
FIG. 3.--Optical micrograph of 60Sn-40Pb solder. Light regions are Sn-rich, dark regions are Pb-rich. Solder is divided into cells, or colonies , of similarly oriented lamella.
FIG. 4.--TEM micrographs of 60Sn-40Pb solder revealing grain structure in (a) lamellar regions, (b) globular regions. Sn-rich regions are lighter areas with a small-feature size of 0.1 μm.
FIG. 5.--Optical micrograph of 60Sn-40Pb solder after conditions of thermomechanical fatigue. Solder heterogeneously coarsens at cell boundaries, which leads to eventual failure through these coarsened regions.
FIG. 6.--Optical micrograph of leaded transistor solder bonded to circuit board.
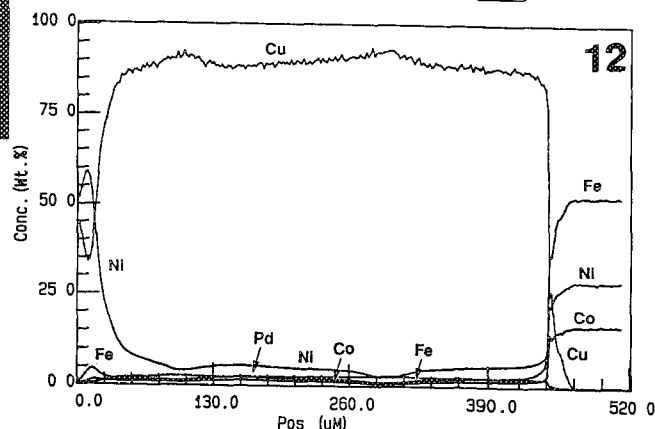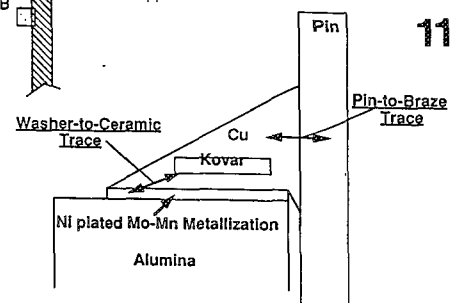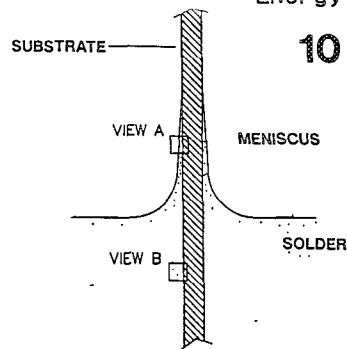
309

FIG. 7.--Optical micrograph of bonding pads of failed transistor.

FIG. 8.--EDS spectrum of emitter lead fracture surface.

FIG. 9.--Gold map of solder film cross section of pretinned lead.

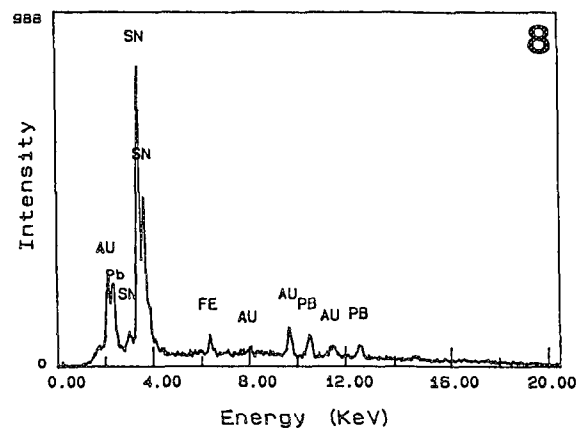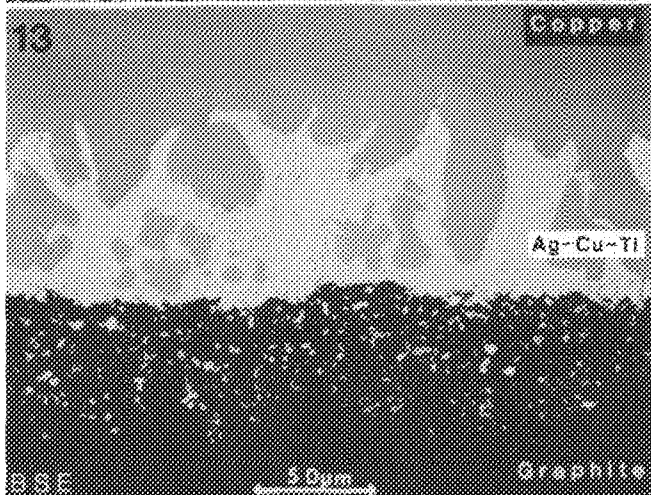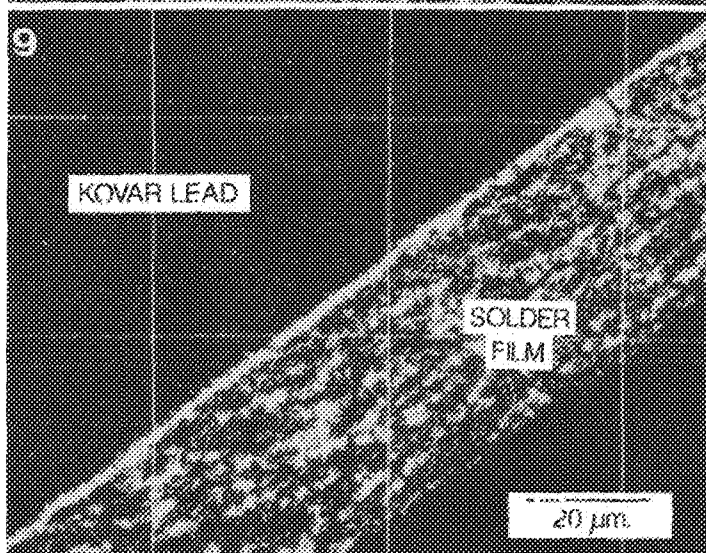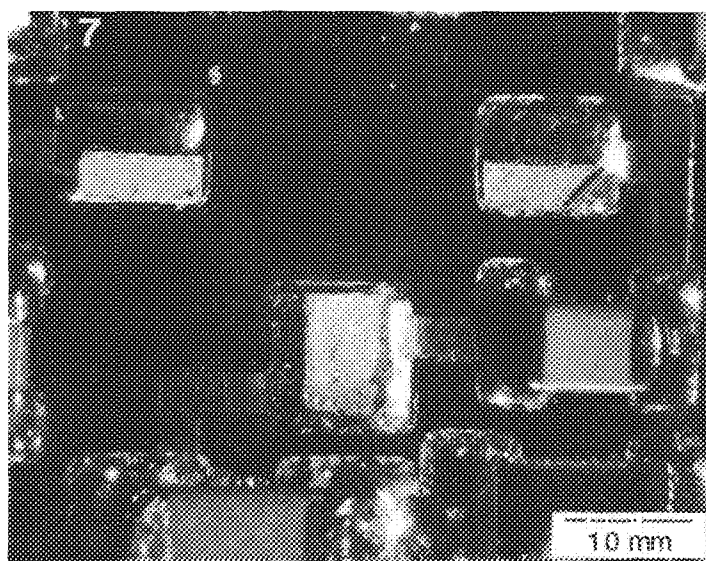FIG. 10.--Geometry of solder meniscus on vertical plate.

FIG. 11.--General location of two types of quantitative electron microprobe linescans performed on brazed area seals: pin-to-braze and washer-to-ceramic traces. Area seal has cylindrical symmetry around middle of pin.

FIG. 12.--Results of "washer-to-ceramic" quantitative linescan performed on area seal with Palco alloy pin brazed for 10 min with peak braze cycle temperature of 1109 C. Trace begins at Ni plated layer on top of Mo-Mn metallization and proceeds through Cu braze to end at Kovar washer.

FIG. 13.--BSE micrograph of isotropic graphite-AgCuTi-Cu braze joint.

face. Increasing the immersion time to as much as 4 s per dip did not eliminate gold from the solder layers.

Microstructural analysis was used to develop the following scenario for the embrittlement of the circuit board solder joints. During the pretinning immersion, gold became heavily concentrated in the limited solder volume comprising the meniscus, as shown in area A of Fig. 10. This hypothesis was confirmed by (1) optical microscopy on sessile drop samples (63Sn-37Pb on Au/Ni plated Kovar) and (2) gold x-ray maps of vertically immersed Au/Ni plated Kovar coupons. The solder bath temperature (250 C) allowed most of the gold to remain in solution and so precluded the formation of the intermetallic compounds. Upon withdrawal of the lead from the solder, a boundary layer of solder developed at the lead surface and remained with the lead as it exited the solder bath. This solder film was heavily alloyed with gold. The lead rapidly cooled, causing most of the gold either to remain in the solder film as a supersaturated solution or to form as finely distributed precipitates, instead of forming an interfacial intermetallic layer. This observation is consistent with SEM, backscatter electron imaging, and EPMA gold maps of solder film cross sections taken from pretinned leads. The gold signal was relatively uniform in the solder volume and lacked the customary needle or blocky morphologies of large intermetallic pounds. During vapor-phase reflow of the circuit board, the leads were heated to 215 C for 20 to 30 s, which quickly promoted the formation of gold-tin intermetallic compounds from the dissolved gold. The limited volume of solder in the surface mount joint was insufficient to dilute the gold concentration below the critical level. The intermetallic crystals developed in the solder near the lead and resulted in a fracture path that followed the contour of the lead. The correspondence between the fracture path lead and the contour of the lead is apparent in the micrograph shown in Fig. 7.

A significant reduction of the Au content in the solder films was achieved by an increase in the number of immersions (dips in solder bath). Each subsequent step served to remove an additional amount of Au, thereby further reducing the Au concentration in the solder coating remaining on the lead. After implementation of the new processing procedure, the final concentration of Au in the solder was below the level required to induce embrittlement.

Microstructural Characterization Metal/ Ceramic Brazes for Electronic Applications. A number of vacuum electronic components utilize a cylindrical joint geometry for metal/ ceramic brazing known generally as an "area seal" (Fig. 11). In this braze joint, the alumina ceramic is metallized with Mo-Mn metallization; the metallization is Ni-plated prior to brazing with Cu in a hydrogen atmosphere. A Kovar alloy washer is used to help control the thermal expansion mismatch between the Cu brazement and the alumina; the pin ma-

terial may be Kovar, Palco alloy (65Pd-35Co), or Ni-plated 316L stainless steel. Despite the use of low-thermal-expansion materials such as Kovar, significant residual stresses may be developed in the alumina, depending on the level of alloying that occurs due to the interaction of the pin, the Ni-plated Mo-Mn, and the Kovar washer with the Cu brazement. If the residual stress in the alumina is high enough, cracks will start at the very tip of the brazement and run in toward the center of the area seal. Although creep-induced stress relaxation of these residual stresses is possible in a batch furnace with extended cooldown times, belt furnaces with fixed belt speeds generally allow very little time for such stress relaxation to occur.[16] In general, if the level of alloying in the Cu brazement can be minimized, crack-free area seals can be consistently produced, because relatively small levels of alloying of the Cu brazement lead to significant increases in creep strength of the braze relative to pure Cu.[17,18]

Materials processing and materials characterization aspects of the metal/ceramic area seal electronic feedthrough study. As part of this study, two groups of area seals were produced: (a) a group of samples with different pin alloys (either Kovar, Palco, or Ni-plated 316L stainless steel) which were all brazed for relatively long times, i.e., 10 min above the melting point of Cu (1084 C), with a peak temperature of 1109 C; and (b) a group of area seals with Palco alloy pins that had various brazing times and peak temperatures. All braze runs were performed with a wet hydrogen process using either pure hydrogen or dissociated ammonia.

The various samples were examined with an automated JEOL 8600 EPMA controlled by the Sandia Task software package.[19] The EPMA was used both for elemental x-ray mapping (analog) and the measurement of quantitative compositional linescans. Although two types of EPMA linescans were performed (Fig. 11), special attention is here given to the "washer-to-ceramic" linescans, since they are closer to the point of maximum stress in the alumina ceramic. In general, the same trends of alloying are observed in both linescans, although the level of alloying for a particular sample is generally higher in the vicinity of the pin.

Effect of pin material on alloying level of the Cu brazement: 10 min/1109 C brazes. The highest alloying levels in the brazes were observed with the Palco alloy pin, the only pin alloy discussed in detail here. Figure 12 shows the results of a linescan that ran from the Ni-plated layer on top of the Mo-Mn metallization through the braze to the Kovar washer. The average braze composition obtained from this sample was found to be 89.6 Cu, 4.75 Ni, 2.55 Pd, 1.96 Fe, and 1.16 Co. Other area seal samples brazed under the same conditions with various pin materials showed generally less alloying. The Palco pins cause the larg-

est amount of alloying under these brazing conditions, followed by the Ni-plated 316L stainless steel pins; the lowest alloying levels are achieved with Kovar alloy pins.

Effect of brazing time and peak temperature on alloying levels in area seals with Palco alloy pins. The second group of samples focused on the reduction in alloying level, which can be obtained by minimizing the amount of time spent above the melting point of Cu during brazing. The 3min/1097 C run represents the fastest braze process cycle that can be achieved with the available belt furnace available, and does show some reduction in alloying level compared to the 10min/1109 C process cycle. Two short-time samples were both run by use of a batch furnace equipped with a viewport, so that the operator could observe flow of the Cu braze and thus minimize time spent above 1084 C. Extremely low levels of alloying are achieved with the batch furnace process. For example, a 7s/1087 C process cycle leads to an average braze composition of 99.59 Cu, 0.20 Ni, 0.01 Pd, 0.11 Fe and 0.01 Co. In comparison with the longer braze cycle shown in Fig. 12, it is apparent that a very large reduction in the level of alloying has been achieved with the batch brazing process. Although only a limited number of developmental batch brazes have been performed similar to the 7s/1087 C process cycle, no cracking has been observed in the alumina near the end of the Cu braze fillet in batch-brazed samples, suggesting that the lower level of alloying these brazes does indeed serve to reduce the residual stress in the alumina ceramic.

In general, the trend in alloying levels observed with the 10min braze time can be understood by examination of the shapes of various binary Cu phase diagrams and (assuming that one actually had a binary system) calculating the expected amount of alloying in the brazement if equilibrium were achieved. If one examines the binary systems of interest, Cu-Pd, Cu-Co, Cu-Ni, and Cu-Fe, it is apparent that the Cu-Pd system predicts very high levels of alloying of the Cu at 1109 C due to the flatness of the liquidus and solidus lines at the Cu-rich end.[20] By contrast, the Cu-Ni system leads to a lower alloying level, and the lowest levels are expected with the Cu-Fe and Cu-Co systems.

Microstructural Characterization of Direct Brazing of Graphite to Copper. A major challenge to the Magnetic Confinement Fusion Energy program is the fabrication of various plasma-facing components that must survive high heat, particle, and eddy-current loading conditions. These components typically consist of graphite armor tiles brazed to a metal substrate. A good joint between the tiles and substrate results in low thermal resistance across the graphite-metal interface with efficient cooling during plasma disruptions. The metal substrate is generally copper because of its excellent thermal properties. The large difference in thermal expansion between graphite and copper can produce relatively high residual brazing stresses and lead to failure at or near the braze joint. It is therefore important to develop a brazing methodology that minimizes these potentially damaging stresses. Engineers at Sandia National Laboratories in Albuquerque, N.M. have been especially interested in studying the effects of compliant interlayers, controlled thermal processing, and active filler metals on producing a thermally resistant joint.[21-24] This case study discusses the microanalytical results of directly brazing isotropic and pyrolytic graphite to oxygen-free high-conductivity (OFHC) copper with an Ag-Cu-Ti filler metal.

Poco AXF-5Q graphite was directly brazed in vacuum to OFHC Cu with Ag-26.7Cu-4.5Ti (nominal weight percent) at 860 C. Graphite cannot be generally wet by most commercial filler metals, but Ti promotes wetting by reacting with the graphite surface. The resulting braze joint should be realtively ductile and resistant to thermal cycling.

SEM analysis of the graphite-Cu joint revealed excellent wetting (Fig. 13). The filler metal penetrates approximately 50 μm into the porous Poco graphite and produces an excellent metallurgical bond. X-ray elemental distribution maps of Ag, C, Cu, and Ti are shown in Fig. 14. The bulk braze microstructure is composed primarily of Ag-rich eutectic and Cu-rich proeutectic regions. There is also a Cu-rich transition region of between the braze and OFHC Cu substrate, caused by filler metal dissolution of the base metal. This produces a leaner Ag-based, hypereutectic composition in the bulk braze. Although most of the Ti constituent diffuses to the graphite interface, Ti is also found in the Cu-rich phase. Quantitative compositional EPMA of the Ag and Cu-rich regions detected 27% Cu and <0.3% Ti in the Ag phase and 8.5% Ag and 2.5% Ti in the Cu phase.

The reaction layer at the graphite and braze interface was examined by TEM, including electron diffraction analysis. The reaction layer was identified as TiC (lattice parameter = 0.432 nm) and its average thickness was 0.35 μm (Fig. 15). The formation of the reaction layer allows the direct wetting of graphite by the active Ag-Cu-Ti filler metal.

More recent hardware designs have used polylytic graphite (PG) in place of isotropic graphite to take advantage of its enhanced thermal properties. Figure 16 shows an optical micrograph of a PG-OFHC Cu substrate brazed with the Ag-Cu-Ti alloy. Comparable wetting results were observed. Prototype components have been tested in a Sandia-designed high heat flux test system with joints surviving peak surface heat fluxes of 3 kW cm² or greater.[25] This technology is being applied to the fabrication of the Tore Supra pump limiter in Cadarache (France).

Summary

Advanced packaging technology is placing new and severe demands on the solders and brazes used in assembly. Demands for higher quality and new environmental legislation are driving
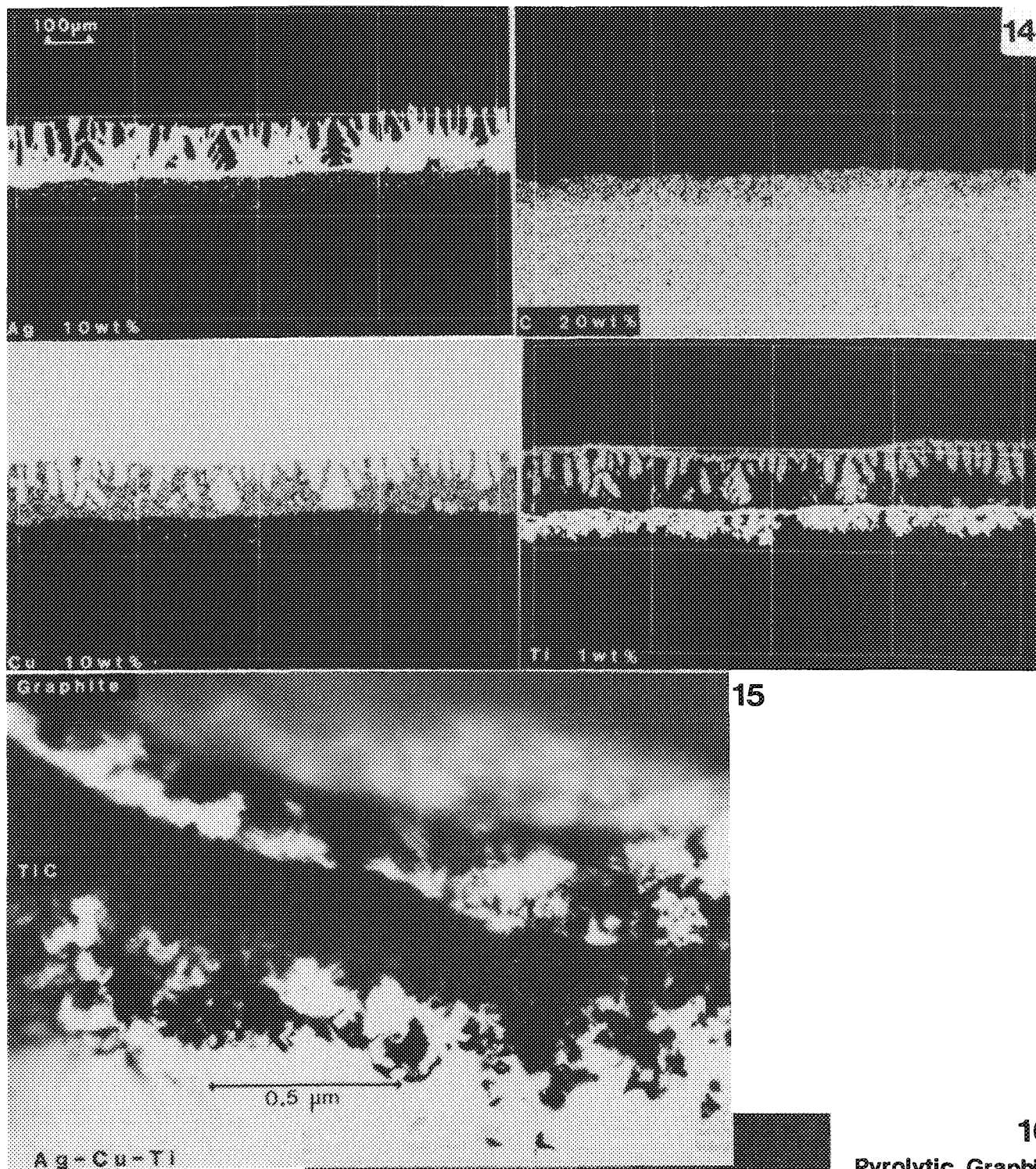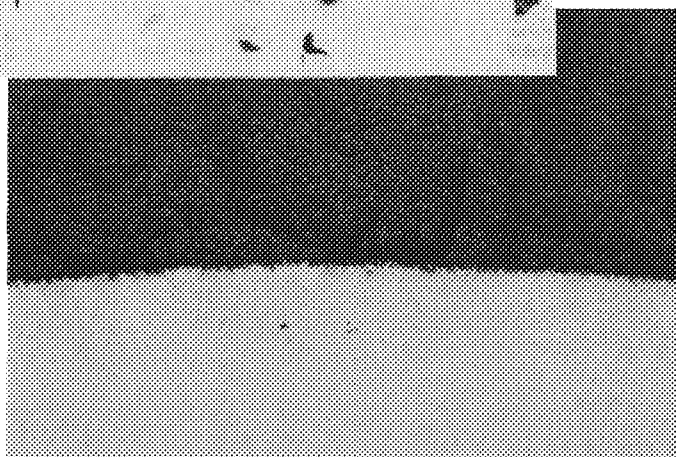
Pyrolytic Graphite

Ag26.7Cu4.5Ti

OFHC Cu

FIG. 14.--X-ray distribu-
tion maps (Ag, C, Cu, Ti)
of isotropic graphite/
AgCuTi-braze joint.
FIG. 15.--TEM bright-field
image of TiC reaction
layer.
FIG. 16.--Optical micro-
graph of pyrolytic graph-
ite to OFHC Cu braze
joint made with active
Ag-Cu-Ti filler metal.

313

the evolution of manufacturing technology, and more severe in-service requirements and a higher level of in-service reliability are driving the evolution of materials and processing technologies. The ability to examine the microstructure and time-dependent microstructural evolution of the brazes and solders used in advanced packaging is essential to meeting these new demands. Studies such as those reviewed here are essential and the design, materials, and manufacturing engineers must work together to develop the new product required for competition in the new international industrialized marketplace.

References

1. D. R. Frear, W. B. Jones, and K. R. Kinsman, *Solder Mechanics: A State of the Art Assessment*, Warrendale, Pa.: Minerals, Metals and Materials Society, 1991.

2. C. Lea, *A Scientific Guide to Surface Mount Technology*, London: Electrochemical Publishers, 1988.

3. H. H. Manko, *Solders and Soldering*, New York: McGraw Hill, 1979.

4. F. N. Sinnaduri, *Handbook of Microelectronics Packaging and Interconnect Technologies*, London: Electrochemical Publishers, 1985.

5. R. J. Klein Wassink, *Soldering in Electronics*, 2nd ed., London: Electrochemical Publishers, 1989.

6. The Metals Handbook, *Metallography and Microstructures*, vol. 9, 10th ed., Materials Park, Ohio: ASM International, 1985.

7. J. I. Goldstein et al., *Practical Scanning Electron Microscopy and Microanalysis*, New York: Plenum Press, 1981.

8. The Metals Handbook, *Materials Characterization*, vol. 10, 10th ed., Materials Park, Ohio: ASM International, 1986. (See especially chapters on OM, SEM/EPMA and TEM.)

9. J. B. Posthill, D. R. Frear, and J. W. Morris Jr., *Proc. 44th Ann. Meet. EMSA*, 1986, 410.

10. D. R. Frear, J. B. Posthill, and J. W. Morris Jr., *Metall. Trans.* 17A: 1325, 1989.

11. D. R. Frear, D. Grivas, M. McCormack, D. Tribula, and J. W. Morris Jr., *Proc. Effect of Load and Thermal Histories on Mechanical Behavior*, Warrendale: TMS, 1987, 113.

12. D. R. Frear and W. B. Jones, *Proc. NEPCON 1990*, 1340.

13. S. M. Lee and D. S. Stone, *Proc. 40th ECTC Conference*, 1990, 491.

14. M. Bester, *Proc. InterNEPCON*, 1968, 211.

15. W. G. Bader, *Welding J.* 48: 551s, 1969.

16. J. J. Stephens, S. N. Burchett and F. M. Hosking, in P. K. Kumar, Ed., *Metal/Ceramic Joining*, 1991, TMS.

17. K. Monma, H. Suto, and M. Oikawa, *J. Japan. Instit. Metals* 28: 253-258, 1964.

18. B. L. Jones and C. M. Sellars, *Metal Sci. J.* 4: 96-102, 1970.

19. W. F. Chambers, *SANDIA TASK8*, Sandia National Laboratories Report SAND85-2037, 1985.

20. T. B. Massalski, Ed., *Binary Alloy Phase Diagrams*, Am. Soc. for Metals, vol. 1, 1986.

21. F. M. Hosking, *DOE IMOG Joining Subgroup Semiannual Meeting*, Miamisburg, Ohio, 1984.

22. F. M. Hosking, *AWS International Brazing and Soldering Conference*, Chicago, Ill., 1987.

23. J. A. Koski, F. M. Hosking, R. D. Watson, and C. D. Croessmann, *Symposium of Fusion Technology*, Utrecht, The Netherlands, 1988.

24. F. M. Hosking, R. E. Semarge, and C. R. Hills, *Microbeam Analysis--1987*, 257.

25. F. M. Hosking, J. A. Koski, R. D. Watson, C. D. Croessmann, and J. A. Rejent, *AWS International Brazing and Soldering Conference*, Washington, D.C., 1989.

ANALYTICAL ELECTRON MICROSCOPY OF RAPIDLY SOLIDIFIED METALS

T. F. Kelly, L. M. Holzman, Keesam Shin, Y.-W. Kim, J. C. Bae,
J. E. Flinn, P. P. Camus, and A. J. Melmed

Analytical electron microscopy has been an important part of studies of rapidly solidified metals since the beginning of these studies. This is largely due to the small dimensions of characteristic microstructural features of rapidly solidified materials. Examples of the need to characterize these materials on the submicron scale are given below for two types of rapidly solidified material: centrifugally atomized steel powder and electrohydrodynamically atomized submicron spheres.

Rapid solidification has a marked effect on the precipitates in a material. A high-purity alloy of Fe-40 wt% Ni was prepared by RSP.[1] There should be no precipitates in the alloy after heat treatment at 1200 C. This fact was confirmed in a conventionally processed sister material. However, the rapidly solidified material has a large number density of small precipitates present. Figure 1(a) is a bright-field image of an extraction replica taken from the alloy. In addition to some $(Fe,Cr)_{23}C_6$ carbides, aluminum oxide particles are found. The x-ray spectrum in Fig. 1(b) is taken from an aluminum oxide precipitate. These oxide precipitates are not distinguishable from the carbides by their appearance in the structure. X-ray and EELS mapping of the elements in the respective precipitates has been pursued in order to learn about the relative number and distribution of the precipitate types.

A 304 SS that has been rapidly solidified by centrifugal atomization[2] was found to contain a large number density of 1-2nm-diameter cavities. These cavities have been imaged by through-focal bright-field and annular dark-field imaging in a field-emission STEM (VG HB501).[3,4] The images are combined in an image processor in order to demonstrate that the two image types indicate the same features. This approach eliminates the possibility of certain artifacts (Fig. 2a). The thickness of the sample was measured by low-loss EELS[5] to determine the number density to be about 10^{23} m^{-3}. We conjecture that these cavities are stabilized by an oxide coating, but they are too small to analyze with confidence with AEM. This material was studied in an energy-compensated atom probe and when oxygen was observed, it was

present in a highly localized region (Fig. 2b). These findings are consistent with our concepts of oxide-stabilized cavities.

Pure elements and alloys have been processed by electrohydrodynamic atomization to produce droplets in the size range of 1 nm to 1 μm in diameter. The droplets cool at greater than 10^6 K/s and as a result, amorphous phases are produced even in pure metals. Since pure amorphous metals solidified from the liquid had never before been observed, the atomic structure is of great interest.[6] We have obtained electron diffraction patterns by microdiffraction in a field emission STEM (VG HB501). The particle shown in Fig. 3 has crystallized only partially, an observation that provides information about the temperature of nucleation and the crystal growth rate. A radial distribution function was determined for a pure amorphous vanadium particle[7] (Fig. 4) by recording of an energy-filtered profile of the scattered intensity as a function of scattering angle. These data were converted into the radial distribution function by standard techniques.

References

1. K. Shin, M. S. Thesis, Dept. Mat. Sci. Eng., U. Wisconsin, 1991.
2. R. N. Wright et al., *Metall. Trans*. 19A: 2399-2405, 1988.
3. D. F. Dawson-Elli et al., Materials Research Society (R. M. Anderson, Ed.) 199: 75-84, 1990.
4. T. F. Kelly et al., *Phil. Mag*. (submitted).
5. R. F. Egerton et al., *Proc. 45th Ann. Meeting EMSA*, 1987, 123-124.
6. Y. W. Kim et al., *Acta Metall*. 37: 247-255, 1989.
7. L. M. Holzman et al., *Proc. XII Int. Cong. Elec. Micros*., vol. 4.
8. This work has been supported by the National Science Foundation, Grant DMR 8451933; and the Department of Energy under Grant DE-FG02-85ER45215 and Contract C87-101251.

T. F. Kelly and L. M. Holzman are at the Material Sciences Program; K. Shin, Y.-W. Kim, and J. C. Bae are at the Department of Materials Science and Engineering; and P. P. Camus and A. J. Melmed are at the Applied Superconductivity Center, all at the University of Wisconsin, Madison, WI 53706. J. E. Flinn is at the Idaho National Engineering Laboratory, EG&G, Idaho Falls, ID 83415.
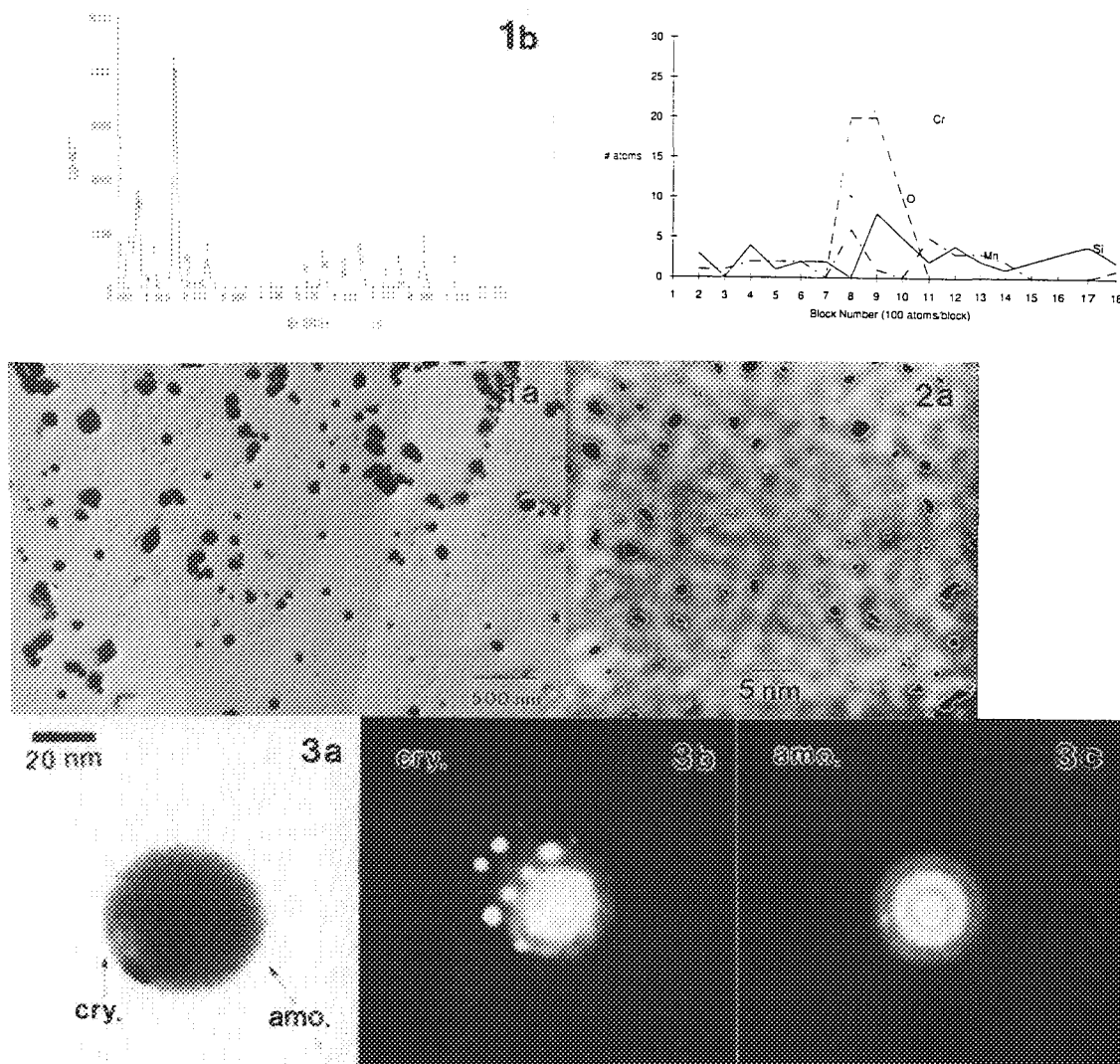
FIG. 1.--(a) Carbon extraction replica
of RSP Fe-40 wt%Ni. (b) X-ray spec-
trum from aluminum oxide precipitate.
FIG. 2.--(a) Image produced by combin-
ing underfocus and overfocus bright-
field and annular dark-field images.
Features with correct contrast for cav-
ities are highlighted. (b) Composition
profile from an energy-compensated atom
probe.
FIG. 3.--(a) Bright-field image of par-
tially crystallized Fe-20 at% Co
sphere. (b) and (c) Microdiffraction
patterns from crystalline and amorphous
regions of sphere, respectively.
FIG. 4.--Radial distribution function
for pure V determined from energy-fil-
tered scattered signal.

CROSS-SECTIONAL TEM SPECIMEN PREPARATION OF FREE-STANDING METAL MULTILAYERED FILMS

M. A. Wall

The cross-sectional preparation of free-standing metal multilayered films is discussed. Production of large flat transparent regions in cross-sectional TEM specimens is usually quite difficult. This difficulty arises from the fact that these types of specimens are usually a composite of dissimilar-ion and chemical etching rate materials. With a unique combination of electroplating,[1] lapping, dimpling, and ion milling, it will be shown that it is possible to produce large thin areas from specimens of dissimilar materials.

Experimental

The material from which a cross-sectional specimen is to be made is a copper/304 stainless steel(ss) multilayer with a repeat period of 20 nm. The total number of periods are 1000, which gives a total film thickness of 20 μm.

The specimen preparation procedure is as follows. A thin strip is cut from the multilayered film measuring 1.5 × 20 mm. One end of this strip is attached with conductive epoxy to a small strip of brass sheet, 10 × 25 mm, for handling purposes. A plating solution with a bath geometry as in Fig. 1 is made. A specimen is attached to an electrical feedthrough. The flat specimen surfaces must be parallel and equidistant from the copper sacrificial anodes. After a diameter of 3 mm is reached, a 0.020in. slice is taken from plated specimen. A disk can now be lapped to a thickness of 75-80 μm. The disk is lapped from both sides with Al_2O_3 lapping film: 30, 12, and 3 μm. Final polish of surfaces is made on a 1μm softcloth. Dimpling is done from one side only with 2μm boron nitride, to a final thickness of <7 μm, and finished with a softcloth tool (Fig. 2). Ion milling is done one side at a time with the use of a single-sided attachment[2] to facilitate ion milling at low angles. A sector speed control[2] is also used, so that the ion milling is mainly perpendicular to the interfaces.[3] Ion milling goes on for 2 h at 4.5°; then the specimen is turned over and the ion milling is continued at an angle of 3.5° until perforation.

Results

The preparation parameters of two Cu/(ss) specimens are listed in Table 1. Specimen B (Fig. 4) was prepared by a more conventional

approach. There is a little thin flat region in specimen B and there is heavy preferential etching of the Cu plating and at the Cu plating/(ss) interface. Specimen A (Figs. 3 and 5) exhibits a large thin flat region, a significant improvement over specimen B.

TABLE 1.--Comparison of two specimens prepared with different parameters.

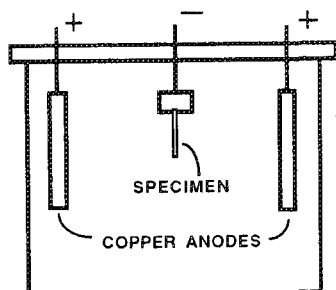|	Specimen A	Specimen B
Initial thickness	75 μm	120 μm
Dimpling	One side	Both sides
Dimple thickness	<7 μm	10 μm
Ion Milling	One side at a time	Both sides
Sector control	Yes	No
Ion milling angle	<5.0°	11°

Conclusion

With the modification of several specimen preparation parameters, it is possible to produce large thin flat areas from materials with differences in thinning rates.

References

1. C. Trybus et al., "Preparation of in situ Cu-Nb composite sheet and wire for TEM analysis," *Mat. Res. Soc. Proc.* 115: 1988.

2. R. Alani et al., "Chemically assisted ion beam etching," *Mat. Res. Soc. Proc.* 199: 1990.

3. U. Helmerson et al., "Cross-section preparation for TEM of film-substrate combinations with a large difference in sputter yield," *J. Electron Microsc. Tech.* 4: 361, 1986.

PLATING SOLUTION

COPPER SULFATE   9 oz./gal.
SULFURIC ACID   25 oz./gal.
HYDROCHLORIC ACID .1ml/gal.
ROOM TEMP
SLOW AGITATION
  1ma/sq in.
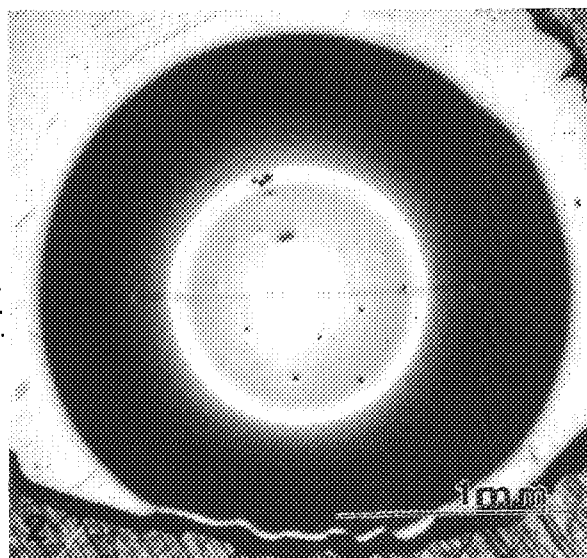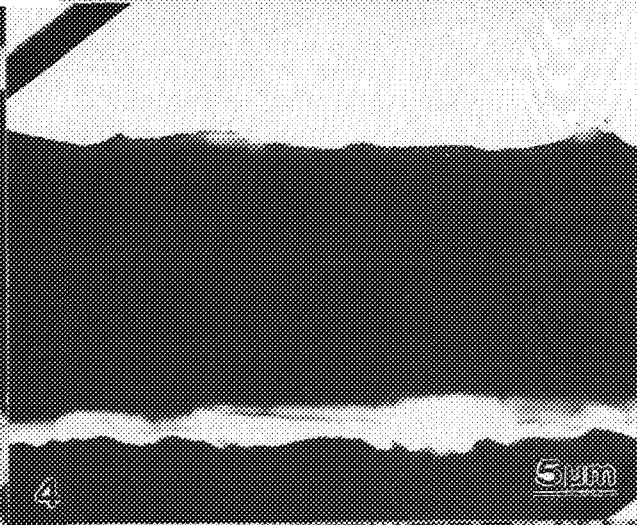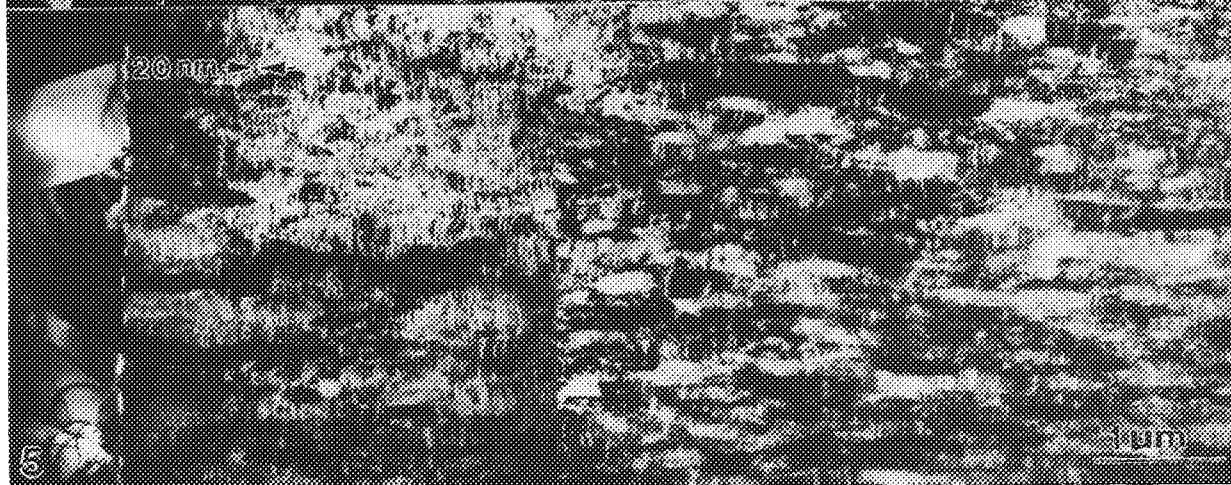
FIG. 1.--Optical micrograph of electroplated, lapped, and dimpled specimen.
FIG. 2.--Schematic of electroplating bath.
FIG. 3.--Electron micrograph of specimen A showing large thin region.
FIG. 4.--Electron micrograph of specimen B showing little thin region.
FIG. 5.--Electron micrograph of specimen A at higher magnification showing multilayered structure within columnar growth.

ANALYSIS OF HIGHLY MOISTURE-SENSITIVE SAMPLES IN AN ELECTRON MICROPROBE

Alfred Kracher, E. E. Ness, S. C. Sevov, J. W. Anderegg, and K. E. Windom

A study of highly reactive intermetallic compounds made it necessary to transfer samples into an electron microprobe without exposing them to air. We have constructed a sample stage subsystem that permits transfer of moisture-sensitive samples from a glove box into an ARL SEMQ electron probe microanalyzer. The subsystem consists of an adapter block and a transfer container with a sealed lid. The lid can be opened and closed while the container is inside the SEMQ vacuum chamber by means of the rotation feedthrough of the SEMQ sample stage. The stage subsystem described here is sufficiently airtight to allow the transfer of pure Na metal without significant corrosion.

Little is known about phase relations in alkali metal-noble metal systems. The intermetallic compound $NaPt_2$ was recently described,[1] prompting a more comprehensive investigation of the Na-Pt system and other alkali-Pt systems. However, the analysis of possible intermetallic compounds presents some problems. The stoichiometry of the compounds cannot always be determined by x-ray diffraction, since the large difference in scattering power between the Na and Pt atoms makes it impossible to determine location and occupancy of all Na sites. The reaction products are usually small crystals, often intimately mixed with unreacted starting material. In this situation, analyzing the run products by electron microprobe seems the most promising approach. Some alkali-bearing compounds are extremely sensitive to moisture and decompose rapidly when exposed to ambient air.

The apparatus in which the intermetallic compounds are synthesized is contained in a glove box flushed with inert gas (N_2 or Ar). In order to analyze these compounds by electron microprobe, we had to ascertain that they would not degrade inside the microprobe and devise a containment system that would allow the transfer of samples between the glove box and the electron microprobe without exposing them to destructive moisture levels.

We assumed that the samples would not degrade significantly at high vacuum. Normally

the vacuum inside the SEMQ sample chamber is better than 10^{-5} Torr, around 1 mP (millipascal). Our instrument employs a permanently connected Spectramass SelecTorr® quadrupole mass spectrometer/residual gas analyzer (RGA), which was used to determine the partial pressures of residual gas components.

The residual gas composition was determined with two different high-vacuum pumps connected to the vacuum system. When this project was begun, a CryoTorr 7 cryogenic pump was attached to the SEMQ microprobe. The advantage of a cryopump for work with sensitive samples is that it produces an exceptionally clean vacuum, free of pump oil and other organic materials. However, owing to mechanical problems the cryopump later had to be replaced with the original high-vacuum pump, a Varian 4-in. oil diffusion pump. The partial pressure of H_2O was found to be around 10^{-7} Torr (13 µP) with both types of pump. Other major components of the residual atmosphere were N_2 and O_2. In addition, during normal operating conditions a significant amount of Ar and CH_4 leaks into the vacuum from the flow proportional counter, which is flushed with a P-10 gas mixture (90% Ar, 10% CH_4). Because of interference, mostly due to $^{36}Ar^{2+}$, the gas flow had to be shut off for accurate measurement of the H_2O partial pressure.

The RGA is primarily a leak detector with limited accuracy. Its quadrupole head is mounted at the vacuum pump manifold, not at the sample location. Partial pressures read by the RGA are thus generally lower than at the location of interest. However, even considering these limitations, our data show conclusively that H_2O partial pressure in the vacuum system is low enough to prevent corrosion of the moisture-sensitive samples used in this study.

For the transfer of samples from the glove box to the SEMQ vacuum system, we have built a special sample substage, which provides continuous protection from ambient air. After analysis the sample can be transferred back into the glove box in the same way. This arrangement makes it possible to perform further investigations on the same material that has been analyzed.

Figure 1 shows the main components of the airtight stage subsystem: (1) the adapter block (right), which attaches to the holding bracket inside the sample chamber in the same way as the original ARL-built sample holders; (2) the transfer container (left), which attaches to the adapter block. Containers can be exchanged without removing the adapter block. The lid of the container is shown partially open, with a mock sample in place. Samples can be up to 1 in. (25.4 mm) in diameter. Two
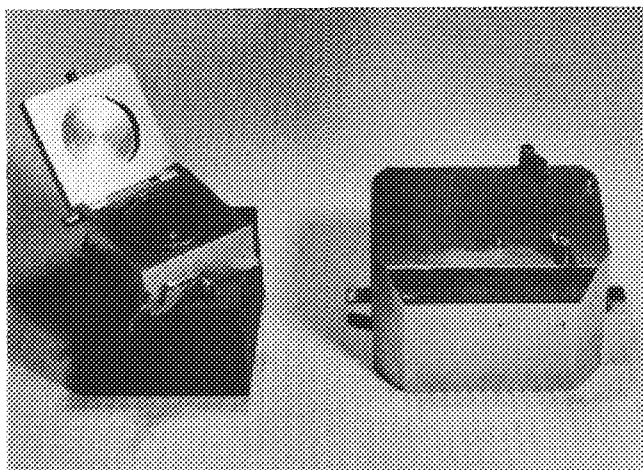
FIG. 1.--Components of airtight sample substage: transfer container (left) and adapter block (right). Lid of transfer container is partly open to show sample (1 in.-diameter disk) and O-ring.
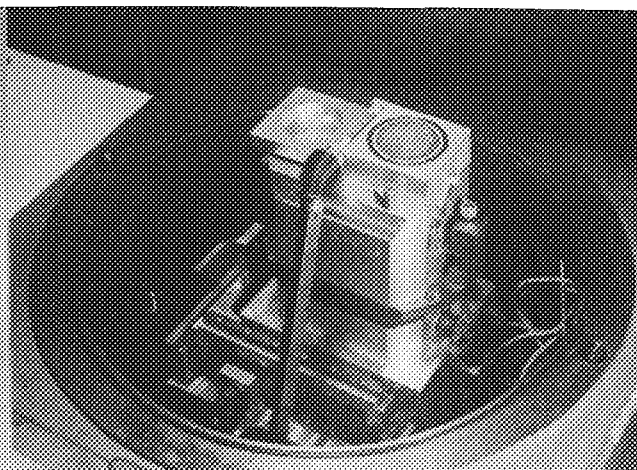
FIG. 2.--Airtight sample substage mounted in SEMQ sample chamber. Telescopic/flexible actuator for lid is connected to rotation feedthrough. Lid shown fully open.

small pins visible on top of the adapter block engage in holes in the bottom of the transfer container, and two brackets hold the container in place on the adapter block. A manual safety lock prevents accidental opening of the container during transfer.

When the transfer container is inside the vacuum chamber, its lid can be opened and closed by the operator by means of the rotation feedthrough on the SEMQ sample chamber. This feedthrough is provided for the optional ARL-built tilt/rotation substage and is not normally used during routine analysis. A telescopic/flexible connection is supplied with the tilt/rotation substage. In the special substage described here, this connection is attached to the lid mechanism of the transfer container. The lid is shown fully open in Fig. 2 to illustrate the function of this mechanism. Normally the lid cannot be opened until the sample chamber is evacuated, and the gate valve between the sample chamber and the main tank of the vacuum system is open. The lid rotates by a full 180°, and during analysis lies flat on the left side of the sample.

A sample transfer cycle consists of the following steps.

1. Place the sample in the transfer container inside the glove box under inert gas, and put in air lock. Partially evacuate air lock, and backfill with inert gas. This procedure will maintain a partial vacuum inside the transfer container, holding the lid in place by air pressure. After the closed container is removed from the air lock, the lid can also be secured with the manual safety catch, which is visible on the front of the transfer container in Figs. 1 and 2.

2. Open the SEMQ sample chamber. Attach transfer container to top of adapter block. Unlatch safety lock.

3. Connect the opening mechanism on the transfer container to the rotation feedthrough

means of the telescopic/flexible connection.

4. Evacuate microprobe sample chamber. Pumping down the sample chamber releases the lid of the transfer container. Thus, for very sensitive samples the sample chamber should be partially evacuated, then backfilled with inert gas before final pump-down. When the evacuation sequence is complete, the gate valve above the sample stage opens automatically; this provides sufficient clearance above the substage so that one can open the lid of the transfer container by turning the rotation drive on the outside of the SEMQ sample stage.

5. The sample can now be raised into analyzing position. With the lid fully open, no part of the substage assembly protrudes above the level of the sample.

6. After the sample is again lowered into the sample change position, the lid is closed. The rotation drive on the SEMQ microprobe has a locking feature, which can be used to maintain slight positive pressure on the lid of the transfer container. This is sufficient to retain vacuum inside the transfer container during the vent cycle of the sample chamber. Since the SEMQ microprobe uses inert gas (normally N_2) to vent the sample chamber, minor leakage of the lid during the beginning of the vent cycle has no adverse effect on the sample.

7. After removal from the microprobe, the transfer container is inserted in the air lock of the glove box. Once the air lock is evacuated, the lid of the container can be opened and the air lock flushed with inert gas.

We have tested the device in two ways. First, we tested the transfer container itself by loading a piece of Na metal under inert gas, closing and latching the container, and removing it from the glove box. It was kept in ambient air overnight, then returned

to the glove box, and the Na metal was optical-
ly inspected for alteration. Second, the en-
tire transfer cycle described above was per-
formed with a Na-Pt reaction product known to
be highly reactive. Both tests showed no al-
teration of the sample. Since Na metal and its
intermetallic compounds are some of the most
reactive substances known, we anticipate that
almost any moisture-sensitive sample can be
transferred into the microprobe with the sub-
stage system described here.

References

1. K.-J. Range, F. Rau, and U. Klement, "So-
dium diplatinum," *Acta Cryst*. C45: 1069, 1989.

EVALUATION OF CRYSTAL DIFFRACTOR PARAMETERS BY USE OF A MICROFOCUS X-RAY SOURCE

W. Z. Chang and D. B. Wittry

Crystal diffractor parameters are still of fundamental interest in the x-ray physics and x-ray spectrometry fields. The width of the rocking curve, the reflection coefficient, and the degree of uniformity of a bent crystal are the parameters that determine the crystal's diffraction efficiency when used in spectrometers for wavelength-dispersive spectrometry with x-ray sources of small size.

A typical rocking curve of a diffraction crystal may be characterized by the peak reflection coefficient P, and the full width at half-maximum (FWHM), called the rocking curve width W; another parameter sometimes used is the integrated reflection coefficient R (also known as the diffracting power.[1,2] In the physical sense, the rocking curve width is an important parameter for determining the actual diffraction area for a particular diffraction geometry. The ability to evaluate these parameters provides the key guidelines to optimize the choice of crystal materials and sizes, and to achieve better diffraction efficiency in the fields of x-ray spectrometry and x-ray fluorescence analysis. In this paper we describe a method for evaluating crystal diffraction parameters based upon the Johann diffraction geometry with a cylindrically bent mica (muscovite) single crystal and a microfocus x-ray source. The method is based on comparison of the area of the diffracting regions with the area predicted by theoretical calculations.

Advantages of the Present Method

In our approach, parallel incident radiation is not required, which eliminates the need for precision collimator alignment for producing a parallel x-ray beam. In double crystal spectrometer measurements,[3,4] the collimator divergence of the beam often complicates obtaining the width of rocking curve, since a deconvolution has to be performed in order to separate the effect of divergence of the beam and the rocking curve width. Moreover, the incident beam in the technique we used is unpolarized. However, in the double-crystal spectrometer configuration, the incident x rays on the second crystal are partially polarized. The integrated reflection coefficient R and the

rocking curve width W of this crystal have, in addition, a polarization factor, which depends on whether the crystal is nearly perfect, ideally mosaic, or in between. Obviously, the results of the evaluation are rather uncertain when the mosaic behavior of the crystals is unknown. Furthermore, the measurement of the crystal parameter is done with a bent crystal, which is of direct interest in wavelength-dispersive spectrometry. The measurement made with a double-crystal spectrometer applies only to a flat cyrstal which provides inadequate information, since the parameters of a crystal under either plastic or elastic bending certainly change from those in its flat form.

If one makes a direct measurement with a curved crystal using the x-ray continuum, one can in addition determine how well the crystal is bent by observing the uniformity of the image of the diffracted beam. It is therefore apparent that this method provides extensive information on crystal parameters and is relatively easy to implement.

Experimental

The experimental configuration is shown in Fig. 1. An x-ray beam was generated by bombardment of a copper target with a focused electron beam. A mica crystal 12 μm thick, 1.5 × 1.5 in. in size was bent to a 4in. radius and located on a focal circle with a 2in. radius. The photographic recording film (Polaroid type 57) was placed close to the crystal. Figure 2 shows (a) a simulated image for a perfectly aligned diffractor viewed normal to the diffractor's surface, and (b) a slightly misaligned diffractor projected on the film plane. For the results shown in Fig. 3 with Cu Kα radiation of 1.54Å wavelength, the
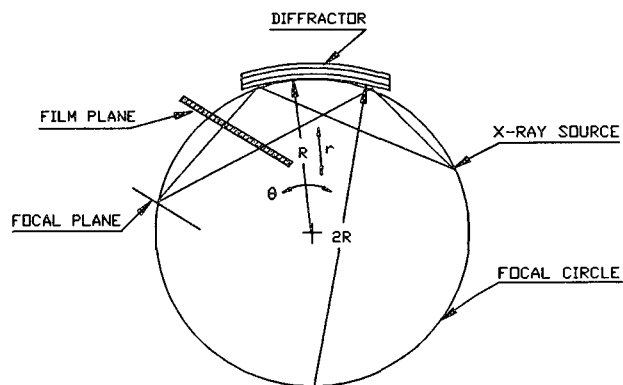
FIG. 1.--Experimental configuration used in the present work.

fifth-order reflection of mica was selected because of its high diffraction intensity[5] and the relatively large Bragg angle of 22.6°.

The alignment was carried out in the following way. We initially recorded the diffraction image on the film and then employed a proportional counter at the focus to search for the characteristic line peak by scanning the crystal diffractor using the θ adjustment shown in Fig. 1. In common practice, a good alignment depends entirely on obtaining a sharp diffraction peak, even if it is not known whether the diffractor is actually ideally aligned. However, in our method, a slightly misaligned crystal is recognized on the recording film by its image in comparison with an ideally aligned one. Thus, the misalignment can be corrected with successive diffractor adjustments (of r and θ) and with the aid of photographic exposures between adjustments.

The image of the diffracted beam obtained, for Cu K radiation, is shown in Fig. 3 and confirmed the theoretical predictions from which the rocking curve width and the effective area of diffraction can be determined; this information, together with experimental intensity measurements, makes it possible to determine the reflection coefficient. (For details, refer to the following section.) In order to demonstrate the potential of revealing the conditions of a bent crystal, Fig. 4 shows topographs of a poorly bent and a well-bent mica crystal. The radiation of 3.358 Å from a Ca Kα target was employed in this case. Figure 4(a) shows the image of the diffracted beam from continuum incident radiation to be
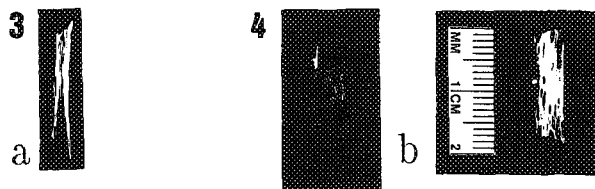
FIG. 3.--Image formed by cylindrically bent mica crystal with Cu Kα radiation generated by focused electron beam (50 μA and 20 kV). One-minute exposure time with type 57 Polaroid film.

FIG. 4.--Images formed by cylindrically bent mica crystal with Ca Kα radiation generated by focused electron beam (50 μA and 20 kV). (a) Poorly bent mica crystal (1.27 cm × 3.81 cm × 12.5 μm) with x-ray continuum; 4min exposure time with Polaroid type 57 film. (b) Well-bent mica crystal (1.27 cm × 3.81 cm × 18 μm) with characteristic radiation; 4min exposure time with Polaroid type 57 film. Difference in size is due to slightly different film position.

uniform in intensity. It is obvious that the mica crystal was bent to a nearly perfect condition with a minimum of cleavage and of distorted lattice planes. In contrast, Fig. 4(b) depicts an excessive number of wiggly lines due to characteristic radiation, which indicate that the mica was poorly bent. Clearly this technique facilitates the assessment of bending accuracy, which is the first important factor in the process of evaluation of crystal parameters.

In diffraction efficiency measurment, a mica crystal 35 μm thick was used and an aperture was placed in front of the detector in order to reduce the excessive counting rate for direct beam measurement. The detector's location for diffracted beam measurement was in the film plane, shown in Fig. 1, and for direct beam, was placed in a plane which was parallel to the film plane and was close to the diffractor. Several corrections to this measurement will be discussed in following sections.

Discussion

The calculations, the results of which are shown in Fig. 2, may be expressed by the following equation for a perfectly aligned diffractor.[6]

$$\Delta\theta_0 = \frac{X^3 \cot^2\theta_B + X^2 \cot\theta_B}{2}$$
$$- Z^2 \frac{1}{2\sin\theta_B \cos\theta_B} + \frac{X}{\sin^2\theta_B} \quad (1)$$

where X and Z are the ratios of the actual coordinates x and z to 2R (twice the radius of the focal circle), θ_B is the Bragg angle, and $\Delta\theta_0$ is the rocking curve half width in radians. A plot of Eq. (1) is shown in Fig. 2(a). The following equation was derived by taking into consideration the misalignment of the diffractor in its radial direction:[7]
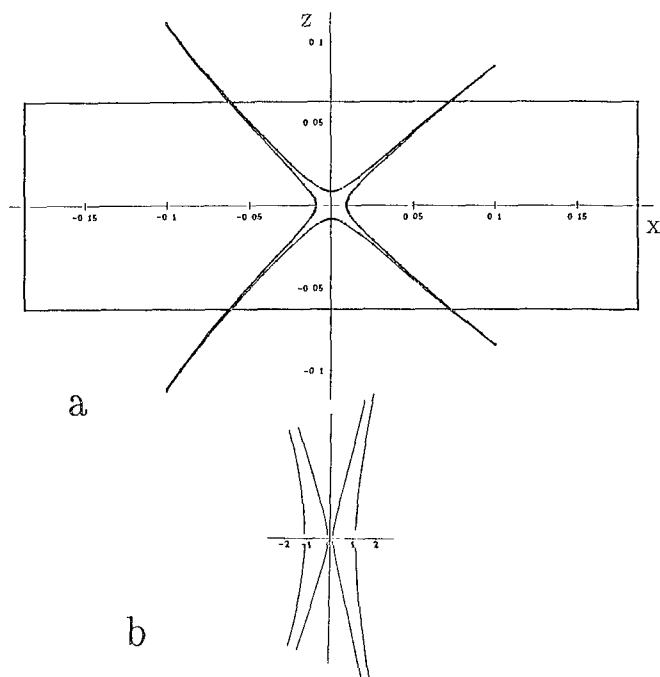

FIG. 2.--Simulated images for Johann diffractor and x-ray point source. (a) Calculated image based on Eq. (1). Rectangle indicates size of diffractor to scale. (b) Calculated image based on Eq. (2) (slight misalignment), and foreshortened to correspond to recorded image.

$$\Delta\theta = \Delta\theta_0 + E \cot an\ \theta_B(1 + X \cot an\ \theta_B) \qquad (2)$$

where E is the displacement of the center of the diffractor in the radial direction away from the center of the focal circle, and $\Delta\theta$ is the corresponding value of the rocking curve half width. For a particular Bragg angle θ_B, selection of values for $\Delta\theta$ and E allows a simulated image with coordinates X and Z at the diffractor's position to be obtained. This image is foreshortened and curved on the photographic film plane through experimentally measured geometric relations. Direct comparisons of both calculated and experimentally recorded images reveal whether the chosen $\Delta\theta$ and E values are appropriate. When the condition is such that the image is similar to that shown in Fig. 2, the correct value of $\Delta\theta$ may be determined by measurement of the width of the image in the plane of the focal circle (Z = 0 in Eq. 1).

The reflection coefficient of mica is calculated as the product of two ratios: first, the intensity ratio of the peak of the diffracted beam to the incident beam striking the full surface of the diffractor; and second, the area factor, which is the ratio of the diffracting effective area to the area of the aperture placed in front of the detector when the intensity of the incident beam is measured. The former ratio, as well as the area of the incident beam, are readily measured during the experiments. The diffracting area is determined by numerical integration of the area bounded by the four curves, within the actual diffractor size limits, in the simulated image (Fig. 2a). In the case of Cu $K\alpha$ radiation and the fifth-order diffraction of the mica crystal, $\Delta\theta$ was found to be 5.1×10^{-4} radians. The two crystals, for the reflection coefficient and the $\Delta\theta$ measurements, were assumed to have the same diffracting areas, even though they differ in thickness. The area factor was calculated with account taken that the incident beam from the point source is not normal to the center of the diffractor surface nor to the plane of the aperture, and that distances from the course to the center of the diffractor, and from the source to the plane of the aperture, are different. From the geometry of the experiment, both areas were projected normal to the incident rays of the x ray source, and the solid angles subtended by the aperture and by the diffracting areas at the source were calculated. The area factor was found to be 0.156, which is the ratio of the solid angles. In addition to the calculations of two ratios, the reflection coefficient was corrected by use of Kramer's theory,[8] along with the experimental conditions to account for the continuum radiation of the incident beam. The correction factor can be obtained by subtraction of the theoretically calculated continuum background from the pulse height distribution of the direct beam and integration of the remaining intensity due to the characteristic x-ray line. Another correction should be made to compensate for the difference in the absorption path for the incident and diffracted

beams in air. However, in our case, the path length difference between the source to the detector (direct beam) and the source to the diffractor, then the detector (diffracted beam), is negligible. Thus, the reflection coefficient was calculated as 0.0342.

The derived $\Delta\theta$ value should be defined as half of an effective rocking curve width compared to the conventional FWHM value. In the curved crystal case, x rays satisfy the Bragg condition, not only on the surface of the diffractor, but also at planes parallel and underneath the surface. As a result, the diffracted image is broadened, and $\Delta\theta$ is expected to be larger.[7] Also, the intensity distribution is not included in the $\Delta\theta$ expression, which implies that the information concerning where the calculated $\Delta\theta$ lies on the rocking curve is unknown. Furthermore, the intensity distribution in the present case does not resemble that of the conventional rocking curve. However, if the rocking curve is assumed to be a Gaussian distribution, the curve can be expressed as an exponential function of X^4 and Z^4, since $\Delta\theta$ varies as X^2 and Z^2. In Fig. 5, the expected intensity versus the coordinates is plotted with Z set equal to zero and the X^3 term in Eq. (1) neglected. It shows that the shape of the intensity distribution in this case has a nearly flat peak and a rather steep slope at the breadth of the curve, which suggests that the curve could be approximated to a rectangular shape, as shown in Fig. 5. Moreover, it also determines the effective rocking curve width if the rectangular area is set equal to the area under the curve which, in fact, has been numerically integrated. Thus, it is found that the boundaries of a rectangular distribution, occurring at ±0.907 on the normalized X axis, intercept the curve at 50.92% of its peak value. This result suggests that the effective rocking curve width measurement taken from the diffraction image is reasonably close to the FWHM value of the curve. Also, the product of the peak P, the reflection coefficient, and the effective rocking curve
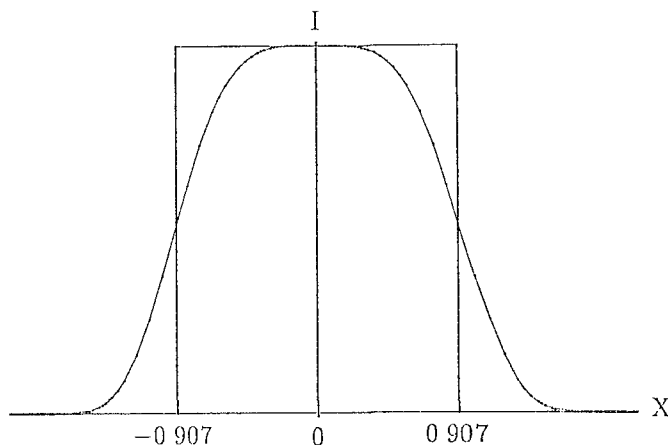

FIG. 5.--Theoretical curve of intensity vs X coordinate, showing shape of intensity distribution. Rectangle shown has same area as area under intensity distribution.

width becomes the integrated reflection coefficient R. In our case R, the product of the coefficient and $2\Delta\theta$, is 3.49×10^{-5} rad, which is close to the measured value 4.0×10^{-5} given by Gilfrich et al.[4]

Accuracy of the Method

Strictly speaking, a more quantitative measurement is needed in order to verify experimentally the shape of the intensity distribution. The necessary procedure would therefore be to characterize the film's response to use a microdensitometer trace of the pattern on the film so that the position of half-maximum intensity can be found, which leads to a more accurate value of $\Delta\theta$.

In addition to the film response, the effect of the finite x-ray source size would also contribute to the accuracy of determining $\Delta\theta$. In relation to the simulated image, which was obtained based on the assumption of an ideal point source, the recorded image pattern exhibits broadening of the diffracting region, due to the finite size of the x-ray source. An estimate of the broadening is 2.5×10^{-4} rad if the previously measured electron beam size is taken to be 25 μm and the radius of the focal circle 50.8 mm. By comparison with the obtained value of $\Delta\theta$, it illustrates the necessity of correcting $\Delta\theta$ due to this significant line braodening effect. The corrected $2\Delta\theta$ is then 7.7×10^{-4} rad, which is in reasonable agreement with the value of 7.9×10^{-4} from the experimental work of Anan'eva et al.[9]

The finite source size effect indicates that it could impose a limitation in measurement of $\Delta\theta$, which has smaller angular width. This limitation can be removed to a certain degree, due to the fact that the electron-beam spot can be further decreased without loss of current in the spot by use of an LaB_6 cathode, and by optimization of the electron-beam aperture size. Furthermore, a more accurate correction to the measured $\Delta\theta$ can be obtained by careful measurement of the size of the x-ray source. The size of the x-ray source can be evaluated by reference to the width of the Kossel lines, since a point source of x rays diffracted from a good-quality planar crystal generates a series of Kossel lines.

The diffra tion image may also be broadened by the width of a characteristic line and/or $K\alpha$ doublets. The angular width of a characteristic line is directly related to the Bragg angle and the wavelength spread by

$$\delta\theta = \tan\theta_B \, \delta\lambda/\lambda \qquad (3)$$

Angular dispersion increases as the Bragg angle of $\delta\lambda/\lambda$ increases, which may induce a significant broadening despite the fact that in the case of Cu $K\alpha_1$ radiation, $\delta\theta$ is equal to 1.43×10^{-4} rad when calculated from the $\delta\lambda/\lambda$ value of 3.43×10^{-4} as given by Blokhin.[10] That is less than the calculated rocking curve width $2\Delta\theta$. In the same fashion, unresolved $K\alpha$ doublets would have to be taken into consideration. According to the value of 2.48×10^{-3} for $\delta\lambda/\lambda$,

as quoted by Heinrich,[11] because of the width of the $K\alpha_1$-$K\alpha_2$ doublet of Cu, $\delta\theta$ is equal to 1.03×10^{-3} rad for Cu $K\alpha$ radiation, which is larger than the obtained value of $2\Delta\theta$. Thus, in some cases, experimentally measured $\Delta\theta$ should be corrected for the presence of $K\alpha$ doublets if the doublets cannot be resolved. The correction could be made either by use of a single $K\beta$ line to avoid the complication of the $K\alpha$ doublets, or by performing deconvolution of the intensity distribution of the $K\alpha$ doublets from the intensity profile.

Conclusions

With our preliminary experimental results and the discussion of a number of necessary corrections, it has been demonstrated that evaluation of crystal diffraction parameters can be accomplished by use of the standard Johann diffraction geometry. As a matter of fact, this is the first attempt to obtain quantitative values of key parameters, such a $\Delta\theta$, and the reflection coefficient in this configuration. The merit of this technique is demonstrated by the fact that the rocking curve width is correlated to the diffraction image from which the effective area of diffraction and the reflection coefficient can also be derived. Further work in progress includes characterization of the photographic film, more accurate measurement of the x-ray source size, and measurements of parameters of other diffracting crystals as well as measurements at various wavelengths. It is believed that the technique presented here will contribute to the fields of research in x-ray diffraction and spectrometry.

References

1. R. W. James, *The Optical Principles of the Diffraction of X-ray*, London: G. Bell and Sons, 1958.
2. J. Vierling et al., "Improving the diffracting properties of LiF: Compariscn with graphite," *Appl. Spectr.* 29: 322, 1975.
3. A. H. Compton and S. K. Allison, *X-rays in Theory and Experiments*, New York: Van Nostrand, 1935.
4. J. V. Gilfrich et al., "Integral reflection coefficient of x-ray spectrometer crystals," *Appl. Spectr.* 23: 342, 1969.
5. Von A. Meisel et al., "Die Intensität der an gebogenen Glimmerspaltflächen in höheren Ordnungen reflektierten Röntgenstrahlung," *Z. Kristallogr.* 122: 148, 1965.
6. D. B. Wittry et al., "X-ray optics of doubly curved diffractors," *J. Appl. Phys.* 67: 1633, 1990.
7. D. B. Wittry et al., "Properties of curved x-ray diffractors with stepped surfaces," *J. Appl. Phys.* (in press).
8. T. S. Rao-Sahib et al., "X-ray continuum from thick elemental targets for 10-50 keV," *J. Appl. Phys.* 45: 5060, 1974.
9. G. V. Anan'eva et al., An x-ray method of determining the state of polycrystallinity of a crystal," in N. N. Sheiftal, Ed., *Growth of*

Crystals, New York: Consultants' Bureau, 1968.

10. M. A. Blokhin, *The Physics of X-rays*, Moscow: State Publishing House of Technical-Theoretical Literature, 1957, 404.

11. K. F. J. Heinrich, *Electron Beam X-ray Microanalysis*, New York: Van Nostrand, 1981, 125.

A CONTROLLED-DISPERSION PARALLEL-WAVELENGTH DISPERSIVE X-RAY SPECTROMETER FOR ELECTRON MICROSCOPY

C. E. Fiori, S. A. Wight, and A. D. Romig Jr.

This paper describes a new technique for the detection of x rays in electron column instruments used in microanalysis. In electron column instruments, the point source of x rays is produced by the interaction of a focused electron beam with the sample. Neither of the conventional methods, wavelength-dispersive (WDS) nor energy-dispersive (EDS) based spectrometry, is optimized for low-Z element quantitative analysis.[1] In WDS applications, where the analyte elements are Be through P, chemical effects complicate the x-ray measurement process. Peak positions and shapes are altered, sometimes very strongly, by the electron configurations of the analyte atoms and neighboring atoms. In these cases, the ideal spectrometer would profile the peak and some small amount of continuum on either side of the peak such that an accurate peak area could be calculated.[2] Present WDS spectrometers are serial in nature and cannot directly measure peak areas, causing errors in the determination of light element concentrations. Bastin and co-workers have developed an elegant method to provide accurate area determinations, using the serial spectrometer, by a three-point procedure.[3,5] The parallel wavelength-dispersive spectrometer (PWDS) we propose here is ideally suited for those applications. The concept of this type of spectrometer was first proposed in 1939 by J. Hillier, who used a flat crystal and photographic film to demonstrate the principle.[6]

Figure 1(a) is a schematic representation of a conventional WDS. A fraction of the x rays emitted from the analytical region of the specimen reach the diffracting crystal; those that have wavelengths that satisfy Bragg's law are diffracted, and then detected by a gas proportional counter. Bragg's law states that $n\lambda = 2d \sin \theta$, where n is an integer representing the order of diffraction, d is the interplanar crystal spacing, λ is the wavelength of the x ray (in the same units as d), and θ is the angle of incidence of the x rays on the crystal surface.[7] At the focus of a conventional focusing Johansson x-ray spectrometer, x rays of the same energy are brought together (Fig. 1a). The x rays incident on the crystal are polyenergetic, but in the diffracted arc all x rays are monoenergetic, where the x-ray energy diffracted can be described by Bragg's law. The source of x rays is defined by point S and the detection point is defined by D. Note that S

and D are always symmetric about the midpoint (midplane) of the diffracting crystal. This symmetry exists because the crystal is bent and ground to the exact curvature of the Rowland focusing circle such that every ray trace from a point source on the Rowland circle is diffracted to another focal point on the Rowland circle (for x rays that satisfy Bragg's law for set conditions). The entire area of the crystal is used to diffract x rays of one energy.[8]

The conventional configuration described above can be altered to produce an interesting and novel effect. Consider what happens when the target, which is for this purpose a point source of polychromatic x rays, is brought closer to the crystal by being deliberately moved off the Rowland circle (Fig. 1b). Now x rays of various energies are brought together at a new focal point that is symmetric to S because each ray trace from the point source to the crystal intersects a different angle with the crystal. Bragg's law states that the emerging x rays are monoenergetic. The x rays have a range of energies but at the cost of efficiency.[9] The range of energies depends on the distance from S to the diffracting crystal. By controlling the distance from the crystal to the specimen and the crystal angle, we can affect a controlled amount of energy dispersion in the diffracted arc. An energy dispersion plane P can now be defined between the diffracting crystal and the focal point. The dispersion of x rays passing through this plane can be detected with an appropriate detector, such as x-ray film or a scintillator/photodiode array. To maximize the utility of the x-ray dispersion, a variety of crystal geometries can be used, curved in either one or two dimensions.[10]
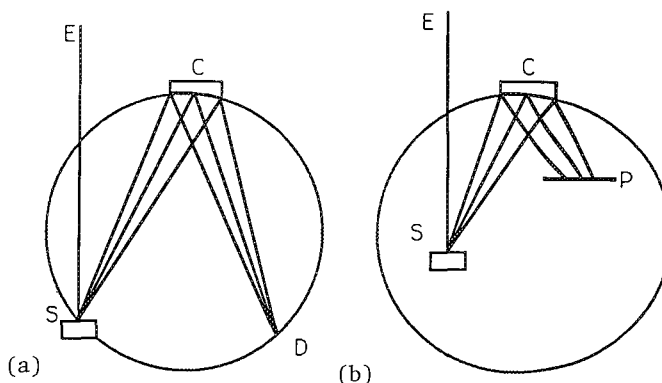

(a) (b)

FIG. 1.--(a) Schematic representation of conventional WDS; (b) schematic representation of PWDS, where E is electron beam, S is sample, C is crystal, D is detector, and P is dispersion plane.

C. E. Fiori and S. A. Wight are at the Chemical Science and Technology Laboratory, National Institute of Standards and Technology, Gaithersburg MD 20899; A. D. Romig Jr. is at the Sandia National Laboratory, Albuquerque NM 87185.

As to efficiency considerations, on the Rowland circle the entire crystal surface is used to diffract a single x ray energy. As the point S is moved closer, the crystal diffracts a range of x ray energies. The larger the range of energies, the smaller the portion of the crystal surface is being used to diffract each of those energies. Crystal efficiency is exchanged for the ability to pass a range of energies that comprise a peak. This is the reason that any attempt to use a flat crystal results in a totally unacceptable efficiency at any one energy.

Diffraction crystals to be used in this application should be chosen very carefully. Many crystals are heat annealed after they are bent, to relieve stress and increase efficiency by the "mosaic" effect. This polygonization results in many small crystals instead of one continuous crystal.[11] The resulting diffracted arc contains a series of bands of x rays that do not inhibit conventional WDS but are not useful for this application. Lithium fluoride (LiF) and quartz (SiO_2) crystals are known to exhibit these Laue patterns.[12]

References

1. S. J. B. Reed, *Electron Microprobe Analysis*. Cambridge: Cambridge University Press, 1975, 318.
2. J. T. Armstrong, "Accurate quantitative analysis of oxygen and nitrogen with a W/Si multilayer crystal," *Microbeam Analysis--1988*, 301.
3. G. F. Bastin and H. J. M. Heijligers, *X-ray Spectr.* 15: 135, 1986.
4. G. F. Bastin and H. J. M. Heijligers, *Microbeam Analysis--1984*, 291.
5. G. F. Bastin and H. J. M. Heijligers, *J. Microsc. Spectrosc. Electron.* 11: 215, 1986.
6. J. Hillier, U.S. Patent No. 2 419 029, 1947.
7. W. L. Bragg, "The intensity of reflexion of x rays by crystals," *Phil. Mag.* 27(ser. 6): 881, 1914.
8. J. I. Goldstein, D. E. Newbury, P. Echlin, D. C. Joy, C. E. Fiori, and E. Lifshin, *Scanning Electron Microscopy and X-ray Microanalysis*, New York: Plenum Press, 1981, 205.
9. S. Brennan, P. L. Cowan, R. D. Deslattes, A. Henins, D. W. Lindle, and B. A. Karlin, "Performance of a tunable secondary x-ray spectrometer," *Rev. Sci. Instrum.* 60: 2243, 1989.
10. M. J. Carr and A. D. Romig Jr., "Normal incidence x-ray mirror for chemical microanalysis," U.S. Patent No. 4 916 721, 1987.
11. B. D. Cullity, *Elements of X-ray Diffraction*, Reading, Mass.: Addison-Wesley, 1978, 260 (2d ed.).
12. L. S. Birks and R. T. Seal, "X-ray properties of plastically deformed LiF," *J. Appl. Phys.* 28: 541, 1957.

ELECTRON PROBE COMPOSITIONAL MAPPING OF PARTICLES AND SAMPLES WITH IRREGULAR SURFACES

J. A. Small, D. S. Bright, R. L. Myklebust, and D. E. Newbury

In recent years quantitative compositional mapping with the electron probe microanalyzer has become a powerful tool for the study of two-dimensional elemental distributions. Unlike x-ray area scans, which photographically record only the presence or absence of a particular element at a given location, compositional maps provide a series of digital images in which the variations in gray level or color are directly proportional to variations in the elemental concentration.[1,2]

A fundamental assumption of quantitative electron probe microanalysis procedures is that the measured intensities depend only on the elemental composition of the target.[3] When irregular specimens, such as particles and rough surfaces, are analyzed, geometric effects such as size and shape modify the measured intensities relative to a polished bulk target. These effects alter the scattering properties of the beam electrons and the x-ray absorption path lengths from the situation that exists for a flat, polished specimen of the same composition.[3,4]

The peak-to-local background (P/B) procedure has been developed to correct the measured X-ray intensities for the effects of sample geometry. This procedure, which is based upon the Hall method[5] for the analysis of biological thin films, was developed for the single-point analysis of particles and rough surfaces by Small et al.[6] and by Statham and Pawley.[7] The basis for the method is that the ratio of peak-to-local background is found to be relatively insensitive to sample geometry:

$$(P/B)_{irreg} \simeq (P/B)_{bulk} \qquad (1)$$

where "irreg" refers to the ratio for a particle or for an irregular, rough surface and "bulk" refers to the corresponding ratio for a flat polished sample of the same composition. In this paper we report on experiments to extend the P/B method to the mapping of rough surfaces and particles.

To provide a suitable specimen to evaluate the use of P/B ratios for compositional mapping of samples with nonconventional geometries, we prepared a rough surface from NIST Standard Reference Material (SRM) 482 (60.3% Au, 39.6% Cu) which is certified as a microanalytical standard to be homogeneous on a micrometer scale. A rough surface (Fig. 1) was prepared by

The authors are with the Microanalysis Research Group, Chemical Science and Technology Laboratory, National Institute of Standards and Technology Gaithersburg, MD 20899.
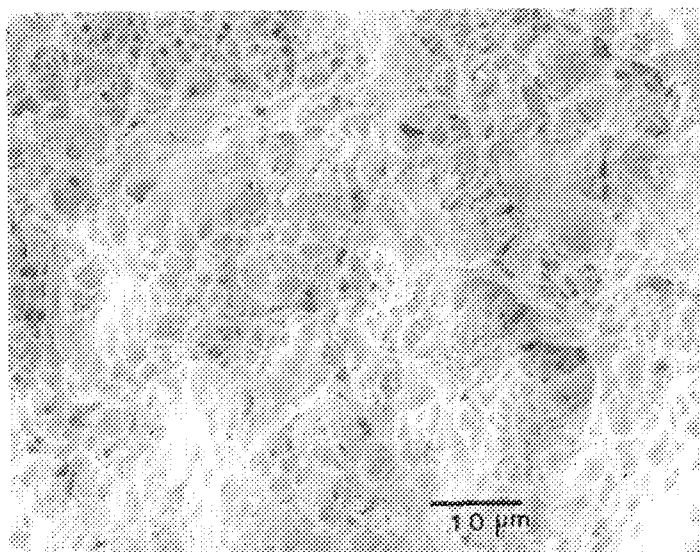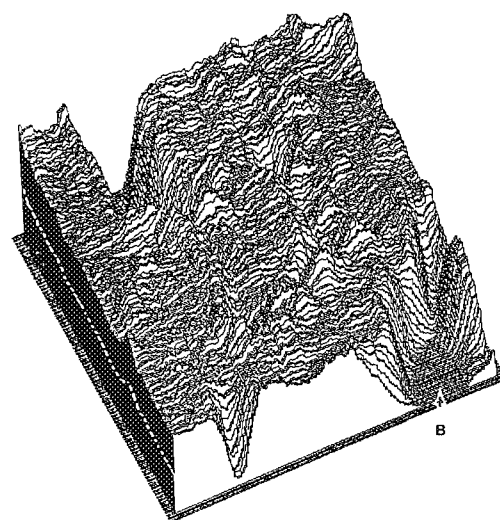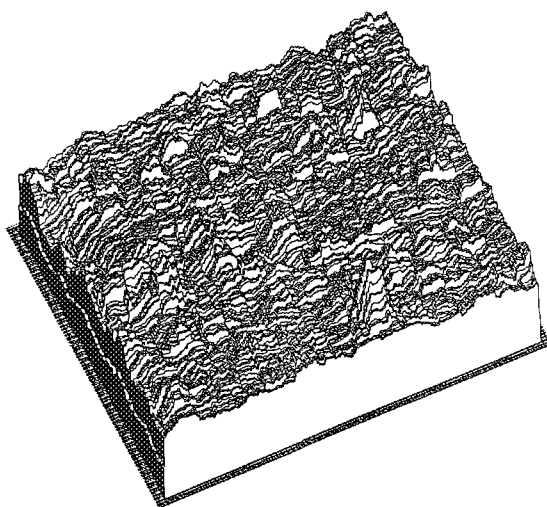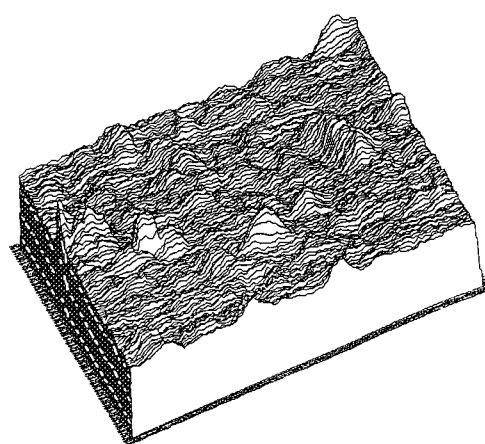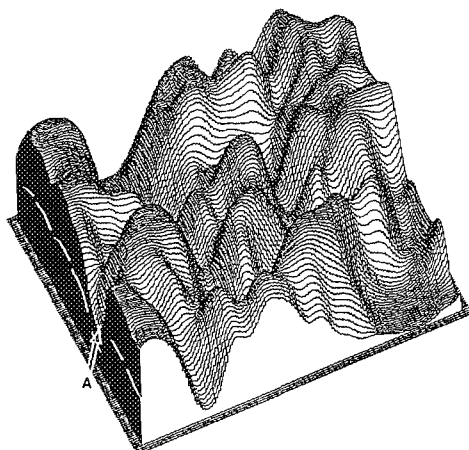
FIG. 1.--Electron micrograph of Au-Cu rough surface.

cryo-fracturing of the alloy under liquid nitrogen. For this experiment, we collected 128 × 128 pixel images from the sample for the Cu Kα, the Au Mα, and Cu Lα x-ray intensities along with their associated background images. Since the sample is electron opaque, the predominant effect of sample topography will be local tilt effects on backscattering and non-uniform x-ray absorption. The varying absorption path lengths for the rough surface result in large variations in the measured x-ray intensities. The P/B corrected images corresponding to each characteristic image were calculated from Eq. (2) at each pixel location:

$$I^1 = (I_p - I_B)/I_B \qquad (2)$$

where I is the P/B corrected intensity and the P and B subscripts refer to the peak and background intensities, respectively. Both wavelength- and energy-dispersive x-ray detectors were used for this initial study. For wavelength spectrometry, the background intensities were determined by collection of an image from a background region set slightly higher in energy than the peak region. For energy spectrometry, the background was determined by a linear fit to a background region immediately adjacent to the peak.

The results are displayed as mesh plots showing the distribution of the raw characteristic x-ray peak intensities and the P/B x-ray intensity-ratios over the sample area. The

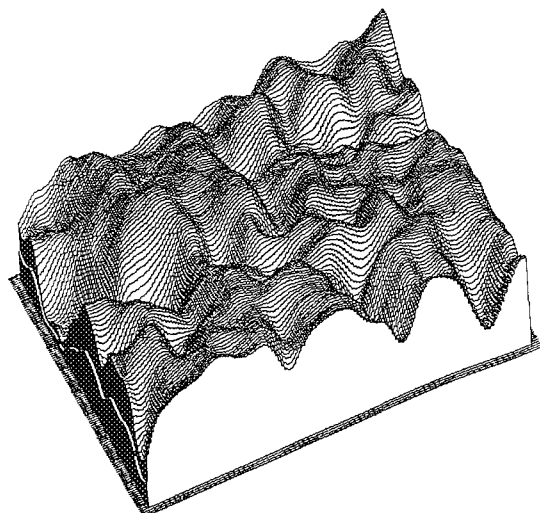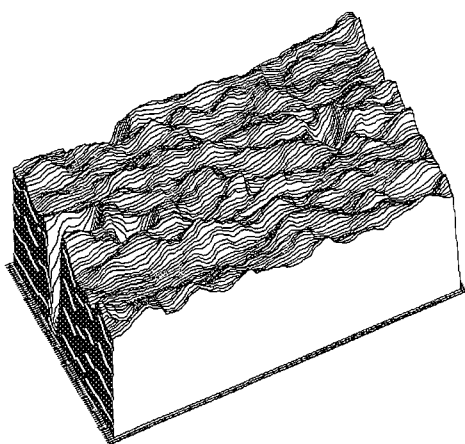FIG. 2.--Contour plot for Cu Kα x-ray intensity.
FIG. 3.--Contour plot for Au Mα x-ray intensity.
FIG. 4.--Contour plot for Cu Lα x-ray intensity.
FIG. 5.--Contour plot for P/B ratio of Cu Kα x-ray intensity.
FIG. 6.--Contour plot for P/B ratio of Au Mα x-ray intensity.
FIG. 7.--Contour plot for the P/B ratio of Cu Lα x-ray intensity.

images were smoothed with a 7 × 7 mean filter to minimize pixel-to-pixel random noise and emphasize the long-range structure in the images.

If there were no effect from sample topography, the raw x-ray intensity plots would be featureless, since the sample is homogeneous. Conversely, the degree to which the x-ray maps are affected by sample topography and the degree to which the P/B method is successful in correcting the images can be evaluated from the intensity variations observed in the P/B plots.

The raw intensity plots for Cu Kα, Au Mα, and Cu Lα lines are shown in Figs. 2-4. All three of the characteristic x-ray plots show large variations in the measured x-ray intensities over the sample surface. The effect of sample topography is smallest for the relatively high energy Cu Kα line at 8.04 keV, since there is minimal absorption; and largest for the Cu Lα line at 0.93 keV, which is highly absorbed. The variations in the Au Mα intensity at an energy of 2.1 keV are between the other two lines.

The corresponding P/B corrected contour plots are shown in Figs. 5-7. The P/B plots for the Cu Kα and the Au Mα lines have less structure than the corresponding raw intensity plots. In both cases the P/B contours are nearly flat with only minor variations in intensity across the specimen surface. The small variations in the plots correspond to areas of the sample where the topography is particularly convoluted and the x-ray path length variation is substantial. The P/B contour plot for the Cu Lα line also shows substantially less variation than the raw intensity plot, even for areas where the variations in the characteristic plot are quite severe, such as that indicated by an "A" in Fig. 4. The regions on the contour plot where the P/B correction does not adequately correct for the variations in intensity, such as region "B" in Fig. 7, correspond to areas of the sample for which the absorption path length is so large that only a relatively few x rays escape. In these cases, where it is not possible to obtain a statistically significant x-ray count for the background, the P/B method fails.

The results of this preliminary test of P/B ratio maps indicate that the P/B ratio procedure effectively reduces the influence of sample topography in the compositional mapping of rough surfaces. The effectiveness of the procedure depends critically on obtaining a statistically significant number of x-ray counts.

References

1. R. B. Marinenko, R. L. Myklebust, D. S. Bright, and D. E. Newbury, *J. Micros.* 145: 207-223 1987.
2. D. E. Newbury, C. E. Fiori, R. B. Marinenko, R. L. Myklebust, C. R. Swyt, and D. S. Bright, *Anal. Chem.* 62: 1159A, 1245A, 1990.
3. J. I. Goldstein, D. E. Newbury, P. Echlin, D. C. Joy, C. E. Fiori, and E. Lifshin, *Scanning Electron Microscopy and X-ray Microanalysis*, New York: Plenum, 1981.
4. J. T. Armstrong and P. R. Buseck, *Anal. Chem.* 47: 2178-2192, 1975.
5. T. A. Hall, *Quantitative Electronprobe Microanalysis*, in K.F.J. Heinrich, Ed., Nat. Bur. Stds. Special Pub. 298, 1968, 269-299.
6. J. A. Small, K. F. J. Heinrich, D. E. Newbury, and R. L. Myklebust, *SEM/1978* II, 445-454.
7. P. J. Statham and J. B. Pawley, *Scanning Electron Microscopy* (vol. 1), 1978, 469-478.

SEM AND EPMA APPLICATION TO THE INVESTIGATION OF ELECTROMIGRATION IN THIN-FILM INTERCONNECTS

A. N. Priymak

The SEM and EPMA techniques have been applied to the detection of grain boundary electromigration in Al and Al-Sn stripes of submicron thickness and various lengths, which were tested under various conditions (temperature, current density) by the drift-velocity method.

The EPMA technique for measuring the "effective" stripe thickness has been developed and applied to the detailed exploration of cathode edge drift kinetics and morphology of the depleted region (behind the shifted cathode edge).

A. N. Priymak is at the Institute of Problems of Microelectronics Technology and Superpure Materials, USSR Academy of Sciences, 142432 Chernogolovka, Moscow District, USSR.

Thus, for the first time, existence of a homogeneous thinning area in front of the cathode was established, as was the dependence of the area length and the thickness and morphology of residual Al in the depleted region on the initial stripe length, temperature, and current density.

To study the Al accumulation at the anode side of the stripe, the SEM technique for detecting the height and volume of hillocks was applied and the dependence of these characteristics on the experimental conditions was established.

The equipment and the technique of in situ investigation (in an EPMA chamber) of edge displacement and hillocks/whiskers growth kinetics have been developed, which enabled us to study the earliest stages of the processes. For the first time, direct measurements of hillocks/whiskers formation and edge drift velocity have been carried out. Possible mechanisms of hillocks/whiskers growth can now be discussed.

ANALYSIS OF HIGH-T$_C$ BULK SUPERCONDUCTORS WITH ELECTRON MICROPROBE COMPOSITIONAL MAPPING

R. B. Marinenko

A barium-yttrium-copper (BYC) high-T$_C$ superconductor specimen from Argonne National Laboratories was analyzed with electron microprobe (EPMA) digital mapping using wavelength spectrometers. The material studied was from a large-bath production technique from the Superconductivity Pilot Center at Argonne. This superconductor has a second silver phase in the superconducting material and a silver electrode on the exterior surface. The objective of this work was to determine whether interactions were present between the superconducting material and the silver.

Experimental

Cross sections and longitudinal sections of the sample were mounted in epoxy and polished with diamond paste. Specimens were examined with the electron microprobe and x-ray spectra were obtained with an energy dispersive spectrometer (EDS). Digitized x-ray intensity maps were obtained for barium, silver, copper, and yttrium using three wavelength spectrometers (WDS), a 20kV excitation potential, and about 29nA aperture current. The 64 × 64 pixel maps were taken at a dwell time of 016 s/pixel with 94 μm along an edge.

Results and Discussion

Two distinct phases are present in the bulk material as can be seen in the secondary electron (SE) images in Fig. 1. EDS analysis showed that the light phase is silver and the darker material is the BYC superconductor. On the outside of the bulk material is a silver electrode layer which was applied to improve electrical conductivity[1] between the superconductor and other components in electrical circuits. The outermost layer, above the silver electrode, is lead-tin solder.

The bulk superconductor contains numerous voids, as has been observed in previously analyzed BYC specimens.[2] The silver electrode also appears to have some voids. The extent of contact between the superconductor and the silver electrode can be seen in the SE and backscatter (BS) images in Fig. 2. In many locations along the boundary the two materials are juxtaposed with no interruptions, but there are also several locations where voids occur along the boundary.

WDS maps[2,3] are in Figs. 3 and 4. In Fig. 3

R. B. Marinenko is at the Surface and Microanalysis Science Division, Chemical Science and Technology Laboratory, National Institute of Stardards and Technology, Gaithersburg, Md 20899.
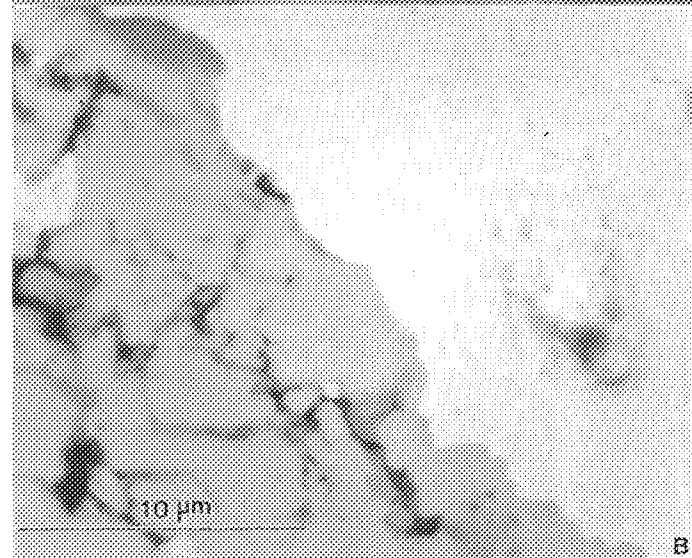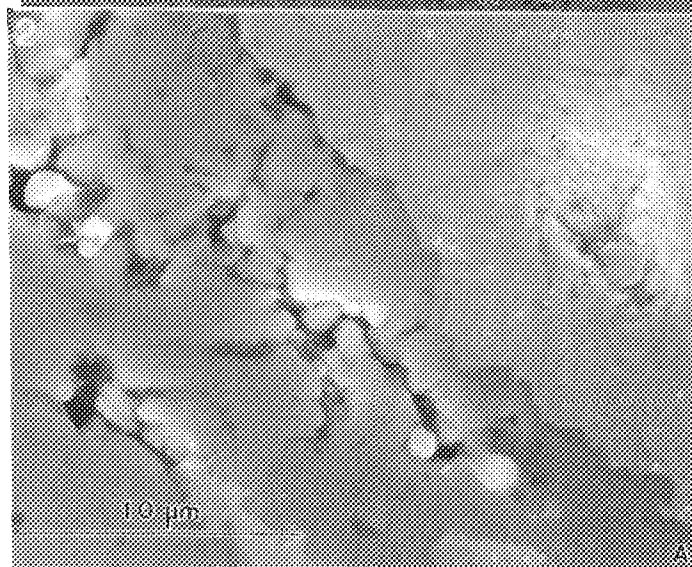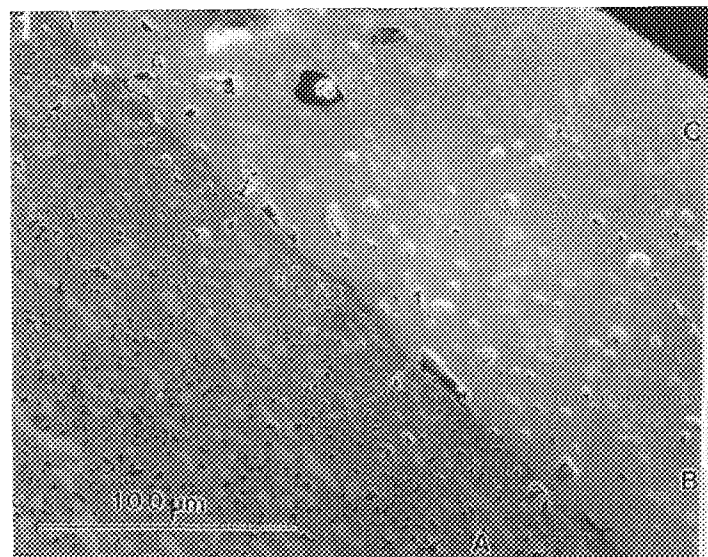
are maps from the cross section taken for elements barium (A), copper (B) and yttrium (C) with an overlay of the three elements in the lower right (D). A second set of maps taken from a longitudinal section of the same specimen but for elements barium (A), silver (B), and copper (C) with the overlay in (D) is in Fig. 4. Since only three spectrometers were available on the electron microprobe used in these analyses, mapping all four elements simultaneously was not possible. In the maps of the longitudinal section, the silver phase appears to be isolated from the superconducting material; i.e., it does not migrate into the superconducting material at the sensitivity level of this experiment, which is approximately 1 wt%. In addition, although the superconducting material appears to be somewhat more homogeneous than the BYC superconductors observed previously in this laboratory,[2] some small regions of copper- and barium-rich compounds are scattered throughout the BYC superconducting material in the specimen.

Conclusions

SE and BS images and WDS digital mapping have been useful in defining the microstructure of this unique superconductor. More analysis such as secondary ion mass spectrometry (SIMS) will be done to determine whether silver does migrate into the superconducting phase. A migration of 1 or 2 μm of low-concentrations of silver would not be detectable with EPMA, since the excitation volume of the electron beam is 2-3 μm in diameter.

References

1. J. W. Ekin et al., "High-Tc superconductor/noble-metal contacts with surface resistivities in the 10^{-10} ohm-cm range," *Appl. Phys. Let.* 52: 1819, 1988.

2. R. B. Marinenko, D. E. Newbury, D. S. Bright, R. L. Myklebust, and J. E. Blendell, "Application of wavelength-dispersive compositional mapping to high-temperature superconductors," *Microbeam Analysis--1988*, 37-40.

3. R. B. Marinenko et al., "Digital x-ray compositional mapping with 'standard map' correction for wavelength dispersive spectrometer defocussing," *J. Microsc.* 145: 207, 1987.

4. R. B. Marinenko et al., "Defocus modelling correction for wavelength dispersive digital compositional mapping with the electron microprobe," *J. Microsc.* 155: 183, 1989.
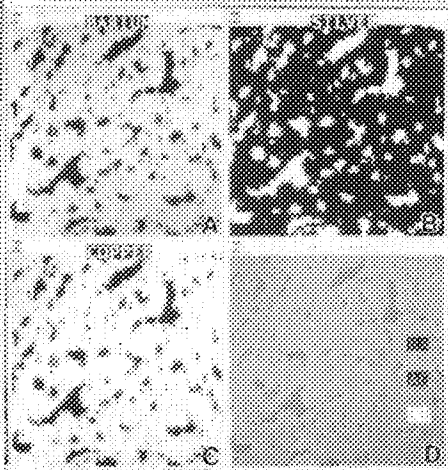
FIG. 3.--WDS element digital maps of super-
conducting material taken for elements
A (barium), B (copper), C (yttrium), and
D (overlay of all three elements).
FIG. 4.--WDS element digital maps of supercon-
ducting material taken for elements A (barium),
B (silver), C (copper), and D (overlay of all
three elements).

FIG. 1.--Secondary electron image of outer edge of
superconductor: in superconducting material A, dark
area is BYC superconductor and light phase is silver;
B is outer silver electrode; C lead-tin solder.
FIG. 2.--(A) Secondary-electron and (B) backscatter
images of contact region between superconducting
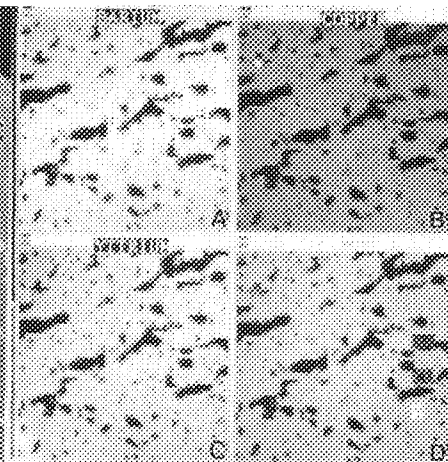material and silver electrode.

COMPARISON OF SCANNING FORCE MICROSCOPE AND SCANNING ELECTRON MICROSCOPE ANALYSIS OF POLY-SILICON

G. D. Aden, R. T. Jobe, P. E. West, and Bill Roth

Poly-silicon is used in the semiconductor industry as a gate material for MOS devices. Of key importance in the preparation of the poly-silicon layer are uniformity, grain size, and thickness. Characterization of this layer can be difficult because the extremely fine grain structures can only be imaged at magnifications in excess of 100 000×.

Poly-silicon is typically grown on a thermal oxide layer of silicon wafers as an early step in the semiconductor process. As a result, this surface is insulating and charges easily under electron bombardment. A conventional tungsten or LaB_6-equipped scanning electron microscope (SEM) cannot be used to image the poly-silicon because of insufficient beam current density.

Techniques using the field-emission SEM are available for direct imaging of nonconducting samples at high resolution images with an SEM, and the excess penetration of the electron beam through the poly-silicon limits the ability to view or measure the surface topography.

With the scanning force microscope[2] (SFM) it is possible to image uncoated poly-silicon in ambient air directly. SFM images provide direct visualization of the poly-silicon, as well as quantitative values for surface and area roughness.[3] The SFM is derived from the scanning tunneling microscope (STM); it provides high resolution, three-dimensional images of a sample's surface in vacuum, ambient air, and liquid. Measuring images of poly-silicon is problematic with an STM because of a requirement for current flow between the probe and sample.[4,5] A primary advantage of the SFM is that it can directly image electrically insulating materials.

Images are created in the SFM by measurement of the three-dimensional position of a sharp probe as it is scanned over a surface in a raster motion. Piezoelectric ceramics capable of controlling motion to a fraction of a micrometer are used for creating the raster motions of the probe. The SFM is nondestructive because the loading force of the stylus on the surface is as small as 0.1 nano-Newtons.

Experimental

Uncoated poly-silicon samples were imaged with a Hitachi S-4000 FE-SEM.[6] The sample was placed at 6mm working distance and at a 30°

G. D. Aden, R. T. Jobe, and P. E. West are at TopoMetrix Corp., 1505 Wyatt Ave., Santa Clara, CA 95054; Bill Roth is at Hitachi Scientific Instruments, Nissei Sangyo America, Ltd., 460 E. Middlefield Rd., Mountain View, CA 94043.

tilt. The microscope was operated at 20 keV and about 1 picoamp. Samples were moved continuously to avoid charging and contamination.

SFM images were measured on the TopoMetrix TMX 2000 SFM system.[7] The loading force of the probe on the sample was approximately 5 nano-Newtons and scan rates were 10 μm/s. Scans required approximately 2 min to complete. 1 × 1cm samples of poly-silicon were secured on the sample stage of the microscope with double sticky tape. The same samples were imaged in the SEM and SFM.

Results

Figure 1 is the SEM image of poly-silicon at 100,000× magnification. Surface grains sized at 0.05-0.2 μm are directly visualized in these images. These grains appear to be isolated islands of poly-silicon because of the high voltage. SEM images at lower voltages show the surface to be continuous, but were of insufficient resolution to permit visualization of individual grains.

A two-dimensional light-shaded image and three-dimensional gray-scale SFM image of the poly-silicon measured at approximately 100 000× is illustrated in Fig. 2. The detailed topography is easily visualized in these images. Figure 3 is a 500 000× image of the poly-silicon grains. The height of the grains ranges from 0.05 to 0.3 μm. Quantitative measurements of surface and area roughness on the poly-silicon image in Fig. 2 are presented in Table 1.

Conclusion

Magnified views of poly-silicon in the SEM and SFM permit direct visualization of submicrometer surface features. Quantitative values for the feature depth and the surface and area roughness are generated with the SFM.

References

1. J. B. Pawley, "Practical aspects of high-resolution LVSEM," *Scanning* 12: 247, 1990.

2. J. D. Baldeschwieler, J. M. Gill, and P. E. West, "The scanning probe microscope: A powerful tool for visualizing the micro world," *American Laboratory*, Feb. 1991, 53.

3. L. Files-Sesler, J. N. Randall, and D. Harkness, "Scanning tunneling microscopy: Critical dimension and surface roughness analysis," *J. American Vacuum Soc.* B9(2), 1991.

4. J. Jahanmir, P. E. West, and A. Young, "Current-voltage characteristics of silicon measured with the STM in air," *J. Vac. Sci. Technol.* A7(4), 1989.
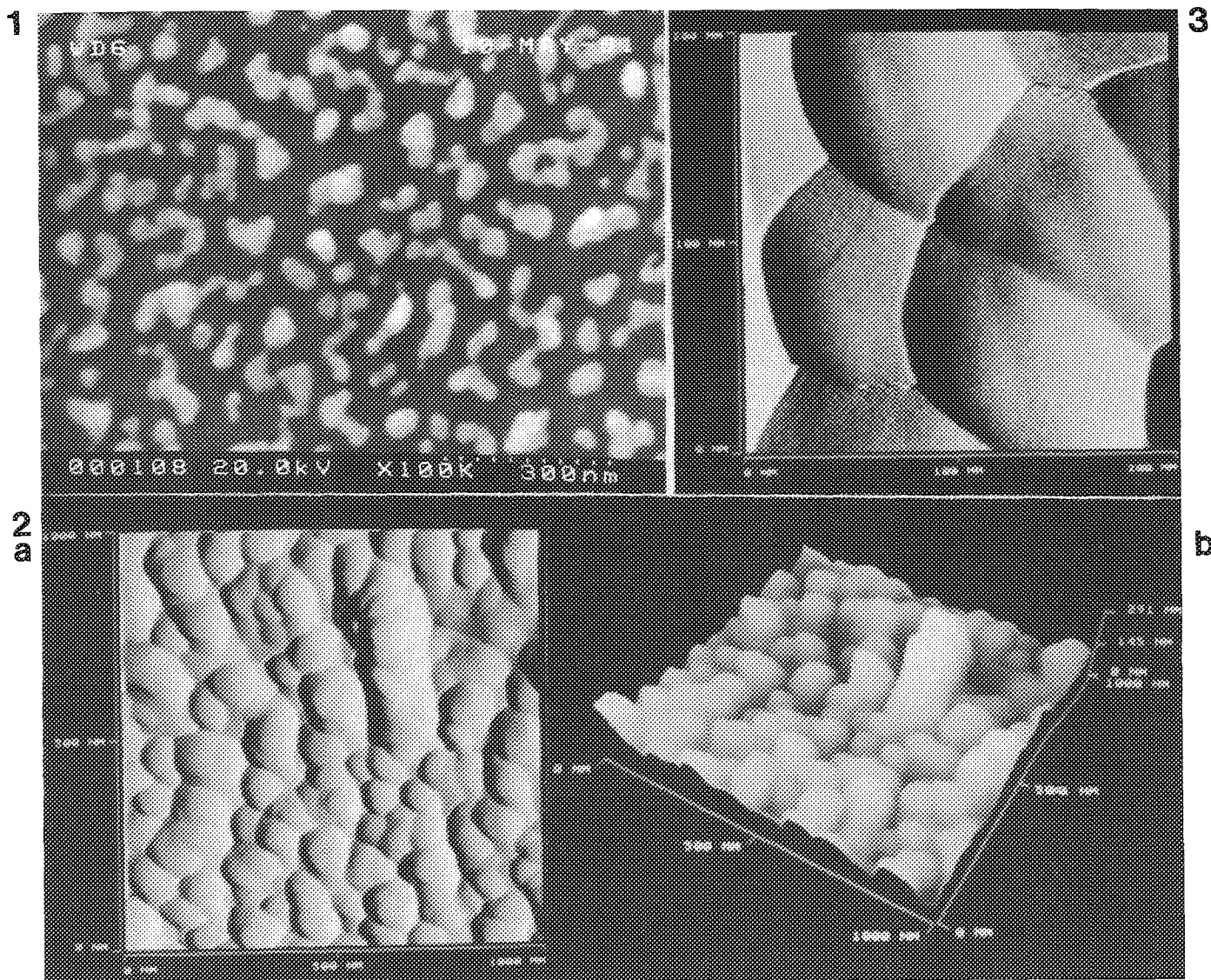
FIG. 1.--SEM micrograph of poly-silicon grains on silicon oxide showing individual 0.05-0.2 μm islands. Taken at 20 keV, 100 000×. Image taken with less than 30 s of electron-beam exposure time.

FIG. 2.--SFM image of poly-silicon grains measured at 100 000× magnification: (a) light shaded display format, (b) 3-D gray-scale display format.

FIG. 3.--Poly-silicon grains measured with the SFM at 500 000× mangification.

TABLE 1.--Line roughness and area roughness of the image displayed in Fig. 2.

Parameter	Value(nm)
Line Roughness	
R_a	23.01
R_b	66.53
R_{pm}	31.92
R_t	138.01
R_{tm}	69.69
Area Roughness	
R_a	29.12
R_{ms}	39.64
Z_{avg}	102.05
Z_{max}	290.50

5. J. Jahanmir, P. E. West, and P. C. Colter, "Local modification of thin SiO_2 films in a scanning tunneling microscope," *J. Appl. Phys.* 67(11), 1990.

6. Hitachi Scientific Instruments, Mountain View, Calif.

7. TopoMetrix Corp., Santa Clara, Calif.

NICHES FOR SIMS IN BIOLOGICAL MICROANALYSIS

M. S. Burns

Secondary Ion Mass Spectrometry (SIMS) has several features that make it potentially useful for addressing questions in biology. New technical developments have enlarged the scope of potential applications, and explorations into specific problems have shown progress in applying SIMS to biological questions. Two problems that need to be addressed are availability of instrumentation and preparation of specimens to take advantage of unique SIMS capabilities.

Isotope Detection

Inherent in instrumentation using mass spectrometric detection systems is the ability to discriminate isotopes. This feature opens the possibility of doing experiments that follow the movement of tracer molecules into cells and localizing them within cells and tissues. Similar to the use of radioactive tracers, "pulse-chase" experiments can be done with a variety of isotopes to follow the course of ions or labeled molecules. Both positively and negatively charged secondary ions have been analyzed.

Recent applications in this area have used stable calcium isotopes (^{42}Ca and ^{44}Ca) to monitor the movement of calcium into both cells in culture and intact tissues. A low-abundance iodine isotope has been used in analysis of thyroid physiology. Other electrolyte substitutions, such as Rb replacement of K and Li replacement of Na, have also been done.

Experiments using labeled molecules have shown the feasibility of detecting organic molecules that are readily labeled with an unusual element. For example, boron-labeled anticancer drugs have been localized. F- and Br-labeled nucleotides have been shown in specific cellular localizations, when incorporated into stable polynucleotide complexes. The demonstration of ^{14}C localization of organic molecules in cell areas opens the possibility of detection of compounds labeled with this radioactive tracer, since a large variety of physiologically important ^{14}C labeled compounds are commercially available.

Although mass interferences are potentially a problem for isotope detection, the available (and being developed) mass resolution on current instruments is generally adequate for detection of specific elements in systems where it has been tested.

Lateral Resolution

The lateral resolution of ion emission is determined by both the probe size and by the

ion detection system, as well as the path of the sputtered ion. Instrumentation using liquid-metal primary-ion beams have probe sizes of ca 30 nm and detection systems have a resolution of ca 1 µm. In practice, however, the preparation of biological materials and maintenance of diffusible elements in their native location is probably more limiting than the instrumental specifications. Cold stages have been developed for biological microanalysis by SIMS but have received only limited examination in biological problems to date. The interplay of resolution and detection sensitivity are more important than any single parameter.

Quantitation

Absolute quantification protocols have been developed using relative sensitivity factors for biological tissue and have given interesting data when compared with other modes of microanalysis. Relative quantitation has frequently been used in published papers for specific applications and has been found useful in addressing many biological problems. There is a need for continuing examination of biological specimens by more than one mode of analysis to give the biologist confirmation that existing biological paradigms are valid. However, given the high sensitivity of SIMS for some elements (notably Na, K, Mg, Ca) of major importance in cell regulation, it is frequently difficult, if not impossible, to have confirmation by an equally sensitive technique on a micro scale.

Applications

The range of SIMS applications in biology is quite wide, encompassing physiological and pathological studies of many tissues such as thyroid, retina, intestine, lung, bone, and many others. In addition, application of this technique to cells in culture gives information on cell processes basic to many disciplines. Some recent studies have been done in botany, which extends SIMS analysis to new types of organisms; now animal, vegetable, and mineral applications for SIMS have been reported. A continuing problem that needs to be addressed is the availability of SIMS instrumentation to the biological scientist.

Instrumentation

New instrumentation and modes of analysis are constantly being developed, which should be useful to the biological community. Higher-resolution instrumentation, both in spatial localization and in mass resolution, could be valuable for given problems. Increasingly surface-sensitive instrumentation will find future applications, although questions concerning preparation of specimens will become even more crucial. The use of microdroplet preparations by SIMS may open areas of micro-wet chemistry.

APPLICATIONS OF SIMS IN COSMOCHEMISTRY AND GEOCHRONOLOGY: PROBING THE EVOLUTION FROM STARDUST TO THE FIRST CONTINENTS

K. D. McKeegan

It is nearly ten years since Shimizu and Hart concluded their landmark review with the opinion that "the ion microprobe is well on its way to revolutionizing the fields of geochemistry and cosmochemistry in much the same way as the electron microprobe revolutionized the field of light." The past decade has seen great progress as techniques for the quantitative determination of elemental and isotopic abundances in complex geologic samples by secondary ion mass spectrometry (SIMS) have been developed, in several important cases, to the point of routine analytical tools. With the availability of second- and recently third-generation SIMS instruments, a wide range of "geologic" problems--from synthesis of the elements in stars to interstellar chemistry and the birth of the solar system, to the formation and differentiation of the Earth, to the more recent emplacement of mineral deposits--is currently under investigation by ion-probe methods in various stages of active development. Obviously, a comprehensive review of the contributions of SIMS to this spectrum of geo- and cosmochemical problems is beyond the scope of these Proceedings; for this purpose the reader is directed to the excellent article by Reed.[2] Instead, this paper briefly highlights progress made in studies of the origins of the solar system and the Earth, in the hope of demonstrating that the enthusiasm of pioneers in the field was fully justified.

The ion microprobe has become an important tool for geochemists because it combines attributes of the two more traditional techniques for studying the distributions of elemental and isotopic abundances in geologic samples: like the electron microprobe, it can perform in situ measurements on polished samples with high (typically a few microns to submicron) spatial resolution; and since it is a mass spectrometer, it also measures isotopes. In addition, SIMS exhibits high sensitivity for most elements, so that detection limits, including those for light elements (Z < 10), are in the ppm to (in favorable circumstnaces) sub-ppb range. A further consequence of this high sensitivity is that certain isotopic measurements may be made on very small samples (see below) or for elements that comprise only trace quantities of some mineral phase. Against these positive features must be set the problems well known in the SIMS community; the propensity for sputtering to produce an abundance of molecular ion species (especially from a com-

plex matrix such as most natural minerals) that cause interferences at the same nominal mass as atomic ions of interest; and the problems for quantitation caused by variations in the ionization efficiencies of different elements (and to a lesser extent, different isotopes), depending on the chemical state of the sample surface during sputtering--the so-called "matrix effects."[3]

For elemental analysis the problem of mass interferences is ameliorated by the use of energy filtering and peak-stripping techniques.[1,4] However, isotopic ratio measurements generally require greater accuracy and thus high mass resolving power (MRP) is the preferred method to separate interfering species. An extremely useful summary of isotopic ratio measurement techniques by SIMS, including a detailed discussion of instrumental aspects and correction procedures for mass fractionation, is presented by Zinner.[5]

Applications in Geochronology

The decay of two isotopes of the same element (^{235}U, ^{238}U) to two distinct isotopes of the same daughter element (^{207}Pb, ^{206}Pb) provides an (almost) unique opportunity for radiometric dating without the need for the assumption of closed-system behavior for parent and daughters. The mineral zircon ($ZrSiO_4$) incorporates high abundances of U and Th, but only trace quantities of Pb, during crystallization. The refractory nature of zircon plus its ability to retain radiogenic Pb make it an excellent geochronometer, particularly for old rocks. However, these same properties can cause zircons to record very complicated histories in their U-Th-Pb isotopic systems, since a single crystal can often survive episodes of crustal melting or erosional transport. The information contained in multiple zones of zircon growth can only be extracted by isotopic measurements on a fine spatial scale such as can be achieved with the ion microprobe.

Early efforts to use the ion microprobe to measure U-Pb ages in zircon met with only partial success owing to the difficulties of measuring the isotopic composition of trace amounts of Pb in the presence of interferences such as Zr_2O and silicides of Hf and the rare earth elements.[2] These problems were overcome by Compston, Williams, and co-workers at the Australian National University using the Sensitive High Resolution Ion MicroProbe (SHRIMP) which, because of its large mass dispersion, is capable of achieving a MRP of about 7000 without a large loss in transmission through the spectrometer.[6] At this MRP, all significant

K. D. McKeegan is at the Department of Earth and Space Sciences, University of California, Los Angeles, CA 90024-1567.

molecular interferences are resolved from the Pb isotopes except PbH[+], which however is negligible in old zircons (since radiogenic $^{207}Pb/^{206}Pb > 0.4$ after 4 Gyr).[7] One can determine U/Pb elemental ratio for a given $\sim30\mu m$ spot in zircon by correcting the measured U^+/Pb^+ ratio by a factor that depends on the UO^+/U^+ ratio, the relation between UO^+/U^+ and U^+/Pb^+ having been established by measurements in standard zircons of known U and Pb content. Although the correction factors depend on instrumental conditions and the matrix analyzed, this empirical method effectively compensates for the differing energy distributions U^+ and Pb^+, yielding an accuracy of better than 2% for U/Pb ratios.[7-9]

A large number of U-Pb studies of zircons performed with SHRIMP have demonstrated its ability to reveal novel information concerning the behavior of the U-Pb system and the complex histories of individual zircons. Perhaps the most exciting result of the ANU group has been the identification of detrital zircons from Western Australia, with crystallization ages of up to nearly 4.3 Gyr.[10-11] These zircons, by far the oldest terrestrial minerals yet discovered, provide us with a unique source of information concerning the evolution of the early Earth. For example, their mere existence constrains the time scale for production of the first continenetal crust, and their Hf isotopic compositions have also provided evidence that the mantle did not undergo extensive melting during formation of the Earth.[12]

Applications in Cosmochemistry

Since the Sun is somewhat less than half as old as the galaxy, the solar system must have formed from a mixture of pre-existing interstellar dust and gas, the nuclear components of which had been produced at different times and in different stars. The discovery of isotopic variations in primitive meteorites that could not be generated by any solar system processes demonstrates that this mixing was not complete and provides important boundary conditions for theories of the origin of the solar system. Because many of these isotopic anomalies occur on a small spatial scale in relatively rare objects, the ion microprobe has played a key role in elucidating both the magnitude of the isotopic effects and the correlations between anomalies in different elements and mineral phases.

Most ion microprobe measurements have been made on Mg isotopic compositions in Ca-Al-rich refractory assemblages from carbonaceous meteorites, where heterogeneous excesses of ^{26}Mg give evidence for the prior presence of live ^{26}Al at the time these minerals formed.[5,13] Because the half-life of ^{26}Al is only 7×10^5 years, these data place severe constraints on the models of the evolution of the solar nebula and its connection to the interstellar medium.[14] Further insights into cosmochemical processes are provided by ion microprobe measurements of large, correlated anomalies in the neutron-rich isotopes of Ca and Ti in individual grains of the ultra-refractory mineral hibonite.[15,16] The data demonstrate that at least four different components are required to produce solar Ca and Ti; one of them can be assigned to a specific nucleosynthetic process (n-rich nuclear statistical equilibrium burning) whose products were ejected by some supernova and transported to the solar nebula as interstellar dust grains. These grains were then partially mixed with other materials and thermally processed to form the hibonites.

In an astonishing series of discoveries made over the past few years, Anders, Zinner, and colleagues have recovered three different types of preserved interstellar dust grains from primitive meteorites: diamond, silicon carbide, and graphite.[17,18] By following tracers provided by anomalous noble gas components, these workers have employed elaborate chemical treatments to purify the exotic phases that constitute but tiny fractions (~400, ~6, and < 2 ppm, respectively) of certain carbonaceous meteorites. The pre-solar origin of individual crystals of SiC and graphite--some of which are smaller than 2 μm in diameter-- has been proved by ion microprobe measurements of extremely anomalous isotopic compositions of C, N, and Si (in SiC); e.g., the $^{12}C/^{13}C$ measured in individual graphite grains ranges from 0.09 to 16 times the solar value.[18] The capability of SIMS to measure correlated isotopic ratios for multiple elements on relict grains formed in the outflows from evolved stars has created new opportunities for astrophysics, as precise laboratory data can now be used to test theories of nucleosynthetic processes in certain types of stars. As an example, recent ion microprobe measurements have found that certain grain size fractions of circumstellar SiC have Ba and Nd isotopic compositions which are almost purely due to s-process nucleosynthesis.[19] Comparison with model calculations for the He-burning shell in red-giant stars (which are one identified source for SiC) whos general overall agreement but significant deviations for some isotopes of Nd.

Conclusions

For many important geologic applications, SIMS is beyond the purely development phase and is fulfilling its promise as the "ultimate weapon of the geochemist,"[20] The use of the ion microprobe as a kind of telescope with which to look through space and time has already provided new and surprising results bearing on the origin and evolution of the Earth and its solar system. In the near future we can anticipate obtaining further insights into such areas as stellar nucleosynthesis, the chemical evolution of the galaxy, and the nature of interstellar dust particles.

References

1. N. Shimizu and S. R. Hart, "Applications of the ion microprobe to geochemistry and cosmochemistry," *Ann. Earth Planet. Sci.* 10: 483,

1982.

2. S. J. B. Reed, "Ion microprobe analysis: A review of geological applications," *Mineral. Mag.* 53: 3, 1989.

3. I. M. Steele, R. L. Hervig, I. D. Hutcheon, and J. V. Smith, "Ion microprobe techniques and analyses of olivine and low-Ca pyroxene," *Am. Mineral.* 66: 526, 1981.

4. E. Zinner and G. Crozaz, "A method for the quantitative measurement of rare earth elements in the ion microprobe," *Int. J. of Mass Spec. Ion Proc.* 69: 17, 1986.

5. E. Zinner, "Isotopic measurements with the ion microprobe," in W. C. Shanks III and R. E. Criss, Eds., *New Frontiers in Stable Isotope Research: Laser Probes, Ion Probes, and Small-sample Analysis*, U.S. Geological Survey Bulletin 1890, 1989.

6. S. W. J. Clement, W. Compston, and G. Newstead, "Design of a large, high-resolution ion microprobe," in A. Beninghoven, Ed., *SIMS*, Münster: Springer-Verlag, 1977.

7. W. Comptston, I. S. Williams, and C. Meyer, "U-Pb geochronology of zircons from lunar breccia 73217 using a sensitive high mass-resolution ion microprobe," *Proc. 14th Lunar and Planet. Sci. Conf., J. Geophys. Res.* 89: B525, 1984.

8. W. Compston, P. D. Kinny, I. S. Williams, and J. J. Foster, "The age and Pb loss behavior of zircons from the Isua supracrustal belt as determined by ion microprobe," *Earth Planet. Sci. Lett.* 80: 71, 1986.

9. T. R. Ireland, W. Compston, I. S. Williams, and I. Wendt, "U-Th-Pb systematics of individual perovskite grains form the Allende and Murchison carbonaceous chondrites," *Earth Planet. Sci. Lett.* (submitted).

10. D. O. Froude, T. R. Ireland, P. D. Kinney, I. S. Williams, W. Compston, I. R. Williams, and J. S. Myers, "Ion microprobe identification of 4100-4200Myr-old terrestrial zircons," *Nature* 304: 616, 1983.

11. W. Compston and R. T. Pidgeon, "Jack Hills: Evidence of more very old detrital zircons in Western Australia," *Nature* 321: 766, 1986.

12. T. Kato, A. E. Ringwood, and T. Irifune, "Experimental determination of element partitioning between silicate perovskites, garnets and liquids: Constraints on early differentiation of the mantle," *Earth Planet. Sci. Lett.* 89: 123, 1988.

13. I. D. Hutcheon, "Ion probe magnesium isotopic measurements of Allende inclusions," in L. A. Cure, Ed., *Nuclear and Chemical Dating Techniques: Interpreting the Environmental Record*, Am. Chem. Soc. Symp. No. 176: 95, 1982.

14. G. J. Wasserburg and D. A. Papanastassiou, "Some short-lived nuclides in the early solar system--a connection with the placental ISM," in C. A. Barnes, D. D. Clayton, and D. N. Schramm, Eds., *Essays in Nuclear Astrophysics*, Cambridge University Press, 1982, 77.

15. A. J. Fahey, J. N. Goswami, K. D. McKeegan, and E. Zinner, "26Al, 244Pu, 50Ti, REE and trace element abundances in hibonite grain from CM and CV meteorites," *Geochim. Cos-*
mochim. Acta 51: 329, 1987.

16. T. R. Ireland, "Correlated morphological, chemical, and isotopic characteristics of hibonites from the Murchison carbonaceous chondrite," *Geochim. Cosmochim. Acta* 52: 2827, 1988.

17. T. Ming, E. Anders, P. Hoppe, and E. Zinner, "Meteoritic silicon carbide and its stellar sources; implications for galactic chemical evolution," *Nature* 339: 351, 1989.

18. S. Amari, E. Anders, A. Virag, and E. Zinner, "Interstellar graphite in meteorites," *Nature* 345: 238, 1990.

19. E. Zinner, S. Amari, and R. S. Lewis, "S-process Ba and Nd in presolar Murchison SiC," *XII Lunar Planet. Sci.* (in press).

20. J. F. Lovering, "Application of SIMS microanalysis techniques to trace element and isotopic studies in geochemistry and cosmochemistry," *NBS Special Publication* 427: 135, 1975.

SECONDARY ION MASS SPECTROMETRY AS A DIAGNOSTIC TOOL
FOR ION IMPLANTATION AND MOLECULAR BEAM EPITAXY

D. S. Simon and Ph. H. Chi

Secondary ion mass spectrometry (SIMS) is the dominant analytical tool of the semiconductor industry for the characterization of atomic dopant concentration profiles. The preeminence of SIMS in this application arises from its low (ppm to ppb) detection limit for nearly all elements in the periodic table, and its excellent depth resolution in single-crystal semiconductor targets. These capabilities are often exploited in following the effects of processing steps such as ion implantation and thermal annealing on a particular dopant species, to compare actual behavior with theoretical models.

Another powerful aspect of SIMS that is less commonly discussed is its ability to detect *unintentional* processing effects, which may take the form of an unexpected depth distribution of intentionally introduced dopants, or unanticipated elements (contamination) that are introduced during processing. During many years of analyzing semiconductor samples by SIMS in our laboratory, we have accumulated a variety of examples of these unintentional effects, primarily in samples produced by ion implantation or by molecular beam epitaxy (MBE). A discussion of these effects demonstrates the variety of unforeseen mechanisms that can occur during these processing procedures.

Ion Implantation

The processing artifacts we have observed for ion-implanted semiconductor samples fall into the general categories of ion channeling, charge-exchange effects, and contamination from extraneous elements. Ion channeling modifies the projected range of the incident ion beam in a crystalline substrate, depending on the orientation of the beam with respect to the crystal axes. In commercial ion implanters the single-crystal wafer is usually tilted by 7° to avoid implantation along a high-symmetry direction. However, a secondary channeling effect known as planar channeling can still occur if the crystal axes in the plane of the wafer are not oriented properly with respect to the scan direction of the implanting beam. In this case, small changes in incident angle as the

beam is scanned electrostatically about a fixed pivot point can lead to large variations in the depth distribution of the implanted species across the wafer.[1] An example of this effect is shown in Fig. 1. Boron ions were implanted over a 100mm-diameter wafer at an energy of 130 keV and a dose of 6×10^{12} atoms/cm^2. The plot shows implanted boron depth distributions that differ substantially in shape between the center and edge of the wafer. The significant shoulder on the deep side of the peak for the center profile is evidence of enhanced planar channeling. Note that even the depth of the implant maximum can be shifted when planar channeling occurs.

Ion implants are sometimes made with multiply charged species to achieve a higher implantation energy for a given accelerating voltage. Figure 2 shows an implantation profile of boron at 400 keV that was made by accelerating $^{11}B^{++}$ through a voltage of 200 kV. The boron beam was first accelerated through a potential of 25 kV and then mass-filtered by a 90° deflection through a bending magnet before final acceleration through a voltage drop of 175 kV. A process that can occur along the flight path is charge-exchange between a doubly charged boron ion and a neutral molecule of residual gas, resulting in a singly charged boron ion and a singly charged gas atom or molecule.[2] If this process occurs before the beam exits from the magnet, the singly charged boron is not bent enough by the magnetic field to pass through the exit slit of the magnet. However, if this charge-exchange process occurs after the mass filter but before final acceleration, the singly charged boron acquires a final energy of $2 \times 25 + 175 = 225$ keV. Charge exchange may have a high probability of taking place if the vacuum after the exit slit of the magnet is poor. In this case, a second peak may be present in the implant profile at a shallower depth than expected due to the singly charged component in the beam. This is the explanation for the shallower peak in Fig. 2.

Not only the profile shape, but also the atom dose is different from the intended but if charge exchange occurs. For a doubly charged implant, the intended atom dose is half the number of electronic charges per unit area accumulated at the target. If an undetected singly charged component is present, it contributes one atom per electronic charge rather than 0.5 atom per charge. Therefore, the actual total atom dose is greater than expected. For the example illustrated in Fig. 2, the B^{++} component is about 50% of the B^+ peak. The total dose is therefore about 20% greater than expected.

Figure 3 shows another example of charge-exchange effects in a multiply charged implant. In this case an implant of Be in GaAs at 5.1 MeV was desired. A high-energy implanter was used to implant Be[+++] accelerated through a voltage drop of 1.7 MV. It is clear from the profile shape measured by SIMS that substantial Be[++] and Be[+] beam components were also present, at energies of 3.4 and 1.7 MeV, respectively, producing the two shallower peaks in the Be profile.

Contamination of the target by extraneous elements during ion implantation may be introduced from the ion source of the implanter,[3] from sputtered metallic components of the end station,[4] or from vacuum contamination. In one case a silicon wafer was amorphized by Si^+ implantation at three different energies in an implanter with a weak Si ion source, at doses in the range of $10^{15}/cm^3$. This procedure required several days of implantation for completion. Following the amorphization, boron was implanted at an energy of 50 keV. When boron was profiled by SIMS, an anomaly was seen at a depth of about 20 nm (Fig. 4). It was also noted that the implanted area of the wafer surface had a straw color. Contamination with carbonaceous material was suspected. When carbon and silicon were profiled, a high carbon signal was seen over a depth of 20 nm, with a corresponding reduction in the silicon signal over the same depth (Fig. 4). It was later learned that the end station of the implanter was pumped by a poorly trapped diffusion pump. Apparently, diffusion pump vapor had condensed on the wafer and had been polymerized by interaction with the energetic Si^+ beam used for amorphization. In this way, an insoluble carbonaceous film was formed on the wafer surface.

Molecular Beam Epitaxy

Molecular beam epitaxy (MBE) is an increasingly popular tool for growing controlled layers of semiconductor material, especially III-V compound semiconductors. Since the source material for the molecular beams is of the highest available purity, and the films are grown in ultrahigh vacuum, one might expect that MBE films would be contamination-free. However, we have not always found that to be true.

Indium was profiled by SIMS in a GaAs-based structure grown by MBE that included an In quantum well. It was noticed that the In background was high in the device away from the quantum well, but dropped by a factor of 100 in the substrate GaAs. This finding led to the conclusion that the MBE system was inadvertently introducing a high level of indium into the growing film. Further investigation and experimentation revealed that indium had been used as a mounting medium in this MBE system to attach the substrate to the sample holder. During MBE growth, the sample is held above 500 C and the indium is in a molten state. We found that the degree of coverage of the wafer substrate over an In-contaminated sample mount was inversely correlated with the concentration of indium in-corporated into the growing film.[5]

Figure 5 shows a typical profile of indium in a nominally pure 1.6µm-thick GaAs film grown by MBE in an In-contaminated system. We also discovered a level of Sb contamination in this same film (also shown in Fig. 5) that was even greater than the In level, approaching 10^{20} atoms/cm^3 near the substrate. It was learned that this particular MBE system had previously been used to grow GaSb. The Sb contamination shows that memory effects from materials previously grown in an MBE system can be quite significant.

A similar example of memory effects from previous operations in an MBE system is shown in Fig. 6. This is a profile of As in a 0.22µm film of InSb, grown in a system that had previously been used to grow GaAs. Cross contamination of Te in InSb from previous CdTe growth has also been reported.[6]

Conclusions

The examples shown in this paper demonstrate that SIMS can be invaluable in diagnosing unintended effects that may occur during semiconductor processing. In particular, our results suggest that memory effects in MBE systems may be much more pervasive than most people would have suspected. To check for unsuspected contaminants, full mass spectral scans should be performed as part of a complete characterization of these materials.

References

1. M. Miyake, M. Yoshizawa, and H. Harada, "Incidence angle dependence of planar channeling in boron ion implantation into silicon," *J. Electrochem. Soc.* 130: 716, 1983.

2. C. P. Wu et al., "Low-energy contaminant in B[++] implantation and its elimination," *J. Electrochem. Soc.* 135: 1735, 1988.

3. D. S. Simons and P. H. Chi, "Ion implantation artifacts detected by secondary ion mass spectrometry," *Microbeam Analysis--1988*, 117.

4. F. A. Stevie, M. J. Kelly, J. M. Andrews, and W. Rumble, "SIMS analysis of contamination due to ion implantation," in A. Benninghoven et al., Eds., *Secondary Ion Mass Spectrometry SIMS V*, Berlin: Springer-Verlag, 1986, 327.

5. D. R. Myers et al., "Unintentional indium incorporation in GaAs grown by molecular beam epitaxy," *Appl. Phys. Lett.* 57: 2321, 1990.

6. G. M. Williams et al., "The growth of high-purity homoepitaxial InSb layers in a molecular-beam epitaxy reactor previously used for CdTe growth," *J. Vac. Sci. Technol.* B8: 79, 1990.
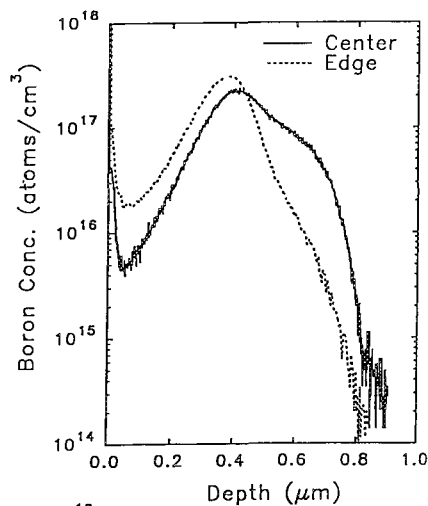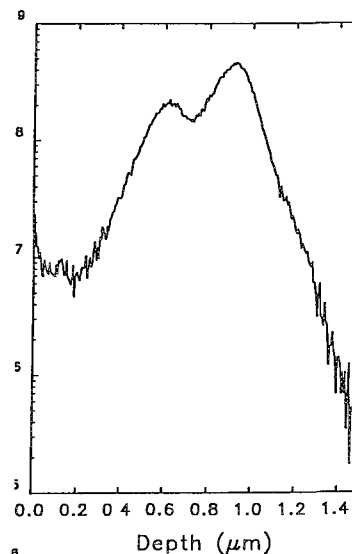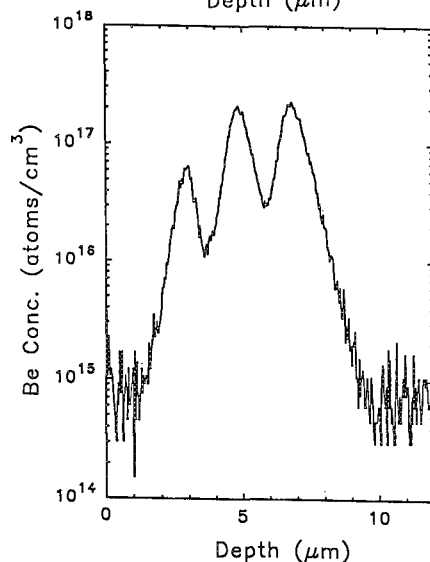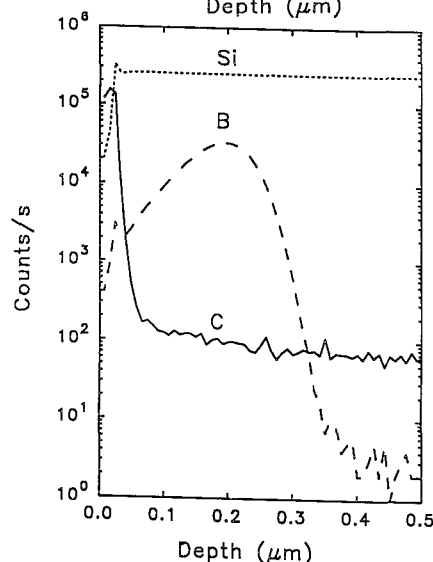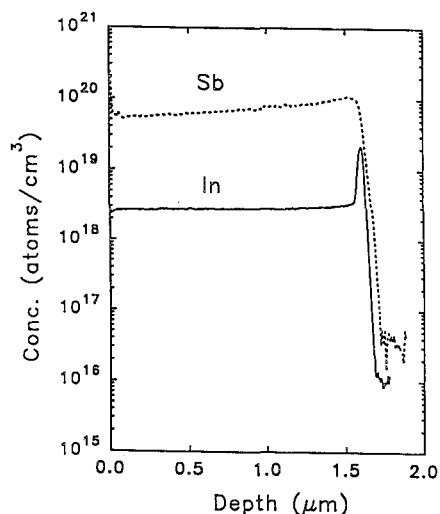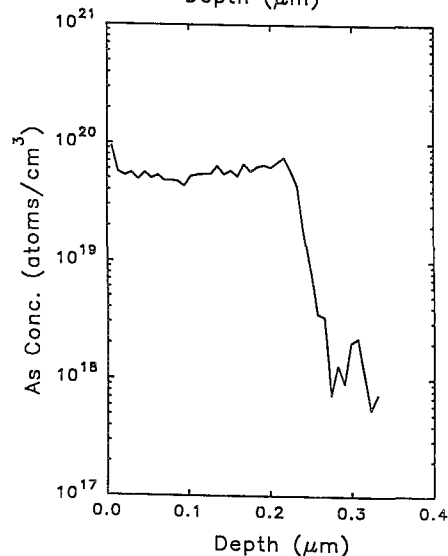
FIG. 1.--Depth profiles of ^{11}B from center and edge of 100mm-diameter Si wafer showing planar channeling effects during implantation.

FIG. 2.--Depth profile of ^{11}B implanted as B^{++} in Si showing shallower peak from charge-exchanged B^+ component.

FIG. 3.--Depth profile of Be in GaAs implanted as Be^{+++} showing shallower peaks from Be^{++} and Be^+.

FIG. 4.--Depth profile of B, C, and Si showing evidence of 20nm carbonaceous contamination layer on Si.

FIG. 5.--Depth profiles showing In and Sb contamination in GaAs layer grown on GaAs by MBE.

FIG. 6.--Depth profile showing As contamination in InSb layer grown on InSb by MBE.

THREE-DIMENSIONAL SIMS IN MATERIALS ANALYSIS

R. H. Fleming

The secondary ion mass spectrometry (SIMS) analysis of heterogeneous elemental, isotopic, and molecular distributions in solid materials requires a suite of strategies. These strategies usually involve ion imaging for characterizing the heterogeneity in the two lateral (surface) dimensions. Acquisition of additional information in the third (depth) dimension converts a lateral analysis into a three-dimensional (spatial) analysis. The lateral analysis of surfaces and the spatial analysis of solids are the subject of this paper.

Why analyze a sample in two or three dimensions? The most obvious reason is to characterize sample heterogeneity. However, a second motive is the simultaneous analysis of two or more samples. For example, when both an unknown and a reference must be measured, the two samples can be arranged in close proximity and analyzed under identical experimental conditions with an imaging technique. Particle analysis is a second example in which many diverse samples can occur in a single image field and be simultaneously analyzed. The heterogeneous features in many samples are isotropically distributed. For these samples, spatial analysis is not required and two-dimensional imaging suffices to characterize the sample.

Besides the added complexity involved in producing the images, there is an inherent disadvantage to imaging analysis. This disadvantage centers around the need to distribute analyte signal intensity among many pixels, 65 536 for a typical 256 × 256 pixel image. The smaller signal allocated to each pixel lower the pixel signal-to-noise ratios. Although these lower ratios are often partly compensated by longer analysis time, they nearly always also reduce analysis precision and raise detection limits.

There are several strategies for converting the SIMS analysis of a surface into a three-dimensional analysis. Because these strategies utilize imaging, the advantages and limitations inherent to imaging also extend to the spatial analysis. The first method for acquiring spatial information is image depth profiling. Repeated images of the secondary ion signal are acquired as the primary ion beam sputters deeper into the sample. Typical sputter rates limit this depth to a few micrometers, thus producing a distinctly different scale in the third dimension. Any sample heterogeneity (crystal orientation in polycrystalline mate-

R. H. Fleming is at Charles Evans & Associates, 301 Chesapeake Drive, Redwood City CA 94063. This work was partially supported by NASA SBIR contracts NAS2-12818 and NAS2-13178.
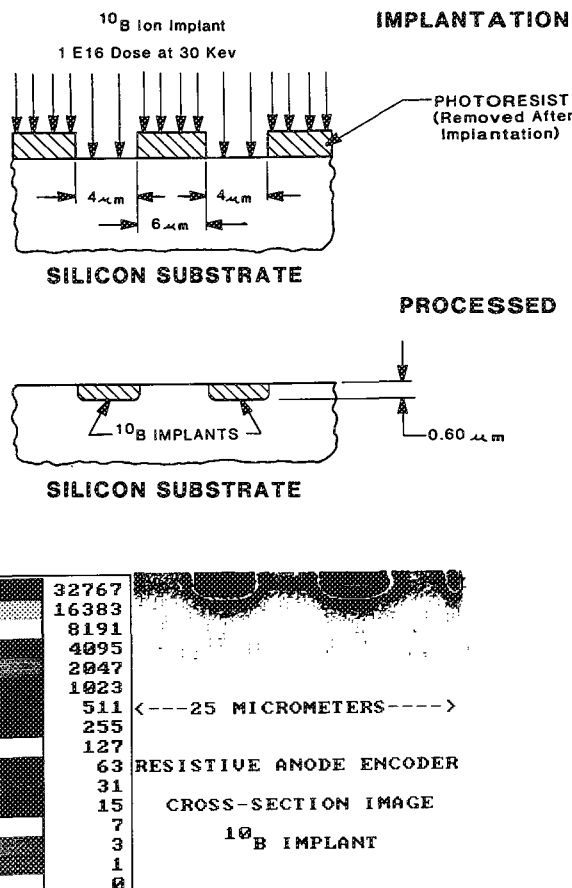
FIG. 1.--Boron cross section recalculated from series of 50 images acquired while sputtering through boron implanted silicon device.

rials for example) can cause variability in the sputter rate. Even single crystals tend to develop uneven sputter crater topography as the crater develops, thereby limiting the depth resolution. Thus, image depth profiling works best for flat, crystalline samples in which the sputter rate is uniform over the image field and the depth of interest is less than a few micrometers. Many semiconductor samples have these characteristics.

Figure 1 shows imaging depth profile results from a semiconductor sample in which silicon had been implanted with [10]B through a mask to produce a spatially heterogeneous boron distribution. Fifty 25μm-diameter images were acquired with a CAMECA IMS-4f instrument in ion microscope mode while the primary ion beam sputtered ~2 μm into the sample. There are several ways to display these results quantitatively. In Fig. 1, the data along a line have been extracted from each image and
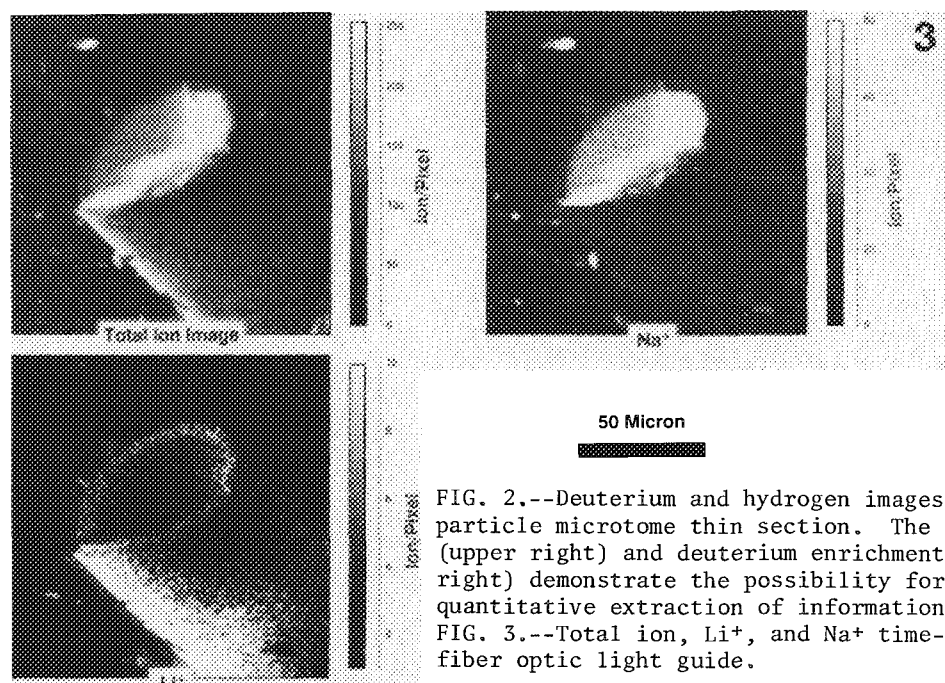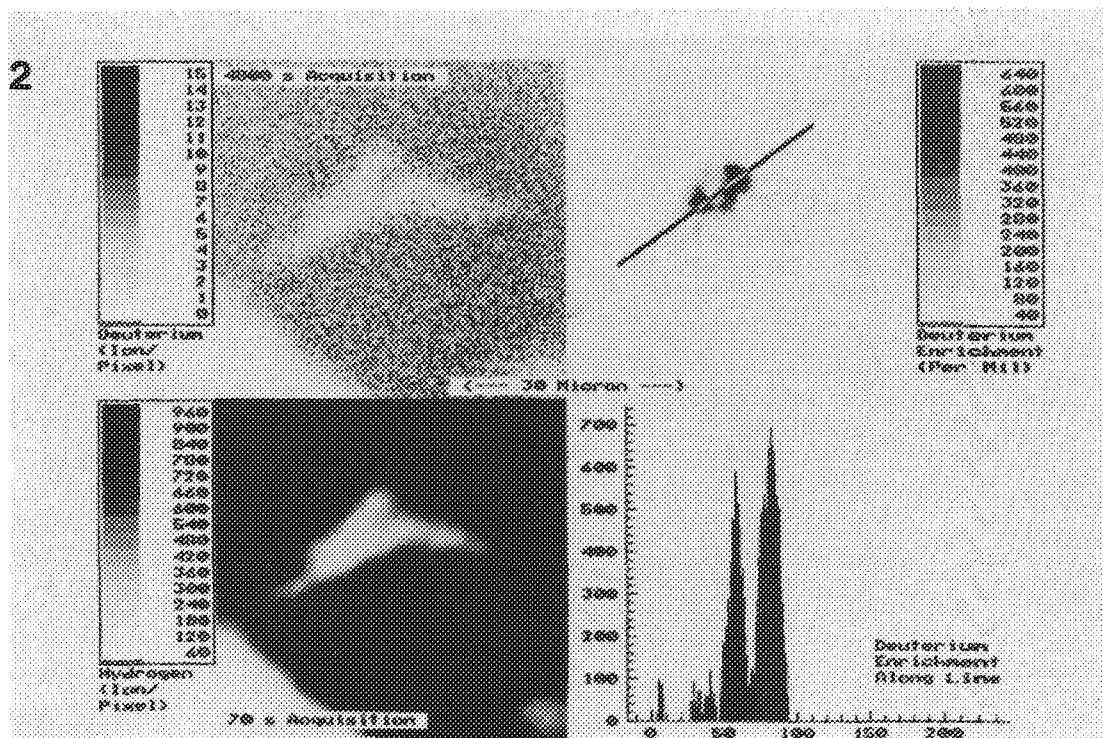
2

3

50 Micron

FIG. 2.--Deuterium and hydrogen images of an interplanetary dust particle microtome thin section. The deuterium enrichment image (upper right) and deuterium enrichment along the line (lower right) demonstrate the possibility for image manipulation and quantitative extraction of information from multiple images.
FIG. 3.--Total ion, Li+, and Na+ time-of-flight SIMS images of a fiber optic light guide.

displayed as a cross section. Two-dimensional images along any plane can be extracted from the three-dimensional data. A second useful display mode is the local area depth profile in which ion intensity from an operator-selected area is plotted as a function of depth. Finally, more complex display schemes provide for projections of multiple cross sections stacked in a two-dimensional display.[1] Different pixel colors or shades usually indicate different ion intensities.

A second strategy for analyzing solid objects exploits microtomy to provide the depth information. The analyst prepares a sequence of ultramicrotome thin sections (typically ~1 μm thick) and selects some or all for analysis. Figure 2 illustrates microtomy on an interplanetary dust particle embedded in an epoxy resin.[2] In this example, a deuterium and a hydrogen image were acquired with a CAMECA IMS-4f instrument in ion microbeam (raster) image acquisition mode. The two images were divided to provide an isotope ratio image that was further modified into the deuterium enrichment image shown. The enrichments are given in parts per thousand (δ) relative to standard mean ocean water (D/H 1.5060×10^{-4}). The normal corrections for spectrometer mass bias, detector dead time, and secondary ion intensity drift are included in the deuterium enrich-

ment image. The epoxy resin D/H ratio has been independently determined, -100δ relative to standard mean ocean water. In this case the epoxy resin portion of the images serves as a reference from which the mass bias correction is calculated. This analysis is an example of sample and reference both analyzed in the same image set. Figure 2 shows that the interplanetary dust particle is heterogeneously enriched in deuterium. The line scan quantitatively indicates the extent of the enrichment.

A third strategy for three-dimensional SIMS analysis depends on sample topography discernible in two-dimensional images. The third dimension is implied by topography. In contrast to the strategies discussed above, this scheme requires nonflat surfaces. Samples with two surfaces at right angles to each other are appropriate. Rather than images at a single mass, total ion images or ion induced secondary electron images, both generated by rastering the primary ion microbeam, tend to reveal topography better. Total ion images are usually acquired with time-of-flight or quadrupule mass spectrometers capable of simultaneously transmitting all masses. Figure 3 demonstrates this third strategy with the analysis of a fiber optic light guide. The three secondary ion images were simultaneously acquired with the Charles Evans & Associates TFS surface analyzer. A pulsed and rastered liquid metal gallium gun produced the ion microbeam image data. The total ion image shows both the fiber shank and its cross section. The Li^+ and Na^+ images indicate that the fiber interior and the cladding have quite different sodium-to-lithium ratios.

References

1. S. R. Bryan, W. S. Larkin, J. H. Gibson, and G. G. Leininger, "Display of three-dimensional data from secondary ion image depth profiles," in A. Benninghoven, A. M. Huber, and H. W. Werner, Eds., *Secondary Ion Mass Spectrometry SIMS VI*, New York: Wiley, 1988, 369.
2. R. H. Fleming, G. P. Meeker, F. Radicati di Brozolo, and D. F. Blake, "Isotope ratio imaging of interplanetary dust particles," in A. Benninghoven, C. A. Evans, K. D. McKeegan, H. A. Storms, and H. W. Werner, Eds., *Secondary Ion Mass Spectrometry SIMS VII*, New York: Wiley, 1990, 385.

QUANTITATIVE DEPTH PROFILING OF ALUMINUM-IMPLANTED SIMOX BY USE OF SECONDARY ION MASS SPECTROMETRY

P. H. Chi, D. S. Simons, P. Roitman, and H. Hughes

SIMOX (separation by implanted oxygen) material has increasingly played an important role in SOI (silicon on insulator) technology because of its radiation-hardening performance and the high-speed and low-power usage of devices made on it. However, the performance of this material can be hampered by the presence, even at low levels, of certain impurities. The impurities may be introduced unintentionally during the oxygen implantation process or during the postimplantation annealing.[1] The high-temperature annealing is needed to reduce the crystalline damage caused by the high-dose oxygen implantation, and to create a stoichiometric SiO_2 layer beneath the silicon layer. Quantifying the impurity levels through Si/SiO_2 interfaces by secondary ion mass spectrometry (SIMS) is a complicated task because of many factors that are known to affect the secondary ion yields. Some of them are matrix effects, sample charging, and changing of the sputtering rate. In general, SIMS is the technique of choice for depth profiling of impurities in semiconductors, since it provides high sensitivity (ppm to ppb level) and is capable of detecting all elements in the periodic table. With the proper standards and methods, the quantitative measurement of impurities through Si/SiO_2 interfaces is achievable.[2-4] In this paper we present the results of SIMS depth profiling by use of the matrix ion species ratio (MISR) method to quantify Al levels in Al-implanted SIMOX samples.

Experiment

Depth profiles of Al-implanted silicon, SiO_2, and SIMOX were obtained in a Cameca IMS 3F ion microscope with a focused and rastered argon primary ion beam. An electron gun was also used to compensate the positive charges that built up on the sample surface during the sputtering process. Secondary ion species were collected from a circular area 60 μm in diameter that was placed at the center of a 250 ×

P. H. Chi and D. S. Simons are at the Chemical Science and Technology Laboratory, National Institute of Standards and Technology, Gaithersburg MD 20899; P. Roitman is at NIST's Electronics and Electrical Engineering Laboratory, and H. Hughes is at Naval Research Laboratory, Washington DC 20375.
Certain commercial equipment, instruments, or materials are identified in this paper in order to specify adequately the experimental procedure. Such identification does not imply recommendation or endorsement by the National Institute of Standards and Technology, nor does it imply that the materials or equipment identified are necessarily the best available for the purpose.

250 m² raster. The SIMOX samples were made on Si(100) wafers. These wafers, while held at 650 C, were implanted with $1.8-2.0 \times 10^{18}$ atoms/cm² of oxygen at 200 keV to create an SiO_2 layer buried beneath the silicon surface. These SIMOX wafers were Al-implanted to 10^{13} atoms/cm² at 200 keV and then annealed for 2 h at 1000 C (first annealed). A second sample was further annealed at 1325 C for 5 h in Ar + 0.5% O_2 (second annealed). At this implantation energy, the Al peak is in the buried SiO_2 layer. Aluminum-implanted Si and SiO_2 standards were also profiled under the same conditions to generate the relative sensitivity factors (RSFs) of aluminum and relative sputtering rates of the Si and SiO_2 matrices. These RSFs were then used in a standard way to establish the aluminum concentration separately in the Si and SiO_2 layers of the SIMOX.[5] The layer thicknesses of the Si and SiO_2 in the SIMOX samples were determined by measurement of the final crater depth with a stylus profilometer, followed by a correction for the relative sputter rates measured in the Al-implanted Si and SiO_2 standard samples. In an alternate approach, the species Si^{2+} and SiO^+ were profiles along with Al^+ and $^{30}Si^+$. The RSF as a function of MIST SiO^+/Si^{2+} was used to quantify Al levels in the Al-implanted SIMOX samples.

The relative sensitivity factors of Al in silicon as function of oxygen backfill pressure were generated by argon bombardment of the Al-implanted silicon sample. The primary current for all measurements was kept constant at 1 μA while the oxygen backfill pressure was varied between 1.3×10^{-6} to 2.6×10^{-4} Pa. We monitored Si^{2+}, Al^+, $^{30}Si^+$, SiO^+ in all depth profiles. For each oxygen backfill pressure, we calculated the sensitivity factor of Al relative to Si and the MISR SiO /Si^{2+}. This particular ratio was selected over other possibilities because it shows a large monotonic variation as a function of the oxygen backfill pressure determined with a constant primary ion beam current. The RSF of Al at each backfill pressure was calculated in the usual way.[6] Figure 1 shows a plot of aluminum RSF vs the matrix ion species ratio SiO^+/Si^{2+}. The RSF values are nearly constant for MISR values between 10^{-4} and 10^{-1} (unoxidized Si). Log RSF values show a linear dependence on log MISR for MISR values between 10^{-1} and 10^2, as the Si becomes more highly oxidized. The RSF calibration curve generated from the data in Fig. 1 can be approximated by a fourth-order polynomial function:

$$\log (RSF) = 19.292 + 0.589x + 0.14x^2$$
$$- 0.041x^3 - 0.011x^4 \tag{1}$$

where $x = \log(SiO^+/Si^{2+})$. The point-by-point aluminum RSF in the Al-implanted SIMOX can be calculated from Eq. (1).

Results and Discussion

In order to verify the validity of this MISR curve, Al-implanted silicon and SiO_2 standard samples were profiled with an argon beam with-oxygen backfill. Figure 2 shows the Al concentration profiles in the silicon sample with the regular (single RSF) and MISR methods. The Al profiles are in good agreement for the two methods. However, for Al-implanted SiO_2 the Al peak concentration from the MISR calculation is higher by a factor of nearly 2 than that obtained by the regular method (Fig. 3). The discrepancy between the methods is attributed to the fact that the $^{30}Si^+$ and the SiO^+ signals in the SiO_2 layer are gradually increasing in intensity from the front to back side of the SiO_2 film. Since the aluminum concentration determined from the regular method is based on a single average value of the matrix $^{30}Si^+$ signal in each layer, this probably leads to the difference in results between the two methods.

The Al-implanted SIMOX was profiled with an 8.0keV Ar^+ beam without oxygen backfill after the first anneal. Fig. 4(a) shows count rate vs depth for Si^{2+}, Al^+, $^{30}Si^+$, and SiO^+. This figure shows sharp Si/SiO_2 interfaces as indicated by the rapid changes in the $^{30}Si^+$ and SiO^+ signals. The concentration profiles of the implanted Al, determined from the MISR calibration curve and by the regular method (single RSF in each layer), are plotted in Fig. 4(b). The regular method shows an anomalously high aluminum level in the first Si layer. The anomaly is due to the fact that the first layer is not a pure silicon layer (as indicated from the $^{30}Si^+$ and SiO^+ signals in Fig. 4a). Rather, an increasing amount of oxygen is found as the SiO_2 interface is approached. The aluminum concentration determined from the MISR method shows about 24% of the Al distributed in the upper Si layer and the remainder distributed through the buried SiO_2 layer. The regular method shows a higher level of aluminum in the top silicon layer (39%) and about 61% distributed in the SiO_2 layer. The re-annealed sample of the Al-implanted SIMOX was also depth-profiled under the same conditions; the results for Al, by the regular and the MISR methods are plotted in Fig. 5. The SiO^+ and $^{30}Si^+$ signals show sharp interfaces (Fig. 5a). A surface oxide layer has grown during the anneal. There are no major differences of the aluminum level in the two methods (Fig. 5b). The oxygen that was originally present in the top Si layer has been incorporated into the SiO_2 films. The profiles show that most of the aluminum is trapped in the new surface oxide under this annealing condition.

Conclusions

The quantification of Al through Si/SiO_2 in-

terfaces using SIMS is not a straightforward process. Matrix effects, sputtering rates, and sample charging can hamper the analysis. The regular method using a single RSF in each layer to determine aluminum levels through SiO_2/Si interfaces is not a suitable choice, as illustrated in the Al-implanted SIMOX sample. The RSF in the regular method does not accommodate the changing of secondary ion yields due to the variation of oxygen levels near the Si/SiO_2 interface and thus leads to incorrect aluminum concentration levels. The MISR method employed in this experiment is preferable for the quantitative analysis of aluminum through SiO_2/Si interfaces.

References

1. P. H. Chi, D. S. Simons, and P. Roitman, *Surf. Interface Anal.* 17: 57-61, 1991.
2. A. E. Morgan, T-Y. J. Chen, D. A. Reed, and J. E. Baker, *J. Vac. Sci. Technol.* A2: 1266, 1984.
3. F. Michiels, L. Butaye, and F. Adams, *Surf. Int. Anal.* 14: 170-177, 1989.
4. F. Michiels, L. Butaye, and F. Adams, *Surf. Int. Anal.* 14: 178-186, 1989.
5. R. G. Wilson, F. A. Stevie, and C. W. Magee, *Secondary Ion Mass Spectrometry: A Practical Handbook for Depth Profiling and Bulk Impurity Analysis*, New York: Wiley, 1989, 3.1-1-3.1-2.
6. F. Michiels, *Aspects of Quantification in Secondary Ion Mass Spectrometry*, Ph.D. Thesis, University of Antwerp, Belgium, 1990.
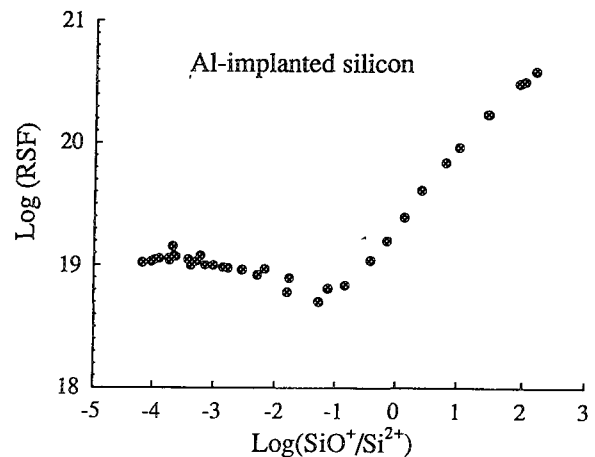
FIG. 1.--Relative sensitive factor curve of aluminum as a function of matrix ion species ratio (SiO^+/Si^{2+}), established by various back-fill pressures.

Fig. 2

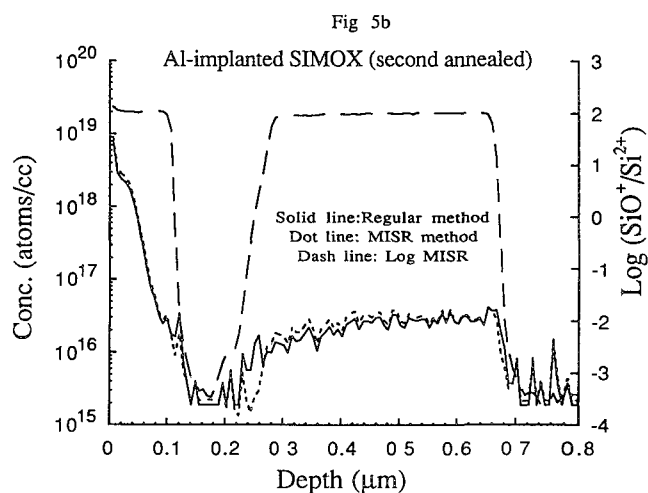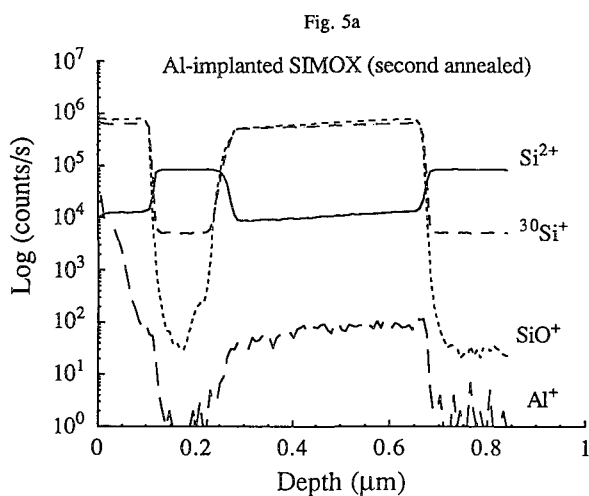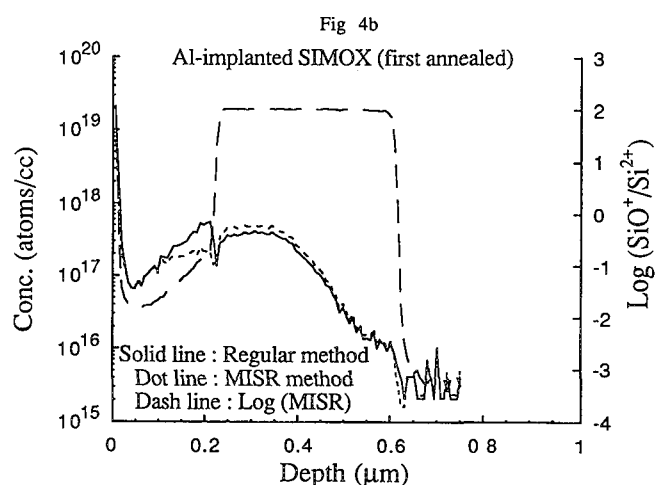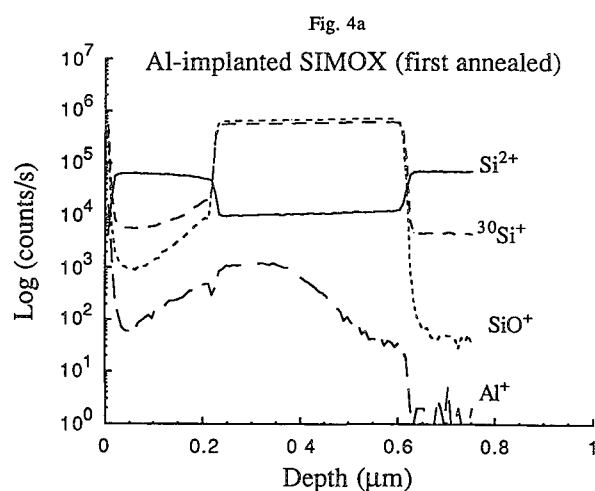Al-implanted silicon

Conc. (atoms/cc) — 10^{20}, 10^{19}, 10^{18}, 10^{17}, 10^{16}, 10^{15}, 10^{14}

Solid line: Regular method
Dot line: MISR method

Depth (μm) — 0, 0.5, 1, 1.5, 2

Fig 3

Al-implanted SiO_2

Conc. (atoms/cc) — 10^{20}, 10^{19}, 10^{18}, 10^{17}, 10^{16}, 10^{15}

Log (SiO^+/Si^{2+}) — 3, 2, 1, 0, -1, -2, -3, -4

Solid line : Regular Method
Dot line : MISR method
Dash line: Log MISR

Depth (μm) — 0, 0.2, 0.4, 0 6, 0 8, 1

Fig. 4a

Al-implanted SIMOX (first annealed)

Log (counts/s) — 10^7, 10^6, 10^5, 10^4, 10^3, 10^2, 10^1, 10^0

Si^{2+}
$^{30}Si^+$
SiO^+
Al^+

Depth (μm) — 0, 0.2, 0 4, 0.6, 0.8, 1

Fig 4b

Al-implanted SIMOX (first annealed)

Conc. (atoms/cc) — 10^{20}, 10^{19}, 10^{18}, 10^{17}, 10^{16}, 10^{15}

Log (SiO^+/Si^{2+}) — 3, 2, 1, 0, -1, -2, -3, -4

Solid line : Regular method
Dot line : MISR method
Dash line : Log (MISR)

Depth (μm) — 0, 0.2, 0.4, 0.6, 0 8, 1

Fig. 5a

Al-implanted SIMOX (second annealed)

Log (counts/s) — 10^7, 10^6, 10^5, 10^4, 10^3, 10^2, 10^1, 10^0

Si^{2+}
$^{30}Si^+$
SiO^+
Al^+

Depth (μm) — 0, 0.2, 0.4, 0.6, 0.8, 1

Fig 5b

Al-implanted SIMOX (second annealed)

Conc. (atoms/cc) — 10^{20}, 10^{19}, 10^{18}, 10^{17}, 10^{16}, 10^{15}

Log (SiO^+/Si^{2+}) — 3, 2, 1, 0, -1, -2, -3, -4

Solid line:Regular method
Dot line: MISR method
Dash line: Log MISR

Depth (μm) — 0, 0.1, 0.2, 0 3, 0.4, 0 5, 0.6, 0 7, 0.8

FIG. 2.--Concentration profile of Al in Al-implanted silicon determined by regular and MISR methods.

FIG. 3.--Concentration profiles of Al in Al-implanted SiO_2. The log(SiO^+/Si^{2+}) of this sample is also shown in this figure.

FIG. 4.--(a) Count rate vs depth for four species in 200 keV, Al-implanted SIMOX after first anneal. (b) Concentration profile of Al determined by regular and MISR methods in Al-implanted SIMOX after first anneal.

FIG. 5.--(a) Count rate vs depth for four species in Al-implanted SIMOX after second anneal. (b) Concentration profile of Al-implanted SIMOX after second anneal as determined from regular and MISR methods.

349

PRTASK: A PC-BASED ACQUISITION AND ANALYSIS SOFTWARE PACKAGE FOR INTERFACING TO THE TRACOR TASK AUTOMATION SYSTEM

J. J. Donovan and V. C. Kress

A PC-based wavelength-dispersive acquisition and analytical software package has been developed for interfacing with the Tracor TASK automation system commonly used with the JEOL electron microprobe. Developmental considerations and capabilities of the program are described. The entire source code (28 000 lines of FORTRAN and Assembler) is available free as shareware for distribution to individuals and institutions. The program may be registered; registration includes free updates and telephone consultation.

Objective

Though well suited for WDS (wavelength-dispersive) microprobe automation, the Tracor TASK software lacks several important analysis features, including the ability to reassign standards and to correct for spectral interferences, the capability to handle large volumes of data, and a flexible means for transferring data to other computers. What we have sought to create is a PC-based software package, interfaced to our existing TASK automation system, using a standard serial port, that will provide high-speed, flexible, and accurate on-line analysis. All procedures are extensively documented to allow even the nonprogrammer quickly to install and configure the interface to an existing TASK automation system. The interface will provide an interactive, real-time acquisition and analysis environment for modern quantitative matrix, interference, and drift corrections.

Description

PRTASK is a modified subset of the previously published PRSUPR software automation and analysis package, with all spectrometer and stage automation support removed, since these functions are handled by the TASK computer system.[1]

PRTASK runs under DOS on any IBM PC or compatible XT, AT, 386 or 486 with 640Kb RAM, a hard disk and a math coprocessor, and a VGA, EGA, CGA or Hercules graphics card and optional mouse or trackball. Real-time multitasking and file sharing by PRTASK is supported with a 386

or 486 CPU in a suitable multitasking environment.

The program graphically displays weight percent, formula or mole/atomic percent, stage coordinate, and beam drift data. A mouse or trackball is supported for point identification and "zoom" features using simple "point and click" actions. Any raw or recalculated data may be output to ASCII text files on disk for use with other spreadsheet, database, or graphics programs.

After each analysis, sample type, sample number (if sample is a standard), sample name (if sample is an unknown), count time, beam counts, X-Y-Z stage positions, and up to 16 channels of x-ray count data are automatically transferred over a standard RS 232 serial connection. X-ray counts may be corrected for background before transfer, using the standard TASK off-peak corrections. The option is also available to transmit uncorrected counts to the PC, allowing nonlinear M.A.N. (Mean Atomic Number) background corrections to be applied in PRTASK.

TASK schedules are also provided to perform automated traverses and 2-dimensional composition maps. Complete documented instructions are supplied to facilitate the necessary TASK source and schedule modifications. The following is a brief discussion of some of the analysis features in the PRTASK software package and how they can be used.

1. PRTASK includes a complete collection of ZAF $\phi(\rho z)$ expressions for fully quantitative analyses from the well-known CITZAF ZAF matrix correction library written by John Armstrong at the California Institute of Technology.[2] All the matrix correction algorithms are fully integrated into PRTASK using simple defaulted menus.

2. In addition to the ZAF corrections, both the traditional constant Bence-Albee expression, the linear UCB expression, and John Armstrong's nonlinear-fit alpha-factors can be calculated and utilized in the analysis of data.[3,4] The program also supports the use of empirically measured calibration curves using k-ratios from literature or user-supplied measurements. The ability to use a modern Bence-Albee type correction such as John Armstrong's nonlinear fit is especially useful when one is reducing large amounts of data from step scans or x-ray images.

3. Because PRTASK requires all element channels in an analytical setup to be measured for each sample, the composition of a standard sample can be calculated as an unknown. This feature provides a very effective way to check

J. J. Donovan is at the Department of Geology, University of California, Berkeley CA 94720; V. C. Kress is at the Department of Geological Sciences, University of Washington, Seattle WA 98195. The assistance and advice of John Armstrong and Paul Carpenter of the California Institute of Technology, and of Scott Kuehner at the University of Washington, are gratefully acknowledged.

for consistency within a suite of standard compositions. In addition, any standard sample can be assigned as the "standard" for that element at any time, either during the probe session or later during off-line data processing. Unknown sample compositions can then be recalculated relative to any standard for which there are data. In cases where the unknowns cover a wide range of compositions, significant benefit may be gained by the use of this standard "reassignment" feature.

4. PRTASK supports the correction of any analytical line for spectral interference by up to two interfering elements. By assigning one of the standard samples as an "interference standard," one can correct for such common interferences as Sr Lα by Si, Ti Kα by Ba, V Kα by Ti and Ba, Cr Kα by V, Mn Kα by Cr, Fe Kα by Mn, and so on. This is a completely quantitative interference correction in that the correction is completely integrated into the CITZAF ZAF iteration loop.

5. Since PRTASK will run on any available PC either on-line or off-line, one does not need to be connected to the TASK system in order to recalculate or plot data from a previous analysis session. This ability for off-line processing provides a considerable savings in time spent actually on the probe, resulting in more efficient use of the probe resources.

6. Because the Intel-based microcomputer is currently a more standard platform than the Tracor Northern PDP-11 based system, one's ability to transfer data between computers and software packages is considerably enhanced.

Summary

Speed, flexibility, connectivity, the ability to handle large quantities of data, the ease of use in the PC environment, and the capability for on- and off-line processing combine to make the PRTASK software analysis package a useful environment for electron-beam microanalysis. Because no expensive hardware upgrade is required, and no programming skills are necessary, we recommend the use PRTASK for any microprobe laboratory currently using the Tracor TASK automation system.

References

1. J. J. Donovan, "PRSUPR: A PC-based automation and data reduction software package for wavelength dispersive electron beam microanalysis," *Microbeam Analysis--1990*, 86.
2. J. T. Armstrong, "Quantitative analysis of silicate and oxide materials: Comparison of Monte Carlo, ZAF, and $\phi(\rho z)$ procedures," *Microbeam Analysis--1988*, 239.
3. A. L. Albee and L. Ray, "Correction factors for electron probe microanalysis of silicates, oxides, carbonates, phosphates, and sulfates," *Analyt. Chem.* 42: 1408, 1970.
4. J. T. Armstrong, "Bence-Albee after 20 years Review of the accuracy of the α-factor correction for silicate and oxide minerals," *Microbeam Analysis--1988*, 469.

OPUS: OLD PROBE—UPDATED SOFTWARE

G. P. Meeker and J. E. Quick

Many older electron microprobes, while still capable of producing quality data, are limited by computer capacity and outdated software. Modern automation systems for new microprobes provide sophisticated graphics, on-line data manipulation, and state-of-the-art correction procedures. These capabilities are beyond the reach of most unmodified older automation systems because the size and flexibility of programs are limited by computer memory capacity. Furthermore, languages used in older commercial software packages may provide limited functions, may be incapable of supporting screen graphics, and may utilize cumbersome editors. Conversion to personal-computer-based automation represents an attractive solution to these problems as personal computers (PCs) have become increasingly powerful over the past 10 years. However, wholesale replacement of entire automation systems can be expensive and result in significant amounts of instrument down time. OPUS (Old Probe--Updated Software) represents a low-cost compromise approach in which a PC provides the higher-level function of the automation system and the original DEC* computer continues to perform basic instrument control.

Hardware

OPUS was developed for a six-spectrometer Applied Research Laboratory (ARL) SEMQ originally automated with ARL software and a 32-kilobyte DEC PDP-11/34 computer interfaced to VT-100 and DECWRITER III terminals. The PDP-11/34 originally controlled spectrometer and stage stepper motors and beam blanking, and performed on-line data reduction using Bence-Albee[1] and MAGIC.[2] The software, written in ARL BASIC, utilized calls to machine language subroutines for instrument control and to compiled FORTRAN routines for data reduction. Original storage media consisted of two 8-in. floppy-disk drives and two 10-megabyte hard-disk drives.

We have recently modified our system to allow an IBM-compatible PC to enslave the PDP-11/34 (Fig. 1). The original hard disk drives and VT-100 terminal were replaced with an 80386-based PC with 4 megabytes of memory, an 80387 math coprocessor, a 150-megabyte hard disk drive, two floppy-disk drives, and VGA color graphics capability. Communication with the PDP-11/34 is accomplished via the standard

RS-232 interface used by the VT-100 terminal. Directions and information are passed between the computers as short arrays of integers at 9600 baud. The addition of the PC to the automation has not significantly increased run times, but has greatly increased the capabilities of the system.

Software

OPUS was written for the PC to suppport a two-tiered approach to machine automation. It is not a terminal emulation program. While running under OPUS, the PC acts as the user interface, passes directions to the DEC computer, and performs on-line data reduction and data output. The PDP-11/34 operates only as a slave system that is reduced to controlling basic instrument functions through a single program, consisting of approximately 50 lines of ARL BASIC code, that invokes machine-language subroutines. This configuration provides access to all existing ARL computer-controlled instrument functions and greatly increases the potential for creating large high-level automation programs on the PC.

OPUS is written in Microsoft QuickBASIC 4.5 and is designed to meet the needs of a multi-user laboratory. The primary functions (Fig. 2) are (1) to lead the user through initial startup of the probe, (2) to direct standardization, and (3) to analyze unknowns. Based on user and instrument input, OPUS directs the PDP-11/34 to perform simple tasks such as moving the spectrometers or reading the beam current. For example, for a given analysis routine selected by the user, OPUS contains instructions for elements to be analyzed, spectrometer assignments, peak and background positions, counting times, and peak and background counts for each standard. OPUS determines the order of elements on each spectrometer, interrogates the PDP-11/34 for current spectrometer positions, calculates the move increment for each spectrometer, and directs the PDP-11/34 to drive the spectrometer motors to appropriate positions. OPUS then directs the PDP-11/34 to count for appropriate intervals, and waits for the PDP-11/34 to report the beam current and the counts on each spectrometer. Matrix correction procedures are performed by CITZAF,[3] which has been incorporated as a subprogram of OPUS.

Potential

The power and flexibility of PC-based automation encourages development of user-friendly capabilities. With increased computer memory and hard disk capacity, complete instructions can be provided to the user for complicated

The authors are at the U.S. Geological Survey, MS 903, Denver Federal Center, Denver, CO 80225. Use of product names is for descriptive purposes only and does not indicate endorsement by the U.S. Geological Survey.
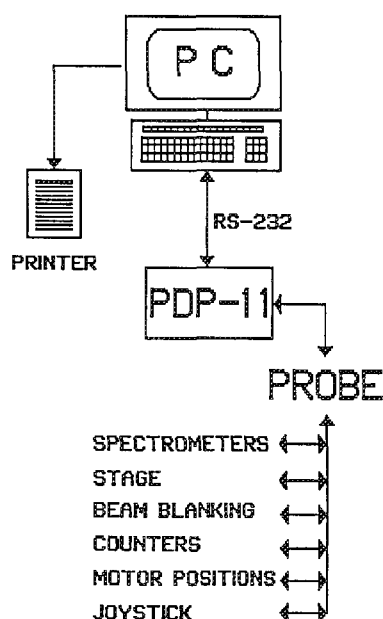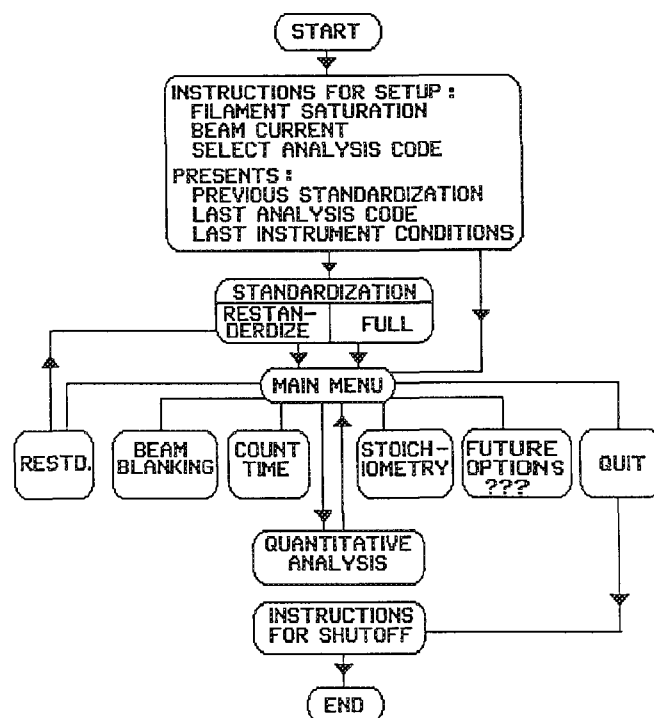
FIG. 1.--Hardware configuration.

FIG. 2.--Flow diagram illustrating basic structures of OPUS.

procedures. Software may be greatly extended for on-line manipulation of data; and QuickBASIC programs, which are increasingly available (e.g., CITZAF), may be incorporated with little or no modification. Screen graphics enable extensive use of diagrams, including pictures of instrument panels or standards, to lead user through tasks. Real-time display of data, including wavelength scans and user-defined plots, can be used to guide analysis. With minimal video equipment, images of unknowns may be captured, processed, stored on disk, and displayed for annotation and location of analysis points. The increased capacity of PC-based storage media permits maintenance of large records, such as a continuous record of standardizations. The ability to write $3\frac{1}{2}$ and $5\frac{1}{4}$ in. floppy disks facilitates transport of the data to other PCs and user databases.

The potential of this system approaches that provided by modern automation systems equipped with more powerful computers. Given the low cost of required hardware (< $5000), OPUS represents an attractive approach for upgrading older automated microprobes.

References

1. A. E. Bence and A. L. Albee, "Empirical correction factors for the electron microanalysis of silicates and oxides," *J. Geol.* 76: 382-403, 1968.

2. J. W. Colby, "Quantitative microprobe analysis of thin insulating films," *Advances in X-ray Analysis* 11: 287-305, 1968.

3. J. T. Armstrong, "Analysis of silicate and oxide materials: Comparison of Monte Carlo, ZAF, and $\phi(\rho z)$ procedures," *Microbeam Analysis 1988*, 239-246.

EXTERNAL COMPUTER CONTROL: ONE VIEW OF THE CURRENT STATUS

J. M. Mackenzie Jr.

The promise of computer control was that it would bring ease of use and allow the extraction of more quantitative information. It was hoped that it might also create new imaging strategies since individual parts of the instrument could be controlled. Although current computer systems are extremely powerful, the state of computer control is pitiful. Although modern digital imaging systems have more capabilities than could be dreamed of just a few years ago, the images obtained from microscopes fail to pass even the minimum standards of a professional microscopist. The reason for this discrepancy is that the interface between the computer and the microscope has not evolved along with the other equipment. In some cases, the evolution has taken an incorrect path. In this paper, the evolution of computer control in both TEM and SEM is examined, starting with the analog instruments.

Although few need or want to understand the hardware issues involved, the lack of response of modern systems is of great concern to everyone. The current generation of users cannot clearly define what they want, since they are for the most part experts in neither hardware nor software. The engineers who manufacture the microscopes rarely get a clear picture of user needs and therefore design their instruments to work well internally without much attention to the outside world.

Here are some of the problems with modern systems that should be examined and discussed. The key to moving data between the microscope and the computer is a good communications system. This system must meet certain design criteria in order to work well.

The first is speed. Data rates in excess of 300 kilobytes/s are easily obtained. All microscope data can be read and written in less than 1 s and should probably be done in far less time.

The second is to create efficient communication protocols. In the Philips C400 computer control system, the total microscope and stage parameters were stored in 321 bytes. The current crop of microscopes convey less information in 2K and 4K blocks. There should also be communication protocols that allow user-defined blocks to increase efficiency.

The third criterion is to have an efficient internal design. One microprocessor can only do one thing. A microscope that communicates safely and quickly with the outside world must have direct access to the analog control of the chosen function.

The fourth is to create a standard that would allow for the creation of more generic software. Achievement of this goal is problematic, as even protocols from major manufacturers are considered proprietary.

We compare all our digital images to film images. Those images are a result of an integration of the electron signal with time. Digitizers that average pixels do not integrate. Two systems are available that do integrate. For the scanning microscope, a gated integrator can achieve results superior to averaging. In the TEM, use of CCD arrays in slow-scan modes can produce superb images. These images, with very little subsequent development, promise to match and then beat film images in terms of accurate quantifiable information. This strategy goes directly against the imaging industry's trend to higher-resolution television rate frame grabbers.

Much of the hardware needed for interfacing is now available from third-party manufacturers. The advances in computers, memory, display printers, mass storage, and cameras can be discussed in terms of developing a modern approach to external control and imaging.

The main area that requires clarification is to determine what pieces are missing in the hardware and to define what it would take in terms of time and effort to obtain those pieces.

The final area that requires discussion is to define what form the software should take. Does our community want turn key systems or does it want flexible primitive routines that can be customized by the individual? Who will define exactly what is needed when no one seems to understand the problem as a whole?

J. M. Mackenzie is at 1219 Gardner Hall, Box 7615, North Carolina State University, Raleigh NC 27695.

IMAGING MOLECULES AND METALS ON METAL SURFACES BY SCANNING TUNNELING MICROSCOPY

S. Chiang, D. D. Chambliss, V. M. Hallmark, R. J. Wilson, J. K. Brown and Ch. Wöll[1]

IBM Research Division, Almaden Research Center, 650 Harry Rd., San Jose, CA 95120-6099

Using an ultrahigh vacuum scanning tunneling microscope (STM),[2] we have imaged naphthalene molecules adsorbed on Pt(111)[3,4,5] and submonolayer metal coverages of Ni, Fe, Ag, and Au on Au(111).[5,6,7,8] The STM is able to observe atomic scale features on both types of systems, giving information on the ordering and binding sites of atoms and molecules on the surface.

High resolution STM images of naphthalene on Pt(111) show the molecules as bi-lobed features with three discrete molecular orientations on the surface, 120° apart, as shown for the ordered layer in Fig. 1.[3] The absolute orientation of the long axis of the molecules is observed to be parallel to the near-neighbor directions of the Pt(111) lattice. The sketch of the observed features, shown in Fig. 2, with the molecules overlayed arbitrarily onto on-top sites of a Pt(111) lattice, demonstrates that the molecules are located on 3x3 lattice sites, with separation of 4 lattice constants between domains. Although the (6x3) LEED pattern reported previously[9] was reproduced, the proposed unit cell is seldom observed in the STM images. Nonetheless, the STM images do show a high degree of order, with ~40% of the molecules satisfying the glide plane symmetry expected from the LEED pattern. Real space images of submonolayer coverage of naphthalene at room temperature also show discrete molecular rotations and translations between adjacent binding sites.[3,4]

For the metal on metal systems, the STM images show the dependence of nucleation and growth phenomena on local atomic geometry and sticking coefficients. Real space images of clean Au(111) show the determination of atomic positions on the Au(111) $(23 \times \sqrt{3})$ stacking-fault reconstruction of the surface. Figure 3 shows pairs of bright ridges, 0.15Å high, which are due to the stacking-fault dislocations of the top layer reconstruction. The ridges change direction, forming a long range "herringbone" arrangement of domains of this structure, as shown in Fig. 3.[5,6] Ni on Au(111) forms an ordered array of islands with a spacing of 73Å along [1$\bar{2}$1] in rows 140Å apart at surface-lattice dislocations located at elbows of the Au(111) "herringbone,"[7] as shown in Fig. 4. The island arrays are explained by a model in which Ni atoms diffuse on the surface and aggregate at these dislocations with a low initial sticking probability. Preliminary work on Fe on Au(111) shows nucleation at the same elbow sites, (Fig. 5) but with less regular island shapes than those of Ni. Ag grows outward from atomic steps on Au(111) in monolayer high, rounded fingerlike structures (Fig. 6);[8] the complex growth front is well described by a model using diffusion-limited aggregation with local relaxation. While Au deposited on Au(111) also shows islands nucleating at the Au(111) elbow sites, Au forms fewer large islands than Ni.(Fig. 7).[10]

References

1. Present address: Angewandte Physikalische Chemie, Universität Heidelberg, Im Neuenheimer Feld 253,D-6900 Heidelberg, Germany
2. S. Chiang, et al., J. Vac. Sci. Technol. A6 (1988) 386.
3. V. M. Hallmark et al., Phys. Rev. Lett. 66 (1991) 48.
4. V. M. Hallmark et al., J. Vac. Sci. Technol. B9 (1991), in press.
5. S. Chiang et al., The Structure of Surfaces III, eds. S. Y. Tong et al., Berlin: Springer-Verlag, (1991).
6. R. J. Wilson et al., Aust. J. Phys. 43 (1990), 383.
7. D. D. Chambliss et al., Phys. Rev. Lett. 66 (1991), in press.
8. D. D. Chambliss and R. J. Wilson, J. Vac. Sci. Technol. B9 (1991), in press.
9. D. Dahlgren and J. C. Hemminger, Surf. Sci. 109 (1981) L513; 114 (1982) 459.
10. This work was supported in part by the Office of Naval Research (N00014-89-C-0099).
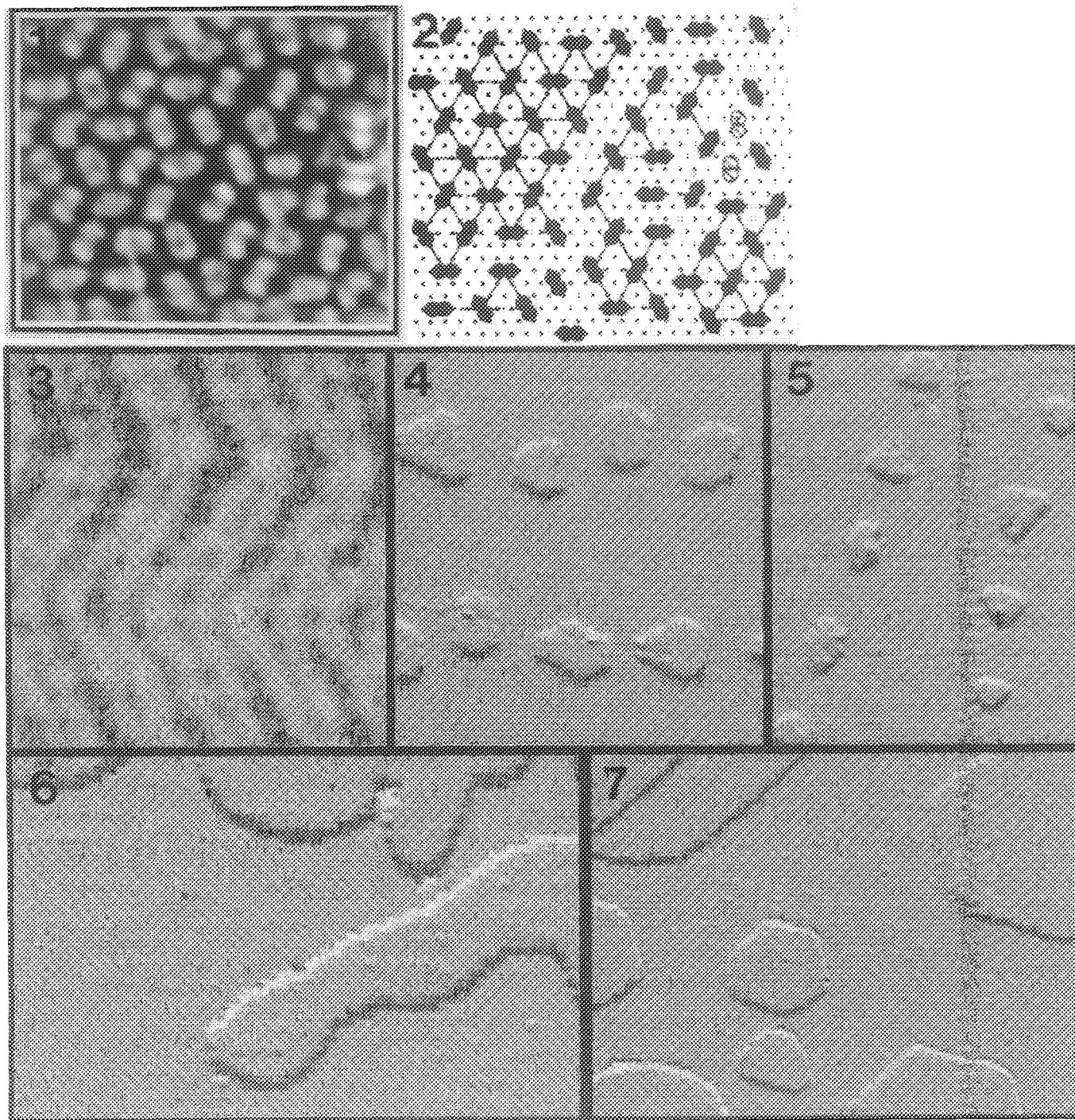
Fig. 1. STM image of naphthalene on Pt(111), showing bi-lobed molecules. Image size 150×90Å^2.

Fig. 2. Sketch of features in Fig. 1, showing arrangement of molecules on Pt (3x3) lattice sites into domains.

Fig. 3. STM image of clean Au(111) surface. Image size 320×300Å^2.

Fig. 4. Differentiated STM image of Ni on Au(111), showing hexagonal islands nucleating at kink sites of Au "herringbone." Image size 290×320Å^2.

Fig. 5. Differentiated STM image of Fe on Au(111), with less regular islands nucleating at kink sites of Au "herringbone." Image size 230×320Å^2.

Fig. 6. Differentiated STM image of Ag on Au(111), showing fingerlike protrusions extending from step edges onto reconstructed Au surface. Image size 840×530Å^2.

Fig. 7. Differentiated STM image of Au on Au(111), showing larger hexagonal islands influencing original reconstruction. Image size 700×530Å^2.

SCANNING TUNNELING MICROSCOPE IMAGING OF THE REAL SPACE STRUCTURE OF A TWO-DIMENSIONAL QUASICRYSTAL

R. S. Becker, A. R. Kortan, F. A. Thiel, H. S. Chen, and A. J. Becker

AT&T Bell Laboratories, 600 Mountain Avenue, Murray Hill, New Jersey 07974

Quasicrystals are a new phase of condensed matter characterized by a lack of translational symmetry, while yet possessing strong orientational symmetry. From their 1984 discovery in Al-Mn by Schectman et. al. [1] until the present, they have remained poorly understood, principally due to their lack of periodicity, which has proved to be a serious stumbling block to the traditional analytical methods of condensed matter physics. Two dimensional decagonal quasicrystals were discovered in 1985 by Bendersky [2]. These unusual compounds are quasiperiodic in two dimensions and periodic in the third, appearing intermediate between periodic and fully quasiperiodic phases. A number of models have been advanced in explanation of the curious symmetry displayed by these materials, falling into three main categories. quasicrystal glasses [3], multiple twinning [4], and tilings [5]. The glass models have been unable to account for the perfection shown by the Al-Cu-Fe quasicrystals, while diffraction methods have difficulty distinguishing between the latter models

Since the decagonal materials show a periodic relationship between successive layers, they are a natural candidate for the atomic resolution real-space imaging capabilities of the scanning tunneling microscope (STM). The first experiment on decagonal quasicrystals using this instrument[6] showed that the surface possessed a high degree of order, exhibiting the five-fold symmetry revealed in high resolution x-ray diffraction measurements[7]. A typical tunneling image is shown in Figure 1. The surface features are plainly seen to form continuous rows of mass density, extending across the entire image. Rotating the image in Figure 1 reveals this to be the case in all five symmetry directions. This feature alone provides convincing evidence for a tiling model description of the order. The continuity of the mass density lines across the terraces shows that a high degree of correlation exists between successive layers, and suggests that the tiling is essentially perfect on the scale (15nm) of the tunneling image

Using images similar to that shown, we have deduced a model structure consisting of a complementary stacking of aluminum pentagonal quasilattices with the transition metals decorating the pentagon centers. Each layer is related to the adjacent layers by an inflation. The terrace step heights are related to the fundamental structure in this model, an icosahedron consisting of two complementarily stacked aluminum pentagons with a transition metal atom capping the top and bottom. This structure has the height of two steps, separating it between the aluminum pentagons accounts for the measured 0.2nm step height.

[1] D Schectman, I. Blech, D. Gratias, and J. W. Cahn, Phys. Rev. Lett. 53, 1951 (1984)

[2] L Bendersky, Phys. Rev. Lett 55, 1461 (1985).

[3] D Schectman and I. A. Blech, Metall. Trans. A 16, 332 (1985).

[4] L. Pauling, Phys. Rev. Lett. 58, 294 (1987).

[5] D Levine and P. J. Steinhardt, Phys. Rev. Lett. 53, 2477 (1984).

[6] A R Kortan, R. S. Becker, F. A. Thiel, and H. S. Chen, Phys. Rev. Lett. 64, 200 (1990)

[7] A. R Kortan, F. A. Thiel, H. S. Chen, A. P. Tsai, A. Inoue, and T. Masumoto, Phys Rev. B 40, 9397 (1989).
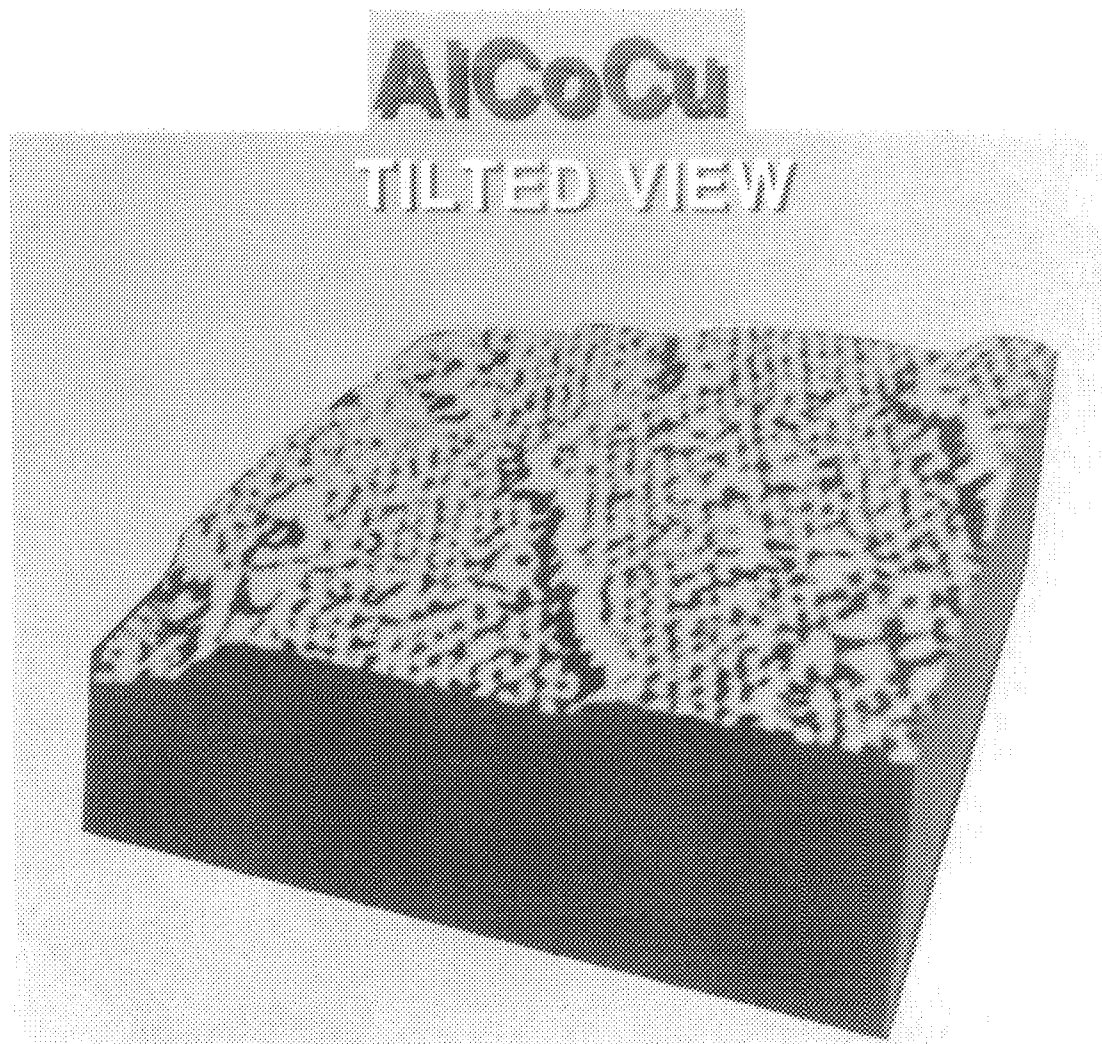
Figure 1. 15nm x 15nm tunneling image of AlCoCu viewed in perspective. The mass density lines lie on one of the five quasiperiodic symmetry directions The 0.2nm high steps running across the image delineate individual terraces. The atomic positions occupy a network of pointlike and circular features characteristic of quasiperiodic order.

SCANNING TUNNELING MICROSCOPY STUDIES OF CRYSTAL GROWTH

M. G. Lagally

University of Wisconsin-Madison, Madison, WI 53706

It has been recognized since the earliest days of crystal growth that kinetic processes of all kinds control the nature of the growth. As the technology of crystal growth has become ever more refined, with the advent of such atomistic processes as molecular beam epitaxy, chemical vapor deposition, sputter deposition, and plasma enhanced techniques for the creation of "crystals" as little as one or a few atomic layers thick, multilayer structures, and novel materials combinations, the need to understand the mechanisms controlling the growth process is becoming more critical. Unfortunately, available techniques have not lent themselves well to obtaining a truly microscopic picture of such processes. Because of its atomic resolution on the one hand, and the achievable wide field of view on the other (of the order of micrometers) scanning tunneling microscopy (STM) gives us this opportunity. In this talk, we briefly review the types of growth kinetics measurements that can be made using STM. The use of STM for studies of kinetics is one of the more recent applications of what is itself still a very young field.

The theoretical framework for investigating surface kinetic processes has been in hand for a long time, and has, in some cases, been developed to a considerable degree. Consider the simplest case: the homoepitaxial growth of a material on itself (A-on-A). Atoms arrive from the vapor phase at a surface. To remain on the surface ("accommodate") they must give up their heat of condensation through one or a series of inelastic collisions. Once bound in the holding potential of the surface, an atom will migrate (surface self-diffusion) until it finds another of its kind, either at the edge of a terrace or another freely diffusing atom. If it becomes incorporated into the edge of an existing island or terrace, we speak of "lateral condensation" with a certain probability (the "lateral condensation coefficient"). If it finds another freely migrating atom, a stable nucleus may form. Nucleation is the first stage, followed subsequently by growth, and eventually by "coarsening" (or "ripening"). The two-dimensional coarsening process, the elimination of small islands at the expense of large ones, driven by a desire of the system to eliminate boundary energy to reduce its total free energy, involves, in addition to migration, a "lateral desorption" process, in which diffusable species are created at the edges of islands.

In addition to these processes, which all involve interactions of atoms on a flat terrace, there are kinetic mechanisms controlling the flow of atoms over edges of terraces and, if three-dimensional crystals instead of layers form, processes that control the formation and shape of these crystals. Anisotropies caused by the low structural symmetry of the substrate can occur in any of the transport, condensation, or desorption processes.

These processes can all be readily and rather straightforwardly investigated in the STM. The procedure is simple. A few atoms are deposited on a well characterized substrate and their behavior observed by measuring the types of structures these atoms form as a function of time, temperature, substrate surface condition, and deposition conditions. All that is really necessary is to count the atoms or islands, measure their size and shape, and relate this information to simple models of diffusion, condensation, or evaporation. Figure 1 shows an STM image that summarizes the types of situations encountered in these experiments. The figure shows a region of Si(001) surface that is typical. The surface shows steps of monatomic height, with terraces about 300Å wide. The surface reconstructs into rows of dimers to reduce surface energy, causing a surface structural symmetry lower than that of the bulk. The crystal symmetry causes the dimer rows on alternate terraces to be orthogonal and causes the edges of terraces to have different structures. The figure therefore illustrates several possible anisotropies in kinetic mechanisms: surface diffusion, transport over steps, and sticking at steps. In addition, about 0.1 monolayer of Si atoms have been deposited onto the surface shown in Fig. 1. These atoms have migrated to form small Si islands, which reflect the kinetic mechanisms and their anisotropies operative in the molecular-beam epitaxial growth of Si on Si(001). These as well as the growth of very small metastable 3-D crystals of Ge on Si(001) will be described in this talk (1-5).

Scanning tunneling microscopy clearly has made a major impact in surface studies. However, much of the early work has consisted of qualitative interpretations of images, a danger that most microscopies are subject to. This talk will demonstrate that with appropriate statistical analysis, quantitative values can be obtained for activation energies, condensation coefficients, and desorption energies, as well as anisotropies in these parameters.

References

1. Y.-W. Mo, B. S. Swartzentruber, R. Kariotis, M. B. Webb, and M. G. Lagally, Phys. Rev. Letters 63, 2393 (1989).
2. M. G. Lagally, Y.-W. Mo, R. Kariotis, B. S. Swartzentruber, and M. B. Webb, in Kinetics of Ordering and Growth at Surfaces, ed. M. G. Lagally, Plenum, New York, NY (1990).
3. Y.-W. Mo, D. E. Savage, B. S. Swartzentruber, and M. G. Lagally, Phys. Rev. Letters 65, 1020 (1990).
4. Y.-W. Mo and M. G. Lagally, Surface Sci., in press.
5. Y.-W. Mo, J. Kleiner, M. B. Webb, and M. G. Lagally, Phys. Rev. Letters, in press, April 15, 1991.
6. Research supported by ONR, Chemistry Program.

$$S_A$$

$$S_B$$
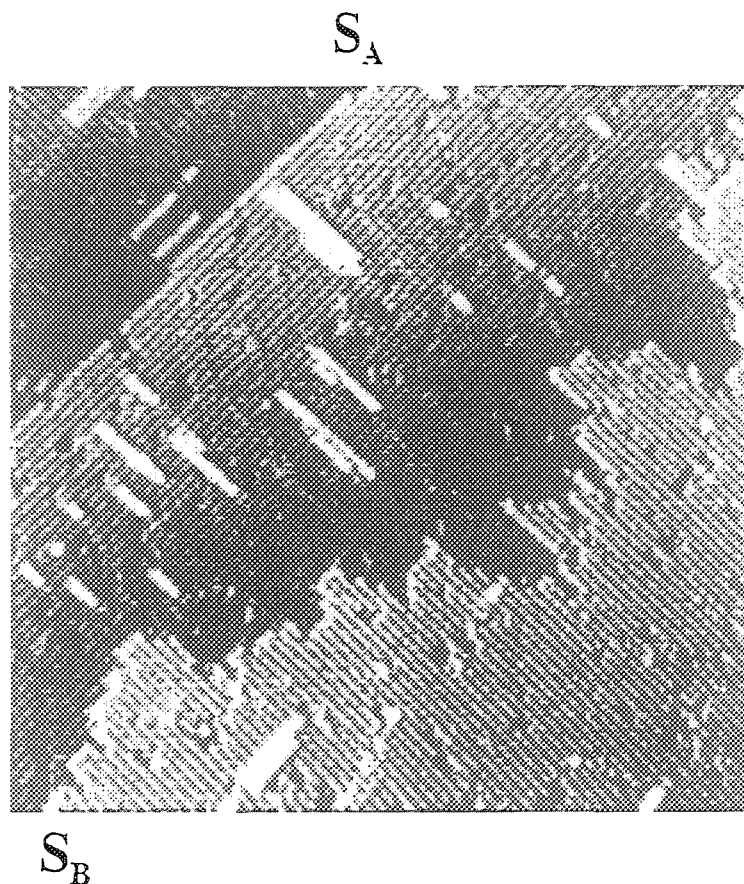
Figure 1 STM image of stepped Si(001) on which ∿ 0.1 monolayer of Si has been deposited. Image size 600x600Å. Dimer rows running orothogonal to each other on adjacent terraces are visible, as are small islands of Si with anisotropic shapes. S_A and S_B indicate the two types of steps.

IMAGING MOLECULES ADSORBED ONTO ELECTRODES UNDER POTENTIAL CONTROL BY SCANNING PROBE MICROSCOPY

N.J. Tao, J.A. DeRose, P.I. Oden and S.M. Lindsay

Department of Physics, Arizona State University, Tempe, AZ 85287

Clemmer and Beebe[1] have pointed out that surface structures on graphite substrates can be misinterpreted as biopolymer images in STM experiments. We have been using electrochemical methods to react DNA fragments onto gold electrodes for STM and AFM imaging.[2] The adsorbates produced in this way are only homogeneous in special circumstances.[3] Searching an inhomogeneous substrate for 'desired' images limits the value of the data. Here, we report on a *reversible* method for imaging adsorbates. The molecules can be lifted onto and off the substrate during imaging. This leaves no doubt about the validity or statistical significance of the images. Furthermore, environmental effects (such as changes in electrolyte or surface charge) can be investigated easily.

We use DNA fragments dissolved in a buffer which does not react with the Au(111) electrode over a wide range of potential. The solution is placed in a three electrode cell[3] which uses a Pt wire counter electrode and a bare silver wire quasi-reference (AgQR). Fresh wires are used for each experiment. The substrates are clean Au(111) epitaxially deposited onto mica (J.A. DeRose *et al.*, to be published). The electrolyte used for the data presented here is 10mM NaH_2PO_4 (pH 6.0) made with distilled and filtered $18M\Omega$ water. The STM tip is insulated so that *no* Faradaic leakage current can be measured.[3] Images are made at tip voltages between -0.1 and -0.7V and tunnel currents of typically 0.5nA.

Figures 1A and B shows a typical area of the Au(111) substrate that is flat to within a single atomic step. The images are taken *in situ* at 0.5V and -0.1V vs. AgQR under the buffer alone. Such images and cyclic voltammetry show that no irreversible reactions occur in this system between -0.3 and +1.0V vs. AgQR. When the solution contains $30\mu g/mL$ of 146 base-pair fragments of DNA and the substrate is held at 0V vs. AgQR images such as 1C are obtained. 1D shows the same area about 10 minutes after the potential was changed to -0.2V vs. AgQR. Most of the 'blobs' have gone. 1E shows the same area after the potential was returned to 0V and another 10 minutes had passed. Many of the 'blobs' have returned. The 146 base-pair DNA should be a double helix of 500Å length in the bulk solution. It appears on the electrode as a globular structure of ~80Å diameter. We believe this is due to a compaction transition in the high ionic strength at the electrode surface (observed in electron microscopy by Eikbush and Moudrianakis[4]). Images of high molecular weight DNA (Figure 1F) are consistent with this view. The material forms thick fibers like those observed in ref. 4. Similar effects can be seen in AFM images, although the contrast appears to be rather different and additional delicate adsorbate structures are visible.

References

1. C.R. Clemmer and T.P. Beebe, Science (1991) **251**, 640.
2. S.M. Lindsay and B. Barris, J. Vac. Sci. Technol. (1988) **A6**, 543 and S.M. Lindsay *et al.*, Science (1989) **244**, 1017.
3. L.A. Nagahara *et al.*, Ultramicroscopy (1990) **33**, 107.
4. T.H. Eikbush and N. Moudrianakis, Cell (1978) **13**, 295.

10mM NaH$_2$-PO$_4$ pH6 on Au(1$\bar{1}$1).

A: V$_s$=0.5V

B: V$_s$=-0.1V

146 bp DNA, 30μg/mL in 10mM NaH$_2$-PO$_4$

C: V$_s$=0V

D: V$_s$=-0.2V

E: V$_s$=0V

High molecular weight DNA, 40μg /mL in 10mM NaH$_2$PO$_4$

F: V$_s$=0V
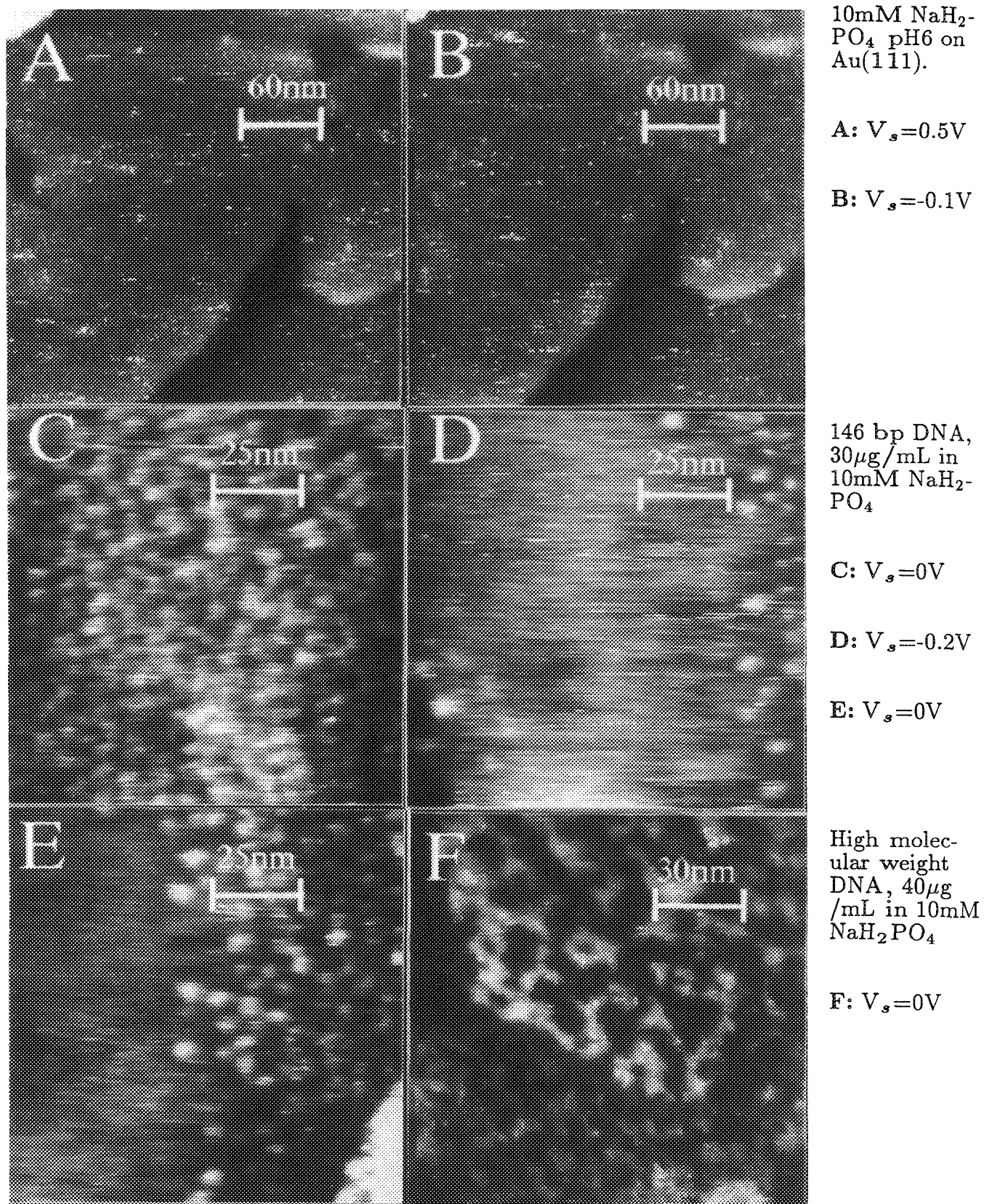
FIG. 1. – STM images (raw data) taken *in situ* on Au(111) in potential control. Black to white is 0 to 5Å height. Solutions and substrate potentials (V$_s$ vs. AgQR) listed at right.

SCANNING TUNNELING MICROSCOPY OF *E. coli* RNA POLYMERASE DEPOSITED ONTO AN Au SUBSTRATE BY AN ELECTROCHEMICAL PROCESS

Rebecca W. Keller,* Carlos Bustamante,** and David Bear***

*Department of Chemistry, University of New Mexico, Albuquerque NM 87131
**Institute of Molecular Biology and Chemistry Department, University of Oregon, Eugene, OR 97403
***Cell Biology and UNM Cancer Center, University of New Mexico Albuquerque, NM 87131

Under ideal conditions, the Scanning Tunneling Microscope (STM) can create atomic resolution images of different kinds of samples. The STM can also be operated in a variety of non-vacuum environments. Because of its potentially high resolution and flexibility of operation, it is now being applied to image biological systems. Several groups[1-6] have communicated the imaging of double and single stranded DNA.

However, reproducibility is still the main problem with most STM results on biological samples. One source of irreproducibility is unreliable sample preparation techniques. Traditional deposition methods used in electron microscopy, such as glow discharge and spreading techniques, do not appear to work with STM. It seems that these techniques do not fix the biological sample strongly enough to the substrate surface. There is now evidence that there are strong forces between the STM tip and the sample and, unless the sample is strongly bound to the surface, it can be swept aside by the tip.

A technique to deposit electrochemically *E. coli* RNA polymerase from a buffer solution on gold surface has been developed. Electrodeposition of biological molecules for use with the STM has two advantages over most other deposition methods[3]: 1) a wide variety of biological molecules can be bound strongly to a normally inert conductive surface such as gold, and 2) electrochemical methods allow control of the solution-substrate interface.

Images of the quaternary structure of *E. coli* RNA polymerase have been obtained in a high humidity (water/glycerol) environment using this deposition technique. No forms comparable to the shapes observed when the enzyme is present have been detected in blanks prepared without the enzyme. The enzyme molecules appear as a group of "jaw-shaped" or "C-shaped" structures (Figure 1), adopting multiple orientations on the surface. The dimensions of the structures observed are consistent with values reported in the literature and their overall shape is reminescent of those previously suggested by TEM studies (Figure 2). Cyclic voltammetry reveals the blocking of the Au electrode as the electrodeposition proceeds and suggests that the attachment of the polymerase takes place by a physisorption mechanism and not by chemical bonding to the surface.

Several problems must still be solved before this method can be fully implemented as a reliable deposition technique for STM. The molecules do not seem to be homogeneously distributed on the substrate surface and finding them can sometimes take several hours. Efforts are now being made to deposit the protein more uniformly on the surface, making the probability of finding them higher. Also a method to control the orientation of the molecules deposited on the electrode surface would be useful. This will allow us to obtain better statistics on the structural parameters and dimensions of the deposited species.

References

1. T.P. Beebee et al., Science 243, 370, (1989)
2. G. Lee et al., Science 244, 475, (1989).
3. D. Keller et al., Proc. Natl. Acad. Sci. USA 86, 5356, (1989).

4. S.M. Lindsay,et al., Science <u>244</u>, 1063 (1989).
5. D.D. Dunlap, and C. Bustamante, Nature <u>342</u>, 204 (1989).
6. R. J. Driscoll et al. Nature <u>346</u>, 294, (1990).
7. W. Tichelaar et al., Micronand Microscopia Acta <u>15</u>, 195 (1984)
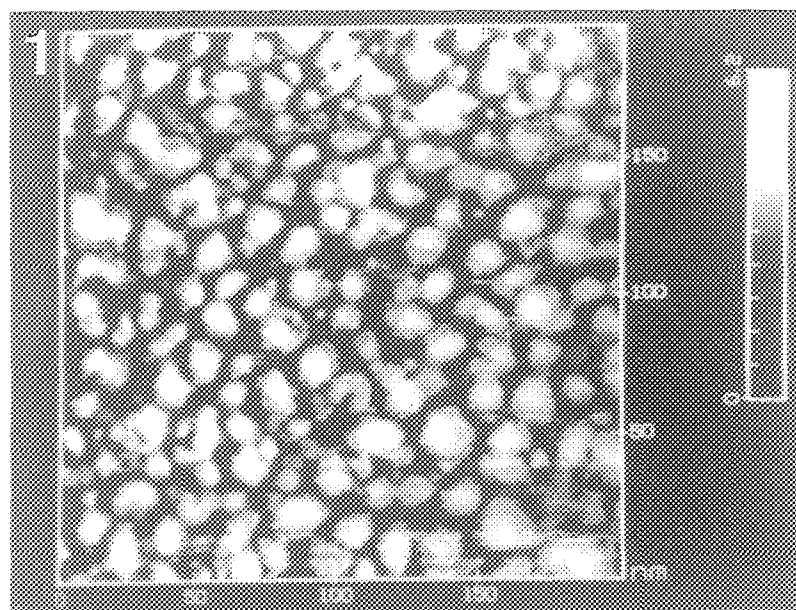
FIG. 1.--STM image obtained after the *E coli* RNA polymerase molecules were electrodeposited on gold for 1 hour at 1.0V. Note the random arrangement of the structures observed.
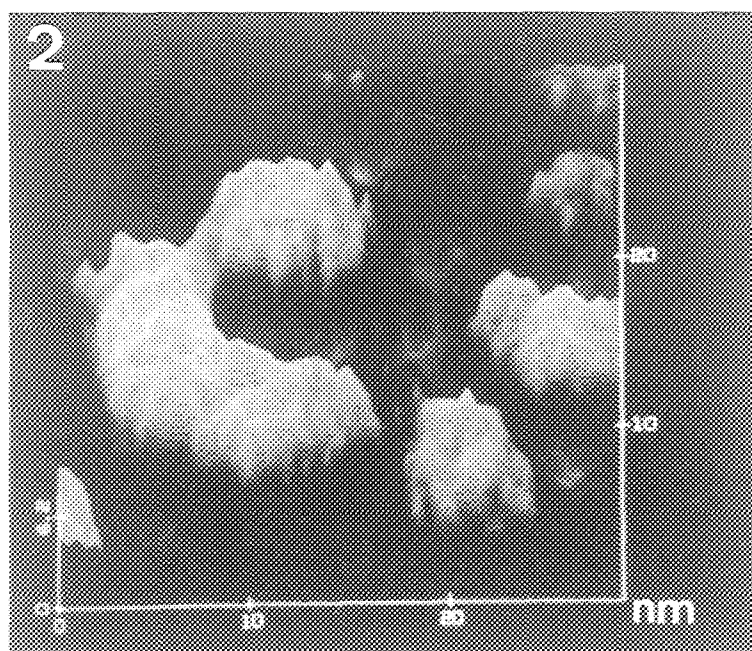
FIG. 2.--STM image of a "jaw shaped" structure. These are identified as the RNA polymerase molecules. The arms of the molecule are about 150Å in length and ~ 50Å high.

ATOMIC FORCE MICROSCOPY OF LANGMUIR-BLODGETT MONOLAYERS AND BILAYERS

J. A. N. Zasadzinski

Chemical and Nuclear Engineering Department, University of California, Santa Barbara, Ca. 93106

Phospholipid monolayers and bilayers prepared by the Langmuir-Blodgett technique are simplified model systems of biological membranes. The molecular organization of these monolayers and bilayers has been intensely studied as they are excellent tools for understanding biological processes such as adhesion, fusion, protein structure and organization, etc. Recent structural studies have included electron diffraction of monolayers deposited on substrates[1] and X-ray diffraction of monolayers at the air-water interface.[2] Both diffraction techniques suggest that in the gel phase, the lipid hydrocarbon chains possess long range orientational order, but relatively short range positional order. As a result, L-B films in the gel state closely resemble the "hexatic" phases better known in thermotropic liquid crystals[3]. However, both short-range and long-range order have not yet been studied in a single Langmuir-Blodgett film.

The Atomic Force Microscope (AFM)[4] should be ideal for visualizing monolayers and bilayers at high resolution. The AFM records interatomic forces between the apex of a cantilevered spring tip and the surface of the sample. Fig. 1 shows a top view of a cadmium arachidate monolayer in air which contains 12 holes, 30 to 140 nm in size. The surface of the films could be imaged repeatedly without damaging the sample. Dark areas correspond to the lower areas in the image, with about 3 nm difference between the bottom of the holes and the top of the monolayer. However, by increasing the applied force on the AFM tip, we could pierce the monolayer to image the 0.5 nm hexagonal lattice of the mica substrate. In this way, we could convince ourselves that we were indeed imaging the cadmium arachidate surface.

Fig. 2 shows a grey scale AFM image of the polar region of a bilayer of DMPE deposited on mica. These images were taken under water at ambient temperature and pressure. The dominant features of the images are long, uniformly spaced rows roughly .7 - .9 nm in spacing. A modulation also can be seen along the rows, with rounded bright spots roughly every .5 nm. We believe that the individual bright spots along the rows correspond to the individual headgroups of the DMPE molecule. The lattice spacing is that measured by X-ray diffraction at the air-water interface. The area per molecule in the AFM image, about .4 nm^2, is also in agreement with the .4 nm^2 area per molecule measured before deposition. These images also show that the DMPE packing is imperfect, that there are a number of defects and vacancies in the lattice, although the rows of molecules extend for several nanometers. This is suggestive of hexatic ordering. The lipid headgroups are not at a uniform height; the bilayer is rough at the nanometer scale.

The resolution and reproducibility of our images suggest that the localized pressures most likely do not reach the level that we may have expected. AFM tips are rounded, with at least a 50 nm radius, with at least a few atomic-scale projections. When the tip is pushed into the LB film covered substrate, the surface deforms smoothly over some fraction of the tip. This smooth deformation will absorb much of the applied force of the AFM cantilever and distribute the force over a relatively large area of several tens or hundreds of square nanometers. The smoothly varying force over the bulk of the tip should not change much as the AFM tip is rastered across the LB film. However, the local interactions probed by the atomic scale projections do change as the tip is rastered across the specimen surface, and it is these changes that likely dominate the AFM image.

1. Kjaer, K, J.Als-Nielsen, C.Helm, L.Laxhuber, H. Möhwald. *Phys. Rev. Lett.* 58:2224-2227 (1987).
2. Garoff, S., H. Deckman, J.Dunsmuir, M.Alvarez, and J.Bloch. *J. Phys.(France)* 47:701-709 (1986).
3. Brock, J. D., R. J. Birgeneau, J. D. Litster, A. Ahorony. *Phys. Today* 42: 52-59 (1989).
4. Binnig, G., C. F. Quate, and Ch. Gerber. *Phys. Rev. Lett.* 56: 930-933 (1986).
5. This work was supported by the Whitaker Foundation, NSF grant CBT86-57444 and ONR grant N00014-90-J-1551. Thanks are especially due to P. K and H. G. Hansma for essential help and continuing collaborations on AFM and STM imaging.
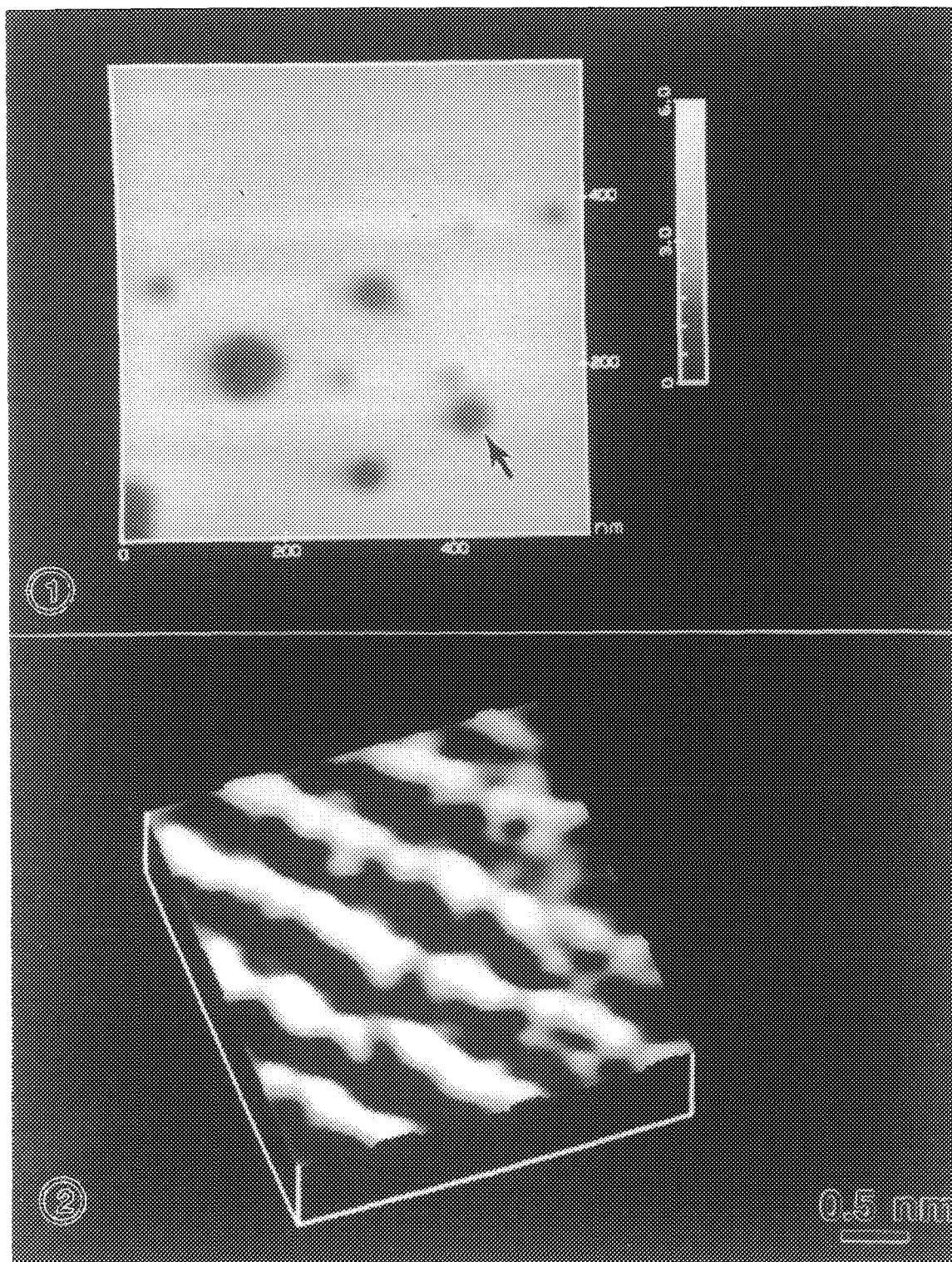
Fig. 1. AFM image of cadmium arachidate monolayer deposited on mica at a surface pressure of 35±3 mN/m. The image size is 500 x 500 nm. Low regions appear dark while higher regions are light. Many irregularly shaped, 3 nm deep holes can be seen in the monolayer ranging in size from about 30 - 140 nm. The smaller holes are more than twice as small as those ever resolved previously.

Fig. 2. Grey scale AFM images of the polar region of a bilayer of DMPE. The images were taken under water at ambient temperature and pressure. The uniform rows are .7 - .9 nm in spacing. The modulation along the rows, with rounded spots every .5 nm, correspond to the headgroups of the DMPE molecule. The lattice spacing is identical to that measured by X-ray diffraction at the air-water interface.

A TWO-SPRING MODEL OF THE TIP SAMPLE INTERACTION USING THE SCANNING TUNNELING MICROSCOPE IN AIR

John T. Woodward

Department of Physics, University of California, Santa Barbara, California 93106

The scanning tunneling microscope (STM) is capable of imaging surface features of electrically conductive samples with lateral resolution of 2 Angstroms and vertical resolution of 0.1 Angstroms.[1] This is accomplished by rastering a conducting tip just above the sample surface using a piezoelectric drive. The tunneling current between the tip and the sample, which depends on the distance separating the two, is then used to keep the tip a constant distance above the sample and generate a height plot of the surface.

When an STM is used in air, a small liquid bridge can be formed between the scanning tip and the sample as shown in Fig. 1. This bridge results from any fluid contamination on the surfaces along with condensation of primarily water from the air. For most applications of the STM, this liquid bridge has little effect on the image. However if the sample is somewhat flexible or only weakly bound on the STM base, as is the case for freeze fracture replicas, the forces exerted by the liquid bridge on the sample as the tip scans the surface can significantly alter measured heights from their actual values. As shown in Fig. 2, when the STM tip pulls away from the sample to go over a surface feature the liquid bridge pulls the sample up as well. This causes the measured height to be larger than the actual height of the feature.

We propose a two spring model for the tip sample interaction. The first spring with a spring constant, k_1, represents the forces between the tip and the sample while a second spring with spring constant, k_2, represents the forces between the sample and the STM base as shown in Fig. 3. With this configuration a surface feature would have its measured height increased by a factor $(k_1+k_2)/k_2$ over its actual height.

The forces between the tip and the sample are the van der Waals attraction and the Laplace pressure of the liquid bridge. Under typical operating conditions these combine to give a spring constant of $k_1 = 15$ N/m. To estimate k_2 we note that we mount the replicas on porous surfaces to allow water or other solvents used to clean the replica to be drawn off. To estimate the worst case, or smallest, value of k_2 we consider the replica suspended over a square pore with the tip at its center.

If standard electron microscopy mounting methods are used $k_2 = .003$ N/m leading to amplifications by a factor of 5000. Relatively simple modifications including the addition of a 200 nm silver backing to the replica and using a membrane with smaller pore size give $k_2 = 400$ N/m which reduces height amplifications to about 4% if the contamination is pure water. Experiments using this method looked at a replica of a freshly cleaved mica surface with the STM. A typical image is shown in fig. 4. Images of 50 nm by 50 nm areas of a replica taken the day it was made had standard deviations in height of 0.51 nm. The same replica after five days covered in a Petri dish gave a standard deviation in height of 0.61 nm and after an additional day exposed to air of 1.64 nm. We therefore conclude that surface contamination does play a role in the amplification of height measurements made by the STM on freeze fracture replicas.[2]

References

1. P. K. Hansma and J. Tersoff, J. Appl. Phys. 61, R1 (1987)
2. This research was sponsored by a Whitaker Foundation Biomedical Engineering Grant
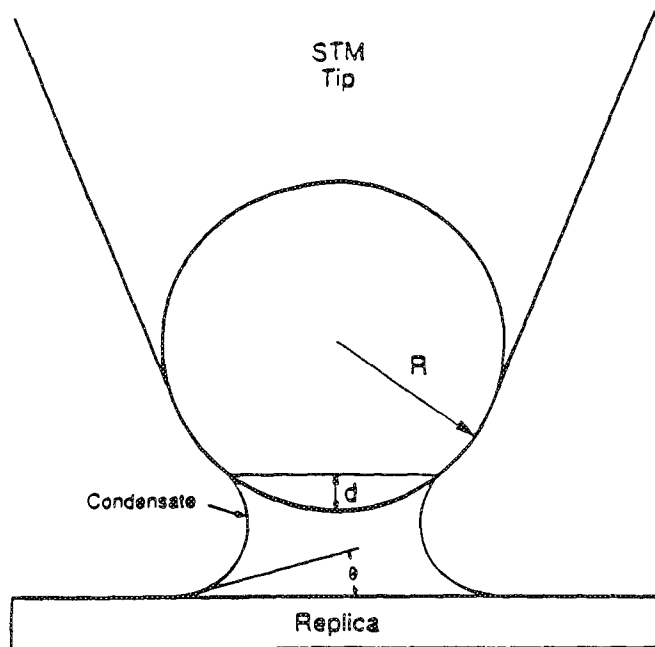
FIG. 1.--Condensation on STM tip and sample forms liquid bridge between them. Surface tension of liquid tries to draw them together.
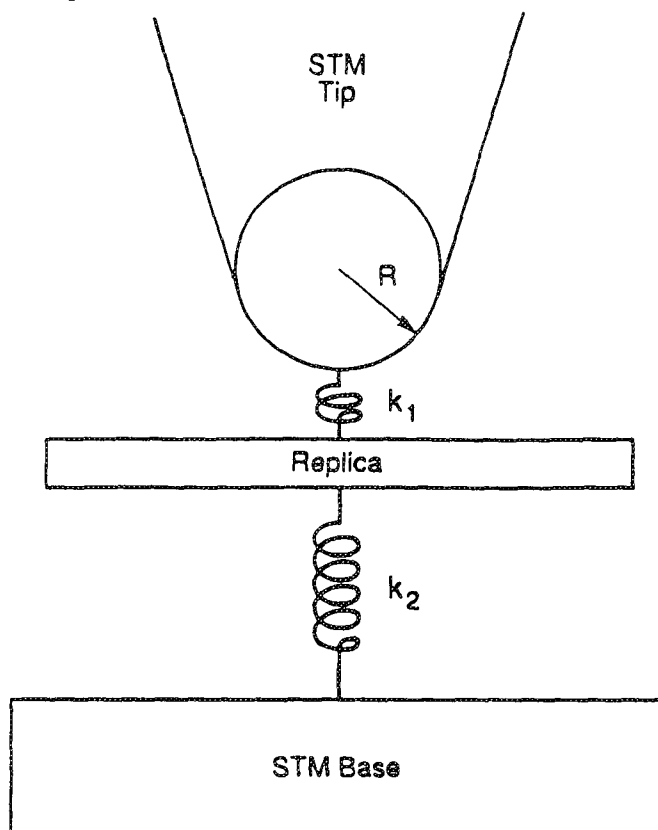
FIG. 3.--In multiple spring model k_1 is effective spring constant between STM tip and sample, and k_2 is effective spring constant between sample and STM base.
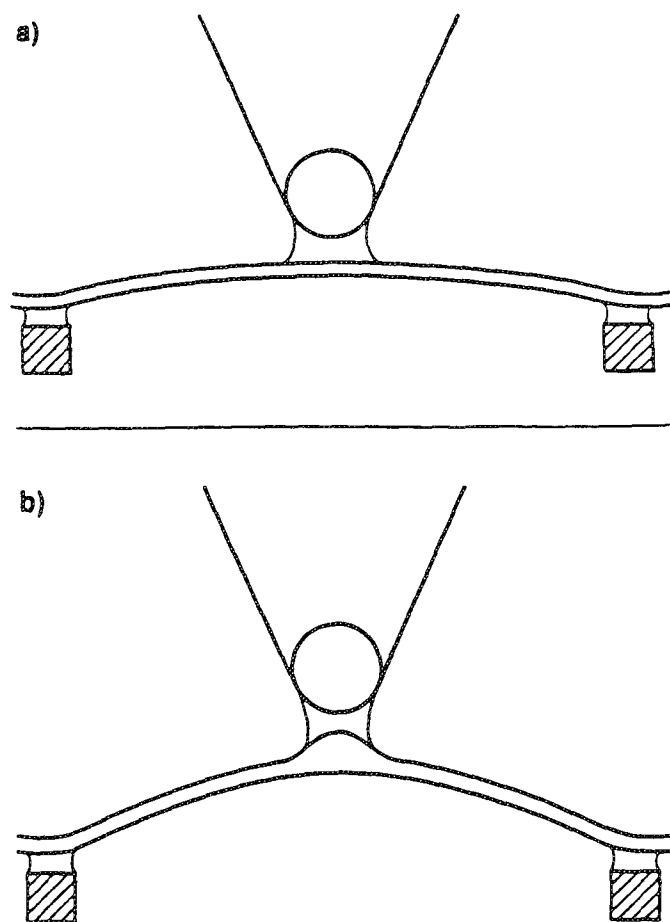
FIG. 2a.--Liquid bridge between STM tip and thin metal replica draws them together by deforming replica and pulling it from mount. 2b.--When tip pulls away from replica to go over surface feature the liquid bridge and van der Waals force pull replica along with tip. STM tip must retract more than actual height of feature to maintain constant tunneling current.
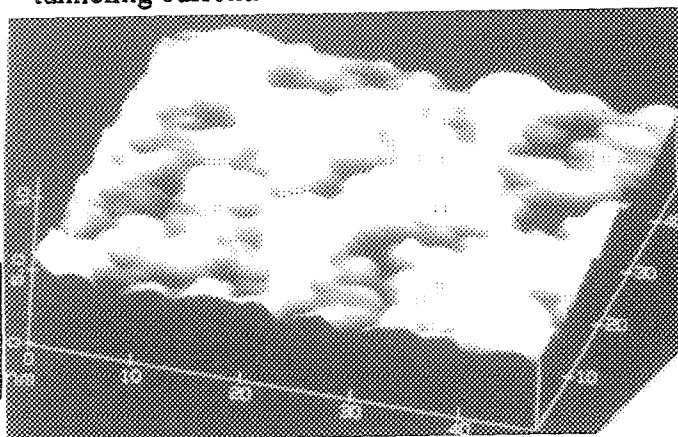
FIG. 4.--Typical image of freeze fracture replica of mica after replica has been in Petri dish five days. Standard deviation in height is 0.60 nm. Scale is in nanometers.

AN IMPROVED DESIGN FOR A SCANNING TUNNELLING MICROSCOPE (STM) FOR USE IN A TRANSMISSION ELECTRON MICROSCOPE (TEM)

W.K. Lo and J.C.H. Spence

Dept. of Physics, Arizona State University, Tempe, AZ 85287, U.S.A.

An improved design for a combination Scanning Tunnelling Microscope/TEM specimen holder is presented. It is based on earlier versions which have been used to test the usefulness of such a device.[1,2] As with the earlier versions, this holder is meant to replace the standard double-tilt specimen holder of an unmodified Philips 400T TEM. It allows the sample to be imaged simultaneously by both the STM and the TEM when the TEM is operated in the reflection mode (see figure 1).

The resolution of a STM is determined by its tip radii as well as its stability. This places strict limitations on the mechanical stability of the tip with respect to the sample. In this STM the piezoelectric tube scanner is rigidly mounted inside the endcap of the STM holder. The tip coarse approach to the sample (z-direction) is provided by an Inchworm which is located outside the TEM vacuum.[3] The Inchworm drives the STM tip assembly via a rod which extends from the Inchworm to the tip assembly through a vacuum seal located at the back end of the STM holder. The rod can be decoupled from the tip through a decoupling joint after the tip has been positioned. The tip assembly is held in place by a spring clip (not shown). This relatively complicated approach to the coarse z-motion of the STM offers the advantage that the mechanical path length between the tip and sample is minimized when the tip is decoupled. Minimizing the mechanical path length decreases the STM's susceptibility to external vibrations. This is critical since the limited space between the pole pieces of the TEM does not allow the use of any form of vibration isolation other than the inherent stability of the TEM.

The joint connecting the rod to the tip assembly is also designed to allow the tip assembly to be rotated by way of the Inchworm and rod. If the tip is mounted off axis it traces out a circle as the tip assembly is rotated. This provides a limited coarse x,y motion of the tip. It is, however, very useful for the occasions when the tip is not located over an ideal region of the specimen. The coarse x,y motion allows the tip to be repositioned while the holder is still in the TEM.

The sample is glued to a cylinder in the specimen mount which is held by friction in the endcap. The specimen mount is separately grounded from the rest of the holder to minimize any electrical interference from the high voltage power supplies of the piezo electric tubes. The cylinder can be rotated to set the specimen tilt while the holder is outside the TEM. This tilt adjustment is used (along with the TEM beam tilt adjustments) to place the reflected beam on the optic axis of the TEM. This is necessary for the optimum imaging conditions of the TEM. Although a tilt that is adjustable while the holder is in the TEM is desirable, its benefits would be outweighed by its complexity. The sample may be tilted about a second direction (along the long axis of the holder) by rotating the whole holder in the TEM.

The completed STM/holder is shown in figure 2. It is held in a stand which is used for STM work outside the TEM. The endcap is at the right end of the holder while the Inchworm is at the left. It is presently undergoing final testing.[4]

References

1. M. Kuwabara, et al., J. Vac. Sci. Tech. A7 (1989) 2745.
2. J. C. H. Spence, et al., Ultramicroscopy 33 (1990) 69.
3. Burleigh Inchworm; Burleigh Instruments, Inc.; Fishers, NY
4. This work is supported by NSF grant #DMR 88-13879 and the NSF/ASU National Center for High Resolution Electron Microscopy at Arizona State University.
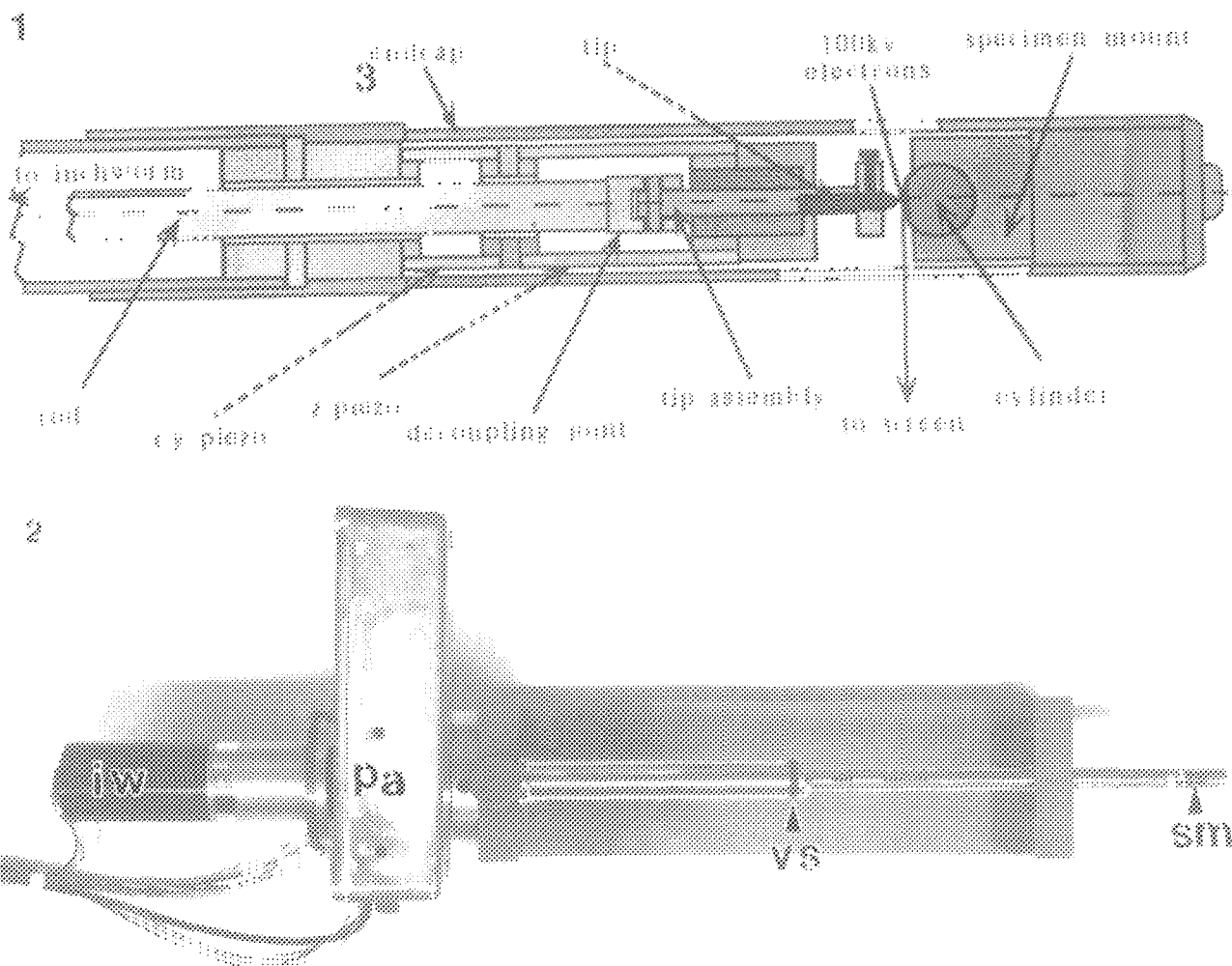
FIG. 1.--Diagram of endcap of STM/TEM holder. Endcap is 4.46cm long and 0.65cm wide at its narrowest point. Decoupling joint allows tip assembly to be disengaged from rod after tip is in tunnelling position. Tip is mounted slightly off axis to provide limited coarse motion when tip assembly is rotated. Specimen is glued to cylinder in specimen mount. This allows specimen tilt to be adjusted. Electron beam enters through top port in endcap. Reflected beam exits through objective aperture cutout at bottom.

FIG. 2.--Picture of completed holder in its stand. Complete holder is 36cm long. I.W. denotes Inchworm motor which provides coarse z-motion (along long axis of holder) of tip. It is connected to a long rod which runs through body of the holder to tip assembly. P.A. denotes preamplifier of STM. It is mounted on STM to minimize length of signal leads. S.M. is sample mount which is visible through objective aperture port of holder. V.S. is one of three vacuum seals of STM holder.

NANOMETER-SIZED TUNGSTEN TIPS FOR STM AND AFM

Mircea Fotino

Department of Molecular, Cellular and Developmental Biology
University of Colorado, Boulder, CO 80309-0347, U.S.A.

An essential requirement in the pursuit of atomic resolution by scanning tunneling microscopy (STM) or atomic force microscopy (AFM) is the use of a tip with an apex of dimensions comparable to or preferably smaller than those of the specimen to be identified. Although atomic resolution of mostly planar specimens has been obtained even with atomically blunt tips, the above requirement appears indispensable for determining 3D surface structures extending equally in all three dimensions.

Tips most commonly used so far in STM or AFM applications are made by grinding or by etching a thin and rigid Pt/Ir or W wire. Mechanical grinding occasionally leaves protruding spikes typically several tens of nm in radius that can play the role of scanning stilus even though neither adequately oriented nor particularly sharp and symmetric.

Etching yields more symmetric and reproducible tips the overall shape and apex radius of which depend on experimental conditions. Fabrication by etching seems to be more frequently adopted by experimenters, but little detailed information is usually given about apex quality and radius beyond an approximate estimation in a broad range between about 0.1μm and 1μm, and only very rarely includes supporting evidence in the form of high-resolution electron micrographs of the tip. A commonly used and typical tip obtained by standard etching of W wire 0.75mm or less in diameter in a 2N NaOH solution under optimum a.c. voltage in the 1V to 5V range is shown in Fig. 1. The overall symmetry and sharpness of the tip look satisfactory at low magnification (Fig. 1a), but when viewed at high magnification by TEM at 200 kV (Fig. 1b) the apex appears consistently blunt by its radius of several hundreds of nm and thus insufficiently sharp for atomic resolution in general.

The tip shape is determined by etching dynamics. Taking advantage of electrolyte dynamics and of the dependence of bubble flow on tip geometry during etching by a.c. currents, a simple method has been developed for reliably and reproducibly etching tips with an elongated apex of nm and sub-nm dimensions (nanotips). These tips should be well suited for atomic-resolution imaging of macromolecules and 3D surfaces.

The two-step procedure involving the etching parameters mentioned above is carried out in a glass cell so it could be monitored at all times through a low-powered optical microscope. In the first step a slender, conical tip such as in Fig. 1 is etched under several volts in some 30 to 60 seconds by routine immersion. The tip cone can be shaped by a combination of voltage between electrodes and depth of immersion into the electrolyte. If the immersion is shallow or the wire barely touching the liquid surface, a large cone angle is obtained. Conversely, the deeper the immersion, the slenderer the cone. In either case the apex remains blunt because the bubbles produced by the a.c. current move away from the tip in a divergent stream by buoyancy along the curved cone.

The orientation of the tip-forming wire is reversed in the second step and the etching voltage reduced to a small fraction of a volt. In this configuration the bubbles move slowly in opposite direction in a convergent stream that squeezes the etching of the blunt apex into one or several elongated and ultrasharp spikes through the growth of pits on the apex surface. Satisfactory results are reliably obtained by

slow etching over tens of minutes. Since at these small dimensions the apex configuration changes quite rapidly even under small etching voltages, continuous monitoring of the etching process is needed to determine the optimal stopping point.

If the tip etched in step 1 has a large cone angle, the apex formed in step 2 quite frequently contains several spikes that may not be noticeable at low magnification (Fig. 2a). At high magnification there appears no clear pattern in the disposition of the spikes (Fig. 2b), which may result from the combination of several parameters such as initial wire diameter, lattice orientation in the wire, or bubble flow. However, when proceeding slowly from a thin wire, there seems to be a correlation between a more orderly disposition of spikes and their individual quality, e.g. symmetry and sharpness, as in the case of the tip shown in Fig. 3a. The apex of   1nm radius shown at high magnification in Fig. 3b is typical of several spikes seen on this tip.

The above discussion of tip and apex characteristics applies to the dense metal clearly distinguishable from the less dense deposits that alter the overall appearance of these structures. The nature and the elimination of these deposits, most likely electrolyte residues and/or atmospheric contaminants, is under study. A more detailed account of this tip-forming procedure is to appear elsewhere*.
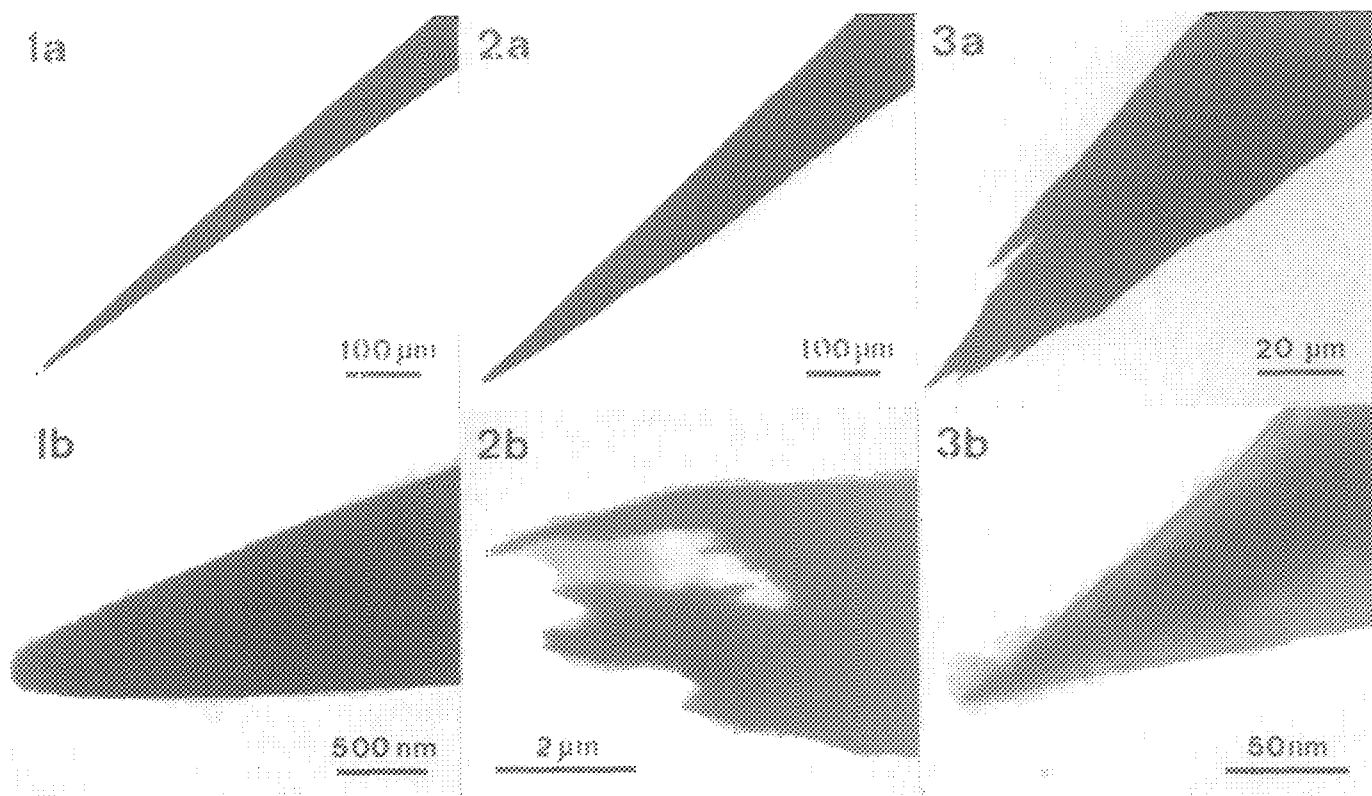
FIG. 1   Tungsten tip etched by standard method: slender (a) yet blunt (b).

FIG. 2   Tungsten tip etched by two-step procedure: almost indistinguishable from standard tip in Fig. 1 at low magnification (a) yet displaying multiple spikes at high magnification (b).

FIG. 3   Tip of 0.37mm tungsten wire etched by two-step procedure (a) and symmetric apex of radius ≲1nm representative of other spikes on the same tip (b).

CRYO-SCANNING TUNNELING MICROSCOPY OF DNA

John Harris, Aaron Partridge, Joshua Partridge and Randy Nielsen

Atomis, Inc., 2946 San Pablo Avenue, Berkeley, CA 94702

Scanning tunneling microscopy has found increasing interest in biological sciences[1]. Several problems face the investigator imaging samples of biological origin. These include low conductivity, poor attachment of the sample to substrate and thermal/mechanical drift of the sample while scanning. Several approaches have tried to overcome these problems. These include coating with metal[2], freeze drying and/or freeze fracturing[3] and tunneling in water[4]. Another useful method is to freeze the sample on the STM holder and image frozen. The biological structure should stay rigid under the scanning tip, should not be swept away from the substrate and should provide highly reproducible images.

Calf thymus DNA (Sigma #D-1501) was mixed in deionized water-tween 20 (0.1%). DNA concentrations varied between 10 µg/ml and 1 µg/ml. The sample was heated slightly, a small drop placed on highly oriented pyrolytic graphite (HOPG) and air dried. The sample holder was immediately placed in an Atomis variable temperature cryo-STM with a 6 micron scan range head (Surface Interface, Inc., Mountain View, CA), frozen and scanned.

Most of the DNA aggregated in clusters with individual segments spreading from a few of the clusters. Some appeared to be associated with graphite flakes reported earlier[5]. Figure 1 shows an isolated, coiled DNA strand before processing. Figure 2 shows the same image after FFT processing. Helical periodicity measured about 3.5 nm with an average diameter of 4 nm. Temperature was critical regarding attachment of the sample to substrate. At -20°C, DNA could be swept aside after a few tip scans.. At -50°C, neither high current nor high bias could dislodge particles, though these conditions could crash the tip easily. Sample drift was negligible once tip and sample temperatures reached equilibria. The lack of sample drift aided resolution since the head was not designed for high resolution (wide scan head).

Cryo-STM offers distinct advantages in the application of STM to biological molecules. Once molecules are frozen, they remain in a native state throughout the analysis. Since the sample is frozen solid onto the surface, tunneling interactions do not change the location or the conformation of the molecule. This is especially significant when you hear of STM stories about the "the perfect sample tha got away". Also, once the temperature becomes cooler, the electronic noise decreases. There are a few disadvantages of the system. Freezing is not a rapid freeze, so ice crystal formation might be a problem for larger, intact biological structures. Consequently, sample surfaces must be dry before they can be frozen nor can they be imaged in a hydrated environment. Drying is achieved at cryogenic temperatures by purging helium gas into the system. A rapid drying technique using dry nitrogen[1] was not used for these images but should help to keep structure intact. Interactions of different biological molecules at different temperatures can be studied with this system. Interactions could be localized at cryogenic temperatures when scanning, allowed to continue at a warmer temperature, then returned to a colder temperature for further imaging. Newer techniques are being developed for cryogenic STM's[6] which could possibly be used for biological conformational studies.

References

1. K. A. Fisher et al., Ultramicroscopy, v.33, 117.
2. M. Amrein, et al, Science v.240, 514
3. J. A. N. Zasadzinski, et al, Science, v.239, 1013
4. S. M. Lindsay, et al, Science, v.244, 1063
5. M. Salmeron, et al, Jl Vac. Sci. Technol., v.8, 635
6. M. Hecht et al., Proceedings of 12th ICEM (Imaging), v.1, 613
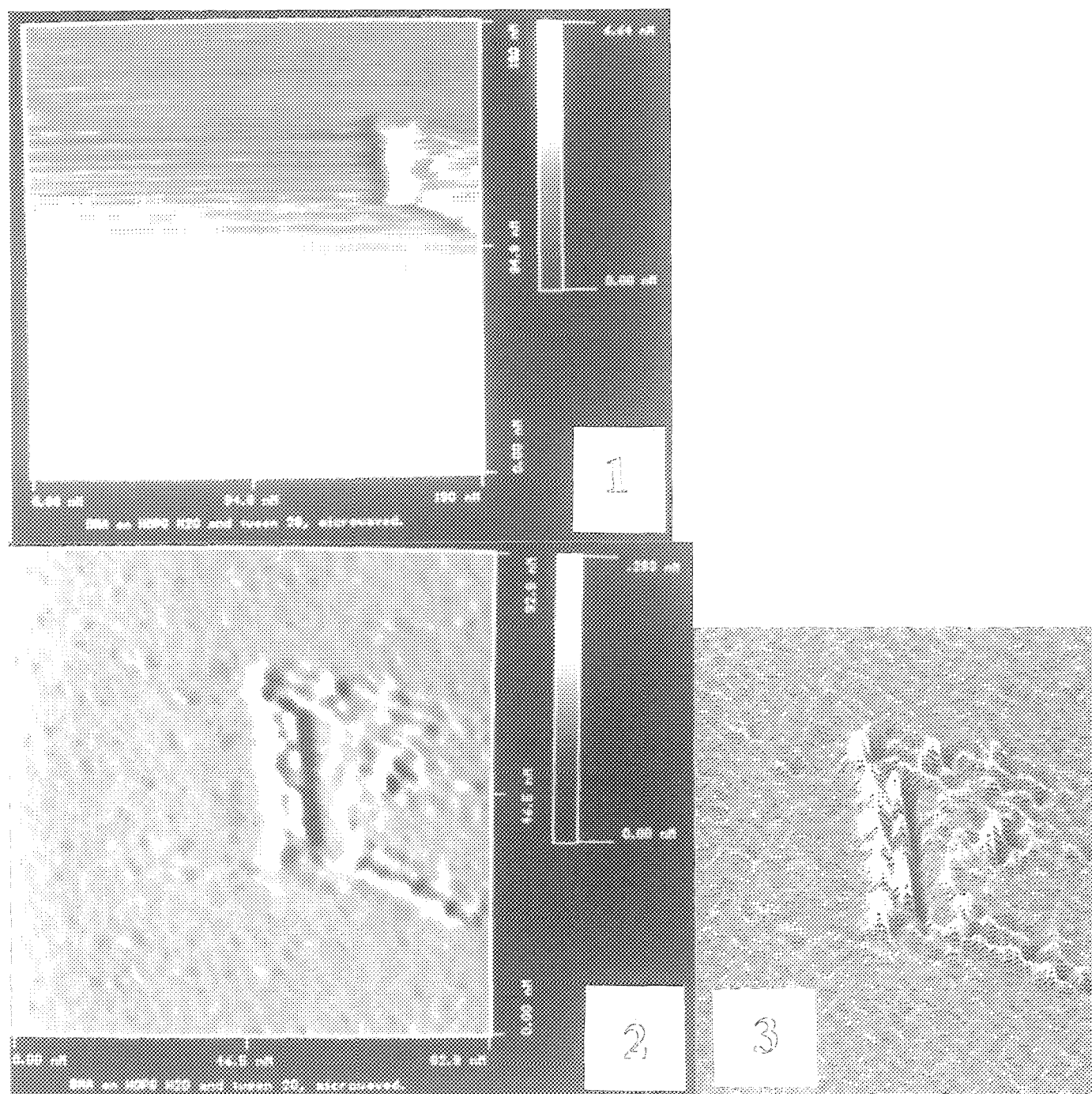
Fig. 1 Raw, unprocessed image of DNA   . 200 mV bias, 0.2 nA current.
Fig. 2 Processed image (FFT) of Figure 1 showing helical structure.
Fig. 3 Line scan of Figure 2.

SCANNING TUNNELING MICROSCOPY AND ATOMIC FORCE MICROSCOPY OF FIBRILLAR STRUCTURES IN LIQUID CRYSTALLINE POLYMERS

I. H. Musselman and P. E. Russell

Department of Materials Science and Engineering and Precision Engineering Center, North Carolina State University, Raleigh, NC 27695.

Hierarchical fibrillar structures have been reported to be present in liquid crystalline polymer (LCP) extrudates such as fibers and tapes.[1] Extensive characterization of Vectran®, a thermotropic copolyester, by light microscopy and scanning and transmission electron microscopy (SEM, TEM), resulted in the development of a well-accepted hierarchical fibrillar structural model for this highly oriented LCP.[1] This structural model has since been extended to lyotropic polymers such as Kevlar® and to the "rigid rod" polymers such as poly(p-phenylene benzobisthiazole) (PPBT). With conventional SEM and TEM, the smallest fibrils were shown to be about 50 nm wide and 5 nm thick.

With the emergence of higher-resolution imaging techniques such as scanning tunneling microscopy (STM) and field emission SEM (FESEM), we have been able to explore the ultrastructures in the LCP fibrils further and to extend the LCP structural model.[2,3] Model extension has been facilitated by the ability to measure microfibril width and thickness at the 1-100nm size scale from the STM images. It is also of particular interest to develop a better understanding of the process-structure-property relationships controlling the thermotropic polymers and the aramids. A higher molecular orientation is known to favor a higher modulus; however, it is unclear whether this molecular orientation is related to the microfibrillar structure. We anticipate that a better understanding of this relationship will be achieved as a result of our access to these higher-resolution microscopy techniques.[3]

Our previous correlative microscopy studies of these LCP materials[2,3] have been extended to include imaging by atomic force microscopy (AFM). In this study, the texture and structure of Vectran and Kevlar LCP fibrils are examined by two scanning probe techniques, STM and AFM. Since STM requires a conducting specimen for signal generation, LCP samples for STM analysis were coated with a thin film of Pt. These same metal-coated samples, along with uncoated specimens of the same materials, were images by AFM. The ease of imaging LCP fibrils with STM and AFM, and the effects of tip geometry, metal coating, and substrate choice on the measured fibril dimensions, are discussed in this paper.

Experimental

The investigated LCP materials consist of highly oriented fibers composed of Vectran [copolyesters of 40hydroxybenzoic acid (HBA) and 2-hydroxy-6-napthoic acid (HNA)], and the aramid fiber Kevlar. These materials exhibit unidirectionally oriented structures as revealed by x-ray diffraction and microscopy studies.[1,4] Ultrasonication was used to disintegrate the LCP fibers to provide fine "fibrillar" samples for STM and AFM studies. The sonicated fibril/ethanol suspension was transferred dropwise to highly oriented pyrolytic graphite (HOPG) substrates. Two samples each of Vectran and Kevlar were prepared. Thin Pt coatings (ca 5 nm) were deposited by ion beam surface for STM imaging. These coatings have been shown to introduce minimal topography to the original sample surface.[5] Two samples were left uncoated for AFM imaging.

All STM and AFM images were acquired with a Nanoscope II instrument manufactured by Digital Instruments, Inc. STM images were acquired from several areas each of the

Pt-coated and uncoated specimens. For each sample area, a large image, 8-12 μm, was acquired to identify the location of the fibrils. Numerous smaller images, down to 150 nm², were obtained within the region of each large scan to better resolve individual fibrils. The Nanoscope II software was used to measure the width and thickness of each fibril.

Results

STM images of sonicated, Pt-coated Vectran (Fig. 1) and Kevlar (Fig. 2) fibers clearly reveal the hierarchical fibrillar structure present in these liquid crystalline polymers. In Figs. 1 and 2, fine microfibrils are observed to be well aligned within the larger Vectran and Kevlar fibrillar units. In addition, distinct texture can be observed along the length of each microfibril (Figs. 1b and 2b). Kink bands, shown for the first time to be a result of microfibril deformation related to the poor compressive properties of highly oriented polymers, are observed in a representative image of Vectran fiber (Fig. 1b).

AFM images acquired from Pt-coated and uncoated Vectran and Kevlar specimens are qualitatively similar to the STM images obtained from the Pt-coated samples. Surprisingly, the uncoated fibrils were not disturbed by the scanning process, which suggests that the metal coating was not necessary to anchor these samples to their substrates. An AFM image (Fig. 3a, bottom) of uncoated Kevlar reveals the same hierarchical fibrillar structure observed by STM. A nonuniform fibrillar texture, revealed in the AFM image of uncoated Vectran (Fig. 4), can be attributed to the inherent nature of the polymer in contrast to the metal coating.

The widths and thicknesses of the 20 smallest fibrils, measured from each of the 6 data sets (STM: Pt-coated Vectran, Pt-coated Kevlar; AFM: Pt-coated Vectran, uncoated Vectran, Pt-coated Kevlar, uncoated Kevlar), are presented in Table 1. Figure 5 demonstrates the fibril measurement method. From Table 1, it is clear that the widths of the Pt-coated microfibrils of Vectran and Kevlar, measured from the AFM images, are more than twice as wide as those measured by STM. This increased width could be attributed to the use of an AFM tip that is broader than the STM tip. The average etched Pt/Ir STM tip used in this study has a 500Å radius of curvature and a cone half angle of 5 to 10°.[6] In contrast, the AFM tip typically has a 300Å radius and a 55° slope.[7]

TABLE 1.--Microfibril widths and thicknesses determined by STM and AFM for Pt-coated and uncoated Vectran and Kevlar.

Sample	Number of Measurements	Width (nm)	Thickness (nm)
STM Vectran, 5 nm Pt	20	17.1 ± 3.8 [0.8]	4.4 ± 1.8 [0.4]
STM Kevlar, 5 nm Pt	20	19.9 ± 8.3 [1.9]	2.8 ± 1.7 [0.4]
AFM Vectran, 5 nm Pt	20	73.2 ± 20.4 [4.6]	14.3 ± 9.3 [2.1]
AFM Kevlar, 5 nm Pt	20	44.3 ± 10.4 [2.3]	9.0 ± 6.4 [1.4]
AFM Vectran, uncoated	20	80.9 ± 22.6 [5.1]	32.3 ± 11.5 [2.6]
AFM Kevlar, uncoated	20	60.6 ± 11.9 [2.7]	17.2 ± 8.0 [1.8]

[ ] Standard deviation of mean, $s/\sqrt{N}$.

In addition to the larger microfibril widths, the AFM thickness measurements for Pt-coated Vectran and Kevlar are more than 3 times larger than the corresponding STM measurements. The vertical calibration of the STM and AFM heads have been checked against a calibration grating. Although the head calibrations may differ by 5-10%, this difference cannot fully account for the observed discrepancy in fibril thickness.
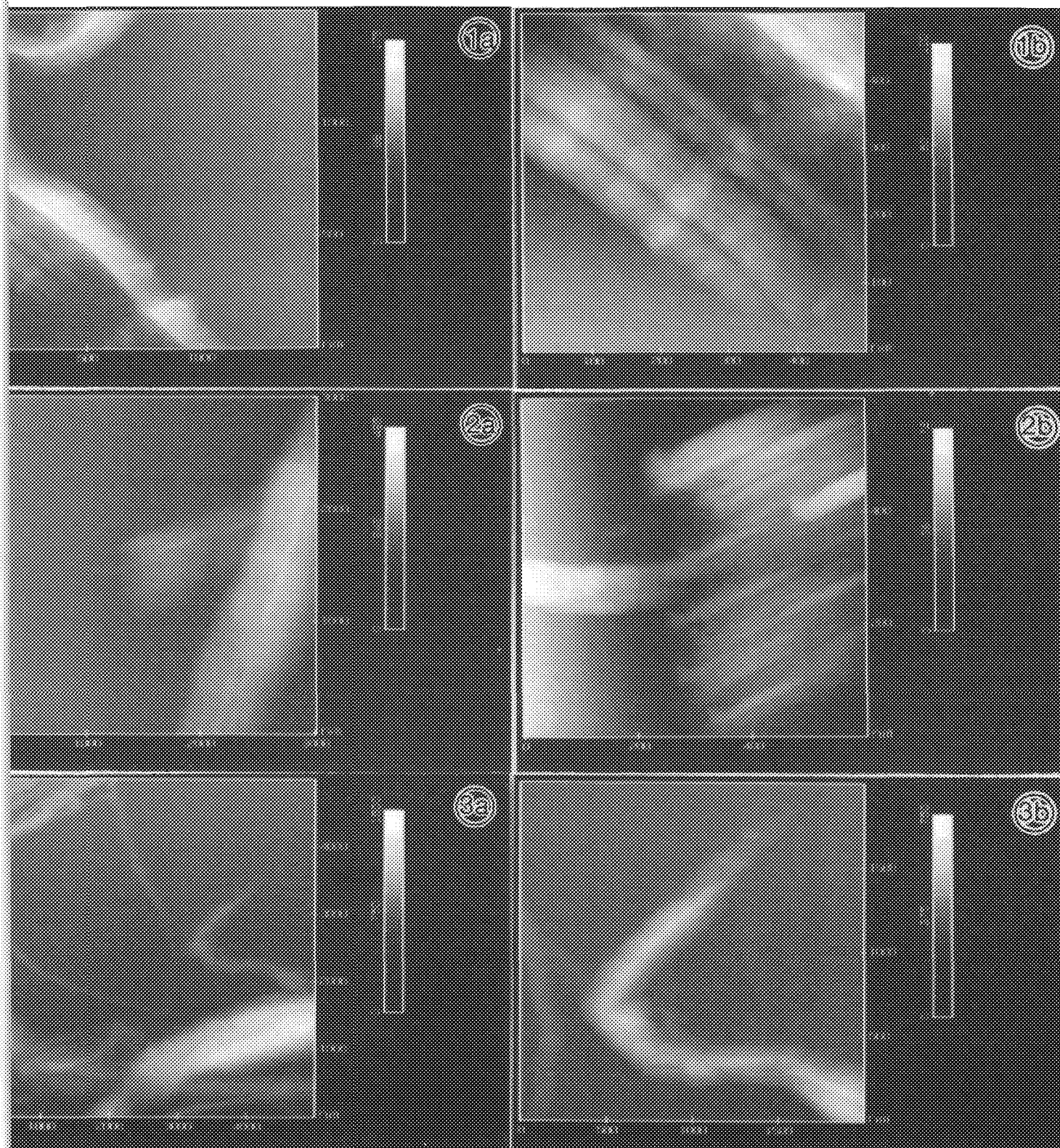
FIG. 1.--STM images of sonicated Vectran on HOPG substrate coated with 5 nm Pt.   (a) Hierarchical fibrillar structure observed. 1500 × 1500 nm. (b) Microfibrillar texture and kink bands observed. 500 × 500 nm.
FIG. 2.--STM images of sonicated Kevlar on HOPG substrate coated with 5 nm Pt.   (a) Hierarchical fibrillar structure observed. 3000 × 3000 nm. (b) Microfibrillar texture observed. 600 × 600 nm.
FIG. 3.--AFM images of uncoated, sonicated Kevlar on HOPG substrate. (a) Hierarchical fibrillar structure observed at bottom of image. 5000 × 5000 nm. (b) 2000 × 2000 nm.

Exhaustive imaging of these four samples by STM and AFM could have reduced the possibility of a sampling error, which might account for the measured difference in microfibril thickness.

An alternative explanation for the increased microfibril thickness observed by AFM vs STM considers variations in the compression of the HOPG substrate by a STM vs an AFM tip. Compression of the HOPG surface during STM imaging has been observed by Shedd.[8] During scanning the tip (STM or AFM) exerts a force on the HOPG substrate over the tip/substrate contact area. In STM, this force is relatively small and is constant during scanning on a uniform metal coating. In contrast, a larger force is applied to the sample by an AFM tip. For an AFM sample consisting of uncoated fibrils on a HOPG substrate, the compressive pressure (force/area) is larger when the tip scans over the bare HOPG substrate than when it scans over a microfibril sitting on that substrate. For a constant applied force, this difference in pressure is the result of a tip/HOPG contact area that is smaller than the fibril/HOPG contact area. This variation in the compression of HOPG for different sample areas could account for the increased microfibril thickness observed by AFM vs STM.

Larger thickness measurements of microfibrils by AFM for the uncoated vs coated Vectran and Kevlar samples (Table 1) may possibly be attributed to sampling or to compression differences as described above. However, in this case the difference in the compression of bare HOPG vs HOPG under a fibril would not be related to tip or technique, but would be rather due to differences in the material, e.g., uncoated vs metal-coated samples. For a metal-coated sample, the compression effect of HOPG described above is expected to be reduced, which coincides with the smaller measured fibril thicknesses for this sample (Table 1). A variation in microfibril thickness for the uncoated vs the coated samples may also be related to the possible nonuniform deposition of metal over the fibrils vs the HOPG substrate.

Conclusions

Both the scanning tunneling and the atomic force microscopes have demonstrated their ability successfully to image sonicated samples of Vectran and Kevlar microfibrils. Acquisition of AFM images from these samples has proved to be more convenient than expected: the uncoated fibrils remain undisturbed for the duration of imaging. The STM and AFM images clearly show the hierarchical fibrillar structure present in these liquid crystalline polymers. With AFM, the true polymer topography can be observed in the nonoameter-size regime from the uncoated samples.

As is apparent from the results of this study, quantification of microfibril widths and thicknesses is difficult. Tip, substrate, and coating effects must be considered when measurement differences observed by STM and AFM are assessed. However, the ability to eliminate the need for a metal coating in AFM studies places this technique at a distinct advantage for quantitative measurements. In the future, we plan to try to resolve the quantitative discrepancies described here. Proposed experiments include imaging these fibril samples with a more controlled geometry AFM tip[9] and exploring the use of alternative, less compressible substrates.

References

1. L. C. Sawyer and M. Jaffe, "The structure of thermotropic copolyesters," *J. Mater. Sci.* 21: 1897, 1986.
2. I. H. Musselman et al., "Correlative STM, FESEM, and TEM studies of fibrillar structures in liquid crystalline polymers," *Proc. XII ICEM*, 1990, 866.
3. L. C. Sawyer et al., "Microfibrillar structures in liquid crystalline polymers," *J. Mater. Sci. Let.* (in press).
4. A. M. Donald and A. H. Windle, "Electron microscopy of banded structures in oriented thermotropic polymers," *J. Mater. Sci.* 18: 1143, 1983.

5. I. H. Musselman and P. E. Russell, "Platinum thin film roughness measurements by scanning tunneling microscopy," *Microbeam Analysis--1989*, 535.

6. I. H. Musselman and P. E. Russell, "Platinum/iridium tips with controlled geometry for scanning tunneling microscopy," *J. Vac. Sci. Technol.* A8: 3558, 1990.

7. T. R. Albrecht, *Advances in Atomic Force Microscopy and Scanning Tunneling Microscopy*, Ph.D. Dissertation, Stanford University, Stanford, Calif., 1989.

8. G. M. Shedd, *Scanning Tunneling Microscopy Studies of Clusters and Materials Modification at the Nanometer Scale*, Ph.D. Dissertation, North Carolina State University, Raleigh, N.C., 1991.

9. Hongyu Ximen and P. E. Russell (personal communication).
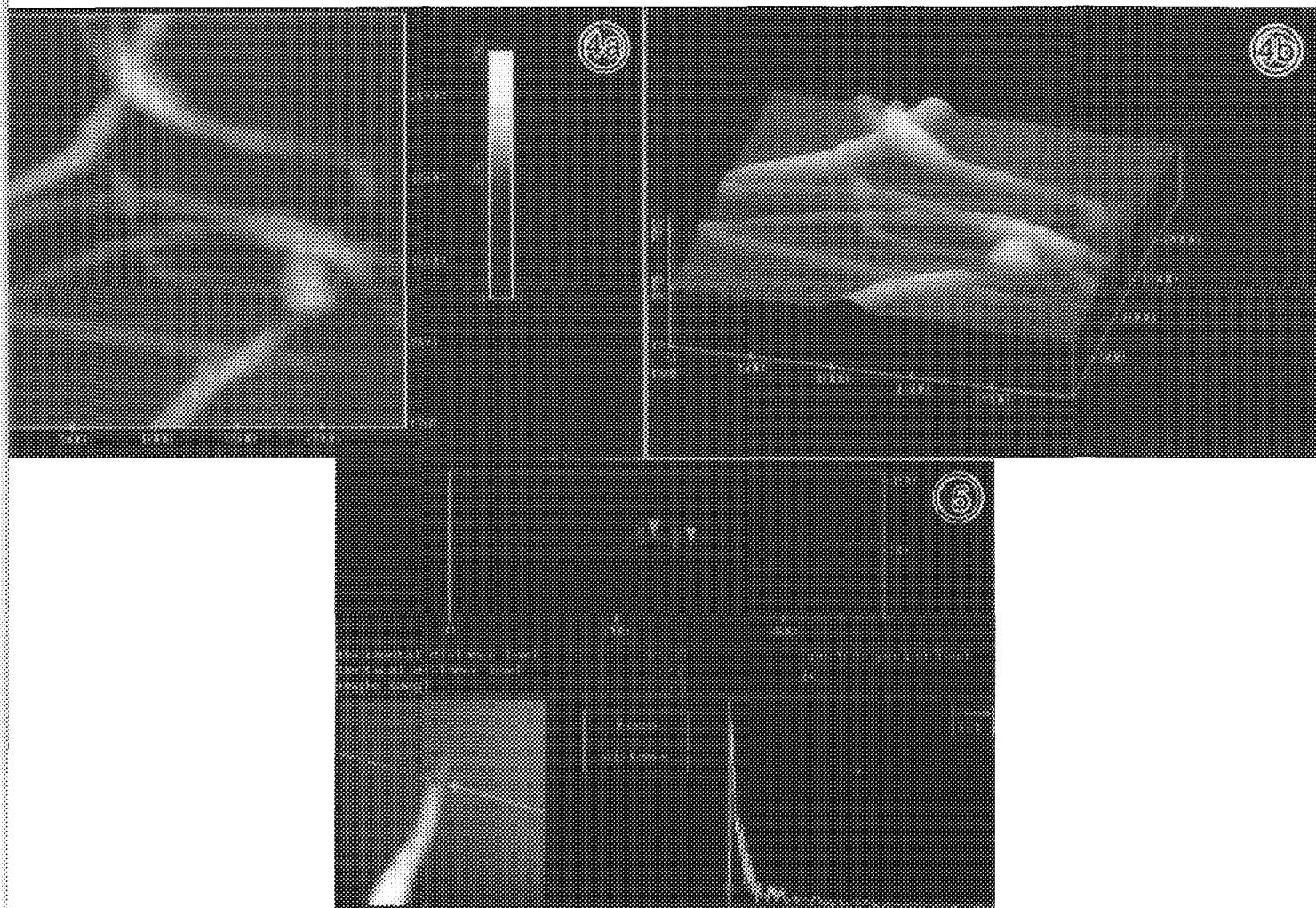
FIG. 4.--AFM image of uncoated, sonicated Vectran on HOPG substrate. Nonuniform microfibrillar texture revealed. 2500 × 2500 nm. (a) Top-down view. (b) Three-dimensional view.

FIG. 5.--AFM image of sonicated Kevlar on HOPG substrate coated with 5 nm Pt. Demonstration of microfibril measurement method. Microfibril width is 42.7 nm. Microfibril thickness is 4.9 nm. 500 × 500 nm.

J-2: Magnetic Materials

MICROMAGNETICS OF LONGITUDINAL RECORDING MEDIA

P.S. Alexopoulos*

IBM Research Division, Almaden Research Center, San Jose, CA 95120

Future needs in high density magnetic storage devices require increases both in linear and track densities. The latest 1 Gigabit per square inch areal density for longitudinal media demonstrated by IBM [1] has reduced the bit size to dimensions comparable to the characteristic micromagnetic length scales of todays media. Improvement or extension of the current recording limits requires detailed knowledge of micromagnetics and their manipulation or tailoring through the microstructure of the utilized magnetic thin films. There is a number of ways that these parameters can be controlled through the microstructure of the thin films including: chemical alloying, use of nucleating underlayers, and deposition parameters [2,3]. Our investigation of written transitions recorded on a series of cobalt based alloys using Lorentz microscopy showed that the domain wall structures observed in the transition zones are very complex (Figure 1). The transition zones contain not only zig-zags shape 180° walls but also vortex structures and intermediate states between the two[4].

Effort has been made by a number of investigators to quantify the micromagnetic structures of written bits by a set of parameters that can eventually be correlated to material microstructural parameters and functional performance. The latest quantification efforts are also accompanied by parallel efforts in the development of modelling using large scale numerical micromagnetic simulations[5,6,7]. This paper presents a review of the micromagnetic studies of thin film magnetic materials performed by the authors referenced below and by our group at the IBM Almaden Research Center.

REFERENCES

1) T. Yogi et al., IEEE Trans. Magn. MAG-26, 5, 2271 (1990).
2) J. K. Howard, J. Vac. Sci. Technol. A., Vol. 4, 1 (1986).
3) T. Yogi et al., IEEE Trans. Magn. MAG-26, 5, 1578 (1990).
4) P.S. Alexopoulos and R.H. Geiss, IEEE Trans. Magn. MAG-22, 566 (1986).
5) I. A. Beardsley and V. S. Speriosu, IEEE Trans. Magn. MAG-26, 5, 2718 (1990).
6) R. Giles, P.S. Alexopoulos and M. Mansuripur to be published in "Computers in Physics".
7) J. G. Zhu and H. N. Bertram, J. Appl. Phys., 63, 3248 (1988)
* Magnetic Recording Institute.
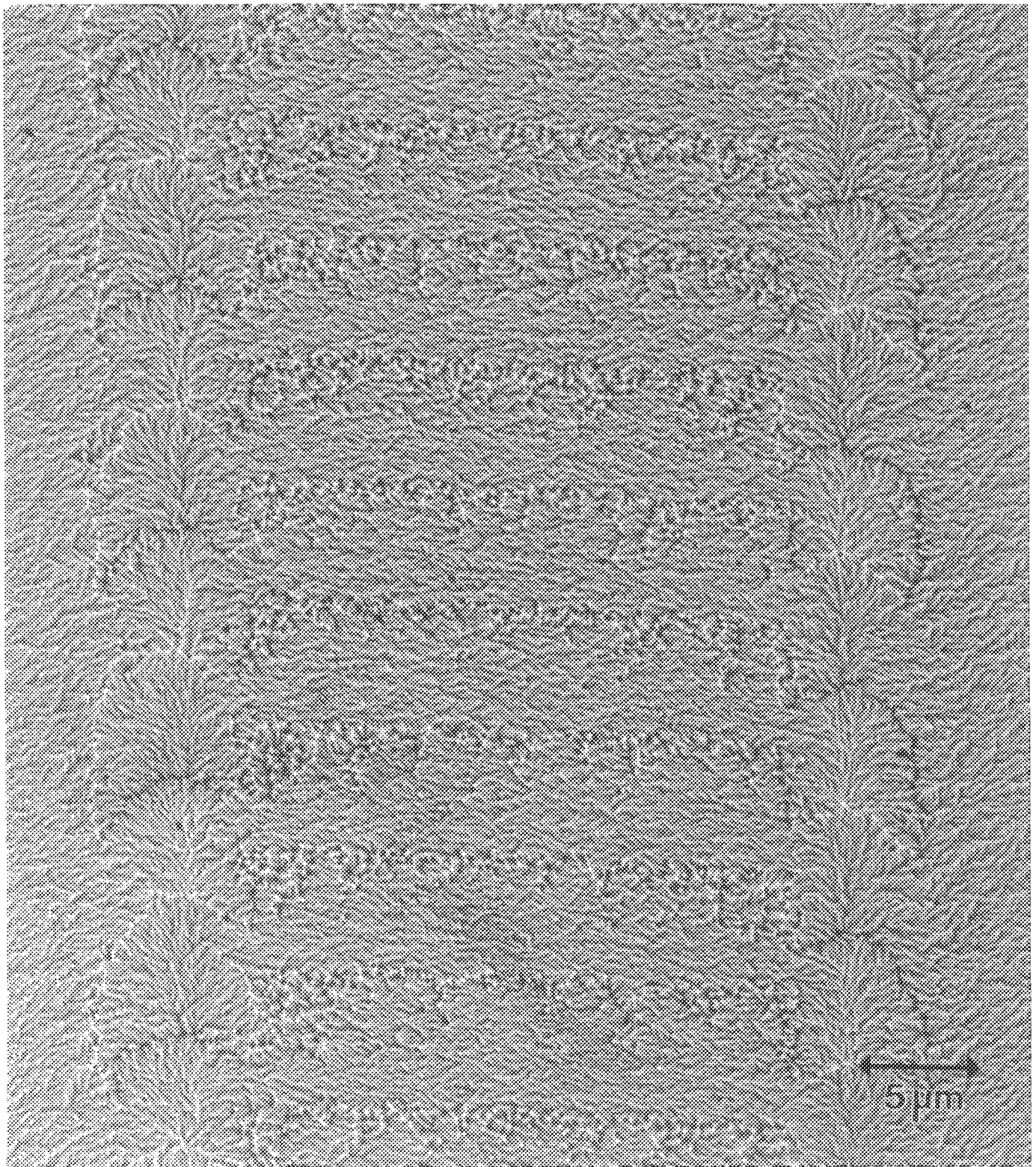
Figure 1. Fresnel image of magnetic bits written quasi statically using a thin film inductive head with 25μm track width

TRANSMISSION ELECTRON MICROSCOPY OF ORIENTED $Co_{84}Cr_{14}Ta_2$ THIN FILMS FOR LONGITUDINAL MAGNETIC RECORDING

T. P. Nolan

Department of Materials Science and Engineering, Stanford University, Stanford, CA 94305

Thin film magnetic media are being used as low cost, high density forms of information storage. The development of this technology requires the study, at the sub-micron level, of morphological, crystallographic, and magnetic properties, throughout the depth of the deposited films. As the microstructure becomes increasingly fine, with grain sizes approaching 100Å, the unique characterization capabilities of transmission electron microscopy (TEM) have become indispensable to the analysis of such thin film magnetic media.

Films were deposited at 225°C, on two NiP plated Al substrates, one polished, and one circumferentially textured with a mean roughness of 55Å. Three layers, a 750Å chromium underlayer, a 600Å layer of magnetic alloy of composition $Co_{84}Cr_{14}Ta_2$, and a 300Å amorphous carbon overcoat were then sputter deposited using a dc magnetron system at a power of 1kW, in a chamber evacuated below 10^{-6} torr and filled to 12μm Ar pressure. The textured medium is presently used in industry owing to its high coercivity, H_c, and relatively low noise. One important feature is that the coercivity in the circumferential read/write direction is significantly higher than that in the radial direction.[1,2] Despite some empirical success in controlling this coercivity anisotropy, the associated structural mechanism has not been determined. Magnetic anisotropy is affected by a number of factors, e.g. magnetic domains in Co align preferentially along the long axis of high aspect ratio grains, parallel to the c axis of hcp crystals, and in directions of compressive stress. Published work has shown indirect, but inconclusive evidence for each of these mechanisms, so more rigorous study is appropriate. Through-foil and cross-section TEM analysis; including BF, DF, SAD, and high resolution imaging is being used to analyse the subtle variations in nanostructure and crystallography which may affect magnetic properties.

Through-foil, BF micrographs (FIG 1) show the morphology of the (a) textured and (b) untextured samples. The directionality in FIG 1a is due to thickness variations caused by the substrate texturing, but the individual grains remain nearly spherical as in the untextured substrate. Grain shape anisotropy does not appear to be a predominant mechanism. If crystallography dominates the magnetic anisotropy in the circumferential direction, one would expext preferred orientation of the magnetically easy c-axis [00.2] in that direction. It has been suggested that this preferred orientation could result from epitaxial growth of the (00.2) planes of the Co alloy (2.04Å) upon the (110) planes of the Cr (2.04Å), both of which would align with the circumferential texturing of the substrate.[6] Both diffraction patterns in Figure 1 show missing (11.0) rings, corresponding to perpendicular orientation of that plane. The directionality in the SAD pattern of the textured sample may be due to preferred orientation of multiple planes, including (00.2), or observation of higher order Laue planes due to the perpendicular (11.0) orientation and the surface tilt of the texture lines. Dark field micrographs (FIG 2) confirm the texturing and show grains of the same orientation following individual texture lines, but the associated mechanism is not revealed yet.

A high resolution through foil image of the textured sample (Figure 3), shows the orientation of the Co grains in more detail. Faulting occurs on the basal (00.2) planes so the predominance of faulted grains is evidence for the suggested c-axis in plane orientation. However, the proposed predominance of grains with c-axis parallel to the texture lines is not observed. It is found to align in a variety of directions in the plane of the film. A cross-section micrograph with the circumferential direction perpendicular to the electron beam, shown in Figure 4, has a diffraction pattern with the Cr (002) and Co (11.0) planes oriented in the growth direction, and the three inner rings all somewhat oriented parallel to the texture direction. These rings correspond to the Co (10.0) (inner ring), Co (00.2) and Cr (110) (middle ring), and Co (10.1) (outer ring) planes. This, along with further evidence from high resolution imaging of cross-section samples (not shown), suggests that the epitaxy is more complicated than previously proposed, with epitaxial growth of multiple planes upon the Cr (110) planes. This could explain the multiple orientations of the Co [00.2] directions in Figure 3.

The power of TEM as a tool for analysing the morphology of the Cr and Co alloy layers and orientation relationships between them is clear. Further careful microscopy should bring about a more complete understanding of the complex crystallography involved. This analysis is essential to the understanding and effective control of magnetic anisotropy in thin film magnetic media.[7]

References

1   E. Teng and N. Ballard, IEEE Trans. Magn., MAG-22, 579 (1986)
2   S. Uchinami, et al., IEEE Trans. Magn., MAG-23, 3408 (1987)
3.   T. Arnoldussen, et al., IEEE Trans. Magn., MAG-20, 821 (1984)
4.   R. Nishikawa, et al., IEEE Trans. Magn., VOL 25, NO. 5, 3890 (1989)
5.   T. Lin, R. Alani, and D. Lambeth, JMMM (1988)
6.   K. Furusawa, et al., IEEE Trans. Magn., VOL. 26, NO 5, 22 (1990)
7.   Partial funding for this work was provided by KOMAG Inc. Contributions to this research from R. Ranjan, T. Yamashita, and L. Chan of KOMAG, and R. Sinclair of Stanford University are much appreciated.
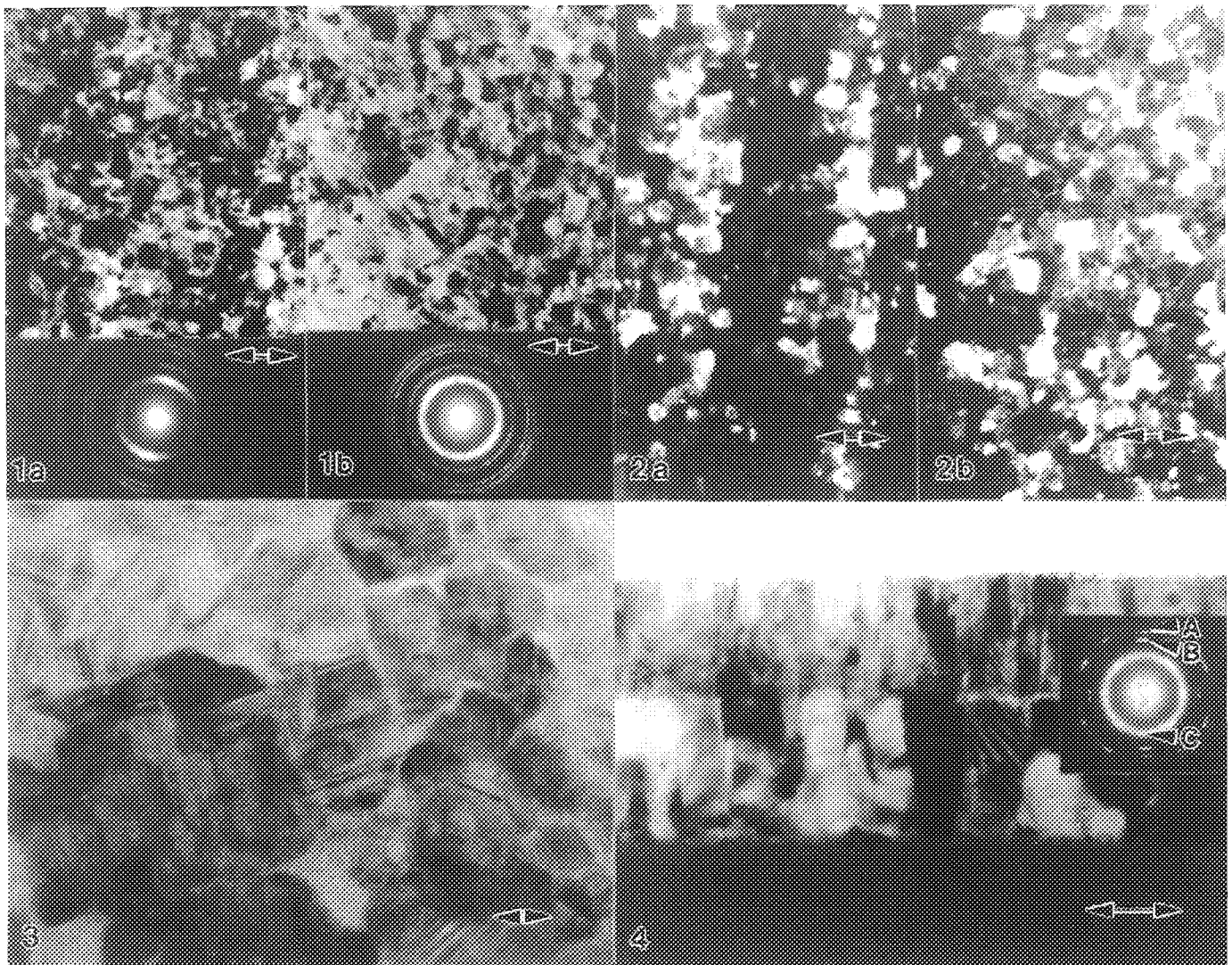
FIG.1. Through-foil BF images of $Co_{84}Cr_{14}Ta_2$ on (a) textured substrate (b) polished substrate. [Bar=100nm.]
FIG. 2. Dark Field of same areas as FIG. 1.
FIG. 3. High resolution through-foil of $Co_{84}Cr_{14}Ta_2$, on textured substrate. [Bar=10nm.]
FIG. 4. Cross-section of $Co_{84}Cr_{14}Ta_2$, on textured substrate. [Bar=50nm.] [A=Cr (002)] [B=Co(11.0)] [C=triple ring in to out Co (10.0), Co (00.2)+Cr (110), and Co (10.1)]

Microstructures and Recording Performances of Longitudinal Media Using Different Atomic Mass Underlayer Materials

Thao A. Nguyen, Tadashi Yogi and Steven Lambert

IBM Research Division, Almaden Research Center, San Jose CA 95120

Magnetic and recording properties of Co-based longitudinal media are strongly influenced by the underlayer and sputtering conditions.[1,2] We have investigated the relationship between magnetics, recording noise and microstructural characteristics of CoPtCr media on Mo and W underlayers over a sputtering pressure range 3-24 mtorr, complementing our earlier work of Cr underlayer.[1,2]

The media structure is C/CoPtCr/Mo or W, with thicknesses of 25/25/100 nm respectively. The film structure was sputter-deposited in a DC S-gun magnetron system. The remanence-thickness product, $M_r t$, was kept in the range of 0.6-1.0 10^{-3} emu/cm^2. The films were characterized by a vibrating sample magnetometer for their magnetic properties. Magnetic recording measurements were made with thin film inductive write heads with a track width of about 10 μm at a flying height of about 5 μm. The microstructures were studied using the JEOL JEM 4000 FX and AKASHI 002-B transmission electron microscopes.

We find a systematic dependence of transition noise on the atomic mass of the underlayer. At low sputtering pressure and for a 100 nm underlayer thickness, the noise performance, $S_0 NR$, decreases in going from Cr to Mo to W where $S_0 NR = 20 \times \log$(Isolated pulse amplitude/Integrated media noise voltage at 2 kfc/mm). As the sputtering pressure is increased to 24 mtorr, $S_0 NR$ improves for all underlayers and converges to high values of 37-39 dB. The improvement is due to better isolation of CoPtCr grains which is controlled by the underlayer morphology. At low pressures, TEM micrographs (Figures 1a, 2a, 3a) reveal that the magnetic grains become more continuous in going from Cr to Mo to W. At highest pressure (Figures 1b, 2b, 3b) the magnetic grains are decoupled on all underlayers. The decoupling of the magnetic grains is associated in media transition noise, similar to our previous report.[2] We can interpret the trend in the underlayer growth morphology in terms of the mobility of the sputtered species upon arrival on the growing film surface. Easily thermalized light elements develop columnar structure whereas the higher mobility of heavier elements promotes more smooth and continuous films. The observed microstructures correspond to Zone 1 and Zone T structures in Thornton's microstructure diagram.[3]

References

1. T. A. Nguyen et al., Proceedings XIIth International Congress
for Electron Microscopy, Vol. 4, 770, 1990.
2. T. Yogi et al., IEEE Trans. Mag., Vol. 26, No. 5, 1990.
3. J.A. Thornton, Proceedings of SPIE. Vol. 821, 95, 1987.
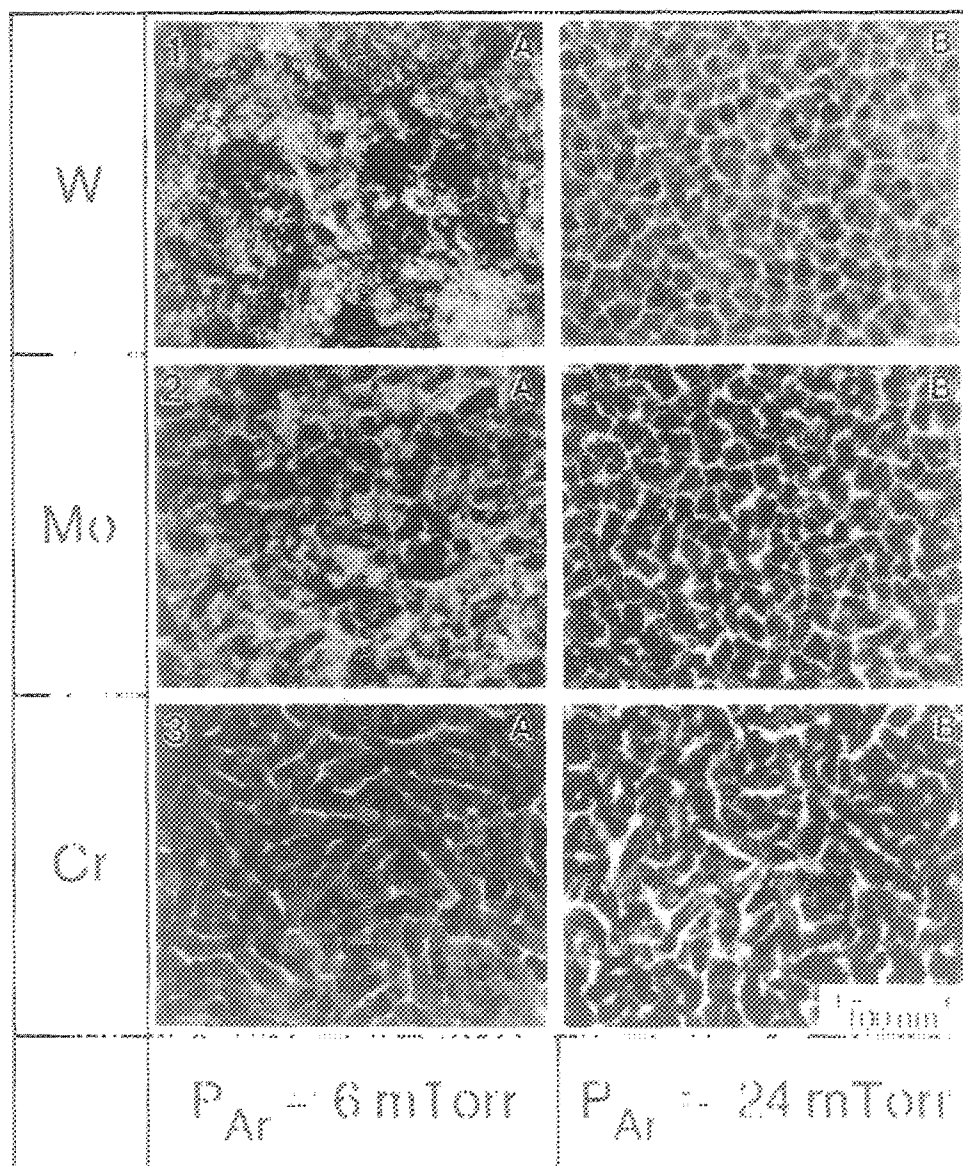
Figures 1a, 2a, 3a. Plane view TEM microstructures of W (1a), Mo (2a) and Cr (3a)/ CoPtCr media sputtered at Argon pressure of 6 mtorr

Figures 1b, 2b, 3b. Plane view TEM microstructures of W (1b), Mo (2b) and Cr (3b)/ CoPtCr media sputtered at Argon pressure of 24 mtorr.

A HIGH-RESOLUTION TRANSMISSION ELECTRON MICROSCOPY INVESTIGATION OF THE INTERFACIAL STRUCTURE OF CoNiCr/Cr BI-LAYER MAGNETIC THIN FILMS+

B. Y. Wong* and D. E. Laughlin*

*Department of Metallurgical Engineering and Materials Science, Carnegie Mellon University, PA 15213

The use of performance enhancement underlayers is a common practice in production of magnetic recording media[1]. In the case of Co-based alloy deposited on chromium underlayers, the enhancement in the in-plane coercivity is phenomenal. Conventional and High Resolution TEM are powerful tools in the investigations of structure of these films because of the very fine grain size of the films. Previous microdiffraction studies on these bi-layer films have revealed the apparent grain to grain orientation relationship (O.R.) between individual grains in the two layers in the plane view sections of these specimens[2]. Since the underlayer exerts such a great influence on the structure and properties of the overlayer, it is of great importance to study the interfacial structure of these bi-layer films. The lattice matching across the interface and the interfacial defects which formed could very well provide explanation(s) to the enhancement in the in-plane coercivity.

The system used for this study is the bi-layer CoNiCr/Cr thin films. They were produced by RF sputtering onto Corning 0211 glass substrate. Cross sectional specimens were made by first binding thin sections of specimen with epoxy, followed by mechanical thinning. The final thinning process was carried out by ion-milling. The specimens were studied in a JOEL 4000EX Electron Microscope.

Two O.R.s were observed in the cross section specimens with HRTEM in the hcp CoNiCr/ bcc Cr bi-layer thin films. The first one is that of Pitsch-Schrader (Fig.1): $(11\bar{2}0)$hcp//(001)bcc, [0001]hcp//[110]bcc. The Cr surface that is parallel to the plane of the film is (001). As a result of this O.R., the hcp c-axis lies preferentially in the plane of the film. The lattice spacing for (0002) CoNiCr and (110) Cr has a misfit of only 0.6% and thus most of the misfit occurs in the normal direction. The extra planes to accommodate the misfit are denoted by the white arrows. The obtuse contrast at the interface in between the arrows is believed to have been caused by the misfit strain/defect at the interface. Figure 2 is an image of the interface with the same O.R. but studied along another zone axis. The interface is not as sharp as in figure 1 and this is because the observed zone axis is not along that of best fit. The contrast can be attributed to the strain or defects at the boundary and it extends beyond two atomic layers at the interface. A total of between five to six atomic layers are involved in the strain relaxation process at the interface.

The other O.R. observed was that of Potter (Fig.3): $(10\bar{1}1)$hcp//$(1\bar{1}0)$bcc, $[\bar{2}110]$hcp//$[\bar{1}11]$bcc In this case, the Cr (110) and the CoNiCr $(10\bar{1}1)$ plane is parallel to the interface. The HR image shows that the atoms in the bcc (110) and the hcp $(10\bar{1}1)$ planes line up with each other. Further studies of the atomic positions indicate that the bcc $[\bar{1}11]$ and hcp $[\bar{2}110]$ are parallel to each other and they lie at an angle of 35° with respect to the plane of the paper. No defect contrast was observed at this interface indicating extremely good matching. As a result of this epitaxial growth, the c-axis of the hcp CoNiCr is situated at 28° with respect to the interface.

References
[1]   J. P. Lazzari, I. Melnick, and D. Randet, IEEE Trans. Magn. MAG-3, 205 (1967).
[2]   K. Hono, B. Y. Wong, and D. E. Laughlin, J. Appl. Phys. 68, 4734 (1990)
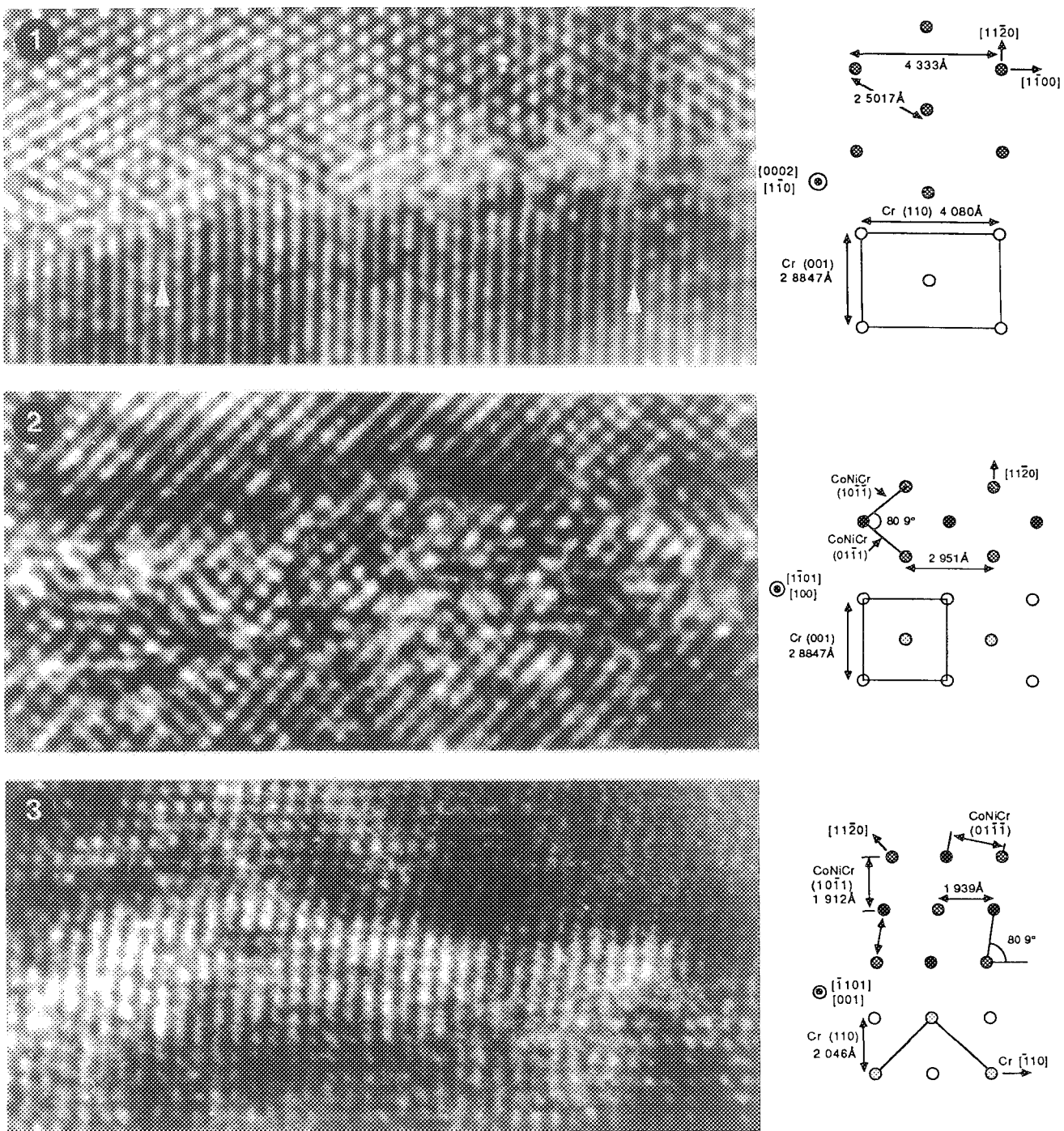
Figure 1. Cross section of a CoNiCr/Cr bi-layer thin film with the Pitsch-Schrader O.R..: (11$\bar{2}$0)CoNiCr//(001)Cr, [0001]CoNiCr//[110]Cr. The extra planes in the Cr underlayer are indicated by the white arrows.

Figure 2. Cross section of a CoNiCr/Cr bi-layer thin film with the Pitsch-Schrader O.R. The observation zone axes for the two layers are [1$\bar{1}$01] and [100] respectively.

Figure 3. Cross section of a CoNiCr/Cr bi-layer thin film with the Potter O.R.: (10$\bar{1}$1)CoNiCr//(1$\bar{1}$0)Cr, [$\bar{2}$110]CoNiCr//[$\bar{1}$11]Cr.

MICROSTRUCTURAL CHARACTERIZATION OF CoPtCr/Cr THIN-FILM DISKS BY CROSS-SECTION TEM AND ELONGATED PROBE MICRO-DIFFRACTION

M.A. Parker*, K.E. Johnson**, C. Hwang*, and A. Bermea*

*IBM Storage Systems Products Division, San Jose, CA 95193
**IBM Storage Systems Products Division, Rochester, MN 55901

We have reported[1] [2] the dependence of the magnetic and recording properties of CoPtCr recording media on the thickness of the Cr underlayer. It was inferred from XRD data that grain-to-grain epitaxy of the Cr with the CoPtCr was responsible for the interaction observed between these layers. However, no cross-sectional TEM (XTEM) work was performed to confirm this inference. In this paper, we report the application of new techniques[3] for preparing XTEM specimens from actual magnetic recording disks, and for layer-by-layer micro-diffraction with an electron probe elongated parallel to the surface of the deposited structure which elucidate the effect of the crystallographic structure of the Cr on that of the CoPtCr.

XTEM specimens were prepared from magnetic recording disks[1] [2] by modifying[3] a technique used to prepare semiconductor specimens.[4] After 3mm disks were prepared per the standard XTEM procedure,[4] these disks were then lapped using a tripod polishing device.[5] [6] A grid with a single 1mmx2mm hole was then glued with M-bond 610 to the polished side of the disk. The specimen was inverted and lapped on a polishing puck with a transparent center post using the tripod until the Si became transparent. The specimen was then transferred to an ion-milling holder, especially modified with two graphite beam stops mounted to blank the ion beam from the side with the magnetic layer. Ion-milling proceeded from the NiP side of the laminated structure, which masked the CoPtCr/Cr layers to produce more uniform thin area. The milling condtions were nominal, except for liquid nitrogen cooling of the stage. This procedure results in specimens with superior drift stability, suitable for the exposures, > 5 min, essential for micro-diffraction. Elongated probes for micro-diffraction can be obtained either by scanning the beam parallel, or by adjusting the condenser stigmation coils to make the beam an astigmatic ellipse of high aspect ratio parallel to the interface of interest. Elongated probe micro-diffraction (EPMD) patterns were obtained on the JEOL 4000FX at 400 keV with an astigmatic probe 10nm wide by 300nm long. The smallest condenser aperture was used to minimize the effect of astigmatism in the reflections.

Figure 1a is a triple exposure consisting of a bright field image of a CoPtCr/Cr bilayer, the corresponding SAD pattern, and the image of the smallest, 10 μm, SAD aperture used to define the area of analysis. Figure 1b shows the SAD pattern alone. It is well known that spherical aberration[7] limits the areal resolution of SAD patterns. Thus, the SAD pattern is a convolution of the electron diffraction patterns due to the CoPtCr, Cr, and NiP layers, as well as the glue layer. Micro-diffraction overcomes this difficulty but at a loss of statistical accuracy because fewer grains are analyzed. However, if the probe is elongated parallel to the interfaces of interest, it becomes possible to average the contributions of scores of grains at a given depth below the surface of the thin film, which in effect allows one to depth-profile the crystallographic structure. Figures 2a-d show the deconvolution of the SAD pattern using EPMD. Figure 2a shows that the amorphous rings in the SAD pattern are due to the NiP; figure 2b, that the Cr has a strong 100* reflection perpendicular to the surface of the film indicative of a <100> fiber texture; figure 2c, that there is pairing of the reflections of the Cr with those of the CoPtCr indicative of epitaxy between the two layers; figure 2d, that the CoPtCr has a strong 11.0* reflection perpendicular to the surface of the film indicative of a <11.0> fiber texture. Similar EPMDs from CoPtCr/Cr layers with thicker Cr underlayers, > 120 nm, show a gradual change from a

<100> fiber texture in the Cr layer adjacent to the NiP to a <110> fiber texture adjacent to the CoPtCr,[2] which results in the loss of the <11.0> fiber texture in the CoPtCr. It is the strong <11.0> fiber axis texture in the CoPtCr with the thin Cr underlayer that gives rise to a greater preponderance of grains with c-axes in the plane of the film which has been correlated with a high squareness.[1]

In summary, XTEM and EPMD have provided insight into the mechanism of grain-to-grain epitaxy for films with thin Cr seed layers, and of the evolution of the crystallographic structure of those films with thicker Cr underlayers. The evoluiton from a <100> fiber texture to a <110> in thicker Cr films revealed by EPMD explains the decreasing values of squareness in films grown on thicker Cr underlayers. In addition, we have applied the technique of XTEM combined with EPMD to numerous other thin film and multilayer systems with equally interesting results.

References

1. K. E. Johnson et al., J. Appl. Phys., 67(1990)4686.
2. M. A. Parker et al., J. Appl. Phys., (submitted to '91 Intermag-MMM).
3. M. A. Parker et al., MRS Symp. Proc., 199(1990)331.
4. J. Bravman and R. Sinclair, J. Elec. Micro. Techs., 1(1984)53.
5. S. J. Klepeis et al., MRS Symp. Proc., 115(1988)179.
6. J. P. Benedict et al., MRS Symp. Proc., 199(1990)189.
7. P. Hirsch et al., Electron Microscopy of Thin Crystals, Huntington, New York: Krieger (1977)18.
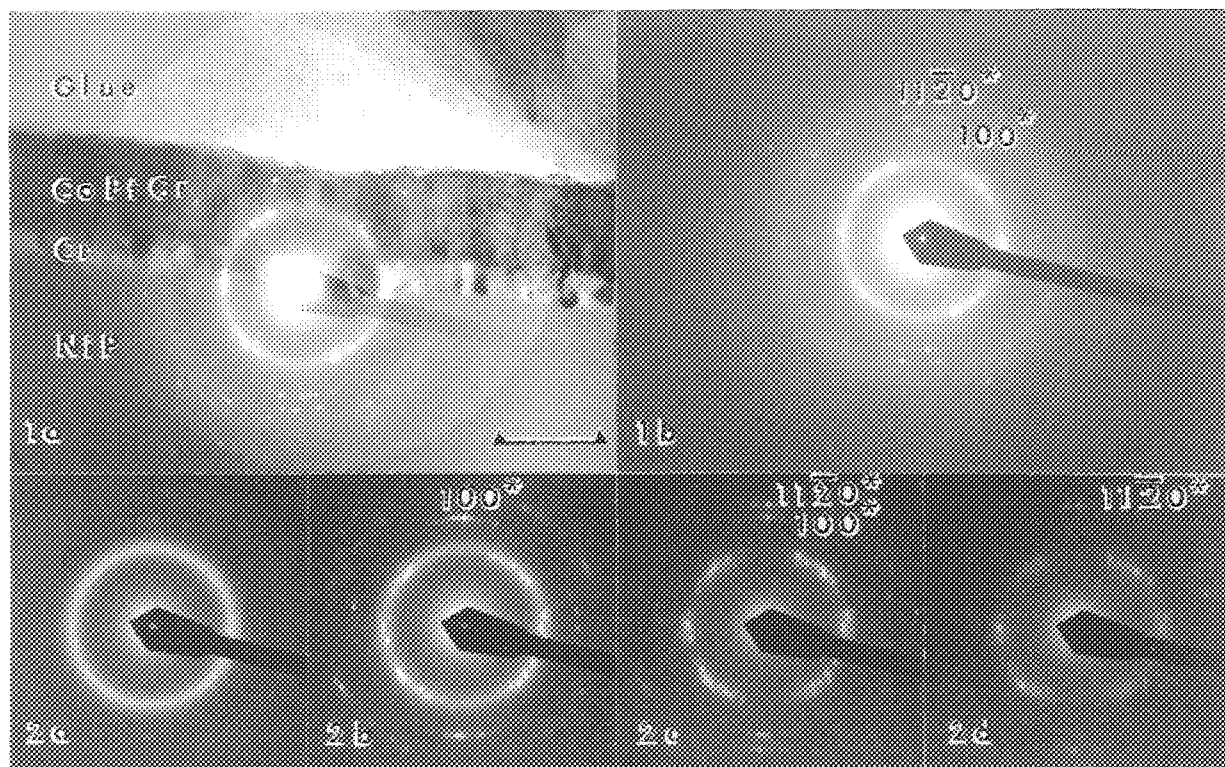
Fig. 1.--Cross-section TEM (XTEM) of CoPtCr/Cr on NiP illustrating a) triple exposure consisting of bright field image, corresponding SAD pattern, and image of field limiting aperture, and b) corresponding SAD pattern alone. Bar = 50 nm.
Fig. 2.--Elongated probe micro-diffraction (EPMD) patterns taken of a) NiP underlayer, b) Cr seed layer, c) interface between Cr and CoPtCr layers, and d) CoPtCr layer.

SCANNING ELECTRON MICROSCOPY WITH POLARIZATION ANALYSIS: AN UPDATE

J. Unguris, M. W. Hart, R. J. Celotta, and D. T. Pierce

National Institute of Standards and Technology, Gaithersburg, MD 20899

Over the past ten years the technique of scanning electron microscopy with polarization analysis (SEMPA) has rapidly evolved from a scientific curiosity to a useful analytical tool for looking at a material's magnetic microstructure. Several reviews of the technique have been published elsewhere[1,2,3]. SEMPA has been successfully used to analyze various technological problems such as: noise in magnetic and magneto-optical recording media, domain wall motion in thin film recording heads, and domain structures in small Permalloy shapes. Basic science applications of SEMPA include quantitative studies of the influence of the surface on the structure of magnetic domains and domain walls, and studies of magnetic microstructures in ultra-thin (0.1 - 1 nm) ferromagnetic films. Many current applications of SEMPA make use of the technique's surface sensitivity to probe the magnetism of thin films and multilayers.

The SEMPA experimental set-up has been described in detail elsewhere[4]. Basically, a SEMPA apparatus consists of a scanning electron microscope, an ultra-high vacuum specimen chamber, and a detector for measuring the spin polarization of the secondary electrons. For conventional transition metal ferromagnets, the electron spin polarization is directly proportional to the specimen's magnetization. A SEMPA measurement therefore provides a direct image of the magnitude and direction of the magnetization. This image is also independent of the samples's topography. SEMPA is easily combined with other ultra-high vacuum compatible surface analysis tools such as Auger electron spectroscopy, reflection high-energy electron diffraction (RHEED), ion milling and thin film evaporators. With these additional tools SEMPA can be used to study the magnetic microstructure of thin films and multilayers prepared in situ.

Two examples of in situ deposited thin films are presented in the figures. Fig. 1 shows the magnetic domain pattern of an electrically insulating Fe garnet film that was coated with a 2 nm thick Fe film. The Fe film eliminates charging and the magnetization of the Fe replicates that of the garnet. Fig. 2 shows a SEMPA measurement of an Fe/Cr/Fe sandwich. The magnetic coupling of the Fe/Cr/Fe system was studied as a function of Cr thickness by depositing a Cr wedge. Fig. 2a shows the domain pattern of the Fe crystal substrate. Fig. 2b shows the domains in the Fe/Cr/Fe sandwich. The domain reversals show that the coupling oscillates between ferromagnetic and antiferromagnetic as a function of Cr thickness.

References

1. J. Unguris et al., in Chemistry and Physics of Solid Surfaces VIII, Springer-Verlag, (1990) 239.
2. K. Hayakawa, K. Koike, H. Matsuyama, Hitachi Inst. News 14, (1988) 11.
3. J. Kirschner, in Surface and Interface Characterization by Electron Optical Methods, Plenum, (1987) 267.
4. M. R. Scheinfein et al., Rev. Sci. Instr. 61, (1990) 2501.
5. This work was supported in part by the Office of Naval Research.
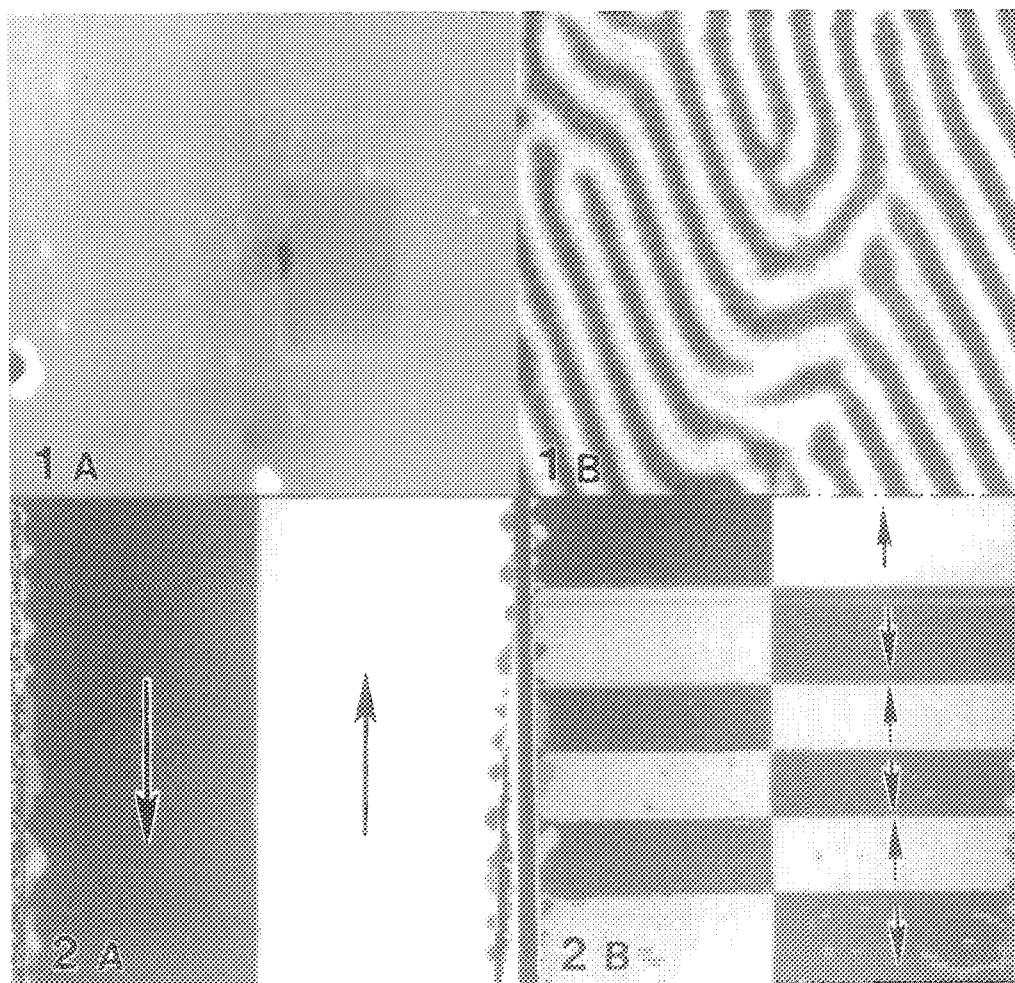
FIG. 1.--SEMPA measurement of Fe garnet coated with 2 nm thick Fe film. (A) is topographic image and (B) is simultaneously measured magnetization image from same region. Images are 40 μm across. FIG. 2.--SEMPA measured magnetization of a clean Fe crystal in (A) and after growing a Fe/Cr/Fe multilayer in (B). Cr spacer layer thickness varies from 0 near the top of the image to 5 nm at the bottom. Domain reversals show reversals in magnetic coupling with Cr thickness variation. Arrows indicate magnetization directions. Images are 400 μm across.

THE DEPTH SENSITIVITY OF TYPE II MAGNETIC CONTRAST

R.P. Ferrier and S. McVitie

Department of Physics and Astronomy, The University of Glasgow, Glasgow G12 8QQ, Scotland

Type II magnetic contrast arises from the change in the effective electron backscattering coefficient due to interaction of the scattered electrons and the magnetic induction present within a ferromagnetic sample; both domain and "domain wall" contrast are observable depending on the relative geometry of the beam, the specimen and the detector (for a review see Tsuno).[1] A major problem with Type II contrast is that it is very weak and can be swamped easily by even relatively low topographic or atomic number contrast. For studies of the domain wall dynamics in thin film recording heads Wells and Savoy[2] overcame this problem by driving the head with an a.c. voltage and detecting, via a lock-in amplifier, the synchronous part of the backscattered signal. This work was performed in an SEM operating at up to 40kV; we have extended the method by employing a modified JEOL 2000FX TEM/STEM (Fig. 1) which operates at up to 200kV and has a special objective lens to allow observation of the magnetic specimen in field-free space whilst the objective lens is excited.[3] In the synchronous detection method the geometry shown gives an image where pairs of black and white lines show the maximum extent of wall movements over one drive period.

In an earlier study Ferrier and Geiss[4] showed that the two layers of permalloy which make up the P2 polepiece of a thin film recording head could exhibit totally different domain structures and this was elucidated by comparing images taken at different accelerating voltages and with different head drive voltages. The capability of depth profiling of the magnetic structure is enhanced with the 200kV now available and provides a feature unique to the electron method and hence an advantage over the more straightforward Kerr optical imaging techniques. We illustrate this with two examples. Thin film recording heads produced by LETI[5] in Grenoble have a structure where the main polepieces are on the surface of the slider and coplanar; the return path for the flux is provided by a lower polepiece of quite different geometry lying some 15μm below the surface A series of images taken at increasing accelerating voltage (Fig. 2) show that at 60kV only the structure in the upper polepiece is visible whereas at 100kV structures in both upper and lower polepieces are seen simultaneously; at 160kV image contrast is dominated by the lower polepiece. In this instance the totally different geometry of the upper and lower polepieces helps to distinguish the structures. In more conventional recording heads the structure is protected by a thick ~20μm alumina layer above the P2 polepiece. Although this can be removed chemically to allow for the synchronous method of Type II imaging at 60kV, there is always the worry that the stress state may be altered and hence change the magnetic structure. We have now demonstrated that by operating in range 160 - 200kV we can image the domain walls in P2 through this very thick film (Fig. 3). For comparison the image of another head which has approximately half the alumina thickener is shown. Undoubtedly, the presence of thick alumina overlayers makes it much more difficult to differentiate different structures in the two permalloy layers which make up P2. Currently we are pursuing both experimental studies and theoretical modelling by Monte Carlo methods to quantify the depth sensitivity of the method in the presence of alumina overlayers of various thicknesses.[6]

References

1)   K. Tsuno, Rev. Solid State Science (1988) 2, 1.
2)   O.C. Wells and R.J. Savoy, IEEE Trans.Mag., MAG-17 (1981), 1253.
3)   R.P. Ferrier et al., IEEE Trans.Mag., MAG-26 (1990), 1337.
4)   R.P. Ferrier and R.H. Geiss, Electron Microscopy 1986, 2, 1725.
5)   J.P. Lazzari and P. Deroux-Dauphin, IEEE Trans.Mag., MAG-25 (1989), 3190.
6)   Support from IBM General Product Division, San Jose and from LETI in Grenoble is acknowledged. In part this work was also supported by the EEC through the CAMST initiative
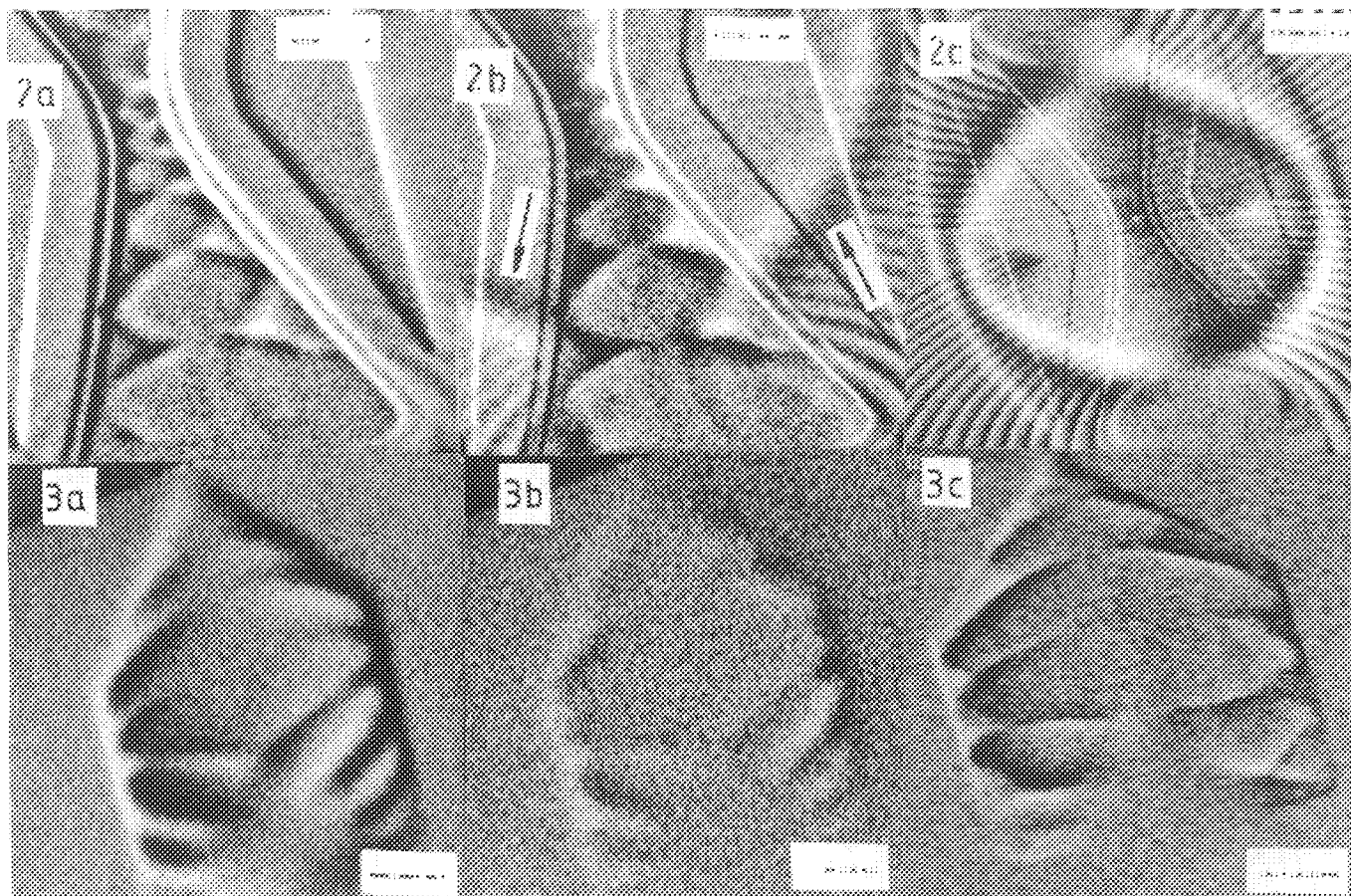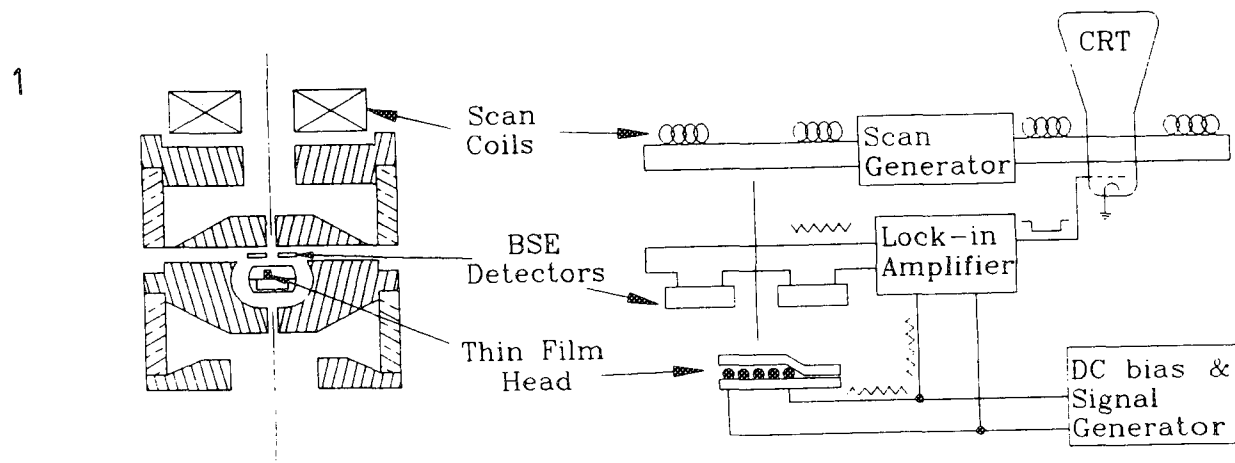
FIG. 1.--Schematic of the arrangement for backscattered electron imaging with synchronous detection.[3] The microscope is the JEOL 2000FX with the special BMP 20 polepiece.

FIG. 2.--Coplanar polepiece thin film recording head produced by LETI, Grenoble.

a) 60kV image, head drive current 10mA peak to peak. Bar = 12μm.

b) 100kV image, head drive current 10mA peak to peak. Bar = 12μm.

Note the appearance of domain walls in the lower polepiece as indicated by the arrows.

c) 200kV image, head drive current 25mA peak to peak. Bar = 20μm.

FIG. 3.--Thin film recording head produced by IBM General Products Division.

a) 200kV image of head A which has ~20μm alumina overlayer; head drive current 10mA peak to peak. Bar = 20μm.

b) 120kV image under same conditions as a).

c) 120kV image of head B which has ~10μm alumina overlayer; head drive current 10mA peak to peak. Bar = 20μm.

MAGNETIC FORCE MICROSCOPY

P. Grütter ▽, D. Rugar, H.-J. Mamin, and T.R. Albrecht

IBM Research Division, Almaden Research Center, San Jose, CA 95120
▽ Present address: Institute of Physics, U. of Basel, Switzerland

The aim of this talk is to give a short introduction to the technique of magnetic force microscopy (MFM), review recent advances in instrumentation and present measurement on various magnetic materials.

MFM [1, 2] is a non-destructive method which allows the imaging of magnetic structures with little or no sample preparation on a 50-100 nm scale. The central component of every MFM is a sharp magnetic tip mounted on a flexible cantilever. The interaction of the magnetic tip with a sample stray field leads to a change of both cantilever deflection and resonant frequency. These changes are measured with a sensitive displacement probe, eg. an interferometer. Images are generated by raster scanning the sample relative to the tip and recording the tip-sample interaction as a function of position

Recent advances in instrumentation have made MFM a more practicel and easier to use technique with a larger scope of applications [3, 4, 5]. In particular, micromachined Si cantilevers with integrated tips have been batch fabricated for use in MFM by coating them with thin ferromagnetic films [3, 4] By choosing appropriate coatings, the magnetic properties of these force sensors can be tailored. Furthermore, these cantilevers achieve high mechanical Q factors (exeeding 20 000) in moderate vacuum (mTorr). This leads to an increase of sensitivity by more than an order of magnitude. A FM detection scheme has been developed which allows force microscopy with these high Q cantilevers without compromising detection bandwidth [5].

Fig. 1 shows MFM images of transitions written in a longitudinal magnetic recording medium acquired with three different thin film tips. The stray field component perpendicular to the sample was imaged with a 15 nm thick Co coated tip magnetized parallel to its tip axis (left image). By magnetizing a 15 nm thick CoPtCr coated tip perpendicular to its axis, the sample in-plane stray field component was measured (middle image). A NiFe (Permalloy) coated tip is magnetically soft. These tips thus respond to the total stray field emanating from the sample (right image). Figure 1 thus demonstrates that different components of the sample stray field can selectively be measured by appropriately magnetizing hard magnetic tips in an external field.

MFM is not limited to the imaging of magnetically hard samples. Thin film tips exhibit a very small magnetic stray field. Permalloy squares of 30 nm thickness and a coercivity of less than 2 Oe can be imaged without observing any tip stray field induced domain wall motion (Fig 2)

References
[1] Y. Martin and H.K. Wickramasinghe, Appl. Phys. Lett 50, 1455 (1987)
[2] J.J. Saenz et al., J. Appl. Phys. 62, 4293 (1987)
[3] P. Grütter et al., Appl. Phys. Lett. 57, 1820 (1990)
[4] P. Grütter et al., J. Appl. Phys. 69, (1991)
[5] T. Albrecht et al., J. Appl. Phys. 69, 668 (1991)

Figure 1· MFM images of transitions in a longitudinal magnetic recording sample imaged with three different tips (see text)
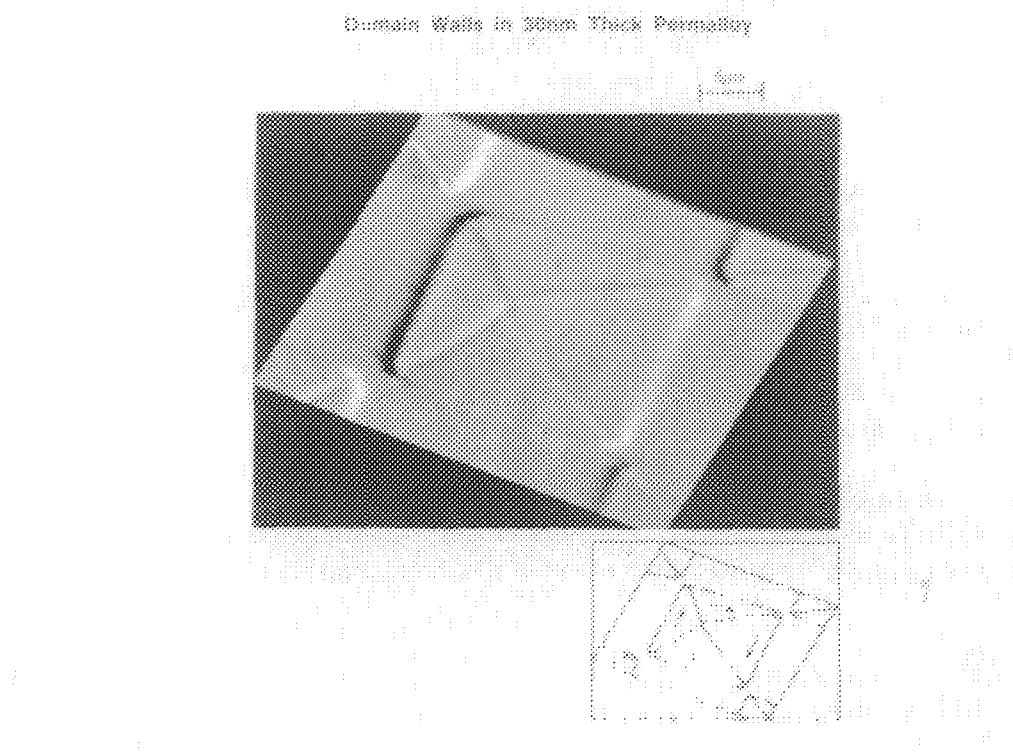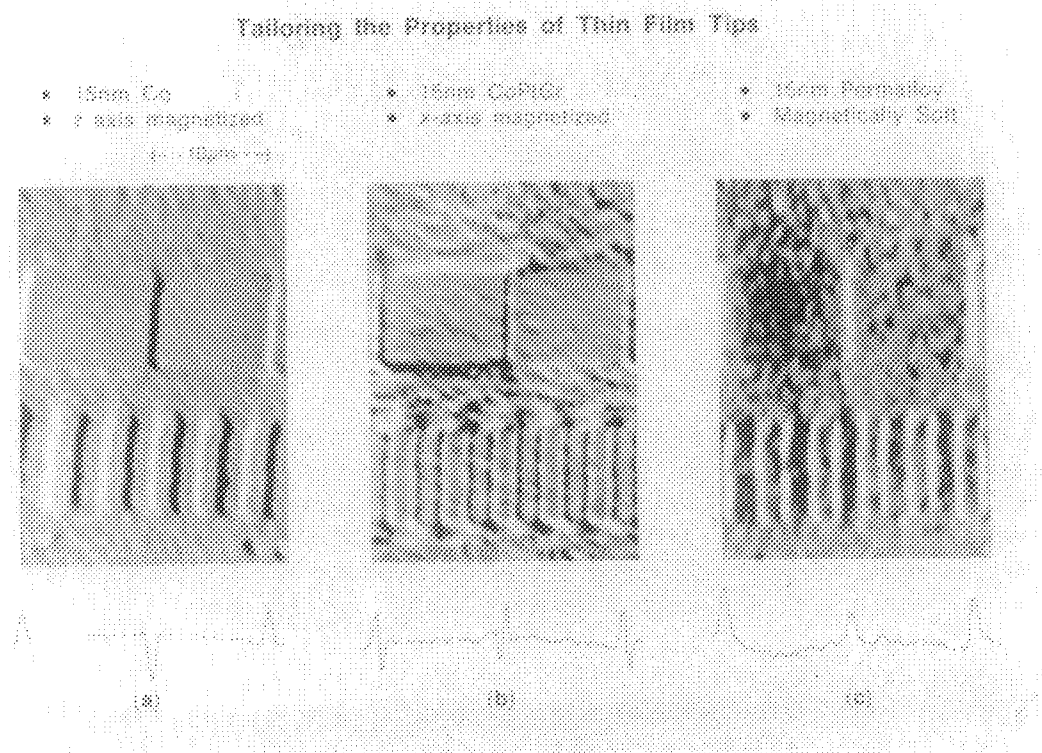
Figure 2: MFM image of a 20 μm NiFe square. The domain walls, including some small bifurcations near the corners, are clearly seen

A STUDY OF THE MAGNETIC STRUCTURE OF MAGNETIC FORCE MICROSCOPE TIPS USING TRANSMISSION ELECTRON MICROSCOPY

S. McVitie[*] and U. Hartmann[**]

*Department of Physics and Astronomy, University of Glasgow, Glasgow G12 8QQ, U.K
**Institute for Thin Film and Ion Technology, Forschungszentrum Jülich, D-5170 Jülich, Germany

Magnetic force microscopy[1,2] (MFM) has become an important tool in the investigation of the micromagnetic structure of magnetic systems. The interaction of stray magnetic field from a sample with a sharp magnetic tip is measured as the tip is scanned across the surface of the sample. Characterisation of the tip-sample interaction is of paramount importance if the measured signal obtained by MFM is to be put on a quantitative basis. In this paper we describe the preliminary results obtained by studying MFM tips using the Lorentz techniques of transmission electron microscopy.

The MFM tips were prepared from 25μm thick Ni wire by an electrolytic etching and polishing technique which produces tips with a sharp apex of radius <100nm[3]. The nature of the tips meant that only the very end of the tips were thin enough to be observed using 200kV electrons in TEM. In order to characterise the magnetic structure of the tips it was therefore necessary to rely on observing the magnetic stray field external to the tips produced by the magnetisation distribution within them. Of particular interest is the extent and magnitude of the stray field from the end of the tip as this field may affect the magnetic structure of the sample under investigation during MFM observations.

Examination of the tips was made using the JEOL 2000FX at Glasgow which is equipped with a special polepiece for magnetic imaging. (This polepiece is very similar to one designed previously[4]). In this microscope both TEM and STEM imaging modes are implemented with the specimen located in field free space. A probe size of <50nm is available in the latter. The imaging techniques used in this study were the Foucault and differential phase contrast (DPC) modes of Lorentz microscopy[5]. Both these modes are suited to the investigation of stray fields from samples and in the latter the detected signals are linearly proportional to in-plane components of magnetic induction integrated along the electron path.

Images obtained using the Foucault mode from a MFM tip indicate that the tips are uniformly magnetised at their apex and in adirection along the axis of the tip from the observations of the stray field (Fig. 1a). Also visible along the length of the tip at the lower edge are changes in contrast revealing that the tip is not uniformly magnetised along the whole of its length (Fig. 1b). The extent of the stray field, from the end of the tip, evident from these images suggest that the uniformly magnetised region covers an area which extends a distance less than ~1μm from the apex. A DPC image of a different tip, sensitive to the component of integrated induction along the axis of the tip, which although appears slightly damaged confirms this magnetic structure (Fig. 2). The advantage of the linear imaging conditions of DPC is illustrated by the intensity profile from the digital image acquired by DPC taken along the axis of the tip from the apex (Fig. 3) Although this intensity variation corresponds to the integrated field component along the electron path it clearly shows the decay characteristics of the field from the end of the tip.

Information provided by analysis of the experimental data presented here will be used to help our understanding of the tip-sample interaction in MFM. Specifically we expect the results to lead to an improved model of the tip's magnetic structure and its response to magnetic interactions. Such information is of crucial

importance in order to put the interpretation of MFM images on a quantitative basis[6].

References

1. Y. Martin and H. K Wickramasinghe, Appl. Phys. Lett , (1987)50, 1455
2. U. Hartmann, J. Magn. Magn. Mat., (1990)83, 545.
3. T. Göddenhenrich et al., J. Micros., (1988)152, 527
4. K. Tsuno and T. Taoka, Japan. J. Appl. Phys., (1983)22, 1047.
5. J. N. Chapman, J. Phys. D:Appl. Phys., (1984)17, 623.
6. This collaborative project was set up with support from the EEC through the CAMST initiative.
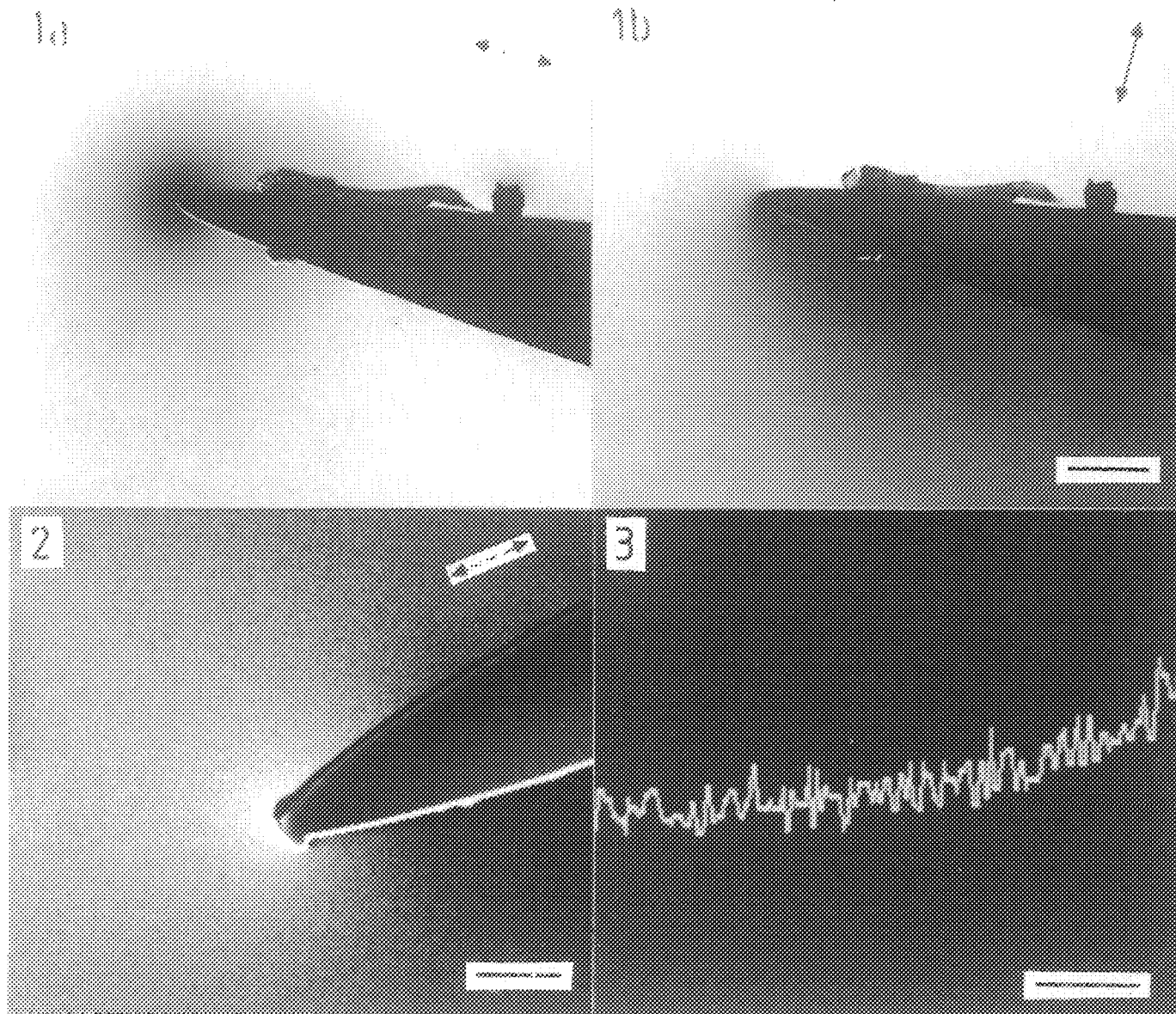
FIG. 1.--Pair of Foucault images of a Ni MFM tip. Direction of sensitivity to in-plane magnetic induction in each image is indicated by arrows Note stray field at end of tip. Bar = 1μm.

FIG. 2.--Digital DPC image of tip which has been slightly damaged. Direction of in-plane induction mapped is indicated by arrow. Bar = 1μm.

FIG. 3.--Intensity profile from FIG. 2 showing nature of decay of integrated magnetic induction from end of tip as function of radial distance from end of tip. Bar = 0.5μm.

HREM CONTRIBUTIONS TO MICROSTRUCTURAL INVESTIGATIONS OF MAGNETIC THIN FILMS AND ULTRATHIN MULTILAYERS

Z.G. Li*, David J. Smith and S.S.P. Parkin**

Center for Solid State Science, Arizona State University, Tempe, AZ 85287
*Present address: DuPont Experimental Station, Wilmington, DE 19880
**IBM Almaden Research Center, San Jose, CA

Magnetic thin films and ultrathin multilayers(ML) have been developed which are of great fundamental and technological interest[1,2].Since their physical properties depend strongly upon growth conditions, it requires microstructural investigations to establish and understand their interrelationship. The required information about thin films includes, for example, layer-layer and layer-substrate interfaces, crystallinity, crystal type, columnar growth, crystal orientations and so on, all of which could influence or even totally change the macrobehavior. Unlike other commonly used structural determination techniques which average over comparatively large volumes, HREM provides real-space information on the atomic scale. It has been demonstrated to be an ideal method for investigating thin film microstructure, especially for ultrathin ML with bilayer thicknesses on the nanometer scale. A limitation of electron microscopy is that the information is obtained from two-dimensional projections of the sample. However, thin films and ML can be prepared in both cross-section and plan-view. It is thus usually possible to obtain quasi-3D information and answer important structural questions about crystalline, polycrystalline and amorphous-like thin films.

Rare-earth transition-metal alloy films. Observations revealed the presence of small microcrystallites, typically 2.5-7nm in size in thin films of TbFeCo which had previously been considered as fully amorphous[3]. Further studies of thin FeCo films revealed considerably bigger crystals, thus confirming the critical role of Tb in influencing the thin film microstructure and magnetic properties. Later studies of encapsulated films indicate that the micro-particles do not result from the method of film preparation. Figure 1 compares a thin TbFeCo film with small crystals of about 3nm and a thin FeCo film with 40nm crystals. After annealing, crystals in the former sample grow considerably, with significant changes in magnetic properties[4].

Multilayers. Multilayer films based upon transition-metal ferromagnets have important prospects for recording media. We have used HREM and other electron microscopy methods to investigate the structural characteristics of magnetic multilayers grown by sputtering. Advantage was taken of the crystalline nature of the substrate to align the plane of individual layers with the incident beam direction, while the lattice fringes of the substrate provided an internal spacing calibration. Figure 2 compares the microstructure of sputtered Co/Cu multilayers in one case with the ML grown directly on the Si substrate where interfacial reactions are apparent, and in the other with an Fe buffer layer where the layer growth is well-ordered. The latter film has been shown to give extremely high values of the saturation magnetoresistance[5,6].

References

1. P. Chaudhari, J.J. Cuomo, J.R. Gambino, Appl. Phys. Letts., 22 (1973) 337.
2. P.F. Carcia, A.D. Meinhaldt, A. Suna, Appl. Phys. Letts., 47 (1985) 178.
3. Z.G. Li, D.J. Smith and K. Sickafus, Appl. Phys. Letts., 55 (1989) 919.
4. Z.G. Li et al. J. Appl. Phys., (in press).
5. S.S.P. Parkin, Z.G. Li and D.J. Smith, Appl. Phys. Letts., (in press).
6. The electron microscopy was carried out at ASU in the National Facility for High Resolution Electron Microscopy supported by NSF Grant DMR-89-13384.
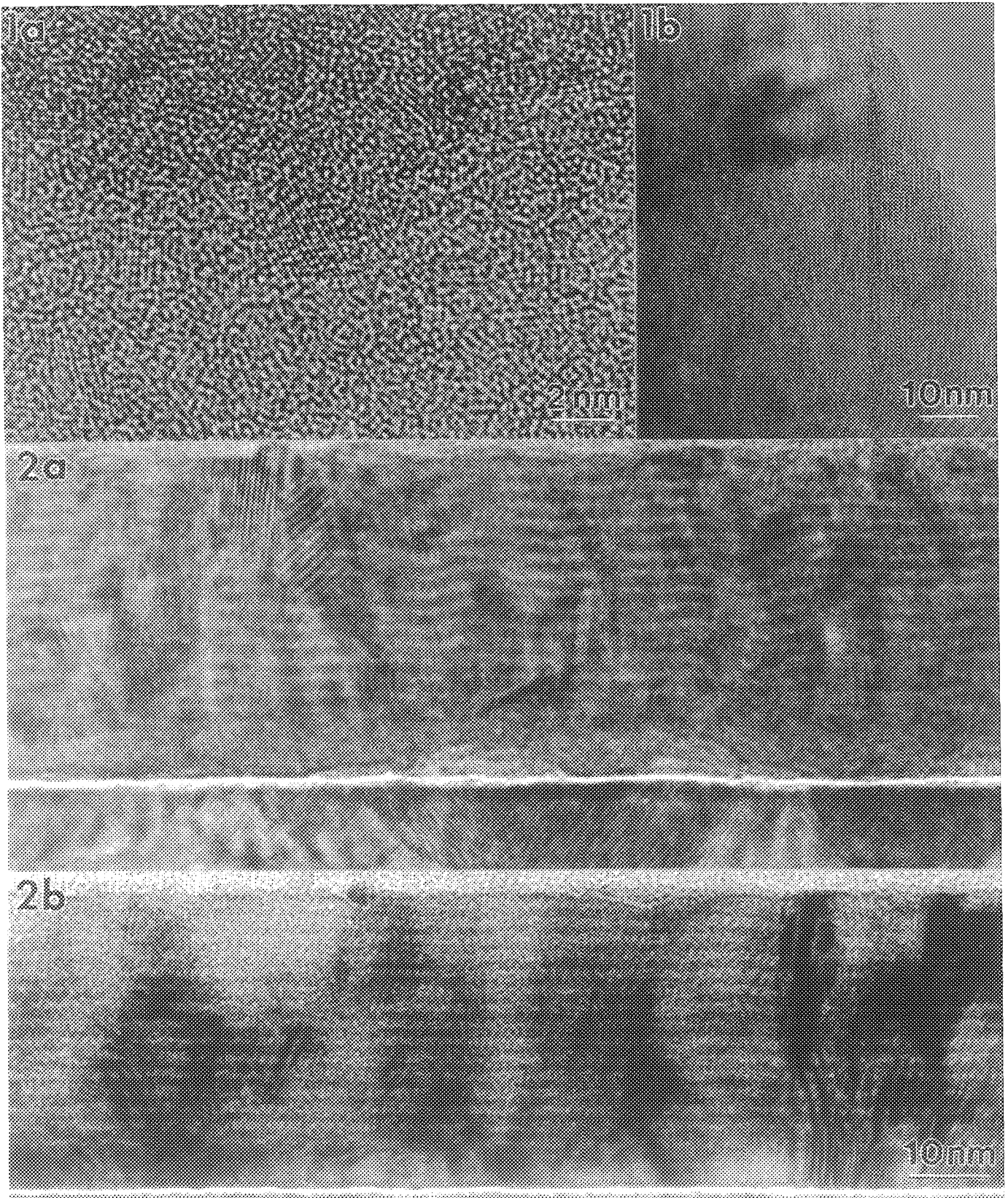
FIG. 1. Thin films of (a)TbFeCo, and (b)FeCo, imaged in cross-section.
FIG. 2.   Thin Co/Cu ML films deposited on Si (100) substrate taken at deliberate underfocus conditions to enhance contrast of successive Co and Cu layers: (a) first Cu layer reacts with Si substrate; (b) Fe buffer layer promotes high quality ML growth.

TRANSMISSION ELECTRON MICROSCOPY STUDIES OF BI-SUBSTITUTED GARNET FILMS

P. A. Labun,* P.A. Crozier,* and T. Suzuki **

*Center for Solid State Science, Arizona State University, Tempe, AZ 85287-1704,
** IBM Almaden Research Center, 650 Harry Rd, San Jose, CA 95120-6099

Bi-substituted garnet films have attracted much attention as possible materials for high density magneto-optical recording media. Recently a new rapid thermal annealing technique has been developed to produce garnet films with improved microstructural and magnetic properties [1]. We have employed in-situ heating in an analytical electron microscope to characterize the microstructural changes to the morphology and chemistry during thermal annealing of garnet films.

Garnet films were produced by an r.f. magnetron sputter deposition method in an Ar atmosphere. The nominal composition of the films was $(BiDy)_3(FeGa)_5O_{12}$ with a thickness of ~ 40 nm. The films were transferred into the hot stage of a Philips 400T transmission electron microscope and heated to a maximum temperature of 720 C. Different rates were used to simulate the effect of heat pulsed annealing.

Fig.1 shows a bright field image of the initial as-deposited films and it's corresponding diffraction pattern. Both the image and the diffraction pattern indicate that the film has an amorphous structure. The corresponding image and diffraction pattern from a heated sample is shown in Fig. 2. The image shows the presence of circular regions (marked B) containing second phase particles indicating that precipitation has occurred. Electron diffraction patterns from the unprecipitated region (marked A) show that transformation to the polycrystalline garnet phase has occurred. Fig.3 shows a higher magnification image of the interface between region A and B. In region A the grains are up to 30 nm in size whereas in region B they are up to 5 nm in size.

The techniques of electron diffraction and electron energy-loss spectroscopy were used to identify the structure and composition of the second phase precipitates. The data was recorded on a Philips 400T equipped with a field emission gun and a Gatan 666 parallel recording system. Diffraction data from one of the particles is shown in the inset of Fig.3 and indicates that the particle is crystalline. Energy-loss spectra from both the particle and the surrounding matrix are shown in Fig.4. The most prominent feature in the spectrum from the particle is the Bi O_{45} edge at 26 eV. Both the energy-loss spectra and the diffraction data confirm that the particles are hexagonal Bi. Further work is in progress to understand the various steps occurring during the transformation from the as-deposited amorphous film to the final polycrystalline garnet film.

References

1. T Suzuki, F. Sequeda, H. Do, T. C. Huang and G Gorman, J. Appl. Phys. 67 (1990) 4435.
2. This work was supported by IBM Almaden Research Center and was performed in the ASU HREM Facility (supported by NSF Grant DMR-8913384).
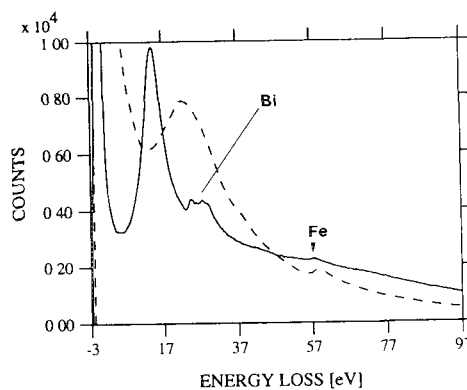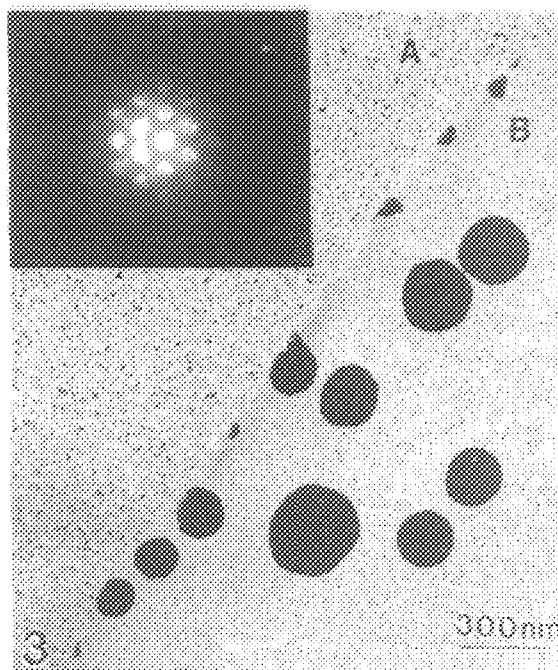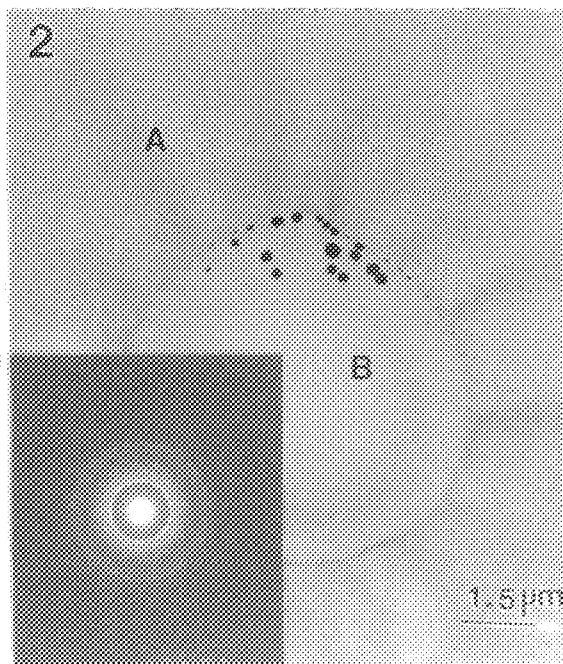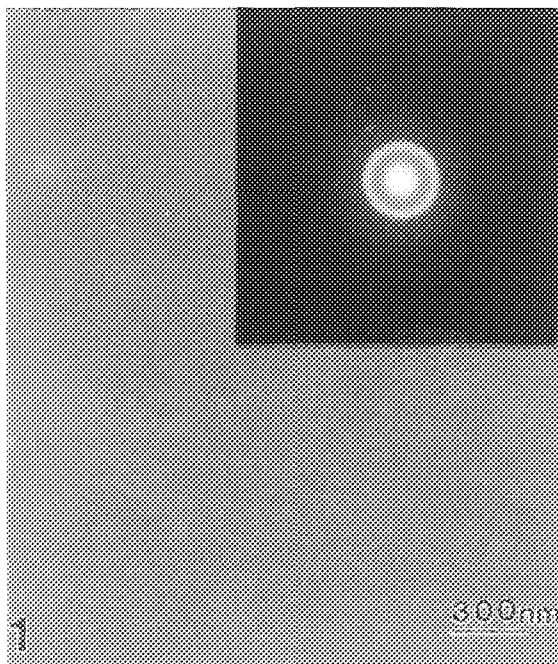
Fig.1: Bright field image (BF) and electron diffraction pattern from as-deposited amorphous films.

Fig.2: BF image and corresponding diffraction pattern from film after rapid heating to 680 C showing circular regions in which precipitation has occurred.

Fig.3: Higher magnification image of interface region showing precipitation. The inset shows the electron diffraction pattern from the precipitate.

Fig.4: Energy-loss spectra from precipitate (solid line) and surrounding matrix (dotted line).

NOVEL MAGNETO-OPTICAL RECORDING MATERIALS
--- Bi-substituted Garnet Films ---

Takao Suzuki and Hossein Nuri

IBM Research Division, Almaden Research Center

650 Harry Road, San Jose, CA 95120-6099

For future high density magneto-optical recording materials, a Bi-substituted garnet film ($(BiDy)_3(FeGa)_5O_{12}$) is an attractive candidate since it has strong magneto-optic effect at short wavelengths less than 600 nm. The signal in read back performance at 500 nm using a garnet film can be an order of magnitude higher than a current rare earth-transition metal amorphous film. However, the granularity and surface roughness of such crystalline garnet films are the key to control for minimizing media noise.

We have demonstrated a new technique to fabricate a garnet film which has much smaller grain size and smoother surfaces than those annealed in a conventional oven. This method employs a high ramp-up rate annealing ($\Gamma = 50 \sim 100$ C/s) in nitrogen atmosphere. Fig.1 shows a typical microstruture of a Bi-susbtituted garnet film deposited by r.f. sputtering and then subsequently crystallized by a rapid thermal annealing technique at $\Gamma = 50$ C/s at 650 °C for 2 min. The structure is a single phase of garnet, and a grain size is about 300A. It should be noted that the grain boundaries are sharp, being indicative of the absence of segregated phase.

Those films thus crystallized by a rapid thermal annealing show high coercivity ($\gtrsim$ kOe), and high squareness of hysteresis loops.

For further reduction of grain size and better morphology, a multi-layer structure of garnet films has been examined. Among various materials as separator, Co metal is likely most effective for controlling coercivity and squareness. A discussion of microstructure in conjunction with magnetic properties will be given.

References:

1) T.Suzuki, F.Federico, H.Doa, T.Huang and G.Gorman; J.Appl.Phys. 67, 4435 (1990).
2) T.Suzuki, G.Zaharchuk, G.Gorman, F.Sequeda and P.Labun, IEEE Trans.MAG.26, 1927 (1990).
3) T.Suzuki, 35th MMM Conference (San Diego, 1990) BB-02.

Fig.1 High resolution electron micrograph of Bi-substituted garnet film crystallized by a rapid thermal annealing technique.

MICROSTRUCTURAL DEPENDENCE OF MAGNETIC PROPERTIES OF PT/CO MULTILAYERS FOR MAGNETO-OPTICAL RECORDING DEVICES

Z.G. Li and P.F. Carcia

Du Pont Research and Development, Experimental Station,
P.O.Box 80356, Wilmington, DE 19880-0356

Pt/Co ultrathin multilayer films are a new candidate for magneto-optical (MO) recording devices[1]. We have previously shown that their magnetic properties are improved by sputtering them with either Kr or Xe instead of Ar[2]. Specifically, Ar-sputtered films have too small coercivity for recording. In this study we demonstrate that high resolution electron microscopy (HREM) is a powerful technique to study the relationship of the multilayer microstructure and magnetic properties. We used a Philips CM30 and a JEM 2000FX microscope to study multilayers with a typical total thickness in the 10 nm range, consisting of only 1-2 atomic layers of Co and 4-6 atomic layers of Pt .

Figure 1 compares the cross sectional microstructure of nearly identical Pt/Co multilayers (~10x[4Å Co+13Å Pt]) sputtered in (A) 7 mTorr of Ar, (B) 7 mTorr of Kr, and (C) 5 mTorr of Xe. The layers sputtered in Ar are extremely flat and continuous. Sputtering with a larger mass gas (Kr or Xe) progressively increased the layer roughness, and the lateral continuity of layers was more frequently interrupted by grain boundaries, which were very distinct in Kr- and Xe-sputtered films compared to Ar-sputtered films. Thus the layering was superior in Ar-sputtered films. However, by comparing electron diffraction images (Fig. 2) from the film cross sections, we found that Kr- and Xe-sputtered multilayers had superior (111)-fcc texture. Whereas diffraction from (111) multilayer planes of the Ar-sputtered film caused a faint circular ring of nearly equal intensity everywhere, diffraction from the Xe-sputtered film was most intense in a direction near normal to the Si substrate, indicating superior (111) film texture. And Fig. 3 is a high resolution lattice image of the (111) atomic planes of the Xe-sputtered Pt/Co multilayer with about 2.23Å spacing parallel to the substrate surface. (The diffraction result for the Kr films was intermediate to that of the Ar and Xe-sputtered films). Thus, one cause for the larger coercivities in Kr- and Xe-sputtered films may be a larger crystallographic contribution (better texture) to their magnetic anisotropy energy.

Finally, we can understand the microstructural features and their relationship to sputtering conditions as follows. By sputtering with either Kr or Xe, energetic bombardment of the growing multilayer is less compared to sputtering with Ar[2]. Although energetic bombardment promotes smoother layers, because of an increase in adatom mobility, it also compromises the (111)-fcc texture, which is crucial for good magnetic properties[3].

References

1. W.B. Zeper, F.J.A.M. Greidanus, P.F. Carcia, and C.R. Fincher, J. Appl. Phys. **65**, 4971 (1989)
2. P.F. Carcia, S.I. Shah, and W.B. Zeper, Appl. Phys. Lett. **56**, 2345(1990)
3. The authors thank L. Hannah for assistance with microscopy.
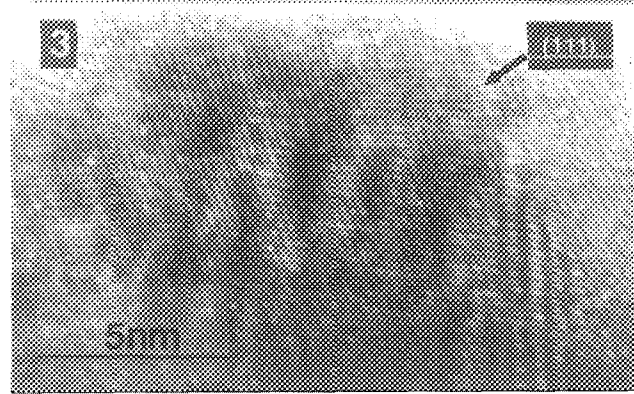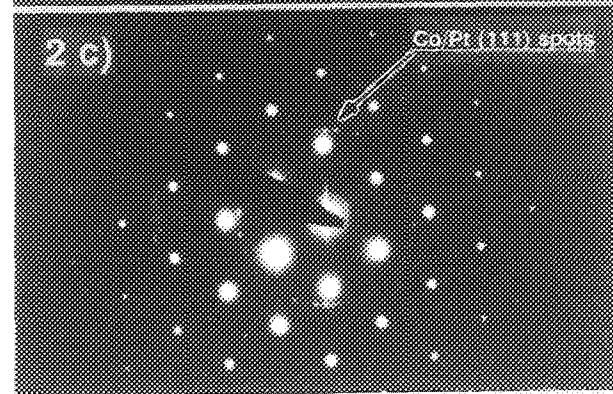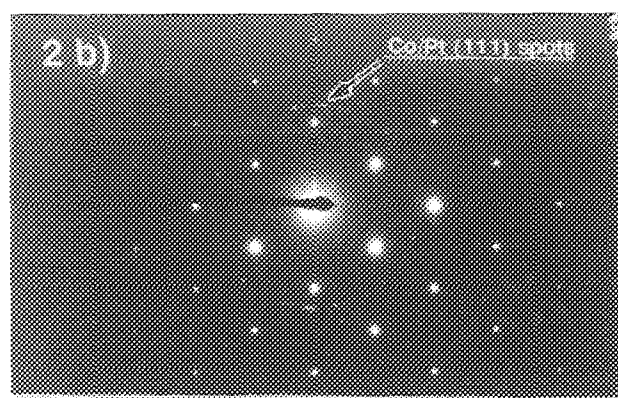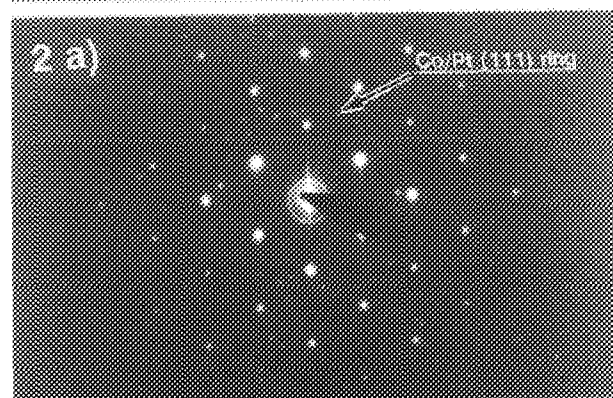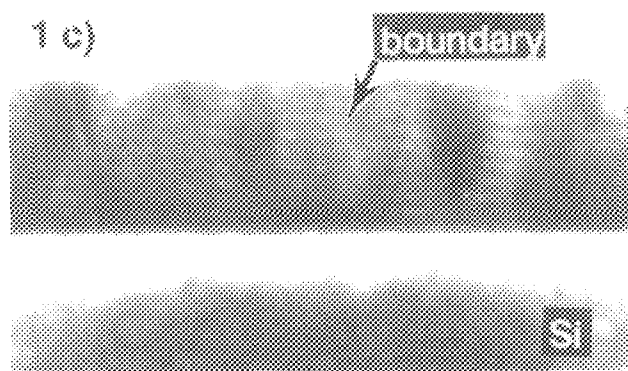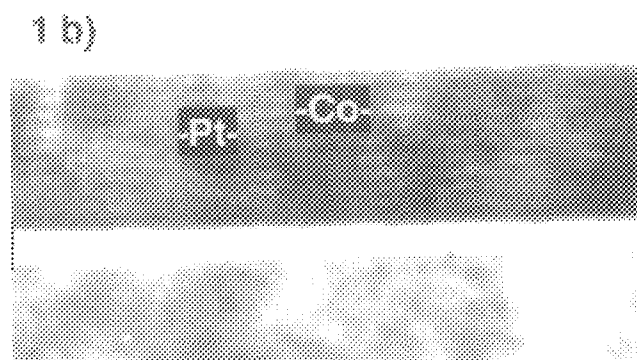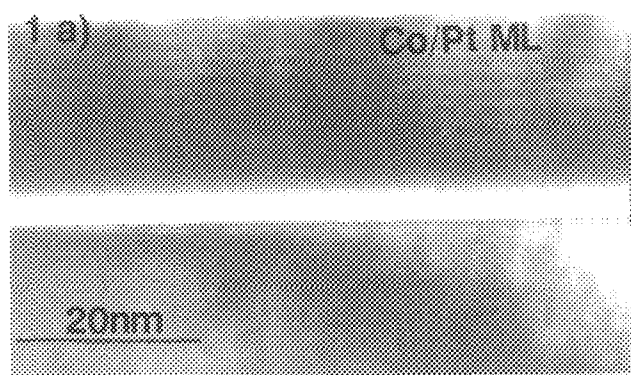
Fig 1. Cross sectional images of Pt/Co multilayers sputtered in (a) 7 mTorr Ar, (b) 7 mTorr Kr, and (c) 5 mTorr Xe.

Fig 2. Corresponding electron diffraction images of (a) Ar-, (b) Kr-, and (c) Xe-sputtered Pt/Co multilayers.

Fig 3. HRTEM lattice image of Pt/Co multilayer sputtered in 5 mTorr Xe.

TEM STUDY OF THIN IRON OXIDE FILMS DEPOSITED BY PULSED-LASER ABLATION

Ian M. Anderson, M. Grant Norton, and C. Barry Carter

Department of Materials Science and Engineering, Cornell University, Ithaca, New York 14853

Iron-oxide-based compounds are of technological interest because of their unique magnetic properties. Thin films of these compounds are especially suited to applications such as magnetic recording devices. The binary Fe–O system provides a model for the study of iron-oxide-based compounds, since the multiple valence of the Fe cations permits the formation of phases having a variety of crystal structures. These structures include rock salt (wüstite, $Fe_{1-\delta}O$), two spinels (magnetite, Fe_3O_4 and maghemite, γ-Fe_2O_3), and corundum (hematite, α-Fe_2O_3). The former three phases have cubic-close-packed oxygen sublattices, while the latter has a hexagonal-close-packed oxygen sublattice. The γ-Fe_2O_3 phase is a metastable, cation-deficient spinel, generally formed by careful low-temperature oxidation of the magnetite phase.

Thin iron oxide films have been deposited by pulsed-laser ablation onto (001)-oriented MgO single-crystal substrates. The microstructure and epitaxy of these films have been studied using transmission electron microscopy (TEM) and selected-area diffraction (SAD). All films were deposited using a KrF excimer laser (λ=248 nm) as the radiation source and a dense, sintered, polycrystalline α-Fe_2O_3 pellet as the iron oxide source. Films were deposited directly onto specially prepared electron-transparent substrates of single-crystal MgO oriented close to (001), as is detailed elsewhere[1]. This technique allows the microstructure of the as-deposited film to be examined without the introduction of artifacts during TEM sample preparation. Films were deposited at a range of substrate temperatures and ambient oxygen partial pressures.

Figure 1 shows TEM images of a very thin film deposited at 500°C and 400 mTorr of oxygen. Figures 2 a) and b) show a diffraction pattern recorded from the film and a corresponding schematic, respectively. The diffraction pattern indicates that the film is a spinel phase, even though the source of the iron oxide was hematite. This is not inconsistent with previous studies of iron oxides deposited using pulsed-laser ablation[2]. The film is epitactic, and there is no detectable mismatch between the lattice parameters of the spinel and the MgO substrate. This is unexpected since the two iron oxide spinel phases as well as magnesium-iron spinel, $MgFe_2O_4$, have lattice parameters which are smaller than that of MgO by about one third of one percent. (This would correspond to a misfit dislocation spacing of about 100 nm.) The spinel reflections are strongly faceted. Weak superlattice reflections are also visible in the diffraction pattern. The presence of the superlattice reflections is not yet entirely understood, but they are consistent with extra reflections of the γ-Fe_2O_3 phase observed in its powder diffraction pattern[3].

The two images shown in Figure 1 were recorded from the same area of the film, and were formed under identical two-beam diffraction conditions close to the (001) pole of the MgO. Figure 1a is a bright-field (BF) image, and Figure 1b is a dark-field (DF) image formed with the spinel (220) reflection. The BF image shows the important morphological features of the film. The film is continuous and covers the entire substrate. The absence of misfit dislocations is consistent with the coherent nature of the film suggested by the diffraction pattern, as is the bending of the film evident in the BF image. In addition to the continuous film, faceted particles with edges parallel to the low-index directions of the substrate are also found dispersed throughout the film. The structure and the chemical composition of the particles are under investigation. The DF image, formed using a reflection characteristic of the film only, verifies the continuous nature of the film and shows a fine domain microstructure. These domains can also be seen in the BF image on a portion of the film which is bent out of the two-beam imaging condition. The domain walls are strongly faceted, and their traces are parallel to the <100> directions.

The stoichiometry of the films and the identity of the faceted particles will be discussed. HREM examination of the domain structure of the films is in progress and will also be presented[4].

References

1. M.G.Norton et. al., Appl.Phys.Lett. (1990) 56, 2246.
2. S.B.Ogale et al., Appl.Phys.Lett. (1988) 53, 1320.
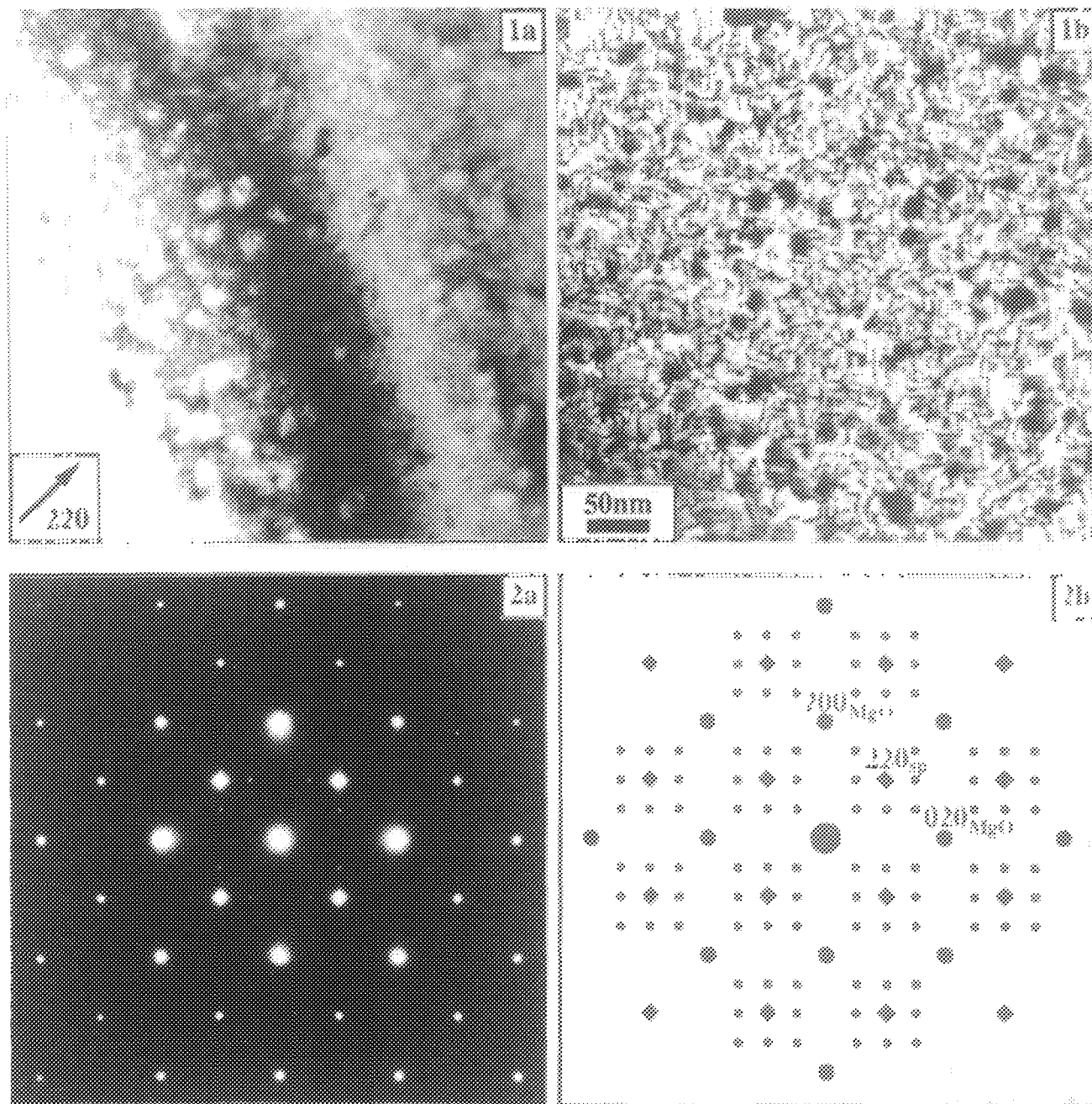3. JCPDS Powder Diffraction File, 24–81.

Figure 1.--A) BF image of as-deposited film imaged in a two-beam condition near the [001] pole of the MgO substrate; B) DF image of the same area, formed with the 220$_{sp}$ reflection.

Figure 2.--A) SAD pattern of the [001] pole of the MgO substrate; B) its schematic interpretation:
◆ : reflection characteristic of spinel only;
● : superposition of reflections of the film and the MgO substrate;
○ : superlattice reflections.

A MICROSTRUCTURAL CHARACTERIZATION OF Co-Zr TYPE PERMANENT-MAGNET MATERIALS

K. R. Lawless and G. C. Hadjipanayis*

Department of Materials Science, University of Virginia, Charlottesville, VA 22903
*Department of Physics, University of Delaware, Newark, DE 19716

Considerable interest has been shown recently in the hard magnetic properties of Co-Zr, Co-Zr-B, and Co-Hf-B alloys, but as yet no detailed microstructural studies have been published.[1,2] The Co-Zr phase diagram seems to be reasonably well known[3], although the crystal structure of the $Co_{11}Zr_2$ phase is only partially determined.[4] This paper will report on some preliminary studies of rapidly solidified Co-Zr-B-Si and Co-Hf-B-Si alloys and binary Co-Zr alloys.

All specimens used in this study were prepared by melt spinning. Specific alloys were heat treated at temperatures from 650 to 900°C. TEM specimens were prepared from ribbon material by ion milling.

X-ray diffraction studies of these alloys all showed a characteristic broad peak centered around d = 0.205nm. Although it was obvious that this was a complex peak, attempts to deconvolute it were unsuccessful. SAD patterns revealed that major phases in the alloys were very heavily faulted, thus giving rise to the very confusing X-ray diffraction patterns.

Both melt spun and annealed samples were microcrystalline and multiphase in character. A typical microstructure for an alloy with the basic overall composition of $Co_{11}Zr_2$, rapidly solidified and then annealed for 20 minutes at 900°C, is shown in Fig. 1. By the use of CBED and EDS, it was possible to confirm the presence of three phases, orthorhombic $Co_{11}Zr_2$, cubic $Co_{23}Zr_6$, and cubic (FCC) Co.

Figure 2 shows a typical unfaulted grain of the minor phase $Co_{23}Zr_6$. Occasional grains of this phase were twinned on {111} planes. The major phase present was orthorhombic $Co_{11}Zr_2$, which is visible as the striated, heavily faulted grains visible in all of the Figures. Long-period anti-phase boundary structures are common in these alloys. Figures 3 and 4 show both this orthorhombic phase and the FCC Co. In many cases, the Co phase was twinned, as can be seen in both Fig. 1 and Fig. 4. No evidence of non-crystalline boundary regions between grains was detected. Similar microstructures observed in Co-Zr-B-Si and Co-Hf-B-Si alloys will be discussed.[5]

1.   C. Gao, H. Wan and G. C. Hadjipanayis, J. Appl. Phys. 67, 4960 (1990).
2.   G. Stroink, Z. M. Stadnik, G. Viau and R. A. Dunlap, J. Appl. Phys. 67, 4963 (1990).
3.   W. H. Pechin, D. E. Williams and L. Larsen, Trans. of the ASM 57, 464 (1964).
4.   S. F. Cheng, W. E. Wallace and B. G. Demczyk, Proceedings, Sixth International Symposium on Magnetic Anisotropy and Coercivity in Rare Earth-Transition Metal Alloys, Pittsburgh, PA. 477 (1990).
5.   This research was supported by the Army Research Office.
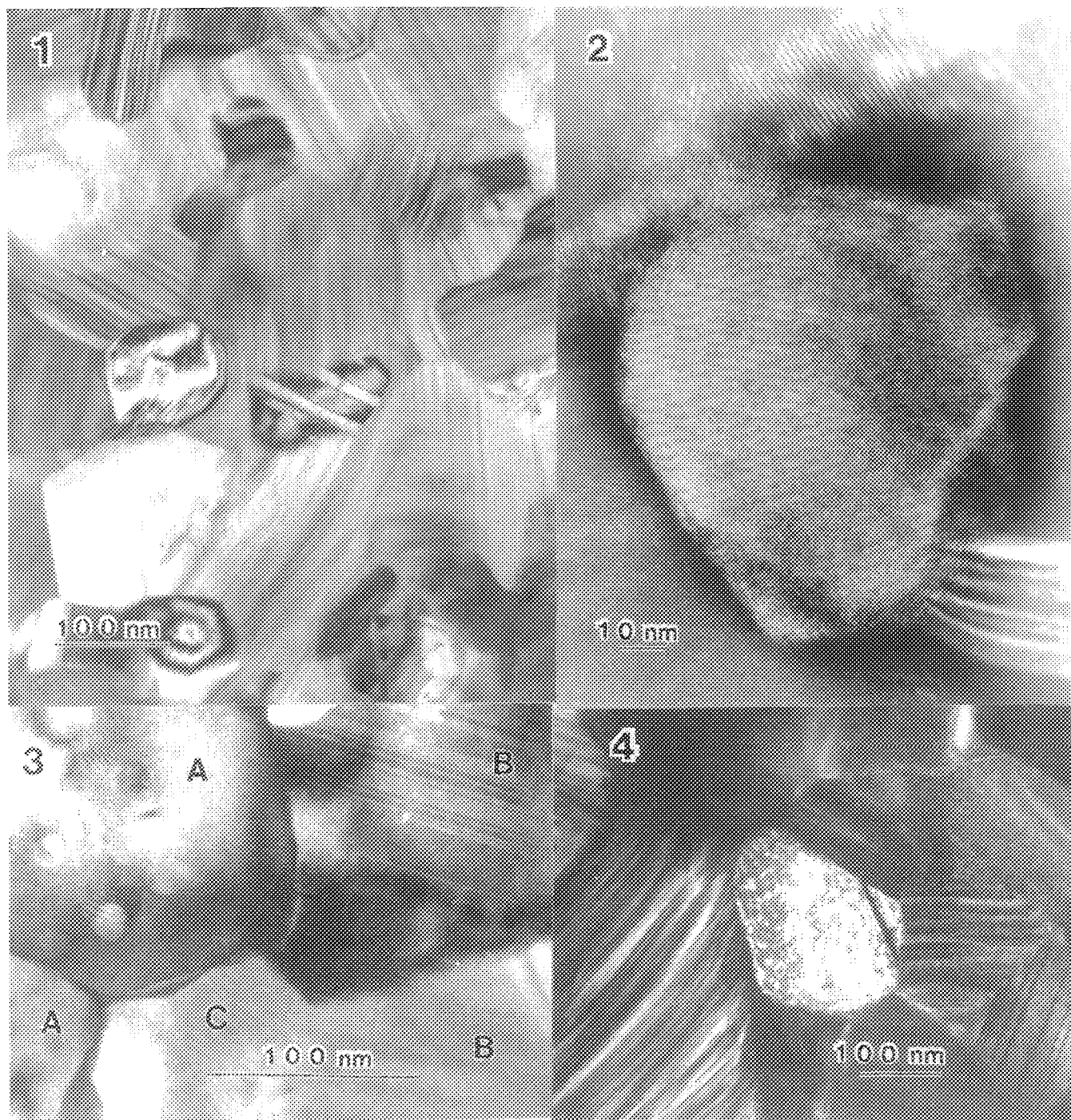
Fig. 1. Multiphase microstructure of annealed $Co_{11}Zr_2$.
Fig. 2. Unfaulted grain of $Co_{23}Zr_6$.
Fig. 3. FCC Co (A), Orthorhombic $Co_{11}Zr_2$ (B) and cubic $Co_{23}Zr_6$ (C) phases.
Fig. 4. Twinned FCC Co surrounded by heavily faulted $Co_{11}Zr_2$ grains.

LORENTZ ELECTRON MICROSCOPY OF MAGNETIC DOMAINS IN RAPIDLY SOLIDIFIED AND ANNEALED Pt-Co-B ALLOYS

N. Qiu and J. E. Wittig

Department of Materials Science and Engineering
Vanderbilt University, Nashville, TN 37235

PtCo hard magnets have specialized applications owing to their relatively high coercivity combined with corrosion resistance and ductility. Increased intrinsic coercivity has been recently obtained by rapid solidification processing of PtCo alloys containing boron. After rapid solidification by double anvil splat quenching and subsequent annealing for 30 minutes at 650°C, an alloy with composition $Pt_{42}Co_{45}B_{13}$ (at.%) exhibited intrinsic coercivity up to 14kOe.[1] This represents a significant improvement compared to the average coercivities in conventional binary PtCo alloys of 5 to 8 kOe.

Rapidly solidified specimens of $Pt_{42}Co_{45}B_{13}$ (at.%) were annealed at 650°C and 800°C for 30 minutes. The magnetic behavior was characterized by measuring the coercive force (H_c). Samples for TEM analysis were mechanically thinned to 100 μm, dimpled to about 30 μm, and ion milled to electron transparency in a Gatan Duomill at 5 kV and 1 mA gun current. The incident ion beam angle was set at 15° and the samples were liquid nitrogen cooled during milling. These samples were analyzed with a Philips CM20T TEM/STEM operated at 200 kV. The magnetic domain structure was investigated by Lorentz phase contrast imaging. Lorentz conditions were achieved by operating the CM20 in the LM mode where the objective lens is turned off and by defocusing the diffraction lens 200 μm to improve the Fresnel contrast. An image intensified Gatan 622 video camera was used to increase the magnification. The Lorentz images were recorded by directly photographing the TV screen.

The rapidly solidified state is a disordered FCC PtCo structure supersaturated with boron. Annealing this metastable state ordered the PtCo matrix into the $L1_0$ face centered tetragonal superlattice and precipitated Co borides. Figure 1(a) shows a representative BF image of the microstructure after annealing for 30 minutes at 650°C. The matrix has been partially ordered into the $L1_0$ superlattice and Co_3B has precipitated within the grains as well as on the grain boundaries. Increasing the annealing temperature to 800°C produced a completely ordered PtCo matrix and changed the precipitate structure from orthorhombic Co_3B to tetragonal Co_2B. At 800 $^\circ$C , both the matrix grains and borides have coarsened as shown in figure 1(b). Magnetic characterization of these two microstructures revealed a factor of two times greater coercivity in the material heat treated 30 minutes at 650°C compared to H_c from the sample annealed 30 minutes at 800°C. Figures 2- (a&b) reveal the complex magnetic domain structure for the 650°C annealed sample. Each PtCo matrix grain contains several domains of different shapes and sizes. Typical closure domain structures are also visible in the samples. No domain walls were detected within the Co_3B precipitates. Although a similar complex domain structure is also observed in samples annealed at 800°C, the domain size is considerably larger compared to the specimen annealed at 650°C. In addition, domain walls were present within the tetragonal Co_2B precipitates.

Magnetic domain wall pinning by precipitates or grain boundaries is partially responsible for the higher coercivity in the 650°C annealed material. However, other factors may also influence the hard magnetic behavior. Since the only requirement for high coercivity is a large and rapid variation of domain wall energy with position, a

partially ordered structure exhibits increased coercivity (domain wall energy is about 4×10^{-2} J m^{-2} for the disordered phase and about 3×10^{-2} J m^{-2} for the ordered phase).[2] Annealing at 650°C for 30 minutes produced the partially ordered FCT matrix that provides the rapid changes in wall energy with position. Also, since Co borides are magnetic, interaction between the precipitates and matrix must be considered. Precipitate-matrix interaction could decrease the local demagnetization field and cause increased coercivity. The absence of domain walls in the Co_3B precipitates of the 650°C material indicate that these borides may be within the single domain size. In addition, Co_3B has a domain wall energy about 1.7×10^{-2} J m^{-2} with substantial easy-axis magnetic anisotropy which is not observed in Co_2B.[3] Therefore, the stronger interaction effects by Co_3B precipitates compared to Co_2B precipitates would also contribute to the total increase in intrinsic coercivity. [4]

References
1. J. A. Teubert, Masters Thesis, Vanderbilt University, May 1989.
2. P. Gaunt, J. Appl. Phys. 43 (1972) 637.
3. J. D. Livingston, J. Appl. Phys. 52 (1981) 2506.
4. This work, sponsored by the Vanderbilt Space Processing Center, is supported by the NASA Office of Commercial Programs under Grant# NAGW 810.
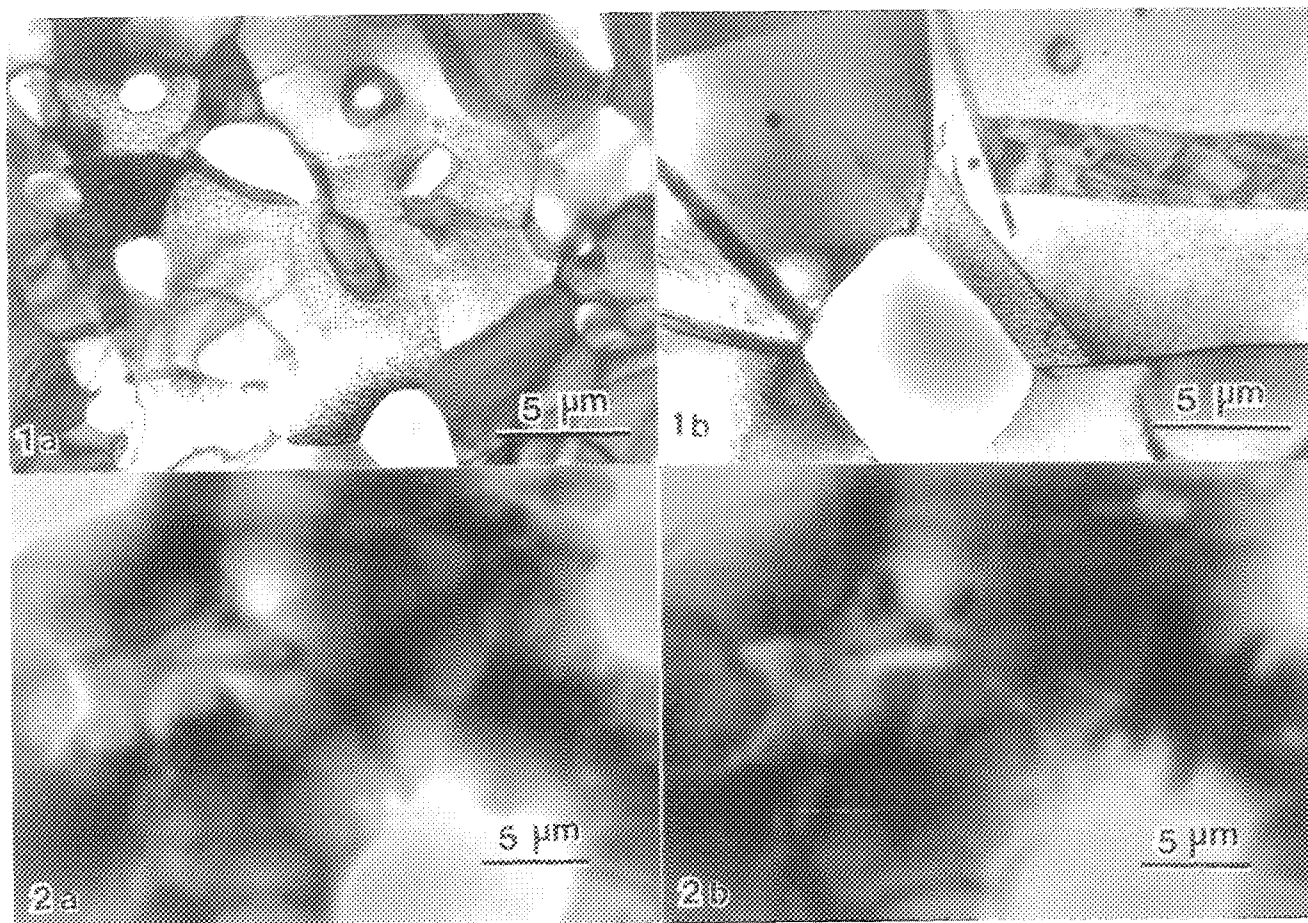
Fig.1- The BF images of the $Pt_{42}Co_{45}B_{13}$ annealed at 650°C for 30 minutes in (a) and at 800°C for 30 minutes in (b) reveal the variation in matrix grain and precipitate size.

Fig.2 - Lorentz imaging of the sample annealed at 650°C for 30 minutes shows the magnetic domain structure in the matrix grains (a) overfocused and (b) underfocused.

J-3: Analytical Electron Microscopy

MATERIALS SCIENCE APPLICATIONS OF A 120kV FEG TEM/STEM: TRISKAIDEKAPHILIA

J. Bentley, A. T. Fisher, E. A. Kenik, and Z. L. Wang

Metals and Ceramics Division, Oak Ridge National Laboratory, PO Box 2008, Oak Ridge, TN 37831-6376

The introduction by several manufacturers of 200kV transmission electron microscopes (TEM) equipped with field emission guns affords the opportunity to assess their potential impact on materials science by examining applications of similar 100-120kV instruments that have been in use for more than a decade.[1] This summary is based on results from a Philips EM400T/FEG configured as an analytical electron microscope (AEM) with a 6585 scanning transmission (STEM) unit, EDAX 9100/70 or 9900 energy dispersive X-ray spectroscopy (EDS) systems, and Gatan 607 serial- or 666 parallel-detection electron energy-loss spectrometers (EELS). Examples in four areas that illustrate applications that are impossible or so difficult as to be impracticable with conventional thermionic electron guns are described below.

Imaging. The high brightness and coherence of illumination provides outstanding TEM phase contrast imaging performance. Not only is this useful in high resolution electron microscopy (HREM) lattice imaging studies, for example dumbbell splitting in Si <110> images was observed with 0.3s exposures,[1] but also in lower resolution work such as imaging the Fe-rich α and Cr-enriched α' nm-scale isotropic modulated structures caused by spinodal decomposition of the ferrite phase of aged duplex CF8 stainless steel.[2] Improved phase contrast in glancing-incidence reflection electron microscopy (REM) increases the fine structure in images of surface steps and dislocations and has allowed the detection of sub-0.1-nm surface steps on α-Al$_2$O$_3$.[3] Bright- and dark-field STEM image resolution for a FEG instrument is superior to that of a non-FEG instrument but is still normally inferior to that of equivalent TEM images. However, in STEM, "dynamical" contrast effects (e.g. bend contours) can be suppressed and image contrast can be adjusted electronically. High-angle annular dark-field (so called Z-contrast) STEM images are even more useful. A nearly equivalent Z-contrast TEM mode has been demonstrated but a FEG provides no advantage.[4]

Diffraction. The highly coherent (parallel) illumination with a FEG allows extremely fine detail in selected area diffraction (SAD) patterns to be easily viewed and recorded. For example, in SAD patterns of SiC made by chemical vapor deposition, the "streaks" along the <111>$_\beta$ (or <0001>$_\alpha$) growth direction are revealed to consist of finely spaced maxima. This material has one-dimensional disorder with neighboring regions corresponding to various α polytypes (predominantly 2H, 4H, and 6H) as well as β, each only one or a few unit cells thick. Similar, but more periodic, maxima are observed in diffraction patterns from long period polytypes. Although a FEG provides no fundamental advantage for producing convergent beam electron diffraction (CBED) patterns containing high-order Laue zone (HOLZ) lines, the fine structure is easily visible on the viewing screen. This was of benefit in determining the long-range-order parameter of (Fe,Ni,Co)$_3$V alloys from changes in lattice parameter measured from changes in the accelerating voltage at which 3 HOLZ lines intersected at a point in <111> CBED patterns.[5] Similarly, crystal symmetry determination from CBED, an important part of phase identification, can be much easier with a FEG, even though equivalent data could be obtained with a thermionic source. In the identification of Al$_{12}$Mo pseudo-lamellar second phase in annealed, molybdenum-implanted aluminum, the ease-of-use and good shadow image resolution were not inconsequential factors in determining the space group by CBED from the highly buckled precipitates.[6]

X-ray microanalysis. Most of the advantages of a FEG-AEM for X-ray microanalysis result from the high source brightness. The compositions of precipitates in stainless steels can be complex, requiring good statistical accuracy for confident modeling of the behavior of minor alloying additions. For the analysis (on extraction replicas) of particles with a size of only a few nm the high current density probes from a FEG are almost essential. Radiation induced segregation (RIS) in stainless steels can lead to dramatic changes in materials behavior and has been studied extensively, not least because of the practical importance for operating nuclear reactors. The

depletion of chromium at grain boundaries is of particular concern, and whereas AEMs with thermionic sources can detect a composition change, a FEG-AEM can provide a more accurate measure of the minimum Cr levels reached and other important subtle details of the segregation profiles for even the minor alloying elements.[7] An even more challenging problem is posed by the measurement of equilibrium segregation of minor or trace solutes at grain boundaries, since the segregant is confined to one or two atomic planes at the boundary. Statistically significant (3σ) levels as low as 0.36 at.% P in the excited volume, corresponding to 6% of a monolayer coverage of the grain boundary, were measured in studies of type 304L stainless steel.[8] The <2-nm-diameter probe was maintained on the (edge-on) boundary through monitoring the diffraction pattern. In earlier work, antimony segregation was detected at individual grain boundary dislocations in an antimony-doped stainless steel.[9] The atom location by channeling enhanced microanalysis (ALCHEMI) technique has been applied to determine the sublattice occupancies of ternary additions to CuAu alloys which have the $L1_0$ structure and typically are micro-twinned as a result of their tetragonality.[10] ALCHEMI analyses thus required the use of small probes. The good shadow image resolution was also helpful in setting up the appropriate diffracting conditions.

Electron energy-loss spectroscopy. The high source brightness of a FEG is likewise an advantage for small area analyses by EELS. Although, in principle, small areas can be selected from high magnification images with the EELS entrance aperture, the chromatic aberrations of the image-forming system limit the area selection for most core-loss studies, and operation in the diffraction mode with area selection by the probe is necessary. These effects were clearly important in the analysis of sub-10-nm intragranular particles of B_4C in crept, sintered α-SiC.[11] The measurement of RIS profiles in stainless steels by PEELS has been performed to complement EDS measurements.[12] For some conditions, the potential higher spatial resolution from the reduced importance of beam spreading, can give more accurate compositions. Another advantage over EDS is the ability to analyze for small manganese levels in radioactive neutron-irradiated steels, or even to be able to analyze very radioactive specimens at all.[12] A final aspect of EELS with a FEG is the improved energy resolution. With cold field emission, less than 1 eV resolution is routinely achievable, opening up many possibilities for detailed low-loss and near-edge fine structure analyses, such as in diamond films or oxide ceramics.

Two kinds of improvement are expected for a 200kV FEG AEM – resolution and penetration. With electron holography, the present HREM performance of 300 or 400kV instruments may be exceeded. The increased penetration may be most helpful in EELS (e.g. less sensitivity to unwanted surface films). With some new FEG designs, the availability of larger spot sizes and beam currents for conventional TEM operating modes could be an important practical improvement.

As for our 120kV FEG AEM, there are, of course, features of the performance (probe size, vacuum, etc.) that are exceeded in newer or more specialized instruments, and limitations that are shared by other instruments (such as beam damage and hole drilling), but the 13 examples described above and 13 years of productive use seem to us to be grounds for triskaidekaphilia.[13]

1. J. Bentley, Proc. 38th Ann. Meet. EMSA (1980) 72-73.
2. M.K. Miller and J. Bentley, Mat. Sci. & Technol. 6 (1990) 285-292.
3. Z.L. Wang and J. Bentley, J. Electron Micros. Tech., in press; also these proceedings.
4. J. Bentley, K.B. Alexander, and Z.L. Wang, Proc. XIIth ICEM (Seattle) 4 (1990) 400-401.
5. D.N. Braski, J. Bentley, and J.W. Cable, Proc. 40th Ann. Meet. EMSA (1982) 692-693.
6. L.D. Stephenson, J. Bentley, R.B. Benson, and P.A. Parrish, Proc. 41st Ann. Meet. EMSA (1983) 262-263.
7. E.A. Kenik, in L.W. Hobbs et al., Eds., Mater. Res. Soc. Symp. Proc. 62 (1986) 209-216.
8. E.A. Kenik, Metall. Trans., 22A (1991) 253-255.
9. E.A. Kenik, Scripta Metall. 21 (1987) 811-816.
10. J. Bentley and K. Hisatsune, Proc. 47th Ann. Meet. EMSA (1989) 234-235.
11. K.L. More, J. Bentley, C.H. Carter Jr., and R.F. Davis, in D.C. Joy, Ed., Analytical Electron Microscopy-1987, 299-302; K.L. More et al., J. Am. Ceram. Soc., 69 (1986) 695-698.
12. E.A. Kenik, J. Bentley, and N.D. Evans., these proceedings.
13. Research sponsored by the Division of Materials Sciences, U.S. Department of Energy under contract DE-AC05-84OR21400 with Martin Marietta Energy Systems, Inc. Thanks to Dr. Neal Evans for Greek lessons.

MICROANALYSIS WITH A 200keV FEG TEM

David C Joy

EM Facility, University of Tennessee, Knoxville, TN 37996-0810

Introduction The Hitachi HF-2000 is a 200keV cold field emitter TEM, designed to offer both high resolution imaging performance and a nanometer probe-forming mode for microanalytical operation. The purpose of this paper is to report some initial microanalytical results obtained from the HF-2000 installed at the University of Tennessee.

General Electron-Optical Parameters The cold field emission gun, which runs at about $5 \times 10^{-9} \mathrm{pA}$ pressure, uses an electrostatic lens configuration and a six stage accelerator. The entire electron gun system is under the control of a dedicated microprocessor which permits all of the operational parameters of the gun to be set, monitored, and adjusted through a keyboard and display. The tip emission current can be adjusted up to $40 \mu A$, and the gun voltage ratio (that is the ratio between the voltage on the second anode and the tip extraction voltage) can be varied from 4.5 to 7.5, permitting a significant degree of flexibility in optimizing the optics of the emitter. For a gun voltage ratio of 4.5 and an emission current of $25 \mu A$ the brightness β that we have experimentally measured at 200keV is between 1 and 3×10^8 amps/cm^2/steradian in either the imaging or analytical electron-optical configurations.

In the 'analysis' mode of operation the beam diameter at the specimen can be varied over a wide range of values. Figure (1) shows a digital microdensitometer trace taken across a micrograph of a scanned beam track recorded at x1,000,000 magnification. The Full Width at Half Maximum (FWHM) height of the profile is 0.8nm while the Full Width at Tenth Maximum (FWTM) height is 1.9nm. The profile in the orthogonal beam direction is identical. The probe shape is closely Gaussian in form with no evidence of a skirt around the central region, and over 85% of the beam current falls within 0.85nm of the axis. For an emission current of $40 \mu A$ and a voltage ratio of 7 a current in excess of 1nA can be put into this probe, corresponding to a current density $>10^5$ amps/cm^2.

EDS results The instrument is fitted with a 30mm^2 KEVEX Quantum™ energy dispersive X-ray detector positioned to give a take-off angle, from a horizontal specimen, of 60°. The solid angle of collection of the detector is estimated to be 0.15str. With a 1 to 2nm probe and a typical metallurgical specimen whole spectrum count rates of between 300 to 1200 cps are obtained. We have estimated the minimum mass sensitivity of the system by means of measurements on small vapor deposited spheres (1 to 10nm in diameter) of pure metal. With a 2nm diameter probe on a 3nm diameter sphere of copper

(i.e. approximately 3×10^{-19} gms) the peak to background ratio is >16, and the estimated minimum detectable mass for a 100 second record period is 5×10^{-21} gms. Over a typical 100 second acquisition period the variation in incident beam current (the sum of long term drift and any short term noise) is less than 2% so no corrections for a time varying incident beam current are required even for quantification.

PEELS results The field emission gun, because it is running at room temperature, has a low energy spread and is therefore well suited for high resolution electron spectroscopy. Figure 2 shows a typical zero-loss peak recorded on the HF-2000 at 200keV using a GATAN PEELS™ system. Depending on the acquisition time of the spectrum, and for a tip emission current of 30μA, the FWHM of the peak was found to be between 0.55 and 0.7eV, essentially the specified resolution of the spectrometer. Deconvolution of this zero-loss peak, assuming the instrument response function of the PEELS to be a 0.5eV FWHM Gaussian, shows (figure 3) the expected, inherently asymmetric, energy profile of the beam. The thermally broadened width of this profile (FWHM) is about 0.4eV, a value which is in good agreement with theoretical expectations.
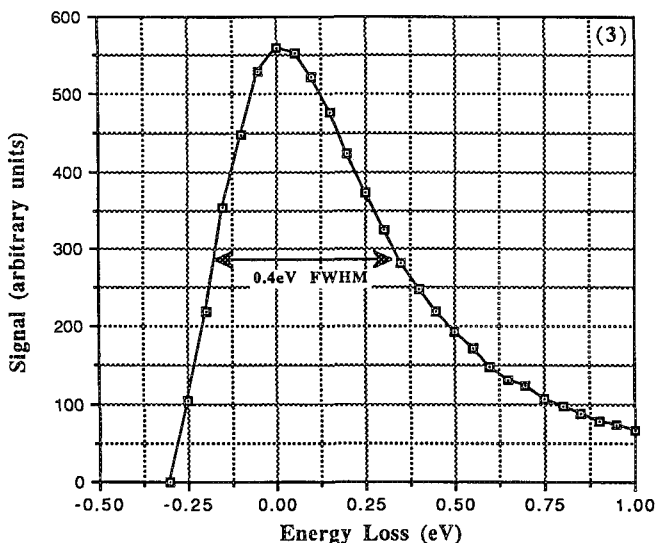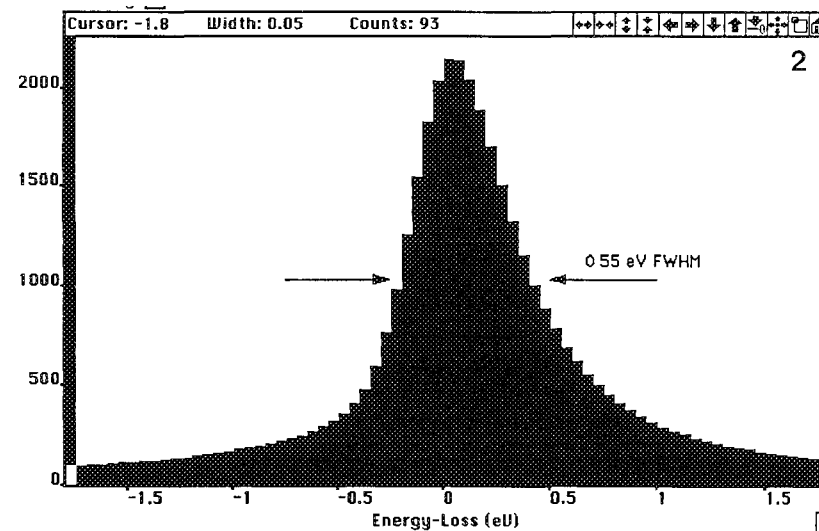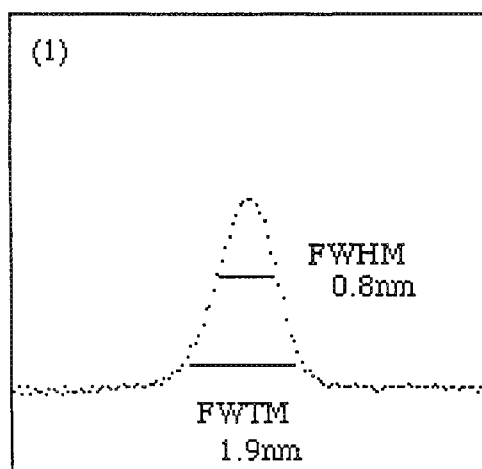
FIG 1.-- Profile of nominal 1nm diameter probe at 200keV from HF-2000.

FIG 2.-- Zero loss PEELS spectrum at 200keV showing 0.55eV FWHM resolution. Single 25ms acquisition period.

FIG 3.-- Measured energy profile of beam showing thermal width of 0.4eV FWHM.

ADVANCES IN ALCHEMI

P. S. Turner,* T. J. White,** A. J. O'Connor,* and C. J. Rossouw***

*School of Science, Griffith University, Nathan, Queensland 4111, Australia
**Electron Microscope Centre, University of Queensland, St Lucia, Queensland 4067, Australia
***CSIRO Division of Materials Science an Technology, Clayton, Victoria 3168, Australia

ALCHEMI - atom location by channeling enhanced microanalysis - is an important technique of analytical electron microscopy, introduced nearly 10 years ago by Spence and Taftø,[1] which utilises the phenomenon of electron channeling to determine the partitioning of impurity species on atomic sites in crystals from ratios of normalised x-ray counts for channeling and non-channeling orientations. The original "ratio" method has been used with success in a number of cases (see reviews by Krishnan[2] and Smyth and McCormick[3]) but is limited in its range of applicability by several factors. We have described an alternative approach to the collection and analysis of electron channeling data for ALCHEMI, which is less sensitive to these factors, and can provide greater precision and reliability.[4] In this paper, a general form of our analysis is described, and the two methods are compared and contrasted.

ALCHEMI data results from the variations in x-ray emission (or in the corresponding EELS edge intensities) from atoms as the orientation of the crystal relative to the electron beam is varied, and the peaks in the standing electron waves move across lattice sites. Microanalysis of impurity species can be performed because their x-ray emissions can be correlated with those from the atoms at different sites in the crystal structure, provided that all emissions are sufficiently localised, so that excitations from both host and substitutional atoms on specific sites respond in a similar way to dynamically induced changes in electron flux in these sites, and that orientations can be found which in projection distinguish between host atom sites.

In the "statistical" approach to ALCHEMI analysis[4] we make the single assumption that for each impurity species j, the counts N_j may be written as a linear combination of the host atom counts N_i for each of the spectra:

$$N_j = \sum_i \alpha_{ij} N_i$$

where the coefficients α_{ij} and their errors are determined by multivariate analysis. The concentration c_j of impurity atom j and the fraction f_{ij} of j atoms which reside on the host sites i may be obtained from the α_{ij} coefficients, from[5] [6]

$$c_j = \sum_i \frac{\alpha_{ij}\, n_i\, /\, k_{ij}}{\left(1 + \sum_l \alpha_{il}/k_{il}\right)}$$

where n_i is the number of host atoms of type i per unit cell and k_{ij} is the k-factor ratio k_i/k_j for atoms i and impurity j. The fractional partition f_{ij} is then

$$f_{ij} = \frac{1}{c_i}\; \frac{\alpha_{ij}\, n_i\, /\, k_{ij}}{\left(1 + \sum_l \alpha_{il}/k_{il}\right)}.$$

Uncertainties in both these quantities are derived from the standard deviations in the α_{ij}.

In order to apply the statistical method, values of the relevant k-factors must be obtained. If these are not available from previous calibrations for the instrument used, suitable standards must be prepared. In determining the k-factors, it is important to avoid channeling orientations. For the determination of impurity species concentration and distribution over host sites, the objective is to record many spectra at and around zone-azis orientations, for which strong channeling effects are observed. The variation in orientation can be achieved by changing the incident beam tilt using dark-field alignment controls.

A few initial spectra will quickly reveal the extent of channeling, through variation in the count ratio for the host atom sites of interest. Typically, about 20 spectra each having about 1000-2000 counts for the impurity species will prove adequate. The accuracy of the final analysis will, of course, depend on the strength of the channeling effects, the quality of background subtraction procedures, uncertainties in the k-factor calibrations, as well as the count rates and number of spectra. Sets of data for different zone-axes and for different areas and thicknesses of the sample can be combined in the final analysis.[5][6] No calculations of diffracted electron intensities within the crystal are required.

Preliminary results for the partitioning of Yb between the Ca and Zr sites of a Yb-doped zirconolite are shown in Table I, for three combinations of x-ray emissions.[5] These were recorded using a Link Ge detector fitted to a Jeol 4000FX, with powdered samples on holey-carbon coated nylon grids mounted in a Gatan double-tilt cold stage at -156^{0}C. The k-factors were only estimated approximately, so there may be a systematic error in the Yb concentrations, to be corrected after the Ge detector has been fully calibrated[7]. The variations in errors for these results are indicative of the effects of low count rates (Yb-K) and delocalised emissions (Zr-L) on the analyses.

Problems with ratio ALCHEMI can arise from uncertainties in the measured count rates, since the ratio-of-ratios analysis amplifies errors.[6] Errors in count rates can result if the channeling effects are weak, if the non-channeling orientation is poorly chosen,[8] but especially when the x-ray emissions from one or more species are delocalised.[9][10] In general, it seems that the ratio method is better suited to planar diffraction geometries. Beam intensity fluctuations over the long counting times required are compensated for through normalisation, but specimen drift (in position and tilt) can be a limitation.

In contrast, the statistical method involves many short measurements, does not amplify errors, averages over random experimental uncertainties, and is less sensitive to the effects of delocalisation. While relative k-factors are required, the method provides both partitioning data and impurity concentrations, together with standard errors consistent with the quality of the data.

These and other comparisons will be illustrated with examples involving several crystal structures, and both axial and planar channeling. The potential of Ge detectors to provide improved ALCHEMI analyses will be considered.[11]

Table I. Partitioning of Yb between Ca and Zr

X-ray emissions	Concentration Yb	Formula (-Ti_2O_7)
Yb-L, Ca-K, Zr-K	0.199 ± 0.008	$(Ca_{0.798}Yb_{0.202\pm0.015})(Zr_{0.805}Yb_{0.195\pm0.015})$
Yb-L, Ca-K, Zr-L	0.20 ± 0.02	$(Ca_{0.84}Yb_{0.16\pm0.03})(Zr_{0.76}Yb_{0.24\pm0.04})$
Yb-K, Ca-K, Zr-L	0.20 ± 0.04	$(Ca_{0.76}Yb_{0.24\pm0.09})(Zr_{0.84}Yb_{0.16\pm0.05})$

1. J.C.H. Spence and J. Taftø, J. Microsc., 130 (1983) 147.
2. K.M. Krishnan, Ultramicroscopy, 24 (1988) 125.
3. J.R. Smyth and T.C. McCormick, Ultramicroscopy, 26 (1988) 77.
4. C.J. Rossouw et al., Phil. Mag. Letts., 60 (1989) 225.
5. P.S. Turner et al., J. Microsc., 162 (1991) in press.
6. C.J. Rossouw et al., Proc. XII Int. Congr. Electron Micr. (1990) 468.
7. T.J. White et al., J. Microscopy, 162 (1991) in press.
8. J.A. Eades et al., Proc. XII Int. Congr. Electron Microsc., (1990) 412.
9. S.J. Pennycook, Ultramicroscopy, 26 (1988) 239.
10. C.J. Rossouw et al., Phil. Mag. B, 57 (1988) 209, 227.
11. Work supported by the Australian Institute of Nuclear Science and Engineering, and by the Australian Research Council.

HIGH-ANGLE ANNULAR DARK-FIELD STEM IMAGING OF DOPED SEMICONDUCTOR LAYERS

D.D. Perovic and J.H. Paterson

Cavendish Laboratory, Madingley Road, Cambridge CB3 0HE, UK

With the development of crystal growth techniques such as molecular beam epitaxy (MBE), it is now possible to fabricate modulation-doped superlattices consisting of alternating ultra-thin layers of n-and/or p-type material abruptly separated by undoped material. At sufficiently high dopant concentrations these abrupt layers may be imaged in cross section by electron microscopy. Pennycook et al.[1] and Treacy et al.[2] have used high angle annular dark-field (HAAD) imaging in the scanning transmission electron microscope (STEM) to image low levels of dopants (~1 at. %) in semiconductors. This work is concerned with imaging boron and arsenic doped layers in silicon at levels <<1 at.%.

Fig. 1 shows a HAAD image of a B-Si superlattice at the <110> zone-axis orientation taken at 100 kV using a VG HB501UX STEM. The bright vertical layers are the B-doped regions, containing ~4 x 10^{20} B/cm^3. The horizontal lines are due to beam instability while the image was recorded. Fig.2 shows a line scan across the same superlattice, recorded by scanning the beam across the specimen in a direction perpendicular to the layers. This shows that the contrast in the B-doped regions is ~6% stronger than in the undoped regions. The part of the line scan off the edge of the specimen at the left of the figure is taken to correspond to zero contrast. Fig 3. shows a HAAD image of a As/B -Si *nipi* superlattice at the same orientation. In this case the doping levels were ~3.5 x10^{20} B/cm^3 and ~8 x 10^{18} As/cm^3. This image was recorded digitally, and the grey-levels remapped using a square-root look-up table to enhance low contrast levels. Contrast from the As-doped layers can be seen between the brighter B-doped layers. The B and As doping levels in these superlattices are known from secondary-ion mass spectroscopy analysis.

The surprisingly strong contrast from the substitutionally B-doped regions has been shown[3] to result from atomic displacement-induced quasi-elastic scattering owing to the large misfit between B and Si. The observed HAAD intensity in fig.1 results solely from Si atoms displaced from their equilibrium lattice sites adjacent to substitutional B-atoms, otherwise, the lower Z of the B:Si regions would give rise to *darker* HAAD contrast relative to the Si matrix from a simple Rutherford scattering argument. The dependence of B:Si contrast on crystal orientation (i.e. Bloch-wave intensity distribution) is consistent with a strain-induced, quasi-elastic scattering description[3] .

The origin of the weak contrast associated with the relatively low concentration As-doped Si layers located between the B:Si layers has also been studied. It is known from several x-ray diffraction studies that substitutionally-doped As induces a negligible strain in Si for concentrations below 1 x 10^{19} As/cm^3. (The As-doped layers shown in fig. 3 are known to be fully substitutional from ion-channelling studies). Accordingly, the observed HAAD contrast is associated with large-angle Rutherford scattering. In light of earlier studies it would appear that Z-contrast would be insignificant at such low impurity concentrations. However, the use of an axial channelling condition should to be best-suited for efficient compositional sensitivity for two reasons. Firstly, for low-index zone axis orientations, complete localization of the Bloch-wave intensity along the atomic columns gives the highest intensity at the atom sites where scattering to high angles occurs. Provided the low-

angle (coherent) Bragg scattering is removed from the image, the incoherent scattering intensity from an impurity atom is therefore maximized. Secondly, a random crystal orientation of the multi-layer structure can hinder the detection of weak contrast. Specifically, for a {100}-oriented multi-layer (cf. fig. 3), the sharpest contrast across a given interface viewed in cross-section is obtained along a <110> crystal direction. In light of the above conditions, we have been able to directly image impurity atom concentrations of ~ 0.01 at.% which to our knowledge is the lowest level attained using electron microscopy techniques thus far. [4]

References

1. S.J. Pennycook, S.D. Berger, and R.J. Culbertson, J. Microsc. 144 (1986), 229.
2. M.M. Treacy et al., Ultramicroscopy 26 (1988), 133.
3. D.D. Perovic et al. , Philos. Mag. (1991) 63 (4).
4. We would like to thank Dr. W.O. Saxton for his help in the preparation of fig. 3.
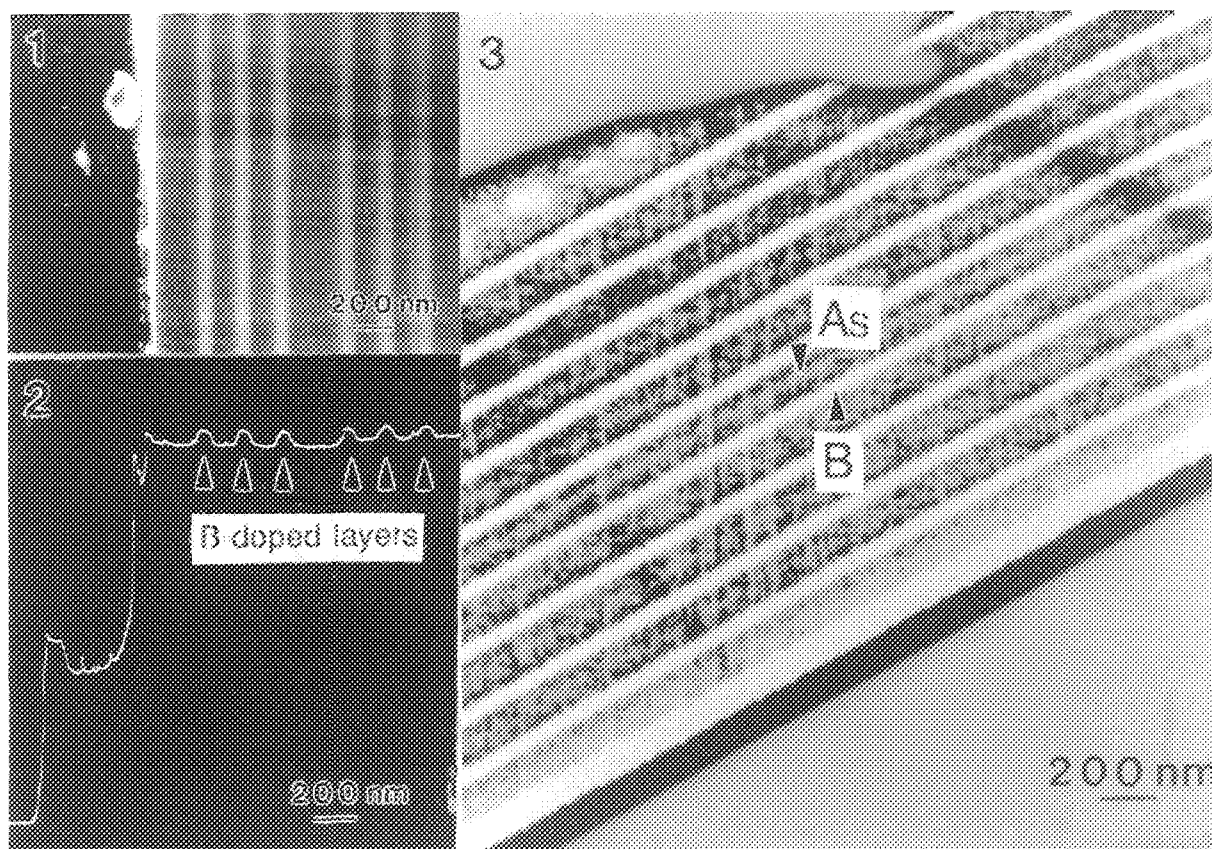
Fig. 1. HAAD image of B-Si superlattice at the <110> zone axis orientation.
Fig. 2. HAAD line scan across the specimen shown in fig. 1.
Fig. 3. Digital HAAD image of B/As-Si superlattice at the <110> zone axis orientation.

ELECTRON SPECTROSCOPIC IMAGING AND DIFFRACTION

M. Rühle*, J. Mayer*, J.C.H. Spence*, J. Bihr**, W. Probst**, E. Weimer**

* Max-Planck-Institut für Metallforschung, Seestraße 92, D-7000 Stuttgart 1, Germany
** Carl Zeiss, Postfach 1380, 7082 Oberkochen, Germany

A new Zeiss TEM with an imaging Omega filter is a fully digitized, side-entry, 120 kV TEM/STEM instrument for materials science. The machine possesses an Omega magnetic imaging energy filter (see Fig. 1) placed between the third and fourth projector lens. Lanio[1] designed the filter and a prototype was built at the Fritz-Haber-Institut in Berlin, Germany[2]. The imaging magnetic filter allows energy-filtered images or diffraction patterns to be recorded without scanning using efficient area detection. The energy dispersion at the exit slit (Fig. 1) results in $\sim 1.5\ \mu m/eV$ which allows imaging with energy windows of ≤ 10 eV. The smallest probe size of the microscope is 1.6 nm and the Koehler illumination system is used for the first time in a TEM. Serial recording of EELS spectra with a resolution < 1 eV is possible. The digital control allows X,Y,Z coordinates and tilt settings to be stored and later recalled.

Three imaging and diffraction modes are possible: conventional imaging without filter, zero-loss filtered imaging and diffraction (at energy E_0) and electron spectroscopic imaging (ESI) with inelastically scattered electrons (with energies $E_0 - \Delta E$, with $0 < \Delta E < 2$ keV). In the conventional mode images are blurred by inelastically scattered electrons. Zero-loss imaging results in an enhancement of the contrast.[3] Energy filtered convergent beam electron diffraction pattern can also be obtained[4] (Fig. 2). Many more details can be recognized on filtered CBED patterns. For the first time, two-dimensional elastic scattering data can be obtained. Fig. 2a,b show unfiltered and filtered CBED of MgO with an 8 eV filtering window (around zero loss). The two micrographs (Fig. 2a,b) were exposed to equal optical density. Pendellösung fringes can easily be seen on filtered images. Such images allow a quantitative two-dimensional evaluation of diffraction patterns which leads to the determination of structure-factor amplitudes and phases[5].

ESI requires an analysis system for image processing. In this system TV images are digitized (512 x 512 pixel) and the intensity for a selected energy loss ΔE is stored for each pixel. Jeanguillaume et al.[6] pointed out that images for (at least) three different energy losses are required for ESI: two images at different energy losses lower than the characteristic edge (ΔE_1 and ΔE_2, intensities: $I(\Delta E_1)$ and $I(\Delta E_2)$) and one image slightly above the energy loss corresponding to the inner shell edge (ΔE_3, intensity $I(\Delta E_3)$). The two images taken at energy losses lower than the edge are used for an extrapolation of the background at ΔE_3: $I_B(\Delta E_3)$. The intensity difference $\Delta I = I(\Delta E_3) - I_B(\Delta E_3)$ between the signal after the edge and the extrapolated background yields information on the concentration of the corresponding element in the specimen for each pixel. A first example is shown in Fig. 3. Fig. 3a represents a BF micrograph of an internally oxidized Pd-Al alloy which contains η-Al_2O_3 particles. Fig. 3b is a processed image for ΔE_3 slightly beyond the K-edge of oxygen: The η-Al_2O_3 precipitates appear bright owing to the oxygen content.

Experiments done so far with the new Zeiss instrument reveal that spectroscopic imaging allows qualitative new possibilities. Such an Omega filter should be available for all TEMs used in materials science research.

References:
1. S. Lanio, Optik 73 (1986) 99
2. S. Kujawa et al., Optik 86 (1990) 39
3. L. Reimer et al., J. Microscopy 155 (1986) 169; 159 (1990) 143; 159 (1990) 161
4. J. Mayer et al., these proceedings
5. J. Zuo et al., Phys. Rev. Letter 61 (1988) 353
6. J. Jeanguillaume et al., Ultramicroscopy 3 (1978) 237
7. The work was supported by the Bundesministerium für Forschung und Technologie (BMFT) under contract No. NTS 0215/8.
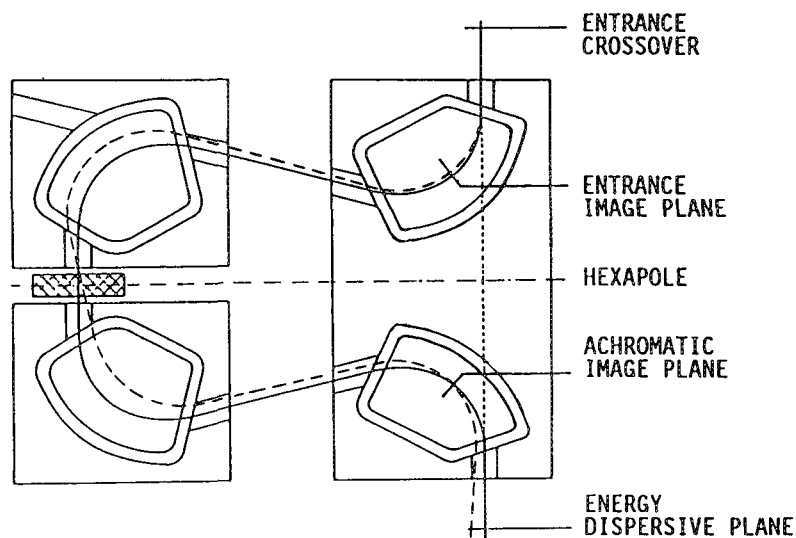
FIG. 1.--Schematic drawing of the Omega filter.
(—— beam path for electrons of energy E_0; – – – beam path for electrons of energy $E_0 - \Delta E$).
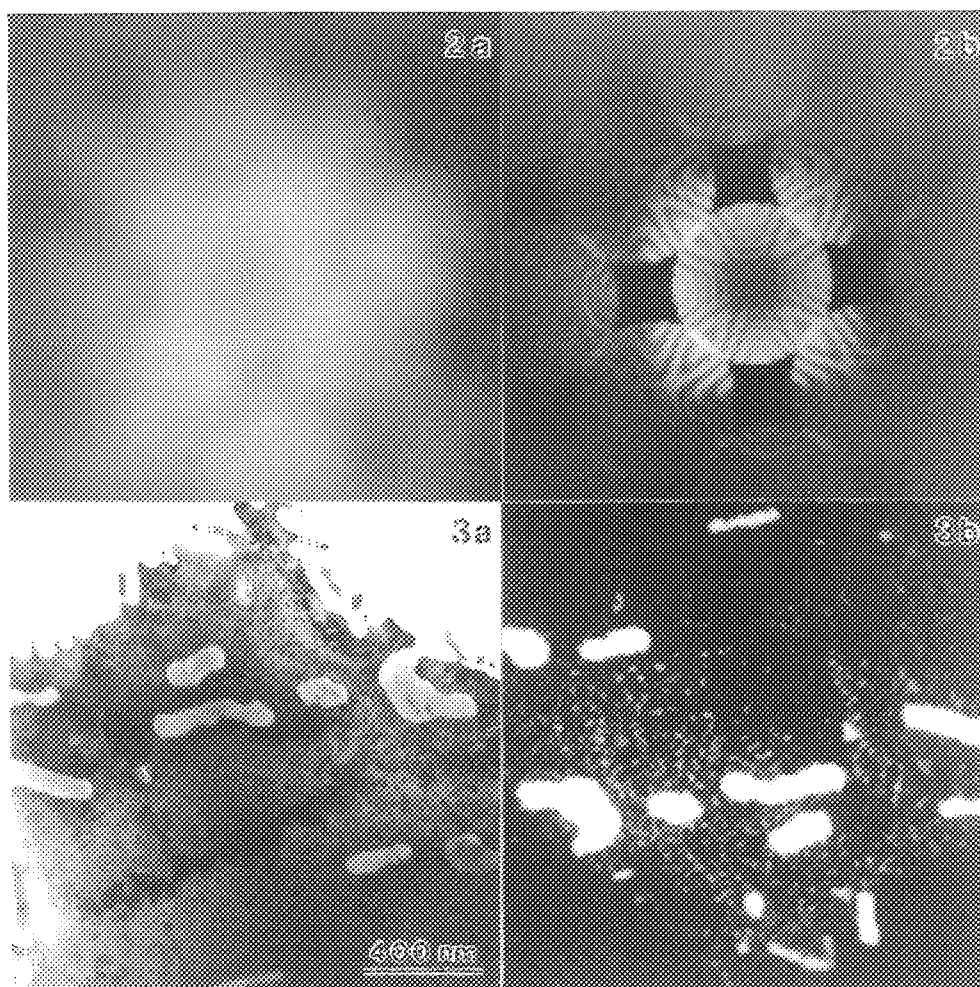
FIG. 2.--Convergent beam diffraction patterns of MgO, zone axis <001>. FIG. 2a--Unfiltered image. FIG. 2b--Filtered image (increased exposure time x 4). The filtered image can be used for comparison with computer simulated CBED (elastic scattering).
FIG. 3.--Oxygen chemical mapping of η-Al_2O_3 particles embedded in Pd. FIG. 3a--Conventional BF image. FIG. 3b--ESI image for oxygen.

CORRECTING CHANNELING AND DIFFRACTION EFFECTS IN QUANTITATIVE REELS SURFACE MICROANALYSIS

Z. L. Wang* and J. Bentley

Metals and Ceramics Division, Oak Ridge National Laboratory, Oak Ridge, TN, 37831-6376
* and Dept. of Materials Science and Engineering, The University of Tennessee, Knoxville, TN, 37996

Channeling conditions or resonance conditions have to be satisfied in order to enhance image contrast in reflection electron microscopy (REM) and the signal-to-background ratio in reflection electron energy-loss spectroscopy (REELS). The introduction of the channeling and diffraction effects can complicate surface microanalysis (Fig. 1). In REELS, the composition ratio for two elements may be determined by[1]

$$\frac{N_A}{N_B} = \frac{I_A(\beta,\Delta)}{I_B(\beta,\Delta)} \frac{\sigma_{eff}(B,\beta,\Delta)}{\sigma_{eff}(A,\beta,\Delta)}, \text{ with } \frac{\sigma_{eff}(B,\beta,\Delta)}{\sigma_{eff}(A,\beta,\Delta)} \equiv \frac{\sigma(B,\beta,\Delta)}{\sigma(A,\beta,\Delta)} \frac{i_B}{i_A} \frac{K_B}{K_A}, \tag{1}$$

where $\sigma(A,\beta,\Delta)$ is the single-atom ionization cross-section of element A for collection semi-angle β and energy window Δ; i_A is the average local (channeling) current density at A atom sites; N_A is the average atomic concentration of A atoms; $\sigma_{eff}(A,\beta,\Delta)$ is defined as an effective ionization cross-section (EICS) of element A; $I_A(\beta,\Delta)$ is the integrated core-loss intensity for element A; and K_A is introduced to take into account the deviation of the final inelastic electron angular distribution from the Lorentzian function due to dynamical diffraction effects. Equivalent symbols apply to element B. The newly defined EICS is determined not only by the property of each single atom (σ) but also by both the dynamical elastic and inelastic electron scattering (K) and the detailed channeling processes (i) of the electrons. In REELS, the elastic Bragg reflections and core-shell inelastic scattering may not be independent events; it is thus necessary to measure their combined effects experimentally. A practical method is described below.

The characteristic features in a reflection high-energy electron diffraction (RHEED) pattern can be observed in a transmission high-energy electron diffraction (THEED) pattern of the same material under identical diffraction conditions.[2] Thus, it should be possible to define the angular distribution of the inelastically scattered electrons within a reflected spot from measurements made in the transmission geometry on a thin foil of the same crystal with the incident beam and specimen tilted to set up conditions equivalent to those in the RHEED case. For a specimen with thickness equal to the mean distance D that electrons travel along the surface in the RHEED case, the effects of dynamical scattering and channeling (or resonance) in the RHEED geometry should be equivalently generated in the THEED geometry and thus be automatically included in EELS measurements of EICS ratios for the equivalent diffraction spot.

For a MgO (100) surface, if one views the crystal along [011], the O and Mg atoms are located in separate rows; it is thus possible to get different O-K and Mg-K excitation signals due to channeling discrimination. For a rough (100) surface and (400) specular reflection case (Fig. 2a), the REELS measured intensity ratio for core-losses is $I(O)/I(Mg) = 17.4 \pm 0.4$ for $\beta = 1.2$ mrad, $V = 300$ kV and $\Delta = 100$ eV. The EICS ratio measured in equivalent THEED case (Fig. 2b) is $\sigma_{eff}(O)/\sigma_{eff}(Mg) = 12.2 \pm 0.6$ (This value has little dependence on specimen thickness). Thus the surface composition determined by Eq. (1) is $N_O/N_{Mg} = 1.43 \pm 0.1$. This result agrees with the ~50% excess oxygen determined previously for an [001] azimuth where there is no discrimination due to channeling.[1] However, an incorrect composition, $N_O/N_{Mg} \approx 0.76$ would be obtained if the EICS ratio, $\sigma_{eff}(O)/\sigma_{eff}(Mg) = 22.9 \pm 1.1$, measured from the (000) spot under weak diffracting conditions was used. The SIGMAK2 program[3] for isolated atoms gives $\sigma_{eff}(O)/\sigma_{eff}(Mg) = 22.0$.

In the (10 00) specular reflection case (Fig. 3a), REELS gives $I(O)/I(Mg) = 15.0 \pm 0.4$ and $\sigma_{eff}(O)/\sigma_{eff}(Mg) = 15.9 \pm 0.4$ (Fig. 3b). Hence $N_O/N_{Mg} = 0.9 - 1.0$, close to the composition of bulk MgO. This result is interpreted as being due to deeper penetration of the electrons into the surface, so that the inelastic scattering is dominated by the bulk effect. The results also show how the relative surface sensitivity of REELS can be controlled.[4,5]

References

1. Z. L. Wang and J. Bentley, Microscopy Microanalysis Microstructures, in press (1991).
2. G. Lehmpfuhl and W. C. T. Dowell, Acta Cryst. (1986) A42, 569.

3. R. F. Egerton, Electron Energy-Loss Spectroscopy in the Electron Microscope, Plenum Press, NY (1986).
4. Z. L. Wang and P. Lu, Ultramicroscopy (1988) 26, 217.
5. Research sponsored by the Division of Materials Sciences, U.S. Department of Energy, under contract DE-AC05-84OR21400 with Martin Marietta Energy Systems, Inc.
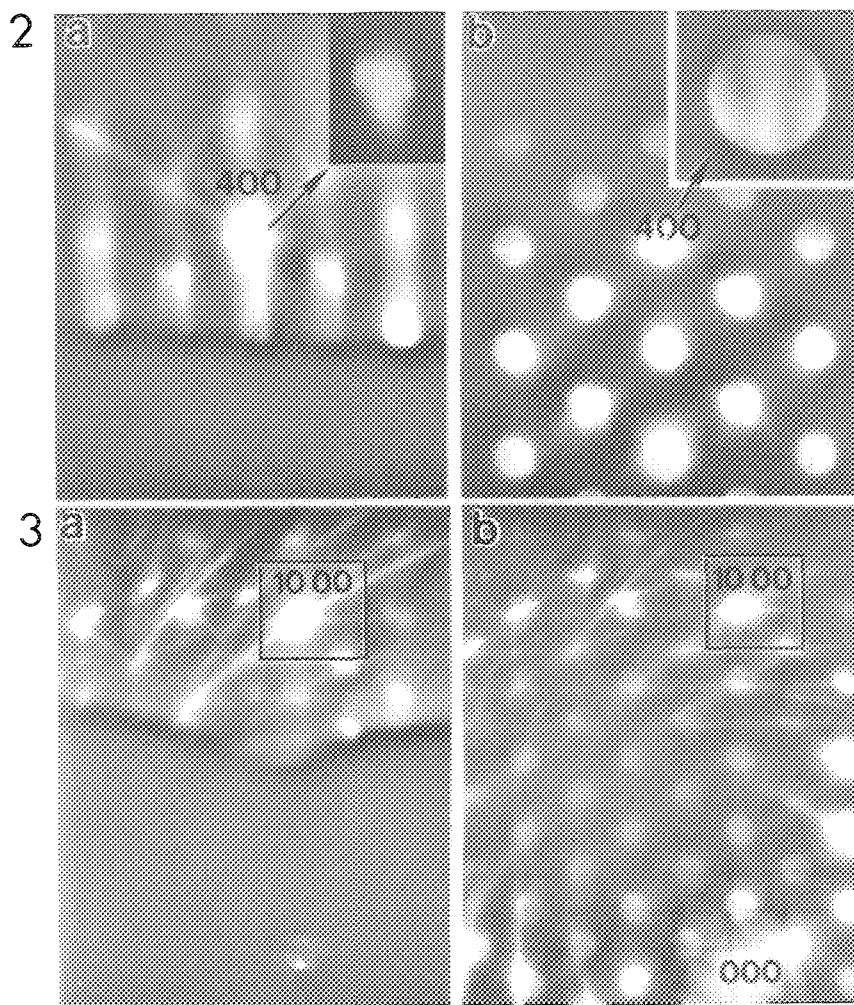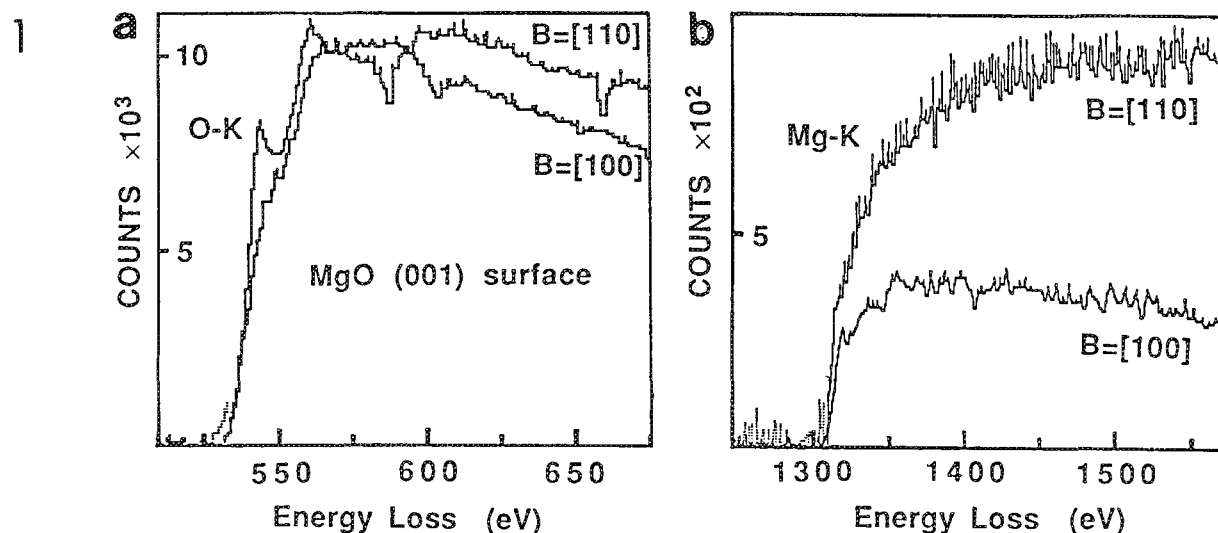
FIG. 1.-- Comparisons of REELS spectra from MgO (001) surface when the beam azimuths are close to [100] and [110] in Philips CM30 TEM (300 kV). Relative increase in Mg-K edge at [110] azimuth case indicates strong electron channeling along the Mg atom rows. In [100] azimuth case, channeling discrimination does not make any difference in the excitation of O-K and Mg-K because both O and Mg are distributed in mixed rows.

FIG. 2.--RHEED (a) and THEED (b) patterns from MgO (100) surface with beam azimuth close to [011] and (400) spot strongly excited. Channeling discrimination may have strong effect in REELS surface microanalysis in this case.

FIG. 3.--Same as Fig. 2 except (10 00) spot is strongly excited.

SHARPENING OF EELS DATA BY DECONVOLUTION

P.E. Batson

IBM Thomas J. Watson Research Center
Yorktown Heights, New York 10598

The IBM Wien filter spectrometer[1] now delivers 0.1eV resolution with a diode array detector. Figure 1 shows the zero-loss distribution, Z(E), in the HB501 STEM. Figure 2 shows the Al $L_{2,3}$ edge obtained at the same time. This report covers a successful application of a suggestion by D. W. Johnson that deconvolution may be possible if Z(E) contains a sharp edge, such as that on the left in Figure 1.

In principle, deconvolution can be done by a simple division of the fourier components of the data $D(\omega)$ by $Z(\omega)$. In practice, severe amplification of noise results by the naive approach. In this work, I use a modified Wiener filter[2] algorithm:

$$D_s(\omega) = \frac{Z(\omega)^\dagger/|Z(\omega)|}{|Z(\omega)| + NS_d(\omega)} D(\omega) \equiv F_d(\omega)D(\omega) \qquad (1)$$

where D_s is the sharpened Data, $NS_d(\omega)$ is the noise to signal ratio, and the dagger indicates a complex conjugate. Equation (1) defines a fourier filter function $F_d(\omega)$. This definition preserves the phases of components in $1/Z(\omega)$ to avoid inducing asymmetries as NS_d is introduced. All of the work and effort is now involved in estimating NS_d. I make a first guess for NS_d as shown in Figure 3, using a characteristic width and power law shape. Notice that the noise is not expected to be constant, and that in the 0.15-0.3eV resolution region the signal is comparable to the noise. Thus, the noise must be accurately evaluated. The first estimate for F_d is then given as curve (a) in Figure 4. If this is multiplied by $Z(\omega)$ we can obtain a resolution function R(E). Figure 5, curve (a) shows that oscillatory wings are introduced into what should be a symmetric, positive definite result. A more desirable shape can be obtained by fitting a smooth power law curve to the wings of R(E). R(E) is then subtracted from the smooth fit to obtain a difference quantity ΔR(E) which quantifies the unwanted oscillatory part. A correction ΔF_d to F_d is then computed:

$$\Delta F_d(\omega) = -\Delta R(\omega)F_z(\omega). \qquad (2)$$

where F_z is defined as F_d above, but uses the noise to signal ratio of Z(E). The justification for this result is easy with some thought and will be covered elsewhere. Now $\Delta F_d(\omega)$ can be added to curve (a) in Figure 4 to obtain a corrected curve (b). In Figure 5, a new R(E), curve (b), is now the result when the new F_d is applied to $Z(\omega)$. After 2-3 iterations, the resolution function converges to the symmetric, positive definite distribution. Finally, F_d is applied to $D(\omega)$ from Figure 2, to obtain the sharpened result shown in Figure 6. Convolution of the resolution function with a step verifies that no oscillations in the deconvoluted data originate with improper correction of the shape of Z(E).

This process can work because the steep edge in Z(E) provides a high resolution source for the measurement. As we noted above, though, the signal to noise at this resolution is not very good. In Figure 4, we can see that the function F_d is unity at the high and low frequencies, but rises to as much as 12 in the frequencies of interest. Thus, the high frequency noise is not amplified, but noise having 0.1-0.2eV periodicity is amplified with the signal. This means that a periodic spectral feature at the limit of resolution can arise from amplification of noise. In the present case, the 0.44eV spin-orbit splitting is resolved, but the shape of the two spin components at the 0.15eV resolution may only be defined with a signal to noise ratio of about 2-3. It is gratifying, therefore, to find a good correspondence with the x-ray absorption data as plotted in Figure 6.[3]

I am indebted to J.C.H. Spence for bringing Johnson's suggestion to my attention. A more detailed description will appear elsewhere.

1. P.E. Batson, Rev. Sci. Inst. 57 43 (1986), 59 1132 (1988).
2. C.W. Helstrom, J. Opt. Soc. Am. 57 297 (1967).
3. C.G. Olson and D.W. Lynch, Sol. St. Comm. 31 601 (1979).
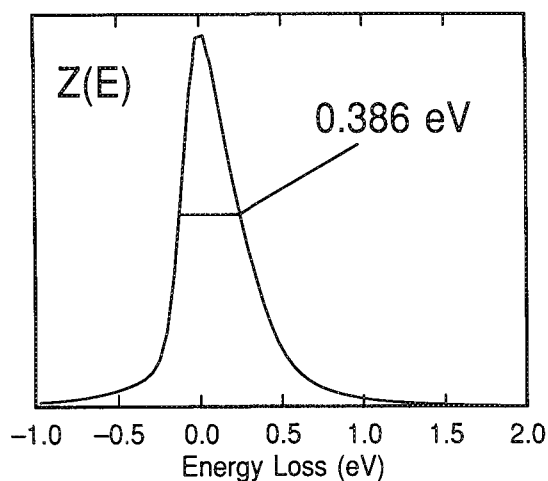
Figure 1 Zero loss energy distribution dominated by the field emission tunneling profile
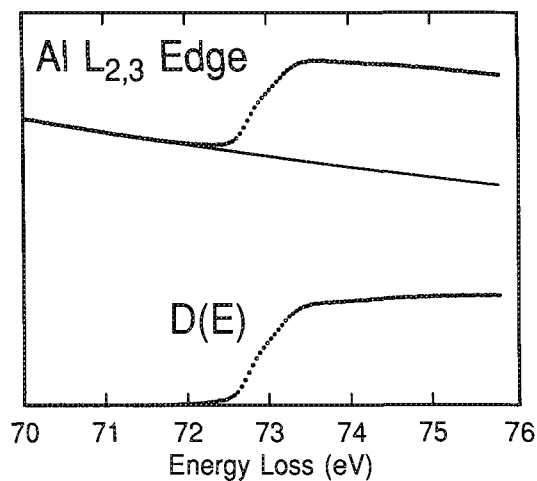
Figure 2. Al $L_{2,3}$ edge raw data, background fit and stripped edge
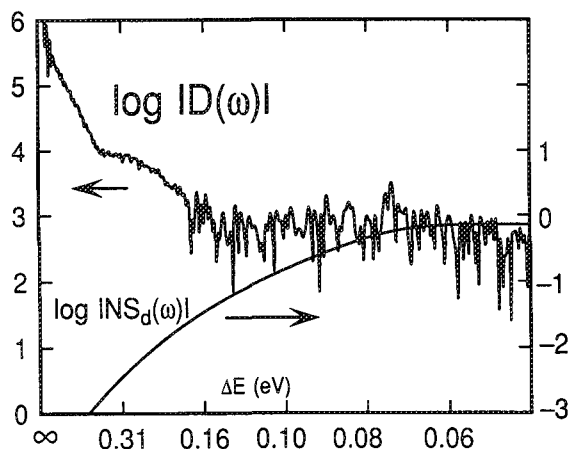
Figure 3. Power spectrum of the data with a first estimate of the noise content. Ordinate is a $\log_{10}$ scale.
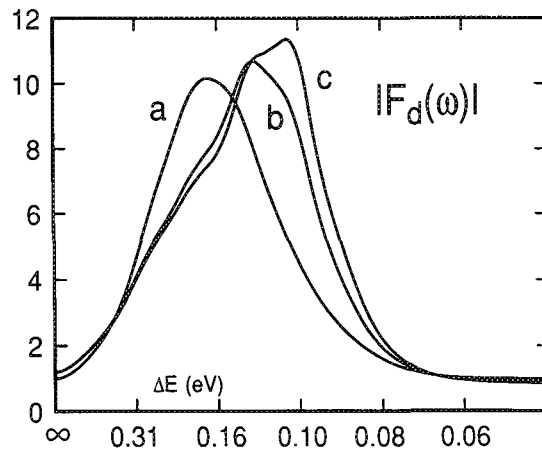
Figure 4. Modulus of successive approximations for fourier filter function, F, used to sharpen the data.
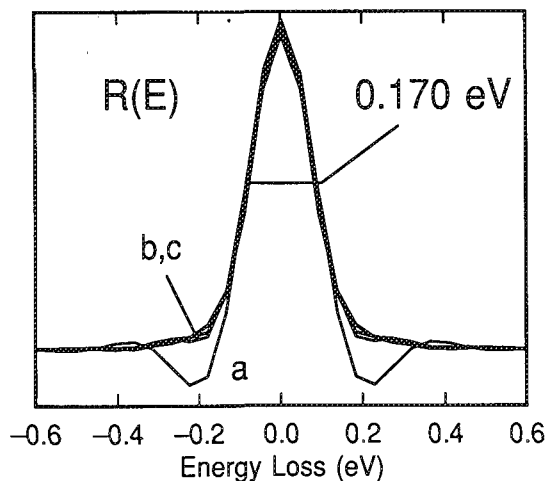
Figure 5 Resolution functions which result from application of successive filter functions to the zero loss distribution
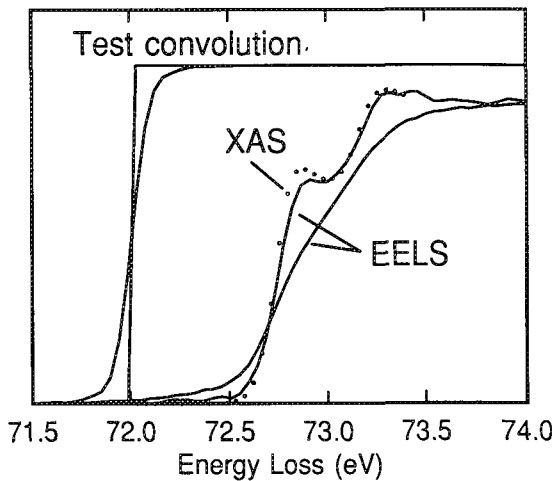
Figure 6. Stripped and sharpened edge compared with XAS results

INELASTIC SCATTERING PROBABILITY FOR ELECTRONS TRAVELLING THROUGH THE OXIDE IN AN MOS HETEROSTRUCTURE

Marek A. Turowski*, Thomas F. Kelly*,**, and Philip E. Batson***

*Materials Science Program, **Department of Materials Science and Engineering, University of Wisconsin. ***IBM Thomas J. Watson research Center, Yorktown Heights, NY   10598

Al/SiO_2/Si (MOS) heterostructures which are typical of actual electronic devices have been studied with high spatial resolution scanning transmission electron microscopy (STEM). As the starting material for a cross-section view TEM sample, the n-type, 4" silicon wafer with 40 nm thick, thermally grown silicon dioxide and 120 nm thick aluminum overlayer was used. Sample preparation procedures and experimental conditions have been described elsewhere [1]. Electron energy loss spectra were recorded over the low-loss region (0 to 100 eV) at 1, 2 and up to 5 nm intervals across interfaces in all three materials. The energy loss function was then obtained from experimental spectra after Fourier-log deconvolution of multiple scattering [2]. We found the structure in the energy loss spectra below the bulk plasmon energy in the vicinity of either interface. They included 3.5 - 4 eV and 7 - 8 eV peaks as clearly seen in Fig.1. The latter is the strongest at the interface and the smaller 3.5 - 4 eV peak reaches its maximum 1.5 - 2 nm away from the interface. For purpose of explaining these features a four-layer model for the electric potential distribution in the MOS heterostructure, as depicted in Fig.2, was developed [1]. The inelastic scattering probability curves were calculated for the electron beam moving through the oxide and compared with the corresponding experimental loss function. The applied potential generated by an oncoming, external electron is a particular solution to the Poisson equation and we called ϕ_{ext} [3]. Homogeneous solutions in one dimension for the planar system are in the form of exp($\pm$ky) and give rise to possible surface excitations [4]. The linear combination of the homogeneous solutions and the particular solution for the bulk modes will give the total potential in any given layer (i). The six multiplication constants can be found from matching the continuity conditions for potentials and normal components of the electric displacement vectors at each interface [1,3].

The results of the computer calculations are included in Fig.3 for the beam at the oxide center and both Al/SiO_2 and Si/SiO_2 interfaces. As the input data we used tabulated values of the refractive index and extinction coefficient [5] for each material, converted to their real and imaginary parts of dielectric permittivity. The energy positions of all features are given in the Table below:

Energy positions of loss features from the model

Features	a	b	c	d	e	f	g
Energy (eV)	1.5	3.8	5-6.5	8.7	11.0	12.5-15.5	20.0

The 8 eV peak, marked as feature d, is attributed to the relaxed surface plasmon from Al or Si depending on which side of the oxide an electron beam is moving[1,6]. The lowest intensity of this feature occurs at the oxide center. The 4 eV peak (feature b) has its origin in the silicon and appears also at the faraway Al/SiO_2 interface. Generally speaking these two and other smaller features are associated with interface contributions to the electron energy loss probability. Full description of the heterostructure should take into account its geometry and component materials, so the appearance of these interface and surface features may lead to a better understanding of the response of composite MOS structures in high electric fields and the phenomenon of dielectric breakdown.

References
1. M.A.Turowski, Ph.D. Thesis, Mat. Sci. Prog., UW-Madison, (1990).
2. R.F.Egerton, "Electron Energy-Loss Spectroscopy in the Electron Microscope", Plenum Press, N.Y. (1986).
3. P.E.Batson, Ultramicroscopy, 11, 299-302 (1983).
4. P.E.Batson, in: Analytical Electron Microscopy, ed. by R.Geiss, San Francisco Press, p. 187 (1981)
5. Handbook of Optical Constants of Solids, ed. E.Palik, Academic Press, Inc. (1985).
6. A.Howie and R.H.Milne, Ultramicroscopy, 18, 427-433 (1985).
7. This work supported by a grant from the International Business Machines Corporation.
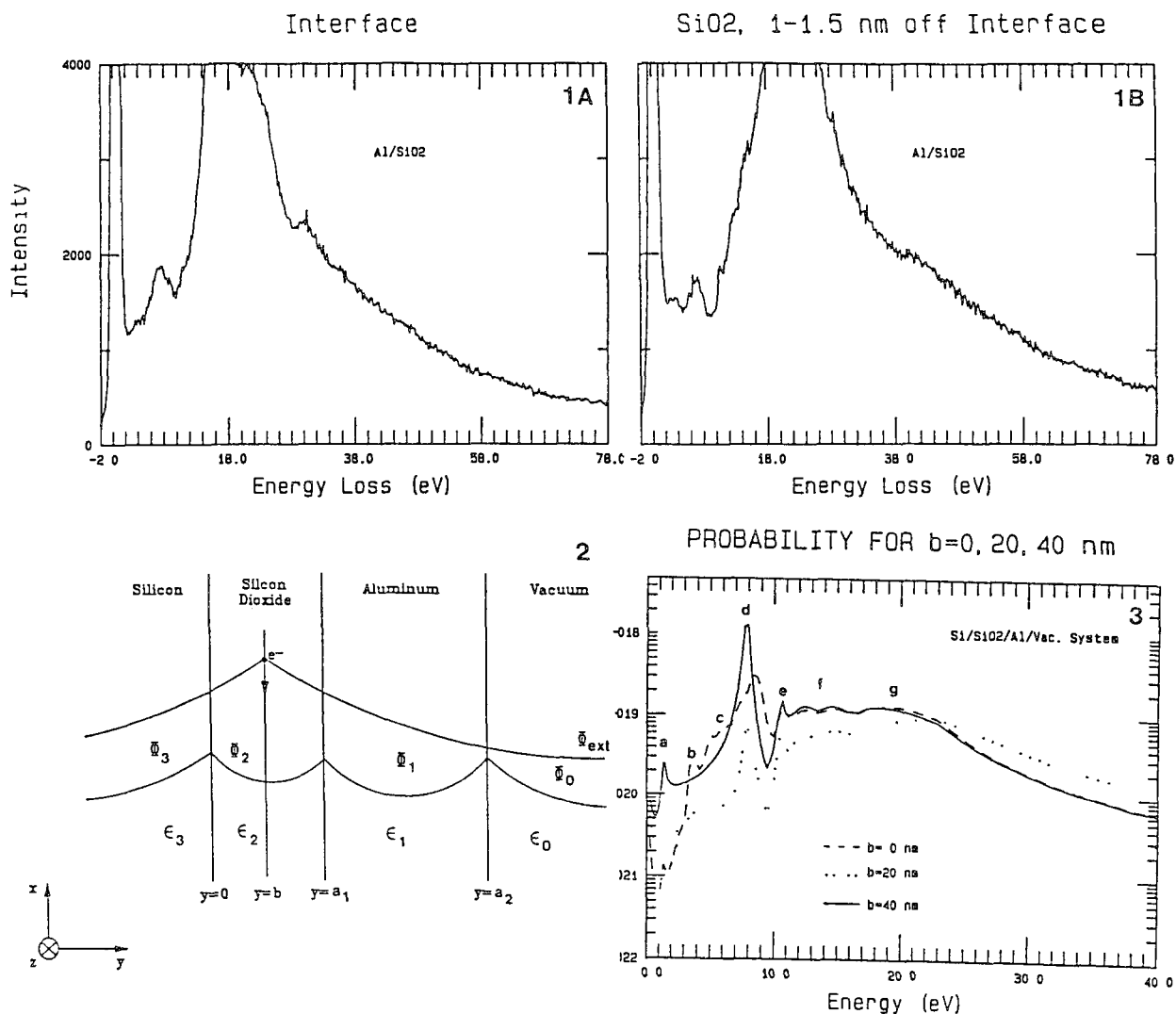
Fig. 1 A) EEL Spectrum at the Al/SiO$_2$ interface. B) EEL spectrum in the SiO$_2$ taken 1-1.5 nm away from the Al/SiO$_2$ interface.

Fig. 2 Four layer geometry of MOS heterostructure with schematic of the potential distribution and an electron beam position.

Fig. 3 Inelastic scattering probabilities calculated from the model for three beam positions: Si/SiO$_2$ interface, the center of the SiO$_2$, and at the Al/SiO$_2$ interface.

TEMPERATURE EFFECTS ON ORIENTATION-DEPENDENT EXELFS

Brad L. Thiel[*] and Christopher Viney[#]

* Department of Materials Science and Engineering; FB-10
# Center for Bioengineering; WD-12
University of Washington, Seattle, WA 98195

Recently, investigations have begun to explore the effects of Mean-Square-Relative-Displacements (MSRD), or thermal damping, on the EXELFS oscillations above electron absorption edges[1,2]. These types of analysis can be extended to include orientation effects in anisotropic crystal systems. Furthermore, as this technique is a direct probe of the electronic structure of a crystal, this information could be combined with the crystal symmetry and Cauchy relations to examine various physical properties. One such property is the elastic compliance quadric.

With the development of the parallel detection EELS spectrometer, EXELFS type studies have become practical. This makes accessible a large field of analysis, previously explored only by EXAFS[3]. Thus, we are able to combine a wealth of experimental and data analysis algorithms from that technique with the high spatial resolution and crystallographic information afforded by the modern analytical TEM. We have developed computer simulation programs which demonstrate the feasibility of this hybrid analysis.

Although the EXELFS equation is somewhat involved, the large number of variables make several types of information available.

$$\chi(k) = \sum_j \frac{N_j}{R_j^2} F(k)\, e^{-2R_j/\lambda} e^{-2\sigma_j^2 k^2} \sin[2kR_j + \Phi_j(k)]\cos^2\omega_j \quad (ref.\ 4)$$

Here, the equation is essentially identical to that of EXAFS, with the addition of the $\cos^2(\omega)$ term which reflects the preferred Bloch state in a two-beam situation. Several techniques exist for isolating the desired piece of information. These range from an actual fitting of the data to taking the ratio of two spectra made while holding all parameters constant except the term of interest. The former method alleviates concerns in dealing with complex edge shapes, multiple scattering, and other complications.

A simple demonstration of this technique is carried out by examining the MSRD (σ^2) in single crystal zinc (hcp), parallel and perpendicular to the basal plane. EXELFS calculations are performed simulating $(10\bar{1}0)$ and (0001) two-beam conditions for several temperatures in the range 100K - 300K (Figs. 1a,b) Values for σ^2_{para} and σ^2_{perp} at each temperature were determined using an equation given by Beni and Platzman[5] and inserting anisotropic Debye temperatures (Fig. 2). As all other terms are temperature independent, if one plots $\log(\chi(k, T)/\chi(k, T_{ref}))$ vs k^2, the slope of the resulting line is related to the vibrational part of σ^2 (Fig. 3). Once the appropriate values of σ^2 have been obtained, they may then be converted into elastic compliance values through lattice dynamics using the known crystal symmetry and spacings determined from the accompanying diffraction patterns[6].

1. M. M. Disko, et al., "Temperature-Dependent Transmission Extended Electron Energy Loss Fine Structure of Aluminum", J. Appl. Phys. Vol. 65, p. 325 (1989)

2. J. Okamoto, et al., "Temperature-Dependent EXELFS of Chemically Ordered and Disordered Fe3Al", Proceedings of the XIIth International Congress for Electron Microscopy, Vol. 2, L. Peachev and D. Williams (eds.), San Francisco Press, San Francisco, p. 50 (1990)

3. B. K. Teo and D. C. Joy (eds.), "EXAFS Spectroscopy, Techniques and Applications", Plenum Press, New York (1981)

4. M. M. Disko, et al., "Orientation-Dependent Extended Fine Structure in Electron-Energy-Loss-Spectra", Phys. Rev. B, Vol. 25, No. 6, p. 4252 (1982)

5. G. Beni and P. M. Platzman, "Temperature and Polarization Dependence of Extended X-ray Absorption Fine-Structure Spectra", Phys. Rev. B, Vol. 14, No. 4, p. 1514 (1976)

6. W. Cochran, "The Dynamics of Atoms in Crystals", Edward Arnold, London (1973)
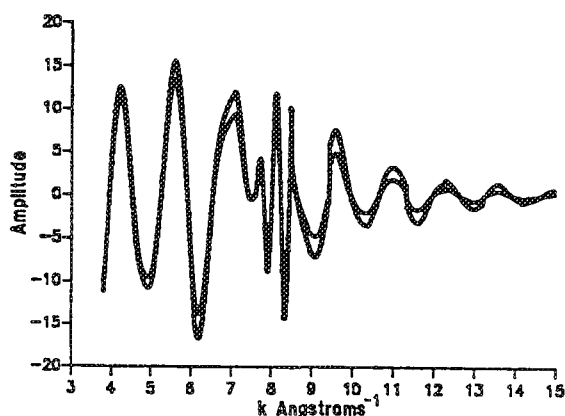
Figure 1a. Simulated EXELFS oscillations in the basal plane of zinc. The larger amplitude corresponds to 100 K, with much stronger damping at 300 K.
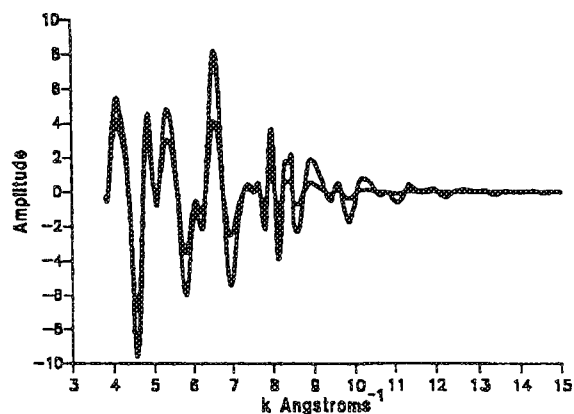
Figure 1b. Simulated EXELFS oscillations perpendicular to the basal plane in zinc at 100 and 300 K. The effects of thermal damping are much more pronounced.
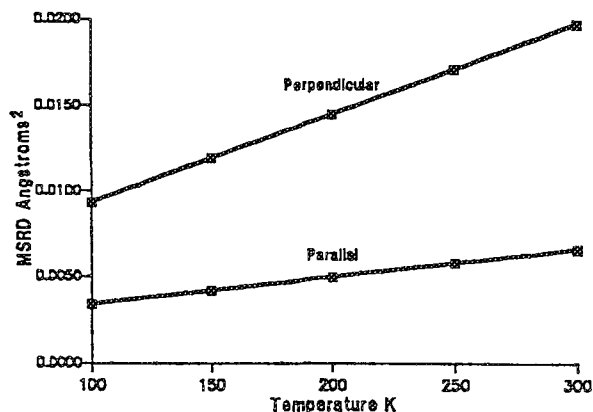
Figure 2. Calculated MSRD values for zinc parallel and perpendicular to the basal plane.
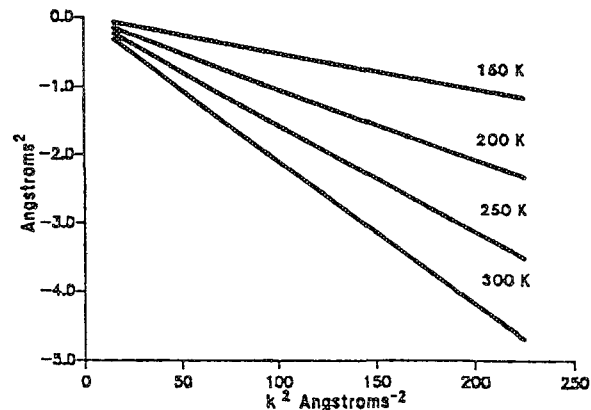
Figure 3. Log ratio plots for spectra at several temperatures relative to 100 K. The increasing slope with temperature reflects the increasing MSRD damping.

QUANTITATIVE LIGHT-ELEMENT ANALYSIS USING PEELS

J. A. Hunt, A. J. Strutt, and D. B. Williams

Department of Materials Science and Engineering Lehigh University,
Whitaker Lab #5, Bethlehem, PA 18015-3095

Electron energy-loss spectrometry (EELS) is theoretically superior to x-ray emission spectrometry (XES) for light element microanalysis. The x-ray fluorescence yield decreases proportional to Z^4, thus dramatically reducing characteristic x-ray production. However, the ionization cross section increases and so EELS becomes more efficient as Z decreases. Despite these advantages light element microanalysis using XES is often preferred to EELS. There are two major reasons why EELS is not more widespread. First, very thin specimens are needed to minimize plural scattering so quantification can proceed assuming single scattering. Secondly, many experimental variables[1] make EELS difficult, particularly for microanalysts accustomed to the x-ray 'turn-key' approach to quantification. The former problem is being overcome with multiple least-squares (MLS) fitting deconvolution routines[2], while the latter has largely been solved by the development of parallel EELS (PEELS) and powerful analysis software. In this paper we show the quality of data currently available using PEELS.

(P)EELS is capable of detecting very light elements such as Li, which is beyond the limits of XES. Analysis of lithium is complicated because the standard power law background fit is inaccurate at low energy losses due to overlap with the plasmon peaks. Difference spectra can suppress the background and PEELS is ideally suited to this approach (Figure 1). Figure 2 shows $\delta'(Al_3Li)$ particles imaged using the background-subtracted Li K edge at 55eV. Spectral collection times are so short that PEELS spectrum-imaging[4] is possible. At each pixel spectra are collected, stored and quantified. Similar data can also be collected using the first plasmon peak shift which varies as a function of Li content[5]. Figure 3 shows a plasmon image where the most intense signal corresponds to the plasmon peak for δ' (14.02 eV) and the background intensity corresponds to the α (Al-Li solid solution) plasmon (14.74 eV). Figure 4 shows quantitative PEELS maps of the Be, Co and Cu distributions in a Cu-Be-Co alloy along with a total inelastic image. Figure 5 shows the change in oxygen concentration across a NiO-ZrO_2 interphase interface measured from changes in the O K-edge which also reflect the change in bonding across the interface. Such analyses are only feasible with PEELS, not serial EELS.

PEELS will only displace XES as the preferred method for all light element microanalysis when it becomes possible to acquire recognizable spectra at the push of a button. Improvements in stability of the electronics, improved (e.g. 2D-CCD) detection systems, combined with on-line reliable and 'turn-key' analysis, are all in progress, but not yet universally available.

References

1.   M. M. Disko, Microbeam Analysis-1986, S. F. Press (1986) 429.
2.   R. D. Leapman and C. R. Swyt, Ultramicroscopy (1989) 26, 393.
3.   D. R. Liu and D. B. Williams, Proc. Roy. Soc. (1989) A425, 91.
4.   J. A. Hunt and D. B. Williams, Ultramicroscopy (1991) in press.
5.   D. B. Williams and J. W. Edington, Phil. Mag. (1974) 30, 1147.
6.   Research supported through NSF DMR 89-05459.
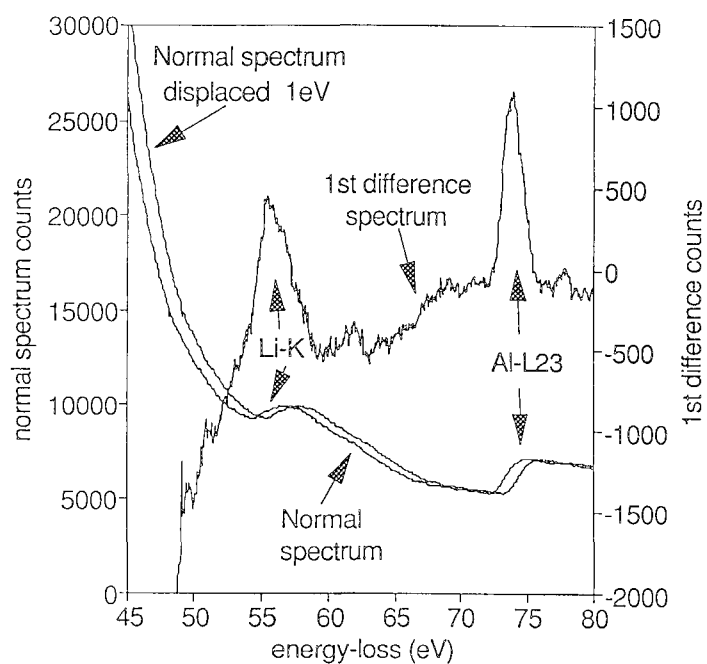
Fig.1 Difference spectrum of Al-Li alloy produced from energy-displaced normal spectra
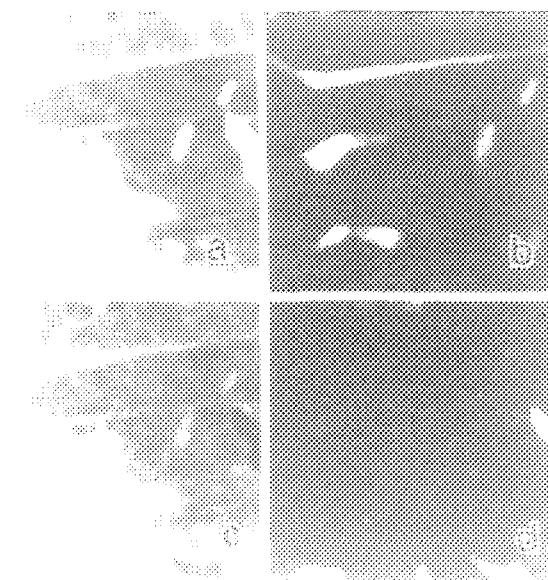
Fig.4 PEELS map of Cu-Be-Co alloy showing (a) the total inelastic map, (b) Be, (c) Cu and (d) Co-distributions

Fig.2 PEELS map of δ'-precipitates in Al-Li alloy using Li-K ionization edge
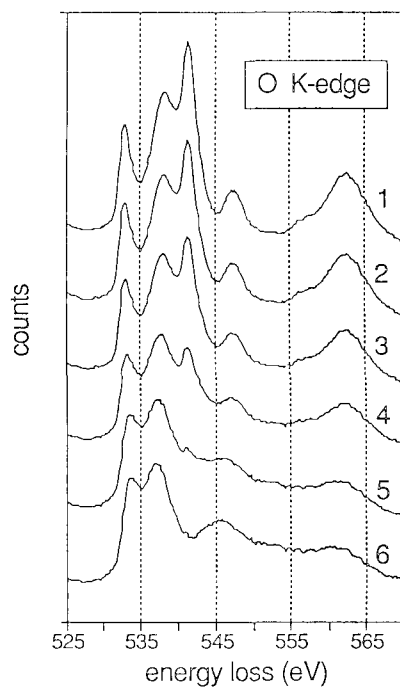
Fig.3 PEELS map of δ'-precipitates using Al-plasmon energy
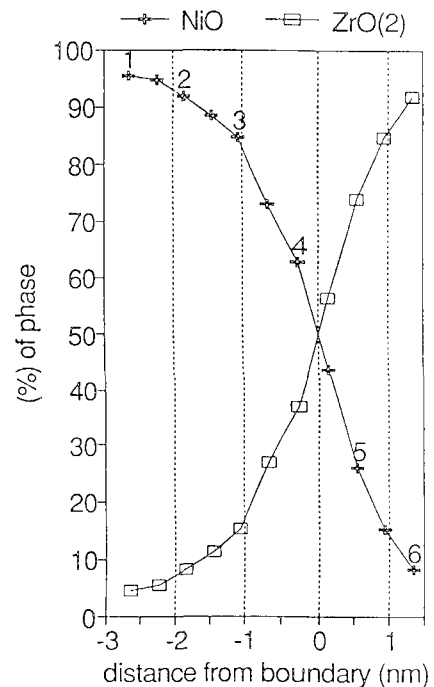
Fig.5 PEELS O-K edge spectra from across a NiO/ZrO2 interface together with calculated chemical composition gradients

IMPROVED DETECTION LIMITS WITH PARALLEL-DETECTION EELS

O.L. Krivanek and M.K. Kundmann*

Gatan Research and Development, 6678 Owens Drive, Pleasanton, CA 94588, USA
*present address: 189A Wildwood Avenue, Worcester, MA 01603, USA

Parallel-detection electron energy-loss spectrometers (PEELS) have improved the detection limits of electron energy-loss spectroscopy (EELS) so much that established comparisons between EELS and energy-dispersive X-ray spectroscopy (EDXS) no longer apply. We have therefore decided to re-investigate the comparative advantages of EELS as a microanalytical technique.

Two types of detection limits are of interest[1]: minimum detectable mass (MDM), and minimum detectable mass fraction (MMF). MDM has been improved by parallel-detection EELS so much that single atoms of elements with favorable cross-sections have become detectable[2]. Since detecting a single atom requires a probe with at least 0.1 nA of current and a diameter of no more than 1 nm, this level of performance needs an electron microscope equipped with an efficient field-emission gun (FEG). On the other hand, because the ratio of the signal from a uniformly dispersed element to the signal from the matrix does not depend on the size of the probed area, MMF depends on the total available probe current rather than the probe current density. This means that MMF should be better for microscopes equipped with thermionic guns than for ones equipped with FEGs.

In order to extract the signal due to a minority element from the strong EELS background, difference techniques[3,4] are used, in which the spectrum is transformed into a first or second difference. The difference spectra are obtained by shifting the spectrum by a few eV between acquisitions, and computing the difference as (A - B) for the first difference, or (2B - A - C) for the second difference, where A, B, and C are mutually shifted spectra. The resultant spectra render weak signals much more visible, and suppress the importance of noise due to the channel-to-channel gain variation of the parallel detector. They consist mostly of peaks and valleys located at edge thresholds, and are amenable to similar methods of quantification as X-ray spectra. Using these types of techniques, Leapman recently showed[5] that MMF attainable with PEELS is similar or lower than MMF attainable using simultaneously acquired EDXS data for elements as heavy as Fe. His study was done in a FEG STEM using less than 1 nA of beam current. Using a standard TEM and a beam current of several nA to several tens of nA, the PEELS MMF can be lowered further, or the same MMF can be obtained in a shorter time.

A state-of-the-art X-ray detector can accept about 30,000 counts per second in the whole spectrum while maintaining a good energy resolution, whereas a more typical X-ray detector can only handle about 5000 counts per second. A parallel-detection EELS detector can accept up to about 10^{10} primary electrons per second in the detected part of the spectrum without saturation. In practice this means that the total beam current has to be restricted to less than a nA for X-ray analysis, while parallel-detection EELS can work with a beam current of several tens of nA as long as the low-loss region is kept away from the detector. Coupled with the much greater geometric collection efficiency of EELS compared to EDXS (about 100 times better) and the fact that typically only one out of around 1000 energy-loss events is accompanied by the creation of an X-ray (fluorescence yield), this means that the signal available to EELS is typically more than 10^6 times stronger. Even though the background is much higher in unprocessed EELS spectra, it is considerably reduced in the difference spectra, especially if there are strong peaks at edge thresholds. The result is that the lowering of MMF by one to two orders of magnitude by EELS compared to EDXS, as originally predicted by Isaacson and Johnson[1], is now within reach.

The practical performance of PEELS and EDXS is compared in Figs 1 to 3. Fig. 1 shows a portion of an undifferentiated PEELS spectrum obtained from gahnite, a naturally occurring mineral whose nominal composition is Al_2ZnO with 3% Fe and 0.3% Mn impurities[6]. The spectrum contains clear oxygen K and iron $L_{2,3}$ edges at 532 and 708 eV respectively, but there is no readily visible manganese $L_{2,3}$ edge at 640 eV. Fig. 2 shows a background-subtracted first difference PEELS spectrum from the same sample, in which a manganese L_3 threshold peak is readily visible. This spectrum was acquired in 132 seconds with a

beam current of about 5 nA. The total count in the Mn L3 threshold peak is 3700 counts, and the background noise in the same energy interval is about 120, giving a signal-to-noise ratio of 30. Fig. 3 shows an X-ray spectrum acquired from the same material in 312 seconds, with a Mn peak showing a signal-to-noise ratio of about 5. If we define a minimum acceptable signal-to-noise ratio as 3, then a 100-second acquisition X-ray spectrum taken under the same conditions would have just detected the 0.3% of Mn in gahnite, and a 100-second PEELS spectrum taken with 5 nA beam current would have just detected about 0.03% of Mn. Had the PEELS spectrum been taken with 50 nA instead, the PEELS MMF in 100 seconds would have been 0.01%, and 0.1% in a 1-second spectrum.

In conclusion, PEELS is turning out to be valuable in detecting small concentrations of uniformly dispersed elements. It is likely to be more sensitive than EDXS for all elements with $Z < 29$, and $Z = 34, 35, 37$-45, 55-69, and 87-101, i.e., for more than 50% of the elements in the periodic table.

1. M. Isaacson and D. Johnson, Ultramicroscopy 1 (1975), 33.
2. O.L. Krivanek et al., J. of Microscopy, Microanal. and Microstruct., to be published.
3. H. Shuman and P. Kruit, Rev. Sci. Instr. 56 (1985), 231.
4. M.K. Kundmann and O.L. Krivanek, J. of Microscopy, Microanal. and Microstruct., to be published.
5. R.D. Leapman and J.A. Hunt, J. of Microscopy, Microanal. and Microstruct., to be published.
6. J. Taftø, Proceedings 10th ICEM (Hamburg, 1982) vol. 1, p. 611.
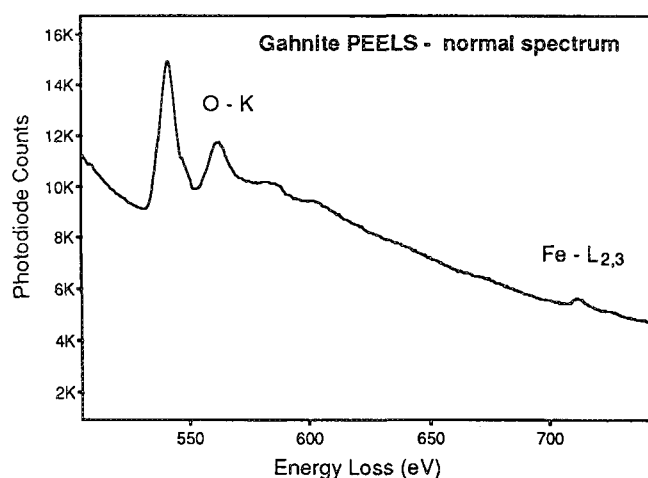
Fig. 1. (above left) Normal PEELS spectrum from naturally occurring gahnite mineral. 100 keV primary energy, 22 seconds acquisition.
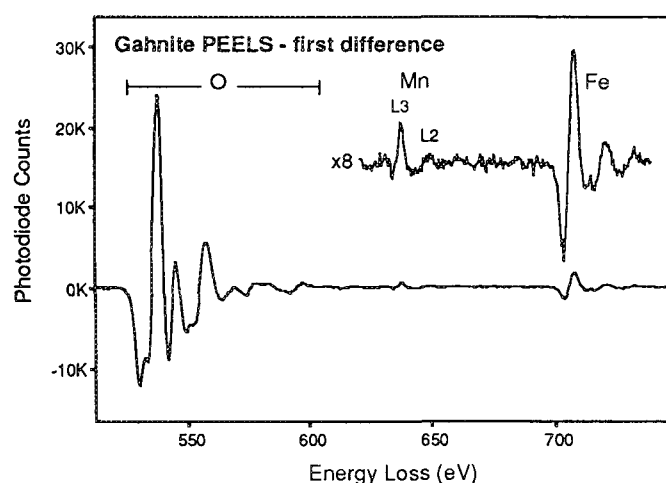
Fig. 2. (above right) First difference PEELS spectrum from gahnite. 132 seconds acquisition. Background subtracted.

Fig. 3. EDXS spectrum from gahnite. 200 keV, 312 seconds acquisition. The inset shows the underlined portion of the spectrum expanded both vertically (8x) and horizontally (4x). The arrowed peak is about one half the size of the Mn peak, but it is due to noise.
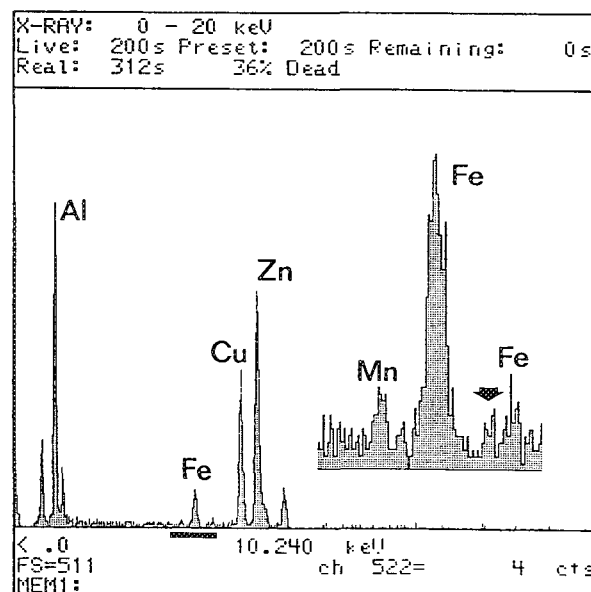
AN EXAMPLE OF SPECTRUM IMAGING USED FOR COMPARISON OF EELS QUANTITATIVE ANALYSIS TECHNIQUES ON Al -Li

John A. Hunt

Department of Materials Science and Engineering, Lehigh University, Bethlehem, PA 18015

Spectrum-imaging is a useful technique for comparing different processing methods on very large data sets which are identical for each method. This paper is concerned with comparing methods of electron energy-loss spectroscopy (EELS) quantitative analysis on the Al-Li system. The spectrum-image analyzed here was obtained from an Al-10at%Li foil aged to produce δ' precipitates that can span the foil thickness. Two 1024 channel EELS spectra offset in energy by 1 eV were recorded and stored at each pixel in the 80x80 spectrum-image (25 Mbytes). An energy range of 39-89eV (20 channels/eV) are represented. During processing the spectra are either subtracted to create an artifact corrected difference spectrum, or the energy offset is numerically removed and the spectra are added to create a normal spectrum. The spectrum-images are processed into 2D floating-point images using methods and software described in [1].

Analysis of Li content in Al-Li alloys using EELS is complicated by an interference between the fourth plasmon and the Li K-edge, and because the power-law background model ($A E^{-r}$) is not accurate at these low energy-losses. Because the energy-scale of the spectra changes slightly as a function both of time and scan position, the Al L_{23}-edge was used to fix the energy scales of each pixel. Spectrum-imaging allowed each of the analysis methods to be repeated several times to hone the processing parameters. Images created using each technique are shown in figure 1. Similarities in the 'noise' of these images suggest energy scale correction errors. The discontinuity in the images around the 52nd scan line is due to an uncorrected spatial drift and does not affect these analyses. The reported image maxima for the methods analyzed correspond to the δ' precipitate composition. They were calculated using slightly spatially smoothed images to reduce the influence of outliers.

Linear least-squares (LLS) was used to fit the background below the Li K-edge by modeling the background before the edge (51-54eV) using a power-law model. A small integration window was used (54.5-56eV) to minimize the errors from the background model and contribution from the fourth plasmon. Analysis of the Al L_{23}-edge is more straightforward; the fitting window was from 66-72eV, the integration window was 72.9-82.9eV. Using a cross-section calculated from SIGMA-K/L [2] the maximum Li concentration ([Li]) is 54.0at%, the mean is 14.7at%. If we assume the foil imaged to be representative of the bulk distribution, the mean [Li] can be set to 10at%, giving a δ' [Li] of 36.7at%. These values are higher than the expected [Li] of about 25at%. Large errors are expected with these calculations because plural-scattering deconvolution was not performed. Figure 1a.

Plasmon energy-shifts can be used to quantify [Li] in Al-Li[3 4] according to $E_p=E_{Al}-[Li]^*C$, where C is a constant, E_p and E_{Al} are the plasmon energies for the unknown and pure Al respectively. An image plane of 3^*E_p was created by measuring the position of the third plasmon and a mean value for E_p was calculated. Assuming the imaged region has a mean [Li] of 10at% the value of C is 4.0, giving a maximum [Li] of 25.8at%. The accuracy of the plasmon shift technique is not sensitive to plural scattering when the first plasmon is used. However, there is a minimum thickness where the third plasmon maxima can be discriminated from the background. For this reason the plasmon shift image in figure 1b terminates further before the edge of the foil than for images of the other techniques. The noise level also increases dramatically as the foil thickness decreases.

Multiple least-squares (MLS) techniques can remove effects of plural scattering.[5] First difference

reference spectra were obtained from an Al foil, and from a LiF film beam damaged to create metallic Li. The first plasmon of a matrix composition Al-Li spectrum was used to convolve the Al and Li references one, two, and three times. The unconvolved references were differentiated again, yielding a total of five reference spectra per element. These references were fit to the edges at each pixel along with the equation of a line and image planes were created for each fit coefficient and its standard deviation (28 images). Figure 1c was created by using the fit coefficients of the unconvolved Li and Al references. Associating the mean [Li] to 10at% yields a peak [Li] of 26.8at%.

The similarities between the contrast of the MLS and plasmon-shift images suggest that these are the methods of choice for analyzing [Li] in Al-Li, and analysis using LLS should not be trusted without deconvolution. The simplicity of the plasmon-shift method and its applicability to relatively thick specimens make it useful for routine microanalysis.

References

1. J. A. Hunt and D. B. Williams, Ultramicroscopy (1991) in press.
2. R. F. Egerton, in:Scanning Electron Microscopy/1984, vol.II, ed. O. Johari, (1984) 505.
3. D. B. Williams and J. W. Edington, Phil. Mag. (1974) 30, 1147.
4. J. A. Hunt, A. J. Strutt, D. B. Williams, these proceedings.
5. R. D. Leapman and C. R. Swyt, Ultramicroscopy (1989) 26, 393.
6. Work supported through NSF DMR 89-05459. Thanks to Dr. A.J. Strutt for the Al-Li specimens, and Dr. R.D. Leapman for providing the VG HB-501 microscope.
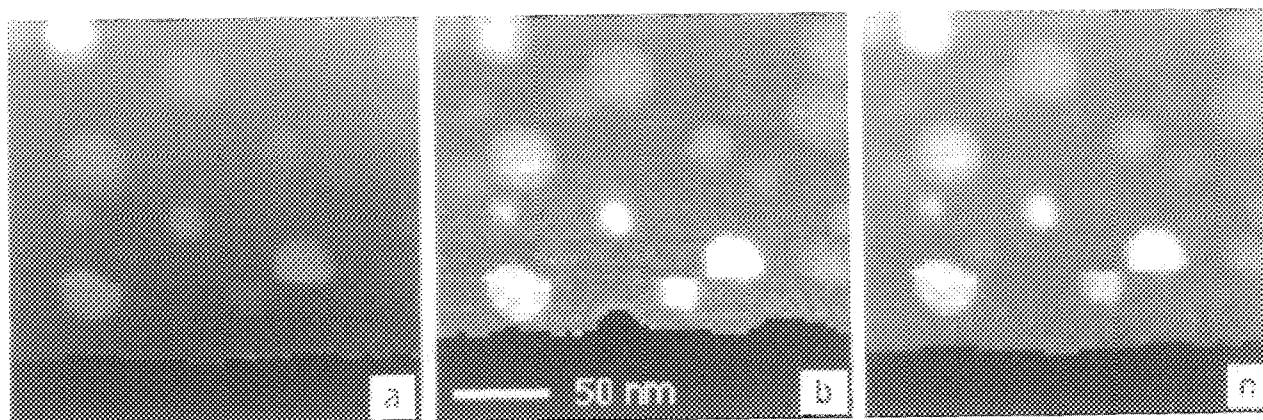
FIG. 1.--Images of [Li] (at%) in a Al-10at%Li foil created using spectrum-imaging with (a) LLS, (b) plasmon-shift imaging, (c) MLS.

QUANTIFICATION OF METALLIC ALUMINUM PROFILES IN Al+ IMPLANTED MgAl₂O₄ SPINEL BY ELECTRON ENERGY LOSS SPECTROSCOPY

N. D. Evans,* S. J. Zinkle,** J. Bentley,** and E. A. Kenik**

* Oak Ridge Associated Universities, P.O. Box 117, Oak Ridge, TN 37831-0117
**Metals and Ceramics Division, Oak Ridge National Laboratory, P.O. Box 2008, Oak Ridge, TN 37831

Magnesium aluminate spinel ($MgAl_2O_4$) is being considered as an insulator material within fusion reactors because of its favorable damage characteristics. The microstructure of material implanted at 650°C with 2 MeV Al^+ ions is shown in cross-section in Fig. 1. Little damage occurs near the surface, whereas at greater depths (0.5 - 1.0 μm) dislocation loops are formed on {110} and {111} planes.[1] Small features thought to be metallic aluminum colloids were observed in the implanted volume near end-of-range. Phase identification by electron diffraction is complicated because the lattice parameter of spinel (0.8083 nm) is almost exactly twice that of aluminum (0.4049 nm). However, the spinel <222> reflection is weak but the aluminum <111> reflection is intense. In $<222>_{sp}/<111>_{Al}$ dark-field images of the implanted volume near end-of-range (Fig. 2) the bright 5-10nm diameter features were presumed to be metallic aluminum colloids.

Since the bulk plasmon loss for metallic aluminum is ~15 eV and the spinel valence loss maximum is at ~24 eV, parallel-detection electron energy-loss spectroscopy (PEELS) for the low-loss region was performed on an implanted specimen prepared in cross-section to attempt to confirm (and quantify) the presence of metallic aluminum. With specimens at -130°C, spectra were acquired with a Gatan 666 PEELS and a Philips CM30 analytical electron microscope (AEM) operated at 300 kV in the diffraction mode (beam convergence $\alpha = 1.5$ mrad, collection semi-angle $\beta = 6$ mrad) and the electron beam converged to define the volumes analyzed. Specimen thicknesses were 40 to 70% of the inelastic mean free path length. A few spectra were acquired in the image mode under equivalent conditions and all spectra were deconvoluted by the Fourier-log method.[2] Reference spectra were obtained from undamaged spinel (well beyond end-of-range) and metallic aluminum, with the relative thicknesses measured from X-ray spectra acquired simultaneously. Acquired spectra were deconvolved into the components due to metallic aluminum and spinel by linear least squares multiple regression analysis with the reference spectra from 10 to 40 eV at ~0.35 eV/channel. The standard error of estimate and 95% confidence intervals about the fitting parameters were also determined.

The two low-loss reference spectra, a spectrum from material at an implant depth of ~1.6 μm, and a spectrum constructed with the best-fit values calculated from the least squares multiple regression analysis are shown in Fig. 3. Overall, the agreement between the constructed best-fit spectrum and the spectrum from the implanted region is quite good; the standard error of the estimate is less than 300 counts. The slight shift of the apparent maximum of the plasmon from the implanted spinel to a lower energy-loss is possibly due to irradiation damage changing the dielectric function of the spinel.

The volume fraction of metallic aluminum in the spinel was measured as a function of implant depth from regression analyses of low-loss spectra and is shown in Fig. 4, where the horizontal error bars define the 200nm probe diameter and the vertical error bars represent the 95% confidence interval. The implant profile calculated by the EDEP-1 computer code, but shifted 0.2 μm deeper, is also shown in Fig. 4. At depths of 0.4 to 1.2 μm, the regression analysis indicated up to 1 vol. % metallic aluminum is present, though none is expected or predicted by EDEP-1. This is probably due to the use of undamaged spinel rather than damaged spinel (with either no or a small amount of metallic aluminum) to obtain the reference spectrum. The confidence intervals for the spectra acquired in the image mode are slightly greater than corresponding spectra acquired in the diffraction mode (±0.8 and ±0.6 vol. % metallic aluminum, respectively); the difference is likely due to the latter being acquired in the same mode as the referencing spectra. Immediately beyond end-of-range, the regression analyses indicated best fits with small negative components of the metallic aluminum spectrum; the reason for this is unclear.

High spatial resolution PEELS was performed at 100 kV with a Philips EM400T/FEG AEM. Initial experiments were performed in the scanning transmission (STEM) mode with a ~0.8nA probe of ~2nm diameter. Large contributions from metallic aluminum were clearly present in the acquired spectra, but

examination of the image showed substantial beam damage (hole drilling) which is known to proceed by reduction to the metallic components in other oxide ceramics.[3] To avoid possible spurious results, spectra were obtained in the image mode at high magnification with area selection by a 2 mm spectrometer entrance aperture. No objective aperture was used because of specimen charging and the need to perform simultaneous X-ray microanalysis when acquiring new reference spectra. Two spectra from the regions indicated in Fig. 2, but obtained under different (weaker) diffracting conditions, are shown in Fig. 5. Regression analyses indicated 3.8 ± 0.5 and 22.8 ± 1.7 vol.% metallic aluminum for spectra (a) and (b), respectively. The pronounced peak at ~15 eV in spectrum (b) confirms the initial interpretation of dark-field images as indicating metallic aluminum colloids.[4]

1. S. J. Zinkle, Proc. 15th Intern. Symp. on Effects of Radiation on Materials (Nashville, TN, June 17-21, 1990) Philadelphia: ASTM in press
2. R. F. Egerton, Electron Energy-Loss Spectroscopy in the Electron Microscope, New York: Plenum Press (1986) 229
3. S. D. Berger et al., Phil. Mag. B 55 (1987) 341
4. Research sponsored by the Division of Materials Sciences, U.S. Department of Energy, under contract DE-AC05-84OR21400 with Martin Marietta Energy Systems, Inc., and under contract DE-AC05-76OR00033 with Oak Ridge Associated Universities (SHaRE Program).
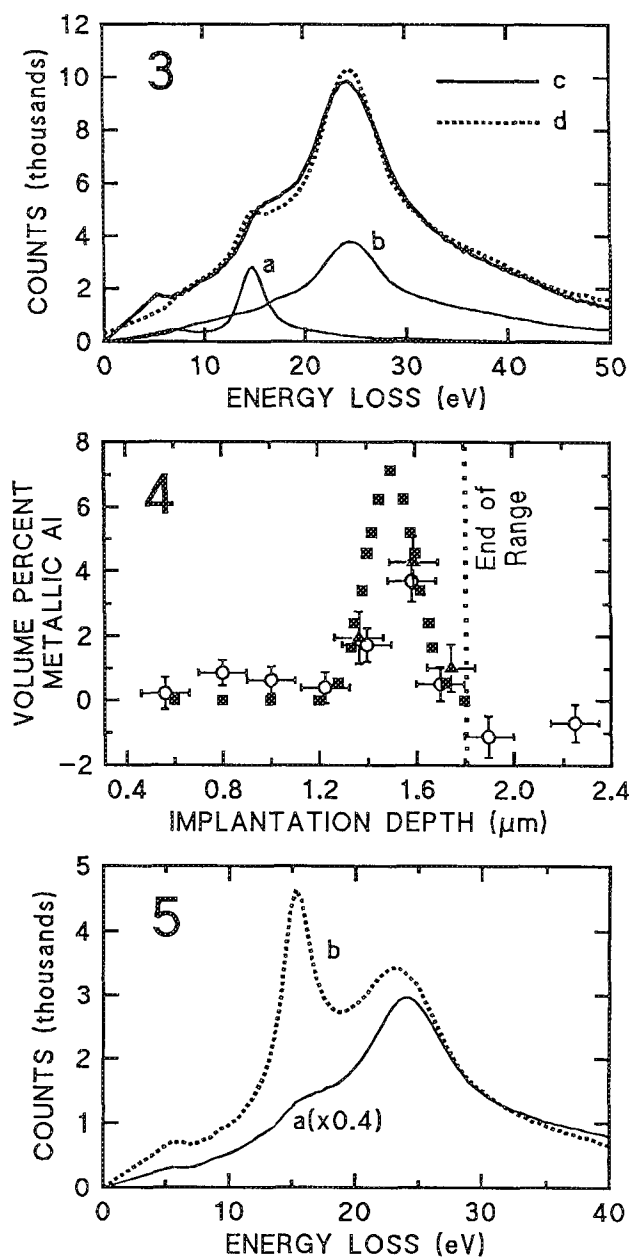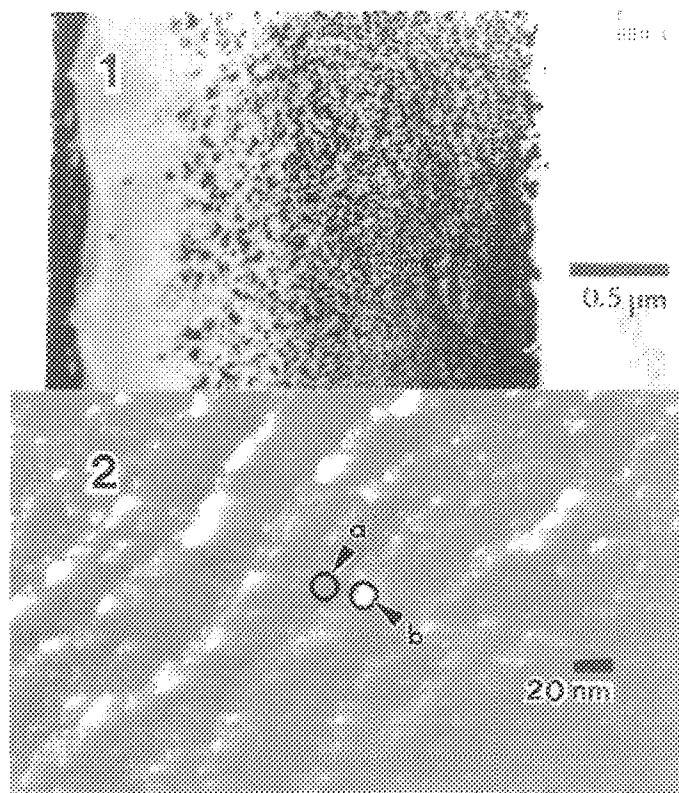
FIG. 1.--Al+ implanted $MgAl_2O_4$ spinel has varying microstructure with implantation depth.
FIG. 2.--Dark-field $<222>_{sp}/<111>_{Al}$ image suggests features near end-of-range are metallic Al colloids.
FIG. 3.--Fourier-log deconvoluted low-loss spectra from (a) metallic Al reference (x1/8), (b) undamaged spinel (x1/3), (c) material at implant depth of ~1.6 μm, and (d) best-fit prediction from multiple regression analysis which indicates 3.7 ± 0.6 vol.% metallic Al is present within implanted spinel.
FIG. 4.--Metallic Al profile: diffraction mode (O), image mode (▲), implant profile from EDEP-1 (▦).
FIG. 5.--High spatial resolution spectra from regions (a) and (b) indicated in Fig. 2.

DETERMINATION OF INTERFACE WIDTH USING EELS FINE STRUCTURE CHANGES

Vinayak P. Dravid*, M.R. Notis** and C.E. Lyman**

*Department of Materials Science & Engineering, Northwestern University, Evanston, IL 60208
**Department of Materials Science & Engineering, Lehigh University, Bethlehem, Pa 18015

The concept of interfacial width is often invoked in many materials science phenomena which relate to the structure and properties of internal interfaces[1]. The numerical value of interface width is an important input parameter in diffusion equations, sintering theories as well as in many electronic devices/processes. Most often, however, this value is guessed rather than determined or even estimated. In this paper we present a method of determining the effective structural and electronic- structural width of interphase interfaces using low- and core loss fine structure effects in EELS spectra.

The specimens used in the study were directionally solidified eutectics (DSEs) in the system; $NiO-ZrO_2(CaO)$, $NiO-Y_2O_3$ and $MnO-ZrO_2(ss)$. EELS experiments were carried out using a VG HB-501 FE STEM and a Hitachi HF-2000 FE TEM. Since oxygen is common to both the phases of the eutectics, oxygen K-edge fine structure was monitored. Both core and low loss spectra were acquired at high energy loss dispersion (0.05 - 0.1 eV/channel) and by moving the electron probe (about 1 nm) from one phase --through the edge-on interface -- to the other, in subnanometer steps. Figure 1A is a montage of oxygen K-edge energy loss near edge structure (ELNES) as a function of the distance from the interface. The transition width of the signal is about 0.8 nm, which is a conservative estimate. If finite localization is taken into account, the effective width may be even less than 0.8 nm. Thus, in the NiO-$ZrO_2(CaO)$ system, the lamellar interfaces are extremely sharp. This result conforms to other measurements using HRTETM and x-ray analysis[2]. In fact this result indirectly reflects high localization of ELNES signal. Similarly, low loss spectra were also obtained as shown in Figure 1B. Even in the case of low loss profiling, the interface width appears to be smaller than 0.8 nm, also implying that the low loss signal is also quite localized under the above conditions.

Using similar strategy, $NiO-Y_2O_3$ DSE interfaces were studied which also indicated sharp interfaces. However, in $MnO-ZrO_2$, the width was a little larger, about 1.2 nm. We believe that it is perhaps due to possible change in valence state in the vicinity of the interface. Figure 2 shows ELNES of O-k edge from MnO (nominal) about 1 nm away from the interface. The ELNES resembles a combination of Mn^{+2} and Mn^{+3} rather than that of just Mn^{+2}. Diffuse intensity was also observed in diffraction patterns, indicative of oxygen vacancies in the crystal due to charge compensation. More work is in progress to confirm and elaborate these observations. It can be summarized that ELNES of common element can be used as a useful probe to determine the effective width of internal interfaces as well as their relaxations.

References
1. see for example, P.G. Shewmon, Diffusion in Solids, McGraw-Hill, New York

(1963), p. 47.
2.V.P. Dravid et al. Ultramicroscopy (1989) Vol.29, p. 60.
3. Research supported by U.S. DoE Grant No. DE-FG02-84ER45150. Many thanks
are due to John Hunt (Lehigh) and R.D. Leapman (NIH) for experimental
assistance.
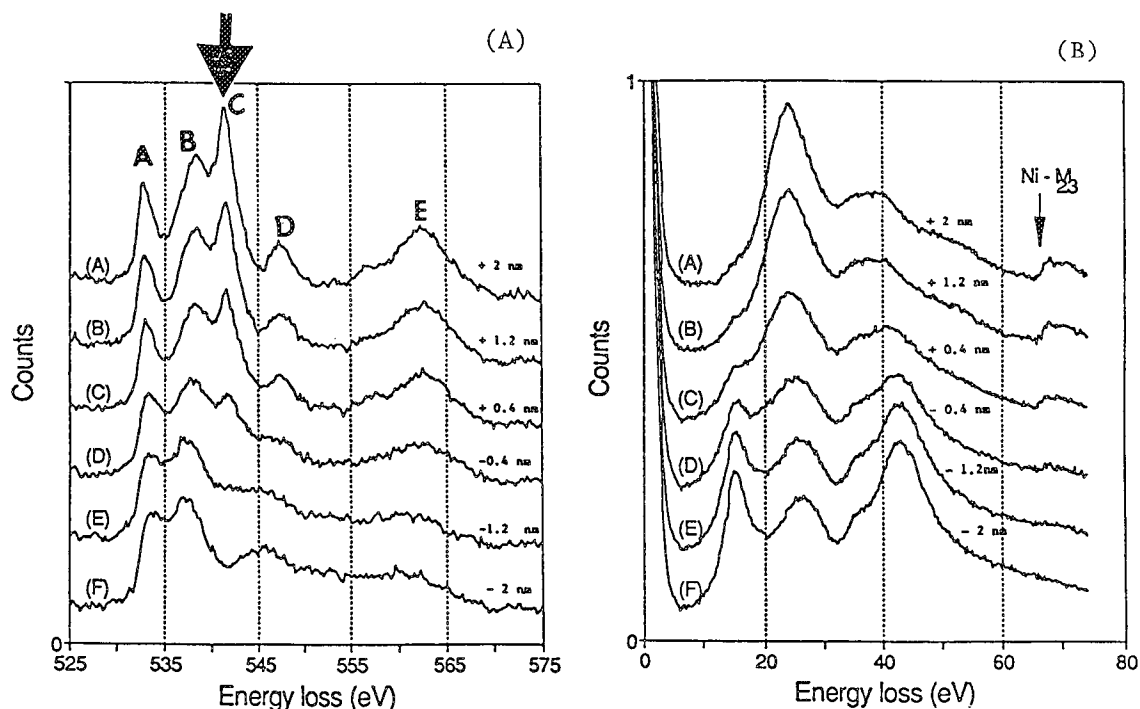
FIGURE 1
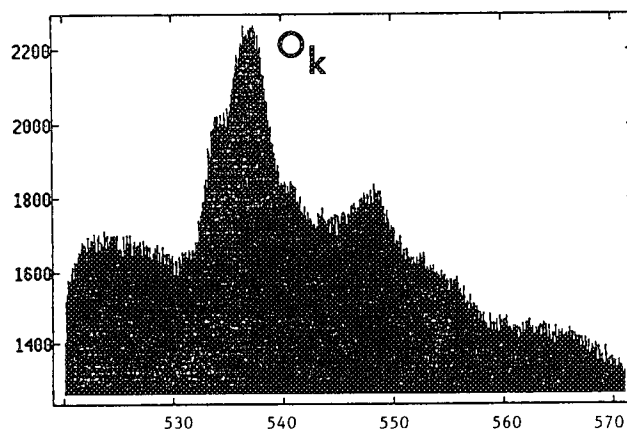
FIGURE 2

FIG. 1 (A) ELNES of O-K edge as a function of probe location from the
interface in DSE. (B) Low loss profiles across the interface. Note sharp
transition of fine structure featues.
FIG. 2 ELNES of O-K edge of MnO, 1 nm away from the interface. The fine
structure indicates possible change in valence state of Mn in the vicinity of
interface.

APPLICATION OF ELECTRON ENERGY LOSS SPECTROSCOPY TO MICROANALYSIS OF IRRADIATED STAINLESS STEELS

E. A. Kenik[*], J. Bentley[*], and N. D. Evans[**]

[*]Metals and Ceramics Division, Oak Ridge National Laboratory, Oak Ridge, TN 37831-6376
[**]Oak Ridge Associated Universities, Oak Ridge, TN 37831

Energy dispersive X-ray spectroscopy (EDXS) has limited application to microanalysis of radioactive materials because of degraded detector performance and the "intrinsic" spectrum associated with the radioactive decay. Electron energy loss spectroscopy (EELS) is not affected by specimen radioactivity and also offers the possibility of improved spatial resolution. Measurements of radiation-induced segregation (RIS) in irradiated stainless steels have been made by both techniques. Analytical electron microscopy was performed at 100 kV in a Philips EM400T/FEG, equipped with an EDAX 9100/70 EDXS system and a Gatan 666 parallel detection EELS (PEELS). Microanalysis was performed in the STEM mode (<2-nm-diam probe with >0.5 nA) with the same acquisition time (50 s) used for both techniques.

Initial measurements were performed on an ion-irradiated modified type 316 stainless steel (designated LS1A), which had moderate-width (~20 nm) RIS profiles at grain boundaries. Profiles measured by EDXS and PEELS match well and show chromium depletion and nickel enrichment (Fig. 1). Such chromium depletion below the 13 at.% Cr required for corrosion resistance would make the irradiated material sensitive to intergranular attack and stress corrosion cracking. Both techniques indicate similar chromium levels at the boundary (~11 at.%), though the PEELS analysis gives ~1 at.% lower chromium. This difference can be attributed to the analyzed volume for EELS being less affected by beam broadening than that for EDXS. In addition, secondary fluorescence of the entire specimen would bias the boundary composition as measured by EDXS slightly toward the matrix composition, whereas no such effect occurs for EELS. Light element detection by PEELS resulted in additional information. The oxygen level detected at the boundary was significantly lower than that in the matrix, indicating that the oxide film responsible for corrosion resistance was thinner or less stable and, as such, less protective. This is consistent with the preferential grain boundary attack observed for such irradiated stainless steels.

Several problems encountered in PEELS of these steels are illustrated in Fig. 2, which shows PEELS spectra from the matrix and a grain boundary in a neutron-irradiated modified type 316 stainless steel (designated PCA). The presence of the oxygen K edge ~40 eV before the chromium L_{23} edge complicates background fitting. The same is true for the proximity and extended structure of the Cr, Mn, Fe, and Ni edges. Fig. 2 shows that manganese is depleted at the boundary. Though manganese analysis is somewhat hampered by a low signal-to-background ratio, the calculated matrix level is 2 at.% Mn, which is the actual manganese content of the alloy. Analysis of manganese by EDXS is precluded by the large Mn K X-ray peaks (from the decay of Fe^{55}) in the "intrinsic" spectrum. Although the levels of chromium and nickel in the matrix are very similar (~15 at.%), the nickel PEELS edge is significantly smaller than the chromium edge, indicating a much smaller nickel cross-section. For the experimental conditions used (beam divergence $\alpha=9$ mrad, collection angle $\beta=14$ mrad, integration window $\Delta=50$ eV), the calculated iron and nickel cross-sections are 0.60 and 0.24, respectively, of that for chromium.

Grain boundary RIS profiles in the neutron-irradiated PCA steel as measured by simultaneous EDXS and PEELS are compared in Fig. 3. There is good agreement between the two techniques in terms of both composition and width of the segregation profiles, but PEELS consistently indicates ~0.5 at.% lower chromium levels at the boundary, as would be expected from reduced beam broadening effects and the elimination of secondary fluorescence. The low matrix nickel levels indicated by PEELS in Fig. 3 are related to the low cross-section of nickel and its associated poor signal-to-background.[1]
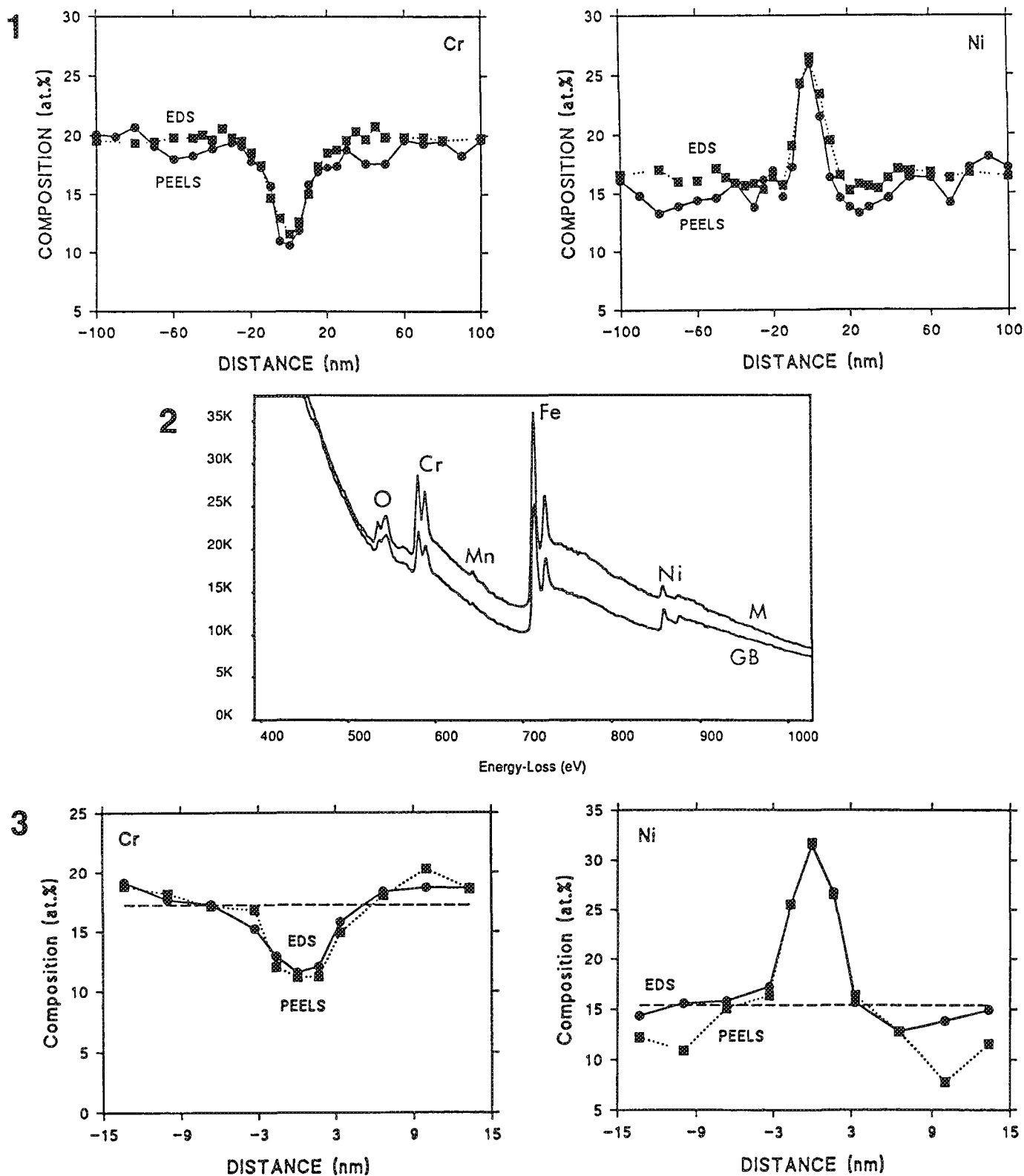
FIG. 1--RIS profiles at grain boundary in LS1A stainless steel ion-irradiated to 1 dpa at 675°C.
FIG. 2--PEELS spectra from matrix (M) and grain boundary (GB) in PCA stainless steel neutron-irradiated to 9 dpa at 420°C.
FIG. 3--RIS profiles at grain boundary in PCA stainless steel neutron-irradiated to 9 dpa at 420°C.

AN AEM CHARACTERIZATION OF INTERFACIAL REACTIONS IN Al-MMC's REINFORCED WITH AS-RECEIVED AND OXIDIZED SiC PARTICLES

J.G. Legoux, G. L'Espérance and M. Suéry[*]

Ecole Polytechnique, Centre de caractérisation microscopique des matériaux, (CM)^2, P.O. Box 6079, Succ. A, Montréal, Québec, H3C 3A7
[*] Institut National Polytechnique de Grenoble, Génie physique et mécanique des matériaux, B.P. 46, 38402 St-Martin-d'Hères, France

Interfacial reactions in MMC's can affect the mechanical properties of the material by changing the composition of the matrix and by forming new compounds at the matrix/ceramic interfaces. These reactions depend on the surface chemistry of the reinforcement, such as the presence of SiO_2 produced by air oxidation of raw SiC particles [1]. These reactions also depend on the processing route, particularly the thermal history of the material (fabrication or subsequent heat treatment or remelting). This paper presents results of an analytical transmission electron microscopy investigation of interfaces observed in Al-1% Mg alloys reinforced with 10 vol. % SiC particles. The composites were produced by the compocasting technique (semi-solid route) using as-received and oxidized SiC particles [2]. The particles were oxidized in air at 1100°C for various times to produce oxidation levels ranging from 0-16 wt % measured by wet analysis.

For composites containing raw particles, no reaction is observed during fabrication. Remelting at 800°C, for 1 hour degrades the reinforcement leading to the extensive formation of Al_4C_3.

For as-cast composites with oxidized particles, the SiO_2 coating reacts rapidly with liquid aluminium during their fabrication. Low oxidation levels ($\approx$ 4%), leads to small spinel ($MgAl_2O_4$) crystals according to the global reaction

$$SiO_2 + 2\ Al + Mg \rightarrow MgAl_2O_4 + 2\ Si.$$
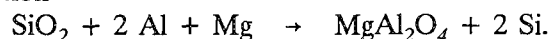
Figure 1 shows the interface obtained for an oxidation level of 16%. The relatively thick ($\approx$ 500 nm) reaction layer also contains $MgAl_2O_4$ with areas rich in Al, Mg and Si. Extensive Energy Dispersive X-ray Spectrometry with a small probe (20 nm) shows the presence of Mg_2Si crystals produced in the layer by the combinaison of the Mg in the alloy with Si rejected by the reaction of $MgAl_2O_4$ formation. The near edge structure of EELS spectra of the Al-rich areas compared with spectra obtained from the Al matrix and from spinel crystals indicate that these areas are metallic in character (Fig. 2).

During remelting of the composites, the metallic Al reaches the SiC particles, attacks them and thus leads to an accumulation of Si at the particle/reaction zone interface and carbon diffuses away from the particle.

Figure 3 shows an EDS linescan across the reaction zone after accounting for the contribution from SiC and $MgAl_2O_4$ compounds. The high Si content near the SiC particles stops the degradation of SiC by liquid aluminium [3,4]. Figure 4 summarizes schematically the reaction zone during remelting which partially protects the SiC particles from liquid aluminium.

References
1. J.G. Legoux, H. Ribes, G. L'Espérance and M. Suéry, Proc. Int. Symp. "Processing and Application of Ceramic and Metal Matrix Composites", 28th Annual Conf. ICM, Halifax, August 20-24 1989, H. Mustaghaci (ed.), Pergamon Press, pp. 324-336 (1989).

2. H. Ribes, M. Suéry, G. L'Espérance and J.G. Legoux, Met. Trans. A., vol. 21A, Sept. 1990, pp. 2489-2496.

3. J.G. Legoux, L. Salvo, H. Ribes, G. L'Espérance and M. Suéry, 119th TMS Annual Meeting, Anaheim, Feb. 18-22 1990, pp. 187-196, (1990).

4. J.G. Legoux, L. Salvo, G. L'Espérance and M. Suéry, Int. Conf. on Fabrication of Particulates-Reinforced Metal Composites", ASM Int., Sept. 16-19 1990, Montréal.
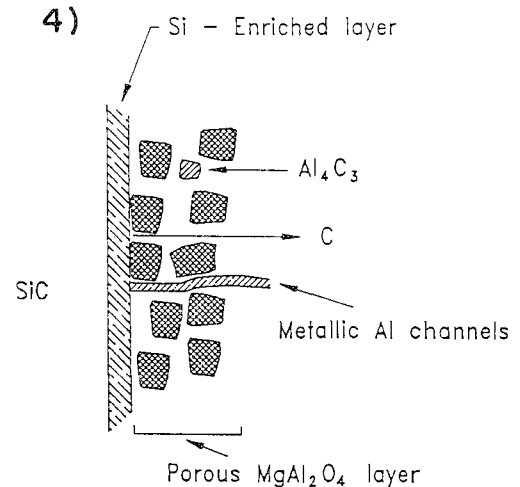
1)
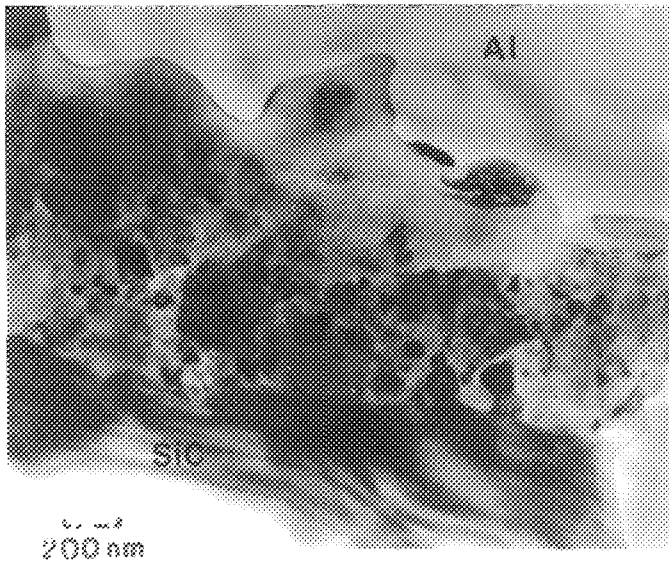
2)
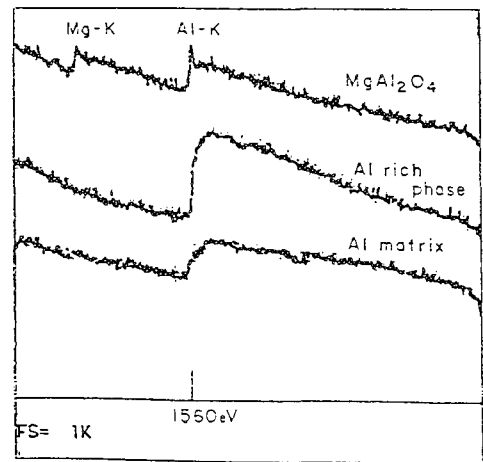
3)
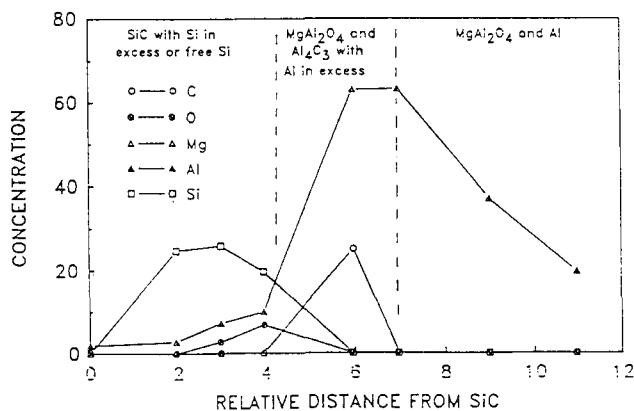
4)

Fig. 1   Interface formed in a composite Al 1% Mg reinforced with SiC oxidized 16%.

Fig. 2   Near edge structure of Al rich compound found in the interface compared with matrix and spinel.

Fig. 3   EDS linescan across the oxide layer after subtraction of the Si, C, Mg, Al and O intensities arising from SiC and $MgAl_2O_4$.

Fig. 4   Possible interphase behavior during remelting of composites reinforced with oxidized particles.

ELECTRON-ENERGY-LOSS SPECTRA OF SILICON CARBIDE OF 4H AND 6H STRUCTURES

D. R. Liu, S. S. Shinozaki, J. W. Hangas and K. Maeda[*]

Research Staff, Ford Motor Company, 20000 Rotunda Drive, Dearborn MI48121,USA
[*]Hitachi Research Laboratory, Hitachi, Ltd., Hitachi, Ibaraki, Japan

The properties of silicon carbide can be tailored with addition of various sintering aides. It is desirable to understand the microstructure of these materials as related to their properties. For example, there is a debate whether there is some Be at all in the 4H structure of SiC doped with BeO.[1,2] It is very difficult to use the conventional EELS quantification procedure to investigate the Be presence of minute amount in SiC. In any spectrum collected from SiC doped with BeO, the huge Si-L23 edge at 100 eV would extend well above 200 eV and make it impossible to identify a small Be-K edge at 111 eV. However, progress has been made in solving this problem as reported in the present paper. A spectrum from SiC with the BeO additive is compared with a spectrum from SiC without BeO, and the difference of the two spectra starting at 111 eV, if present, should be the Be-K edge signal. Thus, one does not have to fit the background before the Be-K edge with the usual power law $A.E^{-r}$, and the background subtraction error is greatly reduced.[3,4]

TEM specimens were made out of SiC-2%BeO (sample #1), SiC-0.5%Al-0.2%B-2%C (sample #2) and a SiC doped with Al at ppm level (sample #3) (all in weight percent). All spectra were collected with a GATAN PEELS unit in a JEOL-2000FX microscope operated at 120 kV. A micrograph from the sample #1 is shown in Fig. 1 where the 4H and 6H are within one grain with their basal planes parallel to the beam direction Spectra collected from the 4H structures of the samples #1 and #2 are shown in Fig 2 with the background before the Si-L23 edge being removed in the usual way The 4H regions were oriented so as to have the basal plane parallel to the electron beam. All spectrum pair shown in this paper were collected from specimen regions of the same thickness as evidenced by comparison of the zero-loss and plasmon loss peaks on their low-loss spectra. For the display clarity in Fig 2, the spectrum of 4H #1 is offset slightly in the Y-axis direction. To extract the Be-K edge signal, the two spectra, having almost the same intensity, were adjusted slightly in X- and Y-directions so that their profiles fit into each other well in the energy range 100-300 eV. The difference of the two spectra in the energy region from 111 eV up should be the Be-K signal. Based on limited data collected, there seems to be some very minute Be-K signal intensity left after the subtraction, representing a Be content much below 1%. Further work is in progress to collect more data so as to enable us to identify the presence or absence of Be in 4H of the SiC-2%BeO with confidence.

It is interesting to compare the Si-L23 edge on the EELS spectra collected from 4H and 6H regions of the same specimen #1 as shown in Fig. 3. The two spectra were collected from adjacent regions as shown in Fig. 1, with their basal planes in the beam direction. The two spectra obviously have different profiles at the peak of 105 eV and in the region 120 eV up. The 4H and 6H structures in SiC are made of the same type of crystal planes, and their only difference is in their stacking sequence with 4H being ABCB and 6H being ABCACB. The result of Fig. 3 appears to indicate that when 6H transforms to 4H, the SiC covalent bond must have experienced some significant electronic structural change. Spectra were also collected from 6H regions of the sample #1 and the sample #3, with one being collected with the basal plane in the specimen plane and the other with its basal plane in the beam direction as shown in Fig. 4. As can be seen, the two spectra are practically the same

447

References

1. S. Shinozaki, J Hangas, K. Maeda and A. Soeta, Ceramic Transactions, 2(1989)113.
2. A. Zangvil and R. Ruh, Ceramic Transactions, 2(1989)63.
3. D. R. Liu and L. M. Brown, J of Microscopy, 147(1987)37.
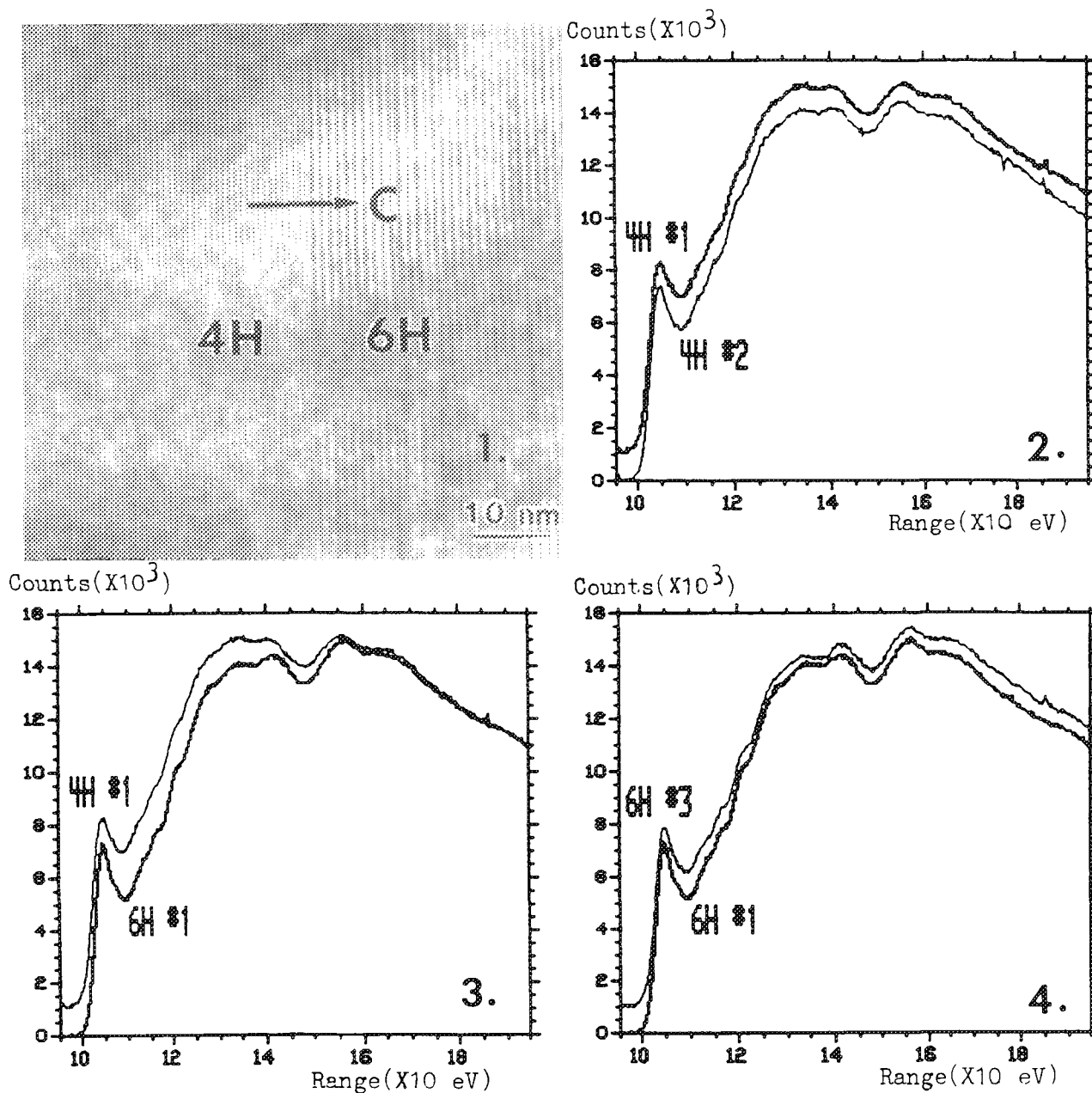4. D. R Liu and D. B Williams, Proc. Roy. Soc. London, A425(1989)91

FIG. 1.--Micrograph showing co-existence of 4H and 6H within single grain
FIG. 2.--EEL spectra from 4H of sample #1 (4H #1) and sample #2 (4H #2) with basal planes in beam direction.
FIG. 3.--EEL spectra from adjacent 4H and 6H regions of same thickness in same sample #1 (4H #1 and 6H #1).
FIG. 4.--EEL spectra from 6H of sample #1 with basal plane in beam direction (6H #1) and from 6H of sample #3 with basal plane in specimen plane (6H #3)

NANOANALYSIS OF SEMI-INSULATING POLYCRYSTALLINE SILICON BY HIGH SPATIAL RESOLUTION ELECTRON MICROSCOPY

M. Catalano,* M.J. Kim,** R.W. Carpenter** and J. Wong***

*Dipartimento Scienza dei Materiali, Università di Lecce, Via Arnesano, Lecce 73100, Italia
**Center for Solid State Science, Arizona State University, Tempe, AZ 85287-1704
***Lawrence Livermore National Laboratory, MSL-369, P.O.Box 808, Livermore, CA 94551

Semi-insulating polycrystalline silicon (SIPOS) has been used extensively as a passivating layer in high-voltage power devices[1,2] and as the wide bandgap material in solar cells.[3] Little information, however, is available on the nano-scale nature of oxygen distribution and its redistribution upon thermal annealing, and the microstructural characteristics of SIPOS thin films. In the present study, the atomic structure of SIPOS layers on Si wafers was characterized by HREM and the oxygen content was quantitatively determined by nanospectroscopy.

SIPOS films were chemical vapor deposited on Si {001} wafers from a preset mixture of SiH_4 and N_2O. Annealing was done in dry N_2 at 900°C for 30 min. Cross-sectional TEM specimens were prepared from both as-deposited and annealed materials. HREM was done in an ISI-002B at 200kV. Nanospectroscopy was performed at 100kV in a Philips EM400ST/FEG microscope coupled to a Gatan parallel-detection EELS, with better than 3 nm spatial resolution.

Figure 1 shows a cross sectional view of the as-deposited SIPOS film on Si (001) surface. The thickness of deposited layer was about 400 nm. HREM and diffraction experiments showed that this film was single phase and amorphous. EELS showed that the amorphous film contained only silicon and oxygen. The quantitative compositional analysis of the SIPOS film was done using core-shell-ionization edges in EELS spectra, following the method described in our previous study.[4] The background stripped experimental Si-L and O-K edges from the amorphous SIPOS film are shown as solid curves in Figs. 2(a) and 2(b), respectively. These were compared with the scaled standard curves (dashed line in Fig. 2) of the net Si-L and O-K edges from experimental standards whose composition are SiO_2. The average oxygen content of the as-deposited SIPOS, determined by this procedure, was 15±1 at.%. Upon annealing at 900°C for 30 min in nitrogen, nanocrystallites appeared in the amorphous SIPOS matrix as shown in Fig. 3. Precipitation of nanocrystals induced by annealing in nitrogen has also been observed in an early TEM study.[5] The structure of these nanocrystals was diamond cubic, with lattice constant corresponding to Si. Microtwins were also observed in a few of the particles. No nanocrystals nucleated from the Si substrate were observed, suggesting homogeneous nucleation from the amorphous SIPOS matrix. It is also interesting to notice the presence of about 1.5 nm denuded zone near the interface with the Si substrate (Fig. 3). The observed plasmon energy E_p for the annealed SIPOS matrix was 18.0±0.3 eV while for Si nanocrystals it was about 17.0 eV. The average oxygen concentration of the amorphous matrix surrounding the nanocrystals was determined to be 36±1 at.%, by comparing the background stripped experimental Si-L and O-K edges from the annealed SIPOS matrix (solid curves) with the scaled standard curves (dashed line) from experimental standards, as shown in Figs. 4(a) and 4(b) respectively. This increase in oxygen content of the SIPOS matrix seems to be the consequence of precipitation of Si nanocrystals from the matrix. In the annealed specimen the amorphous matrix oxygen concentration increase by an additional 15 at.% at the SIPOS-air interface relative to the SIPOS-Si interface was also observed.[6]

References

1. T. Matsushita et al., IEEE Trans. Electron Devices (1976) **ED-23**, 826.
2. T. Aoki et al., J. Electron Eng. (1976) **44**, 265.
3. E. Yablonovitch et al., Appl. Phys. Lett. (1985) **47**, 1211.
4. M.J. Kim and R.W. Carpenter, J. Mater. Res. (1990) **5**, 347.
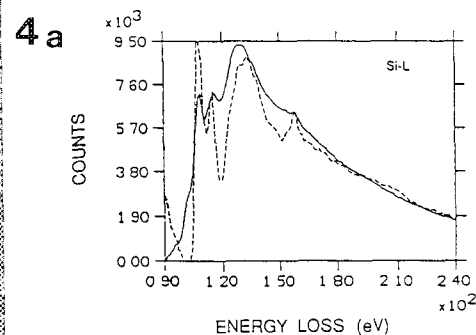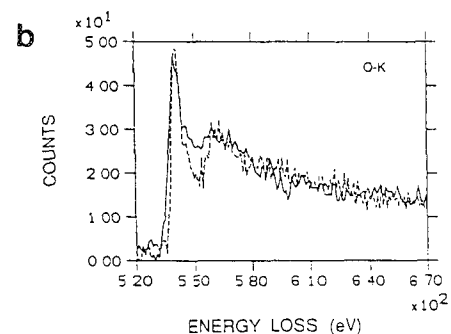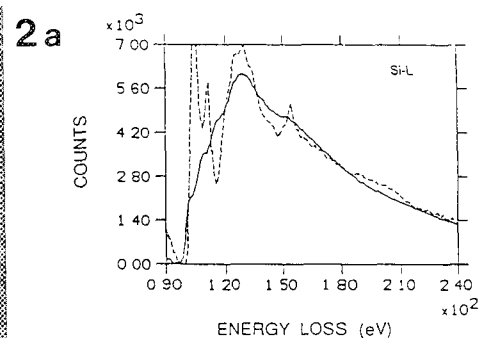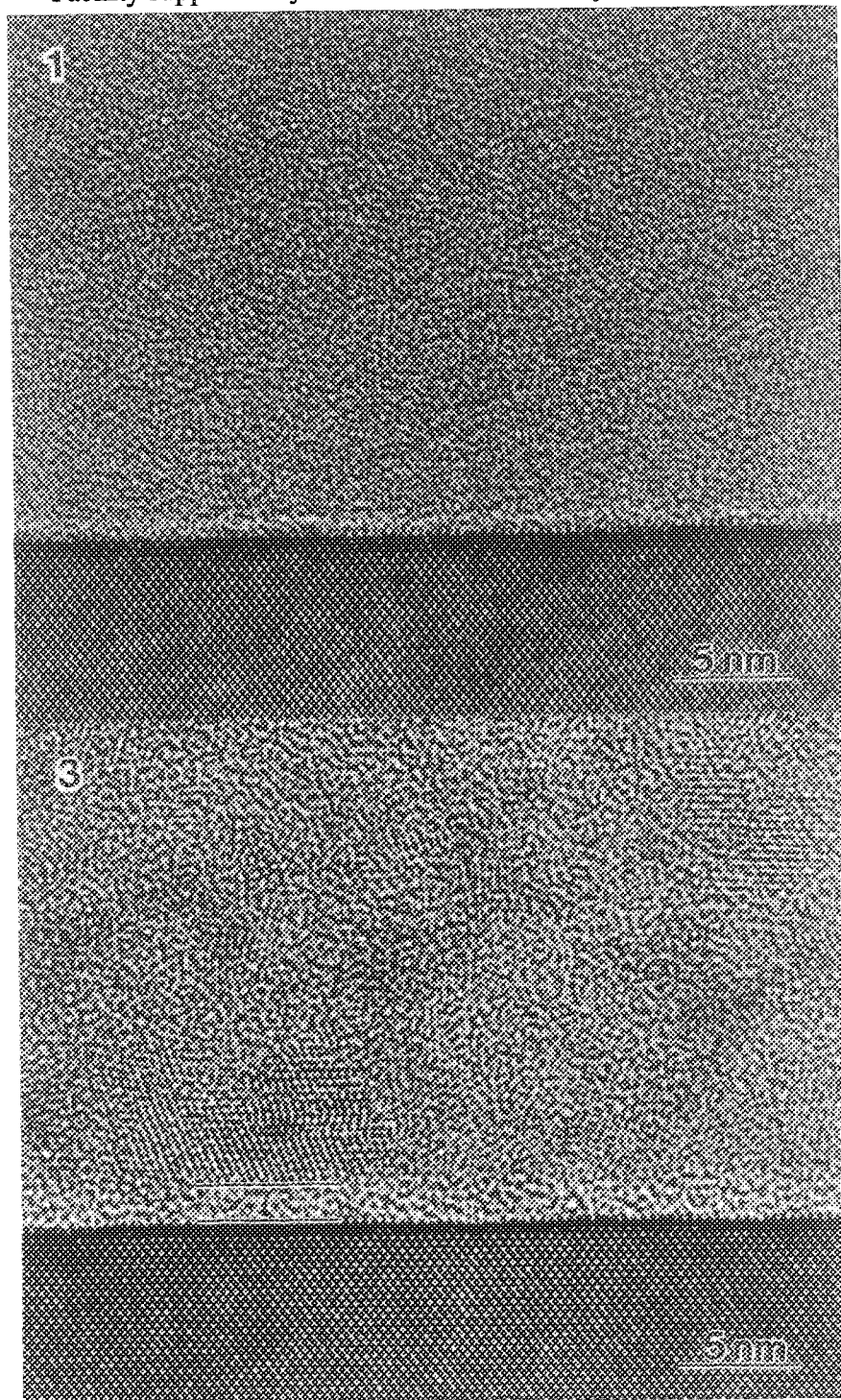5. J. Wong et al., Appl. Phys. Lett. (1986) **48**, 65.
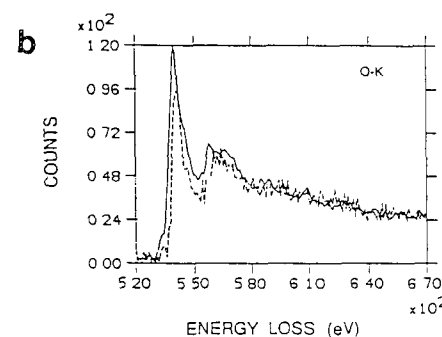
FIG.1.--HREM image of an as-deposited SIPOS film on Si (001). Note the single phase amorphous SIPOS layer.

FIG.2.--Comparison of background stripped (a) Si-L and (b) O-K edges of the as-deposited SIPOS layer (solid line) with the ones of the standard SiO_2 specimen (dashed line). Notice marked differences in the near edge fine structure region of the edges.

FIG.3.--HREM image of the SIPOS layer annealed at 900°C in nitrogen for 30 min. Note nanocrystals in the amorphous SIPOS matrix.

FIG.4.--Comparison of background subtracted (a) Si-L and (b) O-K edges of the amorphous SIPOS matrix surrounding nanocrystals (solid line) with the ones of the standard SiO_2 specimen (dashed line).

ANNEALING EFFECTS ON THE MICROSTRUCTURE OF TITANIUM ELECTRICAL CONTACTS ON DIAMOND FILMS

G-H. M. Ma,* N. D. Evans,** T. Tachibana,* R. E. Clausing,*** and J. T. Glass *

* Department of Materials Science and Engineering, North Carolina State University, Raleigh, NC 27695. ** Oak Ridge Associated Universities, Oak Ridge, TN 37831   *** Metals and Ceramics Division, Oak Ridge National Laboratory, Oak Ridge, TN 37831

With its large band gap and a unique combination of many excellent properties, diamond is regarded as an excellent candidate for making electronic devices for operation at high temperature. In order to fabricate diamond devices, suitable electrical contacts and appropriate deposition techniques must be developed. Titanium is considered a suitable candidate material for diamond electrical contacts based on its properties. Recent current-voltage (I-V) measurements showed that as-deposited titanium contacts on boron-doped semiconducting diamond are rectifying in nature.[1] However, upon post-deposition annealing at 430 °C, these contacts became ohmic. Surface analysis by X-ray photoelectron spectroscopy of these annealed metal contacts showed interfacial metal carbide formation at the metal/diamond interface.[1] Therefore, the microstructural evolution causing these metal contacts to change from rectifying to ohmic in nature is the primary purpose of the present research.

Titanium metal was deposited onto boron-doped semiconducting polycrystalline diamond films (grown by microwave plasma enhanced chemical vapor deposition on silicon) by sublimation from a resistively heated titanium (99.99%) rod and then some films were ex-situ annealed in-vacuo ($\approx 1 \times 10^{-8}$ Torr) at 430°C for 30 minutes. Cross-sectional transmission electron microscopy (TEM) specimens of as-deposited and annealed samples were prepared by ion-milling. Specimens were examined with a Hitachi H-800 analytical electron microscope (AEM), and a Philips EM400/FEG AEM equipped with a Gatan 666 parallel-detection electron energy-loss spectrometer (PEELS). Microstructural evolution was recorded dynamically with the use of a heating specimen holder to anneal an as-deposited specimen in-situ within a Philips CM12 AEM.

The as-deposited contacts were verified to be α-titanium (hcp), of uniform thickness in intimate contact with the diamond films, Fig. 1. There was no interfacial layer evident at the Ti/diamond interface. In an ex-situ annealed specimen, the titanium layer underwent a morphological transformation from an equiaxed to a columnar morphology as shown in Fig. 2. An in-situ TEM heating experiment revealed that this transformation nucleated at the Ti/diamond interface. A thin (≈ 30-50 nm) Ti/diamond interfacial layer developed during annealing (Fig. 3). The near-edge structure of the carbon edge in PEELS spectra from this interfacial layer (Fig. 4) indicated at least some of the carbon in this layer does not have the diamond crystal structure.[2] The studies are underway to discern the nature of this interfacial layer. Carbon was not found in annealed titanium grains but was observed within titanium grain boundary regions (Fig. 5).

Based upon the above findings, it is believed that carbon from the diamond surface or near-surface region diffused into titanium during annealing to form an interfacial layer, and further diffused into the titanium layer along the grain boundaries. This carbon diffusion may leave some electrically active vacancies in the near-surface region of the diamond. Such vacancies may decrease the contact barrier height, and/or decrease the width of depletion region. Either may result in the formation of an ohmic contact.[3]

1. T. Tachibana, et al., to be published (1991).
2. R. F. Egerton, and M. J. Whelan, J. Elec. Spectrosc, 3 (1974) 232.
3. This research is partially supported by Kobe Steel, Ltd., NEDO/MITI of Japan, and in part by the Exploratory Studies Program of Oak Ridge National Laboratory, managed for the Department of Energy by Martin Marietta Energy Systems, Inc., under contract DE-AC05-84OR21400, and in part by the Division of Materials Sciences, U. S. Department of Energy through the SHaRE Program under contract DE-AC05-76OR00033 with Oak Ridge Associated Universities.
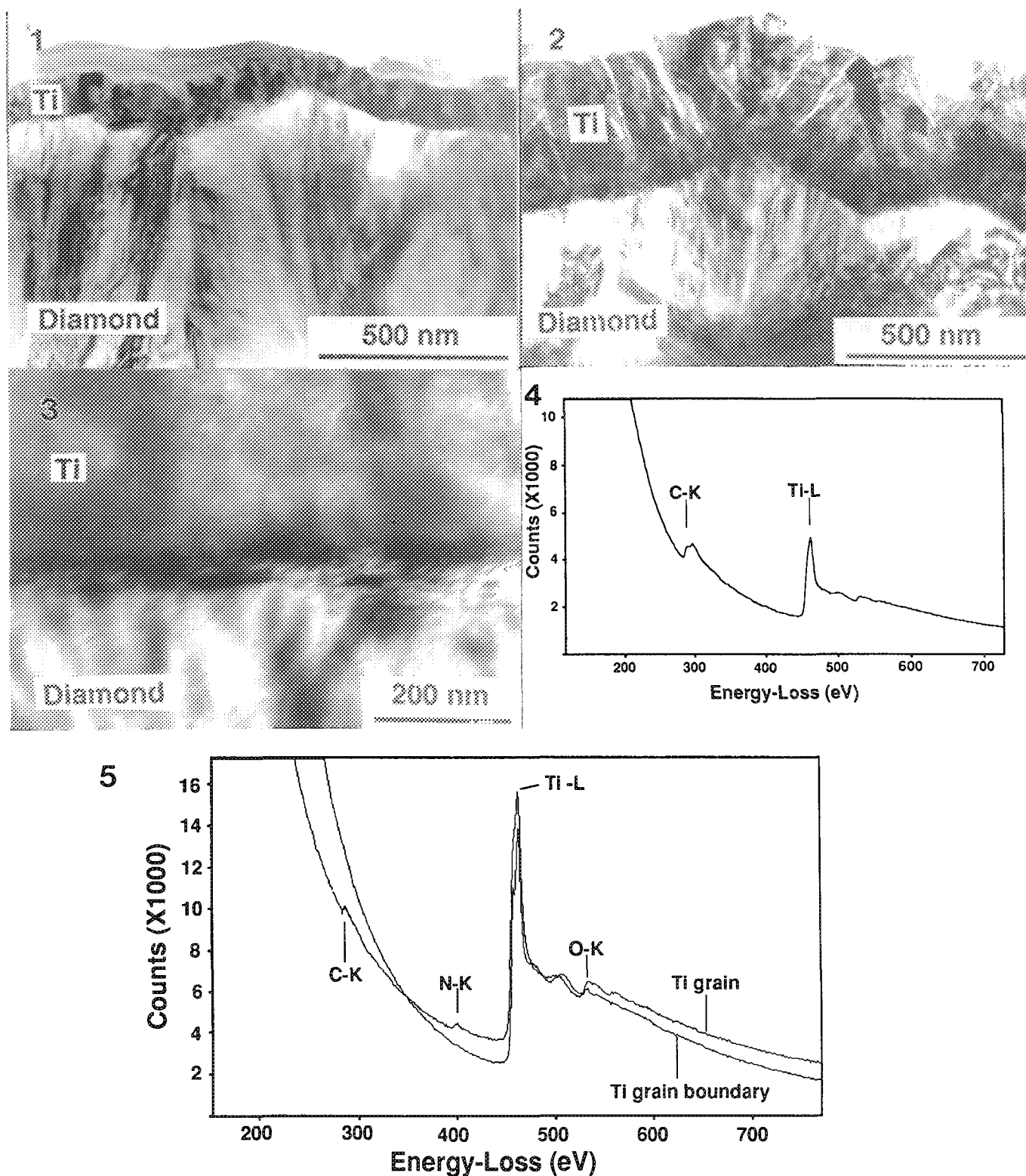
Fig. 1. Microstructure of an as-deposited Ti layer on diamond.
Fig. 2. Microstructure of an annealed Ti layer on diamond.
Fig. 3. Ti/diamond interfacial layer from an ex-situ annealed specimen.
Fig. 4. PEELS spectrum of the Ti/diamond interfacial layer.
Fig. 5. PEELS spectra of annealed Ti grains, and Ti grain boundary regions.

EFFORTS TO IMPROVE THE QUANTIFICATION OF EDX ANALYSES, PARTICULARLY FOR THE LIGHT ELEMENTS

G. L'Espérance

Centre for Characterization and Microscopy of Materials, Department of Metallurgy and Materials Engineering, Ecole Polytechnique de Montréal, P.O. Box 6079, Station "A", Montréal (Québec), Canada, H3C 3A7

The attachment of a Si(Li) energy dispersive X-ray (EDX) detector to a (scanning) transmission electron microscope ((S)TEM) is widely used to carry out quantitative determinations of elemental composition of a localized region of a thin specimen. Although the principles of the technique first proposed by Cliff and Lorimer [1] have been established for some time, there are still a large number of sources of errors [2]. In addition, EDX analyses have been generally restricted until recently to elements with an atomic number (Z) larger than that of sodium (Z > 10) so that electron energy loss spectroscopy (EELS) was the preferred technique for the detection of light elements in an AEM. The relatively recent advent of ultra-thin window (UTW) detectors has offered an alternative (and often complementary) technique to EELS for the analysis of light elements with additional difficulties in the detection and quantification [3]. This paper presents some results of investigations made to improve the quantification of EDX data. Particular attention is given to the detection and quantification of data from light elements on a routine and reproducible basis.

The EDS data were obtained with a Jeol 2000FX or with a Philips CM30 both equipped with a Link LZ-5 detector. The EELS analyses were carried out with the CM30 coupled to a Gatan (model 666) parallel EELS with subsequent processing on an IBM-RT computer.

The quantification of all elements with Cliff-Lorimer's approach is more accurate when using K_{AB} factors experimentally determined from standards of known composition. For light elements, however, the variation of the detector efficiency (ϵ), with time can drastically limit the usefulness of experimental K_{AB} factors to the quantification of data obtained in a time period close to that for which the K_{AB} factors were measured [3]. In cases where appropriate standards are not available, errors in the K_{AB} factors calculated from first principles can arise mainly from the choice of the b_K and C_K parameters needed to calculate ionisation cross-sections, Q, and from the value of the detector efficiency, ϵ, for elements with Z < 20 and Z > 40. Although a considerable amount of work has been carried out to measure Q and to assess various models and the experimental data, considerable caution must be exercised to select appropriate values for the elements and energy of interest [4]. In addition, limited data is available for elements with Z < 10. One possibility to overcome these problems would be to carry out in-situ measurements of Q but then a number of parameters including ϵ and the solid angle must be accurately known [5]. One way that we propose to eliminate the need to know these parameters is the use of ratios of K_{AB} factors obtained at different accelerating voltages. Assuming that b_K is independent of Z, then a value of C_K can be obtained and used to calculate Q. Although the technique can allow for the variation of C_K with Z, values of C_K have been found to vary substantially with small variations in the K_{AB} factors determined so that the choice of E_o and elements must be optimized to minimize the errors [6].

The ability to detect light elements routinely has been found to depend markedly on the experimental conditions when analysing small particles on a grid. The effect has been interpreted in terms of the occurrence of spurious X-rays and/or the presence of uncollimated electrons depending on the experimental conditions particularly the size of the electron beam and that of the platinum aperture.

The difficulty to deal with such effects is that they are probably not accounted for in the standard hole count and can therefore not be entirely removed from the spectrum of the particles.

Another reason which makes the detection and quantification of light elements more difficult is the very significant absorption of the soft X-rays which occurs even for relatively thin specimens. Goldstein et al's. [7] relative criterion can be used to assess the need to carry out an absorption correction but to evaluate in absolute terms the reduction in intensity for each element, Tixier and Philibert's [8] criterion should be used. For example, in BN, an absorption correction would only be necessary for a sample thicker than 3220 nm but then more than 99% of the initially generated B and N X-rays would be absorbed. This explains the very small intensities observed in systems such as BN, B_4C and SiC (in the latter two systems 100 nm thick samples would lead to the absorption of more than 50% of the initially generated C X rays). Such large absorption also increases errors due to the associated lower intensities (poor counting statistics) and the large absorption correction which must be applied. In this context, a potentially very useful procedure to obtain K_{AB} factors and assess the effect of absorption is the extrapolation method [8,9]. The results we obtained using this procedure show its applicability to determine K_{AB} factors for light elements. We also extended its use to enable the microanalyst to assess the various absorption corrections that can be applied, particularly to select appropriate mass absorption coefficients and to assess the role of the specimen-detector geometry.

Quantitative linescans (or maps) involving light elements also become possible. Quantification of the EDX data is carried out by making use of EELS data obtained from a PEELS linescan (or map) of the same area in order to determine the thickness (or t/λ) at each pixel and therefore carry out an absorption correction at each point of the linescan. Knowledge of the net intensities at each point also allows to calculate the errors and the MMF along the linescan. Although EELS can also be used to obtain quantitative linescans (or maps), it appears that the advantage of EDX is the possibility to quantify the data for thicker samples (due to plural scattering and loss of edge visibility in EELS). EELS allowed the detection of smaller MMF values for light elements when measured on thin foils whilst EDX gave lower MMF values for intermediate to heavy elements. In the case of particles on a grid, the size of the smallest particles that could be analysed (and hence the MDM) in EDS and PEELS will be compared for particles containing light elements and using second difference methods to improve the detectability limits in EELS.

References

1.   G. Cliff and G.W. Lorimer, J. Microscopy 103: 203, 1975.
2.   J.N. Chapman and W.A.P. Nicholson, Proc. XIIth Int. Congress for Electron Microscopy, 1990, 458-459.
3.   G. L'Espérance, G. Botton and M. Caron, Proc. 25th Ann. Conf. MAS, 1990, 284-288.
4.   C.J. Powell, Proc. 25th Annual Conference MAS, 1990.
5.   J.H. Paterson, J.N. Chapman, W.A.P. Nicholson and J.M. Titchmarsch, J. Microscopy 154: 1, 1989.
6.   R. Gauvin and G. L'Espérance, submitted to J. Microscopy.
7.   J.I. Goldstein, J.L. Costly, G.W. Lorimer and S.J.B. Reed, SEM/1977, O. Johari, ed., IITRI, Chicago, p. 314, 1977.
8.   R. Tixier and J. Philibert, Proc. 5th Int. Congress on X-ray Optics and Microanalysis, G. Mollenstedt and K.H. Gaukler, ed., Springer-Verlag, Berlin, p. 180, 1969.
9.   Z. Horita, T. Sano and M. Nemoto, J. Microscopy 143: 215, 1986.
10.   E. Van Cappellen, Proc. 11th Int. Congress on X-ray Optics and Microanalysis, J.D. Brown and R.H. Packwood, ed., University of Western Ontario, Canada, 409, 1986.

ABSORPTION CORRECTIONS FOR ANALYSIS OF SEMITHIN SPECIMENS

W. A. P. Nicholson and K. M. Khan

Department of Physics and Astronomy, The University, Glasgow, Great Britain G12 8QQ.

In microanalysis of thin specimens by energy-dispersive x-ray spectroscopy, the peak counts may be converted to elemental concentrations by use of Cliff-Lorimer ratio method.[1] The k-factors may be obtained either from standards or from x-ray production cross sections. The result is only correct if it may be assumed that the absorption of characteristic photons within the specimen is negligible. Differences of absorption in lines of different energy lead to errors in the calculated composition.

A major limitation to performing corrections of specimen self-absorption is the difficulty of determining accurately the specimen thickness, density, and the geometry of x-ray collection; i.e., the absorption path length. Large variations in this path length are frequently encountered in wedge-shape specimens such as those produced by ion beam thinning.

We discuss a method of correcting specimen self-absorption that uses only the data contained in the x-ray spectra collected from a number of analysis points and a knowledge of the general form of absorption function. The method requires negligible absorption of one of the measured lines at even the thickest points analyzed. A second line, which suffers different amounts of absorption at the different analysis points, must also be measured. If this is the L-line corresponding to a K-line that is not absorbed, nothing further is required to deduce the absorption path length at each analysis point. If the second line is from a different element, the atomic ratios of the first and second elements must be approximately the same at all analysis points. Once the absorption path length is known at each analysis point, lines from all elements in the specimen can be corrected for self-absorption.

Formulation

The intensity detected N_{b0} of an element B, after absorption in a specimen of thickness t may be written, following Zaluzec,[2]

$$N_b = N_{b0} \frac{[1 - \exp([\mu/\rho]_b * \rho L)]}{[\mu/\rho]_b * \rho L} \tag{1}$$

where N_{b0} is the generated intensity, $[\mu/\rho]_b$ is the mass absorption coefficient of element B, and $L = t \csc \theta$, where θ is the angle at which the x rays emerge from the specimen surface; $t \csc \theta$ is the path length along which absorption takes place; and ρL, which may be termed the mass path length, is the quantity to be determined at every analysis point at which correction for absorption must be made. If we use the Cliff-Lorimer equation to substitute the elemental ratio for the genrated ratio N_{b0}/N_{a0}, the ratio detected of two lines which are both absorbed in the specimen may be written

$$\frac{N_b}{N_a} = k_{ab} * \frac{C_b}{C_b} * \frac{[\mu/\rho]_a}{[\mu/\rho]_b} * \frac{(1 - \exp(- [\mu/\rho]_b \rho L))}{(1 - \exp(- [\mu/\rho]_a \rho L))} \tag{2}$$

If we assume that the line a is not absorbed in the specimen, that implies that the intensity of a, N_a, is proportional to the specimen thickness t and hence to ρL, so that by substitution of ψN_a for ρL in Eq. (2) and simplification, it becomes

$$\frac{N_b}{N_a} = \frac{C_b}{C_a} * \frac{1 - \exp(- [\mu/\rho]_b \ \psi N_a)}{[\mu/\rho]_b \ \psi N_a} \qquad (3)$$

where ψ is a constant of proportionality in g/cm² and relates the counts of N_a to the specimen (mass) thickness and the path length.

If C_a/C_b is approximately constant for a number of analysis points for which N_a has a range of values, $[\mu/\rho]_b$ will also be approximately constant for these points. A graph of N_a against N_b can be fitted with Eq. (3) by use of k_{ab} and ψ as fitting parameters. The value of ψ can then be used to correct the counts of N_a and those of the other elements for absorption. After calculating "corrected" concentrations of the elements, we can substitute these values of the mass absorption coefficient for B at each point into Eq. (3) for a second approximation of k_{ab} and ψ. If the k-factor k_{ab} is already known, the fitting can be performed more simply with the single parameter ψ. Note that ψ is the slope of the fitting curve in the region of negligible absorption and so corresponds directly to k_{ab0} as defined by Horita et al. as the absorption-free k-factor.[3]

If the K and L lines of the same element can be used, then evidently the ratio C_a/C_b is a true constant (= 1). However, some iteration may still be necessary if variations in composition change the value of $[\mu/\rho]_b$ significantly between the data points.

Experimental

The specimen chosen to investigate the analytical method was a semiconductor multi-layer sample of alternating layers of InGaAs and InP, grown on an InP substrate by metalorganic chemical vapor deposition. The layers of InGaAs varied between 10 and 30 nm wide and the intervening InP layers were 50 nm wide. The sample was prepared as a cross section by ion beam thinning (Fig. 1). It is known that some elemental redistribution has taken place in the sample, that the InP layers contain some small concentrations of both Ga and As, and that P has also diffused into the InGaAs layer.[4] The sample was oriented in the microscope by use of the Kikuchi bands, so that the layers ran vertically through the sample, but away from any strong diffraction condition, since that may affect the relative intensities of the generated characteristic.[5] Spectra were recorded for 30 s from thicker regions and 100 s from the thinner regions from varying thicknesses and several layers of the InP. Figure 2 shows part of a typical spectrum recorded from 0 to 40 keV, so that the In Kα line could be measured. The peak-to-background ratios were such that a simple straight-line background subtraction could be used without a significant effect on the accuracy of the peak counts. The lines measured were In Lα, P K, Ga Kα, As Kα, and In Kα. The k-factors were measured on pure samples of GaAs, GaP, and InP for the same experimental conditions but much longer counting times, to reduce statistical uncertainties. All k-factors are related by the chain rule $k_{ij} = k_{jk} * k_{ki}$ from which other required k-factors were calculated.

Data Available

Figure 3 shows plots of P Kα vs In Kα and In Lα vs In Kα for a range of measured data points with the fitted curves superimposed. The initial analysis was performed on the P and In peaks using the value of 1316 cm²g⁻¹ and 556 cm²g⁻¹ for P Kα and In Lα in pure InP for all data points and assuming that the atomic ratio of In/P was 1. Heinrich's 1987 formulation for mass absorption coefficient was used throughout the data analysis.[6] The resulting values for ψ were used to correct the counts of P K, Ga Kα, and As Kα for self-absorption, and these counts were then used to calculate the first approximation of the specimen composition. After three iterations the process converged so that the calculated atomic fractions had changes by less than 0.3%. Since the specimen is crystalline and atomically perfect, it is to be expected that the group III and group V elements each make up 50% of the specimen composition.

TABLE 1.--Atomic fractions at 12 analyzed regions of different thickness in InPGaAs multilayer sample.

Atomic Fractions

	Cin	Cp	Cga	Cas	(P+As)	(In+Ga)
1	0.474	0.511	0.001	0.013	0.524	0.476
2	0.468	0.434	0.025	0.073	0.507	0.493
3	0.482	0.472	0.009	0.037	0.509	0.491
4	0.468	0.450	0.024	0.058	0.508	0.492
5	0.491	0.482	0.003	0.024	0.506	0.494
6	0.502	0.479	0.004	0.015	0.495	0.505
7	0.503	0.468	0.006	0.022	0.490	0.510
8	0.489	0.478	0.008	0.026	0.504	0.496
9	0.487	0.477	0.004	0.032	0.509	0.491
10	0.492	0.469	0.013	0.027	0.496	0.504
11	0.491	0.466	0.010	0.032	0.499	0.501
12	0.507	0.441	0.013	0.039	0.480	0.520

TABLE 2.--Absorption path length and approximate specimen thickness at 12 analyzed regions with corresponding % absorption of characteristic line.

	Path Length nm	thick-ness nm	P K absb'd %	Ga K absb'd %	As Kα absb'd %	In Lα absb'd %
1	150	45	8.3	1.0	0.6	3.8
2	220	65	12.	1.4	0.9	7.1
3	340	100	16.	2.2	1.4	9.0
4	380	110	18.	2.3	1.6	11.
5	490	140	20.	3.1	2.0	11.
6	560	170	23.	3.5	2.3	12.
7	640	190	25.	4.0	2.7	14.
8	730	210	27.	4.5	3.0	16.
9	770	230	28.	4.7	3.1	17.
10	960	280	31.	5.7	3.9	19.
11	1050	310	33.	6.2	4.2	21.
12	1300	380	36.	7.5	5.1	24.
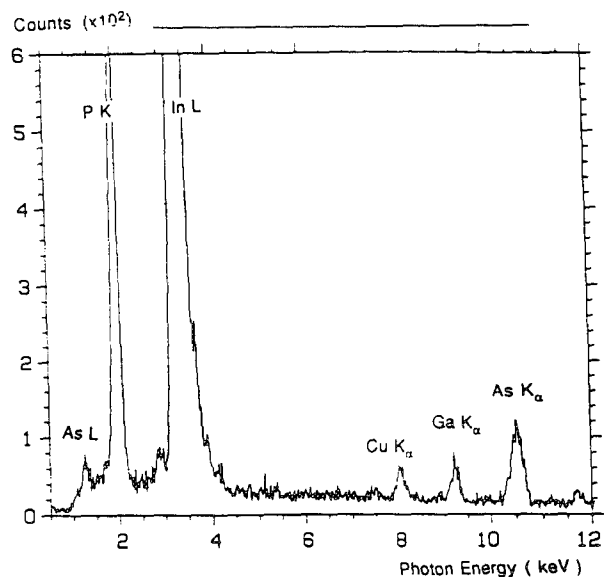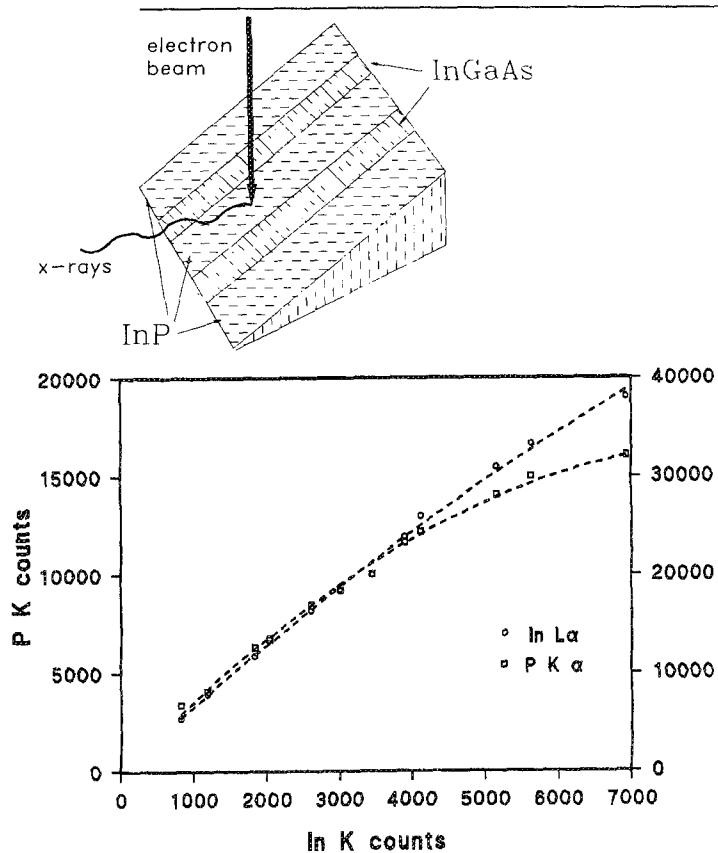
FIG. 1.--Schematic diagram of InGaAs/InP multilayer sample.

FIG. 2.--Part of typical spectrum from InP layer of sample.

FIG. 3.--Plots of normalized P K and In Lα vs In Kα with fitted absorption functions.

(This is not a constraint of the technique.) Table 1 shows that this is the case within 2% relative, except for the thickest and thinnest analyzed points. There is some evidence that very thin InP may change composition due to radiation damage.[7] An approximate calculation of the likely beam broadening in the sample shows that this change is likely to account for the small discrepancy in the analysis at the thickest point.

The final values obtained for k and ψ were $(8.9 \pm 0.4) \times 10^{-8}$ and (6.7 ± 0.4) for In Lα, respectively. As expected the two fitted values for ψ were the same within experimental error. This value was used to calculate the values of the mass absorption path lengths, which have an error of the same order as that of the parameter ψ, i.e., $\pm5\%$. Table 2 shows the absorption path lengths calculated from the approximate mean density of the sample and the % absorption of all the lines in the specimen at each of the data points. The accuracy of the absorption is typically 2% absolute. The approximate specimen thicknesses are also shown, but they have typical errors of $\sim40\%$, mostly due to the uncertainty in the geometric factor cosec θ. Use of the absorption of In Kα is of the order of 0.5%, which is negligible, as is required by the initial assumption in the formulation. The fitted value of k for the K case is in reasonable agreement with the k-factor $k_{InP} = (0.24 \pm 0.02)$ $[k \sim (1/k_{InP})]$.

Conclusions

The analytical approach presented successfully allows corrections of x-ray counts to be made that have been modified by specimen self-absorption. For certain types of specimens for which the composition changes are not too great, the range of thicknesses at which analyses may be made has been significantly increased. Further work will quantify how large the composition variations may be before the analysis technique fails to converge.

References

1. G. W. Lorimer and G. Cliff, "The quantitative analysis of thin specimens," *J. Microsc.* 103: 203, 1975.
2. N. J. Zaluzec, in J. J. Hren, J. I. Goldstein, and D. C. Joy, Eds., *Introduction to Analytical Electron Microscopy*, New York: Plenum Press, 1979, 121.
3. Z. Horita, T. Sano and M. Nemoto, *J. Microsc.* 143: 215, 1986.
4. A. J. McGibbon et al., "X-ray microanalysis of InGaAs/InP multilayer structures grown by metalorganic chemical deposition," *J. Appl. Phys.* 65: 2293, 1989.
5. F. Glas and P. Henoc, "The use of electron induced x-ray emission for the detection of atomic displacement," in G. Tatlock, Ed., *Electron Microscopy and Analysis, 1985*, Bristol: Institute of Physics, 1987, 217.
6. K. F. J. Heinrich, *Mass Absorption Coefficients for Electron Probe Microanalysis*, National Bureau of Standards, Gaithersburg, Md., 1979.
7. G. Bullock et al., "High spatial resolution EDX microanalysis of III-V semiconducting materials," in A. G. Cullis and P. D. Augustus, Eds., *Microscopy of Semiconducting Materials*, Bristol: Institute of Physics, 1987, 643.

THIN-FILM X-RAY QUANTITATION:
NEW INSIGHTS WITH THE AID OF MONTE CARLO CALCULATIONS

J. R. Michael*, A. D. Romig, Jr.* and J. I. Goldstein*†

*Materials and Process Sciences, Sandia National Laboratories, Albuquerque, NM 87185
†Department of Materials Science and Engineering, Lehigh University, Bethlehem, PA 18015

The determination of chemical composition from a ratio of the characteristic x-ray intensities (ratio technique) measured from thin specimens has become a standard technique in analytical electron microscopy.[1] One of the main assumptions used in this technique is that the normalized distribution of characteristic x-ray intensity with mass depth (ρt), termed $\varphi(\rho t)$, is constant with mass depth and approaches one. If this assumption is violated, the x-ray generation must be calculated as a function of mass depth (i.e., a voltage dependence in the ionization cross section is required and the effect of fast secondary electrons must be included) and the standard absorption equation must be modified (since $\varphi(\rho t)$ is not constant with (ρt)).[2] $\Phi(\rho t)$ curves have been experimentally determined only for a limited number of elements because of the difficulty of performing the experiment in thin specimens. Monte Carlo electron trajectory simulations are therefore the most tractable way to calculate the depth distribution of x-ray generation.[3] The recent use of massively parallel computation techniques for Monte Carlo electron trajectory simulations has produced a methodology for near real time simulation of electron scattering in solids.[4] The Monte Carlo electron trajectory simulation executed on a parallel computer allows for the calculation of $\varphi(\rho t)$ curves in real time (about 35 seconds for 5×10^6 electrons), and thus has been used as an aid for quantitative microanalysis of thin film specimens. Massively parallel Monte Carlo simulation has also been used to study the effect of fast secondary generation on light element x-ray quantitation, since a large number of electrons can be rapidly simulated.

Figure 1 shows the $\varphi(\rho t)$ curves, with and without fast secondary electrons, for Al K_α x-rays generated in a 50 nm thick foil of pure Al by 300 keV electrons . The fast secondary electrons increase the number of generated x-rays by approximately 1.3%. For lighter elements the effect of fast secondaries is enhanced. Figure 2 shows the $\varphi(\rho t)$ curve for N K_α x-rays in TiN. In this case the generated x-ray intensity is increased by about 7% at 300 keV and $\varphi(\rho t)$ is not constant with (ρt) . The increase in $\varphi(\rho t)$ above 1.0 and its variation with (ρt) results in errors in the compositions calculated from x-ray intensities using the ratio technique when an absorption correction is required. Figure 3 shows the generated and emitted (after absorption effects are considered) x-ray intensities for N K_α in TiN as a function of depth for an accelerating voltage of 300 kV. For such a strongly absorbing system the emitted intensity is greatly reduced. Figure 4 shows a comparison of the emitted intensities for N K_α in TiN with and without the effect of fast secondary electrons. In systems where large absorption corrections are needed the effect of fast secondary electrons can result in even greater errors.

In a system containing a light and a heavy element, the enhanced x-ray emission from the light element due to fluorescence by fast secondary electrons leads to a compositionally dependent k-factor.[5] Furthermore, for 300 keV primary electrons, the generation of fast secondary electrons will cause significant changes in the $\varphi(\rho t)$ curves for elements with atomic number less than 14.

1. G. Cliff and G. W. Lorimer, J. Microsc. (1975) 103, 203.
2. J. I. Goldstein et al., SEM-1977 I, 315.
3. D. E. Newbury et al., MAS-1983, 168.
4. A. D. Romig, Jr. et al., MAS-1990, 275.
5. R. Gauvin and G. L'Esperance, MAS-1989, 527.
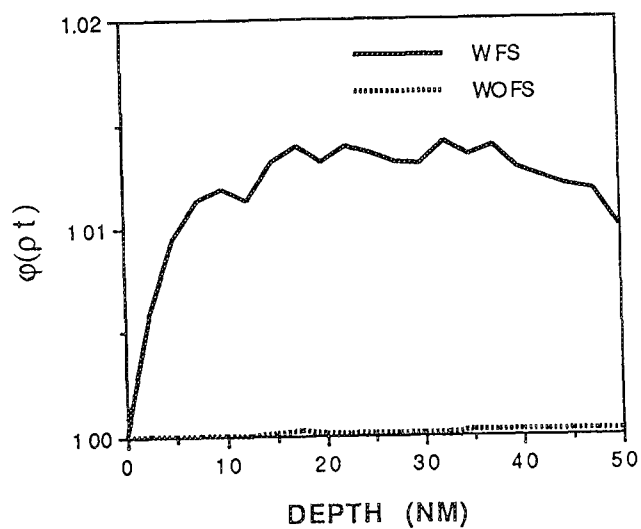
Figure 1. φ(ρt) curves for Al Kα
x-rays generated in 50 nm of Al.
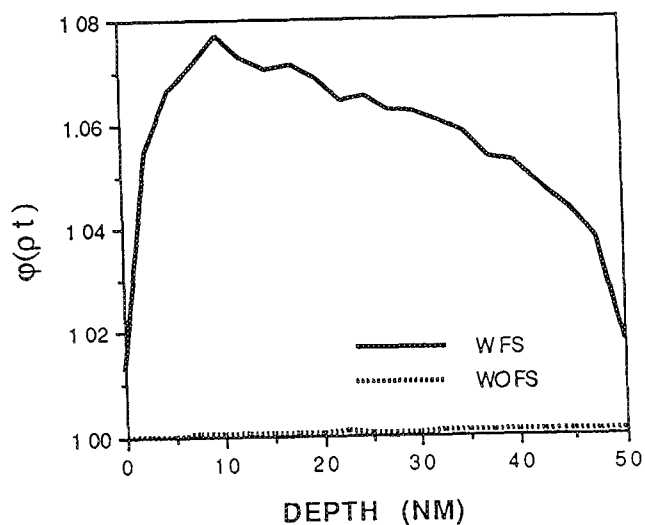
Figure 2. φ(ρt) curves for N Kα
x-rays in 50 nm of TiN.
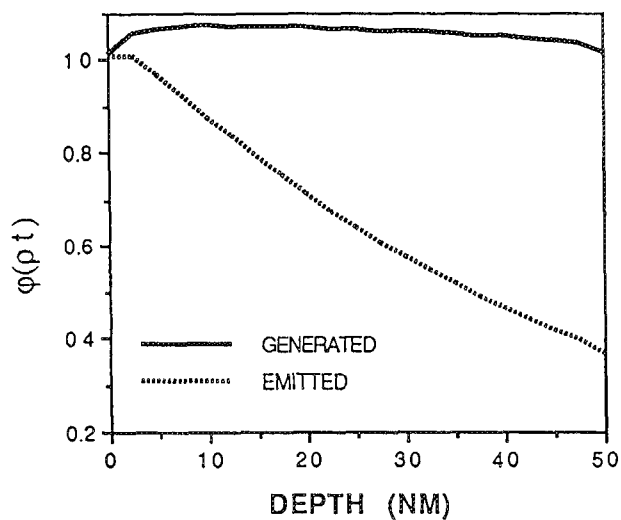
Figure 3. Generated and emitted
N Kα φ(ρt) curves in 50 nm of TiN.
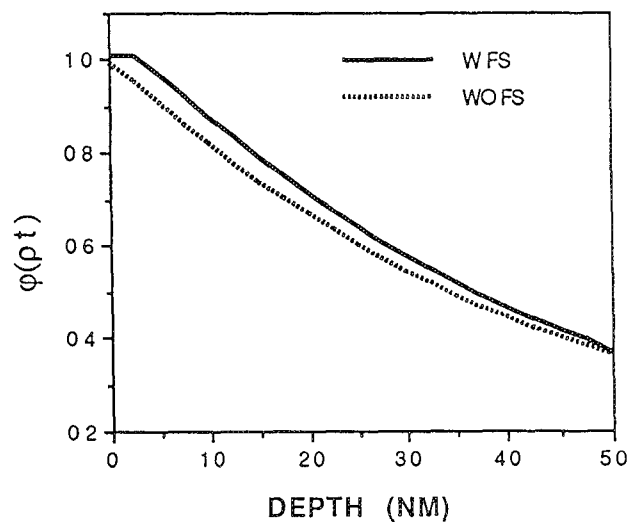
Figure 4. Comparison of emitted N Kα
x-rays in TiN with and without fast
secondaries.

THE STANDARD HOLE-COUNT TEST: A PROGRESS REPORT

C. E. Lyman and D. W. Ackland

Department of Materials Science and Engineering, Whitaker Lab #5, Lehigh University, Bethlehem, PA 18015

Analytical electron microscopy (AEM) was well served by the original hole count test[1,2] that prompted microscope manufacturers to reduce, by an order of magnitude, spurious x-ray generation in the specimen. This spurious x-ray signal is caused by hard x-rays or uncollimated electrons from the illumination system and is typically generated over the entire specimen regardless of where the electron probe is placed for analysis. The original test was performed on an ion-milled thin foil disk specimen of Ag or Mo, but the absolute value of hole count was dependent upon both specimen and operator.[3] To make progress in the reduction of spurious x-rays at intermediate voltages (if the problem is present), a hole-count test on a standard specimen that does not require operator judgement would be useful. The ultimate goal would be to reduce spurious x-rays to a level that would not affect any experiment on any specimen.

The ideal test specimen should be sensitive enough to detect even very low levels of spurious radiation. For the specimen to emit a large signal of characteristic x-rays when struck by high energy x-rays or electrons, it should be made of a relatively thick piece of high atomic number metal. To normalize the spurious signal obtained from the hole, the specimen should also contain a metal film of uniform thickness emitting a characteristic x-ray.[4] In the present work the specimen consists of a 30 nm-thick Cr film sputtered onto a holey carbon film supported on a 400 mesh Au grid[5] and backed by a Au or Mo washer. The uniform Cr film allows the spurious x-ray counts, detected in the hole from Au or Mo, to be ratioed to the Cr peak generated in the same thickness of Cr for each measurement. Figure 1 shows the test specimen configurations used with the Au washer (test specimen A) and Mo washer (test specimen B) placed under the Au grid. The Au washer was 25 µm thick and the Mo washer was 100 µm thick, while the hole in each was about 350 µm in diameter.

The AEM was a Philips EM430, operated in STEM mode, with a special aperture inside the upper objective lens to improve its hole count performance to the level of a Philips CM30. X-rays were detected with a Link Analytical intrinsic Ge detector of collection angle 0.12 sr. The test specimen was loaded into a beam current measuring specimen holder with the Cr film facing the electron beam. A specimen tilt toward the detector of 4° was applied even though the x-ray takeoff angle is 20°. Figure 2 shows the positions on the test specimen where typical measurements were made; for example, in the hole (a) and on the Cr film (b). At each operating condition examined, three "in hole" and three "on film" spectra were collected for 100 seconds live time each.

Figure 3 shows the significant increase in hole count for 200 and 300 kV compared to 100 kV. This test was carried out with test specimen configuration A as shown in Figure 1. The hole count at 300 kV with the standard EM430 50 µm hard x-ray aperture (about 2.8 on Figure 3) can be reduced by one third using a modified hard x-ray aperture consisting of a 50 µm EM400 top hat hard x-ray aperture on top of a 3 mm-long Pt cylinder with a hole in the center. It is important to note that the numerical values for any hole count can only be compared if the test specimens generating them are identical.

Figure 4 shows that this type of test specimen is sensitive to hole count changes produced by different probe demagnifications (spot sizes). This figure shows that a small probe size (spot size 5) has a hole count nearly an order of magnitude higher than a large probe size (spot size 2). The high hole count at spot size 5 is probably caused by 300 kV electrons hitting the C2 aperture holder or the liner tube since at this spot size the beam would have a large convergence angle after the C1 lens. The hole count is actually more strongly revealed by the Au K-line than the Mo K-line since

the Mo washer is nearly four times thicker than the Au grid. The apparent sensitivity of this test specimen may be improved by reducing the Cr film thickness and by selecting specimen materials to ensure that Mo K-to-L analysis[1] can be easily performed (eliminate AuM/MoL peak overlap). [6]

References
1. J.I.Goldstein and D.B.Williams, *SEM/1978* I, ed. O.Johari, SEM,Inc, AMF O'Hare,IL, 427.
2. J. Bentley, N. J. Zaluzec, E. A. Kenik, and R. W. Carpenter, *SEM/1979* II, ed. O. Johari, SEM, Inc., AMF O'Hare, IL, 581.
3. C. E. Lyman, D. W. Ackland, D. B. Williams, and J. I. Goldstein, *Microbeam Analysis-1989*, ed. P. E. Russell, San Francisco Press, 507.
4. This suggestion was originally made by M. N. Thompson of Philips Electronic Instruments, Inc., private communication.
5. Experimental test specimen supplied by N. Alfieri of SPI Supplies Inc., West Chester, PA.
6. This work is supported by the U.S. Dept. of Energy under contract DE-FG02-86ER45269.
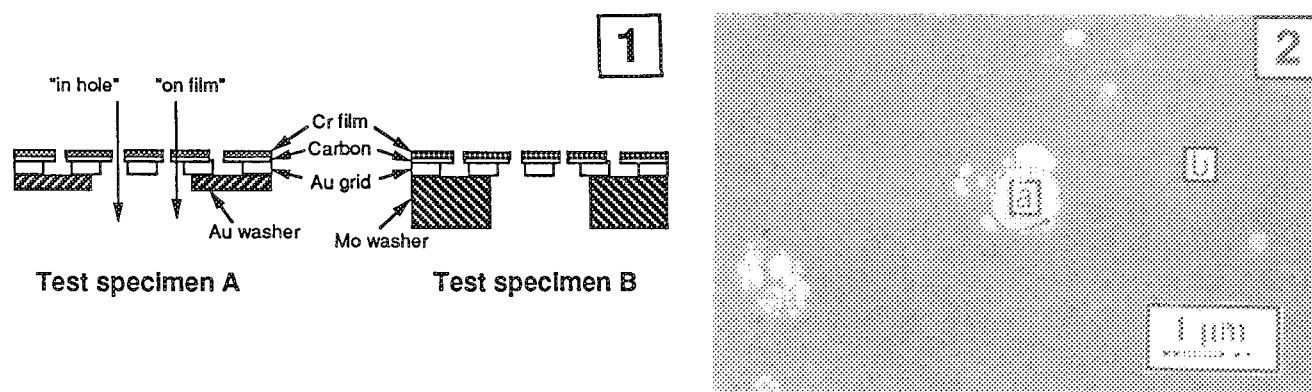
Figure 1. Test specimen configurations used in this work. Cr-coated 400 mesh Au grids backed by a Au washer (test specimen A) or a Mo washer (test specimen B).

Figure 2. STEM micrograph showing a typical "in hole" area (a) and a typical "on film" area (b).
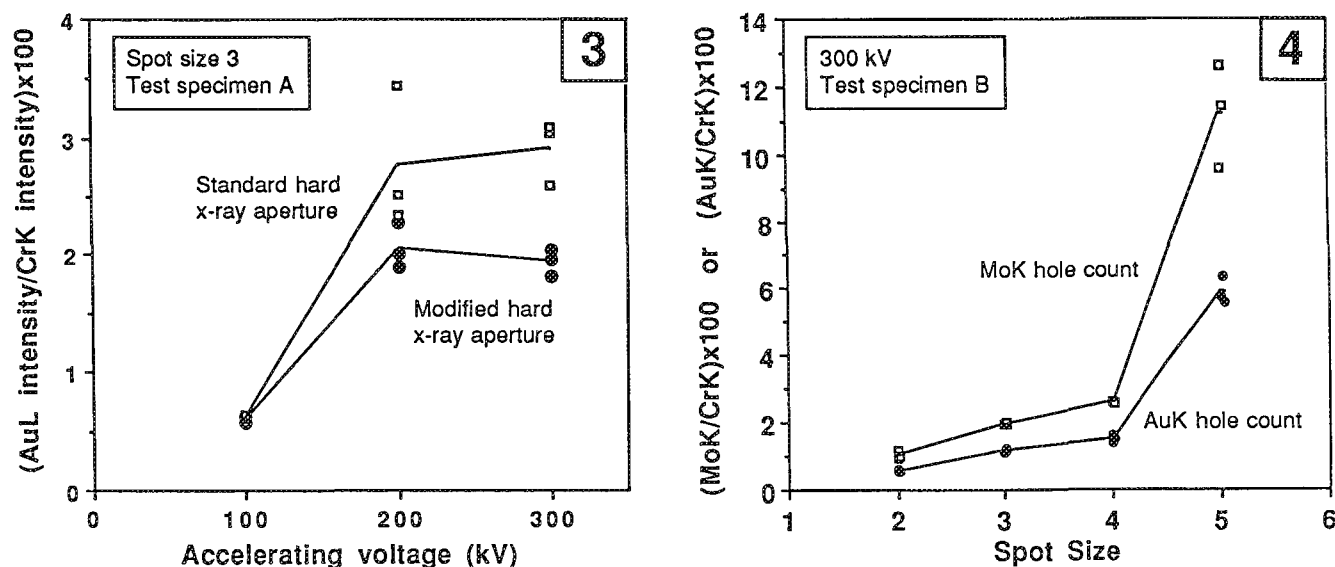
Figure 3. Hole count versus accelerating voltage for the standard EM430 50 μm hard x-ray aperture and for the modified 50 μm hard x-ray aperture.

Figure 4. Hole count versus EM430 spot size at 300 kV with the modified hard x-ray aperture.

MEASUREMENTS OF BEAM BROADENING IN SAMPLES OBSERVED WITH A FEG-STEM

W. A. Furdanowicz,* A. J. Garratt Reed,** and J. B. Vander Sande**

*Homer Research Laboratory, Bethlehem Steel Corp., Bethlehem, PA 18016.
**MIT Center for Materials Science and Engineering, Cambridge, MA 02139.

The issue of what information can be gleaned in the limit from an analytical electron microscope has proved elusive. (It has even been difficult to agree on the terminology to employ!)[1] Central to the debate has been the issue of how the electron beam reacts to its passing through the sample. Early calculations by Goldstein et al., which are now referred to as the "single-scattering model,"[2] have subsequently been refined, although without substantially altering their predictions. Monte Carlo methods, with a complexity increasing with time in parallel with the falling out cost of computational facilities, have produced results generally similar to those of the single-scattering model and its derivatives, as have calculations based on a transport equation. This agreement is hardly surprising, for the three methods are in fact three different descriptions of the same underlying model--that electrons are scattered individually by the nucleii of the atoms, and that the wave nature of the electrons may be ignored. We term this group of models the "ballistic electron models." Despite these limitations, and the fact that other descriptions of broadening have been proposed, the scant available experimental evidence either fitted (perhaps with some imagination) the prediction of this general model, or a plausible reason could be advanced for why it did not fit, so that over the last 14 years it has become generally accepted that the beam broadening b is related to the sample thickness t and density ρ, the atomic weight A, and the atomic number Z of the sample and the beam voltage V by

$$b = S \frac{Z}{V} \left(\frac{\rho}{A}\right)^{1/2} t^{3/2}$$

The constant S varies according to the exact theory used to derive the result, and to the units of b, t, and V.

A few workers have remained uncomfortable with the implicit assumption that the wave nature of the electron can be ignored in modeling its behavior in a solid--periodic or otherwise. Computations by Fertig and Rose, for example,[3] or more recently by Marks,[4] have shown that at least in zone-axis orientations, the beam broadening predicted by wave-mechanical computations is far less than that predicted by the more generally accepted theories, although these computations are open to the criticism that they ignore the effects of inelastic scattering. Because of the great importance of understanding completely the effects of beam broadening in analytical electron microscopy of materials, the present work was undertaken in order to add to the very small amount of available experimental evidence on this topic.

It was decided to study the x-ray signals detected from small precipitates in a matrix, thus avoiding the uncertainties introduced by analyzing grain or phase boundaries. A particle that is small compared to its depth in the foil senses only the probe profile at that depth; the x-ray signal from the precipitate is not influenced by the interaction of the beam at other depths in the specimen. The system chosen was copper with Fe-Co precipitates. Apart from being available and readily prepared, no complications such as fluorescence or absorption were anticipated, which made this system almost ideal for the experiments. The actual bulk composition was 1.8 at.% Fe, 0.9 at.% Co, balance copper; and after the selected thermomechanical treatment, it contained precipitates in the size range 8-28 nm, the matrix containing about 1 at.% Fe + Co.

The samples were prepared by standard metallurgical techniques; the final thinning was performed by jet electropolishing, with extreme care taken to maintain sample cleanliness, including a routine vacuum bake of all samples. The ultimate step taken in this regard was baking several samples in the microscope itself at 140 C for 9 h. As a result, it was possible to study samples for many hours without significant contamination being evident. In all cases, study of an area was terminated once enough contamination to interfere with the observations was present.

A total of 11 precipitates were studied in detail. Several were measured at different orientations, close to two-beam diffracting conditions, or with the deviation parameter s having small positive or negative values, or large positive values. In several cases, the foil was removed from the microscope, inverted, and reinserted, so that the same precipitate could be observed from both sides of the foil. The total number of profiles measured was 39. In the case of five of the precipitates, it was possible to determine the depth from stereo microscopy. In the remaining cases, the precipitate was arbitrarily assigned a depth equal to half the foil thickness. The range of the depths measured directly was 12-80 nm. The sample thickness was either measured directly by stereo microscopy or determined indirectly by observation of the ratio between the copper x-ray signal and the sum of the iron and cobalt signals. By deriving a calibration from those measurements where the thickness was known, one could, given a measurement of the precipitate size (and an assumption, valid in almost all cases, that the precipitates were spherical), to estimate the sample thickness from this ratio. The sample thicknesses were determined to be in the range 16-160 nm, except for one especially thick sample, which was 590 nm thick.

The electron microscopy was performed in a VG Microscopes HBS STEM running at 100 kV. The x-ray detector was windowless and subtended a solid angle of 0.078 sr at the sample; the take-off angle was 13°. The sample tilt varied according to the requirements of selecting the desired diffracting condition, and ranged from approximately horizontal to a tilt of 30° toward the detector. X-ray profiles were obtained by stepping the beam in 21 to 33 equally spaced steps across a distance equal to about twice the apparent particle diameter, centered on the precipitate. The data acquisition was controlled by a specially written set of macros running on a Link Systems AN10000 analyzer. Several (up to seven) scans across the precipitate were summed in order to monitor the build-up of contamination or other sample degradation during the analysis, and to distribute its effects uniformly over the profile area. In fact, no effect of contamination on any detail of the profile could be found. The total acquisition time at each point was in the range 21-120 s. Drift was corrected by manual interaction with the acquisition macro, and a photographic record was maintained of the actual acquisition position of every spectrum. A convergent-beam difference pattern was also photographed for each profile, which provided a record of the crystallographic orientation of the beam with respect to the matrix, with the analysis points marked.

A detailed experiment was performed to estimate the precision of the positioning of the probe, in which photographs of the probe position before and after each acquisition in a profile were digitized and analyzed. This error, which would be (at least at first sight) random, is approximately ±0.75 nm. The full-width-half-maximum (FWHM) of the probe diameter was estimated to be 1.25 nm. Instabilities (magnetic interference and internal instabilities) were estimated to add (in quadrature) effectively another 0.5 nm to the incident beam diameter. Thus an estimate of the "effective beam diameter" was found to be 1.5 nm (FWHM). The error in the beam position is included in the statistical analyses described below; the effective beam diameter is not a random uncertainty, and must be treated differently. We shall return to this issue later in this paper.

In order to compare the data from the various profiles, the following procedure was

devised. From each data point, an "apparent concentration" of iron plus cobalt was determined by the Cliff-Lorimer method,[5] using calculated k-factors. Since the relative k-factors for Fe, Co, and Cu are quite similar, simply plotting the raw ratios in the x-ray intensities would have generated essentially identical results for the purpose of this study. This apparent composition, less the matrix composition of these elements, was plotted as a function of position in the profile. An example is shown in Fig. 2. The positions of the extremes of the precipitate (as determined visually from the photographs) were marked on the plot (but are not shown on Fig. 2). The area of the plot outside the optical diameter of the precipitate was then determined and was ratioed to the total area of the plot. For a given amount of beam broadening, this descriptor will be larger for smaller precipitates, so an alternate descriptor, the "scaled profile broadening" was devised--simply the above-described ratio multiplied by the precipitate diameter. This is believed to be a more useful descriptor for comparison of the results, although a detailed analysis of it has not been undertaken. This descriptor obviously does not directly generate a measure of the beam broadening. However, it does provide a number that should correlate with the beam broadening.

Error bars for the scaled profile broadening were determined empirically by computing the change in the descriptor as the apparent precipitate size (as marked on the data plot) was changed by an amount corresponding to the uncertainty of the probe position.

Detailed statistical analysis was undertaken to investigate the correlation between the beam broadening and, respectively, the precipitate depth in the foil, the diffraction conditions (both the magnitude of the diffracting vector and the magnitude of the deviation parameters), and the beam convergence angle, as well as any correlation between the above and any asymmetry or skew in the profiles. For example, Fig. 3 is a plot of scaled profile broadening vs precipitate depth, for precipitates for which it was possible to determine the depth by stereo microscopy. No correlation is seen in this plot, nor was any found in any other case. Some small amount of broadening, independent of any of the investigated variables, was apparent. (For example, the error bars in Fig. 3 do not cross the zero axis of broadening.) We believe that in almost all cases, that in fact represents the effective probe diameter which, as noted above, was not considered in calculating the errors in these plots. We are currently undertaking computer modeling to verify this interpretation.

A significant variation was found in the apparent composition of the precipitates as the deviation parameter was changed. The data were insufficient to allow a detailed study of this phenomenon. It is believed to represent a manifestation of either x-ray emission enhanced by orientation in the matrix,[6] or of the ALCHEMI effect,[7] or both. Efforts to fit the observed variations to simple-minded interpretations of the rocking curves were not successful.[8]

Discussion

We conclude that in the range of foil thicknesses up to 160 nm in a copper matrix, beam broadening of a 100kV electron beam is small compared with our effective electron probe diameter of 1.5 nm (FWHM) in all conditions.

The implications of this work are profound. The generally accepted ballistic electron models predict broadening in a copper sample 80 nm thick to be in the range 6-10 nm. Our results show that these predictions are too large by about an order of magnitude. We are convinced that the disparity lies in the neglect of the wave nature of the electron in the ballistic models. The limited computations performed by wave-mechanical methods predict that beam broadening of less than 3 nm would be expected, in agreement with our findings. In foils over a few tens of nanometers thick (i.e., a substantial proportion of those we report here) we know that essentially all

the electrons lose energy; evidently, the electrons retain a significant degree of coherence during these energy loss events. Indeed, if such were not the case, it would not be possible to observe good diffraction patterns from solids many extinction distances thick. That such patterns are in fact observed is routine knowledge for the practicing microscopist.

In the literature are a number of measurements of beam broadening as a function of sample thickness, made by a variety of methods. Most of these data appear to show quite plausibly that the beam broadening can be described by the ballistic electron models. We do not believe for one moment that these measurements are incorrect. We observe that in almost all cases, it was necessary for the measurements to be made in samples of extreme thickness. We suggest that in these thick samples the electrons do lose coherence and could then be subject to broadening similar to that described by the ballistic electron models.

However, the recent work of Michael and Williams[9] is not open to this interpretation, since it was performed on samples in the same thickness as used in the present work. It is possible that the geometry chosen by these authors--analysis across a (presumed) sharp concentration step--is complicating the understanding of their results. (That was precisely why we chose to analyze precipitates.) Computations are being performed in an effort to clarify this issue.

For the microanalyst these results are exciting. The sensitivity of grain boundary analysis depends critically on the broadening of the beam as it passes through the sample. Following the logic of Garratt-Reed,[10] but substituting the dramatically smaller broadening demonstrated here, we can see that the optimum experimental conditions for boundary analysis allow far thicker samples and finer electron probes than had been supposed. Alternatively, we now understand that the electron probe in a field-emission microscope can be large compared with the beam broadening, while still being fine enough to give good sensitivity for analysis of boundaries. In this situation the interpretation of the analysis does not depend on the sample thickness. At least qualitatively, it is possible to compare the segregation in different samples, say, simply by measuring the segregation at a few boundaries selected for "being about the right thickness," provided the probe conditions remain constant. Indeed, this has been the practice in our laboratory for many years, and, until now, we have frequently been surprised by the consistency of our results.

Full details of the enture dataset generated in the course of this work are available.[8]

References

1. J. R. Michael and D. B. Williams, "A consistent definition of probe size and spatial resolution in the analytical electron microscope," *J. Microsc.* 147: 289, 1987.
2. J. I. Goldstein, J. L. Costley, G. W. Lorimar, and S. J. B. Reed, "Quantitative x-ray analysis in the electron microscope," *SEM/1977* I, 315.
3. J. Fertig and H. Rose, "Resolution and contrast of crystalline objects in high-resolution scanning transmission electron microscopy," *Optic* 59: 407, 1981.
4. L. D. Marks, "Direct observation of diffractive probe spreading," *Ultramicroscopy* 16: 261, 1985.
5. G. Cliff and G. W. Lorimer, "The quantitative analysis of thin specimens," *J. Microscopy* 103: 203, 1975.
6. A. J. Bourdillon, P. G. Self, and W. M. Stobbs, "Crystallographic orientation effects in energy-dispersive x-ray analysis," *Phil. Mag.* A44: 1335, 1981.
7. J. C. H. Spence and J. Tafto, "ALCHEMI: A new technique for locating atoms in small crystals," *J. Microsc.* 130: 147, 1983.
8. W. A. Furdanowicz, *Effects of Diffraction on Microanalysis of Embedded Precipi-*

tates, Ph.D. thesis, MIT, 1991.

9. J. R. Michael, D. B. Williams, C. F. Klein, and R. Ayer, "The measurement and calculation of the x-ray spatial resolution obtained in the analytical electron microscope," *J. Microsc.* 160: 41.

10. A. J. Garratt-Reed, "Some considerations of the ultimate spatial resolution achievable in scanning transmission electron microscopy," *SEM/1985* I, 21.
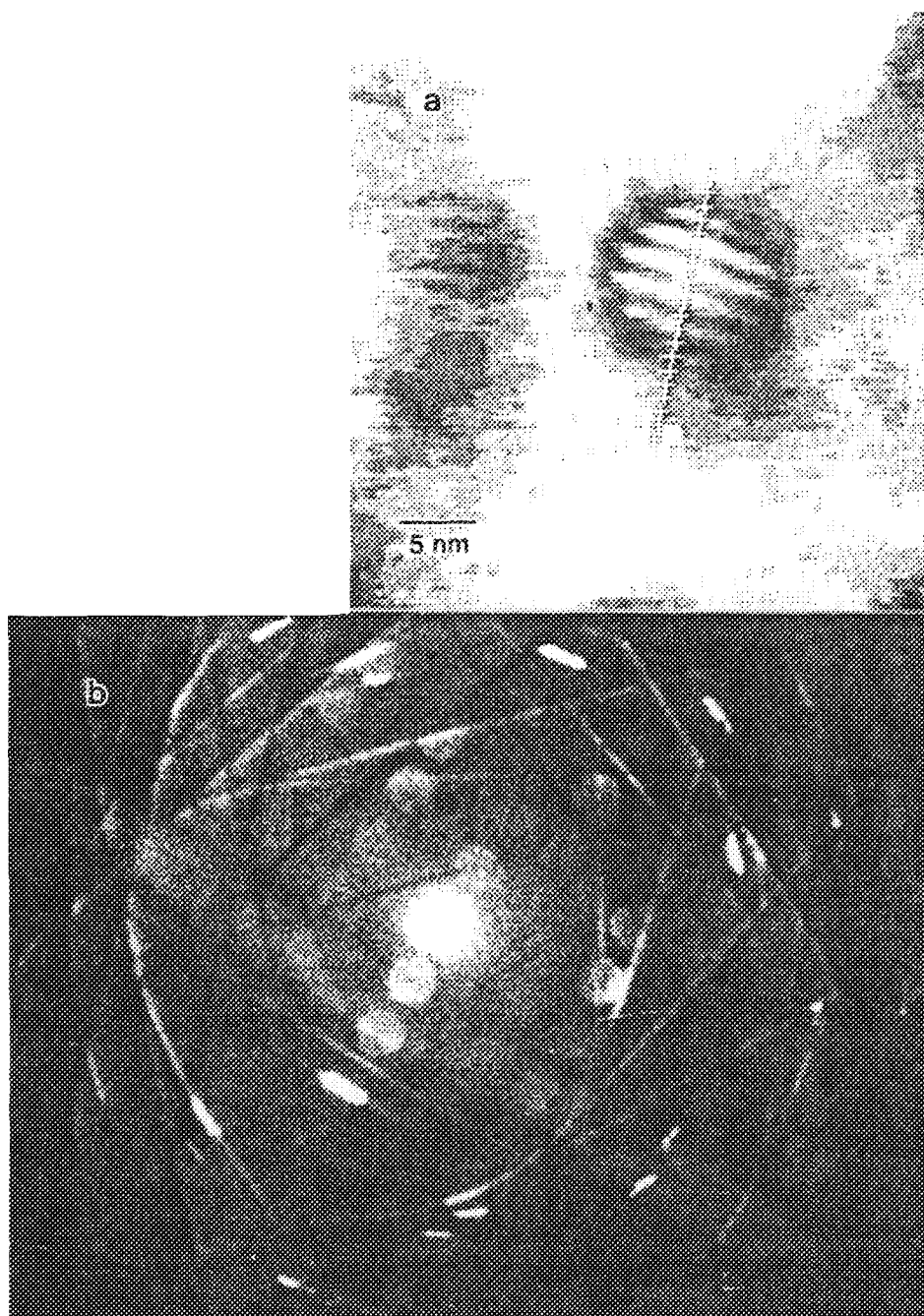
FIG. 1.--Typical precipitate.
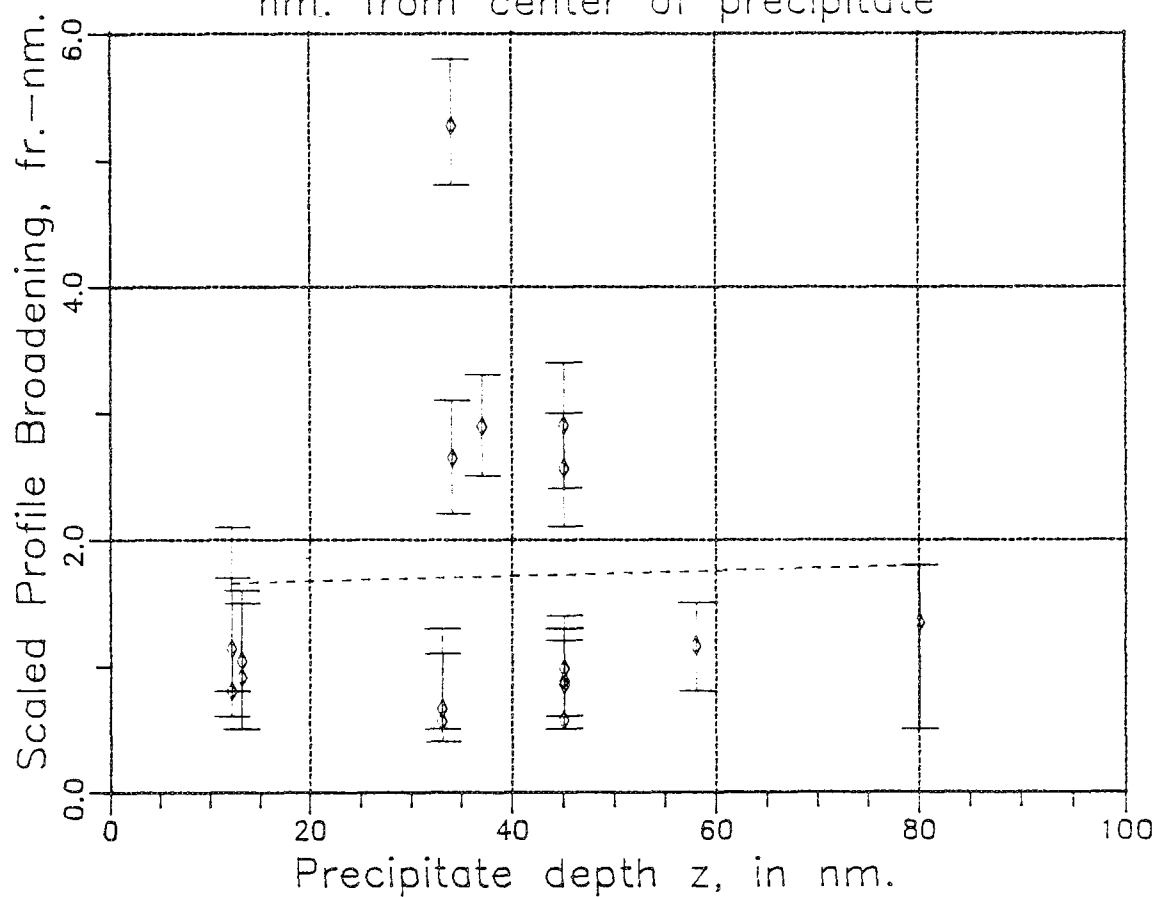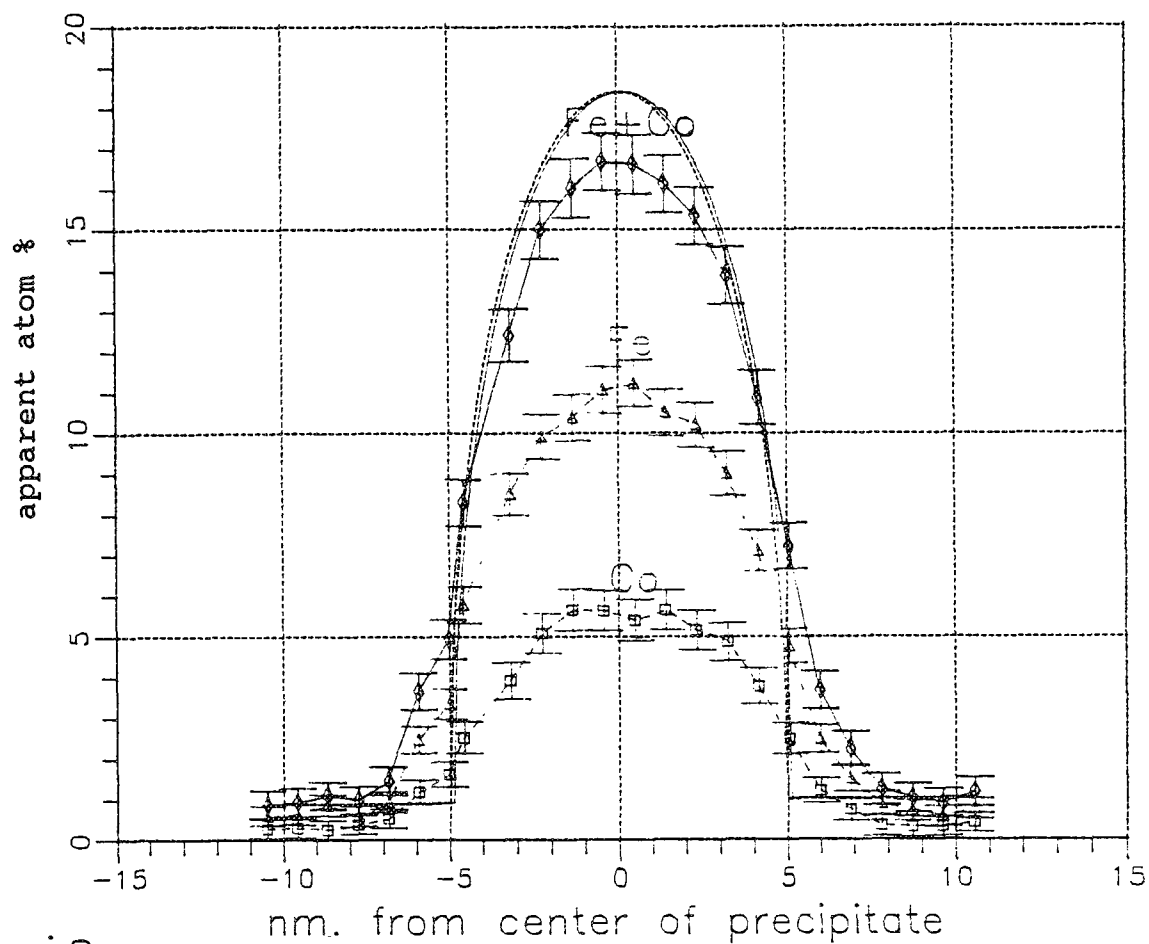
FIG. 2.--Typical plot of composition.
FIG. 3.--Scaled profile broadening.

J-4: EM Applications in Electronics

MICROSCOPY OF VLSI OXIDES

HIROSHI IWASAKI

Matsushita Electric Industrial Co., Ltd., Semiconductor Research Center, 3-15 Yagumo-Nakamachi, Moriguchi, Osaka 570 Japan (present address: The Institute of Scientific and Industrial Research, Osaka University, 8-1, Mihogaoka, Ibaraki, Osaka 567, Japan)

The oxide of silicon and other insulating films form an integral part of every VLSI circuit (e. g. Fig 1 [1]). Thin gate oxide(SiO_2) in the thickness range of 10-20 nm (5-10 nm) is needed for submicron (quatermicron) devices. For such devices, characterization of surface roughness at Si/SiO_2 interfaces becomes increasingly important because it is expected to affect field-dependent dielectric breakdown (FDDB), time-dependent dielectric breakdown (TDDB) and carrier mobility of MOS FETs more sensitively at necessitated higher operating electric fields. The Si/SiO_2 interface is usually considered as the boundary between Si lattice image and granular SiO_2 image.

P-type, CZ- Si(001) substrates with resistivity of 10-13 Ω cm were first cleaned by the RCA method and were oxidized in a quartz tube to 16nm thickness : O_2=100% at 900°C for 53 min (dry oxide), O_2/H_2=1/4 for 11 min (wet oxide).[2] Some MOS structured samples were also studied.[3] Some dry oxide and reoxidized nitrided oxide (ONO) of 7nm thickness were formed by rapid thermal process for electron mobility study.[4] Observations were made using a JEM-4000FX at about 2.5~3.0A resolution. For the STM observations, by means of HF dipping, the oxide was stripped off whereupon it is thought that the Si dangling bonds on the surface are terminated by hydrogen without damaging the interface morphology preventing the surface in air from re-oxidation.[5]

The cross-sectional HRTEM observation revealed for dry oxide bump like interface morphology which is distributed irregularly with small corrugations (5.4~8.1 A in height and 50 A in length), while, the wet oxide interface resulted in smoother undulation with 2.7~5.4 A in height and 400 A in length (Fig. 2).[2] The electron damage problem during HRTEM observation was found to be quite serious, especially for the "wet" oxide specimens.[3,6] For the wet oxide interfaces, regions with large undulations distributed sparsely were found by STM observations (Fig. 3) as well as low magnification TEM.[2] The opposite side of the oxide film to Si substrate is smooth even at the largely undulated portions (TEM). Such large undulations are approximately parallel with <110> directions (Fig. 3) probably reflecting "crystal habit at Si/SiO_2 interface". We also reported previously faceting of Si/SiO_2 interface at inner, concave corners of a trench.[7] For the dry oxide, the bump like protrusions are also observed by STM.[2] Different interface morphologies for dry and wet oxides seem to be related with oxidation Debye lengths beyond which oxidation rate follows the linear-parabolic Deal-Grove oxidation equation : 147 A (dry oxide) and 6 A(wet oxide). Thus unknown initial oxidation process is dominant for the dry oxidation and this may cause the bump like morphology.

We found large difference of electron mobilities for pure oxide and ONO at high electric field and low temperatures (surface roughness scattering regime).[4] At present stage, it seems difficult to detect, by cross-sectional HRTEM, difference of the interface roughness of the oxides that might explain the different electron mobilities.[4] Observation of SiO_2/Si interface morphology in atomic resolution by UHV-STM is in progress and some results will be presented in the conference.[8]

References

1. M. Fukumoto et al. , Proc. ESSDERC 90, Nottingham, (1990) 461.

2. M. Niwa et al., Jpn. J. Appl. Phys., 29 (1990) 2665.

3. M. Niwa et al., Mat. Res. Soc. Symp. Proc., 183 (1990)141.

4. T. Hori and H. Iwasaki, IEDM (1989) 459; T. Hori, IEEE T-ED 37 (1990) 2058.

5. M. Niwa and H. Iwasaki, Jpn. J. Appl. Phys., 28 (1989) L2320.

6. H. Oppolzer, Inst. Phys. Conf. Ser. 93, EUREM '88 2 (1988) 73.

7. R. Sinclair et al., J. Electrochem. Soc., 136 (1989) 511.

8. The author would like to thank Mr. M. Niwa, Drs. T. Hori, R. Sinclair and T. Takemoto for their helpful discussions and encouragement.
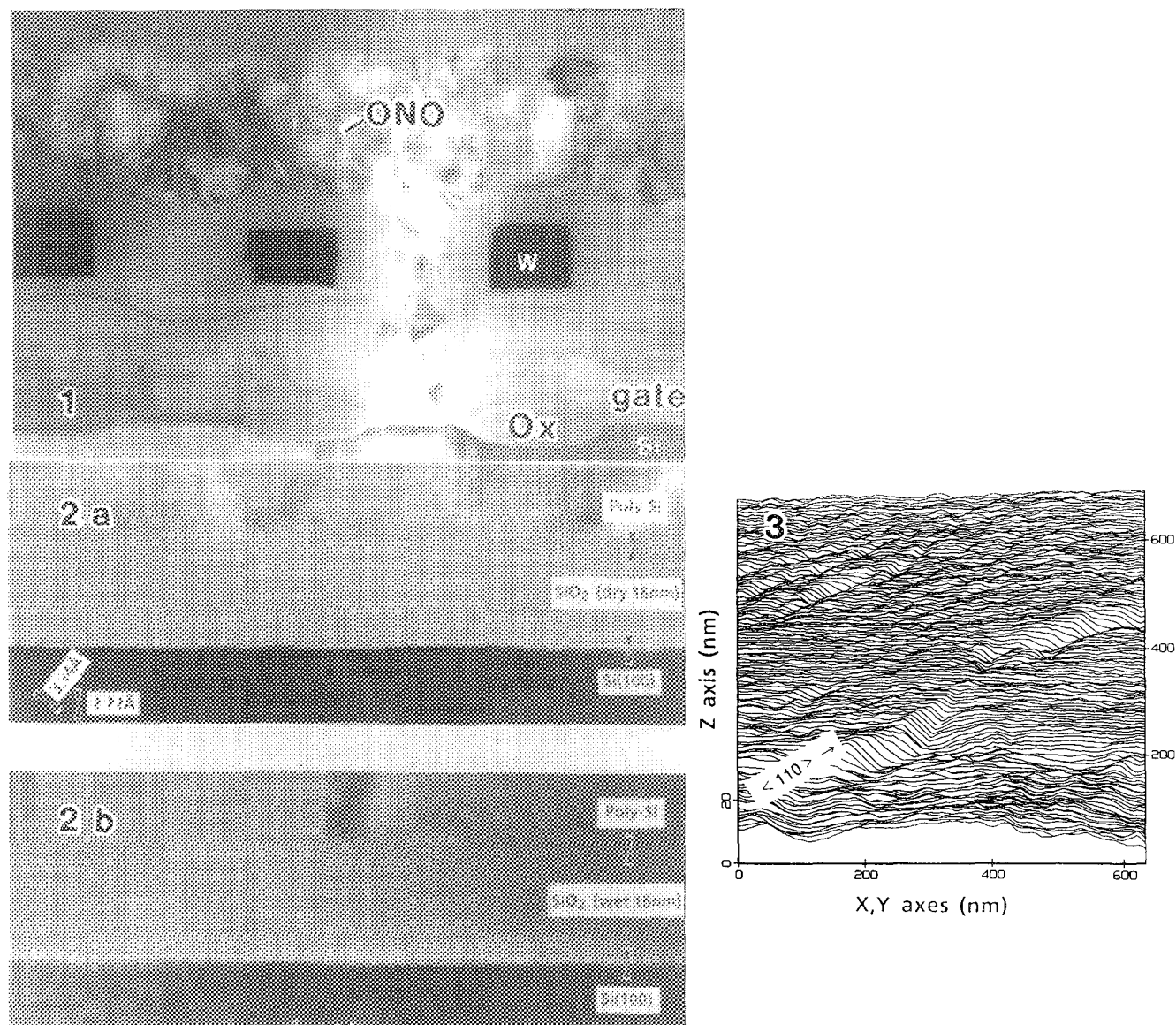
FIG.1.-- Cross-sectional TEM image of stacked capacitor 16M DRAM.

FIG.2.-- Cross-sectional HRTEM image of the dry (a) and wet (b) oxide interfaces of blanket oxides.

FIG.3.-- STM image of wet oxide interface (area=6300×6300 A^2, tunneling current=0.5 nA, sample vias=+1.8 V).

EFFECTS OF SURFACE OXIDE ON LOW-TEMPERATURE EPITAXIAL GROWTH OF Si

K. C. Bretz, T. S. Kuan, P. D. Agnello, and T. O. Sedgwick

IBM T. J. Watson Research Center, Yorktown Heights, New York, 10598

The Si epitaxial growth temperature using Chemical Vapor Deposition (CVD) has been steadily reduced in the last few years to temperatures as low as $600°C$. Blanket and selective Si epitaxy at atmospheric pressure is now achieved at low temperature through purification processes which exclude O_2 and H_2O impurities from the deposition zone (1). In addition to maintaining the deposition system ultra-clean, the initial Si growth surface must be free of surface oxide to achieve low defect density in the epitaxial layer. Previous experiments have shown that a slight presence of surface oxide leads to generation of extended defects. Therefore, an effective surface cleaning process is as important as an oxygen-free environment for achieving perfect epitaxy at low temperatures. In this work we use electron microscopy to study the structure of defects nucleated from surface oxide and the mechanism of defect formation under different growth conditions. High-resolution observations are made to establish quantitative linkage between surface cleanliness and defect population.

To study defect mechanism associated with surface oxide, an ultra-clean, load-locked atmospheric pressure CVD system is used, as described in (1) and (2). Silicon is deposited through the hydrogen reduction of dichlorosilane. Before growth, the (100) Si surface is first annealed in purified H_2 for 10 minutes at $850°C$ to remove residual oxide and then exposed to H_2 and argon carrier gases containing trace amounts of oxygen (25 to 100 ppb) at $650-750°C$ for various lengths of time. In this temperature range, discrete oxide islands form on the Si surface with oxygen exposure. Some of these islands disrupt subsequent Si growth and produce extended defects in the epitaxial layer.

These extended defects give rise to micrometer-sized pyramidal structures that are visible at the film surface under Nomarski illumination or by a SEM. Figure 1(a) shows a typical pyramidal defect in a SEM micrograph. The low angle faces in the pyramidal structure intersect the (100) film surface along the <110> direction. The density of pyramids increases by several orders of magnitude ($10^3/cm^2$ to $10^8/cm^2$) as the surface oxygen content increases from $10^{12}/cm^2$ to $5 \times 10^{14}/cm^2$ as measured by SIMS (2). In cross-sectional TEM images, series of discrete oxide islands of varying sizes decorate and define the film-substrate interface. These TEM images reveal that the dominant defects induced by surface oxide are microtwins which presumably nucleate at larger oxide islands and propagate to the film surface. As shown in Figure 1(b), each twin ends at the apex of a surface pyramid. Twin boundaries enhance local growth rate and, as a result, form low-angle ($4°$) pyramids.

From the dramatic increase of pyramidal defect density with a small increase of surface oxygen, the nucleation of twins must be strongly sensitive to the oxide island size. For each growth condition, only those oxide islands larger than the critical size trigger twin formation. Cross-sectional lattice images can provide accurate measurements of the critical oxide island size for twin formation. Under favorable growth conditions this critical island size can be quite large. One example is shown in Figure 2, where lateral epitaxial growth is able to overcome oxide islands 15 nm in size. Through these cross-sectional lattice images, we learn that growth conditions such as substrate temperature and growth chemistry also affect twin generation. The density of twins tends to decrease with higher deposition temperatures. Under high deposition rates, we observe that even microtwins can be grown over and cured after only a thin layer growth.

References

1. T. O. Sedgwick, M. Berkenblit, and T. S. Kuan, Appl. Phys. Lett. (1989) 54, 2689.
2. T. O. Sedgwick and P. D. Agnello, Proceedings of the 11th International Conf. on CVD, CVD-XI, Eds. K. E. Spear and G. W. Cullen, (The Electrochemical Soc., Pennington, N.J. 1990) p. 254.
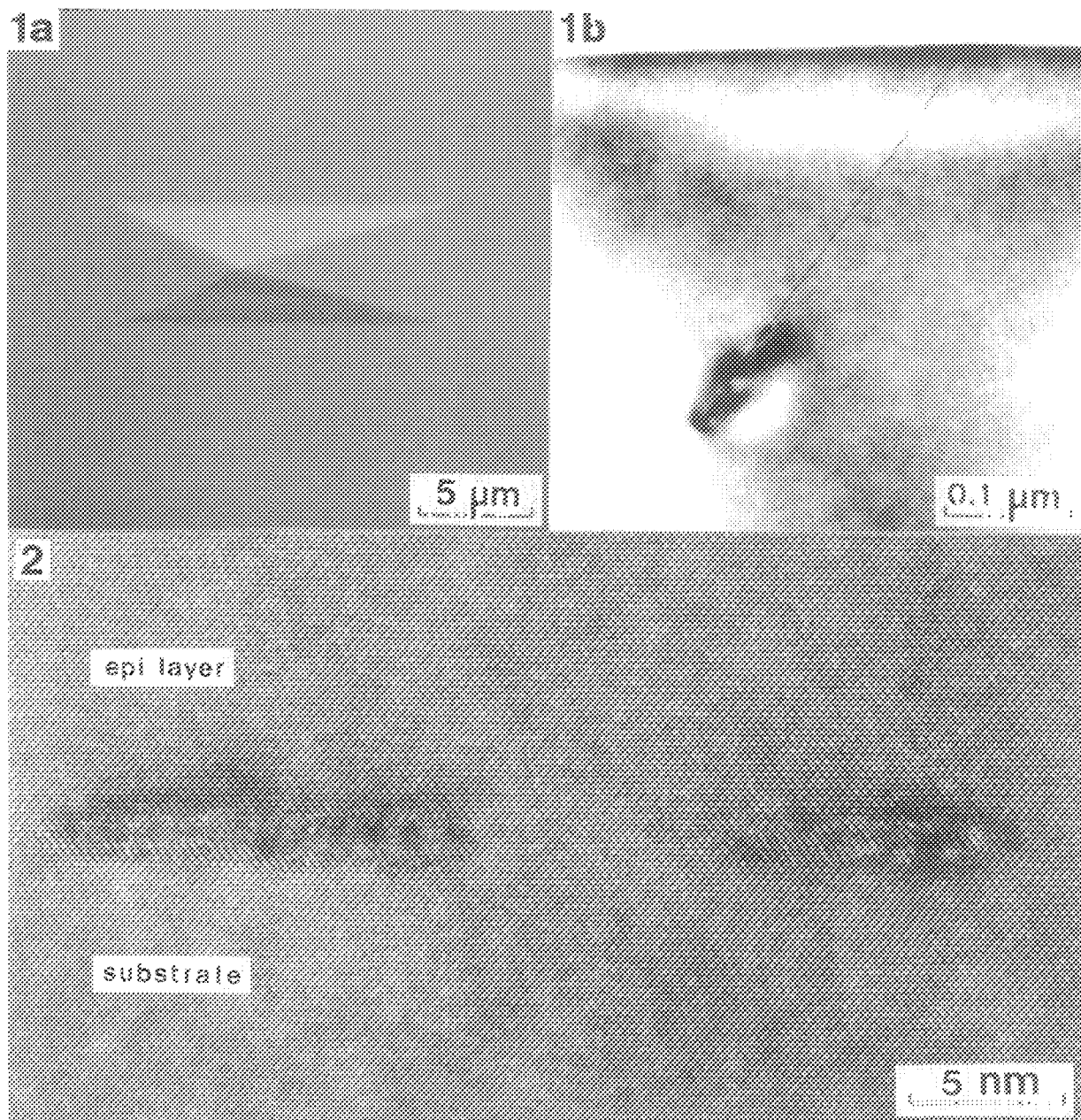
Figure 1   (a) A SEM image of a surface pyramid resulting from extended defects induced by interfacial oxide. (b) A cross-sectional TEM image of a microtwin extended from an oxide island at the interface to the apex of a surface pyramid shown in (a).

Figure 2.   A cross-sectional lattice image of interface oxide islands. These oxide islands are grown over by lateral epitaxial growth.

STRUCTURAL AND COMPOSITIONAL MAPPING AT Si-Ge INTERFACES USING Z-CONTRAST STEM

D. E. Jesson and S. J. Pennycook

Oak Ridge National Laboratory, Oak Ridge, Tennessee 37831-6024

Z-contrast scanning transmission electron microscopy (STEM) is a new technique capable of producing intuitively interpretable images of crystals and interfaces at atomic resolution.[1] A fine (~2.2 Å FWHM) electron probe is scanned across the surface of a thin specimen. Simultaneously, transmitted electrons scattered through high angles are collected by an annular detector with a large inner angle. To understand Z-contrast images requires a fundamentally new approach to image interpretation. The high-angle signal we detect is dominated by incoherently generated thermal diffuse scattering which originates very close to the projected atomic sites. This is sensitive to the composition of the column, approaching the atomic number squared or Z^2 dependence of unscreened Rutherford scattering. As the probe propagates along a major zone-axis, the beam sharpens up (channels) at the column positions with the incident probe profile as an envelope. Physically, this corresponds to s-type Bloch states of the probe wavefunction adding in-phase over the angular range of the objective aperture which enhances scattering to the high-angle detector. The Z-contrast imaging geometry can, therefore, be regarded as a Bloch wave filter. s-states dominate the image, and the filtering precludes interference between other states which explains the weak thickness dependence of the images. The s-state picture is particularly effective in explaining the local nature of images obtained from semiconductor (and indeed all) interfaces. Consider, for example, the very fine scale compositional modulation associated with the $(Si_2Ge_2)_p$ superlattice in Fig. 1(a). The relevant s-state combinations [Figs. 1(b) and (c)] feel either the Ge or Si dumbbells. The states are insensitive to the composition of neighboring columns so that images of interfaces can be regarded as column-by-column compositional maps dominated by high-angle scattering cross sections to the detector. For comparison, we show two strongly excited non-local states [Figs. 1(d) and (e)] which feel both types of dumbbells. Such states, which must be computed for each interface, are responsible for the interface interference patterns obtained in conventional HREM. They do not contribute to Z-contrast imaging, however, because of the filtering effects which affords a major simplification in image interpretation.

We now illustrate the importance of a simply interpretable image in determining the atomic-scale structure and chemistry of interfaces. Consider, for example, the Z-contrast image of the $(Si_4Ge_8)_p$ superlattice shown in Fig. 2. The [110] projection of Si consists of an arrangement of pairs of atoms or dumbbells separated by a distance of 1.36 Å. The 2.2 Å probe will resolve individual dumbbells, but not the atoms comprising the dumbbells. Each bright spot or column in the Z-contrast image corresponds to an individual atomic dumbbell and is slightly elongated along [001] as expected. This illustrates the sensitivity of the shapes of the image features to the detailed arrangement of the atomic columns, thus providing interpretable information well beyond the resolution limit of the microscope. The intensities of the columns in Fig. 2 (to within 10%) directly reflect the scattering power of the columns.[2] The bright horizontal bands, therefore, correspond to deposited Ge layers, and the darker regions deposited Si layers. Figure 2 was obtained at the optimum incoherent defocus[3] corresponding to the most compact surface probe intensity profile. Either side of this condition, the atomic columns blur and gradually fade away, rather like defocusing a camera. All Z-contrast images are, therefore, obtained using identical operating conditions. This is very important since it is not necessary to tune the microscope transfer function based on a preknowledge of the crystal structure. In this way, the material can truly provide the surprises as demonstrated in Fig. 2 by the ordered arrangement of Ge atoms occurring within the deposited Si layers. This unexpected result clearly demonstrates that the structure of ultrathin superlattices is far more intricate than previously imagined and provides important insight into the atomistic processes occurring during MBE growth.[4,5]

References

1. S. J. Pennycook and D. E. Jesson, Phys. Rev. Lett. **64**, 938 (1990).
2. D. E. Jesson, S. J. Pennycook, and J.-M. Baribeau, Materials Research Society Symposia Proceedings **183**, 223 (1990).
3. O. Scherzer, J. Appl. Phys. **20**, 20 (1949).
4. D. E. Jesson, S. J. Pennycook, and J.-M. Baribeau, Phys. Rev. Lett. **66**, 750 (1991).
5. Research sponsored by the Division of Materials Sciences, U.S. Department of Energy, under contract DE-AC05-84OR21400 with Martin Marietta Energy Systems, Inc., and in part by an appointment with the U.S. Department of Energy Postgraduate Research Program administered by Oak Ridge Associated Universities.
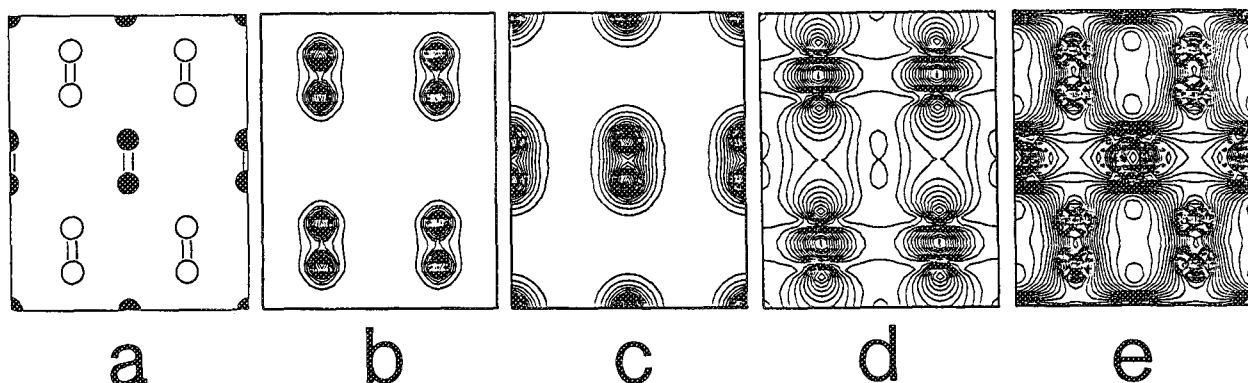
FIG. 1--(a) [110] projection of a $(Si_2Ge_2)_p$ superlattice. Solid circles represent Si columns and open circles Ge columns. Bonding s-state combinations independently feel (b) the Ge dumbbells and (c) the Si dumbbells. Nonlocal states are shown in (d) and (e).
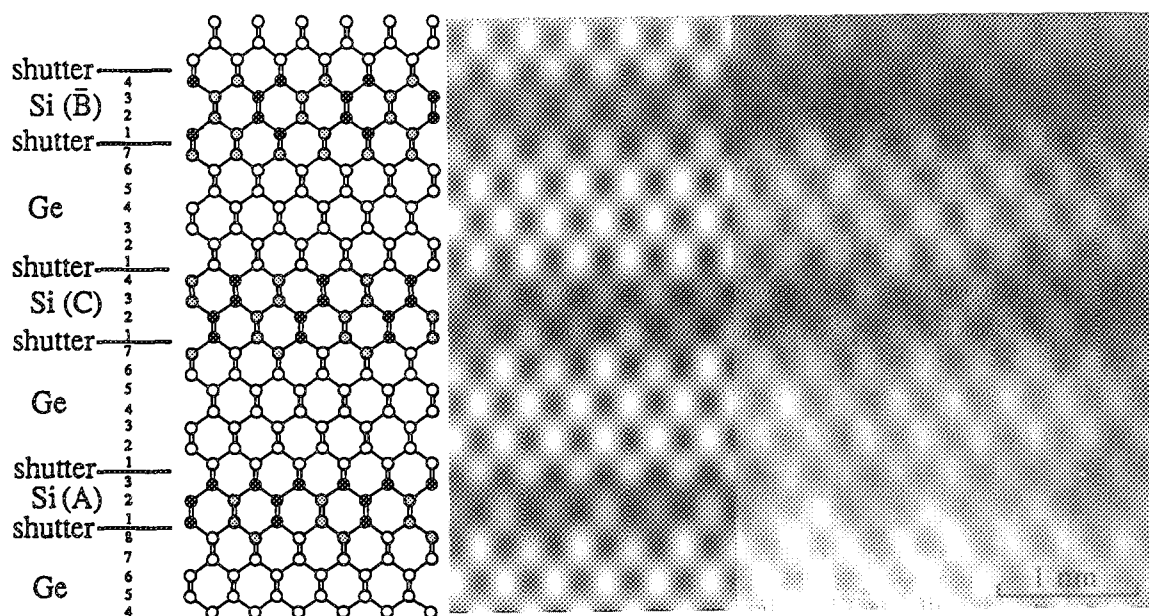
FIG. 2--[110] Z-contrast image of a $(Si_4Ge_8)_p$ ultrathin superlattice showing interfacial ordering. The [001] growth direction is toward the top of the image. From the image simulation, we can determine the ordered phases (see Ref. 4) and deduce precisely how the superlattice has grown in this region. Solid circles represent Si columns, open circles Ge columns, and shaded circles alloy columns. A convergence semiangle of 10.3 mrad, objective lens C_S of 1.3 mm, and defocus of -70 nm was assumed in the simulations.

TEM CHARACTERIZATION OF SILICON EPITAXIAL LAYER GROWN ON Si-TaSi2 EUTECTIC COMPOSITES

C.M.Sung, M.Levinson, M.Tabasky, K.Ostreicher and B.M.Ditchek
GTE Laboratories, 40 Sylvan Road, Waltham, MA 02254

Directionally solidified $Si/TaSi_2$ eutectic composites for the development of electronic devices (e.g. photodiodes and field-emission cathodes) were made using a Czochralski growth technique[1]. High quality epitaxial growth of silicon on the eutectic composite substrates requires a clean silicon substrate surface prior to the growth process. Hence a preepitaxial surface cleaning step is highly desirable. The purpose of this paper is to investigate the effect of surface cleaning methods on the epilayer/substrate interface and the characterization of silicon epilayers grown on $Si/TaSi_2$ substrates by TEM.

Wafers were cut normal to the <111> growth axis of the silicon matrix from an approximately 1 cm diameter $Si/TaSi_2$ composite boule. Four pre-treatments were employed to remove native oxide and other contaminants[2]: 1) No treatment, 2) HF only; 3) HCl only; and 4) both HF and HCl. The cross-sectional specimens for TEM study were prepared by cutting the bulk sample into sheets perpendicular to the $TaSi_2$ fiber axes. The material was then prepared in the usual manner to produce samples having a thickness of 10 μm. The final step was ion milling in Ar^+ until breakthrough occurred. The TEM samples were then analyzed at 120 keV using the Philips EM400T.

The epitaxial layer grown without chemical pretreatments showed a separation of epilayer films from the substrate or a discrete epi/substrate interface. The discrete interface of the epitaxial layer might be composed of impurities along the interface. The remaining samples pre-treated by methods 2-4 generally revealed featureless interfaces between epilayers and $Si/TaSi_2$ substrates (Fig.1). In general, several $TaSi_2$ fibers are dark in contrast and run normal to the surface. Measurements shows the fibers to be 3.3 μm from the surface, in good agreement with the expected epilayer thickness of 2.6 μm plus the 0.5 μm etch-back of the fibers. EDXS and CBED techniques were employed to confirm these fibers as $TaSi_2$ in terms of crystal structure and chemistry (Fig.2). The measurement of Ta:Si peak ratio in the $TaSi_2$ phase was difficult due to peak overlaps between Si K_α and Ta M_α. Thus, the determination of accurate lattice parameters by electron diffraction proved to be the best way to understand the stoichiometry of the phase[3]. CBED patterns from the $TaSi_2$ phase showed a stoichiometric structure of $TaSi_2$ which is hexagonal (a=0.4784 nm, c=0.6570 nm and space group $P6_222$). It was not easy to observe the detailed microstructure of the $TaSi_2$ phase due to preferential thinning of the silicon matrix leaving $TaSi_2$ phases which were considerably thicker. In the sample which had been pretreated with HF a pore was observed at the end of the fiber and associated with a dislocation, Fig. 3. The common plane in $Si/TaSi_2$ eutectic composites was found to be $(0001)_{TaSi2}$ parallel to $(\bar{1}11)_{Si}$. The interfacial study between these two phases is being done using HRTEM. So far there is no evidence for interfacial phases between the silicon matrix and the $TaSi_2$ rods on an atomic scale[4]. No microstructural features aside from bend contours are visible in the silicon matrix. Diffraction contrast images were obtained within a certain range of specimen tilt and correspond roughly to the expected epilayer-substrate interface. Few dislocations and stacking faults were seen propagating from the Si substrate around the $TaSi_2$ fibers into the Si epilayer (Fig.4). The source of this dislocation around the tip of the fiber is not known at this time.

The characterization of strains present in the Si epitaxial layer was also of interest. The measurements of local strains were carried out by using HOLZ line analysis[5]. The accurate measurements of local strains for the Si epilayers and $Si/TaSi_2$ matrix was carried out by fitting computer-simulated patterns to experimental patterns[6]. HOLZ line patterns of the [111] zone axis were obtained from both the silicon matrix and silicon epilayer shown in Fig. 5. No detectable changes of symmetry or lattice parameter changes were obtained within experimental limit.There seems to be negligible strains associated with the silicon epilayers as the result of high quality processing or strain relaxation to the specimen surface.

In summary, these results show that it is possible to grow good quality silicon epilayers on $Si/TaSi_2$ eutectic composite substrate. In most cases, the $TaSi_2$ fibers produce no structural defects in the epilayer, with only a few cases documented where the dislocations reached the epilayer surface. It should be possible to reduce the density of dislocations in the composite substrate which propagate into the epilayers through improved

techniques for both epilayer growth. Nevertheless, the epilayers obtained and observed here are already of nearly sufficient quality for device fabrication.

References

1. B.M.Ditchek and M.Levinson, Appl. Phys. Lett. **49**, 1956 (1986)
2. M.Levinson et al., to be published in Appl. Phys. Lett.
3. C.Sung, to be published.
4. C.Sung et al., to be published.
5. P.J.Jones, G.M.Rackham, and J.W.Steeds, Proc.R.Soc. London Ser.**A354**, 197 (1977).
6. C.Sung and D.B.Williams, Proceedings of Electron Microscopy Society of America, G.W.Bailey ed., San Francisco Press, p384, (1987)
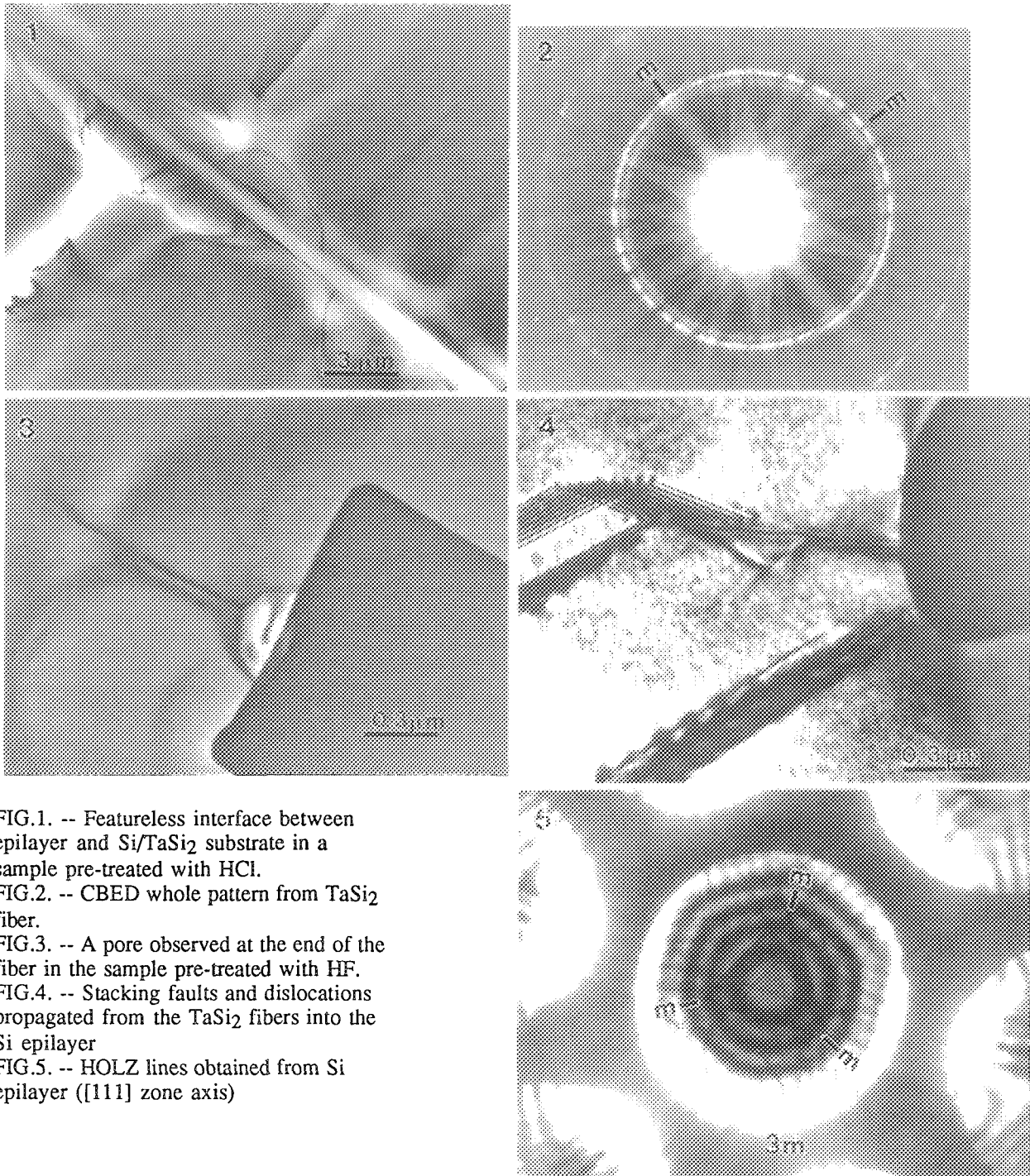
FIG.1. -- Featureless interface between epilayer and Si/TaSi$_2$ substrate in a sample pre-treated with HCl.
FIG.2. -- CBED whole pattern from TaSi$_2$ fiber.
FIG.3. -- A pore observed at the end of the fiber in the sample pre-treated with HF.
FIG.4. -- Stacking faults and dislocations propagated from the TaSi$_2$ fibers into the Si epilayer
FIG.5. -- HOLZ lines obtained from Si epilayer ([111] zone axis)

CHARACTERIZATION OF PLASMA-ASSISTED CVD MULTILAYERS/HETEROSTRUCTURES

M.G. Burke, R.M. Young, C.B. Freidhoff, W.D. Partlow and H. Buhay

Westinghouse Science & Technology Center, Pittsburgh, PA 15235

Amorphous refractory materials can be used in a number of optoelectronic applications when fabricated in multilayer structures. When the layers are deposited with very small thicknesses, heterostructures are produced. Such structures have an adjustable optical bandgap because the wavelength of light is much larger than the distance over which the composition of the film varies (layer to layer). Thicker multilayer structures can be fabricated on metallized, high thermal conductivity substrates. The purpose of the structure is to both protect and modify the substrate's properties. Two types of plasma-assisted chemical vapor deposition (PACVD) techniques have been employed to produce these structures.

In the first deposition technique, remote plasma chemical vapor deposition (RPCVD), the plasma is physically distant from the substrate and the reactant gases which are silane and methane for SiC. Charged species are isolated from the reaction, with only activated neutral species participating in the CVD deposition process. High energy electrons are kept away from the reactants, reducing gas polymerization, and ion damage to the substrate and growing film is eliminated.[1] Several SiC-Si heterostructures were produced using RPCVD. The second set of coarser multilayers have been produced using plasma enhanced chemical vapor deposition (PECVD). In PECVD, the substrate is directly immersed in the plasma, exposing the surface to all of the ionic, radical and neutral species present. We have examined an early sample of a chrome-bonded, aluminized, silicon wafer with silicon oxide and silicon nitride layer pairs deposited on the metal. The layers were deposited using typical gases and conditions for PECVD processes. These include silane, nitrous oxide and ammonia as the precursor gases and a capacitively-coupled, rf plasma discharge.

Cross-sectional specimens were prepared for AEM characterization by mechanically thinning to 100 microns, dimpling to 25 microns, and Ar ion-milling. Electron transparent specimens were examined in a Philips EM400T analytical electron microscope equipped with a Link Analytical LZ5 windowless energy dispersive x-ray spectrometer (EDS) system and an AN10/85S analyzer.

Amorphous SiC-Si Heterostructures-- Two types of specimens were examined: one in which abrupt transitions between the Si and SiC layers were created by halting the CH_4 flow in a square wave manner, and another sample for which the CH_4 flow was regulated by a sin wave. Distinct layers were produced in the first type of sample whereas graded layer transitions were observed for the second set of samples. Representative cross-sectional TEM micrographs of each type of specimen are shown in Figs. 1 and 2. No evidence of crystallinity was obtained from electron diffraction analysis of the layers. Qualitative EDS microanalysis of each layer confirmed the identification of each phase. In each specimen, the first deposited layer adjacent to the [100] Si substrate is amorphous Si. The light bands correspond to the amorphous SiC phase.

SiO_2-Si_3N_4 Multilayers-- Several layers were identified in the cross-sectional samples. These included a thin (18.5 nm) film of Cr, a polycrystalline Al layer 0.18 microns in thickness, and four layer pairs of SiO_2/Si_3N_4. A typical cross-sectional microstructure is shown in Fig. 3. EDS microanalysis revealed that the dark bands were SiO_2 whereas the light, mottled bands were Si_3N_4, Fig. 4. Electron diffraction of the SiO_2 and Si_3N_4 layers confirmed that they were amorphous. Slight perturbations were observed in some regions of the layers. Detailed examination of these regions indicated that these local irregularities were related to polycrystalline grains in the Al layer (local curvature of the grains due to surface effects).

References
1. R.M. Young and W.D. Partlow, Plasma Chemistry and Plasma Processing, in press.
2. The authors thank R.T. Blackham for technical assistance. This work was supported in part by the Air Force Office of Scientific Research and the Naval Weapons Center, China Lake, CA.
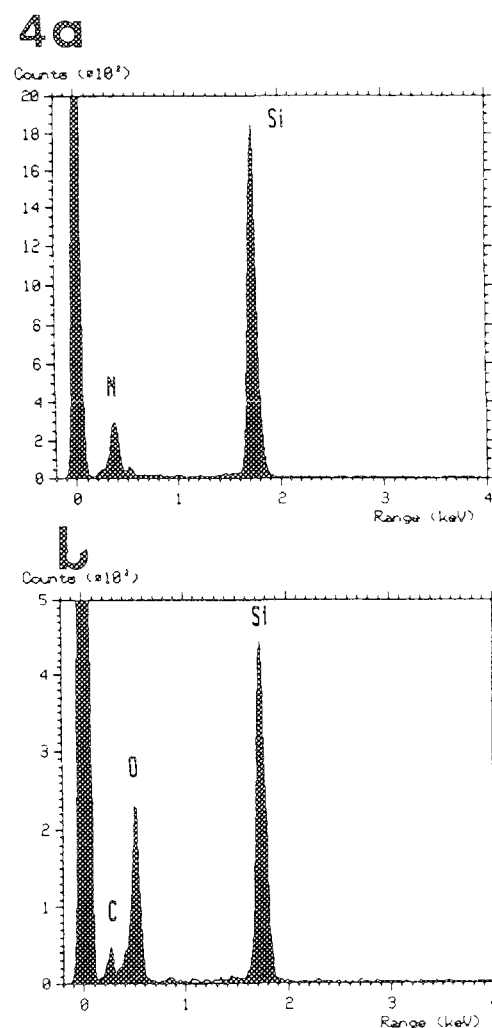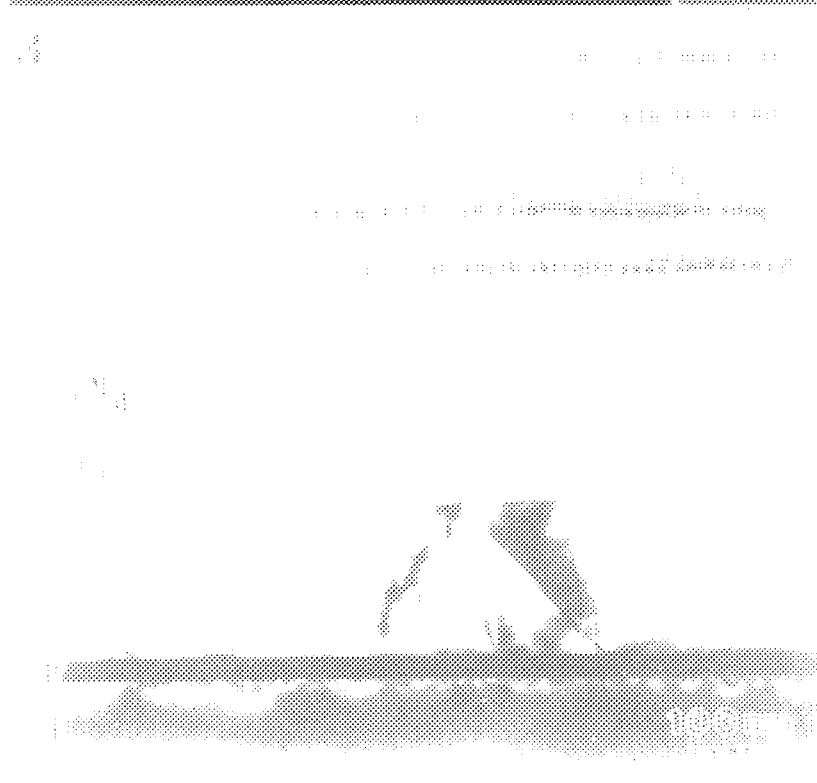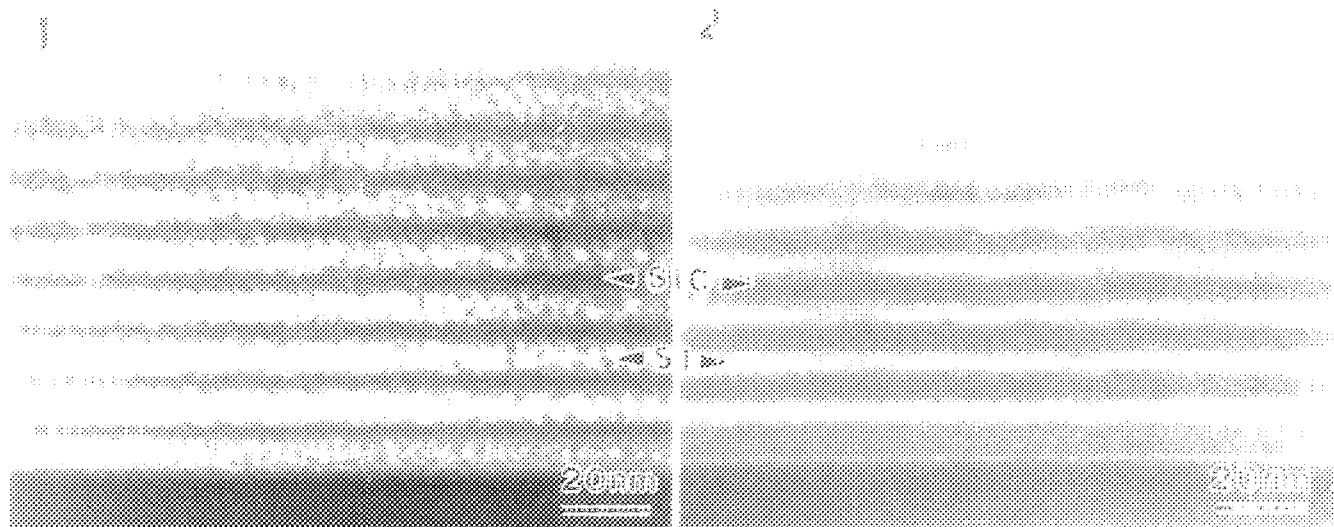
FIG. 1.--TEM micrograph of RPCVD Si/SiC heterostructure produced using square wave CH_4 flow.
FIG. 2.--TEM micrograph of RPCVD Si/SiC heterostructure grown with a sin wave CH_4 gas flow.
FIG. 3.--TEM micrograph of PECVD SiO_2/Si_3N_4 multilayer grown on Cr-bonded aluminized Si substrate. FIG. 4.--EDS spectra of (a) Si_3N_4 and (b) SiO_2 layers (C peak due to contamination).

TRANSMISSION ELECTRON MICROSCOPY APPLICATIONS IN INTEGRATED CIRCUIT PROCESSING

Ki-Bum Kim, Ken Ritz, and Ivo Raaijmakers*

Philips R&D Center-Signetics Company, Sunnyvale, CA 94088-3409
* Present address - Novellus Systems Co., 3950 North First Street, San Jose, CA 94134

The present demand for higher integration density in IC processing with submicron design rules and the development of new materials require a routine application of highly sophisticated characterization techniques as regards both failure analysis and materials development. One such an example is the utilization of conventional and high resolution transmission electron microscopy (TEM) in an IC processing environment. In this paper, we summarize several examples of how TEM can support various IC development programs.

Formation of an Epitaxial Layer

Trends in modern IC processing require the formation of thin, high quality, epitaxial layers with abrupt, well-controlled dopant transition profiles. One of the key factors in achieving such an epitaxial layer is the maintenance of a clean surface during the deposition. Surface residues such as oxygen and carbon form SiO_2 and SiC particles during layer deposition and, thereby, lead to the formation of a poor quality epitaxial layer. In a conventional batch-type low pressure chemical vapor deposition process, the interfacial integrity is deteriorated as the temperature is lowered for deposition from the hydrogen pre-bake temperature of ~ 1000 to 1100 °C. While the recent development of a rapid thermal CVD process guarantees the formation of thin epilayer, it also resulted in the formation of SiC particles at the interface when the surface cleaning was poorly performed (Fig. 1a).

Heteroepitaxial Layer Formation

A continuing effort has been made to incorporate heteroepitaxial layer(s) in present device structures. Two of the most notable examples in Si-based IC's are $Si_{1-x}Ge_x$ and SiC. In forming these heteroepitaxial layers, the growth mode and the defect density of the layer should be carefully investigated since the lattice mismatch between an epitaxial layer and the Si substrate strongly affects the integrity of the layer. In Fig. 1b, $Si_{1-x}Ge_x$ layer formation from excimer laser beam melting of an as-deposited Ge layer and the surface region of the Si substrate is depicted. It will be shown that the evolution of microstructure strongly depending on the average concentration of Ge in the layer. An example of SiC layer formation is shown in Fig. 1c. The surface of a Si substrate was carbonized using C_2H_4 gas in a rapid thermal process. It will be shown that an epitaxial SiC layer forms around 1100 °C. The growth of this layer is self-limited with the final thickness depending upon reaction temperature.

Silicides and Diffusion Barriers

The formation of reliable and reproducible silicide layers is one of the important areas in IC processing. In particular, as the silicide layer is generally formed by chemical reaction between an as-deposited metallic element and the Si substrate, the reaction kinetics, evolution of microstructure, and resultant phase formation should be carefully investigated. In this paper, we shall consider the interfacial reaction between Ti/c-Si and Ti/a-Si as investigated by the cross-sectional TEM (Fig. 1d).
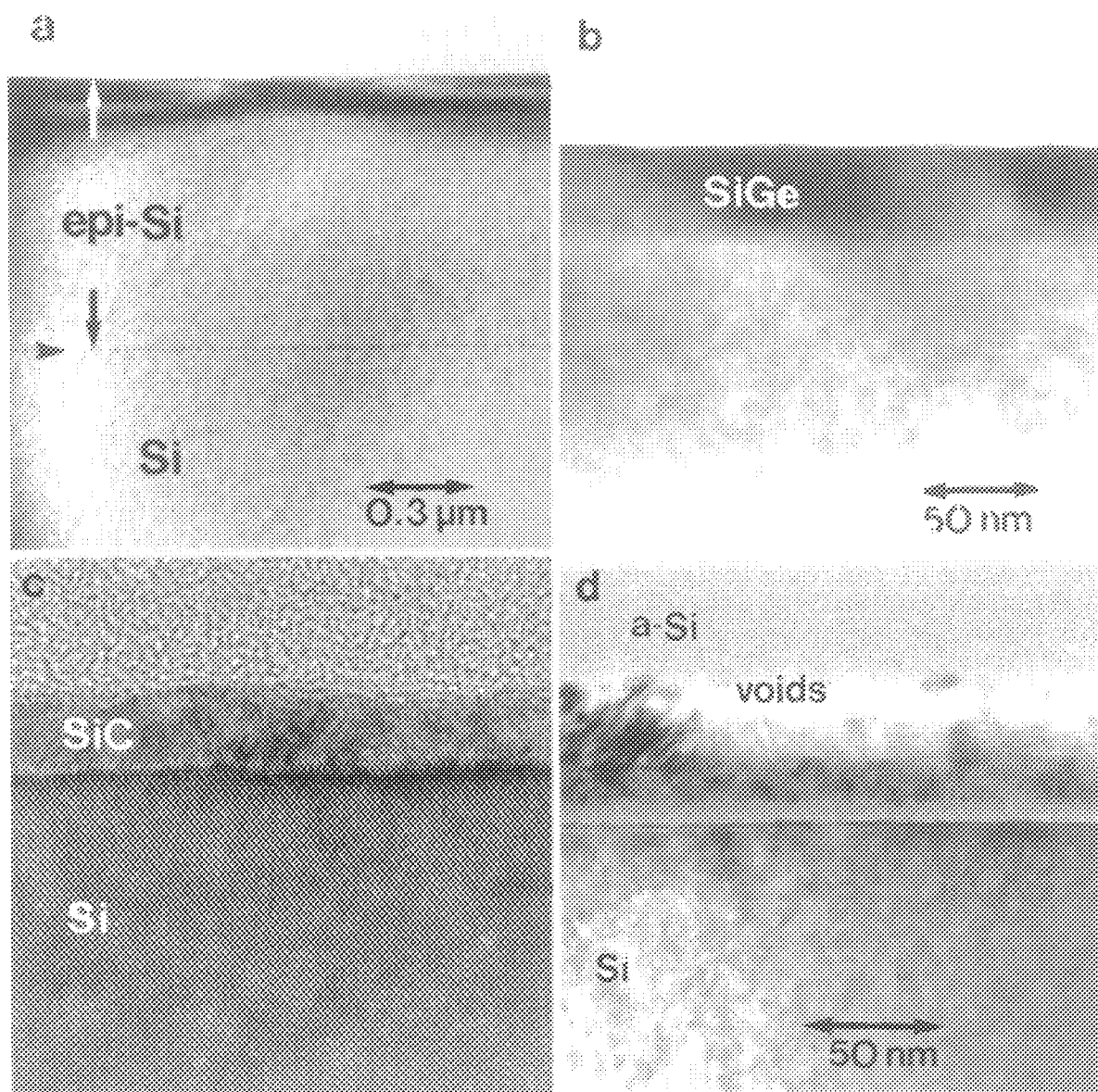
FIG. 1a.-- Cross-sectional TEM micrograph of sample deposited for 90 s at 1000 °C. Interface between substrate and epitaxial layer is deleneated by small SiC precipitates.

FIG. 1b.-- Cross-sectional TEM micrograph of $Si_{1-x}Ge_x$ (x=0.2) layer formed by excimer laser (wavelength 308 nm) process.

FIG. 1c.-- High resolution cross-sectional TEM micrograph of SiC layer formed by rapid thermal process at 1200 °C, 10 sec. C2H4 is used as reacting gas species.

FIG. 1d.-- Cross-sectional TEM micrograph of a-Si/Ti/c-Si sample annealed at 500 °C for 60 min.

A SIMS-TEM STUDY OF FLUORINE IMPLANTS AND ANNEALS INTO SILICON AND POLYSILICON

Vidya S. Kaushik*, Robert L. Hance*, Hsing-H. Tseng** and Philip J. Tobin**

* MOS Surface Analysis Laboratory; and ** Advanced Products Research and Development Laboratory; Motorola Inc., 3501 Ed Bluestein Blvd., Austin, TX 78721

The behavior of fluorine in silicon is important for VLSI applications. The presence of fluorine can lead to improved gate oxide interface reliability and to enhanced boron diffusion in BF_2 implanted devices.[1] We have therefore studied the diffusion behavior of fluorine in silicon and polysilicon using coupled SIMS and TEM investigations on samples implanted with fluorine alone.

Fluorine was implanted into a) (100) silicon and b) polysilicon layers to a dose of $1 \times 10^{16}/cm^2$ at 60 keV at room temperature. The polysilicon layers were grown by LPCVD at 635°C, resulting in small grained columnar polysilicon. The polysilicon layers had a 50 nm grown oxide layer between the polysilicon layer and the (100) silicon substrate. After the fluorine implants, the wafers were subjected to annealing at 750-950°C for 30 minutes. All the wafers were capped with a 13 nm silicon dioxide layer at the wafer surface prior to the ion implantation. SIMS analysis was performed on a Cameca IMS-3F spectrometer with 10 keV O_2^+ ions. XTEM images were obtained on a JEOL 2000 FXII operated at 200 keV with the electron beam parallel to the <110> silicon zone axis.

Figure 1a shows the XTEM image obtained from the as-implanted single-crystal silicon substrate (c-Si), with an overlay of the corresponding SIMS profile. The transition (I) between the region amorphized by the fluorine implant (196 nm deep) and the crystalline substrate is fairly abrupt with nanometer scale roughness. Immediately below this interface, a damaged region was seen in the silicon, probably consisting of clusters of point defects. From the SIMS profile, we estimate the fluorine concentration for complete amorphization of Si to be about $2 \times 10^{20}/cm^3$. Figure 1b is a micrograph of the sample after annealing at 850°C. The micrograph shows a band of defects in the substrate, located at about 20 nm below the amorphous-to-crystalline interface. This band of defects is formed by the annealing of the lightly damaged region below the amorphous region. Also in this micrograph, we see the presence of spherical inclusions (B) within the silicon. These inclusions are believed to be due to segregation of fluorine in the silicon in the form of bubbles. This is consistent with observations of chlorine and fluorine inclusions in the literature.[2,3] HREM images showed that these bubbles were spherical, and filled with amorphous material, with no evidence of strain in the surrounding silicon lattice. The amorphous material could be an artefact of the ion-milling. Correlation with the SIMS profiles shows that the fluorine in the silicon aggregates upon annealing: 1) at the band of defects; 2) at the amorphous-to-crystalline interface; 3) as bubbles near the profile maximum; and 4) at the wafer surface.

Figures 2a and 2b show the polysilicon layer with a fluorine implant before and after annealing at 950°C. Comparison with Figures 1a and b and with the SIMS profiles shows that in the case of polysilicon layers, the implanted fluorine migrates to the oxide layer surfaces below the polysilicon, and to the wafer surface. The fluorine at the profile maximum is drastically reduced during annealing, in contrast to the single-crystal silicon substrate, where it stays almost the same, in the amorphized region as well as in the substrate. These observations suggest that the residual fluorine in crystalline silicon exists as bubbles and that the diffusion of fluorine in polysilicon occurs along grain boundaries. This is confirmed by the observation that in large-grained polysilicon, a larger concentration of fluorine is retained within the polysilicon layer, than in the smaller-grained polysilicon layer. This study has shown that SIMS and TEM analyses can be synergistically coupled to yield important results.[4]

References

1. H-H. Tseng et al., submitted to VLSI Symposium, 1991.

2. C.W. Nieh and L.J. Chen, Applied Physics Letters, (1986) 48, 1528.
3. C.W. Nieh and L.J. Chen, Journal of Applied Physics, (1986) 60, 3114.
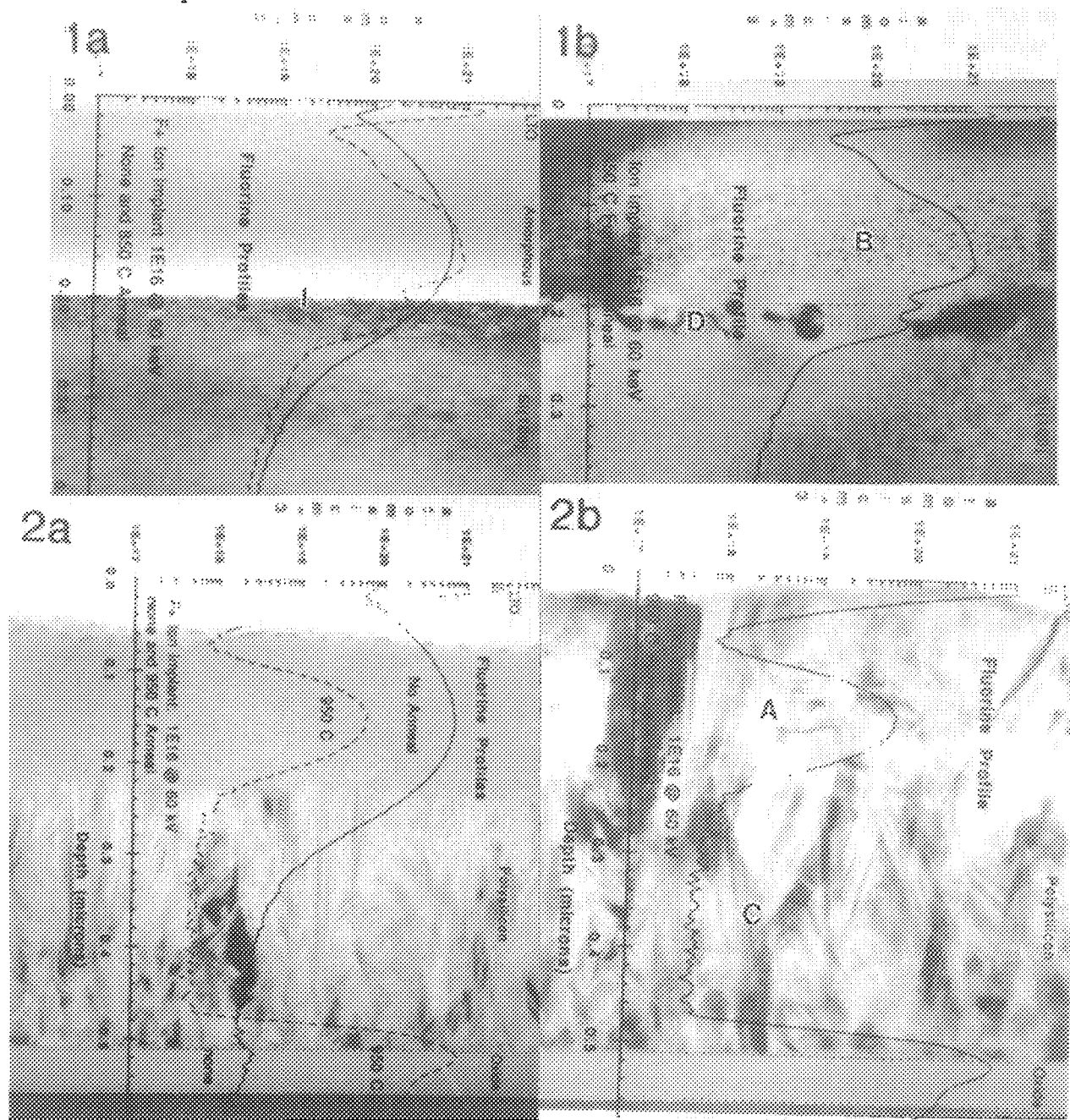
FIG. 1a. XTEM image of Si sample with F implant before anneal with SIMS profile overlay. Note abrupt interface (I) between amorphized region and substrate. Depth scale is in microns.

FIG. 1b. XTEM image of sample in Fig.1 after annealing at 850°C. Compare SIMS profile from 1a and note band of defects (D) and bubbles (B) at profile maximum. Depth scale is in microns.

FIG. 2a XTEM image of poly-Si with F implant before anneal with SIMS profile. Note oxide layer below poly to which F segregates after annealing.

FIG. 2b XTEM image of poly-Si sample of Fig.2a after anneal at 950°C. Note reduction of F concentration after anneal, and differing grain sizes (regions A and C) due to regrowth of amorphous layer.

NANOANALYSIS OF IMPURITY PRECIPITATION ON GRAIN BOUNDARIES IN POLYSILICON

M.J. Kim,* R.W. Carpenter,* D.K. Schroder** and J.H. Wohlgemuth***

*Center for Solid State Science, Arizona State University, Tempe, AZ 85287-1704
**Center for Solid State Electronics Research, Arizona State University, Tempe, AZ 85287-6206
***Solarex Corporation, Frederick, MD 21701

Polycrystalline silicon (polysilicon) has been the subject of extensive studies in recent years due to its wide applications in microelectronics and solar cells, see for example references.[1,2] In most cases of interest impurities segregated to the grain boundaries strongly modify the electronic properties of this material. Understanding the behavior of impurities in polysilicon requires a detailed knowledge of their distribution, phase and thermodynamical stability. In the present study, the structure and chemistry of grain boundaries in polysilicon were characterized by HREM and very high spatial resolution FEG/AEM.

The specimen materials are Solarex cast polysilicon used for solar cells, which are manufactured under a proprietary method called the ubiquitous crystallization process. The samples for TEM observations were cut from the ingot perpendicular to its growth direction and then thinned to electron transparency by mechanical polishing and ion milling. HREM was performed at 200kV in an ISI-002B. Microanalysis was done using a Philips 400ST/FEG microscope coupled to a Gatan parallel-detection electron energy loss spectrometer, at 100kV. A liquid nitrogen cooled specimen holder was used for nanoprobe experiments to minimize specimen contamination and local specimen heating.

The cast polysilicon materials examined were composed of large grains up to many centimeters in size and had lattice defects within the grains, such as stacking faults. Both grain boundaries and lattice defects were found to be electrically active by electron beam induced current (EBIC) experiments.[3] A TEM image of a typical grain boundary is shown in Fig. 1(a). Selected area diffraction experiment showed this to be a twin boundary on the {111} plane (Fig. 1(b)). The observed boundary is also associated with lattice defects and discrete second phase precipitates. Strains associated with them are clearly visible. However, a large portion of the boundary was free from visible defects. The typical appearance of the clean boundary is shown in Fig. 2(a). The boundary is coherent and has the glide mirror symmetry across the common {111} twin plane. Such twin related boundaries are frequently observed in vapor-deposited thin polysilicon film and their structures have been well studied.[4] A stacking fault was also observed very close to the boundary (Fig. 2(b)). It was found to be an extrinsic stacking fault bounded by $a/3<111>$ type Frank partial dislocations. The observed stacking fault was directly attached to the precipitate shown in Fig. 3. Considering the nature of the fault and its close connection to the precipitate, the fault seemed to be formed by the accumulation of Si interstitials produced by the impurity precipitation on the boundary. HREM and diffraction experiments showed that the precipitate was single phase and amorphous. It also appears to be faceted on the Si {111} planes. Nanospectroscopy indicated that the precipitate contained only silicon and oxygen (Fig. 4). Quantitative compositional analysis using core-shell-ionization edges in EELS spectra showed that the precipitate was substoichiometric oxide. A similar oxide precipitate was also observed on the $\Sigma=13$ [001] pure tilt grain boundary in Czochralski-grown Si bicrystal.[5] The above results and further discussion will be reported in detail.[6]

References

1. T. Kamins et al., eds., Mater. Res. Soc. Proc. **182** (1990).
2. H.J. Möller et al., eds., Polycrystalline Semiconductors, Berlin: Springer (1989).
3. M.P. Hanley, MS Thesis, Arizona State University (1991).
4. C. D'Anterroches and A. Bourret, Phil. Mag. (1984) **49**, 783.
5. M.J. Kim et al., Proc. 12th Int. Cong. Electron Microscopy (1990) **4**, 562.
6. This research was supported by grants from NSF-DMR-8901841 and Sandia National Labs., and performed at ASU HREM Facility supported by Arizona State University and NSF-DMR.
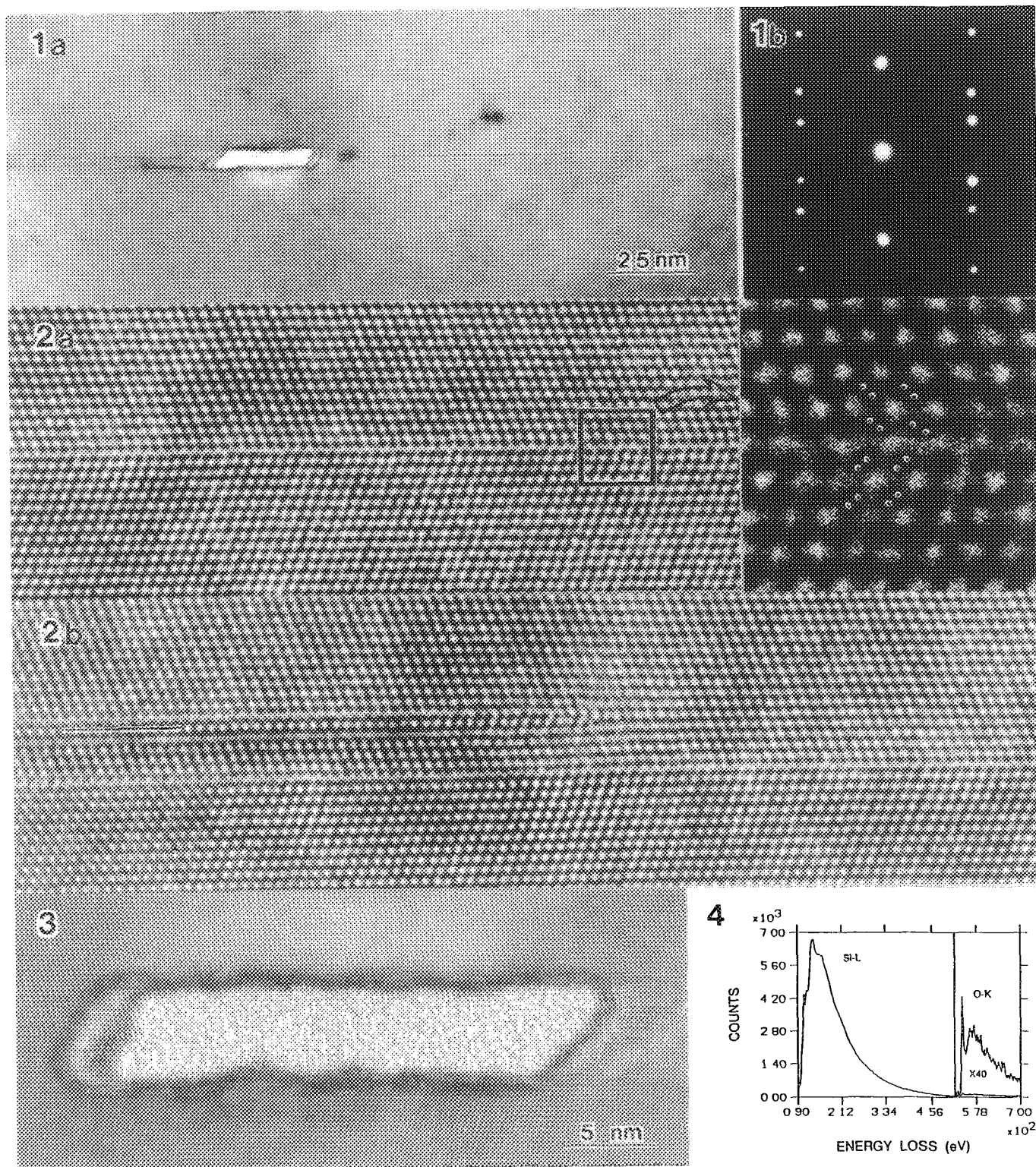
FIG. 1.--(a) TEM image of the grain boundary in Solarex cast polysilicon, and (b) SAD pattern showing the twin relationship of the boundary.

FIG. 2.--HREM images of (a) the boundary which is not associated with impurity precipitates, and (b) the stacking fault observed close to the boundary. The stacking fault was extrinsic type bounded by Frank partials.

FIG. 3.--HREM image of the precipitate on the boundary. The stacking fault shown in Fig. 2(b) was attached to this precipitate.

FIG. 4.--EELS spectrum taken from the precipitate shown in Fig. 3, showing the existence of oxygen in the precipitate.

484

HEXAGONAL PHASE IN TENSILE LPCVD POLY-Si FILM

Tai D. Nguyen

Center for X-ray Optics and National Center for Electron Microscopy, Lawrence Berkeley Laboratory, and Department of Materials Science and Mineral Enginering, University of California, Berkeley, CA. 94720

Polycrystalline silicon (poly-Si) films have found many applications in integrated circuits,[1] and in actuators and sensors.[2] Important considerations in the processing of these devices are structural stability and repeatable mechanical properties of the films. The texture and stress state of the films depend strongly on the microstructures and morphology of the films. Tensile films, which are preferred to compressive films in devices whose lateral dimensions of clamped structures are not to be restricted by compressive buckling,[3] are characterized by equiaxial grain morphology, while compressive films are characterized by columnar grain growth during deposition.[4]

A diamond hexagonal (d.h.) Si structure with lattice parameters of a = 3.8Å and c = 6.28Å was first reported in 1963.[5] More recently, transformation from the diamond cubic (d.c.) Si to the hexagonal phase has been observed in Si under hydrostatic pressure at temperatures between 350 C and 700 C,[6,7] in heavily ion-implanted silicon,[8] and in as-grown, implanted, and annealed CVD Si thin films,[9] in addition to the known high pressure Si phases. Pseudopotential calculation showed that the d.h. Si is not a thermodynamically stable phase, and that the structural energy of the d.c. Si is only slightly lower than that of the d.h. Si under atmospheric pressure.[10] The experimental reports seemed to indicate that the transformation resulted from a stress-induced mechanism. It has been shown that the transformation is related to stress relief when twins in f.c.c. or d.c. materials intersect,[11] and that the d.c. to d.h. transformation may be induced by uniaxial compressive and/or tensile stresses.[8] We have, however, observed the d.h. phase in as-grown LPCVD tensile poly-Si films. In this paper, we report the microstructures of, and the presence of the d.h. phase, determined from the extra rings in the cross-sectional electron diffraction pattern, in LPCVD silicon films.

The deposition, and the structural, texture, and stress properties, of the poly-Si films have been reported elsewhere.[5,12] Undoped poly-Si films of thickness 0.5 to 3.5 μm were prepared from pure silane in a front-injection LPCVD reactor. The film in this study is from a zone transition prepared at temperature near 620 C, in which the wafers closest to the has inlet were tensile with equiaxial grains and the last wafers were compressive with columnar grains. Samples for cross-sectional TEM were prepared by mechanical thinning and ion milling in a cold stage,[13] and were examined in a Philips EM 301 operating at 100 kV, or in a JEOL JEM 200CX operating at 200 kV.

Figure 1 is a HRTEM bright-field image of the film, which shows the Si substrate, the 0.1 μm thick silicon oxide layer, and the tensile poly-Si film. LPCVD Si films grown near crystallization temperature initially form an amorphous solid that subsequently crystallizes during the deposition,[14-15] resulting in the equiaxial grains Amorphous LPCVD silicon films are known to have compressive stress.[16] The transformation from the amorphous state to the crystalline state during deposition results in a volume contraction and hence induces the tensile state in the film. Twins and faulted regions have been observed in the films and at the Si / oxide interface. Figure 2 shows a grain which nucleated near or at the interface. Twin planes are as indicated (T) in the figure. The narrow strip of atomic planes between the arrows has structure different from that of the surrounding [110] silicon, and shows a stacking sequence ABAB... similar to that of hexagonal structure, although first-order twin of the d.c. lattice resulting from shear stress can also results in the same stacking, and formation of twins are more energetically favorable than transformation to the hexagonal phase.[8] It is possible that the twins cross each other and produce a d.h. phase at the intersection, or a twin nucleates inside another twin to produce a long and narrow d.h. region,[7] in such a highly faulted material. However, a larger area of these planes observed is needed for confirmation of it being the d.h phase, since a few or isolated planes as such can be of faulted d.c. structure.[17]

The presence of the hexagonal phase in the LPCVD tensile poly-Si film is determined from the extra rings in the electron diffraction pattern taken from a large cross-sectional area. The dominant d.c. Si rings, and the extra rings corresponding to the d.h. phase are shown in the figure 3. The most visible hexagonal rings are about the $\{111\}_{dc}$ ring, denoted by $\{111^+\}$ and $\{111^-\}$, similar to peaks in x-ray diffraction and rings in electron diffraction patterns reported,[9] and near the $\{311\}_{d.c.}$ ring, or $\{311^+\}$. Rings around $\{331\}_{d.c.}$, however, were not seen probably because of the low intensity of the rings. The inset on the left shows an enlarged section of the $\{111\}_{d.c.}$ ring showing the $\{111^+\}$ and $\{111^-\}$ rings. Measurements from the $\{111^-\}$ ring, or correspondingly $\{100\}_{d.h.}$, and other hexagonal rings yield the values for a and c close to those reported within a few percent. The mechanism for the presence of the d.h. phase in LPCVD tensile Si films, however, is still not understood. It could be one of the mentioned transformation mechanisms from the d.c. structure, or it could nucleate from the amorphous state during deposition. Further studies are needed to understand fully this phenomenom.[18]

1. T.I. Kamins, Polycrystalline Silicon for Integrated Circuits Applications, Kluwer Academic Publishers, Boston (1988). 2. R T Howe, J. Vac. Sci. Tech. B, 6 (1988) 1809. 3. H. Guckel et al., Sensors and Actuators, A21-A23 (1990) 346. 4. P. Krulevitch et al, in Mat. Res. Soc. Symp. Proc. Vol. 202 (1991). 5. R.H. Wentorf and J.S. Kasper, Science, N.Y. 139 (1963) 338 6 V.G Eremenko and V.I. Nikitenko, Phys. Stat. Sol (a) 14 (1972) 317. 7. P. Pirouz et al., Acta Metall. Mater. Vol. 38, No. 2 (1990) 313. 8. T Y Tan, H. Foll, and S.M. Hu, Phil. Mag. A, Vol 44, No. 1 (1981) 127. 9. M. Hendriks et al., Thin Solid Films 113 (1984) 59. 10. M.T. Yin and M.L. Cohen, Phys. Rev. Lett. 45, No. 12 (1980) 1004. 11. U. Dahmen et al., Acta Metall. Mater. Vol. 38, No 2 (1990) 323. 12. J. Huang et al., in Mat. Res. Soc. Symp. Proc. Vol. 182 (1990). 13. T.D. Nguyen et al., accepted to J. Elect. Microsc. Tech. (1991). 14. J. Bloem and A.M. Beers, Thin Solid Films 124 (1985) 93. 15. H. Guckel et al., Digest of Tech. Papers, Transducers (1987) 277. 16. R.T. Howe and R.S. Muller, J. Appl. Phys. 54 (1983) 4674. 17. K.H. Westmacott, private communication.
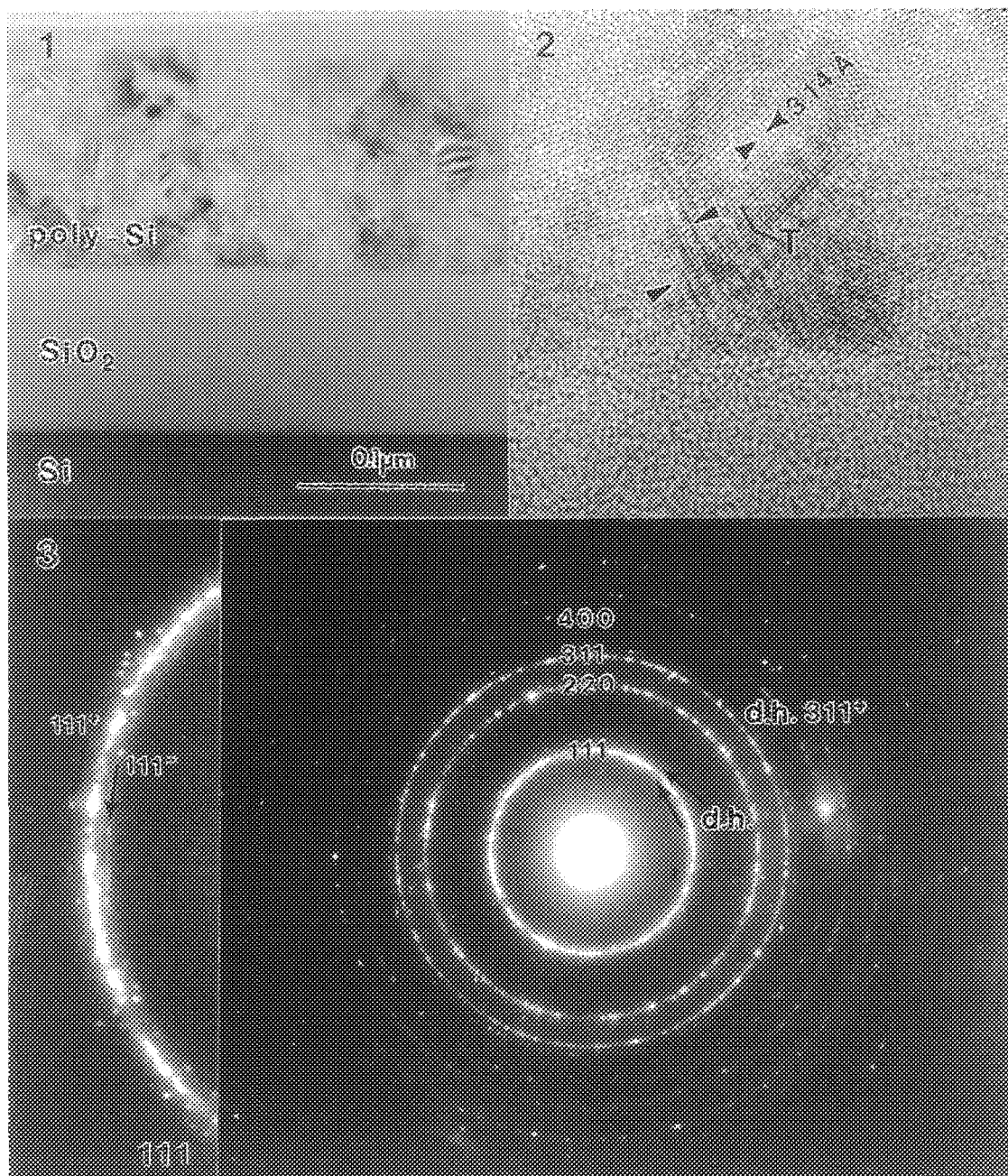
FIG. 1.--HRTEM bright field image of a as-grown LPCVD tensile poly-Si film.

FIG. 2.--Tensile poly-Si at the Si / oxide interface, showing twins and highly faulted region.

FIG. 3.--Electron diffraction pattern of cross-sectional sample, showing the d.c. Si and the extra rings corresponding to the d.h. phase. The inset on the left shows an enlarged section of the d.c. {111} ring with the extra d.h. rings.

Dislocations Induced by Heavy Boron Doping of Silicon

X. J. Ning and P. Pirouz

Department of Materials Science and Engineering, Case Western Reserve University, Cleveland, Ohio 44106

Diffusion-induced dislocations in silicon have long been of interest in semiconducting devices. Several investigations concerning the dislocations induced by doping of Si were carried out during the early sixties[1-3]. However, there are still a number of unresolved questions concerning this problem. Because the boron doped chemical etch-stop technique is widely used in the fabrication of microsensors, new interest has arisen in the role of dislocations induced by boron diffusion and the behavior of these dislocations on the mechanical properties of microsensors. The doping of Si in this technique is heavy ($>5 \times 10^{19} cm^{-3}$) and, consequently, the density of induced dislocations in the wafer is large. The dislocations will probably then play a critical role on the mechanical properties of thin Si wafers used in the etch-stop technique.

Silicon wafers of (001) orientation were diffused with boron at 1125°C for three hours in the presence of a gas of 98% nitrogen and 2% oxygen. A ~250 *nm* thick layer of borosilicate glass formed on the surface of the wafer during the boron diffusion. This glassy layer was removed before TEM specimen preparation and the thin foils were examined by a JEOL 200CX microscope.

Fig. 1 is a low magnification cross-sectional TEM micrograph along the [110] direction. No dislocations are present at depths larger than ~5 μm from the surface. In addition, a ~1.8 μm thick dislocation-free zone was found in the vicinity of the wafer surface. The dislocation density in the dislocated region of the surface was in the order of $10^9 cm^{-2}$. The Burgers vector of these dislocations were determined using the g·b criterion. They were found to be mostly 60° dislocations, although some screw dislocations were also present. The majority of the dislocations were dissociated and a large fraction of them had reacted to form different dislocation locks. For instance, the long dark lines parallel to the surface in Fig. 1 were found to be Hirth locks; these are composite dislocations resulting from the reaction of two dissociated 60° dislocation on two intersecting {111} planes. They consist of stacking faults on two intersecting {111} planes with a $\frac{1}{3}[001]$ edge dislocation along the line of intersection and two $\frac{1}{6}<11\bar{2}>$ 90° partial dislocations bounding the staking faults on each of the {111} planes. Fig.2 is a plan-view TEM micrograph with the electron beam parallel to the [001] direction. A large number of dislocation reactions can be observed. The arrows are dipoles formed, probably by the mechanism proposed by Tetelman[4], during the motion of dislocations from the surface to the lower parts of the wafer. Fig. 3 is a tilted cross-sectional micrograph with the foil surface normal to one of the intersecting {111} planes. Such micrographs allowed the observation of the maximum dissociation: in Fig. 3, the dissociation of dislocations and formation of extended nodes can be observed.

A numerical plot of the boron concentration in silicon according to the complementary error function is shown in Fig. 4. Here $D=2.55 \times 10^{-12} cm^2 sec^{-1}$ and the surface concentration $C_S=5 \times 10^{20} cm^{-3}$. Superimposed on this curve is the resolved shear stress due to boron diffusion in silicon according to the equation given by Prussin[2]. In most of the layer the resolved shear stress is much higher than the yield stress of Si at ~1100°C and thus a high density of dislocations are generated. Since the shear stress falls with depth, i.e. there is a stress gradient, a driving force exists on the dislocations which makes them glide on their {111} slip planes to the lower regions where the shear stresses are lower. Different interactions then take place during the glide of dislocations on different {111} planes.

References
1. H. J. Queisser, J. Appl. Phys. 32, 1776 (1961).
2. S. Prussin, J. Appl. Phys. 32, 1876 (1961).
3. J. Washburn, G. Thomas and H. J. Queisser, J. Appl. Phys. 35, 1909 (1964).
4. A. S. Tetelman Acta Met. 10, 813 (1962).
5. Thanks are due to X. Ding for providing the samples and to Dr. M. Mehregany for useful discussions.

surface ➤

1 μm

0.2 μm
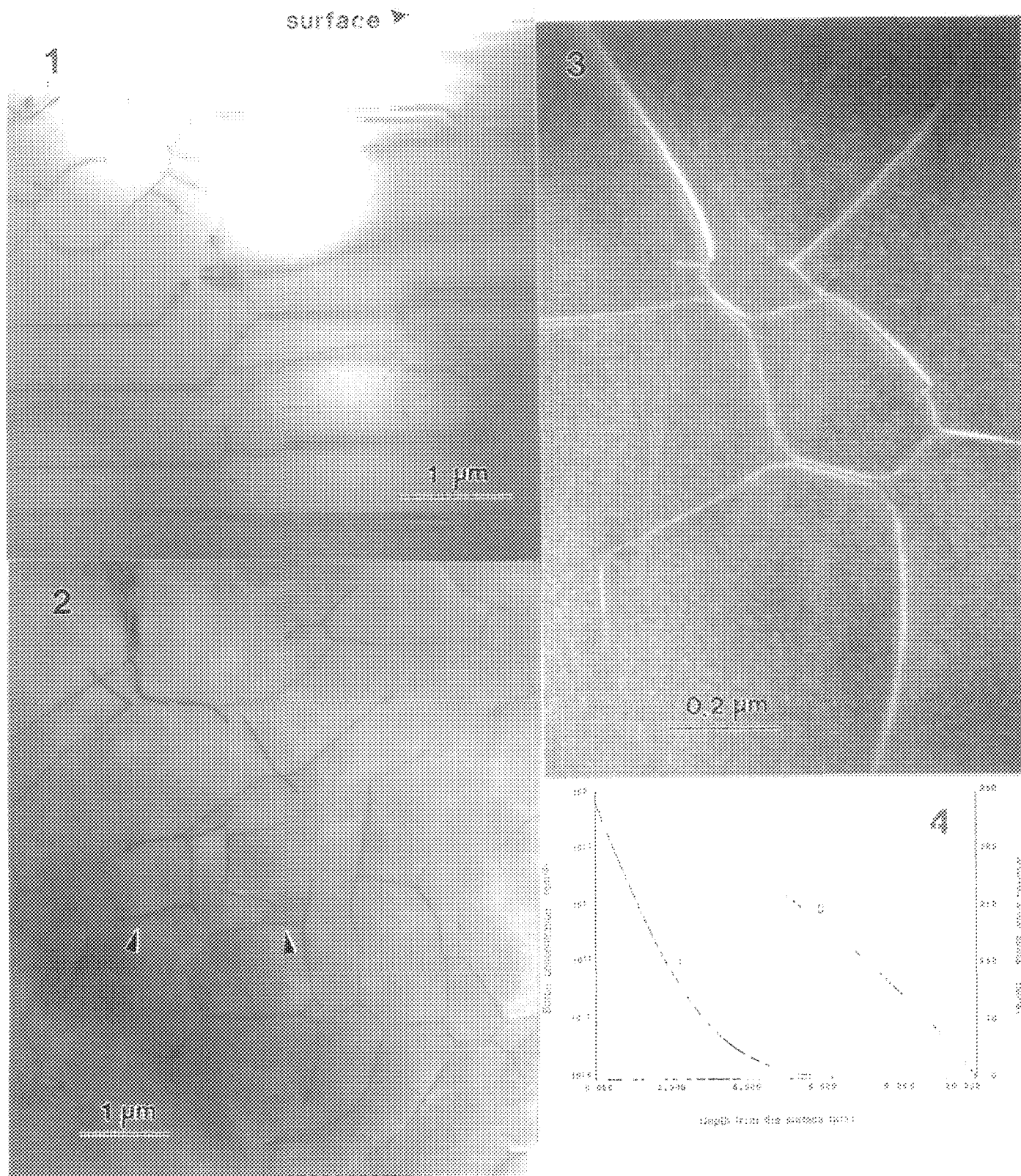
Fig. 1 XTEM micrograph of a heavily boron-doped Si layer. The dark lines parallel to the surface are Hirth locks.
Fig. 2 Plan-view TEM micrograph of the middle part of the boron-diffused layer; the arrows indicate dipoles.
Fig. 3 (111) cross-sectional weak-beam image of dissociated dislocations; note the extended node.
Fig. 4 B-diffusion profile calculated from the complementary error function, and the resolved shear stress vs. diffusion depth.

THE USE OF ELECTRON MICROSCOPY IN CHEMICAL VAPOR DEPOSITION OF TUNGSTEN FOR VLSI/ULSI APPLICATIONS

J.E.J. Schmitz

Genus, Inc. Thin Film Division, Mountain View, CA 94043

Chemical Vapor Deposition of tungsten (CVD-W) is becoming more popular for use as contact fill or interconnect material in high volume production of VLSI/ULSI circuits (see figure 1). The need for contact fill becomes necessary because sputter techniques exhibit certain problems like poor step coverage in deep and narrow contacts (figure 2). Poor step coverage may result in diminished reliability of the circuit. Tungsten technology has been shown to solve many of these problems. In the development of CVD-W technology, electron microscopy proved to be a unique tool contributing substantially to the development of CVD-W. This paper will give an overview of how electron microscopy can and is used in CVD-W IC metallization issues.

CVD-W: This technique uses a chemical reaction between WF_6 and either H_2 or SiH_4 to deposit metallic tungsten on the hot silicon wafer surface. Both chemistries can be used in two modes; blanket or selective tungsten deposition. In the selective mode tungsten is deposited only in certain areas of the wafer i.e. in the contact openings and not on the dielectric layers (see figure 1). In the case of blanket tungsten, tungsten is deposited on the entire exposed area and can be used to fill either contacts or, after patterning, as interconnect material.

Blanket-W: In figure 3 the process flow is shown for a blanket tungsten deposition process followed by etch back. The result is planarized contacts. Also, in place of the etch back step, the tungsten can be patterned and used as a wiring material. A complication of blanket CVD-W is that the adhesion to oxide is extremely poor. Therefore, an adhesion layer is necessary. Scanning electron microscopy (SEM) can be used to check the adhesion at sub-micron dimensions. Important issues of blanket tungsten are a) surface roughness, b) film thickness, c) grain size and d) step coverage. After etch back procedure it is important to know what the tungsten plug level will be related to the oxide surface and how much dimple formation occurred. In the case of dry etching, used to do the patterning of the tungsten film for interconnect, the degree of anisotropy of the etch needs to be evaluated. SEM is sometimes the only tool which allows an accurate evaluation of these issues.

Selective Tungsten: Selective tungsten has its own merits for contact fill when compared to the blanket approach. In this case the deposition chemistry has direct access to the silicon substrate (i.e. the bottom of the contact). Unfortunately, WF_6 reacts very rapidly with silicon under almost all conditions. The silicon encroachment can change the contact properties. Cross sectional TEM pictures can give clear evidence of the extent of the silicon consumption, the quality of the silicon-tungsten interface and other effects. SEM micrographs can give evidence of the degree of selectivity loss and the surface morphology of the tungsten. Electron diffraction techniques can give insight in the tungsten phases present in grains in contacts and other areas.

Other aspects: SEM micrographs can also be helpful to characterize particles, generated either by the deposition process or in the deposition equipment. SEM is also used in the inspection of de-processed samples in which failures occurred to find the failure mode or cause. Another technique often useful is EDAX to find "strange" elements on the wafer surface. From the above it is clear

that electron microscopy can and is extensively in use in IC metallization development. Examples of other analytical techniques such as SIMS and Auger will also be discussed.
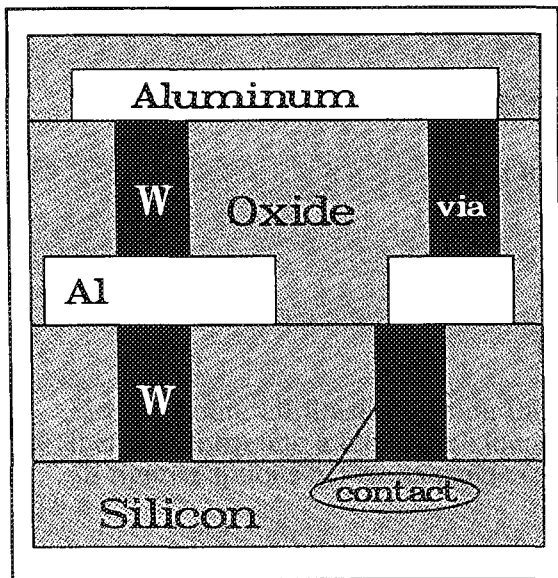
Figure 1. Cross section of a multi-level interconnect system. The contacts are filled with tungsten. The aluminum interconnect lines can be replaced by tungsten.
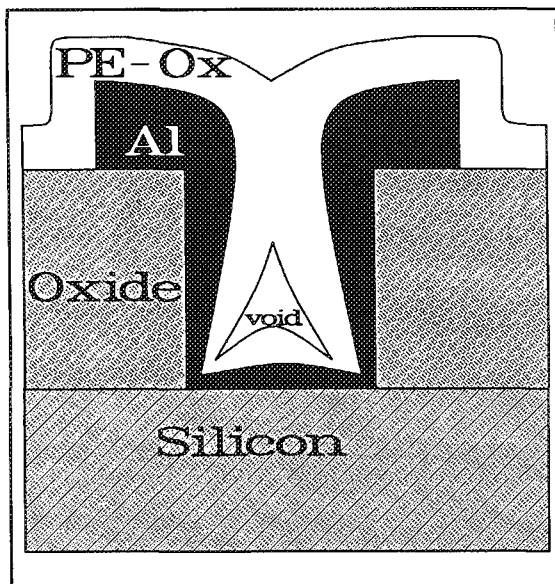
Figure 2. High aspect ratio contact filled with sputtered aluminum. Note the thinning of the aluminum at the side walls. This thinning is a reliability hazard.
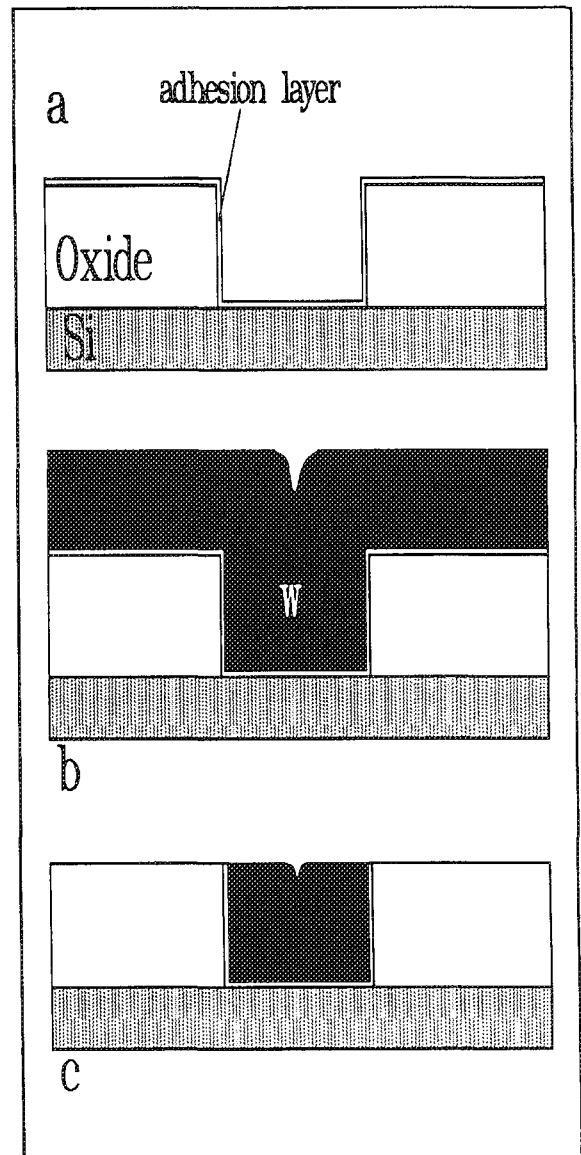
Figure 3. Three steps in the blanket tungsten contact fill process: a) deposition of the adhesion layer; b) after blanket tungsten deposition and c) after tungsten etch back.

TEM CHARACTERIZATION OF METALLIZATION SYSTEMS IN VLSI

A. Mitwalsky and H. Oppolzer

Siemens AG, Research Laboratories, Otto-Hahn-Ring 6, D-8000 Muenchen 83, F.R. Germany

Detailed knowledge of the properties of metallization systems used in silicon VLSI technolgy is essential to evaluate application and to achieve stable device operation. The progressively shrinking device dimensions require analytical techniques allowing to detect interfacial reactions or precipitation with nanometer resolution, particularly for the development of new processes. Transmission electron microscopy (TEM) of thin cross sections represents a powerful tool for obtaining such information directly. In addition to imaging analytical TEM allows phase and element identification with high spatial resolution.

The interaction during processing between silicides of various metals (Ti, Co, Ta and W) and different dopants (B, As) in silicon was investigated since possible metal dopant reactions may lead to dopant depletion in the silicon /1,2/. In the case of Ti and Ta silicide the formation of metal dopant compounds during heat treatment was indeed observed by scanning electron microscopy and TEM. Fig. 1a shows a TEM cross section of a $TiSi_2$ layer formed by silicidation. Boron was implanted in order to use the silicide simultaneously as contacting layer and diffusion source for dopants /3/. The resulting defect clusters are to be seen in the upper part of the $TiSi_2$ layer. After furnace annealing (950°C, 30 min) small precipitates are formed in the damaged region of the silicide in addition to larger crystallites at the $TiSi_2$/Si interface (Fig. 1b). One precipitate in the upper part of the silicide was imaged by high-resolution TEM (HRTEM; Fig. 1c). Moreover, selected area diffraction (SAD) was performed on a plan view sample (Figs. 1d,e). Both HRTEM and more conclusively SAD reveal the small precipitates to consist of TiB_2. For As implantation a similar precipitation behavior leading to the formation of TiAs was found /3/. As a result of the compound formation, the dopant concentration within the Si at the silicide/Si interface is reduced, as found by secondary ion mass spectroscopy (SIMS) leading to irreversibly increased contact resistances. The same effect was also found for preformed junctions after reflow annealing at 900°C used for planarization of doped SiO_2 /3/. ** $TiSi_2$ layers formed by silicidation exhibited an increased sheet resistance after reflow annealing. TEM cross sections of as-silicided samples show that initial thickness variations (Fig. 2a) and especially thin regions at grain boundaries result in breaking-up of the silicide layer after annealing at 900°C (Fig. 2b). Both enhancement of Ti layer tickness and in-situ backsputtering of the Si substrate prior to Ti deposition lead to a more uniform silicide thickness even on polycrystalline Si (Fig. 2c) /4/. On the other hand, the optimized contact between $TiSi_2$ and Si by in-situ backsputtering and the enhanced silicide thickness increase the dopant depletion in the Si adjacent to the silicide by the metal dopant compound formation described above. Therefore, the whole process sequence has to be optimized. ** Non-selective chemical vapor deposition (CVD) of W together with an etchback process allows void-free contact formation for sub-µm technology /5/. Investigations of the various interfaces showed that the only reaction occurred at the W/AlSiCu interface during annealing at 450°C (Fig. 3) /6/. The small (~ 30 nm) grains at the interface were identified by microdiffraction and X-ray micronanalysis (XMA) as hexagonal WSi_2. The consumption of Si atoms by this reaction leads to a Si depletion of the AlSiCu alloy, as found by SIMS. Nevertheless, sufficient electromigration resistance was observed for the Al interconnect /5/. ** Due to the fine vertical channel system (possible fast diffusion paths) within the TiN layer (Fig. 4) which is used together with a Ti layer as diffusion barrier between Al and Si, the barrier function is not obvious. During annealing at 450°C a solid state amorphization reaction occurs at the Ti/Si interface leading

to an interfacial layer with a composition close to TiSi as measured by XMA /7/. At about 500°C the formation of a ternary compound with a composition close to $Ti_5Si_3Al_{12}$ was found at the TiN/AlSi interface /8/.

References

/1/ V. Probst et al., J. Appl. Phys., May 1991, in press
/2/ V. Probst et al., J. Appl. Phys., May 1991, in press
/3/ A. Mitwalsky et al., Proc. 6th Internat. Symp. on Silicon Materials Science and
    Technology, Vol 90-7, 1990, 876-86
/4/ R. Burmester et al., Proc. of 19th European Solid State Device Research Conf.
    (ESSDERC), Berlin, Germany, 1989, 233-6
/5/ H. Körner et al., Proc. of Workshop on Tungsten and Other Advanced Metals for
    ULSI Applications, Dallas, Tx, 1990
/6/ A. Mitwalsky et al., Proc. of 3rd European Workshop on Refractory Metals and
    Silicides (RMS), Saltsjöbaden, Sweden, 1991
/7/ H. Oppolzer et al., Inst. Phys. Conf. Ser. No. 87: Sect. 6, 1987, 433
/8/ M. Mändl et al., J. Appl. Phys. 68 (5), 1990, 2127-32
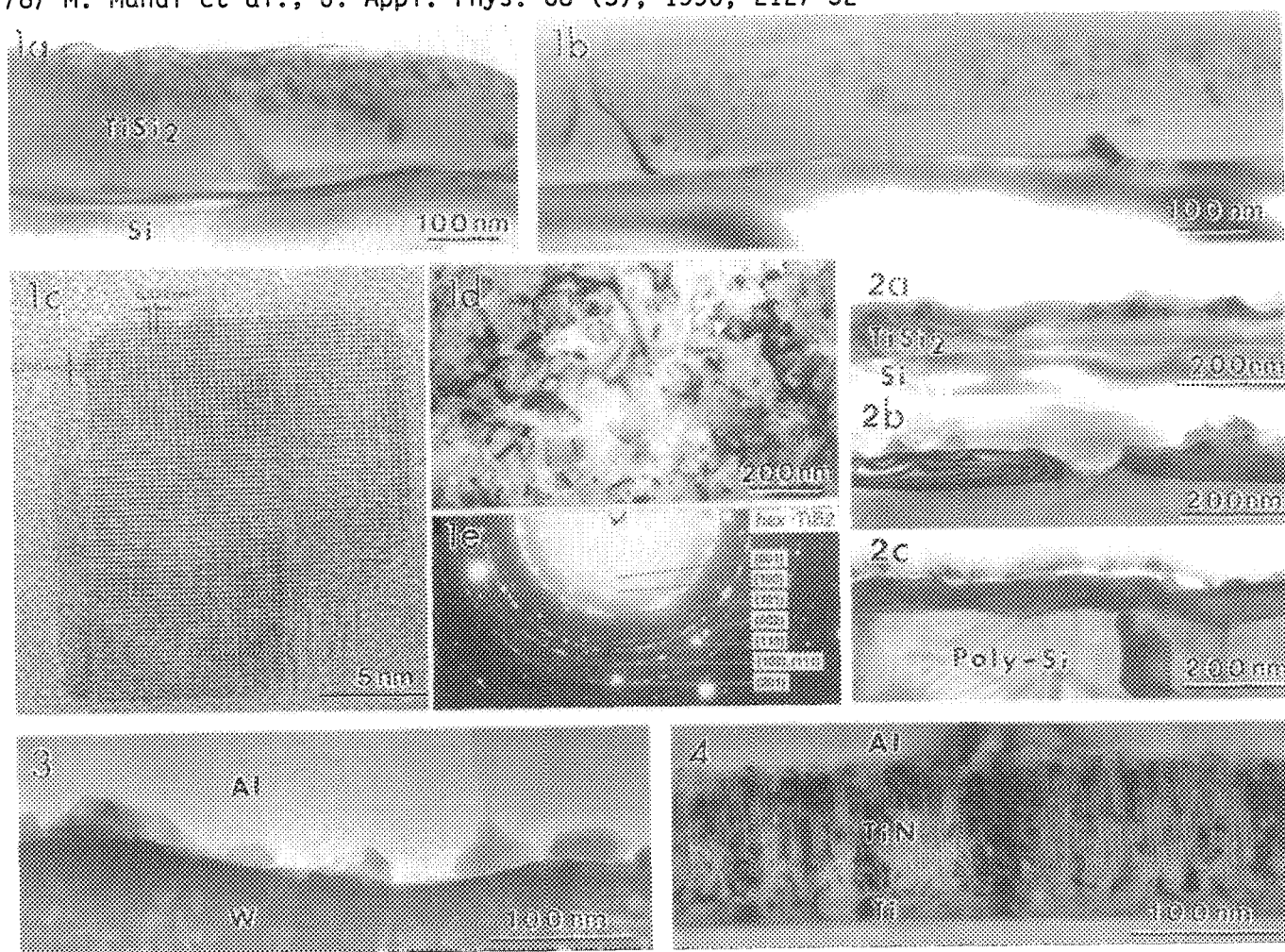
FIG. 1.--Boron implanted $TiSi_2$ (a) with additional annealing (950°C) (b). HRTEM of
        crystalline precipitate (c) and plan view of annealed sample (d) with
        corresponding SAD (e).
FIG. 2.--$TiSi_2$ as-silicided (a) with additional reflow annealing (900°C) (b). $TiSi_2$
        on polycrystalline Si with in-situ backsputtering before Ti deposition and
        reflow annealing (c).
FIG. 3.--Non-selective CVD of W with Al on top and reaction grains after annealing.
FIG. 4.--Ti/TiN diffusion barrier between Al metallization and Si substrate.

MICROSTRUCTURE OF Al-Cu THIN-FILM INTERCONNECT

J. H. Rose, J. R. Lloyd, A. Shepela, and N. Riel

Digital Equipment Corporation 30 Forbes Rd. NRO5/I1 Northboro, MA 01532

The precipitate structure of bulk aluminum alloys was heavily studied with x-ray diffraction commencing in the 1930s and via direct observation with the development of transmission electron microscopy (TEM) techniques in the 1950s.[1] In 1970, recognition of the electromigration performance benefits of Cu additions to Al interconnect in integrated circuit devices precipitated studies on Al-Cu thin films.[2] However, the microstructure of these films remains only partially known, in part due to the many process and interconnect geometry variables.[3-6] In particular, there has been minimal attempt to study films which mimic as closely as possible the environment and thermal history of real interconnect (prior studies typically have examined unpatterned or unpassivated films.) In the present work, Al-Cu films in standard life test devices have been studied. This work is directed at understanding the evolution of microstructure during device processing and life testing and application of this knowledge to a better understanding of the role of microstructure in electromigration in Al-Cu interconnect. The present contribution describes initial microstructural observations on a variety of annealed samples.

Al-1wt%Cu films were sputter deposited onto (100) silicon wafers at a substrate temperature of 450°C (wafers with .3μm of thermal oxide were employed.) Films were patterned to produce life test comb/serpentine structures (lines 1.3μm wide, 0.7μm thick) and lastly passivated with .4μm of oxide (deposited at 380°C for 2 min.) Wafers were divided into quarter sections for annealing. Samples were given single or two-step anneals (150°C/40hr; 150°C/40hr + 200°C/224hr; 280°C/6hr; 280°C/6hr + 200°C/200hr) to induce varying precipitate distributions. As a reference, an unpatterned though otherwise identical wafer was also given the last of these anneals (280°C/6hr + 200°C/200hr.) Samples were prepared for TEM observation by backside mechanical dimpling to a point near perforation followed by removal of the remaining silicon with a solution of 1HF:3HNO$_3$. A portion of each oxide layer was removed via low angle ion milling in a LN$_2$ cooled stage operating at 4kV. Samples were observed in a JEOL 2000FX operating at 200kV. Samples were examined primarily for θ and θ' precipitates, dislocations, and voids.

Microstructural observations for the different sample conditions are as follows;

As deposited - These films are of large grain size, typically several micrometers across (this consequence of a high deposition temperature is desirable for electromigration performance.) Some smaller individual grains or grain clusters are found where the interconnect patterning has by chance crossed small grains in the original film or the boundaries of two or more large grains. There are small θ precipitates (equilibrium CuAl$_2$) at grain boundary/sidewall (GB/SW) junctions and at GB triple junctions (TJ). In addition, there are a few, very small intragranular θ particles on the interconnect sidewalls. Some small voids are found at GB/SW junctions. Dislocation density is about 5.0x10^9/cm^2.

150°C/40hr - There are θ precipitates as above, though larger and of greater number along sidewalls. A few at GB/SW sites are elongated and typically lie at the top (though sometimes at the bottom) surface of the interconnect (Fig. 1a.) In addition, there are θ' platelets in grain interiors (Fig. 1b.) These metastable precipitates are 100nm to 200nm in length. There are relatively large voids along some GB/SW junctions (Fig. 1c.) Dislocation density is about 3.5x10^9/cm^2.

150°C/40hr + 200°C/224hr - θ precipitates have grown with many prominent along sidewalls. The intragranular θ' precipitates have grown and decreased in number. The voids remain. Dislocation density is about 2.0x10^9/cm^2.

280°C/6hr - Large θ precipitates are found, as above. There are a few voids seen at GB/SW junctions. There is a low density of dislocation loops with size range of 20nm to 70nm. Dislocation density is about 2.6x10^9/cm^2.

280°C/6hr + 200°C/200hr - θ particles here are largest and fewest in number. There are a few very elongated precipitates. Due to grain growth, few triple junctions are found after this annealing treatment. Voids remain at some GB/SW junctions. Dislocation density is about 0.9x10^9/cm^2.

Unpatterned, 280°C/6hr + 200°C/200hr - θ precipitates are at triple junctions and along grain boundaries with a

preference for some boundaries over others (likely high energy boundaries, Fig. 2.) Such observations are consist with previous studies. Dislocation density is less than $0.3 \times 10^9/cm^2$, lowest of all samples studied. Apparently, interconnect sidewalls (as in the other samples) tend to trap dislocations in a patterned film. About $2 \times 10^4/cm^3$ dislocation loops are found with size in the 25nm to 100nm range. In cross sectioned samples, some voids are found to lie at grain boundary/top surface junctions.

θ precipitate distributions in these samples are similar to those found in work on unpatterned, polycrystalline films.[4,6] A salient exception is the preferred nucleation of θ at interconnect sidewalls (most noticeable at low temperatures as found during life testing, processing, and device operation.) The GB/SW junction sites tend to produce the largest θ particles due to the adjacent GB acting as a collector plate for Cu atoms.[7] Other observations are novel to passivated interconnect. Trapped vacancy supersaturations have apparently been collected by GBs to form the rounded voids found in all samples (though stress voiding effects are also likely to contribute.) The dislocation loops in the blanket film are likely due to vacancy coalescence and suggest that the GB/SW junctions provide a better site for void formation than available in unpatterned films. A non-equilibrium vacancy concentration may also have aided the formation of the θ' precipitates. The rapid loss of vacancies at free surfaces in thin films has been suggested to suppress formation of GP zones and θ' precipitates.[3] Any effect of these prior existing voids on interconnect electromigration void formation remains to be investigated. The as-deposited films have a high dislocation content - these dislocations are slowly removed during annealing. At life testing and lower temperatures, they are of high enough density to provide a potentially significant diffusion path, feeding Cu to the grain boundaries, θ' precipitates, and θ precipitates at side walls.[8] Given the largely bamboo-like grain structure of this interconnect, dislocations may also contribute to the flux divergences leading to electromigration induced void formation. Clearly, there is dramatic microstructural evolution during life testing (typically performed at 200°C) and during real device operation. The microstructural nature of electromigration failure sites is the subject of continuing studies.

References

1. A. Kelly and R. B. Nicholson, *Progr. Mater. Sci.* 10(1963)149.
2. I. Ames, F. M. d'Heurle, and R. E. Horstmann, *IBM J. Res. Dev.* 14(1970)461.
3. S. Mader and S. Herd, *Thin Solid Films* 10(1972)377.
4. G. A. Walker and C. C. Goldsmith, *J. Appl. Phys.* 44(1973)2452.
5. B. N. Agarwala, L. Berenbaum, and P. Peressini, *J. Electron. Mater.* 3(1973)137.
6. D. R. Frear, et al., *Met. Trans.* 21A(1990)2449.
7. H. B. Aaron and H. I. Aaronson, *Acta Metall.* 16(1968)789.
8. R. W. Balluffi and J. M. Blakely, *Thin Solid Films* 25(1975)363.
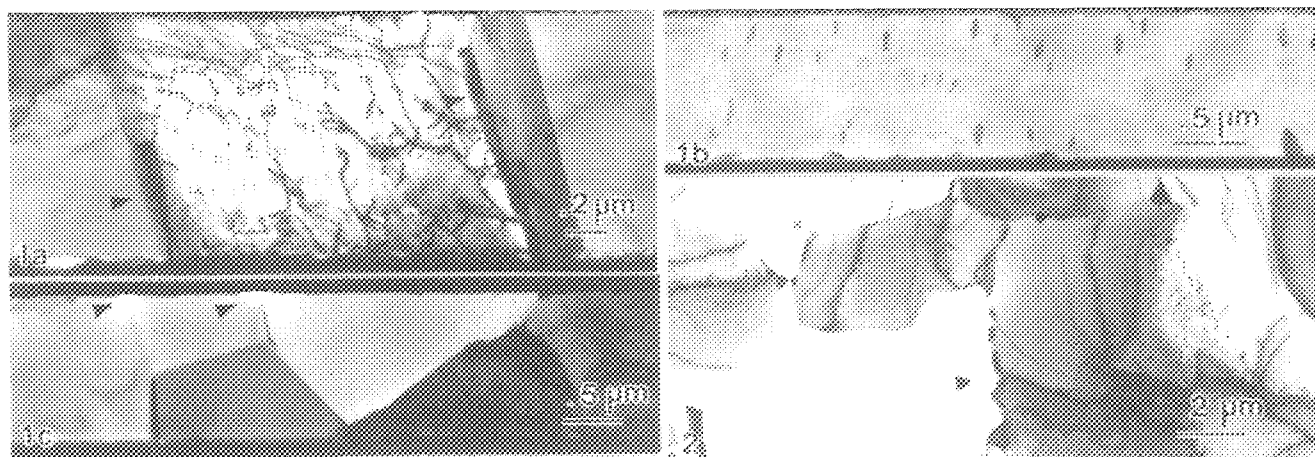
Fig. 1. Interconnect annealed at 150°C/40hr; a) intragranular dislocations and elongated grain boundary precipitates at top surface of the interconnect (arrowed), b) sample oriented so one set of θ' precipitates is in strong contrast, and c) two voids (arrowed.)

Fig. 2. Unpatterned film (annealed at 280°C/6hr + 200°C/200hr); note θ precipitates at triple junctions and clustered along some grain boundaries (arrowed.)

THE EFFECTS OF DEPOSITION AND ANNEALING CONDITION ON THE MICROSTRUCTURAL EVOLUTION OF Al-Cu AND Al-Cu-Si THIN FILMS

M. Park*, S. J. Krause* and S. R. Wilson**
*Department of Chemical, Bio and Materials Engineering, Arizona State University, Tempe, AZ 85287
**Advanced Technology Center, Motorola Inc., 2220 W. Broadway Rd. Mesa, AZ 85202

Aluminum alloys (Al-Cu and Al-Cu-Si) are the most extensively used metals for interconnects in integrated circuits. Cu additions enhance electro-thermal migration resistance[1], but may increase corrosion susceptibility in both reactive ion etching and wet processing due to the formation of Al_2Cu (θ) precipitates[2]. Si was originally added to minimize erosion in contact windows, however it was recently found that the addition of 1.5% or 0.5% Si in Al-Cu alloy improves its corrosion resistance[2]. θ precipitates in binary alloys have been found to occur at the Al/sublayer interface during high temperature (>200°C) deposition due to the fast surface diffusion of Cu[3,4]. For the higher temperature deposition in the Al solid solution region, platelike θ precipitates were also formed at the interface and grain boundaries during a fast cooldown of wafers[4,5]. However, it has not been well understood how the addition of Si in Al-Cu alters the thin film microstructure and increases the corrosion resistance. In this work, the effects of Si addition and deposition temperature on the film microstructure were studied for different alloy compositions and sublayers. The effects of thermal annealing on the interaction of Al films with Ti-W sublayer were also studied.

The alloys studied were; Al-1.5%Cu, Al-1.5%Cu-1.5%Si, Al-0.5%Cu and Al-0.5%Cu-0.5%Si. Al-1.5%Cu was sputter deposited at either 325°C or 465°C. All the other systems were deposited at either 305°C or 435°C. Deposition rate was 1.1μm/min. and wafers were not biased. Either a Ti-W or a SiO_2 film (0.15μm thick) was deposited on the substrate Si wafer prior to the alloys deposition. The as-deposited samples were annealed at 450°C for 30 min. Microstructure was studied with planar and cross-sectional transmission electron microscopy in a JEOL JEM 2000FX at 200keV and a Philips 400-FEG at 100keV. In-situ annealing experiments were performed on a Philips 400T equipped with a heating stage.

Higher deposition temperatures and lower Cu and/or Si additions increased average grain size. In the as-deposited Al-1.5%Cu film, coarse θ precipitates (Figure 1a) were found from the 325°C deposition, while thin platelike precipitates were found from the 465°C deposition. At the maximum concentration of alloy additions (1.5%Cu-1.5%Si), the Al_2Cu and Si particles coprecipitated during the 305°C deposition (Figure 2). The substrate affected the position of precipitate nucleation in 0.5%Cu-0.5%Si films deposited at 435°C. A Ti-W sublayer resulted in formation of Si precipitates at the film's free surface (Figure 3b) whereas a SiO_2 sublayer resulted in formation of columnar Si precipitates which extended from the sublayer interface to free surface (Figure 3a).

The in-situ annealing experiments (Figures 1a-1d) were performed to study precipitation processes of the θ phase in the Al-1.5%Cu alloy deposited at both 325°C and 465°C. During heating at 380°C for 1min, direct coarsening of the particle in the as-deposited sample (325°C) did not occur. Instead, the precipitates split apart and then coarsened (Figure 1b). Complete dissolution occurred at 450°C for 1 min. (Figure 1c). During a fast cooldown, the reprecipitation of the θ particle occurred at more energetically preferred sites (Figure 1d), that were different than the sites (Figure 1b) in the as-deposited sample. Therefore, it is believed that the coarse θ precipitate (Figure 1a) was grown by fast surface diffusion of Cu during deposition at 325°C and was in a metastable state. During in-situ annealing of Al-1.5%Cu deposited at 465°C, dissolution and reprecipitation of θ particles occurred at the same location. The location and size of the precipitates changed little from the as-deposited sample in agreement with the result of Frear et al.[5]. In 1.5%Cu-1.5%Si alloy, the reduction of interfacial energy by the coprecipitation of the particles (Figure 2) can decrease the activation free energy for nucleation. Also it may retard the growth of θ particles during deposition. For 435°C deposition, segregation of Si during deposition may suppress θ phase formation during a cooldown by depleting the preferred nucleation sites for θ phase. It was reported that the possible chemical reduction of SiO_2 by Al may cause the formation Al_2O_3/Si/Al interface which will make the Al/SiO_2 interface the more preferred site for Si to nucleate than the Al free surface[6] or Ti-W/Al interface. This would explain the columnar Si precipitation in 0.5%Cu-0.5%Si deposited at 435°C. The subsequent annealing at 450°C for 30 min. caused a reaction between Al-alloy and Ti-W layer. Localized interactions developed resulting in formation of some regions of $Al_{12}W$ (Figure 4a, 4b). Also localized segregation of W was observed at the grain boundaries in Al thin films (Figure 4a-4d).

Si additions would retard the growth of θ particle by coprecipitation (305°C) and segregation of Si (435°C). Hence overall increase in corrosion resistance can be achieved as previously reported by Weston et al.[2]. Further research will be performed to study the effects of Si and Cu on the precipitation of θ and Si particles and interactions between Al-alloys and Ti-W.

REFERENCES

1. F. M. D'Heurle, Met. Trans., 2A, (1971) 683.
2. D. Weston, S. R. Wilson and M. Kottke, J. Vac. Sci. Tech., A8(3), (1990) 2025.
3. M. Park, S. J. Krause and S. R. Wilson, XIIth ICEM Proc., 4, (1990) 972.
4. M. Park, S. J. Krause and S. R. Wilson, Mat. Res. Soc. Proc. Spring 1991, to be submitted.
5. D. R. Frear et al., Met. Trans., 21A, (1990) 2449.
6. C.-H. Tung et al., J. Appl. Phys., 68(4), (1990) 1592.
7. We acknowledge staff assistance and facility use in the National Center for HREM, Arizona State University, supported by NSF. We also acknowledge the support of this research by Motorola-University Partnership in Research Program.
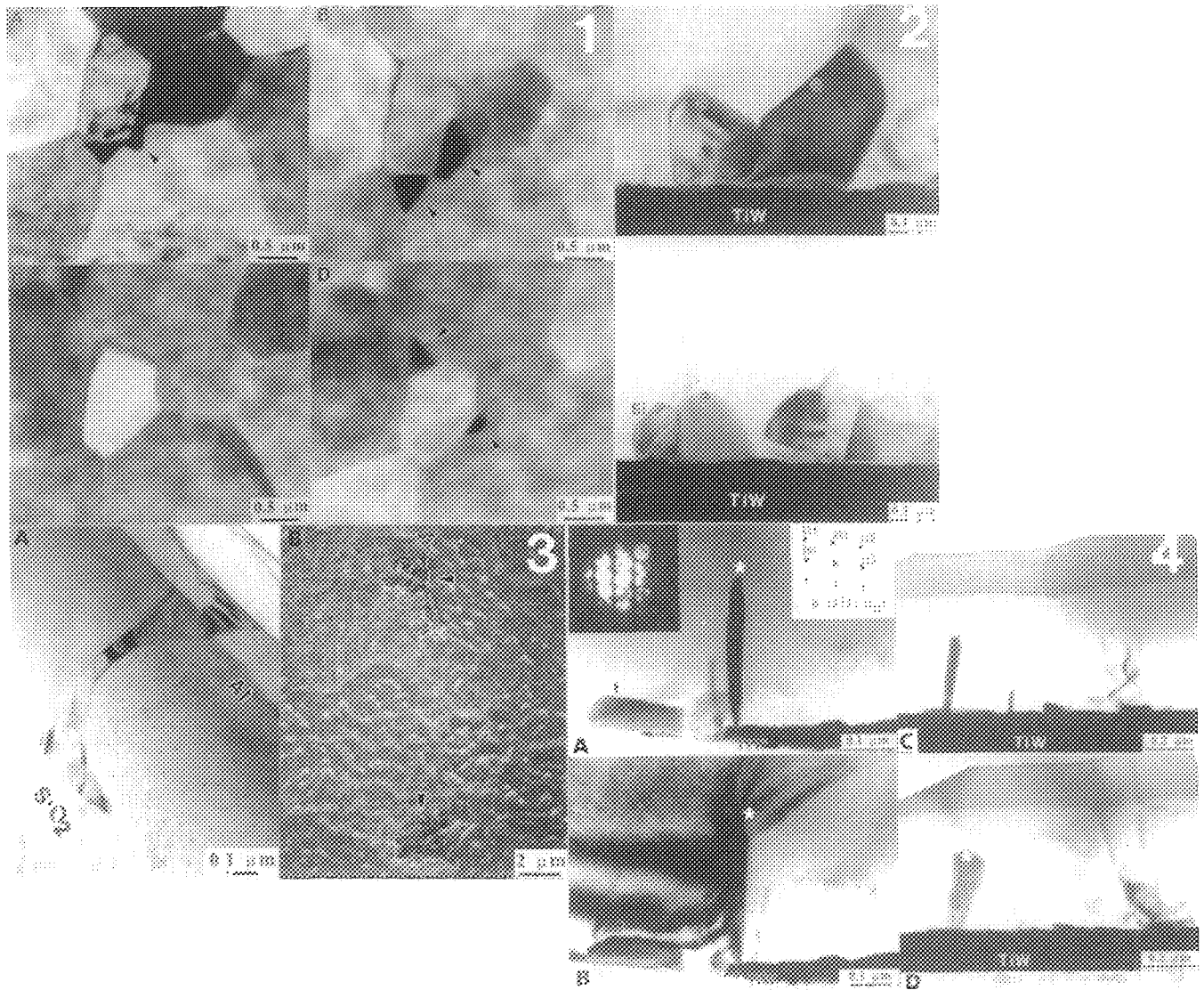
FIG. 1--In-situ annealing of Al-1.5%Cu deposited at 325°C. Coarsening, dissolution and reprecipitation of θ particles (arrow marked) are shown at the grain boundaries.
    1A- Room temperature., 1B- 380°C, (1min.), 1C- 450°C, (1min.), 1D- Room temperature.

FIG. 2--Coprecipitation of Al_2Cu and Si particles in 1.5%Cu-1.5%Si /TiW deposited at 305°C.

FIG. 3--3A- Columnar precipitation of Si in 0.5%Cu-0.5%Si/SiO_2 deposited at 435°C.
    3B- SEM micrograph showing surface Si precipitates in 0.5%Cu-0.5%Si/TiW deposited at 435°C.

FIG. 4--Thin film interactions between Al-0.5%Cu and TiW, annealed at 450°C for 30 min., 4A- Microdiffraction pattern obtained from the planar precipitate of $Al_{12}W$ (arrow marked). Rodlike precipitates (asterisk marked) of W rich compound is shown at the grain boundary., 4B- Grain boundary in contrast, 4C-0° tilted, 4D-20° tilted.

CRYSTALLIZATION OF AMORPHOUS Si IN Si/Al MULTILAYERS

Toyohiko J. Konno and Robert Sinclair

Department of Materials Science and Engineering, Stanford University, Stanford CA94305, USA

Stability of the amorphous Si (a-Si)/Al interface is an important issue from both practical and scientific points of view. Practically, this system can be found in many applications, such as solar cells, thin film transistors, and electrophotography. The normal crystallization temperature of a-Si is close to 700°C. However when in contact with a metallic element with which it forms a binary eutectic phase system, it can crystallize well below the eutectic temperature. The reason for the ease of such a reaction has still not been clarified[1-6]. High-resolution transmission electron microscopy (HRTEM) is a powerful technique to study the mechanism of this behavior because of its ability to identify phases on an atomic scale. This article reports on the crystallization of a-Si observed in a Si/Al multilayer structure.

4000Å thick a-Si/Al multilayers of modulation length of about 120Å were deposited onto a (100) Si wafer by magnetron sputtering. The specimens were subsequently annealed at 175°C for 30 to 90 seconds, followed by quenching into water. A change in color of the film was observed during the annealing. An independent calorimetric study has shown that an exothermic reaction occurs at about 180°C in these multilayer samples[7]. In order to examine this phenomenon, TEM cross-sectional samples were analyzed by bright filed (BF), dark field (DF), and HRTEM. In addition, the same multilayer was deposited on glass substrates and heated in a X-ray diffractometer to observe the evolution of texture.

Figs. 1(a) and (b) are cross-section BF and high-resolution TEM micrographs of the as-deposited a-Si/Al multilayer sample. A (111)texture of Al grains is deduced from the diffraction pattern as well as from the high-resolution image. Figs. 2(a) and (b) are BF and DF images of the sample annealed at 175°C for 37 seconds. The DF image was formed using a part of Si(111) diffraction ring. A large intermixed region is visible, in which crystallized Si (c-Si) is seen to spread over several prior multilayer periods. Apart from the intermixed region, individual small c-Si grains (indicated by arrows) are found inside the Al layers. Fig. 2(c) shows a HRTEM image of one of these incipient Si grains. A large number of twins is observed. A similar observation was made for c-Si nucleated at the a-Si/SiO$_2$ interface[8]. Fig. 3 shows a BF image of the sample annealed for 90 seconds. Crystallization of a-Si is complete at this stage and the original layered structure has almost disappeared due to the grain growth of c-Si as well as the Al phase. Fig. 4 shows X-ray diffraction patterns taken before and after the reaction. An enhancement of Al(111) texture is apparent from the pattern.

Our experimental results are in accordance with an earlier RBS study on metal contact induced crystallization in a-Si/Ag and a-Ge/Al systems[3,4] - namely, crystallization of Si occurs at a very low temperature and primarily within the metal phase. An extensive intermixing of Si and Al grains found in this work indicates that both Si and Al atoms possess a large degree of mobility at relatively low temperatures and that the layered structure is morphologically unstable. Enhancement of texture of the metal phase after the crystallization of the semiconductor phase was also reported in an XRD study done on the a-Ge/Pb system[6]. We speculate that this enhancement is caused by growth of Al(111) grains consuming other less energetically stable Al grains. Complete understanding of this behavior requires further careful TEM analysis, including *in situ* heating experiments.

References

1. F. Oki et al., Japan J.Appl.Phys., 8 (1969) 1056
2. S.R. Herd et al., J. Non-Cryst. Solid, 7 (1972) 309
3. D.Sigurd et al., ibid., 12 (1973) 135
4. G. Ottaviani et al., J.Appl.Phys., 45 (1974) 1730
5. L.S. Hung et al., Mat.Res.Soc.Symp.Proc. 25(1984) 253
6. H. Homma et al., Appl.Phys.Lett., 50 (1987) 594

7. T.J. Konno and R. Sinclair, to be published.
8. A.S. Kirtikar et al., Mat.Res.Soc.Syms.Proc., in press (1990)
9. This research is supported by the National Science Fundation (Grant No. DMR 8902232)
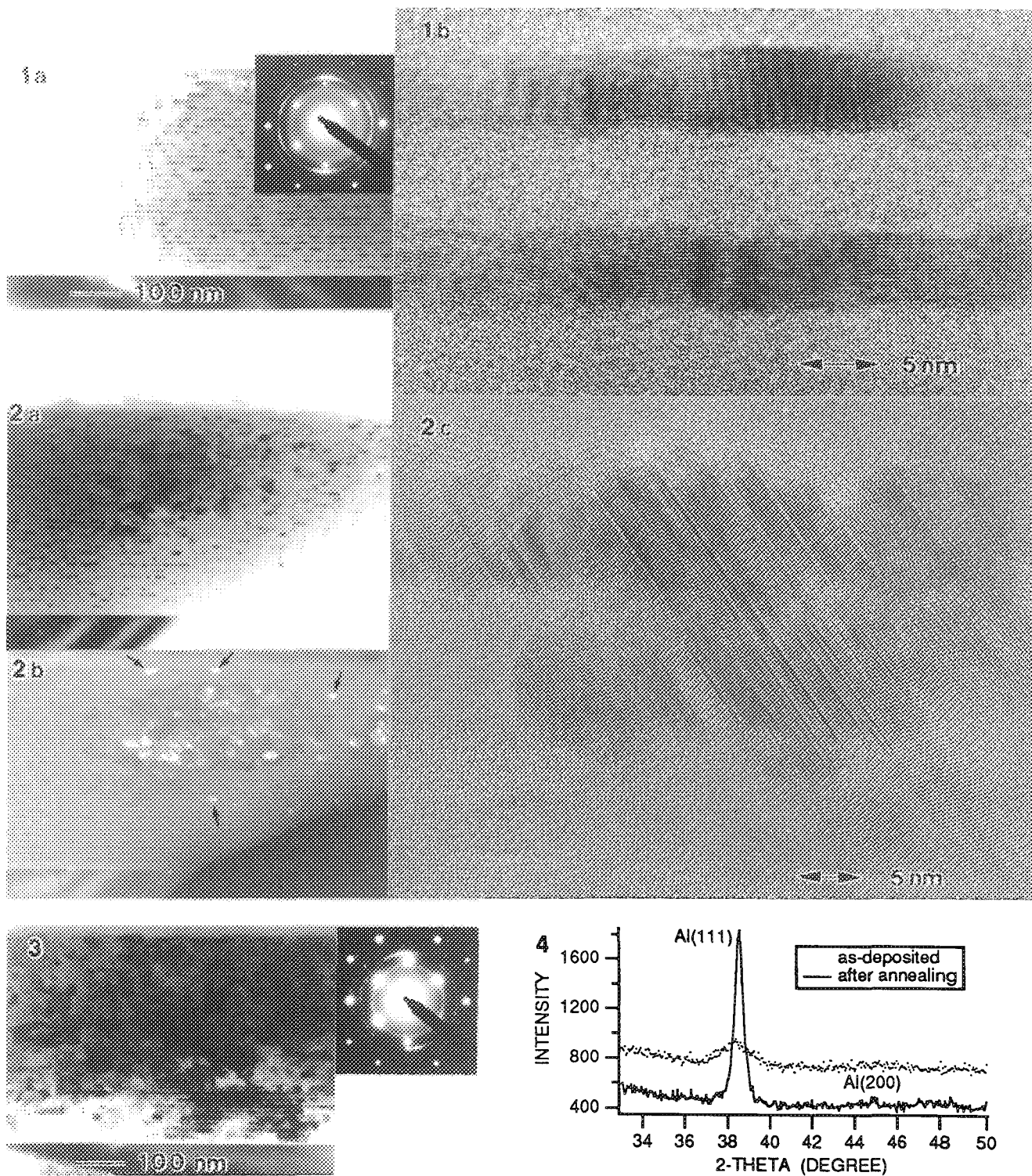
Fig. 1 Cross-section TEM micrographs of as-deposited a-Si/Al multilayer :
   (a) bright field image and diffraction pattern. (b) high-resolution image.
Fig. 2 Cross-section TEM micrographs of the a-Si/Al multilayer, annealed at 175°C for 37 seconds :
   (a) BF image. (b) DF(Si) image. (c) high-resolution image of crystallized Si.
Fig. 3 Bright field image and diffraction pattern of Si/Al multilayer, annealed at 175°C for 90 seconds.
Fig. 4 X-ray diffraction pattern before and after annealing

IN SITU STUDIES OF SILICIDE-MEDIATED CRYSTALLIZATION OF AMORPHOUS Si

C. Hayzelden* and J.L. Batstone**

*Division of Applied Sciences, Harvard University, Cambridge, MA 02138
**IBM T.J.Watson Research Center, P.O.Box 218, Yorktown Heights, NY 10598

Metal silicides in thin films play an essential role in the increasingly fine-scale fabrication of integrated circuits.[1] Although commonly produced by interfacial reaction between metal films and silicon, buried metal silicides have recently been produced in crystalline Si by ion-implantation.[2] Cammarata et al.[3,4], have reported the use of ion-implantation to form buried nickel silicide precipitates in amorphous Si thin films, in which the first (and only) phase to form was $NiSi_2$. The kinetics of the nucleation and growth of $NiSi_2$ precipitates were investigated and an enhancement of the crystallization kinetics of the amorphous Si, apparently due to the migration of silicide precipitates, was found. In this paper, we describe the results of an *in-situ* transmission electron microscopy (TEM) and high resolution electron microscopy (HREM) investigation of the silicide-mediated crystallization of amorphous Si.

Amorphous Si thin films, 95nm thick, were deposited on Si substrates and capped with 100nm thick thermally grown SiO_2 and subsequently ion-implanted with a nickel dose of $5 \times 10^{15} cm^{-2}$ as described previously.[4] Samples were prepared for TEM by chemical jet thinning in a solution of 12.5% HF in HNO_3 to remove the crystalline substrate. In-situ crystallization of amorphous Si was performed in a Philips EM430 TEM operated at 300kV and 150kV with a Gatan single tilt heating holder and recorded dynamically on video tape. After removal of the SiO_2 layer by Ar^+ ion-milling at 3kV with a beam current of 0.5mA, HREM of the crystalline Si - $NiSi_2$ interface was performed in a JEOL 4000EX at 395kV with a point to point resolution of ~1.8Å.

Hot stage microscopy showed that crystallization of the amorphous Si was mediated by the migration of nickel silicide precipitates. Crystallization rates of amorphous Si are strongly temperature-dependent. At 580°C, the growth rate is typically ~5Å/sec.[5] In this study, the silicide-containing Si crystallized at this growth rate at temperatures as low as 500°C. The crystallization onset was not observed within the illuminated area in the TEM at accelerating voltages of 300kV, presumably due to knock-on displacement of Si atoms by the electron beam. At 150kV, no inhibition of the phase transformation was observed. The initial stages of silicide-mediated crystallization are shown in Figs. 1a and 1b. Fig. 1a shows two $NiSi_2$ precipitates oriented in the [011] direction. Crystallization of Si appears to be occurring on the < 111 > faces of the larger precipitate. After 240secs at 507°C, the larger precipitate has begun to migrate, leaving crystalline Si and well-defined Si/$NiSi_2$ interfaces. Fig. 2a shows a partially transformed region at 507°C, in which the characteristic needle-like morphology is shown developing. In Fig. 2b, the needle of Si has grown at an average velocity of 5±0.4Å/sec. At the leading edge of the growing Si needle is a narrow band of $NiSi_2$. Microdiffraction experiments confirmed that the crystalline Si needles grew in < 111 > directions. Fig. 3 shows the planar Si-$NiSi_2$ interface at the end of a growing needle. HREM imaging parallel to [110] revealed a flat Type A (111) interface. In summary, we have directly observed the phase transformation of amorphous to crystalline Si via silicide-mediated nucleation and growth.[6]

References

1. K.N Tu, Advances in Electronic Materials, American Society for Metals, Metals Park, OH (1986) 147.
2. A E. White et al., Appl. Phys. Lett (1987) 50, 95.
3. R.C. Cammarata, C.V. Thompson and K.N. Tu, Appl Phys. Lett. (1987) 51, 1108
4. R.C. Cammarata et al., J. Mater. Res (1990) 5, 2133
5. K A. Jackson, Surface Modification and Alloying, Plenum Press, NY (1983) 70.
6 We thank C V. Thompson, K.N Tu, R C. Cammarata and D A Smith for valuable contributions to this study.
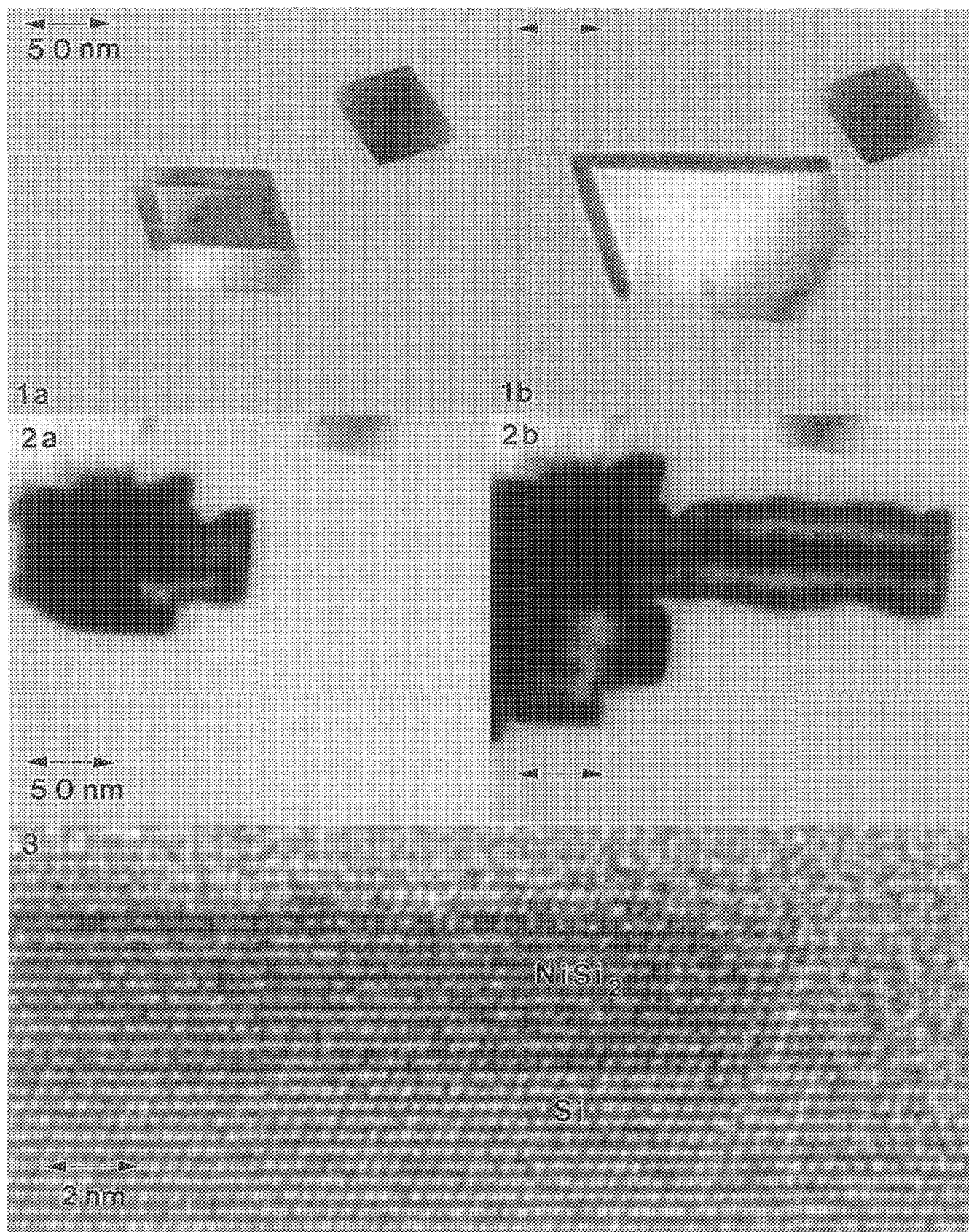
Fig.1 -- NiSi$_2$ precipitates in amorphous Si; a) after 240 secs at 507 °C and b) after 560 secs at 507 °C

Fig 2.--Silicide-mediated growth at 507°C; a) after 560 secs and b) after 720 secs.

Fig.3 --HREM image of the Type A Si/NiSi$_2$(111) interface.

DEVICE FAILURE ANALYSIS: *A PERSPECTIVE FOR THE 1990s*

Ron Anderson

IBM, ZIP E-40, East Fishkill, NY 12533

Historically, analytical TEM and SEM analysis capability has lagged behind the capability to conduct electrical diagnostics on electronic devices. The problem is one of spatial resolution. It isn't a case of TEM and SEM specimen preparation methods not keeping pace with the rapid and steady decrease in dimensions of modern device structures—in reality, the industry as a whole has not been able to do single-device *failure* analysis, much less keep pace with shrinking dimensions. The ability to prepare failure analysis specimens of *pre-specified* individual devices, or small portions of individual devices, has been demonstrated in a very few laboratories only recently. Uncharitably, there has been no pause in diminishing device dimensions. Researchers are now faced with the horrific prospect of the size of the most-meaningful structures in their specimens shrinking well below the one micron spatial resolution of routine light microscopy—just as people are learning how to make specimens of small pre-defined areas. At this writing there is some agreement that a specimen preparation spatial resolution of about 500Å is required. In other words, given the (x,y,z) coordinates of a failed device or structure within a large wafer or chip, it is now required to prepare a SEM cross section or a thin TEM specimen that comes within 500Å of the specified coordinates. The 500Å number is appropriate at this time because many leading manufacturers are thinking in terms of half-micron ground rule structures. Samples must be prepared from slices out of these 5,000Å structures. The spatial resolution required to accurately section any structure is usually taken to be one-tenth the size of the structure: 500Å for 5,000Å features. This means that the spatial resolution needed goes to 300Å for three-tenths micron ground rules, which are just around the corner.

Another fact of life is the changing relationship between TEM and SEM operations in the device failure analysis laboratory. Traditionally, the TEM operation has played a secondary support role to the main failure analysis function. When a failed chip or wafer was submitted for analysis it has traditionally gone to the SEM, after perhaps a brief pause for light-optical microscopy. There is a good chance that TEM was never in the routine failure analysis loop because the TEM specimen preparation procedures used could not prepare the samples. TEM was used, instead, to perform construction analysis—often on "special" TEM chips that got around the spatial resolution problem by preserving x and z dimensions in a structure but extending the y dimension back for hundreds of microns. Also, everyone knew that TEM analysis took about a week to do and couldn't be counted on for same-day turn-around. The above relationships have worked well in the past because device dimensions were large enough that low-tech polishing or specimen fracturing could prepare SEM cross sections satisfactorily and the manufacturing line "customers" were satisfied with the answers the SEMs were providing. SEM manufacturers, driven to a considerable extent by the high-stakes electronics business, have provided instruments with very high SEM spatial and element analysis resolutions to meet this market. As the field evolves it is becoming clear that these relationships are changing. Classes of defects that either didn't exist, or were ignored safely, can now cause device failures. The superior spatial and elemental resolution of TEM analysis, coupled with a diffraction capability and the simple fact that analysis is being performed *in transmission* to identify substrate crystal defects, is now required.

Additionally, in order to interact effectively in today's semiconductor manufacturing environment, TEM samples have to be made with the same high probability of success, same-day turn-around service traditionally offered by SEM operations. It is obvious, then, that the traditional SEM-first exclusive failure analysis protocol has to be modified because one cannot tell *a priori* whether the unique, one-of-a-kind, failure brought in for analysis will not need to be analyzed in the TEM. Compounding the problem is the fact that as the modern device failure rate decreases, the likelihood that any given failure is "one-of-a-kind" increases. At the least, *every* SEM sample prepared must be done so in a manner such that a subsequent TEM sample can be prepared that preserves the same cross section view of the failed region shown in the SEM.

Several things are needed to perform SEM and TEM failure analysis in the above context. First: we, as analysts, have to *really* understand our specimens and the capabilities of the techniques and the instruments. We have to commit to the concept of *solving problems*, not merely completing a pre-determined number of samples or blindly giving the customers only what they ask for. We have to stop doing silly things, like: mechanically fracturing dinner-plate-sized wafers to cross section devices, and smearing-on hundreds of angstroms of carbon (or gold!) for charge collection in a FEG-SEM capable of high resolution, low voltage imaging. Second: we have to learn new ways of preparing specimens with high spatial resolution. The author's laboratory has the capability of turning out 500Å spatial resolution TEM sections with a nearly 100% success rate in about three hours per specimen using simple polishing methods.[1] Other facilities are having similar successes utilizing next-generation dimpling machines and ion milling methods.[2,3] Other, entirely new methods for achieving high-resolution specimen preparation are evolving, such as lithography methods coupled with reactive ion etching and utilizing focussed ion beam instruments to make TEM specimens directly.[4,5] Lastly: the traditional synergism between light-optical, SEM and TEM analysis methods has to be re-evaluated and broadened to include other techniques that have much to offer the device failure analysis team (STM, SXM, SFM μIR, etc.). Analysis should proceed from the least to the most destructive technique with the aim of doing as many things with as many techniques as possible to an individual failure site. We may well experience a renaissance in device failure analysis in the 1990s!

---

[1] Klepeis, S. J., et al., in "*Specimen Preparation for Transmission Electron Microscopy of Materials,*" ed. Bravman, et al., MRS Symposium Proceedings, Vol. 115, p. 179, 1988; Anderson, R.M., et al., *Microscopy of Semiconducting Materials,* 1989, Proceedings of the Physics Conference held at Oxford University, 10-13 April 1989, ed. by Cullis, A. G. and Augustus, P. D., 1989, and Benedict, J. P., et al., *EMSA BULLETIN,* 19, 2, 1989; Benedict, J. P., et al., in "*Specimen Preparation for Transmission Electron Microscopy of Materials-II,*" ed. Anderson, Ron, MRS Symposium Proceedings, Vol. 199, p. 189, 1990.

[2] Dawson-Elli, et al., in "*Specimen Preparation for Transmission Electron Microscopy of Materials-II,*" ed. Anderson, Ron, MRS Symposium Proceedings, p. 75, Vol. 199, 1990.

[3] Alani, R. et al., *ibid.,* p. 85.

[4] Wetzel, T. F. and Kavanaugh, K.L., *ibid.,* p. 43.

[5] Young, R.J., et al., *ibid.,* p. 205.

ELECTRON BEAM TESTING OF MULTILEVEL METAL INTEGRATED CIRCUITS

P. E. Russell, Z. J. Radzimski, D. A. Ricks and J. P. Vitarelli

Department of Materials Science and Engineering,
Box 7916, North Carolina State University, Raleigh, NC 27695

Fundamentally, voltage contrast is a well established technique for determination of voltages on metal surface which can be directly probed with an electron beam[1]. However, actual integrated circuits (IC) consist of two or more conducting layers (metal and doped polysilicon) separated by dielectrics and covered by a dielectric passivation layer. Our work has addressed: i) the removal of dielectric layers (depassivation) by reactive ion etching (RIE) or selectively by focused ion beam etching to allow access to exposed metal lines; ii) modelling effort to understand how the materials and geometric parameters of multilevel IC's affect voltage contrast measurements, and iii) improvements in retarding field spectrometer based measurement techniques.

In relation to the depassivation process we have characterized the reactive ion etching process and have established baseline parameters for existing equipment (Technics RIE system). The basic objective of the RIE optimization was to remove passivation layers from multilevel devices without risking damage to the device. An aluminum etch mask was designed and fabricated to improve the uniformity and control of the etching process. Recently, our efforts have been focused on characterization of the RIE process. The etch rate and selectivity was established for typical materials used in VLSI technology. Moreover the effect of isotropic vs. anisotropic etching was studied in order to evaluate the proper ratio of the physical and chemical factors of the etching process and its effect on the quality of depassivated surfaces. It has been found that using $CH_4 + O_2$ plasma at the discharge power > 100W results in an excessive sputtering of bond wires, the chip base and the etch mask. This in turn leads to a non-uniform etching of passivation layer and subsequent formation of so called "RIE grass". In order to eliminate this effect the physical component of the etching has to be reduced. However, the physical component of RIE cannot be completely eliminated since it is responsible for anisotropic etching.

The second objective was to study theoretically and experimentally the mechanism of charge build-up on passivation layers, as well as the spatial and depth resolution of voltage contrast on specimens with multilevel metallization. To solve this problem theoretically we simulated the device structure and secondary electron extraction conditions using computer modelling techniques. Reliable theoretical methods for predicting voltage levels on passivated lines and trajectories of secondary electrons were established. The steps in creating a model to simulate our experiments are as follows:

a) model electrostatic field lines surrounding the conducting channels on both passivated and depassivated devices in the presence of the extraction voltage, and

b) simulate sample's secondary electron emission and trajectories of secondary electrons in the presence of the resulting electric field.

The first step was implemented using software available at Microelectronic Center of North Carolina (MCNC). The numerical program for secondary electron trajectory computation has been developed for IBM compatible PC/AT systems. Our theoretical results shows that there are fundamental limits for using voltage contrast technique with an electrostatic analyzer due

to a capacitance coupling and capacitance cross talk.[2]

The third objective was to verify the modelling results and to optimize imaging and waveform measurements on passivated and depassivated devices. We were especially interested in studying the effect of extraction field on the charge build up on passivated layer. Preliminary results show only qualitative agreement and indicate that there is a need to evaluate the effect of device geometry, influence of topology and contamination effects more extensively.

While the RIE process is used to remove the passivation layer from the entire integrated circuit, focused ion beam techniques can be used to remove passivation locally. This is important for the waveform measurement technique, where only a small localized region must be exposed directly by the electron. The focused ion beam technique can also be used for repair of areas identified during electron beam testing. This has been demonstrated on an integrated circuits using a liquid metal focused ion beam micromachining system. We are currently investigating the practical aspects of implementing this technique as a standard tool. We are investigating the effect of crater geometry (depth and width) on the ability to measure quantitatively voltage waveforms. Our modelling methods can be extended to this situation and results compared with experiments.

In addition to charging, the contamination build-up is very important during VLSI testing. A preliminary study, not addressed in our previous proposal, shows that this effect can be drastically reduced by cleaning the device in oxygen plasma prior electron beam testing. In order to quantify the contamination build-up process, a measurement technique was recently set-up. We are attempting to establish the optimal procedure for surface cleaning prior voltage contrast measurements.

The theoretical methods for voltage prediction,are being extended to include charging effects. Such parameters as the electron beam energy, beam current and chopping frequency must be taken into account. The complete incorporation of all time dependent effects is quite complex, so the initial efforts will be directed at identification of quantification of the factors, which limit the measurements of high speed voltage waveforms. The effect of device topology must also be addressed. The particular problem of waveform amplitude reduction is addressed and experimental corrections are under development.

References
1. Scanning, Vol. 5, 1983, pp. 14-24.
2. J. Vac. Sci. Technol. B8(6), 1990, pp. 2027-2040.
3. J. Wolcott and J. Cain are gratefully acknowledged for their important contributions to this work. This work was sponsored by NSF DMR-8657813 and by IBM under the SUR program.

CATHODOLUMINESCENCE AND ELECTRON BEAM INDUCED CURRENT INVESTIGATIONS OF SEMICONDUCTOR MATERIALS AND STRUCTURES FOR OPTOELECTRONIC INTEGRATION

E.A. Fitzgerald

AT&T Bell Laboratories, Murray Hill, NJ 07974

Mismatched semiconductor heteroepitaxy has been of interest for both high speed electronics and optoelectronic integration. The largest impact of mismatched epitaxy would be the integration of mature Si electronics with light-emitting III-V materials, such as GaAs.[1] However, the lattice constant of Si is much smaller than the lattice constant of direct band gap III-V materials; therefore, integration through epitaxy introduces many misfit-relieving dislocations, which can terminate at the surface (threading dislocation segments). Any optical devices fabricated from this material degrade rapidly due to the high dislocation density. Cathodoluminescence (CL)[2] and electron beam induced current (EBIC)[3] are extremely valuable in relating optoelectronic quality to microstructure and processing.

We have experimented with both direct growth of GaAs on Si and growth of III-V materials on intermediate Ge_xSi_{1-x} layers. CL was used to investigate the micro-optical properties of the III-Vs, and EBIC was used to examine the threading dislocation densities in the Ge_xSi_{1-x} buffer layers.

For the direct growth of GaAs, if the GaAs is grown on a Si mesa such that the height of the film is nearly equal to the width of the mesa, the dislocation density at the surface should be zero, according to a process we term epitaxial necking.[4] With CL, we observe that the luminescence intensity from a 10μm-thick GaAs film grown on a 40μm-wide mesa is 1.6 times that of unpatterned GaAs/Si. The integrated intensity from the mesa is equal to that of the control GaAs/GaAs sample. However, the GaAs on the Si mesa retains more biaxial compressive strain as well, and the dislocation density at the surface is not zero.

An alternative approach is to obtain a large lattice constant on Si for III-V growth by relaxing Ge_xSi_{1-x} structures without obtaining high dislocation densities. Normally, high dislocation densities are produced when abrupt structures are completely relaxed. By designing appropriate EBIC structures, we were able to easily observe threading dislocation densities in relaxed Ge_xSi_{1-x} structures. For completely relaxed structures grown at high temperatures, we observe remarkably low threading dislocation densities. Fig. 1, 2 and 3 are EBIC images of threading dislocations in completely relaxed 23, 32, and 50% Ge structures, graded at 10%/μm and grown at 900°C. The dislocation densities are 4×10^5 cm^{-2}, 1.7×10^6 cm^{-2}, and 3×10^6 cm^{-2}, respectively.

For comparison, consider an abrupt x=32% sample grown abruptly on Si at the same temperature (Fig. 4). Comparison of Fig. 2 and Fig. 4 show a tremendous difference in dislocation density. The dislocation density in Fig. 4 is so high that the dislcoations have arranged into a cell structure, to minimize energy. The superior quality and large lattice constant of the graded Ge_xSi_{1-x} alloys, with or wothout other dislocation reduction methods, offers great promise for the integration of III-V materials with Si.

References

1. S.F. Fang et al., J. Appl. Phys. 68(1990)R31.
2. B.G Yacobi and D.B. Holt, J. Appl. Phys. 59(1986)R1.
3. H.J. Leamy, J. Appl. Phys. 53(1982)R51.
4. E.A. Fitzgerald and N. Chand, unpublished.
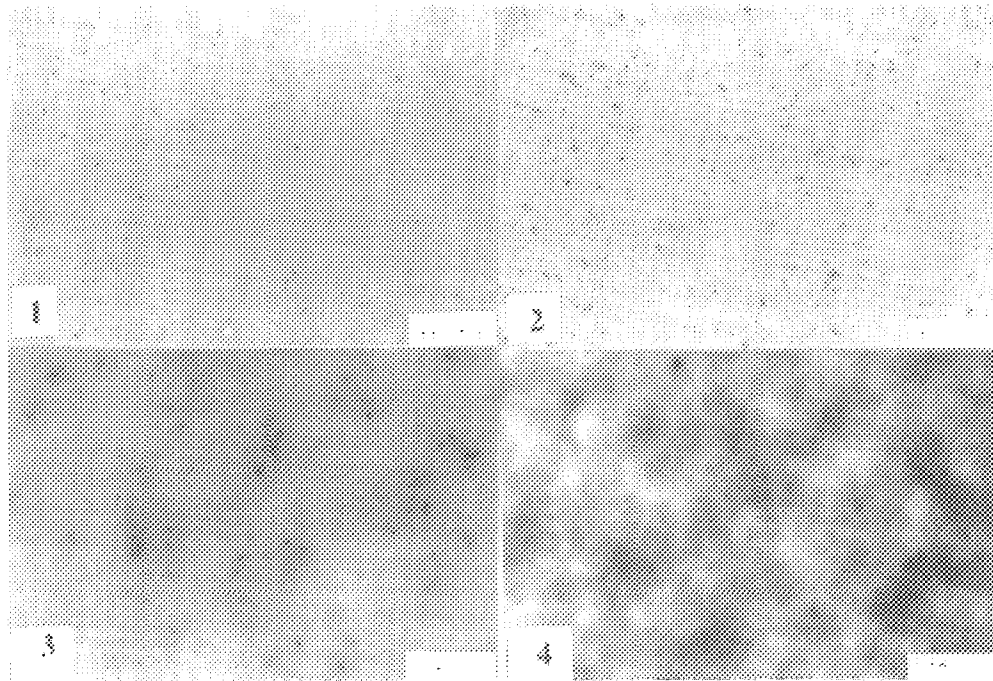
FIG. 1 -- EBIC image of threading dislocations in a completely relaxed, graded $Ge_{0.23}Si_{0.77}$/Si structure. Bar=21 μm.

FIG. 2 -- EBIC image of threading dislocations in a completely relaxed , graded $Ge_{0.32}Si_{0.68}$/Si structure. Bar=21 μm.

FIG. 3 -- EBIC image of threading dislocations in a completely relaxed, graded $Ge_{0.50}Si_{0.5}$/Si structure. Bar=7 μm.

FIG. 4 -- EBIC image of threading dislocations in a relaxed, abrupt $Ge_{0.32}Si_{0.68}$/Si structure. Bar=13 μm

LUMINESCENCE FROM INDIVIDUAL DISLOCATIONS IN II-VI AND III-V SEMICONDUCTORS

J W Steeds

Physics Department, Bristol University, Bristol BS8 1TL, United Kingdom

1. Introduction

There is a wide range of experimental results related to dislocations in diamond, group IV, II-VI, III-V semiconducting compounds, but few of these come from isolated, well-characterized individual dislocations. We are here concerned with only those results obtained in a transmission electron microscope so that the dislocations responsible were individually imaged. The luminescence properties of the dislocations were studied by cathodoluminescence performed at low temperatures (~30K) achieved by liquid helium cooling. Both spectra and monochromatic cathodoluminescence images have been obtained, in some cases as a function of temperature.

There are two aspects of this work. One is mainly of technological significance. By understanding the luminescence properties of dislocations in epitaxial structures, future non-destructive evaluation will be enhanced. The second aim is to arrive at a good detailed understanding of the basic physics associated with carrier recombination near dislocations as revealed by local luminescence properties.

2. Experimental Results

Some of the experimental results of interest to us are not new. In particular the work of Batstone which established the link between dislocations and Y luminescence in ZnSe was published several years ago[1]. The work of Bailey on misfit dislocation in the so-called lattice matched system GaAs/GaAlGaAs are also not new but have not yet been fully reported[2]. More recent work of Wang[3] on the InGaAs/GaAs system represents a systematic effort to introduce misfit dislocations in a controlled fashion, and to study their nucleation and growth in a non-destructive fashion.

3. Interpretation

This lags behind the experiments at present. The clearest story so far relates to dislocations in ZnSe[4]. One of the first issues to resolve is whether the luminescence is intrinsic or extrinsic in character. For the present we believe the balance of evidence favours an intrinsic origin in ZnSe, and this is the assumption behind our interpretation. The second key factor in our interpretation is the strong evidence, summarized by Dean[5] and supported by our own observations that Y luminescence in ZnSe is excitonic in character. The final step is based on our observation that the Y luminescence is remarkably insensitive to parameters such as dislocation character or curvature, and also to whether the dislocations were grown in or freshly introduced. We therefore seek an explanation where one-dimensional electron and hole bands are formed along the dislocation, not by

core states but by long range strain field effects. Based on these starting assumptions, an explanation of the Y luminescence is emerging which seems to match most of the experimental results. Although incomplete at present, the starting point is the work of Bozhokin et al[6] on dislocation excitons. This theory is based on an unscreened classic deformation potential, but a greatly improved potential has now been proposed by Farvacque. Next, classical statistical mechanics are used to interpret the temperature dependence of the Y intensity, and as a result, a value of about 50meV is obtained for the binding energy of the dislocation exciton. To explain the 200meV shift of the Y emission from that of free excitons in ZnSe, it is necessary that the one-dimensional electron and hole bands are shifted from the bulk electron and hole bands by about 75meV. This requirement is consistent with the theory of Farvacque. Finally, the broadening of the Y emission with increase of temperature by acoustic phonons has been explained in detail.

In the case of the dislocation luminescence effects from GaAs/AlGaAs quantum wells, two competing theories exist at present and remain to be evaluated in the future. The first[2] assumes the presence of a Cottrell atmosphere of impurities (probably C) around the misfit dislocations. The higher the impurity concentration, the higher the red shift of the luminescence. Hence, monochromatic images formed at large energy shifts (40meV) from the quantum well peak correspond to high impurity regions near the dislocation cores and show narrow lines as a result. Images formed at energies closer to the peak emission correspond to lower impurity concentrations which extend a long way from the dislocation core and give broad images. An alternative explanation[4] attempts to explain the same results in terms of an in-plane Franz-Keldysh effect associated with charged dislocations.

References

1. S. Myhajlenko et al, J. Phys. C: Solid State 17 (1984) 6477.
2. J.W. Steeds et al, in Evaluation of Advanced Semiconductor Materials by Electron Microscopy, ed. D. Cherns, NATO ASI Series B, Physics Vol. 203, Plenum Press (1989) p 127.
3. J.N. Wang, J.W. Steeds and D.A. Woolf, submitted for publication.
4. Yu. T. Rebane, Yu. G. Shreter, Proceedings of POLYSE '90 Conference, Schwabish Hall, Springer Verlag, in the press.
   J.W. Steeds et al, ibid.
5. P.J. Dean, Phys. Stat. Sol. 81(a) (1984) 625.
6. S.V. Bozhokin, D.A. Parshin and V.A. Kharchenko, Sov. Phys. Sol. State 24 (1982) 800.

CHARACTERIZATION OF DEFECTS AND IMPURITIES IN WIDE BAND GAP SEMICONDUCTORS BY CATHODOLUMINESCENCE IN TEM

R.J. Graham

Center for Solid State Science, Arizona State University, Tempe, AZ 85287-1704

As a characterization technique for semiconductors, cathodoluminescence (CL) performed in TEM has several useful advantages over the more common SEM-based technique, the most important being that the acquisition of CL data from localized regions in an electron transparent specimen allows a correlation of microstructural and optical/electronic information. For example, it is possible to determine the distribution of low concentrations of optically active impurities and their possible association with defects, often at submicron resolution. Examples of TEM CL as a method of characterizing defects in semiconducting materials presented here are taken from wide band gap materials which are of current interest including CVD-grown diamond films and β-GaN on Si.

Experiments were performed in a Philips EM400T equipped with high-resolution TEM CL system[1] which includes a grating spectrometer (Spex 0.22 m Minimate) and an RCA C31034 PMT detector (300-900 nm spectral range). Digital monochromatic CL images were acquired using a STEM attachment and an in-house designed multichannel analyzer. A specimen temperature of 90K and beam voltage of 120 kV were used throughout.

Diamond films grown by chemical vapor deposition (CVD) have potential applications as optical and electronic materials due to the intrinsic properties of diamond such as optical transparency and high carrier mobility. The optical/electronic properties of the many defects currently present in these films have been studied by TEM CL[2]. Fig. 1 shows a typical CL spectrum from a TEM specimen prepared by Ar^+ ion milling from material grown by W filament-assisted CVD from 2% CH_4 in H_2 at 15 Torr and a Si (100) substrate temperature of 750°C[2]. Broad CL bands (band A) observed at 428 ± 1 nm and 551 ± 1 nm are attributed to closely-spaced and widely-separated donor-acceptor (D-A) pairs, respectively (nitrogen and boron). A narrow peak at 737.2 ± 0.5 nm is attributed to interstitial silicon atom impurities. Overall CL intensity varied greatly with growth conditions. The TEM image in fig. 2 shows the typical film microstructure consisting of long grains usually containing many dislocations and other highly faulted regions. CL intensity varied spatially on a submicron scale with both highly faulted and defect-free grains emitting no visible CL. Fig. 3 shows monochromatic CL images of the 428nm band (band A) and 737.2nm peak. Band A CL due to closely-spaced D-A pair impurities was found to be directly correlated with dislocations. Widely-spaced D-A pairs were more uniformly distributed throughout the film. The distribution of interstitial silicon impurities, which probably originate from the Si substrate or silica reactor walls, varied greatly from grain to grain, but was not correlated with any microstructure.

Cubic GaN (β-GaN) offers some interesting device possibilities including blue luminescent devices. Single crystal films of this material, about 1.5μm thick and oriented in the <100> direction, have recently been grown by CVD methods on (100) silicon substrates[3] but the large lattice mismatch with the substrate (about 20%) results in numerous defects in the films. Preliminary TEM CL studies show that any band edge luminescence, expected at around 3.5eV, is quenched by mid gap luminescence associated with extended defects (possibly misfit dislocations) in the β-GaN. For <100>-oriented material, this luminescence, centered at about 2eV, consists of a broad band with about five superimposed peaks, at 549nm, 590nm, 628nm, 680nm and 746nm, which tend to disappear when the material is thinned by Precision Ion Milling (PIMS) and apparently "relaxes" by cracking along <011> directions (fig. 4). Polycrystalline β-GaN with grains oriented close to the <111> orientation on [100] Si gives similar CL with as many as five additional peaks present towards the higher energy green region of the visible at 515nm, 541nm, 559nm, 573nm and 611nm (fig. 5). The origin of these additional peaks may be mid gap states due to the electronic structure of the grain boundaries.

References
1. N. Yamamoto, J.C.H. Spence and D. Fathy. Philos. Mag. B 49, 609. (1984).
2. R.J. Graham, T.D. Moustakas and M.M. Disko, J. Appl. Phys. (in press, 1991)
3. T.D. Moustakas. unpublished results.
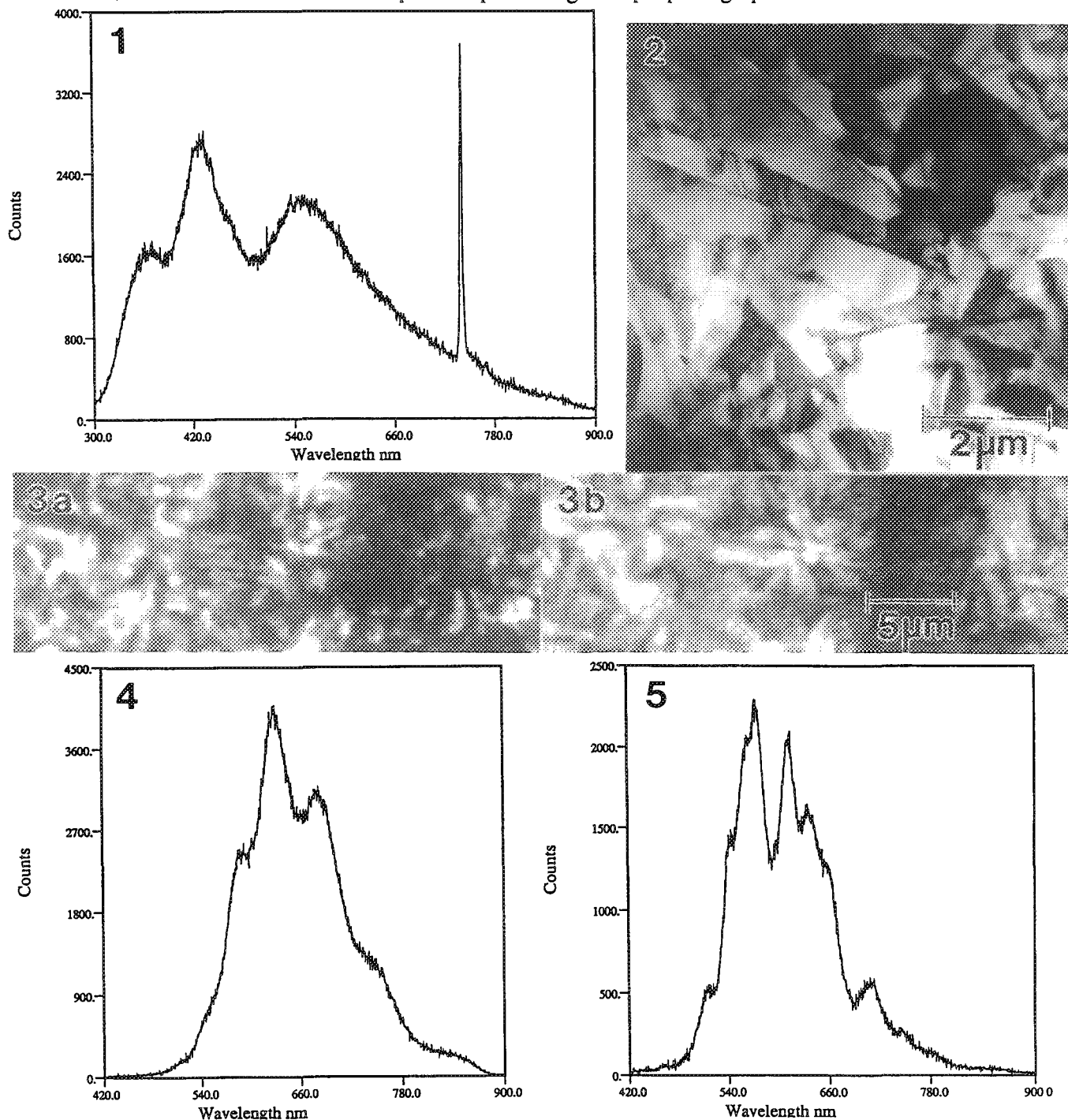
Fig. 1. CL spectrum with emissions at 365 ± 1 nm, 428 ± 1 nm, 551 ± 1 nm. and 737.2 ± 0.5 nm.
Fig. 2. TEM image of typical CVD diamond film microstructure.
Fig. 3. Monochromatic CL images from CVD diamond film; (a) $\lambda = 428$nm, (b) $\lambda = 737.2$nm.
Fig. 4. CL spectrum from $<100>$ β-GaN on (100) Si.
Fig. 5. CL spectrum from textured polycrystalline β-GaN grains oriented close to $<111>$.

A SUPERIOR CATHODOLUMINESCENCE SPECTRAL ANALYSIS AND IMAGING SYSTEM FOR SEMICONDUCTOR CHARACTERISATION

P J Wright

Oxford Instruments Ltd, Eynsham, Oxford

Cathodoluminescence is a useful technique in the structural and electro optical characterisation of semiconductors. When performed in a electron microscope, both high spatial resolution images and spectra may be obtained by use of the correct equipment.

Many designs for instruments suitable for cathodoluminescence spectral analysis and imaging in electron microscopes have been described in the literature during the past 25 years. These have often exhibited improved performance when compared with commercially available systems. The prime reason for this has been the willingness of the dedicated CL researcher to mount large, heavy monochromators directly to the chamber of their microscope. The result has been a microscope committed to CL analysis. However, many potential CL users have to use shared facilities and may not compromise the performance or appearance of the microscope. Subsequently, many CL systems have had the monochromator decoupled from the CL collection optics by either fibre optic bundles or quartz fibres. This has allowed the monochromator and its associated detectors to be easily decoupled from the SEM when not in use. Considerable transmission losses have been incurred and in many cases, it has been necessary to duplicate detectors to allow both spectral analysis and imaging. This has resulted in instruments which were less than optimum in both efficiency and operation.

A low loss CL collection and analysis system has recently been developed that now allows turnkey operation both for imaging and spectral analysis from 0.2 m to 1.8 m.

Fundamental to the design of this system has been the production of a high resolution monochromator with an integral CL collector including a paraboloidal mirror and light guide assembly. The incorporation of lightweight composite materials for most of the structural design has resulted in the entire collector/monochromator being light enough to mount on any SEM chamber without having to modify the vibration isolation.

A set of switching mirrors allows the CL emission to be coupled to the detectors directly for panchromatic imaging or via the monochromator, for either spectral analysis or monochromatic imaging. This has both eliminated the need to duplicate detectors and allows the highest possible transmission efficiency.

Further refinements incorporated in the design of this system include a dual mode, two channel amplifier. The first channel allows photon counting to be performed at low signal intensities and simple V/f detection at higher signal levels. This ensures the system has the widest dynamic range possible.

The second channel accepts the signal from an InGaAs photodiode whose output is modulated by a magnetically sensed chopper.

The integration of a framestore into this system has resulted in two immediately obvious benefits. Firstly, images from low intensity monochromatic signals are easily obtained by averaging over a preset number of frames and secondly the pixel clock from the scan generator is easily monitored and allows the synchronisation of the scans with the modulated signals arising from both the photomultiplier tube and the cooled InGaAs photodiode.

Initial results from a wide range of materials have shown that this system is capable of producing and archiving high quality spectra and both panchromatic and monochromatic images. These have included quantum well structures, semiconductor materials and devices, epitaxial diamond films, bulk diamonds, high temperature superconductors and ceramic materials.

Many of those materials have been studied at room temperature, 77K and 4.2K using compatible cooling stages. This has characteristically increased the signal to noise ratio by orders of magnitude, as well as reducing sample damage by allowing lower operating conditions to be used.

Acknowledgements
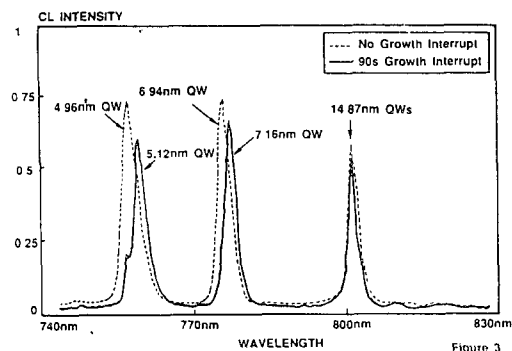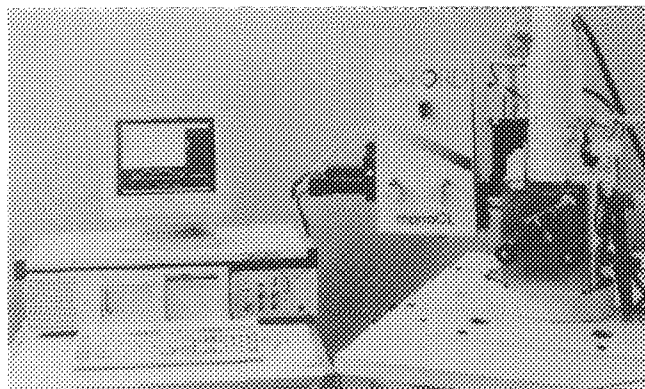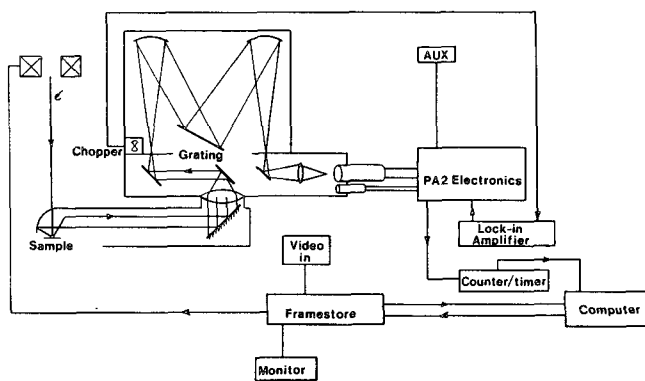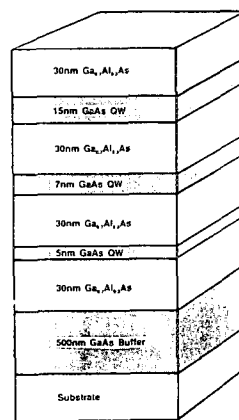
FIG. 1.--Schematic of monoCL system
FIG. 2.--Photograph of monoCL attached to JEOL JSM 840
FIG. 3.--Typical spectral from the quantum well structure shown in FIG. 4.
FIG. 4.--Schematic representation of quantum well structures responsible for the peaks present in the spectra in FIG. 3.

CATHODOLUMINESCENCE OF SEMICONDUCTORS AT 200 eV?

S.Myhajlenko

Center For Solid State Electronics Research,
Arizona State University, Tempe, AZ 85287-6206

Brillson and Vitturo have recently reviewed the application of low energy (300 - 3000 eV) cathodoluminescence (CL) to surface studies of various semiconductors.[1] In principle, the resulting electron penetration (40 - 1500 Å) at these energies should make it possible to differentiate near surface from bulk phenomena. The above authors demonstrated that deep level spectral features could be correlated with changes in the electronic structure of the surface as a result of metallization, laser annealing and thermal desorption. However, the experimental configuration used in the above studies was a room temperature, UHV-based, glancing incidence electron beam apparatus, i.e., no imaging capabilities. A future development in this area would be measurements performed in a regular SEM at cryogenic temperatures. The luminescence efficiency of GaAs greatly increases at low temperatures, and therefore, this would be beneficial to CL signal detection. We also require a better understanding of the factors which may limit progress in this matter. For example, the role of surface recombination velocity, the properties of luminescence dead layers and cross-over voltage phenomena are important to such an investigation. We report on progress in addressing some of these questions.

In this study we have used nominally undoped MOCVD GaAs epilayers (cc < 4 x 10^{14} cm^{-3}).[2] Such samples were chosen in order to optimize spectral quality and sensitivity. On the negative side, the samples possess large 'dark' surface depletion widths (2 - 3 μm). This is important because a functional dependence exists between the luminescence dead layer thickness and the depletion width.[3] Low temperature (15 K) CL measurements were performed in a turbomolecular pumped JEOL 840 SEM (vacuum ~ 3 x 10^{-7} torr with cryogenic pumping) equipped with a single photon counting detection system. In this work we were only able to investigate the near band edge luminescence behaviour owing to detector limitations.

We found that the spectral character and output intensity versus beam voltage was dependent on the excitation power. This in itself was not surprising because of the low temperature injection sensitivity of GaAs . However, a critical voltage/power dosage threshold phenomenon was observed which, when exceeded, produced 'contamination' effects with anomalous CL behaviour. For relatively low excitation power (< 2.5 μW) the CL signal was observed to quench at beam voltages between 1 - 1.5 keV (corresponding penetration depths 300 - 500 Å). See Fig.1 which shows a CL spectrum from n-type GaAs epilayer at 1 keV (1 μW beam power scanned over ~ 1500 μm^2 area). The weak emission can be attributed to the carbon-acceptor transition (eA). This result is consistent with the greater sensitivity of excitons to field ionization than free-to-bound transitions. A similar effect occurs with TEM CL with decreasing sample thickness.[4] The overall quenching of the CL was also consistent with the existence of a dead layer.[5] When the sample was excited with slightly higher beam powers at 1 keV (>10 μW) over a period of minutes, a 'contamination' layer was observed to form on the surface. Once the layer had stabilized, dramatic improvements in CL output were observed, where typical gains were in the range x50 - x500 when re-excited with lower power (1 μW). This effective passivation of the GaAs surface thereby made feasible subsequent CL measurements at 200 eV. In Fig.2 we show a CL spectrum taken at 300 eV (penetration depth ~ 60 Å) in order to highlight the presence of excitons (FE = free exciton, DX = donor-exciton) and free-to-bound transitions (eA = carbon-acceptor, DA = donor-acceptor). Again, the low voltage spectrum was dominated by the carbon-acceptor transition. Two further points: Firstly, the improvement in CL with 'contamination' primarily occured for voltages < 2.5 keV, and secondly, the enhanced CL layer turned into a classical CL contamination 'dark' area for voltages > 3.5 keV.

The nature of contamination at low voltages and low temperatures is clearly complex. We do not address this issue in any detail here. The generation of bright and dark CL areas in a SEM is not unusual. Typically, dark areas are produced by contamination which generate a negative surface charge resulting in deeper surface depletion. What makes the present observations interesting is the voltage regime in which these dramatic effects take place. In semiconductors, the generation of excess electron-hole pairs tends to reduce the surface band bending. Therefore, dependent on the excitation, any residual surface field is responsible for the luminescence dead layer (~ 300 Å from Fig.1 results). However, cross-over phenomena are expected with GaAs in the voltage regime investigated here. A recent calculation for generic GaAs puts the high energy cross-over E_2 at 2.6 keV and the maximum secondary yield at 600 eV.[6] This suggests that for voltages below E_2 the surface voltage will shift to a positive value, and at equilibrium, a surface potential of a few volts or less would exist in the case of GaAs. We speculate that a differential cross-over effect results in a forward bias condition at the GaAs surface. The 'contamination' layer on the GaAs produces perhaps a Schottky like structure? Under certain electron beam injection conditions this could generate a flat band condition. Any residual surface fields, and hence, the dead layer thickness, would be reduced to nearly zero. This could explain the existence of luminescence at 200 eV. The fact that we have not considered surface recombination effects makes these results particularly remarkable. However, it is worth remembering that there is a functional dependence of the surface recombination velocity with surface potential.[7]

REFERENCES:

1. L.J. Brillson and R.E. Vitturro, (1988) Scanning, Vol.2, No.2, 789.
2. Kindly supplied by D.B. Davito.
3. R.E. Hollingworth and J.R. Sites, (1982) J.Appl.Phys., 53, 5357.
4. J. Yuan, S.D. Berger and L.M. Brown, (1989) J.Phys.Condens.Matter, 1, 3253.
5. D.B. Wittry and D.F. Kyser, (1967) J.Appl.Phys., 38, 375.
6. D.C.Joy, (1986) J.Microsc., 147, 51.
7. Illuminating discussions with J.L. Edwards, A.Kriman and R.Puechner are appreciated.
8. This work was supported by ASU-RIA No.021882.
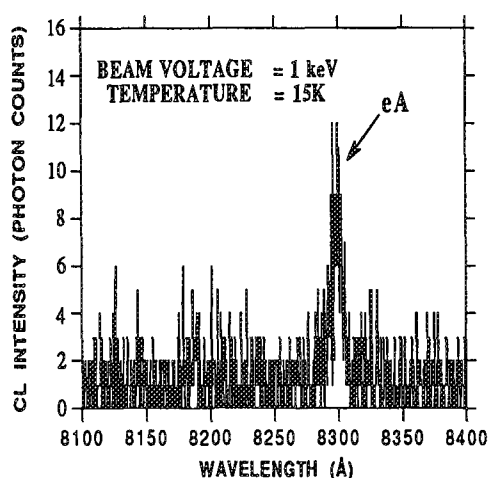
Fig.1 Weak CL emission from GaAs for 1 keV excitation. No CL emission below this value.
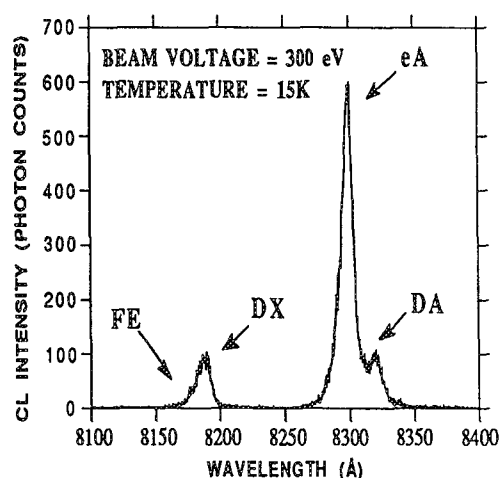
Fig.2 CL at 300 eV from same GaAs sample following deposition of contamination layer.

THE STUDY OF COMPOUND SEMICONDUCTOR HETEROSTRUCTURES BY HIGH-RESOLUTION TRANSMISSION ELECTRON MICROSCOPY

A.G. Cullis

Royal Signals & Radar Establishment, St Andrews Road, Malvern, Worcs WR14 3PS, UK

Heteroepitaxial compound semiconductor systems have increasing importance for the fabrication of advanced electronic devices. Microstructural characterisation of the finest features of these materials can be carried out using transmission electron microscopy (TEM) and this paper demonstrates the use of high resolution work for heterointerface and related investigations in two different areas.

The epitaxial growth of wide band gap II–VI compounds offers potential for a number of optoelectronic device applications[1]. Indeed, in some cases, such as for CdS, it is possible to prepare very high quality Wurtzite–structure layers on Sphalerite substrates, despite the presence of substantial misfit. When hexagonal close–packed CdS is grown by metal–organic chemical vapour deposition on (111)A GaAs, the layer is oriented with $(0001)_{CdS}//(111)_{GaAs}$ and $[11\bar{2}0]_{CdS}//[1\bar{1}0]_{GaAs}$. A cross–sectional, high resolution micrograph of the interface is shown in Fig. 1a where the different atomic stacking in the CdS (ABAB....) and GaAs (ABCABC....) regions is evident. It is also clear that steps of height $1/3[111]_{GaAs}$ are present along the interface and careful consideration of the interfacial stacking shows that these can relieve misfit stress by the introduction of $1/3[1\bar{1}00]_{CdS}$ partial dislocations at alternate step corners[2]. In this way, most of the initial ~3.4% misfit can be relieved without the formation of additional, extensive defect arrays so that only relatively few dislocations bend out of the interfacial plane and thread upwards through the CdS layer. Thus, relatively low threading dislocation densities are achievable in Wurtzite CdS layers of quite limited thickness[2].

It has also been found that the Sphalerite (cubic) forms of the II–VI compounds CdS and CdSe can be produced by growth on (001) GaAs, which provides the appropriate lattice symmetry for the epitaxial layers[2]. However, the cubic structure is metastable and, beyond a certain layer thickness, transforms to the Wurtzite form. Sometimes this can occur quite early in the growth process, as illustrated in Fig. 1b, where blocks of cubic and hexagonal CdSe have been formed immediately. It is also clear that the hexagonal CdSe has formed by multiple twinning on inclined {111} planes of the cubic lattice, leading to the interlocking distribution of the two phases.

In epitaxial alloy systems, for certain device applications, after layer growth it is necessary to modify interlayer properties by intermixing the different components using ion bombardment[3]. This processing is of importance in the GaAs–AlAs system but, for optimum utilisation, it is essential to understand fully ion damage production characteristics in these materials. Indeed, it has been shown[4,5] that AlAs is far less susceptible to ion damage accumulation than GaAs so that damage can be very inhomogeneously distributed in multilayer structures of these materials. This is illustrated by the high resolution TEM study of Fig. 2 which shows a layer system comprising GaAs(70nm)/AlAs(90nm)/GaAs after implantation at 77K with 1.5×10^{14} 150keV–Si$^+$ ions/cm^2. Bands of GaAs on either side of the AlAs have been rendered amorphous (A and D in Fig. 2a) while, as is clear from Fig. 2b, the AlAs has retained a single crystal lattice. The damage resistance of the AlAs persists over a wide dose range up to approaching 10^{16} Si$^+$ ions/cm^2 and represents unusual behaviour for a III–V tetrahedrally-bonded semiconductor. Furthermore, the AlAs also has protected narrow zones of immediately adjacent GaAs crystal (B and C in Fig. 2a) from damage accumulation, the lower zone C being shown at lattice resolution in Fig. 2b. This novel material interaction during bombardment and the intrinsic damage resistance of AlAs probably result from the presence of highly mobile lattice point defects.

References

1. K. Yamaguchi et al., Jpn. J. Appl. Phys. 16 (1977) 1283.
2. A.G. Cullis et al., Appl. Phys. Lett. 55 (1989) 2081.
3. P.G. Deppe and N. Holonyak Jr., J. Appl. Phys. 64 (1988) R93.
4. A.G. Cullis et al., Appl. Phys. Lett. 55 (1989) 1211.
5. A.G. Cullis et al., J. Appl. Phys. 69 (1991) 1278.
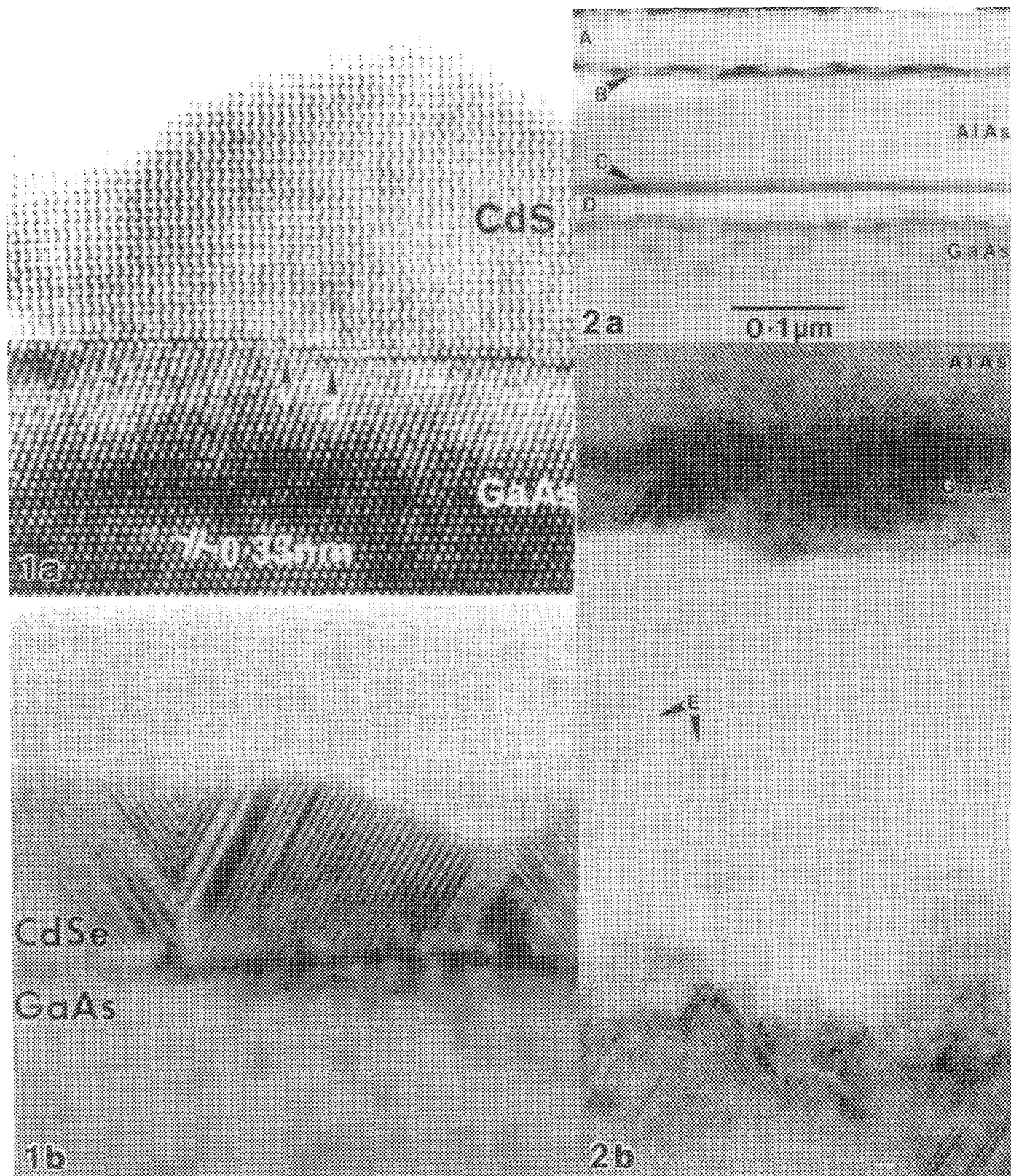
FIG. 1.-- Cross-sectional $[1\bar{1}0]_{GaAs}$-axial TEM high resolution images: (a) hexagonal CdS layer grown on $(111)_{GaAs}$ showing interface with steps at Y and Z; (b) mixed structure CdSe layer grown on $(001)_{GaAs}$.

FIG. 2.-- Cross-sectional $[1\bar{1}0]_{GaAs}$-axial TEM images of implanted AlAs/GaAs layer structure: (a) complete structure; (b) high resolution showing lower edge of crystalline AlAs layer, protected crystalline GaAs zone (dark) and underlying amorphous GaAs containing isolated blocks of crystal (E).

CHEMICAL MAPPING OF MATERIALS AT THE ATOMIC LEVEL

A. Ourmazd, F. Baumann, M. Bode, Y. Kim and J.L. Rouviere

AT&T Bell Labs, Holmdel, NJ 07733

Under appropriate conditions, a conventional lattice image is a map of the sample structure, because the dominant reflections used to form lattice images are relatively insensitive to compositional changes in the sample However, certain reflections, such as the (200) in the zinc-blende structure, owe their existence to chemical differences between the various atomic species present on the lattice sites. Such *chemical* reflections are sensitive to *compositional* changes in the sample. For fundamental reasons such reflections are often weak; they come about because of incomplete cancellation of out of phase contributions from different sublattices. "Chemical lattice imaging" exploits dynamical scattering to maximize the intensity of such reflections, and uses the objective lens as a bandpass filter to enhance their contribution to the image [1,2].

A chemical lattice image encodes the composition of the sample into the local patterns that combine to form the lattice image mosaic. We have developed a vector pattern recognition algorithm [3], which examines each unit cell of the image, measures its composition, and yields a confidence level for this determination For semiconducting materials, the spatial resolution of this technique is a single atomic column. The chemical sensitivity is related to the amount of noise present in the experimental image, and the efficiency with which the signal can be extracted from it. In typical semiconductor samples ~ 30 atoms thick, single- and double- atom substitutions in individual atomic columns can be detected with ~60% and ~90% percent confidence, respectively. The combination of chemical lattice imaging and vector pattern recognition thus provides quantitative maps of the sample composition with near-atomic resolution and sensitivity. (For a more detailed discussion of the spatial resolution and sensitivity of this technique, see [2] and the article in symposium: *Resolution in the Electron Microscope*).

Fig. 1 shows a typical chemical lattice image and its associated quantitative chemical map, directly revealing the compositional change across a GaAs quantum well sandwitched between two Al_4Ga_6As barriers. Using such quantitative chemical maps, it is straightforward to deduce the composition profile atomic plane by atomic plane as a particular compositional inhomogeneity is approached and crossed. Fig. 2 shows the In concentration profile across two (strained) $Al_xIn_{1-x}As/Al_{48}In_{52}As$ layers. This profile demonstrates the remarkable accuracy with which the composition of individual atomic planes can now be measured. When profiles from annealed and unannealed samples are obtained, interdiffusion coefficients as small as $10^{-22} cm^2/s$ can be measured in regions as small as $10^{-19} cm^3$ in volume [4]. The ability to map compositional changes at high spatial resolution and sensitivity allows the microscopic examination of hitherto unexplored areas of materials science [4,5,6].

REFERENCES

[1]   A. Ourmazd et al, Phys. Rev. Lett. (1989) 62, 933.
[2]   A. Ourmazd et al, Ultramicroscopy (1991) 34, 237.
[3]   A. Ourmazd, D.W. Taylor, M. Bode, and Y. Kim, Science (1989) 246, 1571.
[4]   Y. Kim et al, Phys. Rev. Lett. (1989) 63, 636.
[5]   M. Bode et al, Mat Res. Soc. Symp. Proc. (1990) 157, 197.
[6]   F.H. Baumann et al, Bulletin of the American Physical Soc. (1991) 36, 474.
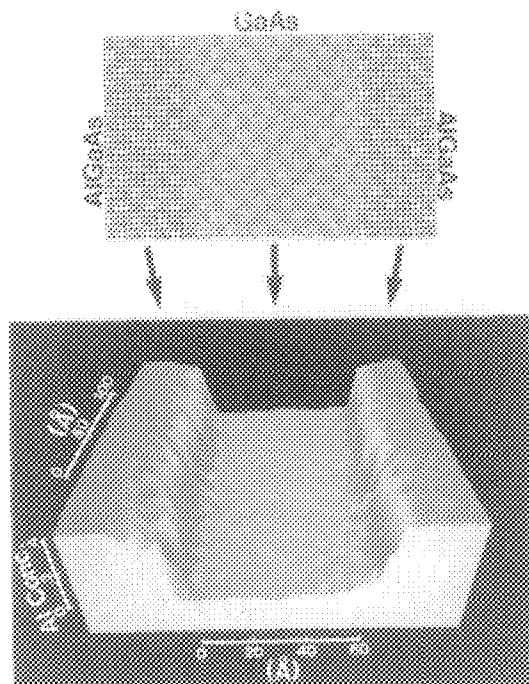
Fig. 1 **Top**: Chemical lattice image of a GaAs quantum well between two AlGaAs barriers, and the resultant interfaces. Analysis of such images by pattern recognition techniques directly yields the local composition of the sample at near atomic resolution and sensitivity. **Bottom**: Three-dimensional representation showing a quantitative chemical map obtained in this way. Height represents the local composition, and color changes represent three standard deviation changes in the signal, i.e. changes in composition with error probability of less than 3 parts in 10^3. *(The quantum well was grown by J Cunningham, chemically imaged by Y. Kim, and analyzed by A. Ourmazd, and D.W. Taylor, at AT&T Bell Labs).*
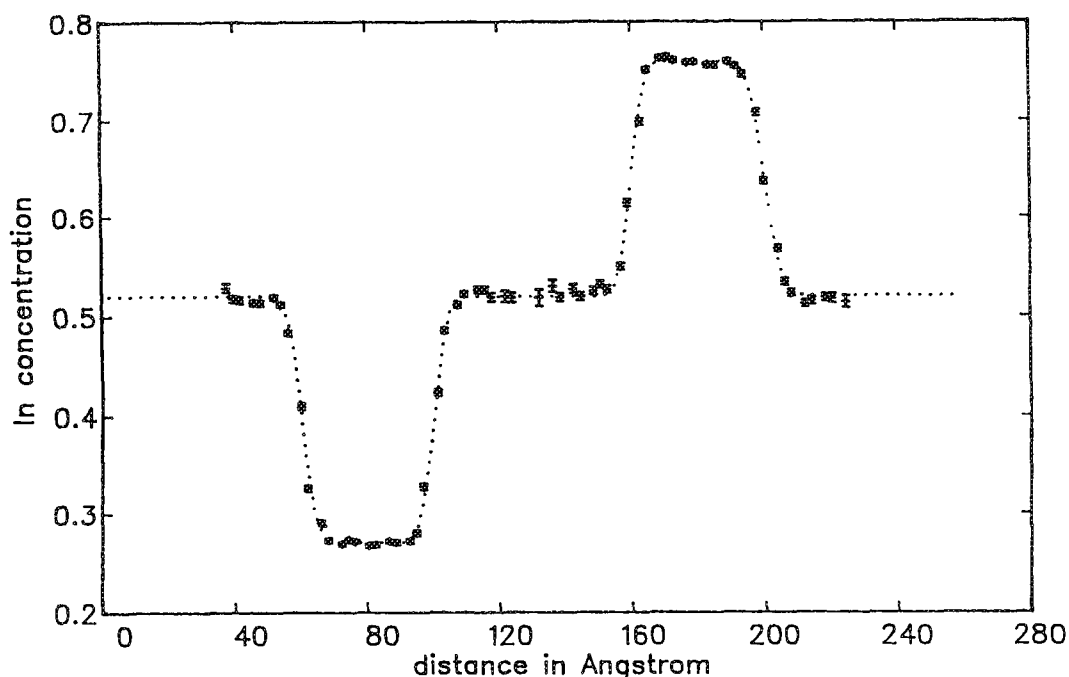
Fig. 2 Indium concentration profile across two $Al_x In_{1-x} As$ layers imbedded in an $Al_{48} In_{52} As$ matrix. Each measurement refers to a 0.15 μm segment of an individual atomic plane. The error bars represent ~60% confidence levels. *(Courtesy of F.H. Baumann, AT&T Bell Labs).*

518

MICROSTRUCTURAL CHARACTERIZATION OF InGaAs/GaAs QUANTUM WELLS GROWN AT LOW SUBSTRATE TEMPERATURES

C.M.Sung, B.Elman, K.J.Ostreicher, J.Hefter, and Emil S.Koteles
GTE Laboratories, 40 Sylvan Road, Waltham, MA 02254

The composition and thickness of $In_xGa_{1-x}As/GaAs$ quantum wells play an important role in the determination of their optical and electronic properties[1]. $In_xGa_{1-x}As/GaAs$ single quantum wells (SQWs) grown at low substrate temperatures with various In compositions (x) and well thicknesses were investigated by reflected high energy electron diffraction (RHEED) and photoluminescence (PL) techniques to determine when the critical thickness for pseudomorphic growth was exceeded. Cross-sectional TEM methods were employed to directly determine the critical layer thickness of InGaAs on GaAs and the presence of the dislocations generated in these layers.

The samples were grown by MBE on semi-insulating (100) GaAs substrates at substrate temperatures of $410^{\circ}C$ and $460^{\circ}C$. They consisted of undoped SQWs and barriers in which the well width was varied from 1 nm to 22 nm. The In composition in the well layers was varied from 0.3 to 0.5. The growth rates and In compositions were deduced from RHEED intensity oscillation measurements[2]. Cross-sectional specimens for TEM studies were prepared in the usual manner, by mechanical thinning followed by Ar^+ ion milling. A Philips EM400T operated at 120 keV was used to observe the specimens.

The accurate measurement of the layer thicknesses by TEM requires that the crystal be imaged under the appropriate diffraction conditions. For instance, interface flatness can be directly monitored at a resolution of ~ 1 nm by using (002) dark field images of cross sections to provide contrast between the different layers[3]. A weak beam dark field (WBDF) imaging technique was also used for the characterization of interfacial roughness and dislocations near the QWs. Very good agreement between the PL and TEM results was observed for the whole range of QW thicknesses. The PL peaks of a sample (x=0.3) grown at $460^{\circ}C$ were narrow, indicating that all four QWs were lattice-matched to the substrate (strained). Notice that the 22 nm SQW exceeds the critical thickness for normal growth temperatures by at least a factor of seven. Theoretical curves (transition energies vs. QW width) with and without strain are shown by solid and dashed lines, respectively in Fig.1. In addition, experimental PL peak energies are plotted as a function of nominal (open circles) and actual (closed circles, measured by TEM) QW widths. The cross-sectional image of the sample used in Fig.1 revealed that all four QWs were strained (Fig.2).

Samples of $In_xGa_{1-x}As/GaAs$ QWs (x=0.4, 0.45, and 0.5) were grown in order to investigate the limitations of low temperature MBE growth. The PL peaks indicated that $In_{0.45}Ga_{0.55}As/GaAs$ QWs of 2.5 nm and thicker were partially relaxed, while no visible relaxation was observed by TEM for the 2.5 nm thick QW (Fig. 3). This discrepancy may result from differences in resolution between the PL and TEM techniques since a local area was observed by TEM as compared to PL. TEM can, however, easily verify a large number of dislocations such as from the 10 nm wide QW in $In_{0.5}Ga_{0.5}As/GaAs$ where no PL was observed due to the very high density of dislocations. The boundary between strained and relaxed regions in the layer thicknesses vs. In composition is shown in Fig. 4. The results of PL and TEM for strained and relaxed layers are indicated by closed and open circles respectively. The steep part of the boundary appears to shift from the x=0.25-0.3 range (at normal temperature growth) to the x=0.4-0.45 range (at low temperature growth). Low temperature data (at x > 0.45) seem to approach Matthews and Blakeslee's double-kink curve[4] while for x>0.3 high temperature results are in good agreement with Matthews and Blakeslee's single kink curve (i.e. single heterointerface relaxation mechanism).

In summary, the low temperature growth produced high quality SQWs and increased the x value of the transition between pseudomorphic and relaxed regions compared with normal growth conditions. These results were confirmed by cross-sectional TEM, indicating that critical thickness at low substrate temperature growth can be increased by at least a factor of seven with no noticeable development of dislocations compared with normal growth temperature.

References
1. P.Melman, et al, Appl. Phys. Lett., 55 (1989), 1436.
2. B.Elman, et al, Appl. Phys.Lett., 55 (1989) 1659.

3. S.Wang, et al, to be published in Superlattice and Microstructure.
4. J.W.Matthews and A.E.Blakeslee, J.Cryst.Growth, 27(1974) 118.
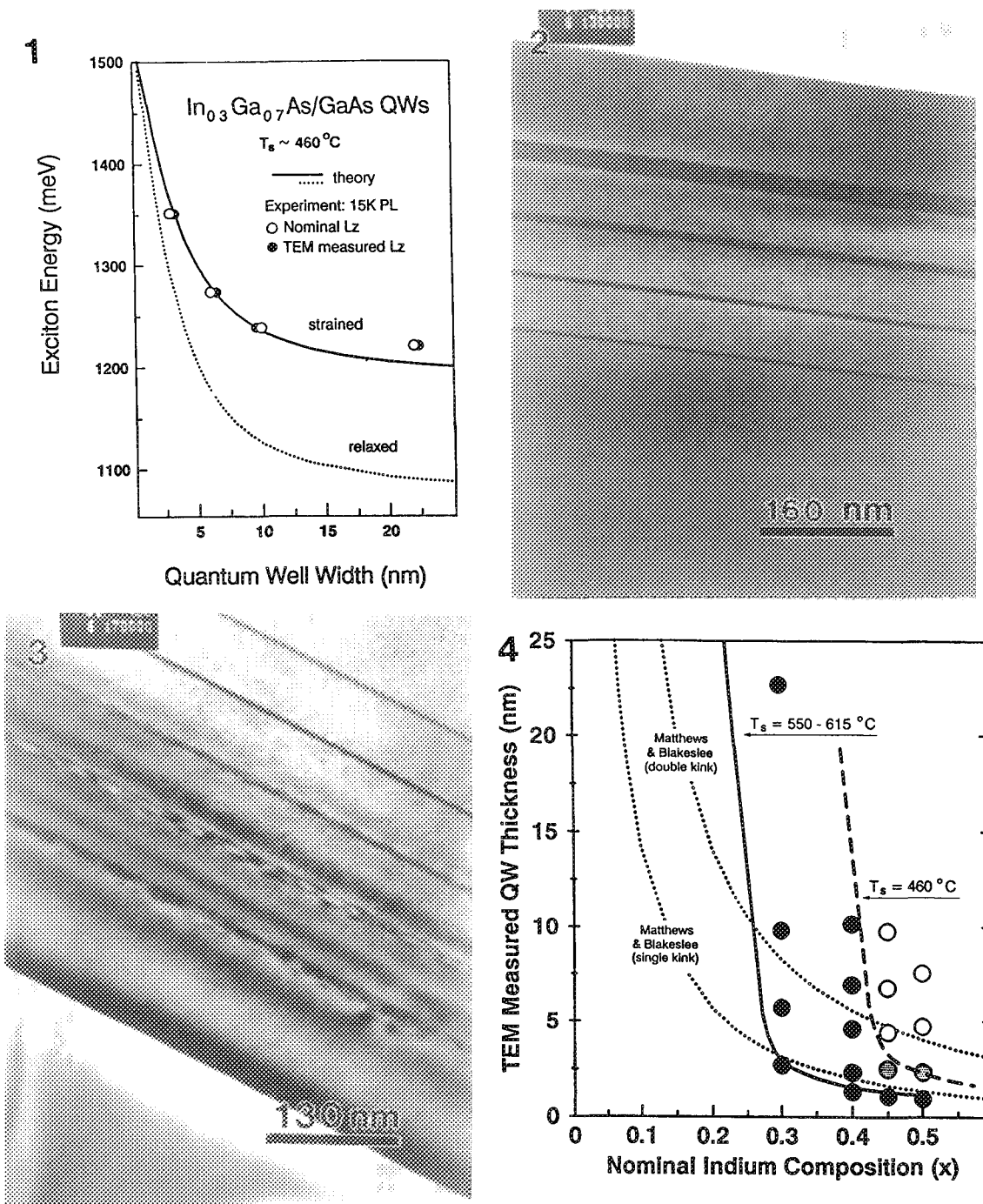
FIG.1. Theoretical curves for transition energies vs. QW width for $In_{0.3}Ga_{0.7}As/GaAs$ SQWs, with and without strain.

FIG.2. Cross-sectional microstructure of a sample containing four $In_{0.3}Ga_{0.7}As/GaAs$ SQWs grown at T_S=460 °C.

FIG.3. TEM micrograph of a sample containing four $In_{0.45}Ga_{0.55}As/GaAs$ SQWs grown at T_S=460 °C.

FIG.4. Calculated (dotted curves) and measured curves of critical layer thickness as a function of nominal In composition for $In_xGa_{1-x}As/GaAs$. Solid and dashed curves are the boundaries between lattice matched (to the left) and relaxed (to the right) layers for normal and low substrate temperature respectively.

A STUDY OF GaAs/Sc$_{0.3}$Er$_{0.7}$As/GaAs HETEROSTRUCTURES GROWN ON NOVEL GaAs SUBSTRATE ORIENTATIONS

Jane G. Zhu, Chris J. Palmstrøm*, and C. Barry Carter

Department of Materials Science and Engineering, Cornell University, Ithaca, NY 14853
* Bellcore, 331 Newman Springs Road, Red Bank, NJ 07701

Compound metallic materials, such as rare-earth (*RE*) monopnictides, are thermally stable and have lattice constants close to those of III-V semiconductors. These materials have been studied in the recent a few years.[1] Epitactic ErAs,[2,3] Sc$_x$Er$_{1-x}$As,[4] ErP$_x$Sb$_{1-x}$,[5] and ErP$_{0.6}$As$_{0.4}$ (ref. 6) have been grown on GaAs by molecular beam epitaxy (MBE). By mixing rare-earth elements or group V elements, or both, rare-earth pnictides can be lattice-matched to almost all group IV, III-V and II-VI semiconductors. Lattice-matched growth of Sc$_x$Er$_{1-x}$As/GaAs, for example, can be obtained using the composition x=0.32.[4] It has been demonstrated that the rare-earth arsenides can be grown on (100) GaAs in a layer-by-layer mode with very good crystal quality, but the GaAs grown on the rare-earth arsenides has far inferior quality to meet the requirement of novel devices.[7] Island growth of GaAs on *RE*As/GaAs has been reported.[8,9]

In the present study, lattice-matched GaAs/Sc$_{0.3}$Er$_{0.7}$As/GaAs heterostructures have been grown by MBE on GaAs substrates with different orientations, including (100), (110), (111), (211), (311) and (511), and characterized using transmission electron microscopy (TEM). The wetting of GaAs on Sc$_{0.3}$Er$_{0.7}$As is significantly improved by growing on (111) substrates instead of (100) substrates. However, twins are observed at both the GaAs/Sc$_{0.3}$Er$_{0.7}$As and the Sc$_{0.3}$Er$_{0.7}$As/GaAs (111) interfaces. Figure 1 shows a plan-view bright-field image from a sample grown on (311)A GaAs substrate with 5.6 nm (average thickness) of GaAs deposited on Sc$_{0.3}$Er$_{0.7}$As(5.6 nm)/GaAs at 490°C. The regions with bright contrast are areas without GaAs on Sc$_{0.3}$Er$_{0.7}$As. The close-to-rectangular areas with the darkest contrast, which are parallel to <01$\bar{1}$> direction, are the projections of inclined {111} microtwins in the top GaAs. In contrast to the growth on (100) Sc$_{0.3}$Er$_{0.7}$As, the coverage of GaAs on Sc$_{0.3}$Er$_{0.7}$As is much better for the samples grown on (311) orientation. A cross-section high-resolution image from another sample grown on (311)A GaAs is shown in Fig. 2. The epitactic crystalline quality of the top GaAs layer has been improved substantially (comparing with the samples grown on (100) GaAs substrates) although there are some stacking faults and microtwins on {111} planes. The ledges and steps with {100} and {111} character on Sc$_{0.3}$Er$_{0.7}$As surface may help the nucleation of epitactic GaAs on Sc$_{0.3}$Er$_{0.7}$As.

References

1. T. Sands et al., Mat. Sci. Reports 5(1990)99.
2. C. J. Palmstrøm et al., Appl. Phys. Lett. 53(1988)2608.
3. J. D. Ralston et al., J. Appl. Phys. 68(1990)2176.
4. C. J. Palmstrøm et al., Appl. Phys. Lett. 56(1990)382.
5. A. Guivarc'h et al., Electron. Lett. 25(1989)1050.
6. A. Le Corre et al., J. Cryst. Growth 105(1990)234.
7. J. G. Zhu et al., Appl. Phys. Lett. 56(1990)1323.
8. J. G. Zhu et al., Mat. Res. Soc. Symp. Proc. 198(1990)177.
9. T. G. Finstad et al., to be published in Mat. Res. Soc. Symp. Proc. (1991).
10. JGZ acknowledges support by the Semiconductor Research Corporation Center for Microscience and Technology under grant No. 90-SC-069. The electron microscopes are part of a central facility provided by the Materials Science Center at Cornell and are supported, in part, by the National Science Foundation.

Fig. 1. Plan-view image of GaAs on $Sc_{0.3}Er_{0.7}As$(5.6 nm)/GaAs grown on (311)A GaAs substrate.
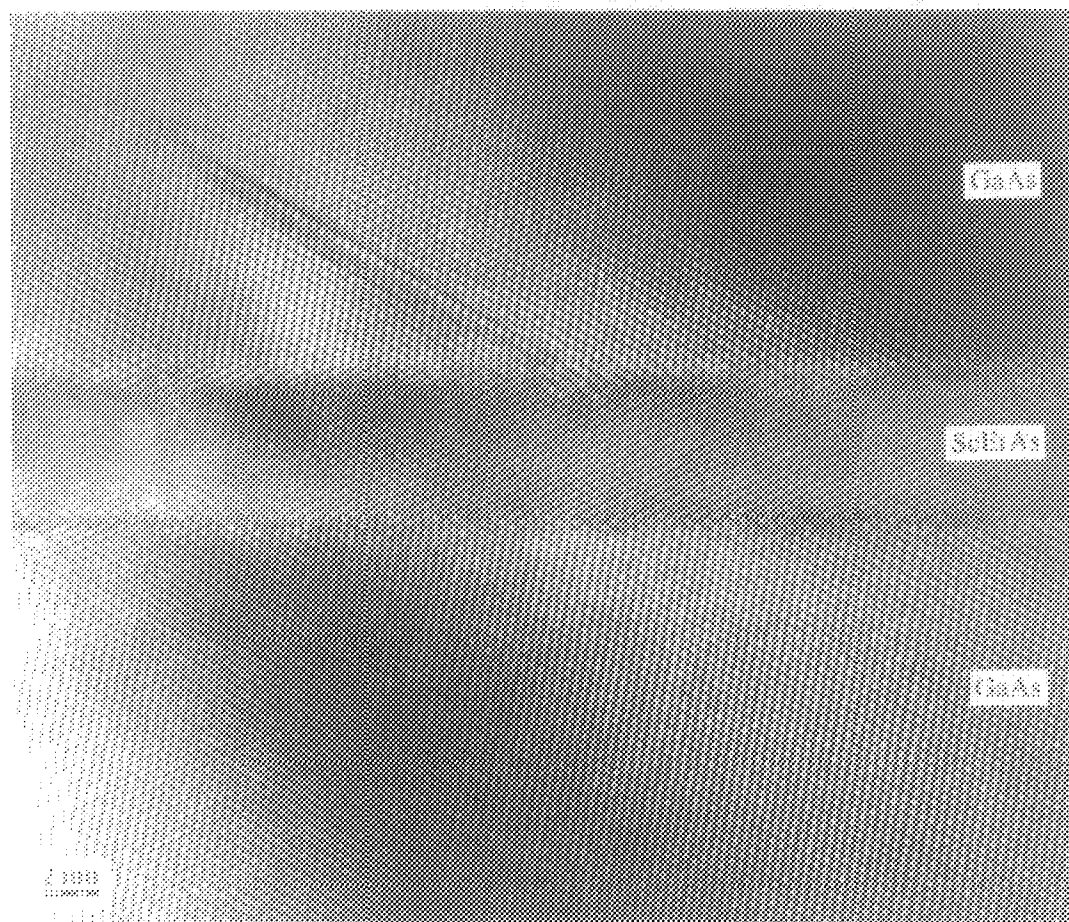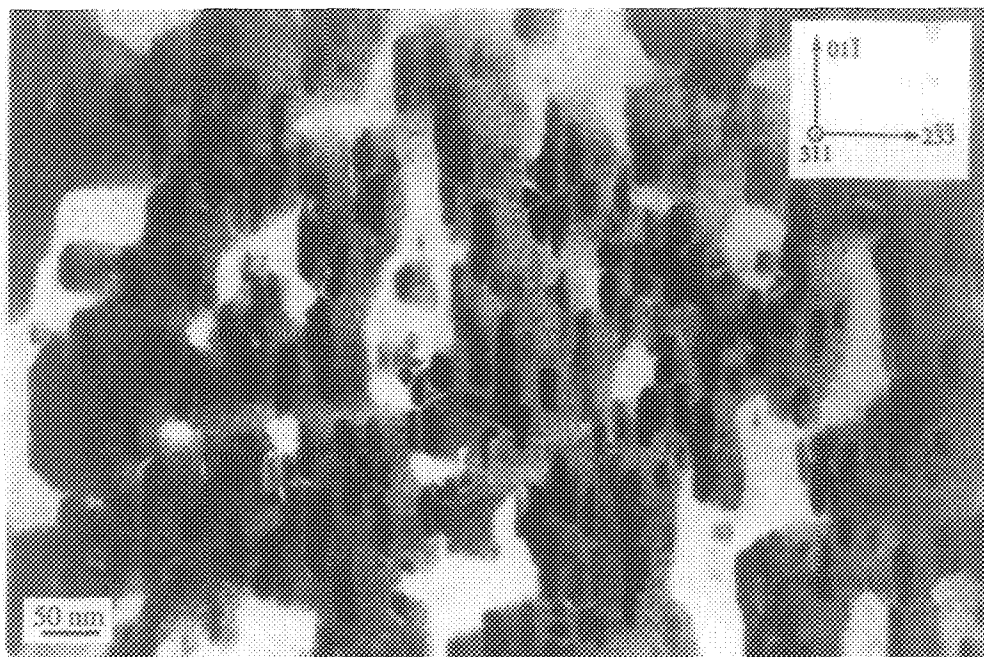
Fig. 2. Cross-section image of GaAs/$Sc_{0.3}Er_{0.7}As$/GaAs grown on (311)A GaAs substrate.

STRUCTURAL ASPECTS OF SILICON DIFFUSION IN QUATERNARY III-V THIN-FILM SEMICONDUCTORS

F. A. Ponce, R. L. Thornton and G. B. Anderson

Xerox Palo Alto Research Center, Palo Alto, CA 94304

The InGaAlP quaternary system allows the production of semiconductor lasers emitting light in the visible range of the spectrum. Recent advances in the visible semiconductor diode laser art have established the viability of diode structures with emission wavelengths comparable to the He-Ne gas laser. There has been much interest in the growth of wide bandgap quaternary thin films on GaAs, a substrate most commonly used in optoelectronic applications. There is particular interest in compositions which are lattice matched to GaAs, thus avoiding misfit dislocations which can be detrimental to the lifetime of these materials. As observed in Figure 1, the $(Al_xGa_{1-x})_{0.5}In_{0.5}P$ system has a very close lattice match to GaAs and is favored for these applications.

In this work, we have studied the effect of silicon diffusion in GaAs/InGaAlP structures. Silicon diffusion in III-V semiconductor alloys has been found to have an disordering effect which is associated with removal of fine structures introduced during growth[1-2]. Due to the variety of species available for interdiffusion, the disordering effect of silicon can have severe consequences on the lattice match at GaAs/InGaAlP interfaces.

The material under study was a 20nm GaAs film grown on a 2μm $Al_{0.3}Ga_{0.2}In_{0.5}P$ film on a GaAs substrate. The films were grown by OMVPE at approximately 750°C. The silicon source was achieved by deposition of a Si film followed by a Si_3N_4 capping layer. Diffusion was performed at 850°C for 24 hours, resulting in silicon diffusion to a depth of approximately 1.2μm into the crystal.

The as-grown AlGaInP film exhibited a well ordered structure shown in Figure 2. The ordering is of the Cu-Pt type[3-4], with a superlattice along $(\frac{1}{2}\frac{1}{2}\frac{1}{2})$ planes and a interplanar distance of 0.646nm. This ordering corresponds to Al and Ga on the same {111}A lattice planes alternating with In {111}A planes. In contrast, the GaInP quantum well in Figure 2 does not show the superlattice structure. The GaAs/AlGaInP interface is strongly affected by the silicon diffusion. Figure 3 shows the structure before and after the diffusion. The unavoidable lattice mismatch which results from the interdiffusion acts as a marker for the interface. The misfit dislocations at the diffusion boundary show the existence of a sharp boundary instead of the expected gradual diffusion profile. This indicates that diffusion on each layer is much faster than across the misfit dislocation boundary. The lattice mismatch in figure 3b is estimated from the separation of misfit dislocations to be 2.2%, and it is thought to be related to In and P diffusing into the GaAs layer. Long range diffusion into the film generates a small lattice mismatch distributed over relatively long distances. Due to the long-range diffusion, dislocations get introduced deep into the crystal as shown in figure 4. These dislocations are detrimental to the electrical and optical characteristics of the film. There is much work still to be done in order to understand the origin and nature of dislocations resulting from the processes here described.

References

1. J. E. Epler, F. A. Ponce, F. J. Endicott, and T. L. Paoli, Appl. Phys. Lett. 64, 3439 (1988).
2. R. L. Thornton, F. A. Ponce, G. B. Anderson and H. F. Chung. Mat. Res. Soc. Proc. 198, 85 (1990).
3. M. Kondow, H. Kakibayashi and S. Minagawa, J. Cryst. Growth 88, 291 (1988).
4. S. R. Kurtz, J. M. Olson and A. Kibbler, Appl. Phys. Lett. 54, 718 (1989).
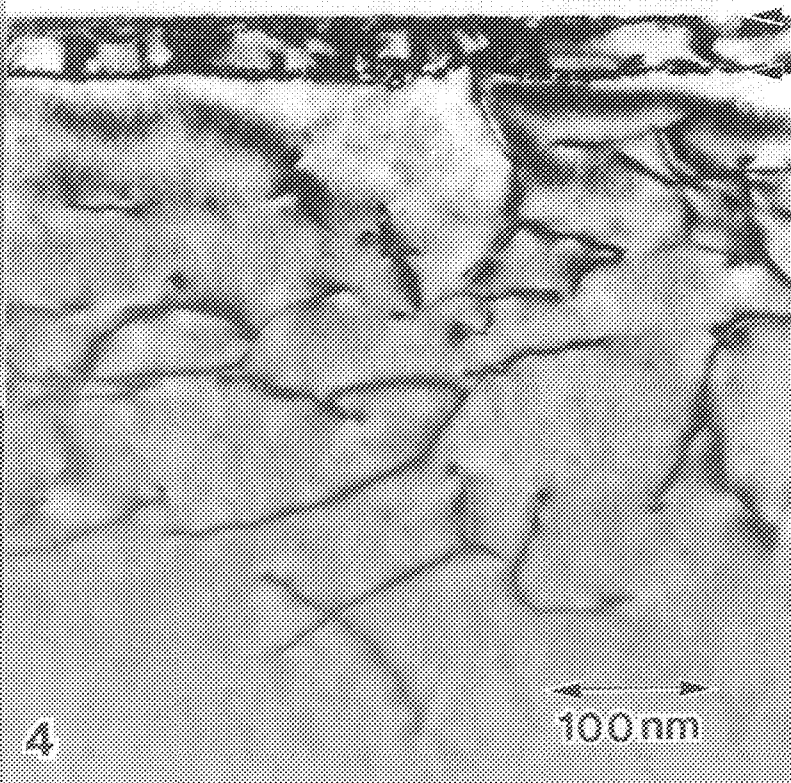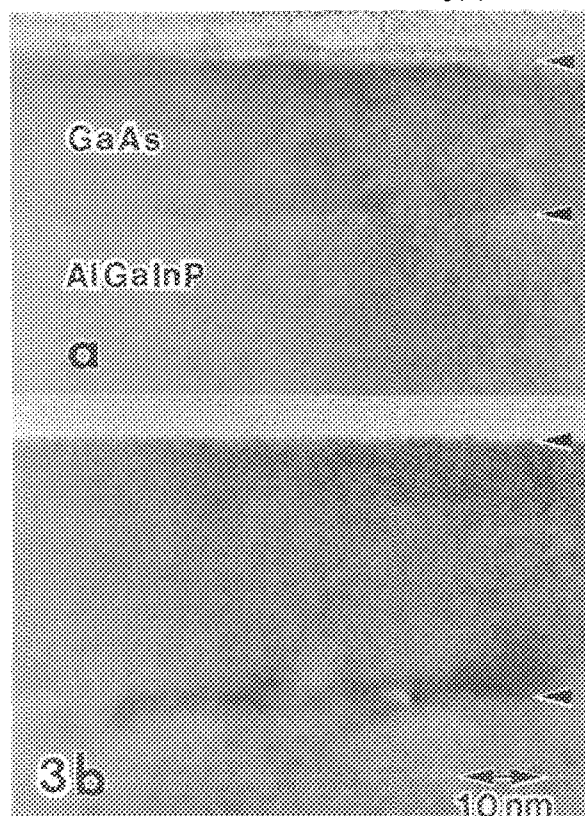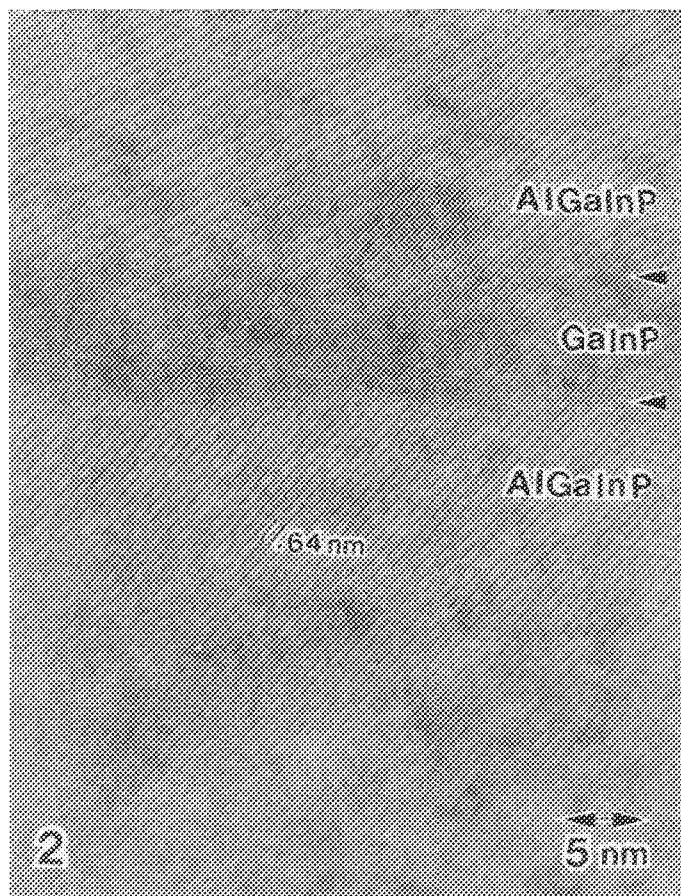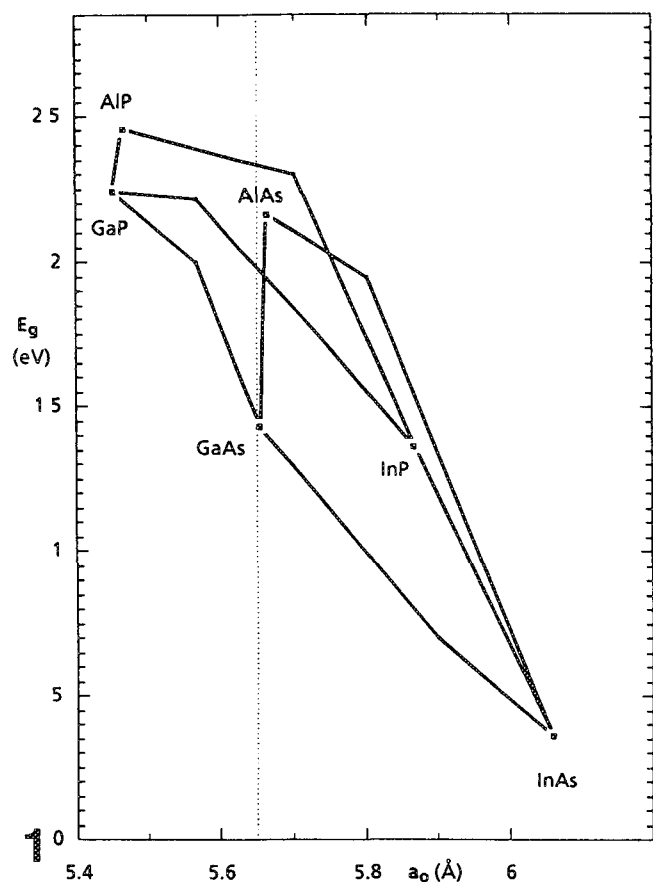
FIG. 1.--Energy gap and lattice constant for the Al-Ga-In-As-P system.
FIG. 2.--GaInP well in the AlGaInP film. Notice double periodicity along {111} in the film.
FIG. 3.--GaAs/AlGaInP interface (a) before and (b) after annealing treatment.
FIG. 4.--Threading dislocations in the AlGaInP film.

DEFECTS IN MBE GROWN InAs$_x$Sb$_{1-x}$ STRAINED LAYER SUPERLATTICES

S. Chadda*, A. K. Datye*, and L. R. Dawson+

* Department of Chemical Engineering, University of New Mexico, Albuquerque, NM 87131
+ Sandia National Laboratories, Albuquerque, NM 87185

III-V alloy devices are being considered for applications as infrared detectors, by several research groups[1-7] due to processing advantages over II-VI alloy devices. InAs$_{0.4}$Sb$_{0.6}$ has the lowest band gap at 77 K among all III-V compounds, which corresponds to a cut off wavelength of 9 µm. The use of strained layer superlattices (SLS) was first proposed by Osbourn[8] for lowering the band gap and achieving absorption at wavelengths greater than 12 µm at 77 K. A schematic diagram of the device is shown in figure 1. It was grown by Molecular Beam Epitaxy (MBE) at 425 °C and it consists of a p-n junction embedded in a InAs$_{0.15}$Sb$_{0.85}$/InSb SLS with layers of equal (110 Å) thickness. The n and p type dopants were S (PbS) and Be respectively. The active device SLS was grown on a composition graded strain relief buffer on the (100) face of an InSb substrate. The samples were sliced, thinned, polished, dimpled and ion milled for making cross-section Transmission Electron Microscope (TEM) samples.

Figure 2 shows a bright field transmission electron micrograph in a two beam condition with g = [400]. The active device region i.e. the top 4.5 microns was defect free and all the defects were contained in the buffer region. However, other areas of the sample (Fig. 3) showed macroscopic cracks which extended right across the buffer and the active device region. These cracks are not desirable as they make the device unusable. The next sample was made at the same conditions as the previous one except that the buffer was grown with Migration Enhanced Epitaxy (MEE). Figures 4 a, b, and c are bright field micrographs with g = [200], [220] and [111] respectively. A large defect density was observed at the interface of the buffer and the active device. These defects were "wiggly" having line directions of [100] and a majority of them terminated at the interface between the n type doped and the un-doped material. The defects were not visible with g = [200] (Fig. 4 a) and the burgers vector of these dislocations was found to be [011] leading us to believe that they are edge dislocations. The invisibility of the defects for g = [200] is consistent with these being edge dislocations with a burgers vector of 1/2 <110>. Further work is being performed on other samples grown by MBE to better understand the role of molecular enhanced epitaxy in the injection of dislocations.

References

1. L. R. Dawson, J. Vac. Sci. Technol. B (1986) 4 (2), 598.
2. S. R. Kurtz, L. R. Dawson, T. E. Zipperian, and S. R. Lee, Appl. Phys. Lett. (1988) 52, 1581.
3. P. K. Chiang and S. M. Bedair, Appl. Phys. Lett. (1985) 46, 383.
4. M. Y. Yen, B. F. Levine, C. G. Bethea, K. K. Choi, and A. Y. Cho, Appl. Phys. Lett. (1987) 50, 927
5. L. O. Bubulac, A. M. Andrews, E. R. Gertner, and D. T. Chueng, Appl. Phys. Lett. (1980) 36, 734
6. L. R. Dawson, G. C. Osbourn, T. E. Zipperian, J. J. Wiczer, C. E. Barnes, I. J. Fritz, and R. M Biefeld, J. Vac. Sci. Technol. B (1984) 2 (2), 179
7. S. Tsukamato, P. Bhattacharya, Y. C. Chen, and J. H. Kim, J. Appl. Phys. (1990) 67, 6819
8. G. C. Osbourn, J. Vac. Sci. Technol. B (1984) 2 (2), 176

Fig. 1

Active device SLS

110 Å InSb

110 Å InAs$_{0.15}$Sb$_{0.85}$

Composition graded buffer SLS

In As$_x$Sb$_{1-x}$

Substrate

p type	
un-doped	2.5 μm
n type	1 μm
x = 0.10	
x = 0.08	
x = 0.06	
x = 0.04	
x = 0.02	0.5 μm
InSb (100)	
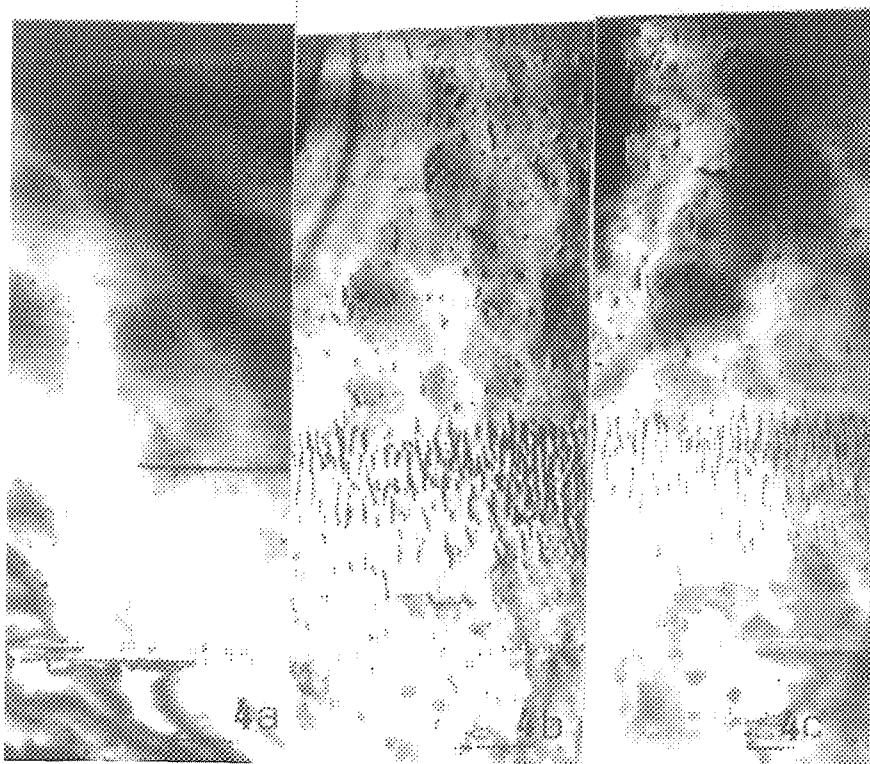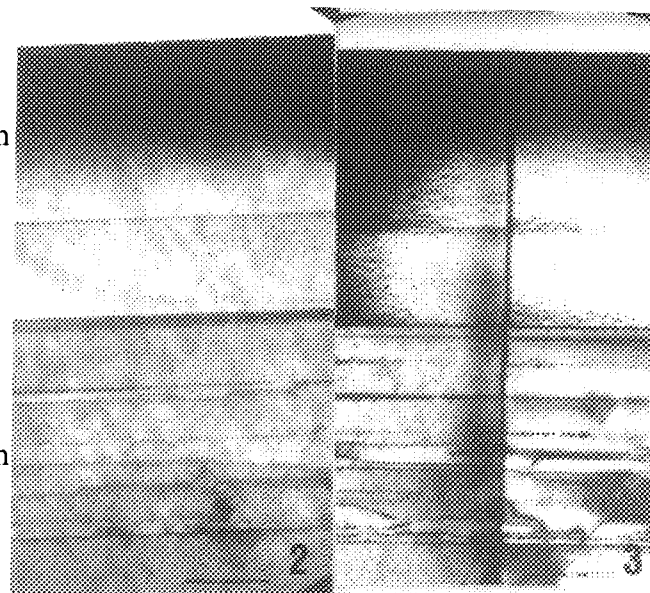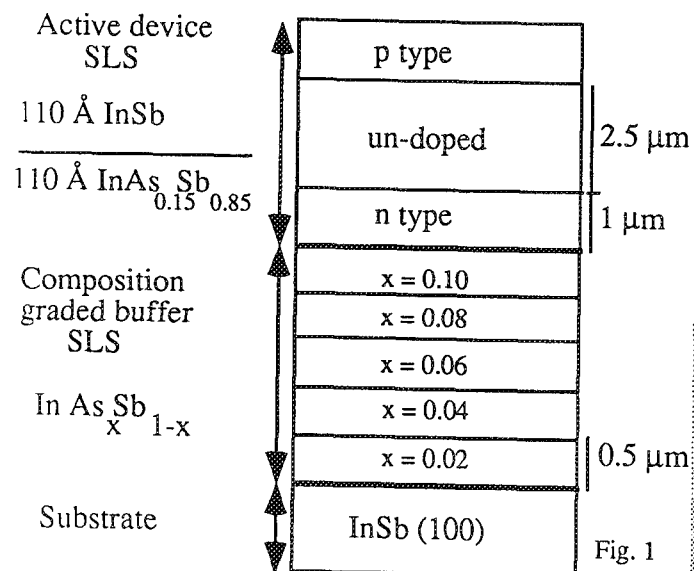
Figure 1. Schematic diagram of device.
Figure 2. Bright field micrograph with g = [400] showing no defects in active device.
Figure 3. Bright field micrograph with g = [400] showing macroscopic cracks.
Figure 4 Bright field micrographs of sample grown with MEE with a) g = [200], b) g = [220], and c) g = [111].
Note: Bar is 1 μm in all micrographs.

ELECTRON MICROSCOPY OF GaAs GROWN ON Si- AND Ge-BASED SUBSTRATES

D.P. Malta, J.B. Posthill, M.L. Timmons, P.R. Sharps, R. Venkatasubramanian, and R.J. Markunas

Research Triangle Institute, Research Triangle Park, NC 27709-2194

A GaAs-on-Si technology is desirable to take advantage of the mobility and direct bandgap of GaAs in combination with the crystalline quality, low cost and established technology of Si Differences in lattice constant (4.1%), thermal expansion coefficient (a factor of $\sim$ 3), and bonding polarity between the two materials can lead to problems such as· threading dislocation formation, thermally induced stress and delamination, and antiphase domain boundaries (APBs),[1] respectively. The lattice mismatch is responsible for the formation of (necessary) misfit dislocations which can concurrently create threading dislocations with typical densities in the range of 10^6 - $10^8 \mathrm{cm}^{-2}$. This density of electrically active defects in a device region is highly undesirable.

A proposed scheme for lattice mismatch accommodation and potential threading dislocation reduction has previously been reported in which each layer of a Si_xGe_{1-x} multilayer structure (MLS) is grown beyond the critical thickness with a progressively higher Ge composition than the previous layer [2] Fig. 1 shows schematically one possibility for this buffer layer structure. The lattice mismatch between layers is determined by their composition difference. In this manner, it may be possible to limit the formation of threading dislocations by limiting the lattice misfit (and therefore the required number of misfit dislocations) at each layer of the Si_xGe_{1-x} MLS In principle, GaAs could then be grown on a high quality Ge terminating layer

A 4-layer MLS was grown at 500°C on vicinal Si(100) tilted 4° off axis toward [011] by molecular beam epitaxy (MBE) with a base pressure of $\sim$ 2 × 10^{-10} Torr. Each layer was 500 nm thick Fig. 2 shows SEM topography and electron beam-induced current (EBIC) images of the structure. The cross-hatching in Fig. 2b is indicative of planar misfit dislocation: arrays. GaAs with an ultrathin InGaAsP prelayer was then grown on the Ge-terminated Si_xGe_{1-x} MLS by organometallic chemical vapor deposition. Fig. 3 shows topography and EBIC images of the heteroepitaxial GaAs film The pits in Fig. 3a were found in most cases to have electrically active defects associated with them (Fig 3c) Based on previous results[1], it is likely that regions that are both electrically active (dark regions in EBIC image) and recessed (secondary electron images) are associated with APBs. Apparently, not all APBs found in this layer are sufficiently electrically active to yield strong EBIC contrast. The visible, electrically active defect density of the GaAs-MLS-Si sample was determined to be $\sim$ $10^7 \mathrm{cm}^{-2}$ from the EBIC data

For comparison, a 50 nm Ge layer was grown on vicinal Ge(100) tilted 6° off axis toward [011] by MBE followed by the same GaAs(InGaAsP) deposition process Fig. 4 shows topography, EBIC, and cross-sectional TEM images of the GaAs film This film is shown to be of lower defect density.[3]

References

1. D P. Malta, et al., Proc. 12th Int. Congress for Electron Microscopy, Eds L D. Peachey and D B. Williams, vol. 4 (San Francisco Press, SF, 1990) 746.

2. J.B. Posthill, et al., Mater. Res. Soc Symp. Proc , vol. 198 (1990) 219.

3. The authors gratefully acknowledge the provision of part of the laboratory facilities used in this study by SDIO/IST through ONR (Contract No. N00014-86-C-0460). We are also pleased to thank J. Hancock and R. Pickett for technical assistance.
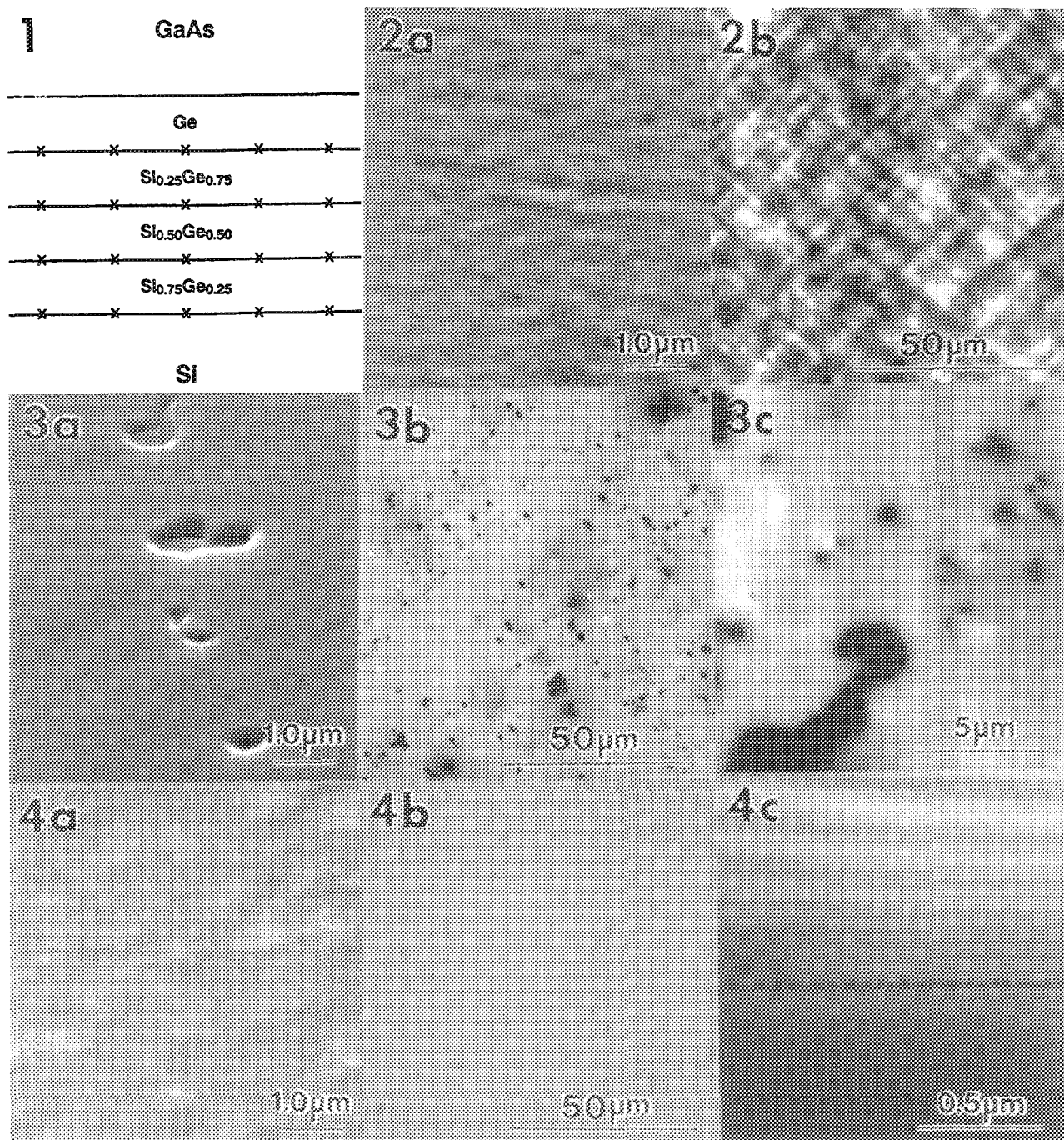
FIG. 1.--Diagram of potential Si_xGe_{1-x} multilayer structure (MLS) grown on silicon ("X" signifies misfit dislocations trapped in interfaces between Si_xGe_{1-x} epilayers).

FIG. 2.--SEM images of Ge-terminated Si_xGe_{1-x} MLS on Si ; (a) secondary electron, and (b) EBIC (14kV).

FIG 3.--SEM images of GaAs(InGaAsP) on Si_xGe_{1-x} MLS on Si; (a) secondary electron, and (b) and (c) EBIC (15kV). Dark regions in EBIC images indicate electrically active defects.

FIG. 4.--SEM images of GaAs(InGaAsP) on MBE Ge on Ge; (a) secondary electron, and (b) EBIC (15kV). Lack of contrast in EBIC image indicates a low electrically active defect density and is consistent with (c) cross-section TEM data.

528

POLISH - INDUCED DAMAGE IN GaAs: A SYSTEMATIC TEM INVESTIGATION

S. Yegnasubramanian and G. E. Carver

AT&T Bell Laboratories, Carter Road, Princeton, New Jersey 08540

Gallium Arsenide Integrated Circuit (IC) Technology demands extremely flat and almost "damage-free" GaAs wafers to maximize the yield in the manufacturing of ICs. These devices are fabricated on oriented surfaces of the crystals, which have been polished to a high degree of flatness and smoothness. The polishing procedures typically involve the use of abrasives successively to result in finer surfaces with a final chemical polishing step to remove the surface damage caused by the abrasives. However, if the final polishing step does not result in damage-free surfaces, local variations in the crystallographic orientation of the surface may lead to defective device structures. Extensive reviews are available in literature on the aspects of etching of GaAs substrates, including procedures for the preparation of polished substrates and on the revelation of defects by selective etchants [1].

The introduction of damage in the GaAs wafers may occur during sawing, lapping, chemical or mechanical polishing etc. It is extremely important to have a knowledge of the depth of such damage, which itself varies with the procedure that has caused the damage. A comprehensive investigation of polish-induced surface strain in <100> and <111> GaAs and InP has been reported [2], where the damage was induced by alumina powder polishing, followed by 1:4 syton in deionized water polish and finally a 0.1% bromine-methanol chemical polish. A comparison of TEM and Raman spectroscopy techniques to study the polish-induced damage in <100> GaAs has also been reported [3]. Some of the other techniques employed in the investigation of polish-damage in GaAs wafers are double-crystal X-ray diffractometry [4], photoluminescence [5], photon backscattering [6] and other optical techniques [7,8]. We present in this paper a systematic investigation of polish-induced damage in GaAs wafers from various stages of polishing such as slicing, lapping, mechanincal and chemomechanical polishing procedures, by TEM.

The following set of samples were characterized in the present investigation: all samples were 2-inch wafers of undoped, seimi-insulating GaAs; i. saw-cut samples (S-1); ii) samples lapped mechanically using alumina (L-1); iii) samples subjected to a half-polish using NaOCl and a grit (HP-1); iv) samples subjected to a final chemomechanical polish with NaOCl and a grit in a finer manner by two different groups, A and B (FP-1A and FP-1B) and v) a lapped commercial sample (C-1), as a reference. TEM specimens were prepared in vertical cross sections using standard procedures and imaged under a JEOL 2000FX microscope. Fig. 1 shows the dark-field image of the saw-cut sample. The surface roughness of the sample is estimated to be ~2 um and the depth of damage is seen even beyond 10 um. The damage density is estimated to be ~10^{10} cm^{-2} within the 2 um region near the surface and dropping off to 10^9-10^8 cm^{-2} between 3 to 5 um depth. The lapped sample exhibited regions of high near-surface damage (Fig. 2) and also regions with less damage. The half-polished samples exhibited a smooth surface with no discernible near-surface damage (Fig. 3). Fig. 4 shows the micrograph of the full polished sample from group A (FP-1A). The sample exhibits near-surface microcracks and sub-surface (~4 um) defects. Fig. 5 shows the micrograph of the full polished sample from group B (FP-1B). The sample exhibited a consistently smooth surface with no-discernible polish damage or cracks. The reference sample, C-1, shows high surface roughness and near-surface damage up to ~2 um (Fig. 6).

References

[1]   D. J. Stirland and B. W. Straughan, Thin Solid Films, (1976) 31, 139.

[2]   Z. Hang, H. Shen and F. H. Pollak, J. Appl. Phys., (1988) 64, 3233.

[3]   T. George, Z. L. Weber, E. R. Weber and F. H. Pollak, J.appl. Phys., (1990) 67, 4363.

[4]   H. Kuwamoto, D. E. Holmes and N. Otsuka, J. Electrochem. Soc, (1987) 134, 1579.

[5]   A. Karpol and B. Pratt, Solid State Commun., (1973) 12, 325.

[6]   R. M. Silva, F. D. Orazio, Jr., and J. M. bennett, Semicond. Int. (1986) 81 (July).

[7]   C. E. Jones and A. Ray Hilton, J. Electrochem. Soc., (1965) 112, 908.

[8]   P. J. Zanzucci and M. T. Duffy, Appl. Opt., (1978) 117, 3477.

200 nm
Fig 1

100 nm
Fig 2

100 nm
Fig 3

100 nm
Fig 4

100 nm
Fig 5

300 nm
Fig 6

530
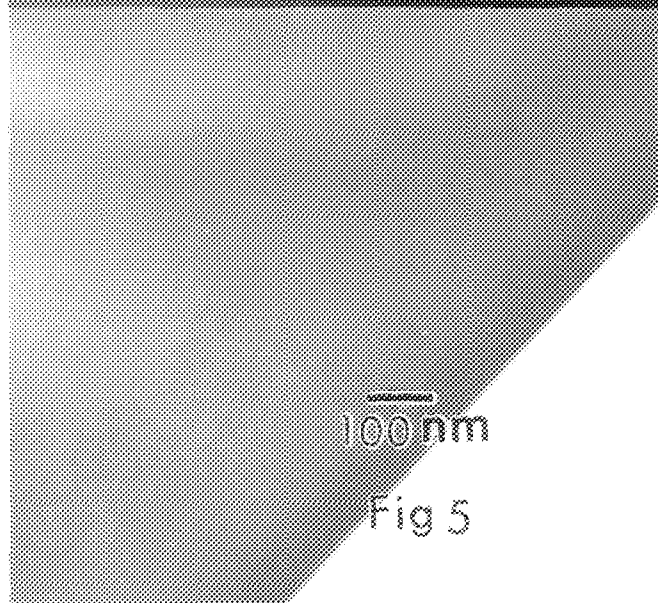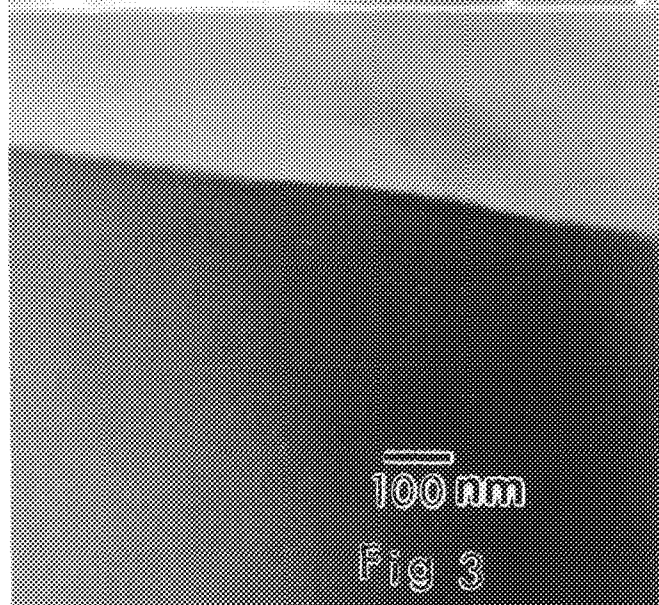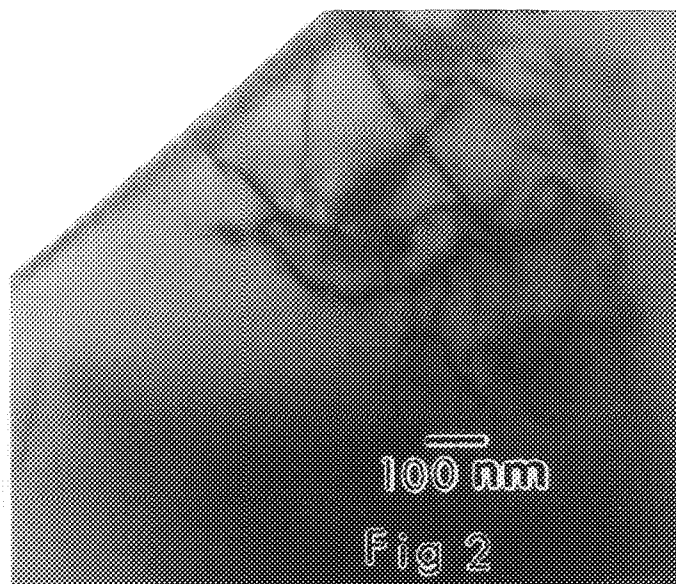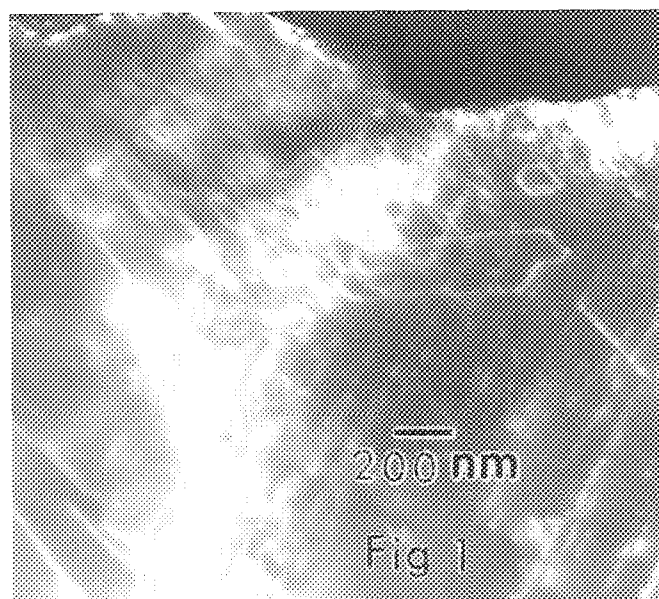
AMORPHOUS-PHASE FORMATION AND INITIAL REACTIONS AT Pt/GaAs INTERFACES

Dae-Hong Ko and Robert Sinclair

Department of Materials Science and Engineering, Stanford University, Stanford, CA 94305

It is now well known that many metals form a 1-2nm amorphous interdiffused layer when deposited onto clean Si surface, which grows upon annealing in some systems but crystallizes into stable, or metastable, phases in others [1,2]. Such behavior can be interpreted in terms of a solid-state amorphization, driven by a negative heat of mixing of the elements with the amorphous phase produced for kinetic reasons [3,4]. Some metal/compound semiconductor systems also show the same reaction behavior. Though there have been some reports, using electron diffraction, on the amorphous phase formation at metal-compound semiconductor interface upon low temperature annealing [5,6], because the expected thickness might only be several atomic layers, it is clear that high resolution transmission electron microscopy (HRTEM) is the most powerful technique to study such a phase[7,8]. This article reports on the amorphous phase formation and the initial stages of reaction occuring at Pt/GaAs interfaces upon annealing with HRTEM, and this is the most direct demonstration of solid state amorphization of a metal with a compound semiconductor.

A 500Å thick Pt thin film was formed by e-beam deposition. TEM cross sectional samples were made by a "cold" method to avoid any possible degradation, and were analyzed in a Philips EM430ST for *in situ* and ex situ HRTEM. In addition we used an AKASHI EM-002B microscope with a probe size of 20Å for microdiffraction and EDS analyses.

Fig. 1(a) is a high-resolution TEM micrograph of a cross section of the as-deposited Pt/GaAs sample, which shows a 2-3nm thick uniform amorphous intermixed layer between the crystalline platinum and the GaAs substrate. We have suggested that this layer is a Pt-GaAs intermixed layer, which is formed by solid-state amorphization reaction during the deposition of the platinum [8]. The amorphous interlayer grew uniformly to 4.5nm toward the GaAs substrate after annealing at 200°C for 30 min, and it shows the same amorphous appearance as the as-deposited sample. Fig. 1(b) shows that after annealing at 200°C for 90 min the intermixed layer grew to 5.5nm and that crystalline nuclei are formed at the region close to the platinum. The lattice spacing and interplanar angles of this phase as well as its location (below the native oxide) suggest that these crystallites are the Pt_3Ga phase. After further annealing for 12 hours at 200°C, the nucleation of another crystalline phase is observed in the intermixed layer, adjacent to the GaAs substrate (see fig. 1(c)). Cross lattice fringes of this crystalline phase correspond to those of $PtAs_2$. Annealing at 250°C results in a crystalline reaction at the platinum-GaAs interface producing a layered structure of Pt_3Ga and $PtAs_2$ between the unreacted Pt and the GaAs substrate (see fig1(d)). After higher temperature annealing at 500°C for 20min. the entire platinum film is consumed, and a bilayer of $PtGa/PtAs_2$ is the final structure on the GaAs substrate. The *in situ* annealing HRTEM experiments also show the growth (see fig. 2) and subsequent crystallization of an amorphous interlayer at the Pt/GaAs interface. The sequence and morphology of the reaction observed *in-situ* correspond to those observed in bulk-annealed samples.

Because platinum is not thermodynamically stable with GaAs, it reacts with GaAs, producing PtGa and $PtAs_2$ phases. Since the crystalline reaction was observed to occur above 250°C, the formation and the growth of an amorphous intermixed layer at the interface is an intermediate step to the crystalline reaction between Pt and GaAs. This finding is consistent with the results observed in a Au-La system[3], and a Ti-Si system[4], both of which are now accepted as examples of solid state amorphization. After the amorphous interlayer grew to some thickness, nucleation of the crystalline phases were observed. Since both Pt and Ga are mobile, Pt_3Ga is first nucleated at the region close to Pt. This phase is formed adjacent to crystalline Pt phase because of the local composition and because Pt_3Ga has similar structure and lattice parameter to the Pt phase. Consequently, the remaining interlayer becomes As rich and so $PtAs_2$ is nucleated after extended annealing at 200°C adjacent to the GaAs substrate.

In summary, a solid-state amorphization reaction and its subsequent crystallization upon low temperature

annealing were observed at the Pt/GaAs interface.

Refences

1. K. Holloway and R. Sinclair, J. Less-Common Metals 140 (1988) 139
2. K. Holloway et al., J. Vac. Sci. Techn. A7 (1989) 1479
3. R. Schwarz and W. Johnson, Phys. Rev. Lett. 51 (1983) 415
4. K. Holloway et al., Mat. Res. Soc. Proc., 187 (1991) 71
5. T. Sands et al., Appl. Phys. Lett. 50 (1987) 1346
6. F. Shiau and Y. Chang, Appl. Phys. Lett. 55 (1989) 1510
7   R. Sinclair et al., Inst. Phys. Conf. Ser. 100 (1989) 599
8. D. Ko and R. Sinclair, To be published in Appl. Phys. Lett.
9. This research is supported by the National Science Foundation (Grant No. DMR 8902232).
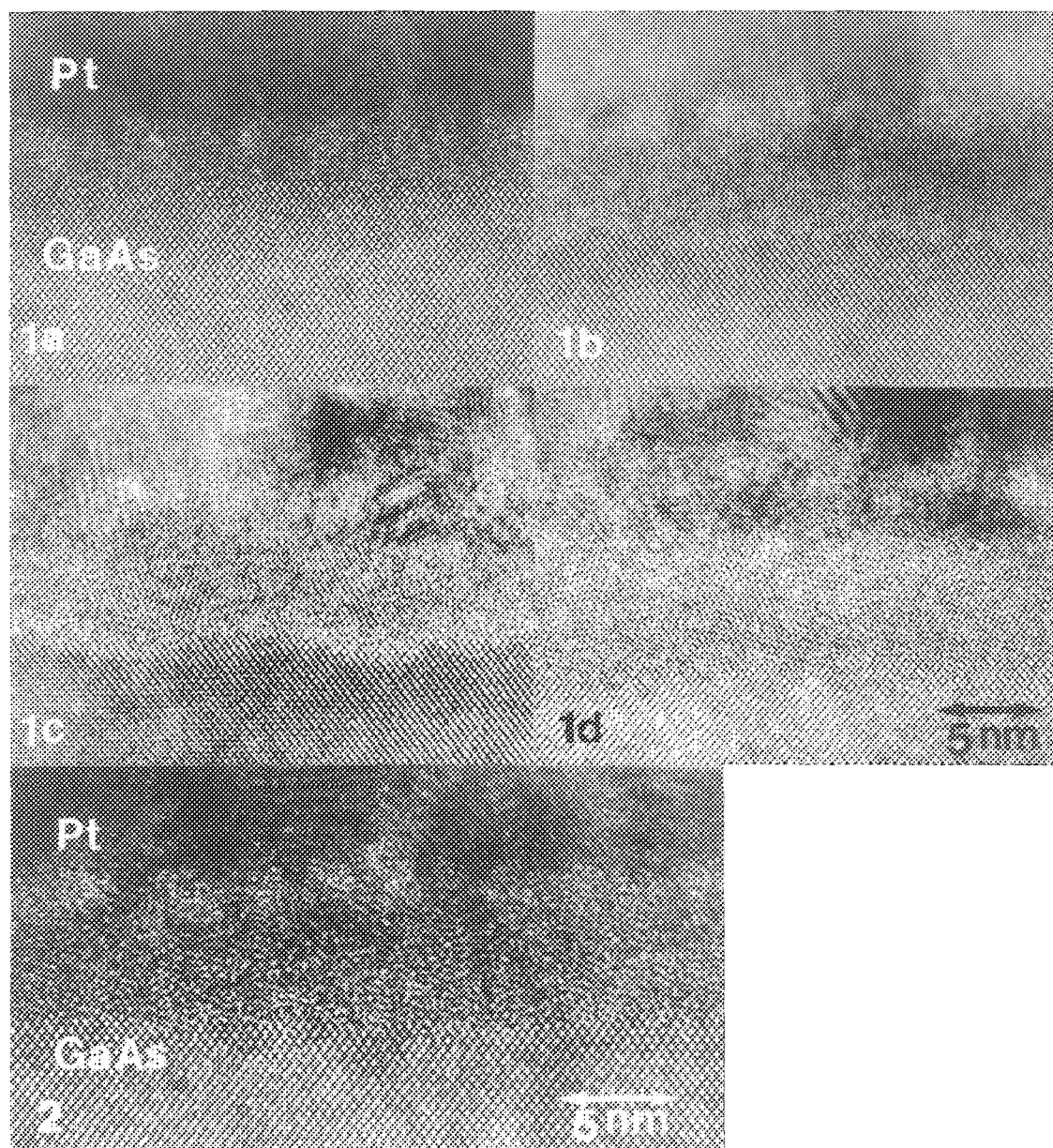
Fig. 1 Cross sectional HRTEM micrographs of the Pt/GaAs samples: (a) as-deposited, (b) annealed at 200°C for 90min, (c) annealed at 200°C for 12hrs, and (d) annealed at 250°C for 10 min.
Fig. 2 Cross sectional HRTEM micrograph of the Pt/GaAs sample *in situ* annealed in the microscope.

PHASE SEGREGATION IN GaAs LAYERS GROWN AT LOW TEMPERATURE

Zuzanna Liliental and Roar Kilaas

Lawrence Berkeley Laboratory, 1 Cyclotron Rd., Berkeley, CA 94720

GaAs device and circuit performance may be impaired by substrate conduction. One such effect, called sidegating, leads to undesirable cross-talk between neighboring devices. This problem can be avoided by isolating the active device layer from the substrate with a GaAs buffer layer grown by molecular beam epitaxy (MBE) at low temperatures (LT GaAs). The LT GaAs layers show high resistivity, a large trap density, and breakdown strengths about ten times that of semi-insulating GaAs. These layers are grown at a substrate temperature of ~ 200°C. A large (~1 at.%) excess of As in these as-grown layers causes an increase (~0.1%) in the GaAs lattice parameter.

The crystal structure of these layers is very sensitive to the growth parameters such as: growth temperature, As/Ga flux ratio and growth rate. With decreasing growth temperature a higher As concentration can be incorporated and only a smaller layer thickness of high crystal perfection can be grown. The layers grown below 200°C using a growth rate of 1µm/h and As/Ga flux ratio corresponding to a beam equivalent pressure ratio of 10 show specific defects with polycrystalline core (mixture of GaAs and As grains) surrounded by dislocations, stacking faults and microtwins. The density of these defects is increasing with layer thickness. For very low growth temperature the material is polycrystalline with As segregated at grain boundaries. The layers grown at 200°C or above do not show any line or extended defects, and their perfection is very encouraging for device application.

The technologically important semi-insulating properties of these layers are observed only after annealing. The annealing is generally part of the growth of an active device structure at 580-600°C on top of the LT GaAs layer. The annealed layers show a decrease of the lattice parameter to the substrate value. The reason of the lattice parameter change is the high density of As precipitates. Their density and their crystallographic structure depends on the growth parameters. Three types of precipitates were identified: a cubic As rich phase, hexagonal As, and amorphous precipitates.

With increasing As/Ga flux rate phase segregation can be observed in these layers. Two types of the precipitates (Fig.1a,b) with different As/Ga ratio can be observed: amorphous Ga rich precipitates and crystalline As rich precipitates. These precipitates are faceted on (111) GaAs planes. At each facet of the amorphous precipitate stacking faults are formed and partial dislocations propagate to the top of the layer, leaving behind stacking faults and microtwins. The crystalline precipitates are new ordered cubic phase. Large areas of the ordered phase was observed at the layer thickness where a deviation from the [001] growth direction to the [31-1] direction took place (Fig.1c). Optical diffraction patterns from such ordered structures show extra diffraction spots at 1/2 [1-11], 1/4 [13-3], and 1/4 [31-1]. A model of the atom arrangement explaining this ordered structure is shown in (Fig.1d). The calculated image and diffraction pattern associated with this image match the experimental image and the related diffraction pattern (Fig.1e). Each fourth (31-1) plane is occupied only by As atoms, whereas three other planes are equally occupied by As and Ga atoms. On these extra planes each As atom is boned to three As atoms and not to Ga atoms as it is observed in the GaAs structure. Ordered structures were predicted theoretically and observed experimentally in ternary semiconductors and in GeSi, however, this type of ordering is observed for the first time in semiconductor materials.
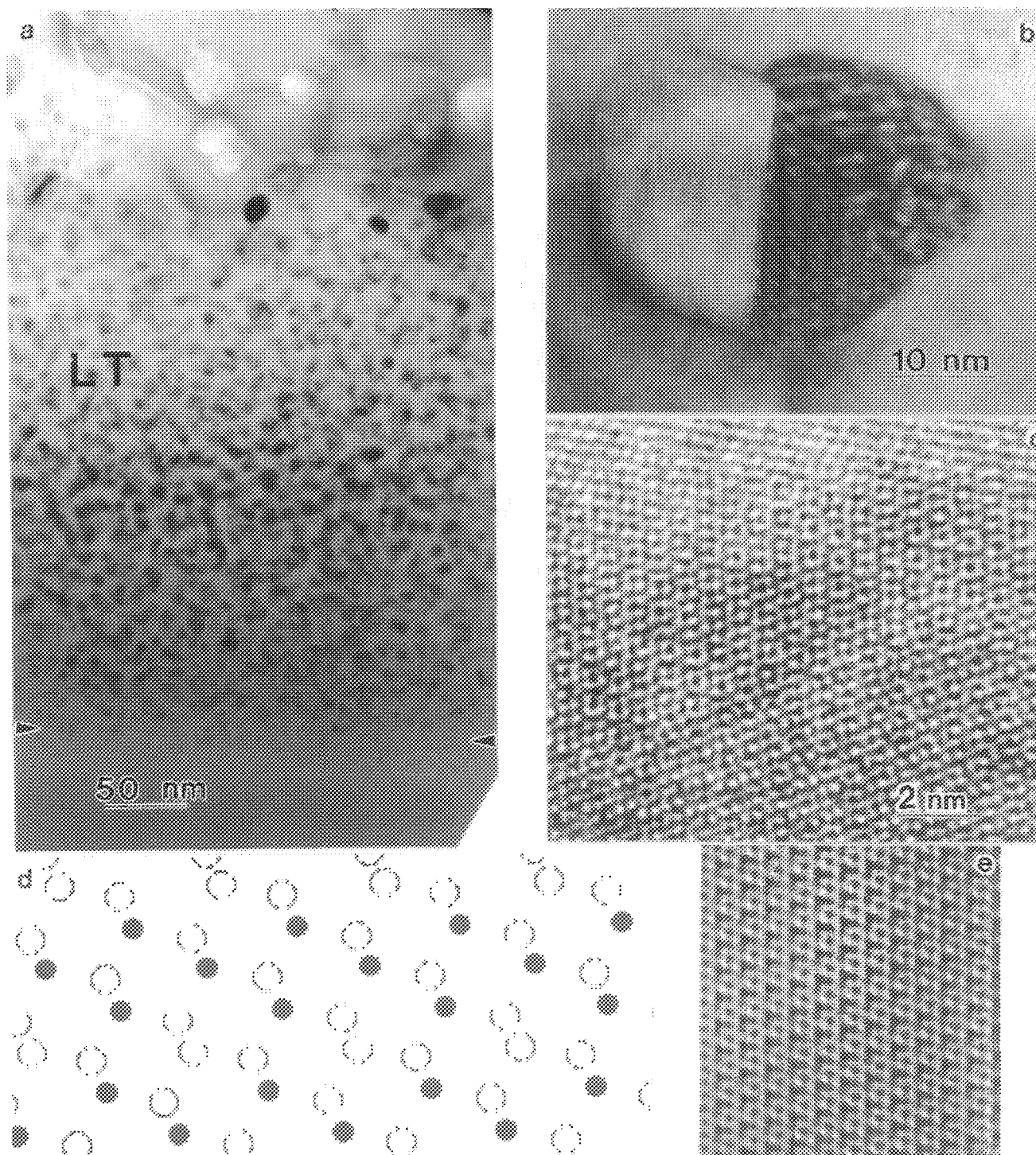
Fig.1: (a) Cross-section micrograph of the GaAs layer grown on GaAs substrate at low temperature. Note high density of hexagonal As precipitates in the part of the layer adjacent to the substrate, large amorphous precipitates Ga rich with light contrast and crystalline As rich precipitates with ordered phase with black contrast. Above the areas with large precipitates close to the layer surface large portion of the layer showed ordered structure; (b) twinned precipitate with ordered structure adjacent to amorphous precipitates; (c) the micrograph showing ordered structure formed close to the top of the layer surface; (d) the proposed model of the ordered structure; (e) the calculated image of the ordered structure for the sample thickness of 30 nm and defocus value of -500 mm;.

J-5: High-Resolution SEM

DIRECT SEM IMAGING OF DEFECTS

J.T. Czernuszka, N.J. Long and P.B. Hirsch

Department of Materials, University of Oxford, Parks Rd., Oxford OX1 3PH, England

It has been 20 years since the theoretical calculations of the possibility of imaging dislocations in bulk specimens using back-scattered electrons were performed.[1,2] It was predicted that a Field Emission Gun SEM would be necessary and this was verified experimentally by Morin et al. who additionally used an energy filter to select only those electrons which had lost only a few hundred eVs.[3] In 1990, we were able to obtain similar images without an energy filter and on a commercial FEG SEM.[4,5] We used a VG HB501 FEG STEM fitted with a highly efficient back-scattered electron detector in the secondary electron port. The image was acquired using a Synoptics Synergy framestore and digital scan generator and subsequently processed using Semper 6. The STEM was operated at accelerating voltages between 30 kV and 100 kV.[6,7] Working at lower accelerating voltages improved the contrast of near surface dislocations but the depth to which useful information could be obtained was reduced. For example at 30 kV the information depth is ~ 95 nm and at 100 kV it is ~ 200 nm. The image width of the dislocations is ~ 10-30 nm. Thus, it is now possible to perform "thin film microscopy" on bulk samples in a commercial FEG SEM. This technique is known as Electron Channelling Contrast Imaging (ECCI) in recognition of the mechanisms giving rise to the contrast. The applications of ECCI are too numerous to detail here but include examination of semiconductor devices (because it is essentially non-destructive) and fractured and worn samples (since specimen preparation is trivial). The following figures present examples of some our work.

Fig.1 shows Ni_3Ga which has been compressed 3% strain at $650^{\circ}C$. The dislocations are predominantly of screw type and are extinct in Fig.1b. This shows that the normal **g.b=0** invisibility criterion holds for screw dislocations in a similar manner to conventional TEM. The general mottling in the figures is thought to be due an oxide surface layer.[4,5] Fig.2 is of a (0001) SiC sample indented at 500 C. Fig.2a is a low magnification image showing lateral cracks associated with the indentations. Fig.2b is a magnified image showing dislocations and radial cracks. It would have been very difficult to prepare a thin foil from this specimen without causing relaxation of the dislocations. Of course, it is possible to image other defects in the bulk such as stacking faults, twins and precipitates. Fig.3 shows a silicide precipitate in a Si sample which had been deformed at 650 C. The strain contrast is shown to be greater than the atomic number contrast. Several of the dislocations appear to have been "punched out" by this precipitate. Only two such precipitates were found on a 4mm x 4mm sample and highlights another positive advantage of ECCI over existing imaging techniques. No precipitates were observed in Si samples compressed at 120 C.

1. D.R. Clarke and A. Howie, Phil. Mag. 24 (1971) 959.

2. J.P. Spencer et al., Phil. Mag. 26 (1972) 193.

3. P.Morin et al., Phil. Mag. A40 (1979) 511.

4. J.T. Czernuszka et al., Proc. XIIth International Congress for Electron Microscopy, Vol. 4, p.410 (1990).

5. J.T. Czernuszka et al., Phil. Mag. Letts. 62 (1990) 227.

6. J.T. Czernuszka et al., MRS Fall Meeting, Boston, USA, December 1st, 1990.

7. J.T. Czernuszka et al., Microscopy of Semiconducting Materials, Oxford, England, 28th March, 1991.

8. JTC wishes to thank the Royal Society for a Research Fellowship.
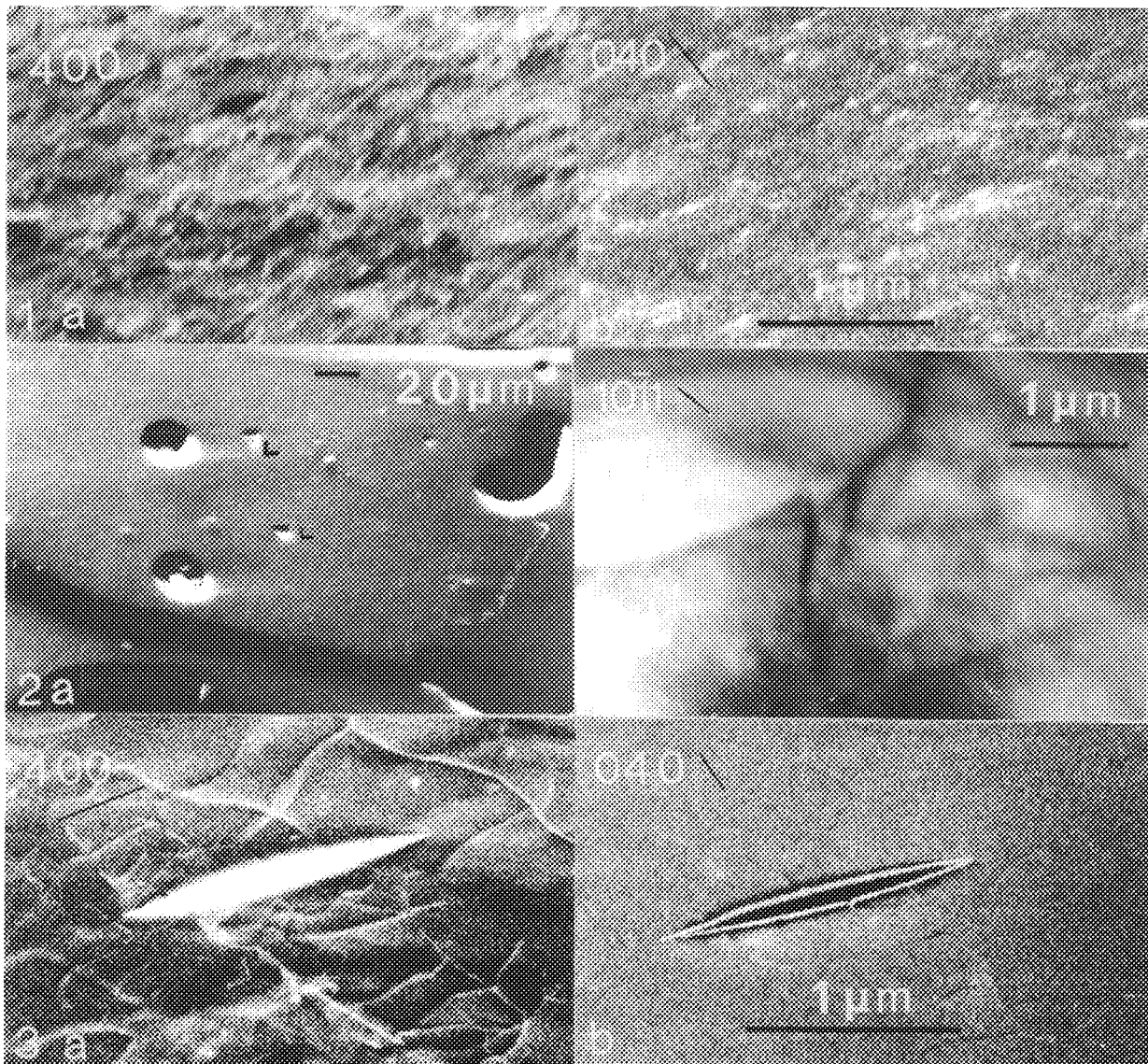
FIG.1 ECCI images of screw dislocations in (111) Ni$_3$Ga. For (b) these dislocations are out of contrast.

FIG.2 ECCI images of indentations on SiC. L are lateral cracks. (b) is a magnified image of part of (a).

FIG.3 ECCI images of a precipitate in (111) Si which had been deformed at 650°C.

STUDIES OF SUPPORTED CATALYSTS BY HIGH-RESOLUTION SEM IN A UHV STEM

J. Liu and G. E. Spinnler[+]

Center for Solid State Science, Arizona State University, Tempe, AZ 85287
+Shell Development Company, Westhollow Research Center, P. O. Box 1380 Houston, TX 77251

In the studies of the materials used in practical heterogeneous catalysis scanning transmission electron microscopy (STEM) is particularly suited for the characterization of particle size, shape, structure and composition of inhomogeneous catalyst systems by the combined use of a variety of techniques. Recently a high resolution surface imaging technique has been realized in STEM by collecting secondary electrons (SE) emitted at the exit surface of the sample.[1,2] The application of this imaging mode to the study of supported metal catalysts has proven very useful in the characterization of the support topography with subnanometer resolution.[1,2] However these studies are confined to extremely thin areas due to the fact that the incident beam will be scattered before encountering the exit surfaces of the sample. This will affect the resolution of SE images, especially for the study of high surface area support materials such as γ-Al$_2$O$_3$ carriers. Furthermore it has been frequently found that metal particles are not usually seen in the SE images even when the particles are situated on the exit surfaces of the supporting materials.[1] As part of an on-going project for characterizing supported catalysts we report here some preliminary results on high resolution SE imaging of supported catalysts in a UHV STEM.

The samples were prepared by dry grinding between two glass slides and dipping a holey carbon coated copper grid into the powder produced. The samples were directly observed without being coated with conducting materials. Such coating would definitely obscure fine scale surface details and make imaging of small metal particles impossible. The experiments were performed in a VG HB-501S UHV STEM codenamed MIDAS.[3] The SE images were formed by collecting SE signals emitted from the entrance surface of the sample.

Support Topography. Two types (type A and type B) of γ-Al$_2$O$_3$ carrier materials were examined. Figure 1 shows a SE image of a type A γ-Al$_2$O$_3$ carrier revealing fine surface details with high resolution. Such detailed surface topography of large agglomerates of γ-Al$_2$O$_3$ particles may not be obtainable if the SE signals were collected at the exit surface of the sample since the contrast and resolution of the exit surface images depend on the thickness of the agglomerates.[2] Figure 2 shows a SE image of a big cluster of a type B γ-Al$_2$O$_3$ carrier sample. It is obvious that type A and type B carriers have very different surface topography. The morphology of the same kind of carrier materials can change from one agglomerate to another. However by examining different fragments of the catalyst a qualitative picture of the carrier and its range of variation can be obtained. These results can be compared with that obtained by macroscopic techniques such as gas adsorption to yield useful information about the behavior of the catalysts.

Particle Studies. It is important for locating the positions of small catalyst particles within the support structures since different positions may have significant consequences on the catalytic activity. Together with examination of the support topography high resolution SE imaging should give information of the topographical relationship of the small active catalyst particles relative to the carrier morphology. Figure 3a shows a SE image of a transition metal/γ-Al$_2$O$_3$ catalyst system and figure 3b is the corresponding ADF image revealing the small metal particles. One can notice that some of the small particles are also revealed in the SE image with weak bright contrast. By comparing SE and ADF images one can, in principle, deduce the relative positions of the particles. Figure 4 shows another SE image of a different fragment of the same sample revealing small particles on the entrance surface of the carrier with contrast varying from very bright (indicated by B) to faint bright (indicated by F). By examining figure 4 and other SE images we concluded that the image contrast of the small particles depends on their relative position with respect to the local tilt of the surface normal of the support. If the particles are situated on a relatively flat area (with respect to the incident beam direction) of the support then the particles will give bright contrast. If the particles are sitting on a deeply inclined surface they may give weak contrast depending on the size of the particle. The relative contrast of small particles also depends on the SE yield of the particles and the support, the size of the particles and contamination of the sample. Detailed study of these problems will be reported elsewhere. Experiments have also been conducted for SE imaging of metal particles, deposited in situ, on low and high surface area carriers.[4,5]

References
1. D. Imeson et al., Ultramicrosc. 17 (1985) 243; D. Imeson, J. Microsc. 147 (1987) 65.
2. J. Liu and J. M. Cowley, Scanning Microsc. 2 (1988) 65, 1957; J. Liu and J. M. Cowley, Ultramicrosc. 34 (1990) 119.
3 G. G. Hembree et al., Ultramicrosc. 31 (1989) 111.   4. J. Liu et al, in these proceedings.
5. This work was supported by Shell Development Company and made use of the ASU Facility for HREM supported by NSF grant DMR-8913384. The authors thank Dr. G. G. Hembree for assistance.
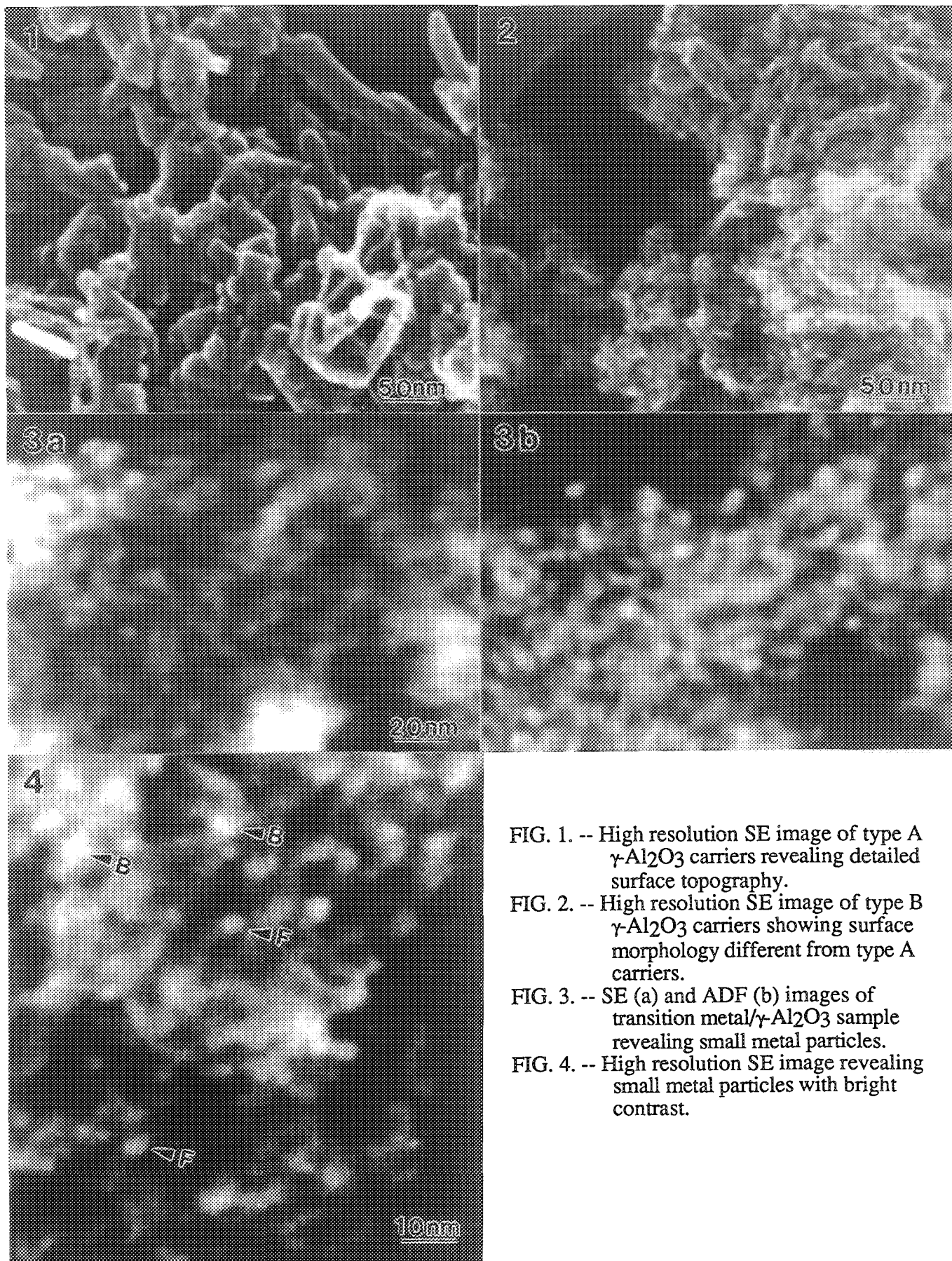
FIG. 1. -- High resolution SE image of type A
γ-Al₂O₃ carriers revealing detailed
surface topography.

FIG. 2. -- High resolution SE image of type B
γ-Al₂O₃ carriers showing surface
morphology different from type A
carriers.

FIG. 3. -- SE (a) and ADF (b) images of
transition metal/γ-Al₂O₃ sample
revealing small metal particles.

FIG. 4. -- High resolution SE image revealing
small metal particles with bright
contrast.

OBSERVATION OF EXTREMELY THIN INSULATING LAYERS FORMED ON A TRENCH WITH AN
ULTRA-HIGH-RESOLUTION SCANNING ELECTRON MICROSCOPE

K. Ogura* and J. Teshima**

*   JEOL Ltd. 3-chome, Musashino 1-2, Akishima, Tokyo, 196 Japan
** JEOL(U.S.A.)INC., 3500 West Bayshore Rd.,Palo Alto, Ca. 94303, U.S.A.

Observation of extremely thin insulating layers of silicon oxide and silicon
nitride formed on a trench with a conventional FE-SEM cannot be satisfactorily
carried out by the conventional method to mechanically polish and chemically
etch the wafer cross section and then investigate the state of layer formation
from the unevenness appearing on the cross section. One reason is that the
resolution of the conventional FE-SEM is not enough for the observation of
several-nm-thick layers even if they are etched. Another reason is that true
layer thickness may be obscured by chemical etching. These are why TEMs have
been used for the observation of extremely thin insulating layers on trenches
with atomic resolution. However, TEM application includes complicated specimen
preparation, and does not allow observation of wide field of view. Therefore,
the ultra-high resolution SEM (UHR-SEM) has recently been used for
similar purposes, using a simply cleaved plane of a wafer.

Since the observation of extremely thin insulating layers on trenches was
started with a UHR-SEM, it has been noticed that the insulating layers appeaing
on a cleaved plane of an wafer showed bright contrast when the observation
magnification was low, and that the contrast was reversed when the magnification
was increased. At an early stage it was thought that the contrast reversal was
caused by change of local electric charging of the insulating layers on a
cleaved plane of the wafer. However, when a specimen heating holder was used to
prevent specimen contamination for high magnification observation, the contrast
reversal of the insulating layers did not occur at any magnification. The
specimen temperature during the observation was 110 ℃.

Photo 1 shows a reversed-contrast image at a 100,000× magnification without
specimen heating. Photos 2 and 3 show 300,000× and 500,000× magnification images
of a trench which appeared on the same cleaved plane of an wafer as the trench
shown in Photo 1, with specimen heating. A double layer which is sandwiched
between silicon and poly silicon is clearly observed with bright contrast in ‚
these two images. From a comparison with TEM results, it was realized that the
outer layer of the bright contrast was approximately 10-nm-thick silicon oxide
and the inner layer was a little more than 10-nm-thick silicon nitride. The
images shown in this paper were obtained with the JEOL JSM-890 UHR-SEM.

Still it is not clear why contrast reversal did not happen when the specimen was
heated up during observation. However, it can be concluded that the UHR-SEM
observation of extremely thin insulating layers appearing on a simply cleaved
plane of an wafer is the simplest and fastest way to get a lot of information
with sufficient resolution from a wide field of view, in order to make a quick
responce to process lines.
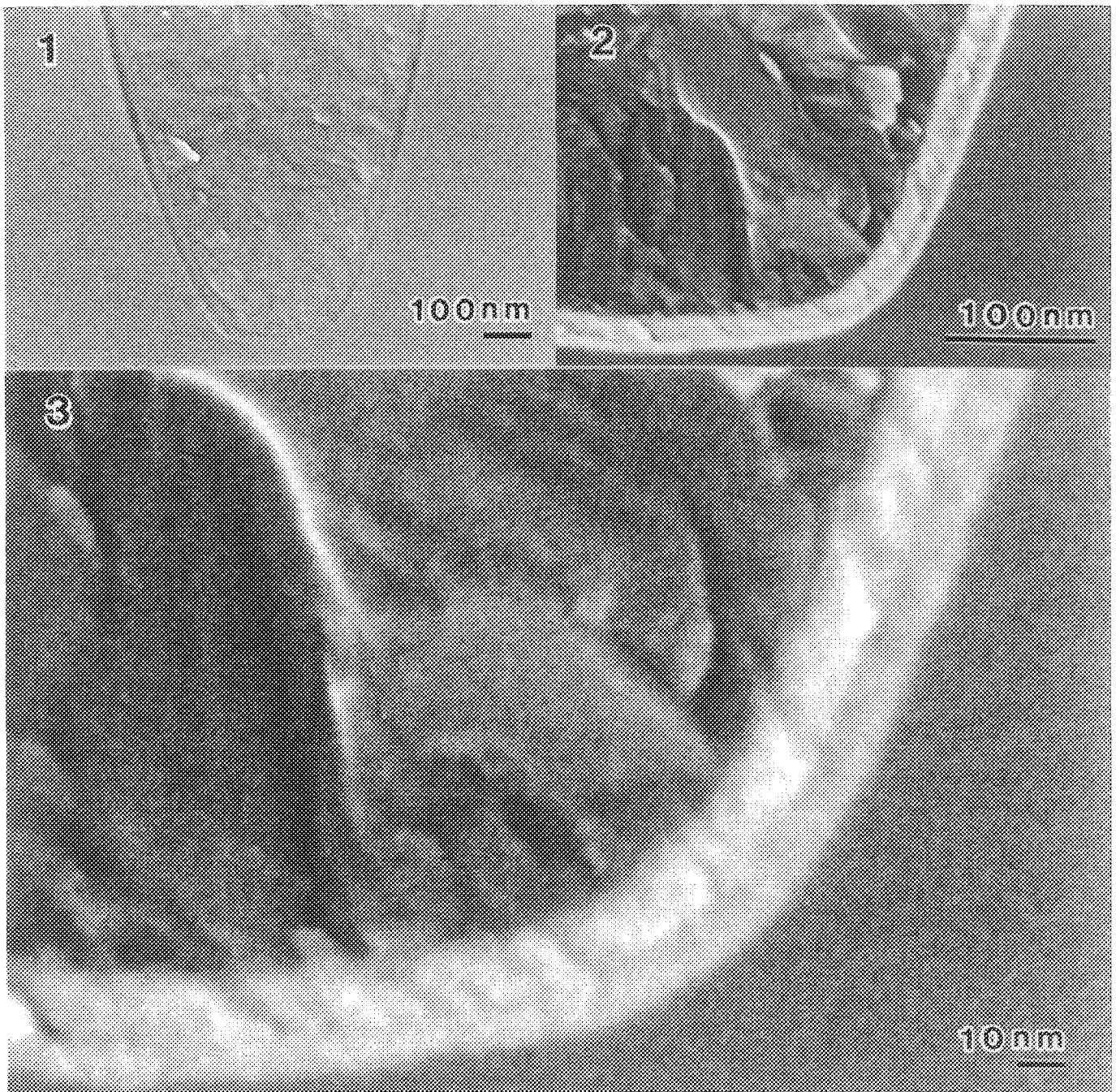
Photo 1.--Trench structure appeared on a simply cleaved plane of an wafer.
Insulating layer is dark in this image. At lower magnification the layer was
observed as a bright line. The specimen was not heated during the observation.
Photo 2.--Higher magnification image of trench. The specimen was constantly
heated at 110 ℃ during the observation. The contrast of insulating layer was
maintained, and a double layer was clearly observed.
Photo 3.--This image was recorded at 500,000× direct magnification. To measure
the thickness of each insulating layer is easy at this magnification. And with
specimen movement, any portion of the trench appearing on a cleaved plane can be
observed with the same quality as this image.

THE EFFECT OF SPECIMEN TILT ON BACK-SCATTERED ELECTRON IMAGE CONTRAST IN SCANNING ELECTRON MICROSCOPY

X. Meng-Burany and A.E. Curzon

Physics Department, Simon Fraser University, Burnaby, B.C., CANADA, V5A 1S6

The present work concerns the back-scattered electron image contrast of a thin film of $Cu_{64}Mo_{36}$ on a silicon substrate. The contrast is defined by the ratio

$$r = I_f/I_b \qquad (1)$$

where I_f and I_b are the backscattered electron signals from the film and from an adjacent bulk reference specimen. In previous work on thin sputtered films of Cu-Mo, Cu-W and Cu-Al[1-3] both the film and the bulk reference specimen were perpendicular to the incident electron beam. It was found that the dependence of r on the accelerating voltage of the electron beam could be used to obtain both the thickness and the composition of the films. It is the purpose of the present work to determine whether the simple method previously used to extract the required information can be extended to include tilted specimens. As will be seen the method can be adapted to films tilted by less than 50°.

Thin films of $Cu_{64}Mo_{36}$ were deposited on the 100 face of single crystal substrates of Si by means of magnetron sputtering from a target containing a copper disk overlaid with a strip of molybdenum. Their mass thicknesses were determined by a Cahn microbalance. The bulk reference specimen was a sputtered thick film of pure molybdenum. A given thin-film specimen and the bulk specimen were mounted adjacent on a flat sample holder so that their top surfaces were coplanar and the contrast ratio was measured with a Robinson back-scattered electron detector in the lower stage of an ISI DS130 scanning electron microscope equipped with an EG&G Ortec EEDS II image analysis system. The dependence of r on accelerating voltage and on specimen tilt were measured in the ranges 7 to 40 kV and 0° to 70° respectively, the tilt angle being changed in 10° steps.

Figure 1 shows a graph of r versus 1/E for tilt angles of 0 and 60°. These curves have two important features: on the left there is a linear section with positive slope and the curves either approach a saturation value or else, at high tilt angles, reach a maximum. It is possible to summarise the present curves by two parameters. These are the maximum or saturation value of r which we will call R and the intercept energy E_i which is the value of beam energy at which the left-hand straight section of the r-$1/E_i$ curve intersects the horizontal line $r = R$ (Point D in figure 1 indicates the position of E_i for the zero-tilt results). The appropriate parameter to specify film thickness in electron scattering studies is the charge thickness t because it is the charge which scatters the incident electrons. It is given by

$$t = T_m Z'/A' \qquad (2)$$

where T_m is the mass-thickness and Z' and A' are the effective atomic number and mass of the alloy in the film. Following previous work[1], Z' was obtained from a root mean square average and A' was taken as the average of the atomic masses of Mo and Cu weighted with their atomic concentrations in the alloy. When the specimen is tilted the distance the beam travels through the film before it reaches the substrate is increased by a factor of $1/\cos\theta$ where θ is the angle of tilt of the film so that the effective charge thickness is t' where

It has been found that when the tilt angle is zero then a graph of $\ln(E_i)$ versus $\ln(t)$ is a single straight line (within experimental error) for Cu-Mo, Cu-W and Cu-Al[1-3] alloys. When the specimen is tilted it might be anticipated that the graph of $\ln(E_i)$ versus $\ln(t')$ would follow the same line because t' for a tilted specimen is the equivalent of t for an untilted specimen. Figure 2 shows a graph of $\ln(E_i)$ versus $\ln(t')$ for the $Cu_{64}Mo_{36}$ alloy and for increments of 10° in tilt angle in the range 0° to 70°. The straight line graph on the figure was obtained from the earlier work[1-3]. The experimental data points for a tilted specimen lie close to the straight line graph provided that the tilt does not exceed about 50°. The straight line graph for untilted specimens was found to apply independently of composition. This fact and the present results for tilted specimens indicate that electron image contrast can be used to measure specimen thickness independent of film composition for angles of tilt up to 50°. Further experiments are being undertaken to confirm this result and to elucidate the reason for the marked departure from linear behaviour which occurs in the graph of $\ln(E_i)$ versus $\ln(t')$ for tilt angles above 50°.[4]
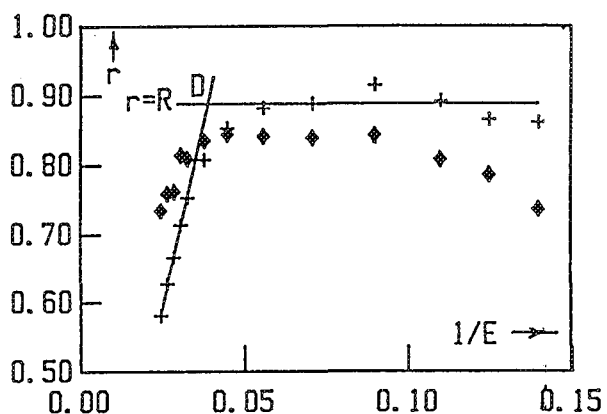
Figure 1

Graphs of r (contrast ratio) versus 1/E where E(kV) is the voltage of the incident electrons.
+ 0° tilt
◆ 60° tilt
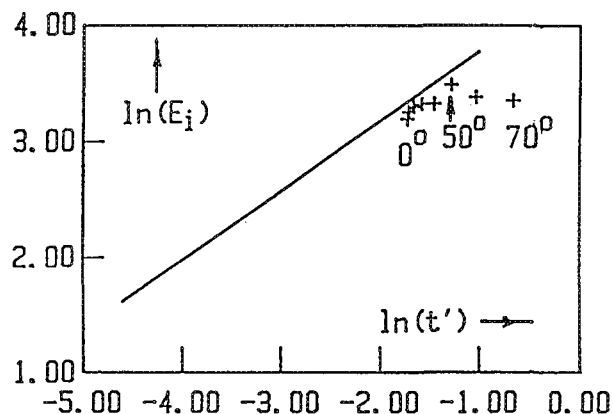
Figure 2

Graph of $\ln(E_i)$ versus $\ln(t')$. E_i(kV) is the intercept voltage and t'(millimoles/cm^2) is the charge thickness.
+ results for tilt angles 0° to 70° in 10° steps from left to right.
The solid line is for 0° tilt[1-3].

References

1. D.J. Wilson and A.E. Curzon, Thin Solid Films, 165 (1988) 217 - 225.
2. O.S. Rajora and A.E. Curzon, Phys. Stat. Sol. (a) 114 (1989) 199 -205.
3. O.S. Rajora and A.E. Curzon, Thin Solid Films, (1991) Accepted for publication.
4. This work was supported by the Nat. Sci. and Eng. Res. Council, CANADA.

Electron penetration effects in the Scanning Electron Microscope applied to Cu/Ta thin films

P. Bailey, K. Holloway, L. Clevenger, N. Bojarczuk

IBM Research, P.O. Box 218, Yorktown Hgts. N.Y. 10598

Current semi-conductor technology uses low-resistivity metals, as Cu, for integrated circuit conductor lines and contact structures. Copper, however, is quite mobile in silicon at elevated processing temperatures and a diffusion barrier such as Ta, is therefore required between the Si and Cu [1] The interdiffusion of Cu and Si with Ta as a diffusion barrier was studied in samples annealed between 500°C and 800°C, using scanning electron microscopy (SEM), and transmission electron microscopy (TEM). [4] Secondary electron images obtained in the SEM, from 5keV to 25keV accelerating voltages were correlated to the structural information obtained by cross-section TEM This work showed that annealing produced a compositionally non-uniform underlayer beneath the Ta film, and that the technique of varying the accelerating voltage in the SEM provides a means of quickly obtaining such information about underlying structures.

The samples were prepared by sputtering 50nm of Ta onto unpatterned Si wafers, then sputtering 100nm of Cu onto the Ta film The samples were annealed, using a temperature range of 500°C to 800°C [2] for 30 minutes in flowing helium purified over a Ti getter. Reactions in these samples were characterized using Rutherford backscattering spectroscopy (RBS) Selected cases were observed using cross-section TEM in a JEOL 4000FX operating at 400keV. TEM sample preparation followed the Bravman-Sinclair process [3] The surface morphology of the annealed samples were observed in a Hitachi S-570LB scanning electron microscope equipped with a LaB$_6$ filament. The secondary electron detector was a standard Everhart-Thornley type and the backscatter electron detector was a solid-state, under the lens type. X-ray infomation was obtained using a Be window EDX detector attached to a Princeton Gamma Tech +4 x-ray/imaging system.

Both the secondary electron (SE) image and the backscattered electron (BSE) image of a solid sample in the SEM are affected by the incident beam voltage [5] With a low enough beam energy, only the surface topography can be seen in the micrograph (Fig 2) As the incident energy increaces, the signal eminating from the surface topography fades away, and is overpowered by the backscattered electrons coming from the underlying structure (Fig 1). With the increace in beam energy, the electron trajectories near the surface become straighter and the electrons penetrate more deeply into the sample before being scattered by the underlying structure back to the surface. At higher energies the electrons also retain a larger fraction of their initial energy after a given length of travel EDX of the "bright" areas (Fig 1) shows a very high concentration of Cu; the other areas show no Cu at all Cross-section TEM of one of the sites where this phenomenon was observed, (Fig 3) shows that there is a layer of Ta over a Cu containing precipitate, as was suggested by the SEM micrographs. The Cu, in the sample annealed at 600°C has penetrated the Ta layer and precipitated in the Si [2] The Cu precipitates were identified as Cu$_3$Si single crystals, and the Ta phase was identified as TaSi$_2$ both by electron diffraction in the TEM Varying the accelerating voltage while viewing the same area of a sample, can produce profoundly different micrographs, with each micrograph containing information from different depths in the sample

References

1. K. Holloway and P. M. Fryer, Tantalum as a diffusion barrier between copper and silicon, *Appl. Phys. Lett.* 57, 17 (1990)

2. K. Holloway *et al*, Tantalum as a diffusion barrier between copper and silicon - failure mechanism and effect of nitrogen additions. (unpublished)

3. J. Bravman and R. Sinclair, *J. Electron Microc. Tech.* 1, 53 (1984)

4. O. Wells, R. Savoy, P. Bailey, Electron beam interactions with solids, *SEM inc., AMF O'hare*, 287-298 (1982)

5. J. Goldstein *et al*, Scanning electron microscopy and x-ray microanalysis; Plenum press, 68, (1984)
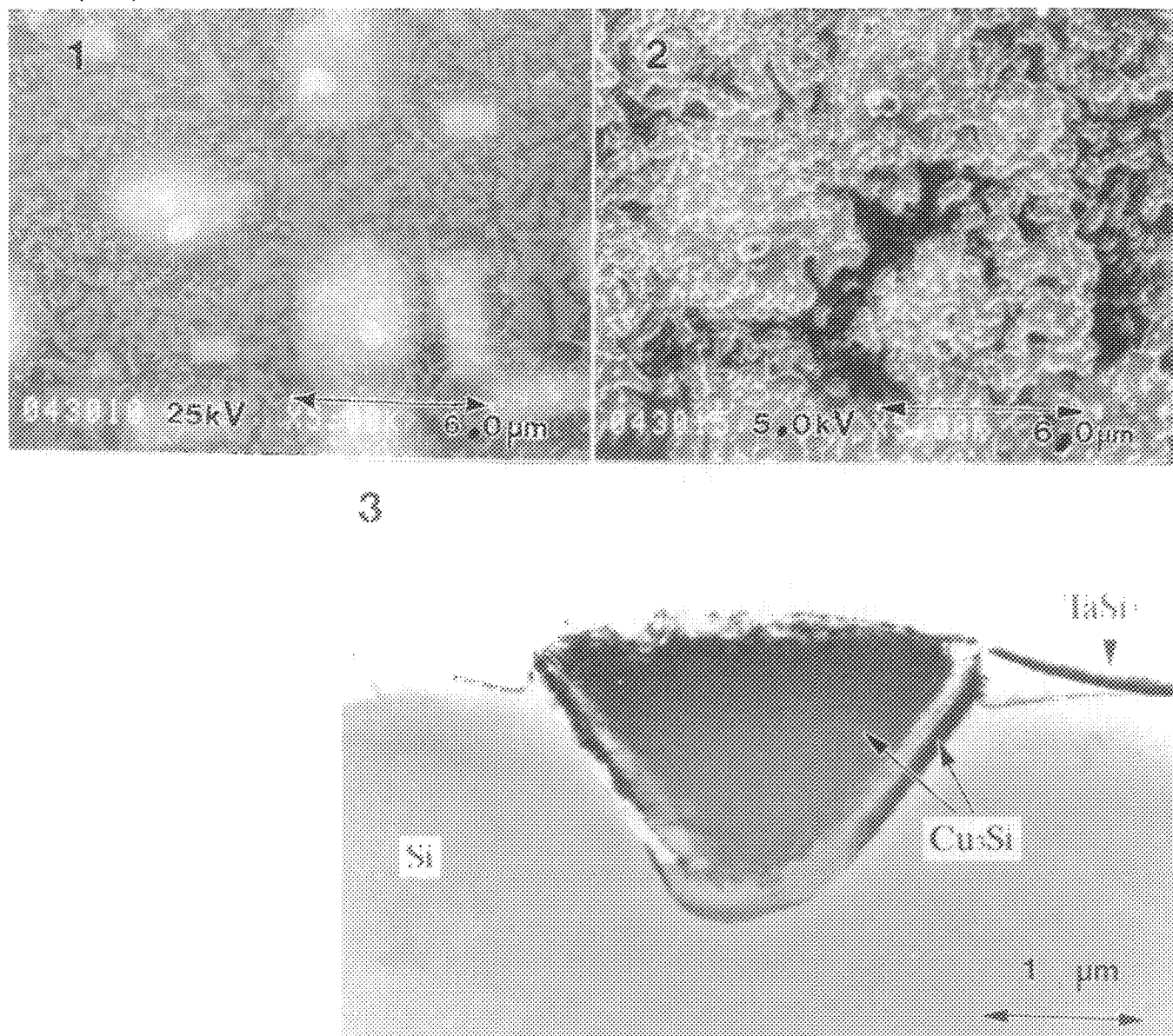
Figure captions

Fig. 1 - Si/Ta/Cu heated to 600°C. Accelerating voltage - 25keV.

Fig. 2 - Si/Ta/Cu heated to 600°C. Accelerating voltage - 5keV.

Fig. 3 - TEM cross-section.

ANALYSIS OF ELECTROLESS NICKEL THIN FILMS

C. W. Price* and E. F. Lindsey

*Chemistry and Materials Science Dept., **Mechanical Engineering Dept., Lawrence Livermore National Laboratory, Livermore, CA, 94550

Thickness measurements of thin films are performed by both energy-dispersive x-ray spectroscopy (EDS) and x-ray fluorescence (XRF). XRF can measure thicker films than EDS, and XRF measurements also have somewhat greater precision than EDS measurements. However, small components with curved or irregular shapes that are used for various applications in the the Inertial Confinement Fusion program at LLNL present geometrical problems that are not conducive to XRF analyses but may have only a minimal effect on EDS analyses. This work describes the development of an EDS technique to measure the thickness of electroless nickel deposits on gold substrates. Although elaborate correction techniques have been developed for thin-film measurements by x-ray analysis,[1,2] the thickness of electroless nickel films can be dependent on the plating bath used. Therefore, standard calibration curves were established by correlating EDS data with thickness measurements that were obtained by contact profilometry.

The plating bath used in this study incorporated a leveling agent that resulted in a phosphorous content in the nickel films of 11 to 12 wt. %.[3] EDS analyses using a standardless quantitative analysis program indicated that the relative variation of phosphorous was not greater than about $\pm$ 5%, so the phosphorous content was assumed to be constant for this study. Since film thickness should be sensitive to the phosphorous content, however, additional calibration will be required to quantify the variation of thickness determined by Ni/Au ratios with the phosphorous content.

Electroless nickel deposits tend to be somewhat rougher than those of vapor deposited films since they tend to develop small nickel-rich nodules on the surface. An example of an electroless nickel film with a nominal thickness of 170 nm is shown at intermediate and high magnifications in Figs. 1a and 1b, respectively. The films used for this study were deposited on 3-μm gold deposits that had been sputtered onto polished silicon substrates. The bumpy surface of the nickel that is apparent in Fig. 1b replicates to some extent the surface of the sputtered gold film that it was deposited on. Small voids, and small regions that appear to have been formed by the rupture of subsurface gas bubbles also are apparent. These features caused noticeable scatter in the profilometer measurements, but as will be shown, reasonable calibration curves were obtained from these specimens.

The thickness range of interest was about 100 to 300 nm. Preliminary studies indicated that optimal sensitivity in this range could be obtained from Ni L_α and Au M_α peaks in spectra generated at 15 kV. The spectra were generated using an optional thin window in a NORAN Micro-Z II Si(Li) EDS mounted on a Hitachi S-800 FESEM; the thin window greatly enhanced the Ni L_α peak intensity. Phosphorous was effectively constant but did have to be monitored in each analysis to verify that it was in the desired range. Therefore, phosphorous was deconvoluted by using standardless quantitative analysis as if the specimen were a homogeneous mixture of nickel, gold and phosphorous, and Ni/Au ratios were obtained from the resulting weight percents. An instrument counting time of 120 s yielded adequate counting statistics; replicate Ni/Au ratios were usually within $\pm$ 2%. Typical spectra from samples with nominal thicknesses of 180 and 290 nm are shown in Figs. 2a and 2b, respectively, and a calibration curve obtained from correlating Ni/Au ratios with profilometer measurements is shown in Fig. 3. The major contribution to the data scatter in Fig. 3 was the effect of surface roughness on the profilometer measurements.

References

1. G. A. Hutchins, The Electron Microprobe, J. Wiley & Sons, NY (1966) pp. 390-404.
2. J. L. Pouchou and F. Pichoir, Scanning, 12, 212 (1990).
3. J. W. Dini, et al. Products Finishing, to be published.
4. Work performed under the auspices of the U. S. Department of Energy by the Lawrence Livermore National Laboratory under Contract #W-7405-ENG-48.
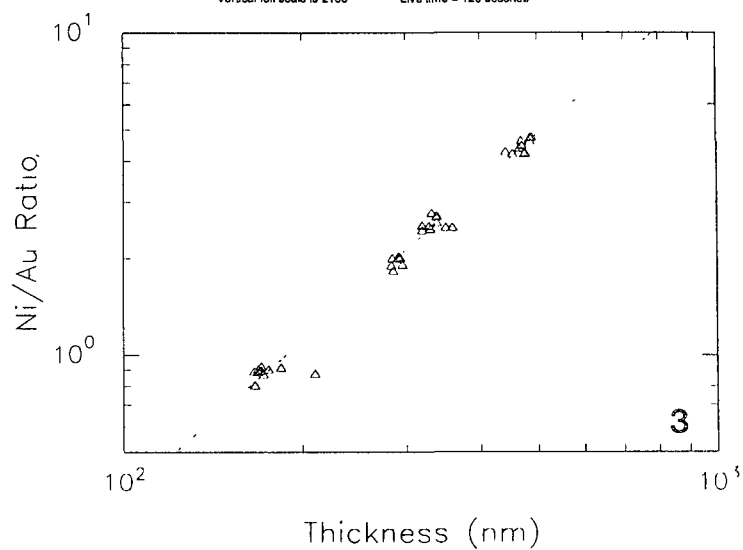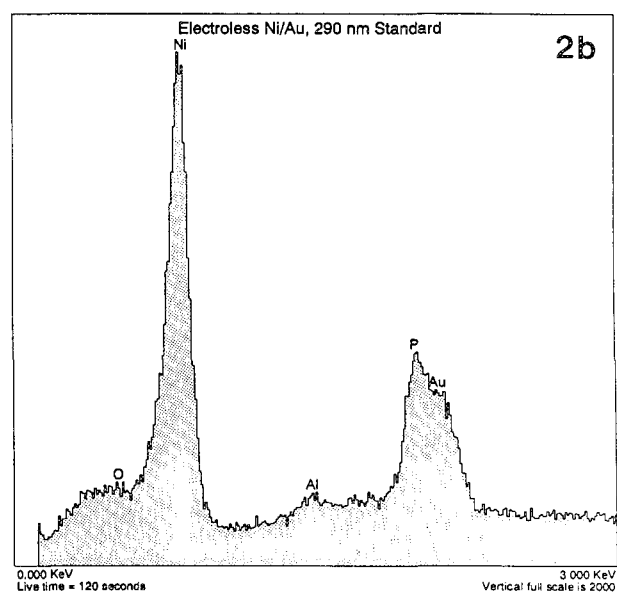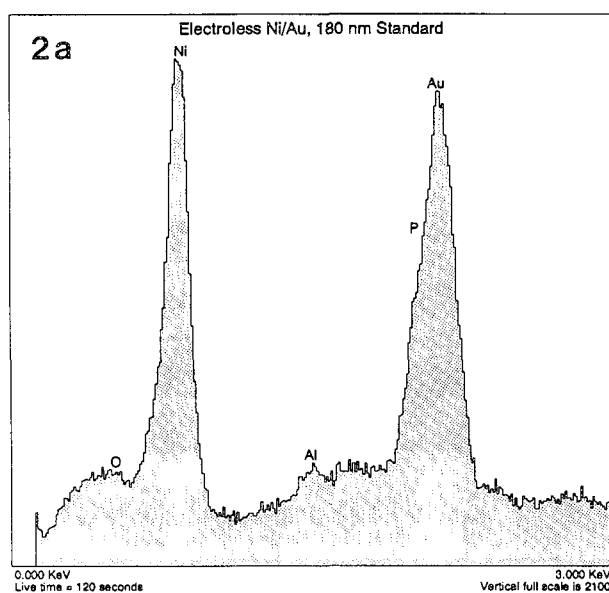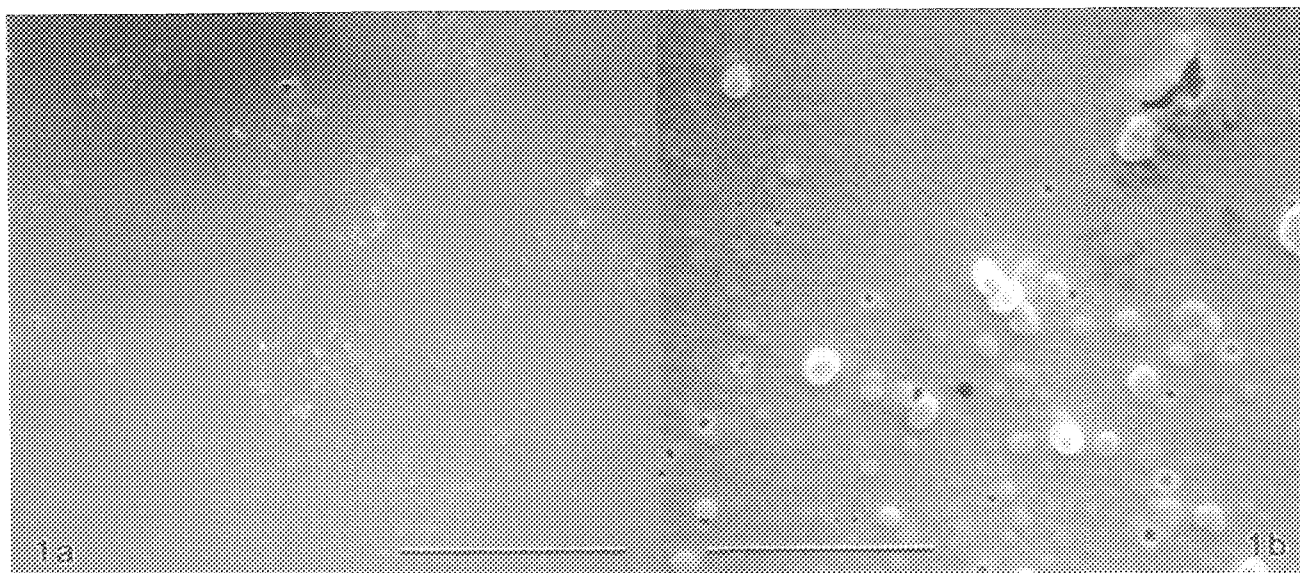
FIG. 1.—Secondary-electron images of an electroless nickel surface; (a) bar = 30 μm, (b) bar = 3.0 μm.
FIG. 2.—EDS spectra at 15 kV for electroless nickel thicknesses of (a) 180 nm and (b) 290 nm.
FIG. 3.—Standard curve generated from Ni/Au ratios and contact profilometry measurements.

HIGH-SPEED ELECTRON COUNTING SYSTEM
FOR TV-SCAN RATE SE IMAGES OF SEM

S. Yamada, T. Ito, K. Gouhara, Y. Uchikawa

School of Engineering, Nagoya University, Nagoya, 464-01 Japan

We reported a system for counting secondary electrons (SEs), with which SE image quality of SEM such as signal to noise ratio (SNR) and linearity were improved, in particular under the condition of low irradiation.[1-3] The system had been developed for slow-scan rates (over 6 sec/flame). The TV-scan rate (1/30 sec/frame) is often used to avoid charging of insulators and biological specimens. We developed a high speed electron counting system with which SE images can be obtained in the TV-scan rate. This paper describes the new system attached to an SEM, and some experimental results obtained with it.

A schematic diagram of the new system is shown in FIG.1, which consists of four main parts; Everhart-Thornley type detector (DT), main amplifier (MA), counter (CNT) and image processor (IP). In designing the system we took precautions for high speed data acquisition in the TV-scan rate. As described in the previous papers,[1-3] the thermal noise and the fluctuations of the pulse height of the SE signal contained in the output of the DT can be removed through the CNT. The data for a pixel (8 bits) from the CNT during the sampling period of 80 ns is sequentially sent to the frame memory (FM2:512x480 Bytes) of the IP. Another bank of the frame memory (FM1) is provided for the analogue image signal. The image data of either FM1 or 2 can be displayed in real time on a CRT.

Observations of a contact hole in the photo resist film were made to compare image quality of the electron counting and the analogue data, as shown in FIG.2. Both the images were obtained by averaging 100 frames in the TV-scan rate under the same imaging conditions. It is clear that the electron counting image is superior to the analogue image in SNR and linearity.

For identical image area on a flat metal surface, we compared the averaged image data (100 frames) in the TV-scan rate of the electron counting and of the analogue signal. (The resist film which is easily charged up by irradiation of primary electrons is not appropriate for repeated measurements.) We estimated SNR from the image data obtained with different values of the primary beam current I_p. The results were plotted in FIG.3. Superiority of the electron counting is quantitatively shown.

References
1 S Yamada et al , *Electron Microscopy 1990 vol 1, San Francisco: San Francisco Press*
   (1990)402.
2. S. Yamada et al., *SCANNING 90 Abst., NJ.FACMS (1990)56.*
3. S. Yamada et al., *Scanning 13[1](1991) (in printing).*
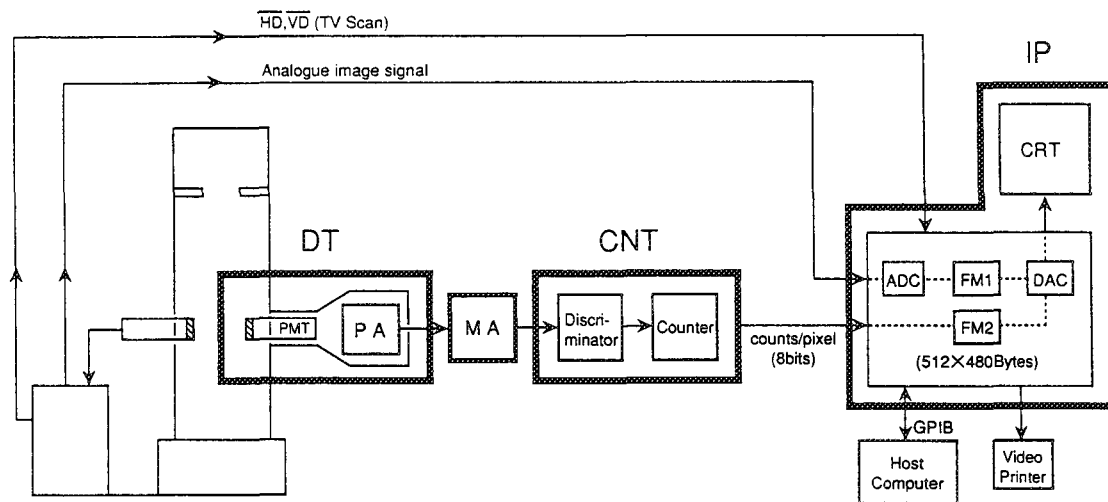
FIG.1--Schematic diagram of high speed electron counting system.
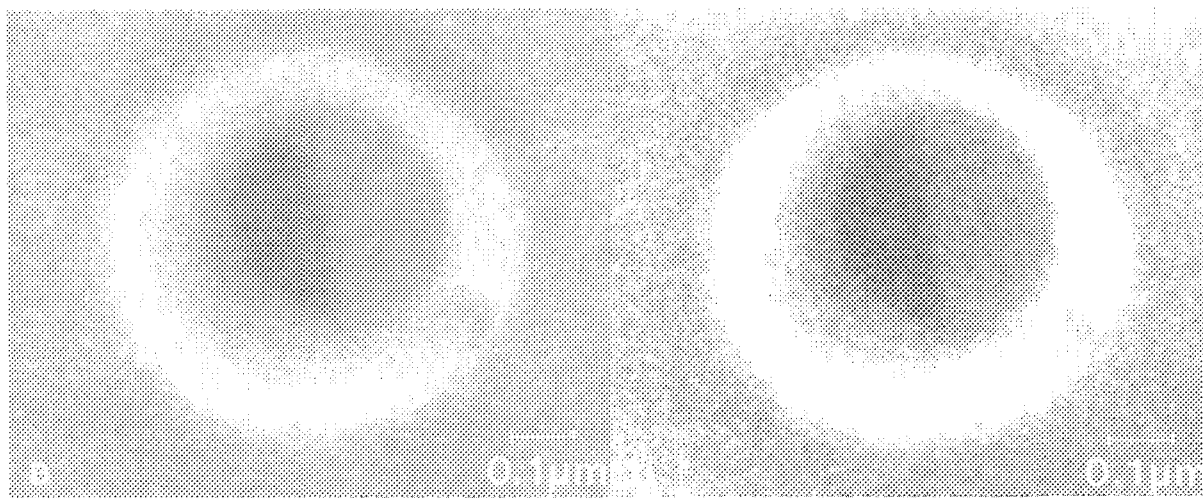
FIG.2--(a)Electron counting image, and (b) analogue image of contact hole in photo resist film obtained by averaging 100 frames in TV-scan rate. Bright ring is side wall of contact hole and half-tone shaded area at hole bottom is unetched remnant of resist. Accelerating voltage is 1.4kV, and primary beam current I_p=0.3pA.
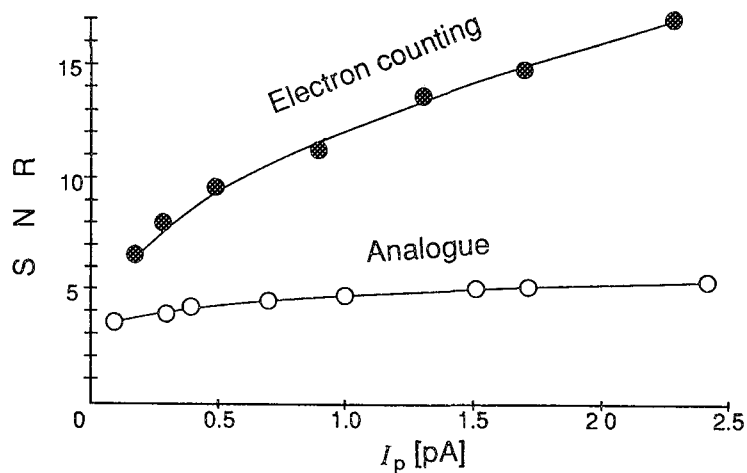
FIG.3--SNR against I_p of electron counting and analogue image data. Accelerating voltage is 1.4kV

USING HIGH-VACUUM EVAPORATION TO OBTAIN HIGH RESOLUTION LOW-TEMPERATURE IMAGES OF FREEZE-FRACTURED MEMBRANES FROM YEAST

William P. Wergin and Eric F. Erbe

Electron Microscopy Laboratory, USDA-ARS, Beltsville. MD 20705

In previous low temperature studies of fractured yeast membranes that were examined in a conventional SEM, Wergin and Erbe demonstrated that resolution could be enhanced by substituting conventional sputter coating of gold with high vacuum evaporation of platinum/carbon.[1] Although this procedure did not clearly resolve membrane particles, the frozen sample could be removed from the SEM and the Pt/C "coat" or replica could be recovered for further examination. Using instruments with greater resolution such as a TEM, as well as a field emission (FE) SEM, to examine the replica did reveal the membrane particles on the replica; therefore the authors concluded that failure to resolve these membrane structures in a conventional SEM probably resulted from limitations of the instrument rather than the coating procedure.[2] Recently, we had the opportunity to interface a FESEM with a cryosystem; this combination was used to determine if samples shadowed in a high vacuum evaporator could be transferred to a cold stage in a FESEM to resolve the macromolecular structure of yeast plasma membranes.

A yeast suspension was frozen, fractured, etched, shadowed with platinum and coated with carbon in a Denton DV-503 high vacuum evaporator with a modified DFE-2 freeze-etch module.[3] Next the frozen sample was transferred to a modified specimen holder for use with the Oxford/Hexland CT 1500 Cryotrans System that was installed on a Hitachi S-4000 FESEM. The specimen was inserted into the microscope (Fig. 1), the temperature of the cold stage was temporarily raised to -98C to remove condensed water vapor (Fig. 2) and individual cells were photographed. Following observation, the frozen sample was removed from the FESEM, the tissue was dissolved from the platinum/carbon replica which was then mounted on a grid for observation and photographic recording in a Hitachi H-500H TEM.

FESEM examination clearly revealed nuclear pores on the surface of the fractured faces of the nuclear envelope (Fig. 3). The P face of the plasma membrane exhibited distinct invaginations and discrete para-crystalline arrays of membrane particles (Fig. 4). The replica of these freeze fractured cells, which was observed in the TEM, more clearly displayed the nuclear pores and the membrane particles (Figs 5 & 6); however, in the TEM, low magnifications of numerous cells frequently revealed replica collapse which occurred while dissolving the tissue and mounting the replica on coated grids.

The use of high vacuum evaporation of Pt/C to coat samples for low temperature FESEM allowed resolution of membrane particles on frozen, fully hydrated cells. This procedure allows one to recover the coating or replica for further analysis in a TEM. At the present time resolution of the replicas is greater in the TEM than that obtained by viewing a replica at ambient temperatures in a FESEM.[4] However, our results indicate that further resolution of structural detail at low temperature appears to be limited by specimen contamination and stage vibration rather than by the grain size resulting from the evaporated Pt/C coating. Reducing contamination and eliminating stage vibration may further increase the resolution obtainable with low temperature FESEM.

References
1. W. P. Wergin et al., Proc. Ann. EMSA Meeting 46(1988)256.
2. W. P. Wergin and E. F. Erbe, Int. Phys. Conf. Ser. 98(1989)715.
3. R. L. Steere, in J. E. Johnson, Jr., Ed. Current trends in morphological techniques, Boca Raton: CRC Press (1981)131.
4. W. P. Wergin et al., Proc. Ann. EMSA Meeting 47(1989)74.
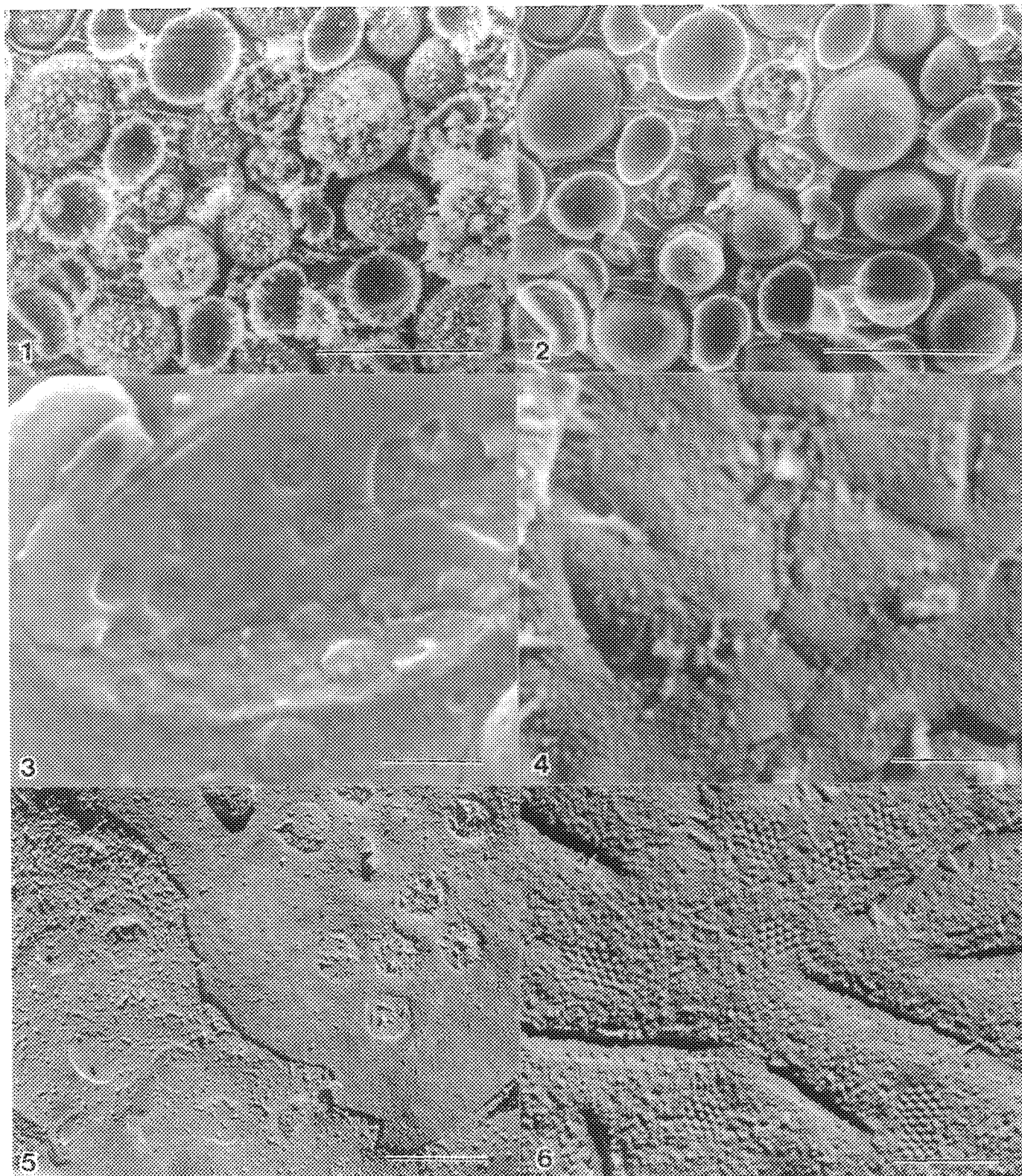
Fig. 1. Freeze etch image of yeast that was shadowed under high vacuum with platinum and transferred to Oxford cryostage in microscope. Bars in Figs. 1 & 2 = 10μm; in Figs. 3 - 6, bars = 200 nm.

Fig. 2. Same preparation as shown in Fig. 1 after temperature of stage was temporarily raised to sublime water-ice contaminants.

Figs. 3 & 4. Low temperature FESEM images of nuclear pores on fractured faces of nuclear envelope (Fig. 3) and hexagonal arrays of particles that can be resolved on P face of yeast plasma membrane (Fig. 4).

Figs. 5 & 6. TEM images of replica that shows nuclear pores (Fig. 5) and membrane particles (Fig. 6).

HIGH-RESOLUTION SE-I IMAGING OF BIOLOGICAL MEMBRANES USING A SCHOTTKY FIELD-EMISSION IN-LENS SEM

R.P. Apkarian

Yerkes regional Primate Research Center, Emory University, Atlanta GA 30322

Previous notes have described efforts to routinely collect quality SE-I image contrasts of biologically significant particulate membrane features (1-10 nm) in the context of whole cells and tissue fragments.[1,2] Utilizing SEMs equipped with in-lens specimen stages and field emission sources (Schottky and cold cathode) operated at 15-30 kV and in conjunction with specimens coated with 1 nm Cr films (Z=24), nanometer resolution of biological samples may be attained.[3] This note describes the definition of optimal electron source conditions for the high resolution imaging of cell membrane features < 10 nm. The Schottky field emitter equipped ISI DS-130F SEM, in-house at the Yerkes Research Facility, was operated at 5-20 kV accelerating voltages (A.V.) and at 4 or 4.8 kV extraction voltages (E.V.). Although we have published images of soft and hard biological sections and isolated cells containing 1-10 nm particle contrasts by operating the SEM at 25-30 kV A.V., we have maintained 4 kV extraction voltage and not attempted using 4.8 kV above 25 kV A.V. since the zirconium/tungsten filament is seven thousand hours old. It is expected that future SEM operation at 25-30 kV will coincide with development of 1 nm colloidal gold-antibody labels that would be directly imaged in association with these small membrane features.

Cell membrane features were assessed on a myelogenous leukemia cell line (HL60) after 4 hour treatment with 2-lyso-phosphatidylcholine (ALP), a synthetic analogue of phosphatidylcholine. Since HL60 cells in culture contain numerous surface blebs in the micrometer range which were absent on this cell type after 4 hrs culture we wished to observe 4 hr treated HL60 cells to determine if there were any remaining nanometer range particulates. Cultured and treated cells were grown on 5 mm silicon chips that were fixed and dehydrated in Beem capsules and subsequently processed in a rotating specimen boat within the Polaron E-3000 critical point dryer.[4] Following delicate handling CO_2 exchange procedures Si chips were mounted onto supports, degassed and Cr sputter coated with a 1 nm thick chromium film in the Denton DV-602 turbopumped system.

In-lens SE-I imaging of these cell surfaces at a CRT magnification of 200,000 times revealed characteristic 50 nm membrane folds when the Schottky emitter was operated at A.V.s of 5,10,&15 kV and E.V. of 4 kV (Figs 1a,b,c). Increased relief contrasts were attained at the higher A.V.s. The Schottky source was bright enough at 20 kV to record 400,000 times CRT magnification images that contained 5 nm particle contrasts (Fig 1d). Increased E.V.s (4.8 kV) improved relief and particle contrasts on these cell membranes particularly at the lower A.V.s (Figs.2a-d). Contamination and beam damage were noticeable when prolonged focusing time was required. The same procedures of focusing, specimen shift, and photography previously developed on the cold cathode in-lens Hitachi S-900 was employed in this study. Although microcollapse is a concern during CPD specimen preparation we feel confident that it is minimal when delicate procedures are employed. This E.M. facility will continue to develop procedures for the high resolution imaging of cell membranes utilizing the ISI DS-130 Schottky field emission SEM.
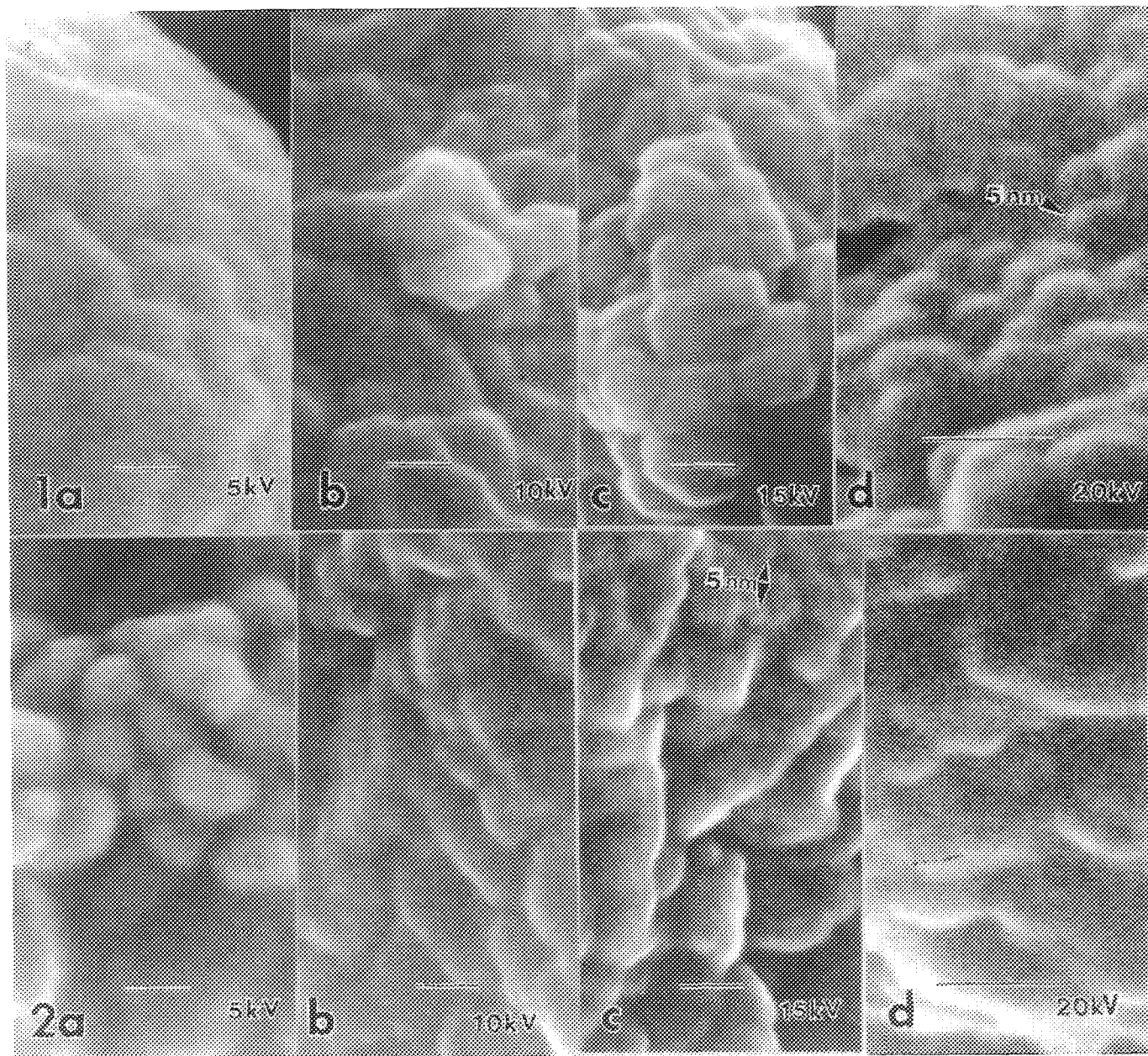
FIG. 1.--HL60 cell surface membrane imaged with 4 kV extracting voltage. Bars = 50 nm.

FIG. 2.--HL60 surfaces imaged with 4.8 kV extracting voltage. Bars = 50 nm.

References
1. R.P. Apkarian, Ann. EMSA Mtg. 45 (1987) 564.
2. R.P. Apkarian, Ann. EMSA Mtg. 47 (1989) 68.
3. R.P. Apkarian, M.D. Gutekunst, and D.C. Joy, JEMT 14(1990) 70.
4. K.R. Peters, J.Microsc.118 pt.4 (1980) 429.
5. Sample courtesy of W. Vogler & M. Shoji, Dept. of Medicine Emory School of Medicine.
6. Technical assistance by S. Park.
7. This research was supported by NIH grant RR-00165 from the National Center for Research Resources to the Yerkes Regional Primate Research Center.

OPTIMIZED IMAGES OF IMMUNOGOLD MARKERS WITH BACKSCATTERED ELECTRONS

Etienne de Harven[1], Cameron Ackerley[2], Richard Leung[1] and Hilary Christensen[1]

Banting Institute[1], Hospital for Sick Children[2], Department of Pathology, University of Toronto, Toronto, Ontario, Canada

The use of colloidal gold markers of small diameter ($\leqslant$ 5nm) may permit direct quantification of the numbers of labeled molecules expressed on cell surfaces (1). To achieve this goal direct immunolabeling must be used and an imaging mode chosen which will reveal <u>ALL</u> the present gold markers, i.e. backscattered electron imaging mode (BEI) (2). Backscattered electron detectors resolving one nm gold particles have recently been described (3) and immunoconjugates prepared with Fab fragments of IgG molecules (4 5) will further increase labeling efficiency for more accurate quantitative studies.

Meanwhile, it is desirable to optimize imaging of 5nm gold markers in the BEI mode, using conventional scanning electron microscopes. To that effect, we have been labeling cells with gold particles of two distinct sizes, 5 and 10 nm. The presence of 15nm particles facilitated fine tuning of the SEM in the BEI mode for subsequent imaging of the 5nm markers. We have compared two types of SEMs, one in which the sample was at a 8mm working distance below the last pole-piece (the JEOL JSM 840), another with the "in-lens" configuration (the JEOL 1200 EXII with the scanning attachments). Both microscopes were equiped with similar lanthanum hexaboride (LaB$_6$) electron emitters and similar solid state BE detectors.

The effects of using different accelerating voltages (from 20 to 80 kV) and of using a 3 lenses condenser system were systematically assessed. The cells (lymphocytes and platelets) were mounted on two types of substrates: formvar coated 300 mesh copper grids, or fragments of glass coverslips. These two types of substrates were (or not) heavily precoated with evaporated carbon. For conductive coating, the cells were coated either with a thin (+10 nm) film of carbon, or with carbon-platinum, or with tungsten or exposed to 0.1% osmium tetroxide for one minute (6).

Optimum imaging of 5nm gold markers on the surface of platelets or lymphocytes was obtained using 1) the "in-lens" configuration, 2) 80 kV accelerating voltage, 3) a heavily carbon pre-coated formvar film substrate, 4) conductive coating either by platinum evaporation or by osmium tetroxide treatment.

The advantage gained by using a platinum, tungsten or osmium coating results probably from a decreased penetration of the incident electrons beneath cell surfaces Cells mounted on a heavily carbon pre-coated formvar film were remarkably stable and free of electrostatic charging when exposed to an incident beam up to 80 kV

References:

1. de Harven E., Christensen H., Leung R., Ackerley C. Proc. 47th Annual EMSA meeting: 1050-1051, 1989.
2. de Harven E., Soligo D., Christensen H. J. Microsc. 146 (2): 183-189, 1987.
3 Erlandsen S.L.; Frethem C., Autrata R.   J. Histochem. Cytochem. 38(12): 1779-1780, 1990.
4. Simmons S.R., Albrecht R.M. Scanning Microscopy Supplement 3: 27-34, 1989.
5. Baschong W., Wrigley N.G. J. Electron Microscopy Technique. 14: 313-323, 1990.
6. Supported in part by a grant from the Leukemia Research Fund of Toronto.
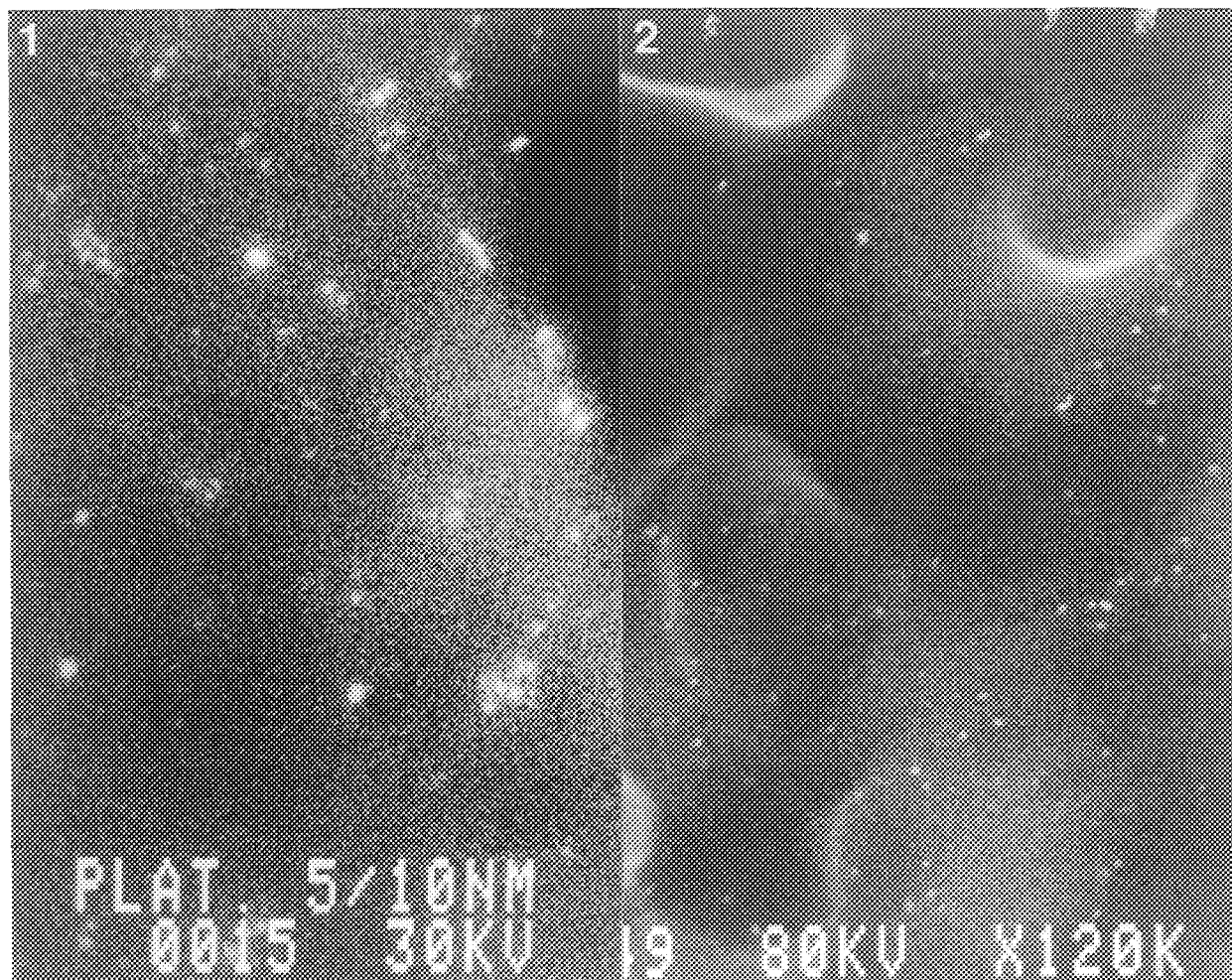
FIG. 1.--Backscattered electron imaging of the surface of a human platelet labeled for the gpIIb/IIIa glycoprotein using sequential labeling with 10 and with 5 nm immunogold markers. To distinct sizes of the gold particles can be clearly recognized.
FIG. 2.--Backscattered electron imaging of the surface of a human lymphocyte labeled with 5 nm gold markers for the presence of the CD3 antigen. The cell was lightly coated with carbon-platinum. The individual 5 nm markers are clearly recognized.

IMAGING OF DRUG COMPOUNDS USING ELECTRON MICROSCOPY, X-RAY MICROANALYSIS, AND ELECTRON DIFFRACTION

J. P. Neilly and M. F. Miller

Department of Cellular and Microscopic Research (45M)
Abbott Laboratories, One Abbott Park Road, Abbott Park, IL 60064

Solid drug delivery systems are becoming increasingly more complex and their development requires the precise control of materials used in their assembly and manufacture (1). Characteristics such as particle size distribution of powders, distribution of various components in tableted mixtures, thickness and continuity of particle or tablet coatings and drug crystallinity all affect the final performance of a drug in vivo. In this paper we describe the use of secondary and backscatter SEM (2), X-ray mapping with an SEM based energy dispersed X-ray spectrometer (EDXS) (2) and electron diffraction (3) to image and help understand the successfulness of a variety of formulation efforts.

Particle size distribution was assessed by mounting the particles either by blowing them onto double-stick tape or suspending them in a solvent followed by rapid air drying on a glass substrate, sputter coating with gold, photographing with the SEM and measuring with a sensitive image analysis system. The distribution of a drug in the matrix of time-release tablets was determined by cross-sectioning tablets, carbon-coating by vacuum evaporation and imaging in the backscatter mode. Distribution of drug on the surface of the tablet was also evaluated. Coated microparticles were cross-sectioned, sputter coated with gold and examined by SEM to measure coating thickness and evaluate continuity. Particles with multiple layers or unclear boundaries between core and coatings were mapped for unique elements by EDXS to visualize the coatings and determine if diffusion had occurred between layers. Finally, the crystallinity of drug compounds was determined by placing thin drug crystals on carbon filmed TEM grids and collecting electron diffraction patterns.

The results clearly demonstrate the utility of combined EM and spectrometry methods for understanding the structural characteristics of dry tablet materials. Backscatter images (Figure 1) clearly show the distribution of a drug and the non-soluble matrix in cross-section and on the surface of time-release tablets. This imaging mode serves to minimize the background topographical information which tends to interfere with evaluation of drug distribution. X-ray maps of coated microparticles (Figure 2) help to discern the boundaries of coatings when layers cannot be clearly seen in the corresponding SEM views. These maps permit evaluation of coating thickness and integrity and show if diffusion between layers has occurred. Electron diffraction patterns (Figure 3) may show the crystalline state of drug compounds as they change from the crystalline to an amorphous state which may help explain the compound's stability. We have found the morphological and spectral data obtained in the manner detailed herein to be useful in the characterization of formulations and for predicting their performance in patients.

References

1. R. Langer, Science, 249 (1990) 1527-1533.
2. J. I. Goldstein et al., Scanning Electron Microscopy and X-ray Microanalysis (1984) Plenum Press, NY.
3. S. W. Hui, J. Electron Micros. Tech., 11, (1989) 286-297.
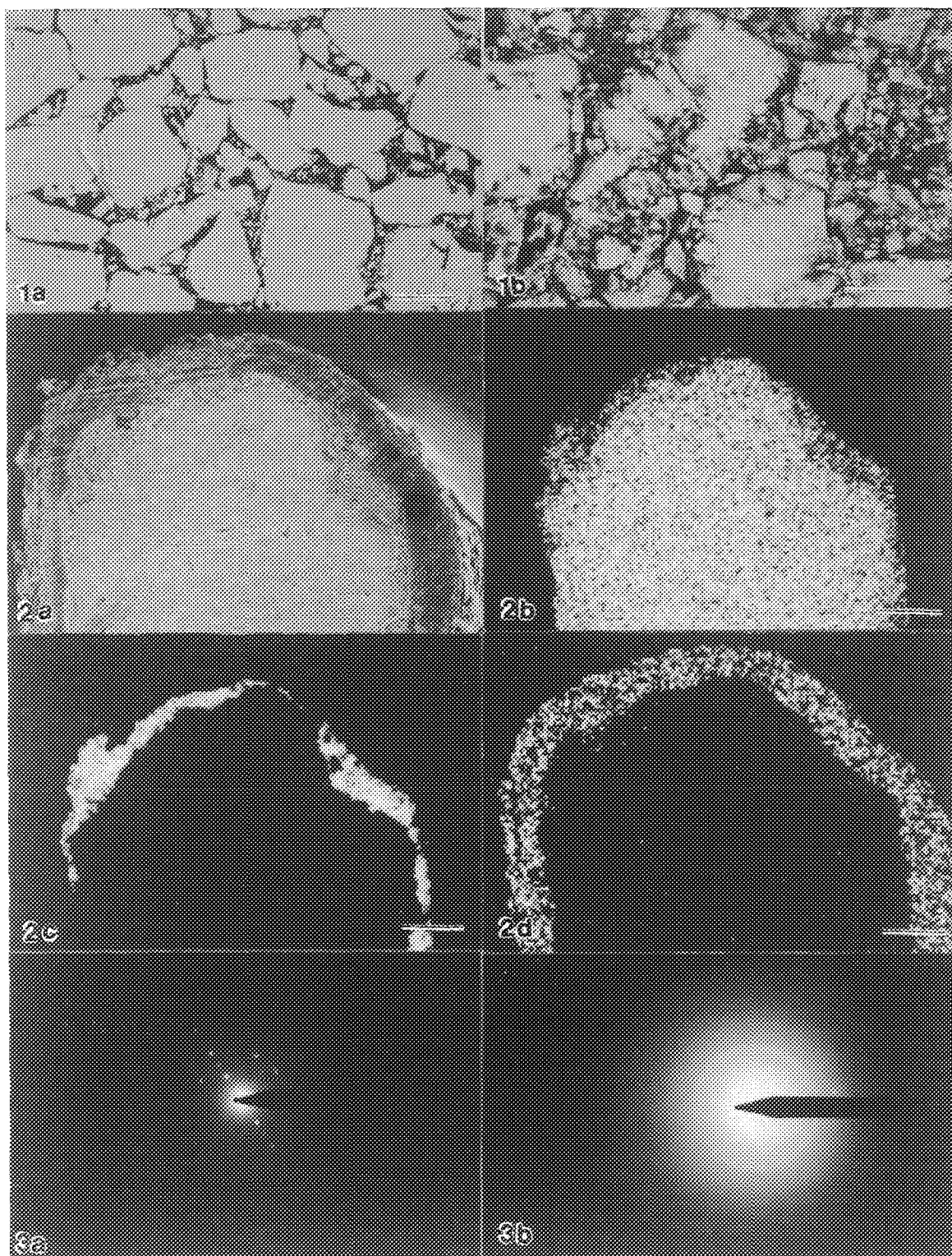
Fig. 1. Backscatter image of time-release tablet showing distribution of the drug and the non-soluble matrix in cross-section (a) and on tablet surface (b). Bar = 100 micron.

Fig. 2. SEM view and X-ray maps of a cross-sectioned, coated microparticle. a) Secondary electron image showing morphology of particle. b) Sodium map showing distribution of drug. c) Magnesium map showing distribution of outer layer. d) Silicon map showing distribution of inner layer. Bar = 100 micron.

Fig. 3. Diffraction patterns showing drug compound transforming from the crystalline (a) to amorphous (b) states.

MICROSCOPY STUDIES OF POWDERY MILDEW ON SUMMER SQUASH

John S. Gardner and W. M. Hess

Department of Botany and Range Science, Brigham Young University, Provo, UT 84602

Powdery mildews are characterized by the appearance of spots or patches of a white to grayish, powdery, mildewy growth on plant tissues, entire leaves or other organs[1]. Erysiphe cichoracearum, the powdery mildew of cucurbits is among the most serious parasites[2], and the most common[3]. The conidia are formed similar to the process described for Erysiphe graminis by Cole and Samson[4]. Theconidial chains mature basipetally from a short, conidiophore mother-cell at the base of the fertile hypha which arises holoblastically from the conidiophore. During early development it probably elongates by polar-tip growth like a vegetative hypha. A septum forms just above the conidiophore apex. Additional septa develop in acropetal succession[4]. However, the conidia of E. cichoracearum are more doliform than condia from E. graminis. The purpose of these investigations was to use scanning electron microscopy (SEM) to demonstrate the nature of hyphal growth and conidial formation of E. cichoracearum on field-grown squash leaves.

Infected, field grown, leaves were harvested during late September and were fixed in 2% glutaraldehyde 3% acrolein in 0.1 M sodium cacodylate buffer (pH 7.2-7.4) followed by dehydration in alcohol. After critical-point drying, samples were sputter coated with 15 nm of gold[5]. Photos were taken at 10-20 kV. Conidia had multiple germ tubes (Figs. 1-2), and hyphae grew in random patterns across the leaf surfaces (Figs. 2-5). Germ tubes and hyphae were not observed entering stomates and direct penetration sites with "halos" were not evident, as was observed with E. graminis on wheat (our unpublished observations). Penetration sites into leaves were not readily evident with SEM. Conidia formed characteristically for powdery mildews (Figs. 4-5), and the surface characteristics of conidia were readily evident (Fig. 6). These findings demonstrate the characteristics observable with SEM which can be compared when hyphal colonies are treated with various air pollutants.

References:

1. G.N. Agrios, Plant Pathology (1978), 250.
2. C.J. Alexopoulos and C.W. Mimms, Introductory Mycology (1979), 310.
3. J.C. Walker, Plant Pathology (1969), 356.
4. G.T. Cole and R.A. Samson, Patterns of Development in Conidial Fungi (1979), 105.
5. E.J Trione, W.M. Hess, and V.O. Stockwell, Can. J. Bot. (1989), 1671.
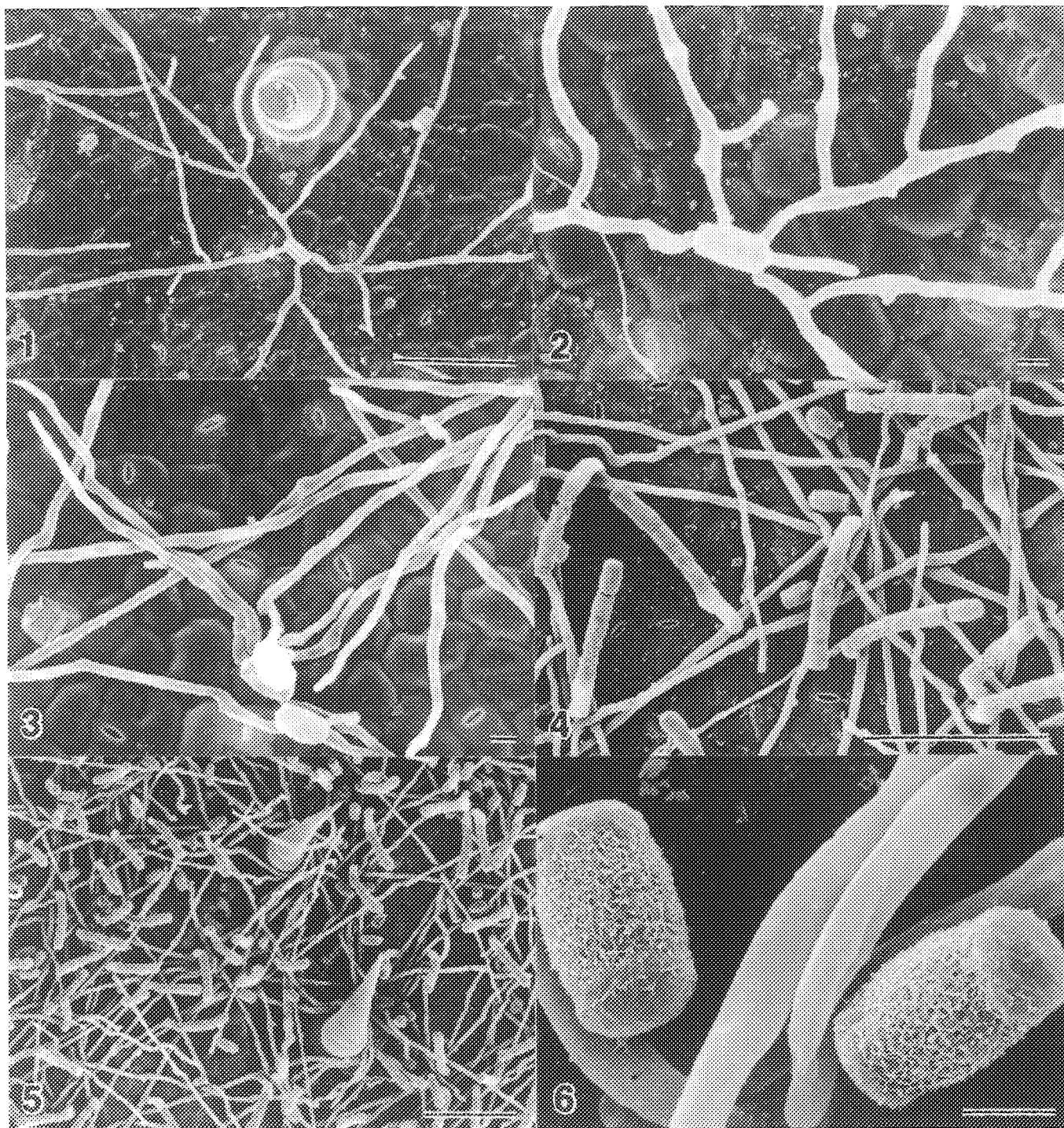
Figs. 1-6. Scanning electron micrographs of powdery mildew (Erysiphe cichoracearum) D.C. on bush squash (Cucurbita pepo L. var. melopepo (L.) Alef. Figs. 1-3. Germination and early hyphal growth. Bar = 100 μm, 10 μm, 10 μm. Figs. 4-6. Hyphal proliferation and conidial development. Bar = 100 μm, 100 μm, 10 μm

MICROSCOPY STUDIES OF FLOWER STRUCTURES

W. M. Hess, Carla A. Hess and John S. Gardner

Department of Botany and Range Science, Brigham Young University, Provo, UT 84602

The flowers of broad-leaved plants have four floral structures which differ significantly in shape from flower to flower. The sepals, petals, stigmas and pistils all have characteristic shapes and examples of all of them have been studied with scanning electron microscopy (SEM)[1,2]. The petals appear to be the most delicate of these structures and are therefore useful as indicators for senescence[3], as indicators for pollution effects or for developmental characteristics[4]. Petals of most flowers are stamens which have switched roles during evolution from sexual organ to agents which attract pollinators. Even though they appear to be smooth to the unaided eye, they have fine sculptured detail when observed with SEM. Adaxial surfaces of some petals have closely packed cells which project from the surface and often have fine ridges or points. The reason for this is unknown, but is likely related to the reflection of light from petals[2].

Floral structures were selected from plants grown in greenhouses and were fixed in 2% glutaraldehyde 3% acrolein in 0.1 M sodium cacodylate buffer (pH 7.2-7.4) followed by dehydration in alcohol and acetone. After critical-point drying, samples were sputter coated with gold. Photos were taken at 5-10 kV.

When visualized with SEM (Figs. 1-6) fine details of flower petals can be characterized. Other floral structures are also easily visualized[2]. Adaxial surfaces of petals appear to be the best indicators for environmental influences. The delicate closely-packed cells which project from the petal surfaces (Figs. 1,3,5) appear to be more vulnerable to environmental influences than the less delicate abaxial surfaces (Figs. 2,4,6). These findings demonstrate that although there are many fine details present on floral structures, the adaxial surfaces of some flower petals may be the most delicate cells and should serve as the best indicators for environmental influences.

References:

1. G. Shih and R. Kessel, Living Images, (1982), 62.
2. J. Burgess, M. Marten, and R. Taylor, Microcosmos, (1987), 78.
3. S.S. Han, A.H. Halevy, and M.S. Reid, J. Amer. Soc. Hort. Sci. (1991), 116, 68.
4. J.W. White, H. Chen, X. Zhang, D.J. Beattie, and H. Grossman, Hortscience (1990), 25, 294.
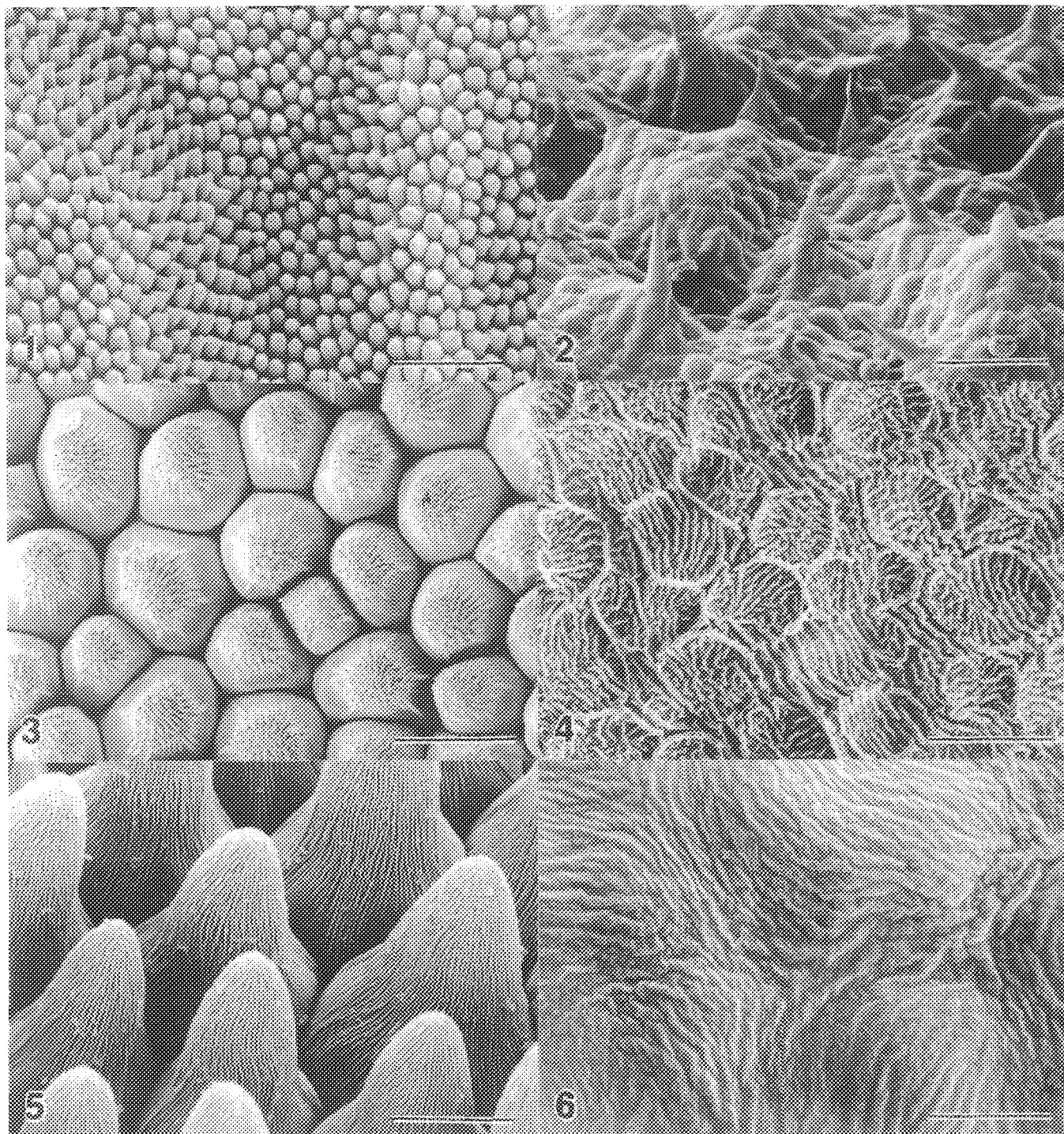
Figs. 1-6. Scanning electron micrographs of floral structures. Figs. 1-2. Lantana (Lantana camara L.) petal surfaces. Fig. 1. Adaxial surface. Fig. 2. Abaxial surface. Figs. 1-2, Bar = 100 µm. Figs. 3-4. Rose (Rosa gallica L.) petal surfaces. Fig. 3. Adaxial surface. Fig. 4. Abaxial surface. Figs. 3-4, Bar = 10 µm. Figs. 5-6. Snap dragon (Antirrhinum majus L.) petal surfaces. Fig. 5. Adaxial surface. Fig. 6. Abaxial surface. Figs. 5-6, Bar = 10 µm.

MONTE CARLO ELECTRON TRAJECTORY SIMULATION OF THE DEPTH SENSITIVITY OF ELECTRON BACKSCATTERING

D. E. Newbury and R. L. Myklebust

Microanalysis Research Group, Surface and Microanalysis Science Division, National Institute of Standards and Technology, Gaithersburg, MD 20899

Backscattered electrons provide one of the most important imaging signals in scanning electron microscopy, providing information on morphology (topographic contrast), composition (atomic number contrast), crystallography (electron channeling contrast), and magnetic microstructure (Type II magnetic contrast).[1] Because of the significant contribution to the generation of secondary electrons made by backscattered electrons while exiting through the specimen surface, even the "pure" secondary electron signal is influenced by the properties of backscattered electrons. Although a considerable base of experimental data exists on backscattered electrons, spatial characteristics of backscattered electrons signals are most easily examined by means of Monte Carlo electron trajectory simulation. In this study, we report on Monte Carlo calculations to show the effect of the sampling depth of backscattered electrons. This subject has been treated previously with Monte Carlo calculations as reported by Shimizu and Murata.[2,3] This study extends the previous work to the prediction of compositional contrast from buried layers.

Calculation Procedure

The NIST Microanalysis Monte Carlo simulation code used for these calculations has been previously described in detail.[4,5] In summary, this simulation makes use of the screened Rutherford cross section for elastic scattering, the Bethe expression for energy loss above 5 keV, and the Rao-Sahib and Wittry expression for energy loss below 5 keV. The step length of the calculation is based on the elastic scattering mean free path, so that the simulation is of the "single scattering" variety, with elastic scattering angles selected from the range 0°-180° based on the formation of Kyser and Murata.[6] The simulation has been tested extensively against a variety of experimental data.[4,5] For the calculations reported in this paper, at least 100 000 trajectories were calculated for each condition simulated. For low backscattering situations, such as is the case for carbon and aluminum, the calculation was increased to 200 000 trajectories to improve backscattering statistics.

To study the depth properties of backscattered electrons, the simulation code was modified to include a counter on each trajectory that records the maximum depth to which the electron penetrated. After each scattering step, the new value of the depth coordinate is compared with the depth coordinate from the previous step, and the counter is incremented when the new depth exceeds the old depth. If a trajectory ends in a backscattering event, the value of the maximum depth counter is recorded in an appropriate histogram. Note that this maximum depth is only rarely the depth of the last scattering event prior to backscattering. The maximum depth of backscattering is an important parameter because it indicates how deeply a feature (e.g., a chemical inhomogeneity) can reside below the surface and still influence the backscattered electron signal. Two different studies were performed: the depth distribution histogram for backscattering was calculated for pure elements, and the backscattering from a buried layer was simulated to calculate compositional contrast.

Depth Distribution Histogram for Backscattering

Figure 1 shows the escape depth histograms for carbon, aluminum, copper, silver, gold

TABLE 1.--Cumulative backscattering depth (E_0 = 20 keV; depths given in terms of D/R_{KO}).

Element	0° Tilt			45% Tilt		
	63%	90%	95%	63%	90%	95%
C	0.21	0.29	0.32	0.15	0.23	0.27
Al	0.18	0.26	0.28	0.13	0.21	0.24
Cu	0.14	0.22	0.24	0.10	0.19	0.22
Ag	0.12	0.19	0.22	0. 85	0.17	0.19
Au	0.10	0.17	0.19	0.075	0.15	0.17

for an incident beam energy of 20 keV and normal incidence (0° tilt). To compare the behavior for different elements, the depth axis of the plot has been normalized by the Kanaya-Okayama range (D/R_{KO}):

$$R_{KO} = 0.0276 \; A(E_0^{1.67}/Z^{0.889})\rho$$

where R_{KO} is the range (μm), A is the atomic weight, E_0 is the incident beam energy (keV), Z is the atomic number, and ρ is the density (g/cm^3).[7] The incremental backscattering from each layer of the histogram is normalized by the total backscatter coefficient. Two features are immediately obvious from Fig. 1. First, as the atomic number of the target increases from carbon to gold, the maximum sampling depth of the backscattered electrons, expressed as a function of the total range, decreases. Second, the position of the peak of the depth distribution also decreases as the atomic number increases.

From the histograms of Fig. 1, the cumulative normalized backscattering coefficient can be determined as a function of depth (Fig. 2). The normalized depths (D/R_{KO}) for specific percentages of the backscattering, e.g., 63% [which corresponds to the value 1 - (1/e)], 90%, and 95%, can be determined from these cumulative curves, as listed in Table 1.

Similar calculations were performed for a surface tilt of 45%. The effect of a tilted surface is to bring the backscatter distribution closer to the surface, as shown for aluminum in Fig. 3, where the backscatter depth distributions are compared for 0° and 45°. The cumulative backscattering plots are shown in Fig. 4, and the depths for various fractions of total backscattering for this condition of specimen tilt are also listed in Table 1.

Contrast from a Buried Layer

The contrast obtained from a layer buried beneath the surface can be readily calculated with the Monte Carlo simulation by appropriate adjustment of the boundary conditions appropriately. For this study, the scattering was calculated from a hypothetical specimen consisting of a layer of carbon, aluminum, copper, or silver over bulk gold. The thickness of the layer was adjusted to place the effect of the enhanced scattering from gold over a range of depth below the surface. The predicted compositional (atomic-number) contrast was calculated between the layered target and the pure element which constituted the layer: C = (ηXAu - ηX)/ηXAu (2) where ηXAu is the backscatter coefficient from the composite target of element X and Au and ηX is the backscatter coefficient from bulk element X. This hypothetical specimen mimics the practical situation that occurs when a two-phase structure is polished and the softer phase smears over the harder phase, burying it. Figure 5 shows the behavior of the contrast as a function of the thickness of the overlayer, where the thickness is listed in linear units. Where element X has a high atomic number, the contrast decreases very rapidly with depth; whereas for a low atomic number, significant contrast for the X-Au binary is preserved to depths exceeding 1 μm.

Discussion

The depth sensitivity of the backscattered electron signal depends strongly on the atomic number of the target, even when the depth is normalized by the range appropriate to each element. When using beam energy experiments to judge the depth of a feature below the surface, one must allow for the atomic-number effect on the depth sensitivity, since there is a 50% difference in behavior between low and high atomic

1

Backscattered Electron Maximum Penetration Depth

$E_0 = 20$ keV

Tilt $= 0°$

* × C
* + Al
* ◇ Cu
* + Ag
* ▣ Au

Vertical axis: $d\eta/d(D/R_{KO})$ — values 0, 0.01, 0.02, 0.03, 0.04, 0.05, 0.06, 0.07, 0.08

Horizontal axis: Depth/Range (Kanaya-Okayama) — 0, 0.1, 0.2, 0.3, 0.4, 0.5

Right axis: Cumulative Backscattering

4

Cumulative Backscattering

* ▣ C
* ◆ Al
* ▣ Cu
* ● Ag
* ▣ Au

$E = 20$ keV

Tilt $= 45$

Vertical axis: 0.0, 0.1, 0.2, 0.3, 0.4, 0.5, 0.6, 0.7, 0.8, 0.9, 1.0

Horizontal axis: Depth/Range (Kanaya-Okayama) — 0.0, 0.1, 0.2, 0.3, 0.4

2

Cumulative Backscattering

Vertical axis: Integrated Backscatter Coefficient (norm) — 0.0, 0.2, 0.4, 0.6, 0.8, 1.0

* ▣ C
* ● Al
* ▣ Cu
* ● Ag
* ▣ Au

$E = 20$ keV

Tilt $= 0$

Horizontal axis: Depth/Range(Kanaya-Okayama) — 0.0, 0.1, 0.2, 0.3, 0.4, 0.5

5

Contrast vs Overlayer Thickness, 20 kV

Vertical axis: Contrast, % — 0, 20, 40, 60, 80, 100

* ▢ C vs Au
* ◆ Al vs Au
* ▲ Cu vs Au
* ✳ Ag vs Au

Horizontal axis: Overlayer Thickness (µm) — 0, 0.5, 1, 1.5, 2

3

Aluminum, $E_0 = 20$ keV

Vertical axis: $d\eta/d(D/R_{KO})$ — 0, 0.01, 0.02, 0.03, 0.04, 0.05, 0.06

* ✳ Al 0 tilt
* ◆ Al 45 tilt

Horizontal axis: Depth/Range (Kanaya-Okayama) — 0, 0.1, 0.2, 0.3, 0.4, 0.5

FIG. 1.--Histograms of the maximum depth of penetration of backscattered electrons for carbon, aluminum, copper, silver, and gold. $E_0 = 20$ keV; tilt = 0°. Vertical axis is normalized backscattering coefficient, depth axis is normalized by Kanaya-Okayama range for each element.

FIG. 2.--Cumulative normalized backscattering coefficient as a function of depth, obtained by summing of curves plotted in Fig. 1. $E_0 = 20$ keV; tilt = 0°. Depth axis is normalized by Kanaya-Okayama range for each element.

FIG. 3.--Comparison of histograms of maximum depth of penetration of backscattered electrons for aluminum target at 0° and 45° tilt; $E_0 = 20$ keV.

Fig. 4.--Cumulative normalized backscattering coefficient as a function of depth, $E_0 = 20$ keV; tilt = 45°. Depth axis is normalized by Kanaya-Okayama range for each element.

FIG. 5.--Atomic-number contrast for binary pair X-Au as a function of thickness of an overlayer of element X on gold. $E_0 = 20$ keV; tilt = 0°.

number of the layer material. Monte Carlo calculations can be used to develop an analytic expression for the depth sensitivity of backscattering as a function of beam energy, atomic number, and tilt.

References

1. J. I. Goldstein et al., *Scanning Electron Microscopy and X-ray Microanalysis*, New York: Plenum, 1981, 75-87.
2. R. Shimizu and K. Murata, *J. Appl. Phys.* 42: 387, 1971.
3. K. Murata, *J. Appl. Phys.* 45: 4110, 1974.
4. D. E. Newbury and R. L. Myklebust, *Analytical Electron Microscopy--1981*, 91.
5. D. E. Newbury and R. K. Myklebust, in *Electron Beam Interactions with Solids*, Chicago: SEM, Inc., 1984, 153.
6. D. F. Kyser and K. Murata, *IBM J. Res. Dev.* 18: 352, 1974.
7. K. Kanaya and S. Okayama, *J. Phys.* D5: 43, 1972.

HIGH-RESOLUTION/LOW-VOLTAGE SEM OF POLYMERS

J. H. Butler

Exxon Chemical Co., Baytown Polymers Center, Box 5200, Baytown, TX 77522

Polymers are notorious for the resistance they offer to examination by conventional electron microscopy methods, which are limited in their ability to address fine surface details or to determine the bulk microstructure of multicomponent polymeric materials. Polymeric materials are generally susceptible to beam-induced radiation damage and, as nonconductors, they charge heavily under the scanning electron microscope (SEM) beam. The charging may be overcome and image resolution increased with the use of a transmission electron microscope (TEM), but that increases the potential for beam damage and forces inordinately large amounts of laboratory resources to be concentrated on the generation of undeformed ultrathin samples. Moreover, the TEM ability to image surface morphology is nonexistent without equally demanding sample preparation (i.e., replication) efforts. An extremely efficient alternative to the TEM for the analysis of polymers is the field-emission gun (FEG) source, ultrahigh-resolution, low-voltage scanning electron microscope (LVSEM). LVSEMs minimize all the above-mentioned problems, and they rival TEMs for image resolution. The high brightness produced by the FEG allows the electron probe to be focused down to nanometer dimensions, yet still retain enough intensity to produce usable signal intensities at extremely low accelerating voltages (nominally 1-2 kV). This feature affords three major advantages: (1) higher resolution, (2) negligible beam damage of samples, and (3) absence of the need for coating samples with conducting films to eliminate charging under the beam. This is a double advantage for high resolution, because at high magnifications one wants information about the "neat" surface, not the detailed morphology of the coating.

Resolution and Contrast

At conventional (∿30 keV) accelerating potentials the SEM beam/sample interaction volume in carbonaceous materials is ∿10 μm in diameter. In this situation, secondary (inelastically scattered) electrons emerge from a shallower, more localized region than the (elastically) backscattered electrons, and consequently provide better image resolution.

The secondary image resolution so obtained is effectively equal to the diameter of the incident electron probe, which in turn depends strongly on the brightness of the electron source and on the accelerating potential. Thus, the highest resolution available in commercial SEMs (equipped with a LaB_6 tip and running at 30 keV) has been about 50 Å. On the other hand, the new FEG/LVSEMs can produce extremely finely focused (∿25Å) probes at very low (1-2keV) energies and can do even better (<10 Å) at higher (>10keV) energies.

In a carbonaceous material the secondaries escape from a depth of ∿200 Å regardless of the incident beam energy. Thus, the only way to improve SEI resolution is to use such a low accelerating voltage E_0 that the interaction teardrop dimensions are less than this 200Å escape depth. This effect is prominent when features of interest in the surface topography are of the same (or smaller) size as the interaction volume. In this situation surface features can be "washed out" because of beam penetration through the structure.

At low voltages the secondary-electron yield increases; thus, SEI contrast can be generated as a result of compositional differences in the sample, as well as from

surface topography (which is the only contrast-producing mechanism available at conventional SEM voltages). This advantage has been illustrated for the case of various polymer blends.[1] The differences in secondary emission of the various phases in these blends depends on a combination of factors, such as the nature of the molecular bonds, the elements present, amorphous/crystalline nature of each phase, etc. Mismatch in properties such as viscosity and ductility of various polymers in the blends shows up as topographical contrast. The great advantage here, of course, is there is no need for heavy atom staining in order to generate compositional contrast in SEIs of multicomponent polymeric materials.

Damage and Charging of Samples

Since most of the energy in the incident electron prove is lost by conversion into heat at the irradiation point, conventional accelerating voltages may cause deterioration, decomposition, sublimation deformation, and cracking of the sample. Although it has never been quantified for polymers, sample damage becomes very small at 2 keV and below. Thus, one can increase the overall electron dose to several hundred times that used at conventional voltages. Residual change buildup can also cause damage and distortion of detailed features.

One of the biggest problems with SEM of polymers at conventional voltages is their great propensity to accumulate negative charge and consequently to reject the incident probe in successive scans. This situation obviously exists because the electrons that impinge on the sample surface do not drain away faster that they are supplied by an intense high-energy probe. The physical attribute of conductivity allows accumulated charge to be dispensed in metals and some semiconductor samples, but is not an advantage enjoyed by polymers and other nonconductors. However, conductivity is not the only way in which materials disperse accumulated charge from an incident probe; they also emit secondary (SE) and backscattered (BS) electrons. At very low accelerating voltages, the fact that the SE escape depth is of the same order as the incident electron penetration depth can be used to eliminate the buildup of surface electron charge. At some given accelerating beam energy E2 the sum of the secondary and the backscattered currents equals that of the incident beam. Under these conditions charge is neither injected into nor extracted from the sample, and it is possible to image nonconducting materials without coating them with metal.

Electron Emission in the LVSEM

Whenever an electron beam of energy E_0 irradiates matter, various types of electrons (secondaries, backscattered, Auger, etc.) are emitted from the surface of the target. The electrons can be classified according to their energy E as belonging to one of two groups: (1) E < 50 eV, secondary electrons; and (2) 50 eV < E < E_0, backscattered (reflected) electrons.[2]

If we define the secondary electron yield δ as the number of secondary electrons emitted per incident electron and by analogy, the backscattered electron yield η as the number of backscattered electrons emitted per incident electron, then (since Kirchhoff's law must apply to this situation) we have the condition

$$I_B = \delta I_B + \eta I_B = I_{SC} \tag{1}$$

where I_B is the beam current and I_{SC} is the current flowing to or from ground to the specimen. If the specimen is not an electrical conductor, I_{SC} is zero and consequently a charge imbalance is generated in the sample of magnitude

$$I_B[1 - (\delta + \eta)] \tag{2}$$

For a polymer irradiated with a beam energy of a few thousand electron volts, $(\delta + \eta)$ < 1, so that the charge accumulates in the sample, which therefore acquires a negative potential; and since the electron source is negative with respect to ground,

the effective potential energy of the beam is reduced.

If the initial incident energy is high enough so that $(\delta + \eta) < 1$, then under constant irradiation the sample will continue to charge negatively until the effective landing energy of the electrons is such that $(\delta + \eta) = 1$ (Fig. 1). At this energy, usually referred to as E2, the sample is in a dynamic charge balance condition. If the initial energy is below E2, the sample will charge positively and re-collect secondary electrons until the effective energy once again becomes E2. Thus, E2 is clearly the single most important parameter describing the charge-up behavior of a polymer.

If the processes of secondary and backscattered electron emission from a polymer can be modeled in enough detail, the value of E2 (as well as of other parameters of interest) could be computed. Since η is typically one-tenth of δ, essentially all theories proposed so far ignore the direct contribution of backscattered electrons to the total emission current. However, the task of deterministically modeling secondary-electron emission is monumental. Thus, the traditional methods are all empirical (or at least semi-empirical) in nature.

Secondary-electron emission is a complex phenomenon that involves (1) SE production via interactions between energetic electrons and a solid; (2) secondary electron transport to the sample surface; and (3) emission of secondaries over the surface potential barrier. Electrons of different E have different escape depths.

There are four basic types of electron-solid interactions: core electron excitation, phonon excitations, valence excitation of single electrons (interband and intraband quantum state transitions), and plasmon excitations (collective excitations of valence electrons via energy coupling to the volume plasma oscillation of the electron gas within a solid). Of these interactions, only the last two play significant roles at low incident beam energies. Thus, our formulation adopts a semi-empirical approach that only considers the sample's constituent elements--the molecular bonds and the density.

The simple "generic" model for secondary emission was proposed originally by Salow[3] and independently in a modified form by Bethe,[4] and was developed, among others, by Dekker.[5] According to these authors, if R is the penetration depth of an incident electron into the sample, ε is the averaging energy required to generate a secondary electron, and λ is the electron's average mean free path length, the integrated value for secondary electron production is:

$$\delta = - \frac{0.5}{\varepsilon} \int_{0}^{R} \frac{dE}{dS} \exp(-S/\lambda) \, dS \tag{3}$$

where S is the path distance measured along the electron trajectory.

If we now make the simplifying assumptions that the electron travels in a straight line (i.e., ignore backscattering), and that the instantaneous stopping power dE/dS is constant and equal to the incident energy divided by the range, we have a closed expression for secondary electron production.

$$\delta = \frac{0.5E\lambda}{\varepsilon R} [1 - \exp(-R/\lambda)] \tag{4}$$

It is readily shown that the maximum secondary yield δ_m occurs when the beam range is about 2.3λ. If the nergy at which the yield reaches the maximum δ_m is E_m, a "universal" yield curve expression can be derived from Eq. (4) that contains only the quantities E, E_m, δ, and δ_m:

$$\frac{\delta}{\delta_m} = 1.11(E/E_m)^{-0.35}\{1 - \exp[-2.3(E/E_m)^{1.35}]\} \tag{5}$$

FIG. 4.--Surface modified polyethylene film: (a) uncoated SEI at 2 keV in FEG/LVSEM; (b) sputter coated (20 nm Au/Pd) in LaB_6 SEM at 30 keV.

FIG. 1.-- $(\delta + \eta)$ for carbon as a function of incident beam energy E_0.

FIG. 2.--"Universal" yield curve for secondary electron emission.

FIG. 3.--Experimental and theoretical E2 data vs ratio of valence electrons to monomeric molecular weight.

Equation (6) has the general graphical form shown in Fig. 2 and like all rate equations can be cast into the form

$$\delta = KE^{-\eta} \tag{6}$$

By fitting measured values for a number of polymers, Burke[6] was able to obtain

$$\delta = KE^{-0.725} \tag{7}$$

K can be written any number of ways; one approach Burke took was to equate the asymptotic energy variation of the yield to an empirical expression involving the number of valence electrons VE and molecular weight MW per monomeric unit:

$$K = 10.64(VE/MW) - 3.15 \tag{8}$$

By use of this quantity, together with values of δ_m and E_m derived from a variety of measurements, Burke's formula can then be used to compute E2 values from a wide range of polymers.

Table 1 lists measured and computed E2 values (in keV) for many commercially available polymers. The values range from a minimum of 0.9 to a maximum of 1.6 keV. All the values were taken at room temperature and are the averaged result of four measurements.

Figure 3 is a plot of these data points as a function of the ratio VE/MW of the constituent monometric units. We see that Burke's equations produce values for E2 which, when plotted against the ratio VE/MW, approximate a lower bound for the experimental data. Although other variants of Eq. (8) produce somewhat different estimates for E2, they all usually lie on the low side of the experimental data.

Although it cannot be claimed that Burke's equations have any predictive value, they do at least suggest that VE/MW is a significant index for E2. Since the "model" involved is a very simplistic one, it is probable that a more detailed analysis might yield a more useful relation. For example, recent work by Kishimoto et al., suggests that the π-electron fraction (i.e., the ratio of π-bonds to σ-bonds in the monomeric unit) also appears to be a meaningful index.[7]

Compositional vs Topographical Contrast

The previous section was chiefly concerned with obtaining and understanding secondary-electron contrast produced as a result of differences in chemical composition within the context of low voltage SEM, which can be operated within the realm of E2 for most materials. Similarly, none of the discussion is relevant in terms of conventional SEM, which is capable of producing only topographical contrast in the secondary-electron imaging mode. Unfortunately, the converse situation (LVSEM in which there is no topographical contrast) never exists; some degree of topographical contrast is always superposed on the compositional contrast in the final stage.

It would then appear that, by ignoring the effects of topographical contrast, we have oversimplified the situation; and for the purpose of secondary-electron imaging, that is so. However, the high topographical resolution attainable in the LVSEM can be advantageous in its own right. For example, if the surface of the sample is rough on a scale comparable to the escape depth for secondary-electron emission (5-15 nm), we might expect that E2 would be much different from what it is for the same material with an atomically smooth surface. Thus an E2 profile may be a useful tool for the characterization of polymer surfaces.

Figure 4 provides high-resolution observations of an undamaged, uncoated polyethylene (PE) film with a highly modified (electrically treated) surface. This sample exhibits a 25-50Å "microstructure," as shown in Fig. 4(a) (taken at 2 keV incident beam

TABLE 1.--Experimental and theoretical second crossover energies (E2) for polymers in keV.

Polymer	Measured E2	Burke's E2	VE	MW
Polysulfone 3703	1.1	0.61	160	442
PBT Celenex 2002	1.1	0.84	83	219
ABS 901 Magnum	1.1	0.98	82	211
HIPS Styron (Polystyrene)	1.3	0.92	40	104
Nylon 6	1.2	1.18	45	112
PET Traytuf 7200	0.9	0.72	70	189
Polyethylene 8054 N	1.5	1.61	18	42
ABS	1.3	0.98	82	211
EVOH	1.4	1.15	28	70
High Density Polyethylene	1.5	1.61	18	42
Isotactic Polypropylene	1.4	1.61	18	42
Kraton 1107	1.5	0.91	38	99
Low Density Polyethylene	1.5	1.61	18	42
Poly(ethylene-co-vinyl acetate)	1.3	1.04	44	112
Poly(ethylene-co-acrylic acid)	1.2	1.06	39	99
Poly(butadiol 1,4-terepthalate)	1.5	0.88	84	220
Poly(caprolactone)	1.4	1.20	46	114
Poly(carbonate)	1.3	0.83	96	254
Poly(styrene)	0.9	0.92	40	104
Poly(styrene-acrylonitrile)	0.9	0.60	56	155
Poly(ethylene terepthalate)	0.9	0.72	70	189
Poly(ethylene-co-propylene)	1.2	1.33	28	68
Nylon 6/Nylon 66 copolymer	1.2	1.23	137	338
EVOH Soranol D 2908	1.3	1.15	28	70
PMMA	1.6	1.87	40	90
Kraton 1901x	1.4	0.91	38	99

energy). Direct observation of this microtexturing can provide important information about the way functionalized polyolefin films work in the adhesion of inks and paints[6]; due to lower resolution and other problems in the past, workers have not detected texutring of treated polymer surfaces.

For comparison, Fig. 4(b) shows the same material at the same magnification as seen in an LaB$_6$-equipped SEM. The microtexturing is not visible here for one or both of two reasons. The LaB$_6$ instrument must operate at 30 keV to yield equivalent resolution of the FEG/LVSEM at 2 keV, so that the sample has experienced beam damage. Also, operation at 30 keV requires the specimen to be coated to prevent charging under the beam; thus Fig. 4(b) is basically a micrograph of the Au-Pd coating.

Applications

The physical properties of any semicrystalline polymer product are ultimately determined by the relative degree and arrangement of the amorphous and crystalline fractions. One way to assess this microstructure is directly to observe the lamellar
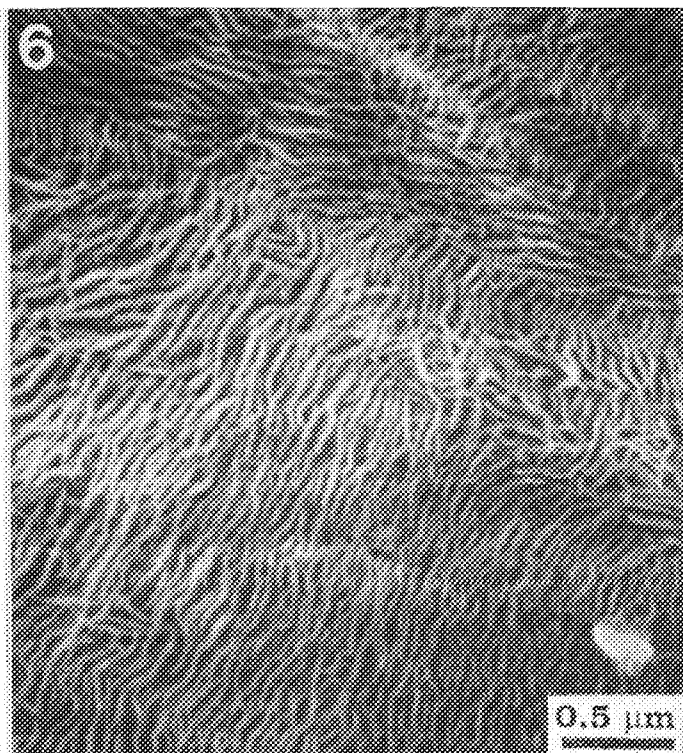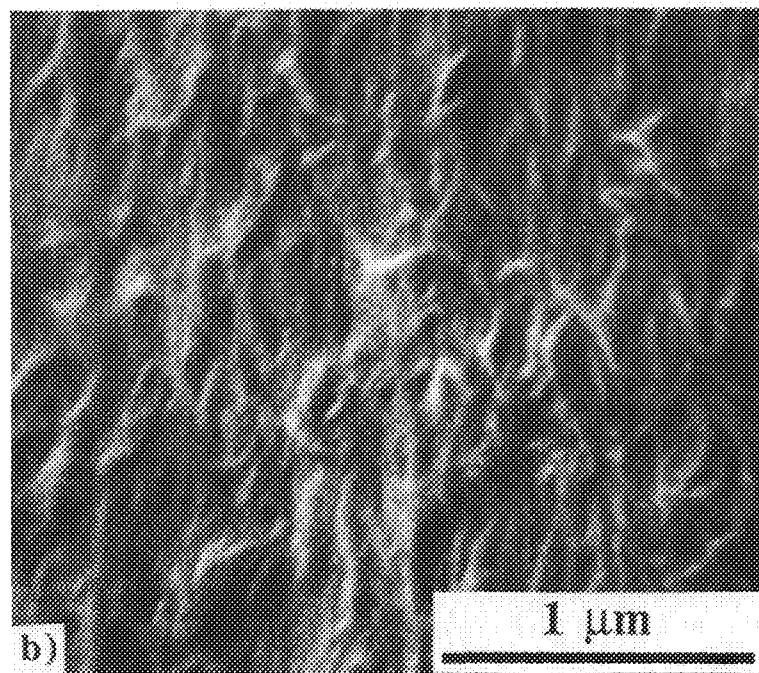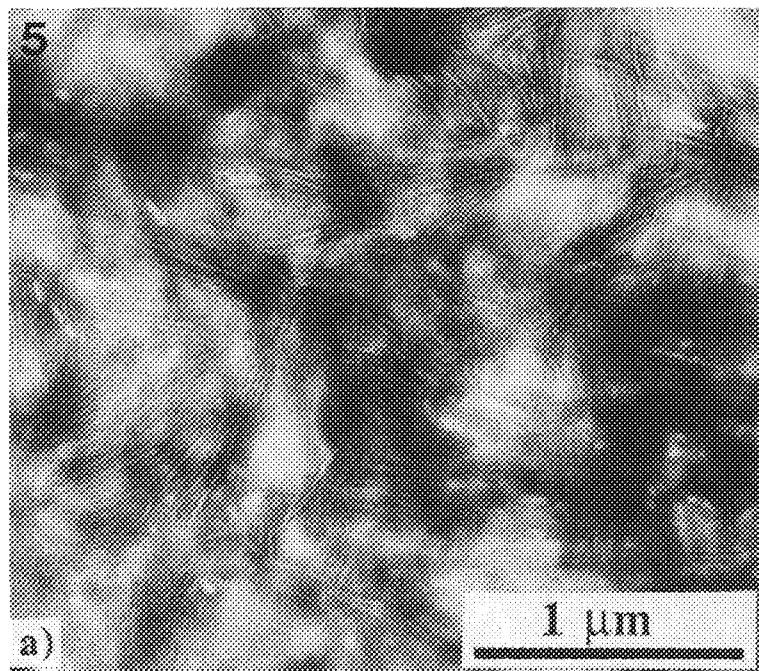
FIG. 6.--Lamellar bundles in an *un-coated, unstained,* and *unsectioned* biaxially oriented PE film surface.

FIG. 5.--Lamellar imaging in polyethylene: (a) high-density PE, OsO_4 stained and cryosectioned in TEM at 35 000×; (b) unprepared, low-density PE film surface at 40 000× in LVSEM.

bundles of crystallites: their relationship to each other and to the amorphous phase. Conventionally this assessment is done by TEM, with the use of heavy metal oxidative stains (such as RuO_4) to promote the amplitude contrast contribution from the amorphous phase.[9]

Figure 5(a) is a TEM micrograph of high-density PE which has been OsO_4 stained and thin sectioned at cryogenic temperatures. The thin (∿300 Å) crystalline lamellae are readily visible. However, the nature of these experiments is not conducive to side-scale experimentation; in any typical case, the required sample preparation time alone can be prohibitive.

Lamellar imaging with the LVSEM is a simple and straightforward application of purely topographical contrast of a microtextured surface: Fig. 5(b) shows lamellar (<500 Å)

571

FIG. 7.--Cross section of failed
LLDPE heat seal: (a) region of
termination of seal failure; (b)
close-up of area containing drawn
polymer (i.e., "microcraze" region).
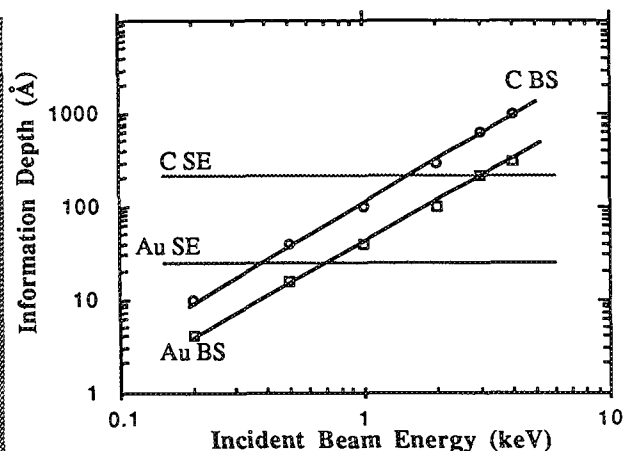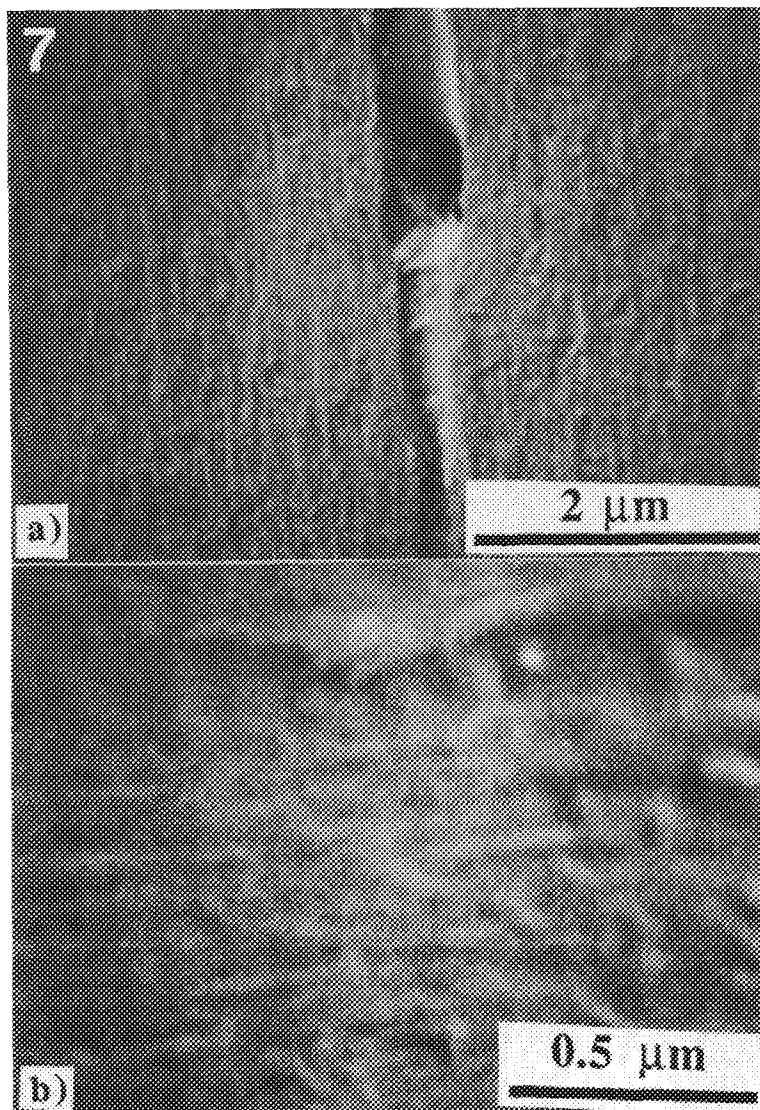
FIG. 8.--Variation of information
depth in backscatter (BS) and sec-
ondary electron (SE) imaging modes
for carbon and gold as a function
of incident beam energy.

detail of an uncoated, unstained and unsectioned low-density PE film surface. A more
dramatic example of LVSEM imaging of lamellar bundles is provided in Fig. 6, which
shows the relative ordering of the lamellae in a film that has been biaxially ori-
ented. Here the effects of stress induced crystallization on the microstructure are
obvious.

Interfaces between heat-sealed surfaces present a special problem for characteriza-
tion. We examined one sample of heat-sealed (linear low-density) PE by cryosection-
ing through a failed portion of the seal and examining this region in cross section.
Figure 7(a) shows the termination region of the failed seal. The failed interface
region extends over a micron into the intact seal and region and terminates in a thin
(<500Å) bright line. Preceding this thin line is a region (∿0.75 µm long) that con-
tains a considerable amount of polymer that has been "drawn" perpendicular to the
direction of the seal. This region is shown at high magnification (60 000×) in Fig.
7(b), where lamellar sized (<500 Å thick) vertical striations are readily observable.
This type of failure is very similar in appearance to the conventional brittle fail-
ure mechanism, in which a microsize (region of vertically drawn polymer) develops
into a propagating crack tip.

Backscattered to the Future

As opposed to secondary-electron images, backscattered images always improve in resolution as E_0 decreases.[10] As can be seen from Fig. 8, at energies below about 1.5 keV the VS depth of information becomes comparable to, and ultimately less than, the SE value. Thus, it will be BSIs that will carry the most useful surface detail at low incident-beam energies. Also, the intensity of BS emission is directly proportional to the specimen atomic number Z; thus the contrast obtained in BSIs is strongly compositional in origin.

Unfortunately, the decrease in BS emission as a function of accelerating voltage (coupled with the low Z = 12 for C) brings the BS signal intensity for polymeric materials below the detectable level of conventional BS detectors; the high resolution theoretically attainable in BSIs remained to be demonstrated. However, there is a new type of BS detector based on microchannel-plate technology that is sensitive to slight variations in very low BS signal intensities; it appears to be just a matter of time until these detectors are incorporated into LVSEM systems.

Summary

It has been repeatedly demonstrated that an LVSEM equipped with a FEG source can produce topographical contrast secondary-electron images of polymers at substantially higher magnifications than a conventional SEM, and with a resolution that rivals TEM. This is straightforward in operation; however, the capability of producing contrast based on differences in chemical composition within the sample is an added advantage not available in any conventional SEM. The ability to produce quality images at low accelerating beam voltages minimizes beam damage to the sample, and affords an operating window (e.g., E2) where the sample does not build up negative charge and thereby obviates the normal requirement to coat samples with a conductive layer.

References

1. V. K. Berry, *Scanning* 10: 19, 1988.
2. H. Seiler, "Secondary electron emission," in D. F. Kyser et al., Eds., *Electron Beam Interactions with Solids* (Proc. 1st Pfefferkorn Conf., Monterey, Calif.) O'Hare, Ill.: Scanning Electron Microscopy, 1982, 34.
3. H. Salow, *Physik. Zeitschr.* 41: 434, 1940.
4. H. Bethe, *Phys. Rev.* 59: 940, 1941.
5. A. J. Dekker, *Sol. State Phys.* 6: 251, 1958.
6. E. A. Burke, *IEEE Trans.* NS-27: 1760, 1980.
7. Y. Kishimoto, T. Oshima, M. Hashimoto, and T. Hayashi, *J. Appl. Polym. Sci.* 39: 2055, 1990.
8. D. M. Brewis and D. Briggs, *Polymer* 22: 7, 1981.
9. H. Sano, T. Usami, and H. Naiagawa, *Polymer* 27: 1497, 1986.
10. D. C. Joy, "Low voltage scanning electron microscopy," *EMAG 87*, Inst. Phys. Conf. Ser. No. 90, Manchester, 1987, 177.

AUTHOR INDEX

Notes

Notes